Lecture Notes in Electrical Engineering 390

Jiadong Sun
Jingnan Liu
Shiwei Fan
Feixue Wang
Editors

China Satellite Navigation Conference (CSNC) 2016 Proceedings: Volume III

Springer

Lecture Notes in Electrical Engineering

Volume 390

Board of Series editors

Leopoldo Angrisani, Napoli, Italy
Marco Arteaga, Coyoacán, México
Samarjit Chakraborty, München, Germany
Jiming Chen, Hangzhou, P.R. China
Tan Kay Chen, Singapore, Singapore
Rüdiger Dillmann, Karlsruhe, Germany
Haibin Duan, Beijing, China
Gianluigi Ferrari, Parma, Italy
Manuel Ferre, Madrid, Spain
Sandra Hirche, München, Germany
Faryar Jabbari, Irvine, USA
Janusz Kacprzyk, Warsaw, Poland
Alaa Khamis, New Cairo City, Egypt
Torsten Kroeger, Stanford, USA
Tan Cher Ming, Singapore, Singapore
Wolfgang Minker, Ulm, Germany
Pradeep Misra, Dayton, USA
Sebastian Möller, Berlin, Germany
Subhas Mukhopadyay, Palmerston, New Zealand
Cun-Zheng Ning, Tempe, USA
Toyoaki Nishida, Sakyo-ku, Japan
Bijaya Ketan Panigrahi, New Delhi, India
Federica Pascucci, Roma, Italy
Tariq Samad, Minneapolis, USA
Gan Woon Seng, Nanyang Avenue, Singapore
Germano Veiga, Porto, Portugal
Haitao Wu, Beijing, China
Junjie James Zhang, Charlotte, USA

About this Series

"Lecture Notes in Electrical Engineering (LNEE)" is a book series which reports the latest research and developments in Electrical Engineering, namely:

- Communication, Networks, and Information Theory
- Computer Engineering
- Signal, Image, Speech and Information Processing
- Circuits and Systems
- Bioengineering

LNEE publishes authored monographs and contributed volumes which present cutting edge research information as well as new perspectives on classical fields, while maintaining Springer's high standards of academic excellence. Also considered for publication are lecture materials, proceedings, and other related materials of exceptionally high quality and interest. The subject matter should be original and timely, reporting the latest research and developments in all areas of electrical engineering.

The audience for the books in LNEE consists of advanced level students, researchers, and industry professionals working at the forefront of their fields. Much like Springer's other Lecture Notes series, LNEE will be distributed through Springer's print and electronic publishing channels.

More information about this series at http://www.springer.com/series/7818

Jiadong Sun · Jingnan Liu
Shiwei Fan · Feixue Wang
Editors

China Satellite Navigation Conference (CSNC) 2016 Proceedings: Volume III

Springer

Editors
Jiadong Sun
Chinese Academy of Sciences
China Aerospace Science and Technology Corporation
Beijing
China

Jingnan Liu
Wuhan University
Wuhan
China

Shiwei Fan
China Satellite Navigation Office
Beijing
China

Feixue Wang
National University of Defense Technology
Changsha
China

ISSN 1876-1100 ISSN 1876-1119 (electronic)
Lecture Notes in Electrical Engineering
ISBN 978-981-10-0939-6 ISBN 978-981-10-0940-2 (eBook)
DOI 10.1007/978-981-10-0940-2

Library of Congress Control Number: 2016937343

© Springer Science+Business Media Singapore 2016
This work is subject to copyright. All rights are reserved by the Publisher, whether the whole or part of the material is concerned, specifically the rights of translation, reprinting, reuse of illustrations, recitation, broadcasting, reproduction on microfilms or in any other physical way, and transmission or information storage and retrieval, electronic adaptation, computer software, or by similar or dissimilar methodology now known or hereafter developed.
The use of general descriptive names, registered names, trademarks, service marks, etc. in this publication does not imply, even in the absence of a specific statement, that such names are exempt from the relevant protective laws and regulations and therefore free for general use.
The publisher, the authors and the editors are safe to assume that the advice and information in this book are believed to be true and accurate at the date of publication. Neither the publisher nor the authors or the editors give a warranty, express or implied, with respect to the material contained herein or for any errors or omissions that may have been made.

Printed on acid-free paper

This Springer imprint is published by Springer Nature
The registered company is Springer Science+Business Media Singapore Pte Ltd.

Preface

BeiDou Navigation Satellite System (BDS) is China's global navigation satellite system which has been developed independently. BDS is similar in principle to global positioning system (GPS) and compatible with other global satellite navigation systems (GNSS) worldwide. The BDS will provide highly reliable and precise positioning, navigation and timing (PNT) services as well as short-message communication for all users under all-weather, all-time, and worldwide conditions.

China Satellite Navigation Conference (CSNC) is an open platform for academic exchanges in the field of satellite navigation. It aims to encourage technological innovation, accelerate GNSS engineering, and boost the development of the satellite navigation industry in China and in the world.

The 7th China Satellite Navigation Conference (CSNC2016) is held during May 18–20, 2016, Changsha, China. The theme of CSNC2016 is Smart Sensing, Smart Perception, including technical seminars, academic exchanges, forums, exhibitions, and lectures. The main topics are as follows:

S1 BDS/GNSS Application Technology
S2 Navigation and Location Based Services
S3 Satellite Navigation Signals
S4 Satellite Orbit and Clock Offset Determination
S5 BDS/GNSS Precise Positioning Technology
S6 Atomic Clock and Time-frequency Technology
S7 BDS/GNSS Augmentation Systems and Technology
S8 BDS/GNSS Test and Assessment Technology
S9 BDS/GNSS User Terminal Technology
S10 Multi-sensor Fusion Navigation
S11 PNT System and Emerging Navigation Technology
S12 Standardization, Intellectual Properties, Policies, and Regulations

The proceedings (Lecture Notes in Electrical Engineering) have 176 papers in ten topics of the conference, which were selected through a strict peer-review process from 440 papers presented at CSNC2016. In addition, another 193 papers

were selected as the electronic proceedings of CSNC2016, which are also indexed by "China Proceedings of Conferences Full-text Database (CPCD)" of CNKI and Wan Fang Data.

We thank the contribution of each author and extend our gratitude to 237 referees and 48 session chairmen who are listed as members of editorial board. The assistance of CNSC2016's organizing committees and the Springer editorial office is highly appreciated.

The 7th China Satellite Navigation Conference (CSNC 2016) Committees

Scientific Committee

Chairman
Jiadong Sun, China Aerospace Science and Technology Corporation

Vice-Chairman
Rongjun Shen, China
Jisheng Li, China
Qisheng Sui, China
Changfei Yang, China
Zuhong Li, China Academy of Space Technology
Shusen Tan, Beijing Satellite Navigation Center, China

Executive Chairman
Jingnan Liu, Wuhan University
Yuanxi Yang, China National Administration of GNSS and Applications
Shiwei Fan, China

Committee Members (By Surnames Stroke Order)
Xiancheng Ding, China Electronics Technology Group Corporation
Qingjun Bu, China
Liheng Wang, China Aerospace Science and Technology Corporation
Yuzhu Wang, Shanghai Institute of Optics and Fine Mechanics, Chinese Academy of Sciences
Guoxiang Ai, National Astronomical Observatories, Chinese Academy of Sciences
Shuhua Ye, Shanghai Astronomical Observatories, Chinese Academy of Sciences
Zhaowen Zhuang, National University of Defense Technology
Qifeng Xu, PLA Information Engineering University
Houze Xu, Institute of Geodesy and Geophysics, Chinese Academy of Sciences
Guirong Min, China Academy of Space Technology

Xixiang Zhang, China Electronics Technology Group Corporation
Lvqian Zhang, China Aerospace Science and Technology Corporation
Junyong Chen, National Administration of Surveying, Mapping and Geoinformation
Benyao Fan, China Academy of Space Technology
Dongjin Luo, China
Guohong Xia, China Aerospace Science and Industry Corporation
Chong Cao, China Research Institute of Radio Wave Propagation (CETC 22)
Faren Qi, China Academy of Space Technology
Sili Liang, China Aerospace Science and Technology Corporation
Shancheng Tu, China Academy of Space Technology
Rongsheng Su, China
Zhipeng Tong, China Electronics Technology Group Corporation
Ziqing Wei, Xi'an Institute of Surveying and Mapping

Organizing Committee

Secretary General
Haitao Wu, Navigation Headquarters, Chinese Academy of Sciences

Vice Secretary General
Wenhai Jiao, China Satellite Navigation Office Engineering Center
Jianjun Wu, National University of Defense Technology
Weina Hao, Navigation Headquarters, Chinese Academy of Sciences

Committee Members (By Surnames Stroke Order)
Qun Ding, The 20th Research Institute of China Electronics Technology Group Corporation
Miao Yu, China Academy of Space Technology
Li Wang, International Cooperation Research Center China Satellite Navigation Engineering Office
Ying Liu, China Satellite Navigation Office Engineering Center
Shuhua Zhang, National University of Defense Technology, Changsha
Xiuwan Chen, Peking University
Xiangan Zhao, China Defense Science and Technology Information Center
Ouyang Guangzhou, Academy of Opto-electronics, Chinese Academy of Sciences
Gang Hu, Beijing Unicore Communications, Inc.
Min Shui, National Remote Sensing Centre of China
Zhong Dou, National Time Service Center, Chinese Academy of Sciences

Editorial Board

Topic S1: BDS/GNSS Application Technology
Qin Zhang, Chang'an University, China
Shuanggen Jin, Shanghai Astronomical Observatory of Chinese Academy of Sciences
Jianping Cao, Air Force Equipment Research Institute
Ruizhi Chen, Texas A&M University (Corpus Christi), USA

Topic S2: Navigation and Location Based Services
Yamin Dang, Chinese Academy of Surveying and Mapping
Jing Li, Telecommunication & Information Center, Ministry of Transportation and Communications
Baoguo Yu, The 54th Research Institute of China Electronics Technology Group Corporation
Kefei Zhang, RMIT University, Australia

Topic S3: Satellite Navigation Signals
Xiaochun Lu, National Time Service Center, Chinese Academy of Science
Yanhong Kou, Beihang University
Zheng Yao, Tsinghua University
Tom Stansell, Stansell Consulting, USA

Topic S4: Satellite Orbit and Clock Offset Determination
Geshi Tang, Beijing Aerospace Control Center
Xiaogong Hu, Shanghai Astronomical Observatory, Chinese Academy of Sciences
Rongzhi Zhang, Xi'an Satellite Control Center
Maorong Ge, Geo Forschungs Zentrum (GFZ) Potsdam, Germany

Topic S5: BDS/GNSS Precise Positioning Technology
BDS/GNSS Precise Positioning Technology
Qile Zhao, Wuhan University
Jianwen Li, Information Engineering University
Song shuLi, Shanghai Astronomical Observatory, Chinese Academy of Sciences
Yanming Feng, Queensland University of Technology, Brisbane, Australia

Topic S6: Atomic Clock and Time-frequency Technology
Lianshan Gao, The 203th Research Institute of China Aerospace Science and Industry Corporation
Chunhao Han, Beijing Satellite Navigation Center
Xiaohui Li, National Time Service Center, Chinese Academy of Sciences
Nikolay Demidov, VCH Corporation, Russia

Topic S7: BDS/GNSS Augmentation Systems and Technology
Junlin Zhang, OLinkStar Co., Ltd., China
Jinping Chen, Beijing Satellite Navigation Center
Rui Li, Beihang University
Shaojun Feng, Imperial College London

Topic S8: BDS/GNSS Test and Assessment Technology
Jun Yang, National University of Defense Technology
Xiaolin Jia, Xi'an Institute of Surveying and Mapping
Wenxian Yu, Shanghai Jiao Tong University
Yang Gao, University of Calgary, Canada

Topic S9: BDS/GNSS User Terminal Technology
Haibo He, Beijing Satellite Navigation Center
Baowang Lian, Northwestern Polytechnical University
Hong Li, Tsinghua University
Yong Li, University of New South Wales, Australia

Topic S10: Multi-sensor Fusion Navigation
Zhongliang Deng, Beijing University of Posts and Telecommunications
Hong Yuan, Academy of Opto-electronics, Chinese Academy of Sciences
Yongbin Zhou, National University of Defense Technology
Jinling Wang, University of New South Wales, Australia

Topic S11: PNT System and Emerging Navigation Technology
Mingquan Lu, Tsinghua University
Wei Wang, The 20th Research Institute of China Electronics Technology Group Corporation
Yin Xu, Academy of Opto-electronics, Chinese Academy of Sciences
Xiangzhen Li, Chungnam National University, Korea

Topic S12: Standardization, Intellectual Properties, Policies, and Regulations
Daiping Zhang, China Defense Science and Technology Information Center
Yonggang Wei, China Academy of Aerospace Standardization and Product Assurance
Haibo Liu, Institute of Policy and Management, Chinese Academy of Sciences
Haibo Wang, Electronic Intellectual Property Center, Ministry of Industry and Information Technology, PRC

Contents

Part I
Satellite Orbit and Clock Offset Determination

Research on the Inversion Method of USO Frequency Stability Joining GNSS and Inter-satellite Distance Measurement

Xuan Liu, Dengfeng Wang, Xingwang Zhong and Yansong Meng

Abstract K-band ranging (KBR) system and GNSS receiver are the key payloads of the gravity exploration satellite which employs LEO satellite tracking LEO satellite technology. Ultra-stable crystal oscillator, providing precise inter-satellite distance measurement with clock frequency reference, is the key component of the KBR-GNSS system. Therefore, real-time and dynamic monitoring on-orbit ultra-stable oscillator (USO)'s frequency stability are very necessary. First of all, the analysis formula of DOWR with time-tag corrected is deduced based on the study of the KBR-GNSS measuring principle. Second, the coupling relationship between Allan variance formula and inter-satellite time difference is analyzed deeply. Two methods of inversing USO Allan variance are proposed, of which one is using inter-satellite time difference measurement and the other one is employing inter-satellite distance measurement. Finally, referring to GRACE satellite payload scheme, a set of KBR-GNSS system is developed, by using which, the effectiveness of the two algorithms is validated and their advantages and disadvantages are compared meanwhile. The research results of this paper have some references to the design of inter-satellite ranging system of Chinese first generation earth gravity exploration satellite.

Keywords GNSS K-band ranging · Dual one-way ranging · Ultra-stable oscillator Allan variance · Gravity field exploration

X. Liu (✉) · D. Wang · X. Zhong · Y. Meng
China Academy of Space Technology, No. 504 Chang'an Eastern Street, Xi'an, China
e-mail: liuxuan0229@126.com

D. Wang
e-mail: wangdf79@163.com

X. Zhong
e-mail: zhongxw1391@qq.com

Y. Meng
e-mail: yansongmeng@hotmail.com

© Springer Science+Business Media Singapore 2016

J. Sun et al. (eds.), *China Satellite Navigation Conference (CSNC) 2016 Proceedings: Volume III*, Lecture Notes in Electrical Engineering 390,
DOI 10.1007/978-981-10-0940-2_1

1 Introduction

The precise measurement of the earth's gravity field shows great application value in oceanography, hydrology, geophysical science, and military aspects. Leo satellite tracking Leo satellite technology, referred to as SST-LL, is one of the most effective means of detection of gravitational field [1]. GRACE (Gravity Recovery and Climate Experiment) satellite jointly developed by The United States and Germany was launched in 2002, in which SST-LL technology was used for the first time. High precision K-band ranging (KBR) and GNSS receiver are the core payloads of the GRACE, of which ultra-stable oscillator (USO) is the key equipment. USO is the standard of time and frequency of KBR and GNSS receiver in which all of the measuring time tags are referenced to USO's output. During on-orbit operation process, USO is influenced by various factors such as temperature, radiation, and aging so that its frequency is not stable, thereby affecting measurement accuracy of KBR and GNSS receiver [2]. Consequently, monitoring of on-orbit USO frequency stability for measurement data processing and analysis are of great help.

China has launched the earth's gravity field exploration program. Related research institutions and scholars have made deep study in KBR, USO, and GNSS receiver [3, 4]. Taking GRACE satellites as the background, based on the principles of two one-way ranging (DOWR) and high precision time difference correction, combining with the self-developed KBR-GNSS experimental systems, this paper intensively studies the indirect calculation method of USO frequency stability. Starting from the original definition of Allan variance, the relative Allan variance mathematical model is firstly proposed by inter-satellites time difference value and then further established using biased distance between satellites. Direct measurement and indirect computing results of USO Allan variance are compared and analyzed, which verifies the accuracy and feasibility of indirect calculation methods. Finally, some suggestions and considerations are put forward to Chinese earth's gravity field exploration satellites.

2 Principle of Measurement

2.1 Dual One-Way Ranging

As showed in Fig. 1, satellite i and satellite j transmit Ka band signal to each other, respectively, and the difference of these signals is 670 kHz. The receiving terminals uninterruptedly monitor the phase changes of 670 kHz signal using phase locked loop to obtain one-way phase measurements φ_i^j and φ_j^i.

The theoretical basis of KBR is DOWR which can effectively suppress the common error caused by medium and long term frequency instability of USO [4], as showed in Fig. 2. At the specified nominal measuring time t, the one-way phase measurement of satellite i can be expressed as [5]:

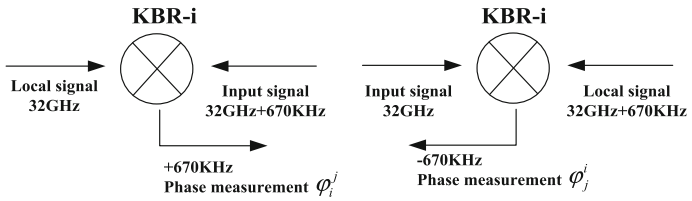

Fig. 1 KBR signal flow graph

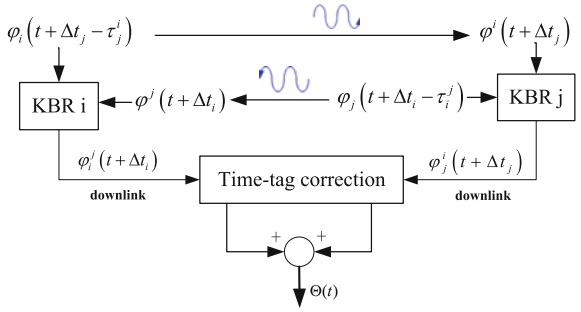

Fig. 2 Schematic of dual one-way phase measurement

$$\varphi_i^j(t+\Delta t_i)=\varphi_i(t+\Delta t_i)-\varphi^j(t+\Delta t_i)+E_i^j \quad i,j=1,2,\ \ i\neq j \tag{1}$$

Formula (1) is the phase difference from the received signal and the local reference signal, among which the phase of received signal in satellite i can be represented by the one of transmitted signal in satellite j.

$$\varphi^j(t+\Delta t_i)=\varphi_j\left(t+\Delta t_i-\tau_i^j\right) \tag{2}$$

where τ_i^j is the signal travel time from satellite j to i. So, formula (1) can be written as:

$$\varphi_i^j(t+\Delta t_i)=\varphi_i(t+\Delta t_i)-\varphi_j\left(t+\Delta t_i-\tau_i^j\right)+E_i^j \tag{3}$$

Δt_i called time-tag error is the difference of actual and nominal sampling time, which needs to be corrected by GNSS measurement. E_i^j is the sum of measurement errors including integer ambiguity, ionosphere error, and other phase measuring errors.

Phase $\varphi_i(t)$ can be decomposed into the reference phase $\bar{\varphi}_i$ and phase errors caused by the oscillator $\delta\varphi_i$

$$\varphi_i(t) = \bar{\varphi}_i(t) + \delta\varphi_i(t) \tag{4}$$

So, formula (3) can be written as:

$$\begin{aligned}\varphi_i^j(t+\Delta t_i) = {} & \bar{\varphi}_i(t+\Delta t_i) + \delta\varphi_i(t+\Delta t_i) \\ & - \bar{\varphi}_j(t+\Delta t_i - \tau_i^j) - \delta\varphi_j(t+\Delta t_i - \tau_i^j) + E_i^j\end{aligned} \tag{5}$$

Formula (5) can be arranged using Taylor polynomial method, in which phase change $\dot{\bar{\varphi}}_i(t)$ is represented by constant standard frequency f_i. Then following four expressions can be obtained:

$$\begin{aligned}\bar{\varphi}_i(t+\Delta t_i) &\approx \bar{\varphi}_i(t) + \dot{\bar{\varphi}}_i(t)\Delta t_i \approx \bar{\varphi}_i(t) + f_i\Delta t_i \\ \bar{\varphi}_i(t+\Delta t_j - \tau_j^i) &\approx \bar{\varphi}_i(t) + f_i\Delta t_j - f_i\tau_j^i \\ \delta\varphi_i(t+\Delta t_i) &\approx \delta\varphi_i(t) + \delta f_i(t)\Delta t_i \\ \delta\varphi_i(t+\Delta t_i - \tau_j^i) &\approx \delta\varphi_i(t) + \delta f_i(t)\Delta t_i - \delta f_i(t)\tau_j^i\end{aligned} \tag{6}$$

In that way, the result of DOWR is [5]:

$$\Theta \equiv \varphi_i^j(t+\Delta t_i) + \varphi_j^i(t+\Delta t_j) \tag{7}$$

Because the frequencies of microwave signal in two satellites are designed differently, f_1 represents the microwave signal in satellite i while f_2 represents that in satellite j. If formula (6) is substituted into (5) and then formula (5) is substituted into (7), it can be got that:

$$\begin{aligned}\Theta(t) \approx {} & (f_i\tau_j^i + f_j\tau_i^j) + (\delta f_i\tau_j^i + \delta f_j\tau_i^j) \\ & + (f_i - f_j)(\Delta t_i - \Delta t_j) + (\delta f_i - \delta f_j)(\Delta t_i - \Delta t_j) + E\end{aligned} \tag{8}$$

Consequently, the biased distance measurement can be written as:

$$R(t) = \lambda\Theta(t), \quad \lambda = c/(f_i + f_j) \tag{9}$$

2.2 Time-Tag Correction DOWR

As mentioned before that DOWR can effectively suppress the phase errors caused by medium and long term frequency instability of USO, a key prerequisite of ensuring noise suppression ratio is that measurement time consistency must reach a certain precision when two one-way phase measurements are superimposed based on Eq. (7). GRACE requires that this time consistency is better than 0.1 ns. In practical projects, it can be ensured that the GNSS pseudorange measurements are

tagged with KBR measuring time if the time-tag produced by local USO is used to sample GNSS and KBR measurements at the same time. In this paper, GNSS and KBR measuring time are denoted by t_i^{gnss} and t_i, respectively.

$$\begin{aligned}\Delta t &= \Delta t_i - \Delta t_j = (t_i - t_{\text{gnss}}) - (t_j - t_{\text{gnss}}) \\ &= (t_i^{\text{gnss}} - t_{\text{gnss}}) - (t_j^{\text{gnss}} - t_{\text{gnss}}) = t_i^{\text{gnss}} - t_j^{\text{gnss}}\end{aligned} \tag{10}$$

As showed in Fig. 2, Δt is used to correct KBR measuring time and two one-way phase measurements from satellite i and satellite j can be resampled at nearly the same time. In practice, it is chosen that measurement of satellite j is resampled at t_i. Where Δt, got through GNSS data post-processing, is used to interpolate one-way phase measurement of satellite j, which is showed in the following expression

$$\begin{aligned}\varphi_j^i(t+\Delta t_j) &= \varphi_j^i(t+\Delta t_i - \Delta t) \\ &= \bar{\varphi}_j(t+\Delta t_i - \Delta t) + \delta\varphi_j(t+\Delta t_i - \Delta t) \\ &\quad - \bar{\varphi}_j(t+\Delta t_i - \Delta t - \tau_j^i) - \delta\varphi_j(t+\Delta t_i - \Delta t - \tau_j^i) + E_j^i\end{aligned} \tag{11}$$

Until now, the equation of DOWR is rewritten after time-tag correction as:

$$\begin{aligned}\Theta(t_i) \approx\ & (f_i\tau_j^i + f_j\tau_i^j) + (\delta f_i\tau_j^i + \delta f_j\tau_i^j) \\ & + (f_i - f_j)\delta|\Delta t_i| + (\delta\dot{\varphi}_i - \delta\dot{\varphi}_j)\delta\left|\Delta t_j\right| + E\end{aligned} \tag{12}$$

where $\delta|\Delta t_i|$ and $\delta\left|\Delta t_j\right|$ are time difference measuring errors which are very small and can be neglected [6] (Fig. 3).

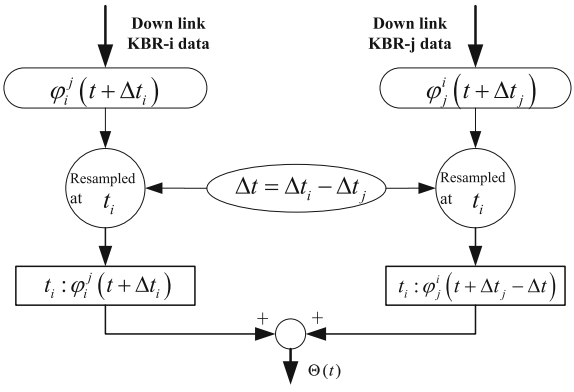

Fig. 3 Principle of time-tag correction

2.3 Relative Frequency Error

Formula (12) subtracts formula (8), neglecting the small terms:

$$\Theta(t_i) - \Theta(t) \approx (f_i - f_j)(\Delta t_i - \Delta t_j) + (\delta f_i - \delta f_j)(\Delta t_i - \Delta t_j) \tag{13}$$

Defining a new composite phase measurement as:

$$\Theta_p(t) = \Theta(t) - (f_i - f_j)(\Delta t_i - \Delta t_j) \tag{14}$$

Formula (15) can be got if formula (14) subtracts formula (12):

$$\Theta_p(t) - \Theta(t_i) \approx (\delta f_i - \delta f_j)(\Delta t_i - \Delta t_j) \tag{15}$$

As a result, relative frequency error is:

$$\delta f_i - \delta f_j \approx \frac{\Theta_p(t) - \Theta(t_i)}{\Delta t_i - \Delta t_j} \tag{16}$$

2.4 Relative Allan Variance

The so-called frequency stability is the degree of any frequency source producing the same frequency in a period after continuous operation for a while, also described as the degree of frequency random fluctuation. The frequency instability, in time domain, is generally characterized by Allan variance. Any oscillator can output a signal that can be described as the following formula:

$$A(t) = [A + \varepsilon(t)] \sin[2\pi f_0 t + \varphi(t)] \tag{17}$$

A is the amplitude and f_0 is the nominal frequency. $\varepsilon(t)$ and $\varphi(t)$ represent the random amplitude and phase fluctuations with respect to the ideal case. Then, phase deviation can be expressed as [7]:

$$x(t) = \varphi(t)/2\pi f_0 \tag{18}$$

$$y(t) = \dot{\varphi}(t)/2\pi f_0 \tag{19}$$

where $\dot{\varphi}(t) = \delta f_i - \delta f_j$, δf_i is frequency error. Formula (18) signifies relative time deviation and formula (19) signifies relative frequency deviation. As a result, Allan variance is defined as:

$$\sigma(\tau) = \left[\frac{1}{2(N-1)}\sum_{i=1}^{N-1}(y_{i+1} - y_i)^2\right]^{1/2} \tag{20}$$

where $y_n = (x_n - x_{n-1})/\tau$ represents the average frequency deviation of Nth interval. So, Allan variance can be rewritten as:

$$\sigma_x(\tau) = \left[\frac{1}{2(N-1)\tau^2}\sum_{i=1}^{N-1}(x_{i+2} - 2x_{i+1} + x_i)^2\right]^{1/2} \tag{21}$$

If $x = \Delta t$, relative Allan variance can be got:

$$\sigma_{\Delta t}(\tau) = \left[\frac{1}{2(N-1)\tau^2}\sum_{i=1}^{N-1}(\Delta t_{i+2} - 2\Delta t_{i+1} + \Delta t_i)^2\right]^{1/2} \tag{22}$$

A new relative frequency deviation expression can be got if substituting formula (16)–(19):

$$\bar{y} = \frac{\delta f_i - \delta f_j}{(f_i + f_j)/2} \tag{23}$$

δf_i and δf_j represent the deviation with respect to the nominal frequency of USO in satellite i and satellite j, respectively. $(f_i + f_j)/2$ signifies average nominal frequency. On these basis, corrected Allan variance based on KBR measurement can be expressed as:

$$\sigma_{\bar{y}}(\tau) = \left[\frac{1}{2(N-1)}\sum_{i=1}^{N-1}(\bar{y}_{i+1} - \bar{y}_i)^2\right]^{1/2} \tag{24}$$

In the end, for computing two USOs' relative Allan variance, the Eq. (22) based on inter-satellites time difference measurement and Eq. (24) based on GNSS and KBR measurements are obtained. What needs to be pointed out is that Allan variance getting from these equations represents the overall level of the two USOs' frequency stability. Given two USOs are running independently in two satellites, it can be estimated that Allan variance of single USO is about half of the two USOs' relative Allan variance.

3 Test and Verification

3.1 Testing System

As shown in Fig. 4, two sets of KBR-GNSS experimental system referenced to GRACE KBR were self-developed and a ground test system was build accordingly. KBR-GNSS system consists of K band and L band antenna, RF transceiver that is used for up-conversion and down-conversion reference signal, USO which produces local reference frequency and digital signal processing unit which handles GNSS signal processing and KBR carrier phase extraction. All the tests were carried out in a special anechoic chamber in order to restrain multipath signal, in which free signal propagation distance was about 3.5 m. Only 32 GHz microwave was used because the ground test did not involve the ionosphere calibration. Digital signal processing unit obtains one-way phase measurements for KBR on one hand and tracks GNSS navigation signal, generating pseudorange measurements. Then packaged KBR and GNSS measurements are sent to special testing equipment. After data preprocessing, precision time-tag acquisition and DOWR arrangement, biased distance and time difference value between the satellites are, respectively, got.

3.2 Testing Results

A lot of KBR and GNSS observations were got under the help of the testing system with the almost constant temperature and pressure environment. Testing results showed that the precision of the measuring time difference values of two KBR got from GNSS data was up to 0.1 ns and KBR biased distance precision using time-tag correction DOWR was better than 10 μm as shown in Fig. 5.

After dealing with the same set of test data using Eq. (22) with (24), respectively, the average frequency stability of individual USO was estimated accordingly. In order to reduce one-way KBR errors apart from error sources caused by

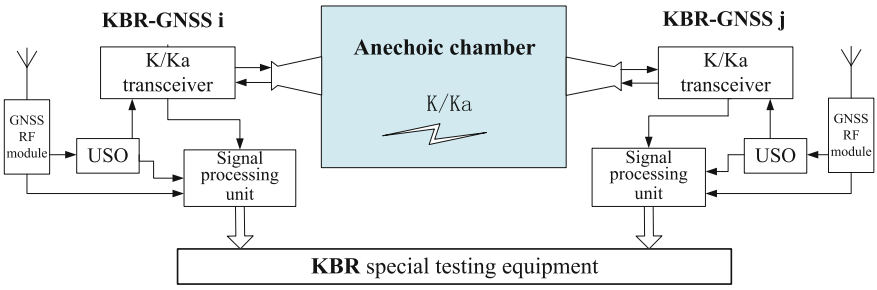

Fig. 4 Experimental system of SST-LL KBR-GNSS

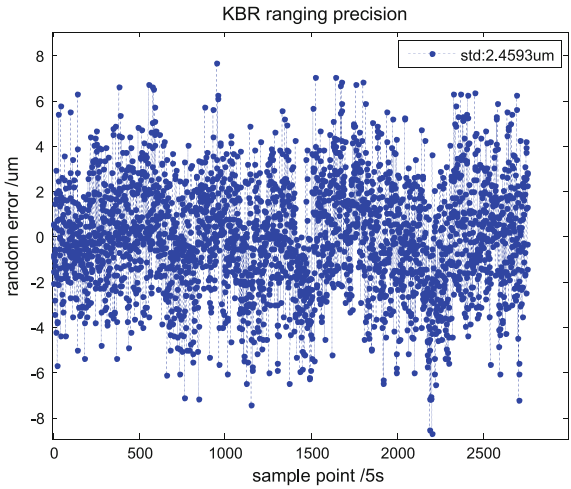

Fig. 5 KBR range error time series

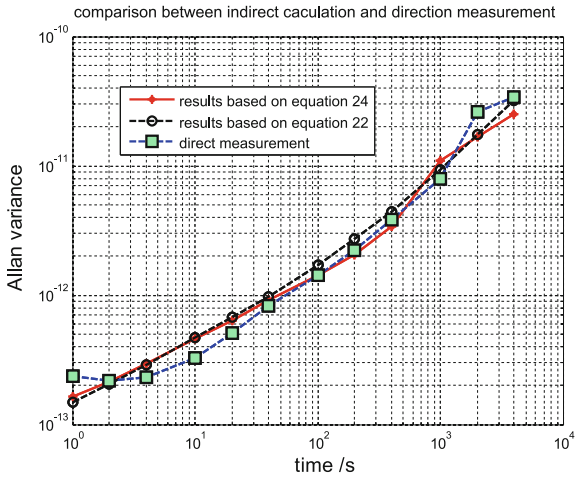

Fig. 6 Allan variance results of indirect calculation and direct measurement

USO frequency instability as much as possible, several tests kept two KBR-GNSS systems relatively static, the receiver carrier to noise ratio consistent and environment temperature basic constant, so that the multipath error, system noise and ranging system error were kept within the reasonable scope, which was advantageous to accurately assessing the validity of the indirect frequency stability calculation method.

For the same set of test data, Fig. 6 shows the individual USO Allan variance estimation curve using two calculation methods and measured curve by TSC5115A cooperated with OSA8607D (10 MHz) for comparison. Allan variance based on time-tag difference is got by Eq. (22), while Allan variance based on distance and time-tag joint model is obtained by Eq. (24). Direct measurement curve is the

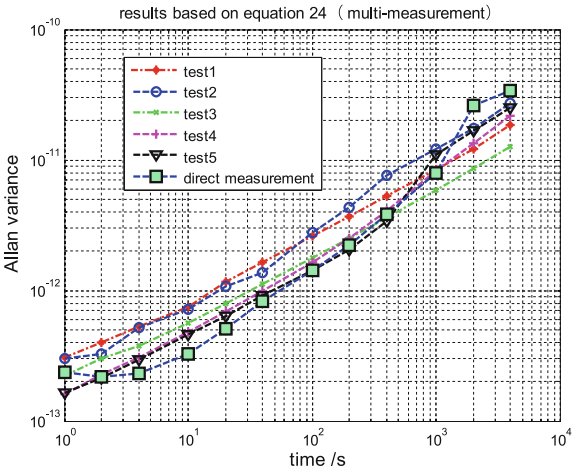

Fig. 7 Allan variance computing results based on the joint model Eq. (24)

average of the two USO Allan variance using TSC5115A. Figure 6 shows that the results of two indirect calculation methods are in good consistency and are consistent with the direct measured results.

Figure 7 shows the Allan variance based on Eq. (24) using five different sets of test data, in which the trend of five indirect calculation results are almost consistent with slightly difference at the same time point and the average of indirect results is higher than direct measurements at the same time point.

However, RF transceiver and USO are very sensitive to tiny changes in temperature. Thus, the instability of temperature difference of two KBRs might introduce offset in phase measurement. In addition, multipath signal and small ground vibration also had influence on the phase measurement. All these factors mentioned above were eventually transformed into phase measurement noise of the short and medium term of KBR, and then influenced Allan variance calculation results. That is why five indirect calculation results in Fig. 7 are not in full accord.

4 Conclusion

The formula of indirectly calculating relative frequency error of two USOs based on KBR phase measurement was deduced, and then the equation of relative Allan variance based on relative frequency error and relative time difference were obtained, respectively. USO Allan variance was estimated indirectly using KBR and GNSS data based on two methods and measured directly using standard instrument. The results of these two ways were compared, showing that the results were basically identical. If a single comparison was made to two kinds of calculation methods, it could be seen that the method based on time difference introduced less errors than the one based on relative frequency error. However, the calculation

model of Allan variance presented in this paper can only reflect the overall distribution of two USOs' relative frequency stability to a certain extent, but not the exact frequency stability of a single USO. While, what needs to be known is that for the data post-processing of KBR data, monitoring the distribution and change trend of USO frequency stability in a certain period of time has already played a very significant role in the effectiveness interpretation of payloads data. The research results of this paper have some reference to the design of inter-satellite ranging system of Chinese first generation earth gravity exploration satellite.

References

1. Wang Z, Jiang W (2011) Theory and method of determining the earth's gravitational field based on satellite tracking satellite technology. Wuhan University Press, Wuhan, pp 5–13
2. She S, Wang K (2006) The technology of high accuracy inter-satellite microwave ranging. J Astronaut 3:402–406
3. Kang K, Li H (2012) Demonstration on the design of filter indexes of inter-satellite high accuracy ranging system for gravity satellite. Chin J Geophys 10:55–110
4. Liu X, Wang D et al (2015) Research on the effect of signal propagation delay between satellites on KBR's measurement performance. In: Academic conference proceedings of China aerospace institute in 2015
5. Kim J, Tapley BD (2003) Simulation of dual one-way ranging measurements. J Spacecraft Rockets 40(3):419–425
6. Thomas JB (1999) An analysis of gravity-field estimation based on inter-satellite dual-1-way biased ranging, Jet Propulsion Lab. JPL Publications. 98-15, Pasadena, CA, May 1999
7. Zhong C, Xia Z (2008) Transform of short-term frequency stability from frequency domain to time domain. The frequency control technology conference proceedings in 2008

Research of Satellite and Ground Time Synchronization Based on a New Navigation System

Yang Yang, Yufei Yang, Kun Zheng and Yongjun Jia

Abstract The new navigation time synchronization method is a breakthrough in existing navigation systems time synchronization accuracy limit, and it is an effective way to reduce system construction costs. By placing more accurate atomic clock in GEO satellites, it can synchronize with ground systems and generate time reference, the GEO satellites can give time to other navigation satellites, the new system can achieve high-precision time synchronization. This paper designs the navigation constellation of the new satellite navigation system, and configures the satellite clocks, simulates all kinds of constellation time synchronization precision, and educes the satellite clock configure scheme in the new navigation system.

Keywords Navigation system · Time synchronization · Satellite clock

1 Introduction

Satellite navigation systems have been widely used in military and civilian aspects of various countries and have achieved great benefits. But still there are various disadvantages in navigation system, as the number of existing satellite onboard atomic clocks demands more and high costs [1, 2]. Therefore, the use of new atomic clock design, to explore new satellite clock configuration is an effective way to reduce system construction costs.

The new time synchronization method is essentially a kind of satellite-ground, inter-satellite system operation control concept: it contains GEO satellites constellation and high accurate atomic clock; its time reference is generated by the GEO satellites and the system Control Segment Operational; it mainly relies on the OCS to do the centralized satellite-ground and inter-satellite measurement

Y. Yang (✉) · Y. Yang
Beijing Satellite Navigation Centre, Beijing, China
e-mail: 112632507@qq.com

K. Zheng · Y. Jia
Beijing Institute of Special Electromechanical Technology, Beijing, China

© Springer Science+Business Media Singapore 2016

J. Sun et al. (eds.), *China Satellite Navigation Conference (CSNC) 2016 Proceedings: Volume III*, Lecture Notes in Electrical Engineering 390,
DOI 10.1007/978-981-10-0940-2_2

processing; it depends on the inter-satellite link to update the ephemeris, and to shorten the data age. So, non-GEO satellite of the navigation constellation can use reasonable algorithm, high-precision satellite-ground and inter-satellite link, and the configuration of the ultra-stable crystal oscillator, to achieve a high precision with low construction cost.

2 The New Time Synchronization Plan

Under the new system time synchronization plan involved basic navigation constellations and star clock design, the link design, and time synchronization plan.

This system needs GEO satellite to provide time service, so the constellation must contain GEO satellites. For new time synchronization system, GEO satellites use more accurate onboard atomic clock which builds a time reference together with the OCS clock [3]. This paper takes two types of optical clocks and hydrogen atomic clock as a time reference installed on the GEO satellite, and non-GEO satellites use ordinary onboard atomic clock or ultra-stable crystal oscillator. The new time synchronization system involves satellite-ground link and inter-satellite link. Inter-satellite link contains timing link between GEO and non-GEO satellite and time synchronization link between non-GEO satellites. The new time synchronization method contains that: non-GEO satellites-ground link use satellite time and frequency transfer method; inter-satellite link use inter-satellite two-way time and frequency transfer method; GEO satellite-ground link use both satellite laser ranging and two-way time and frequency transfer method; OCS and each time synchronization stations use both satellite two-way time and frequency method and satellite common-view method.

3 Time Synchronization Measurement Model

The satellite-ground microwave observation model can be expressed as [4]:

$$\rho' = \rho + c \cdot (\Delta t_S - \Delta t_R) + \Delta\rho_{\text{ion}} + \Delta\rho_{\text{tro}} + \Delta\rho_{\text{rel}} + \Delta\rho_{\text{scc}} + \Delta\rho_{\text{ant}} + \Delta\rho_{\text{ml}} + \varepsilon \quad (1)$$

In this formula, ρ' is microwave observation value, ρ is the true distance from the ground station to the satellite; c is the light speed, Δt_S is satellite clock error, and Δt_R is ground station clock error; $\Delta\rho_{\text{ion}}$ is ionospheric delay error, $\Delta\rho_{\text{tro}}$ is tropospheric delay error; $\Delta\rho_{\text{rel}}$ is relative delay error; $\Delta\rho_{\text{scc}}$ is satellite centroid compensation correction; $\Delta\rho_{\text{ant}}$ is antenna phase center error; $\Delta\rho_{\text{ml}}$ is multipath effect; ε is pseudo range observation noise.

The satellite-ground laser observation model

The observation model of the satellite-ground laser ranging can be expressed as:

$$\rho' = \rho + \Delta\rho_{\text{tro}} + \Delta\rho_{\text{rel}} + \Delta\rho_{\text{scc}} + \Delta\rho_{\text{ec}} + \Delta\rho_{\text{ant}} + \Delta\rho_{\text{ml}} + \varepsilon \tag{2}$$

In this formula, ρ' is laser observation value. ρ is the true distance from the laser station to the satellite; $\Delta\rho_{\text{tro}}$ is tropospheric delay error; $\Delta\rho_{\text{rel}}$ is relative delay error; $\Delta\rho_{\text{scc}}$ satellite centroid compensation correction; $\Delta\rho_{\text{ec}}$ is station coordinate correction; $\Delta\rho_{\text{ant}}$ is antenna phase center error; $\Delta\rho_{\text{ml}}$ is multipath effect; ε is laser observation noise.

Two-way measurement equation

The two-way measurement equation can be obtained from the single direction measurement equation of satellite-ground and inter-satellite.

$$\begin{cases} \bar{\rho}_{ij} = d + c \cdot \delta t_i - c \cdot \delta t_j + n_{ij} \\ \bar{\rho}_{ji} = d + c \cdot \delta t_j - c \cdot \delta t_i + n_{ji} \end{cases} \tag{3}$$

In this formula, $\bar{\rho}_{ij}$ and n_{ij} are pseudorange (microwave, laser) and measurement noise from point S_i to S_j; $\bar{\rho}_{ji}$ and n_{ji} are corrected pseudorange (microwave, laser) and measurement noise from satellite S_i to S_j; δt_i and δt_j are clock error S_i and S_j. c is the light speed and d stands for distance between S_i and S_j, as below: $d = [(x_i - x_j)^2 + (y_i - y_j)^2 + (z_i - z_j)^2]^{1/2}$.

4 Satellite Clock Modeling and Time Synchronization Algorithm

The atomic clock used in the satellite navigation system contains system change and random error. Atomic clock error may be expressed as the difference between the instantaneous clock time and the standard time $x(t)$. Choose quadratic polynomial model as clock error model

$$x(t) = a_0 + a_1(t - t_0) + \frac{1}{2}a_2(t - t_0)^2 + \varepsilon_x(t) \tag{4}$$

In this formula, a_0 is the initial phase(time) deviation, a_1 is the initial deviation of the atomic clock frequency, and a_2 is linear frequency drift rate; $\varepsilon_x(t)$ is the random variation component of clock deviation caused by clock noise; t_0 is the reference time. The step of time synchronization process is as follows: observation data pretreatment, parameters priori information determination, initial clock error calculation, time estimation matrix building, residual edit, and iteration [5].

5 Simulation and Results Analysis

5.1 Atomic Clock and Clock Data Simulation

Allan variance is the most common expression of frequency stability, which depends on the length of time stability, and is divided into short-term frequency and long-term stability. Although the definition of short-term stability and long-term frequency stability is same, they reflect different aspects of signal stability characteristics. Measurement of short-term frequency stability in the time domain is very difficult, or even impossible, but at the same time it is easier to measure in the frequency domain. So, short-term frequency stability measurement can be converted into a time domain phase noise, so as to get the short-term time domain stability indirectly. Phase noise theory and statistical thin phase noise of time domain and frequency domain Allan variance are equivalent. If got the conversion relationship between them, the amount of each physical characterization can be then revealed. This paper use Allan variance as the satellite clock error calculation model.

When calculating the simulation, noise as above is generated by the white noise, and relevant noise generation process is as follows [6]:

$$y_i^{\mathrm{WP}} = \sigma_{y\mathrm{WP}}(\tau) \cdot (\mathrm{rand}_i - \mathrm{rand}_{i-1}) y_i^{\mathrm{WF}} = \sigma_{y\mathrm{WF}}(\tau) \cdot \sqrt{3} \cdot \mathrm{rand}_i$$
$$y_i^{\mathrm{RW}} = y_{i-1}^{\mathrm{RW}} + \sigma_{y\mathrm{RW}}(\tau) \cdot 3 \cdot \mathrm{rand}_i$$
$$y_i^{\mathrm{FF}} = \sigma_{y\mathrm{FF}}(\tau) \cdot \sqrt{5} \cdot [i^{-2/3}\mathrm{rand}_1 + (i-1)^{-2/3}\mathrm{rand}_2 + (i-2)^{-2/3}\mathrm{rand}_3 + \cdots + \mathrm{rand}_i]$$

In this formula, $\mathrm{rand}_i \sim N(0,1)$, N is the number of sampling points.

Atomic clock error is calculated by the following formula:

$$x_i = x_{i-1} + \tau(y_i^{\mathrm{WP}} + y_i^{\mathrm{WF}} + y_i^{\mathrm{FF}} + y_i^{\mathrm{RW}}) \quad i = 1, 2, \ldots N \tag{5}$$

5.2 Simulation of Ultra-Stable Oscillator Data

Crystal error is more complex, so there is no proper mathematical model yet. Since there is no direct ultra-stable oscillator laboratory results, this paper uses Allan variance provided by ACES. Inverse the main Allan variance noise component, and put them together (Table 1).

Table 1 ACES ultra-stable crystal oscillator (USO) Allan variance with interval

Measurement interval (s)	1	2	4	10	20
Sigma	1.49e−13	1.26e−13	1.00e−13	8.82e−14	8.88e−14
Interval (s)	40	100	200	400	1000
Sigma	9.67e−14	1.23e−13	1.30e−13	1.20e−13	2.25 e−13

Table 2 Calculated Allan variance of noise figure

h_{-2}	h_{-1}	h_0	h_1	h_2
1.00e−13	8.82e−14	8.88e−14	9.67e−14	1.23e−13

With the condition of knowing Allan variance value of five typical time interval τ, h_{-2}, h_{-1}, h_0, h_1, h_2 can be calculated; knowing more than five Allan variance value, it can be calculated by least squares method, and then calculate any corresponding Allan variance (Table 2).

Because the random walk, frequency flicker noise, frequency white noise, flicker phase noise, and phase noise are independent random processes, after separated apart, five noises can use its own characteristic to inverse error sequences.

You can utilize these five separate noises respective characteristics, separated these noises and inversion error sequence, the formula shows in Eq. (5).

5.3 Simulation Conditions

In this paper, navigation constellation consists of MEO, GEO, and IGSO numbered 1–35, of which No. 1–27 is MEO satellites, No. 28–30 is IGSO satellite, and No. 31–35 is GEO satellite. Inter-satellite link error is set to 0.1 m (1σ). Satellite-ground link error is analyzed in two ways: Microwave satellite-ground microwave link error is 1.2 m (1σ); Laser microwave link error is 0.1 m (1σ).

There are five domestic time synchronization stations, whose minimum elevation observations are 5°. The simulation period is 7 days. Onboard satellite clock error, initial onboard clock error σ_{X_0}, and covariance matrix P_{X_0} of hydrogen maser, rubidium and cesium clock, optical clocks, ultra-stable oscillator is as [7, 8].

The simulation program is in Table 3.

Table 3 Simulation algorithm design

Scenario	Station	GEO	Non-GEO	Measurement
I	Hydrogen	Cesium	Rubidium/Cesium	Microwave satellite-ground link + Ka inter-satellite links
II	Optical	Optical	Rubidium + Cesium	Microwave satellite-ground link + Ka inter-satellite links
III	Optical	Optical	Ultra-stable oscillator	Microwave and laser joint satellite-ground link + Ka inter-satellite link
IV	Optical	Hydrogen	Rubidium + Cesium	Microwave and laser joint satellite-ground link + Ka inter-satellite link
V	Optical	Hydrogen	Ultra-stable oscillator	Microwave and laser joint satellite-ground link + Ka inter-satellite link

5.4 Simulation Results Analysis

Figures 1 and 2 are traditional satellite time synchronization error statistics. Without navigation constellation two-way filtering time synchronization, or entire constellation drift time, which maximum drift is about 7 ns, the introduction of inter-satellite links increased redundancy observations to help improve the time synchronization accuracy, to keep constellation drift within 0.65 ns in simulation conditions.

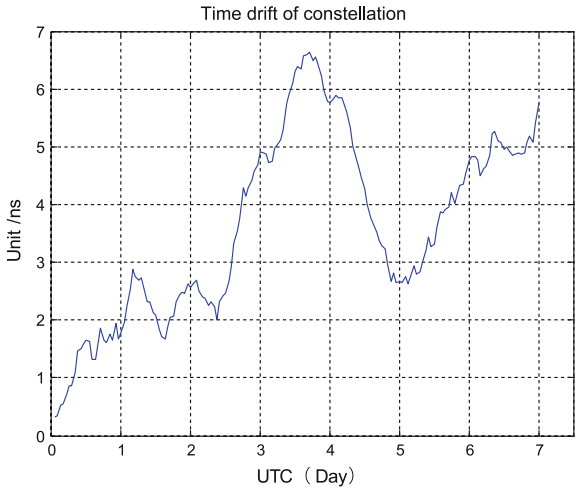

Fig. 1 Option I: constellation time drift error

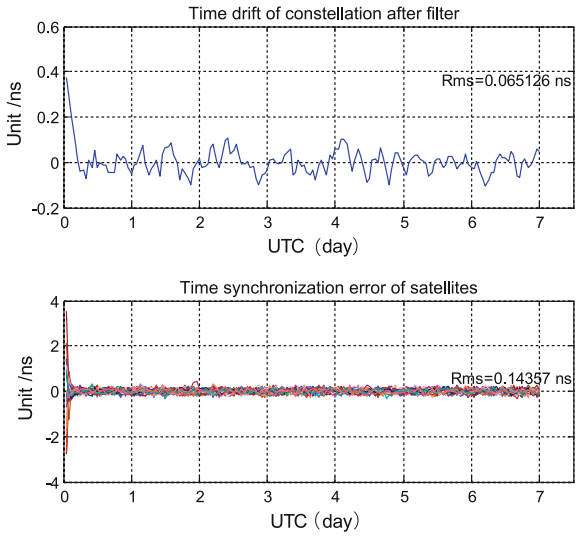

Fig. 2 Option I: constellation drift and satellite time synchronization error

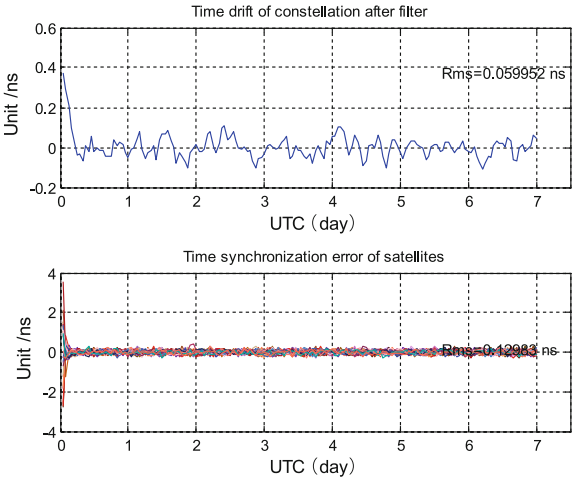

Fig. 3 Option II: constellation drift and satellite time synchronization error

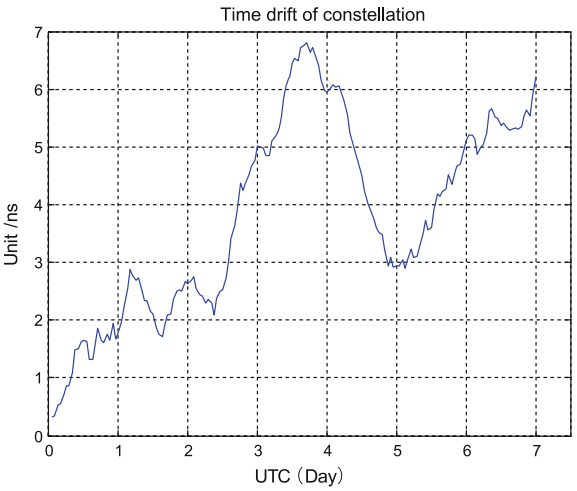

Fig. 4 Option II: constellation time drift error

Figures 3 and 4 are atomic clock + atomic clock(rubidium, cesium). Due to the GEO satellite uses a high-precision optical clocks, the simulation use laser and microwave joint satellite-ground link to take place traditional satellite-ground link; the clock of ground station is optical clock; GEO equipped with optical atomic clock; GEO onboard clock does not participate in time synchronization between non-GEO satellites, and only do time synchronization with ground stations to keep time reference. The time reference in this paper is time reference in navigation system with respect to UTC, not taking the establishment of optical clocks to improve the accuracy of UTC time in consideration. Figure 3 shows that the average constellation time (the constellation drift) and constellations time synchronization accuracy with respect to the traditional model has greatly improved.

At a given simulation conditions, the constellation average time is below 0.06 ns, time synchronization accuracy is below 0.14 ns, non-filtering time synchronization under the same conditions as a whole constellation of synchronization drift reached 7 ns (Fig. 4).

Figures 5 and 6 are the time synchronization accuracy of new optical atomic clock + ultra-stable oscillator clock. Ultra-stable oscillator has a good short-term stability but a poor long stability. Without two-way time synchronization, the whole constellation time shift is about 140 ns (Fig. 6), much larger than the drift of rubidium and cesium clock (Fig. 4). However, when added microwave and laser joint satellite-ground link, the average constellation time (the constellation drift) accuracy is about 0.0488 ns (Fig. 5). Which is slightly better than optical II.

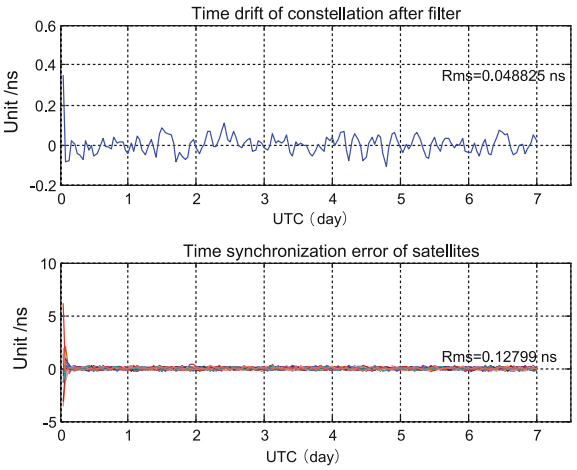

Fig. 5 Option III: constellation drift and satellite time synchronization error

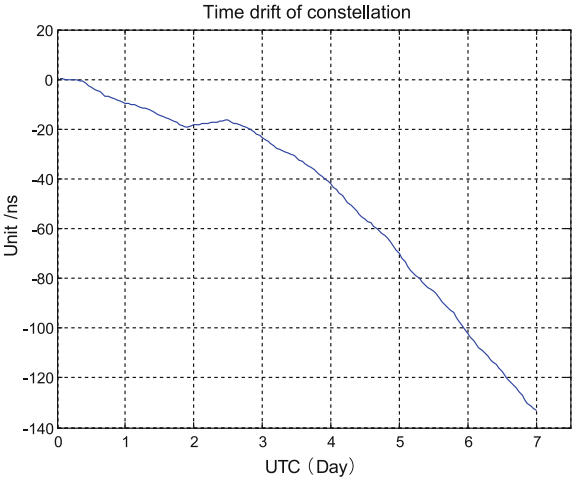

Fig. 6 Option III: constellation time drift error

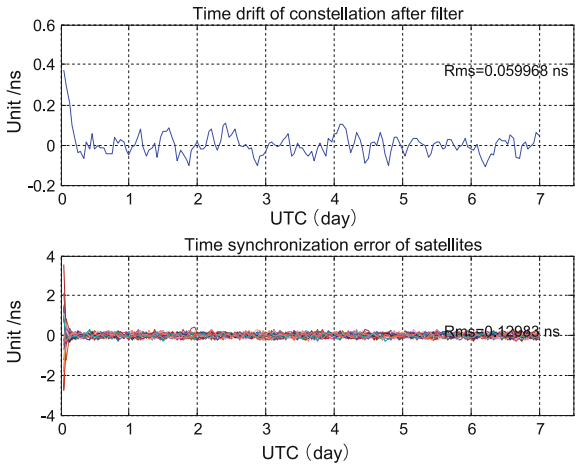

Fig. 7 Option IV: constellation drift and satellite time synchronization error

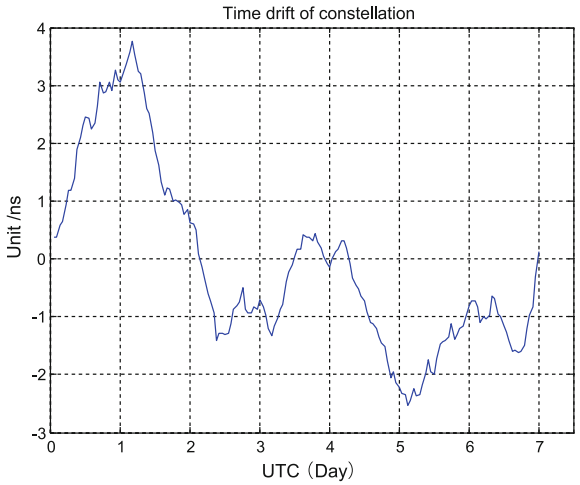

Fig. 8 Option IV: constellation time drift error

Figures 7 and 8 are the time synchronization accuracy of new hydrogen atomic clock + atomic clock(rubidium, cesium). As can be seen from Fig. 7, the average constellation two-way filtering time accuracy is 0.06 ns, time synchronization accuracy is 0.13 ns, and the average two-way filtering time is considerable with option II and III. The time synchronization accuracy of each satellite is lower than option II and III (Fig. 8).

Figures 9 and 10 are the time synchronization accuracy of new hydrogen atomic clock + ultra-stable oscillator clock. GEO is equipped with hydrogen atomic clock; other satellite clock uses ultra-stable oscillator clock. It can be concluded that the overall constellation time drift is about 0.05 ns, time synchronization accuracy is 0.128 ns (Fig. 9). Under the given simulation condition, the accuracy is slightly

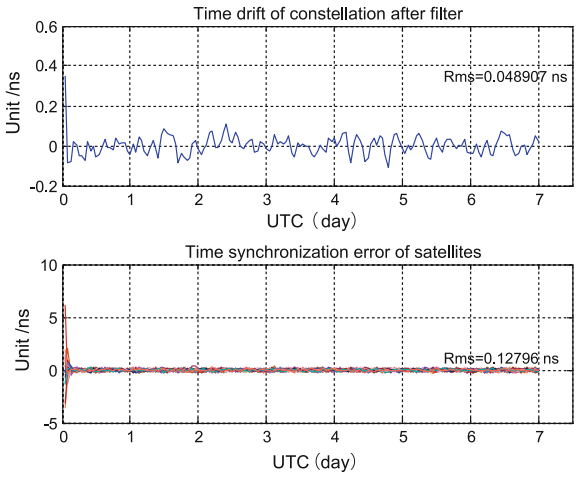

Fig. 9 Option V: constellation drift and satellite time synchronization error

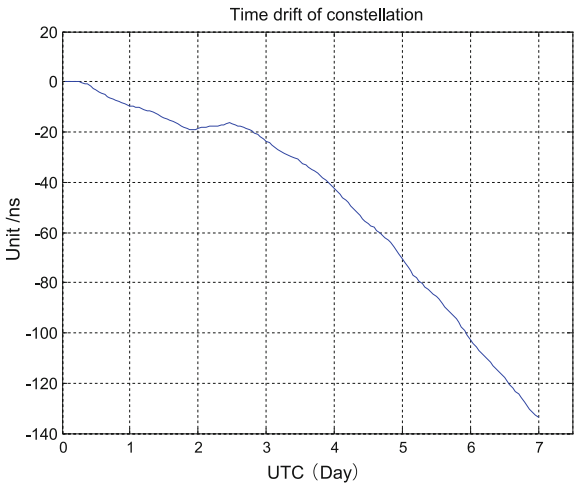

Fig. 10 Option V: constellation time drift error

better than option IV (Fig. 10). The time synchronization accuracy is slightly better than the option IV too.

5.5 In Conclusion

The present problem of onboard atomic clock frequency drift, accuracy will be getting worse with time. In this paper, simulation results show that:

The new time synchronization method can greatly improve the time synchronization accuracy.

In the new satellite and ground joint batch processing mode, the accuracy of hydrogen atomic clock and atomic clock on the GEO satellite is at the same orders of magnitude. This is because: when the satellite and ground joint estimation, all observations is transform to the same epoch, and the overall network adjustment make full use of observation information, in order to improve time synchronization accuracy. When the satellite and ground joint estimation, time synchronization accuracy depends on the satellite, the inter-satellite link precision, and algorithms. When GEO is equipped with optical atomic clock, its stability is about 1.25×10^{-12} s, the stability of hydrogenatomic clock is about 6.25×10^{-11}. In the simulation, the satellite-ground link accuracy is about 0.1 m, and the time synchronization error is about 3×10^{-10} s, the noise of satellite-ground link drowned GEO onboard clock performance, so with respect of satellite and ground joint entire network time synchronization, the accuracy of optical atomic clock and hydrogen atomic clock on the GEO satellite is at the same orders of magnitude.

Under the condition of new method, the ultra-stable oscillator can replace rubidium, cesium clock as onboard atomic clock of non-GEO satellites.

References

1. Gill P, Margolis H, Curtis A et al (2008) Optical atomic clocks for space. National Physical Laboratory
2. Godone A, Levi F, Micalizio S et al (2004) Coherent population trapping maser: noise spectrum and frequency stability. Phys Rev A 70(1):2508–2519
3. Svehla D (2008) A novel design for the navigation system and proposal to unify the timing and the positioning system using GIOVE Follow-on. ACES and future GNSS-based earth observation and navigation, Munich, Germany, 26–27 May 2008, pp 1–27
4. Kou Y (2007) GPS principles and applications. Publishing House of Electronics Industry, Beijing
5. Zhu J. The study of navigation satellite orbit determining and time synchronization method for ISLs. National University of Defense Technology(Ch), Changsha
6. Svehla D, Rothacher M, Ziebart M, Salomon C (2006) Galileo on board International Space Station and synergy with the ACES clock ensemble. European Geophysical Union, General Assembly, Vienna, 2–7 April 2006, pp 1202–1210
7. Diez J, D'Angelo P, Fernández A (2006) Clock errors simulation and characterisation. ION GNSS 19th international technical meeting of the satellite division, Fort Worth, Texas, 2006, pp 815–821
8. Weaver G (2010) The performance of ultra-stable oscillators for the gravity recovery and interior laboratory. 42nd annual precise time and time interval (PTTI) meeting, 2010, pp 369–379

Performance Evaluation of the Beidou Satellite Clock and Prediction Analysis of Satellite Clock Bias

Xueqing Xu, Shanshi Zhou, Si Shi, Xiaogong Hu and Yonghong Zhou

Abstract Satellite clock bias (SCB) is provided by the in orbit atomic clock, which is the key to satellite navigation system. First, the time reference of the satellite navigation system is realized by the SCB, and the SCB prediction accuracy will also affect the positioning accuracy of real-time navigation users. With the development of our Beidou satellite navigation system (BDS), the performance requirement of the satellite clock and accuracy requirement of the SCB prediction are higher and higher. This paper will study on performance evaluation of BDS atomic clock and the prediction analysis of SCB series exclusively. In order to show the results objectively and effectively, we select two data processing centers of the GeoForschungsZentrum Potsdam (GBM), and SHAO Analysis Center (SHA), to obtain the same time BDS clock bias sequence as the base data, for a comparative analysis. First, the performance of the atomic clock is evaluated by statistics of the Allen variance. Meanwhile, we establish the model for each SCB sequence according to the characteristic of the atomic clock, by using a combined method of least squares and autoregressive model (LS+AR), to predict and assess the SCB with root mean square error (RMS). Results show that the performance of BDS in orbit atomic clock is stable, with the day stability in the order of 10^{-14}; And the atomic clock performance is related to the SCB prediction accuracy, that is shown as better performance with higher prediction accuracy; Mean while the LS+AR model predict SCB series based on the performance of different atomic clocks, which can improve the SCB prediction accuracy effectively.

X. Xu (✉) · S. Zhou · S. Shi · X. Hu · Y. Zhou
Shanghai Astronomical Observatory, Chinese Academy of Sciences,
Nandan Road no. 80, Xuhui District 200030, Shanghai, China
e-mail: xqxu@shao.ac.cn

X. Xu · X. Hu · Y. Zhou
Key Laboratory of Planetary Sciences, Chinese Academy of Sciences,
Shanghai 200030, China

S. Shi
Graduate University of Chinese Academy of Sciences, Beijing 100049, China

© Springer Science+Business Media Singapore 2016

J. Sun et al. (eds.), *China Satellite Navigation Conference (CSNC) 2016 Proceedings: Volume III*, Lecture Notes in Electrical Engineering 390,
DOI 10.1007/978-981-10-0940-2_3

Keywords Atomic clock performance · Allen variance · SCB prediction · Least squares · Autoregressive model

1 Introduction

BeiDou Navigation Satellite System (BDS) is a global satellite positioning and communication system developed by China, which contains three departments of the space part, the ground part, and the customer part, and can provide the users with high precision and reliable positioning, navigation and timing services globally and all-weather, and has a short message communication ability. Now the BDS can provide regional navigation, positioning, and timing services. The space constellation of BDS consists of 14 satellites, and each satellite is equipped with four high performance rubidium atomic clocks, one of them is as a measurement of time, and the rest are standby as the spare. The error sources which influence the accuracy of satellite orbit determination are mainly derived from the orbit and satellite clock. The performance of atomic clock has a direct impact on the accuracy of satellite clock bias (SCB) observations and predictions, which will affect the accuracy of satellite orbit determination [4, 12]. The performance of in orbit atomic clock maybe changed with the variation of space environment, in order to effectively control the characteristic of atomic clock (stability), it is important to evaluate the performance of the in orbit satellite clock.

The SCB reliable prediction is also important for satellite navigation, especially for orbit determination of the autonomous navigation satellite. During the space running period, if satellite gets into the arcs that cannot be observed by ground stations, then the atomic clock cannot be compared to the ground time reference. The synchronization between satellite clock and the system time should be maintained by satellite clock itself, which is the prediction of SCB. While the prediction accuracy of SCB is affected by the physical characteristics of atomic clock, which is the performance of in orbit satellite clock mentioned above, but also related with the prediction method [7, 9]. Now the mostly used forecasting models about the SCB are: (1) the linear model (LM) [3, 13], (2) the quadratic polynomial model (QPM) [5, 6]. These prediction methods are simple and suitable for prediction of the regular terms in SCB series, which is the part that can be expressed by quadratic polynomial or periodic function, while ignoring the prediction of the irregular part that cannot be directly expressed by the fitting model, and the SCB prediction accuracy will be restricted.

Considering the points above, this paper selects the two data processing centers of GeoForschungsZentrum Potsdam (GBM), and the Shanghai Observatory Data Analysis Center (SHA), and gets the same time BDS clock sequence as the base data. First, the performance of the atomic clock is evaluated by statistics of the Allen variance. On the other hand, we investigate a combined method of least squares and auto regression model (abbreviated as LS+AR), to establish the model for each SCB sequence according to the characteristic of the atomic clock,

and predict the SCB sequences with prediction accuracy assessment by root mean square error (RMS), which draw lessons from our mature experience in the Earth Orientation Parameters (EOP) forecasting [10, 11].

2 Models

In this work, we first analyze the different SCB data series of two processing centers, with the Allen variance to evaluate the frequency stability of the Beidou satellite atomic clock. Construct a fitting model that mainly contains quadratic term and periodic terms, to separate the regular and irregular terms in SCB sequence, then the fitting model is used for prediction of SCB regular terms, and an AR (p) model is selected as the prediction model for SCB irregular terms. The principles of Allen variance for performance evaluation, fitting models, and AR (p) model are briefly described as follows.

2.1 Performance Evaluation

The stability of atomic clock frequency is a key factor of the real-time positioning performance, and Allen variance is generally used to evaluate the frequency stability. Allen variance, which is also known as the double sampling variance, and at first was used to analyze the phase and frequency instability of the oscillator, and then was defined as the common frequency stability analysis method by IEEE standard [8]. Here we select the Allen variance to evaluate the frequency stability of atomic clock, the standard Allen variance is defined as:

$$\sigma_y^2(\tau) = \frac{1}{2(M'-1)} \sum_{k=1}^{M'-1} (\bar{y}_{k+1} - \bar{y}_k)^2, \tag{1}$$

where

$$\bar{y}_k = \frac{x(t_k + \tau) - x(t_k)}{\tau}. \tag{2}$$

where $x(t_k)(t_k = 1, 2, \ldots, N)$ is SCB series, $\bar{y}_k(k = 1, 2, \ldots, N)$ is the average fractional frequency over a specified interval of interest τ, τ is the sample interval.

2.2 Prediction Model for Regular Terms

Because of the different characteristic of the atomic clock, we construct different fitting models to separate the regular and irregular parts in SCB sequence. For the fitting model, we first identify the main periods of SCB sequence by the spectral analysis method, and then establish the model mainly contains the constant term, linear term, quadratic term, and periodic terms, where the main periods in the SCB sequence are 1 week, 24, 12, and 6 h [8]. The fitting model is expressed as,

$$Y_t = a_0 + a_1 t + a_2 t^2 + \sum_{k=1}^{4} b_k \sin(2\pi t/P_k + \phi_k) + \varepsilon_t \tag{3}$$

where, a_0 is the constant term, a_1 is the linear coefficient, a_2 is the quadratic coefficient, t is time, P_k, b_k and ϕ_k are period signals, amplitude, and phase of periodic signals in satellite clock errors sequence, and ε_t is the noise.

After the regular and irregular parts in SCB sequence are isolated by fitting the clock error sequences, the fitting model is then used as the prediction model of the SCB irregular terms. According to the principle of least squares, the predictions of the SCB regular terms can be extrapolated by the fitted model coefficients above.

2.3 Prediction Model for Irregular Terms

The SCB regular terms can be extrapolated by the fitting model smoothly, while the irregular parts in the SCB series are difficult to predict by a simple fitting model, which should be derived by other methods, here we select the classical autoregressive model (AR model). For a stationary random sequence $z_t (t = 1, 2, \ldots, N)$, the p order of AR model (AR(p)) is expressed as follows,

$$z_t = \sum_{i=1}^{p} \varphi_i z_{t-i} + a_t. \tag{4}$$

where, a is zero-mean white noise, p is order of the model, $\varphi_1, \varphi_2, \ldots, \varphi_p$ are autoregressive coefficients.

We adopt the final prediction error criterion (FPE) to identify the order p of AR model for each forecasting step, which corresponds to the smallest FPE [1]. The coefficients can be obtained for solving the Yule-Walker equations by means of the Burg recursion [2] method. Based on the above methods, the AR (p) model can

be updated for each forecasting step, and the new AR (p) model is more reasonable and accurate.

$$\mathrm{FPE}(p) = \mathrm{P}_p(N+p+1)/(N-p-1), \tag{5}$$

$$\mathrm{P}_p = 1/(N-p)\sum_{t=p+1}^{N}\left(z_t - \sum_{j=1}^{p}\varphi_j z_{t-j}\right)^2. \tag{6}$$

where, N is the number of the data sequence $z_t(t = 1, 2, \ldots, N)$, P_p is the rest mean square error.

3 Calculation Example

At present, there are 14 working satellites in the BDS network, forming a regional navigation and positioning system. This network includes five geostationary satellites (GEO, C01–C05), four middle orbit altitude satellites (MEO, C06–C09), and five periodic tilted earth synchronous orbit satellites (IGSO, C10–C14). Among them, the C13 satellite does not work temporarily, which is unable to obtain the SCB data, and is not included in this article.

This work employs the SCB sequence from the two data analysis center GBM and SHA. First the Allen variance was carried out, to comparatively analyze the frequency stability of BDS atomic clock in different time scales; and then used a combined LS+AR method for SCB short term forecasting, the prediction accuracy verification is obtained by comparing the model predicted values with clock bias data, where the prediction spans are mainly selected as 2, 6, and 12 h.

3.1 Prediction Error Estimates

For the estimation of SCB prediction accuracy, we select the root mean squared error (RMS) as the indicator.

$$\mathrm{RMS}_i = \sqrt{\frac{1}{n}\sum_{j=1}^{n}\left(p_j^i - o_j^i\right)^2} \tag{7}$$

where, o is the SCB observations, p is the SCB predictions, i is the prediction interval, n is the number of total predictions.

3.2 Result Analysis

Allen variance of the SCB sequences is first calculated to evaluate stability of the BDS atomic clocks on different scales, and the results were counted in Table 1. In order to intuitively show the stability of the BDS satellite clock presented by two different processing centers, the representative C01 satellite with continuous and complete SCB data is selected as an example, whose Allan variance results on different time scales are plotted in Fig. 1.

For the SCB sequences of two processing centers, 200 predictions are made by means of LS+AR method, with prediction interval of 2, 6, and 12 h, and the mean square error (RMS) is calculated and listed in Table 2, the unit is nanoseconds (ns). In order to show the trend of the forecast error with time increasing, the C01 satellite is also selected as an example, whose 12 h SCB prediction errors in future of the two processing centers are plotted in Fig. 2.

Table 1 Statistics about the Satellite clock stability of processing center GBM and SHA

Sat/Allen variance	GBM		SHA	
	100,000 s	1,000,000 s	100,000 s	100,0000 s
C01	1.354e−13	1.317e−14	6.865e−14	1.323e−14
C02	2.863e−13	4.546e−14	2.124e−13	3.098e−14
C03	1.175e−13	3.352e−14	1.105e−13	2.125e−14
C04	1.052e−13	2.708e−14	7.388e−14	2.913e−14
C05	1.104e−13	3.248e−14	8.102e−14	1.743e−14
C06	1.981e−13	4.314e−14	2.321e−13	3.805e−14
C07	9.015e−14	2.682e−14	7.955e−14	2.213e−14
C08	1.969e−13	3.921e−14	2.098e−13	4.336e−14
C09	1.207e−13	3.457e−14	9.478e−14	3.304e−14
C10	1.940e−13	4.603e−14	2.013e−13	4.046e−14
C11	1.545e−13	3.143e−14	1.285e−13	3.502e−14
C12	1.031e−13	3.047e−14	8.145e−14	3.206e−14
C14	9.389e−14	2.985e−14	9.069e−14	3.085e−14

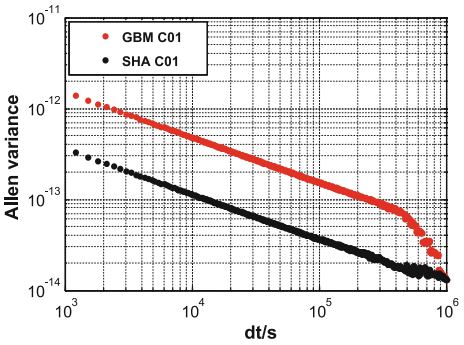

Fig. 1 Satellite clock stability comparison of different time scales of GBM and SHA C01

Table 2 Statistics about the Satellite clock prediction error of processing center GBM and SHA

Sat/RMS	GBM			SHA		
	2 h/ns	6 h/ns	12 h/ns	2 h/ns	6 h/ns	12 h/ns
C01	0.447	1.194	2.582	0.383	0.976	2.109
C02	1.315	3.975	8.977	1.454	4.724	9.287
C03	0.473	2.003	4.407	0.538	2.334	4.696
C04	0.872	2.740	5.897	0.651	2.603	5.198
C05	0.509	1.813	3.415	0.524	1.798	3.271
C06	0.809	3.041	6.524	1.108	3.201	6.754
C07	0.516	1.605	3.245	0.665	1.974	4.031
C08	1.024	3.254	7.479	1.113	4.025	8.492
C09	0.912	1.831	3.858	0.592	1.404	3.517
C10	0.893	3.126	7.273	1.152	3.478	7.972
C11	0.539	1.569	5.102	0.471	1.762	5.119
C12	0.563	1.724	5.756	0.547	1.895	5.937
C14	0.889	3.062	5.698	0.745	2.759	5.477

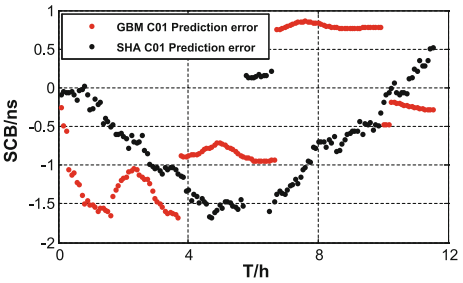

Fig. 2 Satellite clock 12 h prediction error comparison of GBM and SHA C01

Some conclusions can be obtained from the above charts and figures:

(1) we can get some information from Table 1 and Fig. 1, with comparative analysis about the SCB Allan variance of two data processing center, that the current BDS in orbit satellite atomic clock frequency stability is consistent, which is 10^{-13} to 10^{-14} at one hundred thousand second, and 10^{-14} at 1 day.

(2) the SCB predictions of two data processing centers are calculated by using the combined least squares and regression model (LS+AR), the prediction error estimation results in Table 2 and Fig. 2, show that the prediction accuracy performance of satellite C02, C08, C06, and C10 is inferior slightly, mainly due to the quality of the satellite clock itself, while the others present a high prediction accuracy, with 2 h of lower than 1 ns, 6 h of about 2 ns, and 12 h of about 5 ns.

(3) combined the results in Table 1 with Table 2, we find that the satellite (C02, C06, C08, and C10) with poor performance of SCB prediction accuracy,

whose frequency stability of atomic clock is relatively poor, which shows that the stability of the satellite atomic clock will affect the prediction accuracy of the SCB, it further shows that the LS+AR method is effective and necessary by modeling and forecasting the SCB series for each satellite.

4 Conclusion

In this study, the BDS SCB data were obtained from two data processing centers of GBM and SHA. The Allen variance is first listed for comparison analysis on the frequency stability of different satellite atomic clocks. Then we perform the modeling of the SCB sequence for each satellite, by means of LS+AR method, to separate the SCB regular and irregular terms, and their predictions is carried out respectively. Then the prediction accuracy is obtained by comparing the model predicted values with original data.

Here are some conclusions: first, the frequency stability of the BDS in orbit satellite atomic clock shows consistent performance, with 10^{-13} to 10^{-14} at one hundred thousand second, and 10^{-14} at 1 day. Second, the mostly BDS SCB series present a high prediction accuracy, with 2 h of lower than 1 ns, 6 h of about 2 ns, and 12 h of about 5 ns. At the same time, the stability of the satellite atomic clock will affect the prediction accuracy of the SCB, which is shown as better stability performance with higher prediction accuracy relatively. This study uses the LS+AR model to establish the model of the SCB sequence for each satellite, and forecast the SCB regular and irregular terms, respectively, which avoids the problem that error accumulation increases sharply with the increase of the forecast span, in the simple quadratic prediction model,and improve the SCB prediction accuracy remarkably.

Acknowledgments The research is supported by the NSFC grant (11303073, 41574029, 11373057, 11133004), STCSM (06DZ22101). We thank GeoForschungsZentrum Potsdam (GBM) and SHAO Analysis Center (SHA) for providing the GPS SCB data.

References

1. Akaike H (1971) Autoregressive model fitting for control. Ann Inst Stat Math 23:163–180
2. Brockwell PJ, Davis RA (1996) Introduction to time series and forecasting. Springer, New York
3. Dai W, Jiao W, Li W (2009) Research on prediction of GPS B lock IIR (M) atomic clock error. J Geodesy Geodyn 29(4):111–115
4. Gao W, Lin Y, Chen G, Meng Y (2014) The performances assessment methods and results of in-orbit atomic clocks of BDS. J Geomatics Sci Technol 31(4):342–346
5. Guo H, Yang S, Yang Y (2007) Numerical prediction methods for clock difference based on two-way satellite time and frequency transfer data. Geomatics Inf Sci Wuhan Univ 32(1):43–46

6. Liu X, Wu X, Tian Y (2010) Study on atomic prediction of time based on interpolation model with tchebytchev polynomials. J Geodesy Geodyn 30(1):77–82
7. Liu Y, Dang Y, Zheng Z (2011) Study and improvement for the model in satellite clock error long-term forecast. Hydrographical Surveying Charting 31(2):21–23
8. Senior KL, Ray JR, Beard RL (2008) Characterization of periodic variations in the GPS satellite clocks. GPS Solution 12:211–225
9. Tang G, Xu X, Cao J, Liu X, Wang Q (2015) Precision analysis for Compass satellite clock prediction based on a universal clock offset model. Scientia Sinica Phys Mech Atronomica 45 (2):079502-1-6
10. Xu x, Zhou y (2010) Research on high accuracy prediction model of earth orientation parameters. J Spacecraft TT&C Technol 29(2):70–76
11. Xu XQ, Zhou YH, Liao XH (2012) Short-term earth orientation parameters predictions by combination of the least-squares, AR model and Kalman filter. J Geodyn 62:83–86
12. Zhang Q, Wang Y, Sun Y (2015) Performance analysis of atomic clocks on board BDS/GPS/GLONASS Satellites. Hydrographic Surveying Charting 35(2):62–67
13. Zhu L, Li C, Liu L (2009) Research on methods for prediction clock error based on domestic hydrogen atomic clock. J Geodesy Geodyn 29(1):148–151

Relative Navigation for LEO Spacecraft Using Beidou-2 Regional Navigation System

Leizheng Shu and Wenbin Wang

Abstract LEO spacecraft relative navigation method based on Beidou measurement is researched. A series of tri-frequency combinations have been investigated with the purpose to improve the success rate of double-difference carrier phase ambiguity fixing and relative navigation accuracy. The process algorithms for two kinds of approaches, the kinematic relative navigation approach, and dynamic relative navigation approach, are investigated. The ambiguity fixing performance and relative navigation accuracy are validated using the simulated Beidou-2 regional navigation system scenario. The results showed that the single frequency and wide-lane combination ambiguity fixed rate drops rapidly with increasing baseline length, but S0 ultra-wide-lane combination ambiguity can be 100 % accurately resolved under three different baseline lengths. Concern the relative navigation accuracy, single frequency carrier phase especially B1 carrier phase relative positioning accuracy is highest for short baseline. With the increase of baseline length, the advantage of Beidou multi-frequency ionospheric-free combination gradually revealed: when the baseline length increased to 220 km, the relative positioning accuracy of ionospheric-free combination can increase by 75 % at most.

Keywords Beidou-2 regional navigation system · LEO spacecraft · Relative navigation · Tri-frequency combination · Ambiguity fixing

L. Shu (✉) · W. Wang
Key Laboratory of Space Utilization, Technology and Engineering Center for Space Utilization, Chinese Academy of Sciences, Beijing 100094, China
e-mail: shuleizheng@csu.ac.cn

W. Wang
e-mail: wangwenbin@csu.ac.cn

© Springer Science+Business Media Singapore 2016

J. Sun et al. (eds.), *China Satellite Navigation Conference (CSNC) 2016 Proceedings: Volume III*, Lecture Notes in Electrical Engineering 390,
DOI 10.1007/978-981-10-0940-2_4

1 Introduction

GNSS-based spacecraft relative navigation is one of the most important technologies for on-orbit service and formation flying missions. At present, most of the in-orbit LEO spacecraft relative navigation depends on the GPS system. 1998, Japan's space agency (NASDA) demonstrated the GPS-based relative navigation technology for the first time in the ETS-VII mission [1]. German DLR and NASA launched the GRACE (Gravity Recovery and Climate Experiment) mission in 2002, which turns out to be the representation of the relative navigation research, see [2]. Kores et el. [3] adopted the dual-frequency GPS P code pseudorange and carrier phase observations in the reduced dynamic EKF filter to achieve the mm and mu m/s level of accuracy for relative position and velocity, respectively. In recent years, the successful in-orbit implementation of GPS-based relative navigation technology includes: Orbital Express [4] in 2007, PRISMA [5], and TanDEM-X/TerraSAR-X [6] in 2010. In October 2012, China's SJ-9 (Shi Jian-9 Formation Flight Mission) technology demonstration satellites were launched to perform the high precision GPS baseline measurement test [7].

China has launched the plan to expand its Beidou navigation system from the regional operation to global navigation system [8]. To research spacecraft relative navigation technology based on Beidou system is of great significance to improve the accuracy of orbit relative navigation, to enhance the safety of China's space mission autonomy and to extend the application of Beidou in space. Two kinds of Beidou-based LEO spacecraft relative navigation approaches, the kinematic relative navigation approach and dynamic relative navigation approach, are investigated in this article. A series of tri-frequency combinations have been investigated with the purpose to improve the success rate of double-difference carrier phase ambiguity fixing and relative navigation accuracy. The ambiguity fixing performance and relative navigation accuracy are validated using the simulated scenario.

2 Beidou Satellite System and Observation

2.1 Beidou Satellite

The Chinese Beidou navigation system is being gradually perfected in construction. A constellation composed of five geostationary Earth orbit (GEO) satellites, five inclined geosynchronous orbit (IGSO) satellites, and four Medium Earth orbit (MEO) satellites has been deployed by 2012 for providing regional navigation service.

By the end of 2020, China will complete the Beidou navigation satellite constellation, which consists of five GEO, three IGSO, and 27 MEO satellites. The MEO satellites will offer complete global coverage, similar to the GPS and GLONASS.

The IGSO and GEO satellites will improve the visibility and availability for users in China and neighboring regions. The GEO satellites are operating in orbit at an altitude of 35,786 km and positioned at 58.75°E, 80°E, 110.5°E, 140°E, and 160°E, respectively. The MEO satellites are operating in orbit at an altitude of 21,528 km and an inclination of 55° to the equatorial plane. The IGSO satellites are operating in orbit at an altitude of 35,786 km and an inclination of 55° to the equatorial plane [8].

2.2 Beidou Tri-frequency Observation

Beidou system provides three frequency signal, namely, B1, B2, and B3. Taking consideration of the following double-differenced carrier phase measurement equation:

$$\phi_i[m] = \rho + \lambda_i N_i - \left(\frac{f_1}{f_i}\right)^2 I_1 \tag{1}$$

where ϕ_i is the double-differenced phase measurement in meters; ρ is the double-differenced geometrical term which indicates the geometrical distance between receiver and Beidou satellite; λ_i is the wavelength in meters; N_i is the integer ambiguity; I_1 is the ionospheric delay on B1 in meters; and i is the frequency index.

For any integer coefficients i_1, i_2, and i_3, the linear combination which preserves the integer nature of the ambiguities is denoted as:

$$\varphi[cy] = i_1\varphi_1[cy] + i_2\varphi_2[cy] + i_3\varphi_3[cy] \tag{2}$$

By substituting Eq. (1) into Eq. (2) with consideration of the relation: $\phi_i\,[cy] = \phi_i\,[m]/\lambda_i$, one can show that this combination expressed in cycles:

$$\begin{aligned}\varphi[cy] = \rho \Big/ & \frac{1}{\frac{i_1}{\lambda_1} + \frac{i_2}{\lambda_2} + \frac{i_3}{\lambda_3}} + (i_1N_1 + i_2N_2 + i_3N_3) \\ & - \left(\frac{i_1\lambda_1 + i_2\lambda_2 + i_3\lambda_3}{\lambda_1^2}\right) I_1\end{aligned} \tag{3}$$

The resulting integer ambiguity $N = N(i_1, i_2, i_3)$, and the frequency $f = f(i_1, i_2, i_3)$ of this combination correspond to:

$$N(i_1, i_2, i_3) = i_1N_1 + i_2N_2 + i_3N_3 \tag{4}$$

$$f(i_1, i_2, i_3) = i_1f_1 + i_2f_2 + i_3f_3 = f_0(i_1k_1 + i_2k_2 + i_3k_3) \tag{5}$$

According to Cocard's definition, see [9], $k = i_1k_1 + i_2k_2 + i_3k_3$ is called the lane number, which uniquely defines the wavelength of every combination, regardless of any other properties of that combination. For Beidou system, k_1=763, k_2=620, k_3=590, corresponding to the frequency of B1, B3, and B2, respectively. The combination wavelength can be written as:

$$\lambda(i_1, i_2, i_3) = c/kf_0 \tag{6}$$

where base frequency f_0 = 2.046 MHz. We define the wide-lane combination as the resulting wavelength larger than the largest of the three base wavelengths, among which the ultra-wide-lane combinations are those with resulting wavelength larger than 2.93 m; the narrow-lane combinations are those with the resulting wavelength smaller than the smallest base wavelength.

If we assume that the noise on all three frequencies expressed in cycles is the same for all the phase measurements, a noise amplification factor n, with respect to cycles, corresponding to

$$n = \sqrt{i_1^2 + i_2^2 + i_3^2} \tag{7}$$

Taking the first-order ionospheric delay to be inversely proportional to the square of the frequency, we can derive the ionospheric delay amplification factor with respect to B1, q (in units of cycle), and κ (in units of meter) as:

$$q = \frac{1}{\lambda_1}(i_1\lambda_1 + i_2\lambda_2 + i_3\lambda_3) \tag{8}$$

$$\kappa(i_1, i_2, i_3) = \left(\frac{i_1\lambda_1 + i_2\lambda_2 + i_3\lambda_3}{\lambda_1^2}\right) \cdot \lambda(i_1, i_2, i_3) \tag{9}$$

Table 1 summarizes potentially interesting combinations and their relevant features. We regrouped all the possible combinations based on the sum s of i_1, i_2, and i_3.

An investigation of Table 1 leads to the following conclusions:

1. S0 region collects wide-lane and ultra-wide-lane combinations, which corresponds to large wavelength with a low ionospheric sensitivity.
2. S1*a* includes the combinations with the coefficient sum of 1 and small lane number. In this region, the wavelength is larger than 2.93 m, but the ionospheric amplification factor is about 2.3 with respect to cycles. If one considers the amplification factor κ with respect to meters, one obtains huge values since the wavelengths are large in this region.
3. S1*b* includes the combinations with the coefficient sum of 1 and large lane number. In this region, the wavelengths are about 10–12 cm, but they are insensitive to the ionosphere.

Table 1 Feature statistics of Beidou tri-frequency combination

Region	k	(i_1, i_2, i_3)	$\lambda(m)$	n	q	κ
S0	23	(1, −5, 4)	6.3707	6.4807	0.0197	0.6535
	30	(0, 1, −1)	4.8842	1.4142	−0.0626	−1.5921
	43	(1, −4, 3)	2.7646	5.0990	−0.0429	−0.6176
	143	(1, −1, 0)	1.0247	1.4142	−0.2306	−1.2304
	173	(1, 0, −1)	0.8470	1.4142	−0.2932	−1.2931
S1*a*	2	(−6, 15, −8)	73.2631	18.0278	2.1139	806.4319
	11	(−3, −2, 6)	13.3206	7	2.2980	159.3939
	18	(−4, 4, 1)	8.1403	5.7446	2.2158	93.9224
	41	(−3, −1, 5)	3.5738	5.9161	2.2355	41.6009
	48	(−3, −1, 5)	3.0526	6.4031	2.1532	34.2257
S1*b*	1252	(4, −1, −2)	0.1170	4.5826	0.1829	0.1114
	1282	(4, 0, −3)	0.1143	5	0.1203	0.0716
	1312	(4, 1, −4)	0.1117	5.7446	0.0578	0.0336
	1425	(5, −1, −3)	0.1028	5.9161	−0.1103	−0.0590
	1455	(5, 0, −4)	0.1007	6.4031	−0.1729	−0.0907

3 LEO Spacecraft Relative Navigation

Generally there are two kinds of method to implement the carrier differenced Beidou-based relative navigation: kinematic approach and (reduced) dynamic approach.

3.1 Recursive Least-Squares Kinematic Approach

The kinematic approach does not involve any satellite force models at all, and epoch-by-epoch relative positions are computed in purely kinematic mode by processing differential Beidou carrier phase measurements as the main observables.

The kinematic approach mainly implements least squares (LSQ) estimator to solve the ambiguity and the relative position parameters. Least square method can solve the single epoch ambiguity float solution and its covariance matrix, and then employ the LAMBDA method (see [10]) to search for integer solutions. But experiment results show that the single epoch ambiguity fixing success rate is not high, especially when observation noise is high and baseline length is large.

It should be noted that the ambiguities vector is constant in the absence of cycle slips or satellites setting and rising, thus it is possible to obtain a much improved float solution by carrying information from one epoch to the consecutive one. To implement this, a recursive LSQ estimator is developed to process the ambiguity estimate sequentially one epoch at a time. Figure 1 illustrates the algorithm flow

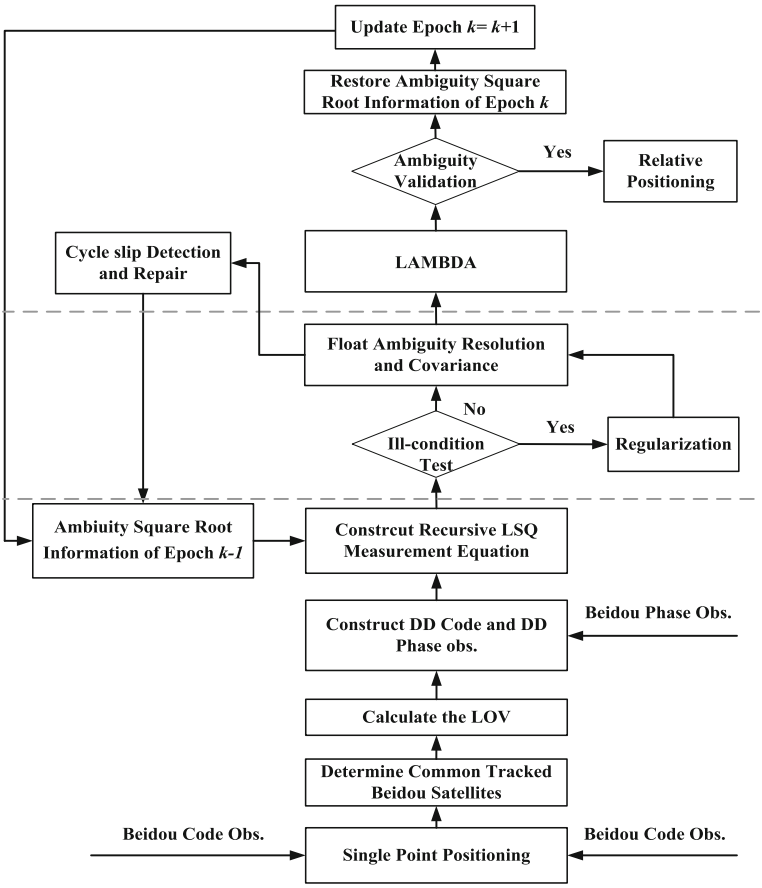

Fig. 1 Algorithm flow chart of the recursive LSQ procedure

chart of the recursive LSQ procedure: a posteriori ambiguity float solution at the previous epoch is exploited as a pseudo-measurement and passed forward to the functional model of the current epoch for improving the float estimates.

3.2 Reduced Dynamic Approach

The basic principle of reduced dynamic approach is: the spacecraft relative dynamic model is first used to calculate a reference relative orbit, and then the high precision Beidou observation is employed to correct the reference relative orbit, results in an optimal estimation of the relative state [11].

Figure 2 shows a conceptual flow chart of the filtering scheme. The Beidou relative navigation filter is implemented in four steps: the time update, the tracked

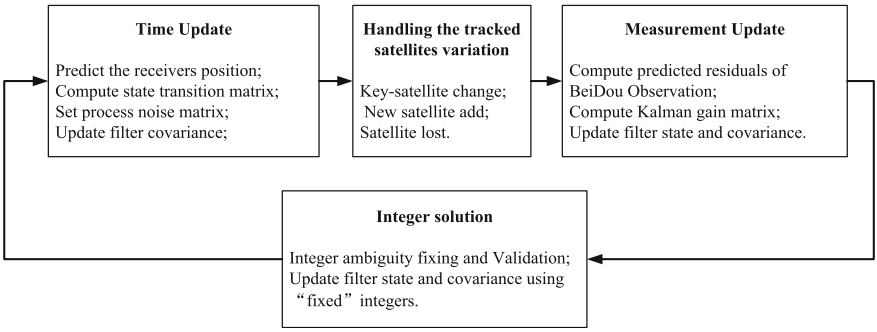

Fig. 2 Algorithm flow chart of the reduced dynamic procedure

satellites variation handling, the measurement update, and the integer solution. Reduced dynamic filter also estimates other parameters at the same time, such as ionospheric delay error, receiver clock error, and empirical acceleration parameter, to improve the fitting degree between the dynamic reference orbit and Beidou observed data.

Therefore the ambiguity float solution solved from the reduced dynamics approach is convergence faster, and the navigation results are smoother at the same time.

4 Simulation and Results

4.1 Simulation Scenario Settings

Simulated scenario is built to test the LEO spacecraft relative navigation performance of Beidou-2 regional navigation system. The Beidou constellation, consists of five GEO, five IGSO, and four MEO satellites, is set up according to the existing 14 satellites' orbit parameters. Figure 3 illustrates the sub-satellite points of the simulated constellation.

Formation spacecraft circles on the GRACE-type orbit, with the orbital inclination of 89° and radius of 6847.75 km. Three groups of simulation are carried out, with baseline length between formation satellites set to 10, 100, and 100 km, respectively. The rest simulation settings can be found in Table 2.

The Beidou satellites visible duration for the first formation spacecraft is given in Fig. 4. It can be seen that frequent tracked satellite variation occurred during 5 h simulation. Due to the less number of Beidou-2 regional navigation system, and the concentration distribution over the Asia-Pacific region, so only when the two spacecraft formation through the Asia-Pacific region can they synchronously observe more than five Beidou satellites. We only investigate the relative navigation performance during this region.

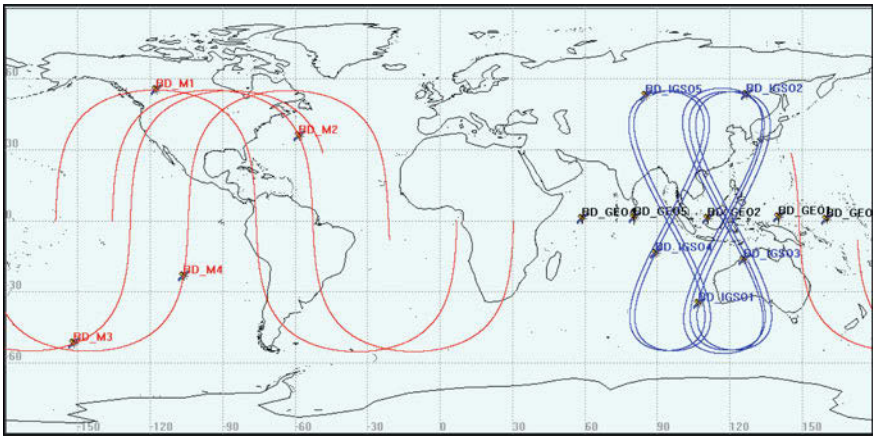

Fig. 3 Sub-satellite points of Beidou-2 regional navigation system

Table 2 The simulation scenario settings

Class	Parameter settings
Beidou constellation	5GEO + 5IGSO + 4MEO
Formation spacecraft	GRACE-type orbit ($i \approx 89°$, r = 6847.75 km) baseline length = 10, 100 and 220 km
Simulation duration	5 h
Simulation step size	1 s
Ionospheric model	CIM(China Ionospheric Model) the ionospheric delay for B1/B2/B3 is inversely proportional to the square of the corresponding frequency
Ambiguity	Fixing integer
Measurement noise	the code noise for B1/B2/B3 is set to 1 times the corresponding carrier wavelength; the phase noise for B1/B2/B3 is set to 0.025 times the corresponding carrier wavelength

4.2 Ambiguity Resolution Performance

The ambiguity resolution is investigated for S0 ultra-wide-lane combination (1, −5, 4), (0, 1, −1), and (1, −4, 3), S0 most used wide-lane combination (1, −1, 0), S1*a* ultra-wide-lane combination (−4, 4, 1) and B1 (1, 0, 0). Tables 3, 4, and 5 summarize the ambiguity success rate for three different methods: recursive LSQ kinematic method, reduced dynamic method, and the famous tri-frequency carrier phase ambiguity resolution method-TCAR.

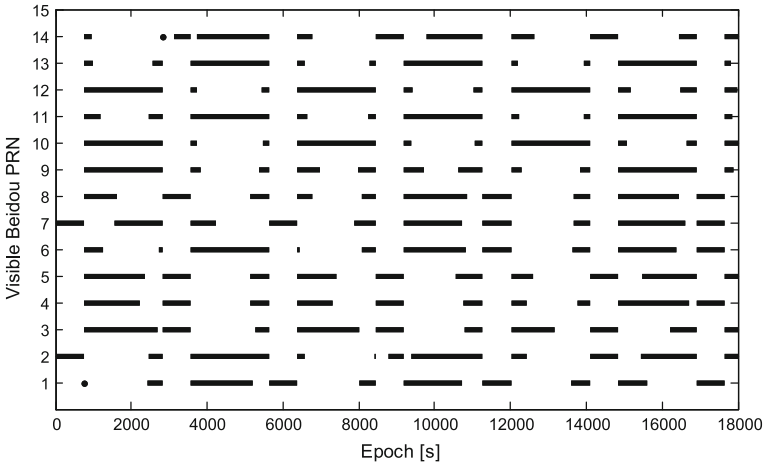

Fig. 4 The Beidou satellites visible duration

Table 3 Ambiguity success rate for recursive LSQ kinematic method

Baseline length	(1, −5, 4)	(0, 1, −1)	(1, −4, 3)	(1, −1, 0)	(−4, 4, 1)	(1, 0, 0)
10 km	100 %	100 %	100 %	100 %	100 %	100 %
100 km	100 %	100 %	100 %	100 %	99.4 %	99.4 %
220 km	100 %	100 %	100 %	100 %	60.97 %	60.88 %

Table 4 Ambiguity success rate for reduced dynamic method

Baseline length	(1, −5, 4)	(0, 1, −1)	(1, −4, 3)	(1, −1, 0)	(−4, 4, 1)	(1, 0, 0)
10 km	100 %	100 %	100 %	100 %	100 %	100 %
100 km	100 %	100 %	100 %	100 %	100 %	100 %
220 km	100 %	100 %	100 %	100 %	100 %	96.21 %

Table 5 Ambiguity success rate for TCAR method

Baseline length	(1, −5, 4)	(0, 1, −1)	(1, −4, 3)	(1, −1, 0)	(−4, 4, 1)	(1, 0, 0)
10 km	100 %	100 %	100 %	100 %	100 %	24.06 %
100 km	100 %	100 %	100 %	97.23 %	89.84 %	12.20 %
220 km	100 %	100 %	100 %	97.01 %	38.89 %	7.14 %

An analysis of Tables 3, 4 and 5 leads to the following conclusions:

1. S0 region ultra-wide-lane ambiguity can be accurately fixed under three different baseline length.
2. S1*a* ultra-wide-lane combination (−4, 4, 1) ambiguity can be 100 % fixed only under reduced dynamic method. The recursive LSQ kinematic method gets

worse success rate while the TCAR gets the worst. This is because even though the wavelength is large for this combination, the ionospheric amplification factor is magnificent. The reduced dynamic method can ensure the ambiguity convergence accurately because we use dynamics parameters to absorb those systemic error.

3. The B1 ambiguity fixing is challenging under long baseline. Even using the orbital dynamics information, the reduced dynamic method can only obtain B1 ambiguity success rate to 96.21 % under the baseline length 220 km.

4.3 Relative Positioning Precision

Figure 5 demonstrates the deviation of relative positioning using only B1 phase for the first 1500 s. Table 6 lists the corresponding ENU deviation statistics for 5 h.

Combined with Fig. 5 and Table 6, we can see that Beidou B1 relative positioning error increases with the increase of baseline length; Consider the ENU deviation, the East accuracy is always better than the North and Up direction. This

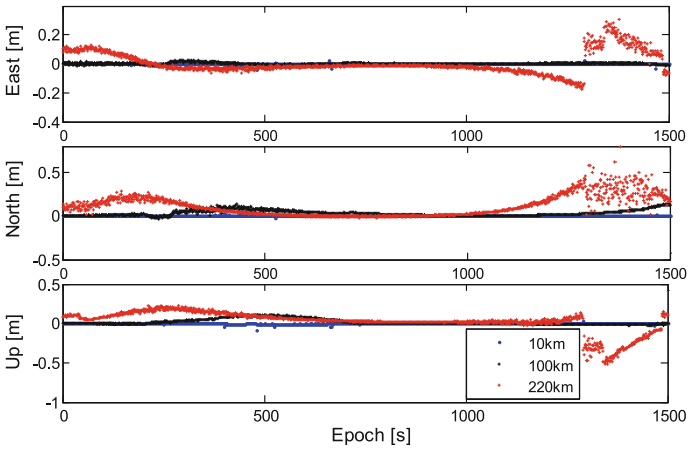

Fig. 5 The deviation of relative positioning using only B1 carrier phase (the first 1500 s)

Table 6 ENU deviation statistics for relative positioning using only B1 carrier phase (5 h)

Baseline length (km)	Mean (mm)			Std (mm)		
	East	North	Up	East	North	Up
10	−0.89	2.02	−1.30	5.05	3.86	6.47
100	1.88	32.14	17.69	5.99	31.52	35.01
220	5.68	109.69	18.58	74.19	113.93	131.21

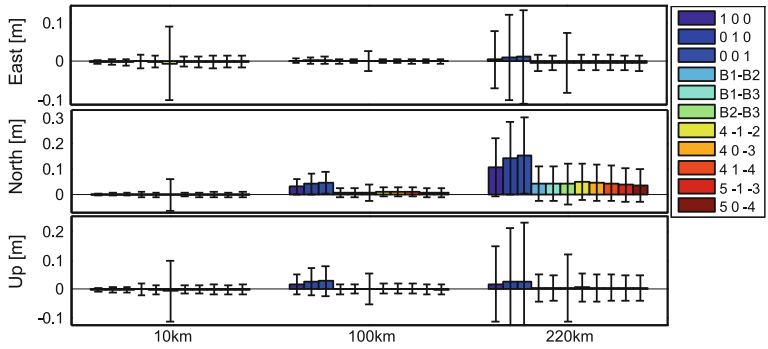

Fig. 6 The deviation of relative positioning using combine measurement (5 h)

can be explained from the Beidou observation geometry: when the formation flies across the Asia-Pacific region, the deployed GEO satellite increases the constraints on East–West direction.

Figure 6 summarizes the relative positioning deviations using different combinations observation. For each baseline length, the first three groups utilize the B1, B3, and B2 single frequency, group 4–6 are three ionospheric-free combinations, group 7–11 are narrow-lane combinations with repressive ionospheric chosen from S1*b* region. The results show that the relative positioning precision is higher using Beidou single frequency carrier phase, especially B1, under the condition of short baseline. With the increase of baseline length, the advantage of Beidou tri-frequency ionosphere-free/repressive combination gradually increases. When the baseline length increased to 220 km, the relative positioning accuracy of ionospheric-free combination can increase by 75 % at most.

5 Summary

A series of tri-frequency combinations have been investigated with the purpose to improve the success rate of double-difference carrier phase ambiguity fixing and relative navigation accuracy. The ambiguity fixing performance and relative navigation accuracy for Beidou-based LEO formation spacecraft are validated using the simulated scenario. The results reveal a variety of optional observation combinations which can be offered by Beidou system under different navigation algorithms and for different baseline length. Future work includes research in Beidou-based high dynamic attitude determination and positioning technology, as well as relative navigation algorithm based on multiple navigation system.

Acknowledgments This study is funded by the ‘Breeding Project’ of Innovation Academy, Chinese Academy of Sciences.

References

1. Mokuno M, Kawano I, Kasai T (1999) Experimental results of autonomous rendezvous docking on Japanese ETS-VII satellite. Guid Control 1999(101):P221–P238
2. Jaeggi A et al (2007) Precise orbit determination for GRACE using undifferenced or doubly differenced GPS data. Adv Space Res 39(10):P1612–P1619
3. Kroes R, Montenbruck O, Bertiger W et al (2005) Precise GRACE baseline determination using GPS. GPS Solutions 9(1):P21–P31
4. Weismuller TP, Leinz MR, Company TB (2006) GN&C technology demonstrated by the orbital express autonomous rendezvous and capture sensor system. American Astronautical Society guidance and control conference, Breckenridge, Co.
5. D'Amico S, Ardaens JS, Larsson R (2012) Spaceborne autonomous formation-flying experiment on the PRISMA mission. J Guid Control Dyn 35(3):P834–P850
6. Montenbruck O, Wermuth M, Kahle R (2011) GPS, based relative navigation for the TanDEM-X Mission—First flight results. Navig J Inst Navig 58(4):P293–P304
7. Chen P, Shu L, Ding R et al (2015) Kinematic single-frequency relative positioning for LEO formation flying mission. GPS Solutions 19(4):P525–P535
8. China Satellite Navigation Office (2013) BeiDou Navigation Satellite System Signal In Space Interface Control Document: Open Service Signal (Version 2.0)
9. Cocard M, Bourgon S, Kamali O et al (2008) A systematic investigation of optimal carrier-phase combinations for modernized triple-frequency GPS. J Geodesy 82(9):P555–P564
10. Teunissen PJG (1995) The least-squares ambiguity decorrelation adjustment: a method for fast GPS integer ambiguity estimation. J Geodesy 70(1–2):P65–P82
11. Wu SC, Yunck TP, Thornton CL (1991) Reduced-dynamic technique for precise orbit determination of low Earth satellites. J Guid Control Dyn 14(1):P24–P30

Analysis on Energy System Safety in GEO Satellite Complex Eclipse

Jinfei Chen, Xingyu Wang, Tao Wang and Ting Wang

Abstract The energy system is one of the key systems of satellite. Once the energy system fails, it can easily lead to failure of other systems. Therefore, the energy system safety is crucial to the satellite in orbit. For GEO satellites, the eclipse is a common astronomical phenomenon. When the satellite is in eclipse, due to the Earth or the Moon blocking the Sun, the energy of solar array will decline, the battery will discharge, and the operation mode of energy system will change. Especially, "*complex eclipse*", which is generated by the continuous alternate block of the Earth and the Moon, will bring the worse influence of satellite energy supply, easily leading to failure of satellite. Therefore, to analyze the impact of complex eclipse to the energy system, safety is quite necessary. First, this paper describes the principles of complex eclipse, GEO satellite energy system and the influence to the energy system caused by the complex eclipse, furthermore determines the relationship between eclipse and the operation mode of energy system, analyzes the energy system safety in GEO satellite complex eclipse, establishes the reasonable disposal strategy based on the result, and applies it. The conclusions show that, the eclipse does affect the energy system of GEO satellite; the method given by this paper is to ensure the energy system safety in GEO satellite complex eclipse with practical value.

Keywords GEO satellite · Eclipse · Energy system safety · Disposal strategy

J. Chen (✉)
Key Laboratory for Fault Diagnosis and Maintenance of Spacecraft in Orbit,
710043 Xi'an, China
e-mail: chen2jin3fei1@163.com

X. Wang · T. Wang · T. Wang
Xi'an Satellite Control Center, 710043 Xi'an, China
e-mail: wxyyx_001@sina.com

T. Wang
e-mail: wang1tao1@163.com

T. Wang
e-mail: wang2ting2@163.com

© Springer Science+Business Media Singapore 2016

J. Sun et al. (eds.), *China Satellite Navigation Conference (CSNC) 2016 Proceedings: Volume III*, Lecture Notes in Electrical Engineering 390,
DOI 10.1007/978-981-10-0940-2_5

1 Introduction

Energy System is one of the core critical systems of satellite, which is mainly constituted by a number of hardware components such as the power produce, power storage, power control, voltage transformation, supply distribution, etc. A large number of fault cases statistical results showed that: the failure of GEO satellites in orbit occurred, the energy system failures account for a large proportion. Especially in the eclipse, due to the effect of the Earth or the Moon obscured the sun for solar array, there is not sufficient power to provide, the battery must discharge to replenish the energy satellite required. When the satellite desired energy consumption exceeds the stored battery power, it will lead to serious consequences that the whole satellite lacks of power, which fails easily. It is quite essential to make an accurate estimate of energy consumption required in eclipse for satellite, to take the necessary avoidance strategy against dangerous situations that may occur [1]. Aiming to a bad case that eclipse shadow caused by the combined effect of the Earth and the Moon, this paper proposed a method of GEO satellite energy system analysis, which can not only predict eclipses occlusion, but also estimate the eclipse of satellite energy consumption. At present, the method has been applied in the actual management of GEO satellite.

2 Fundamental

2.1 Principle and Calculation Model of Eclipse

Eclipse is a kind of astronomical phenomena which is occurred when the Moon or the Earth blocks sunshine to the satellite. Eclipse includes two cases which depend on the blocker is the Earth or the Moon. The Earth eclipse generates because the Earth blocks the sunshine, it took place in spring and autumn every year fixedly, the time span is usually 23 days around the vernal equinox or the autumnal equinox, so the Earth eclipse lasts about 92 days each year. The principle of the Moon eclipse is similar to the Earth eclipse, it generates because the Moon blocks the sunshine. Compared with the Earth eclipse, there is no law of the Moon eclipse. That is because the Moon eclipse is the result of Earth–-Sun revolution, Moon–Earth revolution, and the Earth rotation combined effect. Generally speaking, the Moon eclipse often occurs around the first day of lunar month [2].

One single eclipse process generally contains three stages “penumbra—umbra—penumbra”, uses method based on space visual field to calculate eclipses commonly, which sets the spatial position of the satellite as a reference point of the visual field, by calculating the relative visual angle of the Sun, the Earth, and the Moon to the reference point, to achieve the calculation of eclipse time, eclipse phase [3].

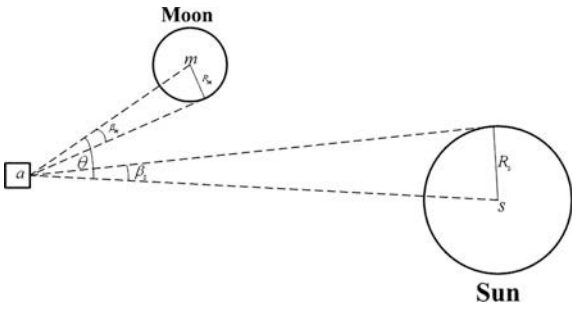

Fig. 1 Principle of eclipse

Take the Moon as the blocker in the discussion of the eclipse's principle, in the J2000 coordinate system as shown in Fig. 1, the position vector of the satellite is $\mathbf{r}_a = [X_a \quad Y_a \quad Z_a]^T$, the position vector of the Sun is $\mathbf{r}_s = [X_s \quad Y_s \quad Z_s]^T$, the position vector of the Moon is $\mathbf{r}_m = [X_m \quad Y_m \quad Z_m]^T$. Therefore

$$\begin{cases} \overrightarrow{as} = \mathbf{r}_s - \mathbf{r}_a = \begin{bmatrix} X_s - X_a \\ Y_s - Y_a \\ Z_s - Z_a \end{bmatrix} \\ \overrightarrow{am} = \mathbf{r}_m - \mathbf{r}_a = \begin{bmatrix} X_m - X_a \\ Y_m - Y_a \\ Z_m - Z_a \end{bmatrix} \end{cases} \tag{1}$$

The visual radius of the Sun is R_s, the visual radius of the Moon is R_m. The visual half field angle of satellite to the Sun is β_s, the visual half field angle of satellite to the Moon is β_m. Therefore

$$\begin{cases} \beta_s = \arcsin\left(\dfrac{R_s}{\sqrt{(X_s - X_a)^2 + (Y_s - Y_a)^2 + (Z_s - Z_a)^2}}\right) \\ \beta_m = \arcsin\left(\dfrac{R_m}{\sqrt{(X_m - X_a)^2 + (Y_m - Y_a)^2 + (Z_m - Z_a)^2}}\right) \end{cases} \tag{2}$$

defines the space angle between vector $\overrightarrow{as}$ and vector $\overrightarrow{am}$ which is θ, therefore

$$\theta = \arccos\left(\frac{\overrightarrow{as} \cdot \overrightarrow{am}}{\left|\overrightarrow{as}\right| \cdot \left|\overrightarrow{am}\right|}\right) \tag{3}$$

So that summarized the judgment basis of the Moon eclipse:

1. When $\theta \geq \beta_s + \beta_m$, there is no eclipse;
2. When $|\beta_s - \beta_m| \leq \theta < \beta_s + \beta_m$, there is penumbra;
3. When $\theta < |\beta_s - \beta_m|$, there is umbra.

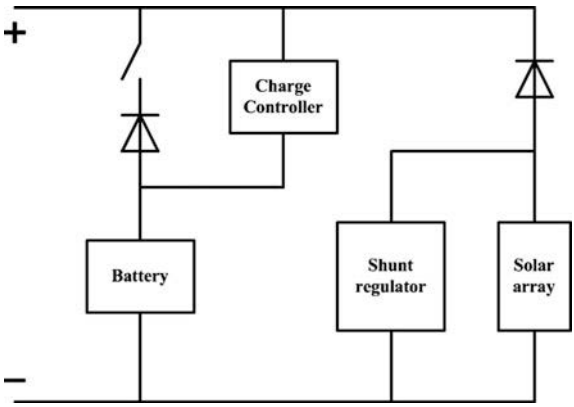

Fig. 2 Structure of GEO satellite energy system

2.2 Introduction of GEO Satellite Energy System

Currently, the vast majority GEO satellites in orbit are designed using the solar array and the batteries as the energy supply.

Figure 2 shows that, GEO satellite energy system consists of solar array, battery, shunt regulator, and charge controller. According to its design, the solar array provides energy to the satellite payload, charges the battery at the same time in illumination. The battery provides energy to the satellite payload in eclipse.

As the input source, the array is exposed to the cosmic vacuum environment, its output could be effected by the incident light intensity, ambient temperature, load power, etc., [4] so that it would lead to a certain amplitude fluctuation. In order to adapt to and regulate the illumination, the shunt regulator is designed to handle the excessive power of solar array. In the illumination, when the solar array output power is greater than satellite payload power consumption, the excessive power is used to replenish the battery; the shunt regulator here is regulating the battery charging current. In the eclipse, the output of solar array decreases because of the block, the shunt current also decreases. When the shunt current drops to zero, which represents the solar array's energy output which is not sufficient to support the satellite, the battery starts to provide energy to the satellite under the control of charge controller.

2.3 The Impact of Eclipse to the Energy System

It is easy to summarize from the above analysis that, there will be two cases of satellite energy supply in eclipse as following: one is the eclipse does not lead shunt current to decrease to zero, in which case the satellite solar array will continue to be used as energy supply, battery does not discharge; the other is the eclipse which

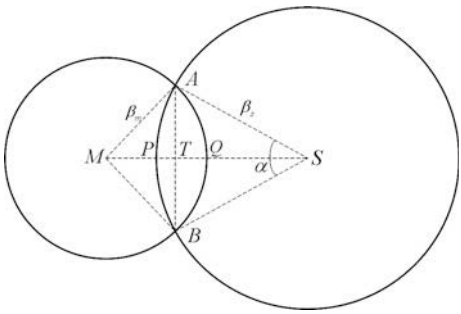

Fig. 3 Model of the Moon eclipse

does lead shunt current to decrease to zero, in which case the satellite will start to use battery as an energy supplement reinforcement, the battery discharges.

Apparently, there is a certain relationship between blocked area and the energy supply mode switch. Therefore, a reasonable solution is to start form the blocked area in eclipse, establish the relationship between blocked area and the energy supply mode switch, so that to forecast the mode switch of energy supply [5, 6].

The model of Moon eclipse shown in Fig. 3 is the example to discuss. The block area W is surrounded by the arc $\overset{\frown}{APB}$ and arc $\overset{\frown}{AQB}$, the area is divided into two parts by the string $\overline{AB}$: one is W_1, surrounded by arc $\overset{\frown}{APB}$ and string $\overline{AB}$; the other is W_2, surrounded by arc $\overset{\frown}{AQB}$, and string $\overline{AB}$. Make the area of sector $APBS$ as W_{APBS}, the area of triangle ABS is W_{ABS}, the central angle is α.

Segment MS is a short arc of circle, which passes through the center of Sun and Moon, takes the satellite as center. As θ is a little angle, it can be approximated as $\overline{AB} \approx \overset{\frown}{MS} = \theta$, the length of arc and string is equal.

According to the law of cosines, in triangle ΔABS

$$\cos\frac{\alpha}{2} = \frac{\beta_s^2 + \theta^2 - \beta_m^2}{2\beta_s\theta} \tag{4}$$

in triangle ΔATS

$$\cos\frac{\alpha}{2} = \frac{TS}{\beta_s} \tag{5}$$

according to the simultaneous equation

$$TS = \frac{\beta_s^2 + \theta^2 - \beta_m^2}{2\theta} \tag{6}$$

so

$$\begin{cases} W_{APBS} = \frac{1}{2}\alpha\beta_s^2 = \arccos\left(\frac{TS}{\beta_s}\right)\beta_s^2 \\ W_{ABS} = \frac{1}{2}\overline{AB} \times \overline{TS} = TS\sqrt{\beta_S^2 - TS^2} \\ W_1 = \arccos\left(\frac{TS}{\beta_s}\right)\beta_s^2 - TS\sqrt{\beta_s^2 - TS^2} \end{cases} \tag{7}$$

similarly

$$W_2 = \arccos\left(\frac{\theta - TS}{\beta_m}\right)\beta_m^2 - (\theta - TS)\sqrt{\beta_s^2 - TS^2} \tag{8}$$

so that the block area is

$$\begin{aligned} W &= W_1 + W_2 \\ &= \arccos\left(\frac{TS}{\beta_s}\right)\beta_s^2 - TS\sqrt{\beta_s^2 - TS^2} \\ &\quad + \arccos\left(\frac{\theta - TS}{\beta_m}\right)\beta_m^2 - (\theta - TS)\sqrt{\beta_s^2 - TS^2} \\ &= \arccos\left(\frac{TS}{\beta_s}\right)\beta_s^2 + \arccos\left(\frac{\theta - TS}{\beta_m}\right)\beta_m^2 - \theta\sqrt{\beta_s^2 - TS^2} \end{aligned} \tag{9}$$

brings formula (6) in

$$\begin{aligned} W = &\arccos\left(\frac{\beta_s^2 + \theta^2 - \beta_m^2}{2\theta\beta_s}\right)\beta_s^2 + \arccos\left(\frac{\beta_m^2 + \theta^2 - \beta_s^2}{2\theta\beta_m}\right)\beta_m^2 \\ &- \theta\sqrt{\beta_s^2 - \left(\frac{\beta_s^2 + \theta^2 - \beta_m^2}{2\theta}\right)^2} \end{aligned} \tag{10}$$

When the satellite in illumination, the energy is provided by the solar array, the battery does not discharged. Suppose the load current of satellite is I_1, the shunt current is I_2, the total current which is outputted by solar array is $I = I_1 + I_2$. When the satellite is in eclipse, the total current decreases to I', which is

$$I' = I\left(1 - \frac{W}{\pi\beta_s^2}\right) \tag{11}$$

Make $\varepsilon = \frac{W}{\pi\beta_s^2}$, the relationship between blocked area and the energy supply mode switch is established:

1. When $I' \geq I_1$, which is $\left(1 + \frac{I_2}{I_1}\right)(1 - \varepsilon) \geq 1$, the battery does not discharge, the mode of energy system does not switch;
2. When $I' < I_1$, which is $\left(1 + \frac{I_2}{I_1}\right)(1 - \varepsilon) < 1$, the battery does discharge, the mode of energy system does switch.

3 Analysis of GEO Satellite Energy in Complex Eclipse

Before the autumn eclipse of a GEO satellite comes in 2015, use the above principle to analysis the energy system as following:

3.1 Eclipse Forecasts

Use the method based on space visual field to forecast autumn eclipse of the GEO satellite in 2015, the result shows that: the eclipse starts in Aug. 30th, ends in Oct. 16th, including three eclipse blocks caused by the Moon. Parts of the results are shown in Table 1.

3.2 Energy Analysis in Eclipse

To facilitate discussion, this paper only discussed in detail the status tail of north energy system in satellites, south part is similar.

Table 1 Parts of the result of eclipse forecast in 2015 autumn

Blocker	Start time	End time
The Earth	2015-08-30 02:37:12	2015-08-30 02:44:16
The Earth	2015-09-13 02:03:23	2015-09-13 03:08:45
The Moon	**2015-09-13 05:21:11**	**2015-09-13 06:03:10**
The Moon	**2015-09-13 14:03:23**	**2015-09-13 14:15:22**
The Earth	2015-10-13 02:10:01	2015-10-13 02:45:02
The Moon	**2015-10-13 17:31:17**	**2015-10-13 21:17:10**
The Earth	2015-10-14 02:12:48	2015-10-14 02:41:51
The Earth	2015-10-16 02:24:27	2015-10-16 02:29:38

3.2.1 Sep. 13th 05:21:11

1. Forecast the blocked area
   Using the orbit of Aug. 28th 2015, set a calculation point every two seconds, calculate the blocked area W, sketch $\varepsilon = \frac{W}{\pi\beta_s^2}$. The abscissa represents time, the ordinate represents the percentage of blocked area.
2. Establish an initial state of energy system
   As introduced in Sect. 2.1, the eclipse caused by the Earth is regular and repeatable. Using data mining algorithms, extract the telemetry parameters in every Spring and Autumn eclipse from 2013 to 2015, summarize the key parameter values of energy system to establish initial state of energy system in this eclipse.
3. Determine the discharging state of battery
   Since an initial state of energy system has been established, it is certain that $\frac{I_2}{I_1+I_2} \approx 27.8\,\%$. So, that when $\varepsilon = \frac{W}{\pi\beta_s^2} > \frac{I_2}{I_1+I_2} \approx 27.8\,\%$, the battery will discharge. As shown in Fig. 4, the shadow area is discharge capacity of battery. Calculate the area with integration, the discharge capacity of north battery is 2.325 A·h.
4. Forecast the battery's status
   This eclipse of the Moon starts about 2 h later since the last eclipse ends, it is a typical "complex eclipse". Since the battery would discharge, it is necessary to determine the battery's status before eclipse occurs. According to the managing files of this GEO satellite: if "North battery pressure 1" or "North battery pressure 2" is less than 4.9, it will be certain that the battery is not full. According to the value in Table 2, before the eclipse occurs, the capacity of battery has been charged approximately 85.4 %.
5. Conclusions of energy system
   Before the eclipse occurs, the battery is not fully charged, the capacity of battery is approximately 85.4 %. During the eclipse, the battery will discharge about 2.325 A·h. According to the managing files of this GEO satellite: the capacity of fully charged battery is 30 A·h, the warning percent of discharging is 73 %.

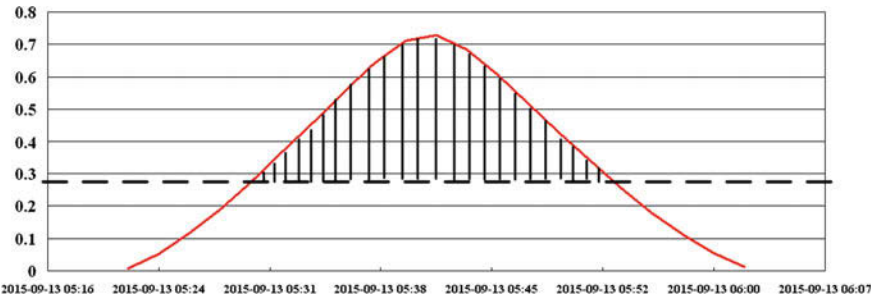

Fig. 4 Curve: the forecast proportion of block and discharge capacity in 05:21:11, 09-13-2015

Table 2 Initial state forecast of north energy system and battery

Parameter	Value	Parameter	Value
North main bus voltage	41.814	North battery voltage	38.784
North main bus load current	19.4025	North battery pressure 1(P1)	4.183
North shunt current	7.4852	North battery pressure 2(P2)	4.208

Table 3 Initial state forecast of north energy system

Parameter	Value
North main bus voltage	42.016
North main bus load current	21.105
North shunt current	12.693

In this eclipse, the battery will discharge about 9.1 %, which is far less than the warning percent, so the conclusion is energy system is safe, no need to take action.

3.2.2 Sep. 13th 14:03:23

1. Forecast the blocked area
2. Establish an initial state of energy system (Table 3)
3. Determine the discharging state of battery
   Since an initial state of energy system has been established, it is certain that $\frac{I_2}{I_1+I_2} \approx 37.6\,\%$. So that when $\varepsilon > 37.6\,\%$, the battery will discharge. As shown in Fig. 5, the largest percent of block is less than 0.8 %, which is far less than the switch value, so that the battery will not discharge at all.
4. Conclusions of energy system
   Since the battery will not discharge at all, the conclusion is energy system is safe, no need to take action.

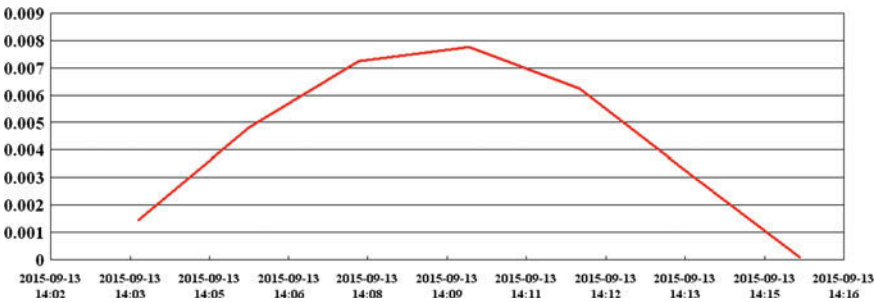

Fig. 5 Curve: the forecast proportion of block in 14:03:23, 09-13-2015

3.2.3 Oct. 13th 17:31:17

1. Forecast the blocked area
2. Establish an initial state of energy system
3. Determine the discharging state of battery
   Since an initial state of energy system has been established, it is certain that $\frac{I_2}{I_1+I_2} \approx 40.6\,\%$. So that when $\varepsilon > 40.6\,\%$, the battery will discharge. As shown in Fig. 6, the shadow area is discharge capacity of battery. Calculate the area with integration, the discharge capacity of north battery is 8.921 A·h.
4. Forecast the battery's status
   This eclipse of the Moon starts about 15 h later since the last eclipse ends, it is also a typical "complex eclipse". As shown in Table 4, before the eclipse occurs, the battery has been fully charged.
5. Conclusions of energy system
   Before the eclipse occurs, the battery is fully charged. During the eclipse, the battery will discharge about 8.921 A·h. In this eclipse, the battery will discharge about 29.7 %, which is less than the warning percent, so the conclusion is energy system is safe, no need to take action.

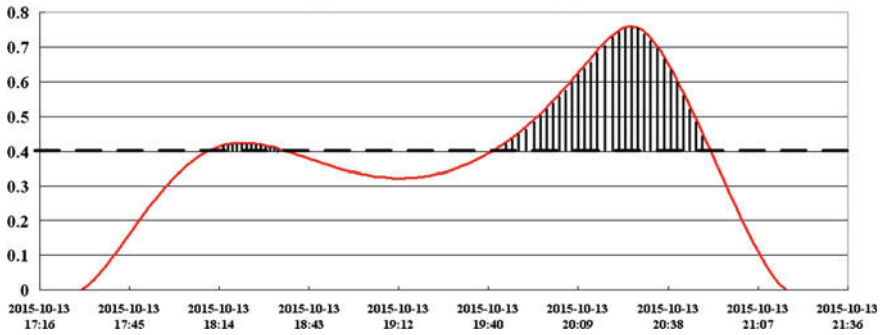

Fig. 6 Curve: the forecast proportion of block and discharge capacity in 17:31:17, 10-13-2015

Table 4 Initial state forecast of north energy system and battery

Parameter	Value	Parameter	Value
North main bus voltage	42.016	North battery voltage	38.986
North main bus load current	20.040	North battery pressure 1(P1)	4.980
North shunt current	13.669	North battery pressure 2(P2)	5.028

3.3 Disposal Strategy for the Eclipse

According to forecast results, the three eclipses in 2015 Autumn will not cause serious impact to the energy system of satellite, so no strategy should be carried out.

According to the analysis, the nature of the serious impact in eclipse is that satellite energy system is insufficient to support the energy consumption of satellite. So, for the serious situation, it is recommended to carry out the strategy such as "switch on the large charging current to increase battery capacity" or "shut down some load to decrease the consumption of energy".

4 Verification of the Analysis in Complex Eclipse

In order to verify the correctness of the analysis and strategy above, use the actual telemetry of satellite during the eclipse in 2015 autumn for inverse calculation.

4.1 Sep. 13th 05:21:11

1. The status of battery discharging
   As shown in Fig. 7, north battery did discharge during the eclipse, the peak value of discharge current is nearly 20 A.
2. The initial status of battery and capacity of discharge
   As shown in Table 5, before this eclipse occurred, the north battery is not fully charged, the capacity is about 90 %. During the eclipse, the north battery discharged about 3.2 %.
3. Analysis of Error
   According to the actual telemetry, it is obvious that energy analysis is correct and effective, it did forecast the discharge, but there is an error about the capacity of discharge, which cannot be ignored. The reason of error as

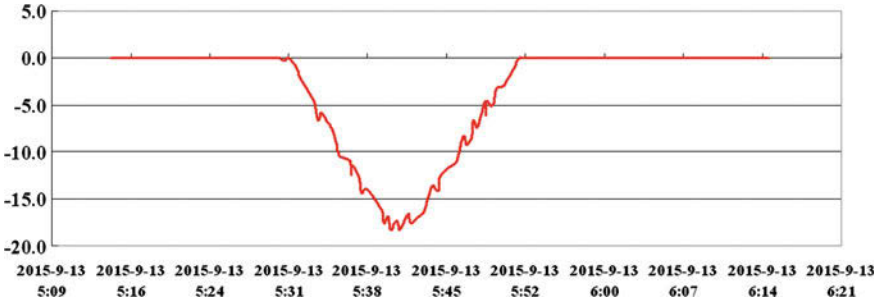

Fig. 7 Curve: discharge current in 05:21:11, 09-13-2015

Table 5 Comparison of the actual and forecast value of north battery's initial state and discharge situation

Parameter	Forecast Value	Actual Value	2015-09-13 05:21:11	2015-09-13 06:03:10
North battery voltage	38.784	38.784	38.784	38.178
North battery pressure 1(P1)	4.183	4.417	4.417	4.27636
North battery pressure 2(P2)	4.208	4.4129	4.4129	4.28996

following: first, this GEO satellite was launched in 2012, it only experienced two Autumn eclipses, such little raw data accumulated. So, that it is easy to bring about error by using data mining algorithms; second, the forecast discharging capacity is based on the forecast value of battery's initial state, it is certain that the errors will be amplified.

4.2 Sep. 13th 14:03:23

As shown in Fig. 8, north battery did not discharge during the eclipse at all.

4.3 Oct. 13th 17:31:17

1. The status of battery discharging
   As shown in Fig. 9, north battery did discharge during the eclipse, the peak value of discharge current is over 20 A.
2. The initial status of battery and capacity of discharge
   As shown in Table 6, before this eclipse occurred, the north battery has been fully charged. During the eclipse, the north battery discharged about 3.1 %.

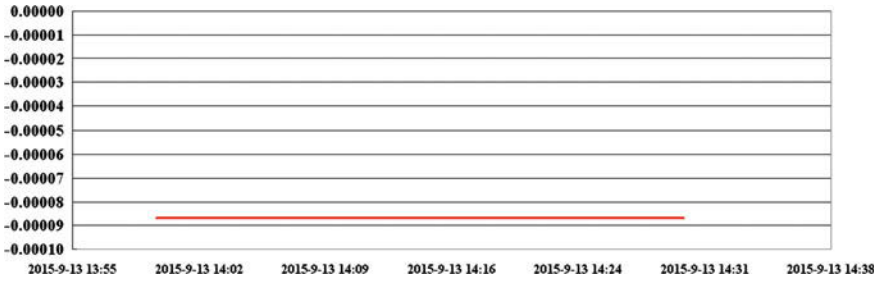

Fig. 8 Curve: discharge current in 14:03:23, 09-13-2015

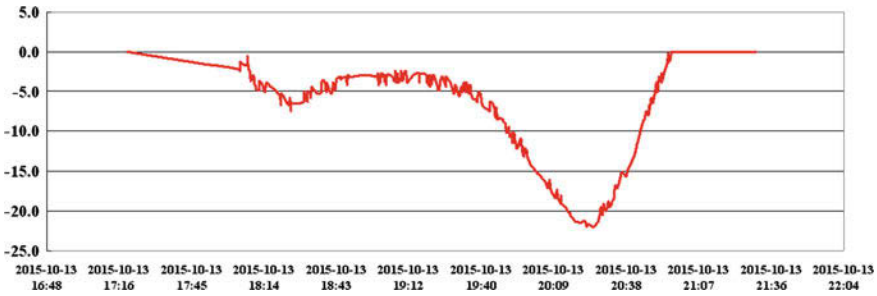

Fig. 9 Curve: discharge current in 17:31:17, 10-13-2015

Table 6 Comparison of the actual and forecast value of north battery's initial state

Parameter	Forecast value	Actual value	2015-10-13 17:31:17	2015-10-13 21:17:10
North battery voltage	38.986	38.986	38.986	36.562
North battery pressure 1(P1)	4.980	4.97956	4.97956	3.4794
North battery pressure 2(P2)	5.028	5.0276	5.0276	3.51134

3. Analysis of Error
   According to the actual telemetry, it is obvious that energy analysis is correct and effective, it did forecast the discharge, it also forecasted the capacity of discharge. As shown in Table 1, this eclipse starts about 15 h later since the last eclipse ends. According to the periodicity and repeatability of the Earth eclipse, the status of battery is stable, which minimize the error.

5 Conclusion

In this paper, a method of energy system safety analysis was proposed, in order to solve the practical problems in GEO satellite management. The method not only can predict the switch of energy system work mode, but also can give a specific forecast values. By applying this analysis and disposal strategy for a GEO satellite in 2015 Autumn eclipse, its correctness and validity has been proved. For the tiny error of forecast, this paper also proposed the reason and would handle it in future work. Currently, this method has been widely used in management of GEO satellites and achieved good results.

Acknowledgments Thanks for the guidance and help provided by Mr. Li Jianyong, Miss Chen Xiaohong, and Mr. Yin Wei.

References

1. Chen F, Jia N (1992) Satellite control manual. Science Press, Beijing
2. Li Y, Zhang Y, Yi K (2005) On celestial body impacts on geostationary satellite. Flight Dyn 23(4):P79–P85
3. Ding J, Qu F, Wei Z et al (2010) Calculating and analysis of satellite umbra based on cartesian coordinate. Sci Survey Map 35(1):P39–P41
4. Zheng J, Chen H, Li Y (2011) Algorithm analysis on energy system state switch time accurate prediction in GEO satellite eclipse. Aerospace Shanghai 28(5):P30–P33
5. Zhang S, Cao X (2001) Calculating method of satellite energy and exit positions and times through Umbra/Penumbra. Aerospace Shanghai (6):P19–P22
6. Yuan M, Shen X, Sun N (2007) Eclipse impacts analysis on energy of satellite. Sci Technol Eng 7(17), P4535–P4527

Autonomous Orbit Determination Method Based on Inter-satellite Doppler Measurement

Kui Lin, Wende Huang, Zhuli Hu, Jianwei Yang and Fanghong Huang

Abstract The autonomous orbit determination of satellite is the premise and the important guarantee of the satellite system to accomplish many space missions, and it is also an important guarantee to improve the security of the satellite system, especially during the wartime. There are many methods for satellite autonomous orbit determination. Since the relative motion of two satellites will produce Doppler Effect, this paper attempts to study the autonomous orbit determination method based on inter-satellite Doppler measurement. First, the autonomous orbit satellite system is established by STK simulation, and the satellite orbit data are generated as the reference orbit of the autonomous orbit. According to the extended Kalman filter theory, an autonomous orbit determination simulation platform is built. The experimental results show that when the observation error is random noise on the order of 0.001 m/s, the URE of orbit determination result is decimeter for 7 days; when the sinusoidal amplitude error of the reference satellite R, T, and N direction is 0.5, 1.0, and 1.0 m, the MEO satellite orbit determination URE is decimeter and the GEO satellite fixed rail URE is at meter level, which proves that using the inter satellite Doppler shift as the measurement of autonomous orbit determination is feasible for medium and high orbit satellite.

Keywords Doppler measurement · Autonomous orbit determination · Kalman filter

1 Introduction

Accurate determination of the satellite orbit is a prerequisite for the success of the satellite to complete its mission. The satellite autonomous orbit determination technology research has become the focus of the common concern of mankind.

K. Lin (✉) · W. Huang · Z. Hu · J. Yang · F. Huang
College of Mechanical Engineering and Automation, National University of Defense Technology, Changsha 410073, China
e-mail: LinkuiNudt@163.com

© Springer Science+Business Media Singapore 2016

J. Sun et al. (eds.), *China Satellite Navigation Conference (CSNC) 2016 Proceedings: Volume III*, Lecture Notes in Electrical Engineering 390,
DOI 10.1007/978-981-10-0940-2_6

The autonomous orbit determination of the satellite is actually determining the satellite orbit depending on the measurement equipment mounted on the satellite without ground support. The scope of future application of this technology in civil and military fields is extremely broad [1–3]. Some achievements have been made in the research of autonomous orbit determination, and the technology based on astronomical observation, sensor, global navigation satellite system, and inter-satellite link have been widely studied [4].

At the end of 1980s, French began to develop DORIS (Doppler Orbitography and Radio-positioning Integrated by Satellite) system, using Doppler principle, through the Doppler frequency shift measurement to achieve the precise measurement for LEO satellite orbit. The DORIS system uses a single pass dual frequency speed measurement system, and the satellite receiver measures the Doppler integral of a period of time (about 10 s) relative to the ground observation station, and then converts it into a mean distance change rate [5–7]. Internationally, the research of DORIS system has been more mature. DORIS system's real time autonomous orbit determination is completed by a real-time autonomous orbit determination software which is composed of a satellite receiver DIODE (DORIS Immediate on-board Orbit Determination). The radial precision of the orbit determination is centimetre level, and the accuracy of 3D is decimetre level [8–10].

DORIS system is only applicable to the orbit determination of low orbit satellite, and its successful operation shows that the satellite orbit determination by using Doppler theory is of great value. For the medium and high orbit satellite, if we use the DORIS ground observation station for orbit determination directly, there will be some problems: for example, the observation geometry is poor. At present, there are few researches using Doppler measurements to determine the orbit of MEO and GEO satellites autonomously. This paper mainly discusses the feasibility of medium and high orbit satellite autonomous orbit determination using the inter-satellite Doppler shift as the observation. First, the autonomous orbit determination satellite system is built by STK simulation, and the satellite orbit data is generated, which is used as the reference orbit of the autonomous orbit determination; then, based on the extended Kalman filter theory, the autonomous orbit determination simulation platform is built, and the orbit determination of the medium and high orbit satellite is realized. Finally, some useful conclusions are made.

2 Characteristics of Inter-satellite Doppler Shift

2.1 Doppler Shift Calculation

In 1842, Austrian physicist Kristen Doppler found that when there is relative radial motion between the source and the receiver, the frequency received by the receiver will be different from the source frequency. This phenomenon is known as the Doppler Effect. The Doppler Effect exists in the propagation of continuous wave

propagation, such as acoustic wave, radio waves, and light waves [11]. The additional frequency shift caused by the Doppler Effect is called the Doppler shift, which is the difference between the frequency of the received signal and the transmit frequency.

If there is a relative motion between two satellites, and mutually observed, the two satellites will produce the Doppler shift. During the satellite motion, the Doppler shift of the receiver is counted, if the time interval is ΔT, the Doppler shift during the ΔT is counted as N, Doppler shift f_d is:

$$f_d = \frac{N}{\Delta T} \tag{1}$$

The relationship between the Doppler shift and the change rate of distance is:

$$v = \frac{\rho_2 - \rho_1}{\Delta T} = -\frac{c}{f_s}(f_d - \Delta f) \tag{2}$$

In the formula, ρ_1 and ρ_2 are two moments of the inter-satellite distance; c is the speed of light; f_s is the transmitting frequency; Δf is the difference between transmitting frequency and receiving frequency.

2.2 Doppler Shift Analysis

Through the STK software, the simulation scenario of autonomous orbit determination system was established. The Walker constellation (24/3/1) was established as the benchmark for other undetermined orbit satellites. There are three orbital planes in the constellation, and each plane is composed of 8 MEO satellites whose orbit heights were 21,528 km. In the distributed autonomous orbit determination mode, the Doppler observation link is established with the reference satellite of different orbits. In this paper, the orbit determination performance of single star is mainly analyzed. The name of the reference satellite is the "MEO + orbital plane number + satellite number inside the orbital plane". The orbital plane number is 1–3, and the satellite number inside the orbital plane is 1–8. For example, "MEO12" is on behalf of the second satellite in the first orbital plane. The orbit parameters of the undetermined orbit satellites are shown in Table 1.

Table 1 The parameters of undetermined orbit satellites

Satellite	Orbit altitude (km)	Eccentricity	Inclination (°)	RAAN (°)	Argument of perigee (°)
MEO	22,000	0	55	60	0
GEO	35,786	0	0	0	0

Different types of inter-satellite observations are analyzed in the following two major categories according to the altitude of satellite orbit:

Observations of the same layer orbit satellites: MEO-MEO;
Observations of different layer orbit satellites: MEO-GEO.

First of all, in preparation for the realization of the follow-up satellite orbit determination, we conduct a corresponding simulation calculation with different types of inter-satellite Doppler measurement. Here we use November 1, 2010 (UTC) as the initial epoch. Satellite orbit data is simulated by STK for one week, the simulation step is 60s. According to the calculation formula of Doppler shift, referencing to the launch carrier frequency $f_s = 23\,\text{GHz}$ proposed in [12], we calculate the Doppler shift of the satellites with different observation combinations, as shown in Tables 2 and 3.

Since the relative position between the same layer and the MEO satellite is basically unchanged, the Doppler shift is almost zero, that case will not be analyzed in this paper. From Tables 2 and 3, there is a significant relative motion between the same layer and different layers, so the Doppler shift value is larger, but because of the Earth shield, there is a gap in the observation of the time slot. Part of the observation of the combination of the inter-satellite Doppler shift curve is shown in Fig. 1.

From Fig. 1, the Doppler shift of both the same layer different track and different layers of the satellite has a certain periodic trend, and the discontinuous part of the curve is not visible.

Table 2 Doppler shift between satellites of the same layers but different orbits (MEO-MEO)

Satellite combination	Minimum Doppler shift (kHz)	Maximum Doppler shift (kHz)	Visibility
MEO-MEO14	−221.7	222.4	There're breakpoints
MEO-MEO24	−224.5	224.0	There're breakpoints
MEO-MEO34	−456.5	456.7	There're breakpoints

Table 3 Doppler shift between satellites of different layers (GEO-MEO)

Satellite combination	Minimum Doppler shift (kHz)	Maximum Doppler shift (kHz)	Visibility
GEO-MEO11	−214.0	213.0	There're breakpoints
GEO-MEO21	−213.8	212.5	There're breakpoints
GEO-MEO31	−212.7	213.8	There're breakpoints

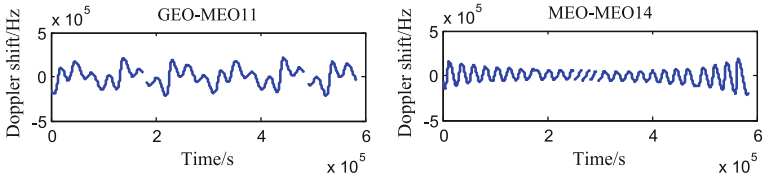

Fig. 1 Curve: Doppler shift between satellites

In summary, inter-satellite Doppler measurement orbit does not apply to the same plane of orbit satellite. The Doppler shift can be obtained by the combination of the different orbit satellites, but there are some time slots in the Earth shield. Therefore, it is necessary to consider visibility constraints when the inter-satellite Doppler shift measurements are used for autonomous orbit determination, so that the reference satellites between which mutual measurements are set up are reasonably chosen, ensuring adequate observed data are obtained at the same time.

3 Autonomous Orbit Determination Algorithm Analysis

In this paper, the dynamic orbit determination method is adopted, and the core algorithm of the autonomous orbit determination is Kalman filter. However, the state equation and the measurement equation are nonlinear, so the extended Kalman filter (EKF) is needed. The flow chart of the algorithm is shown in Fig. 2. We first need to establish the dynamic model of satellite; second, the orbit satellite orbit forecast value integrator is given through "time update module" in the EKF filter; finally, the filtering value of the orbit (i.e., the orbit determination result) is given by the "measurement update module" of the EKF filter after the correction of the satellite Doppler observation data.

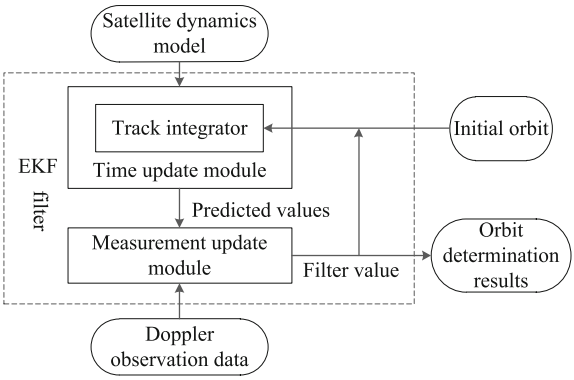

Fig. 2 Autonomous orbit determination algorithm flow chart

3.1 State Equation

The satellite orbit is composed of position vector and velocity vector, which is the state parameter to be estimated $X = (x, y, z, \dot{x}, \dot{y}, \dot{z})^{\mathrm{T}}$, the dynamic model of the satellite is established:

$$\dot{X}(t) = f[X(t)] + w(t) \tag{3}$$

In the formula, $f[X(t)]$ is a nonlinear functional; $w(t)$ is the process noise. Because (3) is a nonlinear equation, it is generally unable to obtain its analytical solution. Therefore, it needs to be linearized:

$$\dot{X}(t) = f[\hat{X}(t)] + \left.\frac{\partial f(X)}{\partial X}\right|_{X=\hat{X}(t)} [X(t) - \hat{X}(t)] + w(t) \tag{4}$$

The sampling interval is $\Delta t_{k,k-1} = t_k - t_{k-1} (k = 1, 2\ldots)$, and the process noise $w(t)$ is constant in a sampling interval, then the solution of differential equation (4) is then discretized and the state equation of the system in which the sampling interval at the k sampling interval is available:

$$X_{k+1} = \Phi_{k+1,k} X_k + w_k \tag{5}$$

In the formula, X_k is the real state vector of the satellite at t_k, $\Phi_{k+1,k}$ is the system state transition matrix of t_k to t_{k+1}, and w_k is the noise of the moment t_k.

3.2 Measurement Equation

If the satellite receiver can get the range change rate between the receiving satellite and transmitting satellite during the period of time by measuring the Doppler count, the measurement equation of the autonomous orbit determination can be described as [10]:

$$V = \frac{c}{f_{\mathrm{s}}} \left(f_{\mathrm{s}} - f_{\mathrm{r}} - \frac{N}{\Delta t} \right) + \varepsilon \tag{6}$$

In the formula, V is the measurement of the range change rate of the two satellites, f_{s} is the signal frequency of the satellite, f_{r} is the signal frequency of the receiver, Δt is the sampling time interval, N is the Doppler count in the sampling time; ε is the random error.

The design frequency of the two satellites is the same, which is $f_s = f_r = f$, and the equation of the measurement can be derived:

$$V = -\frac{c}{f}\frac{N}{\Delta t} + \varepsilon \tag{7}$$

Formula (7) can be discretized, and the measurement equation of the t_k moment can be measured:

$$V_k = \frac{1}{\Delta t_k}(\rho(X_k) - \rho(X_{k-1})) + \varepsilon_k \tag{8}$$

In the formula, $\rho(X_k)$ is the geometric distance between the two satellites at t_k. $\rho(X_k)$ and $\rho(X_{k-1})$ which needs to be linearized:

$$\rho(X_k) = \rho(\hat{X}_k) + H_k(X_k - \hat{X}_k) \tag{9}$$

$$\rho(X_{k-1}) = \rho(\hat{X}_{k-1}) + M_{k-1}(X_{k-1} - \hat{X}_{k-1}) \tag{10}$$

In the formula:

$$H_k = \frac{1}{\Delta t_k}\frac{\partial \rho}{\partial X}\bigg|_{X=\hat{X}_k}, \quad M_{k-1} = \frac{1}{\Delta t_{k-1}}\frac{\partial \rho}{\partial X}\bigg|_{X=\hat{X}_{k-1}} \tag{11}$$

4 Autonomous Orbit Determination and Analysis

4.1 Orbit Determination

The original satellite orbit data needed for the orbit determination is simulated by STK software. We use November 1, 2010 (UTC) as the initial epoch, the simulation time for one week, the simulation step is 10s. The orbit determination strategy is shown in Table 4. Six visible satellites are selected from the reference constellation,

Table 4 Orbit determination strategy

Project	Model
Coordinate system	J2000 inertial coordinate system
Earth gravity field model	JGM3 10 × 10
N body perturbation	Sun and Moon
Ephemeris	DE405 Ephemeris
The solar radiation pressure	Fixed surface to mass ratio (2/1000)
Integrator	RKF78

and the observation relationship is established between the reference satellites and the unfixed orbit satellite.

4.2 Simulation Results Analysis

In this paper, the orbit determination results are compared with the reference orbit, and the error of the orbit and the reference orbit is adopted [13]:

$$\mathrm{URE} = \sqrt{(\Delta R)^2 + 0.0192\left[(\Delta T)^2 + (\Delta N)^2\right]} \tag{12}$$

The ΔR, ΔT and ΔN are, respectively, the radial, tangential, and normal error of the satellite.

In the case of no errors, orbit determination for one week, MEO and GEO satellite orbit determination results URE maximum values as 0.0925 and 0.1095 m. When the observation error is random noise on the order of 0.001 m/s, the variation curves of MEO and GEO satellites are shown in Fig. 3.

The random error of different order of magnitude is added to the observation value, and the maximum value of the orbit determination results URE is shown in Table 5.

From Table 5, the results show that the MEO and GEO of the orbit determination results have shown a rapid deterioration, and MEO's ability to resist error is better than GEO. When the observation error is random noise on the order of 0.001 m/s, two satellite autonomous orbit determination of the URE value is maintained at decimeter level.

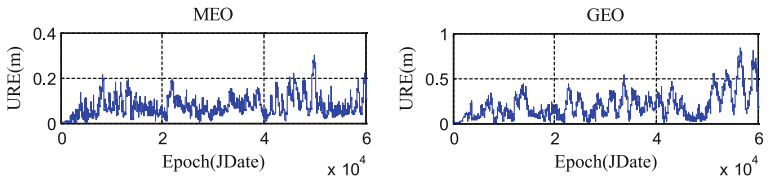

Fig. 3 Curve: the results URE of MEO and GEO satellite orbit determination when the measurement error is 0.001 m/s

Table 5 The maximum value of the orbit determination URE only when the observation error is random noise on the order of 0.001 m/s

Satellite type	Level of error (m/s)		
	0.001	0.005	0.01
MEO	0.3251	1.6181	2.2947
GEO	0.6488	3.9419	6.1854

Due to the complexity of the space motion of the satellite, the orbit precision of the reference constellation will be different from the expected, so it is needed to analyze the variation of the orbit determination accuracy under the condition of the existence of the standard error. If the reference error is only considered, when the amplitudes of *R*, *T,* and *N* directions is 0.5 m/1.0 m/1.0 m, 7 days later, the orbit determination results variation curves of MEO and GEO are shown in Fig. 4.

When the *R*, *T,* and *N* directions of the reference satellite are introduced to the sinusoidal error of different amplitude, the maximum value of the orbit determination results are shown in Table 6.

From Table 6, the sensitivity of MEO to the reference error is weaker than that of GEO. Since this paper is based on the Walker constellation to achieve other satellite orbit determination, therefore, the accuracy of the reference satellite orbit is an important factor to ensure the accuracy.

At the same time, the observation error is random noise on the order of 0.001 m/s, and the reference satellites amplitude of sine error at *R*, *T*, *N* directions are, respectively, 0.5, 1.0, and 1.0 m, the variation curves of MEO and GEO are shown in Fig. 5.

The *T*, *N,* and *R* directions of the reference satellite are introduced with different amplitudes of sinusoidal error, and the URE values of MEO and GEO are shown in Table 7.

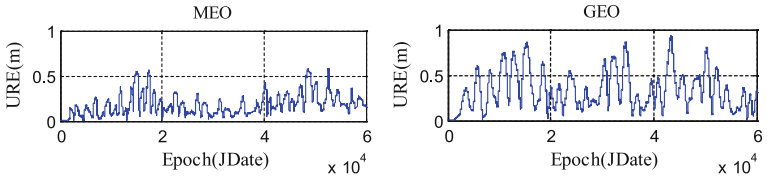

Fig. 4 Curve: MEO and GEO satellite orbit determination URE when the amplitude of the sine error of *N*/*R*/*T* direction is 0.5 m/1.0 m/1.0 m

Table 6 The maximum value of the orbit determination URE only the fiducial error is considered

Satellite type	*R*, *T*, *N* direction sine error amplitude (m)		
	0.5/1.0/1.0	1.0/3.0/3.0	1.0/5.0/5.0
MEO	0.5797	1.6806	2.7489
GEO	0.9360	2.3248	4.1099

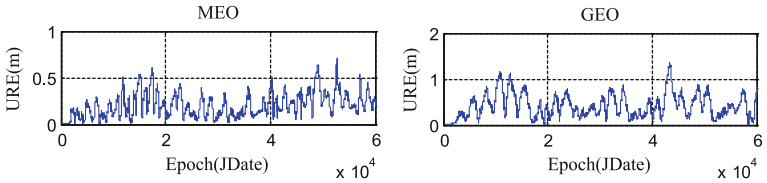

Fig. 5 Curve: MEO and GEO satellite orbit determination URE when the error of observation error is 0.001 m/s, and the amplitude of the sine error of the *R*/*T*/*N* direction is 0.5 m/1.0 m/1.0 m

Table 7 URE maximum value of MEO satellite orbit determination when the fiducial error and observation error are considered at the same time

Observation error (m/s)	*R*, *T*, *N* direction sine error amplitude (m)		
	0.5/1.0/1.0	1.0/3.0/3.0	1.0/5.0/5.0
0.001	0.7108	1.7183	2.7349
0.005	1.5151	2.2805	3.2158
0.01	3.1401	3.2432	3.9715

Table 8 URE maximum value of GEO satellite orbit determination when the fiducial error and observation error are considered at the same time

Observation error (m/s)	*R*, *T*, *N* direction sine error amplitude (m)		
	0.5/1.0/1.0	1.0/3.0/3.0	1.0/5.0/5.0
0.001	1.3540	2.5924	4.1499
0.005	2.1760	3.6527	5.6333
0.01	6.6537	7.4913	8.0001

From Tables 7 and 8 we can see the differences of the URE maximum value of MEO and GEO satellite orbit determination when introducing different error combinations. Under the same error condition, the orbit determination of MEO satellite is better than that of GEO.

In summary, with the inter-satellite Doppler measurement, MEO and GEO satellite autonomous orbit determination can be well achieved. Under the same simulation conditions, the orbit determination accuracy of MEO satellite is always better than that of GEO. Based on the simulation scenario, the calculation verifies that MEO satellites PDOP value is usually less than GEO satellite; that is to say, the observation geometry of MEO satellite is better than that of GEO satellite, so the merits of observing geometry should be an important factor to make the orbit precision of MEO satellite different from the GEO satellite.

5 Conclusions

In this paper, the method of satellite autonomous orbit determination based on inter-satellite Doppler measurement is analyzed. According to the basic principle of Doppler Effect, the observation equation is given, and the autonomous orbit determination of MEO and GEO satellite is calculated by using the extended Kalman filter theory. The simulation results show that, in the case of only considering the observation error, when the observation error is random noise on the order of 0.001 m/s, the URE of orbit determination result is decimeter for 7 days. When the observation error is on the order of 0.001 m/s, sinusoidal amplitude error of reference satellites *R*, *T*, and *N* direction is at 0.5, 1.0, and 1.0 m, MEO satellite

orbit determination accuracy is decimeter, and GEO satellite orbit determination precision is at meter level. Therefore, the autonomous orbit determination of satellite can be realized by the Doppler shift measurement.

In the process of autonomous orbit determination of MEO and GEO satellites, the influence of the results of the observation error and the fiducial error is analyzed. In practice, the frequency offset of the signal and the centroid error of the antenna can neither be ignored. There are some differences in the spatial environment of different satellites, therefore, the autonomous orbit determination method of different satellites should be different. This paper only analyzes single star of MEO and GEO satellite autonomous orbit determination based on the inter-satellite Doppler measurements. This method can be extended to the LEO satellite and the whole constellation of autonomous orbit determination, related content still needs to be further improved. The results of this paper show that the satellite autonomous orbit determination method based on inter-satellite Doppler measurement can be used as an assistant and supplement to other autonomous orbit determination methods.

References

1. Guohua L, Zhailian W, Lin S, Yin X, Yi W (2011) The precision analysis of autonomous navigation satellite cross link-based. In: Proceedings of the second China satellite navigation electronic corpus academic conference, 5
2. Ping S, Guangji Q, Zhonggui C (2006) Studies on autonomous navigation techniques for navigation constellations. Eng Sci 8(3):2–30
3. Zhu Y (2014) Research on autonomous orbit determination of satellite based on Beidou and pulsar. Nanjing University of Science and Technology
4. Hai-sheng L (2010) Autonomous orbit determination of navigation constellation based on crosslink range and orientation parameter constraint. Nanjing University of Aeronautics and Astronautics
5. Liu J (2011) Satellite orbit determination method with DORIS system. National University of Defense Technology
6. Li PJ, Cao JF, Hu XG et al (2010) High accuracy orbit determination with DORIS system. J Spacecr TT&C Technol 29(3):58–64
7. Jayles C, Nhun-Fat B, Tourain C (2006) DORIS: system description and control of the signal integrity. J Geod 80:457–472
8. Jayles C, Chauveau JP, Rozo F (2010) DORIS/Jason-2: better than 10 cm on-board orbits available for near-real-time altimetry. Adv Space Res 46:1497–1512
9. Auriol A, Tourain C (2010) DORIS system: the new age. Adv Space Res 46:1484–1496
10. Liu J, Gu D, Lai Y, Yi D (2012) Study on the method of frequency offset estimation in DORIS real time orbit determination. J Wuhan Univ (Inf Sci Edition) 37(8):956–959 + 966
11. Liu Z-C (2003) Doppler and the origin of his effect. Physics 32(7):488–491
12. Wang K, He X, Zhao H (2007) The simulation of doppler shift in inter-satellite links. Radio Eng 03:36–38
13. Ananda MP, Bernstein H, Cunningham KE, Feess WA, Stroud EG (1990) Global position system (GPS) autonomous navigation. In: Institute of Electrical and Electronics Engineer position location and navigation symposium. Institute of Electrical and Electronics Engineers, New York

Analysis of Ground Anchor Stations' Influence on Autonomous Orbit Determination with Distributed Algorithm

Fanghong Huang, Wende Huang, Yueke Wang, Yifan Zhou and Kui Lin

Abstract The orbit determination of the navigation constellation is the premise for navigation satellite system to realize navigation and position. Autonomous orbit determination based on ground anchor stations can improve the accuracy and survivability of the navigation system, but it has the rotation error. The addition of the ground anchor stations is a valid way to solve the problem. Because of the limited calculation resources on the satellite boards, the algorithm should be a distributed one which, however, is not the optimal. So, it is meaningful to study the influence of the ground anchor stations on the distributed orbit determination algorithm. According to the requirement, first, this article describes the principle of distributed orbit determination algorithm. Second, it analyses the characteristics of it. Third, it studies the effect of ground anchor stations. In the last, it designs a work way in period and tests the feasibility of it. The simulation result shows that ground anchor stations can control the rotation error well, but the simple EKF algorithm used to fuse the data of inter-satellite and satellite-to-ground range measurements constricts slow. In the last an improving algorithm is raised.

Keywords Autonomous orbit determination · Distributed algorithm · Anchor stations · Navigation constellation

1 Introduction

Global navigation satellite system (GNSS) can realize continuous navigation and position which covers the whole earth surface and runs in all the days and on all kinds of weather with high accuracy, so it is widely used in the era of military and commerce. Therefore, many countries began to develop their own GNSS, such as

F. Huang (✉) · W. Huang · Y. Wang · Y. Zhou · K. Lin
College of Mechatronics Engineering and Automation, National University of Defense Technology, Changsha 410073, China
e-mail: 570059217@qq.com

© Springer Science+Business Media Singapore 2016

J. Sun et al. (eds.), *China Satellite Navigation Conference (CSNC) 2016 Proceedings: Volume III*, Lecture Notes in Electrical Engineering 390,
DOI 10.1007/978-981-10-0940-2_7

the GPS of the USA, the GALILEO of the EU, the GLONASS of Russia, the Compass of China, and so on.

The orbit determination of the navigation satellites is the premise for navigation satellite system to realize navigation and position. However, nowadays the ephemeris broadcasted by navigation satellites is usually provided by the ground control system. Once the ground system was destroyed, the whole navigation satellite system would be no longer in force. Also, the net distribution of the ground station for BeiDou cannot cover the whole surface of earth, just like the GPS. So, autonomous orbit determination can improve orbit accuracy and survivability in special time greatly.

But in the process of autonomous orbit confirmation based on inter-satellite range measurement, the constellation's rotation relative to earth cannot be observed when the constellation is treated as a rigid body [1]. It is a key problem to remove or limit the relative rotation in the study of autonomous orbit confirmation. Essentially the rotation error is caused by the rank deficient of the observation equation. So, many scholars put forward several methods to solve this problem [2–4]. Those can be divided into two categories: add virtual basis or add external basis. The methods to add virtual basis are adding prior distribution and adding constraint for the filter, and so on. The methods to adding external basis are methods based on magnetometer measurement; star sensor measurement; three celestial measurement of the Sun, the Moon, and the Earth; pulsar measurement; ground anchor station, and so on. All these methods have their advantages and disadvantages. Under current condition of technology, the method based on anchor stations is the easiest, the most effective way.

Although it depends on the ground, it still has great meaning for the study. On the one hand, in the stage of half autonomous orbit confirmation, the addition of ground station can improve the accuracy of orbit measurement that will provide more accurate initial parameters for complete autonomous orbit confirmation. On the other hand, by the study of how the ground anchor stations affect the autonomous orbit confirmation, we can design a work way which can decrease the satellites' dependency on ground but improve the ability of hiding.

The idea of using anchor to navigate was thought out by J.A. Rajan in 2003. He made elementary simulation for the idea and applied for a patent. At home, Zhu et al. [5–7] conducted a study for the theory and algorithm of anchor station and do the simulation. They used the centralized filtering algorithm to solve the state of the whole constellation, and they got a good result. Shang et al. [8] accessed the performance of anchor station to correct the rotation error in the autonomous orbit determination by simulation.

The algorithm of autonomous orbit determination can be divided into two parts: the centralized algorithm and the distributed algorithm. The centralized algorithm processes all the data of the constellation together, providing an optimal way to solve the orbit estimate problem. But, the process is always done in the ground station for its powerful calculation ability and abundant data resources. However, in order to make the autonomous orbit determination come true, the algorithm needs to be run on the satellites, so it should be easy and quick enough to calculate on the

satellite. Thus, the huge calculation work should be distributed to the single satellite. The question is how to do the distribution to decrease the calculation work for single satellite and communication among the constellation net but meet the orbit accuracy requirement [5].

Because of the background, first, this article briefly introduces the theory of satellite orbit determination with distributed algorithm, and then analyses its characteristics by simulation. In the last, characteristics of the algorithm with ground anchor stations' measurement are analyzed.

2 Theory of Distributed Orbit Determination Algorithm

The basic idea of distributed algorithm is every satellite estimates its own orbit, always by kalman filtering algorithm. Under this circumstance, the main problem is manifested as that: when building a model for the kalman filtering algorithm, the measurement value is bound up with the other satellite's orbit which needs to estimate, too. So, the correct model cannot be built. There are some methods to solve this problem. The first one is approaching the optimal value by iteration which needs much inter-satellite communication [5]. The second one is using the prediction orbit values of the unknown satellites as the real one, which is easy to realize but has big error. The third one is to increase the covariance of the measurement error [5]. The meaning of it is to convert the orbit errors of the reference satellites to the measurement error presented by the covariance of the measurement error. This way improves the accuracy of the model so to improve the accuracy of the orbit estimate. In the following, the principle of the second algorithm is introduced.

In the algorithm based on prediction orbit, the values to be estimated are the position and velocity of the satellite. So, the information needed is the pseudorange relative to this specific satellite and the covariance of the relevant satellites' position and velocity which can be acquired by inter-satellite link.

The state equation and observation equation:

$$X_k = f(X_{k-1}) + G_{k-1}W_{k-1} \tag{1}$$

$$Z_k = h(X_k) + V_k \tag{2}$$

In the equation, X_k is the state vector in the k moment; $f(X_{k-1})$ is the nonlinear state transition function from the moment $k-1$ to the k moment, and W_k is the error vector whose covariance is Q_k in the process of state transition, and G_k is the coefficient matrix of the error; Z_k is the observation vector, and $h(X_k)$ presents the nonlinear function of observation and state, and V_k is the observation error whose covariance matrix is R_k.

The equation of kalman filtering algorithm:

1. Update with the time:

$$\hat{X}_k^- = f\left(\hat{X}_{k-1}^+\right) \tag{3}$$

$$P_k^- = \Phi_{k-1} P_{k-1}^+ \Phi_{k-1}^T + G_{k-1} Q_{k-1} G_{k-1}^T \tag{4}$$

2. Update the measurement:

$$K_k = P_k^- H_k^T \left(H_k^T P_k^- H_k + R_k\right)^{-1} \tag{5}$$

$$\hat{X}_k^+ = \hat{X}_k^- + K_k\left[Z_k - h\left(\hat{X}_k^-\right)\right] \tag{6}$$

$$P_k^+ = (I - K_k H_k) P_k^- \tag{7}$$

In the equation, $\hat{X}_k^-$ is the predicted value of the state to be estimated; P_k^- is the value of the covariance of the states' predicted value; $\hat{X}_k^+$ is the final value of the state; P_k^+ is the covariance of the states' final value; K_k is the coefficient matrix in the process of estimation; Φ_{k-1} is the state transition matrix which along with the $\hat{X}_k^-$ is acquired by orbit integration; H_k is the observation matrix which is acquired by the linearization of $h(X_k)$ in the point of $\hat{X}_k^-$.

Which should be attention here is the set of the covariance matrix. The covariance matrix of the initial orbit P_0 is set according to the estimate of the orbit before the algorithm; Q_k is always set to a constant and R_k is set to a constant here for convenience.

3 Analysis of Distributed Algorithm

In order to analyze the function of the ground anchor stations, we do the analysis on the error characteristics of the distributed algorithm. The kalman filtering algorithm consists of two steps: prediction and correction. Prediction is calculating the prediction value by dynamic equation which is acquired by the analysis of the force applied to the satellite, and the correction is calculating the optimal real-time estimate value according to the measurement and the observation equation. So, in the following chapter, error in the prediction process and error in the end of the algorithm are separately analyzed.

Figure 1 is the process of simulation.

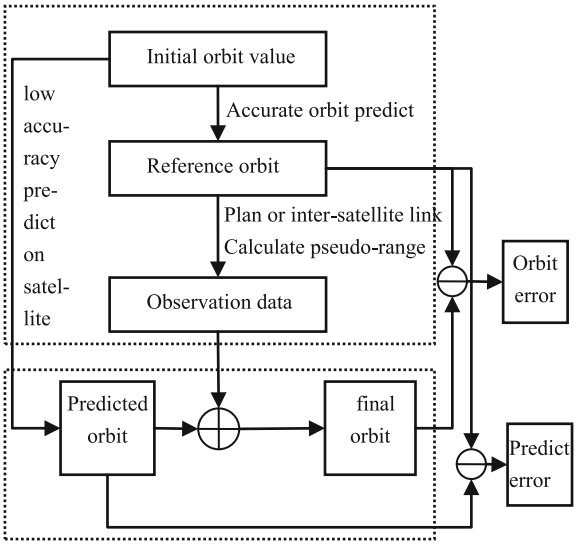

Fig. 1 Process of simulation for characteristics analysis

3.1 Analysis of Error in Orbit Prediction

In this article we analyze the 24 MEOs in Beidou navigation constellation. Because Beidou has not been fully completed, the accurate orbit in the simulation is gotten by simulation. The parameters of simulation are: nine parameters' spherical model of light pressure model; 14 × 14 rank JGM3—gravitational model; JPL DE405 planet ephemeris; 14 ranks KSG multistep integrator; 60s integration step; taking earth tide and sea tide into consideration; IERS final EOP parameters.

When analyzing the characteristics of prediction error, considering an easier model for the limited on-board resources. The parameters are: three parameters' spherical model of light pressure model; 10 × 10 rank JGM3—gravitational model; JPL DE405 planet ephemeris; RKF78 classical numerical integrator; 60s integration step; IERS final EOP parameters.

Then compare the prediction result of the simple model with the accurate model and calculate the mean URE error. Next fit the rotation error for the prediction error (Eq. 8) (see [1]).

$$\begin{aligned} \theta_x &= \frac{2}{N}\sum \cos \Omega_j \Delta i_j \\ \theta_y &= \frac{2}{N}\sum \sin \Omega_j \Delta i_j \\ \theta_z &= \frac{1}{N}\sum \Delta \Omega_j \end{aligned} \tag{8}$$

In the formula, Δi_j and $\Delta\Omega_j$, respectively, are the orbit inclination and RAAN of the ith satellite; N is the number of satellites.

We do so to divide the prediction error to rotation part and structure deformation part. The rotation part cannot be corrected by the inter-satellite range. Thus, without the external basis, error of this part will affect the final result.

Then we got the mean URE error of 60 days prediction (Fig. 2).

It shows that URE error of prediction increase rapidly with time and it comes to 1200 m after 60 days. The orbit determined by prediction is not useful.

The fitting rotation (Fig. 3) shows that the rotation error of long time prediction is relatively small in the inertia coordinate system, the maximum error in the X axis and Y axis is about 0.015as, and maximum error in the Z axis is about 0.04as. Actually the main error in prediction is error in trace direction, which affects little on rotation error.

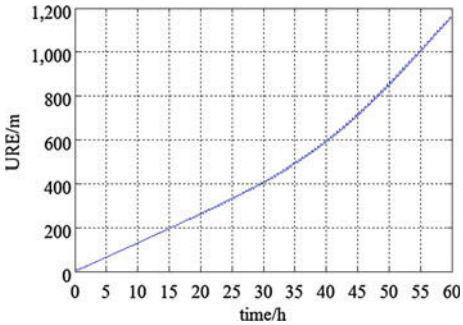

Fig. 2 Mean URE error of simple prediction for 60 days

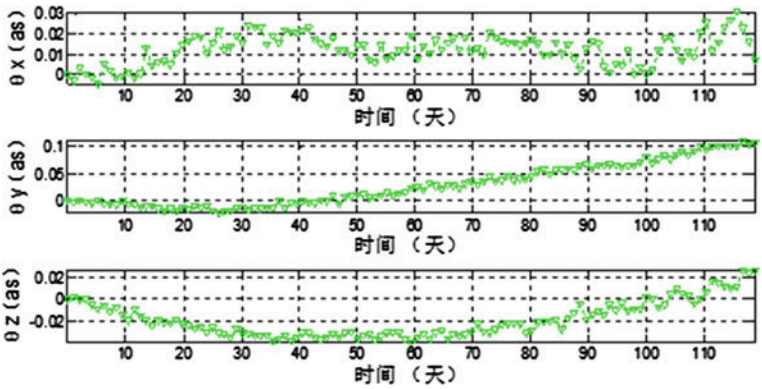

Fig. 3 Curve of rotation error of simple prediction for 60 days

3.2 Analysis of Error in Distributed Algorithm

In the centralization algorithm, the rank defect can be solved by the method of free net adjustment [9], e.g., pseudoinverse adjustment, biased estimate (ridge estimate and generalized ridge estimate), Bayes estimate, and so on. But for the distributed algorithm, there is no relevant theory to solve it accurately. So, we study the issue by simulation. Here we use the algorithm introduced in Chapter "Research of Satellite and Ground Time-Synchronization Based on a New Navigation System".

At first, the range observation is ideal without error. Run the algorithm and we can get the ideal result of this algorithm. Compare it with the prediction result (Fig. 4). It shows that this algorithm can correct most of the prediction error.

Then add random error (0.5 m) to the observation values and compare the result between the observation with error and without error (Figs. 5 and 6). The two pictures show that the results got by the data without and with random error have little difference which has a random distribution after the algorithm going to steady. So, we can draw the conclusion that random error of the range has little effect on the distributed orbit determination algorithm.

Except for that, the figures also show that the orbit diffuses even without the range error. There may be two reasons for it. The first is that the rotation error of prediction has not been corrected. The second reason is the structure deformation error that has not been corrected even if we have inter-satellite range observation. Because EKF straightens the nonlinear observation equation at the prediction

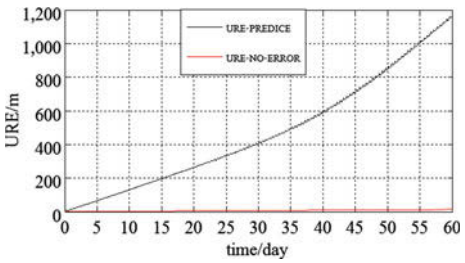

Fig. 4 Error curve of prediction and auto navigation for 60 days

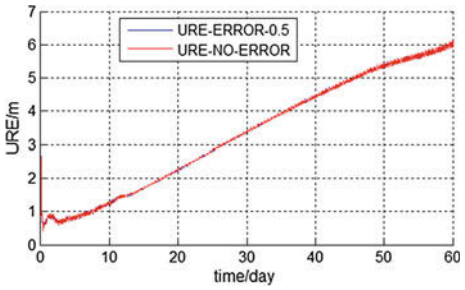

Fig. 5 URE error curve of orbit confirms result with random range error (0/0.5) for 60 days

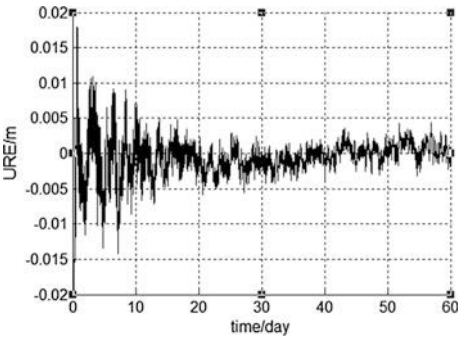

Fig. 6 Difference value between the result with no random range error and error for 0.5 for 60 days

values, so it has linearity error; in the distributed algorithm, the observation model is inaccurate because of the unknown position of the relative satellites. All these reasons affect each other and then make the result more and more worse.

4 Analysis of Anchor Station's Influence

4.1 Analysis of the Function and Work Way of Anchor Stations

According to the analysis before, there are two main reasons for orbit estimate error. One is that error in prediction and correction process results in the orbit diffusing in ECI. The other is the diffusing of the EOP results in the orbit diffusing in ECF after the coordinate convert. So, the ground anchors have two functions. One is to limit the rotation error by satellite-to-ground link, and the other is uploading the newest predicted EOP.

The algorithm still runs on the satellite, when the ground anchor is just like a pseudo satellite lying on the ground. It sends pseudorange signal, data of two-way range, its own position and the clock error data. It would not affect the process of orbit determination when it is destroyed. Adding new anchor stations is easy [8]. In order to hide the station, the link between satellite and ground anchor station is suspended in period. The suspending time depends on the diffusing time of the orbit without anchor stations and the constriction time with them [6].

4.2 Simulation of the Distributed Algorithm with Anchor Stations

Because the influence of the anchor stations come to many factors, including the quantity, position, frequency of the anchor stations, and so on [8, 10]. Here we just analyze the influence of adding 1/3/5 station(s).

Table 1 Positions of anchor stations

Number	Latitude (°)	Longitude (°)	Height (m)
1	40.0861389	116.233361	101
2	18.2950278	109.514750	66
3	39.4589167	76.0205833	1321
4	30.8414167	104.153917	552
5	46.8166667	130.283333	81.2

The positions of the anchor stations are in Table 1.

Set the elevating angle of the ground anchor station as 10°. The link establishment of the inter-satellite-link and satellite-to-ground link are two relatively independent process, so they do not affect each other. The visibility of the satellite-to-ground link decides whether these two ends establish a link in the link plan process. The plan of inter-satellite link is made by specific planning method which here we do not explain. The periods of these two links are both 5 min. Because the satellite-to-ground range observation is affected by the atmosphere, the observation has relatively larger system error than the inter-satellite range observation. So, the random error in the two observations is set as 0.5 m, and the system error in the satellite-to-ground is set as 2 m (Fig. 7).

Several conclusions can be drawn. First, with the satellite-to-ground range observation, the URE error shakes more severely at the beginning of the estimate process, but the tendency of diffusing is controlled. Second, when the number of ground anchor stations goes to specific number, the increase of the station number has no much effect. Third, the constriction speed is relatively slow with this algorithm. In this figure, the error becomes steady in about 50 days. The reason is the EKF algorithm. It has an incorrect model and it does not apply different weights to the different links which have different characteristics.

Consider the plan of running the stations in period. The station number is 3 and set the valid mean URE value as 3 m. Because the constriction speed of the algorithm with stations is too slow, here we suspend the stations for 20 days and then open them for 40 days (Fig. 8). We can see the method is usable but not good.

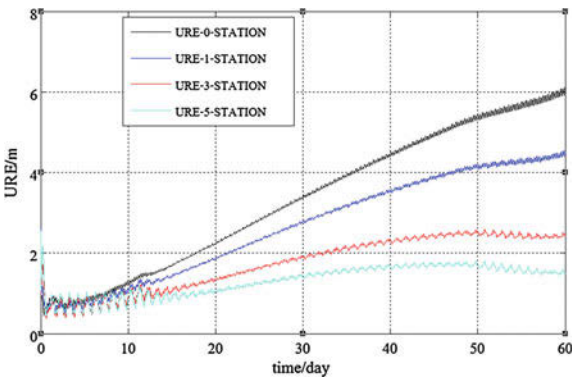

Fig. 7 URE error curve of the orbit determination result by adding 0/1/3/5 station(s) for 60 days

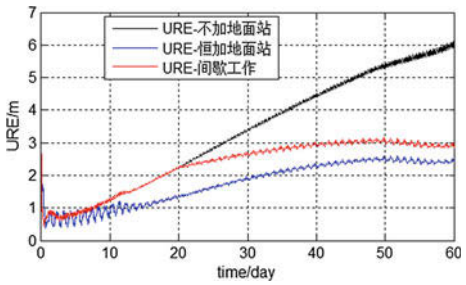

Fig. 8 URE error curve of the orbit determination result with 0/3 station(s) and period work way for 20 days on and 40 days off for 60 days

5 Conclusions

This article analyzes the principle and characteristics of the distributed orbit determination algorithm and the influence of anchor stations. It is tested by simulation with the simple EKF algorithm. The result shows that with the specific algorithm, anchor station range observation can control the rotation error but the constriction speed is slow. In the next step, consider setting the covariance of the error in measurement equation. On the one hand, set different covariance on different links, for the different error characteristics between the satellite-to-ground link and the inter-satellite link. On the other hand, using the method of statistics to analyze the statistical property of the positions of the relative satellites convert them to the covariance in the measurement. Also the simulation scheme still needs to be improved. Introduce part of real data to do the simulation which may improve the reliability of the simulation.

References

1. Menn MD, Bernstein H (1994) Ephemeris observability issues in the global positioning system (GPS) autonomous navigation (AUTONAV). In: Proceedings of position location and navigation symposium, IEEE, pp 677–680
2. Lu Z, Li Z, Liu W (2007) The inspection and correction of the revolution round the earth of navigation satellite constellation. J Astronaut 27(6):1397–1400
3. Cai Z, Han C, Chen J (2008) Constellation rotation error analysis and control in long-term autonomous orbit determination for navigation satellites. J Astronaut 2
4. Shang L, Ren Q, Zhang R (2013) Eliminating constellation rotation error of autonomous orbit determination using differential anchor stations. Geomat Inf Sci Wuhan Univ 8:010
5. Zhu J (2011) Research on orbit determination and time synchronizing of navigation satellite based on crosslinks. National University of Defense Technology, Changsha
6. Su T (2012) The research of the autonomous orbit determination of navigation constellation based on ground-based anchor. National University of Defense Technology
7. Zhu J, Liao Y, Wen Y (2009) The integrated autonomous orbit determination of the navigation constellation based on crosslink range and ground-based emitter. J Natl Univ Def Technol 15–19
8. Shang L, Liu G, Liu S (2012) The evaluation of eliminating the constellation rotation error in autonomous navigation using anchors. In: Proceedings of the 3rd CSNC—S03 accuracy orbit and position

9. Liu L, Y Liu (2000) The rank lack problem in autonomous orbit determination using inter-satellite measurement. J Spacecr TT&C Technol 29(3):80–83
10. Wang F, Guo F, Wen Y (2015) Influence of the quantity and distribution of anchor stations on autonomous orbit determination of navigation constellations. J Spacecr TT&C Technol 34 (3):254–259

Paralleled Geopotential Computing Methods Based on GPU

J. Liu, W. Wang, Y. Gao and L. Shu

Abstract The spherical harmonics model to describe geopotentials relies on recursive algorithms, whose computational efficiency degrades significantly if the order of the expansion into spherical harmonics increases. In order to enhance the computational efficiency for high-fidelity geopotentials, a Global Point Mascon model and a fast algorithm using GPU-based parallel computing are presented in this paper. The GPU-based parallel computing is implemented with compute unified device architecture (CUDA), enabling fast computation of high-fidelity geopotentials. The spherical harmonics and the Global Point Mascon models are evaluated and compared by conducting numerical integration of space trajectories, which show that the latter model with parallel computing leads to one order of magnitude speedup without degradation of numerical integration accuracy.

Keywords Geopotential · Spherical harmonic model · Global point mascon model · GPU · Paralleled computing

1 Introduction

Fast computing of high-fidelity geopotentials is of great significance for space flight concerning satellite on-board real-time navigation, satellite formation maintenance and reconfiguration, space debris orbit prediction, etc. The precise orbits of artificial satellites around the Earth heavily rely on the high-fidelity models for describing geopotentials. In order to achieve high-precision on-board real-time navigation,

J. Liu (✉)
Technology and Engineering Center for Space Utilization,
Chinese Academy of Sciences, University of Chinese Academy of Sciences,
Beijing, China
e-mail: liujiangkai14@csu.ac.cn

W. Wang · Y. Gao · L. Shu
Technology and Engineering Center for Space Utilization,
Chinese Academy of Sciences, Key Laboratory of Space Utilization,
Beijing, China

© Springer Science+Business Media Singapore 2016

J. Sun et al. (eds.), *China Satellite Navigation Conference (CSNC) 2016 Proceedings: Volume III*, Lecture Notes in Electrical Engineering 390,
DOI 10.1007/978-981-10-0940-2_8

dynamic filtering with orbit prediction by computing high-fidelity geopotentials is demanded [1], which is also indispensable for implementing the high-precision formation maintenance and reconfiguration and for precisely predicting the orbits of the huge number of space debris. The spherical harmonics (SH) model is currently used for computing geopotentials, which is an analytic model represented by the coefficients of spherical harmonic expansion of gravity anomalies [2]. The spherical harmonic coefficients reflect the distribution, motion, and changing condition of matters inside the Earth, which is crucial to the research and application in geodesy, oceanography, and space science. Because the SH model is represented by a series of expansions, the computation of geopotentials up to a prescribed order of expansion is convenient to accommodate appropriate precision levels of demanding orbital prediction. Therefore, the SH model is widely used and paid much attention by specialists of astrodynamics. The life-off of satellites for gravity survey starts a new epoch for the development of modeling high-fidelity geopotentials, and currently the SH model has been updated to a degree of an order of 200 and a space resolution of 100 km [3]. However, the higher order means heavier computational burden and lower computation efficiency when the SH model is used, thus making it impossible to use the high-order SH model for on-board navigation or space debris tracking. Fast algorithms of computing the high-order SH model need to be developed.

Improving the performance of a single processor is a choice to improve computing efficiency. However, with the gradually invaliding of Moore's law, this way is coming to the end. An alternative way is parallel computing, which means that using more than one processor to solve a same problem could often achieve a speedup based on the number of processors used. Whether the problem could be split into separate parts and solved by multiple processors simultaneously is the key to obtain significant speedup. With the development of models to describe geopotentials, models implemented by parallel computing have been proposed, for example, the global point mascon model and the interpolation model.

The global point mascon model (or Point Masses model) is based on an assumption: a collection of localized mass elements is an approximate model to enable computation of geopotentials. The mass elements are usually fixed on a spherical face buried below the surface [4] to reduce singularity [5]. Many other works have been done to improve the point mascon model [6, 7]. By using GPU in the modeling and computing process, Ryan and Nitin significantly reduced the number of points needed and published their model [8]. Splitting the geopotential computation into thousands of simple two-body problems, the model can be computed densely and suitable to parallelism, though it loses the physical information of the central planet and could not be used in orbit designing and analysis. The interpolation model is essentially first proposed by Junkins [9], which computes and saves geopotential on the grid points surrounding the central planet, and obtains the geopotential at a target point by interpolation. The interpolation model can achieve orders of magnitude in speedup over the SH model while still preserving the accuracy and robustness. However, that is based on one to two orders of magnitude raised in memory though much work has been done [10–12].

Currently, heterogeneous computing architecture (HSA) systems utilize multi-core processors and customized accelerated coprocessors have become the developing direction of high performance computing architecture [13]. With great advantages of GPU's powerful computational capabilities, high performance/price, and high performance/power consumption ratio CPU/GPU heterogeneous architecture has been used extensively and gets impressive acceleration in different areas [14]. Compute unified device architecture (CUDA) and GPU supporting double precision operation released by NVIDIA company makes it easier to program parallelly in scientific computing.

A Global Point Mascon Model and its paralleled algorithm implemented with CUDA and GPU are presented in this paper. The results of space trajectories' numerical integration using gravitional accelerations computed by the model show that the speed up of integration in high-fidelity gravity field could be one order of magnitude relative to traditional SH model.

2 The Global Point Mascon Model of the Earth

The global point mascon (PMC) model is depicted in Fig. 1. A total of N point mascons with the mass of M_j distribute uniformly on a sphere with a fixed radius and its central coincides with the mass central of the Earth and is buried below the surface. $\mathbf{r}$ is the position of target point in the body fixed coordinate system, $\mathbf{r}_j$ is the target point position relative to the jth mascon.

The PMC model could be represented as the sum of two-body potential, J_2 potential (an unnormalized oblateness parameter) and the potentials that are caused by n point mascons:

$$U_{\mathrm{PMC}}(\mathbf{r}) = U_{2\mathrm{B}+J_2} + \sum_{j=1}^{n} \mathrm{GM}_j / \left|\mathbf{r} - \boldsymbol{\rho}_j\right| \tag{1}$$

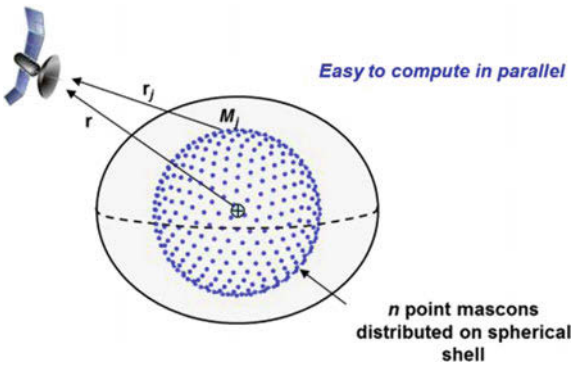

Fig. 1 A sketch of the global point mascon model

where GM_j is the gravitational parameter for the jth mascon, $\boldsymbol{\rho}_j$ is the location of the jth mascon, and U_{2B+J_2} is the potential due to the two-body plus J_2 terms

$$U_{2B+J_2} = \frac{GM_E}{r}\left[1 - J_2\left(\frac{R_E}{r}\right)^2\left(\frac{3z^2}{2r^2} - \frac{1}{2}\right)\right]. \tag{2}$$

where r is the module of $\mathbf{r}$, z is the third Cartesian component of $\mathbf{r}$. GM_E, R_E, and J_2 values come from the GGM02C [15] SH solution and are the gravitational parameter, radius, and unnormalized oblateness parameter for the Earth, respectively.

The distribution of mascon is uniform, so we can fix the mascon locations $\boldsymbol{\rho}_j$ beforehand. The model fitting method estimates only the associated mascon gravitational parameters. We use the geopotential, which is computed by SH model GGM02C, as the pseudo-observations. The observations are taken at surface locations distributed uniformly across the Earth. Once the locations of mascons are fixed and the number of observations exceeds the number of mascons, the optimal estimation problem can reduce to the weighted linear least-squares problem with performance index J:

$$J = \frac{1}{2}\sum_{i=1}^{m} w_i \varepsilon_i^2 = \frac{1}{2}\sum_{i=1}^{m} w_i [U_{PMC}(\boldsymbol{\eta}_i) - U_{SH}(\boldsymbol{\eta}_i)]^2. \tag{3}$$

where m is the number of observations; $\boldsymbol{\eta}_i$ is the location of the ith observations; U_{SH} is the observations and is the potential computed by spherical harmonics for $\boldsymbol{\eta}_i$; U_{PMC} is the observation model and is the potential computed by PMC model; ε_i and $\boldsymbol{\eta}_i$ are the residual and location of the ith observation, respectively.

It is well known that two-body and J_2 have tremendous impact on the whole geopotential. On the other hand, the computational burden of two-body plus J_2 terms is not large. So the Earth PMC model fits only the geopotential terms except the two-body plus J_2 contribution. After the estimation process, the gravitational parameters are determined for different degree and order of spherical harmonics model.

According to the PMC model of Ryan [8] proposed, the models with different degree and order are listed in Table 1. As the degree increases, the number of mascons increases nonlinearly. For a 156 degree model, the mascons number exceeds 30 thousands.

Table 1 Point mascon models and their corresponding fields

Model descriptor	Size of SH fitting field ($d \times d$)	No. of mascons (n)
PMC11n240	11 × 11	240
PMC33n1920	33 × 33	1920
PMC71n7680	71 × 71	7680
PMC156n32720	156 × 156	30,720

3 GPU Parallel Computing

3.1 Introduction of CUDA Programming

The CUDA programming model uses CPU as the host, and GPU as device. CPU is responsible for logical tasks while GPU undertakes the works of highly parallelism. The fundamental unit for GPU programming is thread [16]. As shown in Fig. 2, a number of threads form the block and lots of blocks become one grid which is used to accomplish a task. The fundamental unit for work arrangement is kernel function, all threads belong to one grid execute one same kernel function.

The kernel function is defined as *kernelFunction* ⋘*dimGrid, dimBlock* ⋙ (*Para*), where *dimGrid* is the number of blocks and *dimBlock* is the number of threads per block.

The CUDA device has several memory spaces include global, local, shared, texture, and registers [17], which have different characteristics as shown in Table 2. Of these different memory spaces, global memory is the most plentiful (typically more than 2 GB) and can be accessed by any thread, while shared memory is relatively less (typically 48 kB per block) and can only be accessed by the threads pertaining to the same block. By accessing the values of registers like *blockDim,*

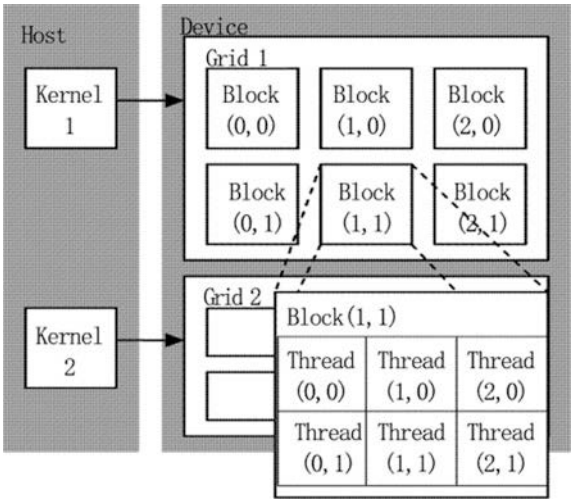

Fig. 2 CUDA's heterogeneous programming

Table 2 Salient features of device memory

Memory	Location on/off chip	Access	Scope	Lifetime
Register	On	R/W	1 thread	Thread
Local	Off	R/W	1 thread	Thread
Shared	On	R/W	All threads in block	Block
Global	Off	R/W	All threads + host	Host allocation
Constant	Off	R	All threads + host	Host allocation

blockIdx and *threadIdx,* a thread gets it's global index in a grid, and executes individual task according to the index.

Different memory type has different data bandwidth. Shared memory has a bandwidth of 1.5 TB/s while global memory only has a bandwidth no more than 190 GB/s. Thus a speedup ratio up to 7 could be achieved if the shared memory is adequately used [18]. In a general case, data that are frequently used in a same block should be loaded in the shared memory to avoid the frequently accessing to global memory and to take advantage of the 'Coalesced Access' mechanism, both of which are essential to improve performance of the programs.

3.2 Strategies to Parallel with GPU

The most time-consuming part in the PMC model is the computation of the gravity forces at the target point. Since the computation is not very large for one point mascon and any point mascon has no relation to other point mascons, it is very suitable to parallel this part of the work with GPU.

On the GPU device, threads could be considered to execute the kernel function simultaneously (actually not). First, every block loads the mass points information (including the position and mass) from the global memory and saves them in its shared memory. According to its global index, every thread in the block uses the corresponding point's information to compute the gravitational acceleration at the target point generated by the single point, and saves it to the shared memory. Second, when every thread in a block finishes its work, a synchronization is triggered, and the reduction method is applied to sum all the results in a block up into a single value and save it to the global memory. Third, a new kernel function is launched to sum the results of every block up into the final results, since it is not supported to synchronize between different blocks. The process in GPU is illustrated by Fig. 3.

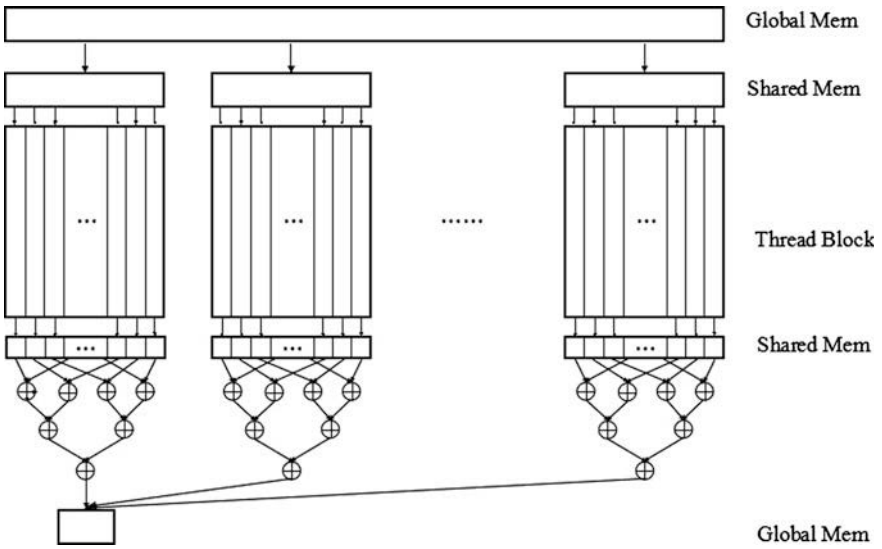

Fig. 3 The PMC model computing process on GPU

4 The Results and Analysis

A simulated scenario is built in order to verify the calculation speed and accuracy of the PMC model. Table 3 summarizes the system configuration of this scenario, in which the spacecraft orbit dynamics model is assumed to consist of the Earth's gravitational only, and the orbit is numerical integrated with the Runge-Kutta 4(5) Dormand–Prince method. The integral results are then compared with the results of corresponding SH model to perform the precision analysis.

4.1 Testing Process

Assuming that the Earth rotates at a constant speed around its spin axis, the dynamic model for the spacecraft in a simplified rotation frame can be denoted as:

Table 3 System configuration of the simulated scenario

Component type	Component
CPU	Intel Xeon E5-1620@3.7 GHz
RAM	8 GB
GPU	Tesla K20C
Operating system	Windows7 64 bit
Development environment	VS2012, CUDA7.5

$$\begin{aligned} \ddot{x} &= 2\Omega\dot{y} + \partial W/\partial x \ddot{y} = -2\Omega\dot{x} + \partial W/\partial y \\ \ddot{z} &= \partial W/\partial z \quad W = (\Omega^2/2)(x^2 + y^2) - U \end{aligned} \tag{4}$$

where x, y, z represents the position coordinates in the ECEF frame, Ω is the rotation velocity and takes the value of 7.292115×10^{-5} for Earth. U is the Earth gravity potential, and the gravity acceleration is corresponding to Eq. 5, where p represents x, y, z.

$$\frac{\partial U}{\partial p} = \frac{\partial U_{2\mathrm{B}+J_2}}{\partial p} - \sum_{j=1}^{n} \frac{\mathrm{GM}_j(p - p_i)}{(\boldsymbol{r} - \boldsymbol{\rho}_j)^3} \tag{5}$$

Parallel computing process is described as Fig. 4. During the preparation stage, CPU reads the mass points' information, including position coordinates and mass, from the data file and sends them to GPU's global memory. Then the integrator on the CPU is initialed and starts working. Integrator is responsible for error controlling, step-size adjusting and the vehicle state updating. The vehicle position coordinates is sent into GPU whenever the gravity acceleration is needed to be calculated. CPU will proceed to the next step once the GPU returns the calculation result.

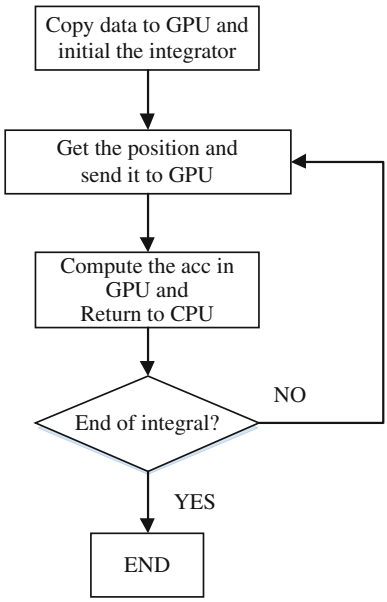

Fig. 4 Flow chart of the testing process on CPU

4.2 Testing Results

4.2.1 Calculation Speed

Three pairs of PMC models and SH models of different order (see Table 4) were chosen to investigate the calculation speed.

A MEO orbit is taken into consider, and the orbit parameters are listed in Table 5. The gravity field is calculated using two kinds of models mentioned above. The numerical integral results are shown in Figs. 5 and 6, for integration duration of 1 and 3 days, respectively.

Results show that, the computation speed-up ratio between the PMC model and SH model increases gradually as the gravitational order increases. A speed-up ratio of an order of 10 can be achieved for high order gravity field. While the length of the integral time has no significant effect to the speed-up ratio.

4.2.2 Calculation Accuracy

High efficiency of orbital numerical integration is the advantage of the PMC model, but the premise is that its calculation precision should be compatible with the same order SH model. Figure 7 shows the position offset of two orbits integrated using those two different 156 order gravity field models as show in Table 4. The position offset in X axis, as shown in the red line, increases linearly with time increased. The blue and green line represents the offset in Y and Z axis, respectively. The offset in these two axes increases volatility over time, but not exceeding a maximum of 2×10^{-3} m after 3 days of integration.

We further compared the integration accuracy for three different types of orbit, including LEO, GEO, and highly elliptical orbit (Molniya orbit). The orbit parameters are listed in Table 5 and the compared results are summarized in Table 6. As can be

Table 4 PMC model and SH model used in the test

Order	PMC model	SH model
33	PMC331920	GGM02C 33 × 33
71	PMC71n7680	GGM02C 71 × 71
156	PMC156n32720	GGM02C 156 × 156

Table 5 Parameters for different orbit types

Orbit type	Perigee altitude (km)	Apogee altitude (km)	Inclination (°)
LEO	400	400	97.1
MEO	1350	1350	80
GEO	35,788	35,788	40
Molniya	500	39,850	63.3

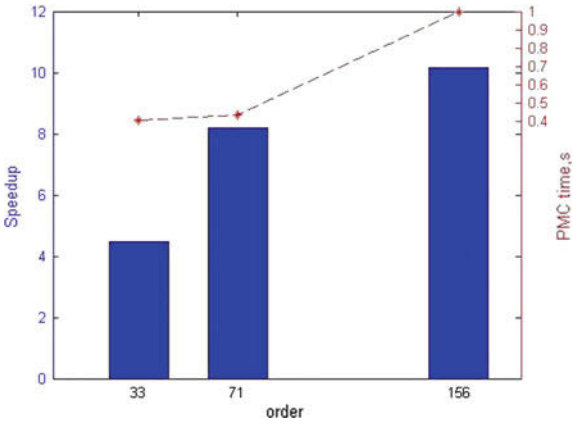

Fig. 5 PMC integral time and speed-up ratio for one day

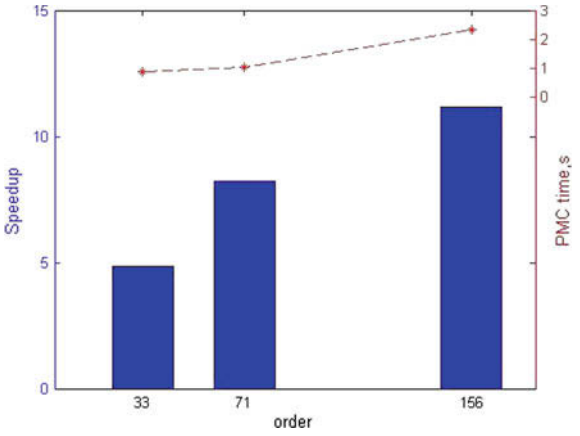

Fig. 6 PMC integral time and speed-up ratio for three days

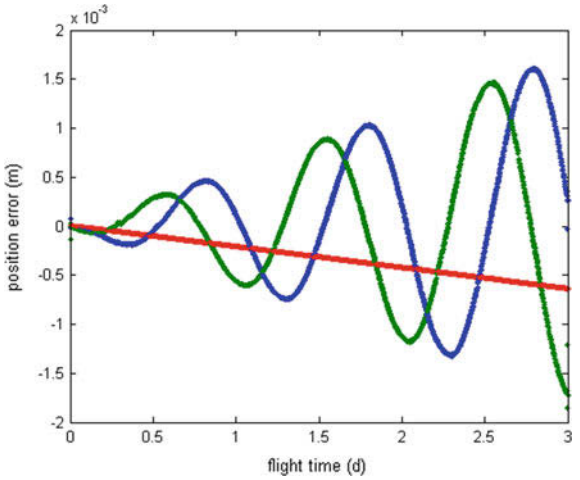

Fig. 7 Orbit position error between 2 model integrating 3 day

Table 6 Error and speed-up ratio on different orbit types

Orbit type	Max error (m)	Speed-up ratio
LEO	0.0167	15
MEO	0.0020	11
GEO	0.00065	14
Molniya	0.0020	15

seen from the results, the calculation accuracy of the PMC model meets the demand of various types of orbit, and the speed-up ratio for high order gravity field are all more than an order of 10.

4.3 Results Analysis

The paralleled PMC model is quite outstanding in accelerating the calculation of gravitational acceleration. Compared with the classical SH model, the speed-up ratio for low order (30) PMC model is about 5; this value increases to 8 when the model order increases to 70. For high-order PMC model, the speed-up ratio can achieve an order of 10. For low order gravity model, the accelerating effect of PMC model is not so prominent as low gravity field computation is relatively inadequate and, the effect of GPU acceleration is concealed by the extra time of the device initialization and data copies. Inversely, a rapid increase in calculation intensity will cause the GPU computing acceleration effect reaching more than 10 times for the high-order gravity field.

For precise orbit determination applications, the higher order integrator, such as Romberg 7(8) method, is generally used to propagate the orbit, which will cause more computation in gravitational acceleration. In this case, paralleled PMC model will result in significant speed up effect. For further work, the fast integration method in high-fidelity gravitational field would be investigated.

Besides the computational efficiency, the PMC model can ensure the accuracy of numerical integration in compatible with the same order of the SH model. For 3 days integration time, the maximum position error is less than 2 cm for a low-Earth-orbit (LEO) satellite, and less than 2 mm for a high-Earth-orbit satellite. This favorable match supports that one can use the PMC model instead of the SH model in the precise orbit determination applications.

5 Conclusions

The PMC model and GPU parallel computing technology are analyzed to realize the orbit integration of the same accuracy comparing with classical spherical model. With the emergence of space-borne GPU technology, on-board autonomous

dynamic navigation and formation control would be significantly promoted. The effectiveness of PMC model in other areas, such as the gravity gradient computation based on PMC model, is still needed to be validated and will be researched later.

References

1. Wang F (2006) Theory and software development on autonomous orbit determination using space borne GPS measurements. Wuhan University
2. Ning JS (1994) The earth geopotential models and applications. Eng Surv Mapp (2):1–8
3. Zhang CD (2005) Three satellites measuring gravity field–CHAMP, GRACE, GOCE. Geophys Geochem Explor 29(5):377–382
4. Weightman JA (1967) Gravity, geodesy and artificial satellites. A unified analytical approach. Use Artif Satell Geod 2:467
5. Chao DB (1992) Global virtual particle model. Geomat Inf Sci Wuhan Univ 02
6. Wu X (2009) A point mascon model based on satellite gravity gradient data, pp 414–417
7. Li ZW (2004) Point mass model tacking account of spectrum. The PLA Information Engineering University
8. Russell RP, Arora N (2012) Global point Mascon models for simple, accurate, and parallel geopotential computation. J Guid Control Dyn 35(5):1568–1581
9. Junkins JL (2012) Investigation of finite-element representations of the geopotential. AIAA J 14(6):803–808
10. Junkins JL, Miller GW, Jancaitis JR (1973) A weighting function approach to modeling of irregular surfaces. J Geophys Res 78(11):1794–1803
11. Engels RC, Junkins JL (2012) Local representation of the geopotential by weighted orthonormal polynomials. J Guid Control Dyn 3
12. Arora N, Russell RP (2015) Efficient interpolation of high-fidelity geopotentials. J Guid Control Dyn 1–16
13. Lu FS (2011) Survey of CPU/GPU synergetic parallel computing. Comput Sci 38(3):5–9
14. http://www.nvidia.cn/object/machine-learning-cn.html. Accessed Sept 2015
15. Tapley B, Ries J, Bettadpur S, Chambers D, Cheng M, Condi F, Gunter B, Kang Z, Nagel P, Pastor R, Pekker T, Poole S, Wang F (2005) GGM02—an improved Earth gravity field model from GRACE. J Geodesy. doi:10.1007/s00190-005-0480-z
16. Nvidia C (2011) Nvidia cuda C programming guide. NVIDIA Corp 120:18
17. Cuda C (2012) Best practices guide. Nvidia Corp
18. Wilt N (2013) The CUDA handbook: a comprehensive guide to GPU programming

Fast Computation Method of Real-Time Precise Satellite Clock Errors for Combined BDS/GPS

Zongpeng Pan, Hongzhou Chai, Kefan Yang, Biao Feng, Di Li, Yingdong Zhou and Feng Ming

Abstract BeiDou Navigation Satellite System (BDS) had been officially operating since the end of 2012. It can provide service of navigation, timing, and positioning in the Asia-Pacific region. In recent years the precise positioning on BDS had been widely studied and the accuracy of BDS Precise Point Positioning (PPP) can reach centimeters. Due to the satellite clock error corrections are fixed in PPP model, the accuracy and stability of real-time satellite clock errors would directly impact the positioning accuracy of real-time PPP (RT-PPP) and are the key points of RT-PPP. In this contribution, the method of fast computation of real-time precise satellite clock errors for combined BDS/GPS was investigated. First, the estimation model of real-time satellite clock based on epoch-differenced observations was studied. Then, the extended Kalman filter (EKF) was used to estimate the satellite clock errors based on real observations which collected from multi-GNSS experiment (MGEX) stations. The accuracy of BDS/GPS real-time clock errors was also analyzed which compared with the final precise clock products. Finally, the performance of BDS/GPS RT-PPP with the real-time BDS/GPS satellite clock errors was investigated. The results showed that the real-time BDS/GPS clock corrections were comparable with the final precise clock corrections and can satisfy the accuracy requirement of RT-PPP.

Keywords Satellite clock errors · Real-time · BDS/GPS · Precise point positioning

1 Introduction

Precise satellite orbit and clock products are the key elements to perform Precise Point Positioning [1] (PPP). In PPP observation equations, the satellite orbits and clock are usually held fixed as known value. The errors of orbit and clock will

Z. Pan (✉) · H. Chai · K. Yang · B. Feng · D. Li · Y. Zhou · F. Ming
Institute of Surveying and Mapping, Information Engineering University, Zhengzhou 450001, China
e-mail: panzongpeng@yeah.net

© Springer Science+Business Media Singapore 2016

J. Sun et al. (eds.), *China Satellite Navigation Conference (CSNC) 2016 Proceedings: Volume III*, Lecture Notes in Electrical Engineering 390,
DOI 10.1007/978-981-10-0940-2_9

contaminate the PPP result [2] directly. For real-time PPP (RT-PPP), the latency of real-time satellite ephemeris must be taken into consideration. Although the accuracy of the predicted part of IGS ultra-rapid orbits (about 5 cm) can meet the requirement of PPP, the accuracy of the predicted satellite clock errors, however, is about 3 ns which equals to 0.9 m in range will introduce large error in PPP solutions. The reason for the low accuracy of predicted satellite clock is that the high frequency of atomic clock on satellite is sensitive to the clock noise which originates from a variety of effects and environment variations, so the accuracy of satellite clock errors will decrease quickly with time goes by and hard to predict [3].

Among the solutions to overcome the accuracy limitation of predicted satellite clock errors, the method of using a network of reference stations to estimate the real-time precise satellite clock errors is commonly used. Since 2013, the IGS real-time group (IGS-RT) had provided real-time satellite orbit and clocks error corrections for GPS and the experimentation products for GLONASS [4]. The GPS/GLONASS real-time satellite ephemeris can meet the accuracy requirement of RT-PPP. However, the real-time satellite ephemeris corrections are not available for other GNSS constellations, such as BeiDou Navigation Satellite System (BDS).

BDS has been officially operation and can provide service of navigation, timing, and positioning in the Asia-Pacific region [5, 6] since the end of 2012. With the distribution of BDS precise satellite orbit and clock errors [7–10], the accuracy of BDS PPP can reach centimeters. However, the above studies were based on post-processed solutions and final precise ephemeris, the performance of real-time satellite orbits, and clocks is less focused on, the same situation is to real-time BDS PPP. Zhang et al. [11] presented the joint estimation model for GPS/BDS real-time clock errors. The results showed that the accuracy of real-time GPS clock errors was agreed with IGS final precise clock products and the accuracy of BDS real-time clock errors can meet the requirement of PPP. Li et al. [12] studied the four GNSSs real-time precise orbit determination (POD) and clock estimation using the zero-differenced raw observations. The results showed that the positioning accuracy and reliability of real-time multisystems PPP was better than GPS-only PPP. However, a large number of ambiguity parameters must be estimated when using zero-differenced carrier phase observations. It will be very time consuming in real-time mode [13] since there are a lot of stations in network. This situation will be even worse with the development of GNSS constellation and station network.

The differenced carrier phase observation between adjacent epochs can eliminate phase ambiguity parameters which will decrease the parameters in equations. In this contribution, the method of fast computation of real-time precise satellite clock errors for combined BDS/GPS was investigated. Then the real-time GPS/BDS clock errors are estimated using the observations collected from IGS multi-GNSS experiment (MGEX) stations. Finally, the RT-PPP-based on real-time GPS/BDS clock errors is performed to investigate the accuracy and availability of real-time clock errors. The following parts of the contribution are organized as follows: first, the clock errors estimation model based on epoch-differenced observations is described in second part. Then the experimental strategies and results analysis are presented. Finally, some conclusions will be drawn.

2 Model for BDS/GPS Satellite Clock Errors Estimation

2.1 Function Model

The ionosphere-free observations of phase and code are used to estimate satellite clocks. For a satellite j of any GNSS s observed by receiver r, considering hardware delays in code observations, the ionosphere-free code and carrier phase observations at epoch (i) can be expressed as follows:

$$P_{\mathrm{if},r}^{s,j}(i) = \rho_r^{s,j}(i) + \delta t_r(i) - \delta t^{s,j}(i) + T_r^{s,j}(i) + d_{\mathrm{if},r}^{s}(i) - d_{\mathrm{if}}^{s,j}(i) + \varepsilon\left(P_{\mathrm{if},r}^{s,j}(i)\right) \quad (1)$$

$$\begin{aligned} L_{\mathrm{if},r}^{s,j}(i) = {} & \rho_r^{s,j}(i) + \delta t_r(i) - \delta t^{s,j}(i) + T_r^{s,j}(i) + b_{\mathrm{if},r}^{s}(i) \\ & - b_{\mathrm{if}}^{s,j}(i) + \lambda_{\mathrm{if}}^{s} N_{\mathrm{if},r}^{s,j}(i) + \varepsilon\left(L_{\mathrm{if},r}^{s,j}(i)\right) \end{aligned} \quad (2)$$

where r is station number, s for any GNSS, such as GPS or BDS, j for a satellite; $L_{\mathrm{if},r}^{s,j}$, $P_{\mathrm{if},r}^{s,j}$ are ionosphere-free phase and code observations, $\rho_r^{s,j}$ is geometric distance between satellite and receiver, δt_r and $\delta t^{s,j}$ are receiver and satellite clock errors, in unit of meter, $d_{\mathrm{if},r}^{s}$, $b_{\mathrm{if},r}^{s}$ and $d_{\mathrm{if}}^{s,j}$, $b_{\mathrm{if}}^{s,j}$ are receiver-dependent or satellite-dependent code and phase hardware delay, $T_r^{s,j}$ is tropospheric delay in line of sight, $N_{\mathrm{if},r}^{s,j}$ is ionosphere-free ambiguity, $\varepsilon\left(P_{\mathrm{if},r}^{s,j}\right)$ and $\varepsilon\left(L_{\mathrm{if},r}^{s,j}\right)$ are the code and carrier phase measurement noise and other unmodeled errors, $\lambda_{\mathrm{if}}^{s}$ is the wavelength of ionosphere-free combination.

Generally, the satellite orbits and station positions are fixed as known component when estimated satellite clocks, which means $\rho_r^{s,j}$ is a known value. The satellite and receiver-dependent hardware delay are respectively combined with satellite and receiver clock errors, due to the linear relationship and cannot directly take them apart. The error correction in observations must be taken into consideration [14] at the same time, such as relativistic effects, antenna phase center, phase windup, troposphere priori model, and Earth tides. The observation equations can be expressed as

$$v_{P,r}^{s,j}(i) = \delta\tilde{t}_r^{s}(i) - \delta\tilde{t}^{s,j}(i) + M_r^{s,j}(i)\delta T_r(i) + \tilde{l}_{P,r}^{s,j}(i) \quad (3)$$

$$v_{L,\mathrm{r}}^{s,j}(i) = \delta\tilde{t}_r^{s}(i) - \delta\tilde{t}^{s,j}(i) + M_r^{s,j}(i)\delta T_r(i) + \lambda_{\mathrm{if}}^{s}\tilde{N}_{\mathrm{if},r}^{s,j}(i) + \tilde{l}_{L,r}^{s,j}(i) \quad (4)$$

where $v_{L,\mathrm{r}}^{s,j}$ and $v_{P,r}^{s,j}$ are the carrier phase and code measurement noise and other un-modeled errors, $\delta\tilde{t}_r^{s}$ and $\delta\tilde{t}^{s,j}$ are receiver and satellite clock errors which include code hareware delay, δT_r is tropospheric zenith wet delay (ZWD), $M_r^{s,j}$ is the wet mapping function. The tropospheric delay can be split into dry and wet component, the dry component can be removed from the observations using a priori model, only

the wet component needs to be estimated, $\tilde{N}_{\mathrm{if},r}^{s,j}$ is float ambiguity which include receiver and satellite-dependent hardware delay, $\tilde{l}_{L,r}^{s,j}$ and $\tilde{l}_{P,r}^{s,j}$ are pre-fit residuals of ionosphere-free phase and code combinations.

Equations (3) and (4) can be directly used to estimate precise satellite clock errors with global stations data. This estimation method is also called the undifferenced method. With the increasing observation stations and satellites of GNSS, there will have a lot of ambiguity parameters in Eq. (4) and it will be time consuming in real-time satellite clock estimation mode.

However, phase ambiguities are quite stable over a period of time if the phase observations have no cycle slip. Using constant character of phase ambiguities, we can form epoch-differenced phase observations and eliminate the phase ambiguity parameters, and then the number of parameters in estimated clock equations will obviously decrease. Since the stable characteristic of code hardware delay of receiver and satellite, they can be both eliminated in the process of epoch differenced [11]. We can only use highly precise epoch-differenced phase observations since the epoch-differenced clocks are estimated [15]. The epoch-differenced phase observations of combined GPS/BDS are expressed as

$$\Delta v_{L,\mathrm{r}}^{G,j}(i) = \Delta\delta t_r(i) - \Delta\delta t^{G,j}(i) + \Delta M_r^{G,j}(i)\delta T_r(i) + \Delta\tilde{l}_{L,r}^{G,j}(i) \tag{5}$$

$$\Delta v_{L,\mathrm{r}}^{B,j}(i) = \Delta\delta t_r(i) - \Delta\delta t^{B,j}(i) + \Delta M_r^{B,j}(i)\delta T_r(i) + \Delta\tilde{l}_{L,r}^{B,j}(i) \tag{6}$$

where Δ is the epoch-differenced operator between two adjacent epochs, G is GPS, B is BDS. It is noted that the difference of ZWD in short time (30 s) is very small and still denotes as $\delta T_r(i)$ in epoch-differenced observations, and we just form epoch-differenced in wet mapping function. The current ZWD and next epoch $(i + 1)$, denoted as $\delta T_r(i+1)$, can be estimated as random walk process in Kalman filter. The parameters in Eqs. (5) and (6) are

$$\left[\Delta\delta t_r(i), \Delta\delta t^{G,j}(i), \Delta\delta t^{B,j}(i),\ \delta T_r(i)\right] \tag{7}$$

Compared to GPS-only processed parameters, only the epoch-differenced BDS satellites clock parameters are added when combined BDS/GPS to estimated satellite clocks. The method of satellite clock estimation using epoch-differenced observations will not significantly increase the estimated parameters when one more GNSS is added, which is important in real-time data processing.

It must be noted that the satellite and receiver clock parameters are linear correlation and the formal equations are singular. It must choose a stable receiver clock as a reference clock and held fixed, then solve the formal equations. At the same time, only the epoch-differenced clocks are estimated when using Eqs. (5) and (6), which must be accumulated with the initial clock bias $\delta t^{s,j}(0)$ if one wants to obtain clock corrections. Then the satellite clock corrections of GPS and BDS are expressed as

$$\delta t^{G,j}(i) = \delta t^{G,j}(0) + \sum_{k=1}^{i} \delta t^{G,j}(k) \tag{8}$$

$$\delta t^{B,j}(i) = \delta t^{B,j}(0) + \sum_{k=1}^{i} \delta t^{B,j}(k) \tag{9}$$

From above equation, the accuracy of estimated satellite clock corrections is influenced by both epoch-differenced clock and the initial clock bias $\delta t^{s,j}(0)$. The temporal change of epoch-differenced clock can be determined accurately using precise phase observations. However, the accuracy of initial clock bias $\delta t^{s,j}(0)$

Table 1 Setting for parameters

	Parameters	Processing strategies
Observations	Phase observations	Epoch-differenced ionosphere-free combination
	Elevation cutoff angle	10°
	Weighting	Elevation-dependent, a priori precision of 0.01 m for phase, for both GPS and BDS
Error corrections	DCB	DCB products provided by CODE for GPS
	Antenna phase center	GPS: igs_08.atx BDS: the estimated value provided by ESA receiver's corrected by igs_08.atx
	Phase windup	Corrected
	Earth tides	Model corrected
	Relativistic effects	Model corrected
	EOP	Provided by IERS
	Position of stations	Network solutions of GFZ
	Satellite orbits	GPS: IGS ultra-rapid-predicted orbits (IGU) BDS: GFZ final orbits (15 min)
Parameters estimation	Receiver clock	White noise with process noise variance of $8.1\,e^7 m^2/s \times \Delta t$ Initial value estimated by code observations and initial variance is $9\ e^6 m^2$
	Satellite clock	White noise with process noise variance of $9\,e^6 m^2/s \times \Delta t$ Initial value provided by IGU and initial variance is $9\ e^6 m^2$
	Tropospheric delay	Dry component provided by UNB3 model Wet component is modeled by random walk process and estimated with process noise variance of $3\,e^{-8} m^2/s \times \Delta t$ Initial value provided by UNB3 and initial variance is $0.25\ m^2$

depends on where it is retrieved from. Generally, the initial clock biases are retrieved from broadcast ephemeris or ultra-predicted ephemeris and also can be estimated by code observations. But the accuracy of initial clock biases which retrieved from those methods is several nanoseconds. The phase measurements which have ambiguity parameters can absorb initial clock biases. The code measurements will be contaminated by those biases. However, the code measurements are down-weighted with respect to phase measurements when perform PPP, which will mitigate the contamination of initial clock biases.

2.2 Parameter Estimation Method

Generally the filter methods are used to estimate parameters in real-time GNSS data processing. In this contribution, extend Kalman filter (EKF) is applied to estimate real-time satellite clock errors. The satellite and receiver clock errors can be modeled as white noise, due to its unstable in adjacent epoch. The parameter of tropospheric zenith wet delay is modeled as random walk process. A detailed and clear discussion of parameters estimation strategies and initial value of all parameters of EKF are summarized in Table 1. The processing strategies of observations and error corrections are also included.

3 Experiments and Results Analysis

3.1 Data and Processing Strategy

In order to investigate the accuracy and availability of real-time satellite clock errors based on epoch-differenced method, the RINEX data (30 s) collected from 50 MGEX stations at doy120 in 2015 are used to estimated clock corrections. The station distribution (red point) is showed in Fig. 1.

In the experiment, the GPS predicted ephemeris is provided by IGS ultrarapid-predicted products. The BDS final ephemeris which provided by GFZ is used since the predicted ephemeris products of BDS are not available. The sampling rate of all ephemeris products is 15 min.

The EKF is used to estimate satellite clock errors based on Eqs. (5) and (6) and the corresponding clock products are GPS-only, BDS-only and combined GPS/BDS clock errors. For detail estimation strategies for all parameters refer to Table 1. Then the estimated real-time GPS clock errors are compared to IGS final cock products (30 s) and the estimated BDS clock errors are compared to GFZ final clock products (5 min). The standard deviation (STD) of each satellite clock errors can be calculated by the formula [2] provided by pan et al. 2015.

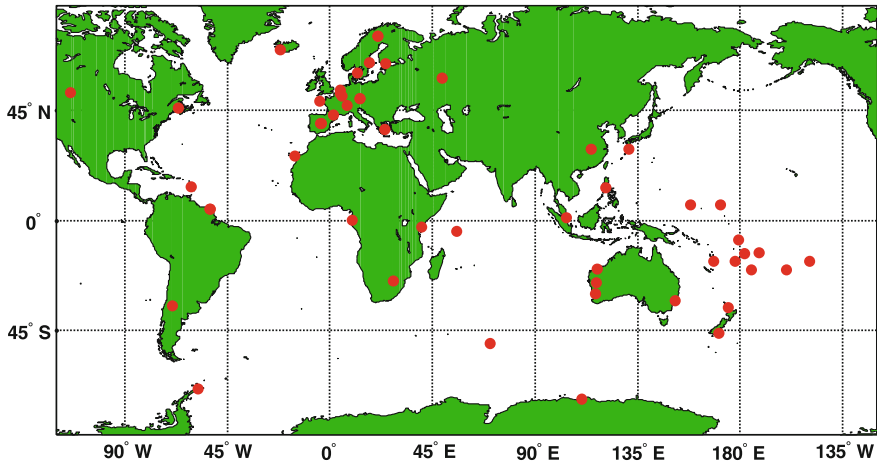

Fig. 1 Station distribution

3.2 GPS/BDS Clock Errors Validation

In order to analysis the influence of combined different systems to the accuracy of the estimated satellite clock errors, the GPS-only, BDS-only and combined GPS/BDS clock errors are estimated, respectively. Figures 2 and 3 present the STD of real-time GPS clock errors, which is estimated by GPS-only and combined GPS/BDS observations, respectively. The clock error of PRN 1 is selected as a referenced satellite clock and the satellite of PRN 8 do not work, so there are no statistical results of both satellite clock errors in Figs. 2 and 3.

It can be seen from Figs. 2 and 3, (1) the accuracy of GPS satellite clock errors, which are estimated by GPS-only and combined GPS/BDS observations, is at the same level. There is no significant difference between GPS-only clock errors and combined GPS/BDS clock errors. (2) The STD values of satellite clock errors are

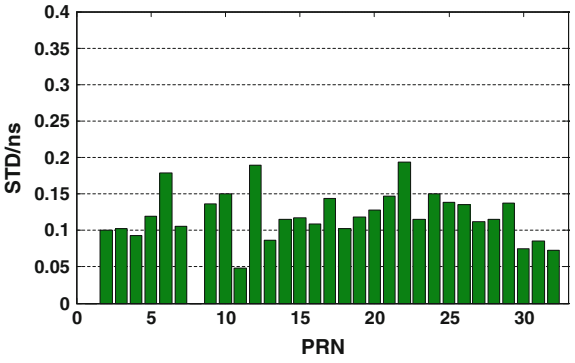

Fig. 2 The STD of clock errors using GPS observations

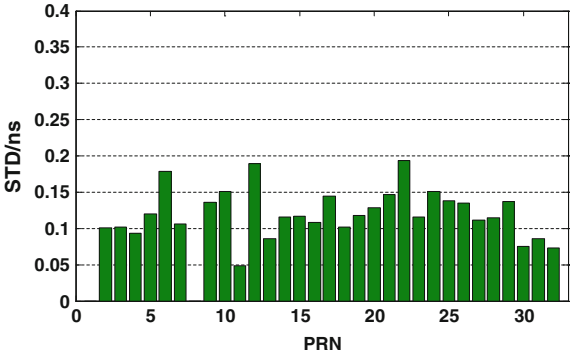

Fig. 3 The STD of GPS clock errors using GPS/BDS observations

smaller than 0.2 ns and the average STD is 0.11 ns. The real-time GPS clock errors which are estimated using epoch-differenced method have a high accuracy.

Figures 4 and 5 present the STD of real-time BDS clock errors, which is estimated by BDS-only and combined GPS/BDS observations, respectively. The clock error of C06 (IGSO) is selected as a referenced satellite clock and the satellite of C13 (MEO) do not work, so there are no statistical results of both satellite clock errors.

As seen from Fig. 4, the STD values of BDS satellite clock errors, which are estimated by BDS-only observations, are smaller than 0.6 ns and the average value is 0.31 ns. The accuracy of different satellites has a significant difference. The STD values of GEO and IGSO are smaller than the MEO ones. The reasons for this phenomenon are that the constellation of BDS has different satellite types and the main satellites of BDS are GEO and IGSO which can be observed at Asia-Pacific area recently. The stations in other places can only observe the MEO satellite and the observed spatial geometry of those stations are poor since the number of working MEO satellites are only 3. Due to the above reasons, the accuracy of MEO satellite clock errors is poor than other satellites when using BDS-only observations from global MGEX stations.

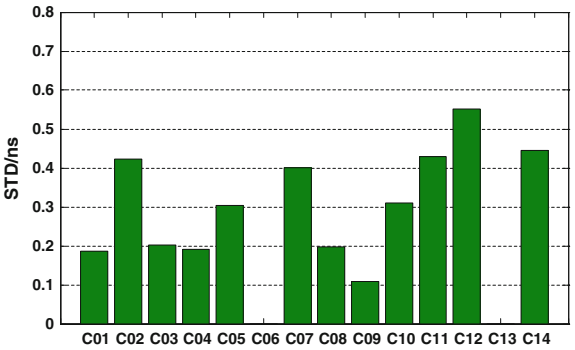

Fig. 4 The STD of clock errors using BDS observations

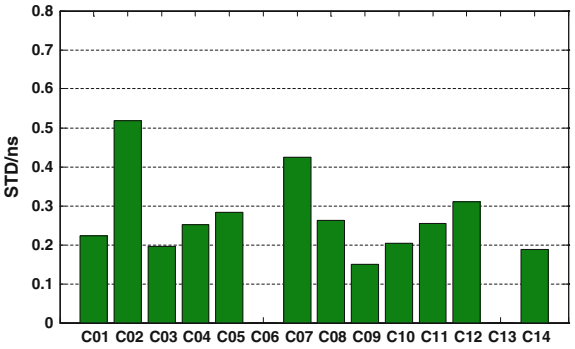

Fig. 5 The STD of BDS clock errors using GPS/BDS observations

Figure 5 presents the STD values of BDS clock errors which are retrieved from combined GPS/BDS observations. As seen from Fig. 5, the average STD of all satellite clock errors is 0.27 ns. Comparing with clock corrections retrieved from BDS-only observations, the accuracy of clock corrections improves 12.9 %. The accuracy of MEO clock corrections improve obviously and at the same level with respect to the accuracy of other satellite clock corrections. It can be seen from formula (5) and (6), the parameters to be estimated are clock errors and tropospheric wet delay. Combined GPS/BDS observations can provide more satellites which will improve the spatial geometry and help take clock parameters and tropospheric wet delay apart, especially in situation of only a few visible BDS MEO satellites. Those are the reasons why the accuracy of BDS clock errors improves when using combined GPS/BDS observations.

3.3 Real-Time PPP

The station of CUT0 and XMIS which is located at Asia-Pacific area, selected for performing PPP are excluded in clock corrections estimation. In order to further analysis the performance of real-time clock corrections, both real-time clock corrections and final precise clock corrections are used to perform static and kinematic PPP, respectively. In kinematic PPP mode, the station position is modeled as white noise. The initial variance is 100^2 m^2.

Figures 6 and 7 present the static positioning bias of different systems combined PPP at station CUT0 and XMIS (note that we plot the absolute value of the positioning bias). The horizontal axis stands for different systems combined mode. Where RT_B is simulated real-time BDS-PPP, RT_G is simulated real-time GPS-PPP, RT_B/G is simulated real-time BDS/GPS-PPP, B is post-processed BDS-PPP, G is post-processed GPS-PPP, B/G is post-processed BDS/GPS-PPP.

As seen from Figs. 6 and 7, the static positioning accuracy of real-time GPS-only and BDS-only PPP daily solutions can reach centimeters. The performance of GPS-PPP is better than BDS PPP either using real-time clock corrections

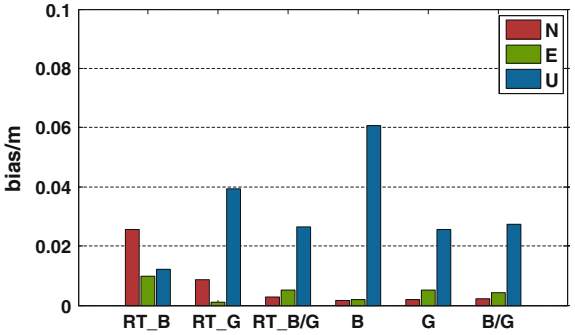

Fig. 6 The positioning bias of PPP solutions at station CUT0

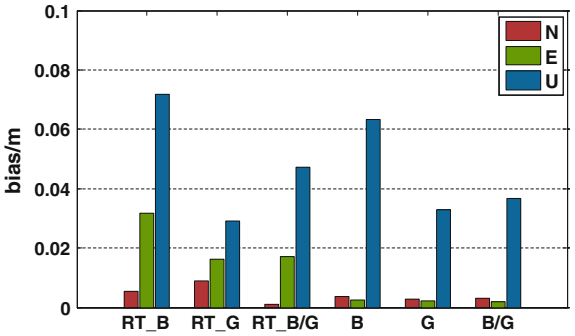

Fig. 7 The positioning bias of PPP solutions at station XMIS

or final precise products. The reasons may be that the satellite ephemeris products of BDS is poor than GPS ones and the precise antenna phase centers correction of BDS is unknown. Both of above reasons can affect the performance of BDS PPP solutions. On the other hand, the performance of combined GPS/BDS PPP is better than single system PPP, especially in horizontal direction. However, the positioning bias in vertical direction is between GPS-only and BDS-only PPP. There are the similar results in the post-processed PPP. Combined GPS/BDS can provide more visible satellites and optimize the spatial geometry which can improve positioning accuracy and reliability of PPP. The phenomenon is more significant in kinematic PPP at station CUT0, presented in Fig. 8. Where the positioning bias series present in (a) is simulated real-time BDS-PPP, (b) is simulated real-time GPS-PPP, (c) is simulated real-time GPS/BDS-PPP and (d) is post-processed GPS/BDS-PPP. The STD values of positioning bias are calculated after one hour of observation which can be considered convergence time of kinematic PPP.

As seen from Fig. 8, the STD of positioning bias series in real-time GPS kinematic PPP is better than real-time BDS ones. The accuracy of real-time GPS kinematic PPP is at centimeter level and the accuracy of BDS kinematic PPP is better than 0.3 m. Due to the BDS constellation, the spatial geometry is changing slowly, resulted in slowly convergence compare to GPS-PPP. On the other, we can find that the big fluctuation of positioning bias series in Fig. 8a, b can be eliminated

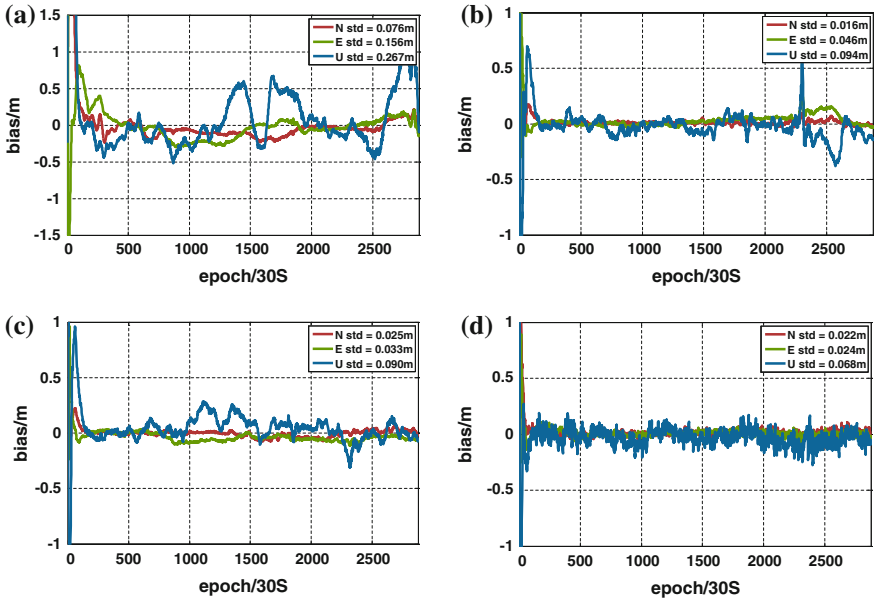

Fig. 8 Different combined kinematic PPP solutions at CUT0. **a** Simulated BDS RT-PPP bias series. **b** Simulated GPS RT-PPP bias series. **c** Simulated GPS/BDS RT-PPP bias series. **d** Post-processed GPS/BDS RT-PPP bias series

by combined GPS/BDS-PPP in Fig. 8c, which indicated the reliability of combined GPS/BDS-PPP is better than single system PPP, especially in situation of only a few visible satellites. Finally, if the accuracy of BDS clock corrections can further improve, the positioning accuracy of combined GPS/BDS PPP will be better, which can be seen from Fig. 8d post-processed PPP, especially in vertical direction.

4 Conclusion

In this contribution, the method of fast computation of real-time precise satellite clock errors based on epoch-differenced observations for combined BDS/GPS was investigated. The extended Kalman filter (EKF) was used to estimate the satellite clock errors based on observations which collected from MGEX stations. The accuracy of estimated BDS/GPS real-time clock errors was also analyzed which compared with the final precise clock products. Finally, the real-time PPP based on real-time GPS/BDS clock errors is performed to investigate the accuracy and availability of real-time clock errors. The results showed that

1. The real-time BDS/GPS clock corrections which are estimated using epoch-differenced method have a high accuracy. The average STD of all BDS

clock errors is 0.27 ns. Comparing with clock corrections retrieved from BDS-only observations, the accuracy of combined BDS clock errors improves 12.9 %. The average STD of all GPS clock errors is 0.11 ns. However, there is no significant difference between GPS-only clock errors and combined GPS/BDS clock errors.

2. The static positioning accuracy of real-time GPS-only and BDS-only PPP daily solutions can reach centimeters. The accuracy of real-time GPS kinematic PPP is at centimeter level and the accuracy of BDS kinematic PPP is better than 0.3 m. The performance of combined GPS/BDS PPP is better than single system PPP.

Acknowledgments Thanks to the IGS MGEX and GFZ for providing GNSS observations and precise ephemeris products. This work was supported by National Natural Science Foundation of China (No. 41274045, 41574010) and State Key Laboratory of Geo-information Engineering (No. SKLGIE2015-Z-1-1).

References

1. Zumberge JF, Heflin MB, Jefferson DC et al (1997) Precise point positioning for the efficient and robust analysis of GPS data from large networks. J Geophys Res Solid Earth (1978–2012) 102(B3):5005–5017
2. Pan ZP, Chai HZ, Liu M et al (2015) Real-time GLONASS precise satellite clock corrections estimation and precise point positioning. J Geod Geodyn 35(6):992–996
3. Huang GW, Zhang Q, Xu GC (2014) Real-time clock offset prediction with an improved model. GPS Solut 18(1):95–104
4. Hadas T, Bosy J (2014) IGS RTS precise orbits and clocks verification and quality degradation over time. GPS Solut 19(1):93–105
5. China Satellite Navigation Office (CSNO) (2012) BeiDou navigation satellite system signal in space interface control document. http://gge.unb.ca/test/beidou_icd_english.pdf
6. Yang YX, Li JL, Xu JY et al (2011) Contribution of the compass satellite navigation system to global PNT users. Chin Sci Bull 56(26):2813–2819
7. Lou Y, Liu Y, Shi C et al (2014) Precise orbit determination of BeiDou constellation based on BETS and MGEX network. Sci Rep 4(8):1255–1264
8. Zhao Q, Guo J, Li M et al (2013) Initial results of precise orbit and clock determination for COMPASS navigation satellite system. J Geodesy 87(5):475–486
9. Montenbruck O, Hauschild A, Steigenberger P et al (2013) Initial assessment of the COMPASS/BeiDou-2 regional navigation satellite system. GPS Solut 17(2):211–222
10. Lou Y, Liu Y, Shi C et al (2015) Precise orbit determination of BeiDou constellation: method comparison. GPS Solut 1–10
11. Zhang W, Lou Y, Gu S et al (2015) Joint estimation of GPS/BDS real-time clocks and initial results. GPS Solut 1–12. doi:10.1007/s10291-015-0476-y
12. Li X, Ge M, Dai X et al (2015) Accuracy and reliability of multi-GNSS real-time precise positioning: GPS, GLONASS, BeiDou, and Galileo. J Geod 89(6):607–635
13. Ge M, Chen J, Douša J et al (2012) A computationally efficient approach for estimating high-rate satellite clock corrections in realtime. GPS Solut 16(1):9–17
14. Kouba J, Héroux P (2001) Precise point positioning using IGS orbit and clock products. GPS Solut 5(2):12–28
15. Bock H, Dach R, Jäggi A et al (2009) High-rate GPS clock corrections from CODE: support of 1 Hz applications. J Geod 83(11):1083–1094

Ultra-Short-Term Stability Analysis of GNSS Clocks

Mingzhe Li, Shaocheng Zhang, Youjian Hu and Lijuan He

Abstract Nowadays, the GNSS applications have been developed not only with high requirement on the positioning accuracy, but also with high frequency and high dynamic observations. In the high frequency and high dynamic application like GNSS radio occultation, single receiver observations are normally used, and the GNSS clocks may became an important error source as differential method cannot be used. In this paper, the ultra-short-term stability of the GNSS clocks are investigated with 20 Hz dual-frequency observations, the receiver clock errors are removed with observation differential between satellites, and first order ionosphere delays are eliminated with ionosphere-free combination. In order to avoid the second order ionosphere delay, ionosphere peace period observations are used for analysis, and the troposphere delay are estimated with mapping function. Finally, the ultra-short-term stability of different atomic clocks onboard GPS and Beidou satellites are analyzed with Hadamard Deviation. The results show that the clock errors stability of 0.05 s in GPS system and Beidou system can reach up to a 10^{-10} degree, and the stability of 1 s interval reach up to a 10^{-11} degree. Hence, it can be concluded that the Beidou satellite clocks have the equivalent performance compared with GPS satellite clocks on ultra-short-term stability, and the accuracy of the Beidou satellite-based radio occultation will be able to achieve the same level as GPS based radio occultation.

Keywords High-frequency data · Clock error · Ultra-short-term stability · Hadamard deviation

M. Li · S. Zhang (✉) · Y. Hu · L. He
China University of Geosciences, 388 Lumo Road, Wuhan, China
e-mail: gnss.zsc@foxmail.com

© Springer Science+Business Media Singapore 2016

J. Sun et al. (eds.), *China Satellite Navigation Conference (CSNC) 2016 Proceedings: Volume III*, Lecture Notes in Electrical Engineering 390,
DOI 10.1007/978-981-10-0940-2_10

1 Introduction

In the GNSS satellite positioning applications, the essence of satellite observations is time measuring. Hence, the atomic clock onboard the GNSS satellite is most important part for a GNSS satellite, and the stability will strongly influence the accuracy and reliability of navigating, positioning, and timing performance [1]. So it is necessary for us to analyze the stability of satellite's clock.

Most of previously scholar researches focus on the analysis of short-term stability or mid-term stability of the GNSS satellite clocks with the observation intervals ranged from 30 s to 1 day, and some very impressive results had been demonstrated. Guo Hairong and Huang Guanwen have worked on the theory analysis of atomic clock's stability, especially Allan Deviation and Hadamard Deviation [1, 2]; Yue et al. [3] have analyzed atomic clock stability onboard some GPS satellites based on IGS 30 s clock products. However, as the development of the high frequency, high dynamic application like GNSS radio occultation, the ultra-short-term stability evaluation, which is several seconds or even less than 1 s interval, became urgently needed.

In this research, the ultra-short-term stability of the GNSS satellite clock will be analyzed. The observation model and satellite clock offset calculation were first introduced in Sect. 2; and then the method used for the stability analysis were introduced in Sects. 3 and 4 shows the statistic results based on the Hadamard Deviation for both GPS and Beidou satellite clocks; and brief conclusion and future research plan were summarized in Sect. 5.

2 Satellite Clock Error Isolation

The pseudorange and carrier phase observation for GNSS positioning is actually the measurement for the differences between signals transmitted time and received time. However, the measurements are influenced with various factors like receiver and satellite clock bias, satellite motions, ionosphere, and troposphere delays, relativistic effects, earth rotation corrections, multipath effect et al. For carry phase measurement, they may also be contaminated with ambiguities and cycle-slips. Hence, various error sources need to be carefully corrected to isolate the satellite clock bias, which is going to be analyzed.

2.1 Observation Models

As the carrier phase observations are much more precise than the pseudorange observation, the carrier phase measurements are used for the satellite clock analysis [4]. The carrier phase and pseudorange observation equation could be listed as follows:

$$\lambda_i \varphi_{r,i}^s = \rho_r^s + c(\mathrm{d}t_r - \mathrm{d}t^s) + \mathrm{dtrop}_{r,i}^s - \mathrm{dion}_{r,i}^s - \lambda_i N_{r,i}^s + \varepsilon_{r,i}^s \quad (1)$$

$$P_{r,i}^s = \rho_r^s + c(\mathrm{d}t_r - \mathrm{d}t^s) + \mathrm{dtrop}_{r,i}^s + \mathrm{dion}_{r,i}^s + e_{r,i}^s \quad (2)$$

where λ_i is the wavelength of carrier phase frequency i, $\varphi_{r,i}^s$ and $P_{r,i}^s$ are the carrier phase and pseudorange observation from satellite s to receiver r, ρ_r^s, is the geometry distances between receiver and satellites, c is the speed of light, $\mathrm{d}t_r$ is receiver clock error, $\mathrm{d}t^s$ is satellite clock bias, $\mathrm{dtrop}_{r,i}^s$ and $\mathrm{dion}_{r,i}^s$ are the signal delays due to troposphere and ionosphere, $N_{r,i}^s$ is carrier phase ambiguities, $\varepsilon_{r,i}^s$ and $e_{r,i}^s$ are random noise for carrier phase and pseudorange correspondingly.

2.2 Single Difference Clock Bias Calculation

For the GNSS satellite clock analysis, one satellite clock needs to be selected as the time reference, thus a single difference between two satellites observations are used for the satellite clock calibration as following:

$$\begin{aligned}\mathrm{d}t^s - \mathrm{d}t^k = &((\rho_r^s - \rho_r^k) + (\mathrm{dtrop}_{r,i}^s - \mathrm{dtrop}_{r,i}^k) - (\mathrm{dion}_{r,i}^s - \mathrm{dion}_{r,i}^k) \\ &- (\lambda_i N_{r,i}^s - \lambda_i N_{r,i}^k) - (\lambda_i \varphi_{r,i}^s - \lambda_i \varphi_{r,i}^k) + (\varepsilon_{r,i}^s - \varepsilon_{r,i}^k))/c\end{aligned} \quad (3)$$

Before calculation work of the satellite clock bias, Melbourne-Wübbena combination and geometry-free combination are used to check cycle-slips. Precise ephemeris is used to calculate the position of satellites, also ionosphere-free combination to eliminate the first order of ionospheric delays. The tropospheric delay is corrected with UNB3 model and estimates the zenith path delay with Neil mapping function [5, 6]. Considering the ambiguities of carrier phase are constant values, they will not affect the stability analysis of the satellite clocks. Beside the above corrections, the relativistic effect and earth rotation corrections are also corrected with empirical model.

3 Analyzing Theory of Atomic Clock's Stability in Time Domain

3.1 Stability Analyzing Method

Frequency standard equipment is the unit of oscillator and the accessory circuit, which can produce standard frequency with high precise and high stability. Atomic clock as a frequency standard equipment, its stability analysis usually included in the analysis of the output frequency random fluctuation which affected by noise. Allan

Deviation and Hadamard Deviation are two typical methods for satellite clock assessment. The former one is usually used for Cs clock analysis, whose frequency drift is not too obviously, and the later one is used for Rb clocks which usually have conspicuous frequency drift [3, 7]. The model of Allan Deviation is written as Eq. 4:

$$\sigma_y^2(\tau) = \frac{1}{2m^2(M-2m+1)} \sum_{j=1}^{M-2m+1} \sum_{i=j}^{j+m-1} [y_{i+m} - y_i]^2 \tag{4}$$

The Hadamard Deviation can be written as in Eq. 5:

$$H\sigma_y^2(\tau) = \frac{1}{6m^2(M-3m+1)} \sum_{j=1}^{M-3m+1} \sum_{i=j}^{j+m-1} [y_{i+2m} - 2y_{i+m} + y_i]^2 \tag{5}$$

where $\{ y_n, n = 1, 2, \ldots, M \}$ is a relative frequency deviation sequence of atomic clocks, τ_0 is the sampling interval, M is the number of data, τ is the averaging interval and m is the averaging sector as $m = \tau/\tau_0$.

The atomic clock error is composed of the certainty parts and the uncertainty parts, whose model can be written as:

$$x(t) = x_0 + y_0 t + \frac{1}{2} D t^2 + \varepsilon(t) \tag{6}$$

Here $x(t)$ is the clock error, x_0 is the initial phase deviation of atomic clocks, y_0 is the initial frequency deviation, D is the frequency drift and $\varepsilon(t)$ is the random part. The initial phase deviation is a constant, which will not affect the stability analyzing results. However, the frequency deviation and frequency drift parts will change with time, both of these two parts will directly affect the Hadamard Deviation results [2]. As a resampling deviation, Allan Deviation can remove the effects due to frequency deviation, but cannot remove the effects of frequency drift. Hence, the Hadamard Deviation as kind of triple sampling deviation is normally used to avoid the frequency drift effect [1].

Considering that GPS and Beidou satellites are now mostly equipped with Rb clocks, the Hadamard Deviation is chosen for atomic clock's stability evaluation in this research.

3.2 *Data Preprocessing*

Before calculating Hadamard Deviation, phase data should be first converted to frequency data. Clock phase data here is equivalent to the time difference measurements, which are directly used for positioning and timing. However, the phase data could be contaminated with gross errors and cannot be detected directly. Hence, the frequency data are normally used for data preprocessing.

For the atomic clock frequency data, it means the relative instantaneous frequency data of atomic clock. The equation used for converting phase data to frequency data is written as following:

$$y_i = \frac{x_{i+1} - x_i}{\tau_0} \tag{7}$$

where y_i is the relative instantaneous frequency data, x_i and x_{i+1} are the atomic clock phase data and τ_0 is the time intervals [3, 4].

Since atomic clock onboard satellites will inevitably generate gross error data in long-term continuous operation. Here a 3σ threshold is used to detect and remove the gross error data. In this research, the data rejection rate is lower than 0.5 %.

4 Results

4.1 Satellites Information of GPS and Beidou

Nowadays, GPS system has 31 operation satellites while Beidou system has about 14 satellites on operation. The satellite specific information is in Tables 1 and 2.

4.2 Analysis

In this research, the Trimble R8 GNSS receivers are used for 20 Hz dual-frequency static observations collection. The data are mainly collected on October 16 2015, November 14 2015, and January 18 2016, and most of the evaluation data are collected during ionosphere peace period between 0:00 am to 7:00 am local time to

Table 1 Satellites information of GPS system (as of January 20, 2016)

Satellite species	PRN
Block-IIA	32
Block-IIR	02, 11, 13, 14, 16, 18,19, 20, 21, 22, 23, 28
Block-IIRM	05, 07, 12, 15, 17, 29, 31
Block-IIF	01, 03, 06, 08, 09, 10,24, 25, 26, 27, 30

Table 2 Satellites information of Beidou system (as of January 20, 2016)

Satellite species	PRN
GEO	C01, C02, C03, C04, C05
IGSO	C06, C07, C08, C09, C10
MEO	C11, C12, C13, C14

avoid the disturbance of second order ionospheric delays, except that some Beidou MEO satellites cannot be observed during this time period.

To analyze the stability of clock bias, different satellites' combination from same GNSS systems are chosen for comparison. Here the GPS satellites G06, G09, G12, G17, G19, G28, and Beidou satellites C01, C03, C06, C08, C11, and C14 are used

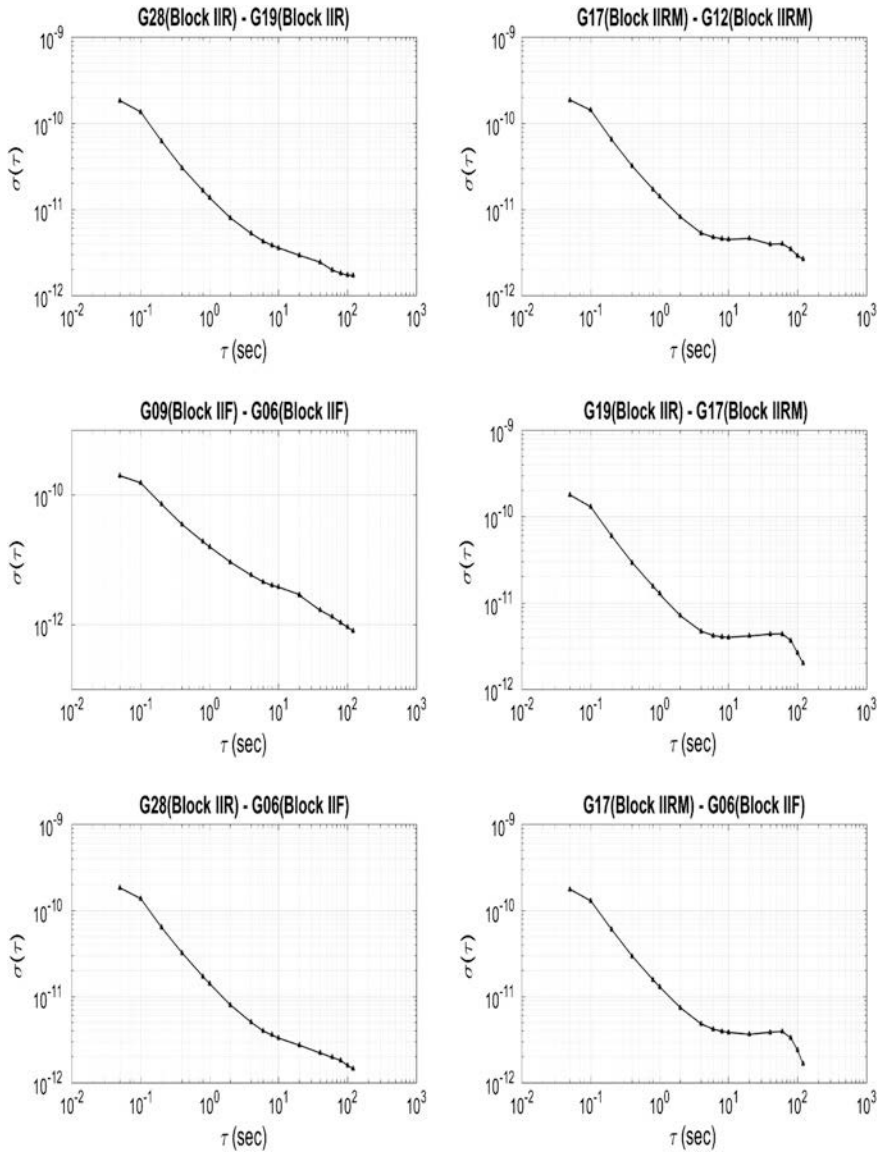

Fig. 1 Hadamard Deviation of atomic clocks onboard GPS satellites

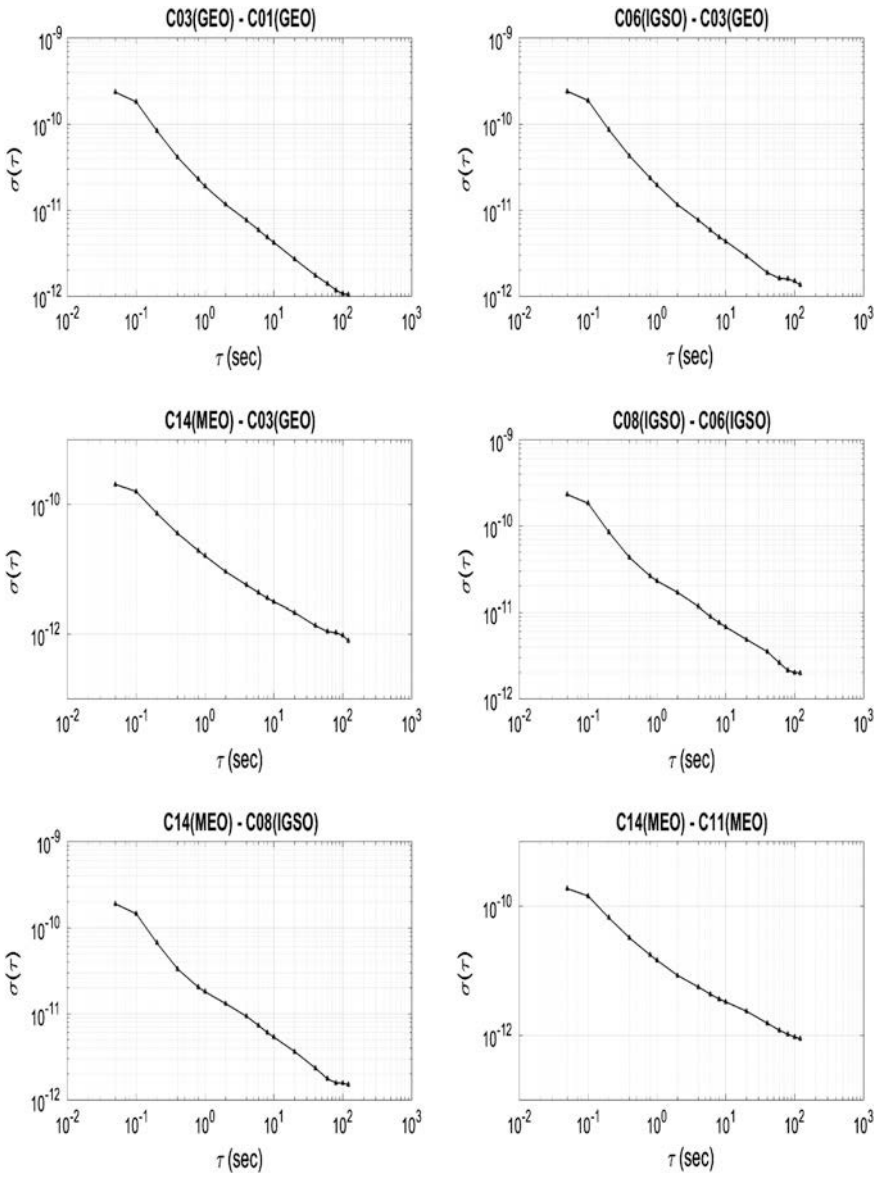

Fig. 2 Hadamard Deviation of atomic clocks onboard Beidou satellites

for the satellite stability evaluation. The Hadamard Deviation is calculated and plotted as in Figs. 1 and 2, where x-axis is for averaging intervals and y-axis stands for Hadamard Deviation results.

The analyze work compared the different type of satellites from the GNSS systems. For the GPS system, six different the combinations of Block-IIR to Block-IIR,

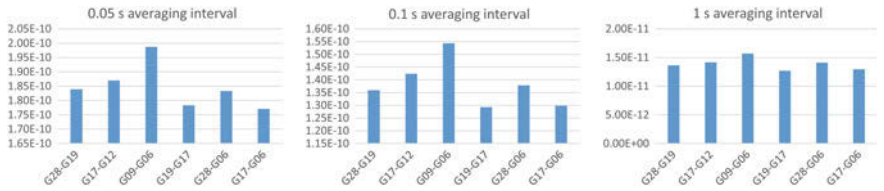

Fig. 3 Ultra-short-term stability of atomic clocks onboard GPS satellites

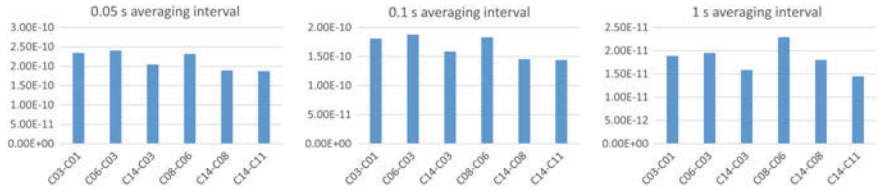

Fig. 4 Ultra-short-term stability of atomic clocks onboard Beidou satellites

Block-IIRM to Block-IIRM, Block-IIF to Block-IIF, Block-IIR to Block -IIRM, Block-IIR to Block-IIF, and Block-IIRM to Block-IIF are chosen. For Beidou system, the GEO to GEO, IGSO to GEO, MEO to GEO, IGSO to IGSO, MEO to IGSO, and MEO-MEO combinations are chosen for Beidou atomic clocks analyzing.

As results shown in Figs. 1 and 2, the clock bias stability of both GPS and Beidou is about 10^{-10} degree at the averaging intervals of 0.05 and 0.1 s, and 10^{-11} degree at the averaging intervals of 1 s. The stability at 10 and 100 s intervals can reach up to 10^{-12} degree. It is obvious that the stability of atomic clocks get better along with the averaging intervals increasing.

Figures 3 and 4 summarized the ultra-short-term stability of GPS and Beidou. The x-axis stands for different satellites combinations and y-axis stands for Hadamard Deviation results.

It shows that the stability of GPS and Beidou at the same averaging intervals has similar performance. Different kinds of satellite combinations did not show much obviously deviation difference at 0.05 s, 0.1 s, and 1 s averaging intervals.

5 Conclusion

In this paper, the Hadamard Deviation is used to study the ultra-short-term clock stability from both GPS and Beidou satellite. The results show that the stability of satellite clock bias can get about 10^{-10} degree at the averaging intervals of 0.05 s, and 10^{-11} degree at 1 s interval. The stability keeps steadily increasing with the averaging interval under 100 s, and could reach up to a 10^{-12} degree on 100 s

interval. The results also show that different generations GPS satellites have the same clock performance while they are all using the Rb oscillator, and for Beidou satellites, the different orbital satellites show the same magnitude ultra-short-term clock stability performance. The comparison between GPS and Beidou satellite clock also show that there is basically not obvious difference on ultra-short-term stability.

The analysis results will help us on making a preliminary estimation on the Beidou based radio occultation performance. As the Beidou satellite clock has the equivalent ultra-short-term stability performance to GPS satellite clock on high rate observation, the Beidou-based radio occultation would be possible with the standard service from IGS. We would like to do more comprehensive study on the high dynamic data LEO observation on future validation work.

Acknowledgements The State Key Laboratory of Geodesy and Earth's Dynamics funding with number of SKLGED2015-3-2-E and China University of Geosciences Fundamental Research Funds for the Central University number 007-G1323511561 are acknowledged for supporting this research.

References

1. Guo H (2006) Study on the analysis theories and algorithms of the time and frequency characterization for atomic clocks of navigation satellites. Information Engineering University, Zhengzhou
2. Guanwen H (2012) Research on algorithms of precise clock offset and quality evaluation of GNSS satellite clock. Chang'an University, Xi'an
3. Yue M, Jianpeng C, Wei D, Xiaolin J (2011) Analysis of on-board atomic clock stability influences. Geomatics Inf Sci Wuhan Univ 36(10)
4. Lou Y, Shi C, Zhou X, Ye S (2009) Realization and analysis of GPS precise clock products. Geomatics Inf Sci Wuhan Univ 34(1)
5. Collins JP (1999) Assessment and development of a tropospheric delay model for aircraft users of the global positioning system. Technical Report University of New Brunswick, Fredericton, Canada
6. Mendes VB (1999) Modeling the neutral-atmosphere propagation delay in radiometric space techniques. Frederiction University of New Brunswick
7. Guanwen H, Zhang Q, Wang J (2009) Research on estimation and prediction of GPS satellite clock error. J Geodesy Geodyn 29(6)

Comprehensive Satellite Clock Performance Evaluation Results Analysis with Multi-data

Xin Shi, Li Liu, Gang Yao, Junping Li and Lei Gong

Abstract The satellite-ground two-way clock correction data is usually adopted in the satellite clock performance evaluation. Two types of new analysis data source including satellite phase difference data and multi-satellites orbit determination clock difference data were introduced in this paper for comprehensive satellite clock performance evaluation. In order to assure the accuracy of the evaluation results, the satellite clock performance evaluation should not only be evaluated by different methods with different data, but also be verified by the satellite clock performance evaluated by different data. The measuring and calculating principle and precision was provided in this paper. The consistency of clock correction and performance evaluation was compared. The results show that satellite phase difference data and satellite-ground two-way clock correction data can preferably evaluate the performance of satellite clock and the evaluation consistency is very high; the orbit determination error in multi-satellites orbit determination clock difference cannot be totally separated, which will influence the satellite clock frequency stability.

Keywords Satellite-ground two-way clock correction · Phase difference data · Multi-satellites orbit determination clock difference · Satellite clock performance

1 Introduction

As the satellite time base of the navigation signal forming and system range measuring, the satellite clock performance determines the navigation satellite time precision and the user positioning accuracy. The satellite clock performance can be evaluated by multi-data source in the satellite navigation system. At present, the satellite-ground two-way clock correction data is usually adopted, but the satellite

X. Shi (✉) · L. Liu · G. Yao · L. Gong
Beijing Satellite Navigation Center, 100094 Beijing, China
e-mail: 876359113@qq.com

J. Li
North China Institute of Computing Technology, 100083 Beijing, China

© Springer Science+Business Media Singapore 2016

J. Sun et al. (eds.), *China Satellite Navigation Conference (CSNC) 2016 Proceedings: Volume III*, Lecture Notes in Electrical Engineering 390,
DOI 10.1007/978-981-10-0940-2_11

phase difference data and the multi-satellite orbit determination clock correction data is not fully used. In order to assure the authenticity of satellite performance evaluation results, the satellite clock performance should adopt multi-data with verification and comparison.

2 Multi-data Source Characteristics

2.1 Satellite-Ground Two-Way Clock Correction Data

The satellite-ground two-way clock correction data is the clock difference between the satellite work clock and the ground main clock separately measured by the satellite and the ground [1]. The frequency accuracy, drift rate, and stability index of the satellite clock relative to the ground reference clock can be calculated by using the satellite-ground two-way clock correction [2]. Because the ground main clock performance is higher than the satellite clock performance at least some order of magnitude, the satellite clock performance analysis results acquired by the satellite-ground clock correction can directly show the satellite work performance. The satellite-ground two-way clock correction data can be direct evaluation data of the satellite clock performance [3].

2.2 Satellite Phase Difference Data

The satellite phase difference data is directly measured by the phase comparison between the main and the backup clock, which shows the measuring precision of the phase-comparison equipment and the work performance of the two clocks. So the satellite phase difference data can directly evaluate the clock performance. With the measuring precision of the phase-comparison equipment, if the performance of the two clocks is consistent, the clock performance of each clock can be got through the phase difference data. But if the performance of one clock is high lower than the other, the phase difference data mainly shows the worse clock performance.

2.3 Multi-satellite Orbit Determination Clock Correction Data

The ground monitor station receiver receives the navigation signal sent by the satellite, which can acquire the observed pseudorange. The pseudorange contains the satellite clock correction and satellite-ground geometric distance. The precise satellite orbit can be calculated by the pseudorange of many monitor stations. Then

the satellite-ground geometric distance can be obtained by using the calculated satellite orbit and the ground station coordinate. We can get the satellite clock correction through removing the satellite-ground geometric distance and error correction from the monitor station pseudorange with the main clock. The satellite work performance can be obtained by relieving the influence of the ground clock, which can be the third-level evaluation data [4].

3 Comprehensive Evaluation and Verification with Multi-data

3.1 Verification with Satellite-Ground Two-Way Clock Correction Data and Satellite Phase Difference Data

The satellite-ground two-way clock correction data and satellite phase difference data was compared and analyzed by using the IGSO satellite data between March 16th and 27th in 2013. During this time, the main satellite clock performance was abnormal. Generally, if the performance of the two clocks is all normal, the clock performance of each clock can be got through the phase difference data. But if the performance of one clock is high lower than the other, the phase difference data mainly shows the worse clock performance. So in this abnormal time of the main satellite clock, the satellite phase difference data mainly indicated the worse abnormal main clock performance. The consistence of the two types of original data and the satellite clock performance was compared as follows.

3.1.1 Consistence Analysis of the Two Types of Original Data

The long-term satellite clock correction data can be expressed by the 2-degree fitting polynomial. The difference between the satellite clock correction real value and the 2-degree fitting polynomial which is called 2-degree fitting error can denote the inner coincidence precision of the satellite clock correction.

In order to compare and analyze on be basis of unchanged data characteristics, the satellite-ground two-way clock correction data and the satellite phase difference data was processed by subtracting 2-degree fitting polynomial to obtain the fitting error, which still could indicate the two types of data characteristics. The fitting error comparison result is shown in Fig. 1, in which x-axis is time (day) and y-axis is 2-degree fitting error (ns).

From the above comparison result, the satellite-ground two-way clock correction data and the satellite phase difference data was totally consistent from the big change tendency to the small periodic regularity. So the satellite clock performance result using the two types of data would have great consistence.

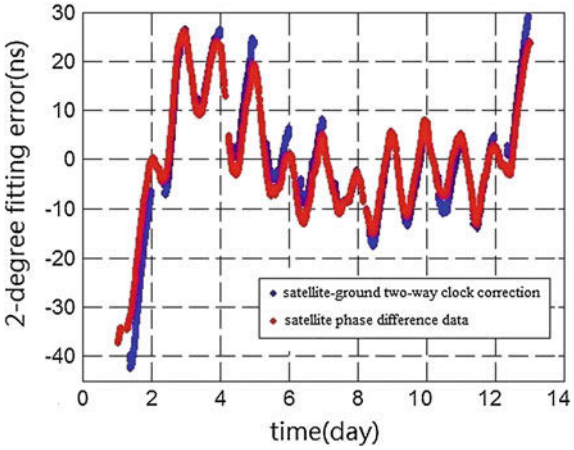

Fig. 1 2-degree ploy-fit error difference

3.1.2 Consistence Analysis of the Evaluation Result Using the Two Types of Data

The satellite clock performance based on the satellite-ground two-way clock correction data between March 16th and 27th is shown in Fig. 2, in which x-axis is time interval (s) and y-axis is Allan variance without drift rate.

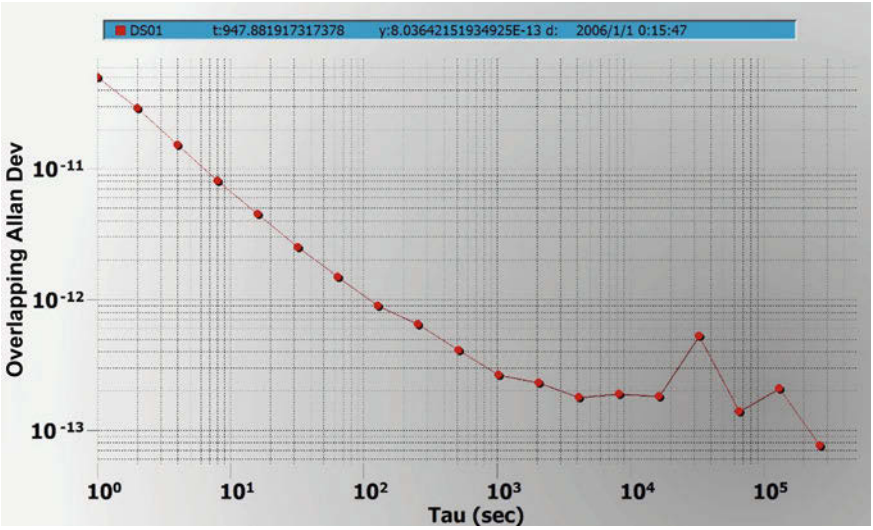

Fig. 2 Allan variance based on satellite-ground two-way clock difference

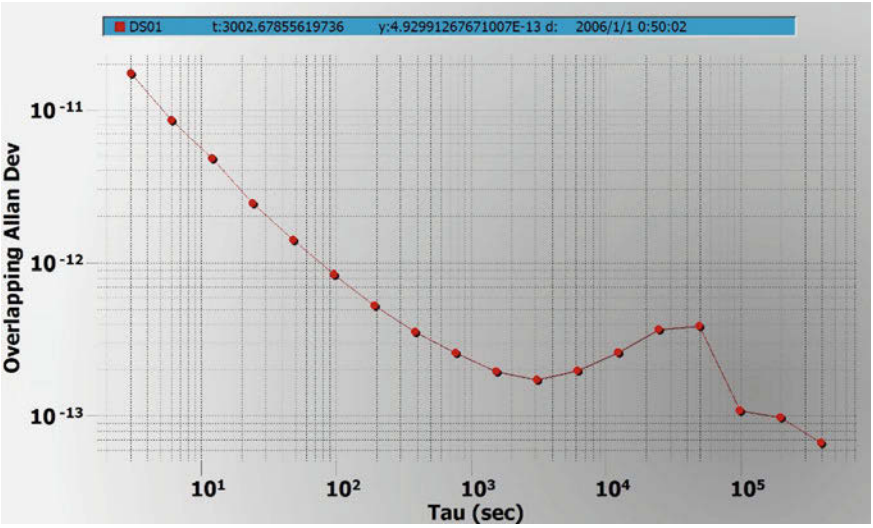

Fig. 3 Allan variance based on phase difference data on-board satellite

The satellite clock performance based on the satellite phase difference data is shown in Fig. 3, in which x-axis is time interval (s) and y-axis is Allan variance without drift rate.

The evaluation results difference analysis between the satellite-ground two-way clock connection data (data 1) and the satellite phase difference data (data 2) is shown in Table 1.

The satellite phase difference data and the satellite-ground two-way clock correction data can estimate the satellite clock performance. Because of different signals estimated by the two types of data, the estimated frequency accuracy and frequency drift rate index is not usable. But 10,000 s stability and day stability index can directly be compared because of its reflecting the satellite clock noise characteristics [5]. The 10,000 s stability and the day stability from the real measured data analysis could meet the index 3E-13, which verified the evaluation consistence of 10,000 s stability and day stability index with the two types of data.

Table 1 Access results difference between two types of data (data 1 and data 2)

Data (Index)	Frequency accuracy (5E-11)	Frequency/day (3E-13)	Allan 10,000 s stability (3E-13)	Allan day stability (3E-13)
Data 1	8.48E-12	−3.84E-14	1.86E-13	1.17E-13
Data 2	3.42E-11	−1.08E-13	2.42E-13	1.38E-13
Data 1–2	2.57E-11	−6.96E-14	5.60E-14	2.10E-14

3.2 *Verification with Satellite-Ground Two-Way Clock Correction Data and Multi-satellite Orbit Determination Clock Correction Data*

The 1 s sampling satellite-ground two-way clock correction data and 1 min sampling multi-satellite orbit determination clock correction data was compared and analyzed by using the GEO satellite data between March 29th and April 6th in 2013.

3.2.1 Consistence Analysis of the Two Types of Original Data

In the same way, in order to compare and analyze on the basis of unchanged data characteristics, the satellite-ground two-way clock correction data and multi-satellite orbit determination clock correction data was processed by subtracting 2-degree fitting polynomial to obtain the fitting error, which still could indicate the two types of data characteristics. The fitting error comparison result is shown in Fig. 4, in which x-axis is time (day) and y-axis is 2-degree fitting error (ns).

The difference between the two types of original clock correction is shown in Fig. 5, in which x-axis is time (day) and y-axis is clock correction difference (ns).

From the above result, there was 9 ns system error and 4 ns day period error between the two types of clock correction data. System error was mainly caused by the difference between the multi-satellite orbit determination receiver and the time synchronization device. It was a constant which had no influence on the evaluation result. The periodic error was mainly caused by the multi-satellite orbit determination clock correction, which absorbing partial periodic orbit error.

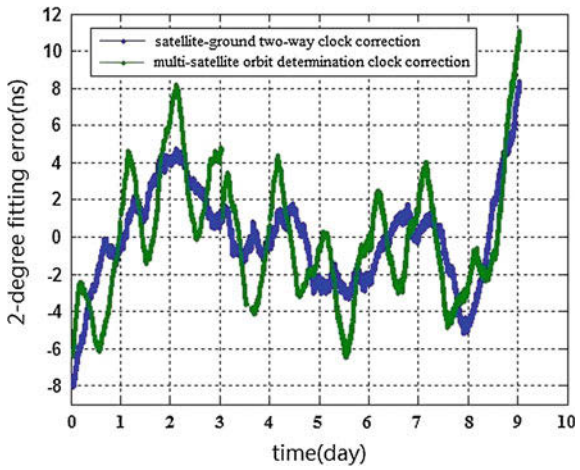

Fig. 4 2-degree ploy-fit error difference

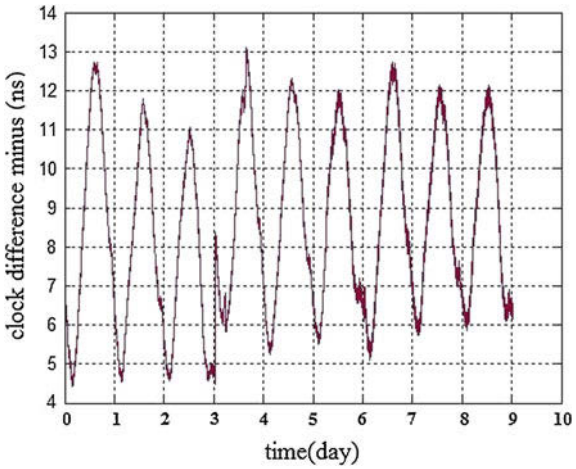

Fig. 5 Clock correction difference between two types of data

3.2.2 Consistence Analysis of the Evaluation Result Using the Two Types of Data

The satellite clock performance based on satellite-ground two-way clock correction data between March 29th and April 6th is shown in Fig. 6, in which x-axis is time interval (s) and y-axis is Allan variance without drift rate.

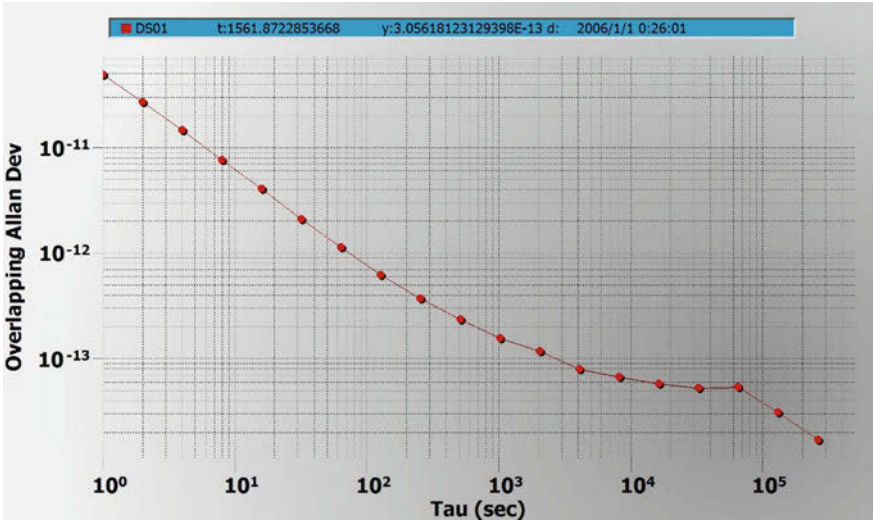

Fig. 6 Allan variance based on satellite-ground two-way clock difference

The satellite clock performance based on the multi-satellite orbit determination clock correction data is shown in Fig. 7, in which x-axis is time interval (s) and y-axis is Allan variance without drift rate.

The evaluation results difference analysis between satellite-ground two-way clock connection data (data 3) and multi-satellite orbit determination clock correction data (data 4) is shown in Table 2.

From the evaluation result consistence of the two types of data, the frequency accuracy and drift rate index evaluation is comparative, which can, respectively, meet the index 5E-11 and 3E-13. The 10,000 s stability and day stability can both meets the index 3E-13, but the precise evaluated by the satellite-ground two-way clock correction data is higher than the multi-satellite orbit determination clock correction data. That is to say, the two types of data can also evaluate the frequency accuracy and drift rate, but the satellite-ground two-way clock correction data is prior to the multi-satellite orbit determination clock correction data in evaluating the stability index because the orbit determination error is not separated from the multi-satellite orbit determination clock correction data, which has an influence on the clock stability.

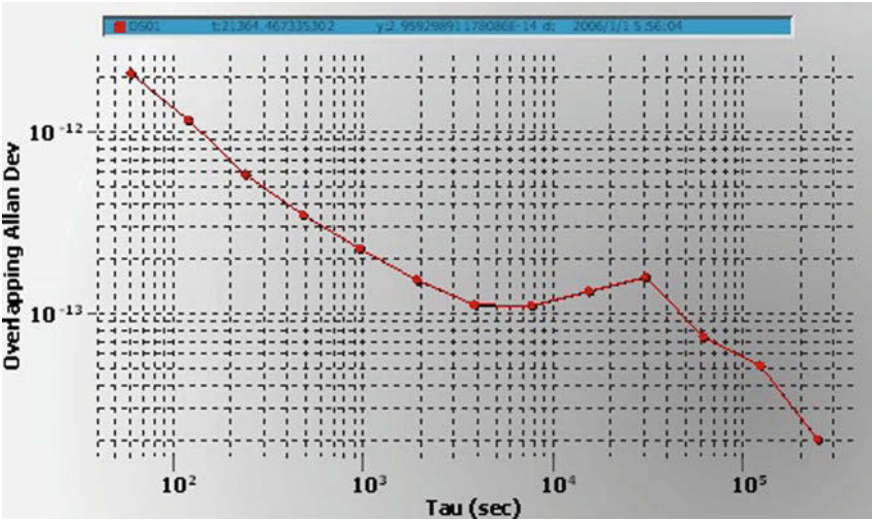

Fig. 7 Allan variance based on multi-satellite orbit determination clock difference data

Table 2 Access results difference between two types of data (data 3 and data 4)

Data (Index)	Frequency accuracy (5E-11)	Frequency/day (3E-13)	Allan 10,000 s stability (3E-13)	Allan day stability (3E-13)
Data 3	2.06E-11	−5.37E-14	6.42E-14	4.32E-14
Data 4	2.07E-11	−5.37E-14	1.19E-13	6.27E-14
Data 3–4	1.00E-13	0E-14	4.77E-14	1.95E-14

4 Conclusions

Two new types of data including satellite phase difference data and multi-satellite orbit determination clock correction data were introduced in this paper for multi-data comprehensive satellite clock performance with the traditional satellite-ground two-way clock correction data, the conclusions are drawn as follows:

1. The original satellite phase difference data and satellite-ground two-way clock correction data is totally consistent from the big change tendency to the small periodic regularity, which has great consistency in evaluating the 10,000 s stability and day stability index.
2. There is some system error and day period error between the multi-satellite orbit determination clock correction data and the satellite-ground two-way clock correction data. The two types of data have comparative evaluation of the frequency accuracy and frequency drift rate, but the satellite-ground two-way clock correction data is prior to the multi-satellite orbit determination clock correction data in evaluating the stability index because the orbit determination error is not separated from the multi-satellite orbit determination clock correction data, which has an influence on the clock stability.

References

1. Weiss MA (1985) Weighting and smoothing of data in GPS common view time transfer. In: Proceedings of precise time and time interval systems and applications meeting, pp 261–275
2. Kirchner D (1991) Two2way time transfer via communication satellites. Proc IEEE 79(7): 983–990
3. Plumb J (2003) Carrier phase time transfer using global positioning system. University of Colorado, Colorado
4. Riley WJ (2002) The Hadamard variance. Hamilton Technical Services
5. Riley WJ (2005) User manual—stable 32 frequency stability analysis. Hamilton Technical Services

Application Characteristics Analysis of the T20 Solar Radiation Pressure Model in Orbit Determination for COMPASS GEO Satellites

Rui Guo, Xiao Gong Hu, Xiao Jie Li, Yan Wang, Cheng Pan Tang, Zhi Qiao Chang and Shan Wu

Abstract For sub-meter precise orbit determination of GEO satellites, solar radiation pressure (SRP) perturbation is the major error and also the main factor that restrains the accuracy of orbit prediction. Compared with MEO satellites, GEO satellites are easier to be influenced by SRP perturbation due to their high altitude orbit feature and the magnitude achieves 10^{-7} (relative to the central gravity). Solar pressure modeling relates to multiple factors, including the satellite platform, attitude controlling, etc., thus it is difficult to accurately model it. It is also the biggest error term that affects the accuracy of precise orbit determination (POD) for medium and high Earth orbit satellites. This paper completes the construction of the time series of the 3.5-year model SRP using the recent 3.5-year real data from COMPASS using the post-processing method. Meanwhile, this paper discovers a secular variation trend and a half-year period of the Cr coefficient. The parameters variation features relating to the seasonal solar activities are investigated. Estimated SPR parameters and periods of solar activities are analyzed, as well as the relationship among the POD accuracy. Therefore, some fruitful conclusions have been got, which helps to establish and refine the COMPASS GEO SRP model.

Keywords Satellite navigation · Precise orbit determination · Solar radiation pressure · Geosynchronous satellite · Time series

Supported by the National Natural Science Foundation Project (2013, 41204022).

R. Guo (✉) · X.J. Li · Z.Q. Chang · S. Wu
Beijing Satellite Navigation Center, Beijing 100094, China
e-mail: shimbarsalon@163.com

X.G. Hu · C.P. Tang
Shanghai Astronomical Observatory, Chinese Academy of Sciences, Shanghai 200030, China

Y. Wang
Institute of Surveying and Mapping, Information Engineering University, Zhengzhou 450052, China

© Springer Science+Business Media Singapore 2016

J. Sun et al. (eds.), *China Satellite Navigation Conference (CSNC) 2016 Proceedings: Volume III*, Lecture Notes in Electrical Engineering 390,
DOI 10.1007/978-981-10-0940-2_12

1 Introduction

Beidou navigation satellite system (COMPASS) is China's self-developed innovative system. Geosynchronous Earth orbit (GEO) satellites are an essential component of COMPASS, and the determination and prediction of their high-precision orbital parameters are the fundamental guarantee of the navigation system services [1].

Compared with the medium Earth orbit (MEO) satellites of GPS, orbit determination of the GEO satellites of COMPASS is a popular and challenging issue in terms of satellite navigation and precise orbit determination (POD). First of all, the high altitude feature limits the baseline length of ground tracking, weakens the geometric conditions of orbit determination, and makes the orbit more easy to be influenced by the error of the dynamic models, which is not beneficial to medium and long-term orbit prediction. Second, the satellite orbit is correlated with clock error because of its geostationary feature. Thus, for the single satellite orbit determination (SPOD) model of GEO satellites with the pseudorange tracking, the technique support of time synchronizing between the satellite and the ground station is required [2–4].

During in-orbit operation, in order to maintain the normal operation of payload, GEO satellites need to gain energy through solar panels on both sides of the satellite. However, SRP is the biggest non-conservative force in the POD process, which affects the orbit of navigation satellites. Its effect relates to multiple factors, including the magnitude of the solar radiation, the irradiated plane of the satellite, the geometrical relationship between the irradiation plane and the Sun, as well as reflection and absorption of the irradiation plane, which is the most difficult to be precisely modeled among all perturbative forces [5–7].

In terms of the sub-meter POD for GEO satellites, SRP perturbation is the major error and the main factor that restrains the accuracy of orbit prediction [8]. Compared with the MEO satellites, GEO satellites are easier to be influenced by the solar pressure perturbation due to the high altitude orbit feature and the magnitude reaches 10^{-7} (relative to the central gravity). Solar pressure modeling relates to multiple factors, including satellite platform, attitude control, etc., thus it is difficult to accurately model it. It is also the biggest error term that affects the POD accuracy for medium and high Earth satellites. Based on the simulation results, when the relative error of the SRP model reaches 15.7 %, the 3-D orbital error will reach 20 m after 13-hour orbit prediction.

With the precise modeling of each physical parameter and the accumulation of the long-term global-tracking orbit measurement data, the SRP model is studied which includes several common models, such as the typical Box-Wing ball model [9], T10 model, T20 model [10], ECOM and SPRINGER model of BERNESE [7], GPSM model of JPL [8], etc. These models are mainly applied to GPS satellites. COMPASS was just completed and commissioned in 2013. Due to the limited

accumulation of the orbit measurement data and the insufficient precision conditions of the SRP model, the orbit determination of COMPASS satellites mainly use the SRP model of the GPS satellites. Since there are some differences between COMPASS and GPS satellite platform, the application characteristics and effects of the GPS SRP model on the COMPASS system is yet to be evaluated [11].

This paper takes the T20 model of GPS satellites as an example, utilizes 3.5-year observation data of COMPASS, completes the characteristic analysis of the T20 SRP model in the GEO POD through the off-line processing approach, and gets some valuable conclusions.

2 The T20 SRP Model

The SRP perturbation stems from the pressure of the solar radiation on the satellite, which is also called pressure perturbation. The SRP perturbation comprises two parts

$$\vec{a}_{\mathrm{SRP}} = \vec{a}_{\mathrm{SRP\_}B} + \vec{a}_{\mathrm{SRP\_}P} \tag{1}$$

In this formula, $\vec{a}_{\mathrm{SRP\_}B}$ represents the solar radiation perturbation acceleration on the satellite body and $\vec{a}_{\mathrm{SRP\_}P}$ expresses the SRP perturbation acceleration in the satellite solar panels. The Sun–Earth shadow relating to pressure perturbation can use the cylinder or biconical Earth shadow model, and there is little difference between these two models. SRP perturbation relates to some coordinate axes, and (e_x, e_y, e_z) is the unit vector of the axes of the satellite-fixed coordinate system. e_z points to the center of the Earth and e_D is defined as the unit vector from the Sun to satellite, and it is defined that $e_y = e_z \times e_D$, $e_x = e_y \times e_z$.

The T20 SRP model of GPS which is mainly used in BLOCK II and BLOCK II-A satellites, and is formulated below

$$\begin{cases} \vec{a}_{SRP} = \frac{a_u^2}{|r_s - r|^2} \cdot (\lambda \cdot \mathrm{SRP}(1) \cdot X(B) \cdot \vec{e}_x + \mathrm{SRP}(2) \cdot D_0 \cdot \vec{e}_y + \lambda \cdot \mathrm{SRP}(3) \cdot Z(B) \cdot \vec{e}_z) \\ X_B = -8.96 \sin B + 0.16 \sin 3B + 0.10 \sin 5B - 0.07 \sin 7B \\ Z_B = -8.43 \cos B \\ D_0 = 8.695/M \end{cases} \tag{2}$$

In this formula, a_u is an Astronomical unit; B represents the angle between the satellite to the Sun direction and points to the +Z axis direction; λ denotes the shadow factor; M is the mass of the satellite; r_s and r, respectively, represent the position vector of the Sun and the satellite in the inertial system.

3 The POD Strategy for GEO Satellites

The RDSS positioning tests were implemented using the RDSS user observation in the region from August 17 to August 18 in 2013. The ranging error and HDOP were analyzed. The positioning error characteristic was analyzed based on different error sources.

In order to check the application characteristics of the T20 model, seven stations are employed from the COMPASS ground tracking network. They are Beijing, Hainan, Sichuan, Heilongjiang, Korla, Kashgar, and Guangdong. The L-band pseuorange and phase data for the COMPASS constellation are employed to carry out the multi-satellite precise orbit determination (MPOD) tests. The orbit determination data is a dual-frequency ionosphere-free combination of the pseudorange and the carrier phase data. The length for the orbit determination is 3 days.

In the MPOD process, EIGEN-GRACE02S Earth gravitation model truncated to 10 by 10 degree and order, IAU80 nutation model, IERS2004 solid Earth tide model, JPL DE403 planetary ephemeris, GPS T20 SRP model, are employed.

The T20 empirical pressure model is applied in the orbit determination. The common pressure scaling factors in the X/Z direction are estimated for a 3-day arc, which are SRP(1) and SRP(3) parameters in Eq (2). The YBias parameter is also estimated, which is the SRP(2) parameter in Eq (2).

The SRP perturbation model of the satellite is an empirical model and there are likely some other dynamic models, i, the orbit period which are not accurately modeled. Therefore, it is necessary to introduce the empirical model into the MPOD process to absorb the model error. Perturbation which has not been molded into periodical functions is divided into three parts—the orbit radial R, the transverse T as well as the normal N.

$$\bar{P}_{\mathrm{RTN}} = \begin{bmatrix} P_R \\ P_T \\ P_N \end{bmatrix} = \begin{bmatrix} \sum_{i=1}^{n} \left(C_R^i \cos^i u + S_R^i \sin^i u \right) \\ \sum_{i=1}^{n} \left(C_T^i \cos^i u + S_T^i \sin^i u \right) \\ \sum_{i=1}^{n} \left(C_N^i \cos^i u + S_N^i \sin^i u \right) \end{bmatrix} \tag{3}$$

In this formula, P_R, P_T and P_N represent the periodical radial, along-track and normal perturbations; u is the satellite latitude; $\left(C_r^i, S_r^i\right)$, $\left(C_t^i, S_t^i\right)$ and $\left(C_n^i, S_n^i\right)$ represent the periodical radial, transverse, and normal direction perturbation of group i. In the conventional MPOD, the evaluation of a group of empirical parameters C_T, S_T, C_N, and S_N in T/N direction is estimated for a 3-day arc. Since parameters C_T and S_T as well as parameters C_N and S_N are strongly correlated, only parameters C_N and S_N are estimated.

4 Application Characteristic Analysis of the T20 SRP Model

The T20 SRP model is designed according to the GPS satellite platform and model parameters are estimated based on the global orbit measurement data. Thus, its application characteristics in COMPASS GEO satellites are yet to be further analyzed. The research work would help to establish and refine the COMPASS SRP model.

In order to complete the application characteristic analysis of the T20 model, the GEO satellite data from COMPASS under China's regional network tracking conditions from January 2011 to May 2014 is applied and processed through off-line POD process, and the processing frequency is every 3 h. More details on POD strategies are in Sect. 3. Then, the time series of dynamic parameters of COMPASS GEO satellites such as the SRP model is analyzed.

4.1 Analysis of Time Sequence of the Cr Parameter

The Cr parameter represents the pressure scaling factor in X/Z direction and Fig. 1 shows its time series results in recent 3.5 years. Notably, the GEO satellite motion has annual features and its POD is unstable in some seasons, during the Sun–Earth eclipse season around Spring/Autumn equinox and also during the Summer/Winter solstices. The estimated dynamic parameters are not stable during these seasons, so the Cr parameters with gross errors are rejected in this time series.

1. **Secular variation trend**

The time sequence results in Fig. 1 show that in recent 3.5 years, Cr parameters have a long-term variation trend. Then, a linear polynomial is employed to fit the Cr time series. Figure 2 shows the residual errors of the Cr time series after the linear fitting. The first order fitting coefficient is about 0.026/year. Because the GEO satellites have to experience orbital maneuvers, in order to maintain optimal signal

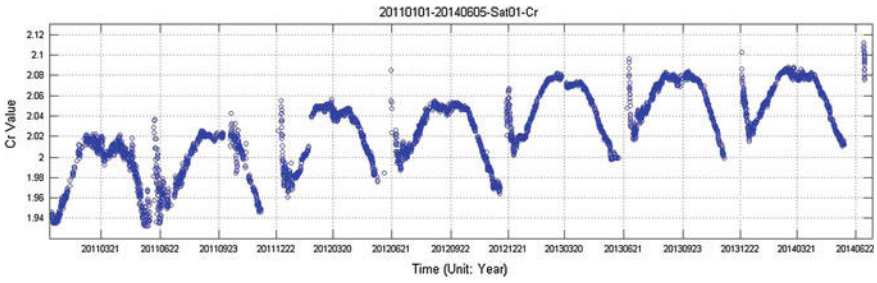

Fig. 1 Time sequence of the Cr parameter

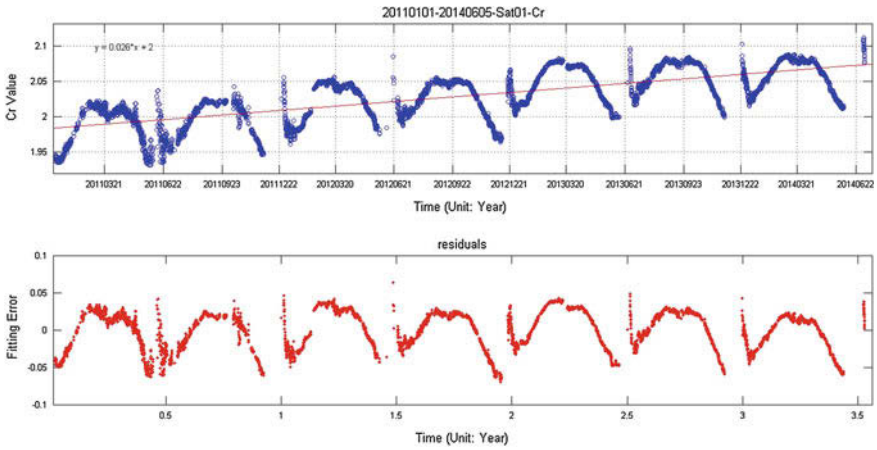

Fig. 2 Time series of Cr parameters and the residual series after the linear fitting

coverage, the fuel is consumed and it leads to the decrease of mass and the increase of area-to-mass ratio for a GEO satellite. Since the given satellite area-to-mass ratio is usually fixed in the POD process, the evaluated reflection coefficient has increasing trend.

The above figure shows that after the linear fitting, the residual errors of Cr parameters no longer have the secular trend, but shows only certain annual variation features.

2. Annual variation characteristics

In order to analyze the annual variation characteristics of the Cr parameter time series, the fast Fourier transformation is applied in order to analyze the period of the Cr parameter after removing the secular trend. For the detrended Cr sequence $\{x\}$, the periodic term is modeled below

$$\begin{cases} \boldsymbol{x} = \sum_{i=1}^{p} (s_i \sin(2\pi f_i \boldsymbol{t}) + c_i \cos(2\pi f_i \boldsymbol{t})) + \boldsymbol{\varepsilon} \\ A_i = \sqrt{(s_i^2 + c_i^2)} \end{cases} \tag{4}$$

In this formula, f_i represents the ith dominant frequency term of the linear fitting residual time series; s_i and c_i are the corresponding coefficient of f_i; A_i represents the amplitude of f_i. Detailed procedures of the analysis of the Cr one order fitting residual frequency are as follows:

1. Data preprocessing, interpolating the rejected gross error data, and achieving the evenly spaced Cr parameter time series;
2. Analyzing data by means of the spectral analysis approach and getting the frequency diagram;

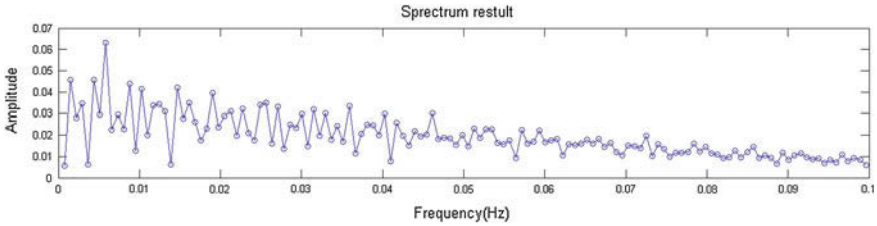

Fig. 3 The periodic frequency diagram of the Cr parameter

3. Choosing the longest period, fitting the Cr parameter time series, deducting this period, and a new residual time series is achieved.

The periodic frequency diagram of the Cr parameter is shown in Fig. 3 as follows. It can be seen that the corresponding frequency of the biggest amplitude (about 0.063) is around 0.005859 and the corresponding longest period is $T_{\max} = 1/0.005859 \approx 171$ days. Figure 4 represents the fitting residual errors based on the 171-day period term, which shows that the red line and the blue line are not completely consistent, and the fitting residual error is still very large because, the Cr time series has some gross errors. These errors are rejected during processing and a completely evenly spaced time series is interpolated. Thus, the results of the fast Fourier transform analysis might have some errors.

The Cr parameter reflects variations of the SRP and its characteristic relates to annual solar activities. The 171-day periodic term is achieved through the Fourier

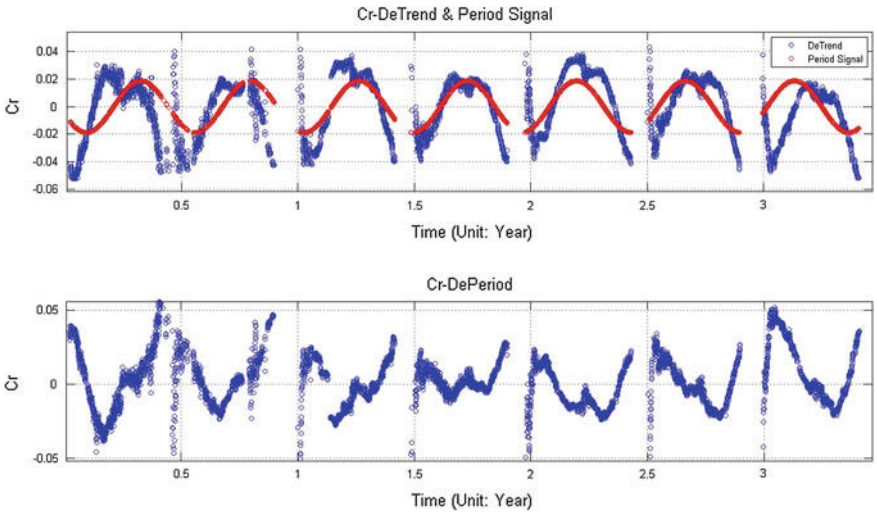

Fig. 4 Residual errors of the Cr parameter after removing the 171-day periodic term (The upper one represents Cr time series and fitting periodic term and the bottom one represents the fitting residual errors)

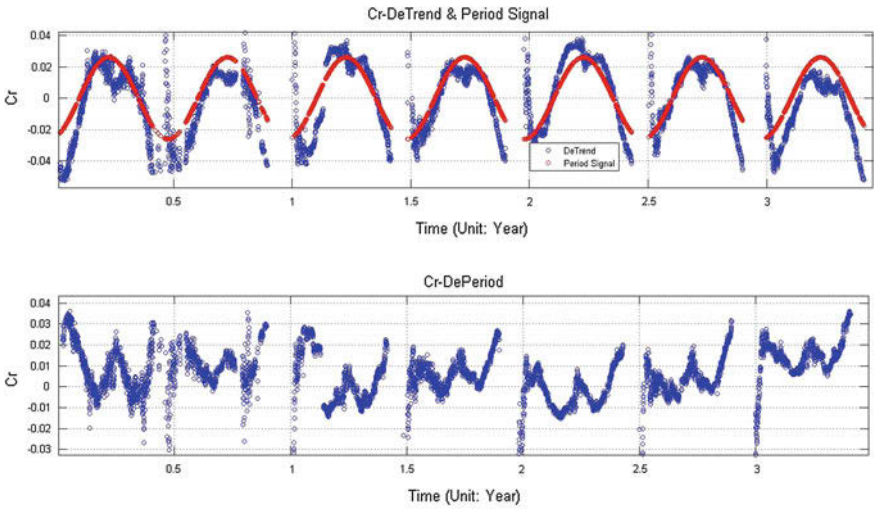

Fig. 5 Residual errors of the Cr parameter after removing the half-year term (The upper one represents Cr and the fitting periodic term and the bottom one represents the fitting residual errors)

transformation, which could not depict the Cr parameter characteristic. Seen from the Cr time series in Fig. 4, the half-year period term is notable. Therefore, we need to correct the periodic term for the Cr parameter time series. A half-year (182.625 days) periodic term is employed to test the fitting error, and tests are carried out again. Figure 5 shows the fitting residual errors based on the half-year periodic term. It can be seen that the red line is pretty close to the blue line and their variation patterns are consistent, and the fitting residual error has been obviously improved. Therefore, theoretically and practically, it is believed that the Cr parameter has a half-year periodic term.

In order to further explain the regularity of the Cr parameter time sequence, the Cr time series is analyzed in an annualized unit throughout 4 years from 2011 to 2014. Figure 6 shows that the regularity of these 4 years is almost the same, with

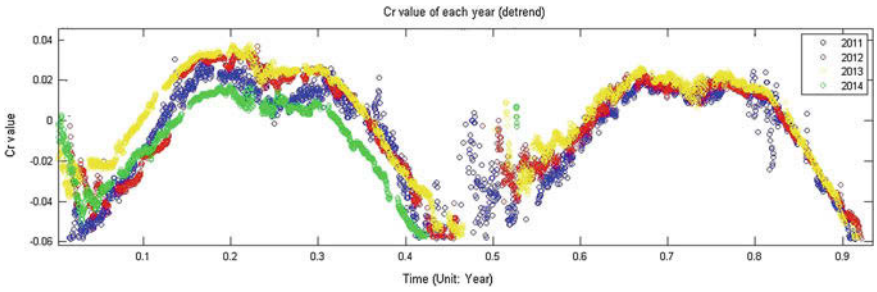

Fig. 6 Time series of the Cr parameter (annualized, secular variation trend term removed)

high similarity among different years. This regularity can be applied in the POD process to perform experimental SPR modeling, in order to improve the accuracy and stability of orbit determination.

4.2 Analysis of the POD Accuracy

The results of Cr time series in Sect. 4.1 show that around Spring equinox, Summer solstice, Autumn equinox, and Winter solstice, the estimated Cr results have large variations and are unstable. Therefore, the orbit overlap errors could be employed to evaluate the POD accuracy in the four different seasons.

The POD results with the tracking data in day $n - 2$, $n - 1$, and n are compared with those in day n, $n + 1$, $n + 2$, and the position error of the overlapping arc in R, T, and N are calculated, so as to evaluate the accuracy of the orbit determination. Table 1 shows the statistical results of the accuracy of the overlap arcs of POD in March, June, September, and December of 2013. The left part of the table represents the statistical accuracy under normal seasons in this month, while the right part shows the statistical accuracy during Spring equinox, Summer solstice, Autumn equinox, and Winter solstice.

On the basis of these results, conclusions can be achieved as follows:

1. In terms of the orbit overlap errors, under normal seasons, satellite radial direction and position error, respectively, register 0.21 and 1.32 m. While in special seasons of spring, summer, autumn, and winter, satellite radial direction and position error are 0.97 and 3.98 m; accuracy attenuates 2–3 times and orbit URE also attenuates from 0.24 to 1.06 m.
2. During Spring equinox and Autumn equinox, the attenuation of satellite radial direction and transverse direction is the most obvious, which leads to the evident URE error. Therefore, during equinoxes, navigation service performance would be affected.
3. During summer solstice and winter solstice, although satellite position precision attenuates distinctly, it is mainly reflected in satellite transverse direction. In terms of the user ranging error (URE), the error of the satellite does not obviously increase, thus navigation service performance is not significantly affected during solstices.

Table 1 Statistical results of the POD accuracy of GEO-1 satellite

Time	R (m)	T (m)	N (m)	Pos (m)	URE (m)	Time	R (m)	T (m)	N (m)	Pos (m)	URE (m)
2013/3/1	0.21	0.56	1.16	1.31	0.24	2013/3/20	**1.73**	3.33	1.46	4.03	1.76
2013/6/1	0.16	0.59	0.57	0.84	0.18	2013/6/21	**0.22**	2.98	0.26	3.00	0.35
2013/9/7	0.21	0.80	1.22	1.47	0.25	2013/9/23	**1.66**	4.50	1.96	5.18	1.72
2013/12/1	0.24	1.57	0.48	1.66	0.28	2013/12/26	**0.26**	3.66	0.39	3.69	0.42
Average	0.21	0.88	0.86	**1.32**	**0.24**	Average	0.97	3.62	1.02	**3.98**	**1.06**

Combining the time series of Cr/YBias parameters and POD accuracy in different seasons, under normal seasons, the T20 SRP model can represent the SRP perturbation of COMPASS GEO satellites. While in special seasons of Spring equinox/Summer solstice/Autumn equinox/Winter solstice, there are large model errors. Main reasons are as follows:

1. There are some differences between the platform of COMPASS GEO satellites and that of GPS satellites. Especially for GEO satellites, their effective payload is larger and their physical configuration is not the same as that of GPS satellites;
2. GEO satellite attitude applies the yaw-steering controlling mode all the time, which is not similar to the yaw-norming attitude controlling approach. Thus, during Spring equinox and Autumn equinox, the T20 model error for GEO satellites is magnified in the Sun–Earth eclipse season, which increases the impact on the POD accuracy.

5 Conclusion

In order to analyze and investigate the application effects of the T20 SRP model in the GEO satellite POD of COMPASS, this paper applies the time series approach to analyze the SRP parameter time series. 3.5-year real data from the COMPASS ground tracking network is utilized to perform tests. The 3.5-year SRP parameters time series is established by the MPOD process. Frequency spectrum analysis is also performed and characteristic analysis of major model parameters is completed. Major conclusions are as follows:

1. In-orbit satellites need to perform regular orbit maneuvering, which changes the satellite area-to-mass ratio. The Cr parameter time series of the T20 model has a secular variation trend, and the coefficient term of one order matching is 0.026/year.
2. In addition to the secular variation trend, the Cr parameter time series of the T20 model also has obvious annual variation characteristics. Its periodic term is about half a year. The Cr parameter time series of different years are distinctly consistent, which is in consistency with the regularity of solar annual motion.
3. Because of the annual motion feature of GEO satellites, the POD is not stable during some seasons. For example, in Sun–Earth eclipse seasons during Spring/Autumn equinox and when GEO satellites pass over the terrestrial equator during Summer/Winter solstices, the estimated results of parameters (Cr) of the SRP model are unstable.
4. In terms of the MPOD accuracy, the T20 SPR model is directly applied. Satellite orbital radial and position error during special seasons is, respectively, 0.97 m and 3.98 m in spring, summer, autumn, and winter seasons. The accuracy attenuates 2–3 times and the orbital URE also attenuates from 0.24 to 1.06 m.

The attenuation is more obvious in Spring and Autumn equinoxes, thus the performance of navigation service during these seasons is affected.

5. Combining the analysis results of the 3.5-year time series of T20 SRP parameters, the direct application of the T20 model in COMPASS GEO satellites has some errors. Under normal seasons, the SRP perturbation for GEO satellites can be represented. While during special seasons of Spring equinox/Summer solstice/Autumn equinox/Winter solstice, model errors would be very large.

References

1. Yang YX, Li JL et al (2011) Contributions of China's Beidou satellite navigation system to global PNT users. Chinese Science Bulletin. 56(21), 1734–1740
2. Guo R, Hu XG, Tang B et al (2010) Precise orbit determination for geostationary satellites with multiple tracking techniques. China Sci Bull 55(8):687–692
3. Guo R, Hu XG, Liu L et al (2010) Orbit determination for geostationary satellites with the combination of transfer ranging and pseudorange data. Sci China Phys Mech Astron 53 (9):1746–1754
4. Guo R, Hu XG, Liu L et al (2010) Orbit determination for geostationary satellites with the combination of transfer ranging and pseudorange data. Sci China Phys Mech Astron 53 (9):1746–1754. doi:10.1007/s1433-010-4092-0
5. Bar-Sever YE (1997) New and improved solar radiation models for GPS satellites based on flight data. Final report of Air Force Material Command Space and Missile Systems Center/CZSF, April
6. Marek Z (2000) Analytical SRP model for GLONASS: initial results. In: International GLONASS experiment—IGEX-98 proceedings, p 315
7. Springer TA, Beutler G, Rothacher M (1999) A new solar radiation pressure model for the GPS satellites, in CODE IGS analysis center technical report, p 673
8. Jay WM, Daniel JS (2010) New solar radiation pressure force model for navigation. J Guidance, Control Dyn 33(5):1418–1425
9. Rodriguez-Solano CJ et al (2012) Adjustable box-wing model for solar radiation pressure impacting GPS satellites. Adv Space Res 49(7):1113–1128
10. Fliegel H, Gallini T, Swift E (1992) Global positioning system radiation force model for geodetic application. J Geophys Res 97(B1):559–568. doi:10.1029/91JB02564
11. Ant S, Willy B et al (2011) An evaluation of solar radiation pressure strategies for the GPS constellation. J Geod 85:505–517

Validation of GPS36 Satellite CODE Precise Orbit with SLR Measurements

Honglei Yang, Tianhe Xu and Dawei Sun

Abstract In this paper, SLR observations are used to validate the CODE precise orbit of GPS36 satellite. First, the comparison of orbit validation is performed by using the SLR normal point (NP) data provided by EDC and CDDIS from July 1 2013 to May 1 2012. Then, a long-term validation of the CODE precise orbit is carried out by using the SLR data from January 1 2003 to March 3 2014 of EDC. The results show that the number of SLR data provided by EDC is larger than those by CDDIS in the same time span, and the orbit validation results have a very good consistency by using EDC data and CDDIS data. The validation from ten years shows that SLR observation accuracy is about in one centimeter level. The data quality of SLR stations is relatively stable, and there is also a relatively stable system error between SLR observation and the computed range between satellite and station. The accuracy evaluated by the SLR data for GPS36 satellite is mostly less than 4 cm.

Keywords Satellite laser ranging (SLR) · GPS · Precise orbit validation · Systematic error

H. Yang (✉) · D. Sun
College of Geology Engineering and Geomatics, Chang'an University,
Xi'an Shanxi, China
e-mail: hozzyee@163.com

T. Xu (✉)
State Key Laboratory of Geo-Information Engineering,
Xi'an Shanxi, China
e-mail: thxugfz@163.com

T. Xu
Xian Research Institute of Surveying and Mapping,
Xi'an Shanxi, China

© Springer Science+Business Media Singapore 2016

J. Sun et al. (eds.), *China Satellite Navigation Conference (CSNC) 2016 Proceedings: Volume III*, Lecture Notes in Electrical Engineering 390,
DOI 10.1007/978-981-10-0940-2_13

1 Introduction

With the development of the satellite laser system and the accumulation of data, satellite laser ranging (SLR), one of the most advanced technologies in modern space geodesy, is widely used in the field of geodesy and geodynamics (see [1]).

In March 1994, the United States launched GPS36 satellite (SVN36, PRN6), one of GPS satellites of Block-IIA, which was equipped with laser reflector arrays (LRAs) (see [2, 3]). Because of equipping the backward laser reflector oriented to earth, GPS36 satellite can receive the laser ranging observation passively, except for broadcasting GPS microwave positioning information actively.

SLR can provide precise distance from stations to satellite. It is important for carrying out external orbit validation and precise orbit determination of spaceborne GPS receiver. By comparing orbits determined by SLR data and GPS microwave observation it can reflect the difference of the two systems directly. The check can be performed by using the observations of one system to evaluate the orbits provided by another system. The orbit precision and reliability will be improved by combining the two kinds of data (see [4, 5]).

Center for Orbit Determination in Europe (CODE) provides GNSS precise orbit with 15-minute intervals, which is computed by 3-day arc data and the precise orbit of the middle day is selected for every GNSS satellite. The number of SLR observation of GPS36 satellite was relatively small since the orbit is very high. In this paper, long-term SLR observation is used to validate CODE GPS36 satellite precision orbit, by comparing the SLR observation and the computed distance between GPS36 satellite and stations with known CODE precision orbit and station coordinate (see [6–8]). When validating GPS36 satellite precise orbit, the unified time system of UTC and the geodetic reference frame of ITRF2008 are chosen.

2 The Principle and Model of SLR Validation

Satellite orbit validation by SLR observation needs to consider three error sources, station coordinate error, satellite orbit error, laser propagation error in the atmosphere. Therefore, each error correction must be carefully considered for the SLR stations and SLR data (see [9, 10]).

2.1 Model Correction of SLR Station

SLR station corrections include the corrections of solid Earth tides, ocean tide, polar tide, and the plate motion which can be computed by SLR stations coordinates and velocities.

The corrections of SLR stations as for datum reference frame use the station coordinates and velocities based on ITRF2008. DE405 is used in the tide perturbation model, JGM-3 for the Earth's gravitational field model, IAU2000 for nutation model, IERS2000 for polar point model, and TIDE2000 for tidal model. In this paper, FES2004 is used for ocean model, IERS C04 used for polar motion correction (see [11–13]).

2.2 SLR Data Correction

SLR data corrections mainly consider tropospheric refraction correction, general relativity correction, centroid compensation correction, and station eccentricity correction (see [6–8]).

Some of the above corrections will use the information of satellite elevation angle and the meteorological parameters attached in the SLR data (see [14]). Tropospheric refraction correction is obtained by using the Marini-Murray model. General relativity correction considers the influence of the sun and the earth's gravitational field (see [9, 10]). The correction vector of GPS36 satellite's mass center compensation is (0.8626, 0.5245, 0.8626 m). Station eccentricity correction refers to the inconsistence between satellite lasering center and the SLR station, which will cause deviation of the theoretical calculated values and measured values (see [9, 10]). In the above corrections, the mass of GPS36 satellite is fixed to 975 kg, and GPS leap second file is used to correct the second jump (see [11–13]).

3 Calculation and Analysis

GPS36 satellite orbit is very high, and the number of available SLR normal points is small. The distribution of global SLR stations is not well located. The numbers of SLR stations in the northern hemisphere are more than those in the southern hemisphere, and distribution is better in Europe. Using long-term SLR data, comparison and analysis of the data quality and the satellite orbit precision can be performed.

3.1 Comparison of the Validation for SLR Observation Data

SLR normal point data of CDDIS (gsfc.nasa.gov) and EDC (dgfi.badw.de) is used for the orbit validation of GPS36 satellite from May 1 2012 (DOY 122) to July 1 2013 (DOY 182). After the error corrections above-mentioned, the difference of the SLR observation and, the computed range between satellite and station by CODE precise orbit and station coordinate, then the statistics of RMS are computed.

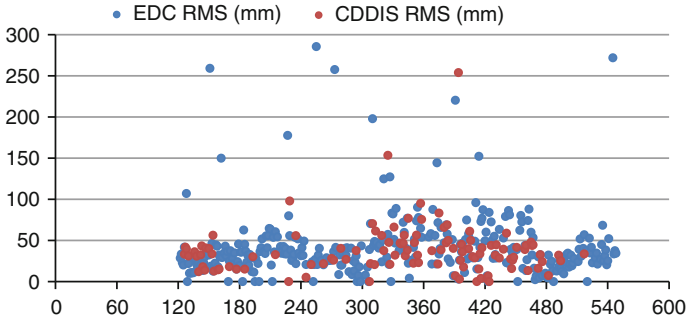

Fig. 1 RMS value scatter diagram for EDC and CDDIS data. (The horizontal coordinate begins in January 1 2012 as the starting day; the vertical coordinate is the RMS with unit of mm)

The RMS that is larger than 300 mm are excluded from SLR data of each station. The reason is due to the assumption of the CODE precision orbit accuracy is better than 100 mm, and 3 times of 100 mm is regarded as the rule of elimination. The cut-off height angle is set as 10 degree. In this period, CDDIS has 12 SLR stations with a total of 636 valid observations, EDC has 17 SLR stations with a total of 2618 valid observations. The distribution of scatter points is shown in Fig. 1.

It can be seen that the EDC has more valid observations than the CDDIS. The scattered point distribution and trend of orbit validation RMS is almost the same. From the point of long-term data, the RMS scatter distribution seems to have a certain periodicity. The main reasons may be followings. (1) The summer season have dense and stable normal points, data quality is also better because of good weather (see Fig. 1). The normal points in winter season are rare, and the data quality is slightly worse. (2) The valid observations distribution is related to the SLR station location.

RMS statistics of orbit validation by SLR data of these two sets are shown in Table 1.

As shown in Table 1, except 7308, 7237 stations, the maximum RMS of the SLR stations is not more than 6 cm. In addition to 7090, 7406, and 7941 stations, the difference between the RMS of SLR data provided by EDC and CDDIS is in the millimeter level, which indicates that the normal point data provided by CDDIS and EDC have good consistency. The statistic valid observation in this period, the CDDIS valid standard point data is about 1/4 of EDC, and the overall RMS of orbit validation is less than 4 cm.

It needs to point out that the total RMS is the weighted average of the RMS value, namely,

$$\mathrm{RMS}_T = \frac{\sum (N_i * \mathrm{RMS}_i)}{\sum N_i}$$

Table 1 Statistics the RMS for EDC and CDDIS data

Station	CDDIS		EDC	
	Normal point	RMS (mm)	Normal point	RMS (mm)
7090	4	12.7	198	39.3
7105	24	48.3	32	48.8
7110	36	28.6	38	28.3
7406	230	30.4	155	57.7
7501	11	15.0	36	18.6
7810	21	22.1	331	24.8
7825	42	13.4	66	13.3
7839	6	14.8	284	18.6
7840	2	30.9	38	23.7
7845	130	47.9	298	46.3
7941	69	15.2	304	30.8
8834	61	27.3	551	28.2
7838			7	4.1
7308			25	133.5
7237			231	72.1
1879			18	26.9
1868			6	24.3
Total	636	30.7	2618	36.2

where RMS_T is the total RMS value, N_i is the number of normal points of each station, RMS_i is the RMS value of each station.

3.2 *Analysis of SLR Normal Point Data for Ten Years*

Through the data analysis of Sect. 3.1, the EDC SLR standard point and CODE precision orbit data provided by the GPS36 satellite from January 1 2003 to March 3 2014 is selected to orbit validation. In this period, there are 29 SLR stations with 35,199 valid observations. The RMS of orbit validation is shown in Table 2, and for the limitation of length, only RMS scattered point figures of 15 stations are shown in Fig. 2. The RMS statistical results are shown in Table 2.

According to the number of valid observations in Table 2, the scatter plots or RMS of the selected 14 stations are shown in the following.

Table 2 The statistical results for SLR validation

Station	Normal points	Mean (mm)	RMS (mm)	Std (mm)
7090	7774	−47.3	52.8	14.0
7810	5149	−26.4	28.5	7.1
7832	4082	−24.8	27.3	4.9
7406	3892	−32.2	44.0	19.6
7839	3380	−25.3	26.4	5.2
7845	1893	−43.8	44.4	4.8
8834	1736	−16.7	24.3	7.0
7840	1286	−30.8	31.9	5.4
7825	1158	−23.0	31.5	11.9
7941	935	−24.6	31.2	9.2
7237	790	−58.6	65.3	12.1
7110	714	−43.9	49.3	12.0
7080	492	−57.5	59.2	9.3
7308	463	−22.2	58.3	21.0
7105	337	−36.7	41.2	12.9
7210	238	−38.5	48.5	23.2
7358	202	−36.6	37.9	5.3
7821	194	−34.5	55.4	8.9
7501	125	−16.3	23.6	9.4
7405	75	15.4	145.4	138.1
1879	63	−20.0	29.4	14.5
7838	53	−18.3	27.5	11.9
7841	51	−14.6	28.7	12.1
1868	36	−18.6	35.8	35.8
1864	25	−46.0	69.7	37.9
7249	21	105.4	152.0	112.7
7355	19	−49.9	72.2	54.0
1873	11	−9.8	115.3	104.1
1884	5	−24.3	34.0	26.6
Total	35,199	−33.6	39.1	10.7

From Table 2, Figs. 2 and 3, the following conclusions can be drawn.

1. Except 7405, 7249, 1873 stations, the RMS of the rest SLR stations are less than 7 cm, and most of them below 5 cm. It shows that the qualities of SLR data of these stations are very high and stable. It could also be concluded that CODE precise orbit has high precision and stability.

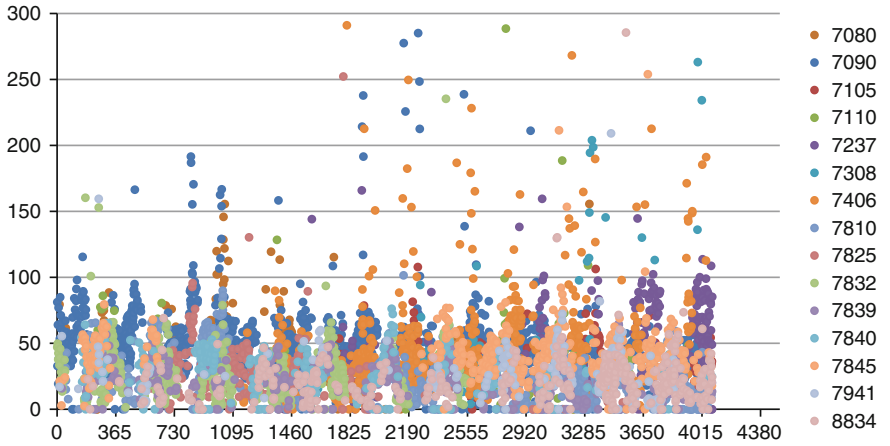

Fig. 2 The RMS scatter diagram of the selected 15 stations using SLR validation. (The horizontal coordinate begins in January 1 2003 as the starting day; the vertical coordinate is RMS value with the unit of mm)

2. There is a good consistency between the SLR observation and the computed range between GPS36 satellite and stations by using CODE precision orbit and station coordinates. There is still a relatively stable system error in the residual. According to the long-term data, the RMS of SLR orbit validation for GPS36 satellite is 3.91 cm, MEAN value is −3.36 cm, STD value is 1.07 cm. It indicates that the accuracy of SLR data is about 1 cm, the orbit precision of the GPS36 satellite is better than 4 cm.
3. The long-term RMS of each SLR station seem to be influenced by some cycle terms, which is related to periodic variation of the distribution of the valid SLR observation. From the overall trend, the quality of the data provided by the SLR station is stable and improved with technological development, such as 7090, 7810, 7839, 7840, and 7845 stations. Data quantity of the SLR station is also enhanced in recent years, such as 7845, 8834, 7941, and 7237 stations.
4. The stations of SLR observation with good quality for GPS36 satellite mostly locate in Europe because of good equipment and stable crust contraction on the European SLR stations.

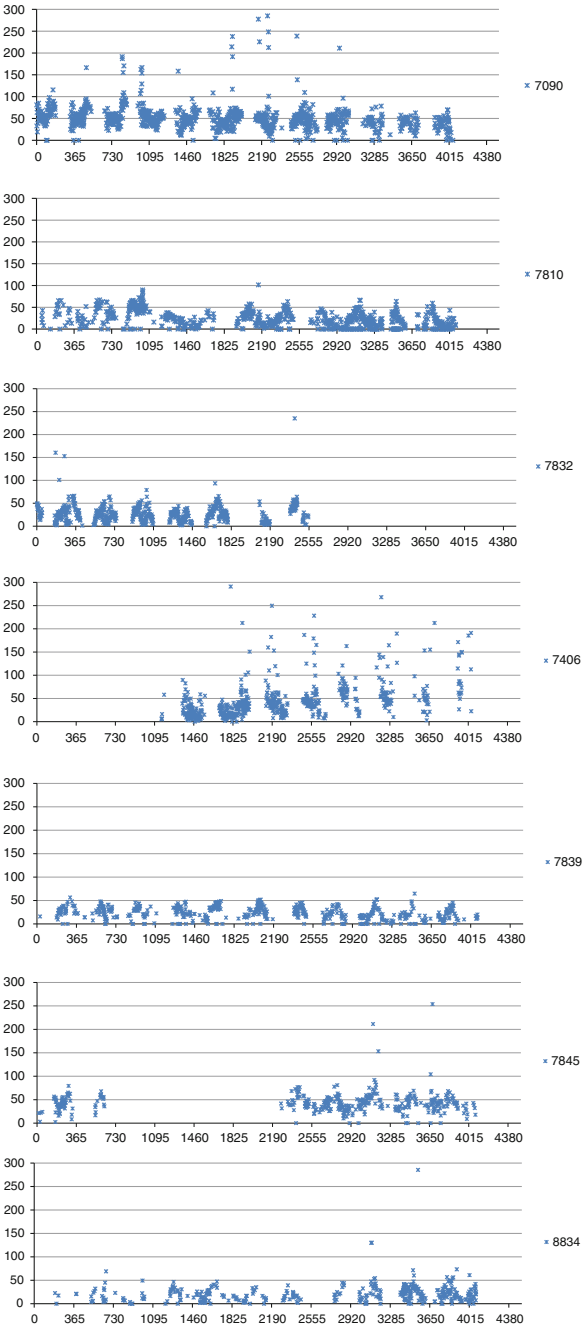

Fig. 3 The RMS scatter diagram of the selected 14 stations. (The horizontal coordinate begins in January 1 2003 as the starting day; the vertical coordinate is RMS value with the unit of mm)

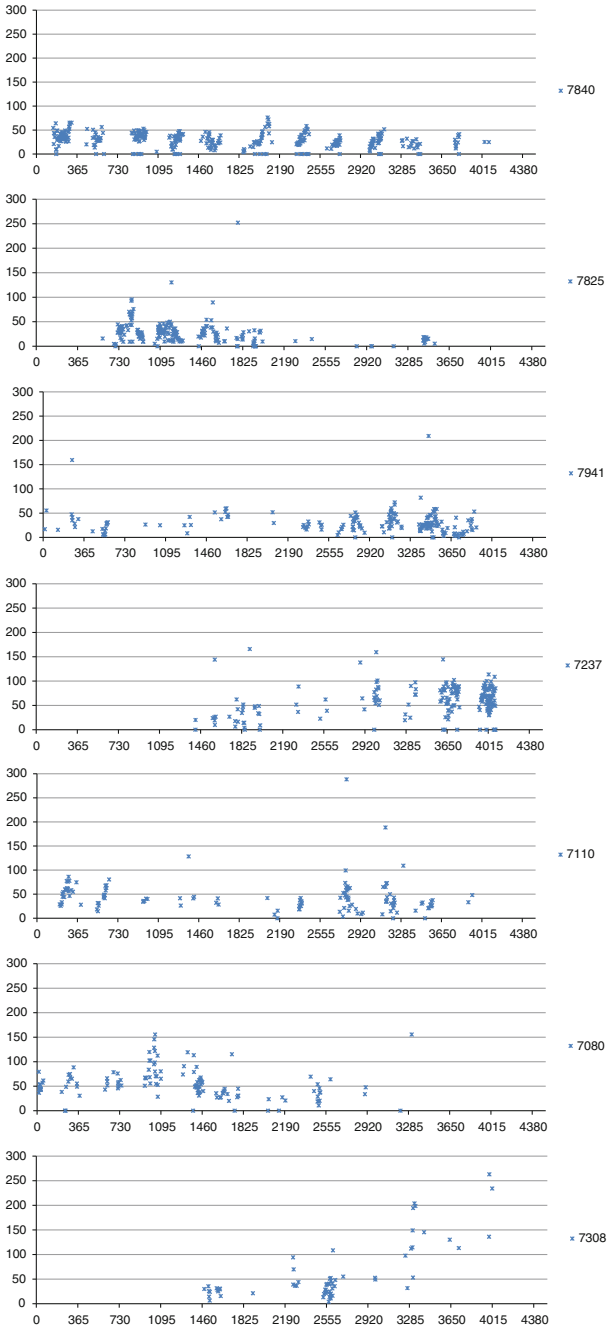

Fig. 3 (continued)

4 Conclusions

The orbit accuracy of GNSS can be validated by using global SLR data, which is up to now the only way of orbit external check. This paper uses long-term SLR data for orbit validation of GPS36, and compares the influence of SLR data from different data sources of EDC and CDDIS on validation accuracy. The results show that EDS can provide more SLR data than that of CDDIS, and their validation accuracies of CODE precise orbit are on the same level. The SLR validation accuracy for GPS36 orbit provided by CODE is less than 4 cm.

Acknowledgements This work is supported by the National Natural Science Foundation of China (No. 41574013 and 41174008) and the open foundation of State Key Laboratory of Aerospace Dynamics (No. 2014ADL-DW0101).

References

1. Qin X (2003) Satellite precision orbit determination based on SLR technology. Master's thesis, The PLA Information Engineering University
2. Xu H (1998) Laser ranging to GPS satellites and its application research. Prog Astron 16(4): P251–P259
3. Timon AS (1999) Modeling and validating orbits and clocks using the global positioning system. Ph.D. dissertation, Astronomical Institute, University of Berne, Berne, Switzerland
4. Xu T, Yang Y (2002) The research on the schemes of combination adjustment of VLBI, SLR and GPS data. Eng Surveying Mapp 11(4):7–10, 21
5. Qu F, Wang T, Chin X, Liu N, Ching B (2002) The comparison of SLR orbit with IGS orbit for GPS35 satellite. Bull Surveying Mapp 2:14–16
6. Qin X, Jiao W, Cheng L, Huo L (2005) Evaluation of CHAMP satellite orbit with SLR measurement. Geomatics Inf Sci Wuhan Univ 30(2):38–41
7. Liu Y, Zhang Y, Wu J (2007) Evaluation of GPS35 satellite precise orbit with SLR measurements. Eng Surveying Mapp 16(2):36–38, 50
8. Zhang Y, Jia X, Mao Y, Liu Y (2008) Evaluation of GPS35 satellite broadcast ephemeris precision by using SLR data. Sci Surveying Mapp 38(3):7–8
9. Li Z, Wei E, Wang Z (2010) Space geodesy. Wuhan University Press
10. Li J (1995) Satellite precision orbit determination. PLA Publication House, Bei Jing
11. Dach R, Hugentobler U, Fridez P, Meindl M (2007) Bernese GPS software version 5.0. Astronomical Institute, University of Bern, Jan 2007
12. Dach R, The Bernese GNSS Software development team (2013) Bernese GNSS software: processing examples in version 5.2, Astronomical Institute, University of Bern, Switzerland Sidlerstrasse 5, CH-3012 Bern, Bern, 2 July 2013
13. Dach R, Walser P (2015) Bernese GNSS software version 5.2. Astronomical Institute, University of Bern, Jan 2015
14. Ricklefs RL, Moore CJ (2009) Consolidated laser ranging data format (CRD) version 1.01, 27 Oct 2009

Orbit Combination of BeiDou Satellites with Pseudo-stochastic Pulse

Weiping Liu, Jinming Hao, Jiantao Xie, Kang Zhang and Yu Zhang

Abstract Multi-days orbit of BeiDou satellites is gotten by the routine method of stacking observation data at present. And moreover, the dynamic model of BeiDou satellites is not perfect because of the little running time, which also limits the precision of multi-days orbit. The method of multi-days BeiDou satellite orbit combination is presented. In this method, normal equation stacking is used to combining some consecutive one-day BeiDou satellite orbits to one multi-days orbit, which can improve calculation efficiency. And meanwhile, pseudo-stochastic pulse is used to compensate the deficiency of dynamic model and improve the precision of multi-days orbit. The analysis shows that it is pseudo-stochastic pulse at the one-day boundary that improves the precision of BeiDou satellite orbits obviously in orbit combination. And the tangential and normal precision is improved more than the radial precision. The orbit precision of GEO and IGSO is improved more than that of MEO. The precision of BeiDou satellite orbit can improve by extending the orbit arc with certain limits, and the result is mostly obvious in the tangential direction.

Keywords BeiDou navigation satellite system · Precise orbit determination · Normal equation stacking · Orbit combination · Pseudo-stochastic pulse

1 Introduction

BeiDou navigation satellite system is a global satellite navigation system, which is constructed and developed by China [1, 2]. The orbit precision of BeiDou satellites is important to affect its application [3, 4]. In the orbit determination of navigation

W. Liu (✉) · J. Hao · J. Xie · K. Zhang · Y. Zhang
School of Navigation and Aerospace Engineering,
Information Engineering University, Zhengzhou, China
e-mail: lwpchxy@sina.com

W. Liu · J. Hao
BeiDou Navigation Technology Collaborative Innovation Center of Henan,
Zhengzhou, China

© Springer Science+Business Media Singapore 2016

J. Sun et al. (eds.), *China Satellite Navigation Conference (CSNC) 2016 Proceedings: Volume III*, Lecture Notes in Electrical Engineering 390,
DOI 10.1007/978-981-10-0940-2_14

satellites, one-day observation data is often processed together. But the error of one-day orbit is often bigger in the starting and ending. So we need to combine some consecutive one-day BeiDou satellite orbits to one multi-days orbit [5, 6].

Multi-days orbit was gotten by the routine method of stacking some one-day observation data first, which is time-consuming and becoming more and more demanding with the increase in the number of tracking stations and one-day observation data. The method of normal equation stacking, which can process one-day observation in parallel and then get multi-days orbit by stacking normal equation, can improve the efficiency of the processing [7, 8]. In late 1990s, Beutler et al. [5] had studied the method of orbit combination by normal equation stacking. And then, Brockman [7] studied combination of solutions for geodetic and geodynamic application. Dong et al. [9] studied estimating regional deformation based on normal equation stacking. Yao [10] had also studied the principle of normal equation stacking and analyzed the effect of orbit combination. Liu et al. [11] studied the method to combine subnetwork solution orbit to the whole network solution orbit. But the above research is mostly focused on GPS and GLONASS. The orbit combination of BeiDou should be studied too. At present, multi-days orbit of BeiDou is mostly gotten by the routine method of stacking observation data [12–17], the precision of which can reach the level of normal equation stacking, but the efficiency is lower. Moreover, the existing research has mainly paid attention to osculating elements and dynamic parameters [18], but ignored the deep study of pseudo-stochastic pulse which is especially important for BeiDou orbit determination because of the deficiency of dynamic model.

To solve the above problem, the principle of normal equation stacking is studied in the paper, and the method of parameter transformation is derived. The method of combining osculating elements and dynamic parameters is introduced, and the method of processing pseudo-stochastic pulse is focused on. At last, the method of orbit combination of BeiDou satellites with pseudo-stochastic pulse is present, which is validated by real observation data.

2 Principle of Normal Equation Stacking

In the method of orbit combination based on normal equation stacking, one-day observation data is processed to form one-day normal equation, and then the equation is transferred and stacked to solve multi-days orbit. The parameter transformation, which can form the new normal equation by reparameterizing the old normal equation through the linear relationship between the new parameters and the old parameters, is often done before normal equation stacking. The method of parameter transformation is derived, and the principle of normal equation stacking is introduced.

2.1 Parameter Transformation

The error equation is expressed as follows:

$$\boldsymbol{v} = \boldsymbol{B}\hat{\boldsymbol{x}} - \boldsymbol{L} \tag{1}$$

The normal equation can be written as

$$\boldsymbol{N}\hat{\boldsymbol{x}} = \boldsymbol{U} \tag{2}$$

where $\boldsymbol{N} = \boldsymbol{B}^{\boldsymbol{T}}\boldsymbol{P}\boldsymbol{B}$ and $\boldsymbol{U} = \boldsymbol{B}^{\boldsymbol{T}}\boldsymbol{P}\boldsymbol{L}$. $\boldsymbol{P}$ is the weight matrix.

Assume to transfer $\hat{\mathbf{x}}$ in the normal equation to $\tilde{\boldsymbol{x}}$, and the linear relationship between them is expressed as follows:

$$\hat{\boldsymbol{x}} = \boldsymbol{C}\tilde{\boldsymbol{x}} + \boldsymbol{d} \tag{3}$$

Equation (3) is taken into Eq. (1), and we have

$$\boldsymbol{v} = \boldsymbol{B}\boldsymbol{C}\tilde{\boldsymbol{x}} - (\boldsymbol{L} - \boldsymbol{B}\boldsymbol{d}) \tag{4}$$

The new normal equation can be expressed as

$$\boldsymbol{N}'\tilde{\boldsymbol{x}} = \boldsymbol{U}' \tag{5}$$

where

$$\boldsymbol{N}' = \boldsymbol{C}^{\boldsymbol{T}}\boldsymbol{B}^{\boldsymbol{T}}\boldsymbol{P}\boldsymbol{B}\boldsymbol{C} = \boldsymbol{C}^{\boldsymbol{T}}\boldsymbol{N}\boldsymbol{C} \tag{6}$$

$$\boldsymbol{U}' = \boldsymbol{C}^{\boldsymbol{T}}\boldsymbol{U} - \boldsymbol{C}^{\boldsymbol{T}}\boldsymbol{N}\boldsymbol{d} \tag{7}$$

Equations (6) and (7) are the formula of parameter transformation. In real application, the linear relationship Eq. (3) should be established first, which is used to get $\boldsymbol{C}$ and $\boldsymbol{d}$. And then the new normal equation can be constructed by Eqs. (6) and (7).

2.2 Normal Equation Stacking

Assume that there are two independent groups of observation data. The observation equation can be written as follows:

$$\boldsymbol{v}_1 = \boldsymbol{B}_1\boldsymbol{x}_{\boldsymbol{c}} - \boldsymbol{L}_1 \quad D(\boldsymbol{L}_1) = \sigma_0^2\boldsymbol{P}_1^{-1} \tag{8}$$

$$\boldsymbol{v}_2 = \boldsymbol{B}_2\boldsymbol{x}_{\mathbf{c}} - \boldsymbol{L}_2 \quad D(\boldsymbol{L}_2) = \sigma_0^2\boldsymbol{P}_2^{-1} \tag{9}$$

where $\boldsymbol{x_c}$ defines estimated parameter. σ_0^2 is unit weight variance. $D(\cdot)$ defines the co-variance matrix. $\boldsymbol{L}_1$ and $\boldsymbol{L}_2$ are the two groups of observation. $\boldsymbol{B}_1$ and $\boldsymbol{B}_2$ are the two design matrices. $\boldsymbol{v}_1$ and $\mathbf{v}_2$ are the two residual vectors. $\boldsymbol{P}_1$ and $\boldsymbol{P}_2$ are the two the weight matrices.

It implies an assumption that all parameters are related to the two groups of observation and there are no parameters only related to one single group of observation. It is possible if the parameters, which are not interested, are pre-eliminated from the normal equation.

According to the least square principle, the normal equations can be expressed as

$$\left(\boldsymbol{B}_1^T\boldsymbol{P}_1\boldsymbol{B}_1\right)\hat{\boldsymbol{x}}_{c1} = \left(\boldsymbol{B}_1^T\boldsymbol{P}_1\boldsymbol{L}_1\right) \tag{10}$$

$$\left(\boldsymbol{B}_2^T\boldsymbol{P}_2\boldsymbol{B}_2\right)\hat{\boldsymbol{x}}_{c2} = \left(\boldsymbol{B}_2^T\boldsymbol{P}_2\boldsymbol{L}_2\right) \tag{11}$$

where $\hat{\boldsymbol{x}}_{c1}$ and $\hat{\boldsymbol{x}}_{c2}$ define the parameter estimation by a single group of observation.

The new normal equation can be gotten by stacking Eqs. (10) and (11).

$$\left(\boldsymbol{B}_1^T\boldsymbol{P}_1\boldsymbol{B}_1 + \boldsymbol{B}_2^T\boldsymbol{P}_2\boldsymbol{B}_2\right)\hat{\boldsymbol{x}}_{\boldsymbol{c}} = \left(\boldsymbol{B}_1^T\boldsymbol{P}_1\boldsymbol{L}_1 + \boldsymbol{B}_2^T\boldsymbol{P}_2\boldsymbol{L}_2\right) \tag{12}$$

where $\hat{\boldsymbol{x}}_{\boldsymbol{c}}$ defines the final parameter estimation by the two groups of observation.

3 Orbit Combination with Pseudo-Stochastic Pulse

When multi-days orbit is solved by normal equation stacking, the parameters in the one-day normal equation can be divided into two categories: one is orbit parameters that are of interest; the other is the parameters that are not of interest, for example, troposphere delay parameters, clock error parameters, and so on. The latter parameters can be pre-eliminated before stacking normal equation, and then solved by back substitution method after orbit parameters are estimated. The method of pre-elimination and back substitution can be referred in [7, 10, 11]. The main concern here is orbital parameters, usually including osculating elements and dynamic parameters. To compensate the deficiency of dynamic model in the BeiDou satellite orbit determination, pseudo-stochastic pulse is focused.

3.1 Combination of Osculating Elements and Dynamic Parameters

If there is a need to combine n one-day orbits, we should establish a linear relationship between the osculating elements and dynamic parameters of the first days and that of the other days, and then use the relationship to transfer parameters of $n-1$

one-day normal equations to unify all the parameters set, and finally, according to the principle of normal equation stacking, we can complete the combination.

To establish the linear relationship, the position and the velocity of the satellite is required to be continuing at the boundary of two days, and the dynamic parameters can be required to be equal among all one-day orbit. We have

$$\begin{cases} \boldsymbol{r_i}(t_{i+1}) = \boldsymbol{r_{i+1}}(t_{i+1}) \\ \dot{\boldsymbol{r}}_{\boldsymbol{i}}(t_{i+1}) = \dot{\boldsymbol{r}}_{\boldsymbol{i+1}}(t_{i+1}) \\ \boldsymbol{q}_i = \boldsymbol{q}_{i+1} = \boldsymbol{q}_c \end{cases} \tag{13}$$

where $\boldsymbol{r}$ and $\dot{\boldsymbol{r}}$ define satellite position and velocity. $\boldsymbol{q}$ defines the dynamic parameters, e.g., solar radiation parameters. $i(i \geq 1)$ defines the number of the day which includes the time span $[t_i,\ t_{i+1})$.

By the relationship between the position and velocity of the satellite and osculating elements and Eq. (13), we can derive the linear relationship as follows:

$$\begin{bmatrix} \Delta \boldsymbol{E}_i \\ \Delta \boldsymbol{q}_i \end{bmatrix} = \begin{bmatrix} \boldsymbol{K}_{i,1} & \boldsymbol{L}_{i,1} \\ 0 & \boldsymbol{I} \end{bmatrix} \begin{bmatrix} \Delta \boldsymbol{E}_1 \\ \Delta \boldsymbol{q}_1 \end{bmatrix} + \begin{bmatrix} \boldsymbol{M}_{i,1} \\ \boldsymbol{N}_{i,1} \end{bmatrix} \tag{14}$$

where $\Delta \boldsymbol{E}_i$ and $\Delta \boldsymbol{q}_i$ define the osculating elements and dynamic parameters of the $i(i = 2, \ldots, n)$ day, and $\Delta \boldsymbol{E}_1$ and $\Delta \boldsymbol{q}_1$ define these of the first day. $\boldsymbol{K}_{i,1}$, $\boldsymbol{L}_{i,1}$, $\boldsymbol{M}_{i,1}$, and $\boldsymbol{N}_{i,1}$ define the relationship matrix [7]. $\boldsymbol{I}$ defines the unit matrix.

Using the linear relationship Eq. (14), parameter transformation is conducted to $n - 1$ one-day normal equations to unify the parameters set with the method referred to Sect. 2.1. And then normal equation stacking is conducted and the combination is done.

3.2 Combination of Pseudo-Stochastic Pulse

In order to reduce the adverse effect of the deficiency in BeiDou satellite dynamic model, it is considered that pseudo-stochastic pulse is added at the boundary of two days when orbit combination is conducted. The pseudo-stochastic pulse is defined as instantaneous velocity increment [19, 20].

$$\boldsymbol{v}_{\text{new}}(\tau) = \boldsymbol{v}_{\text{old}}(\tau) + s \cdot \boldsymbol{o} \tag{15}$$

where s defines the size of pseudo-stochastic pulse. $\boldsymbol{o}$ defines the direction of pseudo-stochastic pulse. τ defines the epoch of pseudo-stochastic pulse. $\boldsymbol{v}_{\text{old}}$ and $\boldsymbol{v}_{\text{new}}$ respectively define the velocity before and after the epoch of pseudo-stochastic pulse.

All pseudo-stochastic pulses should be considered before the current epoch when combining orbits. Assume that τ is the epoch of pseudo-stochastic pulse, and t_i is the epoch of the one-day normal equation. The problem can be solved in two steps.

1. The effect of pseudo-stochastic pulse at the epoch τ to the osculating elements at the epoch τ.

According to Newton's equation of motion [21], the variation of the osculating elements caused by pseudo-stochastic pulse $s \cdot \boldsymbol{o}$ at the epoch τ can be expressed as

$$\begin{cases} \Delta a_s(\tau) = s \cdot \dfrac{2}{n \cdot \sqrt{1-e^2}} \cdot \left(e \cdot \sin f \cdot e_R + \dfrac{a \cdot (1-e^2)}{r} \cdot e_T \right) \\ \Delta e_s(\tau) = s \cdot \dfrac{\sqrt{1-e^2}}{na} \cdot (e_R \cdot \sin f + (\cos f + \cos E) \cdot e_T) \\ \Delta i_s(\tau) = s \cdot \dfrac{r \cdot \cos u}{na^2\sqrt{1-e^2}} \cdot e_N \\ \Delta \Omega_s(\tau) = s \cdot \dfrac{r \cdot \sin u}{na^2\sqrt{1-e^2}\sin i} \cdot e_N \\ \Delta \omega_s(\tau) = \dfrac{\sqrt{1-e^2}}{nae} \left[-e_R \cdot \cos f + e_T \cdot \left(1 + \dfrac{r}{p}\right) \cdot \sin f \right] - \cos i \cdot \dfrac{\mathrm{d}\Omega}{\mathrm{d}t} \\ \Delta M_s(\tau) = n - \dfrac{1-e^2}{nae} \left[-e_R \cdot \left(\cos f - 2e\dfrac{r}{p} \right) + e_T \cdot \left(1 + \dfrac{r}{p}\right) \cdot \sin f \right] \end{cases} \tag{16}$$

where a is semimajor axis. e is orbital eccentricity. i is orbital inclination. Ω is right ascension of ascending node (RAAN). n is mean angular velocity. u is argument of latitude. f is the true anomaly. E is the eccentric anomaly. r is the size of satellite position.$p = a(1-e^2)$ is semi-latus rectum. e_R, e_T, and e_W are, respectively, the unit vector in the radial, transverse, and normal direction.

The effect of pseudo-stochastic pulse at the epoch τ to the osculating elements at the epoch τ is expressed as:

$$\Delta \boldsymbol{E}_s(\tau) = \boldsymbol{\kappa}_s(\tau) \cdot s \tag{17}$$

where $\Delta \boldsymbol{E}_s(\tau)$ defines the variation of the osculating elements at the epoch τ. $\boldsymbol{\kappa}_s(\tau)$ is the coefficient matrix derived from Eq. (16). s is the same meaning as above.

2. The effect of osculating elements at the epoch τ to the osculating elements at the epoch t_i.

According to the variational equation, the state transition matrix can be expressed as

$$(\boldsymbol{M}_s(t_i, \tau))_{jk} = \frac{\mathrm{d}(\boldsymbol{E}(t_i))_j}{\mathrm{d}(\boldsymbol{E}_i(\tau))_k} \tag{18}$$

The effect of osculating elements at the epoch τ to the osculating elements at the epoch t_i can be written as follows:

$$\Delta \boldsymbol{E}_s(t_i) = \boldsymbol{M}_s(t_i, \tau) \cdot \Delta \boldsymbol{E}_s(\tau) \tag{19}$$

According to Eqs. (17) and (19), the effect of pseudo-stochastic pulse at the epoch τ to the osculating elements at the epoch t_i can be expressed as

$$\Delta \boldsymbol{E}_s(t_i) = \boldsymbol{T}_s \cdot s \tag{20}$$

and

$$\boldsymbol{T}_s = \boldsymbol{M}_s(t_i, \tau) \cdot \boldsymbol{\kappa}_s(\tau) \tag{21}$$

In summary, the effect of all pseudo-stochastic pulses before the epoch t_i to the osculating elements at the epoch t_i can be expressed as follows:

$$\Delta \tilde{\boldsymbol{E}}_i = [\boldsymbol{I} \quad \boldsymbol{T}_2^* \ldots \boldsymbol{T}_i^*] \left[\Delta \hat{\boldsymbol{E}}_i^T \quad \hat{\boldsymbol{s}}_2^{*T} \ldots \hat{\boldsymbol{s}}_i^{*T} \right]^T \tag{22}$$

where $\Delta \hat{\boldsymbol{E}}_i$ is the osculating elements of one-day solution at the epoch t_i. $\Delta \tilde{\boldsymbol{E}}_i$ is the osculating elements considered all pseudo-stochastic pulses before the epoch t_i. $\hat{\boldsymbol{s}}_j^* (j = 2, \ldots, i)$ is pseudo-stochastic pulses added at the boundary of two days. $\boldsymbol{T}_j^*$ is the transition matrix.

The parameter transformation is done to the normal equation of the i day. According to Eq. (3), we have

$$\boldsymbol{C}_i = [\boldsymbol{I} \quad \boldsymbol{T}_2^* \ldots \boldsymbol{T}_i^*] \tag{23}$$

$$\boldsymbol{d}_i = 0 \tag{24}$$

According to Eqs. (6) and (7), we have

$$\boldsymbol{N}_i' = \boldsymbol{C}_i^T \boldsymbol{N}_i \boldsymbol{C}_i \tag{25}$$

$$\boldsymbol{U}_i' = \boldsymbol{C}_i^T \boldsymbol{U}_i - \boldsymbol{C}_i^T \boldsymbol{N}_i \boldsymbol{d}_i \tag{26}$$

where $\boldsymbol{N}_i$ and $\boldsymbol{U}_i$ are the normal matrix and free term vector. $\boldsymbol{N}_i'$ and $\boldsymbol{U}_i'$ are the normal matrix and free term vector after the parameter transformation.

The parameter transformation is conducted to all one-day normal equations to unify the parameters set with the above method. And then normal equation stacking is conducted and the combination is done.

In practice, osculating elements, dynamic parameters, and pseudo-stochastic pulses are usually included in one normal equation. First, the parameter transformation is conducted to osculating elements and dynamic parameters. Second, the parameter transformation is conducted to pseudo-stochastic pulses. Last, the normal equation stacking is conducted and orbit combination is done.

4 Numerical Example and Analysis

To validate the method, the real BeiDou observation data is analyzed. First, the function of pseudo-stochastic pulses at the boundary of two days is discussed. And then the practical application of BeiDou satellite orbit combination is validated.

4.1 Function of Pseudo-Stochastic Pulses

The experiment spanned from June 3, 2013 to June 24, 2013, and BDS real observation data from global 24 stations is analyzed. By the way, 12 stations are from Multi-GNSS Experiment (M-GEX) of IGS(●), 12 stations are from BeiDou Experimental Tracking Stations (BETS) of Wuhan University(■). The distribution of stations is given in Fig. 1.

First, one-day observation is processed by the zero-differenced dynamic method and one-day normal equation is saved. And then the three-days orbit combination is done by the method in the paper. Two cases are used, and the strategy of them is given in Table 1. The main difference between them is as follows:

Case 1 (S1) Three one-day orbits are combined to one three-days orbit without pseudo-stochastic pulses at the boundary of every two days.

Case 2 (S2) Three one-day orbits are combined to one three-days orbit with pseudo-stochastic pulses at the boundary of every two days.

The precision of orbit determination is accessed by checking the difference of the overlapped arcs. Table 2 and Fig. 2 have given the mean RMS of BDS orbit in the radial (R), tangential (T), normal (N), and three-dimensional (P) direction.

From the results in Table 2 and Fig. 2, we can see that the precision of all BeiDou satellites orbits are improved obviously after pseudo-stochastic pulses are added at the

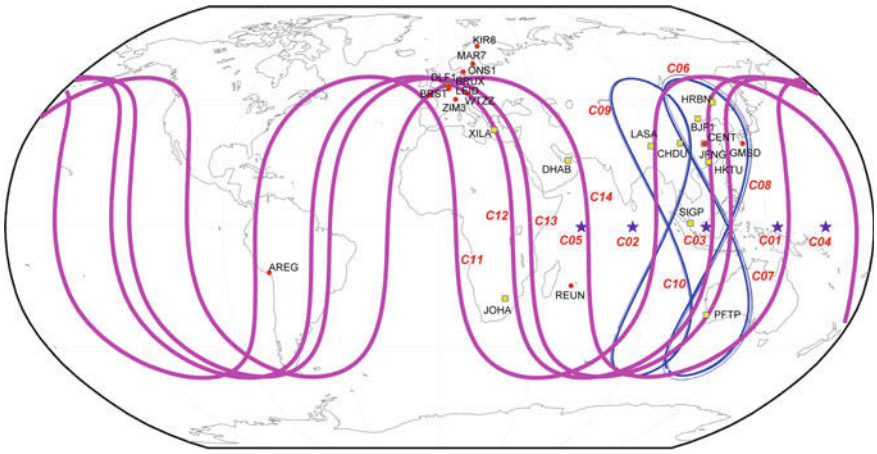

Fig. 1 Station layout

Table 1 Strategy of data processing

Name	Model and parameters
Observation	Zero-differenced iono-free phase and smoothing pseudo-range
Elevation cutoff angle	3°
Sampling rate	180 s
Earth gravity	JGM3 12 ×12
N body attraction	JPL DE200 (sun and moon)
Solid tide	TIDE2000
ocean tide	CSR30
Relativistic effects	IERS2003
Solar radiation	ECOM
Station coordinates	Restrict highly in the system of IGS08
Troposphere modeling	SAAS and NIELL is used for dry delay
	Wet delay is estimated every 4 h
Troposphere modeling	Iono-free combination
Tidal displacements	IERS2003; FES2004
Receiver clock	Taken as epoch parameters
Satellite clock	Taken as epoch parameters
Ambiguity	Float
Orbit parameters	6 orbit state parameters and 5 solar parameters are estimated

Table 2 Statistics of BeiDou satellites orbit precision (units: m)

Type	PRN	*R* (m)		*T* (m)		*N* (m)		*P* (m)	
		S1	S2	S1	S2	S1	S2	S1	S2
GEO	C1	0.151	0.095	0.910	0.731	0.379	0.203	1.019	0.785
	C2	0.082	0.058	0.584	0.456	0.334	0.215	0.705	0.533
	C3	0.111	0.072	0.980	0.825	0.394	0.205	1.099	0.875
	C4	0.347	0.191	2.207	1.813	0.420	0.235	2.286	1.850
	C5	0.106	0.071	0.640	0.542	0.470	0.242	0.830	0.618
	Mean	0.159	0.097	1.064	0.873	0.399	0.220	1.188	0.932
IGSO	C6	0.096	0.068	0.398	0.300	0.449	0.294	0.624	0.437
	C7	0.087	0.068	0.624	0.398	0.462	0.301	0.789	0.512
	C8	0.107	0.069	0.624	0.392	0.254	0.206	0.695	0.454
	C9	0.079	0.060	0.459	0.295	0.312	0.232	0.578	0.393
	C10	0.076	0.060	0.456	0.327	0.337	0.235	0.588	0.418
	Mean	0.089	0.065	0.512	0.342	0.363	0.254	0.655	0.443
MEO	C11	0.061	0.047	0.258	0.208	0.141	0.122	0.309	0.251
	C12	0.098	0.072	0.358	0.288	0.181	0.149	0.421	0.334
	C13	0.070	0.056	0.268	0.215	0.187	0.141	0.343	0.270
	C14	0.059	0.051	0.235	0.184	0.160	0.128	0.298	0.234
	Mean	0.072	0.057	0.280	0.224	0.167	0.135	0.343	0.272

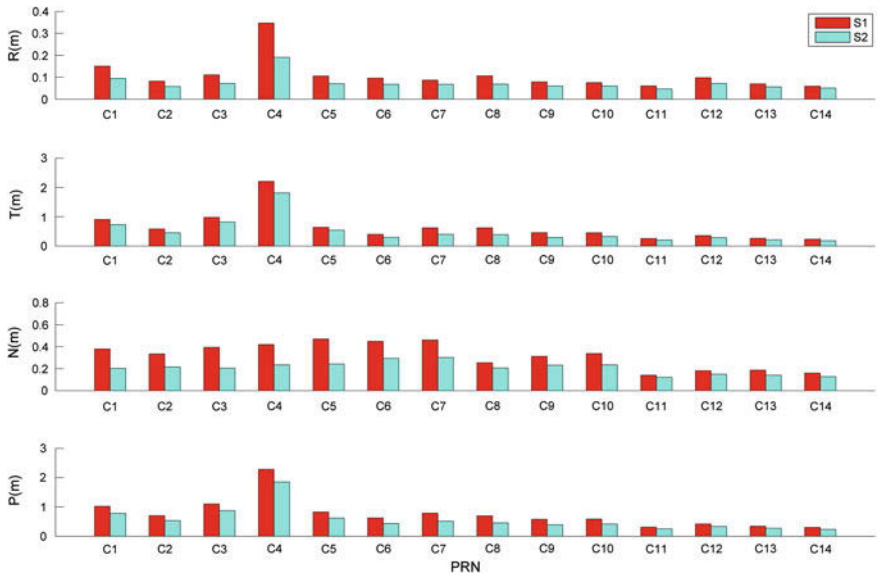

Fig. 2 Comparison of BeiDou satellites orbit precision

boundary of every two days when orbit combination is done. Averagely, the precision of GEO is improved by 0.062, 0.191, 0.179 m in the three directions; that of IGSO is improved by 0.024, 0.170, 0.109 m; and that of MEO is improved by 0.015, 0.056, 0.032 m. The orbit precision of three kinds of BeiDou satellites is improved more in the radial direction than in the tangential and normal direction. In the three-dimensional direction, the orbit precision of GEO, IGSO and MEO is respectively improved by 0.256, 0.212 and 0.071 m. The improvement of GEO and IGSO is obviously more than that of MEO. Pseudo-stochastic pulses can compensate the deficiency of dynamic model in precise orbit determination, so the above results may show that there is bigger error in the tangential and normal direction in the dynamic model of BeiDou satellite. The dynamic model of GEO and IGSO is needed more improved than that of MEO.

4.2 Effect of Multi-days Orbit Combination

To validate the practical application of BeiDou satellite orbit combination, the observation data from June 11, 2013 to June 26, 2013 is used to analysis. The processing strategy is the same with Case 2 in Sect. 4.1. The three-days orbit (S1), five-days orbit (S2), and seven-days orbit (S3) are solved with the method in the paper. The middle day of multi-days orbit is taken as the final orbit. In order to facilitate comparison, the median of the differences at 00:00:00 (or 24:00:00) between two consecutive final orbits is used to assess the orbit precision. Table 3

Table 3 Statistics of BeiDou satellites orbits precision in orbit combination (units: m)

Type	PRN	*R* (m)			*T* (m)			*N* (m)			*P* (m)		
		S1	S2	S3	S1	S2	S3	S1	S2	S3	S1	S2	S3
GEO	C1	0.092	0.058	0.047	0.720	0.520	0.270	0.116	0.066	0.045	0.725	0.534	0.307
	C2	0.030	0.034	0.020	0.195	0.382	0.566	0.050	0.040	0.041	0.274	0.399	0.566
	C3	0.090	0.054	0.041	0.465	0.310	0.181	0.063	0.041	0.040	0.469	0.319	0.204
	C4	0.185	0.127	0.073	1.410	0.817	0.694	0.119	0.072	0.045	1.443	0.819	0.697
	C5	0.032	0.020	0.022	0.499	0.547	0.505	0.126	0.067	0.053	0.518	0.549	0.507
	Mean	0.086	0.059	0.041	0.658	0.515	0.443	0.095	0.057	0.045	0.686	0.524	0.456
IGSO	C6	0.046	0.046	0.048	0.235	0.159	0.125	0.256	0.195	0.175	0.376	0.262	0.200
	C7	0.047	0.028	0.023	0.278	0.151	0.174	0.226	0.203	0.105	0.424	0.236	0.212
	C8	0.051	0.022	0.017	0.318	0.229	0.253	0.110	0.098	0.114	0.361	0.253	0.253
	C9	0.046	0.041	0.040	0.199	0.176	0.103	0.197	0.126	0.128	0.272	0.248	0.183
	C10	0.038	0.032	0.036	0.345	0.200	0.124	0.244	0.150	0.093	0.429	0.265	0.192
	Mean	0.046	0.034	0.033	0.275	0.183	0.156	0.207	0.154	0.123	0.372	0.253	0.208
MEO	C11	0.029	0.024	0.012	0.175	0.093	0.074	0.086	0.075	0.052	0.219	0.142	0.102
	C12	0.020	0.019	0.010	0.143	0.067	0.082	0.069	0.072	0.046	0.241	0.097	0.111
	C13	0.041	0.021	0.013	0.137	0.057	0.044	0.083	0.053	0.043	0.195	0.101	0.076
	C14	0.035	0.019	0.011	0.093	0.056	0.035	0.109	0.051	0.029	0.175	0.087	0.086
	Mean	0.031	0.021	0.012	0.137	0.068	0.059	0.087	0.063	0.043	0.208	0.107	0.094

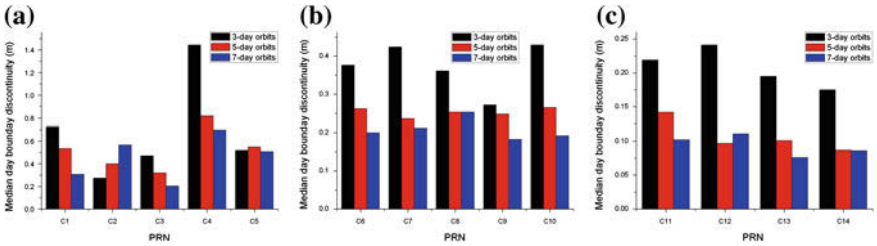

Fig. 3 Comparison of BeiDou satellites orbits precision in orbit combination. **a** GEO. **b** IGSO. **c** MEO

and Fig. 3 have given the median of BDS orbit in the radial (*R*), tangential (*T*), normal (*N*) and three-dimensional (*P*) direction.

From these results in Table 3 and Fig. 3, we can see:

1. With the increase of the arc length, the orbit precision of most of BeiDou satellites is improved, but that of C02 is low. The reason should be analyzed deeply.
2. From the precision in the three-dimensional direction, the average is improved by 23.6, 32.0 and 48.6 % to GEO, IGSO and MEO when the arc length is increased from three days to five days, but it is improved by 13.0, 17.8 and 12.1 % from five days to seven days. It can be seen that it is more improved from three days to five days than from five days to seven days. The reason is that increasing the arc length to a certain extent will not improve the observation structure, and the accuracy of dynamic model also limits the length of the arc. Moreover, when the arc length is increased from three days to five days, the orbit precision of GEO, IGSO, and MEO increases in turn. The reason is that the accumulation of observation data is more meaningful to "kinematic" IGSO and MEO, especially MEO, than "static" GEO. When the arc length is increased from five days to seven days, the difference of the orbit precision improvement of GEO, IGSO and MEO is small.
3. Compared to three-days orbit, the precision of five-days orbit of GEO, IGSO, and MEO is improved by 0.045, 0.013, and 0.019 m in the radial direction, 0.215, 0.119 and 0.078 m in the tangential direction, 0.050, 0.084 and 0.044 m in the normal direction. With the increase of the arc length, the precision is improved most obviously in the tangential direction. The reason is that the orbit in the tangential direction is limited loosely by navigation satellite range observation, and the observation structure in the tangential direction can be better with the increase in the arc length.

These results are basically equivalent to the accuracy in the Ref. [17] in the same condition. The results of this paper are just excellent. Besides pseudo-stochastic pulses added at the boundary of every two days, it also benefits from the use of more stations in the paper. It should be noted that the above assessment is based on the discontinuity at the boundary of a single day. Because the error in the starting and ending of the orbit arc is often bigger, the precision by the assessment method here is more positive than the method of checking the difference of the overlapped

arcs. Moreover, the common data is increasing with the arc length extended, which will also make inner coincidence accuracy be better. Besides the contribution of orbit combination, the orbit precision also benefits from the two factors.

5 Conclusion

Multi-days orbit of BeiDou satellites is gotten by the routine method of stacking observation data at present, which is ineffective. The method of orbit combination based on normal equation stacking is studied. And meanwhile, the dynamic model of BeiDou satellites is not perfect because of the little running time, which also limits the precision of multi-days orbit. The method of combining osculating elements and dynamic parameters is introduced, and the method of processing pseudo-stochastic pulse is focused. Finally, the method of orbit combination of BeiDou satellites with pseudo-stochastic pulse is presented. The analysis of real observation data shows that the precision of all BeiDou satellites orbits are improved obviously after pseudo-stochastic pulses are added. The orbit precision of three kinds of BeiDou satellites is improved more in the radial direction than in the tangential and normal direction. The orbit precision improvement of GEO and IGSO is obviously more than that of MEO. Pseudo-stochastic pulses can compensate the deficiency of dynamic model in precise orbit determination, so the above results may show that there is bigger error in the tangential and normal direction in the dynamic model of BeiDou satellite. The dynamic model of GEO and IGSO is needed more improved than that of MEO. With the increase of the arc length, the orbit precision of most of BeiDou satellites is improved. The orbit precision is more improved from three days to five days than from five days to seven days. With the increase of the arc length, the precision is improved most obviously in the tangential direction. But the orbit precision of C02 is low, and the reason should be analyzed deeply.

It should be noted that the precise orbit, which is gotten from the method with pseudo-stochastic pulses in the paper, can be used to refine dynamic model of BeiDou satellites. The refined method needs to be studied.

References

1. Yang Y (2010) Progress, contribution and challenges of compass/Beidou satellite navigation system. Acta Geodaetica et Cartographica Sinica 39(1):1–6
2. Ran C (2013) Development of Beidou navigation satellite system. CSNC 2013, Wuhan
3. China Satellite Navigation Office (2013) Report on the development of BeiDou navigation satellite system V2.2, Beijing
4. Hao J, Liu W, Yang L et al (2015) Status of precise orbit determination of BeiDou navigation satellite system. J Geomat Sci Technol 32(3):221–225

5. Beutler G, Brockmann E, Hugentobler U et al (1996) Combining n consecutive one-day-arcs into one n-days-arc. J Geod 70(2):287–299
6. Yao Y (2007) Theory and realization of GPS orbit integration. Geomat Inf Sci Wuhan Univ 32 (11):1487–1492
7. Brockmann E (1996) Combination of solutions for geodetic and geodynamic applications of the global positioning system (GPS). University of Bern, Berne, pp 1–7
8. Liu W (2014) Research on precise orbit determination of BeiDou navigation satellite system. Information Engineering University, Zhengzhou, pp 70–90
9. Dong D, Herring TA, King RW (1998) Estimating regional deformation from a combination of space and terrestrial geodetic data. J Geod 72(4):200–214
10. Yao Y (2004) Research on the algorithm and realization of post-processing for GPS precise positioning and orbit determination. Wuhan University, Wuhan, pp 1–7
11. Liu W, Hao J, Qian L et al (2014) Method of satellite combination based on normal equation stacking. J Geomat Sci Technol 31(1):23–27
12. Shi C, Zhao QL, Li M et al (2012) Precise orbit determination of Beidou satellites with precise positioning. Sci China Earth Sci 55:1079–1086
13. Zhao Q, Guo J, Li M et al (2013) Initial results of precise orbit and clock determination for COMPASS navigation satellite system. J Geod 87(5):475–486
14. Liu W, Hao J, Li J et al (2014) Multi-GNSS joint precise orbit determination of BeiDou navigation satellite system. Acta Geodaetica et Cartographica Sinica 43(11):1132–1138
15. He L, Ge M, Wang J et al (2013) Experimental study on the precise orbit determination of the BeiDou navigation satellite system. Sensors 13(3):2911–2928
16. Liu Y, Lou Y, Shi C et al (2013) BeiDou regional navigation system network solution and precision analysis. In: Proceedings of China satellite navigation conference (CSNC) 2013. CSNC2013, Guangzhou, pp 173–186
17. Steigenberger P, Hugentobler U, Montenbruck O et al (2011) Precise orbit determination of GIOVE-B based on the CONGO network. J Geod 85(6):357–365
18. Beutler G, Brockmann E, Gurtner W et al (1994) Extended orbit modeling techniques at the CODE processing center of the international GPS service for geodynamics (IGS): theory and initial results. Manuscripta Geodaetica 19:367–386
19. Liu W, Hao J, Tian Y et al (2015) Fast parameter estimation for pseudo-stochastic pulse. Geomat Inf Sci Wuhan Univ 40(11):1487–1492
20. Beutler G, Jäggi A, Hugentobler U et al (2006) Efficient satellite orbit modeling using pseudo-stochastic parameters. J Geod 80:353–372
21. Liu L (1998) Method of celestial mechanics. Nanjing University Press, Nanjing, pp 45–47

Mitigation of Orbit Integration Errors for Eclipsing Satellites

Bingbing Duan, Junping Chen, Jiexian Wang, Yize Zhang, Sainan Yang, Jiejun Zhang and Qingchen Zhang

Abstract Numerical integration assumes that accelerations at each node are continuous and smooth. However, when satellite enters into shadow, perturbation caused by solar radiation pressure will jump. Therefore, mathematical theory of numerical integrator cannot match the real motion of satellite, which will bring about integration errors. In order to deal with the problem, some experiments are done for different constellations. The result shows that 99 % of error occurs in along-track direction and will accumulate when crossing more shadow boundaries. For different integrators, errors are different. Runge-Kutta4 integrator is sensitive to step size, especially for eclipsing satellites, and is not competent for long arc integration. Adams integrator relies on former steps, needs a fixed step size, and will induce more integration errors when crossing shadow boundaries. Runge-Kutta9 integrator brings less error during eclipsing season than Runge-Kutta4 and Adams integrators, and can change step size flexibly. To mitigate integration errors during eclipses, this contribution introduces an improved method based on Runge-Kutta9 integrator. We use dichotomy to detect the exact epoch of penumbra boundary, change the step size, and restart the integration. Result shows that after boundary detection, accuracy for 1-day arc improves 65.8 %, 2-day arc improves 55.5 %, 3-day arc improves 33.2 %. This method is suitable for both extended filter and least square method.

Keywords Eclipse · Penumbra · Integrator · Runge-Kutta · Adams

B. Duan (✉) · J. Wang · Y. Zhang
College of Surveying and Geo-Informatics, TongJi University, Shanghai, China
e-mail: 410_duanbingbing@tongji.edu.cn

B. Duan · J. Chen · Y. Zhang · S. Yang · J. Zhang
Shanghai Astronomical Observatory, Chinese Academy of Sciences, SHAO, Shanghai, China
e-mail: junping.chen@shao.ac.cn

Q. Zhang
Technical University of Munich, Munich, Germany

© Springer Science+Business Media Singapore 2016

J. Sun et al. (eds.), *China Satellite Navigation Conference (CSNC) 2016 Proceedings: Volume III*, Lecture Notes in Electrical Engineering 390,
DOI 10.1007/978-981-10-0940-2_15

1 Introduction

The International GNSS Service (IGS) is a volunteer organization of more than 200 individual agencies and institutions that maintain a global network of monitoring stations as well as products. Since the IGS started its operations on June 21, 1992, orbits of an unprecedented accuracy are available today for all active GPS satellites with a delay of about 13 days. As the advent of new GNSS, the IGS is fully committed to expand to a true multi-GNSS service. In 2012, the IGS has initiated the Multi-GNSS Experiment (MGEX) to provide Multi-GNSS measurements and products. Accuracy of BeiDou GEO satellite is around 1 meter, BeiDou IGSO satellite is about 30 cm, and BeiDou MEO satellite owns the best trajectory of about 10–15 cm. Galileo orbits provided by TUM show us a precision of 10 cm [1–3]. In some cases, when satellites are in eclipse, it is not easy to get the exact attitude of satellites so that solar radiation pressure model, antenna phase center correction, and phase wind-up cannot be well modeled [4]. In addition, if integration crosses shadow boundary, there will be a perturbation in acceleration caused by solar radiation pressure. Acceleration inside one step size will not be smooth and continue anymore, which can bring about integration errors. In order to solve this problem, dichotomy is used to detect the exact epoch of penumbra boundary and the restart the integration.

2 Character of Integrators

Gauss-Jackson, Runge-Kutta, and Adams integrator are popular among orbit determination, which have already been fully tested in accuracy, efficiency, etc. [5–9]. Laurichesse [10] used Runge-Kutta4 integrator in extended Kalman filter for the purpose of real-time orbit determination. A step size of 60 s was adopted and would change to 10 s when eclipse happens [10]. Li [11] tested Runge-Kutta12 integrator in orbit determination and concluded that high order Runge-Kutta integrator is more precise but also more time consuming. Adams integrator has a stable accuracy but relies on former steps. Li [12] put forward using collocation method to numerical integration and obtained some advantages: a big step size is allowed, positions and velocities of satellite can be obtained directly without any interpolation.

In this paper, Runge-Kutta4, Runge-Kutta9, and Adams integrator are tested based on 2-body problem. As we know, there will be an entirely analytical solution if only the 2-body problem is considered, and at the same time, if we use the same initial orbit excluding all the other force models we shall get a consistent trajectory by numerical integration.

Table 1 presents accuracy of different integrators using different step sizes. It reveals that Runge-Kutta4 integrator is sensitive to step size, a small step size is needed for precise usage. Runge-Kutta9 has an attractive accuracy and is nearly independent of step size. Adams integrator is both efficient and precise but relies on former steps.

Table 1 Accuracy test with different step size (24 h arc)

s	RK4 (m)	RK9 (m)	Adams (m)
10	3.5534E−05	7.1175E−06	1.6901E−06
60	4.9609E−02	1.9425E−06	1.1480E−06
150	2.1973E+00	1.4003E−06	1.0985E−06
300	4.2070E+01	4.3363E−05	2.1257E−06

3 Integration Error of Eclipsing Satellites and Method for Improvement

Models for solar radiation pressure are normally developed for full sunlight, and when in umbra models will be closed. However, there will be about 60 s between completely full sunlight and complete darkness, which is called penumbra. Even if we use Runge-Kutta integrator that is independent of former steps, there will still be a possibility that one separated step cross the shadow boundary, as shown in Fig. 1.

When integrator integrates from epoch n to $n+1$ or from epoch $m-1$ to m, acceleration within this period will not continue and smooth anymore. In order to mitigate integration errors during eclipsing season, a strategy for detecting the boundary of penumbra is put forward. Afterwards, integration is divided into three main parts: full sunlight, penumbra, and umbra. As in Fig. 1, the shadow factor at n epoch is $v = 1$, while $n+1$ epoch is $v = 0$. The boundary is inside the duration, which we can use dichotomy to detect the exact boundary position by doing several iterations. Whenever the shadow factor $v > 0.99$ we can treat it as a boundary epoch. So, boundary epochs b_1, b_2, b_3 and b_4 can be obtained. After that, we can change the step size at epoch n and integrate to epoch b_1, then do the same thing at epoch b_2, $m-1$, b_3 and b_4.

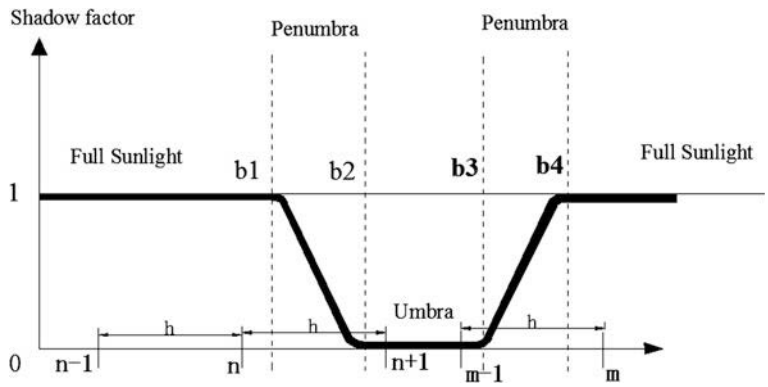

Fig. 1 Integration cross penumbra

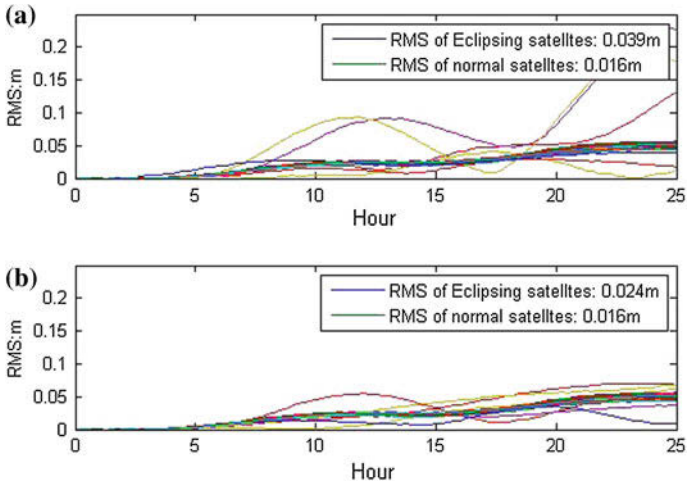

Fig. 2 Comparison of Runge-kutta4 integrator with step size 45 and 60 s

After restarting the integration, we need a standard to judge the precision. However, if the solar radiation pressure model is added, it will be complicated to do analytical solution. But we have already concluded from Table 1 that Runge-Kutta9 and Adams integrator are not sensitive to step size. If we use a very close step size, the results should be the same for the normal satellites, and the difference of eclipsing satellites could be an expression of integration precision.

Figure 2a shows a comparison of Runge-Kutta4 integrator using different step size 45 s and 60 s. It reveals that eclipsing satellites are very sensitive to step size and even normal satellites experience a linear growing difference. Figure 2b shows the same situation but after boundary checking, there is an improvement of 38.5 % for eclipsing satellites, but still not good enough. So, for long time running and precise using, we would not recommend Runge-Kutta4 integrator.

Adams integrator based on former steps is popular among post-processing of orbit determination. When crossing shadow boundaries, some integration errors occur. In order to find out how large the errors can be, we test data from 2015-10-01 to 2015-10-03 for GPS, BeiDou, and Galileo constellations.

Figure 3 shows comparison of Adams integrator with step size 45 s and 60 s for different constellations. The difference is obvious, GPS Block IIF experiences the largest difference, which can reach 1.2 m after 3 days. Table 2 is the time range of penumbra period and times of eclipse.

It is found that difference in Fig. 3 of each satellite increases with the number of eclipse, which means that the more shadow boundaries the integrator cross, the lager difference it will reach. Because that Adams integrator cannot change step size flexibly we do not check the boundary of penumbra and restart the integration.

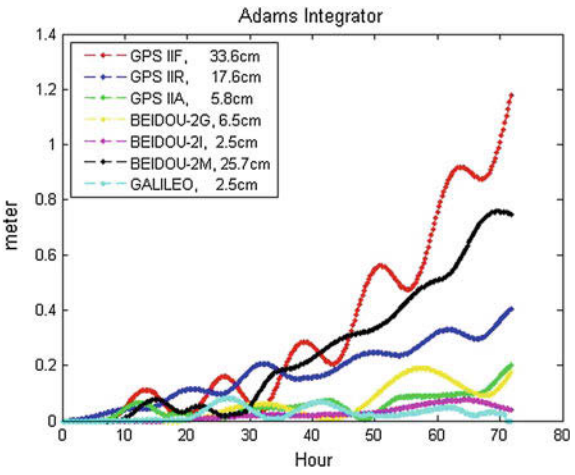

Fig. 3 Comparison of Adams integrator with step size 45 and 60 s

Table 2 Eclipsing information

	Mean penumbra duration (s)	Eclipsing times
GPS IIF	66	6
GPS IIR	62	6
GPS IIA	64	6
BEIDOU-2G	145	3
BEIDOU-2I	230	3
BEIDOU-2M	68	6
GALILEO	220	4

Runge-Kutta9 integrator can achieve the same precision as Adams integrator, but will spend more time. However, Runge-Kutta9 integrator has an advantage that step size can be modified flexibly. We use the boundary checking method that described above and restarts the integration. In order to compare with Adams integrator, the same data is tested for Runge-Kutta9 integrator.

Figure 4 shows the difference of GPS, BEIDOU, and GALILEO constellations after integrating for 3 days. BEIDOU-2M reveals the largest difference, which can reach to 45 cm. Compare Fig. 4 with Fig. 3, we can get that error in Runge-Kutta9 integrator is less than that in Adams. Figure 5 illustrates errors after restart integration. The largest difference drops down to 25 cm, details of improvement are shown as Table 3.

As shown in Table 3, after boundary detection and restarting the integration, accuracy for 1-day arc improves 65.8 %, 2-day arc improves 55.5 %, 3-day arc improves 33.2 %. In addition, 99 % errors occur in along-track direction.

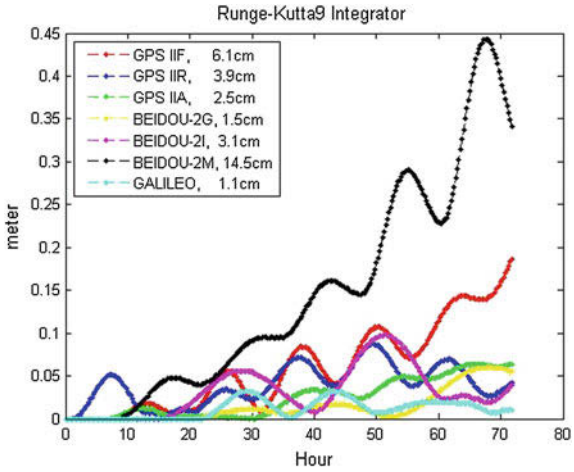

Fig. 4 Comparison of Runge-kutta9 integrator with step size 45 and 60 s

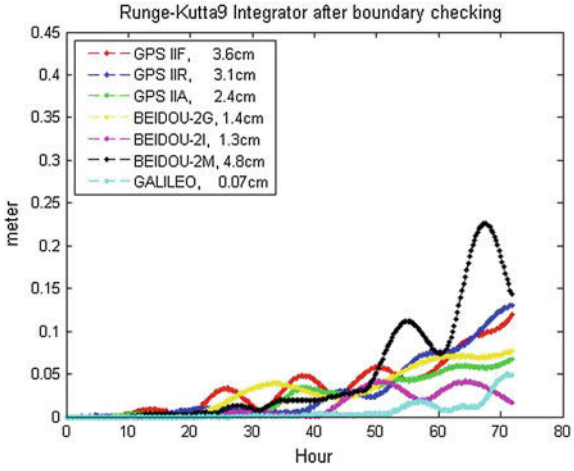

Fig. 5 Comparison of Runge-kutta9 integrator with step size 45 and 60 s after boundary checking

Table 3 Improvement after boundary detection (%)

Day	IIF	IIR	IIA	GEO	IGSO	MEO	IOV	Mean
3	39.9	18.3	2.8	5.6	57.5	66.6	41.9	33.2
2	40.9	74.6	5.3	9.8	80.7	85.2	91.6	55.5
1	44.2	83.1	55.1	21.5	90.4	90.9	75.6	65.8

4 Conclusion

This paper analyzes integration errors caused by crossing shadow boundary. A strategy based on shadow factor is developed to mitigate integration error. Conclusions are as following:

1. Runge-Kutta4 integrator is sensitive to step size especially for eclipsing satellites. The precision decreases after 1 day integration.
2. Adams integrator is precise and stable but relies on former steps. When crossing shadow boundaries, it will bring about errors. As tested in this paper, integration error increases with the number of eclipse. GPS Block IIF satellites can lead to 1.2 m error after integrating for 3 days.
3. Runge-Kutta9 integrator is precise and flexible. It is independent of former steps, and will not cause so much integration error as Adams integrator. Besides, it can modify step size at any epoch. After boundary detection, it will be easy to restart integration.
4. 99 % errors occur in along-track direction. For Runge-Kutta9 integrator, after boundary detection and restarting the integration, accuracy for 1-day arc improves 65.8 %, 2-day arc improves 55.5 %, 3-day arc improves 33.2 %.

Acknowledgements This paper is supported by the 100 Talents Programme of The Chinese Academy of Sciences, the National High Technology Research and Development Program of China (Grant No. 2013AA122402, 2014AA123102), the National Natural Science Foundation of China (NSFC) (Grant No. 11273046, 41174023, 41174024 and 41204022), and the Shanghai Committee of Science and Technology (Grant No. 12DZ2273300, 13PJ1409900), and the State Key Development Program for Basic Research of China (No. 2013CB733304).

References

1. Guo J, Xu X, Zhao Q et al (2015) Precise orbit determination for quad-constellation satellites at Wuhan University: strategy, result validation, and comparison. J Geodesy 1–17
2. Prange L, Dach R, Lutz S et al (2014) The CODE MGEX orbit and clock solution. IAG Potsdam 2013 proceedings. Springer, International Association of Geodesy Symposia, accepted for publication 2014
3. Uhlemann M, Gendt G, Ramatschi M et al (2015) GFZ global multi-gnss network and data processing results 1–7
4. Montenbruck O, Schmid R, Mercier F et al (2015) GNSS satellite geometry and attitude models[J]. Adv Space Res 56(6):1015–1029
5. Montenbruck O, Gill E (2001) Satellite orbits: models, methods and applications. Springer Science & Business Media
6. Zadunaisky PE (1970) On the accuracy in the numerical computation of orbits. Periodic Orbits, Stability and Resonances. Springer, Netherlands, pp 216–227
7. Luo Z, Zhou H, Zhong B et al (2013) Analysis and validation of Gauss-Jackson integral algorithm[J]. Geomatics Inf Sci Wuhan Univ 38(11):1364–1368
8. Berry MM (2004) A variable-step double-integration multi-step integrator. Virginia Polytechnic Institute and State University

9. Fox K (1984) Numerical integration of the equations of motion of celestial mechanics. Celest Mech 33(2):127–142
10. Laurichesse D, Cerri L, Berthias JP, Mercier F (2013) Real time precise GPS constellation and clocks estimation by means of a Kalman Filter. In: Proceedings of the 26th international technical meeting of the satellite division of the institute of navigation (ION GNSS+2013), pp 1155–1163, Nashville, TN, Sept 2013
11. Li D, Yuan Y, Ou J et al (2010) 12 steps Runge-kutta 2 orders algorithm for satellite orbit integration. Geomatics Inf Sci Wuhan Univ 35(11):1335–1338
12. Li ZH, Gong XY, Liu WK (2010) Application of collocation method to numerical integration of satellite orbit[J]. Geomatics Inf Sci Wuhan Univ 35(3):253–256

Precision Evaluation and Consistency Analysis of iGMAS Orbit and Clock Products

Sumei Yu and Tianhe Xu

Abstract This paper evaluates the precision of iGMAS orbit and clock products, and analyzes their consistency. By the methods of orbit comparisons and day boundary discontinuities (DBDs), the iGMAS orbit precision is evaluated. The twice difference method is used to evaluate clock precision. On the basis of precision analysis, consistency of orbit and clock products from different analysis centers (AC) was compared by precise point positioning (PPP) technique. The quality of orbit, clock, and GNSS observation would have a large impact on the accuracy of PPP. Therefore, the experimental data for consistency analysis includes MGEX station observation data with good quality, and the orbit/clock products with comparable precision. Using the proposed method, precision, and consistency of iGMAS orbit and clock products from different AC are analyzed.

Keywords iGMAS · Orbit and clock product · Precision evaluation · Precise point position · BDS

1 Introduction

The international GNSS Monitoring and Assessment System (iGMAS) is the world's continuous monitoring and evaluation system sponsored by China in the international area. iGMAS aims to establish a global distribution network of GNSS signal tracking to provide service to global customers, which can monitor service

S. Yu (✉)
School of Geology Engineering and Surveying, Chang'an University, Xi'an, Shanxi, China
e-mail: ysmxyz@163.com

T. Xu (✉)
State Key Laboratory of Geo-Information Engineering, Xi'an, Shanxi, China
e-mail: thxugfz@163.com

T. Xu
Xian Research Institute of Surveying and Mapping, Xi'an, Shanxi, China

© Springer Science+Business Media Singapore 2016

J. Sun et al. (eds.), *China Satellite Navigation Conference (CSNC) 2016 Proceedings: Volume III*, Lecture Notes in Electrical Engineering 390,
DOI 10.1007/978-981-10-0940-2_16

performance and signal quality of GNSS. GNSS users via the Internet can not only obtain monitoring and assessment service information for each GNSS system, but also get high precision products. Similar to IGS, iGMAS products include Multi-GNSS precise orbit and clock products, iGMAS station coordinates and velocities, earth rotation parameters (ERP), geocentric motion, troposphere and ionosphere products. Precision and consistency of these products are very important for users to carry out high precision navigation and positioning [1, 2]. This paper focuses on precision evaluation and consistency analysis of iGMAS orbit and clock products.

2 Precision Evaluation of iGMAS Orbit and Clock Products

2.1 Orbit Products

In order to assess the orbit precision of iGMAS integration and service center (ISC) and analysis centers (ACs), the following two methods are proposed.

1. Orbit comparison. This approach compares the positions of different orbit products [3, 4]. For GPS system, IGS final product accuracy is regarded as the highest. It can be used to assess GPS orbits precision of iGMAS ACs and ISC by mean RMS of orbit comparison.
2. Day boundary discontinues(DBDS) [4, 5]. This method is developed by Griffiths and Ray in 2009 to use orbit difference of the common epoch of the adjacent day to reflect the precision of satellite orbit. iGMAS ISC and ACs' SP3 files give satellite coordinates from 00:00:00 to 23:45:00, there is no overlap period between the adjacent days' SP3 files. Therefore, Lagrange interpolation method is used to interpolate satellites' coordinates at 23:52:30 epoch.

2.2 Clock Products

IGS final clock products are used as the reference to evaluate ACs and ISC clock products since its accuracy can reach to 75 ps. Usually the clock difference method is used to assess the clock accuracy. The clock difference $\Delta^{j}(i)$ can be expressed as

$$\Delta^{j}(i) = \delta t^{j}(i) - \delta t^{j}_{IGS}(i) \tag{1}$$

Since a relative value GNSS satellite clock can be determined, namely clock solution has a reference clock, the satellite clock calculated by the direct difference contains the system error.

In order to eliminate the influence of the system error, twice difference method is used to assess the clock accuracy as [6].

The steps of clock precision evaluation are as follows.

1. Make a clock difference $\overline{\Delta}^{j}(i)$ between IGS final clock and every satellite clock at the same epoch as

$$\overline{\Delta}^{j}(i) = \delta t^{j}(i) - \delta t^{j}_{IGS}(i) \tag{2}$$

   where $\overline{\Delta}^{j}(i)$ is the jth satellite's clock error, $\delta t^{j}(i)$ and $\delta t^{j}_{\mathrm{IGS}}(i)$ is the jth satellite's clock error at i epoch between ACs or ISC and IGS final clock.
2. Select the satellite n as the reference satellite, the twice difference of clock errors can be expressed as

$$\Delta^{j}(i) = \overline{\Delta}^{j}(i) - \overline{\Delta}^{n}(i) \tag{3}$$

   where $\Delta^{\mathrm{j}}(i)$ is the jth satellite's twice difference at i epoch. $\overline{\Delta}^{n}(i)$ is the reference satellite's clock error at i epoch.
3. Calculate the mean square error (RMS) of the twice difference of clock error to provide the accuracy evaluation without the influence of system error.

3 Basic Principle of PPP

In order to analyze the consistency of iGMAS orbit and clock error, this paper adopts the method of precise point positioning (PPP) [1]. PPP has been widely been used for high precision positioning based on undifferential dual frequency observations, precise orbit and clock error information, and the least squares (LS) or Kalman filtering algorithm. Most of the errors in the procedure of PPP can be corrected by corresponding models and a small amount of unmodeling error such as tropospheric zenith wet delay and the receiver clock error can be estimated as unknown parameters [7]. The accuracy of PPP is generally affected by the quality of observation data, orbit, and clock error. The accuracy of PPP can be used to reflect the consistency analysis of the orbit and clock on the precondition of other error source excluded [8].

PPP uses precise orbit and clock error calculated by the GNSS data of worldwide ground tracking station under indifference mode. The estimated parameters include station coordinates, indifference integer ambiguity, the receiver clock error, and tropospheric delay parameters. PPP mathematical models of GPS, GLONASS, and BEIDOU systems are similar. In the following, GPS PPP model positioning is introduced as an example. GPS observations include pseudo range or phase carrier. The observation equation of GPS pseudo range and carrier phase in the $L_i(i = 1, 2)$ frequency can be expressed as [7]

$$P_i = \rho + c(dt - dT) + d_{\text{orb}} + d_{\text{trop}} + d_{\text{ion}/i} + \varepsilon(P_i) \tag{4}$$

$$\Phi_i = \rho + c(dt - dT) + d_{\text{orb}} + d_{\text{trop}} - d_{\text{ion}/i} + \lambda_i N_i + \varepsilon(\Phi_i) \tag{5}$$

where P_i and Φ_i represent the observed values of the pseudo range and carrier phase respectively, ρ is the geometric distance between the receiver and the satellite, c is the speed of light, dt is the receiver clock and dT is the GPS satellites clock, d_{orb} is GPS satellite orbit error, d_{trop} is tropospheric delay, $d_{\text{ion}/i}$ is ionospheric delay of $L_i(i = 1, 2)$ frequency; $\varepsilon(P_i)$ and $\varepsilon(\Phi_i)$ represent observation noise and multipath error of pseudo range and carrier phase respectively.

The combination model of PPP technology mainly has three kinds: traditional model, UoFc model, and non fuzzy model. The traditional model is the most widely used and uses ionospheric-free combination of dual-frequency pseudo range and phase carrier observation to form the observation equation. The simplified equation of the traditional model can be expressed as

$$P_{\text{IF}} = \frac{f_1^2}{f_1^2 - f_2^2} P_1 - \frac{f_2^2}{f_1^2 - f_2^2} P_2 = \rho + cdt + d_{\text{trop}} + \varepsilon(P_{\text{IF}}) \tag{6}$$

$$\Phi_{\text{IF}} = \frac{f_1^2}{f_1^2 - f_2^2} \Phi_1 - \frac{f_2^2}{f_1^2 - f_2^2} \Phi_2 = \rho + cdt + d_{\text{trop}} + B_{\text{IF}} + \varepsilon(\Phi_{\text{IF}}) \tag{7}$$

$$B_{\text{IF}} = \frac{f_1^2}{f_1^2 - f_2^2} N_1 - \frac{f_2^2}{f_1^2 - f_2^2} N_2 \tag{8}$$

where P_{IF} is the ionospheric-free combination observation of P_1 and P_2 pseudo range, Φ_{IF} is the ionospheric-free combination observation of Φ_1 and Φ_2 carrier phase, f_i (i = 1, 2) is carrier frequency, B_{IF} is ambiguity parameter of ionospheric-free combination observation, $\varepsilon(P_{\text{IF}})$ and $\varepsilon(\Phi_{\text{IF}})$ are observation noises modeled.

In PPP, the preprocessing of observation data and navigation data should be conducted to eliminate outliers in order to gain clean data. The precise orbit and clock should be interpolated to observation epoch. And then station position, receiver clock together with other parameters are solved using the extended Kalman filter (EKF) [9].

4 Calculations and Analysis

The data from October 12, 2014 to October 25, 2014, 14 days is used in this article, which include: IGS and COD final orbit and clock products; IGS ERP file; ISC orbit and clock products of iGMAS; Analysis Centers CHD, LSN, SHA, TLC,

CGS, and WHU orbit and clock products of iGMAS; MGEX Multi-GNSS data of CAS1, GMSD, NNOR, and XMIS stations.

4.1 Precision Evaluation of GPS Orbit and Clock

This paper uses the orbit comparison of iGMAS and COD with respect to IGS final orbit for precision evaluation. The accuracy of the clock is evaluated by twice difference method compared to the IGS final clock.

From Figs. 1 and 2 it can be seen that the precision of COD orbit and clock is higher than others, the orbit difference is less than 5 mm, and the clock difference is less than 0.05 ns. GPS orbit difference of iGMAS ISC is less than 15 mm, the clock difference is within 0.4 ns. Consistency analysis requires products with similar precision, so two sets of products ISC/TLC and CHD/LSN are selected for GPS consistency of orbit and clock products.

For the BDS satellite orbit without a reference orbit for comparison, the DBD method is carried out for the precision assessment of iGMAS ISC and ACs.

The GPS satellite orbit difference and the DBD value are in Fig. 3 of taking two ACs of TLC and WHU as examples.

It can be seen that WHU products have higher precision than TLC. The evaluation results have almost the same conclusion using orbit comparison or DBD. So the DBD method can be used to evaluate the accuracy of BDS satellite orbit.

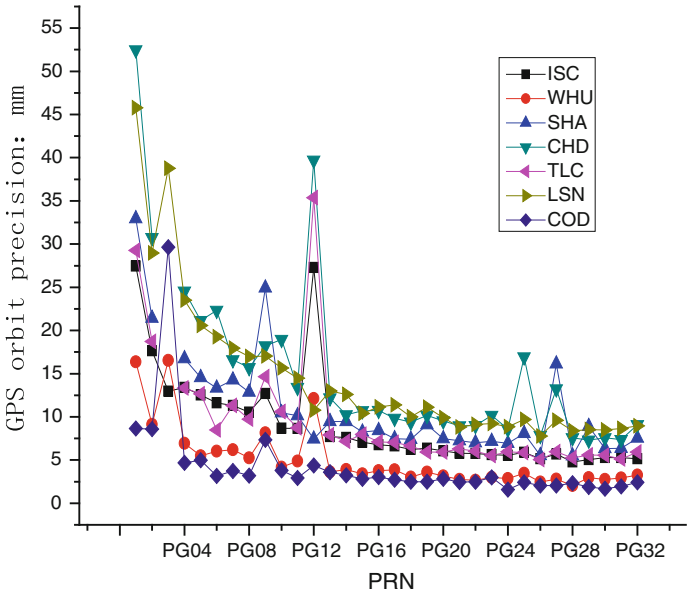

Fig. 1 GPS satellite orbit precision evaluated by orbit comparisons method

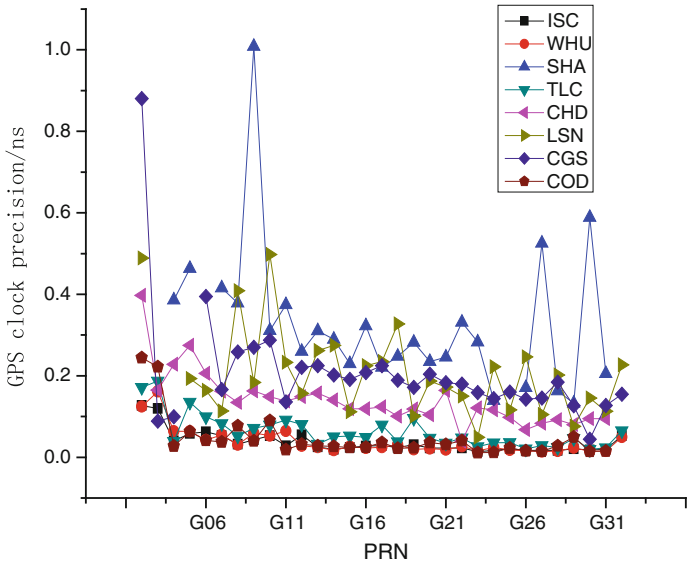

Fig. 2 GPS satellite clock precision evaluated by twice difference method

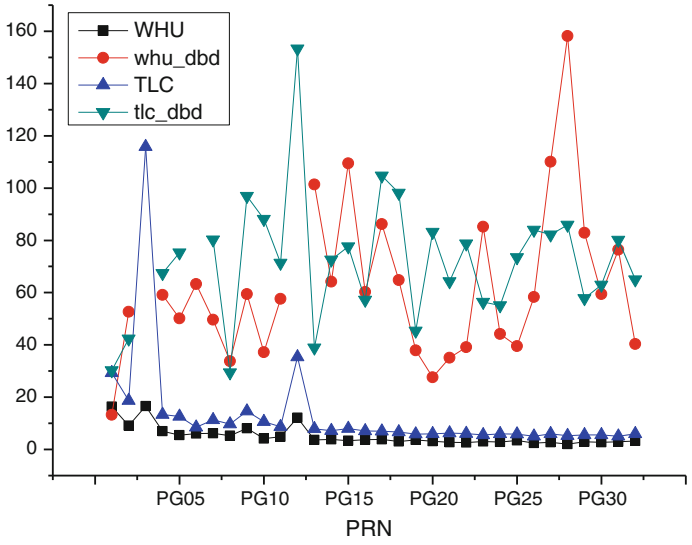

Fig. 3 GPS satellite orbit precision evaluated by orbit comparisons and DBD

It can be seen from Fig. 4 that the precision of BDS orbit products from different AC is equivalent. MEO orbit has the best accuracy with DBD value of 150 mm, DBD value of IGSO orbit is about 250 mm, and GEO orbit has poorest accuracy with DBD value of about 500 mm. Figure 5 shows that GEO satellites clock has

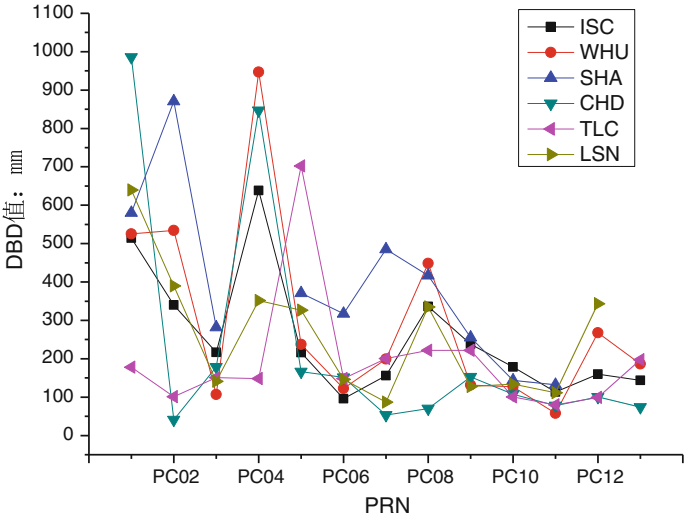

Fig. 4 BDS satellite orbit precision evaluated by DBD method

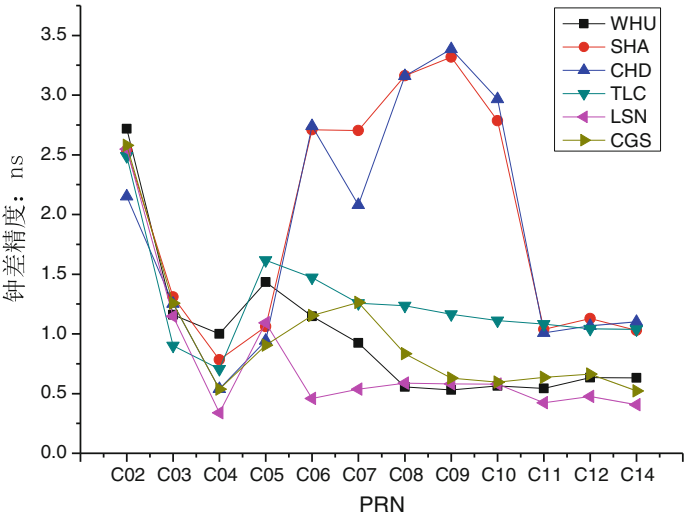

Fig. 5 BDS satellite clock precision evaluated by twice difference method

poor precision compared to IGSO and MEO satellites. The precision of BDS clock is within 1.5 ns except for individual satellite clock of CHD and LSN. Consistency analysis requires products with similar precision, for this reason, this paper selects two sets of products of CHD/SHA and WHU/CGS/LSN for further consistency analysis.

4.2 Consistency Analysis of Orbit and Clock Products

Based on the precision evaluation of satellite orbit and clock, the following data are used for consistency analysis. For GPS satellite orbit and clock products, two groups of ISC/TLC and CHD/LSN are selected. For BDS satellite orbit and clock products, CHD/SHA and WHU/CGS/LSN are selected. Multi-GNSS data of four stations CAS1, GMSD, NNOR, and XMIS are chosen to perform kinematic PPP.

In this paper, the same PPP strategy is used for kinematic solution as [1], and the station coordinate differences between kinematic PPP results and IGS station coordinates are given from 285 to 298 days in 2014. Figure 6 shows the positioning error in the *N*, *E*, *U* directions of GPS kinematic PPP using different orbit and clock products. Figure 7 shows the positioning error in the *N*, *E*, *U* directions of BDS kinematic PPP using different orbit and clock products. Table 1 is the RMS of GPS kinematic PPP in *N*, *E*, *U* directions for the four stations. Table 2 is the RMS of BDS kinematic PPP in *N*, *E*, *U* directions for the four stations The last line in Tables 1 and 2 are the average values of RMS for the four stations.

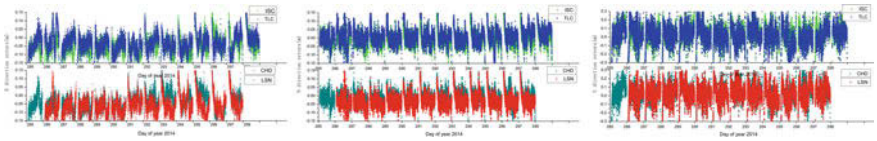

Fig. 6 The residuals in *E*, *N*, *U* direction of GPS kinematic PPP

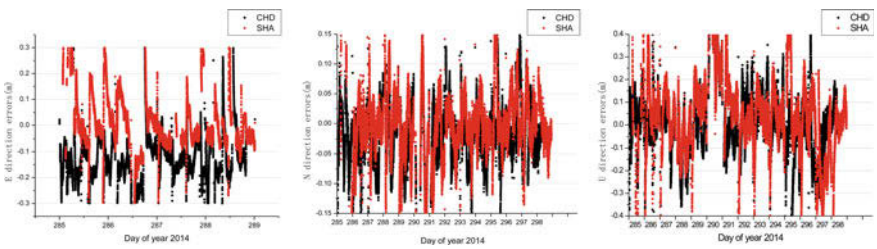

Fig. 7 The residuals in *E*, *N*, *U* direction of BDS kinematic PPP

Table 1 RMS in each direction of GPS kinematic PPP value (unit: cm)

Product	ISC			TLC			LSN			CHD		
	E	*N*	*U*	*E*	*N*	*U*	*E*	*N*	*U*	*E*	*N*	*U*
XMIS	0.60	0.18	1.17	0.43	0.30	1.18	0.74	0.27	1.09	0.64	0.18	1.11
GMSD	0.49	0.64	3.48	0.54	0.94	3.43	0.63	0.41	3.35	0.57	0.69	3.45
NNOR	0.80	0.42	2.09	0.85	0.45	2.53	0.64	0.49	2.28	0.85	0.38	1.83
CAS1	0.87	0.84	4.23	0.57	0.55	3.40	1.06	0.98	4.96	0.91	0.89	4.68
MEAN	0.69	0.52	2.74	0.60	0.56	2.63	0.77	0.53	2.92	0.74	0.54	2.77

Table 2 RMS in each direction of BDS kinematic PPP (unit: cm)

Product	CHD			SHA			WHU			CGS			LSN		
	E	*N*	*U*	*E*	*N*	*U*	*E*	*N*	*U*	*E*	*N*	*U*	*E*	*N*	*U*
XMIS	2.24	0.29	1.85	0.84	0.34	2.57	1.12	0.65	4.06	1.83	0.73	3.45	1.48	0.69	5.99
GMSD	0.95	0.41	2.42	0.45	0.62	1.86	1.75	1.35	1.92	1.69	1.21	3.84	1.01	0.69	2.72
NNOR	1.47	0.69	3.83	0.70	0.81	4.47	1.80	0.86	5.69	1.85	1.25	5.11	1.37	1.18	3.85
CAS1	1.36	1.88	5.52	1.10	2.09	4.01	1.87	1.81	5.06	1.99	2.41	3.55	1.54	2.28	4.14
MEAN	1.50	0.82	3.41	0.77	0.97	3.23	1.63	1.17	4.18	1.84	1.40	3.99	1.35	1.21	4.18

From the results it can be seen that

1. GPS kinematic PPP precision is higher than that of BDS in each direction. The RMSs of GPS PPP in *E*, *N* direction are mostly within 1 cm and the RMS of *U* direction is about 2–5 cm. The RMSs of BDS kinematic PPP in *E*, *N* direction are mostly in 1 cm and the RMS of *U* direction is about 3–5 cm. This is mainly because the accuracy of GPS satellite orbit and clock products is higher than that of BDS products.
2. The results of PPP using different orbit and clock products with the same accuracy level show little difference, which can be used to verify the precision evaluation of the orbit and clock products. Kinematic PPP results with gap in the beginning stage is caused by the convergence of PPP, whose results are not involved in the figures.
3. As for GPS, the consistency of ISC products is better than TLC in *N* direction, and worse than TLC in *E* and *U* direction. The consistency of CHD products is better than LSN in *E* and *U* direction, and worse than LSN in *N* direction.
4. As for BDS, the consistency of SHA products is better than CHD in *E* and *U* direction, and worse than CHD in *N* direction. The best consistency of orbit and clock products in *E*, *N*, and *U* direction are LSN, WHU, and CGS respectively.

5 Conclusions

iGMAS offers satellite orbit, clock, station coordinates and ERP products of GPS, GLONASS, BDS, and Galileo systems, precision and consistency of these products are the basic guarantee for high precision navigation and positioning. With the continuous development of the BDS in China, the PPP technology using BDS or multi-GNSS has been widely used. Orbit and clock products are the basic data of PPP, which directly affects the positioning precision. So it is necessary to study the precision and consistency of BDS satellite orbit and clock products. In this paper, orbit comparisons and DBD method are used to assess the accuracy of GPS satellite and BDS satellite orbit, the twice difference method is used to evaluate the precision of clock products, and kinematic PPP method is preformed to analyze the consistency of the products of orbit and clock in details.

Acknowledgment This work was supported by Natural Science Foundation of China (No. 41174008 and 41574013) and open foundation of State Key Laboratory of Aerospace and Dynamics (No. 2014ADL-DW0101).

References

1. Chen K, Xu T, Chen G et al (2015) The orbit and clock combination of iGMAS analysis centers and the analysis of their precision. In: Proceedings of China Satellite Navigation Conference (CSNC), pp 421–438
2. Wei N, Shi C, Li M et al (2009) Analysis and evaluation of the consistency of IGS products. J Wuhan Univ (Inf Sci Ed) 34(11):1–5

3. Griffiths J, Ray JR (2009) On the precision and accuracy of IGS orbits. J Geodesy 83(3–4):277–287
4. Duan B, Lan X (2012) Precision analysis of IGS precise satellite orbit. Eng Invest 2: 1–4
5. Guo J, Xu X, Zhao Q, Liu J (2015) Precise orbit determination for quad-constellation satellites at Wuhan University: strategy, result validation, and comparison. J Geodesy
6. Yu H, He J, Liu W et al (2014) A method for evaluating the accuracy of satellite clock. Ma Surveying Mapp 34(2):1–3
7. Huang G (2009) Research and software implementation of GPS precision single point positioning and high precision GPS baseline network adjustment. Chang'an University, Xian
8. Xu A, Xu Z, Sui X (2013) The influence of satellite orbit and clock error on the precision of single point positioning. Bull Surveying Mapp 5:1–4
9. Ding H, Luo R, Lu B (2014) Research on precision single point positioning based on RTKLIB. City Surv (5):1–4

Characteristic Analysis and Short-Term Prediction of GPS/BDS Satellite Clock Correction

Weili Zhou, Chao Huang, Shuli Song, Qinming Chen and Zhimin Liu

Abstract The real-time acquirement and prediction of high precise clock error is an important foundation in the field of Global Navigation Satellite System (GNSS) real-time precise point positioning and time service. In this paper, GNSS satellite clock error sequence is analyzed in detail, especially for the Beidou Navigation Satellite System, the periodicity characteristic is compared with distinguished types of satellite clock. The sample length of GPS and BDS clock error sequence are analyzed with the method of Polynomial and Periodic model, the result shows that the short-term prediction is better using one-day sequence than two- or three-day sequence. The ARIMA model is optimized with a new fitting method and determining criteria of the order p and q, which is used to the short-term prediction of satellite clock error. And the precision of satellite clock error is analyzed in 1–6 h prediction length, which is compared with the prediction using Polynomial and Periodic method. The results show that the precision has significantly improved, the mostly GPS rubidium clock error prediction precision of 6 h is better than 0.6 ns and 1 h is better than 0.25 ns which has 50 % improved as statistics for a single month. Meanwhile, the BDS satellite clock error prediction precision of 6 h is better than 2 ns and 1 h is better than 1.4 ns which has 30 % improved.

Keywords GNSS · Satellite clock error · Short-term prediction · ARIMA · Period characteristic

W. Zhou (✉)
Shanghai Key Laboratory of Space Navigation and Positioning Techniques, Shanghai, China
e-mail: wlzhou@shao.ac.cn

C. Huang · S. Song · Q. Chen
Shanghai Astronomical Observatory, Chinese Academy of Sciences, Shanghai, China

C. Huang · Z. Liu
Geomatics College, Shandong University of Science and Technology, Qingdao, China

© Springer Science+Business Media Singapore 2016

J. Sun et al. (eds.), *China Satellite Navigation Conference (CSNC) 2016 Proceedings: Volume III*, Lecture Notes in Electrical Engineering 390,
DOI 10.1007/978-981-10-0940-2_17

1 Introduction

With the increasingly fierce competition of global economy and military, GNSS (GPS, GLONASS, Galileo and Beidou, etc.) has entered a rapid development stage [1, 2]. Real-time Precise Point Positioning has become the goal of all navigation systems [3]. Navigation systems acquire observations based on clock frequency signal of satellite and receiver. Satellite clock and orbit precision are the major factors affecting the capability to provide precise point positioning service.

Currently, the prediction precision of ultra-rapid orbit with the global station observations has reached 5 cm because of the characteristics of navigation satellite orbit and mature orbit determination technology, and the needs of real-time precise point positioning can be fully met. While, selecting the prediction method and enhancing the prediction precision have the difficulties due to satellite clock's instability. At present the researchers at home and abroad have done large relevant work in this aspect. The clock error sequence not only contains a linear or quadratic variation, but also includes periodic variation, found by Reid et al. [4] and Senir et al. [5]. So, IGS using a polynomial model with periodic items to predict the satellite clock error of ultra-rapid production, and the prediction precision is better than 3 ns [3]. Using delay coordinate embedding methods for linear and nonlinear characteristics, a reliable prediction model based on the cyclical changes of satellite clock is presented by Youn et al. [6]. Its precision is slightly better than the prediction section of ultra-rapid products offered by IGS, especially cesium clocks. An improved clock error prediction model combined with the characteristics of GPS and GNSS on-board atomic clock is proposed by Huang et al. [7, 8]. The improved model adds several items to absorb the period effects and determine observation weights using Time Adaptive Function. Meanwhile, a constant correction method is proposed to eliminate and weaken the initial deviation of the prediction sequence. The prediction precision of 6, 12, and 24 h compared to IGU-P solutions increased by 32.9, 26.1, and 17.4 %, respectively. GPS satellite clock error prediction based on least squares and AR model is performed by Xu et al. [9]. The average prediction precision for 12 h is 1 ns. There are orders of magnitude difference between the prediction part and ultra-rapid observation production, which is the constraint of applying to real-time precise point positioning.

In recent years, IGS has started to provide real-time data streams. It can be achieved to calculate real-time satellite clock based on prediction orbit. But there are still some limitations in precision and reliability due to the quality of real-time data streams, tropospheric effects, and other factors. So, high-precision short-term satellite clock error prediction is an effective way to solve the problem of real-time clock service.

Therefore, based on analysis center of iGMAS, variation of different types of satellite clock error is analyzed in this paper. And the feasibility of Polynomial and Periodic model is used in satellite clock error prediction. In-depth study of the ARIMA model prediction method is performed in order to promote the satellite clock error prediction precision of different systems.

2 Periodic Characteristic Analysis of Satellite Clock Error

Quadratic polynomial model is the most commonly used prediction and fitting model to research satellite clock. Polynomial coefficients reflect atomic clock error, clock speed, and clock drift, respectively. In addition, there are also some different items of period for different types of satellite clock error.

2.1 Clock Error Periodic Characteristic of GPS

Using IGS, final clock products released to analyze the periodic characteristic of GPS, and the interval is 30 s. First of all, extracting the quadratic fit residuals is needed. The quadratic fit residuals sequence of G01 and G16 in August 2015 are given in Fig. 1, and there is significant periodic characteristic. So the periodic terms need be considered in the prediction model.

The frequency should be known when fitting periodic terms. The spectral analysis can accurately capture frequency and obtain well results. Amplitude

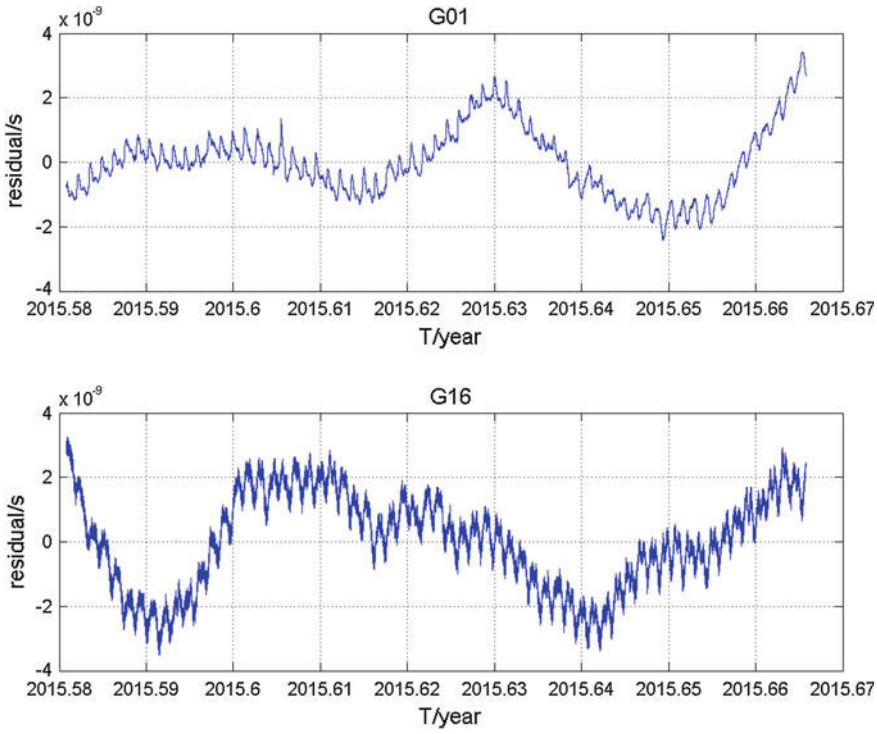

Fig. 1 Quadratic fit residuals sequence of G01 and G16

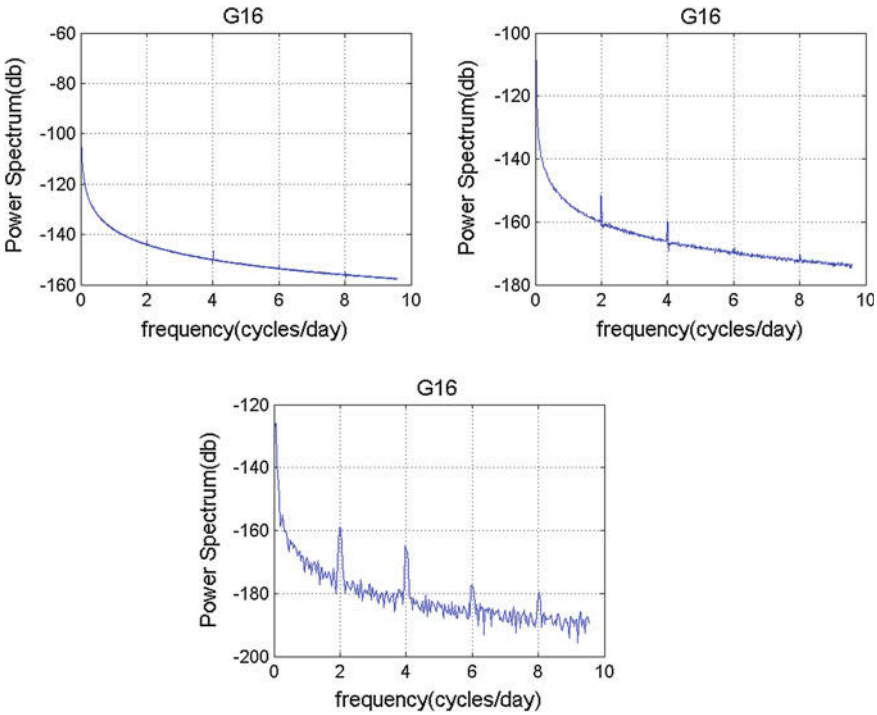

Fig. 2 Amplitude spectrum of different sequences for G16

spectrum of G16 is shown in Fig. 2, and they are the results of 12 months, 3 months, 1 month, respectively. There are stronger power spectrum when the frequency are 2, 4, 6, and 8 cycles/day, corresponding the cycles of 12, 6, 4, 3 h, respectively. The same result can be got through the analysis of all GPS satellite clocks. As is shown in Fig. 2. The shorter the time period, the more obvious the periodic characteristics is. It's caused that the fitting accuracy grow worse over time, and it will impact on capturing the frequency when fitting errors get to a certain extent.

In addition, Reid et al. [4, 10] found that the satellite clock cycle was related to the affection of season, half-year, day, half-day, and other changes by spectral analysis in 2000. Larger cycles have little effect on the results of short-term prediction, so the large cycles are not studied in this paper, only analysis cycles less than one day is analyzed.

Figure 3 presents the amplitude spectrum of four different types of satellite clocks in August 2015, they are G01 (Block IIF Rb), G16 (Block IIR Rb), G31 (Block IIR-M Rb), and G32 (Block IIA Rb), respectively. G32 only has stronger power spectrum when the frequency is two cycles/day (G32 is the only type

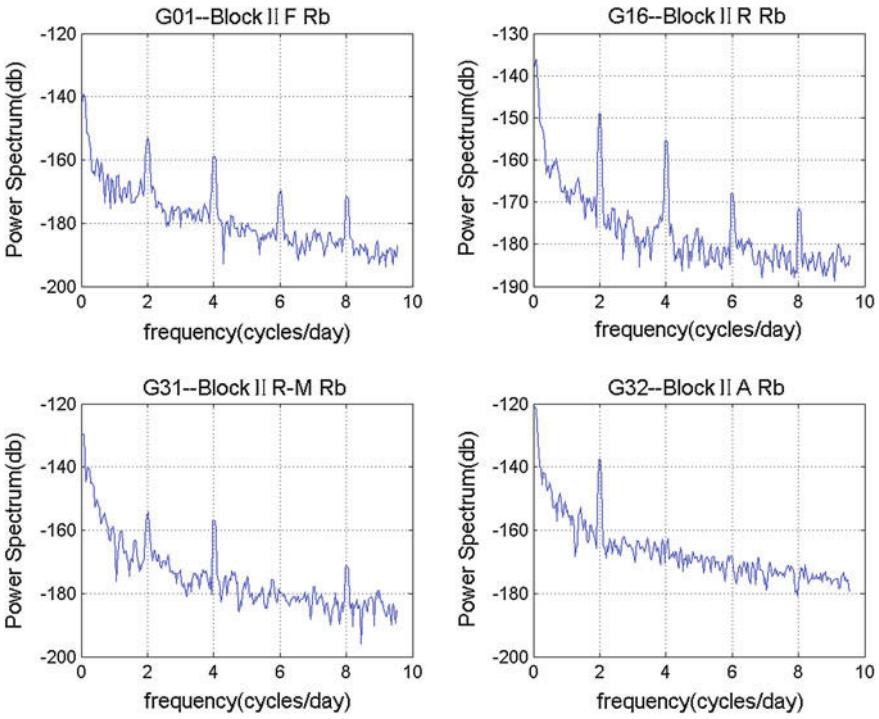

Fig. 3 Amplitude spectrum of G01, G16, G31, G32

Block IIA of GPS at that time), the remaining three types all have stronger power spectrum when the frequency are 2, 4, 6, and eight cycles/day. These indicate that the different types of satellite of GPS have similar characteristics with cycles of 12, 6, 4, and 3 h. The most significant cycle is 12 h, which is approximately equal to the satellite orbit cycle. All the peaks can be understood as harmonics of a fundamental signal [5].

2.2 Clock Error Periodic Characteristic of BDS

Compared with GPS atomic clocks, our BDS on-board atomic clocks still have a long way to go. Meanwhile, there are particularities of its own. Relatively mature research methods and models of GPS may not suitable for domestic rubidium clocks [10].

Here, we analyze the periodic clock error characteristic of BDS using the final products of iGMAS, and choose the date 499th week of BDS (July 26,

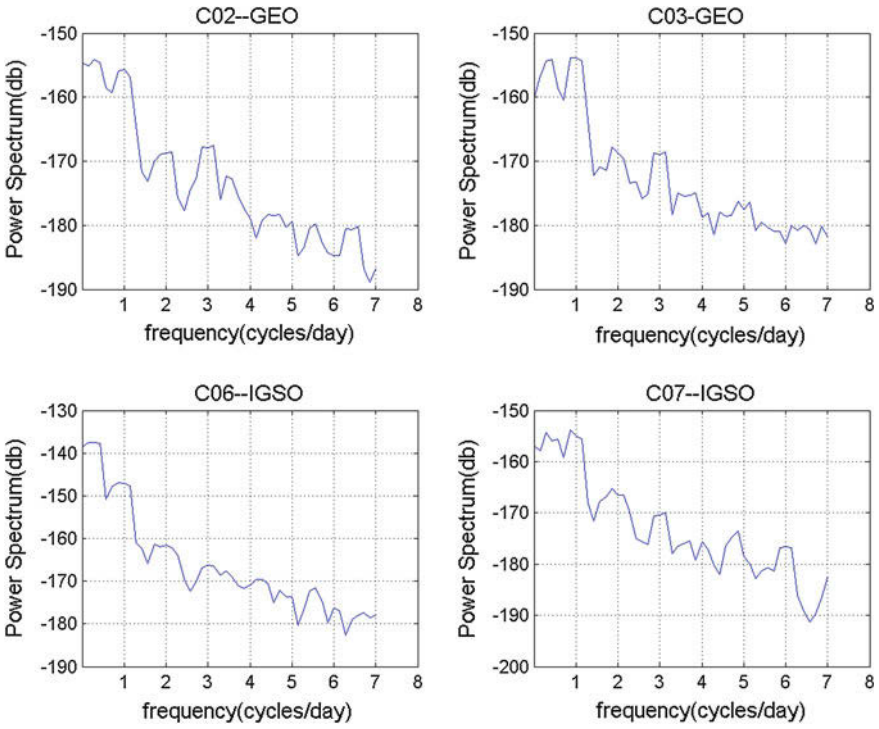

Fig. 4 Amplitude spectrum of GEO satellites and IGSO satellites

2015–August 1, 2015). Figure 4 presents the amplitude spectrum of two different types of BDS satellite clocks. The above two figures are the results of GEO satellites, the following two figures are the results of IGSO satellites. It can be shown that the noise of BDS satellite clock error is relatively large which affects the spectrum analysis comparing with GPS. But the frequency with 1 cycle/day, 2, 3 and 8 cycles/day can be found, which is corresponded to the cycles of 24, 12, and 8 h, respectively. The same conclusion can be obtained after analyzing results of different satellites and dates.

GEO and IGSO satellite clock error has a significant cycle of 1 day compared with the cycles of GPS. The cycle of 24 h is approximately equal to the GEO satellites and IGSO satellites orbital cycle of 24 h, and the conclusion that clock error cycle is approximately equal to the satellite orbital cycle is further confirmed.

Figure 5 shows the amplitude spectrum of MEO satellites. They all have a significant cycle that is larger than 12 h (The frequency is slightly smaller than 2 cycles/day). This is consistent with the MEO satellites orbital cycle of about 12.9 h.

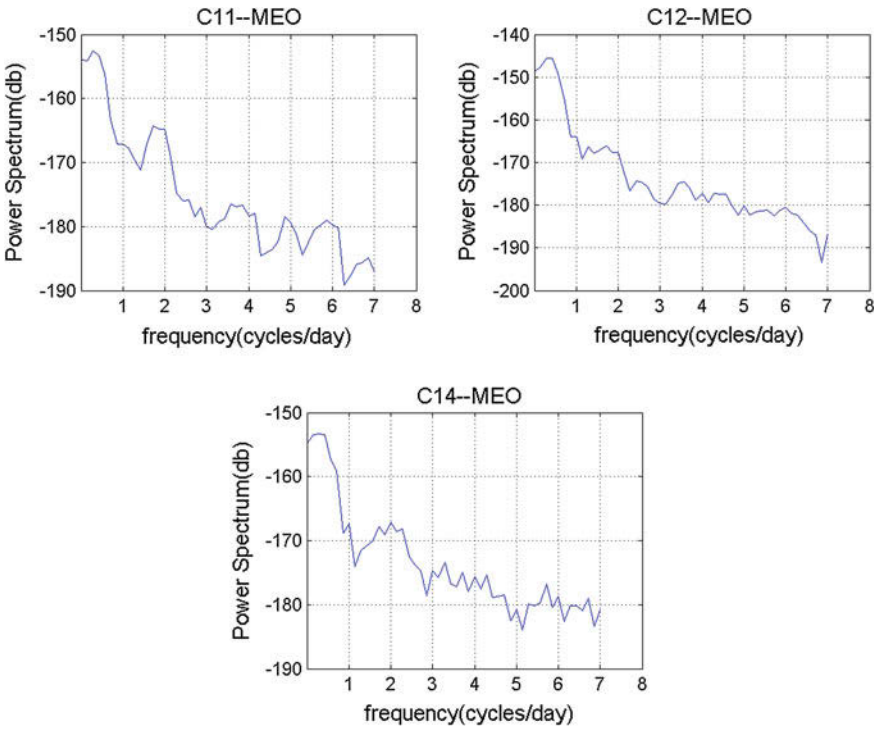

Fig. 5 Amplitude spectrum of MEO satellites

During the operating cycle of satellite, the external factors like thermal and insolation are changing constantly. The temperature change will cause change of the output frequency of the signal produced by atomic clocks, and is the main factor affecting the stability of the satellite clock. Therefore, considering the periodic characteristics of the satellite clock error is due to the physical characteristics of satellite clocks. Senir et al. [5] found that the satellite clock cycle has significant differences during the eclipse. And postulate that on-board clocks are affected by the thermal environment.

In addition, the Cs clocks are more strongly affected than the Rb clocks, whose thermal environment is tightly controlled. And from previous studies, we can see that the periodic characteristic of Cs clocks is more obvious than Rb clocks, which further supports the above results [5].

3 Prediction of Satellite Clock Error

Using polynomial model with periodic terms and ARIMA model to forecast clock error of GPS and BDS combined with the above cyclical characteristics of GNSS.

3.1 Prediction Principle

3.1.1 Polynomial Model with Periodic Items

With the increase of the order, the fitting accuracy is improved after compared with the order of 1, 2, 3, and 4, but the improvement is not obvious. So, selecting the second-order clock error prediction polynomial with the principles of order as low as possible and accordance with the physical characteristics of the satellite clocks [11].

Forecasting model with periodic terms is based on quadratic polynomial. The prediction model is as follows after the analysis of different types of satellite clocks.

$$\Delta t = a_0 + a_1 t + a_2 t^2 + \sum_{m=1}^{n} \left(A_m \sin(\omega_m t) + B_m \cos(\omega_m t)\right) + v \tag{1}$$

Where Δt is the clock error at t, the first three items are the quadratic polynomials. a_0, a_1, a_2 is clock error, clock speed, and clock drift rate, respectively, the fourth is the periodic item, n depends on the number of cycles, and v is the prediction residual.

After the analysis of each satellite clock periodic characteristics, GPS satellite clock error prediction model uses the periodic items of 12, 6, 4, and 3 h. GEO and IGSO satellite clock error prediction models use the periodic items of 24, 12, 8, and 3 h. MEO satellite clock error prediction model uses the periodic items of 12.9 h.

3.1.2 Modified ARIMA Model

ARIMA (p, d, q) model is as follows:

$$\begin{aligned} x_t = {} & \varphi_1 x_{t-1} + \cdots + \varphi_{\mathrm{p}} x_{t-\mathrm{p}} \\ & + a_t - \theta_t a_{t-1} - \cdots - \theta_{\mathrm{q}} a_{t-\mathrm{q}} \end{aligned} \tag{2}$$

where φ_i are parameters of autoregressive model, θ_i are moving average model parameters, x_i are clock error sequence, p/q are orders of autoregressive and moving average model, respectively, d is differential order. ARIMA model prediction precision depends mainly on two aspects: one is preprocessing, to improve the prediction accuracy we need to eliminate the outliers of satellite clock, and to adopt a reasonable method to sequence the clock difference, so that it becomes a continuous and stable random sequence. The other is the selection of p and q the fitting formula is as follows:

$$x(i) = \sum_{j=0}^{m_p} a_j t(i) \wedge j + \sum_{k=m_p+1}^{m} (b_k \cos(\pi * (k - m_p) * t(i)/n) + c_k \sin(\pi * (k - m_p) * t(i)/n)) \quad (3)$$

Where x is clock error, t is time, a is polynomial coefficients, b and c are triangular series coefficients, m_p is the order of the polynomial, which is set as 2 in the next, m is the total number of polynomial and triangular series coefficients, x is the number of clock error.

3.2 Selecting the Length of the Samples

The final IGS products for August 2015 are used for short-term prediction of 27 GPS satellites, and the interval is 30 s. The clock error from August 4 to August 31 is predicted. The final iGMAS products for the 499th BDS week are used for short-term prediction of BDS satellites, and the interval is 300 s. The clock error from the fourth day to the seventh day of the week is predicted. The polynomial model with periodic items described in 3.1 is used to predict the clock error. The following three solutions are employed to forecast the clock error:

Solution 1: Choosing 3 days of clock error sequence to forecast clock error of 24 h.
Solution 2: Choosing 2 days of clock error sequence to forecast clock error of 24 h.
Solution 3: Choosing 1 day of clock error sequence to forecast clock error of 24 h.

Table 1 shows the GPS statistical results, two columns correspond to the probability that 1 day is better than 2 days and the probability that 1 day is better than 3 days, respectively. The proportion that 1 day results is better than 2 days results is about 70 %, and the proportion that 1 day results is better than 3 days results is about 75 %. The proportion reduced gradually with the growth of

Table 1 Comparison of GPS clock error prediction results that using different lengths of sequences

Sequence hour	1–2 days (%)	1–3 days (%)
1	69.60	77.90
2	68.50	74.20
3	67.60	74.50
4	68.10	75.10
5	68.80	74.60
6	69.00	73.70
12	69.20	74.90
24	66.10	71.40

Table 2 Comparison of BDS clock error prediction results that using different lengths of sequences

Sequence hour	1–2 days (%)	1–3 days (%)
1	65.00	85.00
2	71.00	83.00
3	75.00	85.00
4	73.00	87.00
5	65.00	81.00
6	63.00	81.00
12	67.00	75.00
24	73.00	77.00

prediction time. Therefore it can be concluded that 1 day sequence is better than using longer sequences. It is suitable for GPS clock error short-term prediction within 1 day to use 1 day clock sequence, which can be used in the next parts.

Table 2 presents the BDS statistical results. The proportion that 1 day results is better than 2 days results is about 70 %, and the proportion that 1 day results is better than 3 days results is about 80 %. Therefore it can be concluded that 1 day sequence is better than using longer sequences. It is suitable for BDS clock error short-term prediction within 1 day to use 1 day clock sequence, which can be used in the next parts.

4 Example Analysis

Using polynomial model with periodic items and modified ARIMA model to predict clock error of GPS and BDS. The RMS of the prediction error is used as the forecast result.

4.1 Clock Error Prediction of GPS

Polynomial model with periodic items and modified ARIMA model are used to predict the GPS clock error. The sample sequence is chose as the final clock error products of IGS with 30 s sample interval. The sample session is August 2015. It is needed to assess the prediction precision in accordance with the type of statistics, because there are significant differences between different types of satellite clocks. Table 4 is the average results of all types of clock, and Table 5 gives the results with one clock in each type using modified ARIMA model. Table 3 shows the correspondence of satellites and clock types. The satellite of G04, G08, and G10 are changing at that time. G11 and G19 missed the sequence of August 13 and August 25, respectively, so there is no sequence to be predicted. Analyzing the result shown in Tables 4 and 5 can get the following conclusion: prediction precision of

Table 3 Chart of GPS satellite and corresponding clock types in August 2015

Satellite type	Clock	PRN
BLOCKIIA	Rb	32
BLOCKIIR	Rb	2, 11, 13, 14, 16, 18, 19, 20, 21, 22, 23, 28
BLOCKIIR-M	Rb	5, 7, 12, 15, 17, 29, 31
BLOCKIIF	Rb	1, 3, 6, 9, 25, 26, 27, 30
	Cs	24

Table 4 Prediction results of different types of GPS atomic clocks in August 2015/ns

Type hour	BLOCKIIA (Rb)		BLOCKIIR (Rb)		BLOCKIIR-M (Rb)		BLOCKIIF (Rb)		BLOCKIIF (Cs)	
	1	2	1	2	1	2	1	2	1	2
1	0.609	0.479	0.456	0.221	0.377	0.218	0.28	0.139	2.256	0.635
2	0.722	1.114	0.553	0.323	0.45	0.324	0.391	0.255	2.942	1.287
3	0.773	1.55	0.614	0.395	0.488	0.455	0.488	0.35	3.284	1.786
4	0.902	1.65	0.701	0.456	0.538	0.56	0.586	0.422	3.868	2.124
5	0.997	1.401	0.771	0.531	0.578	0.594	0.691	0.462	4.155	2.484
6	1.082	1.082	0.831	0.624	0.612	0.581	0.791	0.489	4.435	3.027
12	1.496	1.419	1.252	1.084	0.888	0.693	1.419	1.103	5.738	4.88
24	2.491	2.388	2.135	2.163	1.568	1.408	3.188	2.94	9.02	7.903

1 is the prediction result using polynomial model with periodic items, 2 is the prediction result using ARIMA model

Table 5 Prediction results of different types of GPS atomic clocks using ARIMA model, only one of each type of satellite is listed/ns

PRN hour	G32	G02	G15	G25	G24
1	0.479	0.162	0.183	0.075	0.635
2	1.114	0.221	0.271	0.118	1.287
3	1.550	0.250	0.319	0.174	1.786
4	1.650	0.266	0.294	0.266	2.124
5	1.401	0.260	0.277	0.296	2.484
6	1.082	0.254	0.259	0.209	3.027
12	1.419	0.558	0.363	0.361	4.880
24	2.388	1.058	0.644	0.809	7.903

BLOCKIIF Rb is the best, precision of BLOCKIIR-M Rb, BLOCKIIR Rb, and BLOCKIIA Rb followed, precision of BLOCKIIF Cs and BLOCKIIA Cs is the worst. Using modified ARIMA model, the prediction precision of most Rubidium in sixth hour is better than 0.6 ns. The result of the first hour improves about 50 % compared to the result of the sixth hour prediction, and the precision is better than 0.25 ns.

4.2 Clock Error Prediction of BDS

Polynomial model with periodic items and modified ARIMA model are used to predict the BDS clock error which includes GEO, IGSO, and MEO satellites. The sample sequence is chose as the final clock error products of iGMAS with 300 s sample interval. The sample session is 499th week of BDS. C04 is not analyzed because of phase jump. The statistics result of MEO satellites uses C11 and C12 (The result of C14 has a large difference). Table 7 is the average results of all types of clock, and Table 8 presents the results with one clock in each type using modified ARIMA model. Table 6 shows the correspondence of satellites and clock types. By analyzing the results, we can obtain the following conclusions: the prediction precision in sixth hour is better than 2 ns. The result of first hour improves about 30 % compared to the result of the sixth hour.

Table 6 Chart of BDS satellite and corresponding clock types in August 2015

Satellite type	Clock	PRN
GEO	Rb	1, 2, 3, 4, 5
IGSO	Rb	6, 7, 8, 9, 10
MEO	Rb	11, 12, 13, 14

Table 7 Prediction results of different types of BDS satellites in August 2015/ns (1 is the prediction result using polynomial model with periodic items, 2 is the prediction result using ARIMA model)

Type hour	GEO		IGSO		MEO	
	1	2	1	2	1	2
1	1.395	1.413	1.047	1.086	1.174	1.053
2	1.167	1.307	1.122	1.051	1.223	1.102
3	1.169	1.422	1.28	1.233	1.255	1.169
4	1.318	1.556	1.4	1.456	1.347	1.26
5	1.663	1.78	1.654	1.685	1.436	1.374
6	2.088	1.975	1.925	1.874	1.541	1.424
12	3.992	3.54	4.554	4.085	2.223	1.988
24	8.327	9.087	7.11	7.834	4.496	4.754

Table 8 Prediction results of C02 C07 and C12/ns

PRN hour	C02	C07	C12
1	1.170	1.030	1.008
2	1.059	0.831	0.936
3	1.191	0.771	0.971
4	1.317	0.715	0.965
5	1.443	0.747	1.012
6	1.544	1.003	1.017
12	1.784	3.023	2.006
24	7.151	4.156	5.626

5 Conclusion

Periodic characteristic of GPS and BDS are analyzed using spectrum analysis. Based on the periodic characteristic, polynomial model with periodic items and modified ARIMA model are used to predict the clock error of GPS and BDS. The conclusions are as follows:

1. The clock error of GPS mainly has four cycles with 12, 6, 4, and 3 h respectively. The cycle of 12 h is the most significant. The clock error sequence of GEO and IGSO has three relatively obvious cycles, with 24, 12, and 8 h, respectively. The cycle of 24 h is the most significant. The clock error of MEO has an obvious cycle of about 12.9 h. The significant cycles are approximately equal to the satellite orbit cycles.
2. Using the sequences of different length to forecast the clock error of GPS and BDS, and the conclusion can be obtained that it is suitable for clock error short-term prediction within one day to use one-day clock sequence.
3. For GPS, the prediction results of using modified ARIMA model is relatively better than that using polynomial model with periodic items. For BDS, the GEO satellites prediction results of using polynomial model with periodic items is better; the MEO satellites prediction results of using modified ARIMA model is better; the IGSO satellites prediction results of using the two methods are close. The results of using polynomial model with periodic items is better to predict the clock error of the coming twenty-fourth hour.

Acknowledgments This study is funded by the National Natural Science Fund (No. 11273048). The IGS is acknowledged for providing the final GPS clock error products. The iGMAS is acknowledged for providing final BDS clock error products.

References

1. Hofmann-Wellenhof B, Lichtenegger H, Wasle E (2008) GNSS-global navigation satellite systems: GPS, GLONASS, Galileo, and more. Springer Wien New York
2. Yang YX, Li JL, Xu JY et al (2011) Contribute of the Compass satellite navigation system to global PNT users. Chinese Sci Bull 56. doi:10.1007/s11434-011-4627-4
3. Gao Y, Chen K (2005) Performance analysis of precise point positioning using rea-time orbit and clock products. J Glob Positioning Syst 3:95–100
4. Reid W, Meeaskill T, Largay M, Oakso J, Buisson J (2000) Performance of GPS Block IIR Rubidium clocks. IONGPS 2000, Salt Lake City, UT 19–22 Sept 2000
5. Senir KL, Ray JR, Beard RL (2008) Characterization of periodic variations in the GPS satellite clocks. GPS Solut. doi:10.1007/s10291-008-0089-9
6. Youn JH, Jeongho C, Moon BH (2010) Improving prediction accuracy of GPS satellite clocks with periodic variation behavior. Meas Sci Technol 21:1–8
7. Huang G, Zhang Q, Li H, Fu W (2012) Research on quality variation of GPS satellite clocks on-orbit using IGS clock products. Adv Space Res. doi:10.1016/j.asr.2012.09.041

8. Huang G, Zhang Q, Xu G (2014) Real-time clock offset prediction with an improved model. GPS Solut 18:95–104
9. Xu X, Hu X, Zhou Y, Song Y (2014) Research on high accuracy prediction model of satellite clock bias. The 5th China Satellite Navigation Conference, vol 5
10. Fu W (2012) Research on prediction and characteristics of GNSS satellite clock on orbit. Chang'an University
11. Hauschild A, Montenbruck O, Steigenberger P (2013) Short-term analysis of GNSS clocks. GPS Solution. doi:10.1007/s10291-012-0278-4
12. Huang G, Yang Y, Zhang Q (2011) Estimate and predict satellite clock error using adaptively robust sequential adjustment with classified adaptive factors based on opening windows. Acta Geodaetica Cartogr Sin 40:15–21
13. Xu J, Fu S (2001) The application of spectral analysis in curve fit. J Geomatics 3:20–22
14. http://acc.igs.org/igsacc_ultra.html
15. IGS http://www.igs.org/rts/products

A Simple Differencing Technology to Improve Prediction Accuracy of Earth Rotation Parameters

Yu Lei, Hongbing Cai and Danning Zhao

Abstract Considering the time-varying characteristics of Earth rotation parameters (ERP) time-series, we attempted to improve the prediction accuracy of ERP using a simple differencing technique. ERP data are first differenced between adjacent epochs. Subsequently the predictions of differenced ERP are generate by means of the combination of (1) least squares (LS) extrapolation of models for Chandler, annual and semi-annual wobbles and for the linear trend, and (2) autoregressive moving average (ARMA) stochastic prediction of LS residuals (LS + ARMA). The results show that the accuracy of predictions is better than that by the conventional method, especially for short- and long-term predictions. Moreover, the significant enhancement can be found in the case of the UT1-UTC predictions in comparison with the prediction of pole coordinates.

Keywords Earth rotation parameters (ERP) · Autoregressive moving average (ARMA) model · Prediction model · Differencing

1 Introduction

The near real-time estimates and forecasts of Earth rotation Parameters (ERP): polar motion (PM), universal time (UT1-UTC) or its first derivative, length of day (LOD), are needed in various fields linked to reference systems such as precise orbit determinations of artificial Earth satellites, space navigation, time-keeping and positional astronomy [1]. ERP predictions enable the real-time transformation between the International Celestial and Terrestrial Reference Frames (ICRF and ITRF). Regularly generated ERP predictions are provided by several international

Y. Lei (✉) · H. Cai · D. Zhao
National Time Service Center, Chinese Academy of Sciences, Xi'an 710600, China
e-mail: leiyu@ntsc.ac.cn

Y. Lei · D. Zhao
University of Chinese Academy of Sciences, Beijing 100039, China

© Springer Science+Business Media Singapore 2016

J. Sun et al. (eds.), *China Satellite Navigation Conference (CSNC) 2016 Proceedings: Volume III*, Lecture Notes in Electrical Engineering 390,
DOI 10.1007/978-981-10-0940-2_18

and national services, e.g., the International Earth Rotation and Reference Systems Service (IERS), or the ERP Service of the Institute for Applied Astronomy (IAA) in Saint Petersburg, Russia.

Different prediction techniques combing the least squares (LS) extrapolation with autoregressive, autoregressive moving average (ARMA) and neural network (NN) predictions were used to forecast ERP [2–6]. The LS extrapolation is employed to extrapolate the linear trend and periodic terms, while the stochastic methods, e.g., AR, ARMA and NN, are actually applied to the residuals after removing a polynomial-sinusoidal curve used for LS extrapolation. Hereafter, the combination of LS extrapolation and a stochastic method is denoted as LS + stochastic. Generally speaking, the LS + stochastic methodologies does not take the non-stationarity of ERP time-series into account. As a result, it is impossible to enhance the prediction quality of ERP using the conventional LS + stochastic methods. In this work, a new LS + stochastic method based on a simple differencing technique is proposed to improve the prediction accuracy of ERP. The new prediction algorithm first makes a one-order difference between adjacent ERP, and then the differenced ERP series are fitted by a LS model. Secondly, an ARMA mode is applied to the LS fitting residuals. Finally, the predicted residual is added to the LS extrapolation, and then this differenced prediction is accumulated to yield the ERP prediction. The results have shown that the proposed prediction algorithm outperforms the conventional LS + stochastic methodologies.

2 Methodology

2.1 De-Trending ERP Time-Series

Observed ERP time-series are always non-stationary, since the variations of Earth rotation is time-varying. Considering the time-varying characteristic of ERP time-series, we utilized a simple differencing technique to make stationarity of ERP series. Suppose that $\boldsymbol{X} = \{x_t, t = 1, 2, \ldots, n\}$ is observed ERP series, a new series $\Delta \boldsymbol{X} = \{\Delta x_t, t = 2, 3, \ldots, n\}$ can be obtained by differencing adjacent ERP values as follows.

$$\Delta x_t = x_t - x_{t-1}, \quad t = 2, 3, \ldots, n \tag{1}$$

Unlike to the conventional LS + stochastic mythologies that are directly to applied to observed ERP series, the new proposed prediction algorithm first de-trend original ERP data using the above differencing scheme, and then uses the LS + stochastic approaches to the differenced series. Finally, the predicted ERP can be obtained using the following formula.

$$\hat{x}_t = x_n + \sum_{k=n+1}^{t} \Delta\hat{x}_k, \quad n+1 \le t \le n+m \tag{2}$$

where $\Delta\hat{\boldsymbol{X}} = \{\Delta\hat{x}_t, t = n+1, n+2, \ldots, n+m\}$ is the forecasted series of differenced series $\Delta\boldsymbol{X}$, and $\hat{\boldsymbol{X}} = \{\hat{x}_t, t = n+1, n+2, \ldots, n+m\}$ is the predicted ERP series.

2.2 LS + ARMA Model

2.2.1 LS Model

As the data intervals are all one day, we use the polynomial-sinusoidal curve for LS fitting, i.e., for approximation the observed series using LS fitting, and then for extrapolation of the deterministic components of ERP time-series.

$$f_{x_t} = a + bt + \sum_{i=1}^{2} c_i \cos(2\pi t/p_i) + d_i \sin(2\pi t/p_i) \tag{3}$$

where a, b, c_i and d_i have to be estimated, $p_1 = 182.62$ and $p_2 = 365.24$ for UT1-UTC, and $p_1 = 365.24$ and $p_2 = 432.08$ for PM.

This model is applied to generate residuals using equation $z_t = x_t - f_{x_t}$ for all t employed to fit the LS model. Subsequently, extrapolation of the above-mentioned model f_{x_t} is used to compute the deterministic prediction of ERP data.

2.2.2 ARMA Model

The univariate component of the residual stationary time-series $\boldsymbol{Z} = \{z_t, t = 1, 2, \ldots, n\}$ may be modeled by the ARMA model with order p and q, denoted as ARMA (p, q). The technique allows one to capture the temporal dependence within $\boldsymbol{Z}$ [7]. A stationary, zero-mean stochastic process (in our case $\boldsymbol{Z}$) is said to be an ARMA (p, q) if it satisfies

$$z_t = \sum_{i=1}^{p} \varphi_i z_{t-i} + \sum_{i=1}^{q} \theta_i \varepsilon_{t-i} + \varepsilon_t \tag{4}$$

where $\varphi_1, \varphi_2, \ldots, \varphi_p$ are the AR coefficients, and $\theta_1, \theta_2, \ldots, \theta_q$ are the moving average (MA) coefficients.

The type of an ARMA model can be identified according to the auto- and partial-correlation functions (ACF and PCF), which are written as belows.

Table 1 Criterion for the ARMA identification

Type	AR (p)	MA (q)	ARMA (p, q)
ACF	Trailing	Truncation	Trailing
PCF	Truncation	Trailing	Trailing

$$\rho_k = \frac{\sum_{t=k+1}^{n}(z_t - \bar{z})(z_{t-k} - \bar{z})}{\sum_{t=1}^{n}(z_t - \bar{z})} \tag{5}$$

$$\begin{cases} \phi_{k,k} = \rho_1 & k = 1 \\ \phi_{k,k} = \frac{\rho_k - \sum_{i=1}^{k-1}\phi_{k-1,i}\rho_{k-i}}{1 - \sum_{i=1}^{k-1}\phi_{k-1,i}\rho_i} & k \geq 2 \end{cases} \tag{6}$$

where $\bar{z} = \frac{1}{n}\sum_{i=1}^{n} z_t$, and $\phi_{k,i} = \phi_{k-1,i} - \phi_{k,k}\phi_{k-1,i-i}$.

The criterion for the ARMA identification is listed in Table 1.

The order p and q can be selected by the Akaike information criterion (AIC). The AIC for an ARMA (p, q) is based on the following statistics.

$$AIC(p,q) = \mathrm{In}\,\sigma^2_{p,q} + \frac{2(p+q)}{n} \tag{7}$$

where σ^2 is an estimate of a variance. One selects p and q which minimize the AIC statistics. ARMA models in general can, after choosing p and q, be fitted by LS regression to find the values of the parameters which minimize the error term. There are several approaches to estimate the ARMA coefficients. In this work, we apply the Yule-Walker procedure.

At last, we utilize the statistics Q to test whether the estimated ARMA model is suitable for time-series forecast. The statistics Q is written as

$$Q_k = [n - \max(p,q)]\sum_{i=1}^{k}\rho_i^2(\alpha) \tag{8}$$

where α is given significance level. when $Q_k \leq \chi^2_{k,\alpha}$, the ARMA model is appropriate. Herein, $\chi^2_{k,\alpha}$ can be found in the χ^2 distribution.

3 Experiment Results

In this contribution, ERP series with daily value from the IERS EOP C04 series are served as data base. Leap seconds are first removed from original UT1-UTC data. The effects of the solid Earth tides with periods from five days up to 18.6 years as well as the diurnal and semi-diurnal ocean tides are then also removed using the tidal models recommended in the IERS Conventions 2010 [8]. Next, UT1R-TAI

data are processed and modelled. At last, in order to obtain UT1-UTC forecasts, the UT1-UTC predictions must be corrected for leap seconds together with tides. However, leap second adjustments and tidal models do not contribute to UT1-UTC prediction error.

3.1 Analysis of Residual Stationarity

In order to validate whether the differencing technique can de-trend the original ERP, two experiments have be carried out.

Case 1: The observed is directly fitted by the LS model, and then the model f_{x_t} is applied to derive the residuals as $z_t = x_t - f_{x_t}$.

Case 2: The original ERP data are first differenced, and then the differenced series are approximated by the LS model. Finally, the residuals are derived from $z_t = \Delta x_t - f_{\Delta x_t}$.

The UT1R-TAI, PMX, LS fitting and residuals series without differencing are given in Figs. 1 and 2, herein the data intervals are from Jan 1, 1990 to Dec 12, 2009. The corresponding series with differencing are given in Figs. 3 and 4. As can be seen in Figs. 1, 2, 3, and 4, the residua series without differencing is non-stationary, while the residuals become stationary after differencing. In order to analysis the characteristics of residual series, Figs. 5 and 6 depict the residual ACF and PCF without and with differencing, respectively. In Figs. 5 and 6 it can be seen that the residuals conform with an AR model since the ACF and PCF are trailing

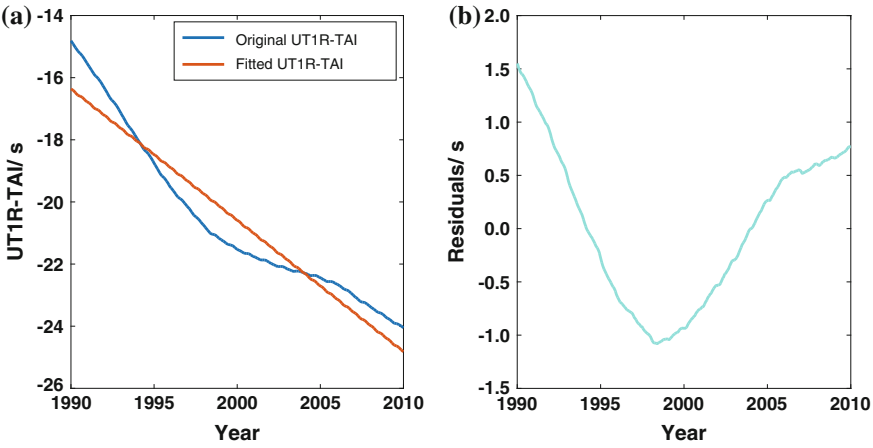

Fig. 1 Original UT1R-TAI, LS fitting series and derived residuals. **a** UT1R-IAI without differencing. **b** LS fitting residuals without differencing

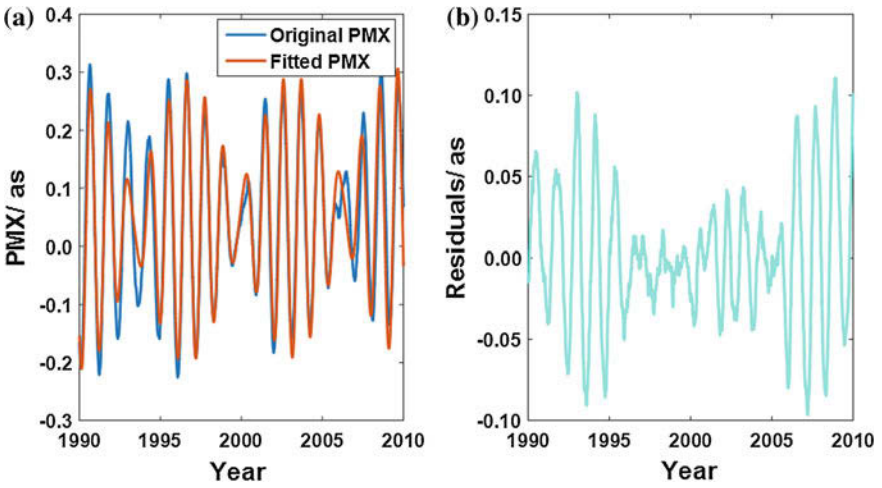

Fig. 2 Original PMX, LS fitting series and derived residuals. **a** PMX without differencing. **b** LS fitting residuals without differencing

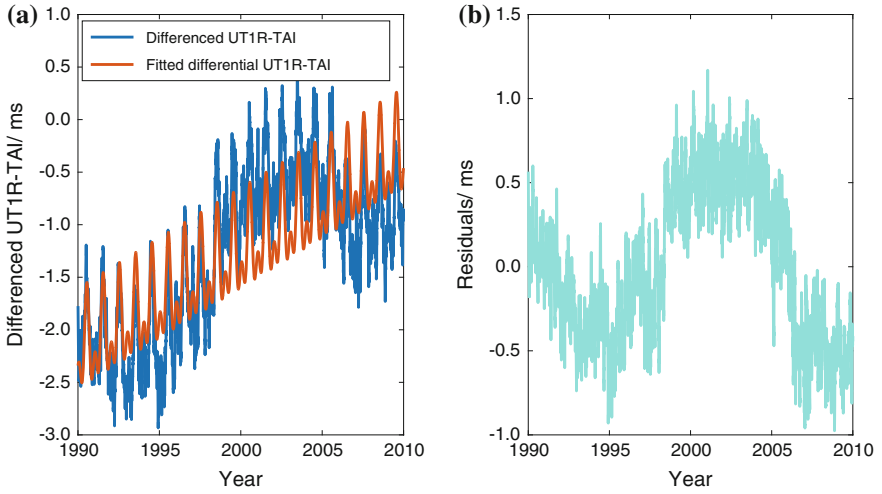

Fig. 3 Differenced UT1R-TAI, LS fitting series and derived residuals. **a** UT1R-IAI without differencing. **b** LS fitting residuals with differencing

and truncation, respectively. Moreover, the residuals after differencing are more matched with an AR model than those without differencing, showing that the former is more stationary. Note that only PMX is analyzed here because PMX and PMX have same property.

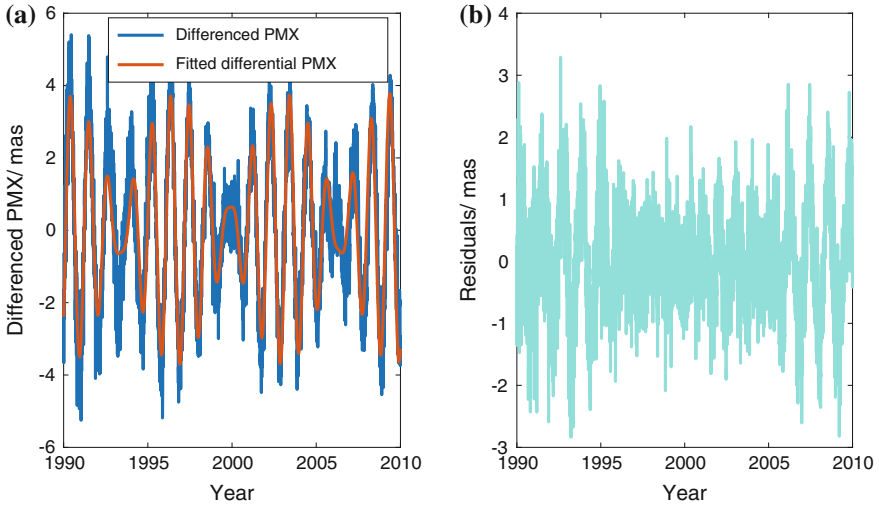

Fig. 4 Differenced PMX, LS fitting series and derived residuals. **a** PMX without differencing. **b** LS fitting residuals without differencing

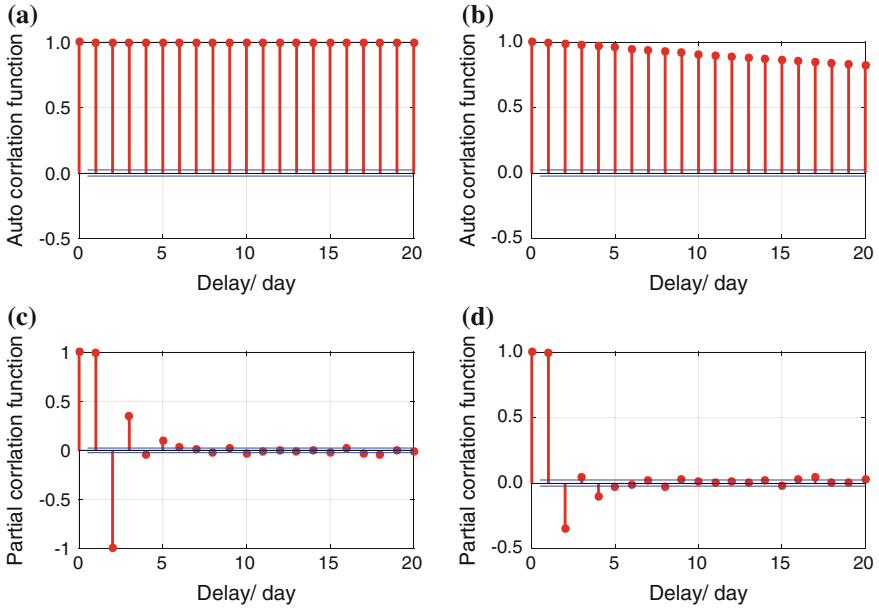

Fig. 5 Auto- and partial correlation function of UT1R-TAI residuals without and with differencing respectively. **a** ACF without differencing. **b** ACF with differencing. **c** PCF without differencing. **d** PCF with differencing

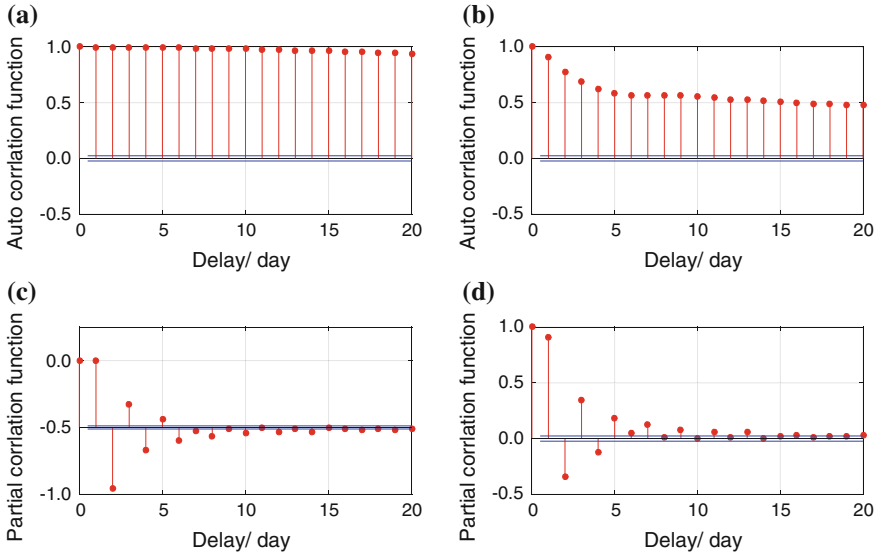

Fig. 6 Auto- and partial correlation function of PMX residuals without and with differencing respectively. **a** ACF without differencing. **b** ACF with differencing. **c** PCF without differencing. **d** PCF with differencing

3.2 Analysis of Prediction Accuracy

The ERP series between Jan 1, 1999 and Dec 31, 2009 are served as data basis for the predictions of 1–360 days in the future. The fitted ARMA model to residuals is used to these residuals using linear prediction operator. The predictions for steps in the future are calculated recursively. The subsequently predicted residuals are then added to the LS extrapolation model to yield the predicted values of ERP.

The root mean squares error (RMSE) of predictions by the LS + ARMA without and with differencing for UT1-UTC and pole coordinates is shown in Figs. 7 and 8.

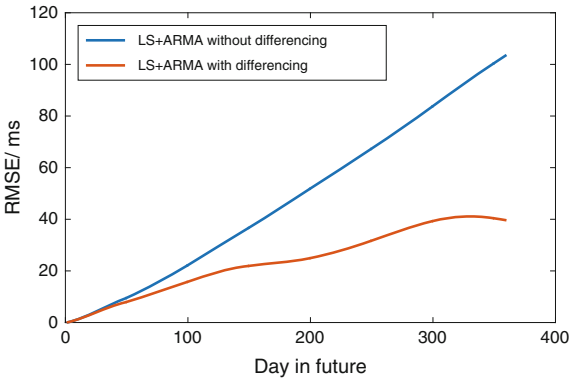

Fig. 7 RMSE comparison between the direct and differential techniques for UT1-UTC prediction

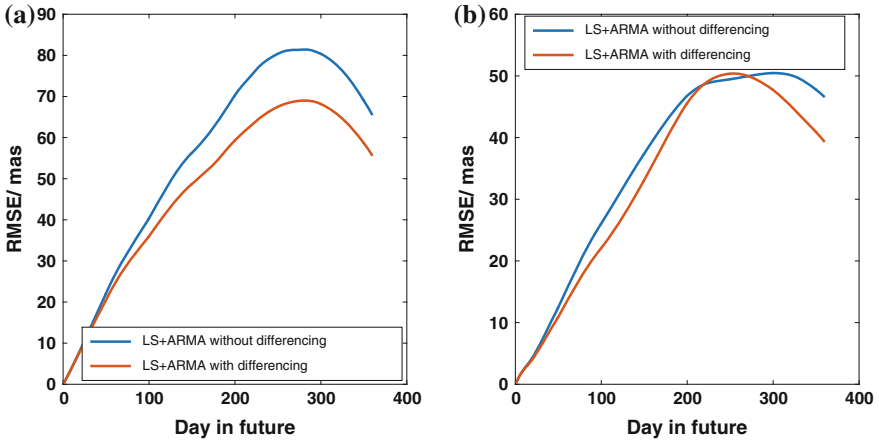

Fig. 8 RMSE comparison between the direct and differential techniques for PM prediction. **a** Prediction RMSE of PMX. **b** Prediction RMSE of PMY

The RMS for different prediction intervals is summarized in Table 2. The RMSE of the prediction day d is calculated by

$$RMSE_i = \sqrt{\frac{1}{N}\sum_{j=1}^{N}(P_j^d - O_j^d)^2} \tag{9}$$

Table 2 RMSE statistics of the direct and differential techniques for ERP prediction

Prediction days	UT1-UTC/ms		PMX/mas		PMY/mas	
	A	*B*	*A*	*B*	*A*	*B*
1	0.04	0.04	0.28	0.28	0.23	0.23
5	0.42	0.42	2.01	2.01	1.40	1.39
10	1.17	1.14	4.09	4.09	2.48	2.40
15	2.13	2.04	6.17	6.10	3.36	3.20
20	3.20	2.99	8.31	8.12	4.34	4.06
30	5.41	4.89	12.91	12.34	6.84	6.23
60	11.79	9.44	26.45	24.37	15.47	13.43
90	19.43	14.20	37.00	33.34	23.81	20.27
120	28.10	18.93	47.67	41.75	30.62	26.03
180	45.78	23.49	63.88	54.58	43.51	40.91
270	73.76	35.05	81.33	68.77	49.96	50.03
300	83.86	39.33	80.36	68.16	50.47	47.71
360	103.65	39.61	65.45	55.55	46.56	39.30

where P the predicted value of the prediction model for day d, O the real observed value of the IERS C04 series, and N the number of predictions made for the particular prediction day, i.e., $N = 300$.

What can be said with the information available from the Figs. 7, 8 and Table 2 is that the prediction accuracy of the 1–10 days prediction by the proposed prediction algorithm is comparable with that by the conventional method, while the former noticeably outperforms the latter beyond 10 days, especially for short- and long-term prediction. In addition, the prediction quality of UT1-UTC is more substantially enhanced when compared to that of pole coordinates, indicating that UT1-UTC data is high time-varying. Referring to the improvement quantification, the UT1-UTC prediction accuracy of 1–30 days and 1–360 prediction days is enhanced by 9.63 and 61.79 % by the developed method, respectively. For pole coordinates, the PMX prediction accuracy of 1–30 days and 1–360 prediction days is improved by 4.39 and 16.30 %, respectively, while 8.95 and 15.60 % for PMY, respectively.

4 Conclusion

ERP time-series can be predicted 360 days in advance with the enhanced accuracy using the combination of LS extrapolation and ARMA stochastic prediction with a simple differencing technology. In all cases analyzed, the extrapolation of the deterministic and stochastic model supported by the differencing strategy yield accurate prediction for all prediction lengths.

In case of the prediction of pole coordinates, the prediction accuracy of the proposed method is better than that of the conventional approach, but only slightly. In contrast, in case of the UT1-UTC prediction, the significant improvement of 360-day predictions (Fig. 7) can be found, claiming that the differencing strategy—even if the data is high time-varying, can be successfully used to enhance the prediction quality.

The differencing scheme seems to a good technique for ERP prediction. It can be hypothesized that the technique can be employed for prediction enhancement of other time-series, e.g., satellite clock bias.

References

1. Gambis D, Luzum B (2011) Earth rotation monitoring, UT1 determination and prediction. Metrologia 48:165–170
2. Niedzieiski T, Kosek W (2008) Prediction of UT1-UTC, LOD and AAM by combination of least-squares and multivariate stochastic methods. J Geodesy 82:83–92
3. Sun ZZ, Xu TH (2012) Prediction of Earth rotation parameters based on improved weighted least squares and autoregressive model. Geodesy and Geodynamics 3:57–64

4. Guo JY, Li YB, Dai CL et al (2013) A technique to improve the accuracy of Earth orientation prediction algorithms based on least squares extrapolation. J Geodyn 70:36–48
5. Lei Y, Zhao DN, Cai HB (2015) Prediction of length-of-day using extreme learning machine. Geodesy and Geodynamics 6:151–159
6. Xu XQ, Zhou YH (2015) EOP prediction using least square fitting and autoregressive filter over optimized data intervals. J Geodyn 56:2248–2253
7. George EPB, Gwilym MJ, Gregory CR (2008) Time series analysis: forecasting and control. Wiley, Hoboken
8. Gerard P, Brain L (2011) IERS Conventions (2010). Verlag des Bundesamts für Kartographie und Geodasie, Frankfurt am Main

The Accuracy Analysis of Autonomous Orbit Determination Based on Onboard Observation Data of Inter-Satellite Link

Jiachao Chang, Lin Shang and Guotong Li

Abstract Autonomous navigation technology of navigation satellite is the key technology of new-generation Beidou navigation system. There are a lot of researches on the autonomous navigation algorithm at home and abroad. But because of the limit of condition, the previous research work is based on the ground simulation data, which includes reference orbit, reference clock error, and inter-satellite pseudorange. The reference orbit data and reference clock error data generally are based on the GPS satellites, which cannot truly represent the characteristics of the orbit and the clock of Beidou satellite. In addition, all kinds of errors those are added to the two-way pseudorange are calculated based on the known error models, which cannot simulate the real space environment. First, this paper gives the accuracy of autonomous orbit determination which is calculated by onboard algorithm. Then the error of the autonomous navigation algorithm is analyzed accurately based on the onboard observation data and precise ephemeris. Finally, using the high accuracy error of system, run the autonomous navigation algorithm at ground and get more precise accuracy of autonomous orbit determination.

Keywords Autonomous navigation · Inter-satellite link · Simulation data · Onboard data · Accuracy of orbit determination

J. Chang (✉)
Student Department, Shanghai Institute of and Microsystem Information Technology, SIMIT, Shanghai, China
e-mail: changjiachao@whu.edu.cn

J. Chang · L. Shang · G. Li
Navigation Department, Shanghai Engineering Center for Microsatellites, SECM, Shanghai, China

G. Li
School of Information Science and Technology, ShanghaiTech University, Shanghai, China

© Springer Science+Business Media Singapore 2016

J. Sun et al. (eds.), *China Satellite Navigation Conference (CSNC) 2016 Proceedings: Volume III*, Lecture Notes in Electrical Engineering 390,
DOI 10.1007/978-981-10-0940-2_19

1 Introduction

At present, China is building the Beidou satellite navigation system. The autonomous navigation technology is a key technology in the design of Beidou satellite navigation system. This technology has great significance in shortening the updating cycle of satellite broadcast ephemeris and increasing the survivability of system [1, 2].

At home and abroad, because of the great significance of autonomous navigation technology, many scholars have researched the autonomous navigation algorithm in depth. There are two main research directions, one is celestial autonomous navigation technology, and the other one is constellation autonomous navigation technology. The constellation autonomous navigation technology includes two kinds of methods: those are centralized autonomous navigation technology and distributed autonomous navigation technology. Distributed autonomous navigation technology has become a hot research topic at home and abroad because of its high precision and low resource overhead.

Each satellite calculates its own position and clock error based on the position and clock error of the other satellites in Beidou system in the distributed autonomous navigation technology. Because of the limit of condition the previous research work is based on the ground simulation data, this has guiding significance to determining the autonomous navigation system and analyzing the accuracy of the autonomous navigation algorithm, but the ground simulation data has limitation. Generally, simulation data is based on the orbit and clock error of GPS satellites, but satellites of Beidou system have different orbit characteristics. The characteristic of clock error is related to the atomic clock strictly, so the clock error of GPS satellites cannot represent the characteristics of atomic clock of Beidou satellites. In addition, all kinds of errors those are added to the two-way pseudorange, such as troposphere error, ionosphere error, relative theory error, device zero range, and phase center correction error, are calculated based on the known error models, which cannot simulate the real space environment. Because of the above reason, the research based on simulation data cannot reflect the performance of the algorithm in the actual engineering completely.

At present, some satellites of Beidou system have worked onboard; they can get real inter-satellite two-way pseudorange, which provides the necessary conditions for onboard autonomous navigation test. In this paper, the results of onboard autonomous navigation test based on three ground stations are analyzed. In addition, based on the observation data of the same period, this paper analyzes the orbit determination accuracy of autonomous navigation algorithm on ground. At last, this paper discusses the main factors which affect the accuracy of the autonomous navigation algorithm by analyzing the onboard result and ground result, which has guiding significance for the further improvement of the algorithm.

2 Introduction of Autonomous Navigation Algorithm

Distributed autonomous navigation algorithm uses inter-satellite measurement two-way pseudorange to calculating its own position and clock error. The commonly used filter algorithms include Kalman filter algorithm, extended Kalman filter algorithm (EKF), unscented Kalman filter (UKF), particle filter (PF), and so on. Considering the performance of the algorithm and the limited calculation resources on the satellite, the EKF filtering algorithm is commonly used in the satellite navigation [1, 3, 4].

The extended Kalman filter is a kind of estimation method that based on the minimum mean square error (MMSE) criterion. This algorithm uses linear method to approximate the nonlinear function by expanding the equation at the estimation value of the state variation using the Taylor polynomial expansion method. Then the nonlinear filter problem is transformed into a linear filtering problem, so we can use conventional linear Kalman filtering method continually [5].

If a discrete time nonlinear state equation and the observation equation can be expressed in the following form

$$\mathbf{X}_k = f(\mathbf{X}_{k-1}) + \boldsymbol{\eta}_{k-1} \tag{1}$$

$$\mathbf{Z}_k = h(\mathbf{X}_k) + \mathbf{v}_k \tag{2}$$

where $\mathbf{X}$ is the state vector, $\mathbf{Z}$ is the observation vector, $f(\mathbf{X}_{k-1})$ is the nonlinear state equation, $h(\mathbf{X}_k)$ is the nonlinear observation equation, $\boldsymbol{\eta}$ is the state noise vector,$\mathbf{v}$ is the observation noise vector, and $\boldsymbol{\eta}$ and $\mathbf{v}$ are the white noise whose average is 0, their statistic characteristics are as follows:

$$\begin{cases} E(\boldsymbol{\eta}_k) = 0, E(\boldsymbol{\eta}_k \boldsymbol{\eta}_j^T) = \mathbf{Q}_k \delta_{kj} \\ E(\mathbf{v}_k) = 0, E(\mathbf{v}_k \mathbf{v}_j^T) = \mathbf{R}_k \delta_{kj} \\ E(\boldsymbol{\eta}_k \mathbf{v}_j^T) = 0 \end{cases} \tag{3}$$

Expand the state equation at the estimation value $\hat{\mathbf{X}}_{k-1}$ using the Taylor polynomial expansion method, and omit the second order and above items; then

$$\mathbf{X}_k \approx f(\hat{\mathbf{X}}_{k-1}) + \left.\frac{\mathrm{d}f(\mathbf{X})}{\mathrm{d}\mathbf{X}}\right|_{\mathbf{X}=\hat{\mathbf{X}}_{k-1}} (\mathbf{X}_{k-1} - \hat{\mathbf{X}}_{k-1}) + \boldsymbol{\eta}_{k-1} \tag{4}$$

If

$$\left.\frac{\mathrm{d}f(\mathbf{X})}{\mathrm{d}\mathbf{X}}\right|_{\mathbf{X}=\hat{\mathbf{X}}_{k-1}} = \boldsymbol{\Phi}_{k,k-1} \tag{5}$$

$$f(\hat{\mathbf{X}}_{k-1}) - \left.\frac{\mathrm{d}f(\mathbf{X})}{\mathrm{d}\mathbf{X}}\right|_{\mathbf{X}=\hat{\mathbf{X}}_{k-1}} \hat{\mathbf{X}}_{k-1} = \boldsymbol{\xi}_{k-1} \tag{6}$$

then

$$\mathbf{X}_k = \mathbf{\Phi}_{k,k-1}\mathbf{X}_{k-1} + \xi_{k-1} + \boldsymbol{\eta}_{k-1} \tag{7}$$

where $\mathbf{\Phi}_{k,k-1}$ is the state transform matrix. Compared with the basic equation of Kalman filter, the state equation adds one nonrandom item ξ_{k-1} at the condition that the filtered last state variable $\hat{\mathbf{X}}_{k-1}$ has been calculated. Such changes have no effect on calculating the mean square error of the state prediction.

Similarly, expand the observation equation at the estimation value $\hat{\mathbf{X}}_{k,k-1}$ using the Taylor polynomial expansion method, and omit the second order and above items; then

$$\mathbf{Z}_k \approx h(\hat{\mathbf{X}}_{k,k-1}) + \left.\frac{\mathrm{d}h(\mathbf{X})}{\mathrm{d}\mathbf{X}}\right|_{\mathbf{X}=\hat{\mathbf{X}}_{k,k-1}} (\mathbf{X}_k - \hat{\mathbf{X}}_{k,k-1}) + \mathbf{v}_k \tag{8}$$

If

$$\left.\frac{\mathrm{d}h(\mathbf{X})}{\mathrm{d}\mathbf{X}}\right|_{\mathbf{X}=\hat{\mathbf{X}}_{k,k-1}} = \mathbf{H}_k \tag{9}$$

$$h(\hat{\mathbf{X}}_{k,k-1}) - \left.\frac{\mathrm{d}h(\mathbf{X})}{\mathrm{d}\mathbf{X}}\right|_{\mathbf{X}=\hat{\mathbf{X}}_{k,k-1}} \hat{\mathbf{X}}_{k,k-1} = \zeta_k \tag{10}$$

then

$$\mathbf{Z}_k = \mathbf{H}_k\mathbf{X}_k + \zeta_k + \mathbf{v}_k \tag{11}$$

where $\mathbf{H}_k$ is the observation vector. Compared with the basic equation of Kalman filter, the state equation adds one nonrandom item ζ_k at the condition that the one step predicts state variation $\hat{\mathbf{X}}_{k,k-1}$ that has been calculated.

Through the first-order Taylor series expansion, we can use linear equation to approximate the state equation and the observation equation. Then we can use the basic equation of Kalman filter to estimate the state variable. Formula (12) gives the recurrence formula which uses EKF to estimate state variable:

$$\begin{cases} \hat{X}_{k+1,k} = \hat{X}_k + \int_{t_k}^{t_k+\Delta t} f(\hat{X}_k, t_k)dt \\ P_{k+1,k} = \Phi_{k+1,k}P_{k,k}\Phi_{k+1,k}^T + \hat{Q}_k \\ K_{k+1} = P_{k+1,k}H_{k+1}^T\left[H_{k+1}P_{k+1,k}H_{k+1}^T + \mathbf{R}_k\right]^{-1} \\ \hat{X}_{k+1} = \hat{X}_{k+1,k} + K_{k+1}\left[Z_{k+1} - h(\hat{X}_{k+1,k})\right] \\ P_{k+1,k+1} = \left(I - K_{k+1}H_{k+1}^T\right)P_{k+1,k}\left(I - K_{k+1}H_{k+1}^T\right)^T + K_{k+1}\mathbf{R}_kK_{k+1}^T \end{cases} \tag{12}$$

We can see that EKF updates the system state variable by calculating a compromise between process noise $\mathbf{Q}_{k-1}$ and observation noise $\mathbf{R}_k$. It can adjust the gain value autonomously according to the relative size of the $\mathbf{Q}_{k-1}$ and $\mathbf{R}_k$ to achieve the optimal estimation of the state of the system. Therefore, we must pay attention to determine $\mathbf{Q}_{k-1}$ and $\mathbf{R}_k$ when we use EKF, otherwise it will cause the filter error increases, and even lead to filter divergence. The process noise and observation noise of the satellite algorithm are calculated on the ground based on prior data, but there are still some errors [1].

In addition to the extended Kalman filter process, the autonomous navigation algorithm is also dependent on the orbit integration algorithm and observation data processing algorithm. Orbit integration algorithm achieves the transform of satellite state variable from current state to next state. Data pre-processing algorithm achieves time reduction of two-way pseudorange, deducting all the ranging errors [7], and so on, to get the real two-way pseudorange at the epoch time. Orbit integral algorithm and observation data processing module working on satellite are simplified because of the limited of satellite resource so that the algorithm has some error. In addition, the models of all kinds of error also have some error. All factors will lead to increase in the error of autonomous navigation increases.

3 Introduction of Test Scenario

The test scenario is that one IGSO satellite determines its orbit and its clock error autonomously based on three stations [8]. Due to the three stations are all in China, satellite cannot be visible all the time, visibility as shown in Fig. 1. The IGSO satellite's trajectory is a fixed "8" shape over China in geocentric earth-fixed

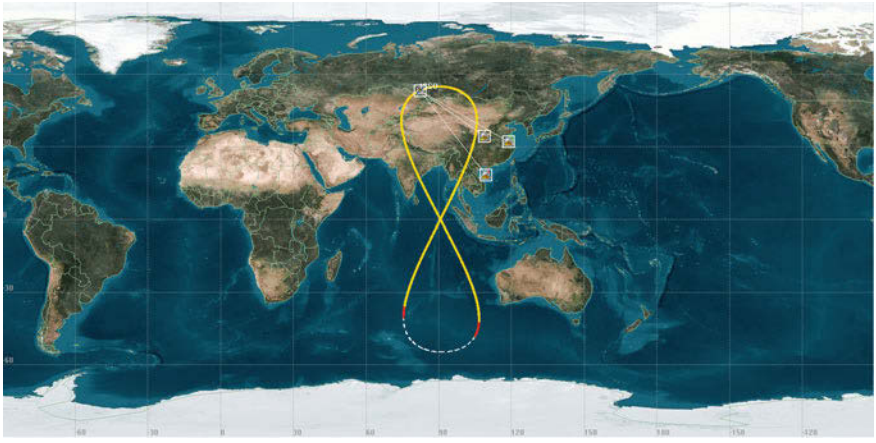

Fig. 1 Test scenario

systems. All the three stations are not visible to the satellite all the time. The solid line in the figure shows that one station is visible to the satellite at least. The dotted line in the figure shows that no station is visible to the satellite. In this way, the observation data is interrupted during some time.

In the actual testing process, due to the problem of ground station support, not all the time the ground station is visible to satellite, the satellite and the ground station build a chain. In addition, even a chain is built between satellite and station; the observation data will become exceptional with a certain probability. So the effective links that the algorithm uses to calculate result are based on the observation data.

4 Analysis of Onboard Test Result

According to the above analysis, the key parameters of autonomous navigation include process noise and observation noise, zero range, and so on. Especially, the zero range used in autonomous navigation algorithm is a relative value, that is, the channel delay of inter-satellite ranging channel relative to the channel delay of navigation signals' broadcast channel. The channel delay of the above two channels that are calibrated on the ground before the satellite was launched usually have big error, so the channel delay must be calibrated when the satellite is launched. Therefore, the above key parameters are calibrated before the test starts based on inter-satellite observation data, the precise orbit, and clock error that were got before the test start. Then, satellite autonomous navigation algorithm calculates the orbit and clock error based on the precise key parameters. The result of orbit determination is transmitted to ground through the telemetry channel. Then we can analyze the accuracy of orbit determination by comparing the result with precise orbit data which is got from ground precision orbit determination system.

The autonomous orbit determination results are shown in Fig. 2. The blue line in above figure of Fig. 2 is the orbit determination result and the red line in below figure of Fig. 2 is the number of effective chain, which are used to autonomous navigation system.

According to Fig. 2, the URE of orbit determination is less than 5 m during 9 days when the autonomous navigation algorithm works at the condition that inter-satellite link is continuous, and there is a fluctuation that is about 3–4 m. At some point because there is no effective inter-satellite link (no ground station is visible or stations transmit abnormal data), the error of orbit determination increases. But once there are effective inter-satellite links, the error will reduce to less than 5 m quickly. The orbit error has a fluctuation even when there are some effective inter-satellite links; there are two main reasons for this. First, the precise orbit has error and the error is fluctuated. Second, the zero range based on precise orbit that has fluctuated error is not precise.

The error of zero range before the sixth day is greater relatively because this zero range is calibrated based on the precise orbit that has error and the precise clock error is not complete. So we transmit new zero range to satellite at sixth day.

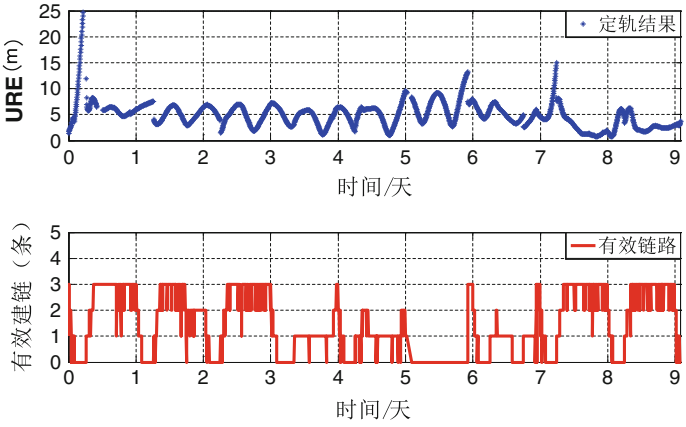

Fig. 2 The result of autonomous orbit determination based on three stations

According to Fig. 2, the orbit error is different before and after the zero range is calibrated again. So we divide the above results into two sections.

Figure 3 shows the result of autonomous orbit determination using old zero range and Fig. 4 shows the result of autonomous orbit determination using new zero range. According to the data of effective inter-satellite number in Fig. 3, time at when there are effective inter-satellite links more than one chain continues long during first day to third day; there is some point at when the number of effective inter-satellite link reduces because sometimes station is invisible to satellite or exchanged data between station and satellite becomes abnormal, but duration time is short. Continuous time of effective inter-satellite link is short during forth day to sixth day; there is only one chain or no chain between satellite and station for long time. Similarly, in Fig. 4, time at when there are effective inter-satellite links more than one chain continues long during eighth day to ninth day; there is some point at

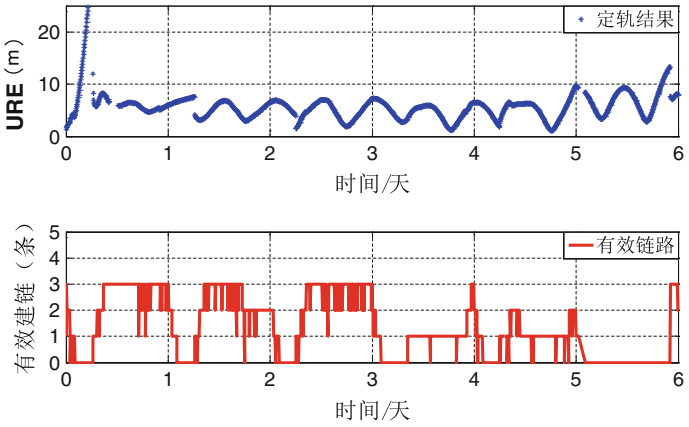

Fig. 3 The result of autonomous orbit determination based on three stations using old zero range

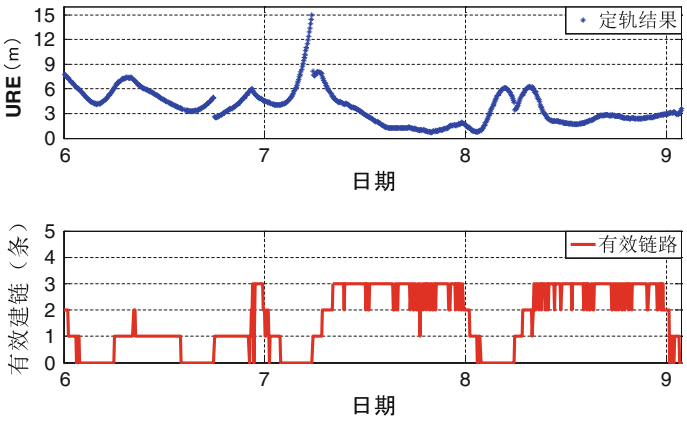

Fig. 4 The result of autonomous orbit determination based on three stations using new zero range

when the number of effective inter-satellite link reduces because sometimes station is invisible to satellite and exchange data between station and satellite becomes abnormal, but duration time is short. Continuous time of effective inter-satellite link is short during seventh day, and there is only one chain or no chain between satellite and station for long time.

Comparing Figs. 3 and 4, the error of orbit determination, which is fluctuated around 5 m and whose fluctuation is 3–4 m, is bigger using old zero range. After using the new zero range, the orbit error has a convergence process. When the effective link between station and satellite becomes stable, the orbit error declines to less than 5 m and the fluctuation is almost 0.

Comparing the time that is between first day and third day in Fig. 3 and the time that is between eighth day and ninth day in Fig. 4, during the first day to third day, the error of orbit determination is fluctuated around 5 m and the fluctuation is about 3–4 m. During eighth day to ninth day, the orbit error has a decrease process and the error declines to less than 3 m when there is effective link.

By the above analysis, the calibration accuracy of zero range has big influence to orbit determination error. So in order to obtain higher autonomous orbit determination accuracy, the zero range must be calibrated precisely based on the precise orbit and clock error before the onboard test starts.

5 Analysis of Afterward Result

By the above analysis, the calibration accuracy of zero range has big influence to orbit determination error. So in order to obtain higher autonomous orbit determination accuracy, the zero range must be calibrated precisely based on the precise orbit and clock error before the onboard test starts. In autonomous navigation algorithm, the parameters for algorithm (process noise Q and observation noise R),

the calibration accuracy of zero range, the error of phase center, and the tropospheric delay correction all have big influence to the accuracy of autonomous navigation algorithm. During the onboard test, the zero range is calibrated based on the afterward precise orbit, but analysis shows that precise orbit still exists error so that the zero range is not calibrated precisely. In addition, the phase center of the station and the adjust parameter for algorithm are not calculated precisely. All the above errors lead to result that the determination orbit has big error.

Afterward, using the two-way pseudorange between station and satellite, zero range that is more precise, the phase center of station that is calculated based on the model of the antenna, and the software parameters that are adjusted accurately, the autonomous navigation algorithm runs on the PC. Considering the completion of the data, the time during which algorithm runs on the PC is selected during first day to fifth day. The result is shown in Fig. 5.

According to Fig. 5, on the first day, the number of the effective inter-satellite link is not stable, and the algorithm cannot converge, so that the error of the orbit determination has fluctuation and the URE > 3 m. After the first day, the links between satellite and three stations tend to be stable. Three effective links can be maintained and the number of effective links reduces occasionally. At this time, the orbit error of the autonomous navigation algorithm converges to 2 m at the end. Thereafter, the links between stations and satellite are stable during the second day to forth day, so the orbit error can maintain less than 2.5 m during this time. From the fifth day, the number of effective links begins to decrease, but the orbit error does not diverge immediately and maintain less than 3 m. When passed half of fifth day, there is no effective link, so that the orbit error begins to diverge. The error is greater than 3 m sometimes. But we can get that the orbit error will reduce to less than 3 m once there is effective link.

Comparing Figs. 2 and 5, the accuracy of orbit determination which is obtained at PC is improved obviously relative to that obtained on the satellite. This result shows that the zero range has error and the algorithm parameters also have error

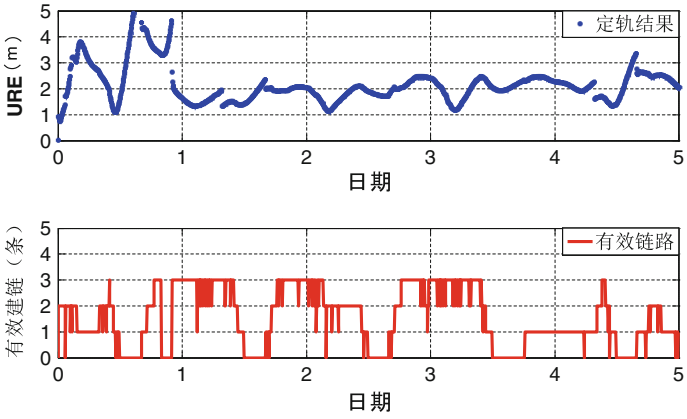

Fig. 5 The result of autonomous orbit determination that runs on PC

during onboard test. To achieve higher accuracy, in the future test process, it is necessary to calibrate these parameters more precisely.

6 Conclusions

According the onboard result of autonomous navigation algorithm, we can get the conclusion that the satellite is able to achieve orbit determination autonomously based on three stations at the condition that there are some effective links. The URE of orbit determination is less than 5 m during 9 days when the autonomous navigation algorithm works at the condition that there are effective inter-satellite link for long time. Afterward, using more precise zero range, calculating the phase center of every plot precise, and adjusting the algorithm parameter, the accuracy of orbit determination improves obviously. But once the number of effective links reduces, the accuracy of orbit determination decreases obviously. Therefore, a certain number of effective links are the pre-condition of precise autonomous orbit determination.

Comparing the above result, many kinds of error are difficult to calibrate accurately in engineering relative simulation data, such as zero range, phase center of antenna, troposphere delay (link between station and satellite), and so on. These kinds of error will affect the orbit results directly. Therefore, to improve the accuracy of autonomous navigation technology in engineering, in addition to researching more precise orbit determination algorithm, it is also needed to pay attention to how to calibrate all kinds of constant value errors in engineering and how to make more accurate model of variable error.

References

1. Shang L (2013) Research on autonomous orbit determination and time synchronization algorithm of navigation satellite. Shanghai Inst Microsys Inf Technol
2. Wang H, Chen Z, Chu H, Wu X, Zheng J (2012) On-board autonomous orbit prediction algorithm for navigation satellites. J Astronaut 33(8):1019–1026
3. Shang L, Liu G, Zhang R, Li G (2013) An information fusion algorithm for integrated autonomous orbit determination of navigation satellites. ACTA Astronaut 85:33–40
4. Shang L, Liu G, Liu S, Zhang R, Li G (2013) an information fusion algorithm of autonomous orbit determination based-on step kalman filter. J Astronaut 34(3):333–339
5. Qin Y, Zhang H, Wang S (2015) Kalman filter and the principle of integrated navigation, 3rd edn. Northwestern Polytechnical University Press, Xian, pp P199–P220
6. Zhang R (1998) Satellite attitude and orbit dynamics and control. Beijing University of Aeronautics and Astronautics Press, Beijing, P7–P12 (Ch)
7. Wen Y (2009) Analysis and simulation technology of satellite navigation system. Beijing University of Aeronautics and Astronautics Press
8. Shang L, Ren Q, Zhang R, Li G (2013) Eliminating constellation rotation error by using the time sequence difference measurement of the station. Geomatics Inf Sci Wuhan Univ 38 (8):920–924

Precise Orbit Determination of Navigation Satellite Using Joint Data from Regional Tracking Station and LEO

Laiping Feng, Rengui Ruan, Xianbing Wu and Bijiao Sun

Abstract The precision of orbit determination for navigation satellites with regional distributed stations may be improved by introducing onboard GNSS observation data. The method of orbit determination combining the onboard data of LEO with the observation data of regional monitor stations is discussed. In order to validate this proposed approach and its performance, the observation data of seven GPS stations in China and onboard data of GRACE-A and GRACE-B during March 16–31, 2011 were collected and orbit determination experiments were carried out. The result shows that, compared with the result of seven stations, the visibility of GPS satellites is increased by about 14 %; meanwhile, the precision of GPS orbit expressed in RTN components is improved by about 35, 44, and 45 %, respectively; when introducing only GRACE-B, improvements in RTN components of 51, 60, and 62 % are achieved when both GRACE-A and GRACE-B are introduced and the visibility of GPS satellites is increased by 18 % in this case. The proposed approach will provide a new idea to improve the orbit determination accuracy of navigation satellite under the restriction of regional monitoring stations.

Keywords LEO · Onboard data · Precise orbit determination · GPS · SPODS · Regional stations

L. Feng (✉) · R. Ruan
College of Geographic Space Information, Information Engineering University, Zhengzhou, China
e-mail: fenglaiping@163.com

L. Feng
National Key Laboratory of Geographic Information Engineering, Xi'an, China

X. Wu
College of Geological Engineering and Surying, Chang'an University, Xi'an, China

B. Sun
Xi'an Research Institute of Surveying and Mapping, Xi'an, China

© Springer Science+Business Media Singapore 2016

J. Sun et al. (eds.), *China Satellite Navigation Conference (CSNC) 2016 Proceedings: Volume III*, Lecture Notes in Electrical Engineering 390,
DOI 10.1007/978-981-10-0940-2_20

1 Introduction

The orbit and clock error of the navigation satellite are calculated by the observation data from the monitoring station, which precision determines the precision of positioning and timing of users. Large quantity and wide distribution of the monitoring station can obtain more observations and may improve the precision of satellite orbit and clock, which is very important. For some new navigation satellite system, as the scale of monitoring station is still small, the overseas monitoring station construction conditions are not available, the full arc tracking of navigation satellite cannot be achieved, and high precision orbit determination is still difficult to achieve, such as the use of pseudo-range of domestic monitoring station to determine the GPS orbit, the precision is about 10 m; the use of carrier phase orbit, the precision is about 1 m; in addition, even if the carrier phase is used, as the affection of the geometric configuration of the constellation, the precision of the BDS MEO satellite orbit determination is 2–3 times lower than GPS, GEO precision is worse [1, 2]. In recent years, the navigation satellite system such as GPS and BDS is hoping realizing the full arc tracking by establishing the link between the navigation satellites, so as to achieve high precision orbit determination [3–6]. In fact, with unique continuous three-dimensional positioning capability the navigation satellite system has become the main method for the orbit determination of LEO. At present, the precision of LEO orbit determination by satellite onboard GPS has reached 1–2 cm [6–8]; many LEO with high precision position requirements have also been equipped with satellite onboard GPS receivers, such as CHAMP, JASON, TOPEX, GRACE, GOCE, etc. The satellite onboard receiver can obtain high precision pseudo-range and carrier observation; if the LEO is seen as the monitoring station, then satellite onboard data and monitoring station data will be used for precision orbit determination of navigation satellite. For monitoring station, the low elevation angle measurement is easy to be influenced by many factors such as multi-path. In order to ensure the quality of observation, it is usually required to set up 0–15° elevation angle of measurement, while there is no barrier around the LEO, in which orbit is higher than troposphere, for GNSS satellite view of low altitude and even negative height, so its influence is small relative to regional observation station; moreover, as the "motion monitoring station," LEO satellite has an enhanced effect on GNSS in space geometric configuration [9], which can improve the precision of orbit determination of GNSS and LEO satellites. Zhu [10] proposed the method of integrating the data of satellite onboard and monitoring stations to determine the orbit, geocentric coordination, and the gravity field coefficients of GPS and LEO (GRACE and CHAMP). The results show that the orbit precision of the two kinds of satellites and earth dynamics parameters can be improved obviously [11]. Geng Jianghui carried out GPS satellite orbit determination experiment using satellite onboard data and regional monitoring station data, and reached similar conclusion. These results clearly show that the use of satellite onboard data can enhance the

precision of navigation satellite orbit determination. All of the studies are based on the global distribution station. The research background of this paper is based on the construction of the Beidou global navigation satellite system (BDS) in China, and the feasibility of using LEO satellite onboard data with regional monitoring station observation to enhance the precision of navigation satellite orbit determination is discussed. The method and mechanical model of combined orbit determination are discussed, and the improvement of the arc tracking and orbit determination precision of GPS satellite are analyzed based on the seven GPS monitoring stations in China by joining GRACE satellite onboard data.

2 Mathematical Model

$$\begin{aligned} \boldsymbol{L}_{\text{sta}} &= \boldsymbol{G}\left(\boldsymbol{x}_{\text{gps}}, \boldsymbol{x}_{\text{sta}}, \boldsymbol{x}_o, \boldsymbol{t}\right) + \boldsymbol{v}_{\text{sta}}, \boldsymbol{v}_{\text{sta}} \in \left(0, \boldsymbol{P}_{\text{sta}}^{-1}\right) \\ \boldsymbol{L}_{\text{leo}} &= \boldsymbol{F}\left(\boldsymbol{x}_{\text{gps}}, \boldsymbol{x}_{\text{leo}}, \boldsymbol{x}_o, \boldsymbol{t}\right) + \boldsymbol{v}_{\text{leo}}, \boldsymbol{v}_{\text{leo}} \in \left(0, \boldsymbol{P}_{\text{leo}}^{-1}\right) \end{aligned} \tag{1}$$

Among them,

$\boldsymbol{L}_{\text{sta}}, \boldsymbol{L}_{\text{leo}}$ GPS observation is obtained from the regional monitoring station receiver and the satellite onboard receiver, respectively; $\boldsymbol{v}_{\text{sta}}, \boldsymbol{v}_{\text{leo}}$ are the corresponding measurement errors; $\boldsymbol{P}_{\text{sta}}, \boldsymbol{P}_{\text{leo}}$ are the corresponding weight matrixes; $\boldsymbol{t}$ is the time parameter; $\boldsymbol{x}_{\text{gps}}$ is the GPS orbit parameters; $\boldsymbol{x}_{\text{leo}}$ is the LEO satellite orbit parameters; $\boldsymbol{x}_{\text{sta}}$ is the station-related parameters, such as station coordinates, tropospheric delay parameters, etc.; and $\boldsymbol{x}_o$ is the measurement-related parameters such as carrier phase ambiguity, clock error parameter, etc.

Above observation equations are linearized and written in matrix form as follows:

$$\underbrace{\begin{bmatrix} l_{\text{sta}} \\ l_{\text{leo}} \end{bmatrix}}_{l} = \underbrace{\begin{bmatrix} \frac{\partial G}{\partial x_{\text{gps}}} & 0 & \frac{\partial G}{\partial x_{\text{sta}}} & \frac{\partial G}{\partial x_{\text{o}}} \\ \frac{\partial F}{\partial x_{\text{gps}}} & \frac{\partial F}{\partial x_{\text{leo}}} & 0 & \frac{\partial G}{\partial x_{\text{o}}} \end{bmatrix}}_{A} \underbrace{\begin{bmatrix} \delta x_{\text{gps}} \\ \delta x_{\text{leo}} \\ \delta x_{\text{sta}} \\ \delta x_{\text{o}} \end{bmatrix}}_{\delta x} + \underbrace{\begin{bmatrix} v_{\text{sta}} \\ v_{\text{leo}} \end{bmatrix}}_{v} \tag{2}$$

Among them,

$$\begin{aligned} l_{\text{sta}} &= L_{\text{sta}} - G\left(x_{\text{gps}}^0, x_{\text{sta}}^0, x_o^0, t\right) \\ l_{\text{leo}} &= L_{\text{leo}} - G\left(x_{\text{gps}}^0, x_{\text{sta}}^0, x_o^0, t\right) \end{aligned} \tag{3}$$

$(\cdot)^0$ initial value of parameter and $\delta(\cdot)$ parameters correction, corresponding to the least squares solution, can be expressed as

$$\begin{aligned} \delta\hat{x} &= (A^T PA)^{-1} A^T Pl \\ \hat{Q}_x &= (A^T PA)^{-1} = \left(A_{\text{sta}}^T P_{\text{sta}} A_{\text{sta}} + A_{\text{leo}}^T P_{\text{leo}} A_{\text{leo}}\right)^{-1} \end{aligned} \tag{4}$$

Among them, $P = \begin{bmatrix} P_{\text{sta}} & \\ & P_{\text{leo}} \end{bmatrix}$, A_{sta} and A_{leo}, respectively, line 1 and line 2 of formula (2), matrix A. $\hat{\boldsymbol{Q}}_{\boldsymbol{x}}$ indicates covariance matrix, its diagonal elements are related to the precision of the corresponding parameters, and the higher the element value is, the lower the precision of the corresponding parameters is.

In orbit determination mission, the station coordinate usually is precisely known, which can be used as a known quantity; while LEO is around the earth in high speed, in which orbit is unknown, its stress is complex, especially the models of solar radiation and atmospheric drag are difficult to be obtained. Compared with the traditional precision of navigation satellite orbit determination, the key of navigation satellite orbit determination is how to accurately describe the orbit of LEO satellite.

3 Orbit Determination Method

The application of GPS satellite onboard observation not only improves the accuracy of orbit determination, but also promotes the great development of LEO satellite orbit determination technology. At present, the main method of orbit determination is dynamic, kinematic, and reduced dynamic method. Over the past 20 years, in foreign countries, the reduced dynamic method and geometric method are mainly used for the orbit determination of gravity and altimeter satellites [7, 8, 12–18] (such as CHAMP, GRACE, GOCE, TOPEX, JASON-1/2) to avoid the error of orbit dynamics models (especially the earth's gravitational field model error) influence, and one of the most important scientific results of these satellites is that the accuracy of earth gravity field model is greatly improved, so that the precision of LEO dynamic model is greatly improved as well. Now the new earth gravity field model is used to LEO orbit determination, and the precision can reach within 5 cm [7]. The dynamic method is an effective method of directly recovering the satellite-related parameters (such as orbit parameters, earth gravity field, geocenter position, etc.), and can be used to obtain satellite position and speed. The purpose of this paper is to use the GPS satellite onboard data to improve the precision of the orbit determination; the kinematic and reduced dynamic method should be avoided because of too many unknown parameters. In addition, by the constraint of current advanced orbital dynamics model for LEO orbit, more information will be obtained which can enhance the geometric construction of GPS satellites [9]. The dynamic orbit determination method is used to describe the LEO satellite orbit in this paper.

Table 1 Force model of GPS and LEO

Force model	GPS	LEO
The gravitational field of the earth	EGM2008 12 × 12 order	EGM2008 120 × 120 order
A tidal gravity	Solid tide and pole tide, tide, ocean pole tide	Solid tide and pole tide, tide, ocean pole tide
Third body gravity	Sun, moon and planets	Sun, moon and planets
The post Newtonian effect	IERS2003 [19]	IERS2003
Solar radiation model	ECOM model	Ball model
Atmospheric drag force	Without consideration	Base on Harri_Pairs atmospheric density model [20]

In order to ensure the accuracy of orbit dynamics model, force model should be considered including the earth gravity field model, the sun gravity, the moon gravity, the planets gravity, and the solar radiation pressure perturbation gravitational force, after the Newton effect. The force models of the GPS satellite and the LEO satellite are shown in Table 1.

The note is that solar radiation and atmospheric drag model in Table 1 has a lot of uncertainty, and their model coefficients should be solved as unknown parameters together with initial orbit state parameters. For the GPS satellite, the study shows that by means of solving the five parameters (D0, B0, Y0, Bc, and GPS) can obtain the ideal orbit solution [21]. For LEO satellite, solar radiation pressure reflection coefficient and atmospheric reflection coefficient should be estimated as a constant for every 6 h; in addition, a set of periodic experience force parameters (R/T/N) will be estimated by each orbit period [22].

On the basis of SPODS (Positioning and Orbit Determination System Satellite) software, we have carried out the function expansion [23], which is based on the combined use of satellite onboard GNSS data and regional monitoring station data. The following experiments are completed based on this software.

4 Experiments and Analysis

4.1 Experiment Data

In order to evaluate the effectiveness of using the LEO satellite onboard observation and regional monitoring station observation to determine the GPS orbit, the satellite onboard data of GRACE-B and GRACE-A together with the observation of seven GPS monitoring stations in China were collected and analyzed. The GRACE project is proposed by American NASA and German DLR to carry out experiments in the earth's gravitational field inversion, atmospheric detection, and ionospheric environment. LEO tracking technology is used for GRACE. There are two satellites

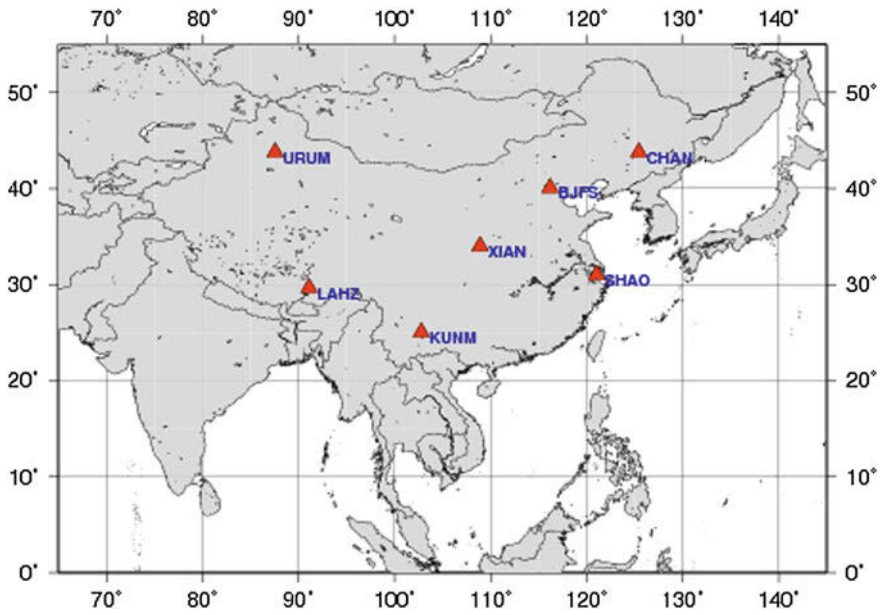

Fig. 1 Distribution of monitoring stations

in the same orbit at a distance of 220 ± 50 km, orbital inclination of 89°, the height of 485–500 km, and a circle around the earth of about 90 min [24]. Two satellites are equipped with a satellite onboard GPS receiver for precision determination of their positions. Seven domestic GPS monitoring stations were chosen including KUNM, LAHZ, BJFS, SHAO, URUM, CHAN, and XIAN; the distribution is shown in Fig. 1. Observation period is from March 16 to March 31, 2011.

In order to facilitate comparison and description of the problem, the following three schemes were set up in the calculation and analysis:

1. scheme 1: using seven domestic GPS tracking station observations;
2. scheme 2: using seven GPS tracking station observations and GRACE-B satellite onboard GPS observation;
3. scheme 3: using seven GPS tracking stations observations and the GRACE-A and GRACE-B satellite onboard GPS observations.

For above three schemes, the orbit determination is carried out respectively. The observations are used for 3 days of arc section and the data sampling interval is for 30 s. In this paper, it is assumed that the accuracy of the satellite onboard observation and the observation of the regional monitoring station is equivalent. According to our experience, the accuracies of the ionosphere-free combination of the pseudo-range and phase are 2 m and 2 cm, respectively; on this basis, the right value will be obtained. As mentioned above, the elevation angle of station is set up to 10° to reduce the multi-path effect, and the elevation angle of LEO is 5°.

The parameters are to be estimated in addition to satellite orbit parameters, including non-difference ionosphere-free combination ambiguity parameters and station tropospheric zenith delay, and the ambiguity parameters using floating-point solution. GPS initial orbit is calculated by broadcast ephemeris: for the GRACE satellite, first broadcast ephemeris and pseudo-range observation data are used for kinematic orbit determination, and then the initial orbit state vector and the initial dynamics model parameters are obtained by dynamic smoothing. In order to analyze the effect of the LEO satellite onboard data, the variation of the geometrical structure of the different schemes of GPS orbit determination is analyzed first, and then the accuracy of the orbit determination is analyzed using IGS precision orbit as the reference.

4.2 Analysis of Geometric Structure for Orbit Determination

The addition of LEO satellite will inevitably lead to the enhancement of the geometrical structure of the orbit determination, in which the first performance is the increase of the visible arc section number. In this definition, visible arc section is the time interval at least one monitoring station observed. Figure 2 shows the visible GPS arc section of the different schemes. It can be seen that in scheme 1, the visible arc of each satellite is between 30.2 and 41.8 %, and the average is about 36.8 %; in scheme 2, the proportion of the visible arc of each GPS satellite is slightly increased except No. 30 satellites, and the average is about 50.8 %, and compared with scheme 1 the addition is about 14 %, and the relative increase is about 38 %. Since the GRACE-B satellite did not observe satellite No. 30, the visible arc segment did not change; in scheme 3, the effective arc of each satellite was significantly increased in the range of 47.3–60.5 %, the average of about

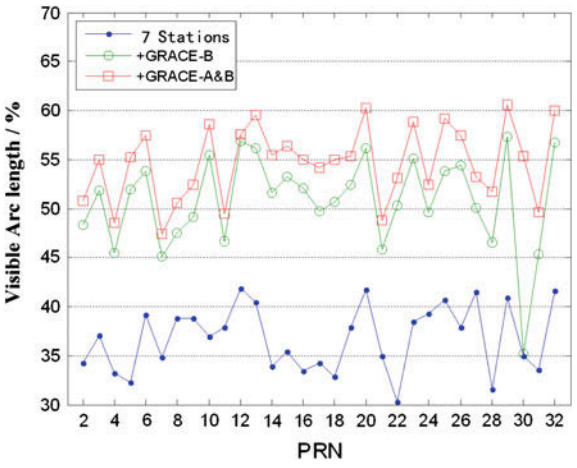

Fig. 2 Comparison of the visibility of GPS satellites from three schemes

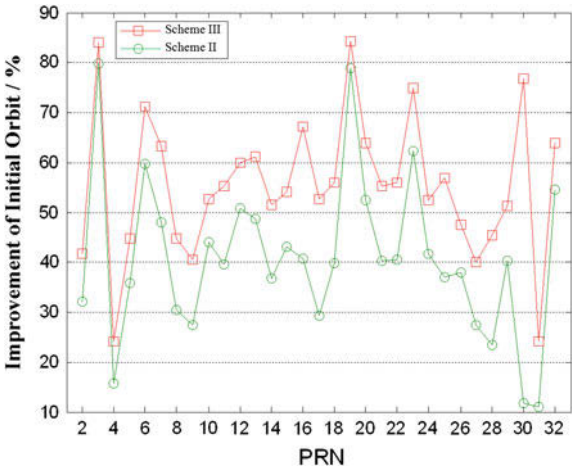

Fig. 3 Improvement of the satellites initial position precision by schemes 2 and 3 compared with solution 1

54.6 %, and compared with scheme 1, the addition is 17.8 %, relative increase of about 48.4 %, and compared with scheme 2, an increase is of about 3.8 %.

By formula (3), the covariance matrix $\hat{\boldsymbol{Q}}_{\boldsymbol{x}}$ obtained by the least square solution is related to the prior right P. In the establishment of the authority matrix P, the design matrix A is determined by $\hat{\boldsymbol{Q}}_{\boldsymbol{x}}$, which is the type of observations, quantity and geometric distribution of the observed values, which reflects the geometrical structure of the orbit determination. If $\sigma_x^2, \sigma_x^2, \sigma_x^2$ are the initial orbit of the satellite $[x, \quad y, \quad z]$ diagonal elements of the covariance matrix, respectively, the 3D position accuracy (STD) can be expressed as $\sigma_{\text{pos}} = \sqrt{\sigma_x^2 + \sigma_y^2 + \sigma_z^2}$. We have shown that the improvement of the 3D position accuracy of the initial orbit of the satellite with different solutions can be seen in Fig. 3. It indicates that the 3D position accuracy of the initial orbit after joining GRACE-B is improved by 11.1–79.8 %, and the average is about 40.7 %. At the same time, the GRACE-A GRACE-B are improved by 24.0–84.2 %, and the average increase is 55.4 %. This is equivalent to the increase of the visible arc length.

4.3 Analysis of Orbit Determination

Figure 4 shows the results of the three schemes for orbit determination compared with the IGS final orbit in RTN direction one day. It can be seen that in scheme 1 R direction RMS is 0.2 m, and RMS (T) and RMS (N) are about 0.6 m; in scheme 2, the RMS of the RTN direction is significantly reduced, the R direction is about 0.1 m, and the T and N directions are less than 0.4 m. Table 2 shows the statistics of the RMS of average orbital (RTN) and three-dimensional position for 16 days. The accuracies of orbit determination by those three schemes are 0.952, 0.521, and

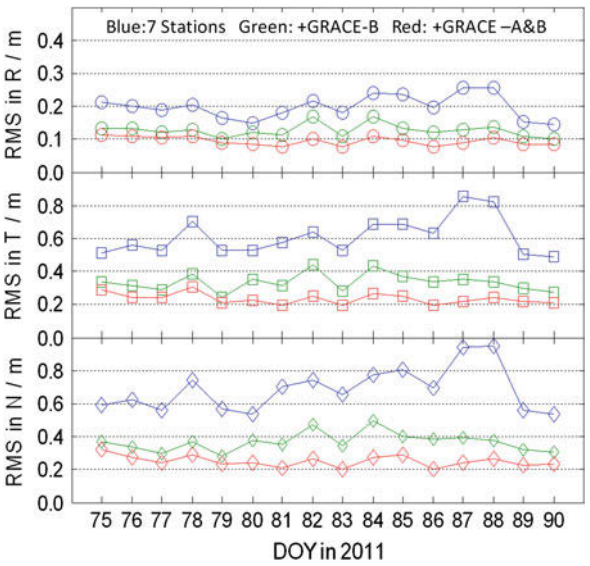

Fig. 4 Daily RMS in RTN of different schemes compared with IGS final orbit

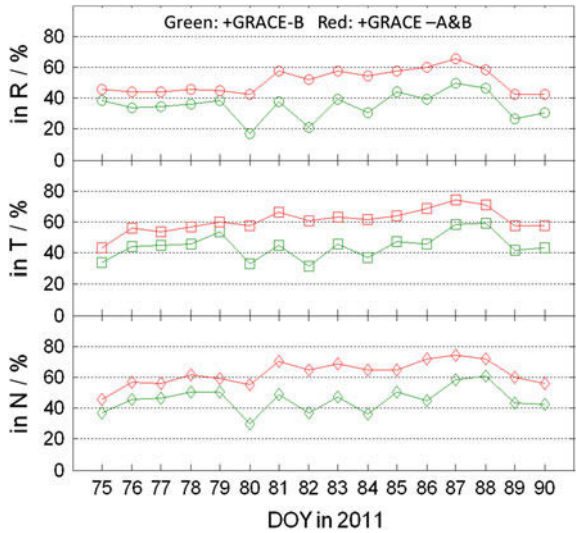

Fig. 5 Improvements of orbit accuracy by solutions 2 and 3 compared with solution 1

0.361 m, respectively, and the radial precision of the orbit with scheme 3 can reach 0.1 m. Compared with scheme 1, the improvements of scheme 3 and scheme 2 are about 45 and 62 %, respectively.

Figure 5 shows the accuracy improvements of schemes 2 and 3 relative to scheme 1. It can be seen that the improvement range of scheme 2, at R direction of the RMS, is between 17 and 49 %, the T direction is between 32 and 58 %, and the N direction is 30–60 %; the average improvement rates of RTN direction are about

Table 2 Average RMS of orbit error (unit: m)

Orbit Component	7 Domestic stations	+GRAC-B	+GRACE-A&B
R	0.198	0.127	0.096
T	0.610	0.336	0.234
N	0.686	0.368	0.251
3D	0.952	0.521	0.361

35, 45, and 44 %, respectively. Scheme 3 of the orbit precision is further improved; the R direction of the improvement is between 42 and 65 %, the T direction is between 43 and 75 %, and the N direction is between 46 and 73 %; RTN directions of the average improvement rate are 51, 60, and 62 %, which indicate that the satellite onboard data bring about the improvement of the orbits T and N. Although the GRACE binary is only 200 km away, it has brought a significant improvement in orbit.

Figure 6 shows the orbit accuracy improvement stated by satellite number, joining a LEO satellite, except No. 30 satellite, and the orbit improvements of the R/T/N direction are about 11–63 %, 25–64 %, and 25–65 %, respectively. It is worth noting that, although the PRN 30 satellite is not directly observed by the GRACE-B satellite, due to the correlation between the satellite orbits in orbit determination process, the R/T/N RMS have been improved by 7, 9, and 13 %, respectively. When the GRACE-A and GRACE-B satellites are joined, the R/T/N RMS of the GPS satellite orbit are improved by 15–76 %, 31–78 %, 37–80 %, respectively.

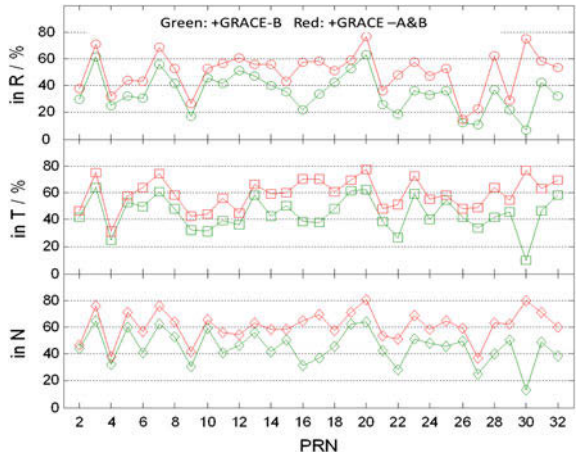

Fig. 6 Improvements of orbit accuracy respective to satellites

5 Conclusion

With the condition of regional monitoring station, the precision of the navigation satellite orbit determination can effectively improve by adding the LEO satellite onboard data to realize the joint orbit determination using monitoring station observation together with the LEO satellite onboard data observation. In this paper, the analysis shows that the satellite onboard GPS observation can effectively improve the visible arc section of the navigation satellites, and enhance the geometrical structure of the orbit. On the basis of the seven domestic monitoring stations, the GPS observation of GRACE-B satellite is added, the visible arc section can be increased by about 14 %, and orbit determination accuracy of RTN direction can be increased by 35, 45, and 44 %, respectively. The accuracy of RTN component is increased by 18, 60, and 62 %. This also shows that, similar to the GRACE satellite formation, compared to the single satellite, its contribution in these two aspects is more significant. It can be assumed that with the help of a certain number of LEO with reasonable orbit distribution, combined with the domestic regional monitoring station is fully possible to achieve the navigation satellite effectively tracking and high precision monitoring.

References

1. Zhou S, Hu X et al (2010) Analysis of orbit determination and prediction accuracy for a regional tracking network. Scientia Sinica Phys Mech Astron, 40(6):800–808
2. Song X (2009) Study on the orbit determination of COMPASS navigation satellites. Chang'an University 47–63
3. Amarillo FF (2011) Inter-satellite ranging and inter-satellite communication links for enhancing GNSS satellite broadcast navigation data. Adv Space Res 47(5):786–801
4. Ananda MP, Bernstein H (1990) Global positioning system autonomous navigation. In: Proceedings of IEEE position, location and navigation symposium, Las Vegas, Nevada, Mar 20–23. pp 497–508
5. Lin Y, He S, Zheng J et al (2010) Development recommendation of inter-satellites links in GNSS. Spacecraft Eng 19(6):1–7
6. Qin X (2009) Spaceborne GPS low earth orbit research theory and method of satellite orbit. PLA Information Engineering University, ZhengZhou, p 166
7. Xu T, Jiang N, Sun Z (2013) Studies dynamics smoothing for GOCE satellite kinematic orbit. Geomatics Sci Eng 33(1):16–20
8. Svehla D, Rothacher M (2003) Kinematic and reduced-dynamic precise orbit determination of low earth orbiters. Adv Geosci 2003(1):47–56
9. Rothacher M (2004) Precise orbit determination for low earth orbiters. In: Colloquium on atmospheric remote sensing using the global positioning system
10. Zhu S, Reigber C, Konig R (2004) Integrated adjustment of CHAMP, GRACE, and GPS data. J Geodesy 78:103–108
11. Geng J, Shi C, Zhao Q et al (2007) GPS precision orbit determination from combined ground and space-borne data. Geomatics Inf Sci Wuhan Univ 32(10):906–909
12. Zhao Q (2003) Research on precision orbit determination theory and software of both GPS naviagation constellation and LEO satellites. Wuhan University, p 6–9

13. Bock H, Jaggi A, Svehla D et al (2007) Precise orbit determination for the GOCE satellite using GPS. Adv Space Res 39:1638–1647
14. Schutz BE, Tapley BD, Abusali PAM et al (1994) Dynamic orbit determination using GPS measurements from TOPEX/POSEiDON. Geophys Res Lett 21(19):2179–2182
15. Svehla D, Rothacher M (2005) Kinematic positioning of LEO and GPS satellites and IGS stations on the ground. Adv Space Res 36:376–381
16. Wu SC, Yunck TP, Thornton CL (1990) Reduced-dynamic technique for precise orbit determination of low earth satellites. J Guidance 14(1):24-24
17. Yunck TP, Bertiger WI, Wu SC et al (1994) First assessment of GPS-based reduced dynamic orbit determination on TOPEX/Poseidon. Geophys Res Lett 21(7):541–544
18. Li J, Zhang S, Zou X et al (2009) Precise orbit determination for GRACE with zero-difference kinematic method. Chinese Sci Bull 54(16):2355–2362
19. McCarthy DD, Petit G (2004) IERS conventions (2003). Verlag des Bundesamtes f¨ur Kartographie und Geod¨asie, Frankfurt am Main, p 127
20. Montenbruck O, Gill E, (2001) Saltellite orbits models, methods, and applications. Springer-Verlag, Berlin
21. Springer TA (1999) Modeling and validating orbits and clocks using the global positioning system. Astronomical Institute, University of Berne, Berne, p 169
22. Bock H (2003) Efficient methods for determining precise orbits for low earth orbiters using the global positioning system (GPS). University of Bern, Bern, p 230
23. Wei Z, Ruan R, Jia X et al (2014) Satellite positioning and orbit determination system SPODS: theory and test. Acta Geodaetica Cartogr Sin 43(1):1–4
24. Chen J (2007) Precise orbit determination of low earth orbiters. Tongji University, ShangHai, p 17

Orbit Accuracy Analysis for BeiDou Regional Tracking Network

Gang Zhao, Shanshi Zhou, Xuhua Zhou and Bin Wu

Abstract In order to evaluate the orbit accuracy of regional network of Chinese BeiDou Satellite Navigation System (BDS), we compare the orbits determined by regional network consisting of ground stations within the border of China and orbits provided by global Multi-GNSS Experiment (MGEX) covering 2-year time span from 2013 to 2014. The results show that, for GEO/IGSO/MEO, mean radial accuracies of regional network orbits are around 0.4, 0.3, and 0.2 m, respectively. The orbit accuracy degenerates significantly during eclipse and IGSO/MEO yaw-fixing season. IGSO/MEO orbit accuracies present possible quasi-periodic oscillation, but show week correlation with sun's elevations above the orbital plane. Assessment of regional network orbits by satellite laser ranging (SLR) shows, for GEO/IGSO/MEO, that the RMS values of station–satellite distance are around 0.6, 0.3, and 0.2 m, respectively, which match the orbit radial errors fairly well but contain significant systematic offsets. The characteristics presented in BeiDou satellites are quite different from those in GPS/Galileo. The dynamic modeling accuracy and orbit processing strategy on BeiDou satellites need further enhancement.

Keywords BDS · Regional network · Orbit evaluation · SLR

1 Introduction

BeiDou Satellite Navigation System (BDS) adopts mixed constellation structure which consists of satellites distributed in Geostationary Earth Orbit (GEO), Inclined Geosynchronous Orbit (IGSO), and Medium Earth Orbit (MEO). Currently, regional

The original version of this chapter was revised: For detailed information please see Erratum. The erratum to this chapter is available at 10.1007/978-981-10-0940-2_66

G. Zhao (✉) · S. Zhou · X. Zhou · B. Wu
Shanghai Astronomical Observatory, Chinese Academy of Sciences, Shanghai, China
e-mail: zhaogang@shao.ac.cn

© Springer Science+Business Media Singapore 2016

J. Sun et al. (eds.), *China Satellite Navigation Conference (CSNC) 2016 Proceedings: Volume III*, Lecture Notes in Electrical Engineering 390,
DOI 10.1007/978-981-10-0940-2_21

BDS which consists of 14 satellites has been put into operation stably. Global BDS has also been implemented gradually, and a few test satellites have been launched or been put into recent launch plan. The final goal of BDS construction is to form satellite navigation system which provides global coverage service. As the onboard reference of navigation system, precise satellite orbit will play important role during the BDS application and spreading in high precision fields.

The networks of monitoring stations of GPS and Galileo systems have achieved global and fairly even distribution. But limited by external conditions, the monitoring stations of BDS are located inside the border of China, which lead to poor geometry structure of carrier phase measurement, and the normal equations of orbit determination have greater probability to become ill-conditioned.

Some dynamical models in BDS orbit processing have not been perfect yet. The solar radiation pressure (SRP) model is the most important perturbation model affecting orbit determination of high-orbit and medium-orbit satellites. The practical SRP models are empirical or semi-empirical, which have been formed on the basis of long-term and large amount data analysis. At present, only for GPS, the SRP model and parameter estimation have been well developed [1, 2]. The modeling for Galileo SRP is still in the stage of investigation and improvement [3]. The modeling for BDS SRP should also been put more efforts.

The nominal coordinate of BDS onboard carrier phase center is adopted in our current data processing. Little difference would appear during the geometry correction for different frequency or to different direction. But only the fixed value is adopted now, in which application should be accompanied by a set of self-consistent parameters to avoid systematic bias of orbits.

Full understanding on accuracies and characters of BDS orbits provided by reginal network is an important approach to investigate the effects of above-mentioned factors and to provide further improvement. For this purpose, comparison and analysis are carried out on the basis of 2-year orbits provided by BDS regional network consisting of a set of ground stations located within the border of China and orbits provided by the multi-GNSS experiment (MGEX) consisting of global ground stations. Multi-satellite orbit determination strategy with simultaneous estimation of orbital elements and clock errors are adopted to obtain the orbits in BDS regional network framework [4]. The external orbit validation on BDS regional network is also carried out on the basis of global satellite laser ranging (SLR) tracking provided by International Laser Ranging Service (ILRS).

2 Orbit Comparison

2.1 MGEX Orbits

MGEX is a huge experimental system organized by International GNSS Service (IGS), in which goal is to explore characters of multiple satellite navigation systems including GPS of US, GLONASS of Russia, Galileo of EU, BDS of China, and QZSS of Japan by

cooperative analysis [5, 6]. A few global satellites navigation analysis centers have joined in MGEX working group, and provide products such as orbit, clock, satellite and station hardware delay, ionospheric correction, earth orientation parameters, etc.

There are around 30 ground stations of BDS in MGEX framework which realized preliminary global distribution even though such distribution is not even very much. Currently, three MGEX analysis centers provide BDS orbit products. Among these, Europe CODE provides orbits of BDS IGSOs and MEOs, and German GFZ and Chinese Wuhan University provides orbits of total BDS GEOs, IGSOs, and MEOs. Preliminary orbit overlap and orbit comparison analysis for the orbit products provided by these three institutions show that 3D orbit accuracies of BDS satellites are around 1–5 m for GEOs and 20 cm for IGSOs and MEOs, in which accuracies are all significantly higher than orbits provided by regional BDS network. The orbit products provided by Wuhan University last longer than the other two centers, so we take orbits of MGEX Wuhan University as reference orbits in this work [7].

2.2 Comparison Results

The orbits provided by regional network and Wuhan University during whole 2013 and 2014 are compared. The evaluation indices include radial (R) accuracy, transverse (T) accuracy, normal (N) accuracy, 3D position accuracy, and user range error (URE). Detailed results are listed in Table 1, in which the comparisons are

Table 1 Statistics of orbit comparisons

Sat type	Sat code	Orbit comparison/cm				
		R	T	N	3D pos	URE
GEO	C01	39.7	2664.0	92.6	2665.9	243.2
	C02	37.0	844.6	59.4	847.4	84.7
	C03	35.6	322.9	73.6	333.1	46.4
	C04	36.5	981.9	94.4	987.1	96.0
	C05	39.1	376.8	74.2	386.1	52.2
	mean[a]	37.1	631.6	75.4	638.4	69.8
IGSO	C06	29.3	113.6	94.9	150.9	32.2
	C07	30.1	95.5	87.0	132.6	32.3
	C08	32.2	111.9	113.2	162.4	35.3
	C09	28.0	107.0	82.3	137.9	30.6
	C10	31.2	106.9	83.3	139.1	33.5
	mean	30.2	107.0	92.1	144.6	32.8
MEO	C11	19.3	77.3	52.2	95.3	23.2
	C12	21.5	81.7	52.2	99.3	25.3
	C13	16.6	72.7	48.9	89.2	20.5
	C14	17.9	73.1	46.8	88.6	21.5
	mean	18.8	76.2	50.0	93.1	22.6

[a] The results of C01 are excluded from statistics

implemented not only in the visible scopes of regional network but in the whole orbits. In this table the values of C01 satellite are excluded from GEOs statistics because of its large deviation from other GEOs.

It is obvious that orbit errors are biggest in T direction and smallest in R direction. The radial errors of GEOs, IGSOs, and MEOs are around 0.4, 0.3, and 0.2 m, respectively. The orbit errors of GEOs are biggest, which attribute to their most poor and almost fixed observational geometry. Such geometry leads to strong correlation between orbit determination and clock estimation, and thus affects the orbit precision and stability seriously. The T direction accuracy of C01 in Table 1 is exceptionally low, which is possibly relevant to the radio phase center difference between its nominal value adopted in our analysis and its estimated value adopted by Wuhan University in the case of vulnerable geometric covering.

Figures 1, 2, and 3 illustrate the details of radial position comparison of GEOs, IGSOs, and MEOs. The red line in each sub-figure (scale in the right side of Y axis) show the elevation of Sun relative to satellite orbit plane (β angle). The shallow gray zone means the satellite is n. In the dark gray zones of Figs. 2 and 3, the β angle are less than 4°, in which the satellites' attitudes will convert into orbit normal (yaw-fixing) modes from usual yaw-steering modes.

Frequent orbit maneuvers should apply to GEOs for the maintenance of sub-satellite point' longitudes. Every maneuver could cause several-day lack of precise orbit. Week negative correlation seems appear between orbit difference and solar β angle in Fig. 1. Dramatic accuracy degeneration or even interruption of orbit will happen when β angle is close to zero.

It is shown in Figs. 2 and 3 that for IGSOs and MEOs, the orbit accuracy may be higher when solar β angle is larger. The orbit accuracy usually degenerates during eclipse season. While the satellite has converted into or approaches to yaw-fixing

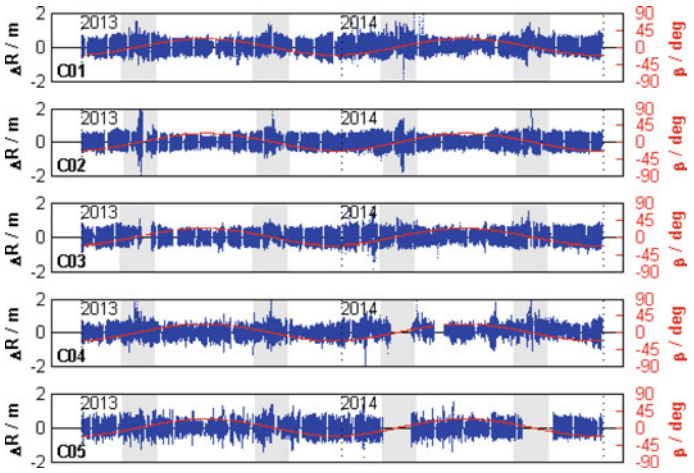

Fig. 1 Radial comparisons of BDS GEO orbits

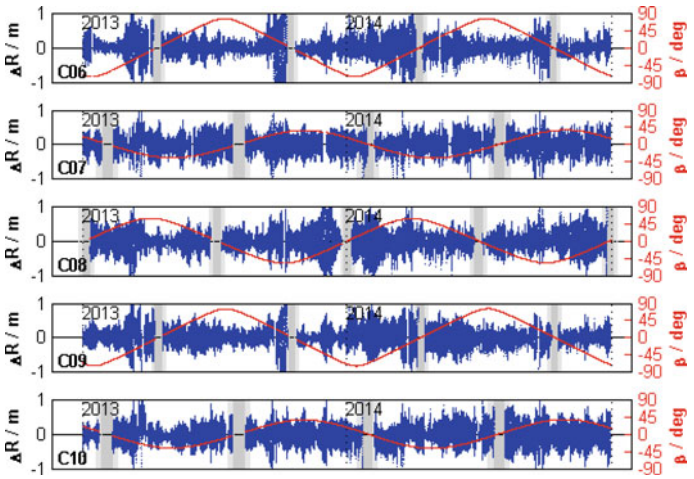

Fig. 2 Radial comparisons of BDS IGSO orbits

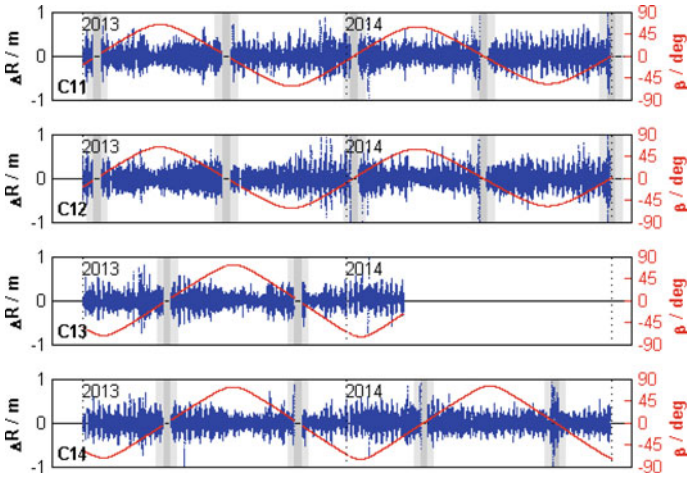

Fig. 3 Radial comparisons of BDS MEO orbits

mode, dramatic accuracy degeneration or even interruption of orbit is possible to occur.

Further detailed survey on Figs. 2 and 3 cannot reveal simple negative correlation between orbit accuracy and solar β angle. It is possible to experience rapid varying process of orbit accuracy during slowly varying process of β angle. The orbit accuracy shows some quasi-wave packet structure. This is possible to relate to parameter estimation of SRP model. Because β angle is taken as SRP parameter in basic frequency item and multiple frequency items, and during the SRP parameter estimation, the effects of these frequency items are involved in orbits.

3 SLR Validation

3.1 SLR Observation

For navigation satellites, SLR is the unique high precision measurement independent to radio carrier phase measurement, and has been taken as an important orbit validation approach [8, 9].

Several satellites in BDS have been taken as international SLR monitoring. Fairly large amounts of SLR tracking data have been gained for one BeiDou GEO (G1, i.e., C01), two BeiDou IGSOs (I3, i.e., C08 and I5, i.e., C10), and one BeiDou MEO (M3, i.e., C11) from 2012. Current global ILRS tracking network consists of around 40 ground stations, which geographical distribution is shown in Fig. 4. On the basis of historical statistics, the observation in 14 stations illustrates the characters of large amount and high performance, so these 14 stations are selected as core stations, which are marked by asterisk symbols in Fig. 4. For BDS, among all core stations, Australian Yarragadee and Chinese Changchun occupy most of observation data, which account for more than 90 % of global sum.

3.2 Validation Results

The orbits provided by regional network are validated by all observation provided by global SLR monitoring network. The precision of tropospheric model correction

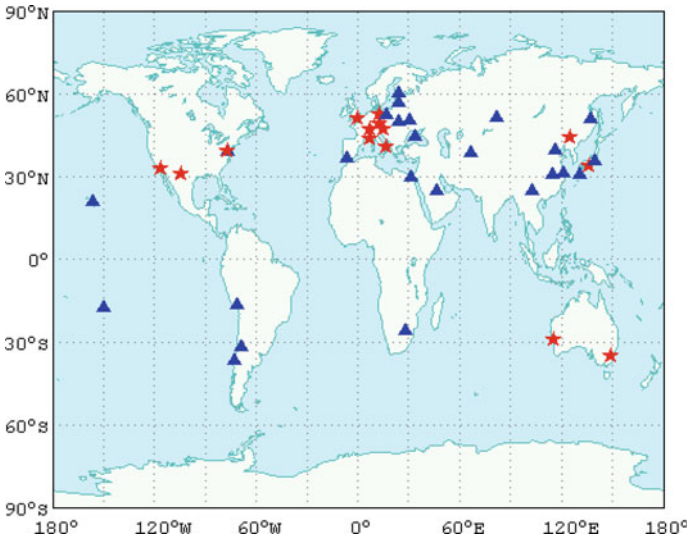

Fig. 4 Global distribution of SLR tracking network

Table 2 Statistics of SLR validation

Sat type	Sat code	Cut-off elevation 20°			Cut-off elevation 60°		
		Points	Mean/cm	RMS/cm	Points	Mean/cm	RMS/cm
GEO	C01	1829	6.3	64.7	–	–	–
IGSO	C08	1820	−18.4	32.8	935	−16.6	29.7
	C10	4306	−14.3	31.0	495	−12.8	25.4
MEO	C11	4913	−0.2	22.2	1767	3.5	18.1

in SLR validation is relevant to observational elevation, so the statistics for cut-off elevation 20° and 60° are carried out separately. The ejection criterion for gross error is 1 m. Table 2 summarizes the bias and dispersion of SLR validation for all core stations.

It can be seen from Table 2 that RMS values of SLR validation show certain degree of reduction when the cut-off elevation increases from 20° to 60°. SLR validation residuals come from orbit error components along satellite–station line of sight, of which majority are orbit radial errors, but the influence of orbit transverse errors and normal errors also involved in the residuals. As shown in Table 1, significant transverse errors and normal errors exist in all satellites. With the increasing of observational elevation, the effects of transverse and normal components decrease, so the RMS values of SLR validation become a bit smaller.

For GEOs, IGSOs and MEOs, RMS values of residuals are around 0.6, 0.3, and 0.3 m. Restricted by the geometrical conditions of the regional network, the observational elevation for C01 is only around 40°, which leads to big value of RMS.

The temporal distributions of SLR validation residuals of these four satellites are illustrated in Figs. 5, 6, 7, and 8. No significant variation of residuals appears along

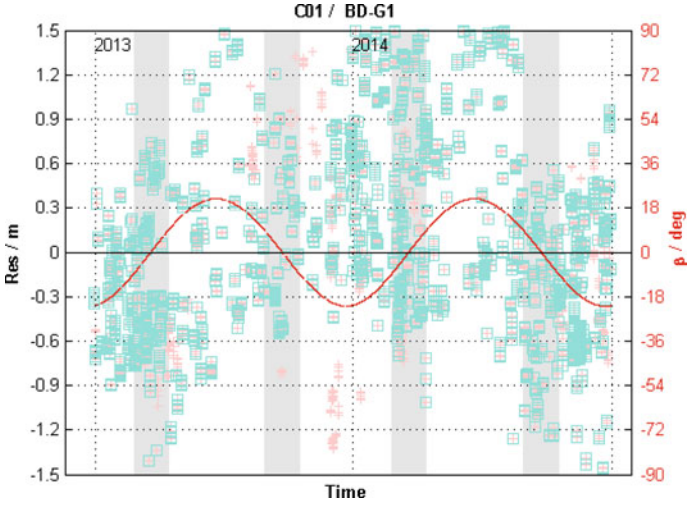

Fig. 5 SLR validation sequence of C01 (GEO) orbit

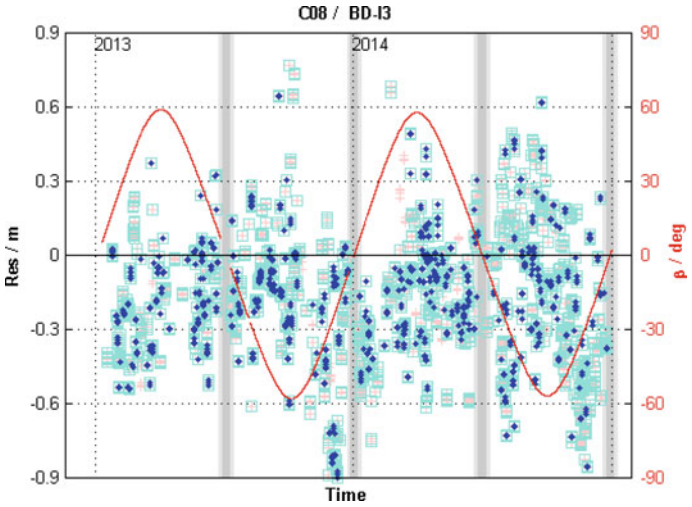

Fig. 6 SLR validation sequence of C08 (IGSO) orbit

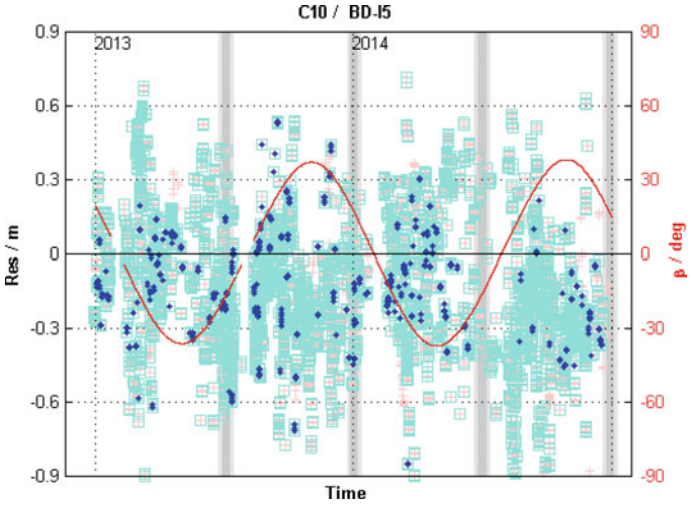

Fig. 7 SLR validation sequence of C10 (IGSO) orbit

with the variation of solar β angle. This is one of BDS' distinctive features because significant negative correlation between residual dispersion and β angle can been seen in GPS and Galileo systems.

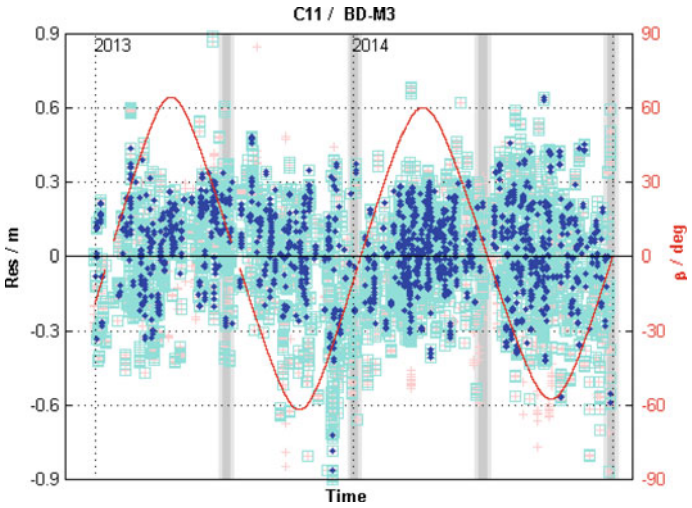

Fig. 8 SLR validation sequence of C11 (MEO) orbit

4 Summary

The accuracies of 2-year orbits from 2013 to 2014 provided by BDS regional network are evaluated by orbit comparison and SLR validation. The main results are as follows:

1. The comparisons with MGEX Wuhan University orbits show, for GEOs, that the 3D orbit accuracies are slightly better than 10 m, and the radial accuracies are around 0.4 m; for IGSOs, the 3D orbit accuracies are around 1–2 m, and the radial accuracies are around 0.3 m; for MEOs, the 3D orbit accuracies are better than 1 m, and the radial accuracies are better than 0.2 m. No significant negative correlation relation exists between orbit accuracy and solar elevation relative to orbit plane, which is different from GPS and Galileo satellites. Orbit accuracies degenerate during eclipse season or attitude mode change.
2. SLR validation accuracies of GEO/IGSO/MEO orbits of regional network are 0.6, 0.3, and 0.2 m, respectively, which are roughly equivalent to orbit radial accuracies. Orbit transverse and normal errors also throw certain effects on validation accuracies.

The evaluations of regional network orbits illustrate that BDSs contain different characters from GPS and Galileo satellites. Further dynamic models and estimation strategy suitable for BDS should be developed.

References

1. Bar-Sever Y (1996) A new model for GPS yaw attitude. J Geodesy 70(1):714–723
2. Springer T, Beutler G, Rothacher M (1999) Improving the orbit estimates of GPS satellites. J Geodesy 73(3):147–157
3. Montenbruck O, Steigenberger P, Hugentobler U (2015) Enhanced solar radiation pressure modeling for Galileo satellites. J Geodesy 89:283–297
4. Rizos C, Montenbruck O, Weber R et al (2013) The IGS MGEX experiment as a milestone for a comprehensive multi-GNSS service. In: Proceedings of the ION 2013 Pacific PNT meeting, pp 289–295, Honolulu, USA, 2013
5. Zhou S, Hu X, Wu B et al (2011) Orbit determination and time synchronization for a GEO/IGSO satellite navigation constellation with regional tracking network. Sci China 54 (6):1089–1097
6. Dach R, Montenbruck O, Prange L (2014) Status of the IGS-MGEX project. In: EUREF symposium, Vilnius, Lithuania, 2014
7. Wang B, Lou Y, Liu J et al (2015) Analysis of BDS satellite clocks in orbit. GPS Solution. doi:10.1007/s10291-015-0488-7
8. Urschl C, Beutler G, Gurtner W et al (2007) Contribution of SLR tracking data to GNSS orbit determination. Adv Space Res 39:1515–1523
9. Montenbruck O, Steigenberger P, Kirchner G (2013) GNSS satellite orbit validation using satellite laser ranging. In: Proceedings of 18th ILRS workshop on laser ranging, Fujiyoshida, Japan, 2013

High Precision Determining and Predicting of Earth Orientation Parameters for Supporting Spacecraft Navigation

Lue Chen, Geshi Tang, Jing Sun, Songjie Hu and Weitao Lu

Abstract Earth Orientation Parameters (EOP) are essential for spacecraft navigation missions, such as deep space navigation and GNSS navigation mission, directly affecting navigation accuracy of spacecraft. First, this paper introduces the theories of EOP determination based on VLBI and EOP prediction in Beijing Aerospace Control Center (BACC), with some new data processing methods and strategies. The systems of EOP determination and prediction in BACC, consisting of VieVS and EOPS software (EOPS), could provide daily products of EOP determination and prediction. Then, The EOP determination products in BACC are compared with the products of International Earth Rotation and Reference Systems Service (IERS) and International GNSS Service (IGS). The EOP prediction products in BACC are compared with the products of IERS, United States Naval Observatory, (USNO) and EOP_PCC. The determination standard deviation of Earth polar motion x-component (PMX) is lower than 0.2 mas, Earth polar motion y-component (PMY) is lower than 0.3 mas, UT1-UTC is lower than 0.02 ms, and the determination accuracy is at the same level of the products of IERS and IGS. Meanwhile, the short-term prediction error of PMX/PMY/UT1-UTC is a little lower than EOP_PCC, and is at the same level of IERS and USNO. These compared results show that EOP products in BACC with high precision could effectively meet the requirement of spacecraft navigation mission. Finally, EOP prediction products in BACC were successfully applied on China's first reentry return flight test mission to support spacecraft's navigation.

Keywords EOP determination · EOP prediction · VLBI · Compared accuracy · China reentry return flight test mission

L. Chen (✉) · G. Tang · J. Sun · S. Hu · W. Lu
National Key Laboratory of Science and Technology on Aerospace Flight Dynamics, Beijing Aerospace Control Center, No. 120, Box 5130 Haidian District Beijing, China
e-mail: luechen0912@163.com

© Springer Science+Business Media Singapore 2016

J. Sun et al. (eds.), *China Satellite Navigation Conference (CSNC) 2016 Proceedings: Volume III*, Lecture Notes in Electrical Engineering 390,
DOI 10.1007/978-981-10-0940-2_22

1 Introduction

Earth orientation parameters (EOP) consist of UT1-UTC, the difference between UT1 (Universal time) and UTC (Coordinated Universal time), polar motion coefficients (PMX, PMY) describing the movement of the Earth's rotation axis to the crust, precession, and nutation [1]. EOP is essential for the transformation of the international terrestrial reference system (ITRS) and the international celestial reference system (ICRS) [2, 3]. EOP has been determined by advanced space geodetic techniques, including SLR, VLBI, GNSS, etc. [4].

The accuracy of EOP determination and prediction directly affects the accuracy of the spacecrafts' orbit measurement and determination. For example, Error in UT1-UTC of 0.1 ms produces an error of 7 nrad in spacecraft right ascension, corresponding to a position error at Mars of 1.6 km [1]. Particularly, high precision determination and prediction of EOP plays the very important role in real-time or quasi-realtime navigation mission.

Geodetic very long baseline interferometry (VLBI) is one of the primary space geodetic techniques providing the full set of Earth Orientation Parameter (EOP) and it is unique for observing long term Universal Time (UT1) and nutation [5]. On the one hand, this paper introduces determining EOP based on VLBI observations in BACC, utilizing VieVS VLBI analysis software, which is developed by Vienna University of Technology. On the other hand, this paper introduces a prediction method of EOP by dual differential least-squares (DDLS) and autoregressive (AR) model (DDLS + AR) [6, 7]. EOP prediction software is developed in BACC, which is called EOP Prediction Software (EOPS) [8]. EOPS could provide daily EOP prediction products automatically.

Then, the determining results of EOP are compared with IERS and IGS results, the prediction results of EOP are compared with IERS, USNO and EOP_PCC results. Finally, the determination and prediction products of EOP were successfully applied on China's first reentry return flight test of lunar exploration (CE-5T1) mission, to support CE-5T1 spacecraft high precision orbit measurement and determination.

2 The Theory of EOP Determining and Predicting

2.1 EOP Determining Method Based on VLBI

EOP determination based on VLBI observation is utilizing the least-squares estimation method [8], the calculation procedure is shown as follows.

The VLBI observation equation is shown in Formula (1) [9].

$$O_t = C(X, t) + V_t \tag{1}$$

where O_t is the obtained delay observation at the time of t, X is the parameter vector related to delay observation. $C(X, t)$ is mathematical model of X, which is also called the theoretical value. V_t is the noise vector. It assumes that X consists of prior value x_0 and correction value x. Thus, the linearization of Formula (1) is shown in Formula (2).

$$O_t = C(x_0, t) + \frac{\partial(X, t)}{\partial X}|_{x_0} \cdot x + V_t \tag{2}$$

Then,

$$y_t = A_t x_t + V_t \tag{3}$$

where $y_t = O_t - C(x_0, t)$, it means the difference of observation value and theoretical value at the time t. A_t is partial derivative matrix.

Then, Formula (3) is expressed in the way of vector, shown in Formula (4).

$$Y = Ax + V \tag{4}$$

Assuming that the observation weight matrix is P_0, the correction value is x, obtained by least-squares method, is shown in Formula (5).

$$x = \left(A^T P_0 A\right)^{-1} P_0 A^T Y \tag{5}$$

In VLBI observation, delay measurement observation $\Delta\tau$ instead of $C(X, t)$ for EOP determining [9], which is shown in Formula (6). The EOP determining procedure follows from Formula (1) to Formula (5).

$$\Delta\tau = -(PNSW\Delta r \cdot \mu) + \Delta\tau_p + (a_{20} - a_{10}) + (a_{21} - a_{11})(t - t_0) \tag{6}$$

where P is precession matrix, N is nutation matrix, S is diurnal rotation matrix, and W is polar motion matrix. (a_{10}, a_{11}) and (a_{20}, a_{21}) are clock error and clock rate in VLBI Station 1 and Station 2.

2.2 2EOP Predicting Method

2.2.1 Dual Differential Preprocessing of the Raw EOP

As to EOP preprocessing, there are some differences of dual differential processing between polar motion and UT1-UTC. Polar motion data could do the direct dual differential processing, yet UT1-UTC data should remove leap seconds and tide correction before dual differential processing. Then, the dual differential processing procedure is shown in Formula (7).

$$\Delta^2 x_t = \Delta(\Delta x) = \Delta x_{t+1} - \Delta x_t = x_{t+2} - 2x_{t+1} + x_t \tag{7}$$

where x_t means the time sequences of EOP, Δ means differential processing.

2.2.2 Least-Squares Method

The dual differential results of EOP could be calculated by Least-squares method shown in Formula (8), it contains linear term and periodic term. For UT1-UTC prediction, the periodic term contains annual, half of a year, 9.3 year, 18.6 year, etc. [10]. For PMX and PMY, the periodic term contains Chandler wobbles, annual, half of a year, third of a year, etc. [6, 7].

$$\begin{aligned} X(t) = A + Bt + Ct^2 + D_1 \cos\left(\frac{2\pi t}{p_1}\right) + D_2 \sin\left(\frac{2\pi t}{p_1}\right) \\ + E_1 \cos\left(\frac{2\pi t}{p_2}\right) + E_2 \sin\left(\frac{2\pi t}{p_2}\right) + \cdots \end{aligned} \tag{8}$$

where, t is UTC time (unit is year). $A, B, C, D_1, D_2, E_1, E_2, \ldots$ are the fitting parameters, $p_1, p_2, \ldots$ are the fitting periods, which could be determined by prior experience.

2.2.3 AR Model

For a stationary sequence $x_t (t = 1, 2, \ldots, N)$, the AR model is expressed as follows [11]

$$x_t = \varphi_1 x_{t-1} + \varphi_2 x_{t-2} + \cdots + \varphi_p x_{t-p} + a_t = \sum_{i=1}^{P} \varphi_i x_{t-i} + a_t \tag{9}$$

where $\varphi_1, \varphi_1, \ldots, \varphi_p$ are model parameters, a_t is white noise, p is model order. Formula (9) is called p order AR model, denoted by AR(p). $a_t \sim N\left(0, \sigma_n^2\right)$, σ_n^2 is the variance of the white noise.

This paper utilizes FPE criterion for determining AR model order. FPE criterion function [10] is shown in Formula (10). The best AR model order is determined by loop search from 1 to 200, and the best AR model has the lowest FPE value.

$$FPE(p) = \frac{N+p}{N-p}\sigma_n^2 \tag{10}$$

2.2.4 Inverse Dual Differential Processing

After least-squares and AR processing of EOP, the inverse dual differential calculation should be done to get the final EOP production results, shown in Formula (11) and Formula (12).

$$\hat{x}_{N+1} = x_N + \Delta x_{N-1} + \Delta^2 \hat{x}_1 \tag{11}$$

$$\hat{x}_{N+i} = \hat{x}_{N+i-1} + \Delta \hat{x}_{N+i-2} + \Delta^2 \hat{x}_i (i = 2 : M) \tag{12}$$

where N is the length of raw EOP, M is the prediction steps of EOP, $\hat{x}$ means prediction results of EOP.

2.2.5 EOP Prediction Error Estimates

Mean absolute error (MAE) is used for evaluating the prediction performance of EOP [10], shown in Formula (13).

$$\mathrm{MAE}_i = \frac{1}{n} \sum_{j=1}^{n} \left(\left| p_j^i - o_j^i \right| \right) \tag{13}$$

where o is the real observation, p is prediction value, i is prediction day, n is prediction number.

3 EOP Results Comparing

3.1 Comparison of EOP Determination Results

In order to evaluate the performance of EOP determination, EOP products of BACC are compared with other international organization's EOP products, IERS EOP products, and IGS EOP products. The Vienna VLBI Software (VieVS) [12, 13] is a new state of the art VLBI analysis software written in MATLAB, this software is utilized to determine EOP based on VLBI observation in BACC. The researcher of BACC participated in the development of VieVS [14]. The raw VLBI observation results are gotten from international VLBI service for geodesy and astrometry (IVS) database, which is from Jan. 1, 2015 to Oct. 31, 2015.

EOP calculation strategy includes VLBI station selection based on geometric baseline, clock jump detection and removal in VLBI station, outlier detection and removal, integral time setting, calculation parameters determination, etc. Meanwhile, lots of model parameters need to be set, such as reference frames,

ephemerides, troposphere, ionosphere, station models, source structure, etc. These parameters setting could be found in VieVS manual [15].

IVS organizes two times conventional VLBI observation every week for EOP monitoring by global VLBI stations. Meanwhile, BACC has developed MATLAB code for conveniently comparing different EOP products, such as EOP of IERS, IGS, and BACC.

EOP products calculated by VieVS are shown in Fig. 1, these are PMX, PMY, and UT1-UTC products. In Fig. 2, the above is IERS results, the middle is BACC results, the underside is IGS results. IERS results is EOP 08 C04 final products, IGS results is IGS final products. The difference value of EOP determination results among BACC, IERS, IGS is shown in Fig. 2. From these figures, these are shown that BACC EOP determination results are mostly identical to IERS and IGS, the numerical compared results are shown in Table 1. The standard deviation of PMX between BACC and IERS is lower than 0.2 mas, the standard deviation of PMY is lower than 0.3 mas, the standard deviation of UT1-UTC is lower than 0.02 ms. This validates the EOP products based on VLBI have high precision results.

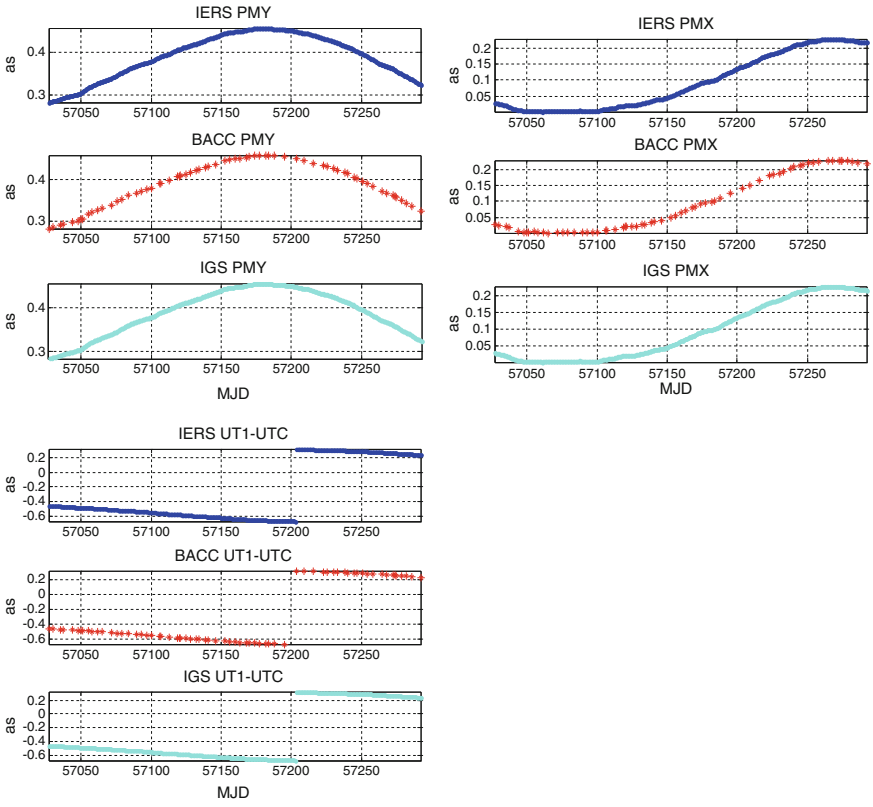

Fig. 1 EOP determination results (PMX/PMY/UT1-UTC) in BACC compared with IERS/IGS

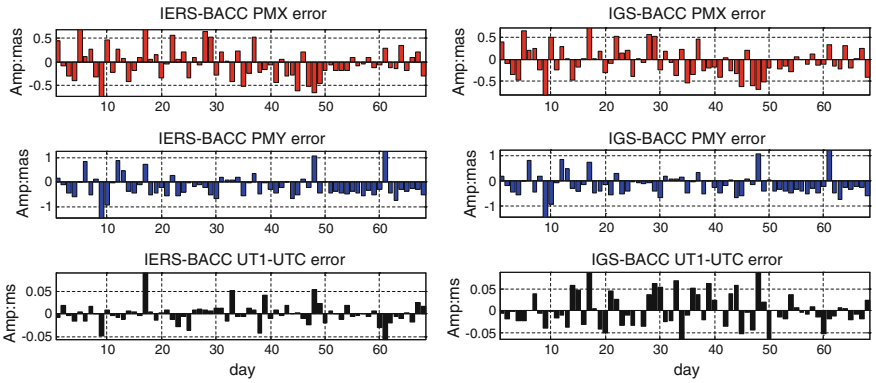

Fig. 2 EOP determination error among BACC/IERS/IGS

Table 1 The error of EOP compare results among BACC/IERS/IGS

EOP	IERS-BACC error (rms)	IGS-BACC error (rms)
PMX (mas)	0.194	0.197
PMY (mas)	0.289	0.294
UT1-UTC (ms)	0.0163	0.0222

3.2 Comparison of EOP Prediction Results

EOP_PCC is the Earth orientation parameters prediction comparison campaign [2], whose aim is comparing EOP prediction performance by different prediction methods. This paper takes UT1-UTC prediction for example to verify EOP prediction performance in BACC. This paper compared EOP_PCC UT1-UTC results with BACC UT1-UTC results [8] in ultra short term prediction (10 days) and short term prediction (30 days), the same UT1-UTC data inputs were utilized. UT1-UTC prediction results are, respectively, shown in Figs. 3 and 4.

From the above figures, it is shown that UT1-UTC prediction error in BACC is lower than EOP_PCC. 1 day prediction error of UT1-UTC in BACC is lower than 0.03 ms, but EOP_PCC minimum 1 day prediction error is at the level of 0.08 ms for UT1-UTC [2]. 30 day prediction error in BACC is lower than 2.5 ms, 30 day prediction error in EOP_PCC is a little larger than 3 ms.

In order to gain daily products of EOP, BACC developed EOP prediction software (EOPS) [8], which could provide daily EOP prediction products automatically. Utilizing EOPS to produce EOP prediction products, the statistical error of EOP prediction in 2015, is shown in Fig. 5 and Table 2.

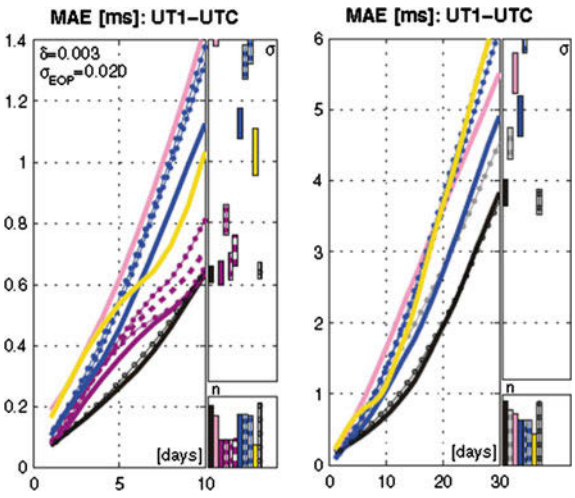

Fig. 3 Short term prediction results of UT1-UTC in EOP_PCC

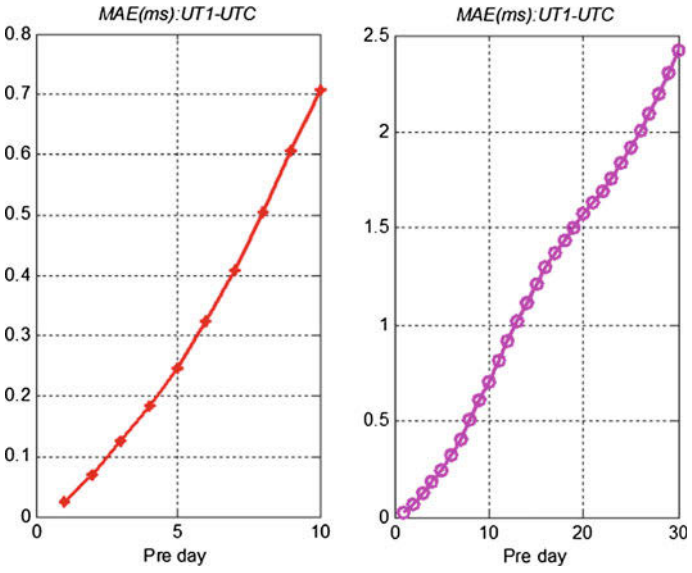

Fig. 4 Short term prediction results of UT1-UTC in BACC

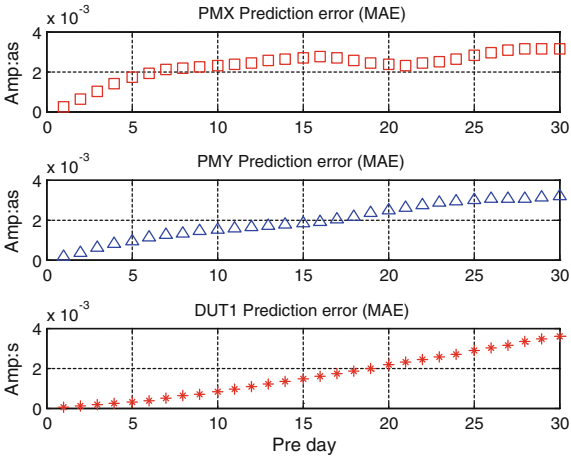

Fig. 5 EOP prediction error in 2015

Table 2 EOP prediction error in 2015

Pre day	PMX pre error (mas)	PMY pre error (mas)	UT1-UTC pre error (ms)
1	0.205	0.179	0.046
5	1.71	0.967	0.291
10	2.28	1.52	0.818
20	2.35	2.47	2.13
30	3.14	3.18	3.58

4 EOP Products Application on Spacecraft Navigation Mission

EOP is the basic data for spacecraft navigation missions. CE-5T1 Mission was successfully implemented from Oct. 24, 2014 to Nov. 1, 2014, which is the first reentry return flight test mission in China, for validating corresponding key technologies for China's lunar sample return mission [16]. EOP prediction results were important for CE-5T1 orbit measurement and determination system.

In CE-5T1 mission, EOP prediction products gained from EOPS were applied to CE-5T1 interferometry measurement mission and orbit determination mission. EOP prediction products error in BACC compared with the products of IERS and USNO is shown in Figs. 6, 7 and 8.

From the above compared figures, it could be concluded that EOP prediction results in BACC were mostly identical to IERS and USNO with a high precision

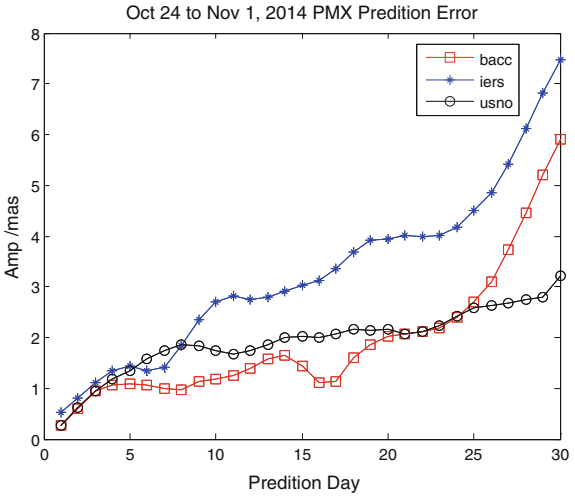

Fig. 6 PMX prediction error of BACC/IERS/USNO in CE-5T1mission

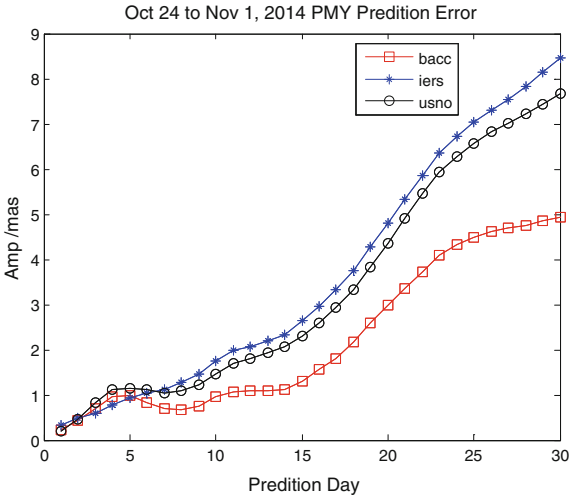

Fig. 7 PMY prediction error of BACC/IERS/USNO in CE-5T1mission

prediction accuracy, and the EOP prediction results of BACC in CE-5T1 mission were very effective for supporting CE-5T1 spacecraft's orbit measurement and determination.

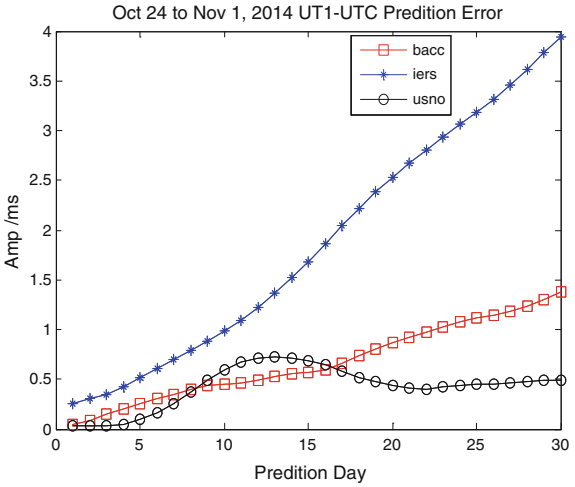

Fig. 8 UT1-UTC prediction error of BACC/IERS/USNO in CE-5T1mission

5 Conclusion

EOP determination results of BACC are quite coincident with the results of IERS and IGS. Compared with BACC results and IERS results, the standard deviation of PMX is lower than 0.2 mas, the standard deviation of PMY is lower than 0.3 mas, the standard deviation of UT1-UTC is lower than 0.02 ms. EOP short term prediction error in BACC is a little lower than EOP_PCC. EOP prediction products which were gained from EOPS were effectively applied to China's CE-5T1 mission for spacecraft navigation. Thus EOP products in BACC could effectively contribute to support China's future spacecraft navigation missions.

Acknowledgements The authors offer our sincere appreciation for BACC iGMAS Analysis Center, IERS, IGS, USNO and EOP_PCC providing EOP products, for IVS providing raw VLBI observations. This work is supported by Equipment Development Foundation (No.9140A24070915 KG13377) and National Nature Science Foundation of China (No. 61304233).

References

1. Vallado DA, Kelso TS (2013) Earth orientation parameter and space weather data for flight operations. A the 23rd AAS/AIAA space flight mechanics meeting. South Carolina, America
2. Kalarus M, Schuh H, Kosek W et al (2010) Achievements of the earth orientation parameters prediction comparison campaign. J Geodyn 62:587–596
3. Nilsson T, Heinkelmann R, Karbon M et al (2014) Earth orientation parameters estimated from VLBI during the CONT11 campaign. J Geodesy 88:491–502
4. Zhang Z, Wang G, Liu X et al (2013) Analysis of EOP determination via Chinese VLBI network. Geomatics Inf Sci Wuhan Univ 38(8):911–915
5. Schuh H, Behrend D (2012) VLBI: a fascinating technique for geodesy and astrometry. J Geodyn 61:68–80

6. Chen L, Tang G, Hu S et al (2014) High accuracy differential prediction of UT1-UTC. J Deep Space Explor 1(3):173–178
7. Chen L, Tang G, Hu S et al (2014) Earth polar motion parameters high accuracy differential prediction. In: Proceeding of the 27th conference of spacecraft TT&C technology in China. Guang Zhou, China
8. Chen L, Tang G, Hu S et al (2015) Determining and predicting UT1-UTC to support China's interplanetary spacecraft navigation. In: 25th international symposium on space flight dynamics ISSFD. Munich, Germany
9. Li Y, Wei E, Wang Z (2010) Space geodesy
10. Xu X, Zhou Y, Liao X (2010) Short-term earth orientation parameters predictions by combination of the least-squares, AR model and Kalman filter. J Geodyn 62:83–86
11. Yang S (2007) Time series analysis in engineering application
12. Sun J, Böhm J, Nilsson T et al (2014) New VLBI2010 scheduling strategies and implications on the terrestrial reference frames. J Geodyn 88:449–461
13. http://vievs.geo.tuwien.ac.at/doku.php
14. Sun J (2013) VLBI scheduling strategies with respect to VLBI2010. Ph.D. thesis. Department of Geodesy and Geoinformation, Vienna University of Technology, Vienna
15. User Manual (2010) The Vienna VLBI software (VieVS) version 1c
16. Liu L, Tang G, Hu S et al (2015) Follow-up flight for the reentry test of China lunar exporation. J Astronaut 36(1):9–17

Part II
BDS/GNSS Precise Positioning Technology

A New Subregional Ionosphere Grid Correction Method Based on Kriging Interpolation and Result Analysis

Wen Li, Hong Yuan, Zishen Li and Xiaokun Zhang

Abstract The correction effect of ionosphere delay is a crucial factor in determining availability, accuracy, reliability, and other key performance indicators of satellite navigation and positioning services. To meet the demands of single frequency and high accuracy users for ionosphere correction, a new subregional ionosphere grid correction method based on Kriging interpolation is proposed in this paper and is further realized with an integrated software program of both server end and client end algorithms. Experiment with observation data from IGS stations in Europe shows that, with only eight reference stations, correction rate of the new method in all subregions can reach about 80–90 %, similar to or even better than that of grid ionosphere maps provided by CODE. So the new method has obvious advantage in comprehensive consideration of correction efficiency and effect, which can serve as important reference for the establishment of ionospheric model in PPP, wide area differential, and regional augmentation systems.

Keywords Ionosphere augmentation model · Kriging interpolation · Subregional ionosphere correction · Grid ionosphere correction

1 Introduction

Ionosphere delay is one of the most important unneglectable main error sources in satellite navigation and positioning systems. Currently, the major basic satellite navigation systems all provide users with broadcast ionosphere correction model in their navigation message. The correction effect, always limited and not very satisfactory, however, cannot meet the demands of users for higher accuracy [1].

W. Li (✉) · H. Yuan · Z. Li · X. Zhang
Academy of Opto-Electronics, Chinese Academy of Sciences,
100094 Beijing, China
e-mail: liwen2015@aoe.ac.cn

© Springer Science+Business Media Singapore 2016

J. Sun et al. (eds.), *China Satellite Navigation Conference (CSNC) 2016 Proceedings: Volume III*, Lecture Notes in Electrical Engineering 390,
DOI 10.1007/978-981-10-0940-2_23

With the development of GNSS, obtaining TEC value with data from various regional and small-area ground GNSS observation network and further establishing more accurate ionosphere correction models that suits the regional ionosphere distribution and variation characteristics or for the purpose of augmentation systems has become a hotspot issue. Many mathematical models and methods have been studied by domestic and overseas researchers with fruitful achievements [2–4].

This paper proposes a new subregional ionosphere grid correction method based on Kriging interpolation and a software program for the whole algorithm flow is established. Moreover, the real correction effect of this method is verified through comparison with that of GIM provided by CODE in Europe.

2 Fundamentals for Kriging Interpolation

2.1 Definition

In the Kriging method, also known as optimum space autocovariance interpolation method, specific weight is assigned to each sample value according to its space location and the degree of correlation with other samples and then the average value of central segment can be estimated through weighted moving average. From the mathematical perspective, it can provide an optimum linear and unbiased estimation for the study subject. So it can reflect the intrinsic characteristics of observation data satisfactorily, which largely owe to its full consideration of both the location correlation between the known and unknown points and the space relativity of the variable itself. Especially for data estimation issue with sparse sample points, the Kriging interpolation method demonstrates unique advantages [5].

Meanwhile, it is known that the ionosphere, as part of the Earth's spatial environment and an open, dynamic and complicated system itself, features distinct diversity in terms of distribution and variation patterns in different regions. This also leads to the fact that every ionosphere correction model has its certain scope of application and often presents different correction levels in different regions. So, how to describe and reflect ionosphere characteristics on a small scale and in a more accurate manner become a key restrictive factor and a difficult problem in this field.

However, it can be found from the above introduction that Kriging's advantage exactly fits the nature of ionosphere and demand for ionosphere modeling. Kriging interpolation is therefore adopted as a basic method in ionosphere estimation [6, 7]. Moreover, as an influential range is always needed in Kriging interpolation, the concept of subregional estimation is introduced. This is where the basic idea of the new subregional ionosphere grid correction algorithm based on Kriging interpolation comes from.

2.2 Methodology

Among the several common categories of Kriging interpolation, it is ordinary Kriging interpolation that is adopted in this paper. Here follows the basic process how it is carried out [8].

For regional variable $z(x)$, assume that the observation values on sample points $x_1, x_2, \ldots, x_n$ are $z(x_1), z(x_2), \ldots, z(x_n)$, respectively, then the value $z(x_0)$ on point x_0 can be estimated by a linear combination as

$$z(x_0) = \sum_{i=1}^{n} \lambda_i z(x_i) \tag{1}$$

where λ_i is weighted coefficient.

Also assume that $z(x)$ comply to intrinsic hypothesis, ordinary Kriging equations can be obtained as:

$$\begin{cases} \sum\limits_{i=1}^{n} \overline{\gamma}(x_i, x_j)\lambda_i + \mu = \overline{\gamma}(x_0, x_j) \quad (j = 1, \ldots, n) \\ \sum\limits_{i=1}^{n} \lambda_i = 1 \end{cases} \tag{2}$$

where $\overline{\gamma}(x_i, x_j)$ is the variogram function value between sample points x_i and y_i; μ is Lagrange constant;

Once the weighted coefficients λ_i are solved from Eq. 2, the estimated value $z(x_0)$ at grid point x_0 can be computed through Eq. 1. So, the key issue in Kriging interpolation lies in selection of theoretical model for the variogram $\overline{\gamma}$ and the model parameters estimation, also called the structural analysis issue for regional variables.

The measurement used for description of the spatial correlation between different points is semivariance, which can be calculated as:

$$\gamma(h) = \frac{1}{2n} \sum_{i=1}^{n} (z(x_i) - z(x_i + h))^2 \tag{3}$$

where h is the distance between two points; n is the number of pair of sample points separated by distance h; z is the attribute value of the corresponding point.

When all the semivariances are worked out for different h, the semi variograms can be plotted with distance and semivariance as the horizontal and vertical axis, respectively. In this algorithm, spherical model (as shown in Eq. 4) is selected as the theoretical variogram model.

$$\gamma(h) = \begin{cases} 0, h = 0 \\ c_0 + c(\frac{3h}{2a} - \frac{h^3}{2a^3}), 0 < h \leq a \\ c_0 + c, h > a \end{cases} \tag{4}$$

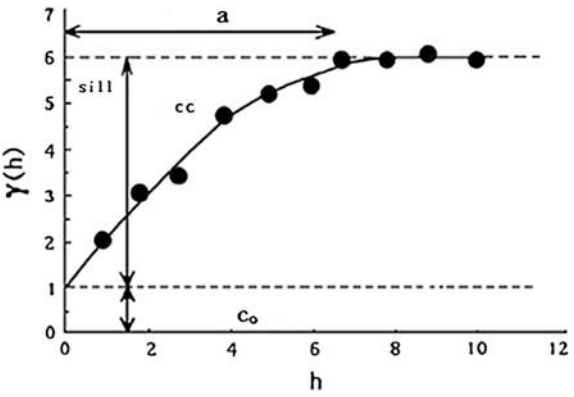

Fig. 1 Characteristic values for variogram function

where c_0 is the nugget value; c is the sill value; a is the range value. Details about these three key characteristic values for the variogram function are shown in Fig. 1.

3 The Subregional Ionosphere Grid Correction Algorithm Based on Kriging and Software Program Realization

The ionosphere correction method proposed in this paper mainly consists of two parts: the server end and the client end. In the software program developed for this algorithm, these two components share a common configuration file for input and output interface control (like data input, product/results output, etc.) and setting of basic information and key parameters (like time interval of ionosphere product, number and latitude/longitude range of subregions, product grid step width, etc.). A detailed flow chart of the software is given in Fig. 2.

The function of the server end is similar to that of the data processing center in a wide area differential system. First of all, preprocess is carried out for the observation data of selected reference stations, such as cycle slip detection and repair, so as to obtain fine observation data and information file of ionosphere pierce points; second, in accordance with the region dividing scheme in the configuration file, estimated VTEC values on target grid points are computed through ordinary Kriging interpolation within each relevant subregion; finally, grid VTEC maps of the whole region for each time interval are stored and displayed in the server end and grid VTEC file (in similar format with CODE GIM [9]) is stored and broadcasted to the users as the final product.

The client end of the software is mainly designed for verification of the accuracy and reliability of the product broadcast by the server end and evaluation of correction effect for the new algorithm. With the selected checking stations from each subregion in the configuration file taken as real users, product broadcast by the server end is used for ionosphere correction and real effects are analyzed. Through comparison between the observation computed VTEC value VTEC for each epoch

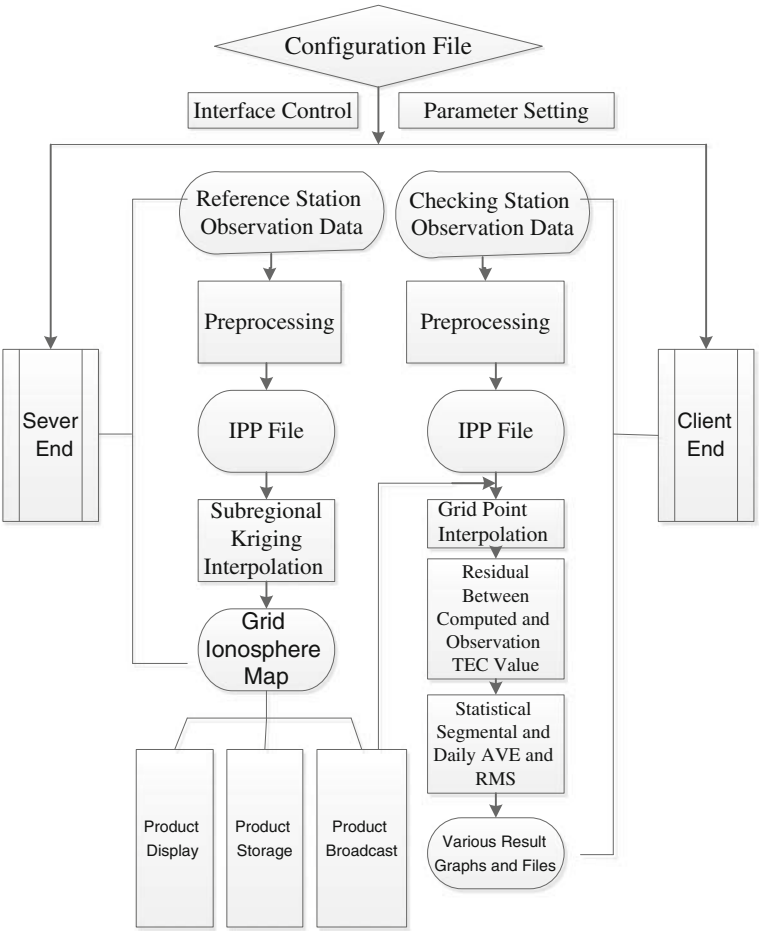

Fig. 2 Algorithm flow chart

and statistical indicators like average, root mean square, and correction rate for each time interval and a single day, various graph and file results (such as scatter time sequence diagram, bar graphs, etc.) are plotted and stored. So, the client end can give us an explicit and detailed reflection of the real correction results of this algorithm in each subregion.

4 Simulation Example

Observation data from IGS tracking stations in the European region are used in this section for verification and test of the algorithm and software program.

4.1 Data and Configuration Scheme

In the test, in consideration of the common relation between latitude and ionosphere variation characteristics, the European region is generally divided into three sub-regions: the mid-low latitude zone (30°N–45°N, 15°W–45°E); the mid-high zone (45°N–60°N, 15°W–45°E), and the high latitude zone (60°N-75°N, 15°W-45°E). There are eight reference stations and three checking stations, which are evenly distributed as shown in Fig. 3, selected for processing. While the IPP information of each epoch from the eight reference stations are used in ionosphere correction product generation, those of the three checking stations are adopted in verification of the actual correction results.

The sample rate of IGS observation data used in this paper is 30 s and the final product is resolved every half an hour. In the final ionosphere grid correction file, the grids are separated by 2.5° in latitude and 5° in longitude. However, in view of the display effect on the server end, the latitude and longitude spacing for grids in the grid ionosphere VTEC maps are both 1 degree.

As a reference, the Global Ionosphere Maps (GIMs) provided by the Center of Orbit Determination [10] in Europe are also introduced on the checking stations for its real correction effects and compared with products of the new algorithm. It should be noted that CODE adopted a 15 * 15 spherical harmonic function model and data from about 95 IGS tracking stations in the same research region (30°N–75°N, 15°W–45°E).

In order to judge the actual correction effect of ionosphere product, here we introduce correction ratio as:

$$\text{Correction Ratio} = \frac{\text{TEC}_{\text{truevalue}}}{\text{TEC}_{\text{computedvalue}}} \tag{5}$$

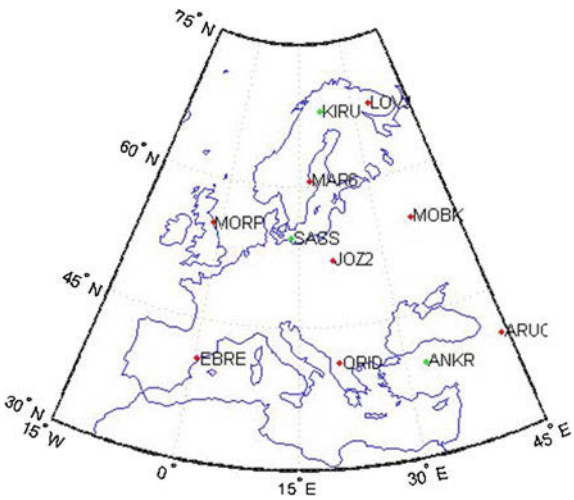

Fig. 3 Distribution of selected reference (*red dot*) and checking (*green dot*) stations in Europe (see color figure online)

4.2 Single-Day Results

Observation data on July 10 2015 (DOY 191) are used for processing according to the above-mentioned configuration scheme.

4.2.1 Server End Products

In the server end, there are 48 grid ionosphere VTEC maps for the European region in total (generated every half an hour), part of which are illustrated in Fig. 4, and also the final ionosphere grid correction file (in similar file naming and format conventions with GIM from CODE).

4.2.2 User End Results

In the user terminal, TEC residuals between the computed value and observation value of each observation epoch are calculated for each checking station. Moreover,

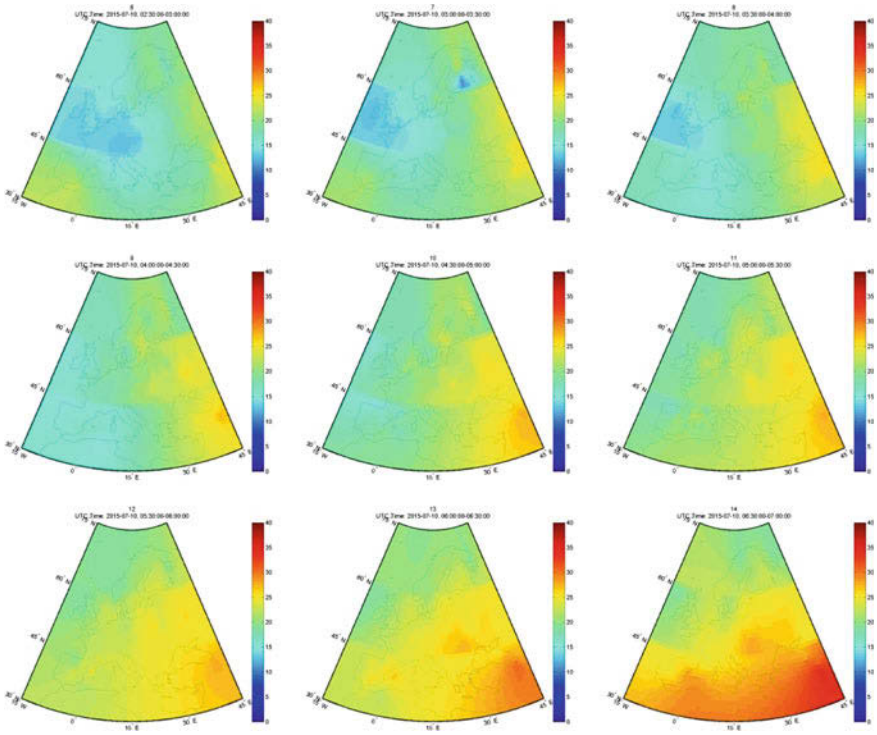

Fig. 4 Grid ionosphere VTEC map in Europe (July 10th 2015, UTC time 02:30:00–07:00:00)

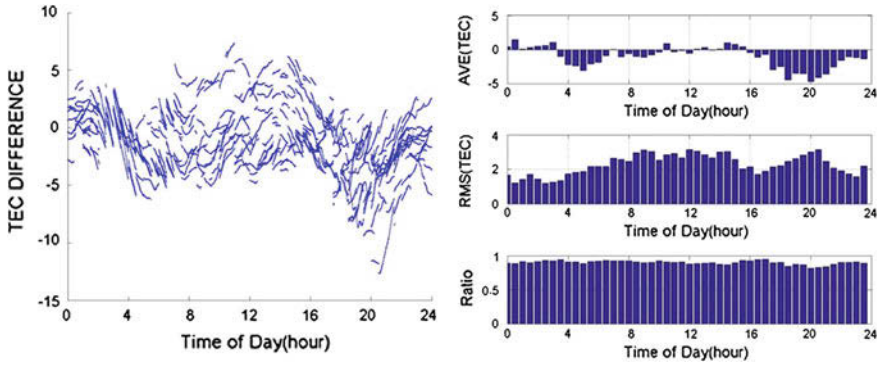

Fig. 5 VTEC residual time series and statistical bar graph on ANKR in mid-low latitude

crucial statistical indicators like TEC residual average and RMS, as well as TEC correction ratio are also given for each segment interval and the whole day in various graphs and files. Some results for station ANKR in the mid-low latitude region are shown in Fig. 5.

4.2.3 Comparison and Analysis

The detailed correction results of GIM provided by CODE on the checking stations can be found in Table 1.

It can be concluded that the correction effect of Kriging subregional interpolation method is equivalent to that of GIM, both of which are very satisfactory with ionosphere delay correction rate all above 90 % in the mid-low, mid-high, and high latitude regions.

4.3 Short Term Results

In order to demonstrate the effectiveness, reliability, and stability of the new algorithm over long time period, the program is deployed on a server for routine auto processing with the same configuration plan. The TEC residual average, RMS, and

Table 1 Correction results comparison on July 10 2015 (DOY 191) (Unit: TECU)

	ANKR			SASS			KIRU		
	AVE	RMS	Ratio	AVE	RMS	Ratio	AVE	RMS	Ratio
Krig	−1.06	2.03	0.91	0.08	1.36	0.94	0.03	2.02	0.90
GIM	0.86	2.26	0.90	0.14	1.46	0.93	0.57	1.85	0.90

Table 2 Statistical results on ANKR (Unit: TECU)

DOY	ANKR					
	Krig			GIM		
	AVE	RMS	Ratio	AVE	RMS	Ratio
223	−0.19	2.18	0.89	0.62	2.06	0.89
224	−0.29	2.03	0.90	0.15	1.99	0.90
225	−0.39	1.97	0.89	0.30	1.87	0.89
226	−0.46	1.51	0.88	0.61	1.41	0.89
227	−0.04	1.85	0.90	0.98	1.81	0.87
228	−0.40	1.77	0.87	0.59	1.65	0.86
229	−0.14	1.75	0.89	0.36	1.68	0.88
230	−0.00	1.88	0.85	0.58	1.86	0.85
231	−0.20	2.01	0.87	0.39	1.93	0.87
232	−0.11	1.77	0.89	0.85	1.67	0.88
233	−0.16	1.67	0.89	0.87	1.66	0.87
234	−0.28	1.67	0.89	0.65	1.67	0.87
235	−0.37	1.79	0.89	0.78	1.73	0.87
236	−0.55	1.82	0.87	0.53	1.71	0.88
237	−0.44	1.74	0.90	0.79	1.67	0.89
238	−0.51	1.78	0.88	0.82	1.75	0.86
239	−0.42	2.02	0.89	−0.36	1.97	0.89
240	−0.26	1.93	0.85	0.32	1.79	0.85
241	−0.34	1.74	0.84	0.57	1.71	0.83

correction rate results on the three selected checking stations from August 11 2015 (DOY 223) to September 5 2015 (DOY 248) are listed in Table 2, Figs. 6 and 7.

It can be seen that, generally speaking, the correction effect of the new algorithm is equivalent to or even better than that of GIM provided by CODE for the European region in this research; both methods have best correction results in the

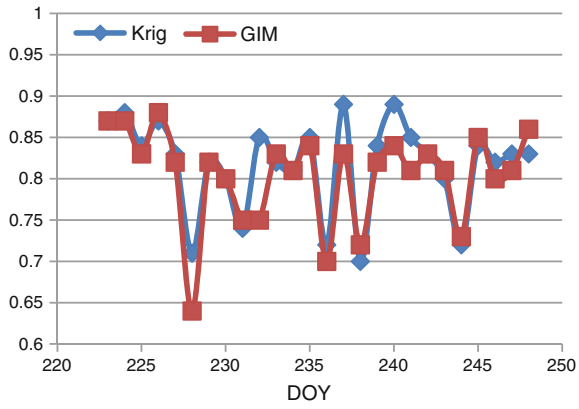

Fig. 6 Correction rate variation on SASS

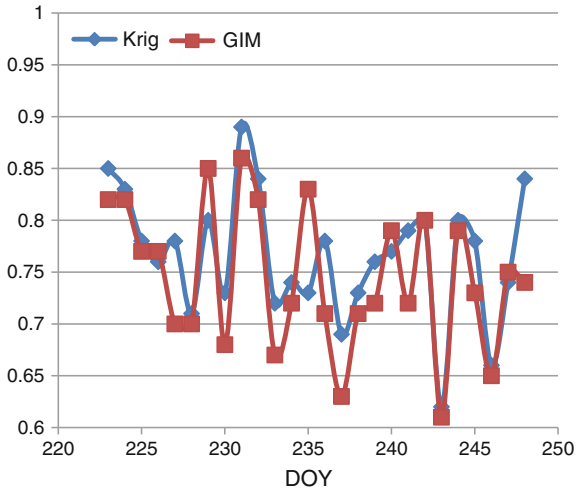

Fig. 7 Correction rate variation on KIRU

mid-low latitude region, while the effect deteriorates slightly as it goes North to higher latitude.

For the subregional ionosphere grid correction method based on Kriging interpolation, the ionosphere delay correction rate in the mid-low latitude region is around 90 %; while in the mid-high latitude region, the majority is about 85 % and all above 70 %; as for the high latitude, the variation range is more obvious, largely between 70 % and 90 % except rare cases about 60 %. This can be partly attributed to the fact that only one reference station is adopted for modeling in this subregion and thus the limited amount of observation data can hardly fully reflect the distribution and diversity characteristics in this area.

Moreover, it should be noted that the new algorithm only uses eight reference stations in the whole European region for the process while CODE adopts data from 95 stations in the same region and the 15-order spherical harmonics function to generate the GIM product. As the new method features much more simple mathematical model and much smaller data volume in processing, its efficiency can be greatly improved. The new method, therefore, enjoys obvious advantage in comprehensive consideration of its efficiency and final effect.

5 Conclusions

In this paper, a new subregional ionosphere grid correction method based on Kriging interpolation is introduced with details on the basic fundamentals and the whole processing flow. A set of software is also programmed to realize the whole algorithm, including both product generation and result verification. Results of test in the European region show that the new algorithm can achieve very satisfactory effect with only eight IGS stations as reference station. The ionosphere delay

correction rate of the new algorithm in mid-low latitude Europe can reach about 90 %, while those for the mid-high and high latitude subreigons are generally around 85 % and 80 %, respectively. This is equivalent to or even better than the correction results of GIM provided by CODE in the same cases. However, in view that CODE adopts data from 95 stations in the same region and a 15-order spherical harmonics function to generate the GIM product, the new method is much more advantageous in processing efficiency. With much smaller observation data volume needed, much simpler mathematical model, much higher processing efficiency, and the very satisfactory correction results, the new method can serve as important reference for the design and establishment of ionosphere correction model needed in regional PPP and augmentation system.

Acknowledgements Sincere thanks to the support of Project No. 41304034 of Natural Science Foundation of China and Sub-Task No. 2014AA123503 of 863 Program.

References

1. Li Z, Huang J (2010) GPS surveying and data processing, 2nd edn. Wuhan University Press, Wuhan
2. Liu J, Wang Z (2008) Comparison and consistency research of regional ionospheric TEC models based on GPS measurements. Geomatics Inf Sci Wuhan Univ 33(5):479–483
3. Schaer S (1999) Mapping and predicting the earth's ionosphere using the global positioning system. Ph.D. dissertation. Astronomical Institute, University of Berne
4. Yuan Y et al (2015) Monitoring the ionosphere based on the Crustal Movement Observation Network of China. Geodesy Geodyn. doi:10.1016/j.geog.2015.01.004
5. Orus R, Hernandez-Pajares M, Juan JM et al (2005) Improvement of global ionospheric VTEC maps by using Kriging interpolation technique. J Atmos Solar-Teer Phys 67(16):159–1609
6. Blanch J (2002) An ionosphere estimation algorithm for WAAS based on Kriging. In: Proceedings of the institute of navigation GPS-02. Portland, OR
7. Tian M, Weixing W (2007) Central and northern China TEC map using the Kriging method. Chin J Space Sci 27(4):P279–P285
8. Zeng H-E, Huang S (2007) Research on spatial data interpolation based on Kriging in terpolation. Eng Surveying Mapp 16(5):P5–P13
9. Schaer S, Beutler G, Rothacher M (1998) IONEX: the IONosphere map eXchange format version 1. In: Proceedings of the IGS AC workshop. Damstadt, Germany, 9–11 Feb 1998
10. Feltens J, Schaer S (1998) IGS product for the ionosphere. In: Proceedings of the IGS analysis centers workshop. Darmstadt, Germany, 9–11 Feb

Research on Integer Ambiguity Resolution Method with BDS and GPS Single Epoch, Dual-Frequency Data

Yong Wang, Xiubin Zhao, Chunlei Pang, Ang Gong and Xiao Wang

Abstract Dual-antenna attitude determination technology based on global navigation satellite system can measure the attitude of transporters continuously and accurately. The correct resolution of integer ambiguity is the basis. Integer ambiguity resolution methods with single epoch data for attitude determination are immune to influence of cycle clip and provide attitude determination immediately, but for most methods, the differences are large between the float solution and the correct integer ambiguity, the search space are large, and the validation of integer ambiguity is difficult. For these problems, baseline constrained iteration least square algorithm used the known baseline length which is proposed to improve the float solution; threshold changes step-by-step to reduce search space; the validation of integer ambiguity is accomplished by comparing the calculated baseline vectors using BDS and GPS data after the baseline length validation. The results of actual testing show that the success rate is more than 98 %, the integer ambiguity resolution method can be effectively used for attitude determination with single epoch data.

Keywords GNSS · Single epoch · Attitude determination · Integer ambiguity · Baseline constrained

Y. Wang · X. Zhao · C. Pang (✉) · A. Gong · X. Wang
Information and Navigation College, Air Force Engineering University,
7, 10077 Xi'an, China
e-mail: chunleipcl@163.com

Y. Wang
e-mail: wangyongnav@163.com

X. Zhao
e-mail: zhaoxiubin926@163.com

© Springer Science+Business Media Singapore 2016

J. Sun et al. (eds.), *China Satellite Navigation Conference (CSNC) 2016 Proceedings: Volume III*, Lecture Notes in Electrical Engineering 390,
DOI 10.1007/978-981-10-0940-2_24

1 Introduction

Global Navigation Satellite System (GNSS) is widely used in positioning and attitude determination in the field of military and civilian because of its characteristics of all-time, all-weather, and wide coverage area. Attitude determination can use carrier phase measurement to resolve the attitude of vehicles, and the integer ambiguity resolution (IAR) is the key. IAR with single epoch data can eliminate the cycle slip and reduce the initialization time, so it will accomplish the attitude determination of dynamic vehicles in real-time. Global Positioning System (GPS) is the most widely used GNSS at present. However, with the development of BeiDou Navigation Satellite System (BDS), combining BDS with GPS data will be a trend. Attitude determination with BDS and GPS data can help IAR and improve the accuracy and reliability, thus it has important research and application value.

Many domestic and foreign scholars had put forward IAR methods with single epoch data used in attitude determination. Teunissen et al. expand and improve the LAMBDA method theoretically based on the known baseline length, then put forward the BC-LAMBDA method [1, 6, 7]. Buist [8] summarizes the IAR methods which can be used in attitude determination systematically and comprehensively, and verify the validity of BC-LAMBDA method with shipboard and airborne test. Liu and Ou [3] puts forward damping LAMBDA method and solve the rank-deficient problem in carrier phase measurement model by adding damping factor to normal equations. Li et al. [4] sets up a model with double frequency pseudorange and carrier phase measurements, and validates ambiguity candidates by dual-frequency correlation and baseline constraint. Qin et al. [10, 11] structure novel measurement equations by transforming the single difference carrier phase equations, and then use modified null space method to verify ambiguity candidate space. Teunissen et al. [9] use two steps searching method to accomplish the attitude determination with BDS single epoch data.

We can conclude from the research of above-mentioned scholars that there are four problems in IAR of attitude determination with single epoch data. They are rank-deficient problem of carrier phase double difference (DD) equations, low precision of float solutions, long span ambiguity searching space, and confirmation of ambiguity candidates. In this paper rank-deficient problem is solved by adding pesudorange measurements. A baseline constrained iteration least square is put forward to improve the accuracy of float solutions. We use double frequency combined carrier phase measurements and threshold changing step-by-step searching method to shrink searching space. At last, we validate ambiguity candidates by comparing the baseline vectors calculated with BDS and GPS data, respectively.

2 Double Frequency Combined Carrier Phase Measurement Equation

GNSS attitude determination uses DD equation. Since its short baseline, DD equation can eliminate many errors, such as ephemeris error, satellite clock error, ionospheric delay, tropsopheric delay, and receiver clock offset. In case of not considering multipath effect, the DD equation can be represented as

$$\begin{cases} \mathbf{\Phi}_{i1} = \frac{\mathbf{B}_i \cdot \mathbf{b}}{\lambda_{i1}} + \mathbf{N}_{i1} + \boldsymbol{\varepsilon}_{i1} \\ \mathbf{\Phi}_{i2} = \frac{\mathbf{B}_i \cdot \mathbf{b}}{\lambda_{i2}} + \mathbf{N}_{i2} + \boldsymbol{\varepsilon}_{i2} \end{cases} \tag{1}$$

where i equals to 1(BDS data) or 2(GPS data), $\mathbf{\Phi}_{i1}$ and $\mathbf{\Phi}_{i2}$ are carrier phase DD measurements on L1 and L2 frequency, respectively, $\mathbf{N}_{i1}$ and $\mathbf{N}_{i2}$ are DD integer ambiguity on L1 and L2 frequency, respectively, $\boldsymbol{\varepsilon}_{i1}$ and $\boldsymbol{\varepsilon}_{i2}$ are carrier noise on L1 and L2 frequency, respectively. λ_{i1} and λ_{i2} are wavelengths corresponding to L1 and L2 frequency. $\mathbf{b}$ is the baseline vector. $\mathbf{B}_i$ is the design matrix.

Supposing j and k are the combination coefficients of $\mathbf{\Phi}_{i1}$ and $\mathbf{\Phi}_{i2}$, respectively, double frequency combined measurement equation, according to Eq. (1), can be expressed as

$$\mathbf{\Phi}_c = \left(\frac{j}{\lambda_{i1}} + \frac{k}{\lambda_{i2}} \right) \mathbf{B}_i \cdot \mathbf{b} + (j\mathbf{N}_{i1} + k\mathbf{N}_{i2}) + (j\boldsymbol{\varepsilon}_{i1} + k\boldsymbol{\varepsilon}_{i2}) \tag{2}$$

From Eq. (2), we can know that combination wavelength is $\lambda_c = \lambda_{i1}\lambda_{i2}/j\lambda_{i2} + k\lambda_{i1}$, combination integer ambiguity is $\mathbf{N}_c = j\mathbf{N}_{i1} + k\mathbf{N}_{i2}$, combination carrier noise is $\boldsymbol{\varepsilon}_c = j\boldsymbol{\varepsilon}_{i1} + k\boldsymbol{\varepsilon}_{i2}$. If we suppose $\boldsymbol{\varepsilon}_{i1}$ and $\boldsymbol{\varepsilon}_{i2}$ are statistical independent and follow the same gauss distribution, the standard deviation is σ, so the standard deviation of combination carrier noise is $\sqrt{j^2 + k^2}\sigma$, the standard deviation of range noise is $\lambda_c\sqrt{j^2 + k^2}\sigma$.

Supposing the carrier noise factor is $\beta_{\mathbf{\Phi}} = \sqrt{j^2 + k^2}$, the range noise factor is $\beta_{\mathbf{b}} = \lambda_c\sqrt{j^2 + k^2}$. We can conclude from double frequency combined equation that $\beta_{\mathbf{\Phi}}$ reflects the difficulty of IAR, $\beta_{\mathbf{b}}$ reflects the accuracy of baseline. A number of double frequency combination of BDS and GPS confirmed by searching method [13] is shown in Table 1.

Table 1 shows that the range noise factor of double frequency combination is greater than that of single frequency, thus solving baseline vector with double frequency will reduce its accuracy. The better way is solving the integer ambiguity of two double frequency combinations, then solving the integer ambiguity of single frequency inversely.

Among the BDS and GPS double frequency combinations in Table 1, although the combination wavelength of (4, −5) and (7, −9) are long, their combination

Table 1 BDS and GPS double frequency combinations

GNSS	j	k	λ_c (m)	$\beta_{\mathbf{\Phi}}$ (cycle^2)	$\beta_{\mathbf{b}}$ (m^2)
BDS	1	0	0.1920	1	0.1920
	0	1	0.2483	1	0.2483
	1	−1	0.8470	1.4142	1.1978
	−3	4	2.0637	5	10.3187
	4	−5	1.4365	6.4031	9.1983
	7	−9	4.7266	11.4018	53.8921
GPS	1	0	0.1903	1	0.1903
	0	1	0.2442	1	0.2442
	1	−1	0.8619	1.4142	1.2189
	−3	4	1.6281	5	8.1403
	4	−5	1.8316	6.4031	11.7278
	−7	9	14.6526	11.4018	167.0655

carrier noise factor is big. That is disadvantage to solving integer ambiguity. So, we use (1, −1) and (−3, 4) to solve double frequency integer ambiguity by multifactor comprehensively considering.

3 Integer Ambiguity Resolution Method with Single Epoch Data

3.1 Baseline Constrained Iteration Least Square Algorithm

Carrier phase measurements have high accuracy, however, the measurement equation with single epoch data is rank-deficient. So, it hardly solves integer ambiguity. In order to accomplish IAR, we have to use pesudorange measurements. Addition of pesudorange measurements can reduce the accuracy of ambiguity float solution, leading to a poor success rate in IAR. Adding the known baseline length to measurement equation as a constraint condition will improve the accuracy of float solution. Teunissen [7] and Tang et al. [12] both use this idea, however, they do not give the specific application methods. In this paper, a baseline constrained iteration least square (BCILS) algorithm is put forward to refer to the idea of [2]. It can improve the accuracy of ambiguity float solution, thus improve the success rate of IAR.

Substituting the pesudorange measurements and carrier phase double frequency combined measurements to the Eq. (2)

$$\begin{bmatrix} \mathbf{L}_P \\ \lambda_c \mathbf{\Phi}_c \end{bmatrix} = \begin{bmatrix} \mathbf{B}_i & \mathbf{0} \\ \mathbf{B}_i & \lambda_c \mathbf{I} \end{bmatrix} \begin{bmatrix} \mathbf{b} \\ \mathbf{N}_c \end{bmatrix} + \begin{bmatrix} \boldsymbol{\varepsilon}_P \\ \lambda_c \boldsymbol{\varepsilon}_c \end{bmatrix} \tag{3}$$

where $\mathbf{L}_P$ is DD pesudorange measurements, $\boldsymbol{\varepsilon}_P$ is the DD pesudorange noise.

Supposing $\mathbf{Y} = [\mathbf{L}_P \quad \lambda_c \mathbf{\Phi}_c]^T$, $\mathbf{A} = \begin{bmatrix} \mathbf{B}_i & \mathbf{0} \\ \mathbf{B}_i & \lambda_c \mathbf{I} \end{bmatrix}$, $\mathbf{X} = [\mathbf{b} \quad \mathbf{N}_c]^T$ and $\mathbf{e} = [\boldsymbol{\varepsilon}_P \quad \lambda_c \boldsymbol{\varepsilon}_c]^T$

Equation (3) can be simplified to

$$\mathbf{Y} = \mathbf{A}\mathbf{X} + \mathbf{e} \tag{4}$$

The least square solution of Eq. (4) is

$$\mathbf{A}^T\mathbf{P}\mathbf{A}\widehat{\mathbf{X}} = \mathbf{A}^T\mathbf{P}\mathbf{Y} \tag{5}$$

where $\mathbf{P}$ is the weighting matrix. Adding $\widehat{\mathbf{X}}$ to both sides of Eq. (5)

$$\left(\mathbf{A}^T\mathbf{P}\mathbf{A} + \mathbf{I}\right)\widehat{\mathbf{X}} = \mathbf{A}^T\mathbf{P}\mathbf{Y} + \widehat{\mathbf{X}} \tag{6}$$

For both sides of Eq. (6) contain $\widehat{\mathbf{X}}$, we can solve it iteratively. The iterative equation is

$$\widehat{\mathbf{X}}^{(n)} = \left(\mathbf{A}^T\mathbf{P}\mathbf{A} + \mathbf{I}\right)^{-1}\left(\mathbf{A}^T\mathbf{P}\mathbf{Y} + \widehat{\mathbf{X}}^{(n-1)}\right), \quad n = 1, 2, \ldots \tag{7}$$

Supposing $\mathbf{q} = \left(\mathbf{A}^T\mathbf{P}\mathbf{A} + \mathbf{I}\right)^{-1}$, Eq. (7) can be expressed as

$$\widehat{\mathbf{X}}^{(n)} = \left(\mathbf{q} + \mathbf{q}^2 + \cdots + \mathbf{q}^n\right)\mathbf{A}^T\mathbf{P}\mathbf{Y} + \mathbf{q}^n\widehat{\mathbf{X}}^{(0)} \tag{8}$$

where $\widehat{\mathbf{X}}^{(0)}$ is the initial value of $\widehat{\mathbf{X}}$. Although $\widehat{\mathbf{X}}^{(0)}$ can be selected any value theoretically, we select the solution of Eq. (4), $\left(\mathbf{A}^T\mathbf{P}\mathbf{A}\right)^{-1}\mathbf{A}^T\mathbf{P}\mathbf{Y}$, as the initial value. So, the variance-covariance matrix of Eq. (8) is

$$\mathbf{Q}_{\widehat{\mathbf{X}}^{(n)}\widehat{\mathbf{X}}^{(n)}} = \left(\mathbf{q} + \mathbf{q}^2 + \cdots + \mathbf{q}^n\right)\mathbf{A}^T\mathbf{P}\mathbf{A}\left(\mathbf{q} + \mathbf{q}^2 + \cdots + \mathbf{q}^n\right) \tag{9}$$

The mathematical expression of baseline constraint in attitude determination is

$$l - \delta \le \sqrt{\mathbf{b}^T\mathbf{b}} \le l + \delta \tag{10}$$

where l is the length of known baseline. δ is the error threshold of baseline. Regard Eq. (10) as terminal condition of above-mentioned iterative method, it can be expressed as

$$l - \delta \le \sqrt{\hat{x}_1^2 + \hat{x}_2^2 + \hat{x}_3^2} \le l + \delta \tag{11}$$

where $\hat{x}_1$, $\hat{x}_2$ and $\hat{x}_3$ are the first to third elements of column vector $\widehat{\mathbf{X}}^{(n)}$, and then the flowchart of BCILS is shown as Fig. 1.

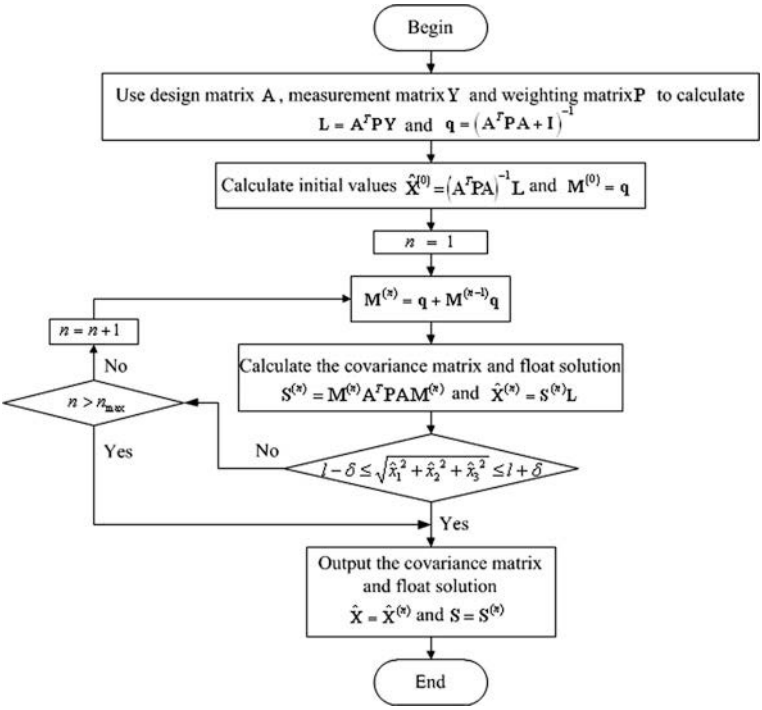

Fig. 1 Flowchart of BCILS algorithm

As shown in Fig. 1, $\mathbf{S}$ is variance-covariance matrix of $\widehat{\mathbf{X}}$. To avoid the iterative time which is too long, we set the maximum of n to 1000. When we have the float solution $\widehat{\mathbf{X}}$ and its variance-covariance matrix $\mathbf{Q}_{\widehat{\mathbf{X}}\widehat{\mathbf{X}}}$, then we can get the float solution of ambiguity $\widehat{\mathbf{N}}_c$ and baseline vector $\hat{\mathbf{b}}$ and their variance-covariance matrix $\mathbf{Q}_{\widehat{\mathbf{N}}_c\widehat{\mathbf{N}}_c}$ and $\mathbf{Q}_{\hat{\mathbf{b}}\hat{\mathbf{b}}}$.

3.2 Threshold Changing Step-by-Step Searching Algorithm

According to Eqs. (5) and (6), the measurement equation can be expressed as

$$\mathbf{Y} = \mathbf{B}\mathbf{b} + \mathbf{C}\mathbf{N}_c + \mathbf{e} \tag{12}$$

where $\mathbf{B} = (\mathbf{B}_i \quad \mathbf{B}_i)^T$ and $\mathbf{C} = (\mathbf{0} \quad \lambda_c\mathbf{I})^T$. The least square problem in Eq. (12) is the minimization problem as

$$\min_{\mathbf{N}_c \in Z^n, \mathbf{b} \in R^3} \|\mathbf{Y} - \mathbf{B}\mathbf{b} - \mathbf{C}\mathbf{N}_c\|^2_{\mathbf{Q}_{\mathbf{YY}}} \tag{13}$$

where $\|\cdot\|^2_{\mathbf{Q}_{\mathbf{YY}}} = (\cdot)^T \mathbf{Q}^{-1}_{\mathbf{YY}} (\cdot)$, and $\mathbf{Q}_{\mathbf{YY}}$ is the variance-covariance matrix of $\mathbf{Y}$. Considering the theory of Teunissen, without baseline constraint, Eq. (13) can be transform into the minimization problem as

$$\min_{\mathbf{N}_c \in Z^n} \left\| \widehat{\mathbf{N}}_c - \mathbf{N}_c \right\|^2_{\mathbf{Q}_{\widehat{\mathbf{N}}_c \widehat{\mathbf{N}}_c}} \tag{14}$$

LAMBDA is an outstanding algorithm to solve the problem. It uses matrix $\mathbf{Z}$ to make Gauss transformation with $\widehat{\mathbf{N}}_c$ and $\mathbf{Q}_{\widehat{\mathbf{N}}_c \widehat{\mathbf{N}}_c}$, to accomplish the ambiguity decorrelation. After that, Eq. (14) can be transform into

$$\min_{\mathbf{z} \in Z^n} \|\hat{\mathbf{z}} - \mathbf{z}\|^2_{\mathbf{Q}_{\hat{\mathbf{z}}\hat{\mathbf{z}}}} \tag{15}$$

where $\mathbf{z} = \mathbf{Z}^T \mathbf{N}_c$ and $\mathbf{Q}_{\hat{\mathbf{z}}\hat{\mathbf{z}}} = \mathbf{Z}^T \mathbf{Q}_{\widehat{\mathbf{N}}_c \widehat{\mathbf{N}}_c} \mathbf{Z}$

By confirming searching threshold, we can search the fixed solution $\breve{\mathbf{z}}$ in the multidimensional ellipsoid whose mathematical expression is

$$\|\hat{\mathbf{z}} - \mathbf{z}\|^2_{\mathbf{Q}_{\hat{\mathbf{z}}\hat{\mathbf{z}}}} \leq \chi^2 \tag{16}$$

The fixed ambiguity $\breve{\mathbf{N}}_c$ can be solved with $\breve{\mathbf{z}}$ and $\mathbf{Z}$, and then the fixed baseline vector will be solved according to the relationship between baseline vector and ambiguity as

$$\breve{\mathbf{b}} = \hat{\mathbf{b}} - \mathbf{Q}_{\hat{\mathbf{b}}\widehat{\mathbf{N}}_c} \mathbf{Q}^{-1}_{\widehat{\mathbf{N}}_c \widehat{\mathbf{N}}_c} \left(\widehat{\mathbf{N}}_c - \breve{\mathbf{N}}_c \right) \tag{17}$$

In attitude determination with single epoch data, for the use of pesudorange, the accuracy of float solution will become low, so the baseline constraint is an important condition. On this occasion, Eq. (13) will transform into

$$\min_{\mathbf{N}_c \in Z^n, \mathbf{b} \in R^3, l-\sigma \leq \sqrt{\mathbf{b}^T \mathbf{b}} \leq l+\sigma} \|\mathbf{Y} - \mathbf{B}\mathbf{b} - \mathbf{C}\mathbf{N}_c\|^2_{\mathbf{Q}_{\mathbf{YY}}} \tag{18}$$

where σ is the error threshold of baseline length. δ in Sect. 3.2 also is the error threshold of baseline length. But they are different, since σ is the error threshold of baseline length with fixed ambiguity, while δ is the error threshold of baseline length with float ambiguity. The value of σ is less than δ.

Apparently, Eq. (18) can not be transformed into Eq. (14) by orthogonal decomposition. The correct ambiguity solution have possibilities to be not contained to the multidimensional ellipsoid expressed by Eq. (16). So LAMBDA algorithm is not suitable for IAR. Teunissen [7] and Qin et al. [10] make the correct ambiguity containing to the searching space by expanding it, however, this method will introduce a large number of incorrect ambiguity into the searching space. It will reduce the search efficiency. A threshold changing step-by-step searching algorithm is put forward in this paper, which can avoid searching a great quantity of incorrect ambiguity candidates by changing the searching threshold.

We can conclude that the correct ambiguity is inevitable to meet the following mathematical expression

$$\chi_{j-1}^2 \le \left\| \widehat{\mathbf{N}}_c - \mathbf{N}_c \right\|^2_{\widehat{\mathbf{Q}}_{\widehat{\mathbf{N}}_c \widehat{\mathbf{N}}_c}} \le \chi_j^2, \quad j = 1, 2, \ldots \tag{19}$$

$$l - \sigma \le \sqrt{\mathbf{b}(\mathbf{N}_c)^T \mathbf{b}(\mathbf{N}_c)} \le l + \sigma \tag{20}$$

where $\mathbf{b}(\mathbf{N}_c)$ is the baseline vector with ambiguity known. χ_j^2 and χ_{j-1}^2 are the high and low thresholds of ambiguity space, respectively. The minimum of low threshold is 0, the maximum of high threshold is $\chi_{\max}^2$. The step size of threshold is $\chi_j^2 - \chi_{j-1}^2 = \theta/j$, and it will decrease with the threshold increasing. If the step size remains unchanged with the increasing of threshold, the ambiguity candidates will increase. θ is the step size constent.

Because the DD ambiguity has serious correlation, it needs to use decorrelation firstly. So, the threshold changing step-by-step searching algorithm can be summarized as

1. Decorrelation of integer ambiguity. Using the same method as LAMBDA algorithm to confirm the gauss transformation matrix $\mathbf{Z}$, then transforming $\left\| \widehat{\mathbf{N}}_c - \mathbf{N}_c \right\|^2_{\widehat{\mathbf{Q}}_{\widehat{\mathbf{N}}_c \widehat{\mathbf{N}}_c}}$ into $\|\hat{\mathbf{z}} - \mathbf{z}\|^2_{\mathbf{Q}_{\hat{\mathbf{z}}\hat{\mathbf{z}}}}$.
2. Confirmation of searching threshold and step size. Supposing the minimum of low searching threshold $\chi_0^2 = 0$, the maximum of high searching threshold $\chi_{\max}^2$, and step size of changing threshold θ/j.
3. Searching of integer ambiguity. Supposing $j = 1$, $\chi_0^2 = 0$ and $\chi_1^2 = \theta$. Searching the fixed ambiguity meeting Eqs. (19) and (20) in the multidimensional ellipsoid expressed by $\chi_0^2 \le \|\hat{\mathbf{z}} - \mathbf{z}\|^2_{\mathbf{Q}_{\hat{\mathbf{z}}\hat{\mathbf{z}}}} \le \chi_1^2$.

In order to improve reliability, ambiguity searching stops when 3 to 5 candidates meeting Eqs. (19) and (20) are found. The correct ambiguity is fixed by validation method finally.

3.3 Validation of Integer Ambiguity

Validation of integer ambiguity is selecting the correct ambiguity from candidates. The common method is ratio test based on residual sum of squares. It supposes the residual sum of squares to obey a Gaussian distribution. It is not suitable for IAR with single epoch [5]. Baseline constraint can be used in validation of integer ambiguity in attitude determination, however, baseline length and baseline vector are not one to one correspondence, and thus its effect is not good.

In IAR with BDS and GPS data, validation can be accomplished by comparing the baseline vector solved with BDS and GPS data, respectively, after the baseline length test. Because the difference between baseline vector resolution with BDS data and GPS data are closed when the correct ambiguity is fixed, this validation method is reasonable. On the condition that $\mathbf{N}_c$ is already known, baseline vector resolution with BDS data is $\mathbf{b}_B(\mathbf{N}_c) = \left(b_{Bx}, b_{By}, b_{Bz}\right)^T$, baseline vector resolution with GPS data is $\mathbf{b}_G(\mathbf{N}_c) = \left(b_{Gx}, b_{Gy}, b_{Gz}\right)^T$. If $\mathbf{b}_B(\mathbf{N}_c)$ and $\mathbf{b}_G(\mathbf{N}_c)$ meet the following conditions, $\mathbf{N}_c$ is fixed as the correct ambiguity.

$$\begin{cases} \|b_{Bx} - b_{Gx}\| \le \eta_1 \\ \|b_{By} - b_{Gy}\| \le \eta_2 \\ \|b_{Bz} - b_{Gz}\| \le \eta_3 \end{cases} \tag{21}$$

where η_1, η_2 and η_3 are difference threshold of 3D coordinate, respectively, of $\mathbf{b}_B(\mathbf{N}_c)$ and $\mathbf{b}_G(\mathbf{N}_c)$. Because the difference between baseline vector with BDS data and GPS data is small, the values of η_1, η_2 and η_3 are small.

When the double frequency ambiguity is fixed, the single frequency ambiguity can be solved according to Eq. (2). Then the high accuracy baseline vector can solve the attitude angles.

4 Experiments and Results

4.1 Experimental Conditions

The experiment is static with two receivers which constitute a single baseline. The receiver OEM board is K501 of ComNav, and the antennae are GPS-702-GG. The experimental location is the roof of research activities building. The sampling interval is 1 s. The masking angle of satellites is 10°. Two experiments were carried out. The baseline length of the first experiment is 3.490 m, and the time is 5492 s. The baseline length of the second experiment is 8.343 m, and the time is 4518 s. The data processing platform is Matlab 2010a. The computer processor is AMD Athlon(tm)II X2 215 with 2.70 GHz main frequency and 1.75 GB RAM. The error

threshold δ is 3 cm, σ is 2 cm. The searching high threshold $\chi^2_{\max}$ is 100, step size constent is 10. The difference thresholds η_1, η_2 and η_3 are 1.5 cm.

4.2 Experimental Results and Analysis

We select one epoch data of the first experiment randomly. The satellite number of BDS and GPS are 8 and 6, respectively. The float $\mathbf{N}_{1,-1}$ and $\mathbf{N}_{-3,4}$ using BDS and GPS data are solved by LS and BCILS algorithms, respectively. Their solutions are shown in Table 2. The LAMBDA fixed ambiguity solutions with multiple epochs data are regarded as the correct ambiguity for comparison.

Table 2 LS and BCILS float solutions

GNSS	Double frequency ambiguity combinations	LS float solutions	BCILS float solutions	Correct solutions
BDS	$\mathbf{N}_{1,-1}$	−48,786.88	−48,786.90	−48,777
		−29,141.94	−29,141.62	−29,141
		−16,427.40	−16,422.58	−16,418
		−2444.66	−2444.51	−2443
		−5273.74	−5269.26	−5267
		−3258.61	−3259.17	−3262
		−26,460.28	−26,459.43	−26,458
	$\mathbf{N}_{-3,4}$	82,790.67	82,791.39	82,794
		62,439.56	62,439.62	62,440
		114,005.48	114,007.54	114,009
		40,831.37	40,831.59	40,832
		48,762.16	48,763.73	48,765
		45,294.66	45,294.13	45,293
		120,837.99	120,837.99	120,838
GPS	$\mathbf{N}_{1,-1}$	−8,636,603.31	−8,636,601.26	−8,636,598
		−20,067.58	−20,066.56	−20,063
		2153.13	2151.96	2148
		−87,891.83	−87,892.81	−87,894
		6,935,880.74	6,935,880.98	6,935,882
	$\mathbf{N}_{-3,4}$	32,035,069.28	32,035,070.67	32,035,072
		−6972.33	−6972.14	−6970
		91,125.03	91,124.84	91,122
		260,276.32	260,275.79	260,275
		−26,759,747.67	−26,759,747.62	26,759,747

Table 3 Success rate and time per request of IAR method

Baseline length/m	Satellite number of BDS	Satellite number of GPS	Total number of epoch	Success number of epoch	Success rate (%)	Time per request (s)
3.490	6–8	5–7	5415	5329	98.43	0.153
8.343	6–8	8–12	4486	4453	99.26	0.207

As shown in Table 2, the accuracy of BCILS float solutions are higher than that of LS float solutions, thus BCILS can improve the accuracy of float solutions. The effective become obvious as the difference between LS float solutions and correct solutions become larger.

The statistical results of IAR method in this paper are shown in Table 3. Because the carrier phase measurements on L2 of some epochs are unavailable, the total number of epoch is not equal to the collective time.

As shown in Table 3, the success rates of two experiments with different baseline length using our method are above 98 %, time per request of two experiments are 0.153 s and 0.207 s, respectively.

We select 1300 s data which the satellite number which is all the same of two experiments to solve the attitude angles. In the first experiment, the satellite number of BDS is 8. Regarding PRN12 whose elevation is maximum as the reference satellite, we make difference with PRN8, 6, 5, 3, 2, 1, and 9. The satellite number of GPS is 6. Regarding PRN4 as the reference satellite, we make difference with PRN12, 2, 17, 10, and 5. In the second experiment, the satellite number of BDS is 6. Regarding PRN10 as the reference satellite, we make difference with PRN8, 7, 3, 5, and 2. The satellite number of GPS is 9. Regarding PRN7 as the reference satellite, we make difference with PRN27, 3, 8, 16, 19, 13, 11, and 23. The attitude solutions are shown in Table 4. The correct attitudes in Table 4 are measured by theodolite. The baseline length, heading angle, and pitching angle of two experiments are shown in Fig. 2.

As shown in Table 4, the error RMS of attitudes solved with GPS data is less than BDS, and the error RMS of attitudes solved with BDS and GPS data is less than anyone of them. The same conclusion can be shown in Figs. 2 and 3.

Table 4 Error RMS of attitudes

Experiment	Baseline length (m)	Attitude	Correct angle (°)	BDS RMS (°)	GPS RMS (°)	BDS+GPS RMS (°)
1	3.490	Heading	65.031	0.169	0.124	0.082
		Pitching	−9.392	0.096	0.067	0.045
2	8.343	Heading	22.966	0.132	0.023	0.021
		Pitching	−11.552	0.021	0.021	0.013

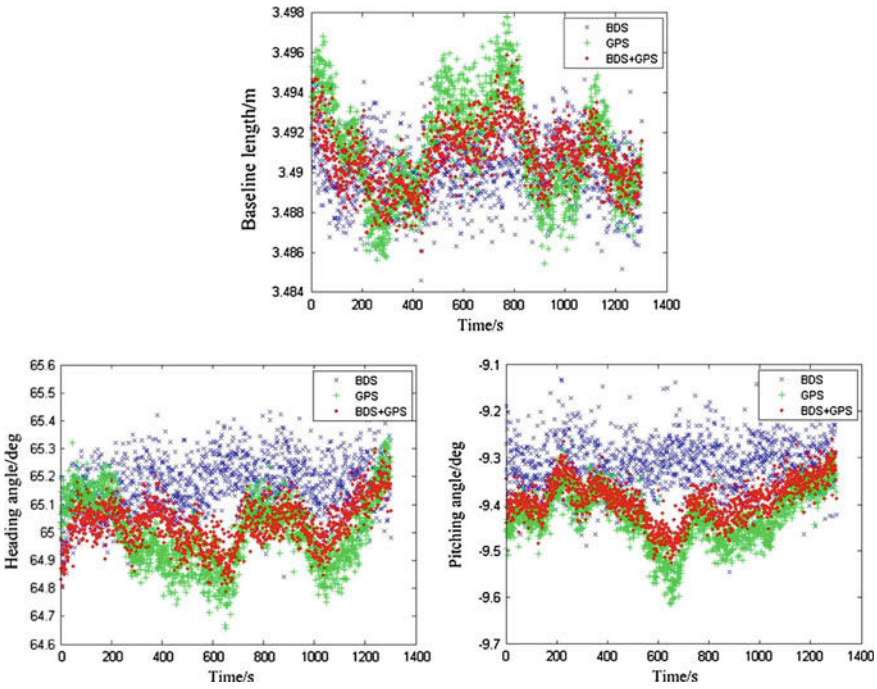

Fig. 2 Baseline length, heading angle, and pitching angle of the first experiment

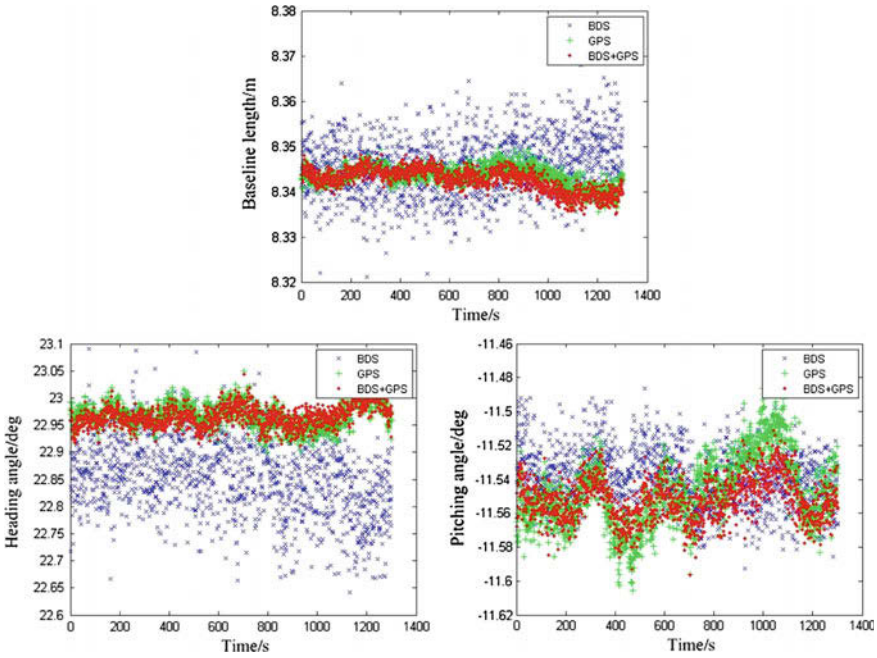

Fig. 3 Baseline length, heading angle, and pitching angle of the second experiment

5 Summary

The IAR method in this paper can improve the accuracy of ambiguity float solutions and have a high success rate, thus it can be used in attitude determination of dynamic vehicles theoretically. Experimental results show that attitude determination with BDS and GPS data is better than anyone of them. But the IAR method in this paper needs to be verified by dynamic experiment.

References

1. Park C, Teunissen PJG (2009) Integer least squares with quadratic equality constraints and its application to GNSS attitude determination systems. Int J Control Autom Syst 7(4):566–576
2. Qian F, Xu C, Ning Z (2010) A new approach to GPS carrier phase ambiguity resolution using single epoch single frequency data. In: International conference on optoelectronics and image processing, IEEE
3. Liu G, Ou J (2003) Determining attitude with single epoch GPS algorithm and its precision analysis. Geomatics Inf Sci Wuhan Univ 28(6):732–735
4. Li Z, Liu W, Lou Y et al (2007) Heading determination algorithm with single epoch dual-frequency GPS data. Geomatics Inf Sci Wuhan Univ 32(9):753–756
5. Liu Z (2003) Research on carrier phase differential GPS. Initial Alignment of Strapdown Inertial Navigation System and their Combination, Changsha, Hunan
6. Teunissen PJG (2006) The LAMBDA method for the GNSS compass. Artif Satellites 41 (3):89–103
7. Teunissen PJG (2010) Integer least-squares theory for the GNSS compass. J Geodesy 84:433–447
8. Buist P (2007) The baseline constrained LAMBDA method for single epoch, single frequency attitude determination applications. Division, Texas
9. Teunissen PJG, Dejonge PJ, Tiberius CCJM (1997) The least-squares ambiguity decorrelation adjustment: its performance on short GPS baselines and short observation spans. J Geodesy 71:589–602
10. Qin H, Chen W, Jin T et al (2011) New attitude determination algorithm for single epoch, single frequency using GPS. J Beijing Univ Aeronaut Astronaut 37(9):1063–1069
11. Qin H, Chen W, Jin T et al (2011) Performance analysis and improved method for single epoch, single frequency attitude determination using GPS. J PLA Univ Sci Technol (Nat Sci Ed) 12(5):431–435
12. Tang W, li D, Chi F (2013) Research on single epoch orientation algorithm of BeiDou navigation system. Geomatics Inf Sci Wuhan Univ 38(9):1014–1017
13. Wang Y, Zhao X, Pang C et al (2014) Selection method and analysis of BDS/GPS four frequency combination observation coefficients. J Air Force Eng Univ (Nat Sci Ed) 15(4):70–74

The Quantitative Analysis of the Mean Nighttime VTEC Based on EMD

Chen Liu, Changjian Liu, Ying Du, Xu Feng and Xuedong Zhang

Abstract Compared with the qualitative analysis, the quantitative analysis of VTEC (vertical total electron content) is more conducive to the modeling, forecasting, and correcting of ionosphere delay. With Empirical Mode Decomposition (EMD), the mean nighttime VTEC are investigated qualitatively using global grid ionospheric data from IGS (the International GPS Service for Geodynamic). The evaluation is done in this paper by comparing GIMs data with the quantitative analysis result and Klobuchar model. The final result indicates that the quantitative analysis result is reliable to describe and forecast the trend of the global mean nighttime VTEC in a solar activity cycle.

Keywords EMD · VTEC · Quantitative analysis · Klobuchar · Solar activity cycle · Prediction ability

1 Introduction

Ionosphere time-delay is one of the main error sources for GNSS users. The quantitative analysis of total electron content is more conducive to the modeling, forecasting, and correcting of ionosphere delay. Since established, the traditional Klobuchar model has been widely applied in navigation and positioning fields [1–3]. The constant value 9.23 TECU, meanwhile, has been generally admissive to describe the nighttime VTEC [1–3], which could introduce 20–30 % errors [4].

The original version of this chapter was revised: For detailed information please see Erratum. The erratum to this chapter is available at 10.1007/978-981-10-0940-2_66

C. Liu (✉) · C. Liu · Y. Du · X. Feng
Institute of Geospatial Information, Information Engineering University, Zhengzhou, China
e-mail: 791387368@qq.com

X. Zhang
Shenyang, China

© Springer Science+Business Media Singapore 2016

J. Sun et al. (eds.), *China Satellite Navigation Conference (CSNC) 2016 Proceedings: Volume III*, Lecture Notes in Electrical Engineering 390,
DOI 10.1007/978-981-10-0940-2_25

Therefore, with the continual increase of the navigation accuracy requirement, more and more significance has been attached to the research of nighttime ionospheric VTEC. Aiming at the problem above, many domestic scholars have revised the nighttime ionospheric VTEC in the elaboration of traditional Klobuchar ionosphere model. Zhu made use of solar flux density to revise the nighttime ionospheric VTEC [5]. Considering the fact that the ionospheric change is closely related to the solar activity cycle, Zhao et al. used sunspot numbers to revise the nighttime ionospheric VTEC [6]. Huang et al. revised the nighttime ionospheric VTEC in consideration of the effect of latitude [7]. Considering the influence of latitude and diurnal variation, Li et al. [8] established a nighttime variational basic model for regional ionosphere modeling.

Except the diurnal variation, ionospheric electron content varies at rates of season, semiyear, year, and solar activity cycle on time series [9–14]. In literature [9–14], many scholars have made the qualitative analysis of different periodic changes about total electron content. However, the quantitative analysis has not been studied. In this paper, EMD was utilized to make the qualitative analysis of the mean nighttime ionospheric VTEC in a solar activity cycle using the GIMs data from IGS.

2 Theory and Methodology

2.1 Empirical Mode Decomposition

Empirical Mode Decomposition (EMD) is an adaptive decomposition method put forward by Huang et al. in 1998, which is applicable to nonlinear and nonstationary signal processing. Based on the time scale characteristics of the signal, the method can break the complex signal up into a number of intrinsic mode function (IMF) component sorted by frequency that contain the local characteristics of the original signal in different time scales [15–18]. An IMF is a function that satisfies two conditions [15, 17]: (1) in the whole data set, the number of extreme and the number of zero crossings must either equal or differ at most by one; (2) at any point, the mean value of the envelope defined by the local maxima and the envelope defined by the local minima is zero.

The EMD method decomposition process is as below.

Step 1: Find the signal sequence of maximum and of minimum, then construct the upper and lower envelopes by cubic spline interpolation.

Step 2: Calculate the average value of the upper and lower envelopes, $m(t)$, and extract $h(t) = y(t) - m(t)$ as the signal details.

Step 3: Repeat step 1 and 2 for $h(t)$ until $h(t)$ meet the IMF component condition and note $IMF(t) = h(t)$.

Step 4: Calculate decomposition residuals $r(t) = y(t) - IMF(t)$.

Step 5: Repeat step 1 to 4 for the residual to get some IMF components and a residual term.

2.2 Strategy of the Quantitative Analysis Based on EMD

Due to different periodic changes, the mean global nighttime ionospheric VTEC sequence is a nonlinear and nonstationary sequence with about 11 years cycle. The information interactions from the various cycles make it difficult to find clear cycles and the extreme points. As a result, it is difficult to make a quantitative analysis of the sequence directly. Owing to the advantage that the decomposition by EMD does not need to input any function in advance, EMD is applicable to any signal decomposition, and dominant to deal with nonlinear and nonstationary signal such as the global nighttime ionospheric VTEC sequence. Therefore, EMD was proposed in this paper to be applied on the quantitative analysis of the mean global nighttime ionospheric VTEC sequence, in order to reduce the difficulty of quantitative analysis and improve the accuracy of quantitative analysis.

Quantitative analysis strategy based on EMD is as below. We get several IMF components and a residual term by multi-scale EMD decomposition of the mean global nighttime ionospheric VTEC sequence. Then we do quantitative analysis of the residual term and these IMF components containing the information of middle-long period variations. With an approximate expression of the trend line of the mean global nighttime ionospheric VTEC sequence shown in Fig. 1, we would realize the quantitative analysis of the mean global nighttime ionospheric VTEC.

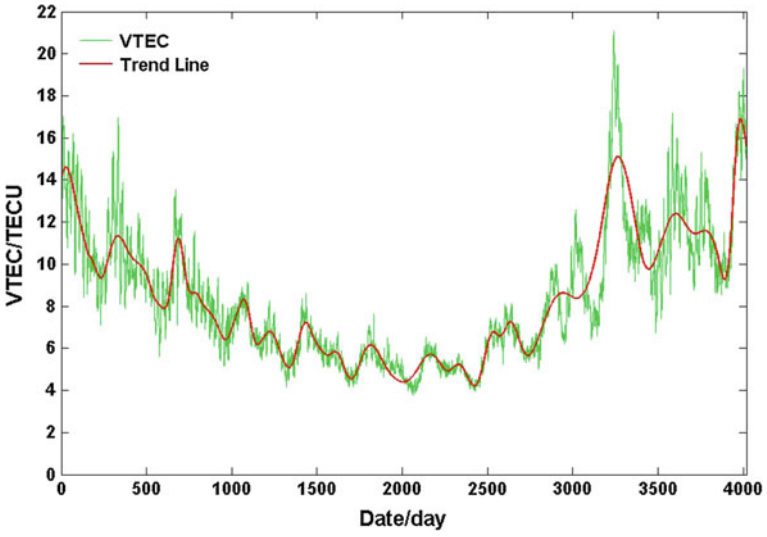

Fig. 1 Trend line of the global mean nighttime ionospheric VTEC

3 Results and Analysis

Based on the GIMs data from IGS, a sequence of global mean nighttime ionospheric VTEC, from January 1, 2003 to December 31, 2013, was selected to be analyzed in this paper. The global mean ionospheric VTEC of nighttime is the mean of the mean nighttime ionospheric VTECs from 68 locations that the latitudinal and longitudinal interval are 10° and 90°, respectively. And the mean nighttime ionospheric VTEC is the VTECs at 0, 2, 4, 6 of local time.

As shown in Fig. 2, the sequence of global mean nighttime ionospheric VTEC has a stable period and a period of dramatic change. And there is an obvious long-term trend of the ups and downs. The fixed value of mean nighttime VTEC in the Klobuchar traditional model, 9.23 TECU, is extraordinary similar to the mean nighttime VTEC (9.13 TECU) in the solar activity cycle selected in this paper. The solar activity cycle is divided into trough and active solar activity by the red line in Fig. 2, the value of which is 9.23 TECU. As shown in Fig. 2, the VTECs and their variation range in trough solar activity are smaller than those in active solar activity.

According to quantitative analysis strategy based on EMD put forward in this paper, we made multi-scale EMD decomposition of the global mean nighttime ionospheric VTEC sequence. In order to meet the decomposition conditions that the upper and lower envelope could contain all the sequence values, two endpoints of the sequence were regarded as both minimum and maximum points to participate in the interpolation calculation of upper and lower envelope curve. Decomposition termination condition is whether the effect of decomposition is not obvious or the residual item is easy to make a quantitative analysis. We get several IMF components and a residual term by multi-scale EMD decomposition shown in Fig. 3.

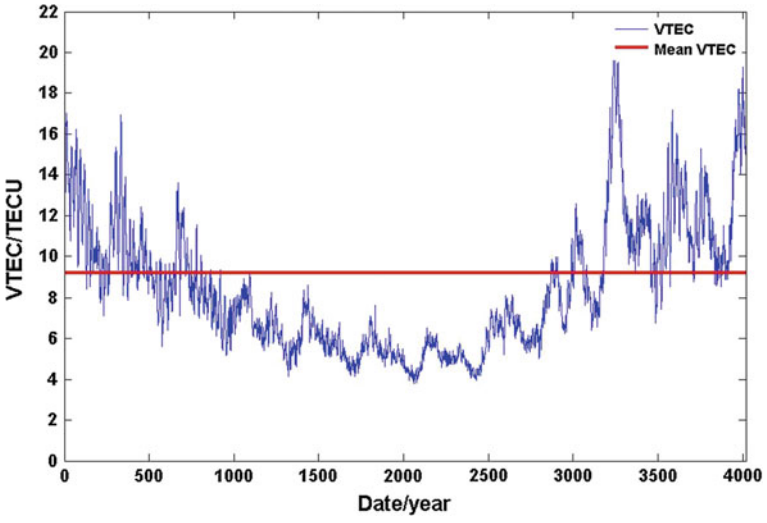

Fig. 2 Series of global mean nighttime VTEC

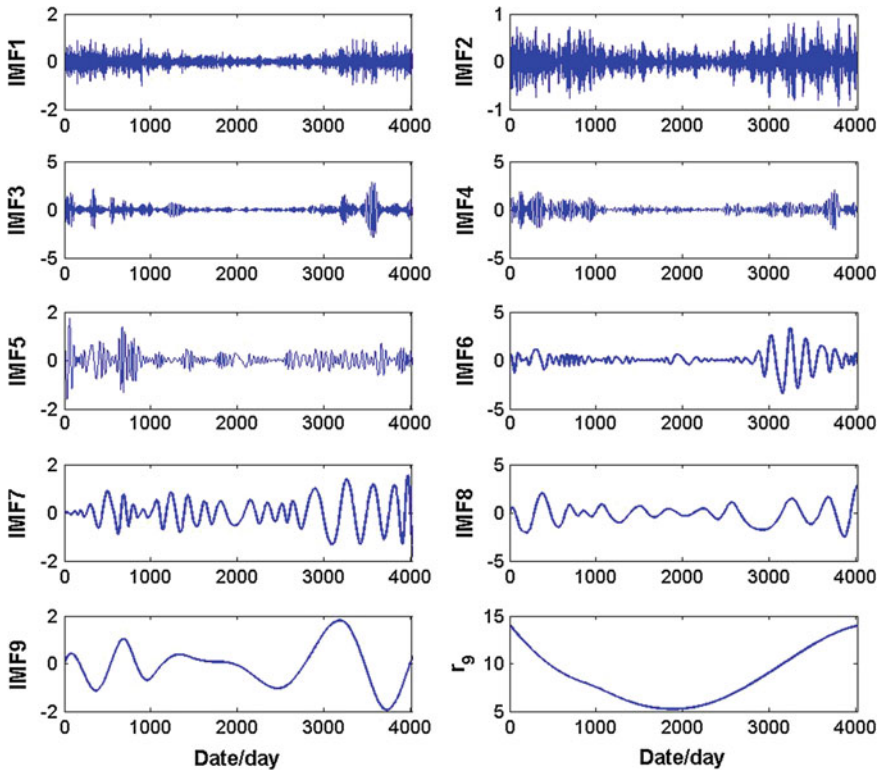

Fig. 3 IMF components and residual term

From the figure, we can find that r_9, the residual term by multi-scale EMD decomposition, can reflect the long-term change trend of the global mean nighttime ionospheric VTEC and the trend of the ups and downs in trough and active solar activity. As a result, the residual term by multi-scale EMD decomposition could be regarded as the long-term variation characteristics of the global mean nighttime ionospheric VTEC in this solar activity cycle. In addition, IMF9 component describes the low frequency change trend of cycle of one year to 3.5 years, and IMF8, IMF7 component describe the intermediate frequency change trend of cycle of one year and half a year respectively, while other components describe the trend of high frequency variations.

According to quantitative analysis strategy based on EMD put forward in this paper, we made quantitative analysis of the residual term and the IMF9, IMF8, IMF7 components. Polynomial curves fitting was adopted in the quantitative analysis of residual term. And the IMF components of low and intermediate frequency were fitted using cosine waves. An approximate expression of the trend line shown in Fig. 1 is the final result of quantitative analysis, which is the sum of the

approximate expressions above. That is, the final result of quantitative analysis is given by Eq. (1).

$$r = r_9 + b_9 + b_8 + b_7 \tag{1}$$

where r_9 is the approximate expression of the residual term, b_9, b_8, b_7 are the approximate expression of IMF9, IMF8, IMF7 respectively. r_9, b_9, b_8 and b_7 are given by the following equations.

$$\begin{aligned} r_9 = {} & -2.7 \times 10^{-13} t^4 + 1.9 \times 10^{-9} t^3 - 1.8 \times 10^{-6} t^2 \\ & - 0.0058t + 13.212 \end{aligned} \tag{2}$$

$$\begin{aligned} b_9 = {} & A_1 \cos\left(\frac{2\pi(t-39)}{653}\right) + A_2 \cos\left(\frac{2\pi(t-3128)}{B}\right) \\ & + A_3 \cos\left(\frac{2\pi(t-1975)}{1500}\right) \end{aligned} \tag{3}$$

$$b_8 = 1.17 \cdot \left(\frac{r_9}{9.13}\right)^2 \cos\left(\frac{2\pi(t+7)}{365.25}\right) \tag{4}$$

$$b_7 = A_4 \cos\left(\frac{2\pi(t-3818)}{188}\right) \tag{5}$$

where A_1, A_2, A_3 and A_4 are the coefficients of fitted cosine wave, B is the cycle of fitted cosine wave. A_1, A_2, A_3, A_4 and B are given by the following equations.

$$A_3 = \begin{cases} 0, & A_1 < 0 \\ -0.0008t + 1.4495, & \text{others} \end{cases} \tag{6}$$

$$A_2 = \begin{cases} 0, & t < 1300 \\ -2.9 \times 10^{-10} t^3 + 2.1 \times 10^{-6} t^2 - 0.0041t + 2.8541, & \text{others} \end{cases} \tag{7}$$

$$A_3 = \begin{cases} 0.5, & 1600 < t < 2350 \\ 0, & \text{others} \end{cases} \tag{8}$$

$$A_4 = 2 \times 10^{-10} t^3 - 1 \times 10^{-6} t^2 - 0.0016t + 0.0728 \tag{9}$$

$$B = \begin{cases} 2000, & t < 1300 \\ 4.8 \times 10^{-8} t^3 - 3.5 \times 10^{-4} t^2 - 0.4894t + 1864, & \text{others} \end{cases} \tag{10}$$

In order to test the fitting effect of the trend line, we calculated the values of difference between the trend line and the result of quantitative analysis, the fixed value of mean nighttime VTEC in the Klobuchar traditional model, shown in Fig. 4.

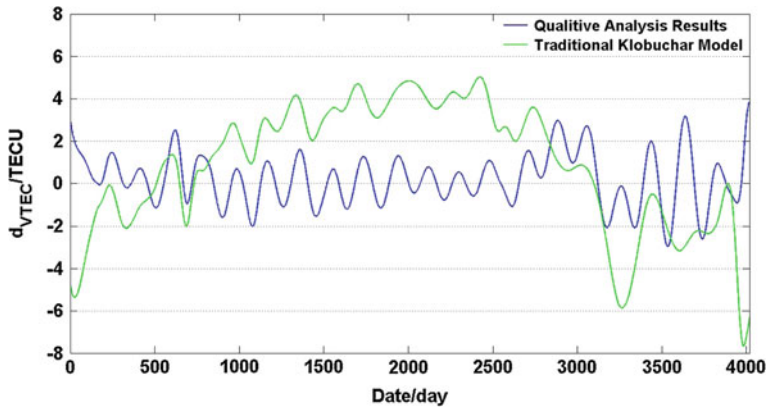

Fig. 4 Deviations of trend line

From the figure, it is obvious that correction effect of the fixed value of mean nighttime VTEC in the Klobuchar traditional model is limited. The values of difference between the trend line and the fixed value of mean nighttime VTEC in the Klobuchar traditional model vary from −8 TECU to +5 TECU. The result of quantitative analysis performs better than the fixed value of mean nighttime VTEC in the Klobuchar traditional model. And the values of difference between the trend line and the result of quantitative analysis vary from −2 TECU to +2 TECU and from −3 TECU to +3 TECU in trough and active solar activity, respectively.

In order to test the fitting effect of the global mean nighttime ionospheric VTEC, we calculated the values of difference between the global mean nighttime ionospheric VTEC and the result of quantitative analysis. The fixed value of mean nighttime VTEC in the Klobuchar traditional model was shown in Fig. 5. From the

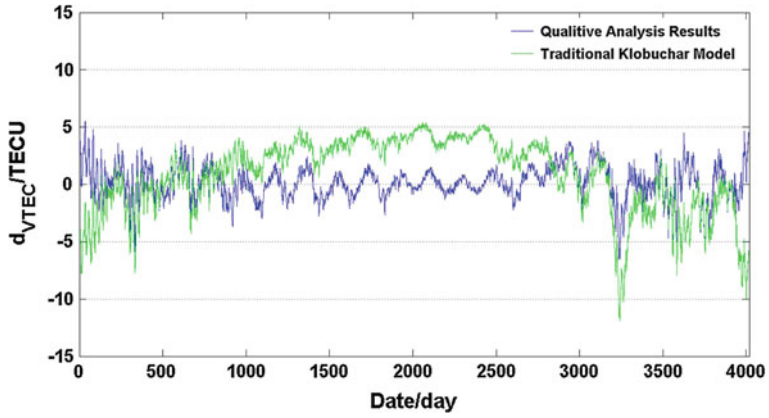

Fig. 5 Deviations of global mean nighttime VTEC

figure, it is obvious that correction effect of the fixed value of mean nighttime VTEC in the Klobuchar traditional model is limited. The values of difference between the global mean nighttime ionospheric VTEC and the fixed value of mean nighttime VTEC in the Klobuchar traditional model vary from −12 TECU to +6 TECU. The result of quantitative analysis performs better than the fixed value of mean nighttime VTEC in the Klobuchar traditional model. And the values of difference between the global mean nighttime ionospheric VTEC and the fitting result of trend line vary from −3 TECU to +3 TECU and from −5 TECU to +5 TECU in trough and active solar activity, respectively.

To quantify the accuracy of quantitative analysis, the correction rate is given by

$$V = 1 - \frac{|\mathrm{VTEC}_{\mathrm{Model}} - \mathrm{VTEC}|}{\mathrm{VTEC}} \times 100\ \% \tag{11}$$

where $\mathrm{VTEC}_{\mathrm{Model}}$ is the VTEC value of a model, and VTEC is the actual value of VTEC. The correction rates of different models, such as the fixed value, the trend line and the result of quantitative analysis, were calculated with the GIMs data regarded as the actual VTEC, shown in Table 1.

Table 1 reveals that the fixed value of mean nighttime VTEC in the Klobuchar traditional model performs worst, with the mean correction rate of 50.4 %. The mean correction rate of the result of quantitative analysis is 86 %, and its ultimate correction rate that is the mean correction rate of trend line is 90.8 %. It is obvious that the mean correction rate of the result of quantitative analysis is in close proximity to its ultimate correction rate. From the Table 1, we can find the minimum correction rate of the fixed value of mean nighttime VTEC in the Klobuchar traditional model is even negative for the following reason. The value of difference between the fixed value and the actual VTEC is more than the actual VTEC, as a result of the fact that the value of VTEC is too low in trough solar activity. It is suggested that the Klobuchar traditional model has some disadvantages in ionospheric correction of nighttime. However, the minimum correction rate of the result of quantitative analysis is 38.6 %, and the same as the minimum correction rate of trend line. The reason for this phenomenon is that the trend line and the fitting value could not reflect the fluctuation caused by ionospheric high frequency variation suitably due to the fact that the ionospheric variation becomes more active in active solar activity. The mean correction rate of the result of quantitative analysis is similar to the average correction rate of trend line, which indicates that the Eq. (1) performs well in fitting trend line and reflecting the trend of the global mean nighttime ionospheric VTEC in this solar activity cycle.

Table 1 Correction rates of mean nighttime VTEC

Correction rates	Maximum (%)	Minimum (%)	Mean (%)
Fixed value	100	−45.1	50.4
Trend line	100	38.6	86.0
Result of quantitative analysis	100	38.6	90.8

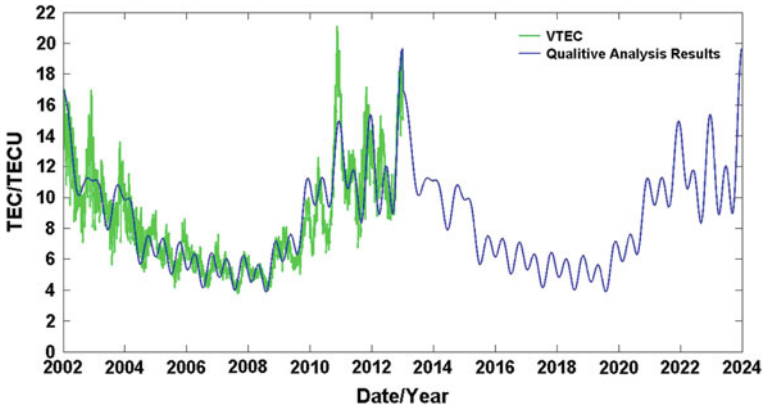

Fig. 6 The comparison of VTEC and the prediction

Figure 6 shows the comparison of the actual calculated values and the forecast values of the global mean nighttime ionospheric VTEC. The values before January 1, 2014 are the results of the quantitative analysis, and the rest are forecast values. As we can see, the result of quantitative analysis can reflect the cycle characteristics and the amplitude of the global mean nighttime ionospheric VTEC, and has a good prediction ability.

For the sake of more intuitive analysis of the prediction ability, the distribution situations of the correction rates in the fitting period, from 2003 to 2013, and the forecast period, from 2003 to 2015, have been count, shown in Table 2.

As shown in Table 2, in the fitting area, the correction rates of the fixed value are distributed in each distribution interval, 58.59 % of which are above 60, and 33.7 % of which are more than 80 %. Most correction rates (about 97.81 %) of the quantitative analysis result mainly concentrate in the distribution interval with correction rates over 60, and 74.81 % of them are more than 80 %. These verify the point mentioned above that the result of quantitative analysis performs better than fixed value in the fitting trend line and reflecting the trend of the global mean

Table 2 The distribution situations of correction rates

	2003–2013		2003–2015	
	Fixed value (%)	Result of quantitative analysis (%)	Fixed value (%)	Result of quantitative analysis (%)
$V \leq 0.0$	5.30	0	4.54	0
$0.0 < V \leq 0.2$	7.39	0	6.34	0
$0.2 < V \leq 0.4$	11.80	0.02	10.11	0.13
$0.4 < V \leq 0.6$	16.92	2.17	18.26	2.99
$0.6 < V \leq 0.8$	24.89	23.00	28.22	26.81
$0.8 < V \leq 1.0$	33.70	74.81	32.53	70.07

nighttime ionospheric VTEC in this solar activity cycle. In the forecast area, the distribution situation of correction rates is accordant well to the one in the fitting period. Therefore, the result of quantitative analysis has a good prediction ability for the global mean nighttime ionospheric VTEC.

4 Conclusions

In this paper, the EMD method has been applied in quantitative analysis of the global mean ionospheric VTEC of nighttime, which has overcome the difficulty in the quantitative analysis of nonlinear nonstationary VTEC sequences. On the comparison of the result of quantitative analysis, the trend line, the actual VTEC from GIMs data and the correction rates, it has verified that the quantitative analysis result given by this paper is reliable and has a good prediction ability. It proves that the fixed value of mean nighttime VTEC in the Klobuchar traditional model is extraordinarily similar to the mean nighttime VTEC in the solar activity cycle selected in this paper, and Klobuchar traditional model has some disadvantages in ionospheric correction of nighttime.

Due to the fact that the quantitative analysis result given by this paper is reliable to reflect and forecast the global mean ionospheric VTEC of nighttime, it can be applied to the elaboration of global ionosphere model, ignoring the influence of the change of latitude.

References

1. Fritsche M, Dietrich R, Knöfel C, Rülke A, Vey S, Rothacher M, Steigenberger P (2005) Impact of higher-order ionospheric terms on GPS estimates. Geophys Res Lett 32(23):23311–23315
2. Liu J (2008) GPS satellite navigation and positioning principle and method. Science press, Beijing
3. Management office of China's satellite navigation system. Public service of the Beidou satellite navigation system space signals interface control file. (2.0), 2013
4. Klobuchar JA (1987) Ionospheric time delay algorithm for single frequency GPS users. IEEE Trans Erospace Electron Syst 23(3):325–331
5. Zhu J (1991) Research of astronomy and geodetic VLBI physical model. Nanjing University, Nanjing
6. Zhao W, Zhang C (2013) Practical analysis and improvement of Klobuchar model. Chin J Space Sci 33(6):624–628
7. Huang Y, Wang M, Han L (2006) Improvement based on the Chinese material for Klobuchar ionospheric model. In: The 19th academic communication of professional committee of China's space science society space detection. Space science society of China, Ningbo
8. Li M, Liao Y, Liang J, Wen Y (2009) Research of ionospheric delay model improvement. Comput Simul 10:21–24
9. Cai C, Gao J, Li Z (2006) The seasonal variation monitoring of ionospheric total electron content by GPS. J Wuhan Univ Ed Inf Sci 5:451–453

10. Liu L, Wan W, Chen Y et al (2011) The relationship between the ionosphere and the solar activity. In: The eleventh academic annual meeting of institute of geology and geophysics of Chinese academy of sciences, pp 477–487
11. Kumar S, Singh AK (2011) Storm time response of GPS-derived total electron content (TEC) during low solar active period at Indian low latitude station Varanasi. Astrophys Space Sci 331(2):447–458
12. Bhuyan PK, Hazarika R (2013) GPS TEC near the crest of the EIA at 95°E during the ascending half of solar cycle 24 and comparison with IRI simulations. Adv Space Res 52:1247–1260
13. Solomon SC, Qian L, Burns AG (2013) The anomalous ionosphere between solar cycles 23 and 24. J Geophys Res Space Phys 118(10):6524–6535
14. Xu Z, Wang W, Zhang R et al (2013) Analysis of the ionospheric TEC characteristics of the twenty-third cycle of the solar activity of WuHan Station. Space Sci J 01(01):28–33
15. Huang NE, Zheng Shen, Long, SR et al (1998) The empirical mode decomposition and the Hilbert spectrum for nonlinear and non-stationary time series analysis. Proc Roy Soc London Ser A, Math Phys Eng Sci 454:903–995
16. Li Q, Wu J, Xu Z et al (2007) To extract the periodic components of solar activity by EMD. Space Sci J 27(1):1–6
17. Wang J, Gao J, Wang J (2008) The calculating of GPS baseline model based on EMD. J Surveying and Mapp 37(1):10–14
18. Gan Y, Sui L, Wang B (2012) EMD threshold denoising method and its application in data processing in inertial navigation system. J Surveying Mapp 41(4):504–509

Convergence Time Analysis of Multi-constellation Precise Point Positioning Based on iGMAS Products

Yulong Ge, Baoqi Sun, Shengli Wang, Pengli Shen and Jinhai Liu

Abstract This contribution focuses on the performance of multi-GNSS precise point positioning (PPP) with iGMAS products. Daily GNSS measurements from 50 stations observed during one hundred days in 2015 are used, the convergence time and positioning accuracy are investigated. As a comparison, the same processing is employed by using GBM products provided by GFZ. The results show that: (1) Compared to GPS-only PPP, multi-GNSS PPP has a great improvement in convergence time, while it is not significant for positioning accuracy. In detail, the averaged convergence time of GPS/BDS PPP is reduced by 14.6 %, and 28.86 % for GPS/GLONASS PPP; the GPS/BDS/GLONASS PPP can further decrease the convergence time, but no obvious improvement is found in four-constellation (GPS/BDS/GLONASS/GALILEO) PPP, compared with GPS/BDS/GLONASS PPP, due to the limited number of GALILEO satellites. As to the positioning accuracy, they are in the same level after the initialization. (2) Using the same observation data, the final position accuracy of both the multi-constellation PPP using iGMAS products and that using GBM products could reach millimeter level in the horizontal, while the convergence time of iGMAS products is relatively slow. Analysis of statistical results shows that the accuracy of positioning is reliable, which could further prove the stability and reliability of iGMAS products.

Keywords Multi-constellation GNSS precise point positioning · Convergence time · iGMAS · Static positioning

S. Wang (✉)
Institute of Ocean Engineering, Shandong University of Science and Technology, Qingdao 266000, China
e-mail: Victory_wsl@vip.126.com

Y. Ge · B. Sun · P. Shen · J. Liu
National Time Service Center, Chinese Academy of Sciences, Xi'an, China

B. Sun
Key Laboratory of Precise Navigation, Positioning and Timing Technology, Chinese Academy of Sciences, Xi'an 710600, China

Y. Ge · P. Shen · J. Liu
University of Chinese Academy of Sciences, Beijing, China

© Springer Science+Business Media Singapore 2016

J. Sun et al. (eds.), *China Satellite Navigation Conference (CSNC) 2016 Proceedings: Volume III*, Lecture Notes in Electrical Engineering 390,
DOI 10.1007/978-981-10-0940-2_26

1 Introduction

Precise point positioning (PPP) is the technology which uses a single dual-frequency GNSS receiver to receive the pseudorange and carrier-phase observations, and the precise orbit and clock products provided by IGS to achieve high-precision absolute positioning. The accuracy of PPP results can be in the millimeter level, and the height accuracy could reach the centimeter level. After years of development, the theory of GPS PPP has been quite mature, and has been widely used in scientific research and industrial applications. Since 2007, with the establishment and development of the four navigation systems, multi-constellation PPP becomes feasible [1–4]. The combination of several navigation systems could greatly improve the satellite's geometric graphics intensity, and significantly increase the positioning accuracy and reduce the convergence time. China's BeiDou navigation system (BDS) began to provide positioning services in December 7, 2012, and plans to provide global navigation services in 2020. The convergence time and positioning accuracy of different constellation combinations are analyzed in this paper [4], including the BeiDou-only PPP which has poorer accuracy than the GPS-only PPP. But GPS/BeiDou significantly improves the positioning accuracy by 28, 6, and 7 % in the east, north, and up components in terms of the RMS statistics, respectively, and the convergence time reduces for 26, 13, and 14 %, respectively. The GPS/GLONASS PPP achieves slightly better positioning accuracy than the GPS/BDS PPP. The triple-constellation PPP further increases the positioning accuracy and decreases the convergence time over the dual-constellation PPP. While, for the limited number of Galileo satellites, in the multi-constellation PPP, its effect on the convergence time and positioning accuracy is not obvious. In this study, the multi-constellation PPP model is developed and its performance is assessed in terms of positioning accuracy and convergence time through static tests by using iGMAS products [5] and the stability of iGMAS products is analyzed.

The main work includes two aspects. One is to develop multi-constellation PPP model and processing method. The second aspect is the comparison of the precision positioning results of iGMAS products and GBM products and analysis on the stability of products.

2 PPP Model with Multi-constellation

The pseudorange and carrier-phase observations can be expressed as:

$$P_j^s = \rho + c \cdot \delta t - c \cdot \delta t^s + d_{\text{trop}}^s + I_j^s + c(d_r + d_i^s) + \varepsilon_p \tag{1}$$

$$\Phi_j^s = \rho + c \cdot \delta t - c \cdot \delta t^s + d_{\text{trop}}^s - I_j^s + \lambda_j N_j^s + \varepsilon_\Phi \tag{2}$$

where the superscript s represents a GNSS satellite, P_j^s is code observations on the jth frequency, Φ_j^s is carrier observations on the jth frequency, ρ is the geometric distance, c is the speed of light, δt is the receiver clock biases, δt^s is the satellite clock biases, d_{trop}^s is the tropospheric delay in meters, I_j^s is the ionospheric delay at jth frequency, the effect of the ionospheric delay on different frequency observations has the following relations: $I_j^s = (\lambda_j^2/\lambda_k^2)I_k^s$, where j, k is the jth or kth frequency, d_r and d_i^s are receiver and satellite terminal hardware delay deviation, λ_j is the wavelength of carrier phase on the jth frequency, N_j is the float ambiguity on the jth frequency.

Using dual-frequency pseudorange and carrier-phase observations of ionosphere-free positioning model, the expression is as follows:

$$P_{\mathrm{IF}} = \frac{f_1^2 \cdot P_1 - f_2^2 \cdot P_2}{f_1^2 - f_2^2} \tag{3}$$

$$\Phi_{\mathrm{IF}} = \frac{f_1^2 \cdot \Phi_1 - f_2^2 \cdot \Phi_2}{f_1^2 - f_2^2} \tag{4}$$

where P_{IF} is ionosphere-free code observation, Φ_{IF} is the ionosphere -free carrier-phase observable, f_1 and f_2 are two carrier-phase frequencies in Hertz.

Multi-constellation GNSS combination can accelerate the convergence rate, improve the positioning accuracy in harsh observation environment, and improve the performance of navigation and positioning, but there is also a problem of compatibility between different systems. These compatibility problems, are mainly caused by the benchmark differences, mainly exist in different navigation systems and the difference of the signal system, the difference of spatial datum is resolved by the orbit of GNSS products, the key problem is to deal with the time difference between different navigation systems. So, if the GPS system time is chosen as the reference time scale, the quad-constellation PPP observation equations may be expressed as follows:

$$P_{\mathrm{IF}}^g = \rho^g + \mathrm{cdt} + d_{\mathrm{trop}}^g + \varepsilon_{P_{IF}}^g \tag{5}$$

$$\Phi_{\mathrm{IF}}^g = \rho^g + \mathrm{cdt} + \lambda N + \varepsilon_{\Phi_{\mathrm{IF}}}^g \tag{6}$$

$$P_{\mathrm{IF}}^o = \rho^o + \mathrm{cdt} + \mathrm{cdt}_{\mathrm{sys}} + d_{\mathrm{trop}}^o + \varepsilon_P^o \tag{7}$$

$$\Phi_{\mathrm{IF}}^{\mathrm{o}} = \rho^o + \mathrm{cdt} + \mathrm{cdt}_{\mathrm{sys}} + \lambda N + \varepsilon_\Phi^o \tag{8}$$

where dt_{sys} is the time difference between GPS and different systems, N and N^o are the parameters of the float ambiguity after being redefined, ε_P and ε_Φ include noise and other measurement error, ρ is the geometric range in meters, c is the speed of light, g refers to GPS, and o refers to other navigation system.

3 Data Description

The data used are collected at fifty IGS stations on 100 days, from June 17, 2015 to October 10, 2015. As iGMAS products in the above time period has a partial loss, the experiment only tests 100 days of observation data. All stations can receive observations from GPS, BDS, GLONASS, and Galileo constellations. Observations have a sampling interval of 30 s, the orbit and clock biases of GBM products have a sampling interval of 15 min and 30 s, respectively, the orbit and clock biases of iGMAS products have a sampling interval of 15 min and 5 min, respectively. The "igs08_1861. Atx" file data generated and released by IGS are used to correct the GPS and GLONASS satellite phase center offset (PCO). The BeiDou and Galileo antenna offsets recommended by the MGEX (The Multi-GNSS Experiment) project are used to correct the PCOs of BeiDou and Galileo satellites [4, 6]. The Kalman filter algorithm is applied in the multi-constellation PPP model. The GPS and GLONASS code observation precision is set to be 0.3 m. The GPS and GLONAS phase observation precision is set to be 0.003 m. The BeiDou and Galileo code observation precision is set to be 0.6 m and the phase observation precision is set to be 0.004 m. The accuracy of orbit provided by iGMAS about GEO satellites and IGSO/MEO satellites is 400 and 15 cm, respectively, so the weight of the GEO satellites is decreased 30 times.

4 Analysis of Positioning Results

The static processing of quad-constellation PPP is carried out by using iGMAS products, and mainly analyzes five different constellation combinations, which are GPS-only, GPS/BDS, GPS/GLONASS, GPS/GLONASS/BDS, and GPS/GLONASS/BDS/Galileo. In the study, the position filter is considered to have converged when the positioning errors reach ±0.1 m and remain within ±0.1 m. And the convergence time is the period from the first epoch to the converged epoch. Figure 1 represents the PPP positioning errors which are based on five processing cases. Among it, G, C, R, and E represent GPS, BeiDou, GLONASS, and Galileo, respectively, the same below. It is obvious that double-constellation PPP positioning results are better than GPS-only PPP. The GPS/BDS PPP has achieved better convergence performance than GPS-only PPP, compared with the GPS/BDS PPP, the GPS/GLONASS PPP has achieved slightly better convergence performance. The GPS/GLONASS/BDS PPP results are extremely similar to those of GPS/GLONASS PPP, and the quad-constellation PPP results are not significantly improved.

Figure 2 shows the number of available satellite and PDOP (position dilution of precision) for five processing cases. There are less available GPS satellites for GPS-only, and the PODP value is relatively big. The dual-constellation combination increases the number of visible satellites and reduces the PDOP value. From dual

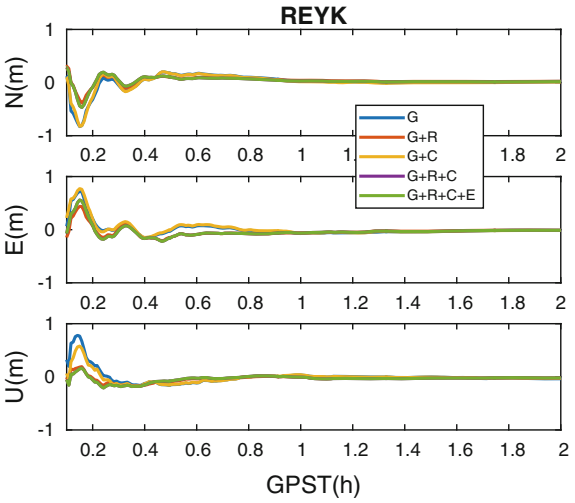

Fig. 1 PPP positioning errors at REYK for five different processing cases

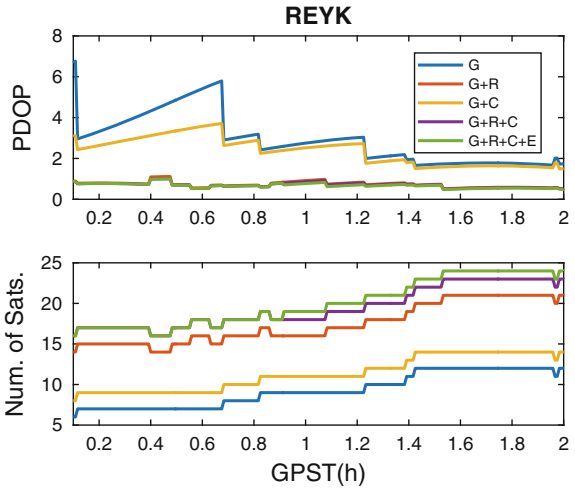

Fig. 2 Satellite of number and PDOP at REYK

constellation to triple constellation, along with the increase of the number of satellites, PDOP value decreases obviously and the PDOP value of quad-constellation combination is similar to the triple-constellation combination. From this, one can draw the conclusion that multi-constellation PPP can improve the structure of the satellite geometry and increase the number of satellites. Figure 3 shows the distributions of convergence time for five combination PPP models by using iGMAS products and GBM products, respectively, whose datasets are collected at fifty stations over one hundred days. It can be seen that the average convergence times of GPS-only PPP, GPS/BDS PPP, GPS/GLONASS PPP, and GPS/BDS/GLONASS PPP are 40.2, 34.3, 28.6, and 28.1 min, respectively. One can draw the conclusion that multi-constellation PPP can decrease convergence time.

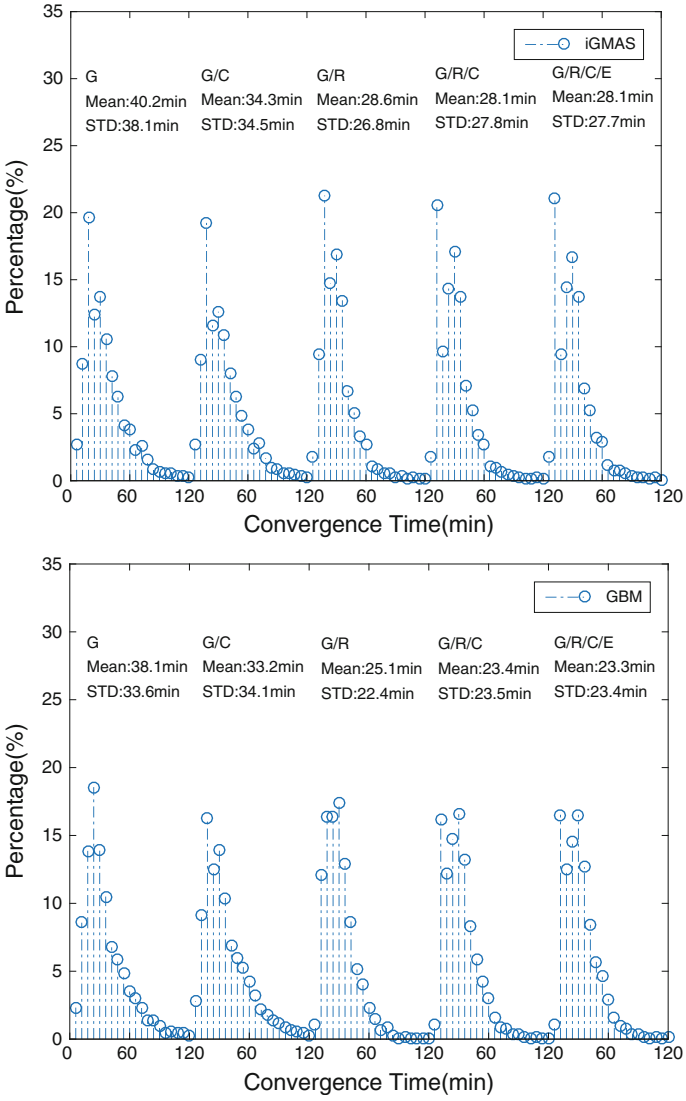

Fig. 3 Distributions of convergence time for five combination PPP models using datasets collected at fifty stations over one hundred days

In the paper [7], as long as the prior information of coordinates is accurate enough, the position filter can be converged within a single epoch. The main reason for why multi-constellation could accelerate convergence includes the following three aspects:

Table 1 Comparison of multi-constellation PPP model

	G	G/C	G/R	G/C/R	G/C/R/E
Observed quantity	2m	2m + 2n	2m + 2p	2m + 2n + 2p	2m + 2n + 2p + 2q
Parameter to be evaluated	m + 5	m + n+6	m + p+6	m + n+p + 7	m + n+p + q+8
Redundancy	m − 5	m + n − 6	m + p − 6	m + n+ p − 7	m + n + p + q − 8

- More satellites can be observed by multi-constellation PPP, thus the accuracy of initial results could be improved.
- Multi-constellation PPP can improve the structure of the satellite geometry, which would accelerate the convergence of parameters to be evaluated [7].
- Table 1 provides comparison of multi-constellation PPP model, where m, n, p, and q refer to GPS, BDS, GLONASS, and Galileo, respectively. Compared with single GPS-only PPP, multi-constellation PPP has higher redundancy, therefore multi-constellation PPP can accelerate the convergence of the parameters to be evaluated.

5 Comparative Analysis of Positioning Results

iGMAS products are analyzed and compared with GBM products from the aspects of positioning accuracy, the convergence time, the tropospheric delay, and the receiver clock biases. Table 2 provides the RMS (root mean square) statistics in the north (N), east (E), and up (U) coordinate components to demonstrate a static positioning accuracy. The RMS computations are based on the average of position solution errors of the last 20 min during one hundred days. Compared with the multi-constellation PPP results obtained by using GBM products, those obtained by using iGMAS products achieve the same positioning accuracy. But the convergence time is relatively slow. Figure 3 shows that the convergence time of several combined positioning is slower than that of GBM for 2.1, 1.1, 3.5, 4.7, and 4.8 min.

Table 2 RMS statistics of positioning errors at stations CUT0

CUT0						
	iGMAS products			GBM products		
	N (m)	E (m)	U (m)	N (m)	E (m)	U (m)
G	0.0017	0.002	0.017	0.0007	0.0023	0.011
G/C	0.0015	0.0023	0.020	0.0011	0.0021	0.021
G/R	0.002	0.002	0.013	0.0010	0.0020	0.011
G/C/R	0.0019	0.0017	0.010	0.0009	0.0017	0.006
G/C/R/E	0.0019	0.0016	0.010	0.0009	0.0016	0.005

Figures 4 and 5 provide troposphere solutions and the difference of receiver clock biases which are calculated by using iGMAS products and GBM products, respectively. The troposphere is basically the same, the difference is in the millimeter level. The difference of the receiver clock biases is less than 10 ns, which is due to the difference between two clock references. Figure 6 provides the statistical results of the RMS in the three-dimensional position, Fig. 7 provides the RMS in the east, north, and up coordinate using 100 days datasets at CUT0. Analyzing Fig. 6, the average RMS values of the three-dimensional position of the two products are 0.059 and 0.0601 cm. One can draw the conclusion that the positioning accuracy of iGMAS products is quite similar to that of GBM products. Analyzing Fig. 7, compared to results calculated by the GBM product, part of the

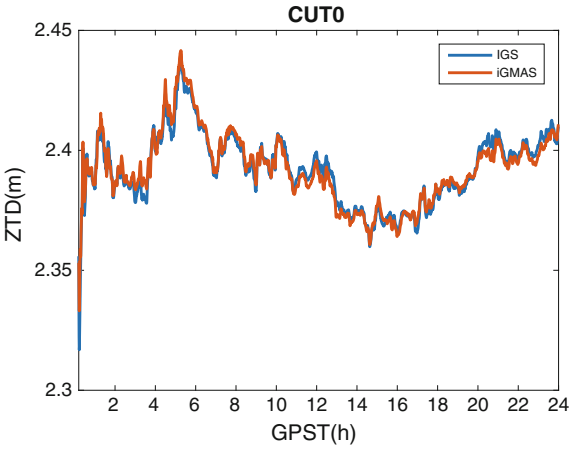

Fig. 4 Troposphere solutions

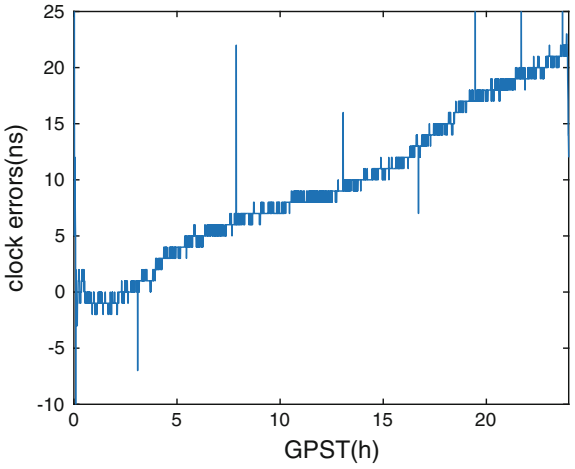

Fig. 5 Difference of receiver clock biases

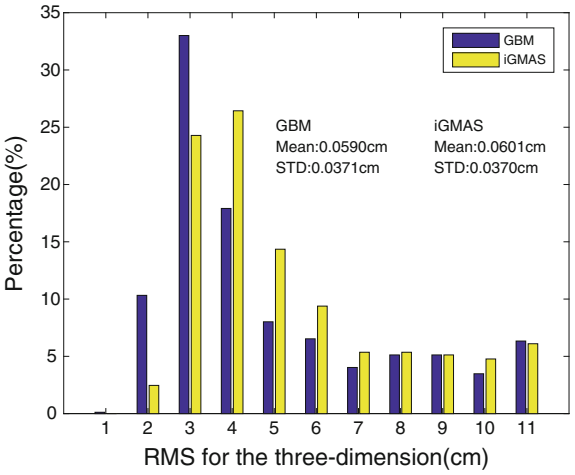

Fig. 6 Distributions of RMS for the three-dimension using 100 days datasets at 50 stations

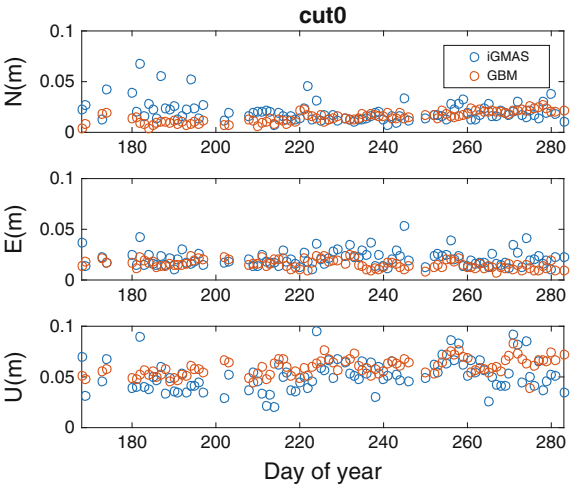

Fig. 7 The RMS in the east, north, and up coordinate using 100 days datasets at CUT0

RMS values of solutions calculated by iGMAS product in the NEU three directions are big, while are stable on the whole. It can be concluded that iGMAS products are reliable in positioning accuracy and stability of products.

6 Conclusions

With the accuracy of BeiDou and Galileo satellite orbit and clock increasing, the results of the multi-constellation PPP are slightly better than GPS-only PPP and dual-constellation PPP. This article focuses on the accuracy of positioning,

convergence time, and the stability of products by using iGMAS products. The GPS/BDS PPP reduces the convergence time by 14.6 % over the GPS-only cases. The GPS/GLONASS PPP decreases the convergence time by 28.86 % over the GPS-only PPP. In the triple-constellation PPP, the convergence time is further reduced by 30.1 %. Because the number of Galileo available satellite is extremely small, so the results of quad-constellation PPP are similar to those of triple-constellation PPP. Compared with the convergence time through using GBM products, the average convergence times of five combination model PPP positionings are 1.1 min, 2.1 min, 3.5 min, 4.7 min, and 4.8 min slow, respectively. The reason why multi-constellation PPP could accelerate the convergence mainly consists of three aspects: (1) it can provide more accurate initial value; (2) it can improve satellite spatial structure; (3) it has higher redundancy, which can accelerate the convergence of parameters to be evaluated. The accuracy of horizontal to be positioned by iGMAS and GBM products could reach millimeter to centimeter level, and the height accuracy is centimeter level, collect single-day solutions at 50 stations and for 100 days, the average RMS values of the three-dimensional position of the two products are 0.059 and 0.0601 cm, respectively. The difference of troposphere average is at millimeter level, and the clock biases difference is less than 10 ns. The 100 test results could show the stability of positioning accuracy, and remain at 0.0212, 0.0217 and 0.0355 m at the three directions of NEU, this illustrates the reliable stability of iGMAS products, and thus it is reliable to use iGMAS products.

Acknowledgments This work is supported by the Open Fund of Key Laboratory of Precision Navigation and Timing Technology, National Time Service Center, CAS(No. 2014PNTT06), National Natural Science Foundation of China (No. 41104021) and National Natural Science Foundation of China (No. 11173026). The authors gratefully acknowledge iGMAS and GFZ for providing products and are really grateful for data from MGEX.

References

1. Li X, Ge M, Dai X et al (2015) Accuracy and reliability of multi-GNSS real-time precise positioning: GPS, GLONASS, BeiDou, and Galileo. J Geodesy 89(6):607–635
2. Li X, Zhang X, Ren X et al (2015) Precise positioning with current multi-constellation global navigation satellite systems: GPS, GLONASS, Galileo and BeiDou. Scientific reports, p 5
3. Li P, Zhang X (2014) Integrating GPS and GLONASS to accelerate convergence and initialization times of precise point positioning. GPS Solutions 18(3):461–471
4. Cai C, Gao Y, Pan L et al (2015) Precise point positioning with quad-constellations: GPS, BeiDou, GLONASS and Galileo. Adv Space Res 56(1):133–143
5. Cai H, Chen K, Xu T et al (2015) The iGMAS combined products and the analysis of their consistency. In: China satellite navigation conference (CSNC) 2015 proceedings: volume III. Springer, Berlin, pp 213–226
6. Rizos C, Montenbruck O, Weber R, et al. (2013) The IGS MGEX experiment as a milestone for a comprehensive multi-GNSSservice. In: Proceedings of ION PNT
7. Song C (2015) Technologies and methods on rapid convergence of precise point positioning. The PLA Information Engineering University

BDS Real-Time Cycle-Slip Detection and Repair Based on Ionospheric Correction

Lingfeng Xu, Changjian Liu, Sai Wang, Chen Liu and Xu Feng

Abstract According to the principle of triple-frequency carrier phase combination and considering the influence of ionospheric delay on combined observation, this paper selects three linearly independent sets of coefficients of combined observation to calculate ionospheric residuals between epochs and correct the wide lane observation; the sum of coefficients of wide lane observation is a nonzero value. Then based on the combined observation of reparation, calculate cycle-slip integer value and repair the cycle slip. By using BeiDou triple-frequency observation data, the experiment shows that proposed method can effectively detect and repair cycle slips of BeiDou triple-frequency observation in real time.

Keywords BDS triple frequency · Independently linear combination · Ionospheric correction · Cycle-slip detection and repair

1 Introduction

As the indispensable steps in data preprocessing of satellite precise positioning, cycle-slip detection and repair can determine the final positioning accuracy. Now, there are many ways to detect and repair the cycle slip, such as high-order difference method, polynomial fitting method, ionosphere residual error method, the pseudorange minus phase linear combination, the geometry-free phase combination, and so on [1]. With the development of BeiDou system, the domestic and foreign scholars have done a lot of researches on triple-frequency data processing. Literature [2] used the similar three carrier ambiguity resolution (TCAR) method which can effectively detect and correct cycle slip in real time.

L. Xu (✉) · C. Liu · S. Wang · C. Liu · X. Feng
Institute of Geospatial Information, Information Engineering University, Zhengzhou, China
e-mail: 495076822@qq.com

© Springer Science+Business Media Singapore 2016

J. Sun et al. (eds.), *China Satellite Navigation Conference (CSNC) 2016 Proceedings: Volume III*, Lecture Notes in Electrical Engineering 390,
DOI 10.1007/978-981-10-0940-2_27

Literature [3] used two triple-frequency geometry-free phase combinations and a pseudorange minus phase linear combination to realize undifferential cycle-slip real-time detection and correction. Literature [4] utilized geometry-free and ionosphere-free combination to detect cycle slips. Literature [5] selected (0, 1, −1), (−3, 1, 3), (1, −7, 6) nonlinear combination to detect and repair well in GPS triple-frequency observations. According to the principle of triple-frequency carrier phase combination and considering the influence of ionospheric delay, this paper uses EWL (0, 1, −1), WL (1, 0, −1), and the sum of coefficients of wide lane observation that is a nonzero value (4, −2, −3). These three sets of coefficients make up of a linear independent array. Then getting the ionospheric residuals between epochs and correcting the WL (4, −3, −2) combined observation. Then, cycle-slip integer value is calculated to repair the cycle slip based on the combined observation of reparation.

2 Principle of Triple-Frequency Carrier Phase Combination

Carrier phase observation equation is as follows: [6]:

$$\phi_i = \lambda_i \varphi_i = \rho - \beta_{\varphi_i} \cdot I + \lambda_i \cdot N_i + \varepsilon_{\varphi_i} \tag{1}$$

Where ϕ_i is the carrier phase measurement in meters; φ_i is the carrier phase observation in cycles; λ_i is the corresponding wavelength; N_i is the integer ambiguity; ρ is the geometric distance between the satellite and receiver, which includes satellite clock error, troposphere delay, and hardware delay of the satellite and the receiver. $\beta_{\varphi_i} = f_1^2 / f_i^2$ is the ratio coefficient of the ionospheric delay of corresponding frequency; ε_{φ_i} is the carrier phase measurement noise.

The linearly combined triple-frequency carrier phase observation can be defined as below [7].

$$\phi_{(i,j,k)} = \frac{i \cdot f_1 \cdot \phi_1 + j \cdot f_2 \cdot \phi_2 + k \cdot f_3 \cdot \phi_3}{i \cdot f_1 + j \cdot f_2 + k \cdot f_3} \tag{2}$$

Where the combined coefficients i, j, and k are integers; the f_1, f_2, and f_3 frequency in accordance with the order from large to small, are corresponding to B1, B3, and B2 of BeiDou, shown in Table 1.

Table 1.1 BDS triple-frequency frequencies and wavelengths

BDS	Frequency (MHz)	Wavelength (m)
B1	1561.098	0.1920
B3	1268.520	0.2363
B2	1207.140	0.2483

The linearly combined frequency, wavelength, and integer ambiguity can be defined as follows: [8].

$$\begin{cases} f_{(i,j,k)} = i \cdot f_1 + j \cdot f_2 + k \cdot f_3 \\ \lambda_{(i,j,k)} = c/f_{(i,j,k)} = c/i \cdot f_1 + j \cdot f_2 + k \cdot f_3 \\ N_{(i,j,k)} = i \cdot N_1 + j \cdot N_2 + k \cdot N_3 \end{cases} \tag{3}$$

Due to the fact that i, j, and k are integers, the ambiguity $N_{(i,j,k)}$ still keeps its integer nature. Therefore, the linearly combined carrier phase observation equation can be shown as:

$$\phi_{(i,j,k)} = \rho - \beta_{(i,j,k)} \cdot I - \lambda_{(i,j,k)} \cdot N_{(i,j,k)} + \varepsilon_{(i,j,k)} \tag{4}$$

Where $\beta_{(i,j,k)}$ is the ratio coefficient of ionospheric delay of the combined observation. It can be expressed as

$$\beta_{(i,j,k)} = \frac{f_1^2 (i/f_1 + j/f_2 + k/f_3)}{i/f_1 + j/f_2 + k/f_3} \tag{5}$$

The carrier phase noises of three frequencies are assumed to be independent and identical in standard deviation. We assume that the carrier phase noises of BDS are $\sigma_{\phi_1} = \sigma_{\phi 2} = \sigma_{\phi 3} = 0.003m$ [9] and the variances of the combined carrier phase observation are

$$\sigma_{\phi_{(i,j,k)}} = \frac{(i \cdot f_1)^2 \cdot \sigma_{\phi_1}^2 + (j \cdot f_2)^2 \cdot \sigma_{\phi_2}^2 + (k \cdot f_3)^2 \cdot \sigma_{\phi 3}^2}{i \cdot f_1 + j \cdot f_2 + k \cdot f_3} \tag{6}$$

When $\sigma_{\phi_{(i,j,k)}}^2 = \mu_{(i,j,k)}^2 \sigma_\phi^2$, $\mu_{(i,j,k)}$ is the phase noise factor:

$$\mu_{(i,j,k)}^2 = \frac{(i \cdot f_1)^2 + (j \cdot f_2)^2 + (k \cdot f_3)^2}{(i \cdot f_1 + j \cdot f_2 + k \cdot f_3)^2} \tag{7}$$

3 Cycle-Slip Detection and Repair

3.1 The Estimation of Combined Cycle Slip

According to the method of TCAR [10], a solution can be given to detect and repair the cycle slip shown as follows:

EWL cycle slips:

$$\Delta N_{(0,1,-1)} = \left(\frac{f_2 \cdot \Delta\phi_2 - f_3 \cdot \Delta\phi_3}{f_2 - f_3} - \frac{f_2 \cdot \Delta P_2 + f_3 \cdot \Delta P_3}{f_2 + f_3} \right) / \lambda_{(0,1,-1)} \tag{8}$$

WL cycle slips:

$$\begin{aligned} \Delta N_{(i,j,k)} = & \left(\Delta\phi_{(0,1,-1)} - \Delta\phi_{(i,j,k)} - (\beta_{(0,1,-1)} - \beta_{(i,j,k)})\Delta I \right) \\ & + \Delta\hat{N}_{(0,1,-1)} \lambda_{(0,1,-1)} / \lambda_{(i,j,k)} \end{aligned} \tag{9}$$

WL cycle slips in which the sum of coefficients is a nonzero value:

$$\begin{aligned} \Delta N_{(l,m,n)} = & (\Delta\phi_{(i,j,k)} - \Delta\phi_{(l,m,n)} - (\beta_{(i,j,k)} - \beta_{(l,m,n)})\Delta I) \\ & + \Delta\hat{N}_{(i,j,k)} \lambda_{(i,j,k)} / \lambda_{(l,m,n)} \end{aligned} \tag{10}$$

3.2 The Estimation of Ionospheric Delay

The combined measurements are heavily affected by the ionospheric delay. So, we need to correct the ionospheric delay when the sampling intervals are large or the ionospheric activity is violent. Then the ionospheric delay between epochs can be calculated by the original measurements:

$$\Delta I = \Delta(\phi_1 - \phi_2) / (f_1^2 / f_2^2 - 1) \tag{11}$$

Where is the ionospheric delay between epochs; and are the originally undifferenced observation; and are the corresponding frequencies.

3.3 Cycle-Slip Repair

Similar to TCAR, the combination EWL (0, 1, −1) and WL (1, 0, −1) of small noise were chosen. Because the sum of two groups of coefficient is zero, the combination (4, −3, −2) of small noise was selected to keep the matrix of coefficient invertible, whose coefficient is not equal to zero. However, the ionospheric delay coefficient is −144.8668, as a result of which the combination (4, −3, −2) is seriously affected by the ionospheric delay. Thus, measures must be taken to correct the ionospheric delay for improving the accuracy of cycle-slip detection. Based on the linear independence of three groups of coefficient, the integers of three original frequency observation cycle slips can be calculated by Formula 12.

$$\begin{bmatrix} 0 & 1 & -1 \\ 1 & 0 & -1 \\ 4 & -3 & -2 \end{bmatrix} \begin{bmatrix} \Delta\hat{N}_1 \\ \Delta\hat{N}_2 \\ \Delta\hat{N}_3 \end{bmatrix} = \begin{bmatrix} \Delta\hat{N}_{(0,1,-1)} \\ \Delta\hat{N}_{(1,0,-1)} \\ \Delta\hat{N}_{(4,-3,-2)} \end{bmatrix} \tag{12}$$

Where $\Delta\hat{N}_1$, $\Delta\hat{N}_2$ and $\Delta\hat{N}_3$ are repaired cycle slips; ϕ_1, ϕ_2 and ϕ_3 are the original observations.

The integer of the original frequency's cycle slips can be calculated from the integers of EWL and two WL cycle slips.

$$\begin{bmatrix} \Delta\hat{N}_1 \\ \Delta\hat{N}_2 \\ \Delta\hat{N}_3 \end{bmatrix} = \begin{bmatrix} -3 & 5 & -1 \\ -2 & 4 & -1 \\ -3 & 4 & -1 \end{bmatrix} \begin{bmatrix} \Delta\hat{N}_{(0,1,-1)} \\ \Delta\hat{N}_{(1,0,-1)} \\ \Delta\hat{N}_{(4,-3,-2)} \end{bmatrix} \tag{13}$$

4 Experiment and Analysis

The triple-frequency data, collected by Sinan receiver with a sample of 10 s from 02:28:20 to 05:00:00 on July 31, 2014, are taken into simulation in this paper.

4.1 The Estimation of Ionospheric Delay

The ionospheric delay between epochs for satellite C01 and C08 was calculated by a software by self, shown in Fig. 1.

From the figure, the ionospheric delay between epochs for satellite C01 and C08 was less than 0.02 m; the average values were 0.0037 and 0.0023 m; RMS were 0.0047 and 0.0045.

4.1.1 Combination Cycle-Slip Detection Residuals

Figure 2 shows the analysis results of the combined cycle-slip detection residuals for satellite C01 and C08. From the figure, we can know that the residuals of EWL's cycle-slip detection are less than 0.1 cycle; the residuals of WL's cycle-slip detection are less than 0.2 cycle; the residuals of WL (4, −3, −2)'s cycle-slip detection are less than 0.3 cycle. The statistical properties are shown in Table 2.

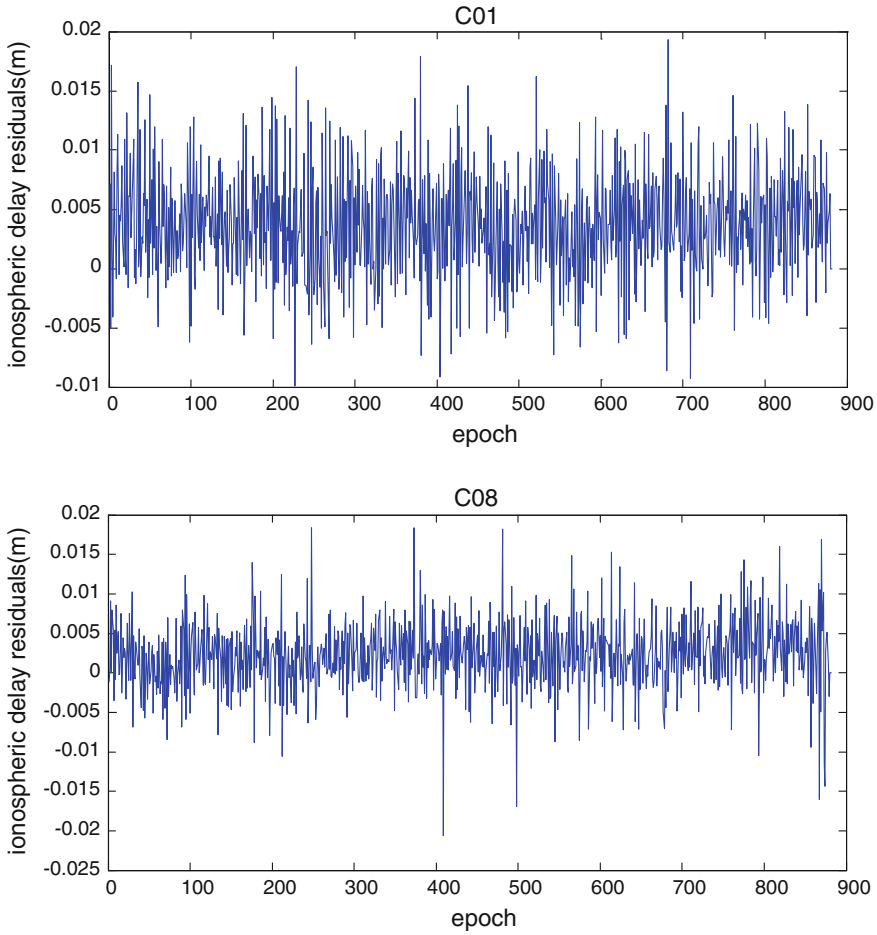

Fig. 1 Ionospheric delay residuals between epochs for satellite C01 and C08 with 10 s observation interval

4.2 Simulate Cycle Slip

The simulate cycle slips (0, 3, 0) and (2, −1, 2) were added to C01 and C08 satellite in 300th epoch and 600th epoch. The analysis results of the EWL's result and the WL's result are shown in Fig. 3. From the figure, we can know that the simulate cycle slips have been successfully detected.

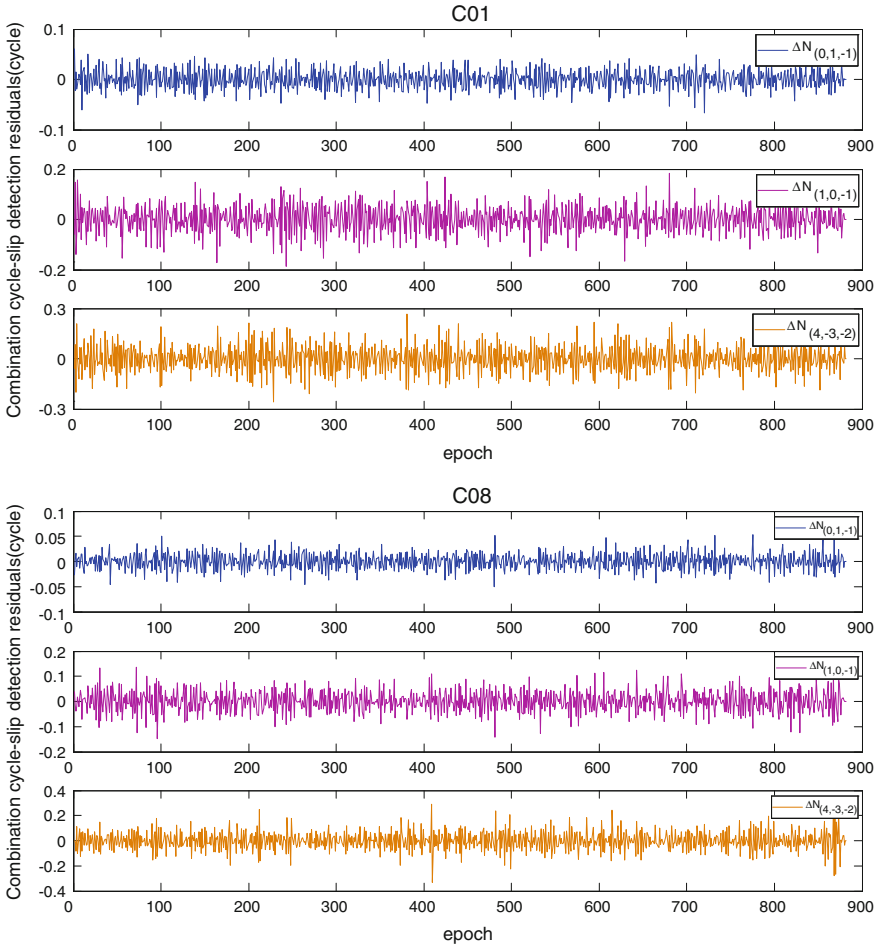

Fig. 1.2 Combination cycle-slip detection residuals for satellite C01 and C08 with 10 s observation interval

Table 1.2 The mean and standard deviation of the residuals of combined cycle-slip detection for C01 and C08 satellite

PRN	Coefficient	Mean (m)	Standard deviation
C01	(0, 1, −1)	0.0001	0.0192
	(1, 0, −1)	0.0011	0.0546
	(4, −3, −2)	0.0001	0.0804
C08	(0, 1, −1)	0.0001	0.0161
	(1,0, −1)	0.0006	0.0436
	(4, −3, −2)	0.0001	0.0755

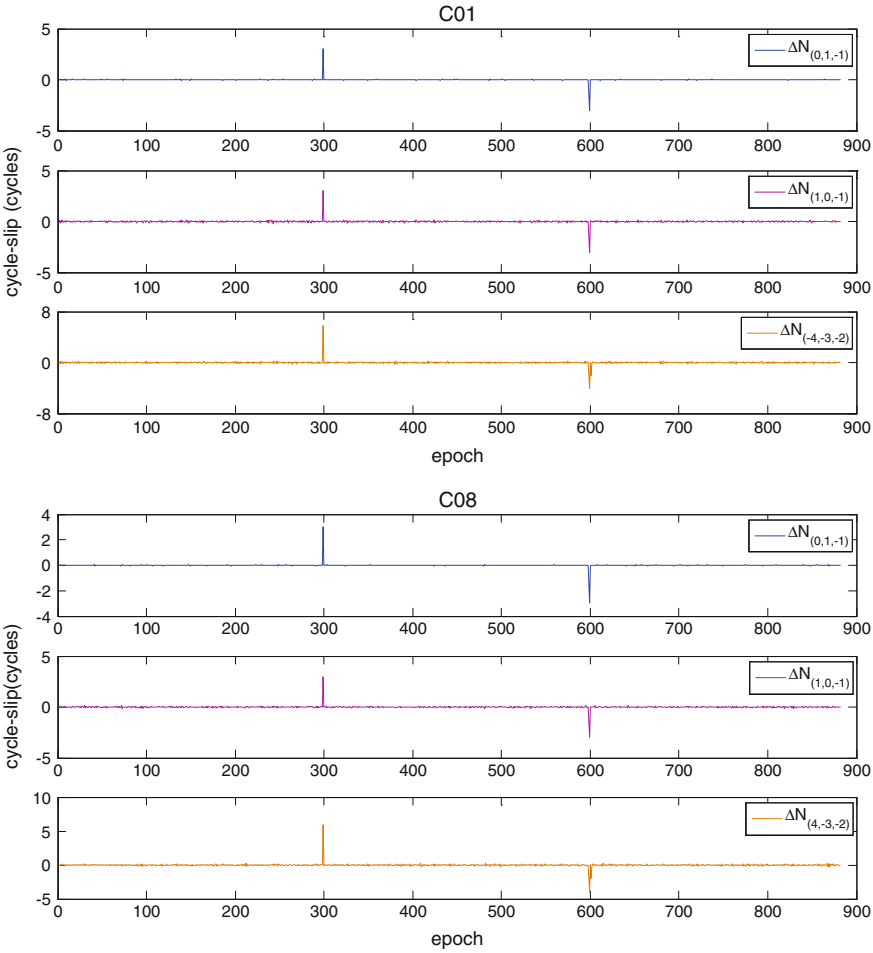

Fig. 1.3 Add simulate cycle slips in satellite C01 and C08 with 10 s observation interval

5 Conclusion

This paper puts out a similar method to TCAR. In consideration of the estimation of ionospheric delay, we corrected the ionospheric delay of WL (4, −3, −2)'s combined measurement, detected, and repaired the cycle slip. The evaluation is done by using BeiDou triple-frequency data in this paper. The final result indicates that the method put forward in this paper is reliable to detect and repair the cycle slip in real time.

References

1. Li Z, Xiaohong Z (2009) New techniques and precise data processing methods of satellite navigation and positioning. Wuhan University Press, Wuhan (Ch)
2. Chen Q, Sui L, Gan Y (2015) Real-time cycle slip detection and repair in triple frequency GNSS. The 6th China Satellite Navigation Conference (Ch)
3. Lingyong H, Lijie S, Yan W et al (2012) BeiDou triple-frequency geometry-free phase combination for cycle-slip detection and correction. Acta Geodaetica et Cartographica Sin 41 (5)763–768(Ch)
4. Wang H, Chai H, Xie K (2015) Study of cycle-slip detection using BDS triple-frequency geometry-free and ionosphere-free combination. J Geodesy Geodyn 35(3):406–411(Ch)
5. Dong L, Yuan Y, Wang H et al (2012) On an optimum selection method of GPS triple-frequency phase combination applied to undifferenced cycle slip detection. J Geodesy Geodyn 32(03):106–109 (Ch)
6. Zhao C (1997) Reformation of triple-differential observation equations of GPS carrier phase. Acta Geodaetica et Cartographica Sin 02:155–159 (Ch)
7. Feng Y (2008) GNSS three carrier ambiguity resolution using ionosphere-reduced virtual signals. J Geodesy 82(12):847–862
8. Li J, Yang Y, Xu J et al (2013) GNSS multi-carrier fast partial ambiguity resolution strategy tested with real BDS/GPS dual- and triple-frequency observations. GPS Solutions 19(1):5–13
9. Li W, Jiang W, Wang Z (2008) Research on the model of GPS triple-frequency phase combination observations. J Geomatics 03:6–8 (Ch)
10. Fan J, Wang F (2015) A method for GNSS three frequency ambiguity resolution based on short baselines. Acta Geodaetica et Cartographica Sin 36(1):43–49 (Ch)

The Performance Analysis of Multi-system Integrated Precise Point Positioning (PPP)

Lingyong Huang, Zhiping Lu, Baozhu Li, Guodong Xin, Wen An, Hao Lv, Ning Wang and Xinfeng Zhou

Abstract Based on the analysis of the GNSS navigation and positioning, this paper studies the key technology and superiority of the PPP based on single difference between satellites. The true observation data are used to compare and analyze the precision and convergence time of PPP based on GPS\GLONASS, GPS\BDS dual system, and GPS\GLONASS\BDS triple system. Finally, the conclusion is drawn as the following: GPS\GLONASS\BDS triple-system PPP technology has the optimal performance on positioning accuracy and convergence time. GPS\GLONASS dual-system PPP almost has the same performance with triple-system PPP. GPS \BDS has no impact on improving performance of GPS PPP, but can improve the performance of BDS PPP greatly.

Keywords PPP · GNSS · GPS · BDS · GLONASS

1 Introduction

PPP technology does not need the reference station, its operation is flexible and its positioning accuracy is high. It can directly obtain the coordinates of the stations which are consistent with the ITRF framework. So, PPP technology research has become a hot spot. Especially with the operation of Beidou system of our country, the research and analysis on BDS PPP become gradually increased. Literature [1] shows that BDS PPP can only achieve dm level positioning accuracy because of the lower precision of precise satellite orbit and clock. But, Literature [2] shows that precise orbit radial accuracy of BDS satellite is less than 10 cm, and the PPP

L. Huang (✉) · B. Li · G. Xin · W. An · X. Zhou
China Aerospace Surveying and Mapping Satellite Center, Beijing, China
e-mail: hlylj87@126.com

L. Huang · Z. Lu · H. Lv · N. Wang
Information Engineering University, Zhengzhou, China

L. Huang
State Key Laboratory of Geo-Information Engineering, Xi'an, China

© Springer Science+Business Media Singapore 2016

J. Sun et al. (eds.), *China Satellite Navigation Conference (CSNC) 2016 Proceedings: Volume III*, Lecture Notes in Electrical Engineering 390,
DOI 10.1007/978-981-10-0940-2_28

can reach cm level accuracy. Through comparing the performance of BDS and GPS PPP, literature [3] shows that dynamic and static BDS PPP can finish convergence in 100–80 min, and can realize the cm and dm level absolute positioning accuracy. No matter the performance of BDS PPP, according to some studies, single-system PPP still exists the following problems: (1) in the occlusion area where the number of visible satellites is less, the worse geometric structure of space satellite easily leads to lower positioning accuracy; (2) because the ambiguity, position parameters, the receiver clock, and troposphere delay cannot be efficiently separated within a short period of time, the convergence time will be longer. So, scholars begin to study the strength of dual-system combination PPP technology. Literatures [4–6] show that, when the GPS satellite is less, the increase of GLONASS satellites can effectively improve the convergence speed and positioning accuracy of GPS PPP.

With the operation of our BDS system and the improving of GLONASS satellite constellation, it is necessary to compare and analyze dual system, even three-system PPP positioning performance combined by GPS, GLONASS, and BDS to achieve the technology accumulation of compatibility and interoperability technology between GNSS system. This paper introduces the GNSS integrated observation model at first. Then the GNSS PPP software developed by Wuhan University and the institute of Naval Oceanographic Surveying and Mapping is used to analyze and compare the accuracy and convergence time of GPS, GLONASS, BDS single system, GPS\GLONASS, GPS\BDS dual system, and GPS\GLONASS\BDS three-system PPP, where the MGEX plan observation data is used.

2 Multi-system PPP Model

2.1 GNSS Observation Model

To realize the multi-system GNSS integrated navigation and positioning, it needs to unify the time, space datum and establish a unified observation model [7]. A multi-system PPP observation model is given as follows:

$$\begin{cases} P_i^G = \rho + cdt_r^G - cdt^{s,G} + T^G + I_i^G + db_i^G + \varepsilon_{pi}^G \\ L_i^G = \rho + cdt_r^G - cdt^{s,G} + T^G - I_i^G + \lambda_i^G (N_i^G + dB_i^G) + \varepsilon_{\Phi j}^G \end{cases}^s \quad (1)$$

where, ρ denotes the distance between the satellite and the receiver, c is the light speed, dt_r and dt^s are receiver and satellite clock errors, respectively, T denotes the troposphere delay, I is the ionospheric delay, N refers to integer ambiguity, db_i^G and dB_i^G denote receiver and satellite equipment delays, respectively, λ refers to carrier phase wavelength, ε_p and ε_Φ refer to carrier observation and code observation errors, respectively, the subscript G and s denote the satellite system and satellite, and the i and r refer to the signal frequency and receiver.

In order to weaken the ionospheric delay, PPP usually adopts the ionosphere-free combination:

$$\begin{cases} P_{IF}^{G} = \frac{f_1^2 P_1^G - f_2^2 P_2^G}{f_1^2 - f_2^2} = \rho + cdt_r^G - cdt^{s,G} + T^G + db_{IF}^G + \varepsilon_{P_{IF}}^G \\ L_{IF}^{G} = \frac{f_1^2 L_1^G - f_2^2 L_2^G}{f_1^2 - f_2^2} = \rho + cdt_r^G - cdt^{s,G} + T^G + \lambda_{IF}^G (N_{IF}^G + dB_{IF}^G) + \varepsilon_{\Phi_{IF}}^G \end{cases} \tag{2}$$

where P_{IF} and L_{IF}^{G} are the code and phase ionosphere-free combination, respectively.

Except the ionospheric delay, PPP still needs to get the precise orbit and clock error, detect cycle slips and carry on the phase center, phase winding, relativistic effect, tidal, and solid tide correction [8, 9]. In the formula (2), the main estimated parameters are the position of the receiver, the float ambiguity, the receiver clock error, and the tropospheric delay. Linearizing the formula (2) and expressing it as follows:

$$\mathbf{L} = \mathbf{BX} + \mathbf{\Delta} \tag{3}$$

where $\mathbf{X}$ denotes the estimated parameter, $\mathbf{B}$ is the matrix coefficients, $\mathbf{L}$ and $\mathbf{\Delta}$ refer to observation and random error.

The corresponding stochastic model of the Eq. (3) is

$$\begin{cases} \mathbf{E}(\Delta) = \mathbf{0} \\ \mathbf{D}(\Delta) = \sigma_0^2 \mathbf{Q} \end{cases} \tag{4}$$

where σ_0^2 is the unit weight variance and the $\mathbf{Q}$ is the factor matrix.

2.2 Adjustment Model of Single Differencing Between Satellites

In order to improve the accuracy of the stochastic model, the method of differencing between satellites is used to eliminate the receiver clock error. The algorithm can greatly reduce requirements for the stochastic model accuracy of pseudorange observation, and the differencing between satellites not only can eliminate the receiver clock error but also can weaken the receiver hardware delay. The differencing between satellites observation equation of GPS\GLONASS\BDS three-system PPP is given as follows:

$$\begin{cases} \mathbf{L}_{m\times 1} = \mathbf{A}_{m\times(m+6)}\mathbf{X}_{(m+6)\times 1} + \boldsymbol{\varepsilon}_{m\times 1} \\ \mathbf{Cov}_{\boldsymbol{\varepsilon}_L} \sim \mathbf{N}(0, \mathbf{Q}_{LL}) \end{cases} \tag{5}$$

with $\mathbf{X} = [x, y, z, dT, dt_{r\_GR}, dt_{r\_GC}, \mathbf{N}_{IF}^s]^T$

where $\mathbf{L}$ is m dimension measurement, $\mathbf{A}$ is the combination coefficients, $\mathbf{X}$ is the estimated parameter, x, y, z is the coordinate parameter, dT is the zenith wet tropospheric component, dt_{r_GR} is the time difference of GPS and GLONASS, dt_{r_GC} is time difference of GPS and BDS, $\mathbf{N}_{IF}^{s}$ is single difference ionosphere-free combination ambiguity set preference to the satellites, and $\mathbf{Cov}_{\varepsilon_L}$ is the stochastic models.

As a result of more parameters in PPP, Kalman filtering algorithm is often used to overcome the high-order matrix inversion difficult and to improve the computing efficiency [10]. The Kalman filter iteration algorithm is used, so the calculation efficiency is high. Kalman filter is composed of the state equation and the observation equation, the state equation describes the state transition of the adjacent moment, and the observation equation describes the information of the state. In order to reduce the influence of gross errors on the Kalman filter, a robust Kalman algorithm is usually introduced (see [10] to get more detail theory).

3 Data Analysis

3.1 Experiment Design

The data got from 4 stations the 342–348 day in 2013 by the Trimble receiver under the MGEX observation program is used to analyze the performance of multi-system combination PPP. Site coordinate position and receiver type are shown in the following table (Table 1).

Data processing strategy: the pseudocode/carrier ionosphere-free combination observation equation is used to correct the phase winding, solid tide, and the relativistic effect; satellite clock and orbit error are corrected by GPS, GLONASS precision products released by ESA and BDS precision products released by WHU; IGS IGS_08.atx absolute antenna phase center model is used to correct satellite antenna phase center; the Saastamoinen model is used to correct the tropospheric dry component; differencing between satellites is used to eliminate the receiver clock error; the wet tropospheric component, coordinate, and float ambiguity are estimated as the parameters by using the Kalman filter. The 4 IGS stations coordinate in the precision clock difference document is defined as the true value to compute the difference dS between true value and the calculation value on ENU direction to evaluate PPP calculation precision. To define the epoch, when distance

Table 1 Station information

No.	Site	Position	Receiver type
1	CUT0	−32.0N 115.9L	TRM59800.00 CIS
2	GMSD	30.6N 131.0L	TRM59800.00 SCIS
3	JFNG	30.5N 114.5L	TRM59800.00 NONE
4	REUN	−21.2N 55.6L	TRM55971.00 NONE

deviation dS for the first time is less than 0.1 m and the 20 epochs after that epoch dS does not exceed 0.1 as the filtering convergence time. Because PPP solution accuracy and convergence speed are better than poor observation time, all PPP solution in this experiment always begin from the for 0 h:0 min:0 s every day recorded by RINEX observation file. Different algorithms and different satellite cutoff angles also can cause different PPP positioning results. Therefore, setting these experiment conditions may lead to the statistical accuracy and convergence time is as same as other scholars do, but the same observation condition and the same data processing strategy can accurately reflect the differences of different satellite navigation systems. The positioning accuracy and convergence time are defined as the evaluation index to evaluate the positioning performance of multi-system PPP.

3.2 Positioning Accuracy Analysis

3.2.1 Single GPS System Static Accuracy Analysis

At first, the site JFNG is selected to analyze the GPS single-system PPP positioning results, the differences of calculation results and true value in the ENU are as shown in Fig. 1. The average value of the static GPS PPP positioning accuracy of every site in 7 days is shown in Fig. 2. In Fig. 1, on the dE and dN horizontal direction single GPS static PPP solution result is less than 0.5 cm every day, in dU direction the accuracy is not very better, but most of them are less than 1.5 cm and the maximum position deviation is only 1.6 cm. As shown in Fig. 2, we can find that the 7 days maximum average positioning error of single GPS PPP is less than 1.5 cm, 4 station average position error is about 1.1 cm. From above, we can see

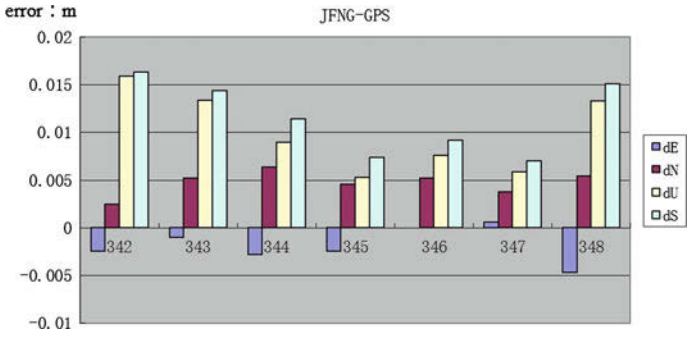

Fig. 1 Analysis of JFNG single GPS system 7 days PPP precision

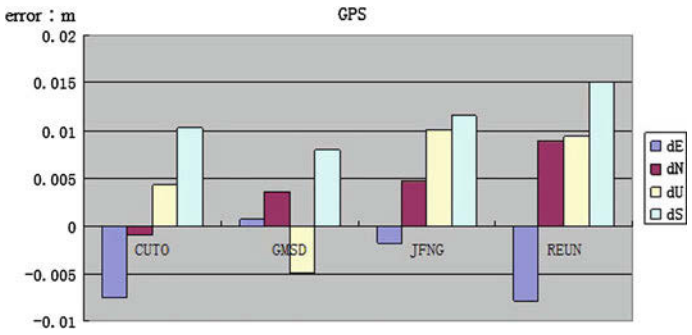

Fig. 2 Single-system 7 days PPP average precision

that the single GPS PPP static positioning precision can finish the cm even mm level positioning.

3.2.2 Dual-System Static Accuracy Analysis

As the same as 3.2.2 does, the JFNG site 7 days GPS\GLONASS and GPS\BDS dual-system static PPP accuracy is analyzed at first. Then every site 7 days average positioning accuracy of GPS\GLONASS and GPS\BDS dual system is analyzed.

As shown in Fig. 3, GPS\BDS combined positioning deviation of the site JFNG is larger than 1.5 cm, and GPS\GLONASS combination position deviation is less than 1.5 cm and even is less than 1 cm in 3 days except that it is more than 1.5 cm in the 342th day. Further comparing the dual-system and single GPS system positioning accuracy, GPS\BDS dual-system combination PPP positioning does not play a role on accuracy improvement. But the GPS\GLONASS double-system combination precision is better than GPS single-system PPP positioning precision. From this, it is found that GLONASS and GPS combined effect is better than that of BDS and GPS combined, which is because that the current accuracy of BDS precision products is worse than GLONASS and the satellite antenna phase deviation of BDS has not been calibrated and corrected.

From Fig. 4, we can see that 7-day average deviation value of GPS\GLONASS dual-system combination static PPP position solution of the REUN site is the largest, about 1.5 cm, while the average deviation of other 3 sites is about 1 cm. Comparing the Fig. 1 with Fig. 3, the positioning deviation changing trend of GPS \GLONASS combination is as the same as the single GPS system PPP positioning, such as, dU direction deviation of GMSD double-system combined PPP solution is −0.491 cm and the dU direction deviation of single GPS system PPP is −0.513 cm. This is because that GPS observation is given a larger weight in the dual-system combined PPP positioning solution, this results to the positioning solution of

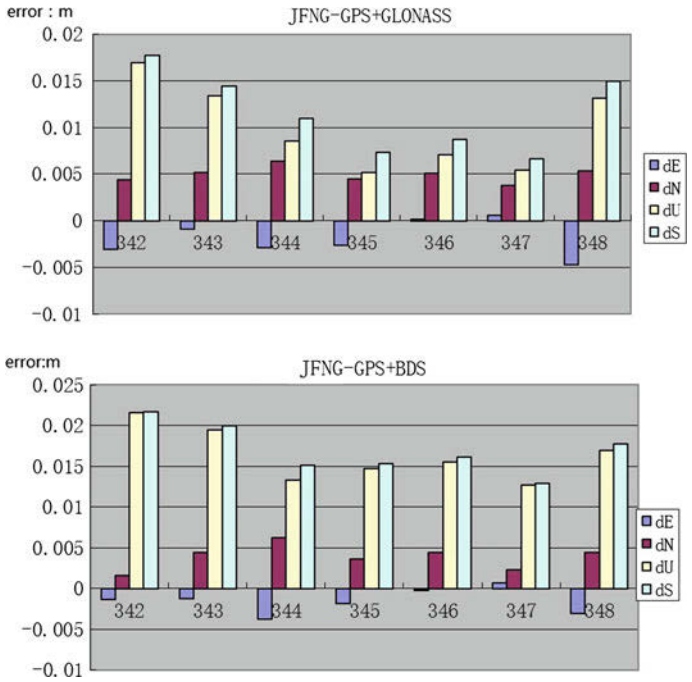

Fig. 3 Dual-system accuracy analysis of station JFNG

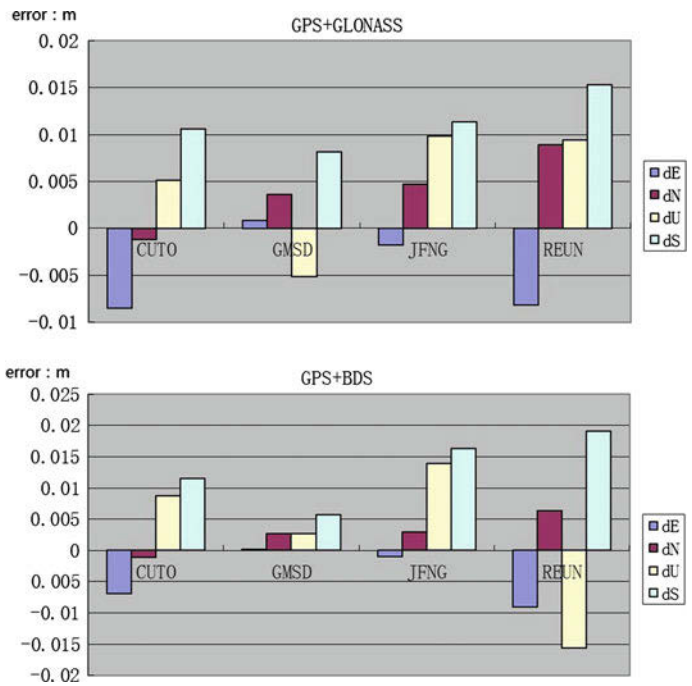

Fig. 4 Dual-system accuracy analysis

Table 2 PPP accuracy analysis unit: cm

	GPS	G\GLO	G\B	G\GLO\B
Position deviation	1.17	1.13	1.32	1.12

dual-system PPP are relatively close to the one of single GPS system positioning results. Also GPS\BDS double-system combined PPP has the same deviation tendency as single GPS system positioning, which is because that usually observation quality of BDS satellite is worse than one of the GPS satellite, so the GPS observation is given a larger weight than BDS observation, which makes the double-system combined PPP positioning has a little difference with single GPS system PPP results. However, according to the accuracy analysis of GPS \GLONASS dual-system PPP positioning, we can know that GPS\GLONASS dual-system combination can improve the GPS single-system PPP positioning accuracy, while the positioning accuracy of the GPS\BDS dual-system PPP positioning does not improve the single GPS system positioning accuracy.

In Table 2, the average deviation of single GPS system PPP is 1.17 cm, GPS \GLONASS double-system PPP average position error of 4 stations is 1.13 cm, which means that GPS\GLONASS double-system PPP can improve the performance of single GPS system PPP. But the mean deviation of GPS\BDS double-system PPP is 1.32 cm and GPS\BDS double-system PPP does not improve the performance of single GPS system PPP. That is because the strength of static PPP model is strong, effect of low-precision BDS observation data on the strength of the model is almost negligible.

3.2.3 Three-System Static Accuracy Analysis

Comparing Figs. 5 and 3, we can find that the accuracy of JFNG three-system PPP positioning accuracy has the similar precision with GPS\BDS dual-system PPP, and has a lower accuracy than GPS\GLONASS dual-system PPP. This is because that JFNG site is located in the territory of China, more BDS satellites can be observed,

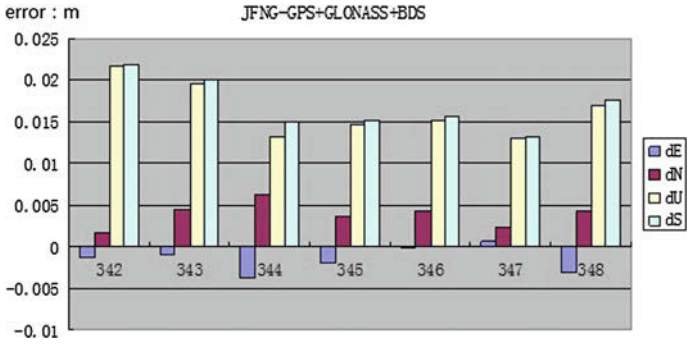

Fig. 5 Three-system accuracy analysis of JFNG station

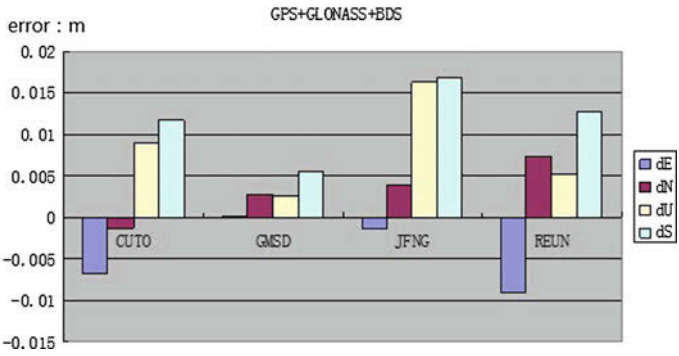

Fig. 6 Triple-system PPP accuracy analysis

which makes the BDS observation to have a larger weight in three-system PPP. So, the positioning accuracy of three-system PPP is less than GPS\GLONASS positioning accuracy. From Figs. 4 and 6, it can be found that positioning accuracy of three-system PPP of other three stations is improved obviously, especially the position deviation of GMSD three-system PPP reduces to 0.5 cm from 1.2 cm of original GPS\GLONASS dual-system positioning solution. As a result, we can see three-system PPP can improve the positioning accuracy of GPS\GLONASS dual system, but whether the system positioning performance is improved or not is depended on the site position and the observation conditions. What is more, according to Table 2, the average deviation of the 4 sites three-system static PPP positioning accuracy is minimal, which means that in most cases, three-system static PPP positioning accuracy is optimal.

3.3 Convergence Analysis

The average convergence time of the static PPP solution of the 4 sites in 7 days was calculated, and the results are shown in Table 3. From Table 3, we can see that the average convergence time of GPS\GLONASS\BDS three system is the shortest for 15.6 min, and the convergence time of GPS\GLONASS system is 16 min. In a single system, the GPS static convergence rate is the fastest for 21 min. From this, we can find that the three-system PPP can shorten the convergence time further, and the combination PPP has a higher efficiency than single GPS system PPP. So in this respect, it is necessary to do integrated PPP.

Table 3 PPP convergence time analysis

	G	G\GLO	G\B	G\GLO\B
Time (min)	21	16	24	15.6

4 Conclusion

Through comparing the PPP accuracy and convergence time of the single GPS system, GPS\GLONASS, GPS\BDS dual system and GPS\GLONASS\BDS three system, we found that the performance of three-system PPP is best; in dual-system PPP, BDS has less effect than GLONASS on enhancing the combination performance. Although BDS is difficult to improve positioning performance when it is combined with other systems, but through the combination with GPS or GPS \GLONASS, BDS can significantly improve its positioning accuracy shorten its convergence time.

Acknowledgment This work was funded by China National Natural Science Foundation (grant number U1431115, 41274015, 41371042, 41574010), National High Technology Research and Development Program 863(Grant number: 2013AA122501) and State Key Laboratory of Geo-information Engineering (grant number SLKGIE2015-M-2-1). The first author is grateful to Tianjin Institute of Hydrographic Surveying and Charting for their help.

References

1. Montenbruck O, Hauschild A, Steigenberger P et al (2013) Initial assessment of the COMPASS/Beidou-2 regional navigation satellite system. GPS Solutions 17(2):211–222
2. Shi C, Zhao J, Li M et al (2012) Precise orbit determination of Beidou satellites with precise positioning. Sci China Earth Sci 55:1079–1086
3. Zhang X, Zuo X, Li P et al (2015) Convergence time and positioning accuracy comparison between BDS and GPS precise point positioning. Acta Geodaetica et Gartographica Sin 44 (3):250–256
4. Cai C, Gao Y (2007) Performance analysis of precise point positioning based on combination GPS and GLONASS, the ION GNSS 20th international technical meeting of the satellite division. Fort Worth, Texas
5. Zhang X, Guo F, Li X et al (2010) Study on precise point positioning based on combined GPS and GLONASS. Geomatics Inf Sci Wuhan Univ 35(1):9–12
6. Li X, Zhang X (2012) Improving the estimation of uncalibrated fractional phase offsets for PPP ambiguity resolution. J Navig 65(3):513–529
7. Huang L, Lv Z, Ren Y et al (2014) Application of multivariate total least square in three-dimensional coordinate transformation. Geomatics Inf Sci Wuhan Univ 39(7):793–798
8. Huang L, Zhai G, Ouyang Y et al (2015) Ionospheric cycle slip processing in triple-frequency GNSS. Acta Geodaetica et Cartographica Sin 44(7):717–725
9. Huang L, Zhai G, Ouyang Y et al (2015) Triple-frequency TurboEdit cycles lip processing method of weakening ionospheric activity. Acta Geodaetica et Cartographica Sina 44(8): 840–847
10. Yuanxi Y (2006) Adaptive navigation and kinematic positioning, surveying and mapping press, 2006. Beijing, China

A Single-Station Ionospheric Model and Satellite DCB Elaboration Method Based on Multi-frequency GPS/BDS Data

Yi Qin, Chenglin Cai and Jinhui Wang

Abstract Ionospheric errors and satellite DCB are important error sources in precise positioning. For area augmentation system, the conventional method is to precisely correct the errors by using the single monitoring stations. For practical application of the area augmentation system of GPS/BDS, this paper uses multi-frequency GPS/BDS data to establish single-station ionospheric model and solves satellites DCB, then the effectiveness of the proposed method is validated with Urumqi iGMAS station data of surveying. The result shows that the relative errors between the method of single-station ionosphere model and the GIM of CODE are controlled within 3.5 TECU; the relative errors between the calculated GPS satellites DCB and CODE published DCB are controlled within 0.5 ns; the relative errors between the calculated BDS satellites DCB and IGG published DCB are controlled less than 1.7 ns; the stability of GPS satellites DCB is better than BDS satellites DCB; and stability of IGSO satellites DCB is better than MEO and GEO satellites.

Keywords Multi-frequency · Single station · Ionospheric · DCB

1 Introduction

Differential code biases (DCBs) is the differential hardware delay that occurs between two different observations obtained at the same or two different frequencies. Previous research shows that the DCB of GPS satellites vary from −10 to 10 ns; some applications of Global Navigation Satellite System (GNSS) such as location, timing, and modeling of ionosphere model will be significantly influenced by the DCB.

Y. Qin (✉) · C. Cai · J. Wang
Guangxi Key Laboratory of Precision Navigation Technology and Application, Guilin University of Electronic Technology, Jinji Road, Guilin 541004, China
e-mail: sml126163@126.com

© Springer Science+Business Media Singapore 2016

J. Sun et al. (eds.), *China Satellite Navigation Conference (CSNC) 2016 Proceedings: Volume III*, Lecture Notes in Electrical Engineering 390,
DOI 10.1007/978-981-10-0940-2_29

Although the individual satellite DCB is calibrated before launch, there are always some reason variations that occur once satellites are in orbit. So, it is necessary to use the ground stations to track data and to accurately estimate satellite DCB. At present, there are two main methods to determine the DCB: (1) The DCBs of satellites are estimated as daily constants which are based on global ionospheric TEC modeling in a solar-geomagnetic frame [1]; (2) The DCBs of satellites are estimated from post-fit ionospheric code residuals whereby the slant TEC is computed from global ionosphere map (GIM) [2]. Therefore, the accuracy of TEC modeling has a great influence on the determination of DCB.

BDS is a satellite navigation system developed by China. There are currently 14 satellites (5 GEO satellites + 5 IGSO satellites + 4 MEO satellites) providing on-orbit services, servicing on the area of China as well as the surroundings. In the service area, the number of current BDS basically equals to that of visible satellites and GPS, but 5 GEO satellites will cause uneven distribution of ionosphere Pierce point. Thus, the ionosphere model established by observation data of BDS cannot comprehensively reflect the daily volatility of ionosphere over the monitoring stations [3]. International GNSS Service monitoring sites are not enough in China and the surrounding areas, so the resolution of GIM over these places is low [4]. In conclusion, it is crucial to calculate DCB of BDS satellites and to establish in service ionospheric delay model.

Given the above consideration, the single-station ionospheric delay model was established by polynomial, to analyze and calculate DCB of GPS/BDS satellites by using International GNSS Monitoring and Assessment Service (iGMAS) GPS/BDS multi-frequency observation data.

2 The Single-Station Ionospheric Delay Model

2.1 Observation Equation

Using dual-frequency and geometric combination to acquire the vertical electronic content, the equation can be described as follows:

$$c \cdot \mathrm{DCB}_r + c \cdot \mathrm{DCB}^g - \frac{F(z)}{9.52437} \cdot \mathrm{VTEC} = \Delta P_r^g \tag{1}$$

$$c \cdot \mathrm{DCB}_n + c \cdot \mathrm{DCB}^b - \frac{F(z)}{8.9932} \cdot \mathrm{VTEC} = \Delta P_n^b \tag{2}$$

where ΔP is the geometry-free combination of the pseudorange observations on dual frequencies; c is the speed of light in vacuum (in m/s); VTEC is the vertical total electron content along the signal propagation path from the satellite to the receiver (in TECu); DCBs stands for differential code biases of satellites and receivers; 9.52437/8.9932 are the frequency of the correlation coefficient when the difference of the GPS/BDS multi-frequency ($f_1 f_2 / B_1 B_2$) pseudorange is translated

into VTEC (because of the limited passage, this paper only analyzes the B_1B_2 frequency DCB of BDS).

Here, the subscript r stands for GPS signal receivers; the subscript n stands for BDS signal receivers; the superscript g stands for GPS satellites; the superscript b stands for BDS satellites

$F(z)$ is mapping function used to convert slant TEC into vertical TEC:

$$F(z) = \frac{1}{\cos(z')} \tag{3}$$

$$\cos(z') = \frac{R}{R+H}\sin(\alpha z) \tag{4}$$

where z is the satellite elevation angle, R is the earth's radius, H is the attitude of the ionosphere shell, and α is the correction coefficient.

Single-station ionospheric model is established through polynomial expansion model by using the multi-frequency GPS/BDS data of the Urumqi station to determine VTEC along the signal propagation path from the satellite to station. The model is to put the VTEC as a function through the latitude difference and angle difference of the sun. The equation can be expressed as follows [5]:

$$\mathrm{VTEC} = \sum_{i=0}^{n}\sum_{k=0}^{m} E_{ik}(\varphi - \varphi_0)^i (s - s_0)^k \tag{5}$$

where φ is the geographic latitude of IPP; φ_0 is the geographic latitude of the central part of the surveyed area. $s - s_0 = (\lambda - \lambda_0) + (t - t_0)$; λ is the geographic longitude of IPP; λ_0 is the geographic longitude of the central part of the surveyed area. In the period of time when the central moment of the solar hour angle, t is the observation time and t_0 is the center of observation time.

2.2 The Data Selection and Processing Strategy

Using DOY 318–329, 2014 of Urumqi station GPS/BDS observation data, the strategy of piece wise constant is adopted to describe the change of the ionosphere model parameters. The day would be divided into 12 times and each time last for 2 h. In this paper, we take 4 orders, and observation would be estimated by the number of parameters in the equation of 12 * (4 * 4) + g + b + 1, (g and b, respectively, represent BDS and the GPS satellites number observed by monitoring stations). According to the theory described above, the DCB and ionosphere coefficients can be estimated from GPS/BDS multi-frequency observations by the least squares method.

When the satellites are observed by monitoring station in a low elevation period, pseudorange differences can be very large. This can explain pseudorange data's

bad quality. In the applications of satellite navigation, if the viewing angle of satellite is very low, the signal is more likely to be totally hided or the signal power attenuation declines below GNSS receiver sensitivity because of the holdbacks such as natural things or architectures. As the result, GNSS receiver channel may fail to track the satellite signal, which means it cannot maintain the stability of signal tracking loop and even lose track of the satellite. This kind of situation is called lock-loss. As the result, this data cannot be participated in calculation, so the elevation mask angle is 15°.

Equations (1) and (2) show the pseudorange differential relationship with the accuracy of VTEC and GPS satellite/receiver DCB. Since the pseudorange ΔP has large noise, to improve the precision of VTEC, the carrier phases are used to smooth the pseudorange. Cycle slips and gross errors in the carrier-phase observations which detected by Turbo-Edit should be removed before using the carrier-phase observations to smooth the pseudorange [6]. To set up corresponding marks for the location of cycle slips, cycle-slips epochs are not involved in smoothing pseudorange processing.

2.3 DCB Treatment Method

As a result, satellite DCB values changed slowly and were relatively stable, the usual processing is within a day of DCB of satellites as a fixed value. Equations (1) and (2) show that the dual frequency and geometric combination values, must be deducted DCB, can be converted to VTEC. However, the DCB of satellites/monitoring station receivers cannot be separated directly, and it need to be added in the appropriate constraint conditions. For the GPS satellites, imposing a zero-mean condition for the validated satellites has to be observed. For the BDS satellites, the DCB of C01 satellite factory defaults is fixed as constraint conditions [7].

As a result, GPS/BDS dual system was used to model the ionospheric delay, and the above two constraints should be added to observation equation.

3 Example Analysis

3.1 Single-Station VTEC Model Calculating Precision Analysis

By Equations (1) and (2), it can be seen that the parameters of single-station ionospheric model and DCB can be calculated by one day data, so that the calculation accuracy of ionospheric model's parameters reflects the precision of satellite DCB.

According to the observation data from the global GPS monitoring stations, the center for orbit determination in Europe (CODE) uses spherical harmonic functions to map the GIM. So far, GIM has become an effective tool for the study of global ionospheric structure changes [8]. The available information shows that the precision

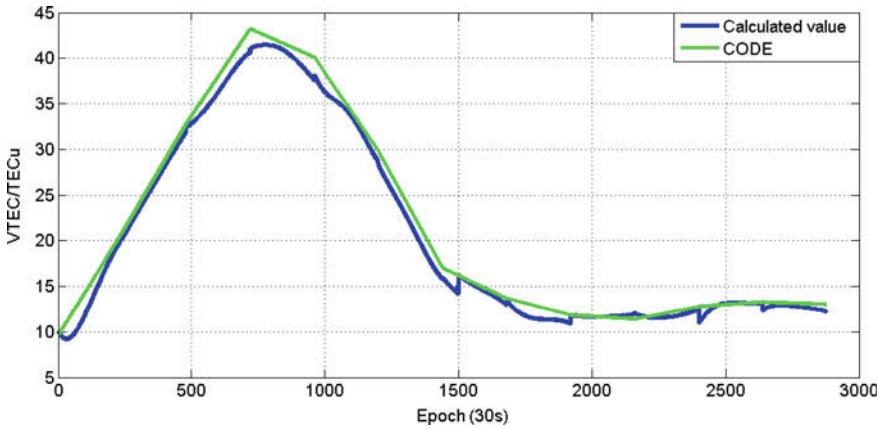

Fig. 1 VTEC value of monitoring station

Table 1 Accuracy statistics of single-station model and CODE VTEC difference unit: TECu

DOY	318	319	320	321	322	323	324
Differences	−0.09	−2.06	−3.43	−3.24	−2.75	−1.70	−2.67
RMS	1.14	2.61	3.67	3.53	2.76	1.69	2.80
DOY	325	326	327	328	329		
Differences	−1.68	−2.48	−3.69	−2.06	−3.08		
RMS	1.81	2.87	3.51	2.08	3.12		

of the GIM is 2–8 TECU [3]. Figure 3 shows that DOY 318, 2014 monitoring station VTEC of calculation value and GIM value is released by CODE.

It can be seen from Fig. 1 that the value of the calculation and CODE with time change tendency is consistent, which can reflect the daily variation of the ionosphere over the monitoring station.

In order to more intuitively reflect the ionosphere single-station-model precision, the single-station model is compared with CODE and the difference in 1 day statistical average. Table 1 shows the DOY 318–329, 2014 VETC difference accuracy of statistics. It can be seen from Table 1 that the mean difference and RMS of less than 3.5 TECU is between the single-station-model measured values and CODE values.

3.2 Satellites DCB Calculating Precision Analysis

3.2.1 GPS Satellites' DCB Calculating Precision Analysis

Currently, the most authoritative international GPS satellites DCB products are provided by the CODE, and its calculating precision is high, which can be taken as

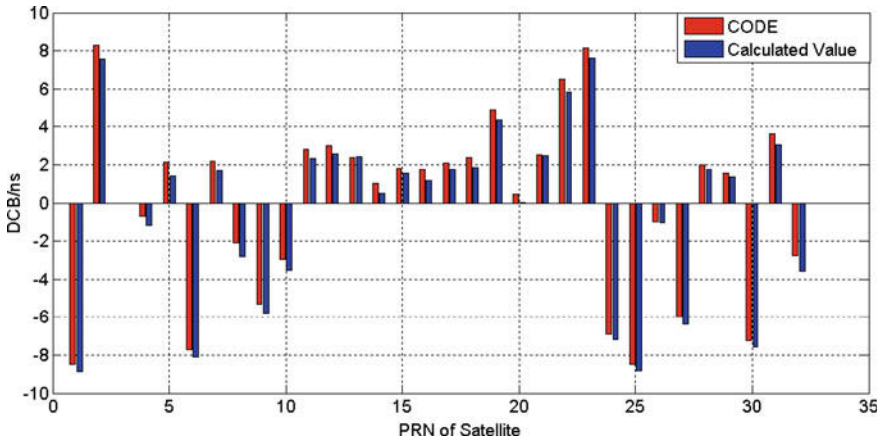

Fig. 2 Mean value of GPS satellites' DCB estimates by single-station model and CODE

reference to the relevant work [9]. The mean differences between DCB calculated by single-station model and those from CODE during DOY 318–329, 2014 are shown in Fig. 2. (There is no PRN 3 observed within the observation period of time, so there is no calculation about its DCB parameters.)

It is shown that the differences are basically the same, and the maximum difference is 0.79 ns (PRN02). From Table 1, it can be concluded that DCB calculated by single-station model and those form CODE is basically at the same precision level. The STD statistical of GPS satellites DCB determined by CODE and single–station model is presented in Table 2; STD reflects the estimate stability of the satellite DCB, and it is also comparable to the formal error of DCB estimates [10].

It can be seen from Table 2 that the STD of DCB provided by CODE range is [0.01, 0.06 ns], and the STD of DCB calculated by single-station-model range is [0.17, 0.50 ns]. The stability of single-station-model calculated values is below CODE values; this is because the CODE release values are based on more than 200 stations observation date to estimate the DCB, and single-station-model values are based on single station, with the decreasing of the number of base station, and the stability of calculated satellites DCB is reduced.

3.2.2 BDS Satellites' DCB Calculating Precision Analysis

The BDS DCB products which developed by the Yuan Yubin's team from the Institute of Geodesy and Geophysics (IGG) are released to users globally [11]. This paper compares and analyzes IGG DCB products with calculated value and the calculated precision is quantitatively analyzed. The mean differences between DCB from IGG and those calculated by single-station model Fig. 3. (There is no C04 and C13 observed within the observation period of time, so there is no calculation

Table 2 The STD statistic of GPS satellite DCB (2014 318–329) unit: ns

PRN	01	02	04	05	06	07	08
CODE	0.02	0.02	0.05	0.03	0.03	0.01	0.06
Calculated	0.17	0.40	0.21	0.55	0.28	0.31	0.42
PRN	09	10	11	12	13	14	15
CODE	0.03	0.02	0.04	0.02	0.05	0.04	0.03
Calculated	0.46	0.43	0.31	0.50	0.38	0.38	0.50
PRN	16	17	18	19	19	20	21
CODE	0.05	0.05	0.05	0.03	0.02	0.04	0.07
Calculated	0.38	0.40	0.37	0.32	0.39	0.27	0.47
PRN	22	23	24	25	26	27	28
CODE	0.05	0.02	0.04	0.04	0.03	0.07	0.01
Calculated	0.24	0.38	0.45	0.46	0.32	0.40	0.23
PRN	29	30	31	32			
CODE	0.05	0.02	0.05	0.02			
Calculated	0.35	0.43	0.51	0.24			

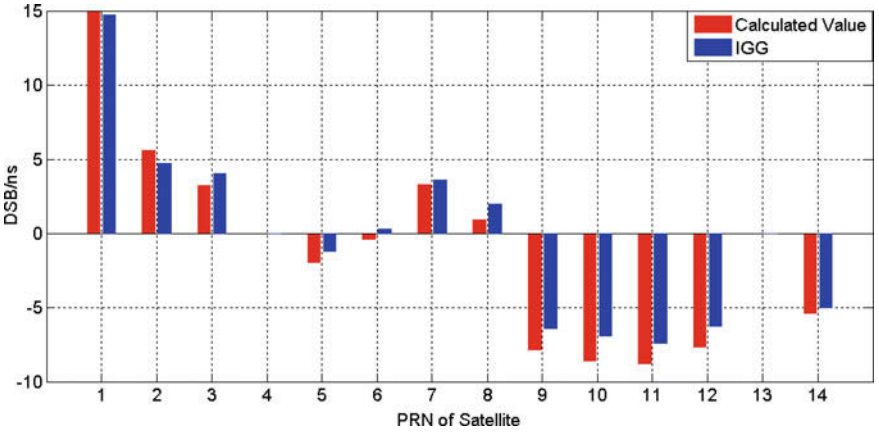

Fig. 3 Mean value of BDS satellites' DCB estimates by single-station model and IGG

about its DCB.) It can be seen that the DCB calculated by single-station model is basically consistent with those from IGG, and the maximum difference reaches at 1.7 ns (C10).

Table 3 shows the STD statistical of BDS satellites DCB determined by single–station model. Due to fixed C01 satellite DCB as the constraint condition, the STD of C01 satellite is 0. (There is no C04 and C13 observed within the observation period of time, so there is no calculation about its DCB.) It can be seen that the STD of BDS satellites DCB range is [0.22, 0.89 ns], and the stability of calculated BDS satellites' DCB is lower than that of GPS; the STD of GEO satellites DCB range is

Table 3 The STD statistic of BDS satellite DCB (2014 318–329) unit: ns

PRN	C01	C02	C03	C05	C06	C07	C08
STD	0	0.61	0.53	0.45	0.33	0.39	0.27
PRN	C09	C10	C11	C12	C14		
STD	0.50	0.41	0.58	0.22	0.60		

[0.53, 0.61 ns]; the STD of IGSO satellites DCB range is [0.27, 0.50 ns]; the STD of MEO satellites DCB is [0.22, 0.60 ns]. The DCB of IGSO satellites relatively to the GEO satellites and MEO satellites is more stable.

4 Conclusion

For the situation that currently regional layout is the main way for the BDS monitoring stations, this paper combined BDS/GPS multi-frequency data, and the single ionospheric model is established on polynomial, which is used to calculate GPS/BDS satellites. The establishment of a single-stand ionospheric model can reflect the daily variation of the ionosphere above the monitoring station, and meet the needs of the ionosphere delay correction and the ionosphere activities under the usual accuracy; the calculated BDS/GPS satellites DCB and official DCB value can be controlled within 0.79 ns/1.7 ns, respectively. Through anglicizing BDS satellites STD, it shows that the STD of IGSO satellites DCB is better than GEO satellites and MEO satellites, and the reasons are as follows:

1. The GEO satellites are relative to the monitoring station in the stationary state, and the low observed altitude angle and geometry-free linear combination can increase the pseudorange noise and multi-path effect.
2. The MEO satellites cannot be constantly tracked by monitoring stations in 24 h, which limits the valid data of observations, affecting the calculating stability of the DCB of MEO satellites.
3. The IGSO satellites, in which orbits are uniformly distributed on both sides of the equator, monitoring stations can do almost 20 h of continuous observation. So, the data qualities are better than those of first two satellites.

Acknowledgments Thanks to the high-precision products provided by international GNSS Monitoring and Assessment System (iGMAS), the support from National Natural Science Foundation of China (61263028), The open foundation of key Lab. of Time and Frequency Primary Standards, CAS (Y000YR1S01) and The open foundation of Guangxi Key Laboratory of wireless broadband communication and signal processing (GXKL0614107).

References

1. Geng C, Zhang H, Zhai C et al (2009) Real time estimation of DCB using kalman filters. Geomat Inf Sci Wuhan Univ 34(11):1309–1322
2. Matsakis D (2007) The timing group delay (TGD) correction and GPS timing biases. In: Proceedings of the 63rd annual meeting of the Institute of Navigation, pp 49–54
3. Tang W, Jin L, Xu K et al (2009) A real-time dual-frequency ionospheric estimation algorithm performance analysis based on BeiDou observational data. Geomat Inf Sci Wuhan Univ 34 (11):1309–1322
4. Liu J (2011) Study of ionosphere prediction models and discussion of preseism ionosphere anomalous. The PLA Information Engineering University
5. Geng C, Tang W, Zhang H et al (2008) A real-time monitoring of ionosphere change by CORS. J Geod Geodyn 28(5):105–108
6. Chen P, Zhang C, Huang K (2010) Cycle slips detection and repairing by use of phase reduce pseudo range law and ionized layer remnant method of difference. J Geod Geodyn 30(2):120–124
7. Wu X, Ping J, Liu L et al (2011) Hardware delay solution of regional satellite navigation system. Geomat Inf Sci Wuhan Univ 29(10):1218–1221
8. Huang Z (2015) Abnormal variation of ionospheric total electron content before the 24 August 2014 M 6.0 California earthquake. Sci Technol Rev 33(4): 22–27
9. Hernandez-Pajares M, Juan JM, Sanz J et al (2009) The IGS VTEC maps: a reliable source of ionospheric information since 1998. J Geod 83(3):263–275
10. Wilson BD, Mannucci AJ (1993) Instrumental biases in ionospheric measurement derived from GPS data. In: Proceedings of the ION GPS-93, Salt Like City, UT, USA, 22–24 Sept 1993
11. http://www.whigg.ac.cn/xwzx/zhxw/201511/t20151106_4455209.html. Accessed 11 Nov 2015

An Algorithm of Single-Epoch Integer Ambiguity Resolution for Reference Stations of BDS Triple-Frequency Network RTK

Ming Liu, Hongzhou Chai, Bingquan Dong, Di Li and Feng Li

Abstract An algorithm of single-epoch integer ambiguity resolution for reference stations of BDS triple-frequency network RTK is proposed in this paper. The mathematic models, resolution process, and result analyses are given in detail. The main idea of this method is to resolve extra-wide-lane and wide-lane ambiguity by using the method of TCAR, determine the ambiguity candidates by linear relation between triple-frequencies ambiguities, and finally, determine the ambiguities depending on residual of nondispersive error. This algorithm was tested, and the advantages of this method are rapid and stable. The double difference integer ambiguity between long-scale BDS reference stations can be fixed at single epoch.

Keywords BDS · Network RTK · Double difference ambiguity · Linear relationship · TCAR

1 Introduction

It is important to fix the ambiguities of reference stations for network RTK, which is the precondition to obtain high-precision combined bias or to establish high-precision model of bias. However, the common distances of network RTK are between 30 and 80 km, which lead to the bias that has relationship with distance becoming weak. Furthermore, it is impossible to resolve ambiguity by the traditional method, for that the influence of ionospheric delay and tropospheric delay is greater than 0.5 cycle to the observations. Even though the coordinates of the reference stations have already been given, it is difficult to determine the ambiguity instantaneous.

In order to solve the above problem, there are some scholars who have researched on it and acquired some achievement. An ambiguity searching method for network RTK baselines between base stations at single epoch was proposed by

M. Liu (✉) · H. Chai · B. Dong · D. Li · F. Li
Institute of Surveying and Mapping, Zhengzhou 450052, China
e-mail: 291410820@qq.com

© Springer Science+Business Media Singapore 2016

J. Sun et al. (eds.), *China Satellite Navigation Conference (CSNC) 2016 Proceedings: Volume III*, Lecture Notes in Electrical Engineering 390,
DOI 10.1007/978-981-10-0940-2_30

Gao, which used carrier-phase data of dual frequencies but not solving the corresponding observational equations, and used the linear relation between dual frequencies ambiguities and known coordinates of base stations directly to search the double difference integer ambiguities by only one epoch. In addition, a new three-step method to determine double difference integer ambiguities resolution of network RTK reference station was proposed by Tang, which included wide-lane ambiguity resolution, narrow-lane ambiguity resolution, and the ambiguities resolution of carrier phase L_1 and L_2. Zhu proposed another method which determined the wide lane by linear relationship between carrier-phase ambiguities first, candidates of double frequency carrier-phase ambiguities could be selected by fixed double difference wide-lane ambiguities, finally, the double frequency carrier-phase ambiguities were searched and fixed through the computation of non-divergent error's residual. Deng realized the instantaneous integer ambiguity resolution in the mode of three frequencies through simulating the observations of L_5. However, there were few researches on BDS network RTK. Therefore, an algorithm of single-epoch integer ambiguity resolution for reference stations of BDS triple-frequency network RTK is proposed in this paper which uses the easy fixed extra-wide-lane and wide-lane ambiguity and linear relationship between carrier-phase ambiguities to determine double difference ambiguities.

2 Linear Relationship Between Carrier-Phase Ambiguities

In the common condition, the reference stations are established on the open place, so the multi-path error can be ignored. Therefore, the equations of carrier-phase measurements between reference stations A and B and satellites p and q can be written as:

$$\frac{c}{f_1}\nabla\Delta\Phi_{1AB}^{pq} = \nabla\Delta\rho_{AB}^{pq} - \frac{c}{f_1}\nabla\Delta N_{1AB}^{pq} - \frac{\nabla\Delta I_{0AB}^{pq}}{f_1^2} + \nabla\Delta T_{AB}^{pq} + \nabla\Delta\varepsilon_{1AB}^{pq} \quad (1)$$

$$\frac{c}{f_2}\nabla\Delta\Phi_{2AB}^{pq} = \nabla\Delta\rho_{AB}^{pq} - \frac{c}{f_2}\nabla\Delta N_{2AB}^{pq} - \frac{\nabla\Delta I_{0AB}^{pq}}{f_2^2} + \nabla\Delta T_{AB}^{pq} + \nabla\Delta\varepsilon_{2AB}^{pq} \quad (2)$$

$$\frac{c}{f_3}\nabla\Delta\Phi_{3AB}^{pq} = \nabla\Delta\rho_{AB}^{pq} - \frac{c}{f_3}\nabla\Delta N_{3AB}^{pq} - \frac{\nabla\Delta I_{0AB}^{pq}}{f_3^2} + \nabla\Delta T_{AB}^{pq} + \nabla\Delta\varepsilon_{3AB}^{pq} \quad (3)$$

where c is the speed of light; f is the frequency of carrier phase; 1, 2, 3 are the number of frequencies, respectively; $\nabla\Delta$ is the symbol of double difference; φ is carrier-phase measurement in the unit of cycle; ρ is the geometrical distance between the receiver and the satellite; N is the integer ambiguity; I_0 is the ionospheric range delay which is independent with frequency; T is the non-divergent error; ε is the noise of observations.

Non-divergent error is mainly the tropospheric delay and the orbit error of satellite which can be eliminated or weakened through correction of model. If we use $\nabla\Delta\eta_{AB}^{pq}$ as the symbol of residual that is corrected by the model of troposphere, the computational formula of $\nabla\Delta\eta_{AB}^{pq}$ can be written as:

$$\nabla\Delta\eta_{AB}^{pq} = \nabla\Delta T_{AB}^{pq} - \nabla\Delta T_{AB}^{\prime pq} \tag{4}$$

where $\nabla\Delta T_{AB}^{\prime pq}$ is tropospheric delay that is computed by the model of Saastamoinen. Eliminating the $\nabla\Delta l_{0AB}^{pq}$ of formula (1)–(3), we can derive the linear relation among triple frequencies ambiguities as below.

$$\nabla\Delta N_1 = \frac{f_2}{f_1}\nabla\Delta N_2 - \nabla\Delta l_{12AB}^{pq} - \nabla\Delta\omega_{12AB}^{pq} \tag{5}$$

$$\nabla\Delta N_2 = \frac{f_3}{f_2}\nabla\Delta N_3 - \nabla\Delta l_{23AB}^{pq} - \nabla\Delta\omega_{23AB}^{pq} \tag{6}$$

All terms in the formula are in the unit of cycle. In addition,

$$\nabla\Delta l_{12AB}^{pq} = \nabla\Delta\varphi_1 - \frac{f_2}{f_1}\nabla\Delta\varphi_2 - \frac{f_1^2 - f_2^2}{c \cdot f_1}\left(\nabla\Delta\rho_{AB}^{pq} + \nabla\Delta T_{AB}^{\prime pq}\right) \tag{7}$$

$$\nabla\Delta\omega_{12AB}^{pq} = \frac{f_1^2 - f_2^2}{c \cdot f_1} \cdot \nabla\Delta\eta_{AB}^{pq} + \frac{f_2^2 \cdot \nabla\Delta\varepsilon_{2AB}^{pq} - f_1^2 \cdot \nabla\Delta\varepsilon_{1AB}^{pq}}{c \cdot f_1} \tag{8}$$

$$\nabla\Delta l_{23AB}^{pq} = \nabla\Delta\varphi_2 - \frac{f_3}{f_2}\nabla\Delta\varphi_3 - \frac{f_2^2 - f_3^2}{c \cdot f_2}\left(\nabla\Delta\rho_{AB}^{pq} + \nabla\Delta T_{AB}^{\prime pq}\right) \tag{9}$$

$$\nabla\Delta\omega_{23AB}^{pq} = \frac{f_2^2 - f_3^2}{c \cdot f_2} \cdot \nabla\Delta\eta_{AB}^{pq} + \frac{f_3^2 \cdot \nabla\Delta\varepsilon_{3AB}^{pq} - f_2^2 \cdot \nabla\Delta\varepsilon_{1AB}^{pq}}{c \cdot f_2} \tag{10}$$

For that, the coordinates of reference stations are known, $\nabla\Delta\rho_{AB}^{pq}$ can be computed precisely. Therefore, $\nabla\Delta l_{12AB}^{pq}$ and $\nabla\Delta l_{13AB}^{pq}$ are constant terms. $\nabla\Delta\omega_{12AB}^{pq}$ and $\nabla\Delta\omega_{13AB}^{pq}$ are residual errors.

3 Ambiguities Resolving of Extra-Wide Lane and Wide Lane

The process of the *TCAR* method is in the sequence of fixing extra-wide-lane ambiguity, wide-lane ambiguity, and narrow-lane ambiguity. For extra-wide-lane ambiguity and wide-lane ambiguity of long baseline, the method of *TCAR* can fix reliably at single epoch. According to the theory of *TCAR*, the computational model

Table 1 TCAR EWL and WL combination of BDS

Combination	Frequency (MHz)	Wavelength (m)
EWL (0, 1, −1)	61.38	4.884
WL (1, −1, 0)	353.958	0.847

Table 2 The ionosphere-delay coefficient and noise influence

Steps	γ	Noise influence (cycle)	
		$\sigma_\upsilon = 0.01$ cycle, $\sigma_e = 0.3$ m	$\sigma_\upsilon = 0.02$ cycle, $\sigma_e = 0.6$ m
EWL	0.016	0.063	0.126
WL	−0.352	0.083	0.166

can be written as below considering the pseudorange measurement R_3 is accurate than others and ignoring narrow-lane ambiguity.

$$\nabla\Delta N_{\mathrm{EWL}} = \nabla\Delta R_3/\lambda_{\mathrm{EWL}} - \nabla\Delta\varphi_{\mathrm{EWL}} - \alpha_{R_3-\mathrm{EWL}} \cdot \nabla\Delta I_1/\lambda_{\mathrm{EWL}} + \nabla\Delta\varepsilon_{\mathrm{EWL}} \quad (11)$$

$$\begin{aligned}\nabla\Delta N_{\mathrm{WL}} = {} & \left(\nabla\Delta\varphi_{\mathrm{EWL}} + \nabla\Delta\widehat{N}_{\mathrm{EWL}}\right) \cdot \lambda_{\mathrm{EWL}} \Big/ \lambda_{\mathrm{WL}} - \nabla\Delta\varphi_{\mathrm{WL}} \\ & - \alpha_{\mathrm{EWL-WL}} \cdot \nabla\Delta I_1/\lambda_{\mathrm{WL}} + \nabla\Delta\varepsilon_{\mathrm{WL}}\end{aligned} \quad (12)$$

where N_{EWL} and N_{WL} are float solutions of wide-lane ambiguity and narrow-lane ambiguity, respectively; $\widehat{N}_{\mathrm{EWL}}$ is the fixed solution of N_{EWL}; I_1 is the ionospheric delay of $B1$. $\alpha_{R_3-\mathrm{EWL}}$ and $\alpha_{\mathrm{EWL-WL}}$ are the ionosphere-delay coefficients of combined observation equations.

From the formula (11) and (12), we can know that the method of *TCAR* eliminates the non-divergent error and is just influenced by ionosphere delay and noise. Using the combinations in Table 1, we can calculate the ionosphere-delay coefficient γ and noise influence which are shown in Table 2.

As shown in Table 2, the extra-wide-lane ambiguity in the first step is influenced weakly by the ionosphere delay; the wide-lane ambiguity in the second step is about 0.1 cycle if ionospheric delay is 0.3 m; what is more, the noise influences to extra-wide-lane ambiguity and wide-lane ambiguity are both less than 0.17 cycle. Therefore, for extra-wide-lane ambiguity and wide-lane ambiguity of long baseline, the method of *TCAR* can fix reliably at single epoch.

4 The Determination and Detection of Ambiguities of Triple Frequencies

A candidate of $\nabla\Delta N_2$ has only one corresponding $\nabla\Delta N_3$ after fixing the extra-wide-lane ambiguity. In the same way, a candidate of $\nabla\Delta N_1$ has only one corresponding $\nabla\Delta N_2$ after fixing the wide-lane ambiguity. The formula (5) gives us

the linear relation between $\nabla\Delta N_1$ and $\nabla\Delta N_2$, which can be taken as an example. For k_{12} = 201,190/260,183 ≈ 0.7733, the integer $\nabla\Delta N_1$ and $\nabla\Delta N_2$ have infinite pairs and have periodicity in theory. But in practice, it is impossible to find the candidates of integer ambiguities that fit the formula (5) absolutely, because of the influence of residual errors and the restriction of precision. Therefore, the ratio that is similar with the slope can also become the candidates of integer ambiguities. However, it does not matter with the use of the searching method. In practice, the influence of ionospheric delay is finite, which does not exceed 10 cycles generally. Therefore, using fixed wide-lane ambiguity and the linear relation (5), we can search the candidates of $\nabla\Delta N_2$ and its corresponding $\nabla\Delta N_1$. In the same way, using fixed extra-wide-lane ambiguity and the linear relation (6), we can search the candidates of $\nabla\Delta N_3$ and its corresponding $\nabla\Delta N_2$.

In the end, we should use the non-divergent error resolved by the candidates to determine the ambiguities. According to formula (5) and (6), the non-divergent error can be derived as below.

$$\nabla\Delta T_{21} = \frac{c \cdot f_1}{f_1^2 - f_2^2}\left(\nabla\Delta\Phi_1 - \frac{f_2}{f_1}\nabla\Delta\Phi_2 + \nabla\Delta N_1 - \frac{f_2}{f_1}\nabla\Delta N_2\right) - \nabla\Delta\rho \tag{13}$$

$$\nabla\Delta T_{32} = \frac{c \cdot f_2}{f_2^2 - f_3^2}\left(\nabla\Delta\Phi_2 - \frac{f_3}{f_2}\nabla\Delta\Phi_3 + \nabla\Delta N_2 - \frac{f_3}{f_2}\nabla\Delta N_3\right) - \nabla\Delta\rho \tag{14}$$

If there are

$$\nabla\Delta\eta_{21} = \nabla\Delta T_{21} - \nabla\Delta T', \quad |\nabla\Delta\eta_{21}| < \sigma_1 \tag{15}$$

$$\nabla\Delta\eta_{32} = \nabla\Delta T_{32} - \nabla\Delta T', \quad |\nabla\Delta\eta_{32}| < \sigma_2 \tag{16}$$

This group of integer ambiguities is considered as the right one. In the above formula, σ_1 and σ_2 are both limited value, which can be obtained by empirical value.

In addition, the fixed ambiguities can be detected by the theory that the algebraic sum of double difference ambiguities of reference stations at one frequency point is zero.

5 Data Test and Analysis

This paper uses the dataset obtained from Shanghai on 14 December 2013 to test the method proposed in this paper. The dataset was recorded in an hour at an interval of 1.0 s and its cutoff elevation is 10°. The reference stations are Ji Gu Jiao (BASE1), Lu Chao Gang (BASE2), and Heng Sha Dao (BASE3), and the distance between BASE1 and BASE2 is 61.7 km, the distance between BASE1 and BASE3 is 60.1 km, the distance between BASE2 and BASE3 is 57.6 km.

Using the method proposed in this paper to resolve ambiguities, the specific process and result are given as below.

1. Taking the PRN1 of BDS satellites as example, we should calculate the constant terms $\nabla\Delta l_{12AB}^{pq}$ and $\nabla\Delta l_{13AB}^{pq}$ according to (7) and (9) and integer extra-wide-lane ambiguity $\nabla\Delta\widehat{N}_{(0,1,-1)}$ and integer wide-lane ambiguity $\nabla\Delta\widehat{N}_{(1,-1,0)}$ according to (11) and (12) first.
2. Determine the ambiguity candidates of L_1, L_2, and L_3 according to fixed extra-wide-lane ambiguity and wide-lane ambiguity and linear relation (5) and (6). Then fix the ambiguity of L_1, L_2, and L_3 according to formula (15) and (16). Taking the first epoch of PRN1 whose reference satellite is PRN7 as example, we can get the inter ambiguities of L_1, L_2, and L_3 shown in the Table 3.
   It is clear that the inter ambiguities of L_1, L_2, and L_3 are right through the detection of closure relationship among reference stations.
3. In the end, we could use the non-divergent error of all epochs calculated by above steps to detect subsequent ambiguities. The results are shown from Figs. 1, 2, 3, 4, 5, 6.
   The non-divergent error includes the residual of tropospheric delay, the error of satellite orbit, and so on. As shown from Figs. 1, 2, 3, 4, 5, 6, the results and changes fit the reality, which proves that the subsequent fixed ambiguities are right and the method proposed in this paper is feasible.

Table 3 The inter ambiguities of L_1, L_2, and L_3 from PRN1-7

Baseline	$\nabla\Delta N_1$, $\nabla\Delta N_2$, $\nabla\Delta N_3$
BASE1–BASE2	(−398885, −4428255, 1359507)
BASE2–BASE3	(1298455, −2076095, −1721896)
BASE3–BASE1	(−899570, 6504350, 362389)

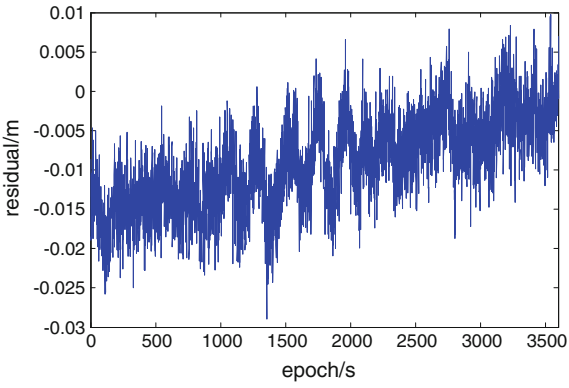

Fig. 1 $\nabla\Delta\eta_{21}$ on baseline BASE1–BASE2

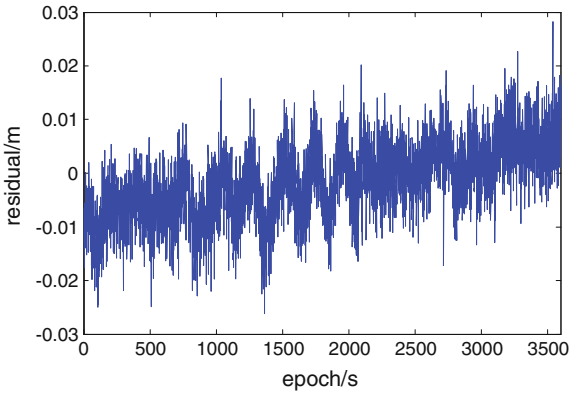

Fig. 2 $\nabla\Delta\eta_{32}$ on baseline BASE1–BASE2

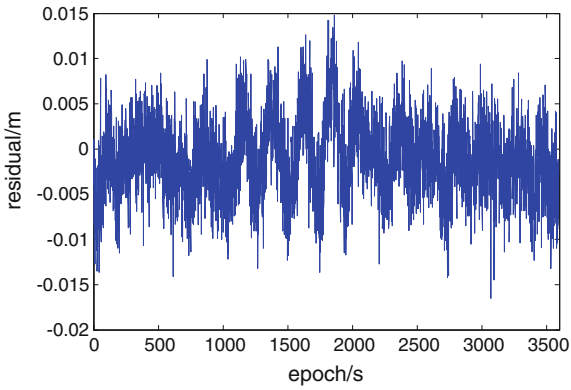

Fig. 3 $\nabla\Delta\eta_{21}$ on baseline BASE2–BASE3

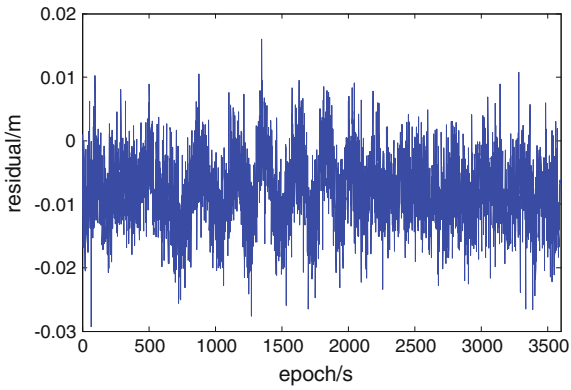

Fig. 4 $\nabla\Delta\eta_{32}$ on baseline BASE2–BASE3

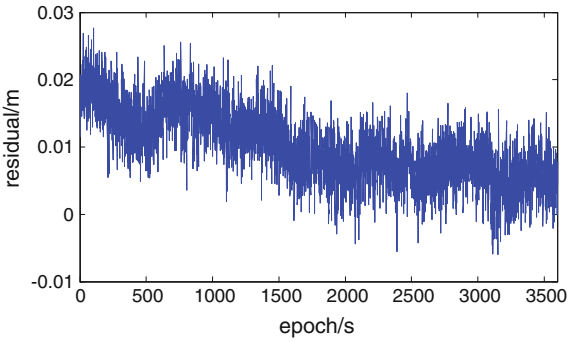

Fig. 5 $\nabla\Delta\eta_{21}$ on baseline BASE3–BASE1

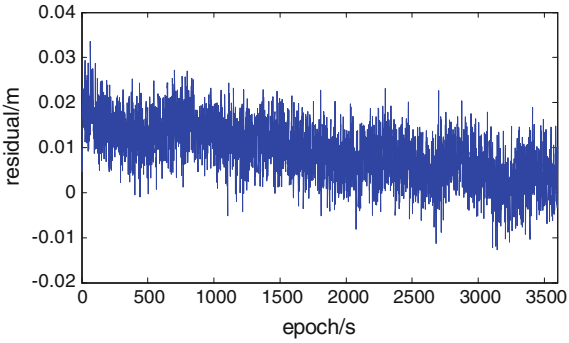

Fig. 6 $\nabla\Delta\eta_{32}$ on baseline BASE3–BASE1

6 Conclusions

An algorithm of single-epoch integer ambiguity resolution for reference stations of BDS triple-frequency network RTK is proposed in this paper. The main idea of this method is to resolve extra-wide-lane and wide-lane ambiguity by using the method of TCAR, determine the ambiguity candidates by linear relation between triple frequencies ambiguities, and finally determine the ambiguities depending on residual of nondispersive error. This algorithm was tested, and the advantages of this method are rapid and stable. The double difference integer ambiguity between long-scale BDS reference stations can be fixed at single epoch. Furthermore, as the time goes on, the determined ambiguities can be judged whether they are reliable according to the changes of the residual of tropospheric delay, which could improve the stability of this method.

Acknowledgment This work is supported by China National Natural Science Foundation of China (No: 41274045, 41574010).

References

1. Dong DN, Bock Y (1989) Global positioning system network analysis with phase ambiguity resolution applied to crustal deformation studies in California. J Geophys Res 94(B4): 3949–3966
2. Blewitt G (1989) Carrier phase ambiguity resolution for the global positioning system applied to geodetic baselines up to 2000 km. J Geophys Res 94(B8):10187–10203
3. Blewitt G (1990) An automatic editing algorithm for GPS data. Geophys Res Lett 17(3): 199–202
4. Gao X, Chen R, Zhao C (2009) A network RTK algorithm and its test. Geomat Inf Sci Wuhan Univ 34(11):1350–1353
5. Gao X, Liu J, Ge M (2002) An ambiguity searching method for network RTK baselines between base stations at single epoch. Acta Geodaetica Cartogr Sin 31(4):305–309
6. Tang W, Liu J, Shi C et al (2007) Three steps method to determine double difference ambiguities resolution of network RTK reference station. Geomat Inf Sci Wuhan Univ 32(4):305–308
7. Zhu H, Liu J, Tang W (2012) The algorithm of single-epoch integer ambiguity resolution between long-range network RTK base stations. Acta Geodaetica Cartogr Sin 41(3):359–364
8. Deng J, Pan S, Wang S (2009) Fast resulotion for three-frequency carrier ambiguity of long-range network RTK based on optional combination. J Chin Inert Technol 25(4):491–495
9. Gao X, Chen R, Li X (2007) The influence and model-correction analysis of non-difference pseudo-distance positioning from neutral atmosphere. Acta Geodaetica Cartogr Sin 36(2): 134–140
10. Hatch R, Jung J, Enge P, Pervan B (2000) Civilian GPS: the benefits if three frequencies. GPS Solut 3(4):1–9
11. Huang L, Ning D, Lv Z (2014) Comparative study on two long-baseline ambiguity resolution methods in application of BEIDOU/COMPASS triple-frequency. J Geod Geodyn 34(5): 101–105
12. Gao W, Gao C, Pan P (2015) Single-epoch positioning method in netwerk RTK with BDS triple-frequency widelane combinations. Acta Geodaetica Cartogr Sin 44(6):641–648
13. Feng Y (2008) GNSS three carrier ambiguity resolution using ionosphere-reduced virtual signals. J Geod 82:847–862
14. Feng Y, Rizos C (2009) Network-based geometry-free three carrier ambiguity resolution and phase bias calibration. GPS Solut 13:43–56

Study on Multipath Effect of GEO Satellite in BeiDou Navigation Satellite System

Peng Wu, Baowang Lian, Yulong Song and Zhe Yue

Abstract For BeiDou navigation satellite system, multipath fading from geostationary Earth orbit (GEO) satellites constraints BeiDou receiver to provide a high-precision positioning service, which is not negligible. By designing multipath fading mathematical model, the mechanism of multipath fading is analyzed. This paper proposes a method, by analyzing the fading trend of the first nulling point and second nulling point of Kepler multipath fading (KMPF) factor, which can reflect variation trend of the multipath error of GEO. Finally, the simulation results verify that the KMPF factor provides an important method to analyze the GEO multipath errors.

Keywords BeiDou GEO satellites · Multipath effect · Kepler multipath fading factor

1 Introduction

The satellite navigation receiver provides PNT information to the user by measuring the pseudorange of the navigation signal. The pseudorange measurement is vulnerable to various errors, which decrease the positioning accuracy of the receiver. The impact of the atmosphere on the navigation signal is characterized by an atmospheric delay, which includes ionospheric delay and tropospheric delay, when the navigation signals transit atmosphere. Besides, the satellite navigation receiver may also suffer from the multipath signal generated by the surrounding environment, which arises loop tracking errors, and ultimately affects the positioning accuracy. In addition, for navigation system, there also exist other unignored errors, such as satellite clock error, ephemeris errors, receiver clock, and so on. Due to each error, source performs the different characteristics in time domain or frequency domain, the corresponding methods can be used to reduce or even eliminate the errors. The common errors

P. Wu (✉) · B. Lian · Y. Song · Z. Yue
School of Electronics and Information, Northwestern Polytechnical University, 710072 Xi'an, China
e-mail: wupengrock@163.com

© Springer Science+Business Media Singapore 2016

J. Sun et al. (eds.), *China Satellite Navigation Conference (CSNC) 2016 Proceedings: Volume III*, Lecture Notes in Electrical Engineering 390,
DOI 10.1007/978-981-10-0940-2_31

resulting from atmospheric delay, satellite ephemeris error, and satellite clock error can be greatly eliminated by differential approach or be remarkably improved by building the corresponding mathematical model. However, the multipath errors cannot be removed by differential technique since multipath is closely related to the environment around the antenna and it is hard to achieve correlation for receivers at different locations. So, the investigation for the mechanism of multipath signal and the mitigation methods has vital significance to reduce the observation errors and to improve the positioning accuracy. For instance, code measurements are used for estimation of atmospheric delay and calculation of satellite orbit parameters in GNSS control segment. If multipath signal infects the code measurements, then the positioning accuracy and timing performance are both directly decreased. Therefore, the influence of multipath error on the navigation system must be paid high attention.

To study the GEO satellites' contribution for improving the system positioning accuracy in Wide Area Augmentation System (WAAS), [1] proposes that "standing multipath" is a main constraint to make WAAS get better performance. Reference [2] shows that even though GEO satellites are not only used for data link to sent correction and integrity messages, but also to be used as additional ranging sources in WAAS, they have a lower ranging accuracy compared with GPS satellites, and multipath is a crucial interference factor for ranging errors. In Refs. [3] and [4], authors research that the multipath fading characteristics of MEO satellites in GPS are much different from multipath fading characteristics of GEO satellites, which indicates that the multipath fading characteristics are closely related with the satellite orbit.

At present, the research on the mechanism of GEO satellite multipath effect is still not sufficient, nevertheless the elimination algorithms for GPS satellites have been studied very deeply. These algorithms provide an effective way to study the multipath effect of GEO satellite in the BeiDou navigation system. Duo to the GEO satellite, location is almost stationary relative to the Earth, the multipath interference varies very slowly with time. Recently, Ref. [5] presents that the GEO multipath interference has more destructive ability than IGSO satellites and MEO satellites.

To solve this problem, this paper acquires the analytic formula of the multipath frequency fading by establishing the ground multipath reflection model. Subsequently, according to the geometric relations between the satellite and the receiver, as well as the theory of coordinate transformation, the Kepler multipath fading (KMPF) factor has been derived, which can reflect the multipath error caused by the satellite orbit parameters. Finally, simulation results verify the analysis on the mechanism of GEO satellite multipath effects.

2 Multipath Fading Mathematical Model

To characterize the influence of multipath signal, it is assumed that the antenna receives a direct signal and a reflected signal simultaneously, then the compound signal $s(t)$ can be expressed as

$$s(t) = \mathrm{Ap}(t)\sin(\omega_0 t) + \alpha \mathrm{Ap}(t - \tau_\mathrm{m})\sin(\omega_0 t + \Delta\Phi_\mathrm{m}(t)) \quad (1)$$

where A denotes the signal amplitude, ranging and data codes are denoted by $p(t) = \pm 1$, ω_0 is the angular frequency including the Doppler shift $\Delta\omega_0 = 2\pi\Delta f_0$, α is the attenuation coefficient of reflected signal, τ_m is the multipath delay, $\Delta\Phi_\mathrm{m}(t) = \Delta\varphi_\mathrm{m} + (\Delta\omega_\mathrm{m} - \Delta\omega_0)t$ denotes the multipath relative phase, where $\Delta\varphi_\mathrm{m}$ is multipath initial phase, and $(\Delta\omega_\mathrm{m} - \Delta\omega_0)$ is the Doppler difference between the direct and the multipath signal. Duo to the satellites, movement is relative to the antenna phase center, the multipath delay τ_m and carrier phase $\Delta\Phi_\mathrm{m}(t)$ vary with time, and the multipath carrier frequency generates an increment that is multipath fading frequency and can be expressed as follows:

$$\Delta f_\mathrm{m} = \frac{1}{2\pi}\frac{\mathrm{d}\Delta\Phi_\mathrm{m}(t)}{\mathrm{d}t} = \frac{1}{2\pi}\frac{\mathrm{d}[\Delta\varphi_\mathrm{m} + (\Delta\omega_\mathrm{m} - \Delta\omega_0)t]}{\mathrm{d}t} \quad (2)$$

According to Eq. (2), the rate of Doppler difference $(\Delta\omega_\mathrm{m} - \Delta\omega_0)$ determines the frequency of the occurring multipath variations. Ideally, since the GEO satellites is stationary to the Earth, the multipath relative phase turns into a constant and the term $(\Delta\omega_\mathrm{m} - \Delta\omega_0)$ becomes zero. Meanwhile, because of the static behavior of the multipath relative phase, the multipath observation will show a fixed bias [6].

As mentioned above, the multipath fading characteristics are determined by the Doppler difference between direct and reflected signals. In other words, the geometry between satellite orbit and reflection point influences multipath effects. Then, we will analyze the GEO satellites multipath fading characteristics by using ground multipath reflection model.

Figure 1 shows the ground multipath reflection model in which the multipath extra-traveled distance $L_\mathrm{m}(t)$ can be expressed as a function of the satellite elevation

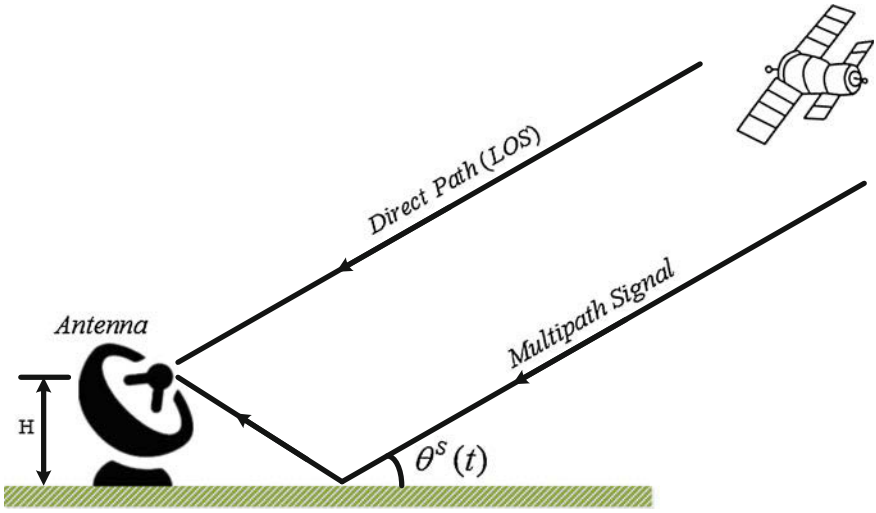

Fig. 1 Model of ground multipath

$\theta^s(t)$, and the height H of the receiver antenna phase center above the reflecting surface at time t. So, we have

$$L_{\mathrm{m}}(t) = 2H \cdot \sin\theta^s(t) \tag{3}$$

According to Eq. (3), the multipath delay of static receiver is closely related to the satellite elevation. In satellite navigation system, the satellite elevation is time-varying relative to the receiving antenna, even for the BeiDou GEO satellites, the elevation could not keep constant over the time. In term of the electromagnetic wave propagation theory, the carrier multipath relative phase can be expressed as

$$\Delta\Phi_{\mathrm{m}}(t) = 2\pi\frac{L_{\mathrm{m}}(t)}{\lambda} = \frac{4\pi H \cdot \sin\theta^s(t)}{\lambda} \tag{4}$$

where the λ is wavelength of the signal.

Substituting Eq. (4) into Eq. (2), and assuming that the receiving antenna and surroundings around the antenna are keeping relatively static, then the multipath fading frequency of the ground multipath reflection model can be expressed as

$$\Delta f_{\mathrm{m}}(t) = \frac{1}{2\pi}\frac{\mathrm{d}\Delta\Phi_{\mathrm{m}}(t)}{\mathrm{d}t} = \frac{2H}{\lambda}\frac{\mathrm{d}[\sin\theta^s(t)]}{\mathrm{d}t}. \tag{5}$$

3 Analysis of the Multipath Parameters

Figure 2 illustrates the geometry between Earth and satellite orbit in the Earth-centered, Earth-fixed (ECEF) system, in which o, R_e, S, $r(t)$, R^s, and A stand for Earth's center, Earth's radius, satellite position, the distance between the satellite and receiver $\|AS\|$, geocentric distance of satellite orbit $\|OS\|$, and location of receiving antenna (A is not the North Pole, but it represents the position of any position on the Earth surface. In order to comply with the visual habits, it points to the zenith direction) at time t, respectively. Besides, plane P is a tangential plane of the Earth surface at point A, as Fig. 2 shows, point D is the projection of satellite S on plane P, and the elevation $\theta^s(t)$ is an included angle between the vector AS and the vector AD. In order to facilitate the geometric relationships among these vectors in Fig. 1, these vectors are presented on a two-dimensional plane as shown in Fig. 1, and according to the law of cosines, we have

$$\sin\theta^s(t) = \frac{R^{s2} - R_e^2 - r^2(t)}{2R_e r(t)} \tag{6}$$

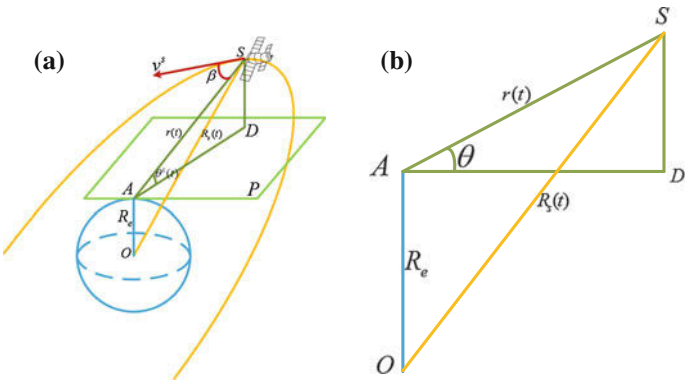

Fig. 2 Geometry between Earth and the satellite orbit. **a** 3D geometry between Earth and satellite orbit, **b** section plan for (**a**)

and substituting Eq. (6) into Eq. (5), the multipath fading frequency is given by

$$\Delta f_{\mathrm{m}}(t) = -\frac{2H}{\lambda}\left(\frac{1}{R_e} + \frac{\sin\theta^s(t)}{r(t)}\right) r'(t) \tag{7}$$

In this equation, the elevation and the distance between satellite and receiver can be extracted from the observables, therefore the characteristic of the multipath fading is mainly restricted by r' at time t. Actually, $r'(t)$ reflects the rate of distance change between satellite and receiver and it is proportional to relative speed along the signal propagation direction. In the ECEF frame, v^s, v, and $\boldsymbol{I}^s$ are the speed of satellite, the speed of receiver, and satellite unit observation vector at the receiver, respectively, thus $r'(t)$ is the dot product of v^s and v, namely

$$\mathbf{r}' = (\mathbf{v^s} - \mathbf{v}) \cdot \boldsymbol{I}^s = (v^s - v)\cos\beta \tag{8}$$

where β is the included angle between $(v^s - v)$ and $\boldsymbol{I}^s$, which is given by

$$\left[\cos\beta = \frac{e\sin f^s}{\sqrt{1 + e^2 + 2e\cos f^s}}\cos\alpha\right] \tag{9}$$

In this equation, $\alpha = \langle SA, SO\rangle$, f^s is the true anomaly. For static scenario, the receiver's speed is zero, then A is the angle between v^s and $\boldsymbol{I}^s$, as shown in Fig. 2b. Based on the analysis of Eqs. (7)–(9), the multipath fading characteristic of static receiver is closely related with the speed of satellite v^s and β.

4 Kepler Multipath Fading Factor

4.1 Derivation of KMPF

As mentioned above, the multipath fading characteristic $\Delta f_{\mathrm{m}}(t)$ is closely associated with the satellite's speed v^s and β. Therefore, the satellite's speed will be as a entry point to further analyze the relationship between the satellite orbit parameters and multipath fading frequency.

Figure 3 depicts the Kepler parameters of satellite orbit, where i is the inclination angle, Ω_0 is the longitude of ascending node, ω is the argument of perigee, $f^s = \omega^s t$ is the true anomaly at time t, and ω^s is the angular rate of the satellite in the Earth-centered, inertial (ECI) coordinate system, which can be achieved from ephemeris. Then, based on the scheme to transform the coordinate systems, the speed of satellite in ECEF system can be calculated as follows:

$$v^s = \frac{R^s}{\sqrt{2}} V \tag{10}$$

where

$$V = \sqrt{(\omega_e^2 + \omega^{s2})(1 + \cos^2 i) - 4\omega_e \omega^s \cos^2 i + [\omega_e^2 \cos(2\omega^s t + 2\omega) + \omega^{s2}]\sin^2 i} \tag{11}$$

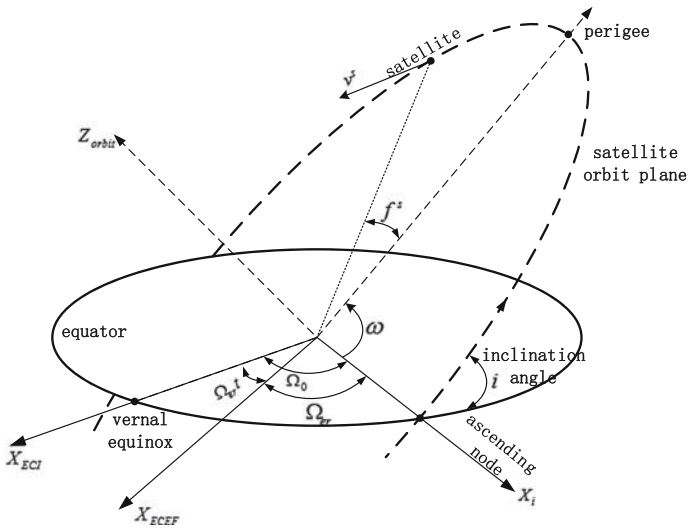

Fig. 3 Kepler parameters of satellite orbit

Meanwhile, according to Eqs. (8) and (9), the Kepler multipath fading factor can be defined as follows:

$$\left[\kappa(t) \triangleq \frac{e \sin f^s}{\sqrt{1+e^2+2e\cos f^s}} V \cos\alpha\right] \tag{12}$$

This equation includes some orbit parameters such as the eccentricity of the satellite orbit e, the inclination angle i, and so on. Subsequently, a deep analysis of these orbit parameters will be discussed in the next section.

4.2 Analysis of KMPF Simulation Curve

4.2.1 Influence of the Orbit Inclination i and Eccentricity e on KMPF

The inclination of GEO satellites in BeiDou system is roughly in the range of 0.03 to 0.09°, and the GEO satellites inclination in WAAS system has a better performance whose range is from 0.01° to 0.02°. In addition, in order to understand deeply the impact of inclination on KMPF, the simulation still takes the situation into consideration when the inclinations are 0.001° and 0.0001°, respectively, as shown in Fig. 4. Meanwhile, some features can be concluded from the curves in Fig. 4.

(i) All the curves show the first nulling at around 11 h.
(ii) When $i = 0.001°$, the amplitude of KMPF factor is greater than others at the first nulling.

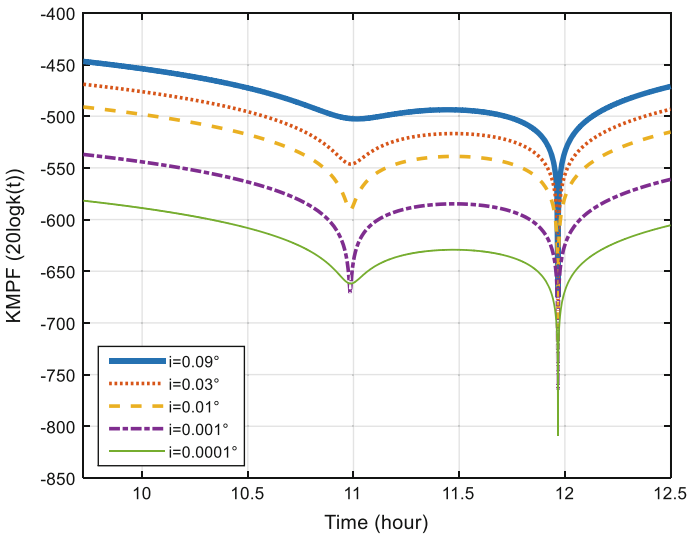

Fig. 4 Fading curve of KMPF

(iii) When $i = 0.09°$ and $i = 0.0001°$, the amplitudes of KMPF factor show a gentle appearance compared with other circumstances at the first nulling.
(iv) The second nulling of all the curves appears at about 12 h.

In order to thoroughly analyze the impact of the inclination i and eccentricity e on KMPF factor, some conclusions can be summarized by comparing with the corresponding curves trend between Figs. 4 and 5. The normalized curves in Fig. 5 derived from Eq. (11), indicate the trends of satellites' speed in ECEF coordinate system. The analyses based on the above four features are shown as follows:

Feature (i) illustrates that the first nulling of KMPF factor curves is closely related to the inclination i. Moreover, in Fig. 5, at the corresponding location to the first nulling, these five curves show an extreme point, which is the reason for the first nulling of KMPF factor curves.

As feature (ii) and (iii) described, by comparing the five curves in Fig. 5, the fading amplitude of the first nulling of KMPF factor curve does not become greater with increase in the inclination. When inclination becomes larger $(i = 0.09°)$ or smaller $(i = 0.0001°)$, the trend of KMPF factor curve at first nulling is gentle. Nevertheless, when $i = 0.001°$, the fading amplitude of the first nulling reaches maximum. By referring Fig. 5, it can be seen that the sharper curve V fades, the larger fading amplitude goes.

Feature (iv) shows the relationship between the curve V and eccentricity e. if $e = 0$, namely the orbit is a standard circle, the movement of satellite will not affect the range rate between the GEO satellites and receiver and the second nulling will vanish from the KMPF factor curve. The fading amplitude of the second nulling is proportional to the eccentricity e.

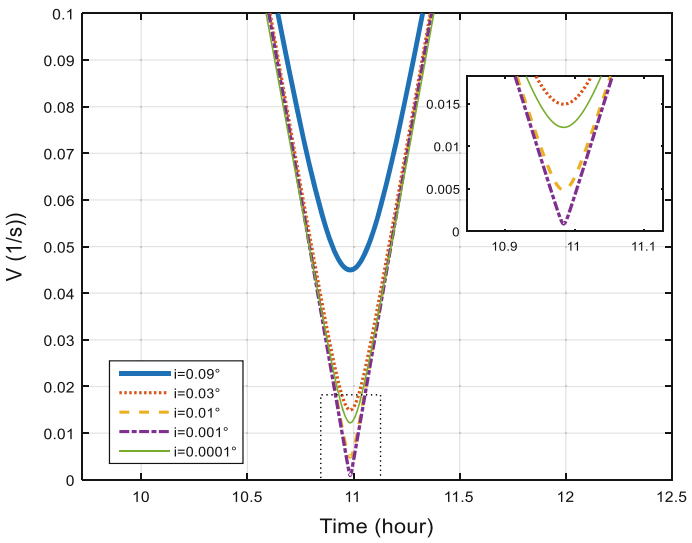

Fig. 5 Relationship between inclination angle and normalized V

4.2.2 Influence of the Argument of Perigee ω on KMPF

As mentioned above, Eq. (11) reflects the relationship between trend of satellite speed and the Kepler orbit parameters, and the first nulling is really close to the trend curve V of the satellite velocity. The further discussions of the location of the first bulling are given below:

Figure 6 shows two KMPF factor curves, and they are plotted by same orbit parameters but the argument of perigee ω. When $\omega = 2$ rad, the first nulling appears at the 6th hour and the 18th hours, respectively. However, for $\omega = 0$ rad, the first nulling occurs at the 10th hour and the 22nd hours, respectively. Hence, the argument of perigee ω can affect the location of the first nulling. Moreover, the cycle of the first nulling fading is about 12 h, which is affected by the angular rate of satellites in orbit plane ω^s, and is inversely proportional to ω^s.

4.2.3 The Relationship Between of the Variable V, Pseudorange $r(t)$ and KMPF

As discussed in above sections, a detailed analysis about KMPF has been developed by selecting different Kepler orbital parameters. This section will research the relationship between of the variable V, pseudorange $r(t)$ and KMPF. The simulation data of curves plotted in Fig. 7 received in Kiri region on August 29th, 2015 and downloaded from the International GNSS Service (IGS) website. The upper panel in Fig. 7, shows the trend of the variable V and the pseudorange $r(t)$ between the NO. 4 GEO satellite and observation point in Kiri region. The lower panel is

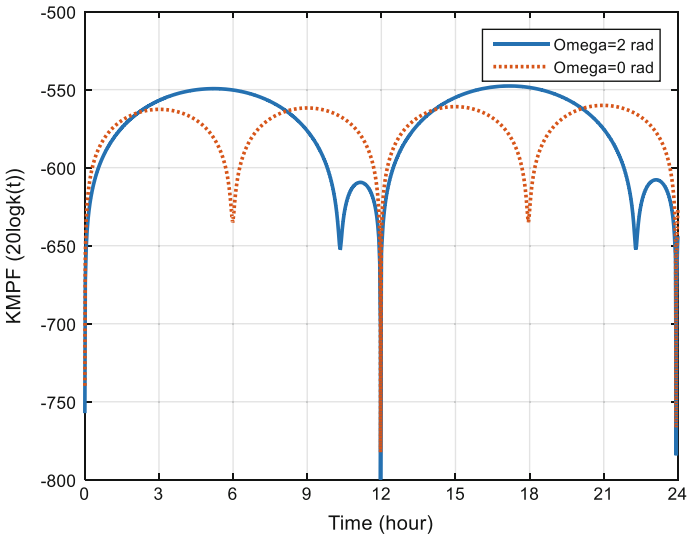

Fig. 6 Relationship between argument of perigee ω and KMPF

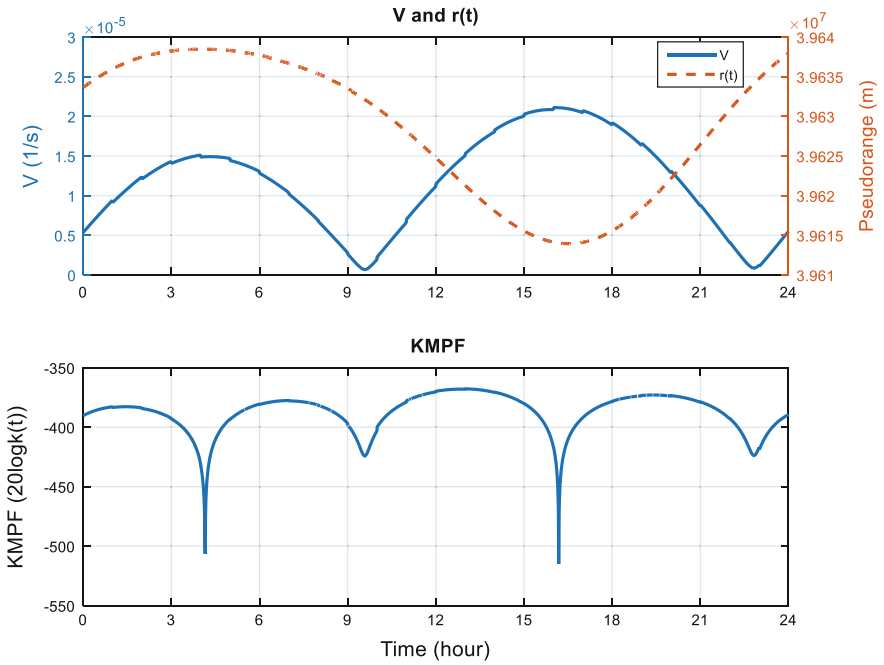

Fig. 7 Relationship between KMPF and pseudorange $r(t)$ and variable V

sketched by the real satellite ephemeris parameters. By analyzing the Fig. 7, some conclusions can be summarized as follows:

(i) The location of the first nulling of KMPF curve is corresponding to the position where the curve V appears the minimal value.
(ii) When the curve V goes to the maximal value, KMPF curve will appear the second nulling, meanwhile the $r(t)$ will show the minimal or maximal value around the position of the second nulling.

5 Simulation Results

This section will verify the theoretical analysis of KMPF factor by simulation. In this simulation, the multipath error envelop curve and Kepler orbit parameters are extracted from data which is received from the real scene at kiri region on August 29th, 2015. The multipath errors on NO. 1 GEO satellite have been calculated by the method mentioned in [7], and this real result is also a reference standard to the simulation.

The top panel in Fig. 8 is a simulation multipath errors, which is based on the ground multipath reflect model proposed in this paper. The middle panel is the real

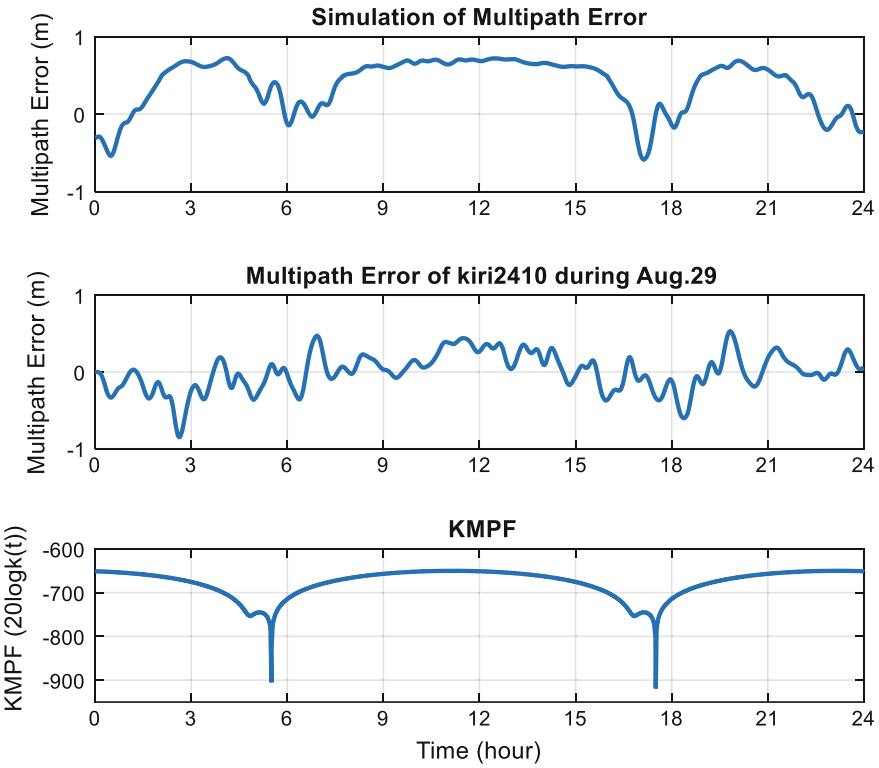

Fig. 8 Characters of multipath of BeiDou NO. 1 GEO

multipath error envelop and the bottom panel is the KMPF factor curve which is plotted by the ephemeris parameters of NO. 1 GEO satellite. According to Eq. (2), GEO satellites multipath effect should present a fixed bias errors, which is called "standing multipath" in [1], and the upper panel also shows this feature.

This article has studied only one reason that may cause the multipath error, the multipath error is related to many factors. Moreover, in a real scene, multipath error is related to many factors, so there exists certain deviation between the simulation curve and practical multipath error curve. However, from the overall trend of these curves, it can be verified that the simulation curve has a certain reference value. The bottom panel shows the waveform of KMPF factor, where the first nulling is not obvious, which means the trend of satellite velocity does not appear large attenuation caused by orbit inclination i. The appearance of the second nulling is caused by eccentricity e. Lastly, comparing the three curves shown in Fig. 8 in a vertical way, when fading in the KMPF waveform occurs, fluctuation in the multipath error appears. So, this verifies the analysis for the multipath effect in this paper.

6 Summary

In order to research the multipath fading effects of GEO satellites, this article analyzes a reason for GEO multipath by building a ground reflect model. In addition, this article deduces the KMPF equation from the multipath fading frequency formula. Finally, some discussions and simulations about GEO satellites orbit parameters are shown as follows:

(i) The first nulling of KMPF factor is related to the inclination i. When i becomes larger or smaller, such as $i > 0.09^\circ$ or $i < 0.0001^\circ$, the trend of first nulling is gentle. But, when i is around 0.001°, the fading amplitude of first nulling becomes lager.
(ii) The location of first nulling of KMPF factor has a relationship with the argument of perigee ω.
(iii) The second nulling of KMPF is mainly related to the eccentricity e, which is in proportion to the eccentricity e.
(iv) When the curve V goes to the maximal value, KMPF curve will appear the second nulling, meanwhile the $r(t)$ will show the minimal or maximal value around the position of the second nulling.
(v) By comparing the simulation multipath error curve and the real multipath error curve, it can be verified that the KMPF factor has a certain reference value for GEO multipath effects.

Acknowledgments This work was supported by the National Natural Science Foundation of China (contract no. 61301094) and BeiDou Special Fund (contract no. GFZX0301040115).

References

1. Timothy S, Jason B, Arthur R (2008) WAAS benefits of geo ranging. In: Proceedings of the 21st international technical meeting of the satellite division of The Institute of Navigation (ION GNSS 2008), Savannah, GA, pp 1903–1910
2. Phelts R, Walter T, Enge P, Akos D, Shallberg K, Morrissey T (2004) Range biases on the WAAS geostationary satellites. In: Proceedings of the ION national technical meeting, San Diego, California, pp 26–28
3. Yang G, Xiaowei C, Mingquan L, Hong L, Zhenming F (2012) The analysis and simulation of multipath error fading characterization in different satellite orbits. In: Proceedings of China satellite navigation conference (CSNC). Springer, Heidelberg, pp 297–308
4. Yang G, Zheng Y, Xiaowei C, Mingquan L (2014) Analysing the orbit influence on multipath fading in global navigation satellite systems. IET Radar Sonar Navig 8(1):65–70
5. Guangxing W, Kees de J, Qile Z, Zhigang H, Jing G (2014) Multipath analysis of code measurements for Beidou geostationary satellites. In: GPS Solutions. Springer, Heidelberg, pp 129–139
6. Markus I (2010) Characterization of multipath phase rates in different multipath environments. GPS Solut 14(4):305–317
7. Byun SH, Hajj GA, Young LE (2002) Development and application of GPS signal multipath simulator. Radio Sci 37:10–110–23

A New Approach of Satellite Selection for Multi-constellation Integrated Navigation System

Guangcai Li, Jiangfei Wu, Weihua Liu and Caixin Zhao

Abstract Based on the analysis of relationship between the satellite elevation as well as the geometry dilution of precision (GDOP) and User-Equivalent Range Error (UERE), a new fast satellite selection algorithm applicable to GNSS receiver was presented with comprehensive considering satellite space geometric distribution and observation error on the result of positioning. In this algorithm, first, the simplified positioning precision evaluation function of elevation and the selecting satellites number model are built with the consideration of GDOP and UERE, through which the minimum elevation thresholds and the number of selecting satellites were quickly decided according to the precision of user's requirement. Then, the partition-weighted method is used to select all the satellites that are greater than the minimum elevation threshold. Parts of satellites are excluded through sorting, differentiating to fulfill satellite selection. Experiment results show that the algorithm has much lower complexity compared to the WPDOP algorithm, and the selection effect is better than the optimal PDOP algorithm.

Keywords Multi-GNSS · Satellite selection · Satellite elevation · GDOP · UERE

1 Introduction

Currently, with the development of GNSS, the number of global navigation satellites in view can be greatly increased to 40 in the same epoch [1]. The GPS/GLONASS/GALILEO/BDS four navigation system can be integrated, which will make the positioning accuracy, integrity, availability, and other navigation performance to greatly improve. However, tracking all visible satellites simultaneously leads unacceptable computation burden for standalone receiver [2], which seriously affects the real-time performance of the navigation and positioning.

G. Li (✉) · J. Wu · W. Liu · C. Zhao
Institute of Geospatial Information, Information Engineering University, Zhengzhou, China
e-mail: LGCGNSS@163.com

© Springer Science+Business Media Singapore 2016

J. Sun et al. (eds.), *China Satellite Navigation Conference (CSNC) 2016 Proceedings: Volume III*, Lecture Notes in Electrical Engineering 390,
DOI 10.1007/978-981-10-0940-2_32

Especially for high dynamic users, the calculation burden of the terminal, the complexity, and the cost of the hardware design are obviously increased. In addition, if the observed data contain large errors it will seriously affect the positioning accuracy [3]. Therefore, the satellite selection algorithm is very important for multi-constellation navigation system.

Most satellite selection methods were proposed to minimum DOP loss due to the reduction of the number of satellite [4], such as best GDOP method [5]. Under this principle, some improved methods are used to reduce computation and quasi-optimal satellite selection algorithm, such as the maximum vector side of tetrahedral volume method [6], the maximum orthogonal projection method [7], the fuzzy selected satellite algorithm [8], the fast selected satellites algorithm based on the elevation and azimuth [8], the dynamic real-time selected satellite algorithm [9], the multi-constellation GNSS using convex geometry [10], and the selected satellite based on recurrent neural networks [11] and genetic algorithm [12]. However, the above algorithms are based on the observation error which is independently and identically distributed, considering the satellite space geometric distribution only, while ignoring the impact by users ranging accuracy (URA), multipath error and the signal-to-noise Ratio (SNR). In the Multi-GNSS, there is a big difference between the different system's satellite observation accuracy. Especially, BDS is composed of geostationary earth orbit (GEO) satellites, inclined geosynchronous satellite orbit (IGSO) satellites and medium earth orbit (MEO) satellites. There is a huge difference between different types of satellites. Based on this, H. Sairo proposed the method of WGDOP (weighted dilution of precision) algorithm [13]. Blanco-Delgado and other scholars have carried on the extension and the consummation to this method [14], but the algorithm computation is still complex, and has been limited in the engineering application.

In this paper, we analyze the relationship between the satellite elevation as well as GDOP and UERE, furthermore, the simplified positioning precision evaluation function of elevation and the selecting satellites number model are built, through which parts of satellites are excluded to fulfill satellite selection. The new fast satellite selection algorithm is proposed, which gives attention to both the influence of GDOP and UERE on the result of positioning, and also reduces the computation. It has important significance for the application of Multi-GNSS.

2 The Analysis of Satellite Elevation in Multi-GNSS

For GNSS, precision can be expressed as the product of GDOP and UERE:

$$\sigma_P = \mathrm{GDOP} \cdot \sigma_{\mathrm{UERE}} \tag{1}$$

In which σ_P is the standard deviation positioning accuracy, σ_{UERE} is a standard deviation of the UERE. This suggests that the positioning accuracy was mainly affected by these two aspects.

2.1 The Relationship Between Satellite Elevation and GDOP

Multi-GNSS and single-constellation navigation system have the same observations model, after the standardization of time and space coordinate system. So, the GDOP of Multi-GNSS also can be defined as follows:

$$\mathrm{GDOP} = \sqrt{\mathrm{trace}(H_{\mathrm{comb}}^{\mathrm{T}} H_{\mathrm{comb}})^{-1}} \tag{2}$$

In which, H_{comb} is the observation matrix of GPS/BDS/GLONASS/GALILEO composite system:

$$H_{\mathrm{comb}} = \begin{bmatrix} H_{\mathrm{GPS}} & 1_{\mathrm{GPS}} & 0_{\mathrm{GPS}} & 0_{\mathrm{GPS}} & 0_{\mathrm{GPS}} \\ H_{\mathrm{BDS}} & 0_{\mathrm{BDS}} & 1_{\mathrm{BDS}} & 0_{\mathrm{BDS}} & 0_{\mathrm{BDS}} \\ H_{\mathrm{Galileo}} & 0_{\mathrm{Galileo}} & 0_{\mathrm{Galileo}} & 1_{\mathrm{Galileo}} & 0_{\mathrm{Galileo}} \\ H_{\mathrm{GLONASS}} & 0_{\mathrm{GLONASS}} & 0_{\mathrm{GLONASS}} & 0_{\mathrm{GLONASS}} & 1_{\mathrm{GLONASS}} \end{bmatrix} \tag{3}$$

where $H_s (s = \mathrm{GPS}, \mathrm{BDS}, \mathrm{Galileo}, \mathrm{GLONASS})$ is the $k \times 3$ matrix and comes from the first three columns of the s navigation system observation matrix, 0_s is $k \times 1$ zero vector and 0_s is $k \times 1$ ones vector, k is the total number of visible satellites for s system. The ith line of the H_s can be represented as

$$H_{si} = (e_{ix}, e_{iy}, e_{iz}) = (\cos \mathrm{EL}_i \sin A_i, \cos \mathrm{EL}_i \cos A_i, \sin \mathrm{EL}_i) \tag{4}$$

where $i = 1, 2, \ldots, k$ is the number of visible satellites for s system, EL_i and A_i is the satellite elevation and azimuth, respectively. (e_{ix}, e_{iy}, e_{iz}) are the unit vectors pointing from the linearization point to the location of the s_i satellite. So, GDOP can be calculated by matrix H_{comb}, and the value is only related to the elevation and azimuth of the visible satellites.

2.2 The Relationship Between Satellite Elevation and GDOP

The UERE for a given satellite is considered to be the statistical sum of the contributions from each of the error sources associated with the satellite. That is

$$\sigma_{i,\mathrm{UERE}}^2 = \sigma_{i,\mathrm{URA}}^2 + \sigma_{i,\mathrm{th}}^2 + \sigma_{i,\mathrm{iono}}^2 + \sigma_{i,\mathrm{trpop}}^2 + \sigma_{i,\mathrm{mpth}}^2 \tag{5}$$

Which are encompasses errors from user range accuracy, thermal noise, ionosphere, troposphere, and multipath. Limited to space, directly gives a simplified calculation models of UERE about satellite elevation [14]:

$$\sigma^2_{i,\mathrm{UERE}}(\mathrm{EL}_i) = \sigma^2_{i,\mathrm{URA}} + \sigma^2_{i,\mathrm{th}} + \frac{1.113}{1.113 - \cos^2 \mathrm{EL}_i} \cdot \sigma_v^2 + (0.017 + 0.28\mathrm{e}^{-11.46\mathrm{EL}_i} + 0.14\mathrm{e}^{-5.73\mathrm{EL}_i}) + \frac{0.0144}{0.002 + \sin^2 \mathrm{EL}_i} \tag{6}$$

The calculation of the parameters in Eq. (6) can be found in [14, 15].

3 Satellite Selection Algorithm Design

3.1 Selecting Satellites Number Model

Choose the number of satellites need to balance position precision and navigation computation. The exponent attenuation model of relationship is built between pre- and post-GDOP and optimal satellites number is given by [16]

$$\overline{\Delta\mathrm{GDOP}} = K/8.5 \cdot \mathrm{e}^{-0.2Kp(1-0.15p)}, \quad (p = m/K, 0.25 \le p \le 0.85) \tag{7}$$

In which, m is the number of selecting satellites, p is selecting satellites ratio, and K is the total number of visible satellites. Through which the number of selecting satellites was decided according to the precision of user's requirement, but m cannot be less than 60 % of K.

3.2 Positioning Precision Evaluation Function of Elevation

Equation (6) shows that UERE is different between different systems, also varies according to the changes in elevation. There is a need to design positioning precision evaluation function (PPE) to simultaneously consider the effect of GDOP and UERE.

The pseudorange equations can be linearized with Taylor's series expansion at the approximate point and associated predicted receiver clock offset. It can be expressed as Eq. (8)

$$\Delta\rho = H_{\mathrm{comb}}\Delta X + \varepsilon \tag{8}$$

In which $\Delta\rho = [\,\Delta\rho_1 \quad \Delta\rho_2 \quad \ldots \quad \Delta\rho_n\,]^{\mathrm{T}}$ is the pseudorange increment vector, $\Delta X = [\,\Delta x \quad \Delta y \quad \Delta z \quad -c\Delta t_1 \quad -c\Delta t_2 \quad -c\Delta t_3 \quad -c\Delta t_4\,]^{\mathrm{T}}$ is the unknown parameter vector of the user's three-dimensional coordinate increment and receiver clock bias for the four systems, the error term ε is the combined effect of the residual errors.

The least square estimation of ΔX is

$$\Delta\hat{X} = (H_{\text{comb}}^{\text{T}} H_{\text{comb}})^{-1} H_{\text{comb}}^{\text{T}} \Delta\rho \tag{9}$$

The position error vector is

$$\begin{aligned} W &= \hat{X} - X = \Delta\hat{X} - \Delta X = (H_{\text{comb}}^{T} H_{\text{comb}})^{-1} H_{\text{comb}}^{\text{T}} \varepsilon \\ &= [\ W_x \quad W_y \quad W_z \quad W_{t_1} \quad W_{t_2} \quad W_{t_3} \quad W_{t_4}\ ]^{\text{T}} \end{aligned} \tag{10}$$

The 3-D positioning error is

$$E_W = \sqrt{W_x^2 + W_y^2 + W_z^2} \tag{11}$$

ε contains random and systematic error, and the positioning precision is mainly affected by the system deviation. ε is unknown, but UERE can be estimated through Eq. (6), so use UERE instead of ε, position error can be predicted. Thus, positioning precision evaluation function can be designed as follows:

$$\begin{aligned} m &= (H_{\text{comb}}^{\text{T}} H_{\text{comb}})^{-1} H_{\text{comb}}^{\text{T}} \text{UERE} \\ &= [\ m_x \quad m_y \quad m_z \quad m_{t_1} \quad m_{t_2} \quad m_{t_3} \quad m_{t_4}\ ]^{\text{T}} \end{aligned} \tag{12}$$

$\text{UERE} = [\ u_1 \quad u_2 \quad \cdots \quad u_n\ ]^{\text{T}}$, u_i is the user equivalent range error of the ith satellite. The positioning evaluation error (PEE):

$$E_m = \sqrt{m_x^2 + m_y^2 + m_z^2} \tag{13}$$

If set $A = (H_{\text{comb}}^{\text{T}} H_{\text{comb}})^{-1} H_{\text{comb}}^{\text{T}}$ then the following equation can be derived

$$m = A \cdot \text{UERE}, \quad m_x = \sum_{i=1}^{n} a_{1i} \cdot u_i, \quad m_y = \sum_{i=1}^{n} a_{2i} \cdot u_i, \quad m_z = \sum_{i=1}^{n} a_{3i} \cdot u_i$$

a_{ii} are diagonal elements of matrix A. The PEE can be calculated as follows:

$$E_m = \sqrt{\left(\sum_{i=1}^{n} a_{1i} \cdot u_i\right)^2 + \left(\sum_{i=1}^{n} a_{2i} \cdot u_i\right)^2 + \left(\sum_{i=1}^{n} a_{3i} \cdot u_i\right)^2} \tag{14}$$

By the calculation Eq. (14), it can be known that when all equivalent range error values are the same, $u_1 = u_2 = \cdots = u_n = \sigma_0$, the PEE will be expressed as follows:

$$E_m = \sqrt{\left(\sum_{i=1}^{n} a_{1i}\right)^2 + \left(\sum_{i=1}^{n} a_{2i}\right)^2 + \left(\sum_{i=1}^{n} a_{3i}\right)^2} \cdot \sigma_0 \tag{15}$$

It is consistent with Eq. (1), and can also prove the validity of the constructor.

From the second section analysis, the observation matrix and UERE are closely related with the satellite elevation, so the accuracy of the positioning can be evaluated as a function of the satellite elevation. Meanwhile, the PEE is also a function of the satellite elevation. Set different elevation mask will cause the change of the PEE, inevitably. So, we can pass through different mask angle to minimize the evaluation error, at this point, the corresponding elevation mask angle is defined as the minimum elevation threshold (Min-ELth). Partition-weighted selection for remaining visible satellites on the basis of set elevation mask to the Min-ELth. That can greatly improve the efficiency and also can ensure positioning accuracy. As a result, a new fast algorithm of the partition-weighted satellite selection method based on the Min-ELth is proposed, hereinafter referred to as PW-ELth.

3.2.1 Simplify PW-ELth

PW-ELth needs to traverse different elevation mask to locate the smallest PEE and determine the Min-ELth. Elevation mask's range is [0°, 45°], if traversal granularity is 1°, it needs 46 times calculation. Although, compared with the best GDOP method and the WGDOP algorithm, the computation amount is greatly reduced, but it still cannot meet the requirements of rapid satellite selection, so it is necessary to simplify the algorithm.

Through the above analysis and a large number of data validation, the PEE increases at first and then decreases along with the increase of elevation mask, so that the Min-ELth can be obtained by the derivative of the extremum method. Due to the satellite elevation angle interval fixed, even if the elevation mask changes in a certain range, the spatial distribution of the satellite will not change. So the PEE is a special piecewise function for elevation mask.

The situation is illustrated graphically in Fig. 1.

Figure 1 shows that PEE and elevation mask are not one-to-one correspondence, but rather a PEE corresponding to a certain range elevation mask. We defined the scope as variable elevation mask area (VEMA). The Min-ELth is the maximum elevation angle in the VEMA (bold identification part) corresponding to the minimum PEE, which is defined as the threshold area (TA).

Through the experimental analysis, TA can be selected as the VEMA with largest domain values, that is, sorted that the satellite elevation has the biggest difference between the adjacent satellite elevations. As the satellite elevation angle increases, the GDOP increases rapidly, so Min-ELth is limited in $0° \sim 45°$. Through the above optimization, Min-ELth selection problem can be converted to a simple

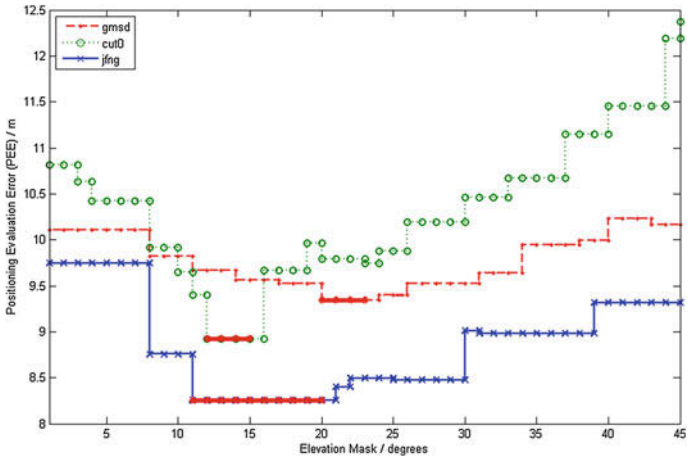

Fig. 1 The relationship between the PEE and the elevation mask

elevation sorting and comparison problem, and the computation is greatly reduced again. Simplified PW-ELth algorithm hereinafter referred to as SPW-Elth.

3.2.2 SPW-Elth Algorithm Design

SNM and PPE were constructed, through which the Min-ELth and the number of selecting satellites were quickly decided. Next, the elevation mask is automatically assigned to Min-ELth excluding the visible satellite below the Min-ELth. If the number of satellite reached the required number of satellite or less than 60 % of the total, there is no longer eliminate satellite. Otherwise, all the satellites, which are greater than the Min-ELth, will be partitioned and weighted to eliminate the redundant satellites.

To sum up, the SPW-ELth algorithm process is as follows:

1. Users according to the requirement of position precision through SNM and PPE decide the required satellite number m and Min-ELth. Automatically exclude some satellites, whose elevation angle is less than Min-ELth, and the rest of the satellite numbers is n.
2. Determine the relationship between n and m, if $n > m$ that all the satellites will be partitioned according to the satellite elevation, whose elevation is greater than Min-ELth (EL_{th}). $EL_{th} \sim 45°, 45° \sim 70°, 70° \sim 90°$ are called low elevation area, middle elevation area, and high elevation area.
3. The satellite elevation in the middle elevation area will be sorted according to their azimuth and calculate the difference between the adjacent satellites azimuth. $n - m$ group satellite will be selected whose difference of azimuth is

smallest, each group has two satellites. To compare each group of two satellites' UERE, eliminate a satellite with bigger UERE.

4. Finally, eliminate redundant satellites and realize indirect selection satellite. Specific flow chart is shown in Fig. 2.

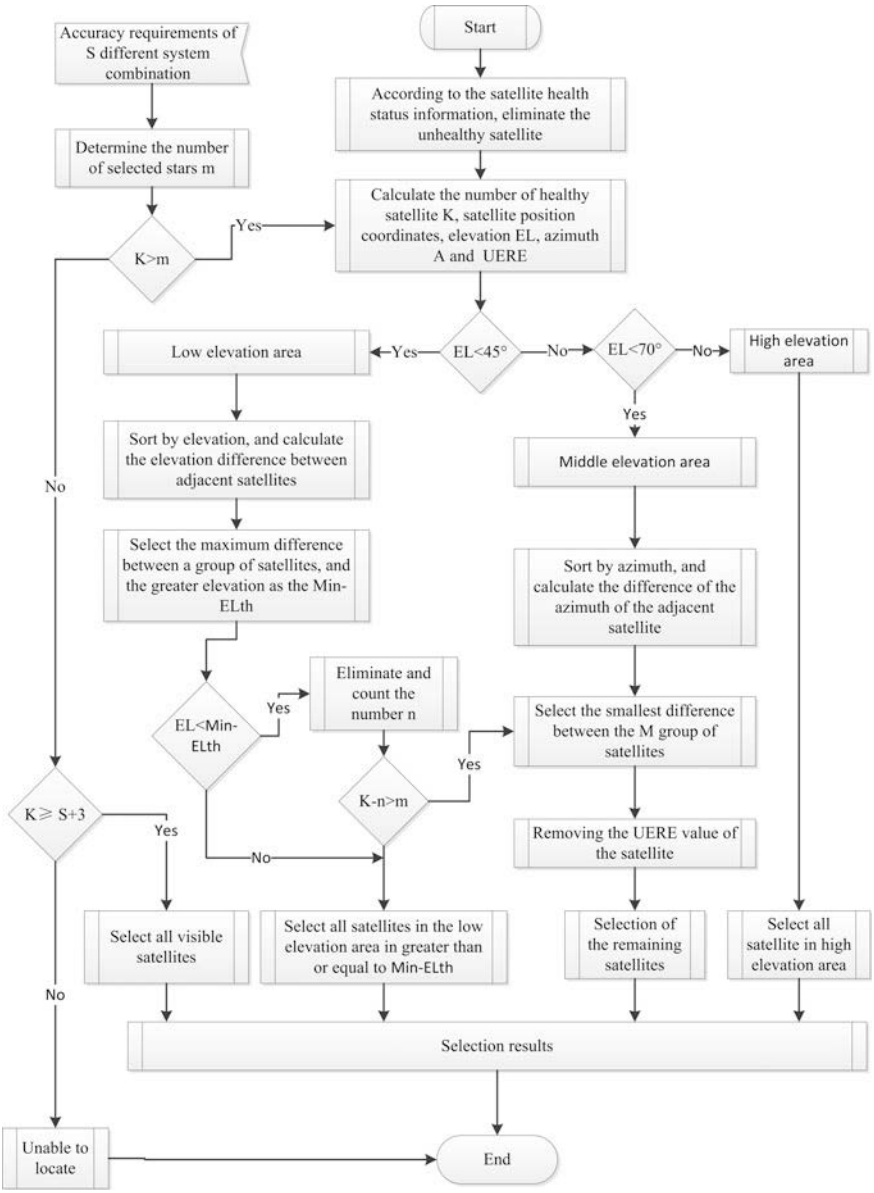

Fig. 2 SPW-ELth algorithm flow chart

4 Experiments and Results

Real data-based experiments were used to evaluate the performance of the proposed algorithm, experimental data provided by IGS-MGEX.

4.1 Experimental Settings

Considering the characteristics of BDS local services, we selected GMSD observatory (30° 33′ 23.2022″, 131° 00′ 56.0331″, 142.336 m) and CUT0 observatory (−32° 00′ 13.9931″, 115° 53′ 41.2807″, 23.992 m) within the scope of BDS services. Data source is RINEX3.2 observation and navigation files provided by the IGS and observation time is from 0:00:00 to 23:59:30 on June 9, 2015, the sampling time interval is 30 s.

In order to verify the validity of the SPW-ELth algorithm, three contrast test is set up: encompasses best GDOP algorithm, best WGDOP algorithm, and PW-ELth algorithm. The calculation complexities mainly depend on the theory of computation. Positioning algorithm uses the weighted least squares estimation (WLS) and comparative positioning accuracy by average position error and root mean square error (RMSE).

4.2 Validity and Computational Complexity Analyses

Due to the traditional optimal PDOP and the optimal WPDOP method along with the increase number of visible satellites, the amount of calculation increases sharply. The GMSD station or CUT0 station can track GPS/BDS/GLONASS/Galileo satellites, the average number of visible satellites reached 30, even choose the least number of satellites according to SNM, and also choose the 18 satellites. Each epoch has to calculate $C_{30}^{18} = 86493225$ times, that the computation is too big to operate. In consideration of the general computer computing ability, without loss of generality choice of an epoch (2015-6-9 0:02:00) and choice of two groups of different combinations of dual system for four methods in GMSD station. The experimental results are in Tables 1 and 2.

Table 1 Performance of four methods for GPS/BDS dual system

GPS/BDS	2D (m)	3D (m)	GDOP
Optimal PDOP	3.436708	3.822289	1.5
Optimal WPDOP	1.974802	2.878967	1.8
PW-Elth-30	2.283885	2.547611	2.8
SPW-Elth-25	2.657797	2.772067	2.4

Table 2 Performance of four methods for GPS/GLONASS dual system

GPS/GLONASS	2D (m)	3D (m)	GDOP
Optimal PDOP	4.550248	5.598056	1.3
Optimal WPDOP	3.544639	3.859836	1.4
PW-Elth-13	3.109068	3.517573	2.5
SPW-Elth-35	3.262601	3.785018	2.3

The result showed that PW-Elth and SPW-Elth have bigger GDOP than optimal PDOP method and optimal WPDOP method. The chief reason was that elevation mask is set as Min-ELth and shielding the low elevation satellite, leads the satellite space geometric distribution structure to not optimal. But for the positioning error, both 2D and 3D, PW-Elth and SPW-Elth are smaller than the optimal PDOP method. The positioning accuracy of SPW-Elth is very close to that of the optimal WPDOP method, and the positioning precision of PW-Elth is the same as that of the optimal WPDOP method, and even better than it. Therefore, the selecting satellite effect of PW-Elth and SPW-Elth is close to optimal.

Compared with PW-Elth, SPW-Elth has smaller GDOP and the positioning accuracy is lower, but the difference is not big. So, SPW-Elth can replace PW-Elth to realize the rapid selection of satellite.

In the actual experiment, we find that the computational complexity between the four algorithms is different, so it is necessary to analyze the theoretical complexity of the above algorithms. Take the experiment of GPS/BDS as an example to calculate the total amount of calculation. The number of visible satellites of the epoch is 20 ($K = 20$), pre-satellite number is 12 ($m = 12$). Statistical results are shown in Table 3.

In Table 3, total count is multiplication times, k is the total number of satellites, m is the number of pre satellite, s is the number of system, and k_i is the number of satellites with an elevation higher than i°, $\dot{k}$ is the number of satellites with an elevation lower than 45°, and n is the number of satellites that are less than the minimum elevation threshold.

Table 3 Comparison of the computational complexity for selection

Algorithms	Expressions (flops)	Total count (flops)
Optimal PDOP	$C_k^m \cdot ((3+s)^2 \cdot m + (3+s)^3 + 4)$	54,041,130
Optimal WPDOP	$C_k^m \cdot (m^3 + (3+s) \cdot m^2 + (3+s)^2 \cdot m + (3+s)^3 + 4)$	362,415,690
PW-Elth-30	$\sum_{i=0}^{45} ((3+s)^3 + 2k_i \cdot (3+s)^2 + (3+s) \cdot k_i + 4) + \frac{1}{2} \cdot [(k-n)^2 + 7k - 3n - 2m - 2]$	84,345
SPW-Elth-25	$\dot{k} \cdot (\dot{k} - 1) + \frac{1}{2} \cdot [(k-n)^2 + 7k - 3n - 2m - 2]$	218

From the above table analysis, the four algorithms have great difference. The calculation of PW-ELth in this paper is much smaller than the optimal PDOP algorithm and the optimal WPDOP algorithm, respectively, about 3 orders of magnitude and 4 orders of magnitude. SPW-ELth is the least and can be realized in real time. Especially with the increase of the total number of visible satellites, the SPW-ELth algorithm is superior.

4.3 Comparative Analysis of Positioning Accuracy

Due to PW-ELth takes into account the effect of GDOP and UERE on the location, it can get a better result in theory. In order to verify this conclusion, the algorithm is compared with the optimal PDOP algorithm, and the efficacy test of the SPW-ELth is also increased.

According to the SNM, the number of satellites is determined to be 60 % of the total number of satellites. The positioning solution is WLS method, the mean and root mean square error (RMSE) are used as the statistical object.

The experiment selects DBS/GPS dual system to use the above three kinds of selected algorithm to carry on the localization analysis to the GMSD station, the experiment results are shown in Fig. 3.

The GPS/BDS/GLONASS/GALILEO four combination system is chosen to use different algorithms to carry on the localization analysis to the CUT0 station, the experimental results are shown in Fig. 4.

As shown in Figs. 3 and 4, the proposed PW-ELth and SPW-ELth algorithms are better than the optimal PDOP algorithm in the 3D positioning accuracy. Mainly because PW-ELth and SPW-ELth algorithm takes into account the UERE can reasonably choose the satellite observation value of Multi-GNSS. Therefore, it can

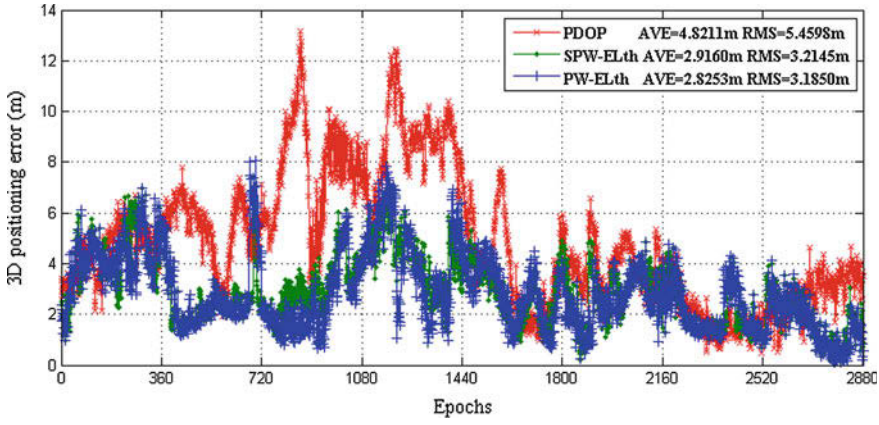

Fig. 3 3D positioning error in real data-based experiment

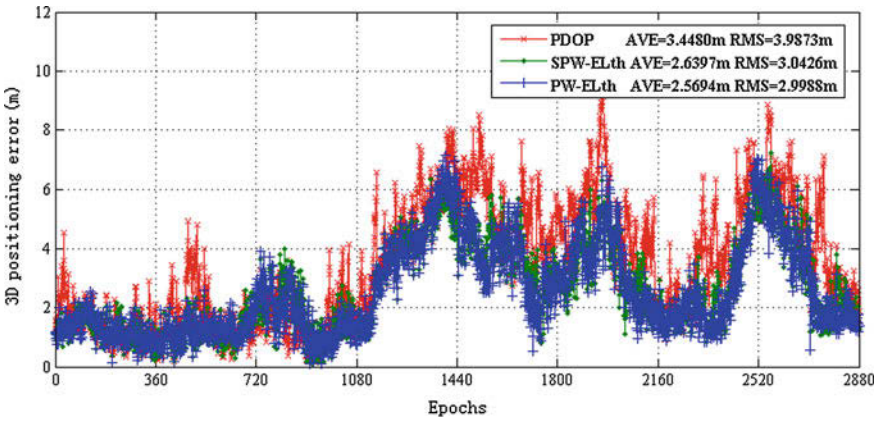

Fig. 4 3D positioning error in real data-based experiment

be a certain resistance to the interference of the non-Health satellite, multipath, ionosphere, troposphere, and other external errors. Therefore, under the condition of continuous observation, the PW-ELth algorithm is more stable than the optimal PDOP algorithm.

The accuracy of SPW-ELth is close to that of PW-ELth and the stability is flat in the case of long epoch. We proved the SPW-ELth algorithm, once again, can replace the PW-ELth algorithm to realize the fast real-time selection.

5 Conclusions

With the improvement and development of the navigation system, the combination of the multi-constellation navigation system will become inevitable. In this paper, a new method named PW-ELth algorithm based on Min-ELth is proposed and the algorithm is extended to simplify practical SPW-ELth algorithm. The results show that the proposed PW-ELth algorithm and the SPW-ELth algorithm are close to the best and calculate amount far less than the optimal PDOP algorithm and optimal WPDOP algorithm. At the same time, because of taking into account the geometric distribution of the satellite space and measurement error, compared with the traditional selection algorithm which only considers the geometric distribution of the satellite space, it improves the positioning accuracy and stability. Considering the positioning accuracy and real-time performance, the proposed algorithm has obvious advantages, especially the SPW-ELth algorithm, which has a high engineering practicability.

Acknowledgments This study is supported by National Natural Science Foundation of China (41174006) and China Postdoctoral Science Foundation (201003772; 20100481458).

References

1. Tian A, Fu C, Dong D et al (2014) The research of satellite selection algorithm in positioning system. Springer International Publishing, Berlin, pp 997–1003
2. Li G, Xu C, Zhang P, Hu C (2012) A modified satellite selection algorithm based on satellite contribution for GDOP in GNSS. Lecture Notes Electr Eng 176(1):415–421
3. Li L et al (2013) GNSS satellite selection algorithm revisited: a weighted way with integrity consideration. In: China Satellite Navigation Conference (CSNC)
4. Roogpiboonsopit D, Karimi H (2009) A multi-constellation satellite selection algorithm for integrated global navigation satellite systems. Intell Transp Syst: Technol, Plann Oper 13 (3):127–141
5. Phatak MS (2001) Recursive method for optimum GPS satellite selection. IEEE Trans Aerosp Electron Syst 37(2):751–754
6. Milliken RJ, Zoller CJ (1978) Principle of operation of NAVSATELLITE and system characteristics. Navigation 25:95–106
7. Bogen HA (1974) Geometric performance of the global positioning system. SAMO–TR-74-169, AD-783210, pp 1–116
8. Kihara M, Okada T (1984) A selection method and accuracy for the global positioning system. Navigation 31(1)
9. Li G, Xu C, Zhang P et al (2012) A modified satellite selection algorithm based on satellite contribution for GDOP in GNSS. J Section Notes Electr Eng 176(1):415–421
10. Blanco-Delgado N, Nunes F (2010) Satellite selection method for multi-constellation GNSS using convex geometry. IEEE Trans Veh Technol 59(9):4289–4297
11. Zhang M, Zhang J (2009) A fast satellite selection algorithm: beyond four satellites. IEEE 3 (5):740–747
12. Monsavi MR, Sorkhi M (2009) An efficient method for optimum selection of GPS satellites set using recurrent neural network. IEEE 2853(3):245–249
13. Sairo H, Akopian D, Takala J (2003) Weighted dilution of precision as quality measure in satellite positioning. IEEE Proc Radar Sonar Navig 150(6):430–436
14. Blanco-Delgado N, Nunes FD (2010) Satellite selection based on WDOP concept and convex geometry. Esa Workshop on Satellite Navigation Technologies & European Workshop on GNSS Signals & Signal Processing, pp 1–8
15. Parkinson B, Spilker J (1996) The global positioning system: theory and applications. Progress in astronautics and aeronautics. American Institute of Aeronautics and Astronautics, vol I, Washington, DC
16. Jin L, Huang Z, Li R, Ma Y (2009) Study on fast satellite selection algorithm for integrated navigation. ACTA Electron Sinica 37(9):1931–1936

A Novel SBAS-Assisted Single-Frequency Precise Point Positioning Method

Yu Zhao, Lin Zhao, Liang Li and Fuxin Yang

Abstract Satellite-based augmentation systems (SBAS) can provide positioning services of 1 m accuracy level by broadcasting real-time error correction products. However, the positioning accuracy of SBAS based on pseudorange has limitation in satisfying high precision navigation service, such as 1-dm accuracy. In view of this situation, one option is the utilization of precise point positioning (PPP) to achieve the global high precision positioning results. However, the accuracy of PPP depends on the quality of various correction products normally difficult to obtain in real-time. It is therefore difficult to acquire real-time PPP resolution. Through combining the real-time characteristics of SBAS with the characteristics of the high precision of PPP, the real-time wide-area PPP can be realized. Although the accuracy of SBAS broadcast ephemeris correction information is little lower than precise ephemeris data, they belong to the corrections of satellite clock and orbit, and can be obtained in real-time. Furthermore, in order to meet the requirement of dynamic navigation, the extended Kalman filter was applied to improve the positioning accuracy. To sufficiently verify the effectiveness of proposed algorithm, the proposed method is compared with the traditional SBAS and PPP methods by using single-frequency GPS data in static and dynamic mode, respectively. The experimental results show that, the static positioning accuracy in horizontal is better than 50 cm, and the dynamic positioning accuracy in horizontal is better than 90 cm, increased by 42 and 40 %, respectively, compared with traditional SBAS method.

Keywords SBAS · PPP · Kalman filter · Real-time dynamic

Y. Zhao · L. Zhao · L. Li (✉) · F. Yang
College of Automation, Harbin Engineering University, Harbin 150001, China
e-mail: liliang@hrbeu.edu.cn

© Springer Science+Business Media Singapore 2016

J. Sun et al. (eds.), *China Satellite Navigation Conference (CSNC) 2016 Proceedings: Volume III*, Lecture Notes in Electrical Engineering 390,
DOI 10.1007/978-981-10-0940-2_33

1 Introduction

Wide-area, real-time and high precision positioning is a very promising technique in the field of GNSS navigation. There is diversity of widely-used high precision positioning methods, in which the real-time kinematic (RTK) is capable of achieving instantaneous centimeter accuracy positioning or even millimeter accuracy in the post-processing mode [1]. Nonetheless, the high accuracy positioning cannot be guaranteed when the baseline dramatically increases, for instance, the order of 1000 km. Precise point positioning (PPP) can realize wide-area high precision locating, but the implementation depends on the precision satellite orbit and clock products provided by IGS that generally are post data [2]. Although IGS has broadcasted ultrarapid ephemeris product on Internet, the accuracy of static real-time positioning can reach 5 cm [3], but it is still difficult for most of GNSS receivers to obtain in real-time. Satellite-based augmentation systems (SBAS) can broadcast wide-area differential correction messages including satellite orbit error correction, clock correction, and ionospheric delay correction by GEO satellites in real-time [4], as well as the wide coverage and the high accuracy in the order of 1–3 m. However, since the SBAS positioning is based on code observation. The positioning accuracy cannot support more demanding navigational applications such as precision approach. Though Euiho and Todd proposed that readjustment of weight matrix can enhance the positioning accuracy of SBAS, it only can make the accuracy reach to submeter level [5]. Thus, it can be seen that these three methods cannot meet the requirements of wide-area, high precision, and real-time performance.

Comparing the advantages and disadvantages of PPP and SBAS comprehensively, it can be found that a combination of two methods is able to achieve wide-area, real-time, and high-precision positioning. First, although the satellite orbit and clock error corrections are different in usage with precise ephemeris, the essences are both corrections to satellite orbit and clock error, thus if we can use satellite orbit and clock corrections broadcasted by SBAS instead of precise ephemeris, the correction in real-time of these two kind of error can be realized in PPP. Second, if the high precision carrier phase observation can be introduced in SBAS positioning method, the accuracy would certainly be improved significantly. Finally, for GNSS dual-frequency receiver users, ionosphere free combination method can be used to eliminate ionosphere error, but majority of users still employ single frequency receiver and the cost of dual-frequency receiver is high, so how to eliminate ionosphere error of single frequency receiver effectively will have more practical significance. SBAS can broadcast single frequency ionosphere delay correction, therefore, single frequency ionosphere delay can be corrected using it directly instead of ionosphere free combination.

Aimed at the above three assumptions, Refs. [6] and [7] have proved the positioning accuracy of PPP with SBAS corrections can reach to decimeter level, but they both use dual-frequency ionosphere free combination to mitigate ionosphere error rather than mitigate it in undifferenced single-frequency measurements

and single-frequency dynamic positioning mode performance is difficult to be guaranteed. The feasibility of single-frequency PPP was proved in Ref. [8], however, ionosphere delay correction computed according global TEC data provided by IGS [9] is adopted in this method. The test results of Ref. [10] showed that the single frequency ionosphere delay correction broadcasted by SBAS is more accurate than the ionosphere delay computed according TEC.

Based on the above assumptions and analysis, a wide-area, real-time single-frequency carrier phase precise point positioning (CPPP) based on extend Kalman filter (EKF) method is proposed in this paper. This method is on the base of wide-area differential correction massages and introducing high precision carrier phase observations, which aims to realize wide-area real-time high accuracy positioning. This paper confirms the feasibility of the method using measured data, the result shows that the proposed method can provide static positioning accuracy in decimeter level and dynamic positioning accuracy in submeter level, respectively.

2 User Positioning Model and Algorithm

According to the instruction in Ref. [11], by receiving satellite ephemeris, clock and ionosphere delay correction messages in real-time, SBAS users normally apply pseudorange for position solution. However, in high precise positioning mode, apparently pseudorange cannot perform competently alone, that makes it is necessary to introduce precise carrier phase observations. Unlike traditional SBAS pseudorange positioning mode, the mode of combining SBAS with PPP will further enhance the positioning accuracy.

2.1 Observation Equations and Error Processing

The basic observation equations of satellite navigation positioning can be expressed as

$$P = \rho + c(\mathrm{d}t_r - \mathrm{d}t^s) + I + T + d_{\mathrm{orb}} + \varepsilon_P \tag{1}$$

$$\varphi = \rho + c(\mathrm{d}t_r - \mathrm{d}t^s) - I + T + d_{\mathrm{orb}} + N + \varepsilon_\varphi \tag{2}$$

where, P is the observed pseudorange and φ is the observed carrier phase, ρ is the geometric range between receiver and satellite, $\mathrm{d}t_r$ and $\mathrm{d}t^s$ are the receiver and satellite clock errors, respectively, I is ionospheric delay, T is tropospheric delay, $\mathrm{d}_{\mathrm{orb}}$ is satellite position geometric error, N is integer ambiguity, ε_p is the unmodeled error including pseudorange noise and multipath error, ε_φ is the phase noise, c is the vacuum speed of light.

Unlike precise ephemeris, SBAS do not broadcast the absolute position and clock error, but the corrections of satellite position and clock error relative to broadcast ephemeris, these two corrections can be divided into long-term and fast error corrections. The long-term corrections contain slow information on the slowly varying satellite orbit and clock errors, and the fast corrections can provide information on the fast varying clock errors [11].

In conclusion, the calculate formulas of SBAS satellite position and clock error correction can be written as

$$\begin{bmatrix} \delta x_k \\ \delta y_k \\ \delta z_k \end{bmatrix} = \begin{bmatrix} \delta x \\ \delta y \\ \delta z \end{bmatrix} + \begin{bmatrix} \delta \dot{x} \\ \delta \dot{y} \\ \delta \dot{z} \end{bmatrix} (t_k - t_0) \tag{3}$$

$$\delta \Delta t_{sv}(t) = \delta a_{f0} + \delta a_{f1}(t_k - t_0) + \mathrm{PRC}/c \tag{4}$$

where, $[\delta x, \delta y, \delta z]^{\mathrm{T}}$ is satellite position correction, $[\delta \dot{x}, \delta \dot{y}, \delta \dot{z}]^{\mathrm{T}}$ is satellite position error variety correction, δa_{f0} is the satellite clock offset error correction, δa_{f0} is the clock drift error correction, t_0 is the time from zero hour in that very day, nothing with toc and toe in broadcast ephemeris, t_{k} is current sample time, PRC is pseudorange correction [6, 11]. Add the above correction to satellite position and clock error computed by broadcast ephemeris together, the corrected satellite position and clock error can be obtained.

SBAS ionospheric delay correction are broadcast as vertical delay estimates at specified ionospheric grid points (IGPs) above the Earth's surface at an altitude of 350 km. The IGP locations are predefined with a spacing of 5° × 5° or 10° × 10°. The IGP locations are denser at lower latitudes because of the fact that the distance represented by a degree of longitude becomes smaller at higher latitudes [12]. In order to obtain the ionospheric correction, the user needs to determine the location of the ionospheric pierce point (IPP) and interpolate from three or four nodes around IPP location to achieve the vertical delay at the IPP at first, then the user can multiply that vertical delay by the obliquity factor to obtain the ionospheric in signal path.

Above all, for single-frequency GNSS receivers, by compensating the above errors, Eqs. (1) and (2) can be changed into

$$P = \rho + c \cdot \mathrm{d}t_r - c(\mathrm{d}t^s + \delta \Delta t_{sv}) + I - I_{\mathrm{corr}} + T + d_{\mathrm{orb}} - d_{\mathrm{corr}} + \varepsilon_P \tag{5}$$

$$\varphi = \rho + c \cdot \mathrm{d}t_r - c(\mathrm{d}t^s + \delta \Delta t_{sv}) - I + I_{\mathrm{corr}} + T + d_{\mathrm{orb}} - d_{\mathrm{corr}} + N + \varepsilon_\varphi \tag{6}$$

where, $\delta \Delta t_{sv}$ is satellite clock error correction, d_{corr} is satellite position error correction, I_{corr} is ionospheric delay correction.

2.2 User Positioning Algorithm

Since SBAS also broadcasts corresponding error variance while broadcasting error corrections, SBAS recommend users applying weighted least square method to calculate user position, the variance relative to each satellite is

$$\sigma_i^2 = \sigma_{i,\text{eph}}^2 + \sigma_{i,\text{UIRE}}^2 + \sigma_{i,\text{tropo}}^2 + \sigma_{i,\text{air}}^2 \tag{7}$$

where, $\sigma_{i,\text{eph}}^2$ is the variance of satellite orbit and clock correction residuals, $\sigma_{i,\text{UIRE}}^2$ is the model variance for the slant range ionospheric error, $\sigma_{i,\text{tropo}}^2$ is the variance of tropospheric error correction residuals. Note that, SBAS do not broadcast any information about tropospheric delay correction, so user should compute tropospheric delay correction on their own by SBAS tropospheric model. $\sigma_{i,\text{air}}^2$ is the variance of airborne receiver errors. Since SBAS is designed for an airborne user initially, when it is applied to other areas $\sigma_{i,\text{air}}^2$ will be no longer suitable. In this paper, this term is replaced by $\sigma_{i,\text{el}}^2$, which is computed based on the satellite elevation

$$\sigma_{i,\text{el}}^2 = R \times \left(a^2 + b^2 / \sin^2(\text{el})\right) \tag{8}$$

where, R is the code/carrier phase error ration; a and b are both carrier phase error factors, el stands for elevating angel.

Using the above variances, the weighting matrix W is constructed as following:

$$W = \begin{bmatrix} \frac{1}{\sigma_1^2} & \cdots & 0 \\ \vdots & \ddots & \vdots \\ 0 & \cdots & \frac{1}{\sigma_n^2} \end{bmatrix} \tag{9}$$

However, since the position solution using pseudorange and least squares method only can reach meter level accuracy, and it cannot meet the requirement of precise positioning. To this issue, the pseudorange and carrier phase are both used and extended Kalman filter (EKF) is employed to replace the least squares method to complete the positioning.

Selected state variable in filter processing is

$$X = (x, y, z, v_x, v_y, v_z, \mathrm{d}t_r, \mathrm{d}f_r, Z_{T,r}, N_1, N_2, \ldots, N_n)^{\mathrm{T}} \tag{10}$$

where, $(x, y, z)^{\mathrm{T}}$ is three-dimensional position of receiver, $(v_x, v_y, v_z)^{\mathrm{T}}$ is three-dimensional velocity of receiver. Here we take dynamic mode as examples, $(\mathrm{d}t_r, \mathrm{d}f_r)^{\mathrm{T}}$ are receiver clock biases and frequency drift, $Z_{T,r}$ is zenith total delay, $(N_1, N_2, \ldots, N_n)^{\mathrm{T}}$ is integer ambiguity float solutions.

According the above equation, applying both pseudorange and carrier phase as system observations, the system model can be obtained.

$$x_k = A_{k|k-1}x_{k-1} + w_k \tag{11}$$

$$y_k = h(x_k) + v_k \tag{12}$$

$$A_{k|k-1} = \begin{bmatrix} I_{3\times3} & T_{3\times3} & 0 & 0 & 0 \\ 0 & I_{3\times3} & 0 & 0 & 0 \\ 0 & 0 & B & 0 & 0 \\ 0 & 0 & 0 & B & 0 \\ 0 & 0 & 0 & 0 & I_{m\times m} \end{bmatrix} \tag{13}$$

where, T is the sample period, $B = [1, T;\ 0, 1]$. Considering Eq. (12) is nonlinear, it needs linearization first and it then becomes as follows:

$$z_k^* \approx He_k^- + v_k \tag{14}$$

$$z_k^* = y_k - h\left(x_k^-\right) \tag{15}$$

$$e_k^- = x_k - x_k^- \tag{16}$$

$$H = \left.\frac{\partial h(x)}{\partial x}\right|_{x_k = x_k^-} = \begin{bmatrix} G_{n\times3} & 0_{n\times3} & 1_{n\times1} & 0_{n\times1} & M_{n\times1} & I_{n\times n} \\ G_{n\times3} & 0_{n\times3} & 1_{n\times1} & 0_{n\times1} & M_{n\times1} & 0_{n\times n} \\ 0_{n\times3} & G_{n\times3} & 0_{n\times1} & 1_{n\times1} & 0_{n\times n} & 0_{n\times n} \end{bmatrix} \tag{17}$$

where, $G_{n\times3}$ stands for direction cosine matrix of observation vector from receiver to satellite. $M_{n\times1}$ is mapping function of tropospheric wet delay. Meanwhile apply the computed covariance matrix W is the measurement covariance matrix of EKF, then according to EKF filter equation, it has

$$x_k^- = A_{k|k-1}x_{k-1} \tag{18}$$

$$P_k^- = A_{k|k-1}P_{k-1}A_{k|k-1}^{\mathrm{T}} + Q \tag{19}$$

$$K_k = P_k^- H^{\mathrm{T}}(HP_k^- H^{\mathrm{T}} + W)^{-1} \tag{20}$$

$$x_k = x_k^- + K_k z_k^* \tag{21}$$

$$P_k = (I - K_k H)P_k^- \tag{22}$$

The above equations explain two important information update process which are state update process and measurement update process. Equation (18) is used to estimate the model state at k time. Equation (19) makes an assessment of the quality

of state estimation. According Eqs. (20)–(22), the state estimation is further corrected. In this paper, since the high precision velocity measurements are added in EKF, thus the algorithm is suitable for high dynamic mode.

3 Data Testing and Analysis

In order to verify the feasibility of the single-frequency CPPP method and compare the positioning results with the traditional SBAS and PPP method, both static and kinematic data are tested in this paper. It should be noted that, in this paper, the positioning results of PPP method is derived from a open source software called RTKLIB (http://www.rtklib.com). The SBAS messages are from the European Geostationary Navigation Overlay Service (EGNOS).

3.1 Static Test

Four IGS stations in Europe are selected in this test, namely, BZRG, IENG, BOR1, and HERT, and use EGNOS data as SBAS information. The first two stations are in Italy, while BOR1 is in Poland and HERT is in England. For each of these four stations, all observation data sets are collected for 7 days. The time interval of the data is 30 s, the cut off elevation angle is 10°. Since these data sets are collected by high-quality receivers and antennas, with none or low multipath. They are thus especially suited to analyze the feasibility of the method.

First we take the observation data of station BZRG from March 26, 2015 to April 01, 201 as example, the error of the three directions of East, North and up in traditional SBAS, PPP, and CPPP Figs. 1, 2 and 3 show the test results, and positioning error statistical information corresponding to the four stations are given in Table 1.

According to Table 1, we can clearly see that, the positioning accuracy of CPPP is significantly higher than traditional SBAS, it is enhanced by 56, 86, and 48 % in direction East, North, and up, respectively, where the accuracy of north axis is most significantly enhanced, and least in up direction. Since all these stations are located in mid-latitude region, while for the station located this position, the north positioning accuracy of ordinary PPP (float solution) is highest, worst in up direction [13], and this conclusion is verified by test results. Although the accuracy in up axis of CPPP is poor, the three dimensional positioning accuracy can completely reach decimeter level. In addition, through the comparison with PPP, CPPP has low precision and long convergence time, but when after the positioning solution convergence, the accuracy is 5, 3, 36 cm lower than PPP, respectively in east-north-up

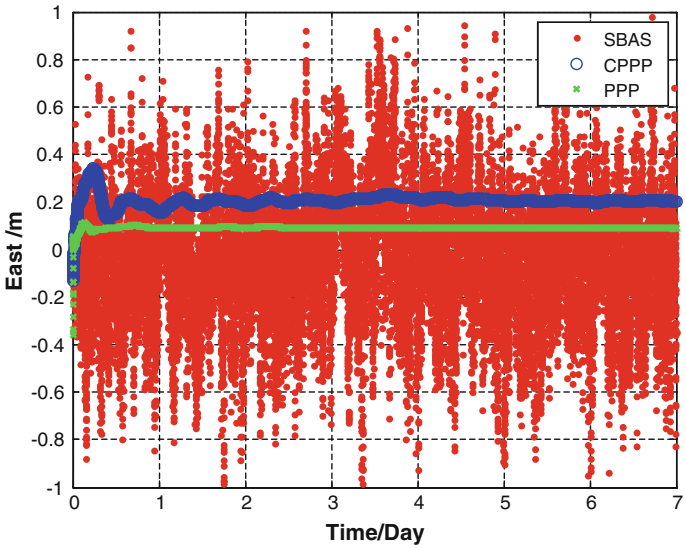

Fig. 1 Static errors in East

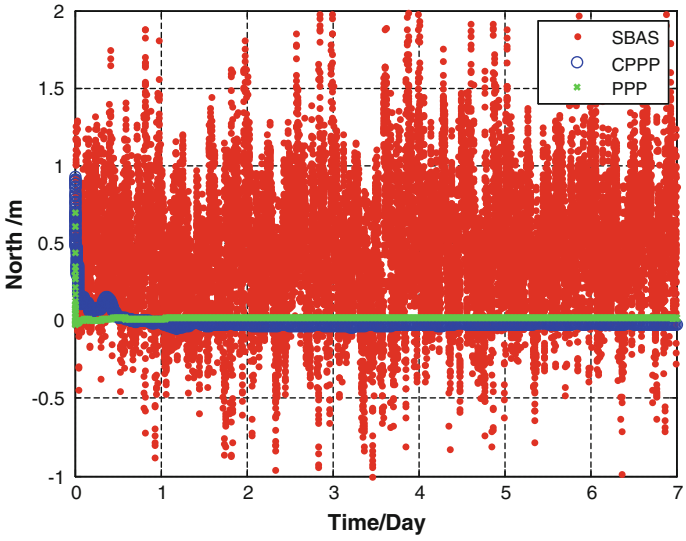

Fig. 2 Static errors in North

direction. Generally, the static positioning accuracy of PPP (float solution) can reach centimeter level, although the accuracy in up axis of CPPP is poor, the three dimensional positioning accuracy can completely reach decimeter level.

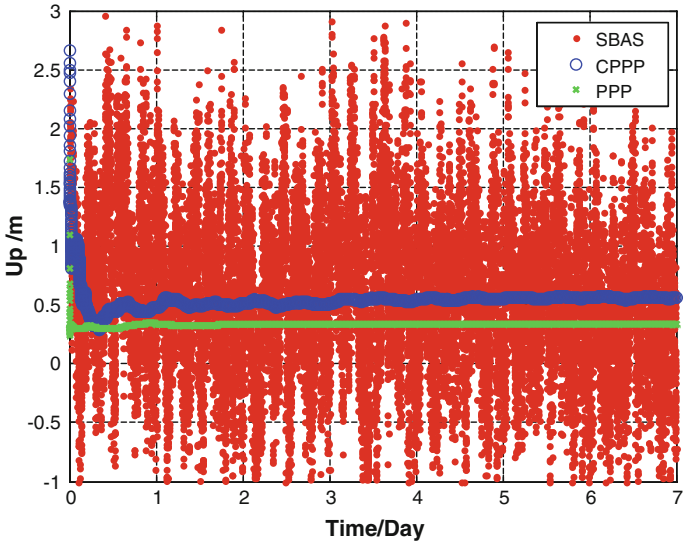

Fig. 3 Static errors in up

Table 1 Positioning performance comparison of three method

	SBAS		PPP		CPPP	
	ENU RMS (m)	CEP95 SEP95 (m)	ENU RMS (m)	CEP95 SEP95 (m)	ENU RMS (m)	CEP95 SEP95 (m)
BZRG	0.259 0.559 0.995	1.114 2.048	0.076 0.011 0.331	0.107 0.356	0.111 0.048 0.522	0.152 0.667
BOR1	0.275 0.548 0.963	1.082 1.959	0.057 0.026 0.079	0.075 0.101	0.110 0.068 0.581	0.214 0.739
IENG	0.356 0.667 0.963	1.335 2.098	0.042 0.035 0.071	0.069 0.097	0.149 0.066 0.485	0.281 0.695
HERT	0.231 0.573 0.769	1.047 1.762	0.066 0.056 0.069	0.087 0.112	0.160 0.047 0.299	0.327 0.511

3.2 Kinematic Test

To further verify the feasibility and dynamic performance of single-frequency CPPP, the high dynamic experiment data of 30 min length in 17/03/2011, TU Delft University, Netherland. The receiver type is Trimble NetR7, antenna type is Trimble Zephyr, sample interval is 0.1 s, the maximum movement velocity of carrier can reach 100 m/h. Figure 4 shows the motion trail.

Fig. 4 Reference trajectory of the rover receiver

For further evaluate the kinematic positioning accuracy of CPPP, we take the positioning results of RTK as the reference position, the distance between experiment section and base station is about several kilometers, and the receiver type of base station is Trimble NetR9, antenna type is Zephyr Geodetic 2.

The positioning results of SBAS, PPP and CPPP are showed in Figs. 5, 6, 7 and 8, Table 2 shows the corresponding error statistics.

Comparing the position errors of the two algorithms in Figs. 6, 7, and 8, it can be seen that, the positioning accuracy of CPPP is higher than traditional SBAS, it is enhanced by 53, 54 and 38 % in direction east, north and up, respectively, and horizontal positioning accuracy has been reached of less than 1 m (95 %) from

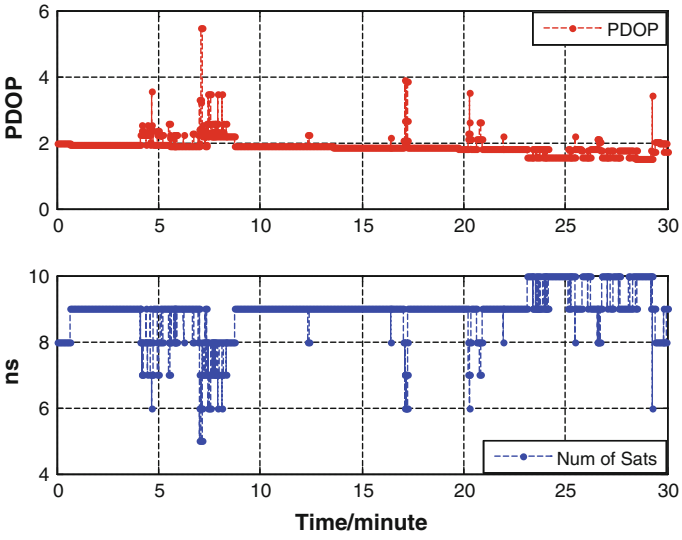

Fig. 5 Number of satellites and the value of PDOP

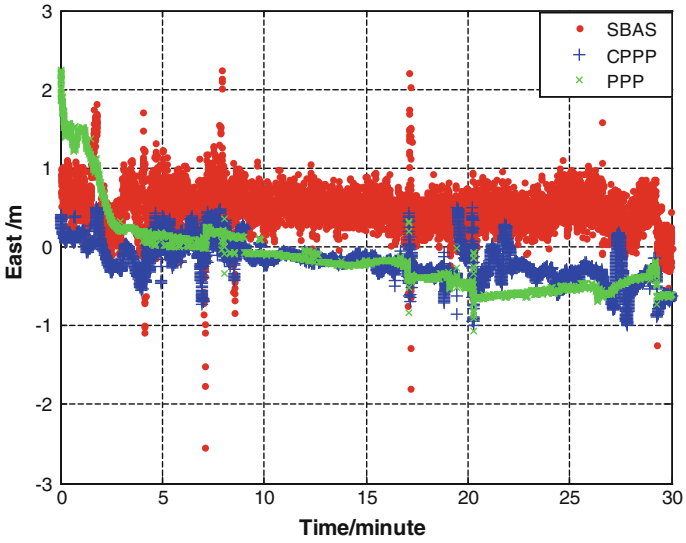

Fig. 6 Kinematic errors in East

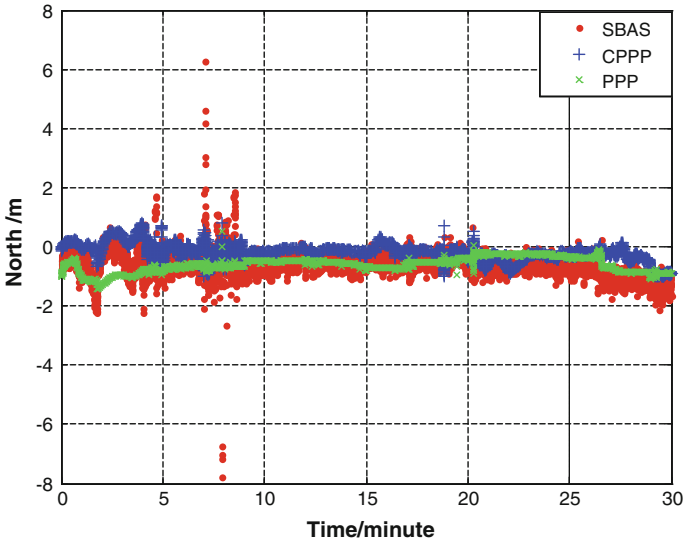

Fig. 7 Kinematic errors in North

Table 2. Compared with static mode, kinematic mode is more complex. In practical environment, the movements of receiver and the environment can be comparatively complex. Although the least squares method is relatively stable, but it ignores the relations between each epoch and may lead to saltation of positioning results. It can

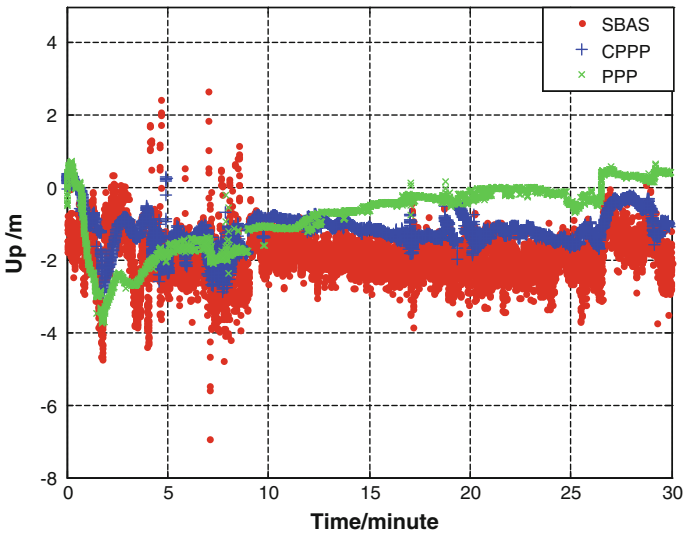

Fig. 8 Kinematic errors in up

Table 2 Kinematic positioning performance comparison of three methods

	SBAS	PPP	CPPP
East-RMS (m)	0.558	0.508	0.261
North-RMS (m)	0.722	0.655	0.330
Up-RMS (m)	1.999	1.211	1.226
CEP95 (m)	1.398	1.271	0.833
SEP95 (m)	3.052	2.837	2.019

be seen from Figs. 6, 7 and 8, there are some points of abrupt change, when Fig. 5 shows that the PDOP of these points is large and the corresponding number of satellites is few. This situation demonstrates the saltation of least squares method. However, also in dynamic mode, the positioning error of CPPP has no abrupt change. This is partly because the high precision carrier phase observation is adopted, but also EKF is applied to instead of least squares method. The position state of users at adjoining times is considered in EKF, thus the unrelated problem of positioning results at different times in least squares method is overcame, then the positioning results after filtering are more accurate and smoother. It also can be found that, the accuracy of PPP is lower than CPPP. Typically, due to the more precise satellite orbit and clock provided by PPP, PPP should have higher positioning accuracy. However, because the positioning results in this paper are derived from RTKLIB, its positioning algorithm is different from ours. As mentioned above, the kinematic mode is more complex than the static mode. The PPP positioning algorithm in RTKLIB is clearly not very applicable for highly dynamic

environment. Thus, it is more significance to study the high-precision positioning algorithm for high dynamic environment, and it shows that the proposed algorithm in this paper has a stronger adaptability for high dynamic environment.

4 Conclusion

Focus on the poor real-time performance of PPP and low positioning accuracy of traditional SABS, on the basis of combination SBAS wide-area differential correction with carrier phase observation, a wide-area single frequency carrier phase real-time precise positioning method based on EKF is proposed and tested. IGS static data test shows that, comparing with SBAS, the precision of horizontal and vertical are enhanced by 77 %(95 %) and 48 %(95 %), respectively. Kinematic experiment shows that, the real-time positioning accuracy is more accurate and smoother by using CPPP algorithm. The horizontal accuracy can be reached within 1 m. The results of static and dynamic tests show that, the proposed method can provide technique for global real-time precise position realization, as well as offer a reference for the further development of wide-area precise position.

Acknowledgments We thank Mr. Yanqing Hou from Delft University of Technology for providing the dynamic GPS data, as well as the IGS for the static data. This research is jointly funded by China Natural Science Foundation (Nos. 61304235, 61273081, 61304234), the fundamental Research Funds for Central Universities (No. HEUCFD1431), and the Post-doctoral Scientific Research Foundation, Heilongjiang Province (Nos. LBH-Q15033, LBH-Q14054).

References

1. Li L, Li Z, Yuan H et al (2015) Integrity monitoring-based ratio test for GNSS integer ambiguity validation. J GPS Solut 1–13. doi: 10.1007/s10291-015-0468-y
2. Zumberge JF (1999) Automated GPS data analysis service. J GPS Solut 2(3):76–78
3. Li X, Ge M, Dai X et al (2015) Accuracy and reliability of multi-GNSS real-time precise positioning. J GPS Solut 89(6):607–635
4. Per E, Walter T, Pullen S et al (1999) J Proc IEEE 84(8):1063–1088
5. Kim E, Todd W, David P (2006) Optimizing WAAS accuracy/stability for a single frequency receiver. Proc ION GNSS 2006:962–970
6. Heßelbarth A, Wanninger L (2013) SBAS orbit and satellite clock corrections for precise point positioning. J GPS Solut 17(4):465–473
7. Rho H, Langley RB (2007) The usefulness of WADGPS satellite orbit and clock corrections for dual-frequency precise point positioning. Proc ION GNSS 2007:9–25
8. Le A, Tiberius C (2006) Single-frequency precise point positioning with optimal filtering. J GPS Solut 11(1):61–69
9. Schaer S, Gurtner W (1998) IONEX: the ionosphere map exchange format version. In: Proceedings of the IGS AC workshop, 1998, pp 2–9
10. Kim J, Lee Y (2014) Using ionospheric corrections from the space-based augmentation systems for low earth orbiting satellites. J GPS Solut 19(3):423–431

11. RTCA (2006) Minimum operational performance standards for global positioning system/wide area augmentation system airborne equipment, RTCA DO-220D, Washington, DC
12. Huang Z, Yuan H (2007) Improving the ionospheric delay correction of satellite-based augmentation systems in equatorial regions. J GPS Solut 39(10):1552–1558
13. Hesselbarth A, Wanninger L (2008) Short-term stability of GNSS satellite clocks and its effects on precise point positioning. Proc ION GNSS 2008:1855–1863

The Methods and Analysis of Zero Baseline and Ultra-Short Baseline Ambiguity Resolution Based on BDS Observations

Yuzhao Li, Qin Zhang, Li Wang, Lihong Fan, Jie Tian and Wenquan Zhuang

Abstract Integer ambiguity resolution is one of the difficult and important points in precision relative positioning. As we all know, LAMBDA (Least-squares AMBiguity Decorrelation Adjustment) method can be regard as the most rigorous algorithm in ambiguity resolution methods, it is still effective in the ambiguity resolution of triple-frequency GNSS precision positioning. So, the algorithms such as LAMBDA, Rounding, and Bootstrapping are adopted in this paper to solve the zero baseline and ultra-short baseline BDS observations, respectively, and the results of ambiguities resolution for pseudorange and carrier-phase double difference observations and increments of ENU direction for baselines are obtained, which the C01 satellite is taken as reference satellite in the whole baselines resolution. Through comparing the consequences of ambiguity resolution and the difference for increment of ENU direction between the three methods and TBC (Trimble Business Center) software, results show that performance of the three methods is at the same level, therefore both of them can be used for ambiguity resolution of zero baseline and ultra-short baseline.

Keywords LAMBDA · Rounding · Bootstrapping · Zero baseline · Ultra-short baseline

Y. Li (✉) · Q. Zhang (✉) · L. Wang · L. Fan · W. Zhuang
College of Geology Engineering and Geomantic, Chang'an University, Xi'an 710054, Shaanxi, China
e-mail: chdlyzhao@163.com

Q. Zhang
e-mail: zhangqinle@263.net.cn

J. Tian
Center for Geodetic Data Processing, National Administration of Surveying, Mapping and Geoinformation, Xi'an 710054, Shaanxi, China

© Springer Science+Business Media Singapore 2016

J. Sun et al. (eds.), *China Satellite Navigation Conference (CSNC) 2016 Proceedings: Volume III*, Lecture Notes in Electrical Engineering 390,
DOI 10.1007/978-981-10-0940-2_34

1 Introduction

As the triple-frequency navigation signals can be broadcasted by BDS in-orbit satellites, it makes China's BDS take the full advantage in high-precision positioning, so it is imperative to research ambiguity fixing methods for triple-frequency precise positioning. Many scholars' researches show that the reliability, accuracy, and solution efficiency of navigation and positioning can be enhanced using triple-frequency observations in GNSS relative positioning.

As the core algorithm for relative positioning, the major ambiguity resolution methods include: first, the Least-squares AMBiguity Decorrelation Adjustment (LAMBDA) proposed by Professor Teunissen and accepted by the industry as the most rigorous theory [1–3]; secondly, TCAR(Three-Carrier Ambiguity Resolution) proposed by Forssell based on European GNSS-2 program is using triple-frequency observations to fix ambiguity progressively; thirdly, considering the additional L5 signal for GPS modernization, Jung proposed a real-time Geometry-free ambiguity resolution algorithm of CIR (Cascading Integer Resolution) in 1999 [4–9].

The TCAR, CIR, and LAMBDA algorithm are analyzed by professor Teunissen in 2002, results show that the first two approaches are Bootstrapping integer estimation algorithm based on Geometry-free model, while the LAMBDA method is suitable for not only Geometry-free but also Geometry-based model, and the corresponding estimation performance is better than or equivalent to TCAR and CIR in Geometry-free model [10]. The BDS triple-frequency ambiguity resolution result shows that the LAMBDA algorithm has significantly improved the short baseline ambiguity resolution using triple-frequency than dual-frequency observations [11].

According to the above researches, the LAMBDA, Rounding, and Bootstrapping algorithms are used to estimate ambiguity of BDS triple-frequency zero baseline and ultra-short baseline observations, the baseline increments in ENU direction are compared and analyzed with results calculated by TBC (Trimble Business Center) software.

2 Ambiguity Resolution Approaches

Ambiguity resolution is the difficulty and key point in GNSS high-precise positioning, and among which the core problem is the improving ambiguity search efficiency. Considering the not full use of ambiguity correlation in past Rounding and Bootstrapping algorithm, Teunissien proposed an approach that use the float ambiguity correlation matrix, according to the minimum of the two-norm for least-squares float ambiguity, and the decorrelation technology is used to search ambiguity, namely LAMBDA.

The observation equations of pseudorange and carrier phase can be expressed as follows:

$$\left.\begin{aligned} P_i &= \rho + \delta_{\text{orb}} + c(\delta_{tR} - \delta_{tS}) + \delta I_{P_i} + \delta_{\text{trop}} + \varepsilon_{P_i} \\ \lambda_i \varphi_i &= \rho + \delta_{\text{orb}} + c(\delta_{tR} - \delta_{tS}) + \delta I_{L_i} + \delta_{\text{trop}} - \lambda_i N_i + \varepsilon_{L_i} \end{aligned}\right\} \tag{1}$$

where P_i (unit: m) is the pseudorange observations in frequency f_i; φ_i (unit: cycle) indicates the carrier-phase measurement in frequency f_i; ρ (unit: m) denotes the geometric distance between the satellite and the receiver; δ_{orb} (unit: m) represents the satellite orbit errors; c (unit: m/s) is the speed of light in vacuum; δ_{tR} (unit: s) is the receiver clock error; δ_{tS} (unit: s) is the satellite clock error; δI_{P_i} (unit: m) indicates the ionosphere delay for pseudorange observations in frequency L_i; δ_{trop} (unit: m) represents the tropospheric delay; δI_{L_i} (unit: m) is the ionosphere delay for carrier-phase observations in frequency L_i; λ_i (unit: m/cycle) is the wavelength for carrier phase in frequency f_i; N_i (unit: cycle) denotes the carrier-phase observations ambiguity; ε_{P_i} (unit: m) is the observation noise for pseudorange; ε_{L_i} (unit: m) is the observation noise for carrier phase.

The satellite and receiver clock errors are eliminated in double difference equations and for zero baseline and ultra-short baseline, the ionosphere delay and troposphere delay are negligible [12]. The double difference equations for pseudorange and carrier phase are expressed as:

$$\left.\begin{aligned} P_{AB}^{ks}(t) &= \rho_{AB}^{ks}(t) + \varepsilon_{AB}^{ks} \\ \lambda\varphi_{AB}^{ks}(t) &= \rho_{AB}^{ks}(t) - \lambda N_{AB}^{ks}(t) + \varepsilon_{AB}^{ks} \end{aligned}\right\} \tag{2}$$

$$\rho_{AB}^{ks}(t) = \rho_{\text{B}}^{s}(t) - \rho_{A}^{s}(t) + \rho_{\text{B}}^{k}(t) - \rho_{\text{A}}^{k}(t) \tag{3}$$

$$N_{AB}^{ks}(t) = N_{B}^{s}(t) - N_{A}^{s}(t) + N_{B}^{k}(t) - N_{A}^{k}(t) \tag{4}$$

where A is the base station for known coordinates, position of satellite k, s can be calculated by ephemeris. So, the unknown parameters in equation are $\rho_{B}^{s}(t)$, $\rho_{\text{B}}^{k}(t)$ and $N_{AB}^{ks}(t)$.

$$\left.\begin{aligned} \rho_{B}^{s}(t) &= \rho_{B_0}^{s} + \frac{X^s - X_{B_0}}{\rho_{B_0}^{s}}\delta X_B + \frac{Y^s - Y_{B_0}}{\rho_{B_0}^{s}}\delta Y_B + \frac{Z^s - Z_{B_0}}{\rho_{B_0}^{s}}\delta Z_B \\ \rho_{B}^{k}(t) &= \rho_{B_0}^{k} + \frac{X^k - X_{B_0}}{\rho_{B_0}^{k}}\delta X_B + \frac{Y^k - Y_{B_0}}{\rho_{B_0}^{k}}\delta Y_B + \frac{Z^k - Z_{B_0}}{\rho_{B_0}^{k}}\delta Z_B \end{aligned}\right\} \tag{5}$$

$$\left.\begin{aligned} \rho_{B_0}^{s} &= \sqrt{(X^s - X_{B_0})^2 + (Y^s - Y_{B_0})^2 + (Z^s - Z_{B_0})^2} \\ \rho_{B_0}^{k} &= \sqrt{(X^k - X_{B_0})^2 + (Y^k - Y_{B_0})^2 + (Z^k - Z_{B_0})^2} \end{aligned}\right\} \tag{6}$$

X_{B_0}, Y_{B_0} and Z_{B_0} represent the approximate coordinates for station B.

The linear form of the above equations is

$$y = Ax + Bz + \varepsilon \tag{7}$$

where the real parameter x represents the location parameters, the integral parameter z denotes ambiguity parameters, A and B are the coefficient matrixes corresponding to the location parameters and ambiguity parameters.

First, the integral characteristics of ambiguity parameters z are ignored, they were treated as a real number. The resolution of least-squares adjustment is as follows:

$$\begin{pmatrix} x_f \\ z_f \end{pmatrix} = \begin{pmatrix} A^{\mathrm{T}}PA & A^{\mathrm{T}}PB \\ B^{\mathrm{T}}PA & B^{\mathrm{T}}PB \end{pmatrix}^{-1} \begin{pmatrix} A^{\mathrm{T}}Py \\ B^{\mathrm{T}}Py \end{pmatrix} = \begin{pmatrix} N_{11} & N_{12} \\ N_{21} & N_{22} \end{pmatrix}^{-1} \begin{pmatrix} A^{\mathrm{T}}Py \\ B^{\mathrm{T}}Py \end{pmatrix} \quad (8)$$

The float covariance matrix is obtained, the inverse of the float ambiguity covariance matrix is decomposed by Cholesky decomposition:

$$\mathrm{N}_{22}^{-1} = \mathrm{LDL}^{\mathrm{T}} \quad (9)$$

The corresponding lower triangular matrix L and positive definite diagonal matrix D are obtained. The ambiguity covariance matrix Qz and ambiguity Zz are obtained under conversion using decorrelation technique.

These above results are calculated by the following three algorithms:

1. LAMBDA Algorithm
   Detailed steps of the algorithm can refer to papers of Teunissien and Li Jinlong, they were not given in detail here.
2. Rounding Algorithm
   The Rounding off algorithm is extracting float ambiguity after decorrelation processing, and the value is rounded to the nearest integer, so the integer is regarded as a fixed ambiguity.

$$Z_{(i)} = \mathrm{round}(Zz_{(i)}) \quad (10)$$

3. Bootstrapping Algorithm
   The Bootstrapping algorithm is used to fix the float ambiguity after integer translation [7]:

$$Z_{(\mathrm{i})} = \mathrm{round}\left(Zz_{(i)} - \sum_{j=i+1}^{n} L_{j,i}\left(\mathrm{round}\left(Zz_{(j)}\right) - Zz_{(i)}\right) \right) \quad (11)$$

3 Analysis

Observation data recorded by three Trimble Net R9 receivers and two Trimble 59900 choke ring antenna arranged in the roof of teaching building II, Yanta District, Chang'an University, Xi'an, China, wherein two receivers are connected to one antenna's zero baseline through a power divider, another receiver is connected to a separate antenna. Zero baseline data observed in December 23, 2014 (day of

year 357), and ultra-short baseline data observed in January 14, 2015 (day of year 014). Satellite elevation mask angle is set to 10°, and data sample interval is 30 s. Supposing that standard deviations of pseudorange observations and carrier phase are 3 and 0.03 m, respectively. During the double difference process, account for the C01 satellite is GEO satellite, it is visible throughout the observation period of a satellite, so it is selected as reference satellite unified.

The GPS observations are processed by TBC software using the broadcast ephemeris. For short baseline data, the accuracy obtained by TBC software is considerable to GAMIT software [13, 14]. The results show that, for zero baseline and ultra-short baseline, the horizontal and vertical accuracy could be reached 1 mm. Increment of ultra-short baseline and zero baseline in ENU direction are −0.048, −10.727, 0.189 m and 0.002, 0.000, −0.001 m, respectively. The above results are regarded as reference incremental of ultra-short baseline and incremental of zero baseline respectively, results of ENU direction incremental obtained by the ambiguity resolution are compared with them.

BDS satellite contains GEO satellites, IGSO satellite, and MEO satellites. Ambiguity resolutions of pseudorange/ phase observation in B3 frequency for C02, C07, and C14 base on the different ambiguity resolution approaches are obtained, and the increment differences between TBC are presented. Results of B1 and B2 frequency are not given, because they were consistent with B3 frequency.

3.1 Zero Baseline

The zero baseline carrier-phase ambiguity in B3 frequency with LAMBDA, Rounding, and Bootstrapping approaches are shown in Fig. 1a–c. From left to right, they are the double difference ambiguity of satellite C02, C07, and C14. It can be seen that the performances of above three algorithms are consistent in GEO, IGSO, and MEO satellites, the fixed ambiguity could be obtained. An outlier existed in epoch 2429 for C02 and C07 satellite, the ambiguity for the rest epoch is the same for single-epoch resolution.

Figure 2 shows that through the entire observation period, the number of visible satellites is equal to or more than 8, and the PDOP value is between 1.5 and 3.5, thus it can be considered that, within observation period, the satellite geometry in space is good and beneficial to positioning.

The increment differences in ENU between TBC and the above three algorithms are shown in Fig. 3. The outlier in 2429 epoch is excluded from the above consequences, and the results for three approaches are consistent. Where the maximum absolute difference in E direction is 8.2 mm, and the values greater than 5 mm are about 4 %, the overall performance is more stable; the maximum absolute difference in N direction is 18.3 mm, and the values greater than 5 mm are about 4.3 %, the overall performance in horizontal is also more stable; the maximum absolute difference in U direction is 40.9 mm, and the values greater than 10 mm are about 3.6 %. On the whole, the performances in horizontal and vertical directions are stable.

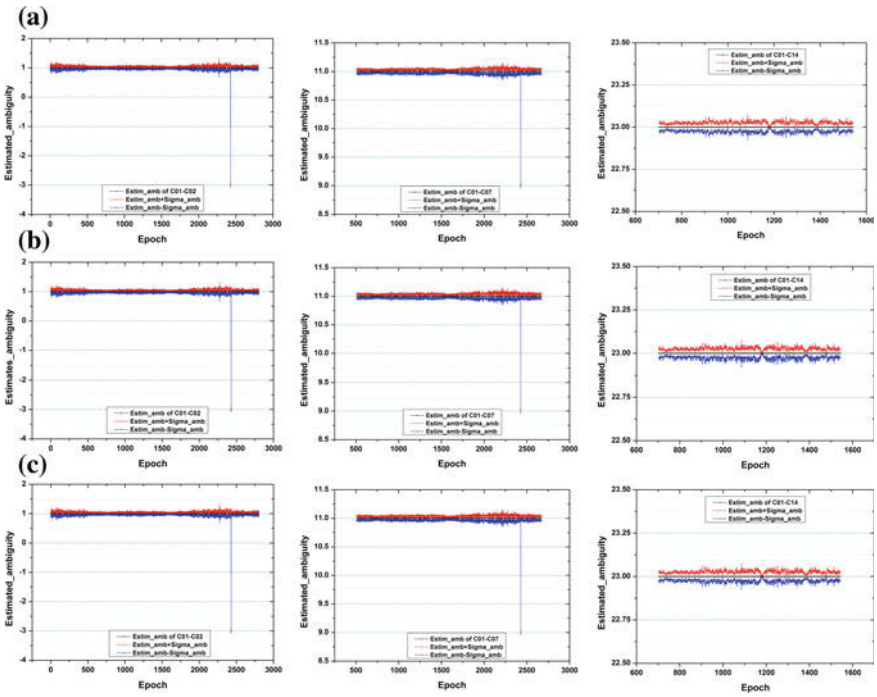

Fig. 1 The estimated ambiguity of zero baseline. **a** LAMBDA, **b** Rounding, **c** Bootstrapping

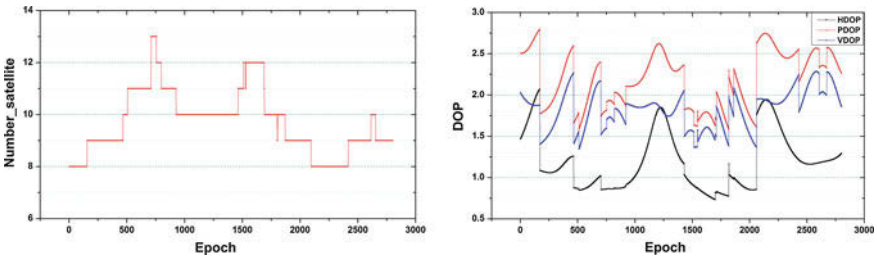

Fig. 2 Number of visible satellites and the DOP value distribution

3.2 Ultra-Short Baseline

Figure 4 shows that the performances of three ambiguity resolution algorithms in ultra-short baseline are consistent, the ambiguity can be fixed by the three approaches. Wherein, the abnormal epochs for LAMBDA appear the most, the Rounding is in the middle, and the Bootstrapping is the least. Overall, the three algorithms are available in short baseline ambiguity resolution.

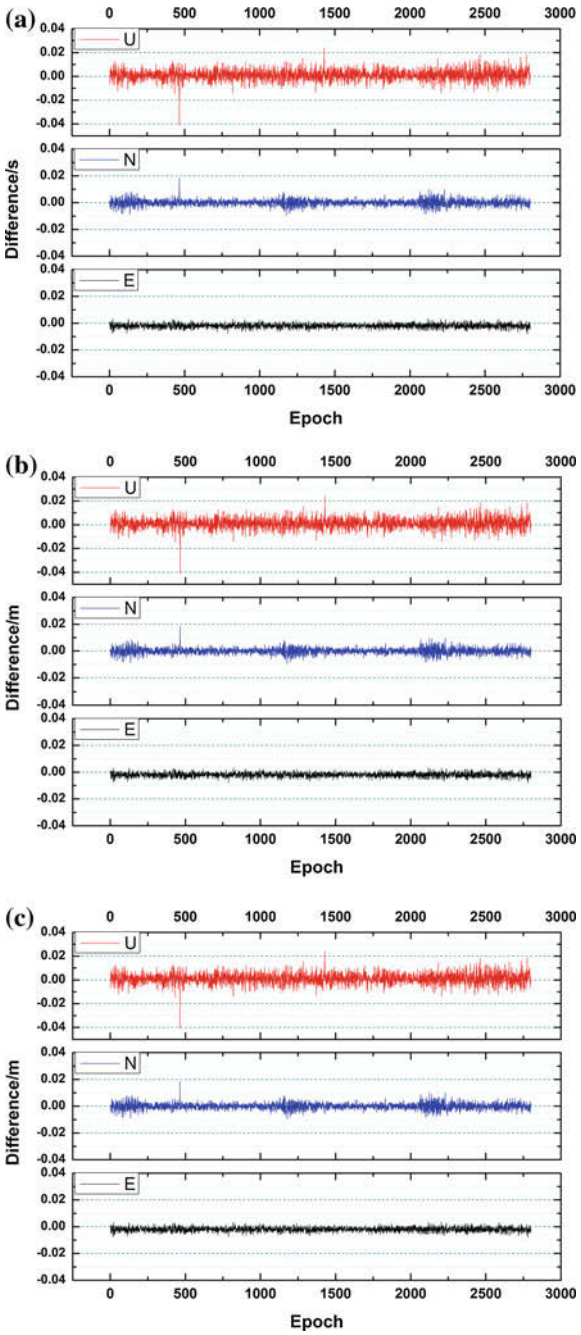

Fig. 3 The difference between ENU increment of zero baseline for different algorithms and result of TBC. **a** LAMBDA, **b** Rounding, **c** Bootstrapping

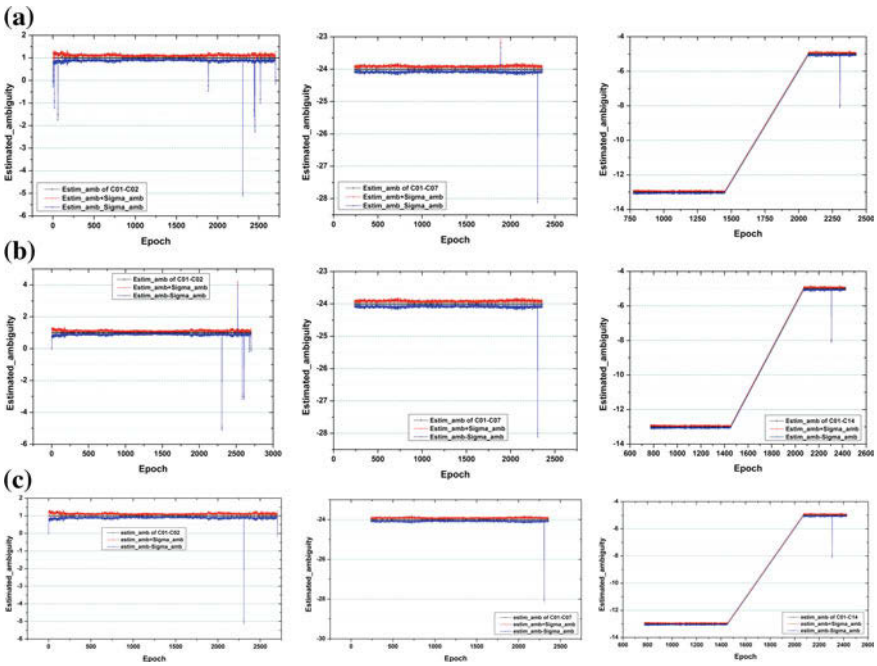

Fig. 4 The estimated ambiguity of Ultra-short baseline. **a** LAMBDA, **b** Rounding, **c** Bootstrapping

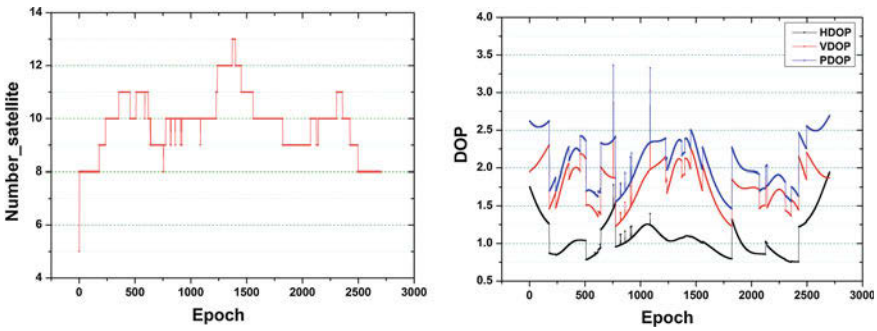

Fig. 5 Number of Visible satellites and the DOP value distribution

Figure 5 shows that the number of visible satellites is equal to or more than 8 except the initial epoch is only 5, and the PDOP during the entire period is between 1.0 and 2.5. It indicates that the satellite geometry in space is good and beneficial to positioning within the entire observation period.

Figure 6 shows the incremental difference between the ENU directions solved by three algorithms and TBC software, the outliers epochs existing in each algorithms resolution result are eliminated in advance. Overall, the results of the three algorithms are basically the same. The statistical result shows that: the maximum

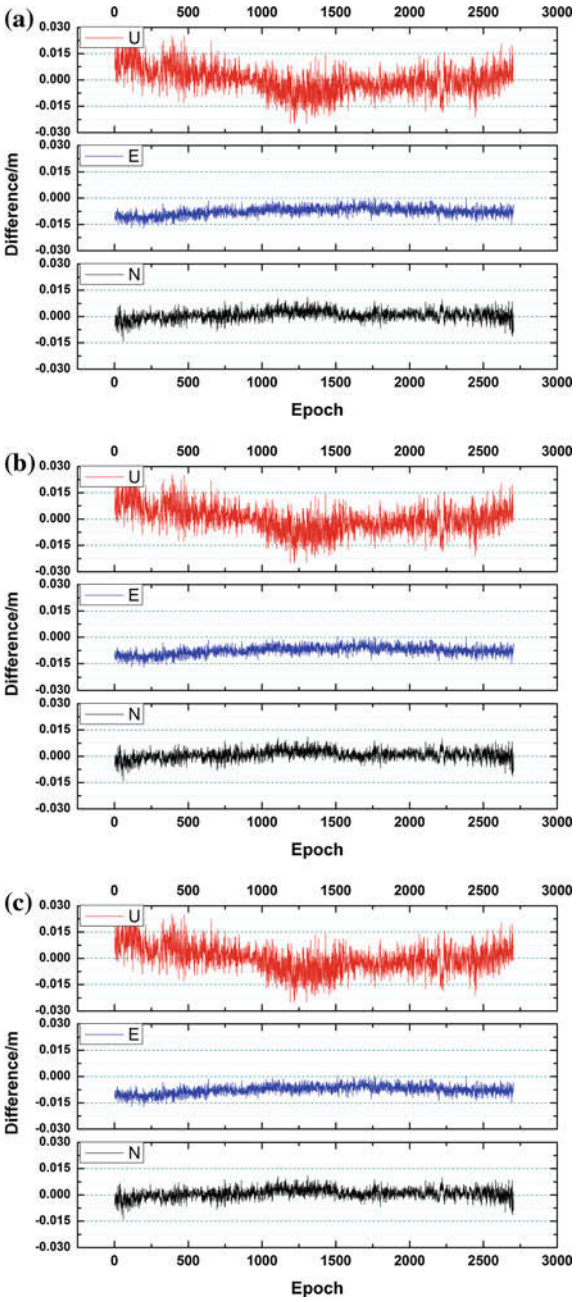

Fig. 6 The difference between ENU increment of ultra-short baseline for different algorithms and result of TBC. **a** LAMBDA, **b** Rounding, **c** Bootstrapping

absolute value of E direction difference is 14.1 mm, but only about 11 % of difference epochs exceed 5 mm, the overall performance is stable. The maximum absolute value of N direction difference is 17.1 mm, but the overall value is basically in -15 to 0 mm, only about 16 % of the difference epochs are less than 5 mm, overall epochs have small fluctuation and perform stable. U direction difference epochs have large fluctuation, the maximum absolute difference reaches to 26.3 mm, and 18.5 % of difference epochs are bigger than 10 mm.

4 Conclusions

LAMBDA algorithm is recognized as the most rigorous theory of ambiguity resolution method, and Rounding algorithm is the easiest way. However, Bootstrapping algorithm is a method which searches and fixes ambiguity gradually. Combining BDS observation data of zero baseline and ultra-short baseline, this paper applies the above three algorithms for calculating ambiguity of GEO, IGSO, and MEO satellites, compares, and analyzes the calculation results. Taking increments of ENU directions solved by TBC software as the references, the differences between ENU directions increments are solved by the three algorithms and the reference value are analyzed. The analysis shows that results of the above three algorithms applied to the single-epoch ambiguity fixing are basically the same for zero baseline and ultra-short baseline. E and N direction differences of zero baseline mainly keep within 5 mm, U direction differences keep within 10 mm, performing stable. 11 % of E direction difference epochs of ultra-short baseline exceed 5 mm; N direction differences basically keep between 5 mm and 15 mm, 16 % of which keep within 5 mm; 18.5 % of U direction differences epochs exceed 10 mm, but the entirety fluctuates within ±15 mm basically. Overall, the performances of three algorithms applied to zero baseline and ultra-short baseline ambiguity resolution are consistent. Therefore, when fixing ambiguity of zero baseline and ultra-short baseline, no matter the simple Rounding algorithm, Bootstrapping algorithm, or tight LAMBDA algorithm can be chosen depending on the situation.

Acknowledgments The authors would like to thank International GNSS Monitoring & Assessment System (GFZX0301040308), The project of National Natural Science Fund (41104019, 41072266, 41304033, 41274005, 41202189) and Central University Research Funds (310826151050) for their support. Thanks to the editors and anonymous referees for providing the valuable comments and suggestions in this paper.

References

1. Teunissen PJG (1995) The least-squares ambiguity decorrelation adjustment: a method for fast GPS integer ambiguity estimation. J Geodesy 70(1–2):65–82
2. Li B (2009) Extended GNSS ambiguity resolution models with regularization criterion and constraints. J Glob Position Syst 8(2):148–153

3. Liu F, Lan X, Chen F (2014) Analysis of Integer Z-Transformation in the LAMBDA method. Geomatics Spatial Inf Technol 4:51–55
4. Li J (2011) Researches on the algorithms of GNSS triple frequency precise positioning. PLA Information Engineering University
5. Feng L (2009) A study on processing and application of GPS multi-frequency observations data. PLA Information Engineering University
6. Huang L (2012) Research on the algorithms and theory of GNSS multi-frequency data processing. PLA Information Engineering University
7. Yu X (2011) Multi-frequency GNSS precise positioning theory and method research. Wuhan University
8. Huang L, Zhai G, Ouyang Y et al (2015) Triple-frequency TurboEdit cycle-slip processing method of weakening ionospheric activity. Acta Geod Cartographica Sinica 44(8):840–847
9. Zhang XH, He XY (2015) BDS triple-frequency carrier-phase linear combinatioinmodels and their characteristics. Sci China Earth Sci 58:896–905
10. Teunissen P, Joosten P, Tiberius C (2002) A comparison of TCAR, CIR and LAMBDA GNSS ambiguity resolution. In: Proceedings of international technical meeting of the Satellite Division of the Institute of Navigation, pp 2799–2808
11. Zhang X, He X (2015) Performance analysis of triple-frequency ambiguity resolution with BeiDou observations. Gps Solut 1–13
12. Wang X (2014) The algorithm study on BDS/GPS baseline solution. Chinese Academy of Surveying and Mapping
13. Li Y, Wang L, Zhuang W et al (2015) Results and analysis of baseline solution with TBC software. Geitech Investig Survey 43(4):60–65
14. Wang L, Zhang Q, Fan L et al (2015) Experiment and results of high precision land subsidence monitoring using fused BDS/GPS data and static relative positioning. J Eng Geodogy 1:119–125

Research on the Feasibility of PPP Technology in Radar Altimeter Calibration

Chao Kong, Zhongmiao Sun, Bin Guan, Hua Lu, Chao Xiong, Meijun Guo and Yingjie Hong

Abstract In the background of the satellite altimeter calibration, the author has discussed the feasibility of using the GPS buoy to determine the sea surface height with high precision based on precise point positioning (PPP) technology. In this study, a number of IGS (International GNSS service) stations data were processed by two different solving modes: single-day solution and single-epoch solution, which the used SPODS software is a high precision positioning and orbit determination software containing the PPP model developed by Xi'an Institute of Surveying and mapping. Under the two different solving modes, we can obtain a positioning solution by period and by epoch, respectively. In addition to the IGS static data, we also processed the reservoir dynamic data collected by the GPS buoy and compared the solution with the result processed by GAMIT/TRACK which is a high precision kinematic positioning software by differential positioning mode. Finally, we concluded that the PPP single-day solution accuracy of the static data in *X*, *Y*, *Z* direction is within 1 cm, indicating the PPP can accurately obtain precise coordinates under the corresponding reference frame; the single-epoch solution accuracy in *X*, *Y*, *Z* directions are within 3 cm whose the processed data were selected from the IGS stations the dynamic buoy solution accuracy in horizontal direction is consistent with TRACK's result, and the accuracy in *U* direction can reach 5 cm which is meeting the accuracy requirements of altimeter calibration.

Keywords PPP · GPS buoy · Water level height · Altimeter calibration

C. Kong (✉) · B. Guan
Information Engineering University, Zhengzhou 450001, China
e-mail: 450698583@qq.com

Z. Sun
Xi'an Research Institute of Surveying and Mapping, Xi'an 710054, China

H. Lu · C. Xiong · M. Guo · Y. Hong
Xi'an Aerors Data Technology Co. Ltd., Xi'an 710054, China

© Springer Science+Business Media Singapore 2016

J. Sun et al. (eds.), *China Satellite Navigation Conference (CSNC) 2016 Proceedings: Volume III*, Lecture Notes in Electrical Engineering 390,
DOI 10.1007/978-981-10-0940-2_35

1 Introduction

In the satellite altimetry, radar altimeter calibration is a very important work. In addition to the traditional tide station technology, using the high accuracy GPS buoy to measure the sea surface height as a reference sea surface to calibrate the radar altimeter's ranging bias has become a commonly used method, and achieved good results at present. For example, the Australia Bass Strait calibration field has got the absolute bias result of Poseidon and JASON-1 altimeter whose value is 10 ± 19 mm and $+147 \pm 21$ mm, respectively, and the most critical equipment used in their experiment is the GPS buoy with centimeter level accuracy, the last result was consistent with other special calibration results [1].

In most cases, GPS differential positioning mode is generally chosen to obtain the position of GPS buoy. That is to say, once the GPS buoy is deployed in the sea area to measure the sea level, the GPS reference station has to be set up on the coast at the same time. The GPS reference station's accurate coordinates could be precisely obtained with the GAMIT/GLOBK or BERNESE software by combining the surrounding IGS (International GNSS service) stations. After that, the buoy accurate position can be obtained by differential treatment with the reference stations set up on the shore [2]. In order to improve the accuracy of differential positioning, the GPS buoy should be as close as possible to the base station. However, the altimeter measurements in the nearshore area have the lower accuracy which will impact the altimeter calibration accuracy at last. So there is a very high demand for the selection of calibration site and the layout of the coastal reference station. Precise point positioning (PPP) is not affected by the reference station, and the accuracy has been constantly improved. Thus, it will have great prospects for application in altimeter calibration. In order to study the feasibility of applying the PPP technology to calibrate the altimeter, we have used PPP software to process the IGS static data and GPS buoy dynamic data, respectively, and compared the solutions with the afterwards relative positioning results processed by GAMIT/TRACK software.

2 Principle of Radar Altimeter Calibration

According to the principle of the radar altimetry, the sea surface height measured by altimeter can be defined as

$$\mathrm{SSH}_{\mathrm{Alt}} = h - (R + R_{\mathrm{dry}} + R_{\mathrm{wet}} + R_{\mathrm{iono}} + R_{\mathrm{ot}} + R_{\mathrm{st}} + R_{\mathrm{pt}} + R_{\mathrm{invb}} + R_{\mathrm{ssb}}) \quad (1)$$

where the h is the height of the satellite's orbit, R is the satellite altimeter measurement value to the sea, R_{dry} is the dry troposphere delay correction, R_{wet} is the wet troposphere delay correction, R_{iono} is ionospheric delay correction, R_{ot} is ocean tide correction, R_{st} is the earth solid tide correction, R_{pt} is the pole tide correction, R_{invb} is the reverse pressure correction, R_{ssb} is the sea state bias correction.

As the satellite altimeter flies over the calibration field, the sea surface height can be calculated by the formula (1). At the same time, sea surface height (SSH_0) at the same area can be obtained by the other level measuring equipment in the calibration field such as the tide technology or ocean array, etc., and refer it as the sea surface reference of the calibration field. Then, the satellite altimeter's ranging absolute bias: R_{bias} can be solved by the formula (2), where the SSH_{Alt} is the sea surface height measured by satellite altimeter; SSH_0 is a reference sea height treated as the true value [3–5].

$$\begin{aligned} R_{bias} &= SSH_{Alt} - SSH_0 \\ &= h - (R + R_{dry} + R_{wet} + R_{iono} + R_{ot} + R_{st} + R_{pt} + R_{invb} + R_{ssb}) - SSH_0 \end{aligned} \quad (2)$$

From the above formula, the absolute bias accuracy is not only depended on the accuracy of the reference sea height, but on the altimeter measurement and the error correction accuracy. Therefore, when we plan to determine the sea surface reference with the GPS buoy, it is necessary to take into account the accuracy of altimeter ranging and the reference sea surface.

In order to avoid the land influence on altimeter measurement and to ensure the measurement accuracy of the altimeter at the calibrating time, the PPP technology is used to determine the height of the GPS buoy which can be deployed anywhere on the wide sea. PPP is generally using the precise orbits and precise clock files released by IGS to eliminate the satellite error term, and using the dual-frequency observation value to eliminate the effect of ionosphere. The position information of the observation equation is solved by combining the dual-frequency non ionosphere observation measurement, the specific algorithm and the model can be found in the reference [6, 7]. PPP solution's location datum is based on the precise ephemeris which is under the IGS08 reference frame. There are small differences between the IGS08 and the ITRF, and the formal errors of the ITRF2008 positions are below 1.5 mm for 92 % of the IGS08 stations [8]. Thus, in most cases, it can be treated equally without distinction.

3 Data Sources and Processing Strategies

3.1 Experimental Program and Data Source

The establishment of calibration field height datum which must be consistent with the altimeter orbit reference frame is the premise work of the altimeter calibration. For the traditional differential positioning method, the height datum of the calibration field is established by setting up the several GPS receivers on the coast and observing continuous several days to get the exact coordinates of the ITRF. Then, based on the relative positioning solving with the reference stations, we can easily obtain the sea surface elevation of deployed GPS buoy area under the same reference frame. This experiment is focused on the analysis of the positioning

accuracy under the ITRF reference frame solved by PPP technology directly according to the static and dynamic processing mode. The software used for the experiment is named SPODS that is developed by Xi'an Institute of Surveying and mapping [7].

We chose total five IGS stations Bjfs, Wuhn, Lhaz, Urum, Chum, and Daej, as the static GPS data whose time is starting from September 16, 2014 to September 21, 2014 whose sampling rate is 30 s and we used SPODS to process the above sites' data by single-day solution mode which could get only one solution for a single period and be available only for static data.

The two days GPS buoy data observed from September 20, 2014 to September 21, 2014 (Doy 263, Doy 264) at Xi'an Lantian reservoir experiments was processed as dynamic data by the single-epoch processing mode which could get one solution for each epoch and be available both for the static and dynamic data. The experiments have used three Trimble SPS852 GPS receivers, one was reformed into GPS buoy, the other two were set as the reference station and observed synchronously with GPS buoy for analyzing the buoy accuracy of relative positioning under the different length baseline to reference station.

3.2 Introduction of SPODS Software

The SPODS is the GNSS positioning and orbit determination software developed by Xi'an Institute of Surveying and mapping. It uses the non difference phase and pseudorange to form the non ionosphere measurement, and the TurboEdit method is used to detect and repair the phase cycle slip. The correct items of the measurements include: satellite and receiver antenna phase center deviation and variation, satellite clock difference, troposphere delay, ionosphere delay, tidal (solid tide, pole tides, and ocean tide loading) displacement correction. Wind-up effect is also considered to correct the phase data. Satellite and receiver antenna phase center deviation and change data are taken from the ANTEX IGS file, and the phase center correction has taken into account the influence of the satellite attitude. The standard Saastamoinen zenith delay model and Beohm and Neill are used to correct tropospheric delay. IERS conventions (2003) are used for tidal displacement correction. According to the preliminary performance test, the GPS satellite orbit solution RMS is 1.1 cm compared with the final orbit of IGS. For the repeatability of the single-day solution of the station coordinates, the horizontal component is 1.5 mm, the height component is 4.5 mm. Detailed information is available in the reference [9]. In this paper, we mainly used the SPODS_PPP module to solve the all of GPS data.

3.3 Data Processing Strategy

Firstly, we should download the IGS final precise ephemeris (.Sp3) and Precise clock products (.Clk) from the IGS website, and then process the GPS data with SPODS_PPP software by two different processing mode, respectively: static single-day solution and dynamic single-epoch solution.

1. For the static data solution, we processed the 5 days IGS stations in Asian region: bjfs, wuhn, lhaz, urum, chum, and daej by the PPP technology. In order to analyze the coordinate accuracy under ITRF and the feasibility for altimeter calibration, we compared each site's single-day results with the precise coordinates released by IGS online site.
2. For the dynamic data solution, first, in order to be able to carry out the accuracy comparison with the true value, we used the static data as dynamic data to be processed whose only difference from static data process is that the processing mode has turned to single-epoch, and the accuracy is evaluated by comparing the results with the known exact coordinates from the IGS website. Then, we processed the real dynamic data collected by GPS buoy in the reservoir. At the same time, two GPS reference stations away from the buoy 20 and 20 m, respectively, were observing synchronously and its precise coordinates were obtained in advance by GAMIT/GLOBK.

For getting the GPS buoy exact positions, we used the differential positioning software (GAMIT/TRACK) to obtain the buoy's position changes relative to the base station, and treated it as the true value of the water surface for the comparison with the PPP solution. The advantages of the TRACK relative positioning is that many common errors can be eliminated using the double difference method in short baseline, thus, its relative positioning accuracy is very high [10]. For the non-differential positioning mode, we got the surface elevation information by processing the high rate data of 1 s sampling rate with SPODS_PPP. In order to analyze the accuracy of water surface processed by the PPP, the dynamic positioning results of single-epoch were compared with the TRACK results [9, 11].

4 Results and Analysis

4.1 Results of Static Data

After downloading the corresponding precise ephemeris and clock products, we processed six IGS stations' 5 days data using SPODS_PPP software by the single-day processing mode, and obtained the corresponding X, Y, Z coordinates. Due to the IGS stations coordinates released by IGS have been accurately known and the accuracy and reliability are very high, the accurate coordinates can be treated as a reference value to be compared with the SPODS_PPP results.

Table 1 Statistics of single-day solution difference between the SPODS_PPP and IGS coordinates/mm

Site	Direction	Doy 1	Doy 2	Doy 3	Doy 4	Doy 5	Average/mm
BJFS	*X*	−1.6	−0.2	−6.2	−2.6	−1	−2.32
	Y	2.9	1.1	1.3	3.5	2.4	2.24
	Z	0.6	−1.3	−1.3	1.2	0.1	−0.14
CHUM	*X*	−1.3	0.4	−4.9	0	2	−0.76
	Y	15.8	15.3	15.5	8.4	11.7	13.34
	Z	9.4	7.4	1.3	1.5	5.4	5
DAEJ	*X*	−1.1	7.4	−2.6	2	3.3	1.8
	Y	1.1	3.3	−0.8	2.8	1.3	1.54
	Z	−2.1	1.1	−4.6	1.3	0.3	−0.8
LHAZ	*X*	−7.1	−4.8	−8.2	−4.3	−4.1	−5.7
	Y	0.2	−1.3	−4.9	−2.6	−0.2	−1.76
	Z	−4.7	−4.3	−8.6	−6	−4.4	−5.6
URUM	*X*	−1.5	−3.4	−2.6	−1.8	−1.3	−2.12
	Y	13.5	12	14.6	6.7	9.6	11.28
	Z	6	1.5	5.5	−0.4	1.1	2.74
WUHN	*X*	−1.2	0	−0.9	−3.8	−5.8	−2.34
	Y	−9.4	−12.2	−8.2	−13.8	−12.3	−11.18
	Z	−5.2	−9.3	−3.3	−6.5	−6.7	−6.2

The results are shown in Table 1, the six stations' deviation in *X*, *Y*, *Z* directions are listed separately.

From Table 1, we can conclude that the PPP positioning results by single-day mode is very close to the exact coordinates, the difference in *X*, *Y*, and *Z* directions is almost within 1 cm at different sites and different observing time. The positioning accuracy of the same station can reach mm level through couple day's continuous observation. Since the differences between the IGS08 and ITRF frame can be neglected, we can see that the PPP solution could get the high precision positions under the ITRF. Thus, we can directly compare the sea surface obtained from PPP results with the altimeter measurements for calibrating.

4.2 Results of Static Data by Dynamic Processing Mode

We selected the single-epoch model to process the static data of the three IGS stations: BJFS, WUHN, and LHAZ. And then, we compared each epoch coordinates with the true value released by IGS. The difference in *X*, *Y*, *Z* directions is shown in Fig. 1.

As can be seen from Fig. 1, it is clear that the stations deviation in *X*, *Y*, *Z* direction is relatively stable and concentrated at each moment during the 24 h.

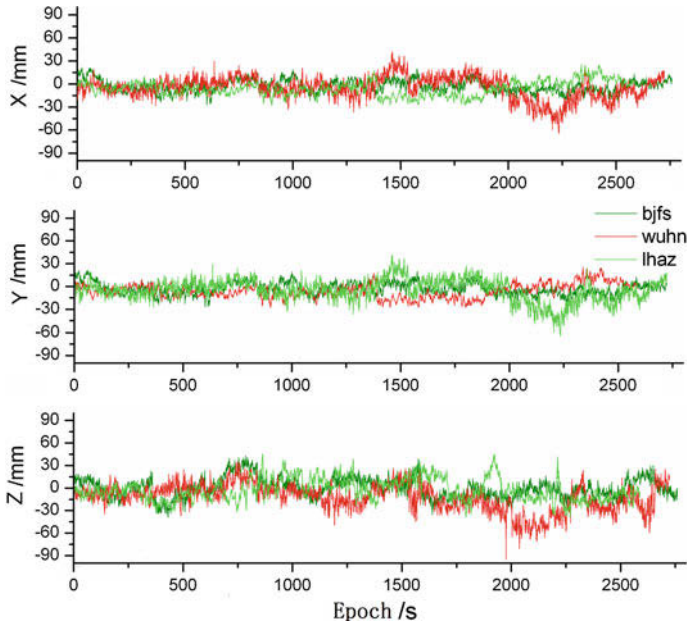

Fig. 1 BJFS, WUHN, and LHAZ's *X*/*Y*/*Z* deviation with IGS

It can be explained that the PPP dynamic processing function and error correction model of the SPODS_PPP is correct whose results are reliable. The overall volatility of the Wuhn site is larger than others and concentrated in the same observation period, which may be affected by the environment factor at the time. Table 2 is statistics of single-epoch solution difference between the SPODS_PPP and IGS coordinates in *X*, *Y*, *Z* direction.

From Table 2, we can conclude that three station's maximum deviation value under the most epochs is within 5 cm, the average of deviation in three directions is within 1 cm, the std value which can reflect the coordinate's deviation size is also within 2 cm.

4.3 Results of GPS Buoy

Actually, the altimeter is only working around the complicated and dynamic water environment. Therefore, the analysis of the dynamic GPS buoy by PPP is necessary. We chose the total 4000 epochs in Doy 263 and total 2000 epochs in Doy 264 buoy data, and converted the *X*, *Y*, *Z* coordinates to *N*, *E*, *U* direction according to the base station, respectively, which is 20 km, 20 m away from the GPS buoy. Its coordinate results in *E*, *N*, *U* direction is shown in Fig. 2.

Table 2 Statistics of single-epoch solution difference between the SPODS_PPP and IGS coordinates/mm

Site	Direction	Max/mm	Min/mm	Mean/mm	Std/mm
BJFS	*X*	21.6	−27.3	−2.7	8.0
	Y	52.8	−41.4	1.6	18.4
	Z	43.1	−39.2	0.0	13.4
WUHN	*X*	42	−64.9	−4.7	14.5
	Y	49.2	−164.6	−21.5	34.4
	Z	34.5	−95.3	−12.7	17.8
LHAZ	*X*	25.6	−28	−5.9	9.3
	Y	119.7	−93.2	5.8	25.1
	Z	45.8	−39.1	−2.4	14.6

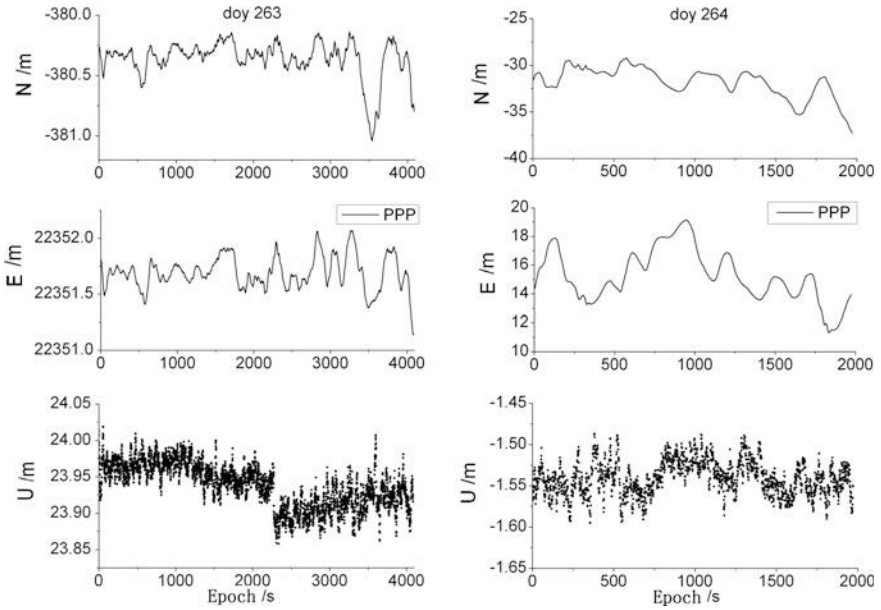

Fig. 2 Buoy's NEU result by SPODS_PPP

In Fig. 2, we can see that the SPODS_PPP could accurately process the GPS buoy dynamic data, its coordinate sequence is quite stable which is in accordance with the actual state of motion of the buoy. While the *U* direction at the Doy 263 appeared a large beating, the reason may be the actual buoy movement or the big mutation in environment. In order to analyze the PPP external accuracy, we made the PPP results to minus the true value from the TRACK solution. The deviation in the *N*, *E*, *U* directions is shown in Fig. 3.

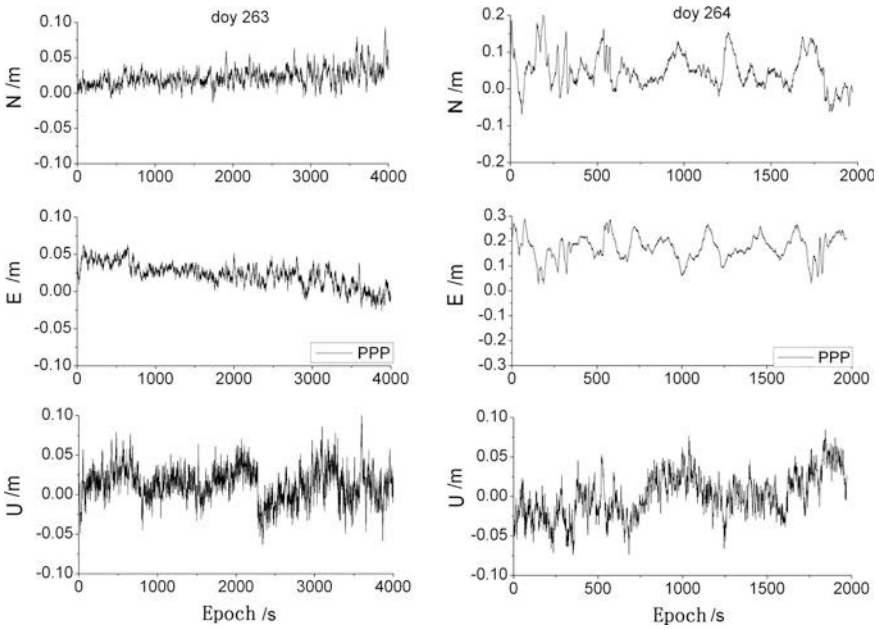

Fig. 3 Buoy SPODS_PPP's result difference with TRACK

Table 3 Statistics of single-epoch solution difference between the SPODS_PPP and TRACK/mm

Time	Direction	Max/m	Min/m	Mean/m	Std/m
Doy 263	*N*	0.093	−0.013	0.022	0.013
	E	0.063	−0.040	0.021	0.016
	U	0.101	−0.063	0.013	0.021
Doy 264	*N*	0.239	−0.0693	0.049	0.047
	E	0.287	0.026	0.174	0.049
	U	0.84	−0.074	0.0	0.027

From the above, we have known the deviation values in *N*, *E*, *U* direction are relatively stable, the deviation in *U* direction basically maintained within the range of 5 cm and is maintained at the zero mean, and the accuracy is consistent with the relative positioning results which can achieve a few centimeters accuracy. It is also verified that the PPP dynamic positioning solution with GPS buoy could be applicable in radar altimeter calibration. The statistics of the solution difference between the SPODS_PPP and TRACK are shown in Table 3.

From Table 3, the standard deviation in *U* direction is found in 3 cm. For the Doy 263, the maximum values in *N*, *E*, *U* direction are 0.093, 0.063, 0.101 m, the mean value is within 3 cm, the standard deviation is 2 cm. Thus, the results of the PPP and TRACK differential results agreed very well. The horizontal accuracy of TRACK is about 2 cm, the vertical accuracy is worse than horizontal direction which may be

Table 4 Statistics of solution difference between the smoothed SPODS_PPP and TRACK/mm

Time	Direction	Max/m	Min/m	Mean/m	Std/m
Doy 263	*N*	0.055	0.0	0.022	0.008
	E	0.051	−0.016	0.021	0.014
	U	0.064	−0.027	0.013	0.014
Doy 264	*N*	0.148	−0.028	0.049	0.032
	E	0.251	0.106	0.174	0.033
	U	0.05	−0.038	0.0	0.021

normal to achieve 5 cm. From the above comparison analysis, we may conclude that the PPP elevation positioning accuracy is very high which the accuracy in *U* direction may be equivalent to the relative positioning even better. In order to eliminate the influence of wave on the buoy, we used a moving average method to smooth the buoy height sequence, the window size was chosen 100 s, and compared the smoothed results each other. The statistics result is shown in Table 4.

Through a comprehensive comparison Table 3 with Table 4, the buoy coordinates in *N*, *E*, *U* direction were improved obviously after a simple average smoothing, that is to say the noise has been obtained with a certain elimination after smoothing. Since the moving average method is a very simple and convenient method, it cannot eliminate the noise in a certain frequency range and cannot remove from the rough. However, the true change of the water surface elevation is generally at the low frequency signal. In order to improve the surface height accuracy by PPP, the high frequency noise has to be removed. Therefore, the denoising effect of different smoothing filtering method is worth further study.

5 Conclusions

Using the IGS precise ephemeris and precise clock products, we processed the IGS stations and GPS buoy data with SPODS_PPP by two different processing mode, and compared it with the corresponding most accurate coordinates, the results show that

1. GPS static data single-day solution: the accuracy in *X*, *Y*, *Z* direction is within 1 cm, and the coordinate can be archived directly under the ITRF which is consistent with the radar altimeter reference frame, thus, it is meeting the basic premise of radar altimeter calibration.
2. GPS static data single-epoch solution: the accuracy in *X*, *Y,* and *Z* directions are within 3 cm, indicating that the PPP dynamic calculation model is correct and has the good accuracy. In the case of perfect environment for observing and the data quality is pretty good, the results are in good agreement with the actual positions.
3. Through processing the GPS buoy dynamic data, the dynamic processing results of GPS buoy in the horizontal direction are basically consistent with the

TRACK result. The *U* direction can reach 5 cm accuracy, which is meeting the altimeter calibration of sea surface altimetry precision requirements.

In summary, The PPP technology can deal with the static and dynamic GPS data at the high precision solution, thus, it is reliable to apply PPP to calibrate the radar altimeter. There are some deficiencies in this contribution such as; the experience was just based on the limited number of GPS buoy data collected data from the static reservoir environment not the real ocean. Because the marine environment is more changeable, GPS buoy operated in the dynamic sea area will be affected seriously, especially in the cycslips and multipath, which would impact the PPP solution at last. Thus, it is necessary to study the PPP influence caused by GPS buoy data quality and find an effective method to improve it.

Acknowledgments Thanks to Dr. Rengui Ruan for providing guidance and the SPODS_PPP software of Xi'an Institute of Surveying and mapping. And the author would like to thank the IGS for providing GNSS observations and precise ephemeris products.

References

1. Watson CS (2005) Satellite altimeter calibration and validation using GPS buoy technology. University of Tasmania, Australia
2. Christopher W et al (2003) Absolute calibration of TOPEX/Poseidon and Jason-1 using GPS buoys in bass strait, Australia. Mar Geodesy, 285–303
3. Watson C, Coleman R, White N, Church J, Govind R (2003) Absolute calibration of TOPEX/Poseidon and Jason-1 using GPS buoys in bass strait, Australia special issue: Jason-1 calibration/validation. Mar Geodesy 26(3–4):285–304
4. Zhang Y, Lin M (2007) Study on the satellite altimeter calibration field and the method. Adv Mar Sci Bull 26(3):87–92
5. Bonnefond P, Exertier P, Laurain O, Jan G (2010) Absolute calibration of Jason-1 and Jason-2 altimeters in Corsica during the formation flight phase. Mar Geodesy 33(S1):80–90
6. Wei J (2007) GPS precise point positioning data processing research. Central South University, Changsha
7. Ruan R, Hao J, Lv Z (2009) Dual frequency precise point positioning software and its precision analysis. GPS Mapp Sci Technol J 26(3):276–279
8. Rebischung P, Griffiths J, Ray J et al (2012) IGS08: the IGS realization of ITRF2008. GPS Solutions 16(4):483–494
9. Zhao J, Wang SP, Zhang HM et al (2008) Long distance. Tidal measurement based on GPS PPK/PPP. J Wuhan Univ Inf Sci Ed 33(9):910–913
10. King RW, Bock Y (2004) Documentation for the GAMIT GPS analysis software. Release 10.2. Mas-sachusetts Institute of Technology, Cambridge
11. Guo J, Zhou M, Tian X (2009) The accuracy analysis of dynamic water measuring with GPS-PPP. Bull Surv Mapp (1):1–3
12. Wei Z, Ruan R, Jia X et al (2014) Satellite positioning system-SPODS: theory and test. J Surv Mapp 43(1):1–4

Cycle-Slip Processing Under High Ionospheric Activity Using GPS Triple-Frequency Data

Lingling Chen and Lixin Zhang

Abstract After making a detailed analyzes on the method of geometric-free (GF) phase combination, we know that misjudged situation will appear when this method is applied to detect cycle slip under the condition of high ionospheric delay. A new method has been proposed to overcome this problem. First, several optimum inter-frequency combination coefficients which not only can reduce the first-order and second-order delay of ionosphere, but also have long wavelengths and low-noise levels were selected. Secondly, the first-order delay of ionosphere is pre-estimated with the three-frequency observation. Lastly, cycle-slip detection is reconstructed. Observation data under the condition of high ionospheric activity is loaded from IGS to verify the validity of the method. The results show that this method can detect all combination of cycle slip under high ionospheric activity and has its own advantage on detecting cycle slip in undifferenced observations.

Keywords High ionospheric activity · Detection of cycle slip · Geometric-free phase combination method · Pre-estimate of ionosphere delay

1 Introduction

The modernization of GPS lead to the signal on L5 frequency broadcasted, and then we can obtain triple-frequency observation data which can provide a new approach to improve the navigation accuracy and efficiency [1]. High-precision navigation and positioning require carrier phase observations which may have cycle slip, so the right pre-treatment of carrier phase observation is the prerequisite for high-accuracy positioning. Since triple-frequency combination observations have several advantages over dual-frequency combination observations which have lower-noise levels,

L. Chen (✉) · L. Zhang
China Academy of Space Technology, 710000 Xi'an, China
e-mail: chenll504zxf@163.com

© Springer Science+Business Media Singapore 2016

J. Sun et al. (eds.), *China Satellite Navigation Conference (CSNC) 2016 Proceedings: Volume III*, Lecture Notes in Electrical Engineering 390,
DOI 10.1007/978-981-10-0940-2_36

longer wavelengths and can reduce the second-order ionosphere effects [2–4], most researches focused on applying triple-frequency observations to detect cycle slip. The main methods include the pseudorange/carrier phase combination method and the geometric-free phase combination method. These two methods defined that the difference of ionospheric delay between epochs is negligible. Generally, they both can detect and repair all cycle slip correctly [5–10]. However, as soon as the difference of ionospheric delay in adjacent epoch is large (electron density TEC $= 4.55\text{e}18/\text{m}^2$), the detection of cycle slip will be incorrect. Literature [11] studied how to handle cycle slip during ionospheric plasma bubble events. Literature [12] is based on the hypothesis to processing the situation of gross errors, cycle-slip, and anomalies ionosphere. In this paper, we propose a modified method taking the advantage of triple observations to select coefficients which can eliminate the second-order effect of ionospheric delay. Then the first-order delay on ionosphere is pre-estimated, and a new detection of cycle slip is constructed. The results indicate that this modified method can detect all combinations of cycle slip in three carriers even under high ionospheric activity.

2 The Method of Geometric-Free (GF) Phase Combination

Based on the multi-frequency theory, we obtain the geometric-free phase expression:

$$i\lambda_1\varphi_1(t) + j\lambda_2\varphi_2(t) + k\lambda_5\varphi_5(t) = -\eta I(t) + N_{i,j,k}(t) + \varepsilon(t) \tag{1}$$

Where (i, j, k) refers to the combination coefficients of carrier phase and satisfy the equation $i + j + k = 0$. In formula (1), the amplification factor of ionosphere delay is

$$\eta = i\lambda_1 + j\lambda_2\frac{f_1}{f_2} + k\lambda_5\frac{f_1}{f_5} \tag{2}$$

The combined ambiguity is

$$N_{i,j,k}(t) = i\lambda_1 N_1(t) + j\lambda_2 N_2(t) + k\lambda_5 N_5(t) \tag{3}$$

The combined noise level is

$$\varepsilon(t) = i\lambda_1\varepsilon_1(t) + j\lambda_2\varepsilon_2(t) + k\lambda_5\varepsilon_5(t) \tag{4}$$

Where λ_i, f_i, $N_i(t)$, $\varepsilon_i(t)$ represent the wavelengths, carrier phase observations, frequency, ambiguity, observation noise (including multi-path, in units of cycle), respectively, on the L_i carrier frequency at the moment of t, I(t) is the ionosphere delay (in weeks) on the frequency L_1.

When cycle slip occurs, using the method of geometric-free phase combination, the difference of adjacent epochs can be expressed as

$$\Delta = \mathrm{i}\lambda_1\Delta\varphi_1 + j\lambda_2\Delta\varphi_2 + k\lambda_5\Delta\varphi_5 = -\eta\Delta I + \Delta N_{i,j,k} + \Delta\varepsilon \tag{5}$$

cycle slip decision conditions is

$$\left|\mathrm{i}\lambda_1\Delta\varphi_1 + j\lambda_2\Delta\varphi_2 + k\lambda_5\Delta\varphi_5\right| \geq n\sigma_{i,j,k} \tag{6}$$

Where $\sigma_{i,j,k} = \sqrt{i^2\sigma_1^2 + j^2\sigma_2^2 + k^2\sigma_5^2}$ is the combination noise level.

If n = 3, the degree of confidence is 97 %.
If n = 4, the degree of confidence is 99 %. (In this paper, define n = 4).

From the formula (5), we can know that the performance of this method is affected by ionosphere delay of adjacent epoch and carrier observations noise level. It has nothing to do with the distance from stations to stars and receiver clock error and tropospheric delay. Moreover, for certain ΔI and Δε, the smaller combination coefficient is, the smaller η is, and the higher the detection accuracy the method has. Thus this method just faced one problem that is when the inter-epoch ionosphere delay is large, the cycle-slip detection accuracy will sharply decreased and even leading miscarriage of justice.

3 Modified Algorithm

Since the triple-frequency combination of geometric-free phase is affected by ionosphere delay between epochs, so first, the first order of ionosphere delay between epochs on L1 frequency is calculated by formula (7)

$$\Delta I_1^1 = \frac{\Delta\lambda_1\varphi_1 - \Delta\lambda_2\varphi_2}{1 - f_1^2/f_2^2} \tag{7}$$

Then cycle-slip detection formula is modified as follows:

$$i\lambda_1\Delta\varphi_1 + j\lambda_2\Delta\varphi_2 + k\lambda_5\Delta\varphi_5 + \eta\Delta I_1^1 = \Delta N_{i,j,k} - \gamma\Delta I_1^2 + \Delta\varepsilon \tag{8}$$

Where ΔI_1^i represents i-order of ionospheric delay on L1 frequency.
Then cycle-slip detection can be decided by formula (9)

$$\left|i\lambda_1\Delta\varphi_1 + j\lambda_2\Delta\varphi_2 + k\lambda_5\Delta\varphi_5 + \eta\Delta I_1^1\right| \geq n\sigma_{i,j,k} \tag{9}$$

The formula (8) shows that the performance of this method is only affected by second order of ionosphere delay and combination noise level. Under high

ionospheric activity (electron density TEC $= 4.55\text{e}18/\text{m}^2$), the error of second order of ionosphere delay is up to 0.19 m in GPS original observation [13]. Because the combination coefficients of the geometry-free phase combination method is chosen in the restrain of low-noise level. It requires small combination coefficients, and the combination wavelength will be small. Therefore, the second order of ionosphere delay must be taken into account.

When the variety of inter-epochs ionosphere delay is larger, first, apply triple-frequency observation data to select out combination coefficients which not only can completely eliminate the first order of ionosphere delay but also can weaken the second-order ionosphere delay, and then reselect combination coefficients in the restrain of low combination noise level. It is shown in the formula (10)

$$\begin{cases} i+j+k=0 \\ i+\frac{f_1^2}{f_2^2}j+\frac{f_1^2}{f_5^2}k \to 0 \\ i+\frac{f_1^3}{f_2^3}j+\frac{f_1^3}{f_5^3}k \to 0 \\ \min(\sqrt{i^2+j^2+k^2}) \end{cases} \tag{10}$$

We select combination coefficients satisfied above formula between [−15, 15] as Table 1. It shows optimal combination coefficients and ionosphere magnification, noise magnification, and detection capability in cycle.

The observation noise in GPS raw carrier phase observations is usually defined as $\sigma_1 = \sigma_2 = 0.03$ cycle on L1 and L2, $\sigma_5 = 0.01$ cycle on L5. Since the carrier phase observation has high stability, the noise level of the inter-epoch difference is negligible. Based on error propagation principle, we know that it will enlarge the noise level to use combination coefficients in Table 1. But the inter-epoch noise level is extremely small, so this method still performs well under the condition of high ionospheric activity.

In order to detect the insensitive cycle slips, we make the optimal combination coefficients pairwise [14]. The number of insensitive cycle in 10 cycles is shown in Table 2.

Although the combination coefficients is used with pairwise type, insensitive cycle slip still exists, and it satisfies $\Delta N_1 = \Delta N_2 = \Delta N_5 = a$ (where a represents integer). For example, cycle slip (1, 1, 1) is the most insensitive cycle slips. The combination coefficient (1, −1, 0) is chosen to detect the most insensitive cycle slips

Table 1 Use the preferred combinations ionosphere magnification and noise magnification

Coefficients	First-order ionosphere magnification	Second-order ionosphere magnification	Noise magnification	Detection capability (cycle)
[1, −6, 5]	0.0847	0.3256	7.8740	0.0906
[2, −11, 9]	0.0230	0.3634	14.3527	0.1104
[1, −5, 4]	0.0616	0.03780	6.4807	0.2010

Table 2 Number of insensitive in 10 cycles

Detect combination	≤10
[1, −6, 5][2, −11, 9]	10
[1, −6, 5][1, −5, 4]	7
[1, −5, 4][2, −11, 9]	8

like the (1, 1, 1) according to the literature [14]. And use the method of twice difference of ionosphere delay inter-epochs to detect cycle slip. It shows that using this method, the jump of (1, 1, 1) will lead a change to the detection volume up to 0.0539 cycle; so that this method can detect the most insensitive cycle slip (1, 1, 1). In order to ensure the accuracy of the cycle-slip detection, four times of the cycle-slip variance is selected as the detecting threshold value. So, if there is no cycle slip when the method of whose formulation is as (11) is used to detect cycle slip, It believe that the cycle-slip correction is right.

$$\lambda_1 \Delta N_1 - \lambda_2 \Delta N_2 = \left[(\lambda_1 \varphi_1 - \lambda_2 \varphi_2)_{t2} - 2(\lambda_1 \varphi_1 - \lambda_2 \varphi_2)_{t1} + (\lambda_1 \varphi_1 - \lambda_2 \varphi_2)_{t0} \right] \tag{11}$$

Where t_0, t_1 and t_2 is continual three epochs. The flow chart of cycle-slips detection and repairing algorithm under high ionospheric activity is shown in Fig. 1.

4 Verification with Real Data

A major magnetic storm happened on March 17, 2013. Stations located around latitude 20°, longitude 20° were severely affected [14], therefore, we select the observation data received by site TOW2 located at North 20°, East 18° whose sampling interval is 30 s as raw data to analyze.

The first order of ionosphere delay on different star is calculated with the original observation data. And then we make a difference on the first order of ionosphere delay of adjacent epoch. The result is shown in Fig. 2.

Figure 2 shows the first order, time difference of ionosphere adjacent epochs delay of different satellite. It is known that the variation rate of ionosphere delay on PRN#9 satellite is biggest after 200 epoch. So we take the observation data on PRN# 9 satellite as an example to analyze in this paper.

In this situation, the detection sequence of the geometric-free phase combination method with coefficients [1, 3, 4] in literature [4] is shown in Fig. 3.

It can be seen from Fig. 3 that the geometric-free phase combination method is significantly affected by the residual effects of the ionosphere. Although there is no cycle slip, the fluctuation range of cycle-slip detection sequence still exceeds its detection threshold. Therefore, this method cannot accurately detect cycle slip in raw data in this condition. In the following chapters, we use the improved algorithms to analyze cycle-slip detection.

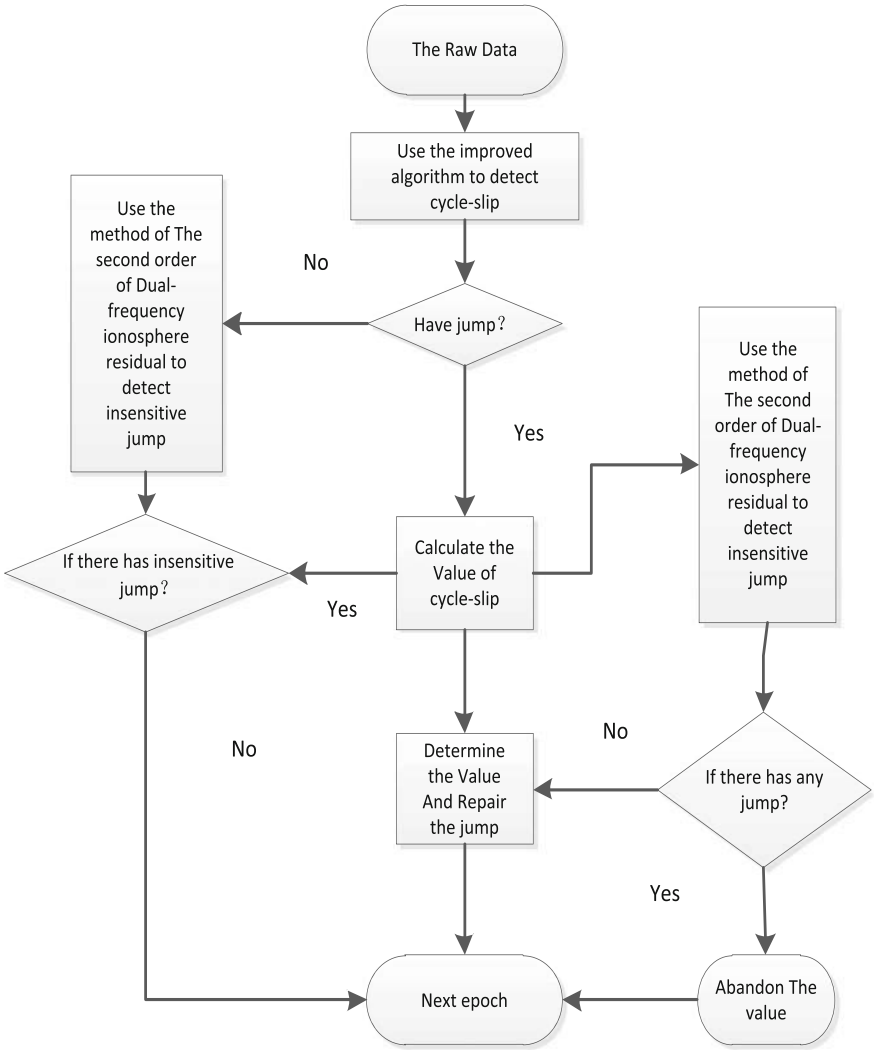

Fig. 1 Cycle slips detect and repair algorithms flow chart under the condition of high ionosphere

4.1 No Jumps

Table 1 and Fig. 4 show that preferred combination coefficients have advantage in weakening the effect of the first order and second order of ionospheric delay. Although the ionospheric delay in adjacent epoch is large, the fluctuation range of

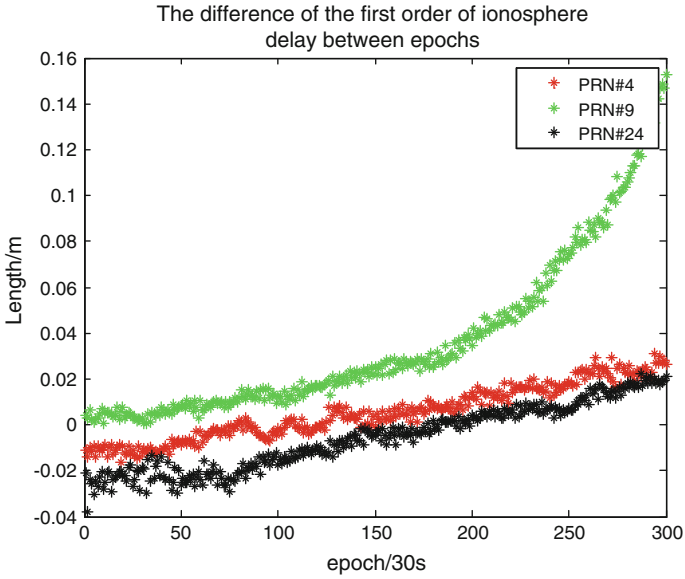

Fig. 2 First order, time difference of ionosphere adjacent epochs delay of different satellite

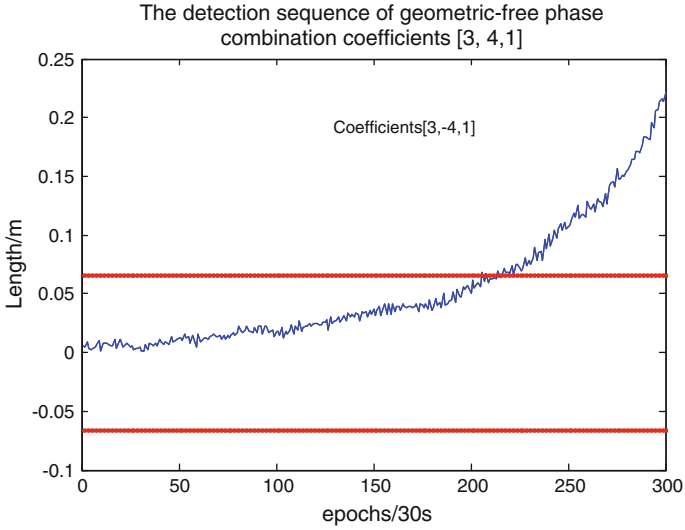

Fig. 3 The cycle-slip detection sequence of geometric-free phase combination coefficients [1, 3, 4]

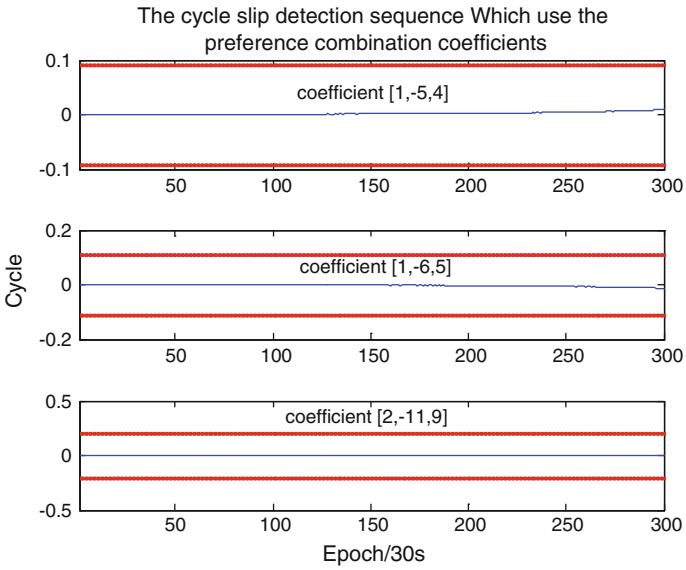

Fig. 4 Cycle-slip detection sequence without any jumps

cycle-slip detection is still small. So the improved algorithms can detect cycle slip under high ionospheric activity with high accuracy.

4.2 Small Jumps

Cycle slip (1, 0, 0) is added to the GPS L1, L2, and L5 carrier phase data at epoch 100. Cycle-slip detection result is shown in Fig. 5.

4.3 Big Jumps and Continuous Jumps

Cycle slip (1, 2, 3) is added to the GPS L1, L2, and L5 carrier phase data at epoch 100. Cycle slip (1, 1, 2) is added at epoch 101, and large cycle slip (4, 1, 5) is added at epoch 200. Cycle-slip detection results are shown as follows (Fig. 6).

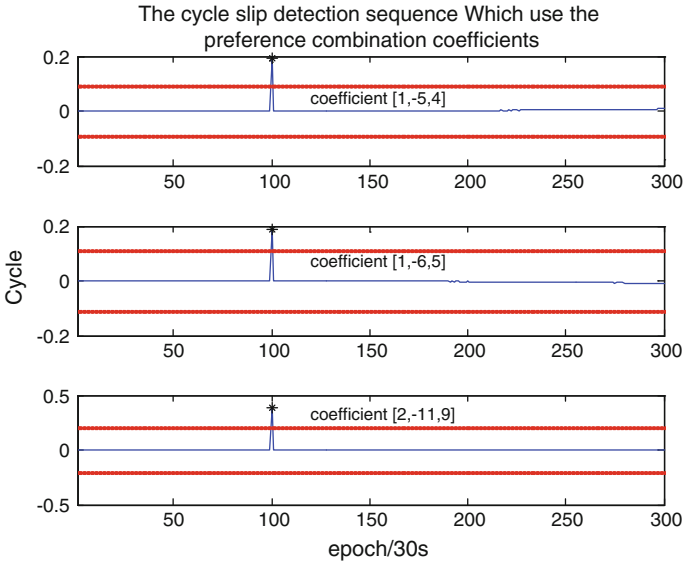

Fig. 5 Cycle-slip detection of small cycle slip (1, 0, 0)

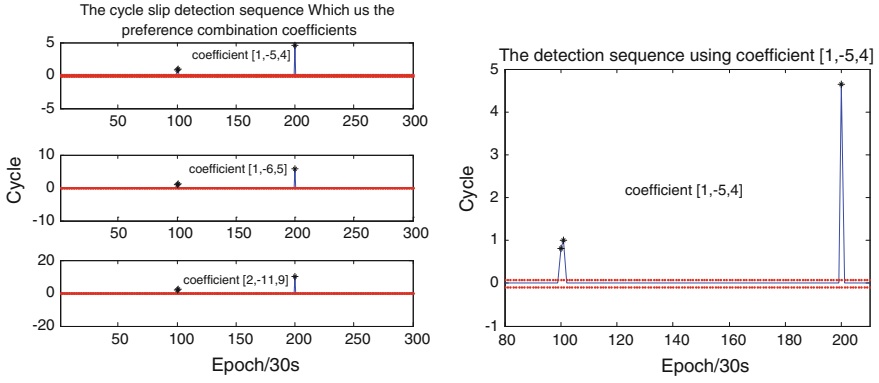

Fig. 6 Cycle-slip detection results of big jump and continuous jump

4.4 Insensitive Jumps

Cycle slip (1, 6, 7) is added to the GPS L1, L2, and L5 carrier phase data at epoch 100, and cycle slip (1, 1, 1) is added at epoch 150. Where cycle slip (1, 1, 1) is the common insensitive jump for that three row combination coefficients, and cycle slip (1, 6, 7) is the insensitive jump only for detection combination coefficient [1, −5, 4].

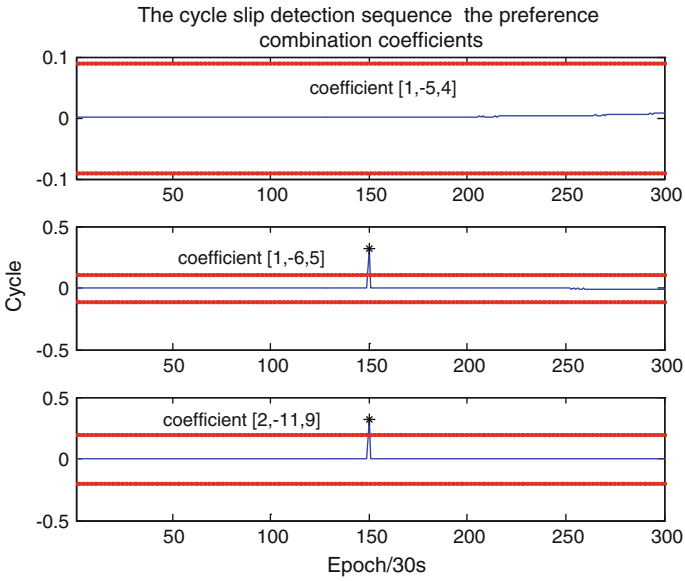

Fig. 7 Cycle-slip detection result of insensitive jump

Based on theoretical analysis and Fig. 7, we can know that the common insensitive jumps are satisfied $\Delta N_1 = \Delta N_2 = \Delta N_5 = a$ (where a represents integer). If cycle slip is times of (1, 1, 1), that all three combinations could not detect it. Generally, dual-frequency, first order, time-difference phase ionospheric residual method is used to detect jump (1, 1, 1). But from Fig. 8a, we know that this method is also affected by the ionosphere delay. The fluctuation range of its cycle-slip detection sequence will exceed its detection threshold under high ionospheric activity, therefore, this method cannot detect the cycle slip (1, 1, 1) accurately either. Based on theoretical analysis and Fig. 8b, we know that the method of dual-frequency second-order, time-difference phase ionospheric residual can significantly weaken the effects of the ionosphere delay. The fluctuation range of its cycle-slip detection sequence does not exceed its detection threshold, so we can use this method to detect the common insensitive jump (1, 1, 1) under high ionospheric activity.

Applying the method of the second-order, time-difference phase ionospheric residual to detect the insensitive jump. The results are as follows (Fig. 9).

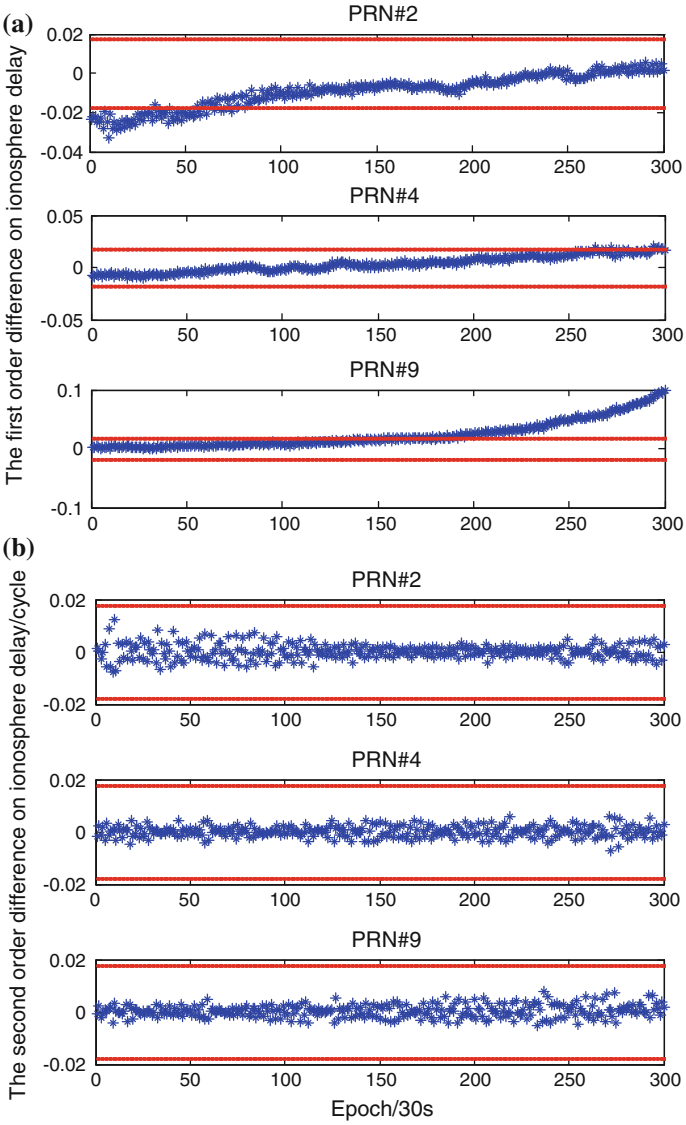

Fig. 8 The result of the first-order residual and the second-order residual of ionosphere

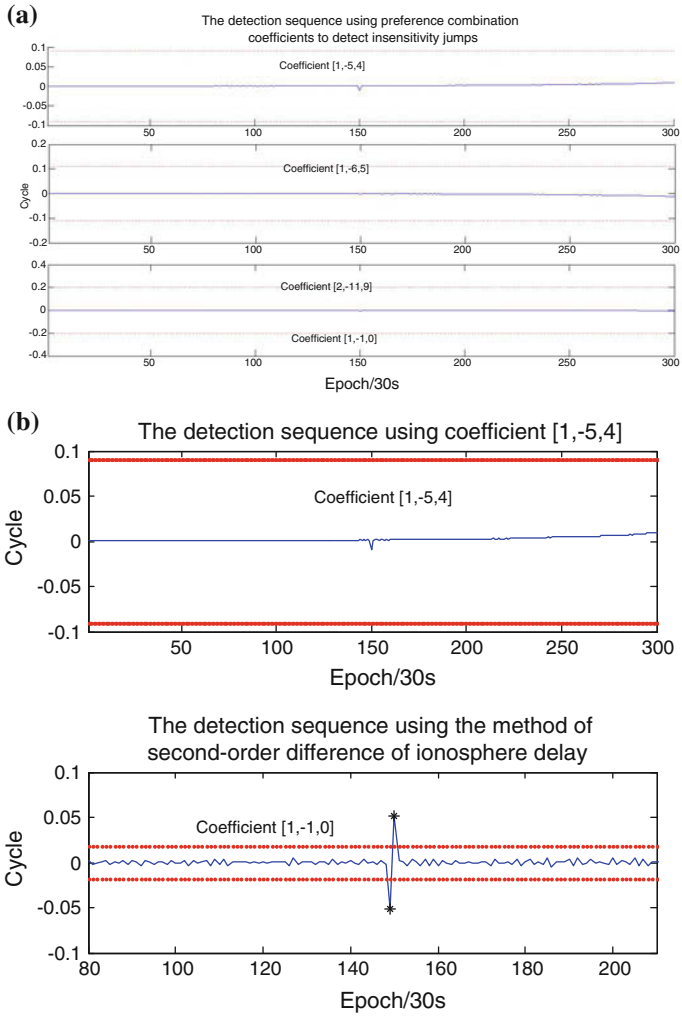

Fig. 9 Cycle-slip detection results applying the second-order, time-difference phase ionospheric residual method

5 Conclusion

The results of experiment reveal that the modified algorithm can overcome the disadvantages of the traditional method such as pseudo range/carrier phase method and triple-frequency geometric-free phase method. And it also can detect all kinds of cycle slip under the condition of high ionospheric activity with high success rate.

The algorithm is very effective to detect the cycle slip in the dynamic, undifferenced observations, and has great significance to enhance the stability of the receiver in harsh environments.

References

1. Yang Y (2010) Progress, contribution and challenges of Compass/BeiDou satellite navigation system. Acta Geodaetica Cartogr Sin 39(1):1–6
2. Wang Z, Liu J (2006) Model of inter-frequency combinations of Galileo GNSS. Geomatics Inf Sci Wuhan Univ 28(6):723–727
3. Cocard M, Bourgon S, Kamali O et al (2008) A systematic investigation of optimal carrier-phase combinations for modernized triple-frequency GPS. J Geodesy 82(9):555–564
4. Huang L, Song L, Liu X (2011) Optimization and selection of GPS triple-carries phase combination observations based self-adaptive clustering algorithm. J Geodesy Geodyn 311(4):99–102
5. Li J, Yang J, Xu J et al (2011) Real-time cycle-slip detection and repair based on code-phase combinations for GNSS triple-frequency undifferenced observations. Acta Geodaetica Cartogr Sin 40(6):717–722
6. Huang L, Song L, Wang Y et al (2012) BeiDou triple-frequency geometry-free phase combination for cycle-slip detection and correction. Acta Geodaetica et Cartographica Sin 41(5):763–768
7. Cao X, Wang J (2014) Cycle-slip detection and repair using GPS triple-frequency undifferent observations. Geomatics Inf Sci Wuhan Univ 39(4):450–456
8. Dai Z, Knedlik S, Loffeld O (2009) Instantaneous triple-frequency GPS cycle-slip detection and repair. Int J Navig Obs 23(1):28–43. doi:10.1155/2009/407231
9. De Lacy MC, Reguzzoni M, Sansof F (2012) Real-time cycle slip detection in triple-frequency GNSS. GPS Solutions 16(3):353–362
10. Yu X (2011) Muti-frequency GNSS precise positioning theory and method research. Wuhan University, Wuhan
11. Banville S, Langley RB, Saito S et al (2010) Handing cycle slips in GPS data during ionospheric plasma bubble events. Radio Sci 45(6):15–31
12. Teunissen PJG, De Bakker PF (2013) Single-receiver single-channel multi-frequency GNSS integrity: outliers, slips and ionospheric disturbances..J Geodesy 87(2):161–177
13. Wu Y (2005) The theory and application multi-frequency data processing of GNSS. Wuhan University, Wuhan
14. Jin R, Jin S, Tao X (2014) Ionospheric anomalies during the March 2013 geomagnetic storm from BeiDou Navigation satellite System (BDS) Observations. Sun JD, Jiao WH, Wu HT et al (eds) China Satellite Navigation Conference(CSNC) 2014 Proceedings, vol I, Springer, Heidelberg, pp 97–104

Resolving the Regional Ionospheric Grid Model by Applying Kalman Filter

Hongliang Cai and Qian Wang

Abstract Ionospheric is the largest error source in the high-precision navigation and positioning. However, single-frequency users can only get the correction by broadcast of the ionosphere models. In this paper, advantages and disadvantages of several kinds of current models are compared, and finally we choose the regional grid modeling. Based on GPS data of "Crustal Movement Observation Network of China" (CMONOC), we extract ionospheric delay from leveled carrier phase observations and take VTEC of the grid points and DCB of receivers as parameters, then describe each state variable with random walk model, thus, setting up the regional ionospheric grid model using the Kalman filter estimation epoch by epoch, which gained good results. Taking global ionospheric maps (GIM) as reference, their variations characteristics of VTEC (vertical total electron content)were consistent. The inner precision of the model ranging from 1 to 3 TECU was detected, and the RMS were about 2.5 TEC and residuals were around 3 TECU. Besides, variations of receiver hardware delay within 2 TECU were relatively smooth. Compared with the regional stations' receiver DCB isolated from the original observation using satellite DCB and spherical harmonic coefficients, the mean differences for a week were all within 2 ns. In addition, the results showed that less stations around grid leading to lower precision of VTEC because of shortage of the observations, and thus the greater the receiver DCB error was.

Keywords Ionosphere · Kalman filter · VTEC · DCB

H. Cai
Beijing Institute of Tracking and Telecommunication Technology, Beijing, China
e-mail: caibanyu@126.com

Q. Wang (✉)
Wuhan University GNSS Research Center, Wuhan, China
e-mail: 2010301610062@whu.edu.cn

© Springer Science+Business Media Singapore 2016

J. Sun et al. (eds.), *China Satellite Navigation Conference (CSNC) 2016 Proceedings: Volume III*, Lecture Notes in Electrical Engineering 390,
DOI 10.1007/978-981-10-0940-2_37

1 Introduction

Since the cancelation of SA policy, ionospheric delay is the most significant error source in the GNSS navigation and positioning. Dual-frequency correction method can be used to eliminate the ionospheric delay by users with the GNSS dual-frequency receivers. However, extensive users with the GNSS single-frequency receivers have to be corrected by ionospheric delay models.

Ionosphere models are divided into empirical and nonempirical models. Empirical models such as Klobuchar model, which sees ionospheric delay as a constant of 5 ns at night and as the positive parts of a cosine function during the day, is simple and practical, but the precision with error of the actual delay about 30–40 % is not high [1]; whereas nonempirical models such as grid model [2–5] is the hotspot of the ionosphere modeling, also a method of high precision. Among them, current common grid models are regional weighted average method, triangle grid interpolation method, kriging interpolation, etc. During practical test, limitations exist [1]. Such as the grid algorithm of regional weighted average method, it cannot separate hardware delay and users have to get the hardware delay accurately first, then estimate ionosphere delay of grid points with absolute ionospheric delay; another example, the parameters of stations and satellites of triangular grid interpolation method, which there are too many parameters and a large amount of calculation, cannot be separated because of their correlation in column [2].

Given that variation of regional satellite hardware delay being small and relatively stable in a short period, we can fix the satellite hardware directly by means of GIM. The algorithm resolves both ionospheric delay and receiver hardware simultaneously. Divide the whole area into uniform grid and apply GPS dual-frequency data, subsequently build the observation equation by adopting a certain spatial interpolation method, and estimate model parameters based on Kalman filter epoch by epoch, thus setting up the regional ionospheric grid model.

2 Establishment of Model

2.1 Calculation of the VTEC

Single-layer ionospheric grid model is based on the assumption that the electrons above the Earth concentrating in an infinitely thin monolayer usually as 450 km (ionosphere highest density of free electron content in the height between 350 and 450 km). Applying a certain projection function, we project the slant total electron content (STEC) onto the single sphere, then convert it to the zenith direction called VTEC. The sphere is divided into a number of grids radially and latitudinally; then VTEC over users can be interpolated with VTEC at the grid points. VTEC at each puncture point (intersection of the satellite signal propagation path and the center of the ionosphere) in the grid area which are obtained with dual-frequency GPS

observations can be used to establish ionospheric delay model within the region by means of mathematical fitting.

In the process of measuring ionospheric STEC with the dual-frequency pseudorange observations, we replace the observations of P1 code by CA code when short of observations of P2 code. Besides, a combination of pseudo-range observations smoothed by carrier phase is used because of the higher accuracy of carrier phase observations than the pseudorange by two orders of magnitude. STEC is calculated as follows:

$$\mathrm{STEC} = 9.52437(\mathrm{P}_2 - \mathrm{P}_1) + 9.52437(b + B) \tag{1}$$

With STEC the slant total electron content between receiver antenna to satellite, $(\mathrm{P}_2 - \mathrm{P}_1)$ the smoothed pseudorange observations, b and B the satellite and receiver hardware delay (difference of hardware delay between satellite and receiver generated by signals of two frequency, which is also known as Differential Code Bias DCB), respectively.

In the process of converting STEC to the VTEC, MSLM projection function is,

$$\mathrm{F}(z) = \frac{1}{\cos(z')}$$

Where z is the zenith distance at the puncture point.

$$\mathrm{VTEC} = \mathrm{STEC}/\mathrm{F}(z) = \mathrm{STEC} * \cos(z') \tag{2}$$

2.2 Grid Model Method

Grid model is built up with the method of linear interpolation by fixing the satellite DCB firstly and setting VTEC of grid nodes and DCB of receivers to be estimated parameters based on the correlation of spatial distances between VTEC at the puncture point and grid points. Observation equations are as follows:

$$\mathrm{VTEC}_{\mathrm{IPP}} - b = \sum_{i=1,2,3,4} W(d_i) \cdot \mathrm{VTEC}_i + B \tag{3}$$

With B and b the DCB of the receiver and satellite, respectively, seen as global variables for several periods a day and one set a day are estimated, VTEC at grid nodes and DCB of the receivers are estimated at the same time; $W(d_i)$ is the weight function for which our algorithm adopts the method of inverse distance weighting. The puncture point diagram is as shown in Fig. 1.

Where IGP represents grid point, d_1, d_2, d_3, d_4 are distances between the puncture points to four grid points, respectively.

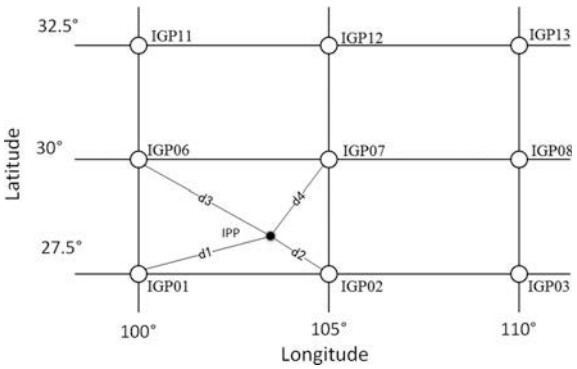

Fig. 1 Puncture point diagram

2.3 Kalman Filter Estimation

Kalman filter estimation uses the state equation to estimate new state values recursively according to the state estimation of the last moment and the current observations. As one of the analysis center, JPL just uses the Kalman filter estimation. Kalman filter is able to overcome the defects of parameters being relevant in the least squares method in different time, which makes filtering results smoother and more accurate.

2.3.1 Observation Equation

Refer to the Fig. 1, set $d = 1/d_1 + 1/d_2 + 1/d_3 + 1/d_4$

$$k_i = \frac{1/d_1}{d}, l_i = \frac{1/d_2}{d} m_i = \frac{1/d_3}{d}, n_i = \frac{1/d_4}{d}$$

Express the VTEC at the puncture points as the function of four grid nodes, respectively. The observation equation correspondingly is

$$\mathrm{VTEC}_i = k_i * x_i + l_i * x_{i+1} + m_i * x_{i+5} + n_i * x_{i+6} + \frac{1}{\mathrm{F}(z)} * B + \frac{1}{\mathrm{F}(z)} * b \quad (4)$$

Where x_i, x_{i+1}, x_{i+5} and x_{i+6} denote VTEC at four grid points around a certain grid, VTEC_i denote the VTEC at the puncture point.

Measurement variances are decided according to the elevation angle of the puncture point, namely the lower the elevation angle is, the greater the variance will be.

In conclusion, we take all parameters to be estimated as state vector in Kalman filter estimation, namely all VTEC at grid points and DCB of all receivers. $\hat{X}_k = [x_1\ x_2 \ldots x_i \ldots B_1\ B_2 \ldots B_j \ldots]_k^T$. Thus the Kalman filter equation is denoted as

$Z_k = H_k X_k + V_k$, where $Z_k = [\mathrm{VTEC}_k^i - \frac{1}{\mathrm{F}(z)} * b_k]$, $H_k = [0 \ldots k_k^i \ l_k^i \ m_k^i \ n_k^i \ldots 0 \ldots \frac{1}{\mathrm{F}(z)} \ldots]$,$V_k$ stands for measurement noise of Gaussian.

2.3.2 State Equation

Between each period, aiming at the characteristics of random walk of VTEC and DCB, we describe each state variable with random walk model in accordance with zero-mean and random process characteristics of a linear variance transformation over time, thus spacial state model is denoted as follows:

$$\hat{X}_{k/k-1} = \Phi_{k,k-1}\hat{X}_{k-1} + W_k \tag{5}$$

Where W_k is Gaussian white noise whose mean value is 0, and the rate of the variance is obtained by experience

$$\Delta\sigma = \dot{q}t \tag{6}$$

Where $\Delta\sigma$ is the increment of the standard deviation, $\dot{q}$ is the rate of change of the standard deviation with time, which means standard deviation is a random quantity changing over time. High-precision results could be acquired by selecting appropriate $\dot{q}$ according to experience.

2.3.3 Recursive Algorithm

Applying the observation equation and state equation above, the recursion procedure of Kalman filtering is as follows:

$$\begin{aligned}
&(1)\hat{X}_{k/k-1} = \Phi_{k,k-1}\hat{X}_{k-1},\\
&(2)\hat{X}_k = \hat{X}_{k/k-1} + K_k(Z_k - H_k\hat{X}_{k/k-1}),\\
&(3)K_k = P_{k/k-1}H_k^T(H_kP_{k/k-1}H_k^T + R_k)^{-1},\\
&(4)P_{k/k-1} = \Phi_{k,k-1}P_{k-1}\Phi_{k,k-1}^T + Q_{k-1},\\
&(5)P_k = (I - K_kH_k)P_{k/k-1}(I - K_kH_k)^T + K_kR_kK_k^T
\end{aligned} \tag{7}$$

Among them, I is the unit matrix, Q_{k-1} is covariance matrix for the system process, $Q(k) = E[W_kW_k^T]$,R_k is the covariance matrix of the observation noise,$R_k = E[V_kV_j^T]$, initially recursive value namely $\hat{X}_0$, P_0 need to be predesigned.

3 Results

3.1 Data Declaration

In order to verify the validity of the algorithm, we adopted the data of "Crustal Movement Observation Network of China" (CMONOC) for 97 stations in 2014. First of all, pseudorange observations are leveled by carrier phase to get high-precision ionospheric delay measurements. Then model with the grid algorithm, finally estimate the VTEC at grid points and DCB of receivers using Kalman filter of each epoch. The grid range is as follows: north latitude for 27.5°–40° and east longitude for 100°–120°, the size for 2.5° × 5°, temporal resolution for 30 s. Station distribution figure is shown in Fig. 2.

3.2 Selection of Initial Value

Calculate data for a week by applying the least squares estimation method on the measurement equation, and take the VTEC at grid points at first epoch everyday as initial VTEC of $\hat{X}_0$. Then the average value of diurnal DCB variation for each station for a week is recalculated, which are assigned to each station as the initial DCB values, that is as the initial DCB in $\hat{X}_0$. Set P_0 to be a unit matrix.

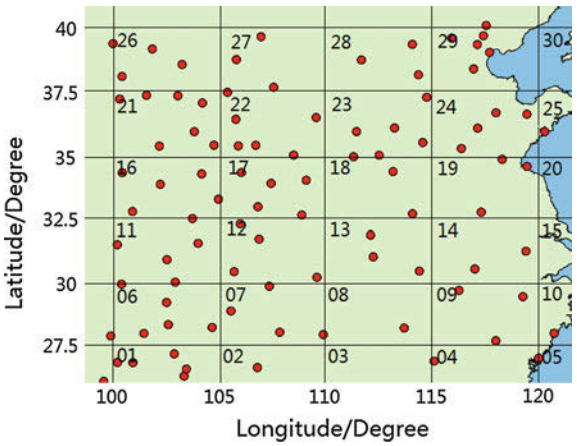

Fig. 2 Station distribution figure

Table 1 Statistical table of daily mean RMS

Doy	309	310	311	312	313	314	315
Mean RMS/TECU	2.28	2.96	2.18	2.45	2.23	2.63	2.13

3.3 Result Analysis

RMS in November 5–11 (doy 309–315) were calculated, and their mean values are shown as Table 1.

The from shows the mean RMS is around 2.5 TECU, and the precision of inner coincidence of the model is good.

3.3.1 Analysis of VTEC of Grid Point

With GIM as reference, compare the VTEC between grid algorithm and GIM. For clarity, Fig. 3 shows the difference of VTEC for doy310 with CODE to check the

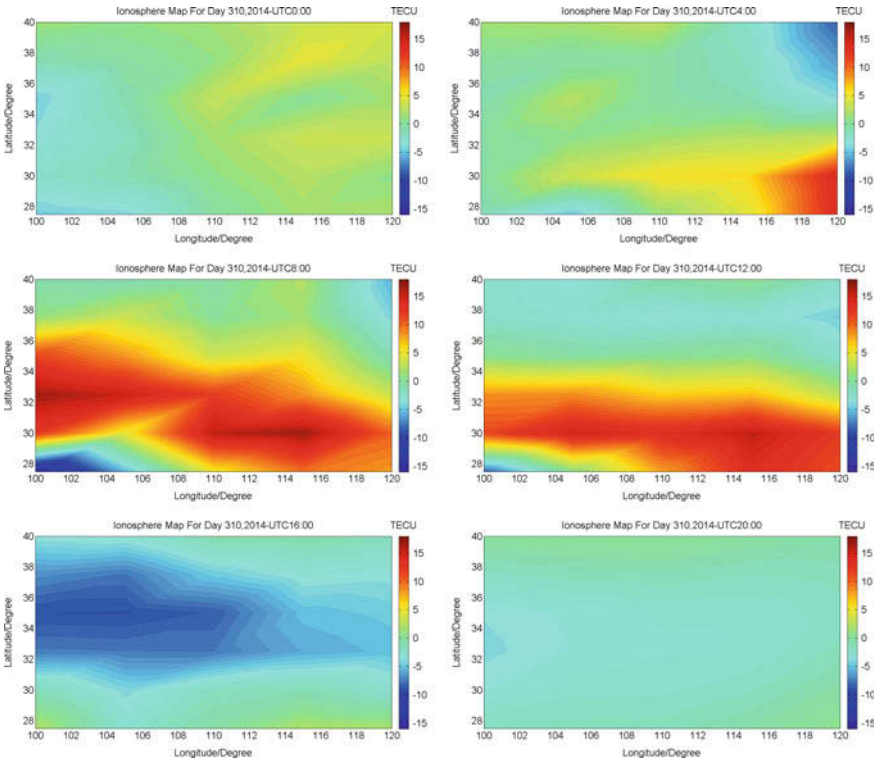

Fig. 3 Differentials of VTEC in doy310

variation of VTEC precision during a day. Due to limited space, we choose the interval to be 4 h, and plot the difference figures in UTC0:00, UTC4:00, UTC8:00, UTC12:00, UTC16:00, UTC20:00 as follows:

Obviously, the difference in low latitude area is greater than in high latitudes, because the closer to the equator, more violent the ionospheric variations will be, and thus greater the error will be, which accords with the characteristics of ionosphere. Besides, it seems the difference is greater during the day than at night, and more obvious in UTC8:00 and UTC12:00, which is caused by the violent solar activity and inaccurate descriptions in detail of the GIM resulting from building globally with less Chinese stations and regionally smoothed. However, in this paper, full consideration to the temporal and spatial variation of the grid parameters are taken by applying the Kalman filter algorithm, which fits the regional changes better, thus resulting in greater bias in the noon.

3.3.2 Analysis of Receiver Hardware Delay DCB

The maximum error of ionospheric delay is hardware delay (the sum of the hardware delay of both satellites and receivers) of GNSS system, so the stability of the receiver DCB is also an important method to evaluate the accuracy of ionosphere modeling.

Four stations located in the inner region were selected to show the receiver DCB obtained by using Kalman filter estimation as shown in Fig. 4.

It is observed that the variations of the DCB are stable, and the accuracy with daily variation about 1 ns is better.

Compare the receiver DCB of last epoch with the regional station receiver hardware delay isolated from the original observation using satellite hardware delay and spherical harmonic coefficients, whose differences reflect outer precision of DCB. By analyzing data for a week and comparing their mean daily difference, results are shown in Fig. 5. Among the figure, the red points correspond to the

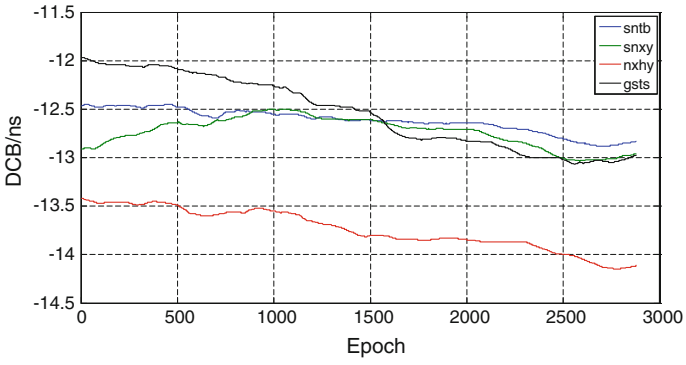

Fig. 4 Estimated DCB of four stations

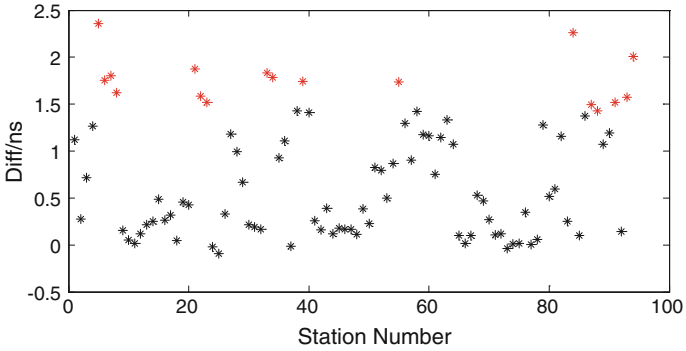

Fig. 5 Daily differences of receiver DCB for a week

stations in edge regions, and the black points correspond to the stations in the central area.

There is greater receiver DCB bias beyond 1.5 ns of the stations in the edge region, however, most of the central stations are within 1 ns, which is caused by less stations and insufficient observations in the edge region. Whereas, stations in the central region were more, which contributed to the better fitting effect and higher precision.

4 Conclusions

With the algorithm of fixing satellite DCB, and setting up the regional ionospheric grid model based on the Kalman filter estimation, we took GNSS data for 7 days from November 5, 2014 to November 11 to test. The results show that the accuracy of ionosphere delay a grid points are higher, the receiver hardware delays within 2 ns are relatively stable. Besides, the results demonstrate that grid point with less station around lead to poorer accuracy of receiver DCB. Further studies will apply the grid model to the regional positioning to test the accuracy of the model.

Acknowledgements Thanks to Key Program of National Natural Science Foundation of China (41231064) and National High Technology Research and Develop Program of China (2014AA123101) and other subjects for subsidizing research. At the same time, thanks to the Crustal Movement Observation Network of China" (CMONOC) for providing the observation data.

References

1. Zhang X, Li Z, Zhang J Research for regional VTEC ionospheric models by using GPS observation
2. Zhang H (2006) Regional ionospheric monitoring and delay correction based on the ground-based GPS in China. Graduate University of the Chinese Academy of Sciences, Beijing, pp 10–16
3. Yuan Y (2002) Theory and method of regional ionospheric monitoring and delay correction based on the GPS. Beijing: Graduate University of the Chinese Academy of Sciences. Graduate University of the Chinese Academy of Sciences, Beijing, pp 3–4
4. Liu J, Chen J, Zhang Y et al (1999) Wide-area differential GPS principle and method. Publisher of surveying and mapping, Beijing, pp 90–100
5. Geng C (2011) Theory and method of ionospheric real-time monitoring and delay correction based on the ground-based GNSS. Wuhan University
6. Ciraolo L, Azpilicueta F, Brunini C, Meza A, Radicella SM (2007) Calibration errors on experimental slant total electron content (TEC) determined with GPS. J Geodesy 81(2)
7. Huang L, Zhang H, Xu P VTEC modeling with Kriging algorithm over China Area
8. Geng C, Zhang H, Zhai C (2009) Solving the hardware delay in real time by applying Kalman filter. Geomatics Inf Sci Wuhan Univ (Sci Inf Part) 11:1309–1311+1323
9. Zhang H, Shi C, Tang W (2008) Unified calculation and analysis of ground-based GPS regional ionospheric polynomial model and the hardware delay. Geomatics Inf Sci Wuhan Univ (Sci Inf Part) 08:805–809
10. Ciraolo L, Azpilicueta F, Brunini C, Meza A, S.M. Radicella S (2007) Calibration errors on experimental slant total electron content (TEC) determined with GPS. J Geodesy 81(2)
11. Zhang H, Han W, Huang L, Geng C (2012) Modelling global ionospheric delay with IGS ground-based GNSS observations. Geomatics Inf Sci Wuhan Univ (Sci Inf Part) 10:1186–1189+1261–1262

Study in BDS Triple-Frequency Phase Ionospheric Delay Estimation and Code Hardware Delay Separation Method

Huarun Wang, Hongzhou Chai, Yang Chong and Yulong Kong

Abstract Precise phase ambiguity resolution is needed to obtain high-precise ionospheric delay with the phase observations, extreme wide-lane (EWL) combination can be easily fixed owing to the long wavelength, MW combination wide-lane (WL) ambiguity fixing may fail because of the influence of code hardware delay, observation noise, and multipath. In this paper, BDS triple-frequency observation and GIM production is applied to fix the WL ambiguity with the fixed EWL ambiguity and phase WL geometry-free (GF) combination, then high-precise ionospheric delay is reconstructed with the fixed ambiguities, also the satellite and receiver code hardware delay is separated. The test results show an obvious improvement of WL ambiguity success rate of fixing, and a systemic bias of 0.5–0.8 m exists between the reconstructed ionospheric delay and GIM correction, meaning an equivalent ionospheric delay correction precision of 3–5 TECU. The separated code hardware delay is stable and the stability of GEO and IGSO satellites is obviously better than MEO satellites, also the code hardware delay bias between different frequencies of IGSO satellites coincides best with DCB estimated from ionosphere modeling.

Keywords BDS triple frequency · Ambiguity fixing · GIM · Ionosphere reconstruction · Code hardware delay separation

1 Introduction

As one of the key influence factor to GNSS users, providing high-precision ionospheric delay is the most important approach to improve the precision in navigation and positioning [1–3]. Currently, the most used methods to deal with ionospheric delay include eliminating the ionosphere information such as ionosphere-free (IF) combination and correcting with ionosphere model, IF combination may

H. Wang (✉) · H. Chai · Y. Chong · Y. Kong
Geography Space Information Institute, Information Engineering University, Zhengzhou 450052, China
e-mail: 593855433@qq.com

© Springer Science+Business Media Singapore 2016

J. Sun et al. (eds.), *China Satellite Navigation Conference (CSNC) 2016 Proceedings: Volume III*, Lecture Notes in Electrical Engineering 390,
DOI 10.1007/978-981-10-0940-2_38

enlarge the observation noise, Kloubchar ionosphere model that navigation users adopt most can only correct for about 60 % of the ionospheric delay. Although post-processing precise ionosphere grid product based on global monitoring stations observation provided by international organizations like IGS analyzing center may reach the precision of 2–8 TECU (1TECU arouses near 0.165 m ionospheric delay error on BDS L1 frequency) [4], GIM correction precision may distribute nonuniform in different regions due to the limitation of monitoring stations location, and decreases when ionosphere severe variation incident occurred [5]. In recent years, multi-frequency technology has developed rapidly, the increase of frequency provides more redundancy observations and promotes carrier phase ambiguity fixing aided by excellent combinations [6]. Jian et al. [7] used GPS EWL ambiguity to resolve the double-difference ionospheric delay; Li [8, 9] proposed a method to get distance-independent triple-frequency ambiguity resolution using semi-generated triple-frequency GPS signals. Fan et al. [10] introduced an approach to analyze BDS satellites DCB precision based on triple-frequency observations. In this paper, multi-frequency WL ambiguity fixing idea is first adopted to propose a method to fix BDS triple-frequency WL ambiguity with the aid of GIM correction, and then high-precision triple-frequency ionospheric delay is reconstructed, lastly the sum of satellite and receiver code hardware delay is separated using MW combination ambiguity.

2 Principle and Methodology

2.1 Ambiguity Fixing and Ionosphere Reconstruction

Triple-frequency pseudorange and phase observation equations (unit: m) can be expressed as follows:

$$\begin{aligned} P_1 &= \rho + \frac{I}{f_1^2} + d_{P1} + \varepsilon_{P1} \quad L_1 = \rho - \frac{I}{f_1^2} + d_{L1} + \lambda_1 N_1 + \varepsilon_{L1} \\ P_2 &= \rho + \frac{I}{f_2^2} + d_{P2} + \varepsilon_{P2} \quad L_2 = \rho - \frac{I}{f_2^2} + d_{L2} + \lambda_2 N_2 + \varepsilon_{L2} \\ P_3 &= \rho + \frac{I}{f_3^2} + d_{P3} + \varepsilon_{P3} \quad L_3 = \rho - \frac{I}{f_3^2} + d_{L3} + \lambda_3 N_3 + \varepsilon_{L3} \end{aligned} \tag{1}$$

Where ρ represents the geometry term independent of frequency, I represents ionosphere parameter, λ represents the wavelength, N represents phase ambiguity on origin frequency, d represents the sum of satellite and receiver code hardware delay, ε represents the influence of observation multipath and noise.

In general phase, geometry-free combination is used to calculate the high-precision ionospheric delay, WL combinations with longer wavelength and

Table 1 The character of BDS triple-frequency phase combinations

Combination coefficient			Wavelength (m)	Ionosphere parameter (cycle)	Ionosphere parameter (m)	Noise parameter (cycle)	Noise parameter (m)
i	*j*	*k*					
Combinations with long wavelength							
0	−2	2	2.442	−0.652	−1.591	2.828	6.907
0	−1	1	4.884	−0.326	−1.591	1.414	6.907
1	−1	0	0.847	−1.527	−1.293	1.414	1.198
1	0	−1	1.025	−1.201	−1.231	1.414	1.449
1	1	−2	1.297	−0.875	−1.135	2.449	3.176

smaller noise are chosen to resolve the phase ambiguity. Table 1 shows the BDS triple-frequency combinations that meet the need of the proposed character [11, 12].

In this paper combinations (0, 1, −1) and (1, 0, −1) are chosen to resolve the ambiguity, the corresponding phase EWL and WL combinations can be expressed as follows:

$$\begin{aligned}\Phi_{\mathrm{ewl}} &= \frac{f_2 L_2 - f_3 L_3}{f_2 - f_3} = \rho + \frac{I}{f_2 f_3} + \lambda_{\mathrm{ewl}} N_{\mathrm{ewl}} \\ \Phi_{\mathrm{wl}} &= \frac{f_1 L_1 - f_3 L_3}{f_1 - f_3} = \rho + \frac{I}{f_1 f_3} + \lambda_{\mathrm{wl}} N_{\mathrm{wl}}\end{aligned} \tag{2}$$

Where $\lambda_{\mathrm{ewl}} = \frac{c}{f_2 - f_3}, N_{\mathrm{ewl}} = N_2 - N_3$ represents the EWL wavelength and ambiguity, respectively, $\lambda_{\mathrm{wl}} = \frac{c}{f_1 - f_3}, N_{\mathrm{wl}} = N_1 - N_3$ represents the WL wavelength and ambiguity, respectively, the geometry-free combination can be got by differing the two equations according to (2).

$$\Phi_{\mathrm{GF}} = \Phi_{\mathrm{ewl}} - \Phi_{\mathrm{wl}} = \left(\frac{1}{f_2 f_3} - \frac{1}{f_1 f_3}\right) I + (\lambda_{\mathrm{ewl}} N_{\mathrm{ewl}} - \lambda_{\mathrm{wl}} N_{\mathrm{wl}}) \tag{3}$$

So we get the ionospheric delay corresponding to L1 frequency.

$$\mathrm{sTEC} = \frac{I}{f_1^2} = \frac{\Phi_{\mathrm{GF}} - (\lambda_{\mathrm{ewl}} N_{\mathrm{ewl}} - \lambda_{\mathrm{wl}} N_{\mathrm{wl}})}{f_1 (f_1 - f_2)} f_2 f_3 \tag{4}$$

In general, high-precision ionospheric delay is obtained through getting phase geometry-free combination and the fixed origin ambiguity, often EWL and WL and narrow-lane (NL) ambiguity fixing is needed in this process [13], however narrow-lane ambiguity is difficult to fix because of its short wavelength. Though the WL geometry-free combination enlarges the noise in (4), only WL ambiguity N_{ewl} and N_{wl} are needed to get high-precision ionospheric delay, which avoids fixing the NL ambiguity. Generally MW combination is adopted to resolve WL ambiguity as follows:

$$\begin{aligned}\hat{N}_{\mathrm{wl,km}} &= \left(\frac{f_k}{c}L_k - \frac{f_m}{c}L_m\right) - f_{\mathrm{km}}\left(\frac{f_k}{c}P_k + \frac{f_m}{c}P_m\right) \\ &= N_{\mathrm{wl,km}} + \frac{f_k}{c}\left(d_{L,k} + \varepsilon_{L,k}\right) - \frac{f_m}{c}\left(d_{L,m} + \varepsilon_{L,m}\right) \\ &\quad - f_{\mathrm{km}}\frac{f_k}{c}\left(d_{P,k} + \varepsilon_{P,k}\right) - f_{\mathrm{km}}\frac{f_m}{c}\left(d_{P,m} + \varepsilon_{P,m}\right)\end{aligned} \tag{5}$$

Where k, m represents different frequency and $f_{km} = \frac{f_k - f_m}{f_k + f_m}$, phase hardware delay and noise can be ignored compared to code pseudorange, so the main factors that influence WL ambiguity are code hardware delay, multipath, and noise, WL ambiguity can be expressed as follows:

$$\begin{aligned}\hat{N}_{\mathrm{ewl}} &= \left(\frac{f_2}{c}L_2 - \frac{f_3}{c}L_3\right) - f_{23}\left(\frac{f_2}{c}P_2 + \frac{f_3}{c}P_3\right) \\ &= N_{\mathrm{ewl}} - f_{23}\frac{f_2}{c}\left(d_{P2} + \varepsilon_{P2}\right) - f_{23}\frac{f_3}{c}\left(d_{P3} + \varepsilon_{P3}\right) \\ \hat{N}_{\mathrm{wl}} &= \left(\frac{f_1}{c}L_1 - \frac{f_3}{c}L_3\right) - f_{13}\left(\frac{f_1}{c}P_1 + \frac{f_3}{c}P_3\right) \\ &= N_{\mathrm{wl}} - f_{13}\frac{f_1}{c}\left(d_{P1} + \varepsilon_{P1}\right) - f_{13}\frac{f_3}{c}\left(d_{P3} + \varepsilon_{P3}\right)\end{aligned} \tag{6}$$

According to the random character of observation noise, smoothing can weaken the influence of noise obviously. Benefiting from the long wavelength up to 4.88 m of the combination (0, 1, −1), EWL ambiguity is limitedly influenced by code hardware delay and noise, so the single epoch success rate of fixing is rather high after smoothing. However, the wavelength of the combination (1, 0, −1) is only 1.03 m, WL ambiguity is more easily influenced by code hardware delay and noise, resulting a lower success rate of fixing. In order to avoid involving the noisier pseudorange observations, phase geometry-free combination is adopted to resolve WL ambiguity under the condition of the fixed EWL ambiguity [14].

$$\begin{aligned}\hat{N}_{\mathrm{Dwl}} &= \varphi_{\mathrm{wl}} - \left(\varphi_{\mathrm{ewl}} - N_{\mathrm{ewl}}\right)\frac{\lambda_{\mathrm{ewl}}}{\lambda_{\mathrm{wl}}} \\ &= N_{\mathrm{wl}} + \frac{f_2 - f_1}{f_1 f_2 f_3 \lambda_{wl}} I\end{aligned} \tag{7}$$

According to (7), WL ambiguity is mainly influenced by ionospheric delay, supposed that the magnitude can be expressed as (8).

$$\frac{f_2 - f_1}{f_1 f_2 f_3 \lambda_{\mathrm{wl}}} I = \Delta N_{\mathrm{wl,Ion}} + \delta N_{\mathrm{wl,Ion}} \tag{8}$$

Where $\Delta N_{\mathrm{wl,Ion}}$ and $\delta N_{\mathrm{wl,Ion}}$ represents the integer and fractional part of the influence of ionospheric delay to WL ambiguity, respectively.

$$\hat{N}_{\mathrm{Dwl}} = N_{\mathrm{wl}} + \Delta N_{\mathrm{wl,Ion}} + \delta N_{\mathrm{wl,Ion}} \tag{9}$$

Smoothing the float WL ambiguity and rounding it to the near integer, we get $\bar{N}_{\mathrm{wl}} = \left[\hat{N}_{\mathrm{wl}}\right]$.

$$\bar{N}_{\mathrm{wl}} = N_{\mathrm{wl}} + \Delta N_{\mathrm{wl,Ion}} \tag{10}$$

Here, GIM product is used to resolve the integer influence of ionospheric delay to WL ambiguity, however the GIM correction precision is not homogeneous in different regions in global, supposed that the integer influence of GIM correction errors to WL ambiguity can be expressed as $\Delta N_{\mathrm{wl,error}}$, according to (4) we can get the equation as (11).

$$\mathrm{sTEC}_{\mathrm{GIM}} = \frac{\Phi_{\mathrm{GF}} - \left[\lambda_{\mathrm{ewl}} N_{\mathrm{ewl}} - \lambda_{\mathrm{wl}}\left(N_{\mathrm{wl}} + \Delta N_{\mathrm{wl,error}}\right)\right]}{f_1(f_1 - f_2)} f_2 f_3 \tag{11}$$

The estimated ionospheric delay with the float WL ambiguity can be expressed as follows:

$$\mathrm{sTEC} = \frac{\Phi_{\mathrm{GF}} - \left[\lambda_{\mathrm{ewl}} N_{\mathrm{ewl}} - \lambda_{\mathrm{wl}}\left(N_{\mathrm{wl}} + \Delta N_{\mathrm{wl,Ion}} + \delta N_{\mathrm{wl,Ion}}\right)\right]}{f_1(f_1 - f_2)} f_2 f_3 \tag{12}$$

Differencing the above two equations.

$$\begin{aligned} \Delta\,\mathrm{sTEC} &= \mathrm{sTEC} - \mathrm{sTEC}_{\mathrm{GIM}} \\ &= \frac{\lambda_{\mathrm{wl}}\left(\Delta N_{\mathrm{wl,Ion}} - \Delta N_{\mathrm{wl,error}} + \delta N_{\mathrm{wl,Ion}}\right)}{f_1(f_1 - f_2)} f_2 f_3 \end{aligned} \tag{13}$$

So we get the influence of ionospheric delay to WL ambiguity.

$$\Delta \hat{N}_{\mathrm{wl,Ion,error}} = \Delta \hat{N}_{\mathrm{wl,Ion}} - \Delta \hat{N}_{\mathrm{wl,error}} = \frac{f_1(f_1 - f_2) \cdot \Delta\,\mathrm{sTEC}}{\lambda_{wl} f_2 f_3} \tag{14}$$

According to (14), the influence of GIM correction errors is directly involved to the integer cycle errors influenced by ionospheric delay to WL ambiguity. After smoothing the float ambiguity and rounding it to near integer, we get the integer influence of ionospheric delay to WL ambiguity as $\Delta N_{\mathrm{wl,Ion,error}} = \left[\Delta \hat{N}_{\mathrm{wl,Ion,error}}\right]$, the fixed WL ambiguity $N_{\mathrm{wl}} = \bar{N}_{wl} - \Delta N_{\mathrm{wl,Ion,error}}$ is obtained and triple-frequency ionospheric delay can be reconstructed with the fixed WL ambiguity.

$$\mathrm{sTEC}_{\mathrm{Triple\_frequecy}} = \frac{\Phi_{\mathrm{GF}} - \left[\lambda_{\mathrm{ewl}} N_{\mathrm{ewl}} - \lambda_{\mathrm{wl}}\left(\bar{N}_{\mathrm{wl}} - \Delta N_{\mathrm{wl,Ion,error}}\right)\right]}{f_1(f_1 - f_2)} f_2 f_3 \tag{15}$$

Differencing the reconstructed ionospheric delay and GIM correction values we get.

$$\begin{aligned} \Delta\,\mathrm{sTEC}_{\mathrm{Ion,error}} &= \mathrm{sTEC}_{\mathrm{Triple\_frequecy}} - \mathrm{sTEC}_{\mathrm{GIM}} \\ &= \frac{\lambda_{\mathrm{wl}}(\Delta N_{\mathrm{wl,Ion}} - \Delta N_{\mathrm{wl,Ion,error}} - \Delta N_{\mathrm{wl,error}})}{f_1(f_1 - f_2)} f_2 f_3 \end{aligned} \tag{16}$$

Supposed that GIM correction errors lead to several integer cycles, the variation of $\Delta\mathrm{sTEC}_{\mathrm{Ion,error}}$ can easily exceed 2.84 m according to (16), we can decide whether the WL ambiguity has been fixed or not through the variation, if failed, we can revise the WL ambiguity with $\Delta N_{\mathrm{wl,error}}$ resolved from $\Delta\mathrm{sTEC}_{\mathrm{Ion,error}}$.

2.2 Code Hardware Delay Separation

Code hardware delay on each frequency can be separated according to the reconstructed ionospheric delay, WL ambiguity and pseudorange geometry-free combination as follows:

$$\begin{aligned} \hat{N}_{\mathrm{ewl}} &= N_{\mathrm{ewl}} - \frac{f_{23} f_2}{c} d_{P2} - \frac{f_{23} f_3}{c} d_{P3} \\ \hat{N}_{\mathrm{wl}} &= N_{\mathrm{wl}} - \frac{f_{13} f_1}{c} d_{P1} - \frac{f_{13} f_3}{c} d_{P3} \\ P_i - P_j &= \left(\frac{1}{f_i^2} - \frac{1}{f_j^2}\right) I + d_{Pi} - d_{Pj} \end{aligned} \tag{17}$$

The above equations can be further expressed as

$$Ax = L \tag{18}$$

Where the GF combination in free term L can be consisted of $P_1 - P_2, P_1 - P_3, P_2 - P_3$, and the corresponding coefficient matrixes are as follows:

$$A_{12} = \begin{bmatrix} 0 & -\frac{f_{23}f_2}{c} & -\frac{f_{23}f_3}{c} \\ -\frac{f_{13}f_1}{c} & 0 & -\frac{f_{13}f_3}{c} \\ 1 & -1 & 0 \end{bmatrix}$$
$$A_{13} = \begin{bmatrix} 0 & -\frac{f_{23}f_2}{c} & -\frac{f_{23}f_3}{c} \\ -\frac{f_{13}f_1}{c} & 0 & -\frac{f_{13}f_3}{c} \\ 1 & 0 & -1 \end{bmatrix} \quad (19)$$
$$A_{23} = \begin{bmatrix} 0 & -\frac{f_{23}f_2}{c} & -\frac{f_{23}f_3}{c} \\ -\frac{f_{13}f_1}{c} & 0 & -\frac{f_{13}f_3}{c} \\ 0 & 1 & -1 \end{bmatrix}$$

The condition number of coefficient matrix is $\mathrm{cond}(A_{12}) = 97.16, \mathrm{cond}(A_{13}) = 14.32, \mathrm{cond}(A_{23}) = 11.68$, also the corresponding term related to ionosphere information in the free term is $(\frac{1}{f_1^2} - \frac{1}{f_2^2})I = -0.6724\mathrm{sTEC}$, $(\frac{1}{f_1^2} - \frac{1}{f_3^2})I = -0.5145\mathrm{sTEC}$, $(\frac{1}{f_2^2} - \frac{1}{f_3^2})I = 0.1579\mathrm{sTEC}$ respectively. In general, it can be more easily effected by observation noise because of the bigger condition number. The condition number of coefficient matrix from L2/L3 combination is the smallest, and the same reconstructed ionosphere error results the smallest effect to free term of L2/L3 combination. From all of the analysis above it can conclude that the L2/L3 GF combination is the best choice to separate code hardware delay.

$$A = \begin{bmatrix} 0 & -\frac{f_{23}f_2}{c} & -\frac{f_{23}f_3}{c} \\ -\frac{f_{13}f_1}{c} & 0 & -\frac{f_{13}f_3}{c} \\ 0 & 1 & -1 \end{bmatrix} \quad x = \begin{bmatrix} d_{P1} \\ d_{P2} \\ d_{P3} \end{bmatrix} \quad L = \begin{bmatrix} \hat{N}_{\mathrm{ewl}} - N_{\mathrm{ewl}} \\ \hat{N}_{\mathrm{wl}} - N_{\mathrm{wl}} \\ P_2 - P_3 - (\frac{1}{f_2^2} - \frac{1}{f_3^2})I \end{bmatrix} \quad (20)$$

In a short period, code hardware delay keeps stable and contributes to forecasting, deducting the influence of code hardware delay from float WL ambiguity can accelerate the ambiguity fixing process which is independent of extra ionosphere information.

3 Experiments and Analysis

In this paper, BDS triple-frequency observation data of MGEX monitoring station CUT0 from April 25th to 29th (DOY 115th–119th) in 2014 are selected to verify the method, the sample interval is 30 s, and the visibility of BDS satellites in this period is shown in Fig. 1.

It can be seen that GEO satellites (C01–C05) are visible in all day owing to their earth synchronous orbit; the visibility of IGSO satellites (C06–C10) is more than 90 % however less than 50 % for MEO satellites (C11–C14) in all day. To be

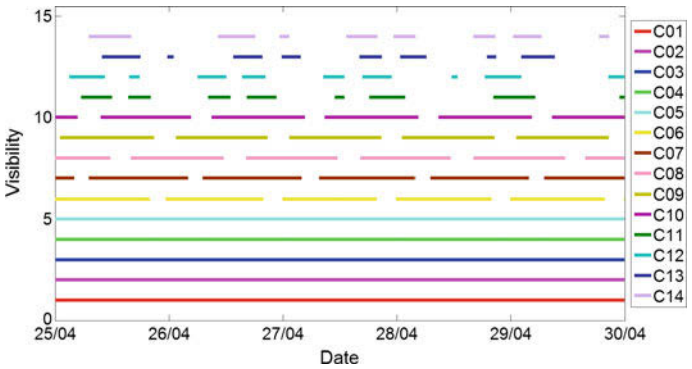

Fig. 1 The visibility of BDS satellites

convenient for discussion and analysis, here the data of station CUT0 on 115th is first selected, and C04, C08, C12 corresponding to GEO, IGSO, MEO satellite, respectively, are focused to get the ambiguity resolution.

3.1 WL Ambiguity Resolution

As known, the MW WL ambiguity is mostly influenced by code hardware delay, multipath, and noise, the distribution of ambiguity residual after rounding to near integer reflects somewhat the character and magnitude of the influence factor. Figure 2 shows the histogram density and Q–Q quantiles of EWL ambiguity residual of the three satellites.

From the histogram in Fig. 2, the EWL ambiguity residual mainly presents a trend of normal distribution, meaning that observation noise coincides with the random character of Gauss distribution. The non-zero mean value of residual is mainly due to the stable influence of code hardware delay on ambiguity in a short period, and the mean difference represents a different magnitude of code hardware delay. For Q–Q quantiles plot, the horizontal ordinate is the quantiles of standard normal distribution, and the vertical ordinate is the sample value, it is closer to normal distribution when sample values coincide with middle position of the slant line. In Fig. 2 EWL ambiguity residual coincides with the slant line on the whole, especially for the middle position of the line, however large difference exists on the both ends of the line. The intercept of the line on vertical ordinate does not equal to zero showing that the ambiguity residual corresponds to a normal distribution with non-zero mean value, which coincides with the results in histogram density plot. The mean EWL ambiguity residual of the three satellites is no more than 0.4 cycles and the biggest residual is less than 0.5 cycles. Figure 3 shows the time series of EWL ambiguity estimated from MW combination.

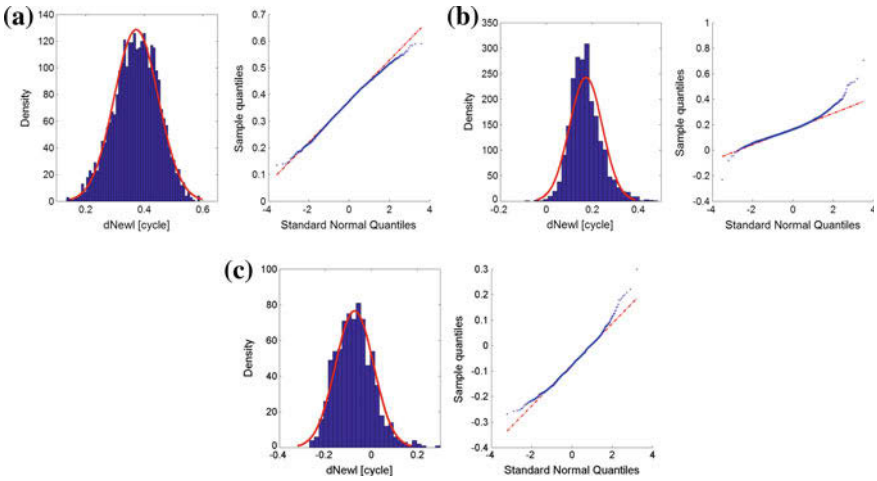

Fig. 2 Histogram density and Q–Q quantiles plot of the EWL ambiguity residual. **a** C04. **b** C08. **c** C12

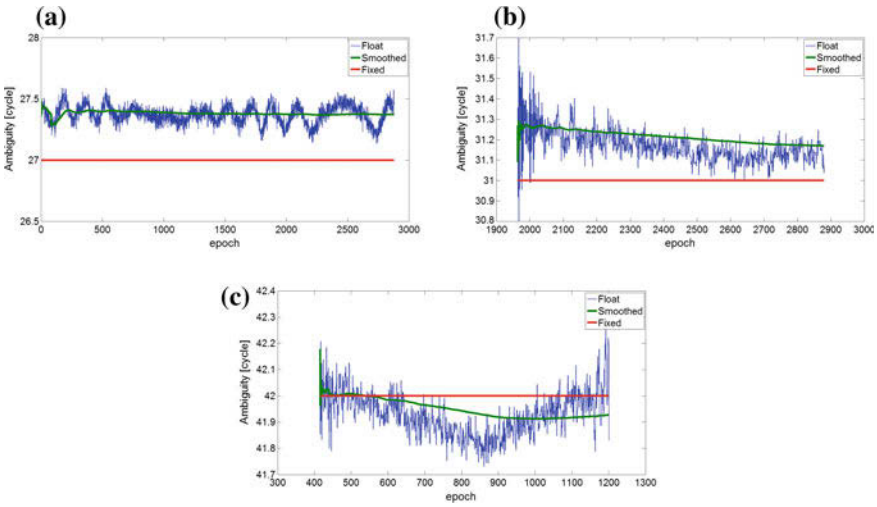

Fig. 3 The time series of EWL ambiguity. **a** C04. **b** C08. **c** C12

In Fig. 3 the EWL ambiguity fluctuates slightly due to the long wavelength, the amplitude is no more than 0.5 cycles. The ambiguity of C04 presents an obvious seasonal waviness mainly due to the multipath influence of GEO satellite, however the ambiguity of C08 and C12 shows an obvious white noise character. All ambiguities present more stable after smoothing, and the single epoch success rate of fixing can reach up to 100 %.

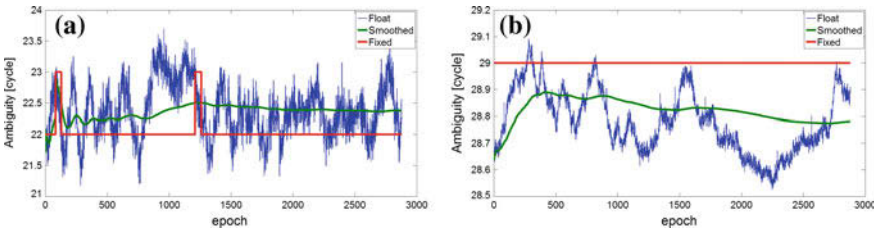

Fig. 4 The time series of C04 WL ambiguity. **a** MW method. **b** Phase WL GF combination method

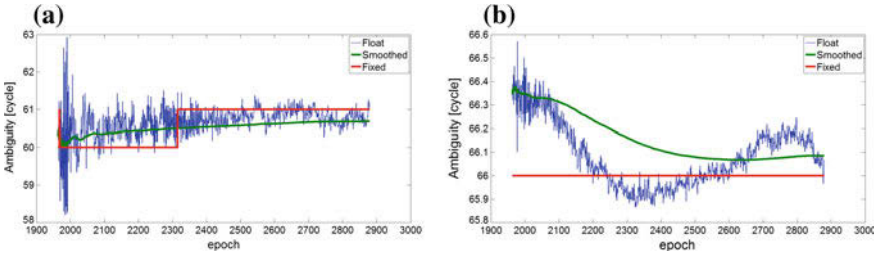

Fig. 5 The time series of C08 WL ambiguity. **a** MW method. **b** Phase WL GF combination method

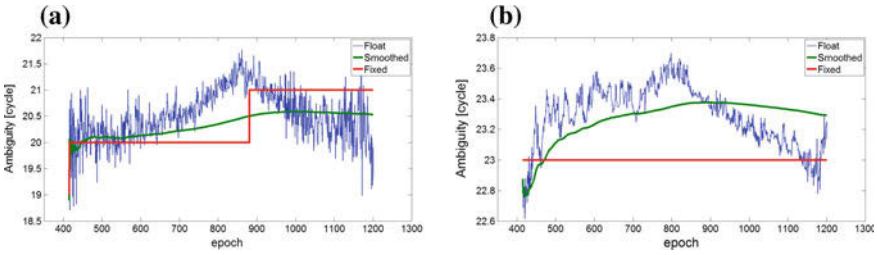

Fig. 6 The time series of C12 WL ambiguity. **a** MW method. **b** Phase WL GF combination method

WL ambiguity has shorter wavelength compared to EWL combination, so it can be more easily influenced by multipath and noise. Figures 4, 5 and 6 give the time series of WL ambiguities estimated from MW combination and phase WL geometry-free combination, respectively.

As for WL ambiguity estimated from MW combination, it also appears an obvious seasonal waviness due to the multipath influence of GEO satellite, and a white noise character of IGSO and MEO satellites. Also it is clear that the variation range is up to 2–3 cycles, which may lead to a wrong fixed value after smoothing such as at the 100th, 1250th epoch for C04, the 1980th, 2340th epoch for C08, the

410th, 890th epochs for C12 when no one cycle-slip occurs, result from the involvement of pseudorange in MW combination which enlarges the noise. WL ambiguity is more easily influenced by multipath and code hardware delay even though the smoothing process can weaken the noise, which is just because of the shorter wavelength compared with EWL combination. However, phase geometry-free combination has smaller noise, the estimated WL ambiguity varies no more than 0.8 cycles when EWL ambiguity has already been fixed and ionospheric delay corrected by GIM production, the stability can be improved a lot and the single epoch success rate of fixing is up to 100 % after smoothing. Also, it can be seen that the WL ambiguity estimated from the above two approaches differs several cycles, just because the ambiguity estimated from MW combination contains code hardware delay. If the GIM correction is precise enough, the WL ambiguity estimated from phase WL geometry-free combination can be fixed to the true value when ionospheric delay has been corrected.

3.2 Ionosphere Reconstruction and Precision Analysis

The slant ionospheric delay can be reconstructed with the phase WL geometry-free combination and fixed WL ambiguities. Figure 7 shows the time series of ionospheric delay estimated of station CUT0 on DOY 115th–119th.

Figure 7 shows a similar variation trend of the estimated ionospheric delay at the same station in different days. Effected by inner ionosphere activities, the estimated ionospheric delay differs most at the local time about 12:00 when ionosphere is active, and almost coincides from 1:30 a.m. to 8:00 a.m. when ionosphere is stable in different days.

In order to evaluate the precision of the estimated ionospheric delay with the fixed WL ambiguities, Figs. 8, 9 and 10 show the ionospheric delay difference of C04, C08, C12 between the estimated value and GIM correction.

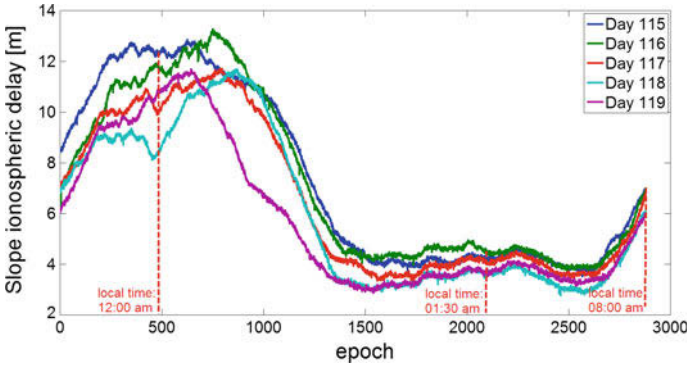

Fig. 7 The time series of C04 ionospheric delay in different days

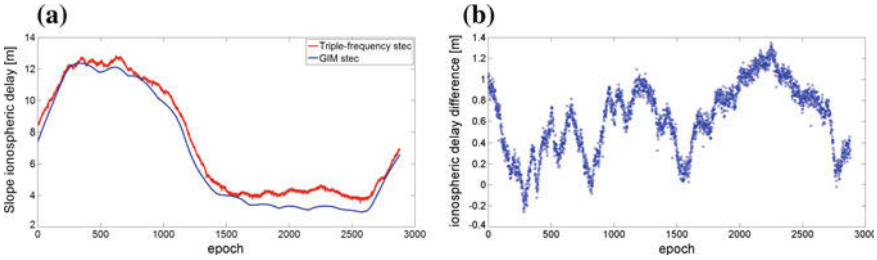

Fig. 8 The comparison and difference between C04 ionospheric delay estimated and GIM correction. **a** The slant ionospheric delay. **b** The ionospheric delay difference

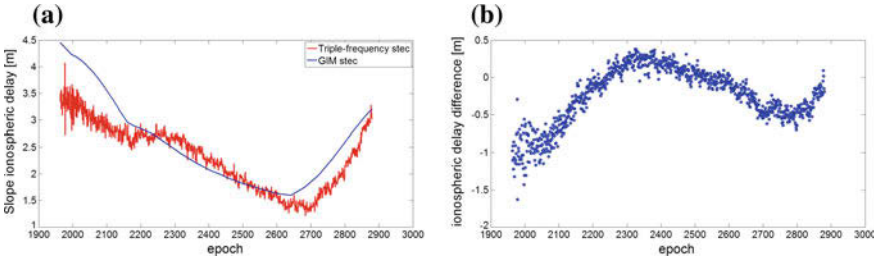

Fig. 9 The comparison and difference between C08 ionospheric delay estimated and GIM correction. **a** The slant ionospheric delay. **b** The ionospheric delay difference

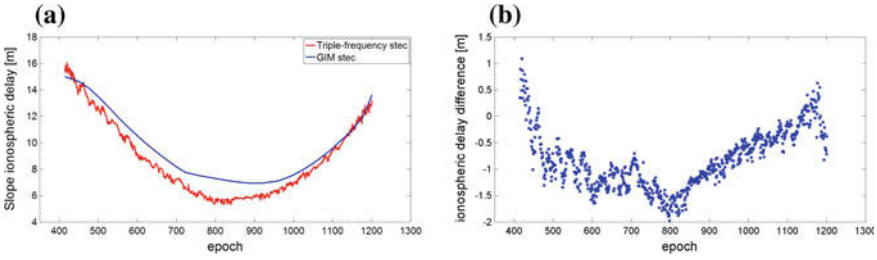

Fig. 10 The comparison and difference between C12 ionospheric delay estimated and GIM correction. **a** The slant ionospheric delay. **b** The ionospheric delay difference

According to (4), one cycle error in fixed EWL and WL ambiguity will trigger 13.54 and 2.84 m variation in estimated ionospheric delay, respectively. From the above figures, it can be seen that the ionospheric delay difference of C04, C08 between estimated value and GIM correction is no more than 1.5 m, and less than 2 m for C12. There exists an ionospheric delay systemic bias of about 0.5–0.8 m between estimated value and GIM correction, meaning an equivalent ionospheric delay correction precision of 3–5 TECU, however this does not influence the triple-frequency WL ambiguity fixing process.

3.3 *Code Hardware Delay Separation and Precision Analysis*

The sum of satellite and receiver code hardware delay on each frequency can be separated when high-precision ionospheric delay is reconstructed. Figure 10 gives the mean residual of WL ambiguity and pseudorange geometry-free combination between L2/L3 deducting ionospheric delay of station CUT0 in 2014 on DOY 115th–119th (Fig. 11).

From the mean value of ambiguity residual, it can be seen that the influence of code hardware delay to EWL ambiguity is stable and less than 0.38 cycles because of the long wavelength, however it can be up to several cycles for WL ambiguity; this is just the reason that the WL ambiguity estimated from MW combination is difficult to fix. The pseudorange geometry-free combination deducting ionospheric delay may differ 1.2 m in different days, which relates to the observation noise and ionospheric delay correction precision. Figure 12 gives the variation of the mean code hardware delay estimated every day on each frequency of the three satellites.

The sum of satellite and receiver code hardware delay keeps stable in a short period, the stability of GEO and IGSO satellites is better than MEO satellite, which may result from the shorter visible period of MEO in a day. Though the magnitude of code hardware delay may exceed 10 m, it can be absorbed into receiver clock offset when positioning which will not influence the precision. With the BDS observations of about 88 global MGEX monitoring stations on April 25th in 2014, satellite and receiver hardware delay biases are separated through ionosphere modeling with 12 order spherical harmonic function, and Fig. 13 gives their comparison with the difference of code hardware delay between L1 and L2 frequency.

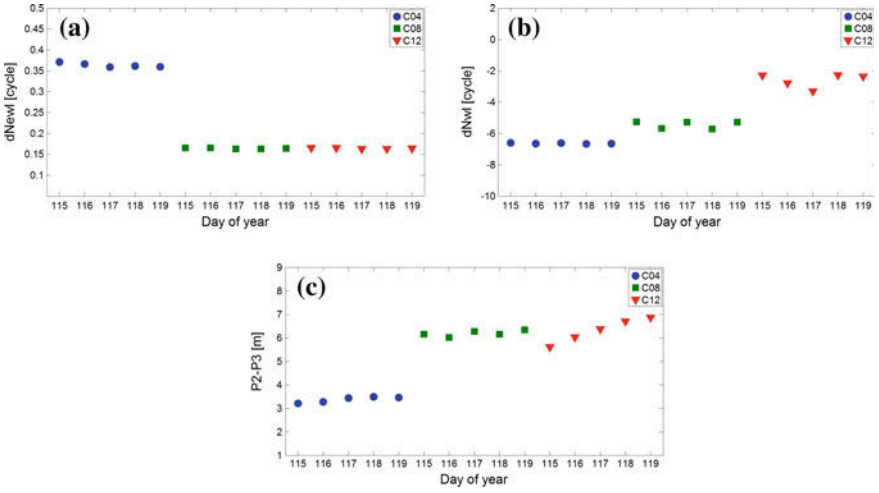

Fig. 11 The mean value of EWL/WL ambiguity residual and code pseudo-range GF combination. **a** EWL ambiguity residual. **b** WL ambiguity residual. **c** Code pseudo-range GF combination

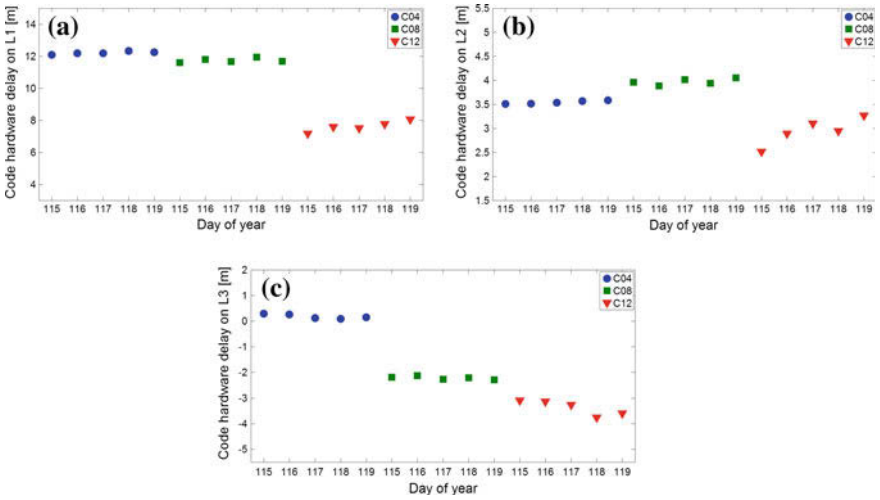

Fig. 12 The sum of satellite and receiver code hardware delay on different frequencies. **a** Code hardware delay on L1. **b** Code hardware delay on L2. **C** Code hardware delay on L3

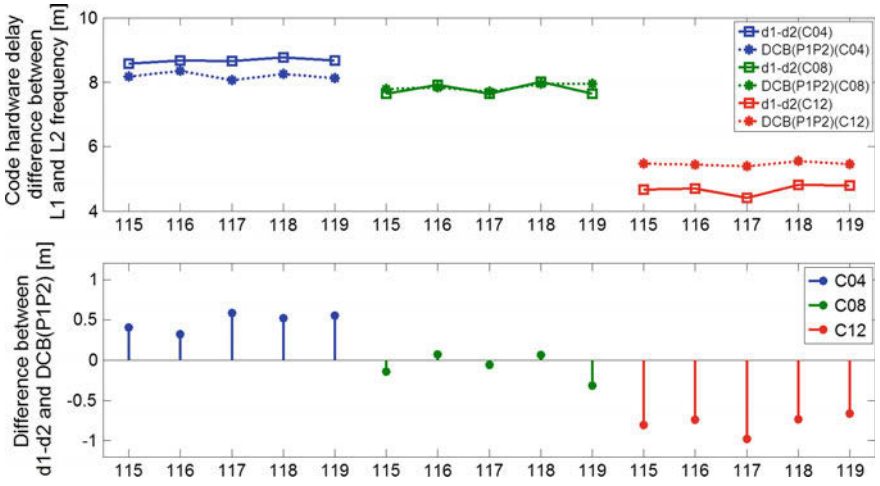

Fig. 13 The comparison of code hardware delay bias between L1/L2 frequencies

It can be seen that the code hardware delay biases from ionosphere modeling with geometry-free combination coincide with the difference of code hardware delay between L1 and L2 frequency. The mean bias is no more than 0.5 m for GEO and about 0.8 m for MEO, however it fits the best for IGSO, the probable reason is that IGSO satellites have a better space geometry distribution compared to GEO satellites and longer visible period compared to MEO satellites, when ionosphere

modeling with original observation, the point of puncture of IGSO signals distribute more widely and homogeneously which describes the distribution characteristics of ionosphere best and thus improves the precision of satellite and receiver DCB separated from ionosphere modeling.

WL ambiguity of MW combination can be easily fixed without GIM correction when assisted by the estimated high-precise and stable code hardware delay, which improves the efficiency and precision of ambiguity resolution in geometry-free mode.

4 Conclusions

Owing to the long wavelength of EWL combination, EWL ambiguity varies less than 0.5 cycles, and the single epoch success rate of fixing can reach up to 100 % after smoothing. In contrast, WL ambiguity from MW combination can vary up to 2–3 cycles because of the influence of code hardware delay and observation noise. In this paper, a method is proposed to resolve the WL ambiguity with the fixed EWL ambiguity and phase WL geometry-free combination, the resolved WL ambiguity presents smoother and higher in success rate of fixing compared to WL ambiguity from MW combination.

There exists an obvious ionospheric delay systemic bias of about 0.5–0.8 m between estimated value and GIM correction, meaning an equivalent ionospheric delay correction precision of 3–5 TECU.

It also turns out that the satellite and receiver code hardware delay separated with reconstructed triple-frequency ionospheric delay and WL ambiguity from MW combination is stable and the stability of GEO and IGSO is obviously better than MEO satellites. The code hardware delay bias between different frequencies coincides well with DCB separated from ionosphere modeling, especially for IGSO satellites which have a better space geometry distribution and longer visible period.

Acknowledgments This work is supported by National Natural Science Foundation of China (No: 41274045;No: 41574010).

References

1. Yuan Y (2002) Study on theories and method of correcting ionopheric delay and monitoring ionosphere based on GPS. Institute of Geodesy and Geophysics Chinese Academy of Sciences, Wuhan
2. He H (2002) Precise kinematic GPS surveying and quality control. Information Engineering University, Zhengzhou
3. Zhang H (2006) Study on method of correcting ionopheric delay and ionosphere monitoring in chinese region based on GPS. Shanghai Observatory Chinese Academy of Sciences, Shanghai

4. Sanz MH-PJMJJ (2009) The IGS VTEC maps a reliable source of ionospheric information since 1998. J Geod 83(11):263–275
5. Zhang R, Song W-W, Yao Y-B, Shi C, Lou Y-D, Yi W-T (2014) Modeling regional ionospheric delay with ground-based BeiDou and GPS observations in China. GPS Solution
6. Li J (2014) BDS/GPS multi-frequency real-time kinematic positioning theory and algorithms. Information Engineering University, Zhengzhou
7. Deng J, Pan S, Hong Z (2014) A resolution method for ionospheric delay with optimal combination of three-frequency data. Geomatics Inf Sci Wuhan Univ 39(5):600–604
8. Li B, Shen Y (2010) Three carrier ambiguity resolution: distance-independent performance demonstrated using semi-generated triple frequency GPS signals. GPS Solutions 14:177–184
9. Li B, Shen Y (2009) A new method for medium and long rang three frequency GNSS rapid ambiguity resolution. Acta Geodaetica Cartogr Sin 38(4):296–301
10. Fan J, Wu X, Li Y (2013) COMPASS satellites DCB parameter accuracy assessment based on triple-frequency data. Chin Space Sci Technol 4:62–69
11. Wang H, Chai H, Xie K (2015) Study of cycle-slip detection using BDS triple-frequency geometry-free and ionosphere-free combination. J Geodesy Geodyn 35(3):406–411
12. Xie K (2014) Research on ambiguity resolution based on BDS triple-frequency. Information Engineering University, Zhengzhou
13. Yanming F (2008) GNSS three carrier ambiguity resolution using ionosphere-reduced virtual signals. J Geodesy 82:847–862
14. Spits J, Warnant R (2011) Total electron content monitoring using triple frequency GNSS: Results with Giove-A/-B data. Adv Space Res 47:296–303

The Effect of Colored Noise on the Coordinate Time Series Analysis of Continuous GPS Stations in Antarctic Peninsula

Chao Ma, Fei Li, Sheng-kai Zhang, Jin-tao Lei, Qingchuan Zhang and Wenhao Li

Abstract Recent researches show not only white noise but also colored noise widely existed in various continuous GPS station coordinate time series, and the colored noise also has an important influence on GPS time series analysis. To determine the optimal noise model of GPS time series in the Antarctic Peninsula, and analyze the influence of colored noise and spatial filtering on the parameters estimation and uncertainty of GPS coordinate time series, the GAMIT/GLOBK 10.5 software is used to solve the measured data of eight GPS stations from 2010 to 2014, and the CATS software is used to estimate the parameters of the coordinate time series in different noise models. The results show that, (1) the combination of white noise, flicker noise, and random walk noise is the best noise model in the Antarctic Peninsula; (2) The main component of the noise model is flicker noise, and the random walk noise only exists in the east direction of a few stations; (3) In Antarctic Peninsula area, regional spatial filtering can greatly reduce the uncertainties in the linear and periodic parameter estimation of GPS time series, by effectively reducing the white noise, flicker noise, and random walk noise.

Keywords Antarctic Peninsula · GPS · Time series · Colored noise

1 Introduction

It was originally assumed that the GPS data are independent random distributed and there is only white noise (WN) in coordinate time series. In recent years, not only WN, but also flicker noise (FW) and random walk noise (RWN) have been studied in GPS time series. Williams et al. [1] analysed noise of 954 consecutive GPS coordinate time series in 9 global GPS solutions by maximum likelihood estimation (MLE) and the results showed that optimal noise model was white noise + flicker

C. Ma · F. Li · S. Zhang (✉) · J. Lei · Q. Zhang · W. Li
Chinese Antarctic Center of Surveying and Mapping, Wuhan University, Wuhan 430079, China
e-mail: zskai@whu.edu.cn

© Springer Science+Business Media Singapore 2016

J. Sun et al. (eds.), *China Satellite Navigation Conference (CSNC) 2016 Proceedings: Volume III*, Lecture Notes in Electrical Engineering 390,
DOI 10.1007/978-981-10-0940-2_39

noise. Jiang et al. [2] used power spectrum analysis and MLE to estimate the noise characteristics of the CORS network coordinate time series in CGCS2000 framework and found that the optimal noise model is WN + FN + RWN. Li et al. [3] used 11 IGS stations in China to analyze the noise of 1995–2010 coordinate time series and found that the noise model of IGS station in China is WN + FN and WN + BPPRN (band pass power rate noise). Jiang and Zhou [4] analysed the noise of 10 consecutive GPS time series in Australian, and found that the optimal noise model in horizontal is WN + FN.

Antarctica is one of most important areas in international geodynamics research field. Polar Earth Observing Network (POLENET) is an international project and it aims to layout GPS and seismograph in the polar regions in the 2007/2008 International Polar Year (IPY) [5]. In recent years, the number and distribution of stations in Antarctic Peninsula is improving largely and the noise analysis of the coordinate time series in the region is possible.

2 Noise Analysis Method

White noise is a random signal or process, and its power spectrum density is distributed uniformly in whole frequency domain, and the other noise has no such property. The high frequency part of the signal usually represents white noise, and the middle and low frequency part represent the flicker noise and random noise. If there is colored noise in the time series, the variance of the parameter estimates will not decrease with the increase of observations. In the calculation of displacement and velocity of base station by GPS repeated observation method, it will be too optimistic velocity error estimation and cannot reflect the actual accuracy if the colored noise is not considered.

At present, there are three noise analysis methods: maximum likelihood estimation (MLE) [6], spectral estimation [7], and empirical method based on Williams [8]. The CATS software is an independent C program developed by Williams [9] to study and compare the random noise process and the distribution of its real uncertainty. The main analysis method of CATS is MLE, so we are mainly concerned about MLE.

MLE is a statistical method for estimating the noise components and parameters of linear equations. That means the likelihood of a set of observation values X must be maximized. The likelihood L of a Gauss distribution is

$$L(x, C) = \frac{1}{(2\pi)^{N/2}(\det C)^{1/2}} \exp\left(-0.5\hat{v}C^{-1}\hat{v}\right) \tag{1}$$

where det is the determinant of a matrix, C represents the covariance matrix of the assumed noise, each kind of noise has a particular covariance matrix. N is the number of epochs and are the post-fit residuals to the linear function using weighted

least squares with the same covariance matrix C. In order to make the numerical more stable, we maximize the logarithm of the likelihood

$$\ln[L(x, C)] = -\frac{1}{2}\left[\ln(\det c) + \hat{v}^T + N\ \ln(2\pi)\right] \tag{2}$$

3 Data Processing

In order to facilitate the reader to understand data processing process, Fig. 1 shows the flow chart of data processing.

3.1 GPS Data Sources

The daily observations of eight GPS stations from 2010 to 2014 in the Antarctic Peninsula are used as GPS raw data (see Fig. 2), and among them there are two IGS stations (PALM, PALV) and six POLENET stations (DUPT, VNAD, HUGO, FONP, ROBI, CAPF). The data sources are from the Scripps orbit and permanent array center (SOPAC) and University NAVSTAR Consortium (UNAVCO).

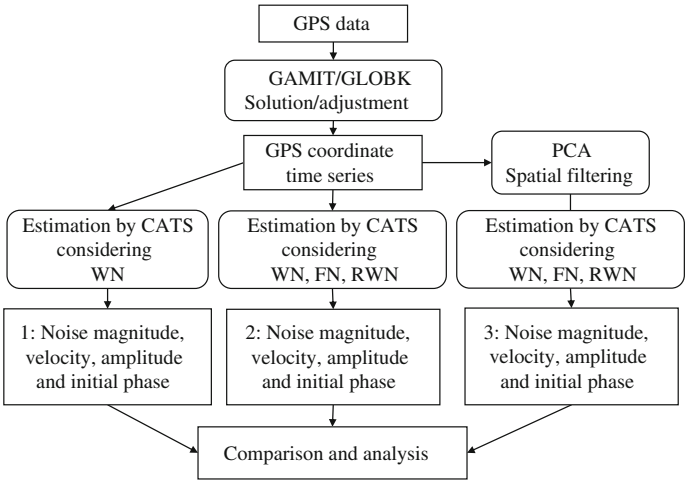

Fig. 1 The flow chart of data processing

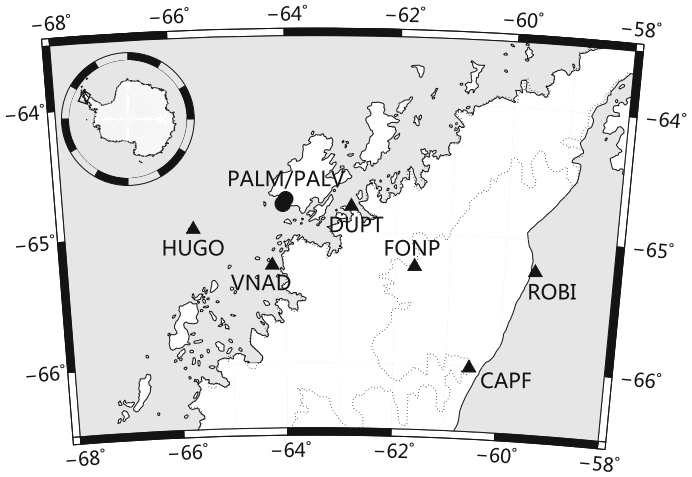

Fig. 2 The distribution of GPS stations in Antarctic Peninsula, the solid triangles represent the POLENET stations and the solid circles represent IGS stations

3.2 GPS Data Processing

GAMIT/GLOBK10.5 is a high-accuracy GPS comprehensive analysis software package for estimating station coordinates and velocities, stochastic or functional representations of post-seismic deformation, atmospheric delays, satellite orbits, and Earth orientation parameters. GAMIT software is used to get the baseline solutions of GPS data in this paper and we modified some of the processing strategies, as shown in Table 1.

Table 1 The strategies of baseline solutions

Entries	Strategies
Choice of experiment	RELAX
Choice of observable	LC_AUTCLN
Reference station constraints (m)	0.05, 0.05, 0.10
Other station constraints (m)	100, 100, 100
Elevation cutoff	15°
Epoch interval	30 s
Troposphere model	Saastamoinen
Tidal model	FES2004
Radiation force model	BERNE
Reference frame	ITRF2008

3.3 Network Adjustment

GLOBK was used for network adjustment in ITRF2008 reference frame after getting baseline solutions. In order to maintain the stability of reference frame, we use the H files of global subnetwork (which can be downloaded from the SOPAC website) and select 91 core stations in IGb08 as stable stations. The time series of GPS station has a step due to earthquakes or antenna changes and other reasons, so we use the latest earthquake file itrf08_comb.eq to correct them.

3.4 Regional Spatial Filtering

The common mode errors are some errors with temporal and spatial correlations in regional GPS network, which has important implications on the analysis of GPS time series. The common mode errors of the GPS network can be eliminated effectively by regional spatial filtering. The principal component analysis (PCA) method [10] is used in this paper for the spatial filtering of GPS network in Antarctic Peninsula. The method is successfully used in the study of coseismic deformation and the decomposition of geodetic data. PCA allows the data itself to determine its spatial distribution. By means of a linear combination, the explained variances of some certain variables will become larger and the variables with larger explained variances are called principal components.

4 Time Series Analysis

4.1 Noise Analysis

We analyzed two kinds of noise combinations, one was white noise (C1), and the other was white noise + flicker noise + random walk noise (C2). Noise magnitude of GPS time series are estimated by CATS software in this paper. Table 2 shows the noise comparisons of GPS time series between two kinds of noise combinations. The time series of all sites in C1 have only white noise, while the time series of most of sites in C2 have white noises and flicker noises and only the north components of FONP and DUPT have only white noises and only the east components of PALM, PALV, and DUPT have random walk noises. Because PALM, PALV, and DUPT have similar latitudes (see Fig. 1), so the random walk noise in east components may be related to the local environmental factors. The white noises of C1 is larger than those of C2, but obviously smaller than total noises of C2. So, if the colored noise is not considered, the white noise in the time series would be overestimated and the total noise magnitude would be underestimated. Because white noise, flicker noise, and random walk noise of GPS network in the Antarctic Peninsula are all significant, the optimal noise model is white noise + flicker noise + random walk noise.

Table 2 Noise comparisons of GPS time series between two kinds of noise combinations (C1 and C2)

Name	Component	C1WN (mm)	C2WN (mm)	C2FN (mm)	C2RWN (mm)
CAPF	N	3.62 ± 0.07	2.38 ± 0.14	9.27 ± 0.70	0.00 ± 0.02
	E	3.42 ± 0.07	2.60 ± 0.10	7.25 ± 0.60	0.00 ± 0.00
	U	10.28 ± 0.21	5.11 ± 0.46	29.47 ± 1.78	0.00 ± 0.00
DUPT	N	2.40 ± 0.04	1.67 ± 0.06	5.42 ± 0.34	0.00 ± 0.00
	E	2.55 ± 0.04	1.51 ± 0.07	5.49 ± 0.43	2.91 ± 1.18
	U	7.78 ± 0.12	3.63 ± 0.27	22.47 ± 1.00	0.00 ± 0.00
FONP	N	2.80 ± 0.05	1.83 ± 0.09	6.68 ± 0.48	0.00 ± 0.00
	E	2.52 ± 0.05	1.67 ± 0.08	5.76 ± 0.42	0.00 ± 0.00
	U	8.36 ± 0.16	4.16 ± 0.35	24.11 ± 1.37	0.00 ± 0.00
HUGO	N	2.98 ± 0.05	1.73 ± 0.09	7.54 ± 0.43	0.00 ± 0.00
	E	3.83 ± 0.07	3.32 ± 0.09	5.50 ± 0.64	0.00 ± 0.00
	U	11.24 ± 0.21	7.39 ± 0.36	27.65 ± 1.81	0.00 ± 0.00
PALM	N	2.28 ± 0.04	1.40 ± 0.06	5.78 ± 0.31	0.00 ± 0.00
	E	2.28 ± 0.04	1.36 ± 0.07	5.26 ± 0.45	3.33 ± 1.17
	U	7.84 ± 0.12	3.58 ± 0.31	23.79 ± 1.07	0.00 ± 0.00
PALV	N	2.25 ± 0.04	1.35 ± 0.07	5.83 ± 0.31	0.00 ± 0.00
	E	2.21 ± 0.04	1.31 ± 0.08	5.27 ± 0.48	2.72 ± 1.45
	U	7.82 ± 0.12	3.61 ± 0.30	23.74 ± 1.07	0.00 ± 0.01
ROBI	N	4.00 ± 0.07	2.27 ± 0.15	10.84 ± 0.64	0.00 ± 0.00
	E	4.57 ± 0.08	3.44 ± 0.11	8.12 ± 0.70	0.00 ± 0.02
	U	11.85 ± 0.22	7.76 ± 0.37	28.92 ± 1.86	0.00 ± 0.00
VNAD	N	2.63 ± 0.04	1.47 ± 0.08	6.90 ± 0.35	0.00 ± 0.00
	E	2.82 ± 0.04	1.36 ± 0.10	7.94 ± 0.37	0.00 ± 0.00
	U	8.30 ± 0.13	4.12 ± 0.29	23.92 ± 1.13	0.00 ± 0.00

4.2 Parameter Estimation and Uncertainty

In order to understand the effects of different noise combinations on parameter estimation, we compared the velocities and annual period amplitudes. It can be seen from Table 3 that estimated parameters have significant differences between C1 and C2. The max difference of the velocities and annual period amplitudes in C1 and C2 are 1.73 mm/a and 0.65 mm, respectively. The max errors of the velocities and annual cycle amplitude in C2 are 47 and seven times greater than those in C1. This indicates that considering white noise only would greatly underestimate the uncertainties of parameters.

Table 3 The comparisons of parameter estimation between two kinds of noise combinations (C1 and C2)

Name	Component	C1Velocity (mm/yr)	C2Velocity (mm/yr)	C2Amplitude (mm)	C2Amplitude (mm)
CAPF	N	8.88 ± 0.07	9.06 ± 0.65	2.10 ± 0.32	2.00 ± 1.33
	E	14.27 ± 0.07	14.48 ± 0.52	1.51 ± 0.22	1.68 ± 0.88
	U	5.47 ± 0.21	5.91 ± 2.06	6.95 ± 2.97	6.56 ± 13.76
DUPT	N	10.88 ± 0.03	10.68 ± 0.31	0.84 ± 0.06	0.97 ± 0.29
	E	11.66 ± 0.03	10.61 ± 1.28	0.71 ± 0.06	0.53 ± 0.22
	U	13.79 ± 0.10	14.88 ± 1.27	2.73 ± 0.66	2.58 ± 2.98
FONP	N	7.45 ± 0.05	7.59 ± 0.45	1.38 ± 0.15	1.39 ± 0.63
	E	14.45 ± 0.05	14.49 ± 0.39	1.19 ± 0.12	1.22 ± 0.47
	U	17.02 ± 0.16	17.39 ± 1.62	3.79 ± 1.21	3.74 ± 6.14
HUGO	N	11.12 ± 0.06	11.88 ± 0.49	1.07 ± 0.12	0.65 ± 0.29
	E	14.62 ± 0.07	14.46 ± 0.39	1.20 ± 0.18	1.30 ± 0.46
	U	5.10 ± 0.22	6.56 ± 1.82	6.39 ± 2.73	5.74 ± 9.66
PALM	N	11.05 ± 0.03	11.11 ± 0.33	0.49 ± 0.04	0.50 ± 0.16
	E	12.67 ± 0.03	11.63 ± 1.44	0.44 ± 0.03	0.25 ± 0.11
	U	7.68 ± 0.11	8.76 ± 1.34	2.40 ± 0.60	2.55 ± 3.31
PALV	N	11.07 ± 0.03	11.14 ± 0.33	0.50 ± 0.04	0.48 ± 0.16
	E	12.68 ± 0.03	11.83 ± 1.21	0.27 ± 0.02	0.37 ± 0.14
	U	7.75 ± 0.11	9.48 ± 1.35	2.50 ± 0.64	2.47 ± 3.19
ROBI	N	7.93 ± 0.07	8.47 ± 0.73	2.54 ± 0.38	2.66 ± 1.87
	E	15.65 ± 0.09	15.75 ± 0.56	1.71 ± 0.29	2.02 ± 1.09
	U	9.62 ± 0.22	9.65 ± 1.96	1.06 ± 0.46	1.45 ± 2.74
VNAD	N	10.23 ± 0.04	10.20 ± 0.39	0.68 ± 0.06	0.71 ± 0.27
	E	12.79 ± 0.04	12.04 ± 0.45	0.41 ± 0.04	0.76 ± 0.32
	U	6.94 ± 0.11	7.43 ± 1.35	2.46 ± 0.64	2.39 ± 3.07

4.3 The Effect of Spatial Filtering on Noise Analysis

By comparing the noises of time series before and after spatial filtering, we analysed the influences of spatial filtering on GPS time series. In order to estimate the parameters of GPS time series, we applied the optimal noise model (WN + FN + RWN) and estimated their magnitudes and uncertainties. It can be seen from Fig. 3 that the average magnitudes of all noises in GPS time series are significantly reduced after filtering. The average magnitudes of white noise and flicker noise fell by 81 and 65 %, respectively, and random walk noise completely disappeared. So the common mode errors of Antarctic Peninsula GPS network contain the majority of WN and FN and all of RWN. Figure 4 shows that

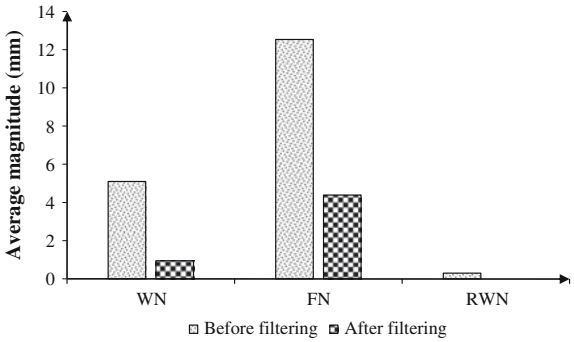

Fig. 3 Comparison of average noise magnitudes of GPS time series between before and after spatial filtering in Antarctic Peninsula

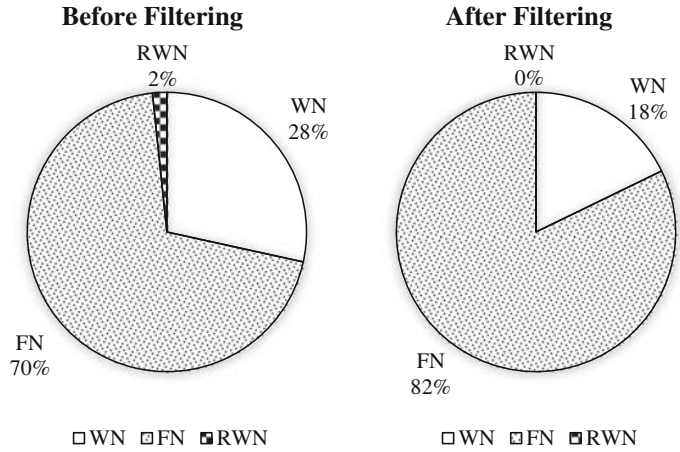

Fig. 4 Comparison of noises percentage of GPS time series between before and after spatial filtering in Antarctic Peninsula

comparison of noises percentage of GPS time series between before and after spatial filtering in Antarctic Peninsula. It can be seen that the main noise type in the Antarctic Peninsula GPS network are not white noises (28 %), but flicker noises (70 %).

By comparing the estimated parameters of GPS time series, we found that the uncertainties of velocities and amplitudes are significantly reduced. But the magnitudes of velocities and amplitudes have little change, for example, the max difference of velocity is less than 1 mm/yr. So the spatial filtering can significantly reduce the uncertainties of parameter estimation in Antarctic Peninsula GPS network, but it has little effect on the magnitudes of estimated parameters.

5 Conclusions

By analyzing the GPS time series of eight stations in the Antarctic Peninsula using different noise models, the optimal noise model in Antarctic Peninsula GPS network is WN +FN + RWN. The main noise type is not WN, but FN. The random walk noises in partial stations may be related to the local environmental factors. The results indicate that considering white noise only would greatly underestimate the uncertainties of parameters and so as to affect the assessment of accuracy, and accuracy in parameter estimation of GPS time series. The regional spatial filtering can effectively reduce the magnitudes of WN, FN, and RWN and the uncertainties of the estimated linear terms and periodic terms.

References

1. Williams SDP, Bock Y, Fang P et al (2004) Error analysis of continuous GPS position time series. J Geophys Res Solid Earth (1978–2012) 109(B3)
2. Jiang ZH, Zhang P, Mi JS et al (2010) Velocity estimation on the colored noise properties of CORS network in China based on the CGCS2000 frame. Acta Geodaetica Cartogr Sin 39 (4):355–363
3. Li Z, Jiang WP, Liu HF et al (2012) Noise model establishment and analysis of IGS reference station coordinate time series inside China. Acta Geodaetica et Cartographica Sinica 41 (4):0–590
4. Jiang WP, Zhou XH (2014) Effect of the span of Australian GPS coordinate time series in establishing an optimal noise model. Sci China Earth Sci 11:010
5. EDC, Zhang SK (2006) Infrastructure and progress of international Antarctic geodetic reference framework. J Geodesy Geodyn 26(2):104–108
6. Johnson H (1997) Correlated errors in geodetic time series: implications for time-dependent deformation. J Geophys Res 102(B1):591–603
7. Beran J (1994) Statistics for long-memory processes. CRC Press
8. Williams SDP (2003) The effect of coloured noise on the uncertainties of rates estimated from geodetic time series. J Geodesy 76(9–10):483–494
9. Williams SDP (2008) CATS: GPS coordinate time series analysis software. GPS Solutions 12 (2):147–153
10. Dong D, Fang P, Bock Y et al (2006) Spatiotemporal filtering using principal component analysis and Karhunen-Loeve expansion approaches for regional GPS network analysis. J Geophys Res Solid Earth (1978–2012) 111(B3)

Information Transmission Path Selection of Navigation Satellite Network Based on Directional Crosslink

Zhenwei Hou, Xianqing Yi, Yue Zhao and Yaohong Zhang

Abstract Autonomous navigation using an intersatellite ranging and communication with intersatellite links (ISL) is the trend of satellite navigation system development. By controlling the direction of phased array antenna flexibly, the directional crosslink can achieve more information from other satellites. However, the efficiency of communication is affected at the same time. In this paper, we analyse the navigation satellite network assembled directional crosslink, and then we propose a solution to describe the progress of information transmission based on building directional graph. Then we present a method of finding *Earliest Journey* and *Shortest Journey*. According to simulation result, the method we present is practicable and we also achieve some valuable conclusions.

Keywords Directional crosslink · Satellite navigation · Path selection · Routing algorithm

1 Introduction

ISLs technology is so important for satellite navigation system to improve the positioning accuracy of the system and to achieve autonomous navigation that the world's major satellite navigation systems are actively exploring and building intersatellite links. ISLs can shorten the ephemeris update cycle and achieve navigation satellite constellation's precision orbit determination. As well, ISLs can forward measurement and control signals, complete navigation constellation indirect monitoring and control. As a result, the number of ground stations and maintenance costs of the system is reduced. Meanwhile, the establishment of ISLs makes the navigation constellation have a shorter route delay, greater communication capacity, and can enhance the viability of the system [1].

Z. Hou (✉) · X. Yi · Y. Zhao · Y. Zhang
Science and Technology on Information Systems Engineering Laboratory, National University of Defense Technology, Changsha, China
e-mail: houzhenwei@nudt.edu.cn

© Springer Science+Business Media Singapore 2016

J. Sun et al. (eds.), *China Satellite Navigation Conference (CSNC) 2016 Proceedings: Volume III*, Lecture Notes in Electrical Engineering 390,
DOI 10.1007/978-981-10-0940-2_40

Directional crosslink has a great advantage in terms of intersatellite ranging and has become the development trend of satellite navigation systems. Currently there is little research on the information transmission path selection of navigation satellite network based on directional crosslink.

Reference [2] uses and extends a graph theoretic model which helps capture the evolving characteristic of satellite networks, in order to propose and formally analyze least cost journeys in a class of dynamic networks, where the changes in the topology can be predicted in advance. Cost measures investigated here are hop count (shortest journeys), arrival date (foremost journeys), and time span (fastest journeys). Reference [3] proposes a method of selecting information transmission path based on the features of directional crosslink. It solves the path selection problems of multiple pieces of navigation information when they are transmitted between any different satellites.

In this paper, we aim at the navigation satellite network which is assembled directional crosslink and propose a solution to describe the progress of information transmission based on building directional graph. A method of finding Earliest Journey and Shortest Journey is described in detail in the paper. Absolutely, we draw some lessons from the traditional Dijkstra algorithm. The paper is organized as follows. Features of directional crosslink and the information transmission process are described in the next section. Section 3 describes the calculation method of the Earliest Journey and the Shortest Journey. In Sect. 4 we do some experiments with the two algorithms we propose and analyse the experiment results. We close the paper with concluding the whole work of this paper in Sect. 5.

2 Directional Crosslink

2.1 Features of Directional Crosslink

Directional crosslink generally works in Ka (23 GHz) or V (60 GHz) band. A higher frequency band can reach higher communication speed and accuracy. And with the spot beam of higher frequency band, directional crosslink can enhance the anti-jamming capability.

The direction of directional crosslink changes frequently over time. The link keeps switching and reconstructing. It generally relies on the phased array antenna to achieve measurement and communication. Intersatellite ranging and communication are main functions of directional crosslink in satellite navigation system. The flexibility of the phased array antenna is beneficial to acquire observations of pseudorange measurements among satellites. The more intersatellite observations are acquired, the more accurate the system will be. It is not realistic for a single satellite using directional crosslink to acquire all the observations of satellites simultaneously. The observations can only be measured in turn. The time of measurement should be as short as possible, that is, we need to obtain the

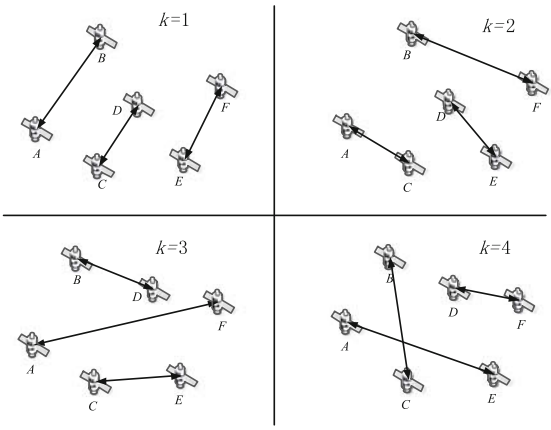

Fig. 1 Working progress of directional crosslink. It describes that the directional crosslinks are established and switched among different satellites in different time slots. k is the time slot number

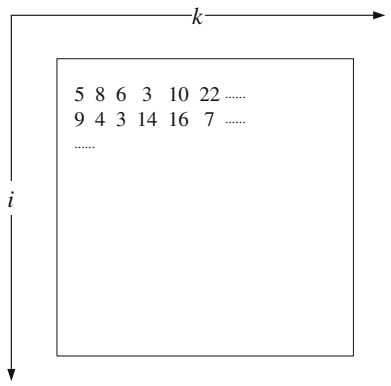

Fig. 2 Link assignment matrix, its row number represents satellite number i, its column number represents the time slot k. If $Q_{i,k} = j$, an ISL is established between satellite i and j at time slot k

observation among as many as satellites within the shortest possible time. So in a cycle period of link assignment, any two satellites establish the link only once.

Because the energy and computing capacity on satellite are limited, a satellite can only assemble one link, which makes navigation satellite network become typical Delay Tolerant Network (DTN). The working progress of directional crosslink is shown in Fig. 1. The progress can be noted by a matrix Q named link assignment matrix which is shown in Fig. 2 [4].

2.2 Progress of Information Transmission

If we do not consider the actual situation of resource constraints and satellite transmission requirements, etc., the satellites connected by ISLs can share the information with each other. For example, in Fig. 1 when $k = 1$, A and B are connected by a link. So the two satellites share the information with each other and

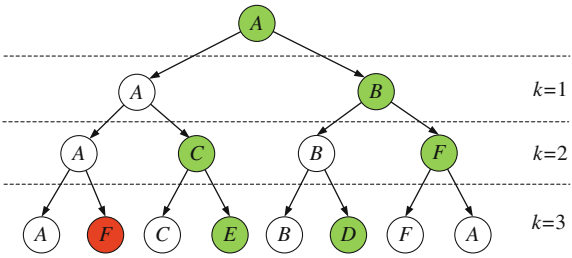

Fig. 3 Information transmission progress under the control of *Retain* and *Forward*. *A* is the source node. The node colored *red* is in the shortest journey, while the one colored *green* is in the fastest journey

have the same information. Then when $k = 2$, B and F are connected by a link. All the information on the B is shared to F, including that which came from A in the slot 1. As a result, information generated on A in slot 1 is transferred to F in slot 2. The example shows that even if A and F are not connected by a link directly, information on A can be transmitted to F by the relay of satellites.

In fact, when a link between two satellites is built, there are two possibilities for the information in the satellite: forwarded to a paired satellite or retained on this satellite. We assume that the satellite can retain the information for enough long time if it is necessary. So by the control of *Retain* and *Forward*, information is transmitted in different journeys, which is shown in Fig. 3. The link assignment is shown in Fig. 1.

The progress of *Retain* and *Forward* can be described by a binary tree. The left branch represents the progress of *Retain*, while the right branch represents the progress of *Forward*. For example, under the control of *Retain* → *Retain* → *Forward*, the information is transmitted to F from A. If the information is under the control of *Forward* → *Forward*, it will be transmitted to F too. However, the first journey only needs one hop (the information is forwarded once) but it costs three slots, while the latter journey needs two hops but it only costs two slots. Of all the journeys, we are interested in two types of them, which are the earliest journey and the shortest journey. The earliest journey can transmit the information to the destination node in the earliest time. We name it with *Earliest Journey*. The shortest journey can transmit the information to the destination node with the minimum hops. We name it with *Shortest Journey*. The above discussion is based on that the information transmit rate of ISLs is fast enough that the information transmission can be finished in one time slot.

In the next section, the *Shortest Journey* algorithm and *Earliest Journey* algorithm will be discussed in detail.

3 Path Selection

In this section we show how to compute *Shortest Journey* and *Earliest Journey* from a source node s to all other nodes. On the assumption that the storage space on the satellites is large enough, we take the idea of information flooding broadcast in

Table 1 Variables and its definition in the following algorithm

Variables	Definition
N	Total numbers of satellites
K	Total numbers of time slots in a period of
$O(s)$	Outdegree of node s in the directed graph
$v_{x(i)}$	Node connected with v_i by an directional edge which points to v_i

the satellite network to find the earliest journey and the shortest journey. The so-called flooding broadcast is a greedy algorithm, assuming that all of the information can be kept on any satellite for enough long time and can be shared between two paired satellites.

The progress of information transmission can be described by a graph G_k (v_k, E_k). v_k represents the satellite nodes. $E_{i\to j}$ represents information generated in satellite i at slot k has been spread to the satellite j in the current time slot. In this paper, the *Shortest Journey* algorithm and *Earliest Journey* algorithm are based on the construction of a directed graph. It will be discussed as follows. The variables and its definition used in the followed algorithm are shown in Table 1.

3.1 Earliest Journey

Information transmission by the way of broadcast will inevitably lead to the flood of the same information in a satellite network. The same satellite may receive the same information multiple times. Apparently, we can get the following conclusions: If the satellite i at time slot t generates information and it is spread to the whole network after n slots ($n < K$), then the information will be transmitted to any satellite before or at slot $n + t$. Thus, when we calculate *Earliest Journey*, we cannot consider the information transmission process after the time slot $n + t$.

The initial state of graph G_k (v_k, E_k) is $E_k = Null$. Information is generated in the time slot s. If the satellite i, j are paired and connected by a link in time slot k ($s < k$), then add the edge $E_{i\to j}$ and $E_{j\to i}$ to the graph G_k. Then, connect all the nodes which are connected with node v_i by an edge pointing to node v_i with an edge. Similarly, connect all the nodes which are connected with node v_j by an edge pointing to node v_j with an edge at the same time. The directed edge in the graph represents that the information generated on the starting node of the edge has been transmitted to the end node of the edge. When the outdegree of source node turns to $N-1$, it indicates that the information on the source node has been transmitted to all other nodes. We also need to maintain two tables to record the prior node of arrival node and arrival slot of information. So the data structure of each node in the algorithm is shown in Table 2.

The idea of *Earliest Journey* algorithm is based on traditional *Dijkstra* shortest path algorithm. The shortest path can maintain a forward path attribute, that is, any

Table 2 Data structure in *Earliest Journey* algorithm

Satellite no.	Prior node	Arrival slot
i	j	k

Table 3 *Earliest Journey* algorithm

Earliest Journey

Input: Link Assignment Matrix Q; Time Slot k; Source Node $s \in V_G$.
Output: Arrival Slot Array $t[v]$; Prior Node Array $f[v] \in V$.
Variables: Directed Graph $G(V_G, E_G)$; Counter c.

1. Initialize: $E_G = Null$; c=0; For all $v \in V$ *and* $v \neq s$, $t[v]=\infty, f[v]=Null$; $t[s]$=0 , $f[s]$=s.
2. While $O(s)<N$-1 do
   if($c>K$) break;
   else
   for all i,j s.t $Q_{i,k+c \bmod K}=j$
   $E_G=E_G+E(v_i->v_j)+E(v_j->v_i)$
   $E_G=E_G+E(v_{x(i)}->v_j)+E(v_{x(j)}->v_i)$
   for all new generated $E(v_s->v_q)$ do
   $l=i$ or j which is not q
   if ($t[q]>c$)
   $t[q]=c$
   $f[q]=l$
   endif
   endfor
   endfor
   $c=c+1$
   endif
   end

forward path of shortest path is the shortest path. While seeking the earliest path, if an edge $E_{s\to a}$ is added to G_k because of the establishment of link between i and j, then the information has been transmitted to a and either i or j is a and the other one is the prior node of a. At last, according to the forward path attribute and the two tables recording the prior node and arrival slot, we can get the *Earliest Journey*. The algorithm is shown in Table 3.

From the following process we can conclude that the spread speed of information is exponential growth pattern. After k slots, due to the repeated received information, the maximum number of satellites which have received the information is $2^{k+1}-1$.

3.2 Shortest Journey

The shortest journey can transmit the information to the destination node with the minimum hops. The *Shortest Journey* algorithm is similar to the *Earliest Journey* algorithm. A difference between two algorithms is that *Fastest Journey* algorithm keeps updating the fastest journey until all the link assignment of a cycle period is completed. In addition, in order to obtain the path of the least number of hops, each satellite node needs to maintain an additional table recording the number of hops of each node. Therefore, the data structure of each node in the algorithm is as shown in Table 4.

The basic idea of *Shortest Journey* algorithm is similar to the *Earliest Journey* algorithm. The algorithm is shown in Table 5.

Table 4 Data structure in *Shortest Journey* algorithm

Satellite no.	Prior node	Arrival slot	Hop count
i	j	k	d

Table 5 *Shortest Journey* algorithm

Shortest Journey

Input: Link Assignment Matrix Q; Time Slot k; Source Node $s \in V_G$.
Output: Hop-Count Array $d[v]$; Arrival Slot Array $t[v]$; Prior Node Array $f[v] \in V$.
Variables: Directed Graph $G(V_G, E_G)$; Counter c.

1. Initialize: $E_G = Null$; $c=0$; For all $v \in V$ *and* $v \neq s$, $d[v]=\infty$, $f[v]=Null$; $d[s]=0$, $f[s]=$s.
2. While $c \leqslant K$
   for all i,j s.t $Q_{i,k+c \bmod K}=j$ do
   $E_G=E_G+E(v_i->v_j)+E(v_j->v_i)$
   $E_G=E_G+E(v_{x(i)}->v_j)+E(v_{x(j)}->v_i)$
   for all new generated $E(v_s->v_q)$ do
   $l=i$ or j which is not q
   if ($d[q]>d[l]+1$)
   $d[q]= d[l]+1$
   $t[q]=c$
   $f[q]=l$
   endif
   endfor
   endfor
   $c=c+1$
   end

4 Experiment and Result Analysis

In this section, the experiment is based on constellation model of Walker 24/3/2 and we use the link assignment schedule in literature [3] for reference. Supposed that satellite 1 generates the information in slot 1, we compute *Shortest Journey* and *Earliest Journey* from satellite 1 to all other satellites. The results are shown in Tables 6 and 7. The comparisons on arrival slot and the number of hops between two journeys is shown in Figs. 4 and 5.

From the results shown in Tables 6 and 7, we can get the earliest and fastest paths from satellite 1 to all other satellites. For example, the earliest path of satellite

Table 6 Experimental result of Earliest Journey algorithm. The earliest path of satellite 5 receiving the information from satellite 1 is 1(1) → 4(2) → 7(5) → 5

i	1	2	3	4	5	6	7	8	9	10	11	12	13	14	15	16	17	18	19	20	21	22	23	24
j	1	4	1	1	7	1	4	6	11	4	17	6	7	20	1	14	1	12	13	4	23	6	7	22
k	1	5	5	1	5	2	2	5	5	4	4	3	3	4	4	5	3	4	4	3	5	4	4	5

Table 7 Experimental result of Shortest Journey algorithm. The shortest path of satellite 5 receiving the information from satellite 1 is 1(5) → 3(6) → 5

i	1	2	3	4	5	6	7	8	9	10	11	12	13	14	15	16	17	18	19	20	21	22	23	24
j	1	1	1	1	3	1	1	1	15	4	17	6	1	13	1	1	1	17	1	4	3	6	17	1
k	1	9	5	1	6	2	6	10	6	4	4	3	7	9	4	11	3	9	8	3	7	4	6	12
d	0	1	1	1	2	1	1	1	2	2	2	2	1	2	1	1	1	2	1	2	2	2	2	1

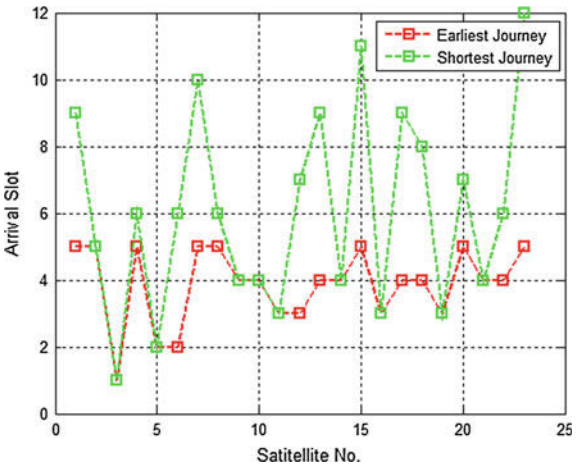

Fig. 4 Comparison on arrival slot between two journeys. The *X-axis* is satellite number. The *Y-axis* is the arrival time slot

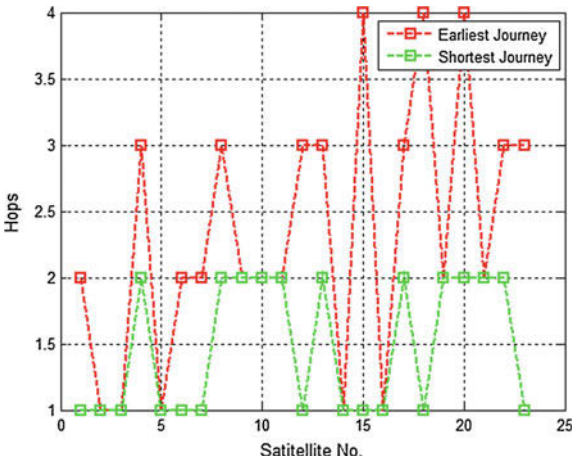

Fig. 5 Comparison on hops between two journeys. The *X-axis* is satellite number. The *Y-axis* is the number of hops

5 receiving the information from satellite 1 is 1(1) → 4(2) → 7(5) → 5. The shortest path is 1(5) → 3(6) → 5. The figures in () represent the slot number.

From the experimental results shown in Figs. 4 and 5 we can get that the earliest path in terms of time is better than the shortest path, but it takes more hops. Similarly, the shortest path in terms of hops is better than the earliest path, but it takes more time slots. In the information transmission process, it will take up less communication resources if the information is transmitted via the shortest journey, for it needs less times of forwarding. However, it is at the cost of longer waiting time and more cache resources. If the information is transmitted via the earliest journey, it will take up less time slots. But it will need more times of forwarding which will take up more communication resources. In practice, the specific choice between the shortest journey and the earliest journey is determined by different needs and constraints.

5 Conclusions

In this paper, we propose a solution to describe the progress of information transmission based on building directed graph and come up with two algorithms to find the earliest route and the shortest route from a source satellite to all the other satellites. According to the simulation results, it turns out that the two algorithms are feasible.

References

1. Luo D, Liu Y, Liu YF et al (2014) Present status and development trends of inter-satellite link. Telecommun Eng 54(7):1016–1024
2. Xuan BB, Ferreira A, Jarry A (2003) Evolving graphs and least cost journeys in dynamic networks. WiOpt'03: modeling and optimization in mobile, ad hoc and wireless networks. Sophia Antipolis, France
3. Hou Z, Yi X, Zhong T et al (2015) Path selection of navigation information transmission under the rules of polling chain-built. J Equip Acad 26(3):69–73
4. Yan H, Zhang Q, Sun Y (2015) Link assignment problem of navigation satellite networks with limited number of inter-satellite links. Acta Aeronautica et Astronautica Sinica 36(7): 2329–2339

Performance Analysis of China Regional VTEC Kriging Grid Algorithm

Ling Huang, Hongping Zhang and Peiliang Xu

Abstract The ionospheric delay is the predominant error source limiting the required positioning accuracy of GNSS whose estimation accuracy affects the effectiveness of ionospheric delay correction directly, especially in mid- and low-latitude regions where the irregularities of ionosphere are prominent. And a certain spatiotemporal variation exists in ionosphere which is caused by the fact that the intensity of ionospheric delay depends on the solar activities. Considering the spatiotemporal distribution characteristics of the ionosphere, data from the Crustal Movement Observation Network Of China (CMONOC) are processed to achieve the ionospheric TEC grid modeling in real time based on spatial variability and correlation theory, and its performance is analyzed under different solar activities. By processing the measured data, the accuracy of Kriging modeling under solar maximum (2014.02) and solar minimum (2015.03) since 2014 are analyzed and verified by the data from external rover stations located at different latitudes and longitudes. The statistics show that the inner precision can still reach about 2.63 TECU, and the Mean Square Error (MSE) of estimated grids VTEC is about 4.52 TECU under intense solar activity condition. The effect of correction at each rover station and the overall average of correction is generally 80 and 90 % or more, respectively, which is nearly equal to than that under low solar activity. This work reveals that the Kriging approach presented here which takes into account the spatial correlation and variability structure of the ionosphere TEC is appropriate for the areas with complex ionospheric variations such as China, and is also suitable for the situation under different solar activities.

L. Huang · H. Zhang (✉)
GNSS Research Center, Wuhan University, Wuhan 430079, China
e-mail: hpzhang@whu.edu.cn

L. Huang
e-mail: huangling_gnss@whu.edu.cn

P. Xu
Kyoto University, Tokyo 611-0011, Japan
e-mail: pxu@rcep.dpri.kyoto-u.ac.jp

© Springer Science+Business Media Singapore 2016

J. Sun et al. (eds.), *China Satellite Navigation Conference (CSNC) 2016 Proceedings: Volume III*, Lecture Notes in Electrical Engineering 390,
DOI 10.1007/978-981-10-0940-2_41

Keywords Ionospheric delay · Solar activity · Spatial variability and correlation · Kriging spatial interpolation · VTEC grid model

1 Introduction

As the predominant error source, the ionospheric delay imposes negative influence on the positioning accuracy of single-frequency users, the performance of PPP convergence and the global navigation service. The accuracy, reliability, and instantaneity of ionospheric delay model are demanded increasingly for constantly improving the positioning accuracy with the competition and development of GNSS. For the users that demand high precision and real-time navigation and positioning, wide area differential systems such as WAAS and EGNOS, employ the ionospheric grid model [1].

For the fact that the latitude and longitude span of China is larger than Europe, the United States and other areas, the ionospheric activity is more complex than the global average, and the ionospheric TEC varies obviously in different latitudes. The setting of model parameters for the common used regional ionospheric delay models such as polynomial, trigonometric series, low-degree spherical harmonic function model, directly influences the fitting effect and scope of application, furthermore, the correction effect is not ideal in the case of the ionosphere varies dramatically [2, 3].

The comprehensive effect of solar activities, the geomagnetic field and the neutral wind result in the ionosphere becoming a complex system with a certain spatial correlation and random variation. And yet, Kriging interpolation estimation method originating from geostatistics takes full consideration of the spatial correlation and variability of observations, which can effectively describe the spatial structure and the random variation of regionalized variables [4]. At present, this method has been widely used in geology, hydrology, remote sensing, meteorology, and other field which is related with spatiotemporal variables [5]. Various researches have been conducted in ionosphere utilizing this method with successful application in WAAS, UPC Global Ionospheric Maps (GIM) and regional real-time ionospheric foF_2 reconstruction and prediction of parameters of ionosphere F_2 layer [6–12].

Aiming at the special situation that China crosses the mid-low latitude with comprehensive variability of the ionospheric TEC, the Kriging interpolation method is employed into the ionospheric grid VTEC real-time estimation integrating the spatial variability and correlation information of the ionospheric TEC. The applicability and reliability of the Kriging spatial interpolation method for China area is demonstrated by analyzing its modeling accuracy and performance under different levels of solar activities from various perspectives.

2 Regional Ionospheric VTEC Kriging Grid Algorithm

2.1 The Ionospheric Delay Estimation Algorithm Based on Kriging Interpolation

The striking feature of Kriging estimator is that under the hypothesis of the second-order stationarity, it takes use of the regionalized variables spatial variability correlation to determine the optimal weights of sampling points around the unknown point under the constraints condition of unbiasedness and optimality and then to obtain the best linear unbiased estimation.

Based on the ionospheric single-layer assumption, the Ordinary Kriging (OK) method is applied to estimate the ionospheric delay at unmeasured ionospheric pierce points (IPP) by expressing it as the weighted linear combinations of the IPPs in a certain range:

$$\tilde{I}(x_0) = \sum_{i=1}^{N} \lambda_i I(x_i) \tag{1}$$

where $\tilde{I}(x_0)$ and $I(x_i)$ are the ionospheric delay values at the estimated point x_0 and sampling points $x_i (i = 1, 2, \ldots, N)$, and their corresponding weights are λ_i.

The expectation of the estimation error is:

$$E(\tilde{I}(x_0) - I(x_0)) = \sum_{i=1}^{N} \lambda_i E(I(x_i)) - E(I(x_0)) = m\left(\sum_{i=1}^{N} \lambda_i - 1\right) \tag{2}$$

The estimation error variance is given below:

$$\mathrm{var}(\tilde{I}(x_0) - I(x_0)) = 2\sum_{i=1}^{N} \lambda_i \gamma(x_i, x_0) - \sum_{i=1}^{N}\sum_{j=1}^{N} \lambda_i \lambda_j \gamma(x_i, x_j) \tag{3}$$

where m is the expectation of the ionospheric delay $E(I(x_i))$, $\gamma(x_i, x_j)$ is the semivariogram between x_i and x_j [5].

To minimize the error variance (3) under the unbiasedness constraint, the Lagrangian function is constructed as below by introducing the lagrangian multiplier μ:

$$L(\lambda, \mu) = 2\sum_{i=1}^{N} \lambda_i \gamma(x_i, x_0) - \sum_{i=1}^{N}\sum_{j=1}^{N} \lambda_i \lambda_j \gamma(x_i, x_j) - 2\mu\left(\sum_{i=1}^{N} \lambda_i - 1\right) \tag{4}$$

By computing the partial derivatives of the Lagrange function with respect to λ_i and μ setting them to be zero, the normal equations can be obtained:

$$\begin{aligned} &\sum_{i=1}^{N} \lambda_i \gamma(x_i, x_j) + \mu = \gamma(x_j, x_0), \quad j = 1, 2, \ldots, N \\ &\sum_{i=1}^{N} \lambda_i = 1 \end{aligned} \tag{5}$$

Equation (5) can be written in matrix form as follows:

$$\begin{bmatrix} \gamma_{11} & \gamma_{12} & \cdots & \gamma_{1N} & 1 \\ \gamma_{21} & \gamma_{22} & \cdots & \gamma_{2N} & 1 \\ \vdots & \vdots & \ddots & \vdots & 1 \\ \gamma_{N1} & \gamma_{N2} & \cdots & \gamma_{NN} & 1 \\ 1 & 1 & \cdots & 1 & 0 \end{bmatrix} \begin{bmatrix} \lambda_1 \\ \lambda_2 \\ \vdots \\ \lambda_N \\ \mu \end{bmatrix} = \begin{bmatrix} \gamma_{10} \\ \gamma_{20} \\ \vdots \\ \gamma_{N0} \\ 1 \end{bmatrix} \tag{6}$$

The solution for λ_i and μ can be obtained by Eq. (6). The error variance is simply given as follows:

$$\tilde{\sigma}_{OK}^2 = \sum_{i=1}^{N} \lambda_i \gamma(x_0, x_i) - \gamma(x_0, x_0) + \mu. \tag{7}$$

2.2 The Computation and Fitting of the Semivariogram

Kriging is a best linear weighted moving average method that the weighted coefficients depend on the relative position of the observation points and semivariogram. In the Kriging interpolation estimation theory, the semivariogram is used to describe the spatial correlation of observations, and is defined as half of the variance of the difference between variables at point x and $x + h$ in any interval h.

$$\begin{aligned} \gamma(h) &= \frac{1}{2}\mathrm{var}[Z(x+h) - Z(x)] \\ &= \frac{1}{2}E[Z(x+h) - Z(x)]^2 - \frac{1}{2}\{E[Z(x+h)] - E[Z(x)]\}^2 \end{aligned} \tag{8}$$

Under the hypothesis of second-order stationary, for any distance h, we have:

$$E[Z(x+h)] = E[Z(x)] \tag{9}$$

Then,

$$\gamma(h) = \frac{1}{2}E[Z(x+h) - Z(x)]^2 \tag{10}$$

The classical formula defining the experimental semivariogram is:

$$\gamma(h) = \frac{1}{2N(h)} \sum_{[h-\delta, h+\delta]}^{N(h)} (Z(x_k) - Z(x_l))^2 \tag{11}$$

Because we do not have pairs of measurements separated by exactly h, we will have to allow a certain tolerance δ. $N(h)$ is the number of point pairs in the distance lag. In ionospheric TEC estimation, $Z(x_k)$ and $Z(x_l)$ are the VTEC at IPP x_k and x_l, respectively. h is the spatial distance between IPPs, and its unit is in km. The computation formula is shown as following:

$$h = (R_e + H)\cos^{-1}(\sin\varphi_k \sin\varphi_l + \cos\varphi_k \cos\varphi_l \cos(\lambda_k - \lambda_l)) \tag{12}$$

where R_e is the average radius of the Earth. H is height of the ionosphere layer. (φ_k, λ_k) and (φ_l, λ_l) is the geographic latitude and longitude at IPP x_k and x_l, respectively.

In order to distribute the weight of each observation accurately, the semivariogram is needed to accurately calculate. Therefore, choosing an appropriate theoretical semivariogram model is the premise to guarantee the quality of the Kriging interpolation results. The commonly used semivariogram models include the spherical model, the exponential model, the Gaussian model, etc. [4]. In this paper, the spherical model with nugget is chosen, as shown in (13), and the model parameters are estimated by means of least squares fitting.

$$\gamma(h) = \begin{cases} C_0 + C\left(\frac{3}{2}\cdot\frac{h}{a} - \frac{1}{2}\cdot\frac{h^3}{a^3}\right), & 0 < h \le a \\ C_0 + C, & h > a \end{cases} \tag{13}$$

where C_0 is the *nugget* indicating the random part of the observations caused by the measurement error. The smaller the C_0, the stronger the spatial correlation of observations, and the weaker the randomness; the greater the C_0, the worse the correlation and stronger the randomness. $C_0 + C$ is the *sill* that reflects the biggest variation extent of the variables. C is the arc rise on behalf of the structural parts of the observations. a is the *range* which is the limit of spatial correlation; the greater the value of a, the larger the range of the spatial correlation.

3 Data Processing and Analysis of the Modeling Accuracy in China

The layout of the reference stations network has direct impact on the valid number, the geometric distribution and the density of IPPs [3], and then affects the external accuracy of the ionospheric grid model. In addition, the ionosphere is continually varying in response to changes in solar activity, and the sun spot number (SSN) is an important indicator of solar activity level. Therefore, the SSN can reflect the intensity degree of the ionosphere variation to a certain extent [13].

GPS data from 80 tracking stations with a reasonable level of a homogeneous distribution from Crustal Movement Observation Network of China (CMONOC) in February 2014 and March 2015 are selected. The regional range is 5°–60°N, 70°–140°E with temporal and spatial resolution of 2.5° (latitude) × 5° (longitude) × 60 s with a total of 345 grids. The SSN in 2014.02 and 2015.03 reaches the solar activity peak value (102.3) and valley value (38.4) since 2014, respectively. Figure 1 shows the distribution of the selected stations (red star) and IPPs at local time (LT) 14:00 on 2014.02.01 (DOY032). The monthly mean of SSN since 2014 and the daily mean of SSN in the peak and valley months are shown in Fig. 2. The data is obtained from the National Oceanic and Atmospheric Administration (NOAA) National Geophysical Data Center [14].

In this paper, the ionospheric delay is extracted by carrier-to-code leveling process. Due to the well stability of satellite DCB, they are calibrated using the GIM products processed by Wuhan University [12]. And the receivers DCBs are extracted from the raw observations of ionospheric delay at regional stations using the GIM products and the known satellites DCBs. Then the Kriging method is applied to the regional ionospheric TEC modeling in real time. The MSLM (Modified Single Layer Model) mapping function used by CODE is applied in this paper [16].

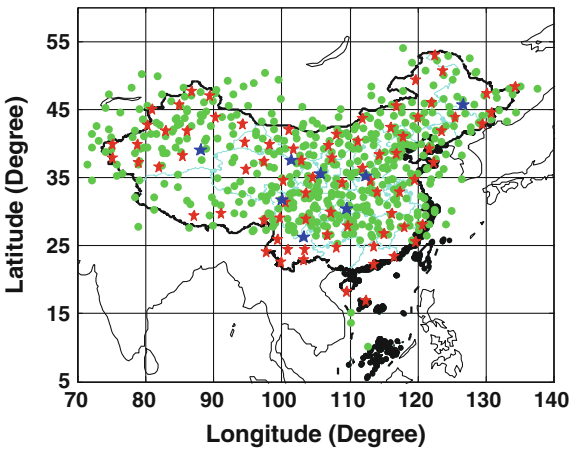

Fig. 1 Distribution of GPS stations and IPPs in China

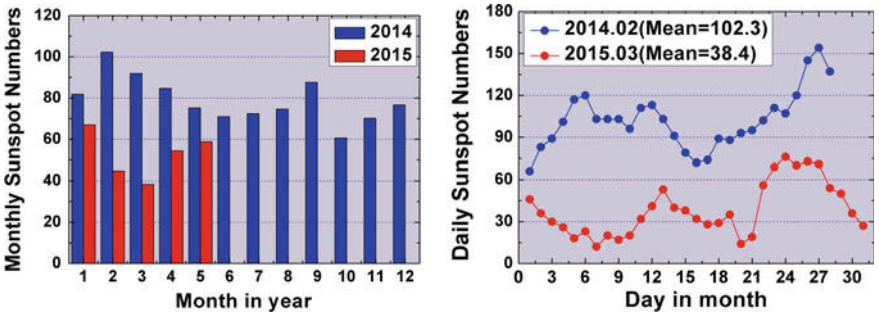

Fig. 2 The variation of SSN since 2014

3.1 The RMS Analysis of the Modeling Residuals

The fitting residuals are obtained by the statistics of the difference between the observations and the model values. Then the inner precision can be evaluated by the root mean square (RMS) of residuals, as is shown in Eq. (14).

$$RMS = \sqrt{\frac{1}{N}\sum_{i=1}^{N}\left(STEC_{obs} - STEC_{Krig}\right)_i^2} \tag{14}$$

where $STEC_{obs}$ is the STEC (Slant TEC) observation along the LOS, and $\mathrm{STEC}_{\mathrm{Krig}}$ is the interpolation value of the grid model along the same LOS. N is the observation number of STEC.

Figure 3 shows the time series of epoch fitting residuals in 2014.02 and 2015.03 when the solar activities reached peak and valley. It can be seen that the epoch RMS of Kriging interpolation has no obvious jump value and all within 1–4 TECU. The monthly mean of RMS in 2014.02 and 2015.03 are 2.63 TECU and 2.60 TECU, respectively. The results indicate that the Kriging modeling accuracy under the

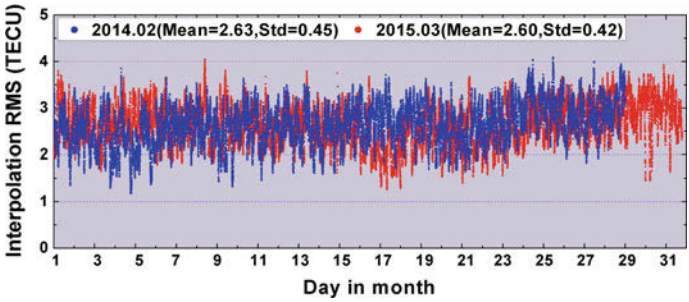

Fig. 3 The time series of epoch RMS in 2014.02 and 2015.03

condition of high solar activity level is still comparable to the accuracy in case of low solar activity level and is very stable. This is reasonable because although the ionosphere is intense at the high solar activity level, the Kriging greatly reduces the influence of the ionospheric irregularities by fully considering the spatial variability effects of the ionosphere to optimize the estimation. And the TEC observations around the estimated IPPs have strong spatial correlations at the low solar activity level with the smooth ionospheric varieties, small structural part, and large variation range. In this case, the accuracy of the Kriging interpolation largely depends on the precision of observations. In addition, because the Kriging interpolation is based on the vertical TEC, therefore the RMS is also associated with the elevation angle of observations and the mapping function.

3.2 The MSE Analysis of the IGPs VTEC Estimation

The Mean Square Errors (MSE) $\tilde{\sigma}_{OK}$, as shown in Eq. (7), which reflects the estimation accuracy can be calculated when estimating the grid VTEC. Figure 4 presents the epoch mean of the MSE during the solar maximum and minimum. The MSE are all within 14 TECU with overall averages 4.52 TECU and 4.35 TECU, respectively. The mean of MSE reaches 10–14 TECU at LT 14:00–16:00 on 2014.02.04. During the period, the ionosphere change was relatively strong, and the sunspot number reached 101, and the solar activity was strong which exacerbated the ionospheric activity levels. In addition, due to the lack of observations at the boundary, the IGPs in low latitudes have no interpolation values in the blank area which results in poor estimation accuracy or having no estimation values.

Figure 5 presents the MSE nephograms and the corresponding distribution of the IPPs at the epoch (LT15:21) which the MSE is larger. It can be found that the estimation accuracy is closely related to the distribution of IPPs. The more IPPs, the higher estimation accuracy and the smaller the MSE. The MSE is mainly in 5–10 TECU within the range of IPPs. Even though in low latitudes, the VTEC estimation

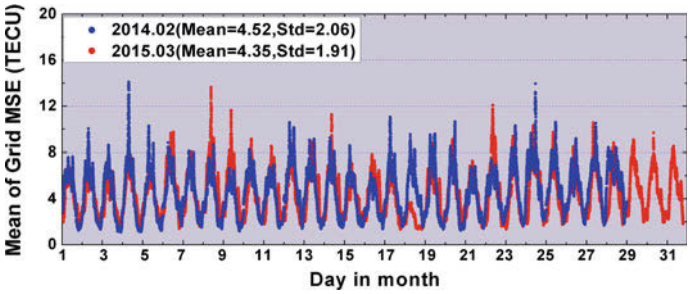

Fig. 4 The mean MSE at epoches on 2014.02.04

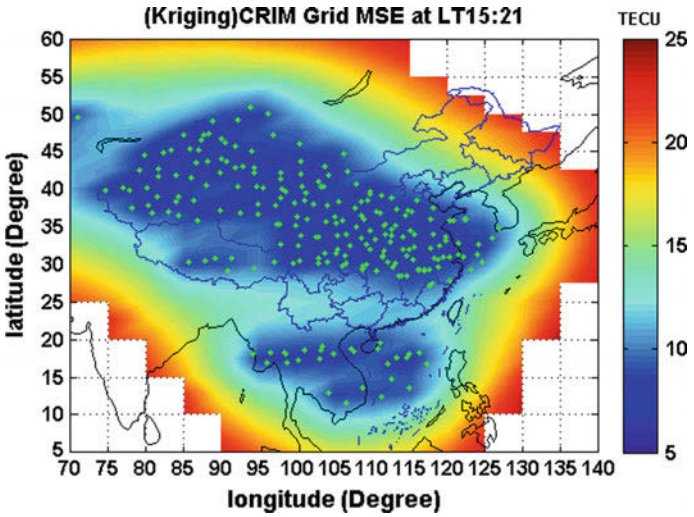

Fig. 5 The distribution of grid MSE and IPP at China local time 15:21 on 2014.02.04

accuracy can be improved obviously as long as there are sufficient IPPs, such as the area (10–15°N, 90–120°E). In the surrounding area where is lack of IPPs, the MSE is within 15–25 TECU. In the blank area, the corresponding grid VTEC cannot be estimated because the interpolation has no ability to extrapolate. Overall, the RMS and MSE have no significant mutations which demonstrate the good stability and reliability of the Kriging interpolation method.

3.3 The Evaluation Using the Rover Stations

In order to further verify the effect of the Kriging interpolation method, 8 rover stations which locate in different longitude and latitude were selects (the blue pentagrams as shown in Fig. 1. The correction effect of the Kriging VTEC grid model was assessed through the statistics of the differences between the STEC observations and the model values along LOS directions. The computation formula of the correction percentage is as follows:

$$\mathrm{CorPer} = \frac{1}{N}\sum_{i=1}^{N}\left(1 - \frac{\left|\mathrm{STEC}_{\mathrm{Krig}} - \mathrm{STEC}_{\mathrm{obs}}\right|}{\mathrm{STEC}_{\mathrm{obs}}}\right) \tag{15}$$

The meaning of each symbol is the same as Eq. (14).

Figure 6 shows the results of the model correction effect at the selected rover stations at the different levels of solar activities. The daily mean correction

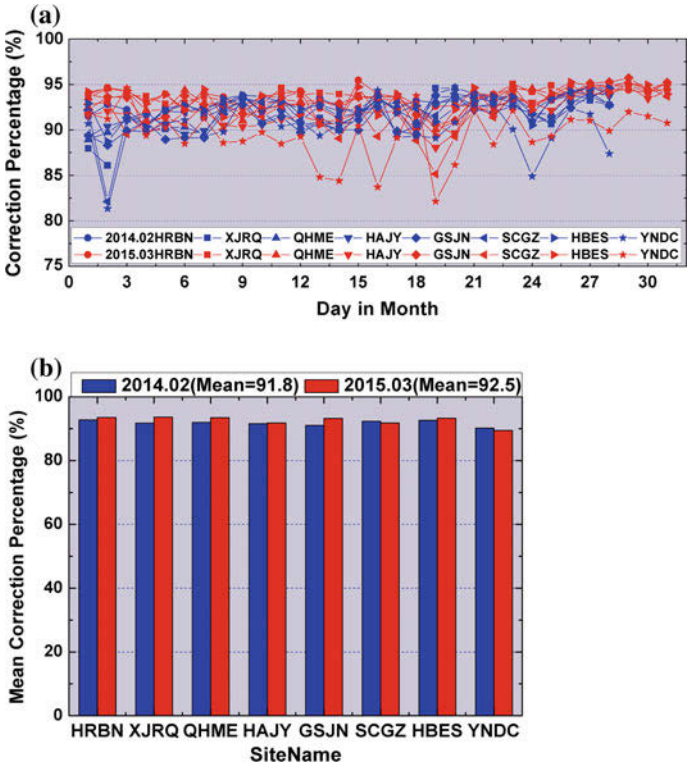

Fig. 6 **a** Daily mean correction percentage of rover stations 6. **b** Monthly mean correction percentage of rover stations

percentage of each station reaches more than 80 %. Except for the site YNDC which locates in low latitude, the correction effect at other stations which locate relatively high latitudes where the ionospheric activities decrease are all above 90 % as is shown in Fig. 6a. Figure 6b presents the monthly mean correction percentages of rover stations in the order from the mid-latitudes to low latitudes with effects of 90 % or more. For all stations, the whole correction effects reach 91.8 and 92.5 % on average in 2014.02 and 2015.03, respectively. This shows that the correction effect of the Kriging grid model under the condition of strong solar activities is almost equal to that in the quiet solar activities period. This is mainly because the Kriging interpolation method possesses the characteristic that takes full use of the correlations of the observations to reduce the effects of the ionospheric irregularities. Therefore, the differences of correction effect at different latitudes under different solar activities are not obvious. The correction effect of this model is comparatively ideal through verification at different latitudes stations which further verifies the reliability of the method.

4 Conclusions

In this paper, taking account of the complex physical properties of the ionosphere and giving full consideration to the structural and random characteristics in ionosphere, the ionospheric grid model for China was reconstructed in real time based on the Kriging theory of the spatial correlation and variability in geostatistics. The ionosheric VTEC grid model based on Kriging spatial interpolation possesses high and stable accuracy which is verified under different solar activities from various perspectives including the RMS of the model fitting residuals and the grid estimation error MSE in statistical analysis, and the external validation is also analyzed using different latitudes rover stations. The RMS is around 2.6 TECU on average, MSE is around 4.5 TECU, and the correction effect is mainly more than 90 %. Therefore, this model could provide reliable and accurate real-time ionospheric correction information for navigation and positioning.

Acknowledgments This work is supported partly by grants from the Key Program of National Natural Science Foundation of China (No. 41231064), the National High Technology Research and Develop Program of China (No. 2014AA123101). And we are grateful to the CMONOC authorities for providing the data for this study.

References

1. Komjathy A, Spark L, Mannucci AJ et al (2002) An assessment of the current WAAS ionospheric correction algorithm in the South American region. In: ION GPS 2002. Oregon Convention Center Portland
2. Yuan Y (2002) Study on theories and methods of correcting ionospheric delay and monitoring ionosphere based on GPS. PhD thesis, Institute of Geodesy and Geophysics Chinese Academy of Sciences
3. Zhang H (2006) Study on China ionospheric delay and monitoring ionosphere based on GPS. PhD thesis, Shanghai astronomical observatory
4. Zhang R (2005) Theory and application of spatial variability. Science Press, Beijing
5. Sarma DD (2002) Geostatistics with applications in earth sciences. Capital Publishing Company, New Delhi
6. Blanch J (2002) An ionospheric estimation algorithm for WAAS based on Kriging. In: Proceedings of the Institute of Navigation GPS-02, Portland, OR
7. Orús R, Hernández-Pajares M, Juan JM, Sanz J (2005) Improvement of global ionospheric VTEC maps by using Kriging interpolation technique. J Atmos Solar Terr Phys 67:1598–1609
8. Sayin I, Arikan F, Arikan O (2007) Synthetic TEC mapping with ordinary and universal Kriging. In: Proceedings 3rd international conference on recent advances in space technologies, RAST'07. IEEE, pp 39–43
9. Wang S, Jiao P, Liu W (2006) Improved Kriging technique of ionospheric parameter foF2 instantaneous mapping. Chin J Radio Sci 21(4):166–171
10. Mao T, Wan W, Sun L (2012) Central and northern China TEC map using the Kriging method. Chin J Space Sci 32(2):209–215
11. Liu RY, Liu GH, Wu J et al (2008) Ionospheric foF2 reconstruction and its application to the short-term forecasting in China region. Chin J Geophys 51(2):300–306 (in Chinese)

12. Huang Z, Yuan H (2012) Ionospheric refraction correction based on spatial statistic for China region. Chin J Space Sci 32(2):209–215
13. Ma LH, Han YB, Yin ZQ (2009) Periodicities in global mean TEC from GNSS observations. Earth Moon Planet 105(1):3–10
14. NOAA National Geophysical Data Center. http://www.ngdc.noaa.gov/stp/space-weather/solar-data/solar-indices/sunspot-numbers. Accessed 11 Nov 2014
15. Zhang HP, Xu PL, Han WH et al (2013) Eliminating negative VTEC in global ionosphere maps using inequality-constrained least square. Adv Space Res 51(6):988–1000
16. Stefan S (1999) Mapping and predicting the Earth's ionosphere using the global positioning system. The Univesity of Bem, Bem

The Tropospheric Product Combination of iGMAS Analysis Centers and the Analysis of Their Precision

Yuguo Yang, Tianhe Xu and Zhangzhen Sun

Abstract Several analysis centers (AC) and a product integration and service center (ISC) have been built by the international GNSS continuous Monitoring and Assessment System (iGMAS) currently. ISC analyzes the quality of product provided by ACs of iGMAS, and then reprocesses to generate a combined product. The tropospheric solution is the key product of ISC and important data for satellite navigation and precise point positioning (PPP). First of all, this paper introduces the method and theory of tropospheric product combination by means of weighted average based on robust estimation. Then, the precision of combined tropospheric product of ISC and the AC's product with respect to the JPL final tropospheric delay is compared and analyzed. Furthermore, the tests of using iGMAS data are implemented to verify the accuracy and reliability of combined tropospheric solution. The results show that the RMS of the combined tropospheric solutions of IGS stations are better than those of most analysis centers, and meet the accuracy requirement of iGMAS. Finally, the precision of ACs' tropospheric products of iGMAS stations with respect to the ISC final products is compared and analyzed.

Keywords iGMAS · Tropospheric product combination · Robust estimation · Weighted average · iGMAS station

Y. Yang (✉)
School of Geology Engineering and Geomatics, Chang'an University,
Xi'an 710054, China
e-mail: yyguo514@163.com

T. Xu (✉)
State Key Laboratory of Geo-information Engineering, Xi'an 710054, China
e-mail: thxugfz@163.com

T. Xu
Xian Research Institute of Surveying and Mapping, Xi'an 710054, China

Z. Sun
Insititute of Space Science ShanDong University, Weihai 264209, China

© Springer Science+Business Media Singapore 2016

J. Sun et al. (eds.), *China Satellite Navigation Conference (CSNC) 2016 Proceedings: Volume III*, Lecture Notes in Electrical Engineering 390,
DOI 10.1007/978-981-10-0940-2_42

1 Introduction

Product integration and service center (ISC) is an important part of the international continuous monitoring and assessment system (iGMAS) and is also the reprocessing center of high-precision products. Meanwhile it is the window of products distribution center whose products are open for users. Currently, most of iGMAS analysis centers (AC) have submitted the final and ultrafast tropospheric products to ISC. ISC analyzes the quality of all AC's products on time, and provides the combination products and the report of their precision assessment at the same time.

From the 1990s, the International GNSS Service (IGS) and the International VIBL service (IVS) have provided tropospheric zenith delay product ZTD, and many studies on tropospheric combination had been done. Keshin [1] introduced the methods of sequential combination of regional tropospheric solutions in the technical report of GPS 2004, and proposed a method of combination troposphere time series by Kalman filter. Pacione et al. [2] combined the time series of troposphere using the least squares (LS) and Kalman filtering, and compared the accuracy of the two methods. Heinkelmann et al. [3] combined a long-term tropospheric time series from VLBI, and compared the precision with eight IVS Analysis Centers. Thaller [4], studied a method of combining the tropospheric products of GPS and VLBI on the normal equation level and parameter level, respectively, in the report. Li and Xu [5] focus on a method of robust Kalman filtering for combination of troposphere time series. Once given the time series from various ACs, with the theory of robust Kalman filtering and least-squares variance component estimation, the average accuracy of the combined solution of tropospheric delay can approach 0.85 mm. A new method of weighted average based on robust estimation is put forward in the paper. A numerical example of iGMAS data is used to test the precision and reliability of the proposed method.

2 The Combination and Assessment of Tropospheric Products

With the differences in the coordinate and time reference frame between the ACs' products, the outlier may be found in products of a single AC. The optimal data processing algorithm and robust estimation method should be used in product combination in order to obtain accurate and reliable combined products [6].

2.1 The Method of Tropospheric Delay Estimation

Tropospheric products of AC are generally calculated by the Precise Point Positioning (PPP) with satellite orbit and clock parameters fixed [6]. The parameter estimation methods of PPP commonly include the LS and Kalman filtering [7].

Assume the error equation of GNSS data to estimate the tropospheric delay as:

$$V = B\,\delta\hat{x} - l \tag{1}$$

where $\delta\hat{x}$ is the correction of unknown parameters. The estimator of least squares adjustment can be expressed as

$$\delta\hat{x} = (B^T PB + P_{X_0})^{-1} B^T Pl \tag{2}$$

where X_0, P_{X_0} are the initial value of parameters and its weight matrix. It should be noted that equivalent reduction and recovery of parameters are involved in parameter estimation procedure. Details about the tropospheric delay estimation can be found in the literature [8, 9].

2.2 The Method of Tropospheric Combination

Robust least squares (RLS) estimation is proposed to combine the tropospheric product of each AC in this paper. Meanwhile, the initial unit weight is calculated by median method. The RLS estimation can eliminate observation with outlier directly, and reduce the weight of low quality observation. The median method can ensure the reliability of initial unit weight, which can influence the following LS estimation [10].

Since there inevitably exist outliers in ACs' tropospheric products, the equivalent weight should be iteratively calculated using robust estimation. Robust estimation is constructed based on the idea of double-elimination combination method [10]. Because the combined tropospheric product belongs to one-dimensional parameter estimation, the median of all the AC tropospheric corrections of the same epoch can provide a reliable initial value. Their median is chosen as the initial value for the following iteration. The error equation of median can be expressed as

$$v_i = L_i - \mathrm{med}(L_i) \tag{3}$$

where L_i is troposphere total delay of AC, $\mathrm{med}(L_i)$ is the initial value of the combination solution by median estimation. The initial residual is obtained by the difference between AC troposphere solution and the initial solution.

The initial residual is used to calculate variance factor σ_0 of unit weight by median estimation. IGG-III scheme is chosen as the iterative weight function [10].

$$\bar{p}_i' = \begin{cases} \bar{p}_i & |v_i'| \le k_0 \\ \bar{p}_i \frac{k_0}{|v_i'|}\left(\frac{k_1 - |v_i'|}{k_1 - k_0}\right)^2 & k_0 < |v_i'| \le k_1 \\ 0 & |v_i'| > k_1 \end{cases} \tag{4}$$

Finally, the combination troposphere can be calculated based on the weighted average method.

$$\mathrm{tro}_{\mathrm{com}}^{\mathrm{sta}} = \frac{\sum_{\mathrm{ac}}^{\mathrm{Nac}} W_{\mathrm{AC}}^{\prime\mathrm{sta}} \cdot \mathrm{tro}_{\mathrm{AC}}^{\mathrm{sta}}}{\sum_{\mathrm{ac}}^{\mathrm{Nac}} W_{\mathrm{AC}}^{\prime\mathrm{sta}}} \tag{5}$$

where Nac is the total number of analysis center. $W_{\mathrm{AC}}^{\prime\mathrm{sta}}$ is the equivalent weight calculated by formula (4) after the iteration.

2.3 Precision Assessment of Tropospheric Combination

After getting the combined tropospheric solution, the comparison and analysis on the precision of combined products is needed. The tropospheric delays of all ACs and ISC in the same epoch are compared, where interpolation method may be used if the sample intervals are different. Then, the tropospheric residuals of ACs in each station can be obtained as follows:

$$V_j^i = X_{sj}^i - X_{cj} \tag{6}$$

where X_{sj}^i $(i = 1\ldots n, j = 1\ldots m)$ are zenith tropospheric delay of ACs in different station, m is the number of stations, X_{cj} is the combined tropospheric delay in the same station.

According to the residuals of ACs for all stations, the mean, standard deviation, and root-mean-square error can be calculated for all ACs in different station as the following formula:

$$\bar{V}_{\mathrm{trp}}^i = \frac{\sum_{k=1}^m V_k^i}{m} \tag{7}$$

$$\mathrm{STD}_{\mathrm{trp}}^i = \sqrt{\frac{\sum_{k=1}^m \left(V_k^i - \bar{V}_{\mathrm{trp}}^i\right)\left(V_k^i - \bar{V}_{\mathrm{trp}}^i\right)'}{m}} \tag{8}$$

$$\mathrm{RMS}_{\mathrm{trp}}^i = \sqrt{\frac{\sum_{k=1}^m V_k^i V_k^{i\prime}}{m}} \tag{9}$$

Based on the residuals of ACs, the precisions of combined products and ACs' products can be estimated.

Precision assessment process is shown as in Fig. 1.

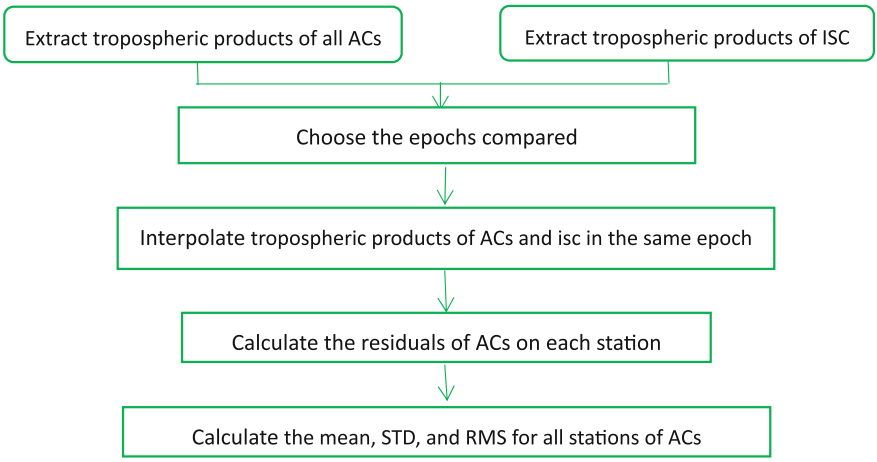

Fig. 1 Flowchart for precision assessment of tropospheric delay combination

3 Calculation and Analysis of Tropospheric Delay on IGS Stations

In order to compare and analyze the accuracy of combined products and ACs' products, we selected 53 weeks' data from 271 of day of year in 2014 to 283 of day of year in 2015 (BDS weeks 0456–0509) for calculation provided by ACs of iGMAS.

The combined tropospheric delay were calculated using 10 ACs' final and ultrafast products of iGMAS on IGS stations during BDS week 0456–0509. Then, the root-mean-square errors (RMS) of ACs' tropospheric delay with respect to the JPL final product were computed. Figure 2 shows the RMS of final tropospheric products of iGMAS with respect to the JPL final products. Figure 3 shows the RMS of ultrafast tropospheric products of iGMAS with respect to the JPL final products. isc refers to a combined tropospheric product, bac, …, xsc represent 10 ACs in chart.

From the statistical results in Table 1, the following conclusion can be drawn:

1. The accuracies of the final tropospheric products of iGMAS ACs and ISC are significantly higher than those of the ultrafast products.
2. The RMSs of isc, cgs, lsn, and tlc are less than 4 mm and the tropospheric products of isc have the highest accuracy; The RMS of bac, sha, tac, and whu is a little bit higher. The RMS of isc is about 3 mm, which has a greatly improvement compared to ACs. It indicates that the proposed method of weighted average based on robust estimation can efficiently and robustly combine all the products of ACs.

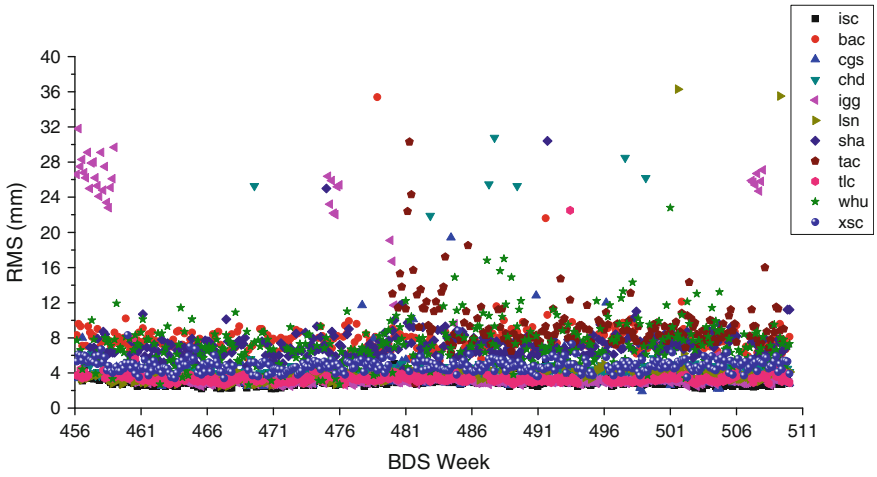

Fig. 2 The RMS of final tropospheric product on IGS stations with respect to the JPL final

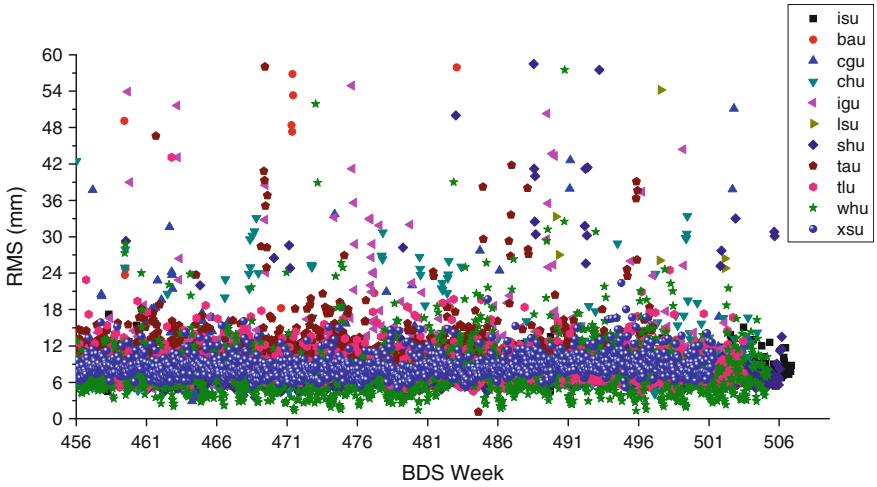

Fig. 3 The RMS of ultrafast tropospheric product on IGS stations with respect to the JPL final

3. The accuracy of ultrafast tropospheric product is obviously lower than that of the final product which is related to the fact that the ultrafast products have a poor accuracy itself. For most of the ACs, the accuracy is less than 8.5 mm for the ultrafast products, and the accuracy of isc is about 7.7 mm, which is still the best one compared to the products of ACs.

Table 1 The RMS of tropospheric on IGS stations with respect to the JPL final (unit: mm)

AC	Final	Ultrafast
isc	3.0	7.7
bac	8.0	8.5
cgs	4.0	9.0
chd	4.6	8.0
igg	5.4	9.2
lsn	3.9	8.1
sha	7.6	7.7
tac	9.6	11.2
tlc	3.4	8.5
whu	7.2	7.7
xsc	4.8	8.7

4 Calculation and Analysis of Tropospheric Delay on iGMAS Stations

Up to now, iGMAS tracking stations are mainly located at the domestic. International organization such as IGS does not involve these stations for data processing. So there are no external reference products during the combination. From the above analysis, the weighted average based on robust estimation method can be efficiently applied to tropospheric product combination of the iGMAS stations and the isc products can be regarded as reference to assess the tropospheric product accuracy of ACs.

Six weeks' data provided by 9 ACs' final tropospheric products from 0499 to 0504 of BDS week is selected for calculation and analysis. The RMS of ACs' tropospheric products on iGMAS stations are compared to those of ISC.

From the calculation results shown in Figs. 4 and 5; Table 2, the following conclusions can be drawn:

1. Only three ACs meet the accuracy requirements (less than 4 mm) of the final tropospheric product in terms of iGMAS stations. Among them, cgs, chd, and lsn have the highest accuracy and their RMS is about 3.8 mm. Most of ACs' accuracies are within 6.5 mm and the few of them is very low. In terms of ultrafast products only tlc meets the accuracy requirement of RMS less than 6 mm.
2. There are many gaps in tropospheric products of iGMAS stations compared to isc. The reasons are fall in two aspects, on one hand, there are few ACs to provide tropospheric products of iGMAS stations which do not always meet the condition of at least three analysis centers involved in the combination. On the

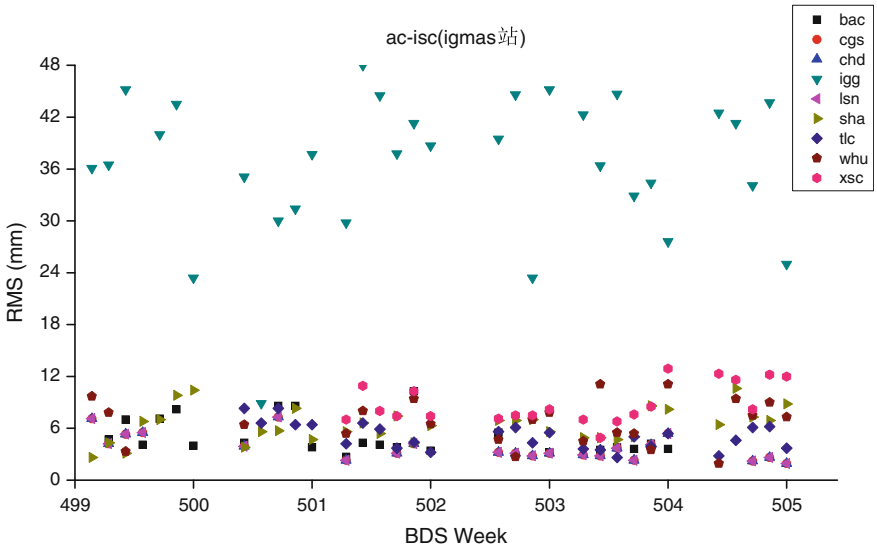

Fig. 4 The RMS of final troposphere on iGMAS stations with respect to the isc final

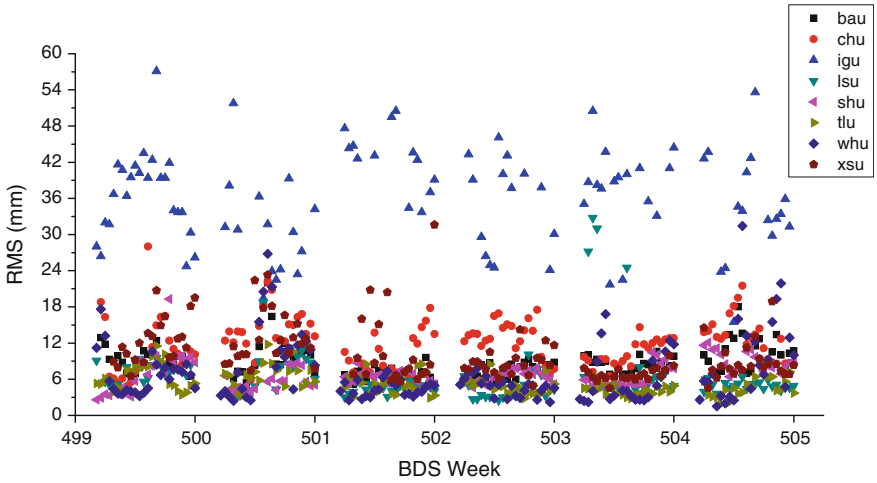

Fig. 5 The RMS of ultrafast troposphere on iGMAS stations with respect to the isc final

other hand, the solution of iGMAS stations products of ACs is unstable and the accuracy is relatively poor, which leads to big difference among the accuracies of the tropospheric products by ACs and isc failure in the combination.

Table 2 The RMS of troposphere on iGMAS stations with respect to the isc final (unit: mm)

AC	Final	Ultrafast
bac	5.1	8.7
cgs	3.8	–
chd	3.8	12.0
igg	36.9	36.3
lsn	3.8	6.4
sha	6.4	6.9
tlc	5.1	5.4
whu	6.7	6.9
xsc	8.8	10.0

5 Conclusions

Tropospheric delay is an important error source in GNSS observation which directly impact on the accuracy of PPP. Combined tropospheric product is one of the main product provided by iGMAS and ISC need to guarantee the accuracy and reliability of tropospheric product. This paper introduces the tropospheric delay combination of ISC and compares the accuracy and reliability of the combination tropospheric product. There still exist some shortcomings in the process of combination and analysis. At present, iGMAS ACs and ISC are at the early stage of construction, and face many problems and challenges. Among them, how to improve the accuracy and stability of iGMAS tropospheric products needs to be urgently solved. Although weighted average based on robust estimation meets accuracy requirement, the RMS is still large. Improved weighting strategy is the future work to be carried out.

Acknowledgments Thanks to the ACs of iGMAS and JPL to provide the tropospheric products. This work is supported by the National Natural Science Foundation of China (No. 41574013 and 41174008) and the Foundation of State Key Laboratory of aerospace dynamics (No. 2014ADL-DW0101).

References

1. Keshin M (2007) Sequential combination of troposphere time series. GPS Solut 11:37–47
2. Pacione R, Pace B, Vedel H et al (2011) Combination methods of tropospheric time series. Adv Space Res 47(2):323–335
3. Heinkelmann R, Boehm J, Schuh H et al (2007) Combination of long time-series of troposphere zenith delays observed by VLBI. J Geod 81(6):483–501
4. Thaller D (2008) Inter-technique combination based on homogeneous normal equation systems including station coordinates, Earth orientation and troposphere parameters. GFZ, Helmholtz-Zentrum, Potsdam
5. Li M, Xu TH (2015) A combined Kalman filter for troposphere time series. J Navig Position 3 (3):79–84

6. Chen K, Xu T, Chen G et al (2015) The orbit and clock combination of iGMAS analysis centers and the analysis of their precision. In: Proceedings of China satellite navigation conference (CSNC) 2015, vol II. Springer, Heidelberg, pp 421–438
7. Byun SH, Bar-Sever YE, Gendt G (2005) The new tropospheric product of the international GNSS service. In: Proceedings of international technical meeting of the satellite division of the Institute of Navigation, pp 241–249
8. Ge MR, Liu JN (1996) The estimation methods for tropospheric delays in global positioning system. Acta Geodaetica Cartogr Sin 4:285–291
9. Byun SH, Bar-Sever YE (2009) A new type of troposphere zenith path delay product of the international GNSS service. J Geod 83(3):1–7
10. Yang YX (1993) Robust estimation theory and it's applications. Bayi Publishing House, Beijing

BDS Zero-Difference Zero-Combination Precise Point Positioning Algorithm Study

Kefan Yang, Hongzhou Chai, Bingquan Dong, Yingdong Zhou, Di Li and Zongpeng Pan

Abstract Because of the characteristics of BDS satellite constellation and the accuracy of satellite orbit and clock error, the initialization time of the traditional ionosphere-free combination precision point positioning (LC-PPP) is longer. To solve this problem, we use the Zero-difference Zero-combination PPP (ZDZC-PPP) algorithm to quickly initialize BDS PPP. The algorithm can take advantage of a priori information of ionosphere as a prior restraint enhancing the equation strength. Therefore it makes it possible to shorten the PPP initialization time. This paper introduces the ZDZC-PPP algorithm and analyzes the difference between it and the LC-PPP. Compared with the traditional LC-PPP, the calculation results show that the ZDZC-PPP can effectively shorten the initialization time and can obtain the high accuracy of the positioning results by MGEX observation data.

Keywords Precise point positioning · Zero-difference zero-combination · Ionosphere delay · Initialization time

1 Introduction

Precise Point Positioning (PPP) using a single GNSS receiver and the precise ephemeris and satellite clocks provided by International GNSS Service (IGS) and combined pseudorange and carrier phase observations can achieve millimeter to centimeter level positioning accuracy [1]. With the gradual improvement and development of BeiDou Navigation Satellite System (BDS), BDS based on PPP has attracted wide attention of scholars both at home and abroad. However, at present, the research mainly focuses on the positioning accuracy of BDS PPP, while the research on the convergence speed is relatively weak. As a kind of effective and convenient

K. Yang (✉) · H. Chai · B. Dong · Y. Zhou · D. Li · Z. Pan
Institute of Surveying and Mapping, Information Engineering University, Zhengzhou 450001, China
e-mail: ykfbpy@163.com

© Springer Science+Business Media Singapore 2016

J. Sun et al. (eds.), *China Satellite Navigation Conference (CSNC) 2016 Proceedings: Volume III*, Lecture Notes in Electrical Engineering 390,
DOI 10.1007/978-981-10-0940-2_43

high precision positioning technology, PPP has immeasurable prospects in engineering application, but its convergence speed and short time positioning accuracy are the main factors that affect the efficiency of the work. The BDS has provided the positioning services to the Asia Pacific region, so it is important to study the positioning performance of the BDS PPP, especially the convergence speed and short time positioning accuracy [2]. Traditional PPP positioning technology is based on the original concept of measurement ionosphere-free combination (LC). However, the mixed BDS satellite constellation characteristics make the space satellites geometric transformation slowly and the current precise BDS satellite antenna phase center correction model and the solar radiation model are unknown, which make the BDS ionosphere-free precise point positioning (LC-PPP) initialization longer.

Reference [3] showed that use of the zero-differenced and zero-combined observables can make full use of a priori information of the ionosphere delay, which can enhance the intensity of the equation and make it possible to shorten the PPP initial time. In this paper, we study the fast initialization of BDS PPP by using the zero-difference zero-combination PPP (ZDZC-PPP) algorithm. The second part of the paper describes the zero-difference zero-combination observation model, stochastic model and parameter estimation model, and the third part is the experimental strategies and results, the last part is the conclusion.

2 BDS PPP Model and Data Processing Strategy

2.1 Observation Equation

1. Zero-differenced and Zero-combined equation

The traditional PPP algorithm uses the dual frequency pseudorange and the carrier ionosphere-free combination to eliminate the ionospheric delay, but the combination makes the pseudorange and the carrier observation noise to expand nearly three times [4]. To limit the observation noise amplification, we use a ZDZC-PPP algorithm based on original observations, with the oblique ionospheric delay as a parameter to estimate and taking into account a priori information of the ionospheric delay to constraint the estimated ionospheric delay parameter, which can speed up the convergence of PPP. The observation equation is as follows:

$$P_{i,r}^{j} = \rho_r^j + c\left(dt_r - dt^j\right) + d_{\text{orb}}^j + T_r^j + \alpha_i I_{\text{ion}/f_i}^j + c\left(b_{p_i,r} - b_{p_i}^s\right) + \varepsilon\left(P_{i,r}^j\right) \quad (1)$$

$$L_{i,r}^{j} = \rho_r^j + c\left(dt_r - dt^j\right) + d_{\text{orb}}^j + T_r^j - \alpha_i I_{\text{ion}/f_i} + c\left(b_{L_i,r} - b_{L_i}^j\right) + \lambda_i N_{i,r}^j + \varepsilon\left(L_{i,r}^j\right) \quad (2)$$

where, $\alpha_i = f_1^2/f_2^2, P_{i,r}^j, L_{i,r}^j$ are the original pseudorange and carrier phase observation, respectively; the superscript j denote the satellites, subscript i and r denote

the observation frequency and receivers, respectively; ρ_r^j denote the geometry distance between the receiver and satellite; c is the speed of light in vacuum; dt_r and dt^j denote receiver and satellite clock offset, respectively; T_r^j denotes satellite orbit error; $b_{p_i,r}, b_{L_i,r}$ and $b_{p_i}^j, b_{L_i}^j$ denote receiver and satellite DCB, respectively; d_{orb}^j and I_{ion/f_i} denote troposphere and ionosphere delays, respectively; λ and N denote carrier wavelength and ambiguities, respectively; $\varepsilon\left(P_{i,r}^j\right)$ and $\varepsilon\left(L_{i,r}^j\right)$ are the observation noise of pseudorange and carrier phase and other corrections, respectively. Usually, the satellite's orbit and clock errors can be corrected by the precise ephemeris and the above equation is linearized. At the same time, the error correction of measurement must be taken into considered, such as DCB correction, earth tide correction, relativistic correction, antenna phase center correction, phase winding correction, etc. Detailed correction method can be referred to the reference [5]. The parameters to be estimated in equations are as

$$\hat{\mathbf{x}} = \left[\delta x, \delta y, \delta z, dt_r, d_{\text{trop},r}, \mathbf{d_{ion}}, \mathbf{N}\right] \tag{3}$$

where, $\hat{x}$ is the vector of parameters to be estimated, the right hand side followed by station coordinates, receiver clock error, tropospheric zenith wet delay, ionosphere delays and ambiguity parameters.

2. Ionosphere-free combination observation model

To facilitate the comparative analysis of the ZDZC-PPP model with the traditional PPP, we get the LC-PPP model for the linear combination of formula (1 and 2). Since the receiver and the satellite DCB cannot be separated directly with other parameters, they are usually estimated together with the receiver and satellite clock error parameters, respectively. The ionosphere-free combination observation equation is as follows:

$$P_{3,r}^j = \frac{f_1^2 \cdot P_1 - f_2^2 \cdot P_2}{f_1^2 - f_2^2} = \rho_r^j + \left(cdt_r + b_{P_3,r}\right) - \left(cdt^j + b_{P_3}^j\right) + d_{\text{orb}}^j + T_r^j + \varepsilon\left(P_{3,r}^j\right) \tag{4}$$

$$\begin{aligned} L_{3,r}^j = &\frac{f_1^2 \cdot L_1 - f_2^2 \cdot L_2}{f_1^2 - f_2^2} = \rho_r^j + \left(cdt_r + b_{P_3,r}\right) - \left(cdt^j + b_{P_3}^j\right) + d_{\text{orb}}^j + T_r^j \\ &+ \left(\lambda_3 N_{3,r}^j + b_{L_3,r} - b_{P_3,r} + b_{P_3}^j - b_{L_3}^j\right) + \varepsilon\left(L_{3,r}^j\right) \end{aligned} \tag{5}$$

Make $\lambda_3 B_{3,r}^j = \lambda_3 N_{3,r}^j + \left(b_{L_3,r} - b_{P_3,r}\right) - \left(b_{L_3}^j - b_{P_3}^j\right)$; in this situation, $\lambda_3 B_{3,r}^j$ containing pseudorange and carrier phase hardware delay and ambiguities parameters, so that the ambiguity parameter lose integer property, usually used real solutions [6].

IGS analysis centers typically use ionosphere-free combination (P1, P2 observation combination) to estimate precise satellite clock error, therefore the estimated

precise satellite clock error is: $cdt^j_{p_3} = cdt^j + b^j_{p_3}$. When the client uses ionosphere-free combination measurements (P1, P2 observation combination) positioning, the satellite hardware delay can be eliminated, without performing correction. Otherwise, the satellite hardware delay should be corrected, namely DCB corrections, to ensure the positioning model and the IGS ephemeris product self-consistent.

From the derivation of the above equations, we can find that the ionosphere-free combination is a linear combination of the original observations. Therefore, in essence, the results of the parameters estimation are equivalent in theory [7]. However, when we use the ZDZC-PPP model to estimate the ionosphere delay as a parameter, the priori ionospheric delay information can be used as a virtual measurement that can enhance the intensity of the equation, which is conducive to the PPP initialization [5].

Currently, high precision ionospheric delay information can be obtained from the GIM model provided by CODE. The accuracy of GIM is between 0 and 8 TECU, which is quite similar to that of the GPS pseudorange measurement. So it can be used to improve the performance of the PPP initialization. At the same time, the prediction GIM products can be used for real-time PPP.

2.2 Stochastic Model

Due to the accuracy of the measurement, concerning about the observed signals, the satellite signal with low elevation angle is easily influenced by atmospheric delay and noise. Therefore, the following trigonometric function model can be used to calculate the measurement accuracy of the satellite view of different heights.

$$\sigma^2 = \frac{\sigma_0^2}{2\sin(E)} \tag{6}$$

where, E denote the satellite elevation angle; σ_0 denote the standard deviation of the observation noise.

2.3 Parameter Estimation

In this paper, we use the Kalman filter to estimate the parameters and the error equation of the filter model is

$$\underset{2m\times 1}{v} = \underset{2m\times n}{H}\ \underset{n\times 1}{\hat{x}_k} - \underset{2m\times 1}{l}\ \underset{2m\times 2m}{\Omega} \tag{7}$$

$$\underset{n\times 1}{\bar{x}_k} = \underset{n\times n}{\Phi_k}\ \underset{n\times 1}{\hat{x}_{k-1}}\ \underset{n\times n}{Q_k} \tag{8}$$

$$\hat{\mathbf{x}}_{\mathbf{k}} = \left[\delta x, \delta y, \delta z, dt_r, d_{\text{trop}}, \delta^1_{\text{ion}}, \ldots, \delta^m_{\text{ion}}, N^1_k, \ldots, N^m_k\right] \tag{9}$$

where, subscript k denote the current one epoch; $\hat{\mathbf{x}}_{\mathbf{k}}$ is the n dimensional state vector optimal estimation; H is the coefficient matrix; Ω is the Covariance matrix of observations; $\bar{x}_k$ is the k moment prediction state; Φ is the state transition matrix; Q_k is the variance matrix of the system process noise sequence.

The handling method of the unknown parameters and the error term of BDS PPP are similar to GPS PPP. For the position coordinate parameters, under the static condition, the prior constraint is 10^2 m and the process noise is 0. The receiver clock error is estimated as white noise, and the variance of the process noise is $10^8\ \text{m}^2/\text{s} \times \Delta t$. The troposphere parameters are estimated as a random walk process, and the process noise variance using the process noise power spectral density q multiply by Δt, which is before and after epoch interval. When the cycle slip did not happen, the ambiguity parameters should be as constant to process and the corresponding process noise variance can be set to 0. Otherwise, ambiguity parameters need to re-initialize and the process noise variance is consistent with the initial epoch.

3 Test Results and Analysis

In order to evaluate the influence of the ionosphere prior constraint on the PPP initialization speed of ZDZC-PPP model, this paper selects the BDS and GPS observation data of the DOY 115 days in 2015, and takes a comparison experiment of static PPP. The experimental data get from 10 observation stations of the MGEX (Experiment muti-GNSS) observation network, and the selected station is shown in Fig. 1, and the observation data sampling interval is 30 s.

In data processing, we use the static positioning mode and fix the satellite orbit and clock with the precise ephemeris and clock provided by GFZ (the German Research Centre for Geosciences). In this paper, we use the model to correct the deviation of phase center of satellite and receiver antenna, antenna phase wind up error, relative error, Earth's rotation error, and solid tide error. However, at present, MGEX only provides a priori BDS satellite PCO correction, and there is no organization to provide the information of BDS satellite PCV and receiver PCV and PCO. Therefore, we cannot carry out accurate PCV and PCO correction. The receiver DCB of LC-PPP model is absorbed by the receiver clock, and the satellite DCB is contained in the satellite clock products, so we do not consider the DCB of LC-PPP. For ZDZC-PPP, the receiver DCB parameter is to be estimated. At the same time, we take advantage of the hardware delay products provided by CODE for BDS and GPS satellite DCB correction.

In the experiment, the 24 h observation data of each station was cut by 3 h, a total of eight arcs, and each arc is reinitialized. To analyze the convergence speed and the positioning accuracy of BDS and GPS PPP, we make the difference

between the results of the PPP solution of the arc segment and the results of GFZ network adjustment.

3.1 Experimental Results and Analysis

In this paper, we use the LC-PPP and ZDZC-PPP to handle the one day observation data of the 10 MGEX observation stations, a total of 80 arcs. The convergence speed of the two PPP algorithms is statistically analyzed according to the different positioning errors in the same observation time, and the partial abnormal data are removed, and the statistics of the 10–60 min in the three-dimensional deviation is performed.

Figures 1 and 2 show the mean deviation of the CUT0 and GMSD station in the three-dimensional positioning for each region. In the picture, the horizontal coordinate is the observation time and the vertical coordinate is the average value of the deviation of the three-dimensional position with respect to truth position provided by GFZ.

From Figs. 2 and 3, we can see that in the same observation time whether GPS ZDZC-PPP or BDS ZDZC-PPP positioning accuracy is higher than the positioning accuracy of the LC-PPP, which shows that the convergence speed of ZDZC-PPP is faster than that of LC-PPP. Taking the BDS PPP average positioning error of

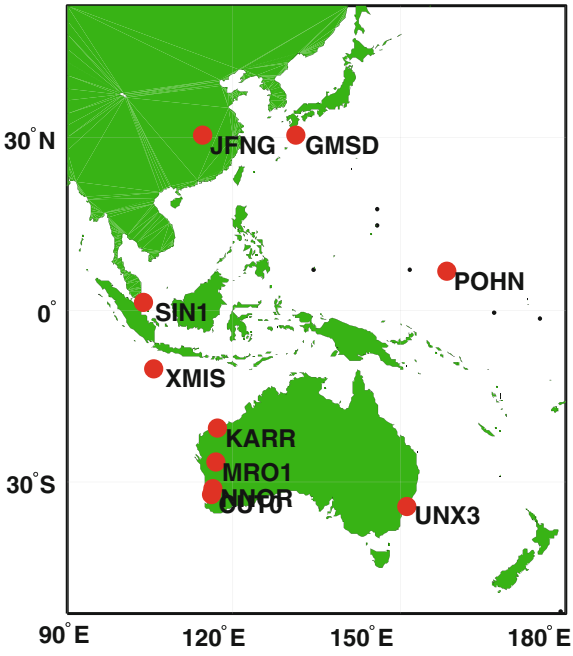

Fig. 1 Distribution of the 10 observation stations

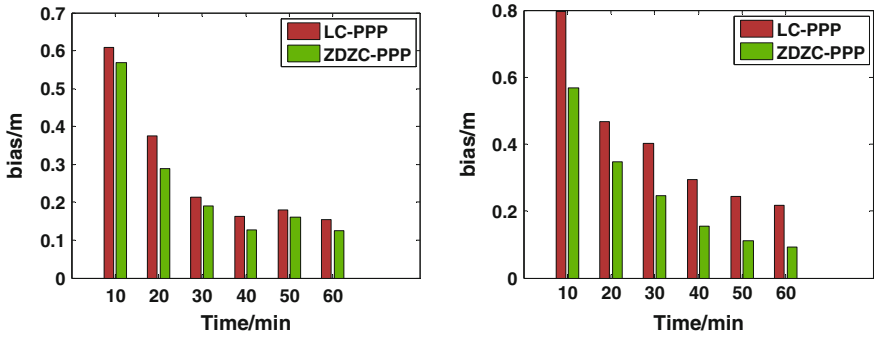

Fig. 2 Each section static GPS PPP positioning results of CUT0 and GMSD station

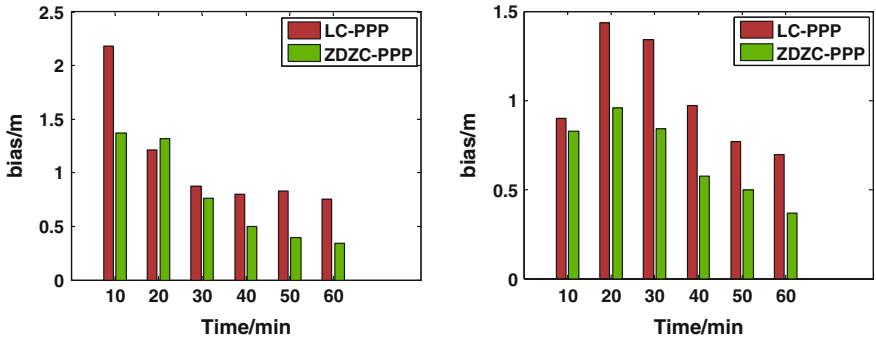

Fig. 3 Each section static BDS PPP positioning results of CUT0 and GMSD station

10 min for CUT0 station as an example, the positioning error of LC-PPP is 2.185 m, and the positioning error of ZDZC-PPP is 1.366 m. At the same time, the positioning accuracy of BDS PPP is obviously lower than that of GPS. The main reason for this situation is that the precise BDS orbit accuracy is lower, and the precise antenna phase center correction is unknown. In addition, the current satellite distribution of BDS making the geometry structure change significantly worse than GPS is also the reason.

In order to further analyze the convergence speed of the two PPP algorithms, the 10–60 min three-dimensional positioning errors of the 80 convergence arcs for the 10 stations are averaged. Table 1 shows the mean value of three-dimensional positioning deviation of the two PPP algorithms at different observation time.

As we can see from Table 1, in the same observation time, the mean value of ZDZC-PPP positioning deviation is less than that of LC-PPP, and a difference of GPS is 2–5 cm, and BDS is 23–70 cm, which shows that the convergence speed of ZDZC-PPP is significantly faster than LC-PPP. At the same time, the ZDZC-PPP

Table 1 The mean value of 3D positioning deviation of GPS and BDS PPP (unit: m)

System	PPP	10 min	20 min	30 min	40 min	50 min	60 min
GPS	LC-PPP	0.782	0.531	0.366	0.231	0.196	0.162
	ZDZC-PPP	0.724	0.437	0.297	0.193	0.168	0.137
BDS	LC-PPP	2.521	2.041	1.638	1.420	1.265	1.066
	ZDZC-PPP	1.713	1.528	1.290	1.108	0.990	0.828

algorithm for improving the BDS PPP convergence speed is more obvious than that of GPS.

The above test results show that, compared with LC-PPP algorithm, when the oblique ionospheric delay as parameters to be estimated and taking into account a priori information of the ionospheric delay to constrain the estimated ionospheric delay parameters can speed up the convergence rate, especially in the current situation that the change of BDS space geometry is slow.

4 Conclusion

To study the problem of the BDS PPP long initial time, this paper uses the ZDZC-PPP algorithm to carry out the test of BDS PPP fast initialization. The ionospheric delay as a parameter is estimated, and the prior information of the ionospheric delay is combined to the estimated ionospheric delay parameters. There are 10 observation stations' observation data of MGEX which are used to perform two PPP algorithms. The experimental results show

In static conditions, compared with the LC-PPP algorithm, the ZDZC-PPP algorithm can improve the convergence speed of PPP. During the same observation time, the mean value of ZDZC-PPP positioning deviation is less than that of LC-PPP, and a difference of GPS is 2–5 cm, and BDS is 23–70 cm, which shows that the convergence speed of ZDZC-PPP is significantly faster than that of LC-PPP. At the same time, the ZDZC-PPP algorithm for improving the BDS PPP convergence speed is more obvious than that of GPS PPP.

References

1. Zhang X, Zuo X, Li P et al (2015) Convergence time and positioning accuracy comparison between BDS and GPS precise point positioning. Acta Geod Sin 44(3):250–256
2. Kouba J, Heroux P (2001) GPS precise point positioning using IGS orbit products. GPS Solut 5 (2):12–28
3. Roesler G, Martell H (2009) Tightly coupled processing of precise point position (PPP) and INS data. In: Proceedings of the 22nd international meeting of the satellite division of the Institute of Navigation, Savannah, GA

4. Tu R et al (2013) A real time ionospheric model based on GNSS precise point positioning. Adv Space Res
5. Hongping Z et al (2013) On the convergence of ionospheric constrained precise point positioning (IC-PPP) based on undifferential uncombined raw GNSS observations. Sensors 13:15708–15725
6. Geng J (2011) Rapid integer ambiguity resolution in GPS precise point positioning. University of Notinghanm, Notinghanm
7. Li X, Ge M, Zhang X et al (2013) A method for improving uncalibrated phase delay estimation and ambiguity fixing in real time precise point positioning. J Geod 1:1–12

Analysis and Correction of BDS Code Multipath Bias

Wenke Yang, Haibo Tong, Lei Pan, Donghui Xu, Wenpu Guo and Jian Yang

Abstract In view of the problem of the long-term variation of code multipath error (called code multipath bias) in the IGSO and MEO satellite observable, code multipath bias of BDS is analyzed using iGMAS data of multiple earth stations. In addition, the GPS and BDS multipath error variation is analyzed comparatively. The results show that the variation of BDS multipath error is related to the elevation angle, satellite orbit type and carrier frequency, but independent with the location of the receivers. And for the carrier frequency $B1$, $B2$, and $B3$, the code multipath bias for MEO satellite is 1.66, 1.05 and 0.53 m, respectively. For IGSO satellite the code multipath bias is 0.65, 0.44, and 0.31 m accordingly, which are smaller than that reported by earlier papers. Especially, for IGSO at frequency $B2$ and $B3$, the code multipath bias is smaller than half of that reported earlier. At the same time, in order to reduce the multipath bias, a two-order polynomial fitting algorithm is proposed in this paper. The results show that: compared with the results of piecewise linear model with 10 correction parameters, the two-order polynomial correction algorithm with three correction parameters can correct the multipath error and reduce the RMS of the multipath error more effectively. The two-order polynomial model in this paper is more convenient considering broadcasting the correction information to the users.

Keywords BDS · IGSO · MEO · iGMAS · Multipath error

W. Yang (✉) · L. Pan · D. Xu · W. Guo · J. Yang
Xi'an Institute of High Technology, Xian 710025, China
e-mail: wenkeyang@foxmail.com

H. Tong
Information and Navigation College, Air Force Engineering University, Xian 710077, China

© Springer Science+Business Media Singapore 2016

J. Sun et al. (eds.), *China Satellite Navigation Conference (CSNC) 2016 Proceedings: Volume III*, Lecture Notes in Electrical Engineering 390,
DOI 10.1007/978-981-10-0940-2_44

1 Introduction

Since December 27, 2012, Beidou satellite navigation system (BDS) provides navigation positioning and timing services for the Asia Pacific region formally [1], which includes five geostationary orbit (GEO) satellites, five inclined geosynchronous satellite orbit (IGSO) satellites, and four medium earth orbit (MEO) satellites [2]. Wanninger [3] and Hauschild [4] discover and analyze the long-term variation of code multipath error (code multipath bias) for IGSO, MEO satellites of BDS using observable from IGS MGEX(International GNSS Service Multi-GNSS Experiment) [5]. It is reported that the bias is independent with the location of the receivers and the receiver types. The code multipath bias is reported as large as nearly 1.5 m for MEO satellite at $B1$ frequency. The code multipath bias can introduce positioning error in single frequency PPP (Precise Point Positioning) [3], and can introduce bias larger than half of the wide lane wavelength into Melbourne–Wuebbena linear combination which serves for fixing the widelane ambiguity [3, 6]. Based on the observable of multiple earth stations of iGMAS (International GNSS Monitoring and Assessment System) [7] in China, the code multipath error is analyzed in this paper. Especially, the long-term variations of the code multipath error of BDS IGSO and MEO satellites for triple frequencies are examined carefully.

Wanninger [3] proposed a piecewise linear model to model and modify the code multipath bias. However, considering broadcasting the correction information to the users, the piecewise linear model requires many parameters to be sent. For example, when the elevation angle range of 0°–90° and the interval of 10° is considered, at least 10 parameters of the piecewise linear model should be included. Meanwhile, a two-order polynomial fitting model with only three parameters is proposed in this paper.

In the following, code multipath observable is analyzed first. Then, based on this, with the observation data of iGMAS stations in China, the code multipath error of BDS is analyzed by comparing BDS with GPS. The code multipath observable of different iGMAS stations from DoY 185 to 192 in 2015 for BDS MEO and IGSO satellites is compared with the reported results by Wanninger [3]. At last, two-order polynomial fitting model is applied and is compared with the piecewise linear model [3].

2 Code Multipath Observable

The multipath error of single-frequency can be analyzed in Eq. (1) with linear combination of single-frequency code and dual-frequency phase observations, which usually is called multipath (MP) observable [3, 8].

$$\mathrm{MP}_i = \rho_i + (m_{ijk} - 1) \cdot \varphi_j - m_{ijk} \cdot \varphi_k - B_i \tag{1}$$

In which

$$m_{ijk} = \frac{\lambda_i^2 + \lambda_j^2}{\lambda_j^2 - \lambda_k^2}$$

$$B_i = (m_{ijk} - 1) \cdot N_j \lambda_j - m_{ijk} \cdot N_k \lambda_k + D_i$$

where ρ_i is the code measurement (m); $\lambda_i, \lambda_j, \lambda_k$ is the wavelengths of the three frequencies i, j, and k; φ_j, φ_k is carrier phase measurements (m) at frequencies j and k; N_j, N_k is carrier phase integer ambiguity at frequencies j and k; D_i is the constant part of the linear combination of code and carrier phase hardware-induced delays and code multipath error; B_i is the linear combination of $N_j\lambda_j, N_k\lambda_k$ and D_i with constant coefficients. As a result, B_i is a constant when there is no cycle clips. To deal with the observation data, it is necessary to detect the cycle clips by comparing carrier phase difference with Doppler [9]. The observation data with no cycle clips is used to determine B_i as the mean of MP_i.

The linear combination in the right of Eq. (1) can cancel out the geometrical distance, satellite and receiver clock offset, ionospheric and tropospheric delays of the single-frequency code observation, the linear combination of code and phase hardware-induced delays, and the constant part of code multipath error.

In fact, the multipath observables of $B1$ (1561.098 MHz), $B2$ (1207.14 MHz) and $B3$ (1268.52 MHz) can be written as:

$$\mathrm{MP}_1 = \varepsilon_{M\rho 1} + \varepsilon_{\rho 1} + 15.9214(\varepsilon_{M\varphi 2} - \varepsilon_{M\varphi 3}) - 16.9214(\varepsilon_{\varphi 2} - \varepsilon_{\varphi 3}) \quad (2)$$

$$\mathrm{MP}_2 = \varepsilon_{M\rho 2} + \varepsilon_{\rho 2} + 5.1943(\varepsilon_{M\varphi 3} - \varepsilon_{M\varphi 1}) - 6.1943(\varepsilon_{\varphi 3} - \varepsilon_{\varphi 1}) \quad (3)$$

$$\mathrm{MP}_3 = \varepsilon_{M\rho 3} + \varepsilon_{\rho 3} - 4.7395(\varepsilon_{M\varphi 1} - \varepsilon_{M\varphi 2}) + 3.7395(\varepsilon_{\varphi 1} - \varepsilon_{\varphi 2}) \quad (4)$$

where $\varepsilon_{M\rho 1}$, $\varepsilon_{M\rho 2}$, $\varepsilon_{M\rho 3}$ are code MP observables for $B1$, $B2$, and $B3$, $\varepsilon_{\rho 1}$, $\varepsilon_{\rho 2}$, $\varepsilon_{\rho 3}$ are thermal noises of code measurement for $B1$, $B2$, and $B3$, $\varepsilon_{M\varphi 1}$, $\varepsilon_{M\varphi 2}$, $\varepsilon_{M\varphi 3}$ are carrier phase multipath errors for $B1$, $B2$, and $B3$, $\varepsilon_{\varphi 1}$, $\varepsilon_{\varphi 2}$, $\varepsilon_{\varphi 3}$ are thermal noises of carrier phase measurement for $B1$, $B2$, and $B3$.

In theory, absolute value of phase multipath error is not more than 1/4 of the wavelength, which means 4.80 cm in $B1$, 6.21 cm in $B2$ and 5.91 cm in $B3$. These values are two orders of magnitude smaller than the code multipath error [10]. Since the magnitude of thermal noises of phase measurement is a few millimeter [11], the third and fourth components in the right of Eqs. (2)–(4) can be ignored. It can be deduced that MP_1, MP_2, and MP_3 are the sum of the code multipath errors and the thermal noises of code measurement. Furthermore, it is generally considered that thermal noise is zero mean white noise, and the constant part of code multipath observable is reduced, so MP observable is the variation part of code multipath error.

3 Multipath Observable Data Sets of BDS

3.1 Comparison of Multipath Observables Between BDS and GPS

Figure 1 shows the BDS $B1$ and GPS $L1$ code multipath observable of MEO satellites as a function of time and as a function of elevation angle at iGMAS station chu1 in DoY 185 of 2015. The fluctuation ranges of code multipath observable in GPS $L1$ and in BDS $B1$ decrease with the elevation angle. The code multipath observable in BDS $B1$ contains additional long-term bias (called code multipath bias) which is elevation-dependent and absent for GPS $L1$.

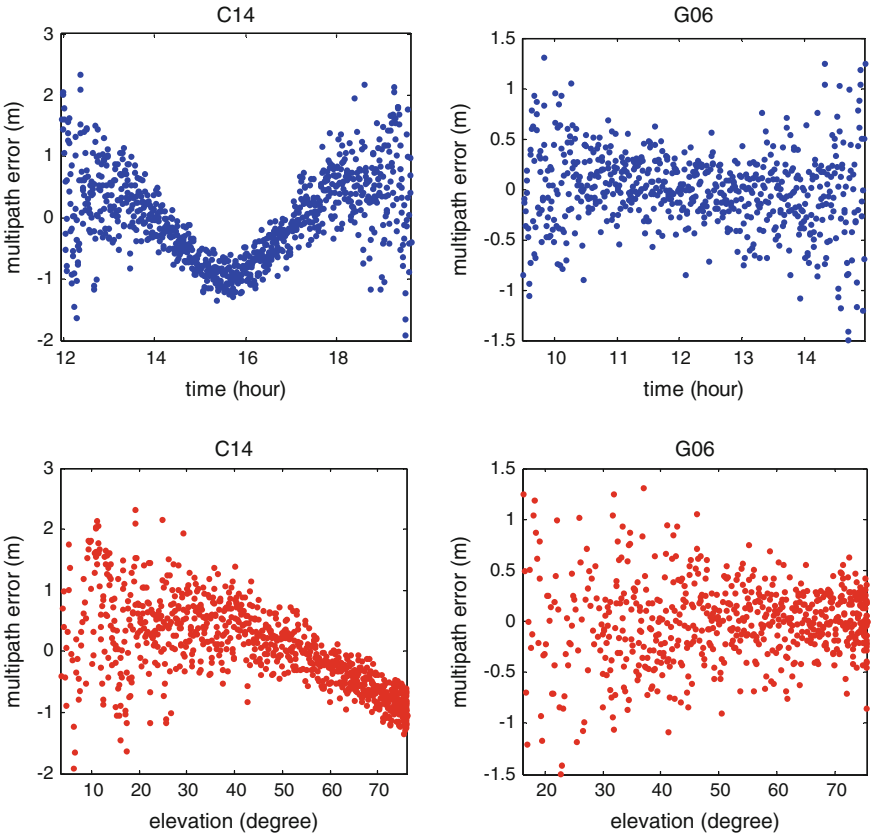

Fig. 1 Examples of MP time series of MEO satellite passes of BDS and GPS of one observation station as a function of time (*upper panels*) and a function of elevation angle (*lower panels*)

3.2 *Comparison of BDS Multipath Bias of Different Observation Stations*

The MP for BDS IGSO and MEO satellites (exclude PRN C13, which is end of signal transmission since Oct. 2014 [12]) for *B*1, *B*2 and *B*3 frequencies are calculated, respectively, based on the observable from eight stations of iGMAS [13] from DoY 185 to 192 in 2015. In order to analyze the relationship between code

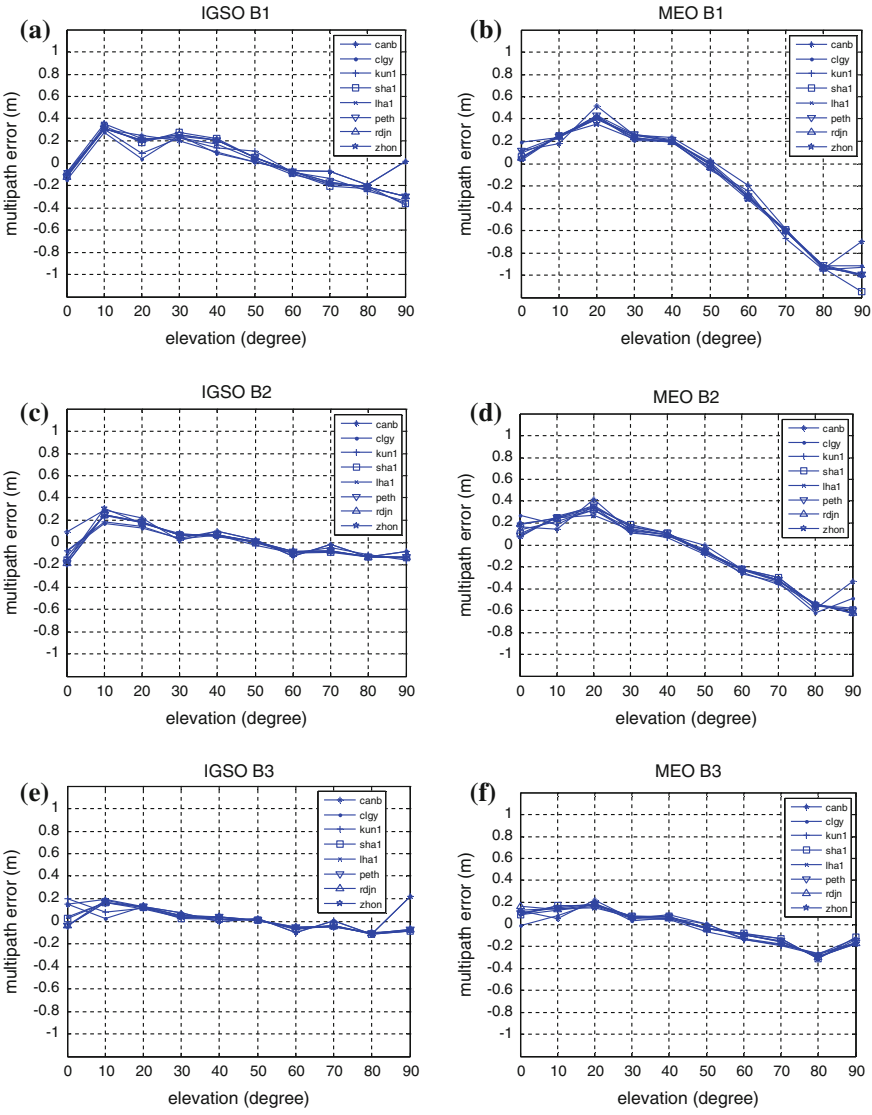

◀ **Fig. 2** The code multipath biases of IGSO satellites for *B*1, *B*2, and *B*3 frequencies as a function of elevation angle for eight stations (*left panel*) and the code multipath biases of MEO satellites for *B*1, *B*2, and *B*3 frequencies as a function of elevation angle for eight stations (*right panel*). **a** IGSO MP (*B*1), **b** MEO MP (*B*1), **c** IGSO MP (*B*2), **d** MEO MP (*B*2), **e** IGSO MP (*B*3), **f** MEO MP (*B*3),

multipath bias and elevation angle, we selected the nodes separated by 10° of elevation. The piecewise linear fitting is applied to the MP observables for the BDS IGSO and MEO satellites, respectively, for each observation station and each of the three BDS frequencies. The multipath bias is showed in Fig. 2 as a function of elevation angle.

The multipath biases of IGSO satellites for *B*1, *B*2, and *B*3 frequencies as a function of elevation angle are plotted in the subgraph a, c, and e in Fig. 2, respectively. It is shown that the multipath biases of each observation station agrees well with each other with the decreasing trend for each carrier frequency, which proofs that the multipath biases of IGSO satellites are independent with the locations of stations. The variation amplitude of multipath biases of IGSO satellites is 0.65, 0.44 and 0.31 m for *B*1, *B*2, and *B*3, respectively.

The multipath biases of MEO satellites for *B*1, *B*2 and *B*3 frequencies as a function of elevation angle are plotted in the subgraph b, d, and f in Fig. 2, respectively. It is shown that the multipath biases of each observation station also agrees well with each other with the decreasing trend for each carrier frequency, which proofs that the multipath biases of MEO satellites are independent with the locations of stations. The variation amplitude of multipath biases of MEO satellites is 1.66, 1.05 and 0.53 m for *B*1, *B*2, and *B*3, respectively.

The variation amplitude of multipath biases of BDS MEO and IGSO satellites at the triple frequencies obtained by iGMAS data in this paper compared with that reported by Wanninger [3] are listed in Table 1.

Compared with the data based on the observation data of MGEX stations in 2014 [3], it shows that the variation amplitude of multipath biases of IGSO satellite at each frequency obtained here based on iGMAS stations in 2015 is much smaller, especially for *B*2 and *B*3 which is half of that in paper [3]. And the variation amplitude of multipath biases of MEO satellites obtained by iGMAS data here is smaller, except for MEO satellites at *B*1 frequency.

Table 1 List of variation amplitude of code multipath observables of BDS MEO and IGSO satellites at triple frequencies obtained by iGMAS data in this paper compared with that reported by Wanninger [3]

	Carrier frequency	Variation amplitude of code multipath biases (m)	
		This paper	Wanninger [3]
MEO	B1	1.66	1.50
	B2	1.05	1.03
	B3	0.53	0.70
IGSO	B1	0.65	1.05
	B2	0.44	0.98
	B3	0.31	0.63

4 BDS Multipath Observable Correction

The two-order polynomial fitting coefficients are calculated by the MSE (Minmum Square Error) estimator for each type satellite (MEO or IGSO), for each frequency. To take iGMAS observation station canb as an example, BDS observation data sets are from DoY 185 to 191 in 2015. The fitted coefficients are shown in Table 2.

The MP observable correction (corr) is calculated with the two-order polynomial coefficients by:

$$\text{corr} = a_2\theta^2 + a_1\theta + a_0 \tag{5}$$

where θ is the elevation angle, a_2, a_1 and a_0 are the polynomial coefficients shown in Table 2.

Figures 3 and 4 show the IGSO and MEO satellites code multipath correction curves, respectively. It can be seen from Fig. 3 that the multipath correction values of $B1$, $B2$, and $B3$ increase with the elevation angle. The values of $B1$ increases linearly, while the values of $B2$ and $B3$ increase quickly at low angles and slowly at high angles.

Table 2 Two-order polynomial fitting coefficients

	Carrier frequency	a_2	a_1	a_0
MEO	B1	0.0003991	−0.0185942	−0.1122992
	B2	0.0001788	−0.0048206	−0.1940369
	B3	0.0001000	−0.0032524	−0.0853314
IGSO	B1	−0.0000085	0.0070683	−0.3600908
	B2	−0.0000588	0.0100994	−0.3532883
	B3	−0.0000670	0.0092607	−0.2790053

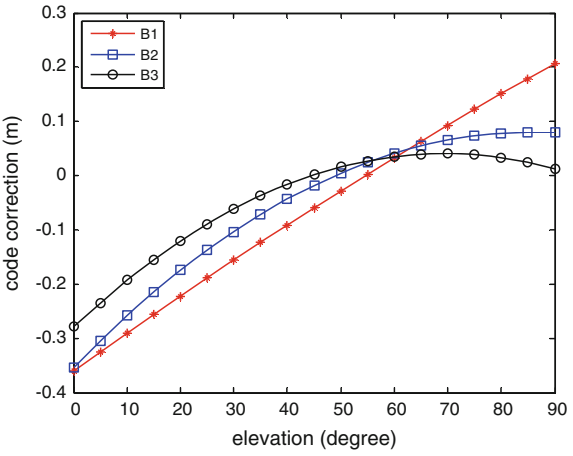

Fig. 3 The code multipath biases two-order polynomial correction model of IGSO satellites for $B1$, $B2$ and $B3$ frequencies as a function of elevation angle

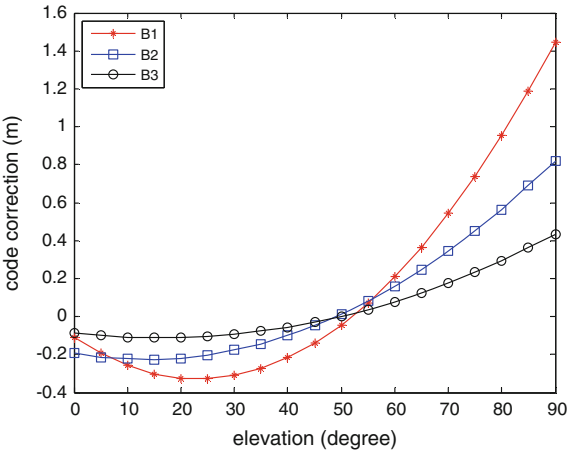

Fig. 4 The code multipath biases two-order polynomial correction model of MEO satellites for $B1$, $B2$, and $B3$ frequencies as a function of elevation angle

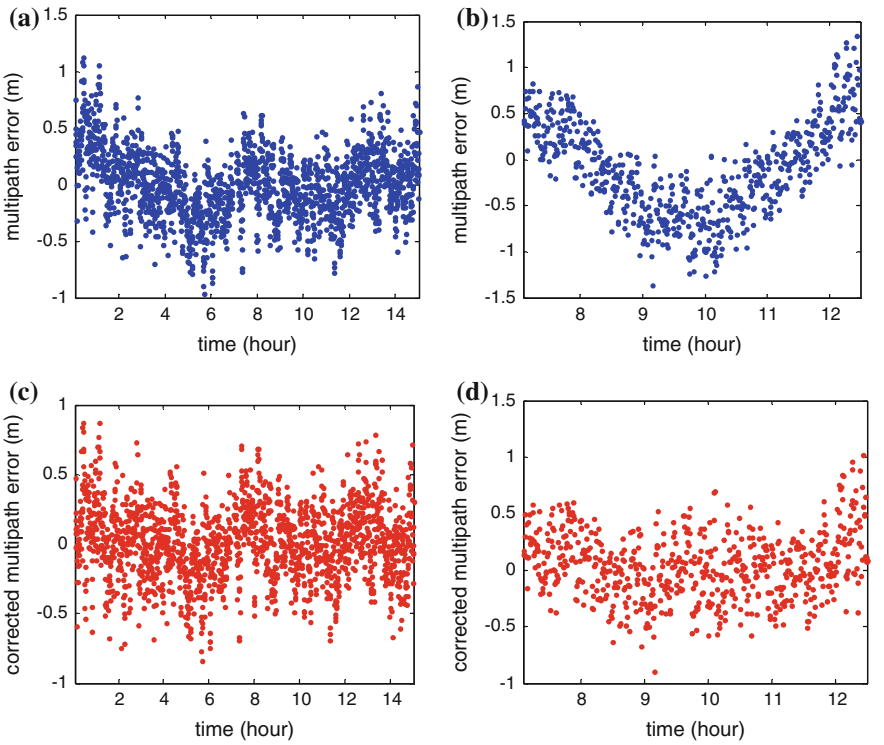

Fig. 5 MP observables of BeiDou IGSO/MEO satellite for uncorrected and corrected $B1$ measurements

Table 3 MP RMS of BDS IGSO and MEO satellite corrected by piecewise linear model and two-order polynomial model

RMS (m)	IGSO			MEO		
	*B*1	*B*2	*B*3	*B*1	*B*2	*B*3
Raw data	0.327	0.286	0.222	0.523	0.382	0.241
Corrected by piecewise linear model	0.313	0.289	0.232	0.378	0.306	0.213
Corrected by two-order polynomial model	0.301	0.269	0.212	0.361	0.295	0.207

As shown in Fig. 4, the multipath correction values of MEO *B*1, *B*2 and *B*3 also increase with the elevation angle. The corrections of the three frequencies increase slowly at low angles and fast at high angles, which differs from IGSO as shown in Fig. 3.

Furthermore, we evaluated the MP observable correction model in Table 2 with the observation data sets at station canb of DoY 192 in 2015, Fig. 5 shows the uncorrected and corrected MP observables at *B*1 of IGSO and MEO satellites. With the application of correction, the bias is suppressed within the multipath observables.

Furthermore, the comparison analysis of the two-order polynomial model and the piecewise linear model [3] is given. Table 3 shows RMS (Root Mean Suqare) of MP correction residuals of BDS IGSO and MEO satellite with piecewise linear model and two-order polynomial model.

It is shown in Table 3 that the MP RMS of BDS IGSO and MEO satellite corrected by two-order polynomial model is smaller than that of the raw data, and is also smaller than that corrected by the piecewise linear model. In the piecewise linear method, the MP RMS decreases after correction with piecewise linear model of MEO satellites, except for IGSO satellite.

5 Conclusions

It is shown that there are long-term variations in code multipath errors (called code multipath bias) of BDS MEO and IGSO satellites as a function of elevation angle by analysis of observations at triple frequencies from multiple domestic stations of iGMAS. The code multipath biases of IGSO and MEO satellites at triple carrier frequencies are independent with the locations of stations, but are related with the satellite orbit type: for each frequency, the variation amplitude of the code multipath biases of MEO satellites is larger than that of IGSO satellites. And biases are related with the carrier frequency: for each satellite orbit type, the variation amplitude of the code multipath biases of *B*1 is largest, that of *B*2 is smaller and *B*3 is smallest.

The variation amplitude of code multipath biases of MEO satellites is 1.66, 1.05 and 0.53 m for *B*1, *B*2, and *B*3, respectively. And that of IGSO satellites is 0.65, 0.44 and 0.31 m for *B*1, *B*2, and *B*3, respectively. Except for MEO satellites at *B*1, the above data are smaller than that reported earlier [3]. Especially for *B*2 and *B*3, the variation amplitude of code multipath biases of IGSO satellites obtained by iGMAS data is smaller than half of that reported earlier [3].

The possible reasons for that difference are two folds. First, paper [3] is based on the observation data from IGS MGEX stations of DoY 70–79 and DoY 160–169 in 2014, and here it is based on the observation data from iGMAS stations of DoY 185–192 in 2015. It is more than one year apart and it is possible that the code multipath bias decrease with time. Second, the analysis of IGSO satellite in paper [3] is based on only three stations (in China, Japan and Australia, respectively) with Trimble NetR9 receiver. And the data here is from eight iGMAS stations in China with receivers from CECT54 and Unicore. It is worthy to examine the possible impact of different types of receivers and parameter settings. Besides, the station-independent characteristic of code multipath bias implies that it is mostly satellite-induced as pointed out earlier [3].

Meanwhile, compared with the results of piecewise linear model with 10 correction parameters [3], the two-order polynomial correction algorithm with 3 correction parameters proposed in this paper can correct the multipath error and reduce the RMS of the multipath error more effectively. The two-order polynomial model in this paper is more convenient considering broadcasting the correction information to the users.

Acknowledgments The authors are grateful for international GNSS Monitoring and Assessment System (iGMAS) to provide BDS and GPS observation data. This study is funded by National Science Foundation of China (61501471).

References

1. Liu J (2013) Status and development of the Beidou navigation satellite system. J Telem Track Command 34(3):1–8
2. Yang Y, Li J, Wang A et al (2014) Preliminary assessment of the navigation and positioning performance of BeiDou regional navigation satellite system. Sci China Earth Sci 57(1):144–152
3. Wanninger L, Beer S (2015) BeiDou satellite-induced code pseudorange variations: diagnosis and therapy. GPS Solut 19(4):639–648
4. Hauschild A, Montenbruck O, Sleewaegen J et al (2012) Characterization of compass M-1 signals. GPS Solut 16(1):117–126
5. Montenbruck O, Steigenberger P, Khachikyan R, Weber G, Langley RB, Mervart L, Hugentobler U (2014) IGS-MGEX: preparing the ground for multi-constellation GNSS science. Inside GNSS 9(1):42–49
6. Lou Y, Zheng F, GuS et al (2015) Multi-GNSS precise point positioning with raw single-frequency and dual-frequency measurement models. GPS Solut 29 Oct 2015 (Online)
7. Jiao W, Ding Q, Li J et al (2011) Monitoring and assessment of GNSS open services. Sci Sin Phys Mech Astron 41(5):521–527

8. Wang G, Jong KD, Zhao Q, Hu Z, Guo J (2015) Multipath analysis of code measurements for BeiDou geostationary satellites. GPS Solut 19(1):129–139
9. Lei Y, Gao Y (2010) Comparison between dual frequency differenced carrier-phase and Doppler in cycle slips detection and reparation. Eng Surv Mapp 19(3):10–13
10. Wu X, Zhou J, Wang G, Hu X, Cao Y (2012) Multipath error detection and correction for GEO/IGSO satellites. Sci China Phys Mech Astron 55(7):1297–1306
11. Gang X (2009) Principles of GPS and receiver design. Publishing House of Electronics Industry, Beijing
12. IGS MGEX Constellation-BDS. http://www.igs.org/mgex/status-BDS. Accessed 26 Jan 2016
13. Chen L, Geng C, Zhou Q, Jiao W (2015) Estimation strategy and accuracy analysis of GNSS real-time precise satellite clock error. In: Proceedings of China satellite navigation conference (CSNC), vol III. Lecture Notes in Electrical Engineering 342, pp 57–66

An Initial Analysis and Assessment on Final Products of iGMAS

Hongliang Cai, Guo Chen, Wenhai Jiao, Kangkang Chen, Tianhe Xu and Hongchen Wang

Abstract The international GNSS Monitoring and Assessment System (iGMAS) is developed as a service platform for multi-GNSS and the Product Integration and Service Center (ISC) is the products reprocess center which provides global users with different time-delay products. The present paper focuses on the final products combination from different analysis centers and the emphasis is put on the consistency between different final products, then an initial assessment about the precision of final products is inhibited with one-year data from iGMAS, including final satellite orbits, clock bias, Earth rotation parameters, global ionosphere map, and troposphere products, and SLR measurements from ILRS are collected for validation of BDS and Galileo satellite orbits; meanwhile, the consistency between final orbits and ERP is analyzed.

The original version of this chapter was revised: For detailed information please see Erratum. The erratum to this chapter is available at 10.1007/978-981-10-0940-2_66

H. Cai · W. Jiao
Beijing Institute of Tracking and Telecommunication Technology, Beijing 100094, China
e-mail: caibanyu@126.com

G. Chen
School of Geodesy and Geomatics, Wuhan University, Wuhan, Hubei 430079, China
e-mail: wuhandaxuexinxibu@163.com

K. Chen
School of Geology Engineering and Geomatics, Chang'an University, Xi'an, Shanxi, China

T. Xu
State Key Laboratory of Geo-Information Engineering, Xi'an, Shanxi, China

T. Xu
State Key Laboratory of Astronautic and Dynamics, Xi'an, Shanxi, China

T. Xu
Xian Research Institute of Surveying and Mapping, Xi'an, Shanxi, China

H. Wang (✉)
Journal of Natural Science, Research and Development Office of Wuhan University, Wuhan, Hubei 430079, China
e-mail: wanghc@whu.edu.cn

© Springer Science+Business Media Singapore 2016

J. Sun et al. (eds.), *China Satellite Navigation Conference (CSNC) 2016 Proceedings: Volume III*, Lecture Notes in Electrical Engineering 390,
DOI 10.1007/978-981-10-0940-2_45

Keywords iGMAS · Products combination · Final products · Consistency

1 Introduction

With the development of global navigation satellite system (GNSS), the GNSS-related technology has been widely applied in different fields, from the concept of IGS proposed at the twentieth IUGG Conference in year 1991 and with a long time-development for more than twenty years, currently, the IGS provides global users with multi-GNSS satellite orbit products, and the one-dimension precisions are 2.0 and 3.0 cm for final GPS and GLONASS orbit, respectively. Meanwhile, with the Multi-GNSS Experiment (MGEX) carrying on, the IGS also provides other satellite navigation orbit/clock products such as BDS, Galileo, and regional navigation system [1–3].

The international GNSS continuous Monitoring and Assessment System (iGMAS) is developed by China at the beginning of 2011 based on the state satellite navigation system (i.e., Beidou Navigation Satellite System, BDS), the iGMAS consists of thirty global-distributed tracking stations, three data centers, eight analysis centers, one monitor and assessment center, one function management center, and one Product Integration and Service Center (ISC). The main task is to track the GNSS satellites by global stations and serve as a platform of data collection, store, analysis, management, and distribution, and provide global GNSS users with different kinds of products, such as satellite orbit/clock, Earth rotation parameters (ERP), station coordinates, global ionosphere maps, station zenith troposphere delay products, and GNSS integrity products.

Currently, ten analysis centers participate in the products combination and assessment, the system basically is in stable function and all kinds of combined products are produced on routine by ISC, according to the timeliness, the ISC can provide three types of combined products, that is ultra-rapid, rapid, and final products, similar to IGS products, the ultra-rapid products are updated every six hours with a delay by three hours, the rapid products are updated every day with a delay about forty and one hours while the final products are produced one time for each week with a delay about twelve days.

The present paper focuses on the analysis of final products, including satellite orbit/clock, ERP, ionosphere and troposphere products, and the external products from IGS are used for comparison of iGMAS products, what is more, the combined products are used to assess orbit products of iGMAS analysis centers which can make the assessment results more objective and reliable, additionally, SLR measurements are used for validation for BDS and Galileo orbit products, the consistency between final combined orbits and ERP is also analyzed in this paper.

2 Combination Strategy for Final Products

Unlike the ultra-rapid and rapid products, when producing the final products, analysis centers adjust all the parameters of stations coordinates, orbits, satellites/receivers clock bias, ERP, and troposphere delay at the same time with lose constraints. For each analysis center, the different final products are consistent within each other, considering that the different stations and processing strategy are used for different analysis centers, it is important to keep the consistency between different combined products for the products reprocess center [4].

2.1 Final Station Coordinates/Orbit/ERP/Clock Bias Combination Strategy

For a long time, the combination of the station coordinates and the ERP products is separately carried out which is adopted by the IGS [5]. Altamimi et al. (2005) proposed a rigorous combination method for station coordinates and ERP, he suggested that the station coordinates and ERP products should be combined together to keep the consistency between the two products, this method is used by IGS nowadays [6–12].

The station coordinates and ERP are in the solution independent exchange format (SINEX) files, given that the solution of analysis center is s and the station coordinates are X_s, the polar motion parameters are x_s^p, y_s^p and the corresponding rate parameters are $\dot{x}_s^p, \dot{y}_s^p$, respectively, the length of day parameter is LOD_s; while the combined solution is c, according to the similarity transformation formula, the observation equation for the combination of station coordinate can be expressed as

$$X_s = X_c + T_c + D_c X_c + R_c X_c \tag{1}$$

where $T_c = [\,TX_c \quad TY_c \quad TZ_c\,]^{\mathrm{T}}$ are the three translation parameters, $R_c = [\,RX_c \quad RY_c \quad RZ_c\,]^{\mathrm{T}}$ are the three rotation parameters along the axis and D_c is the scale parameter.

The combination model for ERP can be expressed as

$$\begin{aligned} x_s^p &= x_c^p - RY_c \\ y_s^p &= y_c^p - RX_c \\ \dot{x}_s^p &= \dot{x}_c^p \\ \dot{y}_s^p &= \dot{y}_c^p \\ \mathrm{LOD}_s &= \mathrm{LOD}_c \end{aligned} \tag{2}$$

The combination of station coordinates and ERP can follow these two steps, first of all, the priori constraints applied in the solution of analysis center should be removed

and minimum constraints are replaced for each solution, the weight for each analysis center is redistributed by variance component estimation method, during the iteration process, the outliers are detected and deleted, secondly, the rotation parameters are fixed with minimum constraints and weighed for station coordinates and ERP is derived from the former step, then the combination solution is aligned to ITRF.

To keep the consistency between final orbits and station coordinates, the consistency correction for orbit solution should be applied for each analysis center [13, 14]

$$\begin{aligned}\Delta\mathrm{orb}_x &= -RZ_{\mathrm{snx}} \cdot \mathrm{orb}_y + RY_{\mathrm{snx}} \cdot \mathrm{orb}_z \\ \Delta\mathrm{orb}_y &= RZ_{\mathrm{snx}} \cdot \mathrm{orb}_x - RX_{\mathrm{snx}} \cdot \mathrm{orb}_z \\ \Delta\mathrm{orb}_z &= -RY_{\mathrm{snx}} \cdot \mathrm{orb}_x + RZ_{\mathrm{snx}} \cdot \mathrm{orb}_y\end{aligned} \tag{3}$$

where Δorb are the corrections for the three directions, orb is the analysis center solution, RX_{snx}, RY_{snx}, and RZ_{snx} are the rotation parameters between analysis center and combined solution of station coordinates. After the application of consistency correction, the orbit solution of each analysis center is consistent with the combined stations coordinates and the orbit combination is processed in the same reference system with weight average method.

Since some analysis centers do not provide station coordinates solution with ERP, another ERP combination method is adopted by this present paper, the ERP products are combined with orbit solution together and the consistency correction for ERP of each analysis center is applied as

$$\begin{aligned}\Delta PMx &= -RY_{\mathrm{orb}} \\ \Delta PMy &= -RX_{\mathrm{orb}} \\ \Delta\mathrm{LOD} &= -RZ_{\mathrm{orb}}/f\end{aligned} \tag{4}$$

where $[\,RX_{\mathrm{orb}} \quad RY_{\mathrm{orb}} \quad RZ_{\mathrm{orb}}\,]^{\mathrm{T}}$ are the rotation parameters between analysis center and combined orbit solution, $f = 1.002737909350795$ is the conversion factor from UT into sidereal time, the weight for each analysis center is computed by the posterior variance then a weighted orbit solution can be obtained by some iterations until no outliers are detected.

After finishing the combination of station coordinates, satellite orbit and ERP, then the clock bias combination can begin. The consistency corrections between these combined solution and clock solution should also be accounted in the clock product combination [15]

$$\begin{aligned}\Delta\mathrm{clk}_{\mathrm{sat}} &= ((X_{\mathrm{ac}} - X_{\mathrm{com}}) \cdot X_{\mathrm{ac}})/R_{\mathrm{sat}}/c \\ \Delta\mathrm{clk}_{\mathrm{sta}} &= ((Y_{\mathrm{ac}} - Y_{\mathrm{com}} - DX) \cdot Y_{\mathrm{ac}})/R_{\mathrm{sta}}/c\end{aligned} \tag{5}$$

where $\Delta\mathrm{clk}_{\mathrm{sat}}$ and $\Delta\mathrm{clk}_{\mathrm{sta}}$ are the consistency corrections for satellites and receivers clock bias, respectively, X_{ac}, X_{com}, and R_{sat} are the satellite position of analysis center, combined solution, and the position vector, respectively, Y_{ac}, Y_{com}, and R_{sta}

are the station coordinates of analysis center, combined solution, and the position vector, respectively, *DX* is the geocenter motion included in the station coordinates combination. The time datum of analysis center is aligned to the broadcast satellite clock after the application of the consistency correction to remove the systematic error results from the different reference stations clock, an iteration process is completed without outliers any more.

2.2 Combination Strategy for Final Troposphere and Ionosphere Products

For the final troposphere products combination, two methods can be used, one is the PPP method with final combined satellite orbit and clock products to estimate the station zenith troposphere delay parameters, and the other is based on the robust weighting method. The former method can keep the combined troposphere products consistent with the orbit/clock products but with a relatively lower reliability and efficiency. Currently, the second method is used in the combination procedure and a similar way is adopted for ionosphere product combination [16, 17].

3 Analysis and Assessment on Final Products

3.1 Final Orbit

Two kinds of reference orbit solutions are used for orbit comparison, the first one is the IGS orbit solution and the other one is the iGMAS combination. For the former, the IGS combined GPS and GLONASS orbit solution are collected to evaluate iGMAS GPS and GLONASS orbit, respectively, while the MGEX orbit provided by GFZ and TUM are used for BDS and Galileo satellite orbit evaluation. About one-year products are collected from iGMAS and the systematic error is removed by similarity transformation between different orbit solutions, the media value of average one-dimension RMS is taken as the precision indicator for each satellite system.

Figure 1 exhibits the RMS series for the four satellite systems, Tables 1 and 2 summarize the statistics results for each analysis center.

The precision of ISC combined GPS and GLONASS orbits is the best among the analysis centers when compared to IGS combination, 1 and 1.7 cm for GPS and GLONASS, respectively, while the orbit precisions of all analysis centers are less than 5 and 8 cm for GPS and GLONASS, respectively. On the other hand, the differences between the precision of analysis centers with regard to IGS and ISC are less than 3 and 7 mm for GPS and GLONASS, respectively, it indicates that the

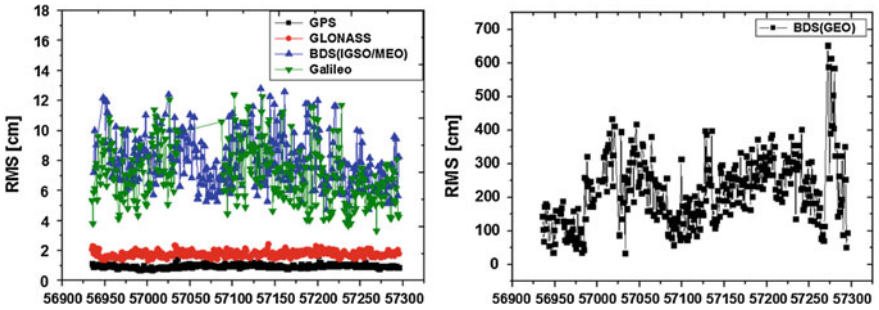

Fig. 1 The RMS series of iGMAS quad-constellation satellite orbits

orbit precision of iGMAS combined GPS and GLONASS solutions has a same level as IGS products.

The precision of BDS GEO is about 3 m compared to the MGEX solution from GFZ while it changes to 1 m compared to the combined solution, significant different precisions show that the assessment may need another way to check the orbit solution such as SLR. For the BDS IGSO/MEO satellites, the precision for all analysis centers is about 15 cm while the combined solution archives the best performance with a 8.4 cm level precision compared to GFZ solutions.

Since there is a lack of broadcast ephemeris for Galileo satellites from Julian Day 57050 and this condition lasts about one month, no orbit solutions are provided by iGMAS analysis centers. For the combined orbit of Galileo satellites, the precision is about 6 cm while the average value of all analysis centers is about 10 cm when compared to the orbits provided by TUM. No matter the BDS or Galileo satellites orbits solution, it is clear that with more track stations used in precise orbit determination, the precision is improved.

Considering that the assessment results are not enough reliable for BDS and Galileo satellites when compared to the MGEX solutions, an external method with SLR is used for these satellites, Table 3 lists the SLR validation results and some residuals larger than 100 cm are treated as outliers and removed in the statistics results, BDS GEO satellites adopt Orbit-Normal (ON) attitude control mode while the IGSO/MEO satellites adopt both ON mode and yaw-steering (YS) mode, limited by the relative static observation geometry, a lower precision for GEO satellites is obtained than non-GEO satellites in POD [18]. The SLR results mostly reflect the orbit error in radial direction and the statistics results show that the RMS of C01 is about 58 cm, the IGSO/MEO satellites during YS mode are better than ON season which are 14 and 6 cm, respectively, for Galileo satellites, the SLR validated RMS is about 10 cm.

Table 1 RMS of iGMAS satellite orbits w.r.t IGS (unit: cm)

AAC	AC01	AC02	AC03	AC04	AC05	AC06	AC07	AC08	AC09	AC10	ISC
GPS	3.8	3.1	2.2	1.9	1.8	1.5	2.2	1.4	1.2	1.4	1.0
GLONASS	7.9	4.3	4.3	2.7	4.2	4.8	6.5	2.6	2.6	3.3	1.7
BDS (GEO)	273	260	265	236	261	212	232	256	236	245	225
BDS (IGSO/MEO)	21.7	13.4	10.0	16.9	15.8	10.5	14.6	18.8	10.4	16.9	8.4
Galileo	20.1	7.4	14.7	8.1	7.8	9.9	8.2	4.8	8.3	17.4	6.1

Table 2 RMS of iGMAS satellite orbits w.r.t ISC (unit: cm)

AAC	AC01	AC02	AC03	AC04	AC05	AC06	AC07	AC08	AC09	AC10
GPS	3.4	3.3	1.9	1.7	1.5	1.2	1.9	1.1	0.8	1.0
GLONASS	7.2	4.4	3.6	2.6	4.0	4.0	6.3	2.2	2.3	2.7
BDS(GEO)	136.9	116.5	97.5	85.6	69.4	57.9	69.2	102.2	69.4	110.0
BDS (IGSO/MEO)	18.7	13.7	9.7	13.4	12.8	9.3	11.4	15.0	8.5	13.8
Galileo	20.3	7.3	14.6	6.8	5.4	6.9	5.7	3.5	5.2	18.6

Table 3 SLR residuals statistics results (unit: cm)

PRN	YS			ON		
	Mean	STD	RMS	Mean	STD	RMS
C01	–	–	–	−51.4	27.0	58.1
C08	−0.9	5.9	6.0	7.9	10.6	13.2
C10	0.2	6.22	6.2	1.9	11.4	11.6
C11	−1.3	4.2	4.4	−3.3	15.6	15.9
E11	−4.3	9.1	10.1	–	–	–
E19	−4.4	8.7	9.7	–	–	–
E20	−4.9	9.7	10.9	–	–	–

3.2 Final Satellite Clock Products

For the assessment of iGMAS final clock products, the corresponding clock products from IGS are used as reference and the same time period as orbit products are in statistics, that is the IGS-combined GPS satellite clock is used for iGMAS GPS satellites clock products, the ESA products are used for GLONASS and the GFZ products are used for comparison of BDS and Galileo. The systematic error between the iGMAS products and the reference products is removed by fitting the data with a second-order polynomial, the average RMS for each satellite system is summarized in Table 4 (values larger than 2 ns are removed in statistics) and Fig. 2 show the mean RMS series of all satellites for the four satellite navigation systems.

From the statistical results, the differences of precision among analysis centers within the same satellite system are obvious, and for the same analysis center, its GPS satellite clock product obtains the best precision among the four systems and is significantly better than other satellite systems. While for the combined clock solution, the precisions are 0.06 ns and 0.1 ns for GPS and GLONASS, respectively, limited by the impact of GEO satellite clock products, the precision for BDS final clock is some worse than GPS and GLONASS with a precision about 0.36 ns, while the precision for Galileo satellites is about 0.27 ns. According to the statistical results, the precision of satellite clock products is a little worse than the

Table 4 RMS of iGMAS satellite clock products w.r.t IGS (unit: ps)

AAC	AC01	AC02	AC03	AC04	AC05	AC06	AC07	AC08	AC09	AC10	ISC
GPS	268	171	265	83	102	221	125	96	65	69	56
GLONASS	802	727	724	165	310	273	545	137	121	173	110
BDS	602	587	597	766	397	450	372	433	367	410	363
Galileo	518	357	464	764	260	285	270	217	342	742	269

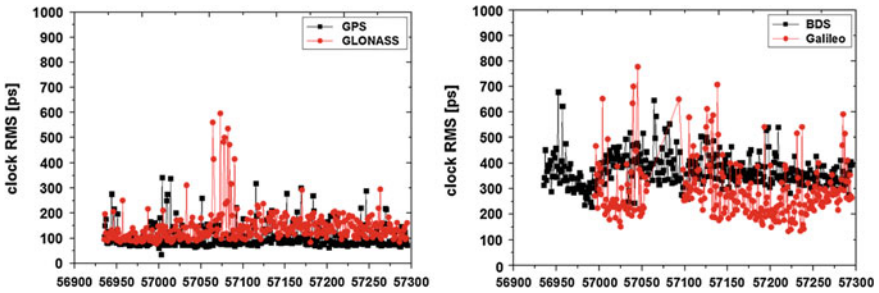

Fig. 2 The RMS series of iGMAS quad-constellation satellite clock products

combined orbits, a possible cause is that the different time systems for IGS (based on GPST) and iGMAS (based on BDT) products which results in accuracy loss in clock products interpolation.

3.3 Final ERP Products

For most analysis centers of iGMAS, the final ERP products are generated in the GPS/GLONASS orbit determination with other products, to have a clear knowledge about the precision of ERP, the ERP products of iGMAS from September 2015 to October 2014 are collected and compared to IGS ERP product in this study.

Figure 3 shows the residuals for different Earth rotation parameters between iGAMS combination and IGS.

The mean of absolute deviation is computed for each parameter as the precision of iGMAS ERP products and the statistical results are shown in Table 5.

The difference of ERP products between most analysis centers and IGS are significant, it indicates that there are some obvious reference differences between the products which related to the specific process strategy and conventions. However, with the consistency correction introduced in Sect. 2.1, the difference between ISC and IGS is less obvious than most analysis centers.

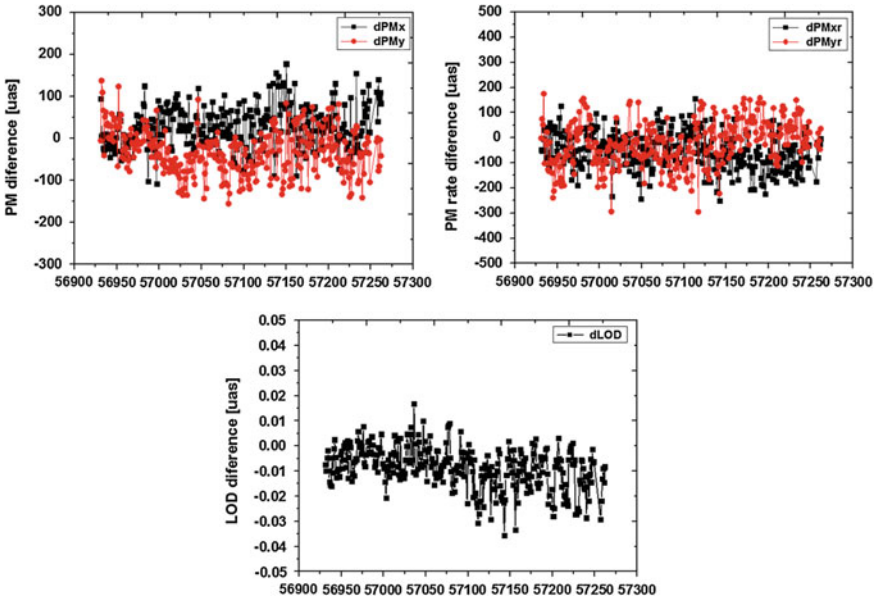

Fig. 3 The difference series of iGMAS ERP products

Table 5 Absolute bias of iGMAS ERP products w.r.t IGS (unit, PM: uas, PM rate: uas/d, LOD: us)

AAC	AC01	AC02	AC03	AC04	AC05	AC06	AC07	AC08	AC09	AC10	ISC
PMx	38	89	37	144	401	32	223	155	59	74	36
PMy	81	161	103	157	425	39	64	215	45	63	44
PMxr	180	103	111	511	162	96	1214	105	72	96	63
PMyr	219	118	143	514	129	109	1055	127	93	98	67
LOD	13	11	18	23	12	19	473	13	17	7	8

In order to further analyze the consistency between combined orbit and ERP products, the rotation parameters (RX, RY) between combined GPS orbit and IGS in the similarity transformation as well as the difference $(\mathrm{d}PM_x, \mathrm{d}PM_y)$ of polar motion parameters between combined and IGS. With the assumption that the orbit products are well consistent with its ERP products, then the equation can be obtained (i.e., $RX = -\mathrm{d}PM_y$ and $RY = -\mathrm{d}PM_x$), Fig. 4 reveals the variation of orbit rotations parameters and the corresponding difference of polar motion parameters. The same variation trend can be found which implies the consistency between combined orbit and ERP is promising.

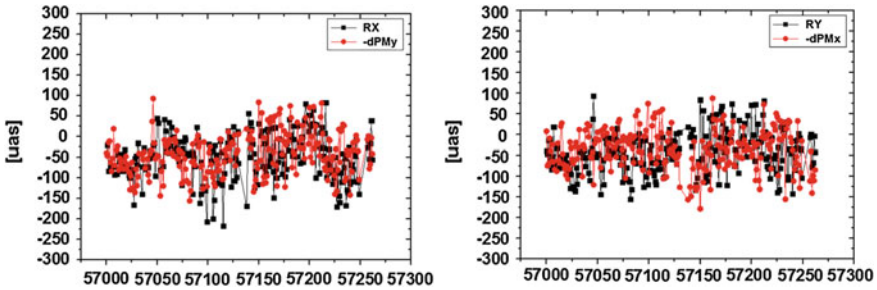

Fig. 4 Consistency between final orbits and ERP

3.4 Final Ionosphere Products

To assess the precision of iGMAS ionosphere products, one-year products are collected from October 2014 to October 2015 and the IGS combined solution is used as reference, Fig. 5 (left) shows the ISC solution precision and the RMS values for the analysis centers are listed in Table 6.

Except the AC07, the precision for other centers are best among 7 TECU and the precision for ISC is about 1.7 TECU which is the better than the analysis centers. What is more, with an improvement of process strategy for some analysis centers, the precision for ISC becomes more stable.

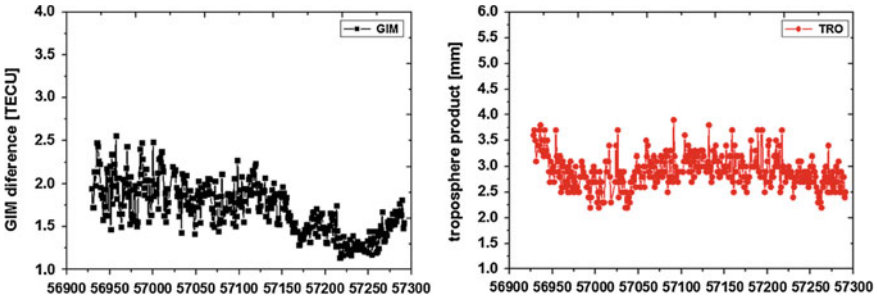

Fig. 5 The RMS series of iGMAS ionosphere (*left*) and troposphere (*right*) products

Table 6 RMS of iGMAS ionosphere products w.r.t IGS (unit: TECU)

AAC	AC01	AC02	AC03	AC04	AC05	AC06	AC07	AC08	AC09	AC10	ISC
RMS	6.10	4.81	3.07	2.78	2.27	3.07	10.83	2.77	3.57	1.93	1.71

Table 7 RMS of iGMAS troposphere products w.r.t JPL (unit: mm)

AAC	AC01	AC02	AC03	AC04	AC05	AC06	AC07	AC08	AC09	AC10	ISC
RMS	7.7	3.6	4.1	3.1	3.6	6.9	8.8	3.3	6.9	4.8	2.9

3.5 Final Troposphere Products

To analyze the precision of iGMAS troposphere products, 54-week products are collected from October 2014 to September 2015 and the JPL products are used as reference for comparison. Figure 5 (right) shows the variation of precision for iGMAS combination and the statistics results are listed in Table 7.

The precision for ISC is about 3 mm and better than the analysis centers, other four centers obtain a precision better than 4 mm while the performance of the rest centers are not promising and a further investigation should be needed.

4 Conclusions

The Product Integration and Service Center (ISC) is the products reprocess center which provides global users with different time-delay products. The present paper focuses on the final products combination from different analysis centers and the emphasis is put on the consistency between different final products. Then one-year final products from iGMAS are assessed and analyzed.

The precisions of iGMAS combination are 1 and 2 cm for GPS and GLONASS, respectively, and the difference is less than 1 cm whether the reference product is IGS or ISC for the precision of iGMAS analysis centers, which indicates that the assessment is reliable and the iGAMS combination of GPS/GLONASS can obtain a same precision level to IGS. However, for BDS GEO satellites, the precision is about 2 m and the IGSO/MEO satellite orbit can achieve a precision about 8 cm while it is about 6 cm for Galileo satellites. On the other hand, with more tracking stations are employed in the precise orbit determination for BDS and Galileo, the corresponding precision improves significantly. Moreover, the SLR validation shows that the precision for BDS IGSO/MEO satellites during YS is better than ON season and the refined process strategy for ON needs further investigation.

The precision difference among analysis centers within the same satellite system is obvious, and for the same analysis center, its GPS satellite clock product obtain the best precision among the four system and is significantly better than other satellite systems. The precision of satellite clock products is a little worse than the combined orbits, a possible cause is that the different time systems for IGS (based on GPST) and iGMAS (based on BDT) products which result in accuracy loss in clock products interpolation. In order to promote the iGMAS orbit/clock products based on BDT in different fields, a further verification of products high-precision application is necessary.

The difference of ERP products between most analysis centers and IGS is significant, it indicates that there are some obvious reference differences between the products which related to the specific process strategy and conventions. However, with the consistency correction introduced in this present paper, the difference between ISC and IGS is less obvious than most analysis centers and the consistency between orbit and ERP combination is promising.

The precisions are 3 mm and 2TECU for troposphere and ionosphere combination products, respectively, and some improvement should be made by some analysis centers in the future.

References

1. Beutler G, Moore A, Mueller I (2009) The international global navigation satellite systems service (IGS): development and achievements. J Geodesy 83(3–4):297–307
2. IGS (2014) IGS quality of service. http://igs.org
3. Steigenberger P et al (2009) Quality of reprocessed GPS satellite orbits. J Geodesy 83(3–4):241–248
4. Na Wei et al (2009) Analysis and assessments of IGS products consistencies. Geomatics Inf Sci Wuhan Univ 11:1363–1367
5. Mireault Y, Kouba J, Ray J (1999) IGS Earth rotation parameters, GPS Solutions
6. Altamimi Z, Collilieux X (2009) IGS contribution to the ITRF. J Geodesy 83(3–4):375–383
7. Altamimi Z, Collilieux X (2013) Reference frames for applications in geosciences
8. Altamimi Z, Collilieux X et al (2007) ITRF2005: a new release of the International Terrestrial Reference Frame based on time series of station positions and Earth Orientation Parameters. J Geophys Research 112
9. Altamimi Z, Collilieux X, Métivier L (2011) ITRF2008: an improved solution of the international terrestrial reference frame. J Geodesy 85(8):457–473
10. Altamimi Z, Collilieux X, Métivier L (2013) ITRF combination: theoretical and practical considerations and lessons from ITRF2008
11. Altamimi Z, Métivier L, Collilieux X (2012) ITRF2008 plate motion model. J Geophys Res 117
12. Altamimi Z, Boucher C, Gambis D (2005) Long-term stability of the terrestrial reference frame. Adv Space Res 36(3):342–349
13. Mireault Y, Kouba J, Lahaye F (1996) IGS combination of precise GPS satellite ephemerides and clocks. In: Beutler G et al (eds) GPS trends in precise terrestrial, airborne, and spaceborne applications. Springer, Berlin, p 14–23
14. Beutler G, Kouba J, Springer T (1995) Combining the orbits of the IGS analysis centers. Bulletin Géodésique 69(4):200–222
15. Kouba J, Springer T (2001) New IGS station and satellite clock combination. GPS Solutions 4 (4):31–36
16. Hernández-Pajares M, Juan JM, Sanz J et al (2009) The IGS VTEC maps: a reliable source of ionospheric information since 1998. J Geodesy 83(3–4): 263–275
17. Feltens J (2002) IONO_WG status report and outlook-position paper. In: IAC workshop, editor. Ottawa, Canada
18. Zhao Q, Guo J et al (2013) Initial results of precise orbit and clock determination for COMPASS navigation satellite system. J Geodesy 87(5):475–486

Evaluating PPP Ambiguity Resolution Methods with Ionosphere-Free and Raw GPS Observation Models

Peiyuan Zhou and Jinling Wang

Abstract Precise point positioning (PPP) is a powerful technique to achieve homogeneous positioning accuracy globally and is becoming the dominating service for precise positioning. Typically, PPP still takes about 30 min of initialisation time to obtain a converged solution of better than 10 cm. In order to shorten the initialization time, integer ambiguity fixing approaches for PPP (PPP-AR) have been developed in the recent years. In most of the existing ambiguity resolution approaches, ionosphere-free observation models are used and therefore they are restricted by the noise of range observations and the short wavelength of the narrow-lane ambiguities as well. However, with the GNSS modernization, a unified processing strategy without forming combinations and differencing is more appealing. In this work, we apply this new approach in uncalibrated phase delay (UPD) estimation and zero-difference (ZD) AR and compare it with the traditional model. The satellite UPDs associated with ionosphere-free model and raw observation model are first estimated from a global distributed GNSS network. 70 stations tracking both GPS and Beidou (BDS) are used in positioning validation. The potential contribution of BDS is also investigated.

Keywords GNSS · Precise point positioning · Raw observation model · Ambiguity resolution · Uncalibrated phase delay

P. Zhou (✉) · J. Wang
School of Civil and Environmental Engineering, University of New South Wales, Sydney, NSW 2052, Australia
e-mail: peiyuan.zhou@unsw.edu.au

J. Wang
e-mail: jinling.wang@unsw.edu.au

© Springer Science+Business Media Singapore 2016

J. Sun et al. (eds.), *China Satellite Navigation Conference (CSNC) 2016 Proceedings: Volume III*, Lecture Notes in Electrical Engineering 390,
DOI 10.1007/978-981-10-0940-2_46

1 Introduction

Integer carrier-phase ambiguity resolution (AR) is the key to fast and high-precision GNSS positioning and navigation. The integer property of the ambiguity parameter is often ignored in precise point positioning (PPP) [19] due to the difficulty of separating UPD from the ambiguity parameter for a single receiver.

In recent years, AR techniques relying only on a single station have been developed successfully to further improve the positioning accuracy of PPP. Generally, we can distinguish between two approaches, presented in recent studies, to recover the integer feature of the undifferenced ambiguities by applying improved satellite-specific correction products, where satellite UPDs have been separated from the integer ambiguities in different ways. The first approach is called UPD estimation model [2, 5]. The satellite UPDs of WL and NL are estimated using the MW and ionosphere-free combination measurements. The other is so-called Decoupled clock model [1, 8]. They redefined the satellite clock products such that the integer nature of ambiguity is preserved after applying their clock products. A comparison of these methods can be found in [3, 15]. Traditionally, PPP-AR is achieved by MW and ionosphere-free combinations in which the ionosphere effect is eliminated. To exploit the ionosphere characteristics, PPP-AR with L1 and L2 raw observables have also been developed recently by Gu et al. [6], Li et al. [12].

In this study, we apply this new approach in uncalibrated phase delay (UPD) generation and ZD AR and compare it with the traditional model. The positioning accuracy and convergence time are investigated in detail.

2 Multi-GNSS PPP Model

The basic mathematical models of pseudorange and carrier-phase between satellite s and receiver r of raw observation model can be expressed as:

$$\begin{aligned}
P_{i,r}^{s,G} &= \rho_r^{s,G} + c(dt_r^G - dt^{s,G}) + \mu_i^G I_r^{s,G} + (d_{i,r}^G - d_i^{s,G}) + \varepsilon_{P_i}^G \\
L_{i,r}^{s,G} &= \rho_r^{s,G} + c(dt_r^G - dt^{s,G}) - \mu_i^G I_r^{s,G} + \lambda_i^G (b_{i,r}^G - b_i^{s,G}) + \lambda_i^G N_{i,r}^{sG} + \varepsilon_{L_i}^G \\
P_{i,r}^{s,C} &= \rho_r^{s,C} + c(dt_r^C - dt^{s,C}) + \mu_i^C I_r^{s,C} + (d_{i,r}^C - d_i^{s,C}) + \varepsilon_{P_i}^C \\
L_{i,r}^{s,C} &= \rho_r^{s,C} + c(dt_r^C - dt^{s,C}) - \mu_i^C I_r^{s,C} + \lambda_i^C (b_{i,r}^C - b_i^{s,C}) + \lambda_i^C N_{i,r}^{s\,C} + \varepsilon_{L_i}^C
\end{aligned} \tag{1}$$

where G stands for GPS; C stands for other constellations like BDS, GLONASS, GALILEO and so on; i is the frequency index; ρ is the non-dispersive geometric distance between receiver and satellite including troposphere delay; t_r and t^s are the receiver and satellite clock errors; I_r^s is the slant ionospheric delay on frequency f_1, μ_i is the frequency-dependent coefficient; $d_{i,r}$ and d_i^s are the frequency-dependent pseudorange hardware delays on receiver and satellite; $b_{i,r}$ and b_i^s their counterpart on carrier phase, which is a combined effect of initial phases and hardware delays

on carrier phase; $N_{i,r}^{s}$ is the unknown integer ambiguity with wavelength λ_i; ε_{P_i} and ε_{L_i} are the unmodeled errors on pseudorange and carrier phase, respectively. Other errors such as the phase center offsets and variations, phase windup, relativistic effect and tide loading are corrected according to [7].

The slant ionospheric delay is estimated as unknown for each satellite observed. In this manner, a priori ionosphere correction model can be employed as constraints for strengthening the solution [11, 12]. In this work, the global ionosphere maps (GIMs) from Center for Orbit Determination in Europe (CODE) is applied as constraints in raw observation model. The estimable ambiguities on each frequency are no longer integers due to the existence of phase hardware delays and application of IGS precise satellite clocks (based on P1–P2 combination).

In a conventional PPP model, the following ionosphere-combinations are normally used to eliminate the first-order ionospheric delays on both pseudorange and carrier phase observations,

$$\begin{aligned} P_{r,3}^{s} &= \rho_r^s + t_r - t^s + \epsilon_{P_3} \\ L_{r,3}^{s} &= \rho_r^s + t_r - t^s + \lambda_1 B_{r,3}^{s} + \epsilon_{L_3} \end{aligned} \tag{2}$$

As a result of ionosphere-free combination and the application of IGS precise satellite clocks, the estimable ambiguity $B_{r,3}^{s}$ becomes a combination of original integer ambiguity and corresponding hardware delays on both pseudorange and carrier phase and therefore lost its integer property [16].

3 UPD Separation and Ambiguity Resolution

In this section, a brief introduction on UPD separation algorithm and PPP-AR at user end will be given. The UPD estimation algorithm for both PPP models is based on the method discussed in [12, 13].

3.1 UPD Separation Algorithm

Based on [2], all undifferenced wide-lane and narrow-lane ambiguity estimates in a continuous arc without cycle slip can be expressed as an integer value plus a bias for the satellite and other for the receiver (regardless of the arc). These biases are shared by all the observations from a specific receiver or satellite and can be expressed as,

$$B_i^j - \tilde{N}_i^j = \bar{b}_i - \bar{b}^j \tag{3}$$

where B_i^j denotes the float ambiguity; $\tilde{N}_i^j$ denotes the sum of integer ambiguity and integer part of UPD; $\bar{b}_i$ and $\bar{b}^j$ are the UPDs of receivers and satellites respectively. The separation ensures that any double-differenced (DD) ambiguity is integer in nature.

Even if we knew all the integer ambiguities, there would still be a rank deficiency of one between receiver UPD and satellite UPD. To estimate UPD, extra condition has to be applied to eliminate the rank deficiency. Often, we choose to fix one of the UPDs to, for example, zero. Then the UFO can be estimated by means of the least squares adjustment. Proper quality control is needed here to exclude inconsistent or bad quality float ambiguities. Under the condition that all integer ambiguities are known and one UPD is fixed, all other UPDs can be estimated according to Eq. (3).

The above equation is suitable for both WL and NL UPD estimation. For conventional PPP model, WL ambiguity is obtained from MW combination [14, 18] and NL ambiguity is derived from float ionosphere-free ambiguity and fixed WL ambiguity [2, 4, 8]. While for the raw observation model, both WL and NL ambiguities are constructed from float ambiguities on L1 and L2. For a detailed description of the algorithm, we refer to [12, 13]. The fundamental difference between ionosphere-free model and raw observation model in UPD separation is the float ambiguity estimates.

3.2 Ambiguity Resolution on Single Station

As shown in Eq. (3), satellite UPDs estimated from a reference network can be directly applied to any single rover anywhere not necessarily included in the network. The satellite UPDs are removed with the estimated UPD products, whereas the receiver UPDs can be separated by enforcing one ZD ambiguity to its nearest integer or by forming single-differences (SD) between satellites. Afterwards, the corrected ambiguities have integer feature and can be fixed by applying LAMBDA method [17].

In real data processing, it is often difficult to fix all ambiguity parameters reliably for PPP, especially resolving the ambiguities of a newly risen satellite or a re-initializing ambiguity after a cycle slip [9, 15], therefore partial AR is attempted if a full AR is not possible. The ambiguities are sorted according to their standard deviation and ambiguities with bad quality are excluded from AR.

Finally, the fixed ambiguities are reconstructed and used to update the positions and we can get the ambiguity-fixed solutions. For conventional PPP model, it can be done according to the following equation,

$$B_3 = \frac{f_1}{f_1 + f_2}(N_n + \bar{b}_n) + \frac{f_1 f_2}{f_1^2 - f_2^2}\tilde{N}_w \tag{4}$$

where N_n and $\tilde{N}_w$ are the already fixed NL and WL ambiguities, respectively; $\bar{b}_n$ is the NL UPD correction. For the raw observation model, a similar procedure can be applied to obtain fixed ambiguities.

4 Results and Discussion

In this section, the results of UPD estimation and PPP positioning with both ambiguity-float and ambiguity-fixed solutions are analyzed in details.

4.1 UPD Quality Analysis

The UPDs estimated from above two separate models are analyzed. In theory, the WL/NL UPDs should be the same for both models; the only difference between them is how the input ambiguities are constructed, either from observation space or state space.

In the following example, observations from around 190 globally distributed IGS stations on DOY 214, 2015 were used to derive UPDs. The distribution of the SD NL UPD differences is shown in Fig. 1. Due to the long-term stability of wide-lane UPDs, the wide-lane UPD was estimated as a daily constant for each satellite, while narrow-lane UPD was estimated as a constant for every 15 min [2]. There are 96 sets of NL UPDs in total in one day for each satellite. Satellite G07 was used as the reference satellite here. Only UPDs for GPS system were estimated

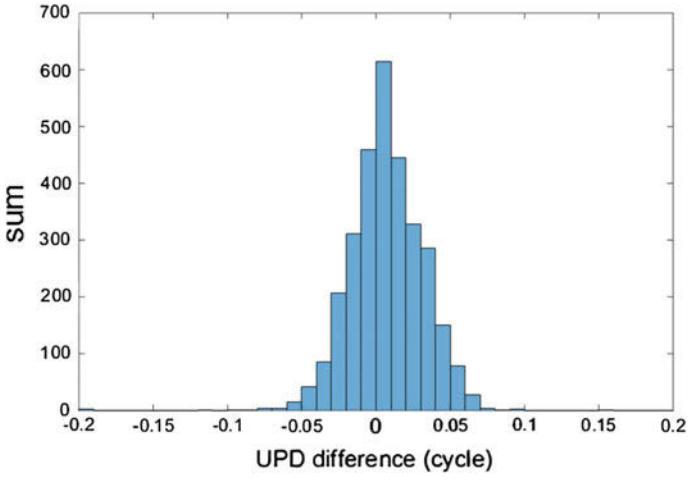

Fig. 1 SD NL UPD differences between ionosphere-free and raw observation model

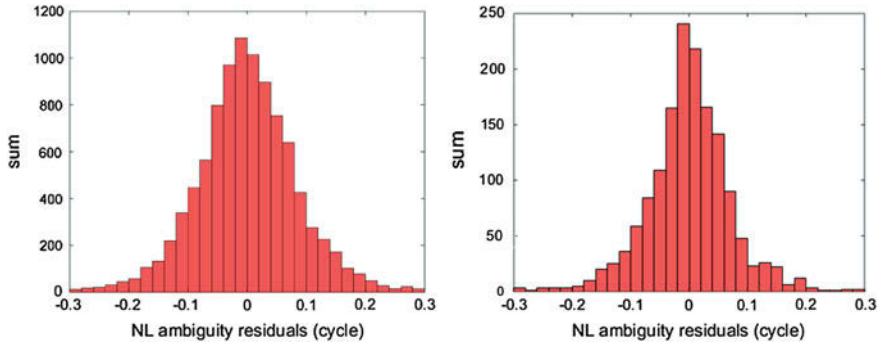

Fig. 2 WL ambiguity residuals on DOY 214, 2015 (*left*), NL ambiguity residuals on DOY 214, 2015 (session 60) (*right*)

in this study. In total, 95.3 % of their differences are within 0.05 cycle and 99.6 % are less than 0.075 cycles, which indicates that UPDs from ionosphere-free and raw observation model are highly consistent with each other. As their differences are ignorable, in the following analysis only UPDs from ionosphere-free model were used for analysis.

The quality of UPD estimates can also be evaluated by checking the residuals of float ambiguities used for UPD estimation. The left figure in Fig. 2 shows the residual distribution of WL ambiguities. Generally, a more consistent UPD solution is expected if the residuals are closer to zero.

In total, 9761 float WL ambiguities were used for WL UPD estimation, and 95.4 % of them are within 0.2 cycles. Again, a high consistency is achieved among all float ambiguity observations. The corresponding NL ambiguity residuals in 60th session are also displayed in right of Fig. 2. In this session, 1559 valid NL ambiguities were used for deriving UPD, and 96.7 % of their residuals are less than 0.2 cycles.

To further validate our UPDs with the products from other sources, our UPDs from ionosphere-free model were compared with the UPD products from SGG in Wuhan University [10], which are publicly available recently and are also based on ionosphere-free model. Overall, 99.2 % of the differences are less than 0.05 cycles and 99.9 % are less than 0.075 cycles. Our UPDs agree well with each other.

4.2 Positioning Results

70 MGEX stations tracking both GPS and BDS were used in this positioning analysis. And none of these stations were included in UPD estimation. For each station, the 24-h dataset was divided into 24 hourly sessions. In total, there are 1680 tests used in the experiment. All these datasets were processed in a kinematic mode to analyze the performance of both ionosphere-free and raw observation model with and without AR.

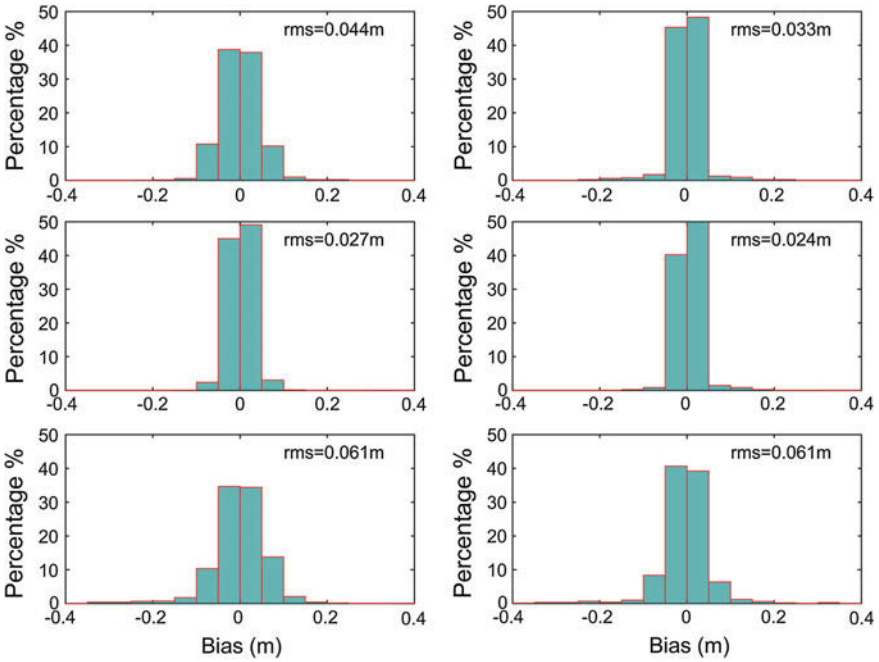

Fig. 3 Distribution of positioning bias, achieved by ionosphere-free float (*left*) and fixed (*right*) PPP

Figure 3 shows positioning biases of ionosphere-free model against "ground truth" in East, North, and Up directions. All these results were obtained from a pure kinematic processing. The left column represent biases achieved with ambiguity-float solution, while the right panel shows ambiguity-fixed solution with our UPD estimates. By fixing ambiguities, the RMS of positioning biases on horizontal directions is improved from 4.4, 2.7 to 3.3 and 2.4 cm, respectively, while on the vertical component, no improvements were found in this study. The east component was improved by 25 %. These UPDs significantly improve the accuracy of hourly kinematic position estimates, especially in the east direction.

Figure 4 shows positioning biases of raw processing model. The left column represents ambiguity-float solution and the right panel is ambiguity-fixed solution. By fixing ambiguities, the RMS of positioning biases on three directions was improved from 4.8, 3.3 and 5.8 to 3.7, 2.0 and 5.7 cm, respectively. The east component is improved by about 23 % by fixing ambiguities in raw model.

By comparing, the columns on the right in Figs. 3 and 4, we can see the RMS from raw observation model on the east component is a little worse than the ionosphere-free model, while on north and up component, the raw model can achieve a better result. Their 3D RMS is 0.073 and 0.070 m, respectively. Overall, with ambiguity-fixing, the raw processing model achieves slightly better results than ionosphere-free model.

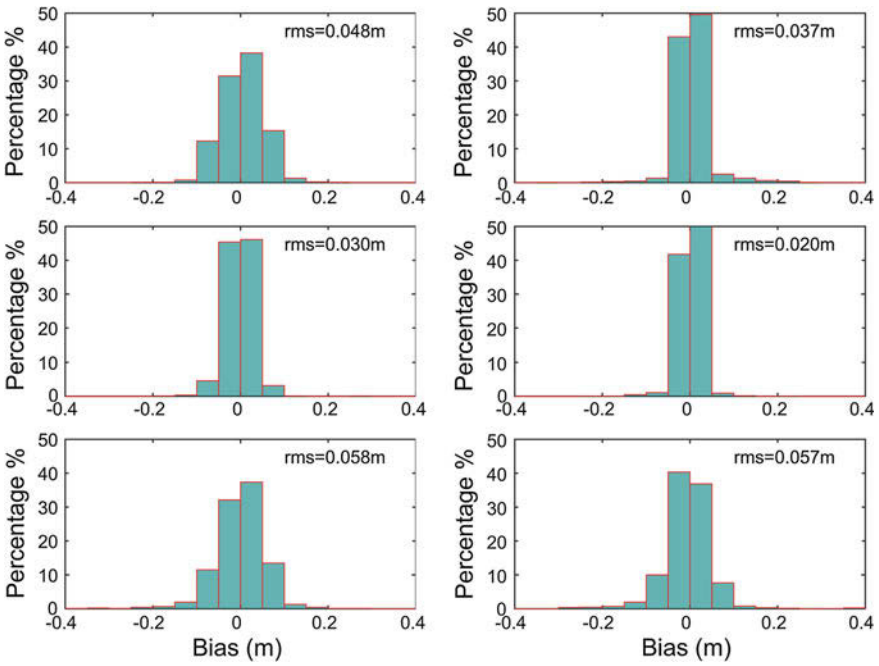

Fig. 4 Distribution of positioning bias, achieved by raw observation float (*left*) and fixed (*right*) PPP

To further investigate the contribution of BDS to conventional PPP, the same data sets were processed again including both GPS and BDS observations. The positioning biases are shown in Fig. 5. The left panes are results from GPS + BDS combined float PPP and right panel is ambiguity-fixed GPS + BDS solution. (Only ambiguity of GPS is fixed). By incorporating BDS, the position accuracy of ambiguity-fixed PPP is slightly improved, both in north and up components. The overall improving is about 6 %.

4.3 Convergence Results

We have also analyzed the time to first fix (TTFF) for the ambiguity-fixed solutions between ionosphere-free and raw observation model. The result is shown in Fig. 6. The averaging TTFF time for these two models is 28.5 and 30.4 min, respectively. Slightly better convergence was achieved with ionosphere-free model here. The longer convergence time for raw observation model might attribute to the use of dm-level accuracy ionosphere model constraints in this study.

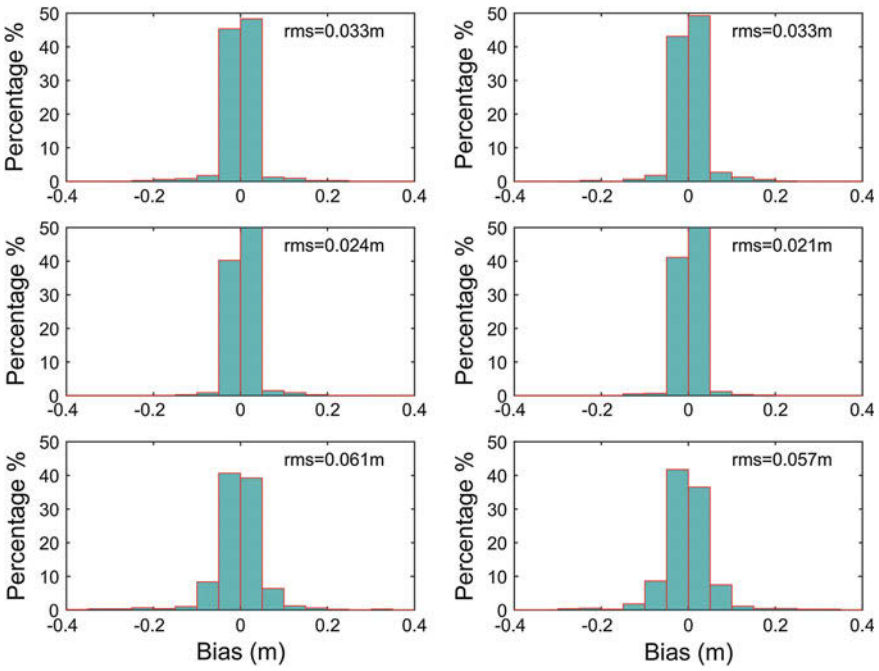

Fig. 5 Distribution of positioning bias, achieved by ionosphere-free float (*left*) and fixed (*right*) PPP (GPS + BDS)

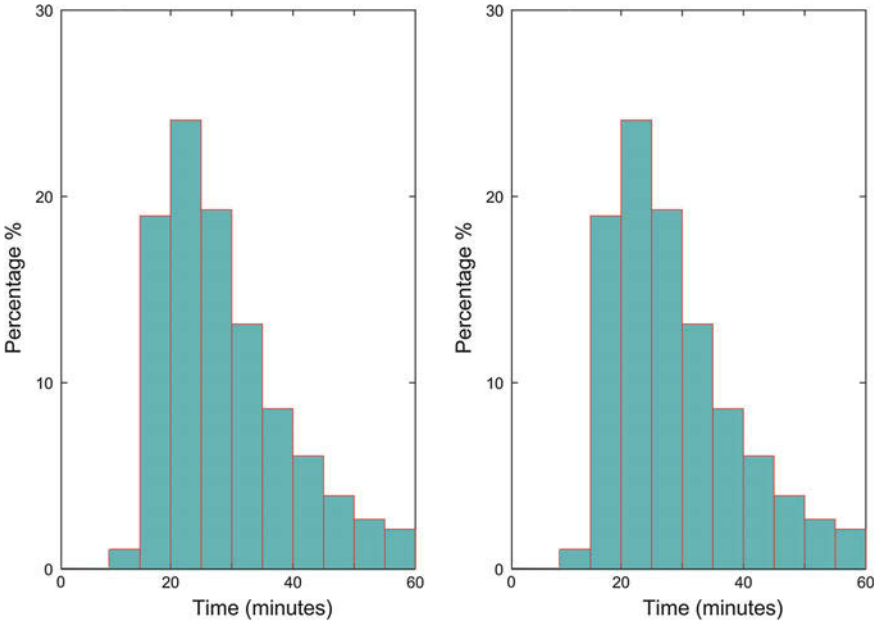

Fig. 6 Distribution of TTFF for ionosphere-free (*left*) and raw observation (*right*) PPP

5 Concluding Remarks

In this work, we have evaluated ambiguity-resolution performances of two commonly used PPP models, ionosphere-free model and raw observation model. UPDs estimations derived from both models confirm their equivalence. Then, based on our own estimated UPDs, the positioning biases and convergence time of both models are evaluated with kinematic tests. These two models show almost similar performances in terms of position accuracy and convergence speed. The raw observation model achieves smaller biases overall, while its TTFF is slightly longer than the ionosphere-free model. The contribution of BDS system to both models has also been investigated. The 3D RMS is reduced by about 6 % after including BDS into processing.

Further research is being performed to extend integer ambiguity resolution to all GNSS constellations, including BDS and Galileo in the near future. With the GNSS modernization, more navigation satellite systems are operating and satellites with multi-frequency observations are also increasing. The accuracy of current ionosphere models is also to be improved. With more accurate ionosphere constraints, the potential of raw observation model can be better exploited.

References

1. Collins P, Lahaye F, Heroux P, Bisnath S (2008) Precise point positioning with ambiguity resolution using the decoupled clock model. In: Proceedings of the 21st international technical meeting of the satellite division of the institute of navigation (ION GNSS 2008), pp 1315–1322
2. Ge M, Gendt G, Rothacher M, Shi C, Liu J (2008) Resolution of GPS carrier-phase ambiguities in precise point positioning (PPP) with daily observations. J Geodesy 82:389–399
3. Geng J, Meng X, Dodson A, Teferle F (2010) Integer ambiguity resolution in precise point positioning: method comparison. J Geodesy 84:569–581
4. Geng J, Teferle FN, Meng X, Dodson AH (2011) Towards PPP-RTK: ambiguity resolution in real-time precise point positioning. Adv Space Res 47:1664–1673
5. Geng J, Teferle FN, Shi C, Meng X, Dodson AH, Liu J (2009) Ambiguity resolution in precise point positioning with hourly data. GPS Solutions 13:263–270
6. Gu S, Shi C, Lou Y, Liu J (2015) Ionospheric effects in uncalibrated phase delay estimation and ambiguity-fixed PPP based on raw observable model. J Geodesy 1–11
7. Kouba J, Héroux P (2001) Precise point positioning using IGS orbit and clock products. GPS Solutions 5:12–28
8. Laurichesse D, Mercier F, Berthias J-P, Broca P, Cerri L (2009) Integer ambiguity resolution on undifferenced GPS phase measurements and its application to PPP and satellite precise orbit determination. J Inst Navig 56:135
9. Li P, Zhang X (2015) Precise point positioning with partial ambiguity fixing. Sensors 15:13627
10. Li P, Zhang X, Ren X, Zuo X, Pan Y (2015) Generating GPS satellite fractional cycle bias for ambiguity-fixed precise point positioning. GPS Solutions 1–12

11. Li X (2012) Improving real-time PPP ambiguity resolution with ionospheric characteristic consideration. In: Proceedings of the 25th international technical meeting of the satellite division of the institute of navigation (ION GNSS 2012). Nashville, TN, pp 3027–3037
12. Li X, Ge M, Zhang H, Wickert J (2013) A method for improving uncalibrated phase delay estimation and ambiguity-fixing in real-time precise point positioning. J Geodesy 87:405–416
13. Li X, Zhang X (2012) Improving the estimation of uncalibrated fractional phase offsets for PPP ambiguity resolution. J Navig 65:513–529
14. Melbourne WG (1985) The case for ranging in GPS-based geodetic systems. In: Proceedings of the first international symposium on precise positioning with the global positioning system
15. Shi J (2012) Precise point positioning integer ambiguity resolution with decoupled clocks. Dissertation, University of Calgary
16. Shi J, Gao Y (2010) Analysis of the integer property of ambiguity and characteristics of code and phase clocks in PPP using a decoupled clock model. In: Proceedings of the 23rd international technical meeting of the satellite division of the institute of navigation (ION GNSS 2010), pp 2553–2564
17. Teunissen PJG (1995) The least-squares ambiguity decorrelation adjustment: a method for fast GPS integer ambiguity estimation. J Geodesy 70:65–82
18. Wübbena G (1985) Software developments for geodetic positioning with GPS using TI-4100 code and carrier measurements. In: Proceedings of the first international symposium on precise positioning with the global positioning system. sl]:[sn]
19. Zumberge JF, Heflin MB, Jefferson DC, Watkins MM, Webb FH (1997) Precise point positioning for the efficient and robust analysis of GPS data from large networks. J Geophys Res Solid Earth 102:5005–5017

Kinematic Precise Point Positioning Algorithm with Constraint Condition

Shaoguang Xu, Yongliang Xiong, Dejun Wang and Xiaoying Gong

Abstract The post processing accuracy of traditional kinematic PPP is at decimeters level, this is a key factor to limit the wide application of kinematic PPP. There may be some prior information during kinematic PPP by GNSS, and this information contains the relation between estimated parameters or external information about the parameters. If this prior information has enough precision, the solution precision of traditional kinematic PPP can be largely improved. A kinematic PPP function model, incorporating some prior information, was purposed in this paper, and the corresponding formulas based on Kalman filter is derived as an example. The proposed algorithm was verified by real GNSS data collected in April 2013. The research results showed the accuracy of kinematic PPP can reach 5 cm after adopting the relaxed line constraint. The accuracy of position can be improved at a certain extent even if partial constraint was adopted, the most effective improvement is the up component, then the east component. In addition, the precision of ZTD can be improved 6 mm at least by adopting either the line constraint or partial constraint.

Keywords Traditional kinematic precise point positioning · Constraint condition · Kalman filter · Troposphere zenith delay

1 Introduction

Precise point positioning (PPP) is favored by the geodetic community for its convenience without base station [1, 2]. From the current progress, long-time static PPP can reach the same precision as differential GPS. But there are too many parameters to be estimated in traditional single system kinematic PPP, with respect

S. Xu (✉) · Y. Xiong · D. Wang · X. Gong
Department of Surveying Engineering, Southwest Jiaotong University, Chengdu, China
e-mail: shaoguangxu@home.swjtu.edu.cn

© Springer Science+Business Media Singapore 2016

J. Sun et al. (eds.), *China Satellite Navigation Conference (CSNC) 2016 Proceedings: Volume III*, Lecture Notes in Electrical Engineering 390,
DOI 10.1007/978-981-10-0940-2_47

to const-acceleration mode, the unknown parameters in each epoch contain position vector, velocity vector, acceleration vector, receiver clock error, troposphere delay and ambiguities. Besides, parameters between adjacent epoch have only two relations. First, the position, velocity and acceleration should meet the physical law of motion, second, the ambiguities keep const if no cycle slip or lose of lock happening. As the result of above reasons, the traditional kinematic PPP solution's position is not accurate enough; the accuracy of post processing is at decimetre level [3].

During the motion of GNSS receiver, there is some prior trace information which may improve the accuracy of navigation and positioning at a certain extent can add to the computation equation of navigation and positioning. Algorithm with constraint condition has been applied in some field and their results have been improved more or less compared to the situation without constraint [4–9]. The algorithm for PPP with constraints is rarely introduced. This paper derived the expression formula of kinematic PPP with constraint condition based on Kalman filter and the validation of the proposed algorithm was investigated using experimental data. Some conclusions are given at last.

2 Kinematic PPP Mode with Constraint Condition

2.1 Traditional Kinematic PPP Mode

The traditional kinematic PPP mode mainly contains: Mode without the estimation of velocity, const-velocity mode and const-acceleration mode. As an example of const-acceleration mode, suppose n satellites are observed at current epoch, then parameters to be estimated include n ambiguities (N), three position parameters (X, Y, Z), three velocity parameters (V_x, V_y, V_z), three acceleration parameters (a_X, a_Y, a_Z), one troposphere delay parameter (Trp), and one receiver clock error (d_t), they can be expressed as follows [10]:

$$\overrightarrow{X} = [X, Y, Z, V_X, V_Y, V_z, a_X, a_Y, a_Z, d_t, \mathrm{Trp}, N_1, N_2, \ldots, N_n]^T \tag{1}$$

Parameter estimation adopts extended Kalman filter algorithm, and the prediction of parameters X_k and its covariance P_k can be expressed as follows:

$$X_{k,k-1} = \Phi_{k,k-1} X_{k-1} + \varpi_k, \quad \varpi_k \sim N(0, Q_k) \tag{2a}$$

$$P_{k,k-1} = \Phi_{k,k-1} P_{k-1} \Phi_{k,k-1}^T + Q_k \tag{2b}$$

where $\Phi_{k,k-1}$ is state transition matrix depicting the relation among position, velocity and acceleration which can be determined by physical law of motion.

Receiver clock error and troposphere delay are regarded as random walk, and ambiguities keep const if there is no cycle slip. Q_k is process noise matrix, and the corresponding process noise is described in related document [11] if all parameters' residual error obey the distribution as formula (2a). It is worth noting that troposphere delay's noise is usually set as 5 mm/sqrt(hour) [12], but kinematic GNSS receiver's elevation during motion may vary largely, so this parameter's noise should be enlarged according to elevation difference between adjacent epoch.

The linearized equations for iono-free observation Z_k are as follows:

$$Z_k^0 = H_k X_k + \omega_k, \quad \omega_k \sim N(0, R_k) \tag{3}$$

The elements of H_k in formula (3) are the corresponding coefficient of position, velocity, acceleration, receiver clock error, troposphere delay, and ambiguities related to satellites, respectively. R_k is the measurement noise matrix and the measurement noise of iono-free pseudorange observation in zenith is about 2 m, and the noise of iono-free carrier phase observation in zenith is about 2 cm, the noise in other directions is the function of elevation angle [2].

Based on the above prediction Eq. (2a, b) and observation Eq. (3) the following equation can be obtained [10]:

$$K_k = P_{k,k-1} H_k^T \left(H_k P_{k,k-1} H_k^T + R_k\right)^{-1} \tag{4a}$$

$$X_k = X_{k,k-1} + K_k \left(Z_k - h\left(X_{k,k-1}\right)\right) \tag{4b}$$

$$P_k = (I - K_k H_k) P_{k,k-1} \tag{4c}$$

2.2 Kinematic PPP with Constraint Condition

Before adding the constraint condition to traditional kinematic PPP mode there must be a classification of constraint conditions, because different adjustment adopted during data process leads to different constraint pattern. If sequential least square is adopted, prior information can be considered as quasi-observation equation, and make combination adjustment with real observation equation [13]; On the other side if Kalman filter is selected, there are several choices, first state transition can be constrained, second filter gain can be constrained, last results can be corrected too [14]. Constraint condition can be divided into equality and inequality constraint, linear and no linear constraint, hard constrain and relaxed constraint. Kalman filter with linear constraint is chose as a case for analyzing kinematic PPP mode with constraint condition [7, 14].

Linear constraint with parameters to be estimated can be expressed as:

$$D \times \overrightarrow{X} = m_k \tag{5}$$

where m is const, what should be care is that the coefficient matrix D can not be rank defect, in other words there can't exist redundancy condition in Eq. (5). For nonlinear constraint function, linearization is made as following:

$$g(x_k) = m_k \tag{6}$$

$$g(x_k^0) + g'(x_k^0)(x_k - x_k^0) \approx m_k \tag{7}$$

Assume GNSS receiver moves on a line, then constraint condition in each epoch is the same, but the constraint condition may different epoch from epoch in practice, and remember to make bijection between them. As the common line for example, if two point coordinates are known: (x_1, y_1, z_1), (x_2, y_2, z_2), the equation of a space line is as:

$$\frac{x - x_1}{x - x_2} = \frac{y - y_1}{y - y_2} = \frac{z - z_1}{z - z_2} \tag{8}$$

The formula is equal to the following:

$$\frac{z_2 - z_1}{x_2 - x_1} \times x - z = \frac{x_1 \times z_2 - x_2 \times z_1}{x_2 - x_1} \tag{9a}$$

$$\frac{z_2 - z_1}{y_2 - y_1} \times y - z = \frac{y_1 \times z_2 - y_2 \times z_1}{y_2 - y_1} \tag{9b}$$

The derivation of above equation for time is:

$$\frac{z_2 - z_1}{x_2 - x_1} \times v_X - v_Z = 0 \tag{10a}$$

$$\frac{z_2 - z_1}{y_2 - y_1} \times v_Y - v_Z = 0 \tag{10b}$$

Once more time for derivation about time is:

$$\frac{z_2 - z_1}{x_2 - x_1} \times a_X - a_Z = 0 \tag{11a}$$

$$\frac{z_2 - z_1}{y_2 - y_1} \times a_Y - a_Z = 0 \tag{11b}$$

The unknown for Kalman filter is as formula (1). According to formula (5), (9a, b), (10a, b), and (11a, b) the following constraint equation can be obtained:

$$\begin{bmatrix} \frac{z_2-z_1}{x_2-x_1} & 0 & -1 & 0 & 0 & 0 & 0 & 0 & 0 & 0 & 0 & 0_1 & \cdots & 0_m \\ 0 & \frac{z_2-z_1}{y_2-y_1} & -1 & 0 & 0 & 0 & 0 & 0 & 0 & 0 & 0 & 0_1 & \cdots & 0_m \\ 0 & 0 & 0 & \frac{z_2-z_1}{x_2-x_1} & 0 & -1 & 0 & 0 & 0 & 0 & 0 & 0_1 & \cdots & 0_m \\ 0 & 0 & 0 & 0 & \frac{z_2-z_1}{y_2-y_1} & -1 & 0 & 0 & 0 & 0 & 0 & 0_1 & \cdots & 0_m \\ 0 & 0 & 0 & 0 & 0 & 0 & \frac{z_2-z_1}{x_2-x_1} & 0 & -1 & 0 & 0 & 0_1 & \cdots & 0_m \\ 0 & 0 & 0 & 0 & 0 & 0 & 0 & \frac{z_2-z_1}{y_2-y_1} & -1 & 0 & 0 & 0_1 & \cdots & 0_m \end{bmatrix} \times \begin{bmatrix} X \\ Y \\ Z \\ v_X \\ v_Y \\ v_Z \\ a_X \\ a_Y \\ a_Z \\ d_t \\ Trp \\ N_1 \\ \vdots \\ N_m \end{bmatrix}$$

$$= \begin{bmatrix} \frac{x_1 \times z_2 - x_2 \times z_1}{x_2 - x_1} \\ \frac{y_1 \times z_2 - y_2 \times z_1}{y_2 - y_1} \\ 0 \\ 0 \\ 0 \\ 0 \end{bmatrix} \tag{12}$$

If constraint condition is more relaxed, and assume only the relation between X and Y exists, the corresponding condition equation can be got:

$$\begin{bmatrix} \frac{y_2-y_1}{x_2-x_1} & -1 & 0 & 0 & 0 & 0 & 0 & 0 & 0 & 0 & 0 & 0_1 & \ldots & 0_m \\ 0 & 0 & 0 & \frac{y_2-y_1}{x_2-x_1} & -1 & 0 & 0 & 0 & 0 & 0 & 0 & 0_1 & \ldots & 0_m \\ 0 & 0 & 0 & 0 & 0 & 0 & \frac{y_2-y_1}{x_2-x_1} & -1 & 0 & 0 & 0 & 0_1 & \ldots & 0_m \end{bmatrix} \times \begin{bmatrix} X \\ Y \\ Z \\ v_X \\ v_Y \\ v_Z \\ a_X \\ a_Y \\ a_Z \\ dt \\ Trp \\ N_1 \\ \vdots \\ N_m \end{bmatrix} = \begin{bmatrix} \frac{x_1 \times y_2 - x_2 \times y_1}{x_2 - x_1} \\ 0 \\ 0 \end{bmatrix} \tag{13}$$

If Kalman filter wants to satisfy formula (12) or (13), the following formula exists:

$$X_k^c = \min\left\{ \left(\overrightarrow{X} - X_k\right)^T W_k \left(\overrightarrow{X} - X_k\right) : D\overrightarrow{X} = m_k \right\} \tag{14}$$

In formula (14), W_k must be positive definite symmetrical weighted matrix, the optimal constraint estimation can be realized by Lagrange maximum likelihood estimation:

$$X_k^c = X_k - W_k^{-1} D_k^T \left(D_k W_k^{-1} D_k^T\right)^{-1} (D_k X_k - m_k) \tag{15}$$

For convenience we define $\gamma = W_k^{-1} D_k^T \left(D_k W_k^{-1} D_k^T\right)^{-1}$, formula (15) can be short as:

$$X_k^c = X_k - \gamma (D_k X_k - m_k) \tag{16}$$

For further exchange:

$$\begin{aligned} \overrightarrow{X} - X_k^c &= \overrightarrow{X} - X_k + \gamma \left(D_k X_k - m_k - \left(D_k \overrightarrow{X} - m_k\right)\right) \\ &= -(I - \gamma D_k)\left(X_k - \overrightarrow{X}\right) \end{aligned} \tag{17}$$

Then covariance after constrained changes to:

$$P_k^c = E[(\overrightarrow{X} - X_k^c)(\overrightarrow{X} - X_k^c)^T] = (I - \gamma D_k) P_k \tag{18}$$

Obviously, when $W_k^{-1} = P_k$, the gain covariance is the least, so from formula (16) and (18) the final results are:

$$X_k^c = X_k - P_k D_k^T \left(D_k P_k D_k^T\right)^{-1} (D_k X_k - m_k) \tag{19}$$

$$P_k^c = P_k - P_k D_k^T (D_k P_k D_k^T)^{-1} D_k P_k \tag{20}$$

The above two formulas are with respect to hard constrain, in order to change it to relaxed constrain, adjust formula (20) to:

$$P_k^c = P_k - P_k D_k^T \left(D_k P_k D_k^T + R_c\right)^{-1} D_k P_k \tag{21}$$

The R_c is as noise matrix of constraint equation, which can be determined according to allowable error range of constraint conditions

3 Test Result and Analysis

3.1 Experiment Strategy

Experiment was done on the roof of one university, the instrument type is UniStrong E660, which can receive L1, L2, C1 and P2 signals. From 22nd Mar to

25th Mar in 2013, about half an hour kinematic observation was collected everyday, the sample interval is 30 s. For the reason that the antenna phase center offset and variety is unknown, so this error was not corrected during PPP, all the left error corrections were referenced the standard PPP mode [15]; Turboedit algorithm was selected during data reprocessing, and the cycle slip was only detected but not repaired [16]; Parameter estimation process adopts Kalman filter mode with forward smooth [17, 18]. The calculation datum is IGS final precise ephemeris and 30 s interval satellite clock error.

Before the test, a rigid chute was made by ourselves, and fixed on the roof. (Fig. 1) A receiver with rope can only slide along the chute's groove when the rope was promoted. On 22nd Mar receiver 024 J kept observing for 5 h in static mode and was shutdown, the position of this point was selected as one known point, then this receiver was restarted to move, nearby there were two receiver named 014 J and 018 J to keep observing during the process. On 23rd 024 J was placed on the another place of the chute and kept observing for 4 h then was shutdown, this position was selected as the second known point, the same 024 J was powered on to move for about half an hour. After two sessions' static observing on the chute on 22nd and 23rd Mar the line equation of receiver motion can be determined, the movement speed of moving receivers was random. On 24th and 25th the receiver was promoted on the chute for half an hour. During the whole experiment, for the limited number of receiver, there is no time overlapping among the rover station, base station and known point observation, the rover station is only a few meters from base station, this allows the LGO (Leica Geo Office) to successfully solve the short baseline to validate our algorithm, the base station 014 and 018 J coordinates in LGO solution was computed by static PPP. Both kinematic and static PPP solutions are finished by our software PLAOD.

$$R_C = \begin{bmatrix} 0.1^2 & 0 & 0 & 0 & 0 & 0 \\ 0 & 0.1^2 & 0 & 0 & 0 & 0 \\ 0 & 0 & 0.06^2 & 0 & 0 & 0 \\ 0 & 0 & 0 & 0.06^2 & 0 & 0 \\ 0 & 0 & 0 & 0 & 0.03^2 & 0 \\ 0 & 0 & 0 & 0 & 0 & 0.03^2 \end{bmatrix} \tag{22}$$

Fig. 1 Test platform

When added line constraint to the filter, the constraint equation noise matrix was set as formula (22), where the prior sigma of position, velocity, and acceleration was established as 0.1 m, 0.06 m/s and 0.03 m/s^2.

3.2 Line Constraint Results

Coordinates of known point 1 and known point 2 were used to determine the line equation, this line constraint was added to the kinematic PPP for solution, at the same time the traditional kinematic PPP result was obtained, besides, LGO solution result can be obtained. Without the base station on 25th, corresponding result can only compare with line constraint result, as can be seen from Fig. 2, where as "free" means traditional kinematic PPP solution, "constrain" means constraint solution, it is obvious that the result after constraint is located on the line of two known point. With regard to 22nd–24th Mar, their results before and after constrained and LGO solution are compared, taking the 22nd result as example shown in Fig. 3, it is easy to see that LGO solution result shows high coincidence with constraint result. From

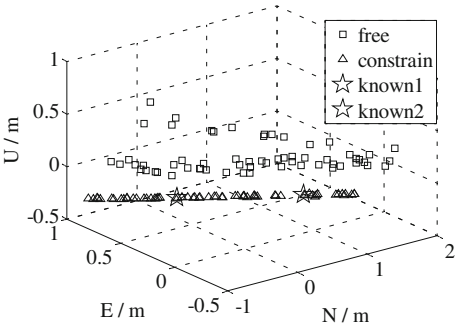

Fig. 2 Results before and after constrained on 25th Mar

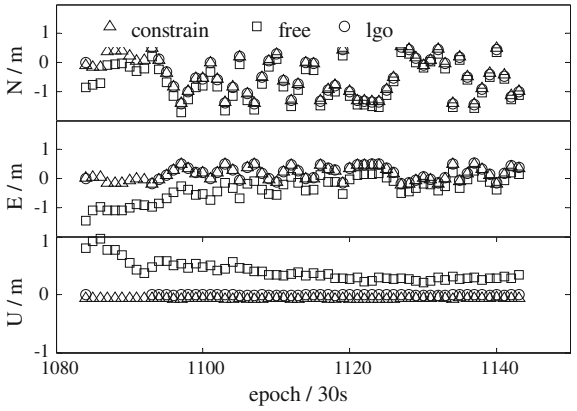

Fig. 3 Results before and after constrained on 22nd Mar

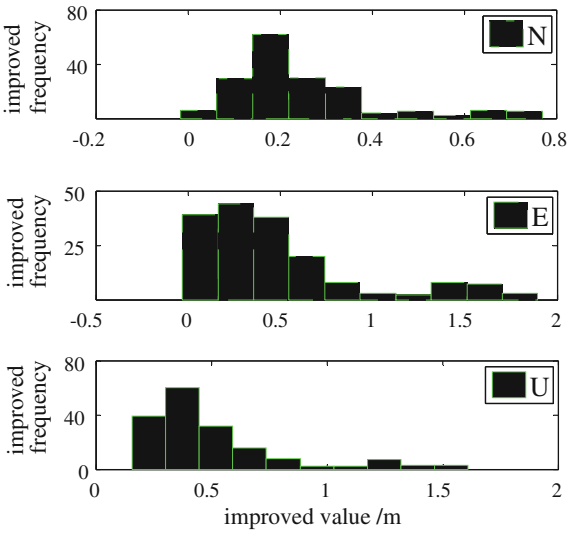

Fig. 4 Improvement statistics of north, east, up compoment

Table 1 RMS before and after constrain

Doy	Free (m)			Constrain (m)		
	N	E	U	N	E	U
22nd	0.238	0.522	0.385	0.025	0.015	0.058
23rd	0.425	0.822	0.868	0.062	0.025	0.052
24th	0.258	0.539	0.523	0.053	0.022	0.059

this picture, we can obtain that the North component's accuracy is the highest in traditional kinematic PPP, then the East direction, the worst is Up component, but constraint condition may change this situation, the detailed improvement can be expressed by Fig. 4, and the root mean square (RMS) is shown as Table 1, from this table we know that all components' accuracy is raised to a few centimeters.

3.3 Partial Constraint Results

For further relaxing the constraint, assume that prior information is only between *X* and *Y* or between *X* and *Z*, which may be happening for plane motion, take 22nd Mar as an example, the results are shown as Figs. 5 and 6, where as "*c*0" is equal to the former line constrain, "*c*1" represents partial constrain, in other words *X*-*Y* constrain or *X*-*Z* constrain, "lgo" and "free" are the same as before, from the two pictures, it can be concluded that this partial constraint can improve the final result at a certain extent, the most effective improvement is the Up compoment which reaches a few centimeters. Besides, corresponding results of zenith total delay (ZTD) were shown in Figs. 7 and 8, obviously, the partial constraint results tend to

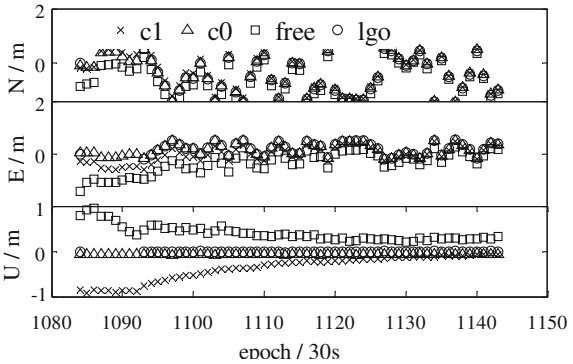

Fig. 5 Results after *X-Y* constraint and comparison

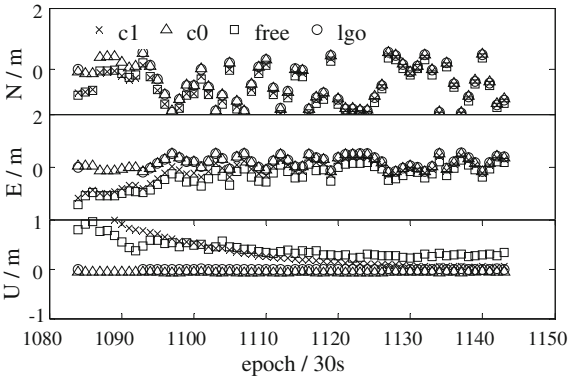

Fig. 6 Results after *X-Z* constraint and comparison

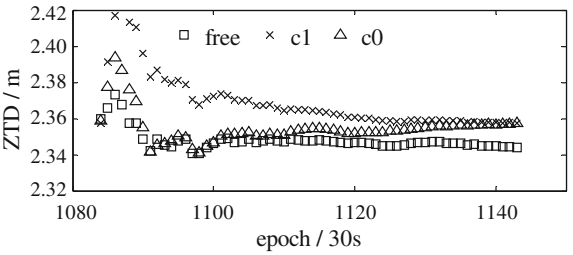

Fig. 7 ZTD before and after *X-Y* constrain

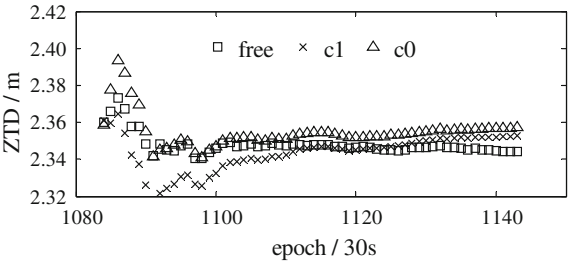

Fig. 8 ZTD before and after *X-Z* constrain

line constraint result, in fact, the line constraint ZTD result is more coincide with static ZTD result despite the static ZTD is not divergent in this time series, ZTD with constraint PPP can be improved at least 6 mm.

4 Conclusion

With respect to the limitation of current kinematic PPP, known information in the observing process was used for purposed algorithm of kinematic PPP with constraint condition. The algorithm was applied to kinematic data with line constrain and partial constraint, results shows that line constraint can improve the traditional kinematic PPP to 7 cm level accuracy, improve the accuracy of East and Up components more effective, and the initialization process is very fast. Partial constraint is also useful for North, East and Up component accuracy improvement, but the Up is most effective, then the East is followed. Data analysis shows that after long time observing the horizontal accuracy especially North component is comparable with traditional mode's result despite constraint is added, but Up component can be improved with several centimeters even 1–2 dm. In fact, what unavoidable is that the accuracy and strength of constraint condition may seriously affect the final result, it is strongly suggested that if accuracy of prior information is higher than 1 dm you would better add this constraint, and your result will be largely improved especially in difficult observation environment. Furthermore, the ZTD's accuracy can be improved at least 6 mm whether line constraint or partial constraint is adopted.

The centimeter level accuracy of the experiment illustrate that kinematic PPP mode with constraint condition has a great application prospect in practice. Some research has shown that train's trail information was used as constraint condition to improve the pseudorange positioning accuracy on the train [19, 20], if the curve measurement information for railway construction is added to kinematic PPP mode the positioning accuracy may further largely improved.

Acknowledgements We thank Professor Dan Simon for his useful suggestions and the support of the Natural Science Foundation of China (Project Number: 41274044, 41374032, 41504021) are gratefully acknowledged. The science and technology project of Sichuan Province (Project Number: 2015JQ0046) also provided lot of support to this research.

References

1. Zumberge JF, Heflin MB, Jefferson DC et al (1997) Precise point processing for the efficient and robust analysis of GPS data from large networks. J Geophys Res 102(B3):5005–5017
2. Kouba J, Héroux P (2001) Precise point positioning using IGS orbit and clock products. GPS Solutions 5(2):12–28

3. Martín A, Anquela AB, Berné JL et al (2012) Kinematic GNSS-PPP results from various software packages and raw data configurations. Sci Res Essays 7(3):419–431
4. Simon D, Chia TL (2002) Kalman filtering with state equality constraints. IEEE Trans Aerosp Electron Syst 38(1)
5. Guo F, Zhang X (2015) Performance enhancement for GPSpositioning using constrained Kalman filter. Meas Sci Technol 26:1–9
6. Tahk M, Speyer JL (1990) Target tracking problems subject to kinematic constraints. IEEE Trans Autom Control 35(3):324–326
7. Alouani AT, Blair WD (1993) Use of a kinematic constraint in tracking constant speed, maneuvering targets. IEEE Trans Autom Control 38(7):1107–1111
8. Li Z, Gao J, Wang J et al PPP/INS tightly coupled navigation using adaptive federated filter. GPS Solutions (published online)
9. Zhu J, Xie J, Chen Y (2011) Analysis of inequality constrains influence to adjustment results. Acta Geodaetica Cartogr Sin 40(1):411–415
10. Welch G, Bishop G (2001) An introduction to the Kalman filter. Course 8, SIGGRAPH
11. Xu S, Xiong Y, Zhou G et al (2016) Kinematic zenith total delay obtained by un-difference car-born GPS. J Geodesy Geodyn Chin 36(1):45–49
12. Kouba J (2009) A guide to using international GNSS service (IGS) products [EB/OL]. IGS Doc
13. Yang Y, Gao W, Zhang X (2010) Robust Kalman filtering with constraints: a case study for integrated navigation. J Geodesy 84(6):373–381
14. Gupta N, Asok A, Doran B, Arroyo A, Markarian R (2009) Mathematically equivalent approaches for equality constrained Kalman filtering [J/OL]. Arxiv preprint arXiv: 0902. 1565
15. Kouba J (2009) A guide to using international GNSS service (IGS) products. IGS Doc
16. Blewitt G (1990) An automatic editing algorithm for GPS data. Geophys Res Lett 17(3):199–202
17. Witchayangkoon B (2000) Elements of GPS precise point positioning. Ph.D thesis of University of Maine, Maine
18. Abdel-salam M (2005) Precise point positioning using un-differenced code and carrier phase observation. Ph.D thesis of University of Calgary
19. Wang J, Liu J, Wei S et al (2010) Switch curve information based train positioning method. J Transp Syst Eng Inf Technol 10(2):64–69
20. Liu J, Cai B, Wang J (2014) A BDS-based train positioning method considering track characteristics. J Transp Syst Eng Inf Technol 14(5):43–48

Instantaneous and Controllable Ambiguity Resolution Based on Linear Integer Aperture Estimator: Principle and Application

Jingyu Zhang, Meiping Wu and Tao Li

Abstract Ambiguity resolution is of importance in precise GNSS application and ambiguity validation is one of critical steps. It is usually realized by the so-called integer aperture (IA) estimator. Though ratio test based on look-up table satisfies the instantaneous and controllable application, its effectiveness in practice is not sufficiently verified and comparison with other IA estimators is not enough. Besides, there is no evaluation standard for the quality of look-up table. In this contribution, we will propose a modified instantaneous and controllable (iCON) method which can apply linear IA estimators to instantaneous applications. This method is easy to be implemented and can realize the instantaneous control to failure rates. In order to verify the effectiveness of this method, simulation experiments are implemented to test the performances of four linear IA estimators. Furthermore, this method is applied into GNSS compass application. Simulation and field test results show that the linear IA estimation based on this method can realize the quality control of ambiguity resolution, and the precision of GNSS compass can be better than integer estimation. In the field test, linear IA estimators have similar, or a little better, performance as ratio test in the precision of GNSS compass. All results prove the effectiveness of linear IA estimation in the quality control of ambiguity resolution for the first time and provide the guidelines for the usage of IA estimators.

Keywords Ambiguity resolution · Integer aperture estimator · Quality control · Fixed failure rate approach · GNSS compass

J. Zhang (✉) · M. Wu · T. Li
National University of Defense Technology, Changsha, China
e-mail: zjy8712@126.com

© Springer Science+Business Media Singapore 2016

J. Sun et al. (eds.), *China Satellite Navigation Conference (CSNC) 2016 Proceedings: Volume III*, Lecture Notes in Electrical Engineering 390,
DOI 10.1007/978-981-10-0940-2_48

1 Introduction

As the prosperity of GNSS systems, precise GNSS applications such as precise positioning or attitude determination have begun to widely spread. In order to quickly achieve centimeter or millimeter precision, ambiguity resolution is the fundamental problem.

Commonly, the procedures of ambiguity resolution can be divided into four steps. In the first step, the integer constraint of ambiguity is disregarded and float solutions are estimated. The float solutions and their variance-covariance (vc) matrix are given as $\begin{bmatrix} \hat{a} \\ \hat{b} \end{bmatrix}$ and $\begin{bmatrix} Q_{\hat{a}\hat{a}} & Q_{\hat{a}\hat{b}} \\ Q_{\hat{b}\hat{a}} & Q_{\hat{b}\hat{b}} \end{bmatrix}$. Part of quality control can be implemented here to detect and adapt outliers. The second step takes into the integer constraint and realizes the integer estimation. The integer estimation can be realized by various estimators. Integer least-square (ILS) [1] is the most widely used one. In order to improve its efficiency, least-square ambiguity decorrelation adjustment (LAMBDA) [2, 3] is often implemented. After integer estimation, ambiguity validation is usually implemented, which can be realized by various acceptance tests. Here the combination of integer estimation and validation is the so-called IA estimation [4], which provides the theoretical foundation of ambiguity validation. After these steps, if ambiguities are correctly fixed, users can take advantage of the precise range data.

Due to the importance of ambiguity quality control, IA estimation has attracted many researchers for more than 10 years [5, 6]. Many IA estimators and their performance have been studied and compared. Some of them have been applied into research. The most representative one is ratio test IA (RTIA) estimator. Based on the created look-up table [7], RTIA can realize instantaneous and controllable ambiguity resolution. However, since the creation of look-up table relies on numerous GNSS samples and Monte Carlo simulation, it is very inefficient. Besides this, according to the creating step of look-up table or fitting function [8], many artificial measures have to be taken to obtain suitable results which are applicable to most GNSS cases. Hence, how to evaluate the quality of different look-up tables also needs to be taken into consideration. In order to tackle these problems, this contribution will propose a modified instantaneous and CONtrollable (iCON) ambiguity resolution approach based on linear IA estimators. This approach can calculate the required critical value for each GNSS model, and it is quick and easy to be implemented. Linear IA estimators which share certain properties can be used based on this approach.

2 Integer Aperture Estimator

2.1 Integer Aperture Pull-in Region

Since integer estimators are the subsets of IA estimators, all properties of integer estimators can be derived from IA estimation. The function of IA estimator is to

give users the control over integer estimation. The definition of IA pull-in region is given as [9].

Definition 1 Let $\Omega \subset \mathbb{R}^n$ and $\Omega_z \subset \Omega$, then the estimator $\breve{a}_{IA} = \begin{cases} z & \text{if } \hat{a} \in \Omega_z \\ \hat{a} & \text{if } \hat{a} \notin \Omega_z \end{cases}$ is an IA estimator only if its aperture pull-in regions satisfy the following requirements

$$\begin{aligned} &(1) \underset{z\in\mathbb{Z}^n}{\cup} \Omega_z = \Omega \subset \mathbb{R}^n \\ &(2) \operatorname{Int}(\Omega_u) \cap \operatorname{Int}(\Omega_v) = \emptyset, u \neq v \\ &(3) \Omega_z = z + \Omega_0, z \in \mathbb{Z}^n \end{aligned}$$

when $\Omega = \mathbb{R}^n$ in condition (1), then IA estimator will be transformed into integer estimator and $\Omega_z = S_z$ with S_z the pull-in region of integer estimator. Condition (3) indicates the translational invariant requirement, and condition (2) clarifies that there is no overlapping between different regions.

The connection between IA estimator and integer estimator relies on acceptance tests. The general form of acceptance test is summarized as [10]

$$\gamma(x) \leq \mu \tag{1}$$

where $\gamma(\cdot)$ is the testing function and μ its critical value. The IA estimator based on $\gamma(\cdot)$ is written as

$$\Omega_z = \{x \in \mathbb{R}^n, z \in \mathbb{Z}^n | x \in S_z, \gamma(x) \leq \mu\} \tag{2}$$

where $\Omega_z \subset S_z$. In practice, the integer estimation is realized by searching which satisfies

$$S_z = \underset{c\in\mathbb{Z}^n}{\cap} \left\{ x \in \mathbb{R}^n, z \in \mathbb{Z}^n \middle| \left| c^T Q_{\hat{a}\hat{a}}^{-1}(x - z) \right| \leq \frac{\|c\|^2_{Q_{\hat{a}\hat{a}}}}{2} \right\} \tag{3}$$

where $c = \breve{z}_2 - z$. z is the best integer candidate, and $\breve{z}_2$ the second best integer candidate. It can be proved that, the $|\cdot|$ can be deleted based on the relation between integer candidates and float solutions. Then we can derive a uniform formula for IA estimation, which is given as

$$\Omega_z = \underset{c\in\mathbb{Z}^n}{\cap} \left\{ x \in \mathbb{R}^n, z \in \mathbb{Z}^n | c^T Q_{\hat{a}\hat{a}}^{-1}(x - z) \leq \frac{\|c\|^2_{Q_{\hat{a}\hat{a}}}}{2}, \gamma(x) \leq \mu \right\} \tag{4}$$

Actually, the formula of Ω_z can be further simplified if $\gamma(x) \leq \mu$ is the subset of $c^T Q_{\hat{a}\hat{a}}^{-1}(x - z) \leq \frac{\|c\|^2_{Q_{\hat{a}\hat{a}}}}{2}$, which will be presented based on specific acceptance test. Note that the simplified transformation of Ω_z in the following subsections is

equivalent to testing function of (1). Hence, the geometry reconstruction of IA pull-in region can be realized by different methods.

2.2 Linear IA (LIA) Estimators

In the analysis to difference test IA (DTIA) estimator [12], we first see that IA estimator can be derived by scaling to integer estimator. The scaling direction is from the second best integer candidate to the best integer candidate. According to the scaling methods, we can classify the IA estimators into LIA estimators and nonlinear IA estimators. LIA estimators can be defined as the IA estimator which has the constant scaling factor in each direction. As contrast, the scaling factor of nonlinear IA estimators depends on the float ambiguities and is varying even at the same scaling direction. Note that ILS can be seen as one special kind of IA estimator, which can be derived from linear and nonlinear IA estimator. In this contribution, we will mainly study the properties of LIA estimators.

2.2.1 DTIA

DTIA was first proposed in [12]. As analyzed in [11], DTIA can be derived by linear scaling to integer estimator. Its original expression is given as

$$R_2 - R_1 \geq \mu_{\mathrm{DT}} \tag{5}$$

with $R_i = \left\|x - \breve{z}_i\right\|^2_{Q_{\hat{a}\hat{a}}}$. Its pull-in region and relation with ILS can be written as

$$\begin{aligned} \Omega_{0,\mathrm{DTIA}} &= \bigcap_{c\in\mathbb{Z}^n/\{0\}} \left\{ x \in \mathbb{R}^n \middle| \frac{\|c\|^2_{Q_{\hat{z}\hat{z}}} c^T Q^{-1}_{\hat{z}\hat{z}} x}{\|c\|^2_{Q_{\hat{z}\hat{z}}} - \mu_{\mathrm{DT}}} \leq \frac{\|c\|^2_{Q_{\hat{z}\hat{z}}}}{2} \right\} \\ &= \bigcup_{c\in\mathbb{Z}^n/\{0\}} T_{\mathrm{DT}}(c) S_{0,\mathrm{IALS}}(c) \end{aligned} \tag{6}$$

with $T_{\mathrm{DT}}(c) = \frac{\|c\|^2_{Q_{\hat{z}\hat{z}}} - \mu_{\mathrm{DT}}}{\|c\|^2_{Q_{\hat{z}\hat{z}}}}$. Note that the IA estimator is realized in decorrelated space so that its performance or success rate can be maximized. Here the decorrelated GNSS model is denoted with $Q_{\hat{z}\hat{z}}$. $T_{\mathrm{DT}}(c)$ is the scaling factor whose value may be changing with the second best integer candidate. DTIA has a distinct performance among IA estimators, since it can be seen as the approximation of optimal IA estimator with strong GNSS models [13].

In order to demonstrate the characteristics of LIA estimator, the geometry reconstruction of DTIA is presented in Fig. 1. According to this figure, we can see that ILS is constructed by different regions, and each region corresponds to a unique

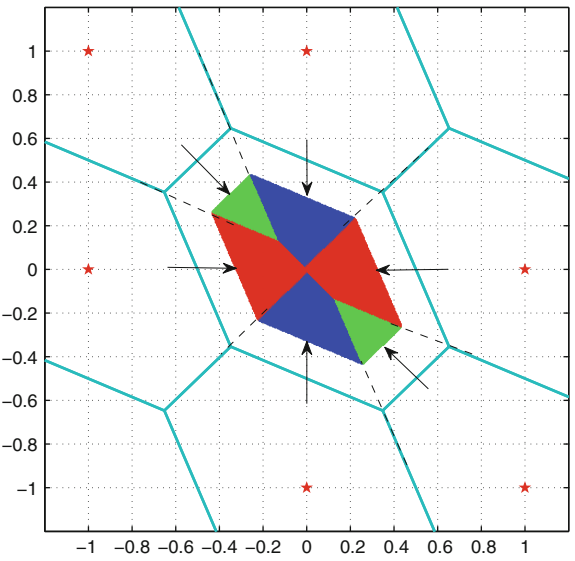

Fig. 1 Geometry reconstruction of DTIA. The *arrows* denote the scaling directions from the second best integer candidates to the best candidate. *Red stars* are the second best integer candidates. *Green*, *blue* and *red* regions denote three kinds of aperture pull-in regions with different scaling factors

integer candidate. The aperture pull-in region of DTIA is constructed by scaling the ILS pull-in region from the directions of second best integer candidates to the best candidate.

2.2.2 Integer Aperture Least-Square (IALS)

IALS is first defined in [14]. Obviously, the original definition of IALS is different from other acceptance tests. However, according to the definition of its pull-in region, we still can derive similar testing formula for IALS. Its pull-in region can be written as

$$\Omega_{0,\mathrm{IALS}} = \bigcap_{c\in\mathbb{Z}^n/\{0\}} \left\{ x\in\mathbb{R}^n \middle| \frac{c^T Q_{\hat{z}\hat{z}}^{-1} x}{\mu_{\mathrm{IALS}}} \le \frac{\|c\|^2_{Q_{\hat{z}\hat{z}}}}{2} \right\} = \bigcup_{c\in\mathbb{Z}^n/\{0\}} T_{\mathrm{IALS}} S_{0,\mathrm{IALS}}(c) \qquad (7)$$

with $T_{\mathrm{IALS}} = \mu_{\mathrm{IALS}}$. The advantage of IALS is that it is easy to be connected with ILS. It has the same scaling factor for each direction, whose value is $\mu_{\mathrm{IALS}} (0 < \mu_{\mathrm{IALS}} \le 1)$. According to the relation of scaling factors, IALS can be seen as one special case of DTIA, and DTIA can be regarded as the generalized IALS.

Note that in [6], the procedures to implement IALS is given, which is complicate and time-consuming. Besides this, it is essentially not rigorous, since it only considers the adjacent integer candidates for the pull-in region of the best integer candidate. The correct testing formula can be directly derived from its pull-in region, which is written as

$$\frac{2(\breve{z}_2-\breve{z}_1)^T Q_{\hat{z}\hat{z}}^{-1}(x-\breve{z}_1)}{\|c\|_{Q_{\hat{z}\hat{z}}}^2} \le \mu_{\mathrm{IALS}} \tag{8}$$

with $\breve{z}_1$ and $\breve{z}_2$ the best and second best integer candidates.

2.2.3 W-Test IA (WTIA)

WTIA is proposed by Wang et al. [15]. Though in [5] WTIA is summarized as one kind of projector tests, it has obvious difference with the other one. The original expression of WT is given as

$$\frac{R_2-R_1}{2\left\|\breve{z}_2-\breve{z}_1\right\|_{Q_{\hat{z}\hat{z}}}} \ge \mu_{\mathrm{WT}} \tag{9}$$

Note that in decorrelated space, $\breve{z}_2$ is the adjacent or closest integer candidates to the best integer candidate. Hence, its pull-in region can be rearranged as

$$\begin{aligned}\boldsymbol{\Omega}_{0,\mathrm{WTIA}} &= \bigcap_{c\in\mathbb{Z}^n/\{0\}} \left\{ x\in\mathbb{R}^n \middle| \frac{\|c\|_{Q_{\hat{z}\hat{z}}}^2 c^T Q_{\hat{z}\hat{z}}^{-1} x}{\|c\|_{Q_{\hat{z}\hat{z}}}^2 - \mu_{\mathrm{WT}}\|c\|_{Q_{\hat{z}\hat{z}}}} \le \frac{\|c\|_{Q_{\hat{z}\hat{z}}}^2}{2} \right\} \\ &= \bigcup_{c\in\mathbb{Z}^n/\{0\}} T_{\mathrm{WTIA}}(c) S_{0,\mathrm{IALS}}(c)\end{aligned} \tag{10}$$

with $T_{\mathrm{WTIA}}(c) = \frac{\|c\|_{Q_{\hat{z}\hat{z}}}^2 - \mu_{\mathrm{WT}}\|c\|_{Q_{\hat{z}\hat{z}}}}{\|c\|_{Q_{\hat{z}\hat{z}}}^2}$. Notice that in (10), there exist obvious similarities between DTIA and WTIA. When $\mu_{\mathrm{WT}}\|c\|_{Q_{\hat{z}\hat{z}}} = \mu_{\mathrm{DT}}$, WTIA will be equivalent to DTIA. However, due to the variation of c, it is difficult to satisfy this condition. Hence, WTIA may have similar performance as DTIA, but not the same.

2.2.4 Projector Test IA (PTIA) and Improvement

PTIA is proposed in [16]. However, the research about PTIA is not so much. Part of reason is due to its testing method. Actually, in decorrelated space, the testing of PTIA can be simplified as

$$c^T Q_{\hat{z}\hat{z}}^{-1}(x-\breve{z}_1) \le \mu_{\mathrm{PT}}\|c\|_{Q_{\hat{z}\hat{z}}} \tag{11}$$

with $c = \breve{z}_2 - \breve{z}_1$. Here we analyze the testing formula of PTIA. At the left side of (11), it can be seen as the projection of $x - \breve{z}_1$ on c with the metric of $Q_{\hat{z}\hat{z}}$. The left side of (11) can be taken as the weighted projection of $x - \breve{z}_1$ on c. However, the right side of (11) is the weighted norm of which means the comparison of two sides

is not balanced. The comparison in (11) tends to be conservative especially when $\|c\|_{Q_{\hat{z}\hat{z}}} > 1$. This means PTIA is not suitable to strong GNSS model if $\|c\|_{Q_{\hat{z}\hat{z}}} > 1$ at that time. In order to improve the performance of PTIA, we change (11) into

$$c^T Q_{\hat{z}\hat{z}}^{-1}(x - \breve{z}_1) \le \mu_{\mathrm{MP}} \|c\|^2_{Q_{\hat{z}\hat{z}}} \tag{12}$$

According to this modified PTIA (MPTIA), its pull-in region can be written as

$$\begin{aligned} \Omega_{0,\mathrm{MPTIA}} &= \bigcap_{c\in\mathbb{Z}^n/\{0\}} \left\{ x \in \mathbb{R}^n \middle| \frac{c^T Q_{\hat{z}\hat{z}}^{-1} x}{2\mu_{\mathrm{MP}}} \le \frac{\|c\|^2_{Q_{\hat{z}\hat{z}}}}{2} \right\} \\ &= \bigcup_{c\in\mathbb{Z}^n/\{0\}} T_{\mathrm{MP}} S_{0,\mathrm{IALS}}(c) \end{aligned} \tag{13}$$

with $T_{\mathrm{MP}} = 2\mu_{\mathrm{MP}}$. It is obvious that this modified PTIA is equivalent to IALS when $\mu_{\mathrm{IALS}} = 2\mu_{\mathrm{MPTIA}}$. This condition is easy to be satisfied. Hence MPTIA is mathematically equivalent to IALS.

2.3 Probability Evaluations of LIA Estimators

In Sect. 2.1, the LIA estimators are summarized into the union of aperture pull-in regions with constant scaling factors independent of float ambiguities. Actually, their probability evaluations also have uniform expressions.

Before we derive the uniform formulas, we first give the definition of LIA bootstrapping (IAB) [17] estimator. They are necessary to approximate the probability evaluations of previous IA estimators.

Definition 2 The pull-in region of linear IAB estimator (LIAB) is defined as

$$\begin{aligned} \Omega_{z,\mathrm{LIAB}} &= \bigcap_{i=1}^{n} \left\{ x \in \mathbb{R}^n \middle| \frac{c_i^T L^{-1}(x - z)}{T_{\mathrm{LIAB}}(c_i)} \le \frac{1}{2} \right\} \\ &= \bigcup_{i=1}^{n} T_{\mathrm{LIAB}}(c_i) S_{0,\mathrm{IB}}(c_i) \end{aligned} \tag{14}$$

with $c_i = \breve{z}_2 - z$ and

$$\begin{cases} T_{\mathrm{LIAB}}(c_i) S_{z,\mathrm{IB}}(c_i + z) = \left\{ x \in \mathbb{R}^n \middle| \frac{x-z}{T_{\mathrm{LIAB}}(c_i)} \in S_{0,\mathrm{IB}}(c_i) \right\} \\ S_{0,\mathrm{IB}} = \bigcup_{i=1}^{n} S_{0,\mathrm{IB}}(c_i) \\ S_{0,\mathrm{IB}} = \bigcap_{i=1}^{n} \left\{ x \in \mathbb{R}^n \middle| c_i^T L^{-1} x \le \frac{1}{2} \right\} \end{cases}$$

where c_i is the canonical vector on the ith coordinate axis. L is the uniquely lower triangular matrix of the decomposition $Q_{\hat{z}\hat{z}} = L^T \mathrm{DL}$. $S_{0,\mathrm{IB}}(c_i)$ and $S_{z,\mathrm{IB}}(c_i + z)$ are parts of IB pull-in region whose second best integer candidate are c_i and $c_i + z$, respectively.

Based on this definition, it is easy to derive a uniform formula for the LIAB probability evaluations. The analytical formulas are given as

$$\begin{cases} P_{s,\mathrm{LIAB}} = \prod_{i=1}^{n} \left(2\Phi(\frac{|x_i|_{\mathrm{LIAB}}}{\sigma_{z_i|I}}) - 1 \right) \\ P_{f,\mathrm{LIAB}}(k) = \prod_{i=1}^{n} \left(\Phi(\frac{z_i(k) + |x_i|_{\mathrm{LIAB}}}{\sigma_{z_i|I}}) - \Phi(\frac{z_i(k) - |x_i|_{\mathrm{LIAB}}}{\sigma_{z_i|I}}) \right) \\ P_{f,\mathrm{LIAB}} = \sum_{k=1}^{\infty} P_{f,\mathrm{LIAB}}(k) \end{cases} \tag{15}$$

with $z(k) = (z_1(k), \ldots, z_n(k))^T$ the kth integer ambiguity candidate. $\sigma_{z_i|I}$ is the ith element of LDL-decomposition of decorrelated matrix $Q_{\hat{z}\hat{z}}$. Different LIAB can be discriminated by $|x_i|_{\mathrm{LIAB}}$ which means the absolute intersecting points between original aperture pull-in region and coordinates. Here we list the expressions of $|x_i|_{\mathrm{LIAB}}$ for the derived IAB of previously mentioned IA estimators

$$\begin{cases} |x_i|_{\mathrm{IAB}} = \frac{\mu_{\mathrm{IAB}}}{2} \\ |x_i|_{\mathrm{DTIAB}} = \frac{\|c\|^2_{Q_{\hat{z}\hat{z}}} - \mu_{DT}}{\|c\|^2_{Q_{\hat{z}\hat{z}}}} \\ |x_i|_{\mathrm{WTIAB}} = \frac{\|c\|^2_{Q_{\hat{z}\hat{z}}} - \mu_{\mathrm{WT}} \|c\|_{Q_{\hat{z}\hat{z}}}}{\|c\|^2_{Q_{\hat{z}\hat{z}}}} \end{cases} \tag{16}$$

MPTIA is equivalent to IAB and $|x_i|_{\mathrm{MPTIAB}} = \mu_{\mathrm{MPTIAB}}$. In decorrelated space, the performance of IAB will approach to that of IA. Hence, we can directly use IAB to approximate IA estimators. When $|x_i|_{\mathrm{LIAB}} = 1$, LIAB can be seen as the decorrelated ILS estimator. Then $P_{s,\mathrm{LIAB}} = P_{s,\mathrm{ILS}}$ and $P_{f,\mathrm{LIAB}} = P_{f,\mathrm{ILS}}$.

3 Instantaneous and Controllable Ambiguity Resolution Method

In order to do the quality control of ambiguity resolution, fixed failure rate approach has been proposed and initially applied. Without consideration of time cost, fixed failure rate approach is the most suitable one. The advantage of fixed failure rate approach lies on that it is general, and can be applied to any IA estimator. Its controllability is determined by the number of simulation samples. More the samples, stronger the controllability of IA will be. However, since fixed failure rate approach relies on Monte Carlo sampling, it is impossible to realize instantaneous application. In order to solve this problem, several alternative approaches have been

proposed by researchers, such as look-up table, fitting functions [18]. Though these methods are feasible, they have to rely on numerous GNSS samples to represent the characteristics of critical values, and then summarize them into the look-up table or fitting functions. Besides this, how to create a specific look-up table or choose which kind of fitting function has to be artificially determined for each acceptance test.

Due to these shortcomings, the iCON approach based on GNSS model was first proposed in [19] and analyzed in [20]. Though it is effective, it can be further simplified and modified. Here we mainly introduce a new version, which can be used by previous linear IA estimators.

3.1 The Simplified and Modified iCON Approach

The procedures of the simplified iCON approach are listed below:

1. Set initial values for P_f, P_μ, μ_0 and other parameters. Calculate probability mass function (PMF) for M aperture pull-in regions. Then sort these PMF into descending order, and choose m so that

$$P_{f,\mathrm{ILS}}(m) > P_\mu, P_{f,\mathrm{ILS}}(m+1) \le P_\mu$$

2. Construct the nonlinear equation and implement numerical optimization t

$$\sum_{i=1}^{m} P_{f,\mathrm{LIAB}}(i,\mu) = \kappa P_f, \kappa < 1$$

Here we give two remarks to this simplified iCON approach:

1. The computations of ILS failure rates and LIAB failure rates are based on (15) in decorrelated space;
2. P_μ is the critical element to control the time cost of Step 2. Since the LIA estimators are approximated by their lower bounds, LIAB estimators, κ is introduced to compensate the approximation errors;
3. The setting of M correlates with the strength of GNSS model. The stronger of GNSS model, the smaller M will be. However, since the order of PMF is not monotonous, we usually choose an empirical value for various situations;
4. The numerical condition to apply this modified iCON approach requires that the choice of P_μ may have to balance the time cost and approximation errors in Step 2.

As the modified version of iCON approach, it still inherits the advantages of iCON. First, it is instantaneous. The only time-consuming part is the numerical optimization in Step 2. In order to further shorten the time cost, some extra measures can be taken, such as choosing suitable M and P_μ or designing better numerical optimization method; Second, the critical value obtained by this approach realize the

quality control to the failure rate of ambiguity resolution. Though there exist approximation errors in Step 2, a small choice of P_μ can limit the errors so that it can be neglected; Third, the time cost of iCON approach based on DTIA satisfies the instantaneous requirement in ambiguity resolution of low frequency.

3.2 Comparison of LIA Estimator Based on Fixed Failure Rate Approach

Based on this simplified iCON approach, previously mentioned LIA estimators can realize instantaneous and controllable ambiguity resolution. However, due to the differences in IA estimators, they may have different performances. Here we make comparison between these LIA estimators by simulation experiment. The simulation setting is detailed listed in Table 1. Note that in the simulation experiment, only the GNSS models whose success rates are larger than 0.8 will be used, since weak GNSS models are difficult realize reliable ambiguity resolution. 100,000 samples will be generated for each GNSS model.

First, we will verify the effectiveness of the probability evaluation formulas based on Monte Carlo simulation. Since the probability evaluations include success rate and failure rate, we will compare the fix rate computed by approximation formulas with that computed by simulation. Note that $P_{\text{fix}} = P_{s,\text{LIA}} + P_{f,\text{LIA}}$ with P_{fix} the fix rate. Table 2 summarizes the statistics in different cases to compare the performances of all estimators.

According to Table 2, it is obvious that DTIA has the smallest approximation errors among the LIA estimators. IALS and MPTIA have the same statistics in approximation errors. When the fixed failure rate becomes larger or GNSS model becomes stronger, the approximation errors will decrease. When $P_f = 0.01$, all IA estimators have almost the same approximation errors. Though there are approximation errors, most of these errors are contributed by success rates approximation, and the approximated failure rates are very small which can be controlled within acceptable range by the iCON approach.

Table 1 Simulation settings for the comparison of LIA estimators

Items	Settings
GNSS systems	GPS, BeiDou, Galileo and all combinations
Time range	July 15, 2014
Frequencies	L1, L2, L5, E5a, E5b, B1, B2, B3
Locations	Changsha, China
STD of ionosphere delay	0.02 m
STD of undifference observations	Code: 20 cm; Phase: 2 mm

STD means the standard deviation

Table 2 The differences of fix rates between LIA estimation and probability approximation, $\delta P_{\text{fix}} = P_{\text{fix}} - P_{\text{fix}}^{\dagger}$ with $P_{\text{fix}}^{\dagger}$ the fix rate by approximation. δP_{fix} can be seen as the approximation error

P_f	Systems	$E(\delta P_{\text{fix}}^{\text{DT}})$	$E(\delta P_{\text{fix}}^{\text{WT}})$	$E(\delta P_{\text{fix}}^{\text{IALS}})$	$E(\delta P_{\text{fix}}^{\text{MPT}})$
0.001	1	0.0064	0.0067	0.0151	0.0151
	2	0.0045	0.0046	0.0056	0.0056
0.01	1	0.0009	0.0010	0.0030	0.0030
	2	0.0001	0.0001	0.0001	0.0001

'1' denotes GPS + BeiDou, and '2' means GPS + BeiDou + Galileo

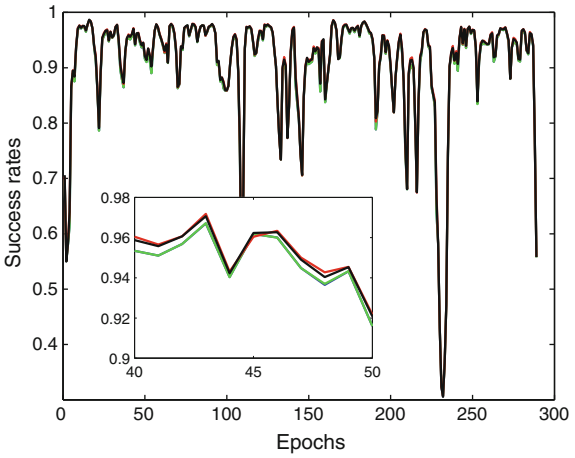

Fig. 2 Success rates of LIA estimators for GPS + BeiDou models when $P_f = 0.001$. *Red line* DTIA; *black line* WTIA; *green line* IALS and MPTIA

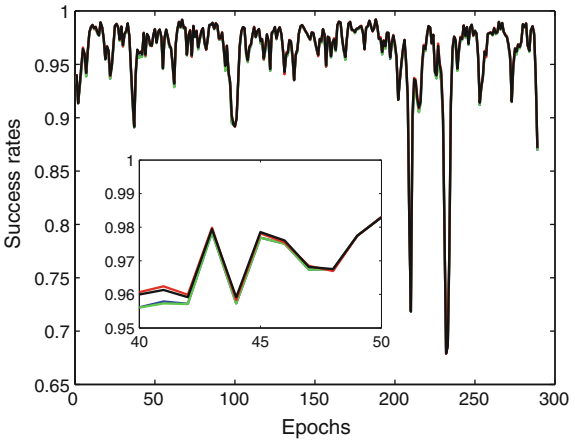

Fig. 3 Success rates of LIA estimators for GPS + BeiDou + Galileo models when $P_f = 0.001$. *Red line* DTIA; *black line* WTIA; *green line* IALS and MPTIA

Based on the critical values obtained from the fixed failure rate approach, we compare the performances of four linear IA estimators. The success rates of four LIA estimators are presented in Figs. 2 and 3. Two kinds of GNSS models are

Table 3 Comparison between the success rates of LIA estimators

P_f	Systems	$E(P_{s,\mathrm{DT}})$	$E(P_{s,\mathrm{WT}})$	$E(P_{s,\mathrm{IALS}})$	$E(P_{s,\mathrm{MPT}})$
0.001	1	0.9096	0.9090	0.9059	0.9059
	2	0.9627	0.9624	0.9611	0.9611
0.01	1	0.9779	0.9778	0.9778	0.9778
	2	0.9912	0.9912	0.9912	0.9912

'1' denotes GPS + BeiDou, and '2' means GPS + BeiDou + Galileo

simulated, GPS + BeiDou and GPS + BeiDou + Galileo. Here we only give the figures when $P_f = 0.001$. The statistics of both figures are summarized in Table 3.

According to Figs. 2, 3 and Table 3, we can see that when $P_f = 0.01$, IA estimators have higher success rates than those when $P_f = 0.001$. This means that loose requirement in failure rate leads to optimistic performance in IA estimation. Besides this, notice that DTIA has a higher success rate than those of others. It means that most of times DTIA has better performance than other IA estimators based on the fixed failure rate approach.

3.3 Comparison of LIA Estimator Based on the Simplified ICON Approach

Previous subsection analyzes the effectiveness of probability approximation in LIA estimators. In this subsection we will compare the performances of these LIA estimators by the simplified iCON approach. The GNSS models are still generated based on previous simulation settings. The controlled failure rates are summarized in Table 4. Here we only give their expectations. On contrast, the success rates of IA estimation are also listed in Table 4 to compare their performances.

In Table 4, it is obvious that the expectations of all controlled failure rates are smaller than the setting of initial failure rates. This is because the approximation formulas in iCON approach are lower bounds of the probability evaluations for IA estimators. Hence, the obtained critical values are conservative choices in controlling failure rates.

Comparing with Table 2, the differences between IA estimators can be seen from their success rates. When $P_f = 0.01$, there is no obvious difference between

Table 4 Comparison of the controlled failure rates of LIA estimators based on iCON approach

P_f	Systems	$E(P_{f,\mathrm{DT}})$	$E(P_{f,\mathrm{WT}})$	$E(P_{f,\mathrm{IALS}})$	$E(P_{f,\mathrm{MPT}})$
0.001	1	0.0007	0.0007	0.0008	0.0008
	2	0.0007	0.0008	0.0008	0.0008
0.01	1	0.0088	0.0088	0.0088	0.0088
	2	0.0071	0.0071	0.0071	0.0071

'1' denotes GPS + BeiDou, and '2' means GPS + BeiDou + Galileo

Table 5 Comparison of the success rates of LIA estimators based on the simplified iCON approach

P_f	Systems	$E(P_{s,\mathrm{DT}})$	$E(P_{s,\mathrm{WT}})$	$E(P_{s,\mathrm{IALS}})$	$E(P_{s,\mathrm{MPT}})$
0.001	1	0.8893	0.8910	0.8919	0.8919
	2	0.9527	0.9533	0.9527	0.9527
0.01	1	0.9777	0.9777	0.9776	0.9776
	2	0.9912	0.9912	0.9912	0.9912

'1' denotes GPS + BeiDou, and '2' means GPS + BeiDou + Galileo

four IA estimators. If $P_f = 0.001$, WTIA, IALS and MPTIA seem to be slightly better than DTIA. This is because the approximation errors in the analytical formulas of IA estimators influence their controllability. It is noted that the loose control over failure rate may lead to optimistic success rate.

Comparing the results of Table 5 with the corresponding results in Table 3, we can give the following remarks:

1. The simplified iCON approach gives conservative control to failure rates. Hence, the success rates of IA estimation based on iCON approach is also more conservative than the results in Table 3;
2. The performances of IA estimators based on the simplified iCON approach are influenced by their approximation errors;
3. Conservative choice in μ will lead to conservative success rate, which can be seen in the comparison of DTIA and IALS;
4. IALS and MPTIA have the same performance all the time. Hence, they are mathematically equivalent.

Even though we still can see that when $P_f = 0.01$ and GNSS model is very strong, the controllability difference between the simplified iCON approach and fixed failure rate approach is trivial. However, until now there are no clear criteria about how to set P_f. The importance of P_f is still obscure. Besides this, when the true ambiguities are not known, comparison between IA estimators is almost impossible. At that time, the feasible criterion should be determined by specific application, such as the precision of positioning or attitude determination. Hence, in next section, we will introduce another criterion to compare the performances of IA estimators.

4 Application in GNSS Compass

In order to test the performance of LIA estimators, a static field test for GNSS compass was carried out. It was implemented on January 9, 2013 at Delft, the Netherlands. Two low-cost, single-frequency mu-blox receivers are connected with the baseline length 9.71 m. One GNSS station with high precise Septentrio receiver is used as reference. Three receivers are connected according to the layout in Fig. 4. Only single-frequency observations are collected more than 1 h. In the data process,

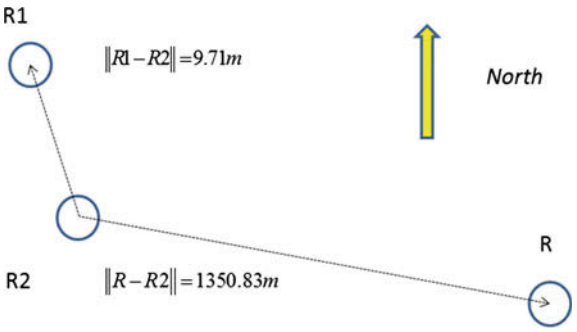

Fig. 4 The layout of field test. $R1$ and $R2$ are two low-cost mu-blox receivers, and R is high-end Septentrio receiver

Table 6 Comparison of fix rates between LIA estimators based on iCON approach and RTIA based on look-up table for two baselines

基线	P_f	$P_{\text{fix}}^{\text{DT}}$	$P_{\text{fix}}^{\text{WT}}$	$P_{\text{fix}}^{\text{IALS}}$	$P_{\text{fix}}^{\text{RT}}$
R1–R2	$P_{f,\text{ILS}}$	0.9997			
	0.01	0.9995	**0.9808**	0.9997	0.9834
	0.001	0.9987	**0.9810**	0.9989	0.9832
R–R2	$P_{f,\text{ILS}}$	0.9997			
	0.01	0.9988	**0.9560**	0.9991	0.9749
	0.001	0.9979	**0.9578**	0.9982	0.9743

IA ambiguity resolutions are implemented based on Kalman filter so that most of epochs can be fixed reliably. Note that in practice the true ambiguities are not known, hence we only can compare the fix rates of four linear IA estimators. Besides this, since one single baseline can determine the heading and pitch, we will compare the heading precision of two baselines based on different IA estimators.

First, we will analyze the ambiguity resolution results for two baselines, which are summarized in Table 6. When $P_f = P_{f,\text{ILS}}$, ILS will be implemented instead of IA estimation. According to Table 6, WTIA has the smallest fix rate. IALS and MPTIA have the same estimation results, and their fix rates are the biggest ones. It means that, based on the simplified iCON approach, WTIA is conservative in quality control. IALS (MPTIA) is optimistic, and more apt to accept the best integer candidate than other IA estimators. The fix rates of RTIA and DTIA are better than that of WTIA but worse than those of DTIA and IALS (MPTIA). The value of P_f also influences the ambiguity fixed rates. Smaller P_f will lead to smaller fixed rates. However, WTIA is different. By analyzing the data process in float ambiguity estimation, many outliers were detected and adapted. This fact also influences the ambiguity resolution and leads to more rejection in ambiguity validation. The same results also can be seen in the precision of heading, which are shown in Table 7.

The precision of heading for two baselines is demonstrated in Table 7. Notice that the float precision of heading in R–R2 is much smaller than that of R1–R2. According to relationship between float precision and baseline length [21], the longer baseline will have more precise float estimation results. After IA estimation, the precision of heading is further improved, though their differences are very small.

Table 7 Comparison of heading precision between LIA estimators based on the simplified iCON approach for two baselines

基线	P_f	$\breve{\sigma}_{\varphi,\mathrm{DT}}$	$\breve{\sigma}_{\varphi,\mathrm{WT}}$	$\breve{\sigma}_{\varphi,\mathrm{IALS}}$	$\breve{\sigma}_{\varphi,\mathrm{RT}}$
R1–R2	$P_{f,\mathrm{ILS}}$	0.0403°			
	0.01	0.0330°	**0.0329**°	0.0331°	**0.0329**°
	0.001	0.0330°	**0.0329**°	0.0331°	**0.0329**°
R–R2	$P_{f,\mathrm{ILS}}$	4.4e-4°			
	0.01	2.611e-4°	**2.535e-4**°	2.611e-4°	2.558e-4°
	0.001	2.610e-4°	**2.538e-4**°	2.609e-4°	2.557e-4°

The float precision for the heading of R1–R2 is $\hat{\sigma}_{\varphi} = 0.2303$, and that of R–R2 is $\hat{\sigma}_{\varphi} = 0.0027°$

This proves the effectiveness of quality control of ambiguity resolution. Among these IA estimators, WTIA still has the best precision. RTIA is a little worse than WTIA. IALS is the worst. It indicates that the rejection of wrong ambiguity is helpful to improve the precision of GNSS compass. The value of P_f has trivial influence in GNSS compass due to the small number of epochs.

Based on previous analysis, we can conclude the following remarks:

- Integer aperture estimation is effective in the quality control of ambiguity resolution, and can improve the precision of GNSS positioning or compass;
- When the number of epochs is not so much, the setting of P_f has no obvious influence. We can neglect its influence in small-scale data process;
- In this static field test, the performance of LIA estimator based on the simplified iCON approach can be better than that of RTIA based on look-up table. This indicates that the research about the selection of IA estimators is necessary and meaningful.

5 Conclusion

Ambiguity validation is an important step in ambiguity resolution to realize quality control. Its value in GNSS data process and the effectiveness of different methods have been the hot topic over the decades.

Based on the theoretical foundation of ambiguity validation, the so-called integer aperture estimation, this contribution selected several popular IA estimators to analyze and classify. From the perspective of geometry scaling, this paper connects integer estimator with IA estimators. Linear IA estimators are classified based on their common properties. Based on their approximated and analytical probability formulas, this contribution proposed a simplified instantaneous and controllable ambiguity resolution method which can be applied to linear IA estimators. As the RTIA based on look-up table, the linear IA estimators based on this simplified approach can realize the quality control to ambiguity resolution, and its implementation procedure is simple.

According to multi-GNSS simulation experiment, the error characteristics of LIA estimators were analyzed, and the performances of LIA estimators were compared by the fixed failure rate approach and the simplified iCON approach. In the GNSS compass field test, heading precision was used to compare the performances of IA estimators. The results showed that LIA based on the simplified iCON approach can realize the quality control of ambiguity resolution, which is helpful to further improve the heading precision. Moreover, the performance of WTIA based on the simplified iCON approach is better than that of RTIA based on look-up table. In the future, it is necessary to verify and compare the performances of LIA estimators in more GNSS applications and data process modes.

Acknowledgment This research is supported by the National Science Foundation of China (Grant No. 61104201) and China Scholarship Council (CSC) (Grant No. 201206110010). The field test was implemented with Yanqing Hou, Dr. Christian Tiberius when the first author worked in Delft University of Technology, the Netherlands. The first author would like to thank their assistance in experiment and discussion about data process. Dr. Sandra Verhagen is also acknowledged for the permission to use GNSS simulation software.

References

1. Teunissen PJG (1999) An optimality property of the integer least-squares estimator. J Geod 73 (11):587–593
2. Teunissen PJG (1993) Least-squares estimation of the integer GPS ambiguities. In: IAG general meeting. Beijing, China
3. Teunissen PJG (1995) The least-squares ambiguity decorrelation adjustment: a method for fast GPS integer ambiguity estimation. J Geod 70(1–2):65–82
4. Teunissen PJG (2003) Integer aperture GNSS ambiguity resolution. Artif Satell 38(3):79–88
5. Verhagen S, Teunissen PJG (2006) New global navigation satellite system ambiguity resolution method compared to existing approaches. J Guid Cont Dyn 29(4):981–991
6. Verhagen S (2005) The GNSS integer ambiguities: estimation and validation
7. Verhagen S, Teunissen PJG (2013) The ratio test for future GNSS ambiguity resolution. GPS Solutions 17(4):535–548
8. Wang L, Verhagen S (2014) A new ambiguity acceptance test threshold determination method with controllable failure rate. J Geod 89:361–375
9. Teunissen PJG (1998) On the integer normal distribution of the GPS ambiguities. Artif Satell 33(2):49–64
10. Teunissen PJG (2013) GNSS integer ambiguity validation: overview of theory and methods. In: Proceedings of the institute of navigation pacific PNT
11. Zhang J et al (2015) Integer aperture ambiguity resolution based on difference test. J Geod
12. Tiberius C, de Jonge P (1995) Fast positioning using the LAMBDA method
13. Li T, Zhang J et al (2015) Integer aperture estimation comparison between ratio test and difference test: from theory to application. GPS Solutions
14. Teunissen PJG (2005) Integer aperture least-square estimation. Artif Satell 40(3):149–160
15. Wang J, Stewart MP, Tsakiri M (1998) A discrimination test procedure for ambiguity resolution on-the-fly. J Geod 72(11):644–653
16. Han S (1997) Quality-control issues relating to instantaneous ambiguity resolution for real-time GPS kinematic positioning. J Geod 71(6):351–361

17. Teunissen PJG (2005) Integer aperture bootstrapping: a new GNSS ambiguity estimator with controllable fail-rate. J Geod 79(6–7):389–397
18. Brack A (2015) On reliable data-driven partial GNSS ambiguity resolution. GPS Solutions 19:1–12
19. Zhang J, Wu M, Zhang K (2015) Instantaneous and controllable GNSS integer aperture ambiguity resolution with difference test. In: China satellite navigation conference 2015. Xi'an
20. Zhang J, Wu M, Li T (2015) Instantaneous and controllable integer ambiguity resolution: review and an alternative approach. J Geod
21. Teunissen PJG (2010) Integer least-square theory for the GNSS compass. J Geod 84:433–447

Ambiguity Fixing for Kinematic PPP with Integer Phase Clock

Kang Zheng, Rengui Ruan, Xiaolin Jia and Hua Lu

Abstract The implementation of precise point positioning ambiguity fixing depends on the products which can be used to recover the characteristics of ambiguity by the service side. When users need to implement single difference between satellite method and the decoupled clock method they have no way to achieve the products, so they must provide the products themselves hard, but when users need to implement the integer phase clock method they can use the wide-lane FCB and integer phase clock provided by CNES. Therefore, in this paper we put forward the algorithm of sequential ambiguity fixing with direct rounding and analyze the effects of ambiguity fixing kinematic PPP based on this method. First we analyze the principle of PPP ambiguity fixing based on the models, and then we introduce the algorithm and how the users have to implement integer phase clock method. Last, based on the principle analysis we design the single-day and two-hour dynamic experiments, which are simulated by static data. Results of numerous stations show that: the algorithm of sequential ambiguity fixing with direct rounding can significantly improve the accuracy of positioning and the east shows more obvious effects, the improvement proportion of single-day and two-hour were approximately 30 and 60 %, so the result can verify the validity of the method proposed.

Keywords PPP · Ambiguity fixing · Integer phase clock · Accuracy

K. Zheng (✉)
Information Engineering University, Zheng Zhou 450001, China
e-mail: kangz002015@163.com

R. Ruan · X. Jia
Xi'an Research Institute of Surveying and Mapping, Xi'an, China

H. Lu
Xi'an Aerors Data Technology Co., Ltd., Xi'an, China

© Springer Science+Business Media Singapore 2016

J. Sun et al. (eds.), *China Satellite Navigation Conference (CSNC) 2016 Proceedings: Volume III*, Lecture Notes in Electrical Engineering 390,
DOI 10.1007/978-981-10-0940-2_49

1 Introduction

When we are processing the traditional precise point positioning, because of the influence of the receiver and the satellite terminal phase delay and the initial phase bias, ambiguity parameters do not have integer properties [1], so they can only be treated as a float solution, and this makes it difficult to achieve the accuracy which can be compared to differential positioning. So in recent years many scholars have done a lot of research about this problem of precise point positioning ambiguity fixing and made a number of effective methods [2–4]. Currently some methods are focused on extensive research, which is mainly inter-satellite single-difference FCB (fractional cycle bias) method [5, 6], integer clock method [7, 8] (IRC, integer recovery clock), and decoupled clock method [1–3]. The three methods are dependent on the FCB product which can be used to restore the integer property of wide-lane ambiguity and narrow-lane ambiguity provided by the service, but users have no public way to achieve the product provided by inter-satellite single-difference FCB and decoupled clock method, so we must use algorithm to achieve the product by ourselves when we need the product. This is not convenient, but when we need to use integer clock method to implement ambiguity fixing, we have the available product provided by CNES publicly.

Therefore, this paper proposes a method based on integer clock which is called sequential ambiguity fixing algorithm with direct rounding to study the effect to dynamic precise point positioning when we use this algorithm. First, the principle of PPP ambiguity fixing was analyzed in detail, when we have obtained accurate float solution of ionosphere-free ambiguity we can take the method called a simple test for independence to select independent single-difference ambiguity considering the fixed success rate of wide-lane ambiguity. When wide-lane and narrow-lane ambiguity with inter-satellite single difference was fixed we adopt a new procedure for sequential ambiguity fixing based on updating the upper triangular square root of covariance matrix [9] to implement PPP ambiguity fixing. Last, we adopt data from a number of IGS stations to implement dynamic test simulated by static, then we can verify the validity of the method when used in dynamic precise point positioning by analyzing the accuracy.

2 Principle of PPP Ambiguity Fixing

When Laurichesse and Mercier [7] adopted integer clock method, the mathematical model used in integer clock method is slightly different from the traditional PPP mathematical model. The satellite and receiver phase delay was mainly analyzed; we will analyze the model in detail following this thought.

Dual ionosphere-free pseudorange and carrier-phase combination of observations are widely used in GPS positioning and observation equation is as follows:

$$P_{\mathrm{IF}} = R + \mathrm{c} \cdot \delta \mathrm{t}_r - \mathrm{c} \cdot \delta \mathrm{t}^s + T + B_{r,P} - B_P^s + \varepsilon_{P_{\mathrm{IF}}} \tag{1}$$

$$L_{\mathrm{IF}} = R + \mathrm{c} \cdot \delta \mathrm{t}_r - \mathrm{c} \cdot \delta \mathrm{t}^s + T - N_{\mathrm{IF}} + B_{r,L} - B_L^s + \varepsilon_{L_{\mathrm{IF}}} \tag{2}$$

$$\begin{aligned} N_{\mathrm{IF}} &= \frac{f_1^2}{f_1^2 - f_2^2}\lambda_1 N_1 - \frac{f_2^2}{f_1^2 - f_2^2}\lambda_2 N_2 \\ &= \frac{c}{f_1 + f_2} N_1 - \frac{c \cdot f_2}{f_1^2 - f_2^2}(N_2 - N_1) \end{aligned} \tag{3}$$

P_{IF}, L_{IF} are pseudorange and phase measurements (in m), R is the true distance between satellite and receiver, the offset and variation of antenna phase center, solid tide, ocean tide, pole tide, and phase windup, such correction have been carried out on default. $\delta \mathrm{t}_r$ is receiver clock error, $\delta \mathrm{t}^s$ is satellite clock error, N_{IF} is ionosphere-free ambiguity (in m), c is the speed of light, N_1, N_2 are respectively corresponding ambiguity parameters L_1, L_2, namely, λ_1, λ_2 is the wavelength of L_1, L_2. T is tropospheric delay, $B_{r,P}$ is the pseudorange delay in receiver. B_P^s is pseudorange delay in satellite, $B_{r,L}, B_L^s$ is appropriate phase delay.

The satellite clock used in traditional PPP was the pseudorange clock based on combination of ionosphere-free, including the pseudorange delay in satellite, so the pseudorange delay was brought into the carrier-phase observations. We can clearly see this difference by comparing the following equation (Eq. (4) with the original equation, Eq. (5) shows the case of traditional PPP when pseudorange clock was used).

$$L_{\mathrm{IF}} = R + \mathrm{c} \cdot \delta \mathrm{t}_r - \mathrm{c} \cdot \delta \mathrm{t}^s + T - N_{\mathrm{IF}} + B_{r,L} - B_L^s + \varepsilon_{L_{\mathrm{IF}}} \tag{4}$$

$$\begin{aligned} L_{\mathrm{IF}} = R &+ (\mathrm{c} \cdot \delta \mathrm{t}_r + B_{r,\mathrm{P}}) - (\mathrm{c} \cdot \delta \mathrm{t}^s + B_P^s) + T + \varepsilon_{L_{\mathrm{IF}}} \\ &- N_{\mathrm{IF}} + (B_{r,L} - B_{r,\mathrm{P}}) - (B_L^s - B_P^s) \end{aligned} \tag{5}$$

From Eq. (4) it can also be seen that the original ambiguity $N = N_{\mathrm{IF}} - B_{r,L} + B_L^s$ does not have integer property, because ambiguity parameter and the phase delay cannot be separated. In order to restore the integer property of ambiguity parameter, Laurichesse proposed integer clock method, Eqs. (6), (7), (8) reflect the specific process.

$\gamma = \frac{c}{f_1 + f_2}, \beta = \frac{c \cdot f_2}{f_1^2 - f_2^2}$, $N_{\mathrm{WL}} = N_2 - N_1$, $N_{\mathrm{IF}} = \gamma N_1 - \beta N_{\mathrm{WL}}$, $\tau_{r,\mathrm{WL}}$ τ_{WL}^s is appropriate the wide-lane phase delay in receiver and satellite.

$$\begin{aligned} \mathrm{MW} &= (\varphi_1 - \varphi_2) - \frac{f_1 - f_2}{f_1 + f_2}\left(\frac{P_1}{\lambda_1} + \frac{P_2}{\lambda_2}\right) \\ &= N_{\mathrm{WL}}^s + \tau_{r,\mathrm{WL}} - \tau_{\mathrm{WL}}^s + \varepsilon \end{aligned} \tag{6}$$

$$\mathrm{L_{IF}} - \beta N_{\mathrm{WL}} = \mathrm{R} + \mathrm{c} \cdot \delta \mathrm{t_r} - \mathrm{c} \cdot \delta \mathrm{t^s} - \gamma N_1 + \varepsilon_{\mathrm{L_{IF}}} \tag{7}$$

$$L_{\mathrm{IF}} - \beta N_{\mathrm{WL}} + \gamma N_1 = R + \mathrm{c} \cdot \delta \mathrm{t}_r - \mathrm{c} \cdot \delta \mathrm{t}^s + \varepsilon_{L_{\mathrm{IF}}} \tag{8}$$

First, Eq. (6) is used, we adopt the MW combination of observations to estimate wide-lane fractional bias. When we achieve the fixed wide-lane ambiguity, the fixed wide-lane ambiguity was substituted in the Eq. (7), then we can get the left of the equation to fix the narrow-lane ambiguity. Finally, the fixed narrow-lane ambiguity was substituted in the Eq. (8) to composite equation without ambiguity parameter. Then we use this equation to estimate a group of satellite clock, it is called integer clock products, including the phase delay in satellite. This is the algorithm applied in the service, and you can get the products of wide-lane FCB and integer clock error with fractional cycle bias in satellite.

When the users adopt the integer clock method to achieve the fixed PPP ambiguity they can use the non-difference or single-difference approach, the essence is same. They can eliminate the impact of error in receiver by the method of inter-satellite single-difference. The phase clock products released by CNES have absorbed the fractional cycle bias in satellite, so we can fix the wide-lane ambiguity and narrow-lane ambiguity with the wide-lane FCB products. Thereby we can achieve the fixed ionosphere-free ambiguity and make them as constraints to update non-ambiguity parameters (three-dimensional coordinates, the receiver clock error).

In this paper we carry out the ambiguity fixing method based on the above idea. The position mode is postprocessing whether we use static or dynamic data. We solve the non-difference ambiguity parameters together with station coordinates and receiver clock by utilizing the recursive least squares method [10, 11], and the normal equation is addicted epoch by epoch. After receiving the non-difference float ambiguity throughout the observation period, we can use the method called "a simple test for independence" to select a group of independent ambiguity, and then we can obtain the float single-difference ionosphere-free ambiguity. By adopting the wide-lane FCB products in satellite we can obtain the fixed wide-lane ambiguity and then we can fix the narrow-lane ambiguity by the sequential way. Last, we can obtain the fixed ionosphere-free ambiguity and make it a constraint to update the non-difference ambiguity and its covariance matrix, so we can obtain the fixed solution.

3 Algorithm of PPP Ambiguity Fixing

3.1 The Process of Implementing Ambiguity Fixing

In this paper we implement the algorithm by making some improvement in the original PPP function of SPODS [10] (Satellite Positioning and Orbit Determination System) software. This software is independently researched by Xi'an Institute of Surveying and Mapping.

When we utilize the PPP function of SPODS, the observations are dual-frequency ionosphere-free pseudorange and phase measurements. We utilize the TurboEdit approach to achieve cycle slip detection and repair in the preprocessing stage. Posterior residual analysis is performed after parameter estimation to detect cycle slip by iteration until there are no more cycle slips.

We have considered comprehensively the offset and variation of antenna phase center, troposphere error, ionosphere error, and the tide error. The parameters to be estimated are divided into two categories, global and local parameters. The global parameters include static station coordinates, troposphere zenith wet delay, and horizontal gradient and ambiguity parameters; the local parameters include dynamic station coordinates and receiver clock error. In the estimation of parameters we will first make the local parameters disappear and then obtain the global parameters such as ambiguities and its covariance matrix. Last we can obtain the values of local parameters in every epoch by substituting the global parameters into the normal equation [10].

The fixing of ambiguity parameters depend on relatively accurate float solution. Since the wavelength of wide-lane ambiguity is longer, about 0.86 m, it is relatively easily fixed. But the wavelength of narrow-lane ambiguity is only 0.19 m, when the accuracy of float solution is not enough there will be some wrongly fixed solution which may make the final result worse.

3.2 *The Fixing of Wide-Lane Ambiguity and the Selection About Independent Groups of Ambiguity*

We make some simple process about Eq. (6), and give the following forms:

$$N_{\mathrm{WL}}^{jk} = \mathrm{MW}^{jk} + (\tau_{\mathrm{WL}}^{s}(j) - \tau_{\mathrm{WL}}^{s}(k)) + \varepsilon \tag{9}$$

Because there may be multiple satellite ambiguity parameters during the observation period, the program has made some process by giving numbers according to the certain order, such as j, k, they are the segment number obtained by the mark of observations based on the cycle slip.

According to the segment of the observed value of each satellite, we can obtain the average MW combined observations for each segment, and this is the wide-lane float value. For each alternative single-difference combination we can obtain the inter-satellite single-difference wide-lane ambiguity, and then we can extract the daily wide-lane FCB products $\tau_{\mathrm{WL}}^{1} \sim \tau_{\mathrm{WL}}^{32}$ from the satellite clock products or wsb file provided by CNES to correct the single-difference wide-lane ambiguities in satellite. After achieving the corrected wide-lane ambiguities, we can screen out the group which meets the demands such as the fractional part after rounding is less than the threshold value (such as 0.15 cycle) and the fixed success probability is higher than threshold value; and then we can calculate the fixed probability of

narrow-lane ambiguity. So we can obtain the final fixed probability by using both of the fixed probability of wide-lane ambiguity and narrow-lane ambiguity. Based on the reverse order of the group of satellites according to the final fixed probability we can use the method called "simple test for independence" proposed by Mervart to select a group of independent single-difference ambiguity.

3.3 Sequential Fixing of Single-Difference Narrow-Lane Ambiguity

We can obtain the float solution of single-difference narrow-lane ambiguity according to the independent groups of single-difference ambiguity, the float solution of ionosphere-free ambiguity $\hat{N}_{\mathrm{IF}}^{jk}$ and the fixed solution of single-difference wide-lane ambiguity $\breve{N}_{\mathrm{WL}}^{jk}$.

$$\hat{N}_{1}^{jk} = \left(\hat{N}_{\mathrm{IF}}^{jk} + \beta \breve{N}_{\mathrm{WL}}^{jk}\right)/\gamma \tag{10}$$

Then we can obtain the fixed solution of single-difference ionosphere-free ambiguity according to the fixed solution of single-difference wide-lane ambiguity and narrow-lane ambiguity after using the rounding method to obtain the integer cycle.

$$\breve{N}_{\mathrm{IF}}^{jk} = \gamma \breve{N}_{1}^{jk} - \beta \breve{N}_{\mathrm{WL}}^{jk} \tag{11}$$

We can use Eq. (11) as a constraint to achieve the fixed solution of PPP by adopting the procedure for sequential ambiguity fixing based on updating the upper triangular square root of covariance matrix. We need to fix a single-difference ionosphere-free ambiguity when we obtain a fixed single-difference narrow-lane ambiguity, and then we can update the non-ambiguity parameters and its covariance matrix by updating the covariance matrix of non-difference ambiguity. So we can obtain the fixed solution of station coordinates.

4 Experiment and Analysis

4.1 The Experiment of Dynamic Simulated by Static in Single Day

We adopted data from 76 IGS stations on January 12, 2015 to make experiments based on dynamic simulated by static conditions and compared the results obtained

from the float solution and fixed solution of ambiguity. The reference coordinate was extracted from the snx file released by IGS, then the position error RMS value (N/E/U/PLANE/3D) of every station was obtained, and the mean value and STD of the position error RMS were obtained [4].

Note: When we achieved the fixed solution the fixed success rate of wide-lane and narrow-lane are all above 90 %.

Station distribution shows as the following:

In Fig. 1 all stations are involved in a single-day solving test, blue stations are involved in the two-hour experiment.

To save space of paper, we only show a single day of POLV station float solution and fixed solution positional error sequence, this is shown in Fig. 2.

As can be seen the position error sequence of POLV station from Fig. 2, the fixed solution is significantly smoother than float solution; when we consider the RMS and standard deviation indicator from Table 1, we can find that all directions of the station reflect better positioning accuracy and stability.

Table 2 shows the statistics of all stations in a single day which is mainly about the improvement of mean and standard deviation indicator. Figure 3 shows the position results of all stations with the way of visual representation.

As can be seen from Table 2, the fixed solution is better than float solution on both mean and standard deviation, this shows that the stability and PPP positioning accuracy of the fixed solution have been significantly improved compared to float solution. And when we consider the improvement of all directions we can see that the improvement in east is better than other directions, the improvement in plane is better than the three dimensions. This conclusion is consistent with the experiment provided by Liu et al. [4] at 2014.

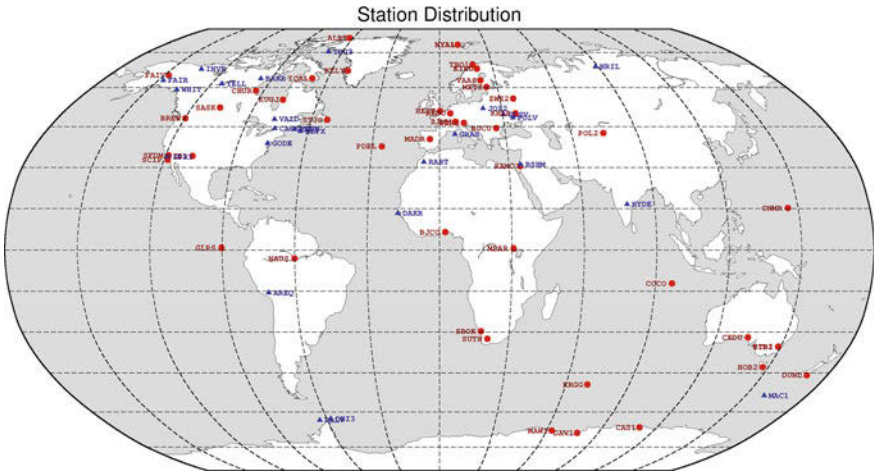

Fig. 1 Station distribution

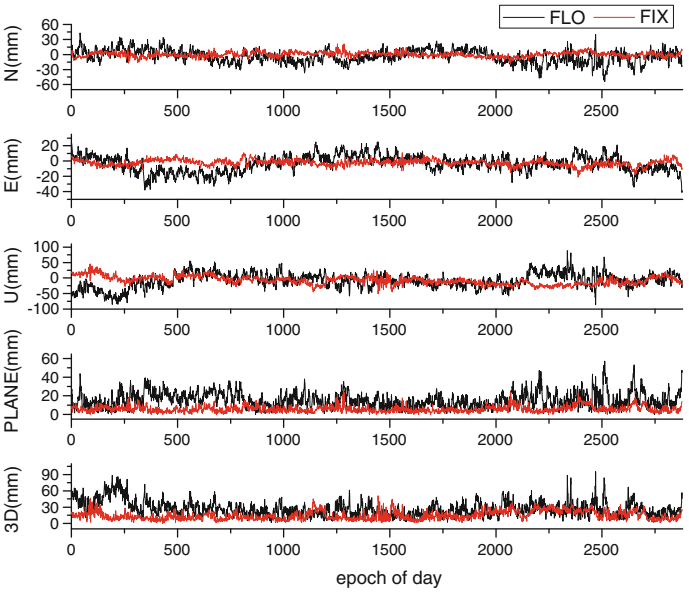

Fig. 2 The sequence of position error of float and fixed solutions on POLV

Table 1 The position RMS of float and fixed solutions on POLV in single day

POLV		N	E	U	Plane	3D
RMS	Float	13.5	11.1	24.6	17.5	30.2
	Fixed	11.5	7.5	18.8	13.8	23.3
Std	Float	13.0	10.5	23.3	8.4	14.2
	Fixed	4.8	4.0	13.4	3.3	8.2

Table 2 The position RMS of float and fixed solutions on all stations in single day

		N	E	U	Plane	3D
Mean	Float	8.4	8.6	24.6	12.2	27.6
	Fixed	7.3	6.0	21.6	9.5	23.6
	Ratio of improvement (%)	13	30	12	22	14
Std	Float	2.8	3.5	10.0	4.3	10.5
	Fixed	2.0	2.4	6.5	2.9	6.7
	Ratio of improvement (%)	29	31	35	33	36

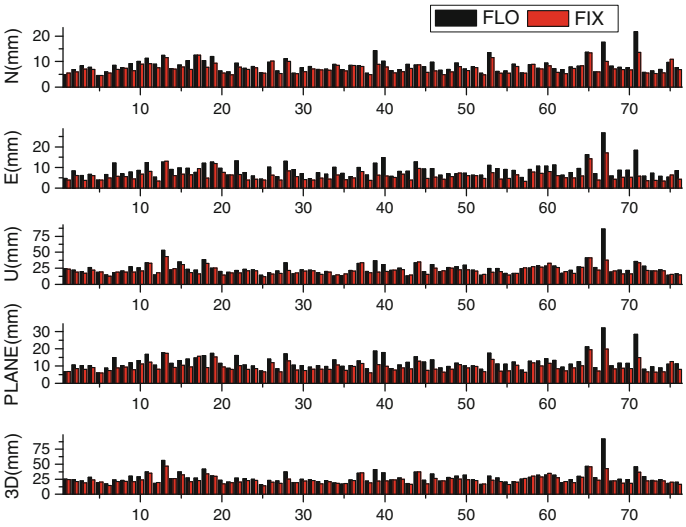

Fig. 3 The position RMS of float and fixed solutions on all stations in single day

4.2 The Experiment of Dynamic Simulated by Static in Two Hours

When we made the experiment of dynamic two hours, we adopted data from 29 IGS stations on January 12. And we utilized the same way as single day to make statistics.

Same as the experiment of single day, we only show position error sequence of POLV station on both float and fixed solutions, this is shown in Fig. 4.

As can be seen from Fig. 4, when POLV station position error sequence of fixed solution is compared with float solution, both solutions have basically the same trend; this phenomenon can also be seen from the standard deviation in Table 3. The standard deviation of the fixed solution is close to the float solution; the fixed solution shows a bias term compared with the float solution, which is equivalent that the entire sequence moves a certain distance to zero, combined with RMS indicators Table 3, we can see that fixed solution shows better solution than the float solution.

Table 4 shows the statistics of all stations in two hours which is mainly about the improvement of mean and standard deviation indicator. Figure 5 shows the position results of all stations with the way of visual representation.

It can be seen in Table 4 and Fig. 5, the results of experiments of dynamic simulated by static in two hours have the same trend with the results in single day. So the results show that the mean and standard deviation of fixed solution is better than float solution, and the improvement in east is better than other directions. The special case is that the position accuracy of float solution in two hours is lesser than

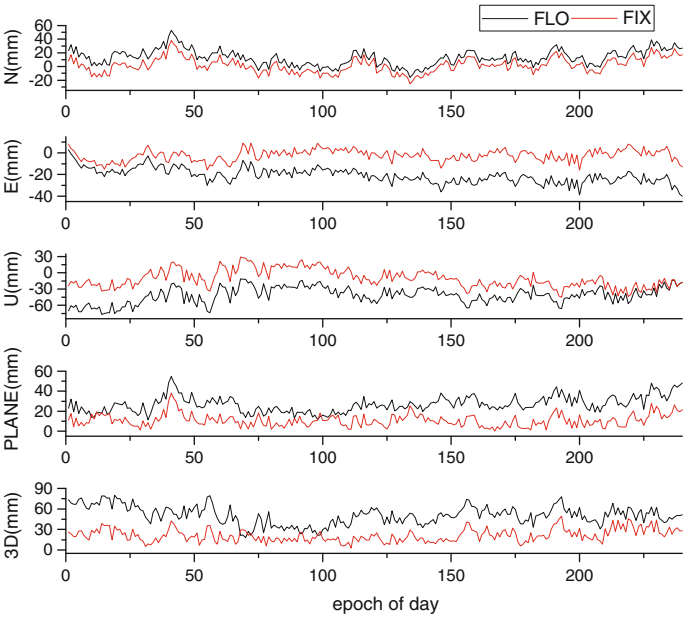

Fig. 4 The sequence of position error of float and fixed solutions on POLV

Table 3 The position RMS of float and fixed solutions on POLV in two hours

POLV		N	E	U	Plane	3D
RMS	Float	17.5	22.0	44.2	28.1	52.4
	Fixed	11.1	5.7	19.5	12.5	23.2
Std	Float	11.6	6.7	14.9	8.0	13.5
	Fixed	10.9	5.2	16.3	6.2	9.3

Table 4 The position RMS of float and fixed solution on all stations in two hours

		N	E	U	Plane	3D
Mean	Float	13.6	19.2	28.6	24.6	38.8
	Fixed	6.9	6.6	21.0	9.9	23.6
	Ratio of improvement (%)	49	66	27	60	39
Std	Float	8.0	15.2	17.7	15.4	21.7
	Fixed	2.6	7.8	10.9	7.6	12.5
	Ratio of improvement (%)	68	49	38	51	42

the accuracy in single day, but the position accuracy of fixed solution in two hours is consistent with the results in single day, so the improvement in two hours is more obvious than the improvement in single day.

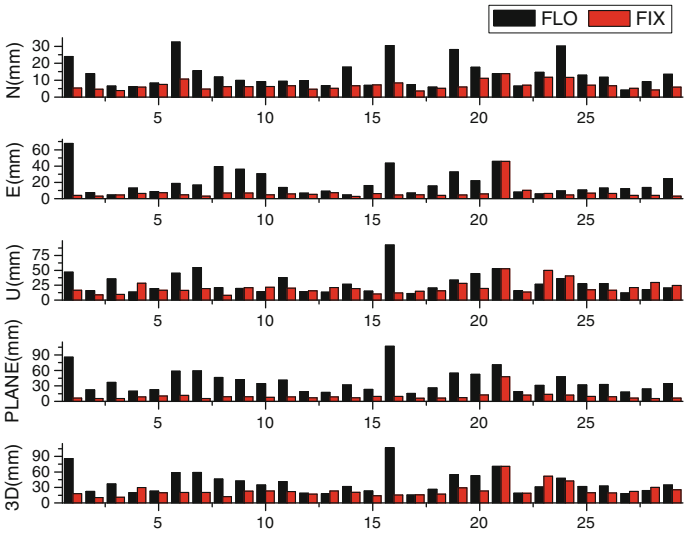

Fig. 5 The position RMS of float and fixed solutions on all stations in two hours

5 Conclusion

In this paper we put forward the algorithm of sequential ambiguity fixing with direct rounding based on the integer clock method, and then we adopt some IGS stations to make the experiments of the dynamic simulated by static in two hours and single day after introducing the principle of this method. Then we can verify the validity of the method when it was used in dynamic PPP by analyzing the accuracy. The results show that the improvement of the dynamic solution in two hours and single day has no significant difference and we can make the similar conclusion below.

(a) The fixed solution of PPP can significantly improve the position accuracy whether seen from the mean or the standard deviation.
(b) The improvement in east is better than the improvement in elevation, the ratio is approximately 30–60 %;
(c) The improvement in plane is better than the improvement in three dimensions.

We implement the integer clock method by using non-difference function model of ambiguity and making single difference to the ambiguity to obtain fixed solution of ambiguity, the experiments show that this method can improve the accuracy of precise point positioning to some extent. Since the adjustment method used in this paper is mainly adopted for postprocessing, while the current accuracy of single-day float solution can achieve millimeter level with static and 2–3 cm or less with dynamic. On this basis, based on the algorithm of sequential ambiguity fixing with direct rounding we can see that the improvement in single day in each

direction solution is up to 10–30 %, the improvement in two hours in each direction solution is up to 30–60 %, so the result can explain significantly how much positive meaning the proposed method have to improve the positioning performance of PPP. In the next we need to make further study about its application in the real-time processing.

Acknowledgments Thanks to the data provided by IGS and the precise orbit products, clock products and wide-lane fractional cycle bias products provided by CNES.

References

1. Zheng Y (2013) Research on integer ambiguity resolution in GPS precise point positioning. Wuhan University
2. Geng J, Meng X, Dodson AH et al (2010) Integer ambiguity resolution in precise point positioning: method comparison. J Geodesy 84(9):569–581
3. Shi J, Gao Y (2014) A comparison of three PPP integer ambiguity resolution methods. GPS Solutions 18(4):519–528
4. Liu S, Sun F, Hao W et al (2014) Modeling and effects analysis of PPP ambiguity fixing based on integer phase clock method. Acta Geodaetica et Cartographica Sin 43(12):1230–1237
5. Ge M, Gendt G, Rothacher M et al (2008) Resolution of GPS carrier-phase ambiguities in precise point positioning (PPP) with daily observations. J Geodesy 82(7):389–399
6. Geng J, Teferle FN, Shi C et al (2009) Ambiguity resolution in precise point positioning with hourly data. GPS Solutions 13(4):263–270
7. Laurichesse D, Mercier F (2001) Integer ambiguity resolution on undifferenced GPS phase measurements and its application to PPP. In: Proceedings of the 20th international technical meeting of the satellite division of the Institute of Navigation (ION GNSS 2007), pp 839–848
8. Loyer S, Perosanz F, Mercier F et al (2012) Zero-difference GPS ambiguity resolution at CNES–CLS IGS analysis center. J Geodesy 86(11):991–1003
9. Ruan R (2015) Ambiguity resolution for GPS/GNSS network solution with SPODS. Acta Geodaetica Cartogr Sin 44(2):128–134
10. Wei Z, Ruan R, Jia X et al (2014) Satellite positioning and orbit determination system SPODS: theory and test. Acta Geodaetica Cartogr Sin 43(1):1–4
11. Ruan R (2009) Study on GPS precise point positioning using un-differenced carrier phase. Information Engineering University, Zheng Zhou
12. Pan L, Cai C, Zhu J (2014) The methods and results of precise point positioning with between-satellite-difference integer ambiguity fixing. J Geodesy Geodyn 34(5):90–93
13. Chang X, Zuo X, Zhang W (2014) The method of ambiguity fixing and analysis of experiment based on dynamic PPP. Geometrics Inf Sci Wuhan Univ 3:006
14. Wang M (2013) Real-time precise point positioning and its application in atmosphere sensing. Information Engineering University, Zheng Zhou

Estimating Tropospheric Slant Delay Based on Improved Ray Tracing Method

Wenyi Wu, Xihong Chen, Zan Liu and Chenglong Li

Abstract Tropospheric slant delay is one of the most significant error sources in navigation satellite systems. Its obvious randomness is mainly attributed to meteorological parameters (temperature, pressure, water vapor pressure, etc.). Aiming at the poor performance of tradition Tropospheric models, and the restrictions of radiosonde data in ray tracing, an improved method based on ray tracing is proposed. In this method, refractive index is improved by inserting in global grid of meteorological parameters, which gets rid of the restrictions of radiosonde data. Meteorological data from Tsukuba (TSKB) stations in Japan are analyzed based on ray tracing technology and tradition models like Hopfield and Saastamoinen. Slant delay for 15 directions, from the zenith to 4° elevation, was computed. The results were compared with ray tracing tropospheric slant delays from nearby radiosonde measurements, which demonstrate that the accuracy and stability of improved ray tracing method is superior to tradition models. The method can precisely provide the tropospheric slant delay in the circumstances where measured meteorological data are absent, so it is of practical engineering significance.

Keywords Tropospheric slant delay · Ray tracing · Hopfield · Saastamoinen. · Refractive index

1 Introduction

Tropospheric slant delay contains more information than tropospheric zenith delay [1–5], which is one of the main error sources in navigation satellite systems positioning. In the analysis of Global Navigation Satellite Systems (GNSS) observation, tropospheric delay is about 2 m at zenith, and will be added to 20 m with the elevations increasing [6]. The neutral atmosphere is not dispersion

W. Wu (✉) · X. Chen · Z. Liu · C. Li
Air and Missile Defense College, Air Force Engineering University,
Xi'an 710051, China
e-mail: 18092161443@163.com

© Springer Science+Business Media Singapore 2016

J. Sun et al. (eds.), *China Satellite Navigation Conference (CSNC) 2016 Proceedings: Volume III*, Lecture Notes in Electrical Engineering 390,
DOI 10.1007/978-981-10-0940-2_50

medium. In order to correct the delay, the model for zenith tropospheric delay is first used to compute the zenith delay which is related to the desired slant directions by the mapping function. The common models contain Hopfield model [7], Saastamoinen model [8], and Neil mapping function (NMF) [9]. However, the traditional models for tropospheric delay are mainly depended on surface atmospheric parameters, and the accuracy is finally restricted.

Ray tracing model can estimate the propagation delays of radio waves [10], while the accuracy normally depends on radiosonde data. Based on this problem, a method based on improved ray tracing is proposed to estimate the tropospheric slant delay. The method improves the process of refractive index, which conquers the restriction of radiosonde data in a high accuracy. The simulation results for meteorological data from TSKB stations in Japan are analyzed and the validity and reliability of the improved method are proved.

2 Method Based on Improved Ray Tracing

2.1 Ray Tracing

Ray tracing which is based on the sell theorem can be the most accurate method for deriving the neutral atmosphere delays if it uses real-time atmosphere parameter values [11]. Radiosonde observation is still an important source of data for neutral atmosphere studies. Figure 1 shows the theory of ray tracing:

Where β stands for the real elevation, in degree, r is the distance between any spot and the center of earth. r_1 is the radius of earth. The neutral atmosphere delays can be computed as

$$\Delta S = \int_{r_1}^{r_2} \frac{rn^2(r)}{\sqrt{r^2n^2(r) - A_0^2}} dr - \sqrt{r_1^2 + r_2^2 - 2r_1 r_2 \cos\theta} \tag{1}$$

Fig. 1 Schema of ray tracing

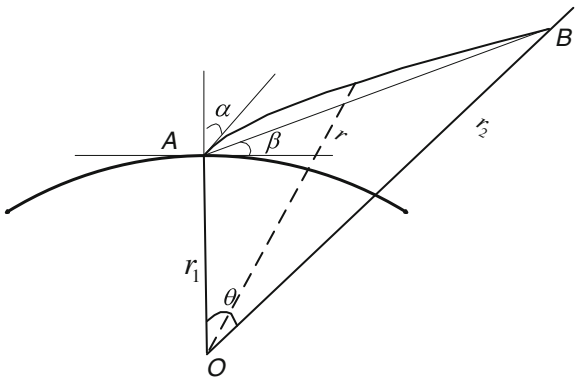

$$A_0 = rn(r)\sin\alpha \tag{2}$$

where ΔS is tropospheric slant delay. $n(r)$ is the refractive index.

2.2 Improved Ray Tracing

Analyzing the model of ray tracing is easy to find that the restriction of radiosonde data can overcome if the model for refractive index can be built [12]. Refractive index can be showed as

$$N = k_1\frac{P-e}{T} + k_2\frac{e}{T} + k_3\frac{e}{T^2} \tag{3a}$$

$$N_w = k_2\frac{e}{T} + k_3\frac{e}{T^2} \tag{3b}$$

$$N_d = k_1\frac{P-e}{T} \tag{3c}$$

where N_w and N_d stand for nonhydrostatic and hydrostatic refractive index. P, e, and T are the meteorological parameter values. k_1, k_2, and k_3 are refactivity constants with values 77.604, 64.79 K mbar^{-1}, and 377600 K^2 mbar^{-1}, respectively.

In order to overcome the restriction of radiosonde data, the model of the neutral atmosphere is used to compute the meteorological parameters [13]. The expression can be showed as

$$T = T_0 - \beta h \tag{4a}$$

$$P = P_0\left(\frac{T}{T_0}\right)^{\frac{g}{R_d\beta}} \tag{4b}$$

$$e = e_0\left(\frac{T}{T_0}\right)^{\frac{g(\lambda+1)}{R_d\beta}} \tag{4c}$$

where P_0, e_0, and T_0 are the meteorological parameter values of sea surface. h is the orthometric height in m. R_d is the gas constant for dry air (287.054 J kg^{-1} K^{-1}). g is the surface acceleration of gravity in ms^{-2}. β and λ are temperature lapse rate and water vapor pressure height factor, which can be computed through inserting in global grid of meteorological parameters.

Table 1 shows the look up table values. The data [12] is divided into two groups, to account for the annual average (mean) and amplitudes of a cosine function for each parameter. Both amplitudes and averages vary with respect to latitude, for all parameters. The annual average of a given parameter [14] can be computed as

Table 1 Value of global troposphere atmosphere parameter

$\Phi/(^\circ)$	Avg				
	P_0	T_0	e_0	β	λ
15	1013.25	299.65	26.31	0.00630	2.77
30	1017.25	294.15	21.79	0.00605	3.51
45	1015.75	283.15	11.66	0.00558	2.57
60	1011.75	272.15	6.78	0.00539	1.81
75	1013.00	263.65	4.11	0.00453	1.55
$\Phi/(^\circ)$	Amp				
	P_0	T_0	e_0	β	λ
15	0.00	0.00	0.00	0.00	0.00
30	−3.75	7.00	8.85	0.00025	0.33
45	−2.25	11.00	7.24	0.00032	0.46
60	−1.75	15.00	5.36	0.00081	0.74
75	−0.50	14.50	3.39	0.00062	0.30

$$\xi(\Phi,\ t)=\begin{cases}\xi_{\text{avg}}(\Phi_i)+[\xi_{\text{avg}}(\Phi_{i+1})-\xi_{\text{avg}}(\Phi_i)]m-\{\xi_{\text{amp}}(\Phi_i)+[\xi_{\text{amp}}(\Phi_{i+1})-\\ \xi_{\text{amp}}(\Phi_i)]m\}\cos[2\pi(t-28)/365.25], & 15^\circ<|\Phi|<75^\circ\\ \xi_{\text{avg}}(\Phi_i)-\xi_{\text{amp}}(\Phi_i)\cos[2\pi(t-28)/365.25], & |\Phi|\le 15 \text{ or } |\Phi|\ge 75^\circ\end{cases} \tag{5a}$$

$$m=(\Phi-\Phi_i)/(\Phi_{i+1}-\Phi_i) \tag{5b}$$

where Φ stands for the latitude of interest in degrees, ξ_{avg} is the computed average, i is the index of the nearest lower tabled latitude. ξ_{amp} stands for the computed amplitude. t is day of year.

If the meteorological parameter values are gained through the method mentioned before, the refractive index can be computed as

$$N_d(h)=k_1\frac{P_0}{T_0}\left[1-\frac{\beta h}{T_0}\right]^{\frac{g}{R_d\beta}-1}-k_1\frac{e_0}{T_0}\left[1-\frac{\beta h}{T_0}\right]^{\frac{g(\lambda+1)}{R_d\beta}-1} \tag{6a}$$

$$N_w(h)=k_2\frac{e_0}{T_0}\left[1-\frac{\beta h}{T_0}\right]^{\frac{g(\lambda+1)}{R_d\beta}-1}+k_3\frac{e_0}{T_0^2}\left[1-\frac{\beta h}{T_0}\right]^{\frac{g(\lambda+1)}{R_d\beta}-2} \tag{6b}$$

Combining the model of ray tracing, the refractive index anywhere can be gained if $r = h + r_1$. The refractive index can be computed as

$$n(r)=[N_d(r)+N_w(r)]\times 10^{-6}+1 \tag{7}$$

Tropospheric slant delay can be estimated accurately by putting the refractive index into ray tracing.

3 Data Processing and Results

In order to verify if the improved ray tracing model is truly more realistic than traditional model for tropospheric delay, a validation process was realized. In this approach we have used radiosonde-derived delays as reference (truth). We choose meteorological and radiosonde data from TSKB station in Japan in the year 2012. The information of TSKB station is showed in Table 2.

In order to verify the accuracy of the improved model, two schemes are proposed to compare; Scheme one: using the improved ray tracing model to estimate the slant delays at different elevations, such as 90°, 80°, 70°, 60°, 50°, 30°, 25°, 20°, 10°, 9°, 8°, 7°, 6°, 5°, 4° and Scheme two: taking the zenith delays computed by traditional models as Hopfield model and Saastamoinen model mapping to the same elevations through Neil mapping function. Comparing the results from two schemes with the truth, bias and RMS can be used to verify the accuracy. Table 3 summarizes the results. Absolute results are gained in order to analyze conveniently.

According to our results in Table 3, bias and RMS in the model of Hop-NMF and Saas-NMF are increasing with the angle decreasing, and close to zero, above 20

Table 2 Value of global troposphere atmosphere parameter

Station	ID	Lat.(N)	Lon.(E)	Hgt.(m)
TSKB	A	36.11	140.09	67.3

Where "Lat." stands for latitude, "Lon." stands for longitude, and "Hgt." is height

Table 3 Value of global troposphere atmosphere parameter

Angle	Hop-NMF		Saas-NMF		Improved model	
	Mean	RMS	Mean	RMS	Mean	RMS
90	0.0009	0.0032	0.0009	0.0029	0.0005	0.0001
80	0.0012	0.0033	0.0012	0.0033	0.0005	0.0001
70	0.0016	0.0035	0.0015	0.0036	0.0006	0.0002
60	0.0019	0.0036	0.0018	0.0037	0.0007	0.0003
50	0.0023	0.0038	0.0022	0.0039	0.0008	0.0004
30	0.0027	0.0039	0.0025	0.0041	0.0010	0.0005
25	0.0031	0.0041	0.0029	0.0047	0.0011	0.0006
20	0.0035	0.0043	0.0033	0.0069	0.0013	0.0008
10	0.0099	0.0681	0.0094	0.0508	0.0015	0.0019
9	0.0143	0.0713	0.0135	0.0558	0.0017	0.0022
8	0.0257	0.0749	0.0249	0.0624	0.0020	0.0025
7	0.0399	0.0790	0.0389	0.0713	0.0024	0.0029
6	0.0488	0.0838	0.0473	0.0739	0.0029	0.0035
5	0.0586	0.0904	0.0567	0.0826	0.0035	0.0036
4	0.0654	0.1020	0.0621	0.1015	0.0042	0.0042

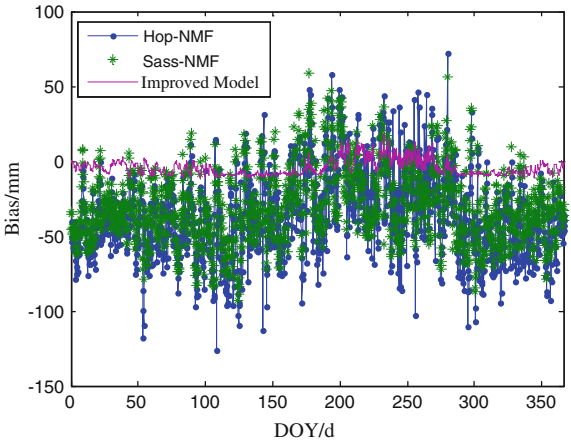

Fig. 2 Bias at 4° on TSKB station

angles. The results of Saas-NMF model are better than Hop-NMF, while the improved model in scheme one is better than Saas-NMF model. Especially at low angles, model in scheme one has improved one quantity.

Figures 2 and 3 show the bias vary at 4-angle and 10-angle by three models at TSKB station in 2012. From two figures, we can find that the trend of models of Hop-NMF and Saas-NMF are similar. Both of them appear major system bias, typically present seasonally. However, the improved model is better than others. Typically presenting randomly rise and fall, it shows that bias of improved model is also seasonally in a certain extent. It may account for the high variability of meteorological parameters in most regions and times.

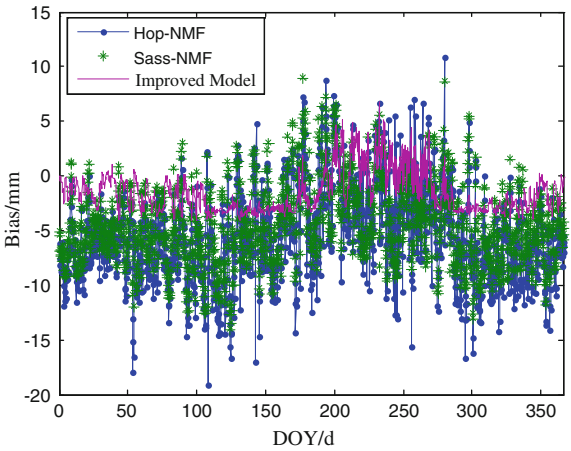

Fig. 3 Bias at 10° on TSKB station

4 Conclusions

In order to estimate tropospheric slant delays accurately, we introduce the model of ray tracing, and improved the refractive index model in ray tracing to overcome the dependence of radiosonde data through inserting in global grid of meteorological parameters. Meteorological data from four stations in Japan are analyzed based on ray tracing technology and tradition models, which demonstrate that the accuracy and stability of improved ray tracing method is superior to tradition models. Not only can the method adapt to the GNSS navigation position, it can also be used in the beidou second generation navigation and positioning. The method can precisely provide the tropospheric slant delay in the circumstances where measured meteorological data are absent, so it is of practical engineering significance to our national navigation position.

References

1. Heikki J, Reima E, Henrik V et al (2007) A variational data assimilation system for ground-based GPS slant delays. Q J R Meteorol Soc 133(625):969–980
2. Thomas P (2003) Tropospheric GPS slant delays at very low elevations. In: Proceedings of international, workshop on GPS meteorology. Institute for Geodesy and Navigation, University FAF Munich, Munich
3. Zhao H, Jiang C (2005) Phase corrections of spaceborne synthetic aperture radar in practical application. Chin J Radio Sci 20(1):48–51
4. Wang Z-B, Zhao L, Wang S-G et al (2014) COMPASS time synchronization and dissemination-Toward centimetre positioning accuracy. Sci China (Phy, Mech Astron) 57 (9):1788–1804
5. Lin HT, Huang YJ, Tseng WH et al (2012) Recent development and utilization of two-way satellite time and frequency transfer. J Metrol Soc India 27(1):13–22
6. Dodson AH, Chen W, Baker HC (2001) Assessment of EGNOS tropospheric correction model. J Navigation 54(1):37–55
7. Hopfield HS (1969) Two-quartic tropospheric refractivity profile for correction satellite data. J Geophys Res 74(18):4487–4499
8. Saastamoinen J (1973) Contribution to the theory of atmospheric refraction. Bulletin Geodesique 107(1):13–34
9. Neil AE (1996) Global mapping function for the atmospheric delay at radio wavelengths. J Geophysic Res 101(B2):3227–3246
10. Fang SUN, Wang H-G, Kang S-F et al (2008) A ray tracing algorithm for duct environment. Chin J Radio Sci 23(2):331–334
11. Zhu Q-L, Z-S WU, Zhao Z-W et al (2010) Tropospheric slant delay measured by singular ground-based satellite navigation receiver. Chin J Radio Sci 25(1):37–41
12. Zhao J-S, Song S-L, Chen QM et al (2014) Establishment of a new global model for zenith troposphere delay based on functional expression for its vertical profile. Chin J Geophys 57 (10):3140–3153
13. Zhang J-P (2013) Methods of retrieving tropospheric ducts above ocean surface using radar sea clutter and GPS signals. Doctoral dissertation, Xidian University, Xi'an
14. Huang L-K, Liu L-L, Wen HY et al (2014) Single-site improvement and accuracy analysis for zenith tropospheric delay of EGNOS model over asia area. Acta Geodaetica et Cartographica Sin 43(4):341–347

A Improving Method for Validating Ambiguity Resolution of BeiDou Static Baseline Solution with Medium-Long Baseline

Junjun Ying, Chuanzhen Sheng and Jingkui Zhang

Abstract In BeiDou static baseline solution with medium-long baseline (20–60 km), there are two problems: (1) selection of algorithm model; (2) selection of ambiguity validation value and validation methods. Theories and methods of static baseline solution of medium-long baseline are analyzed and compared respectively based on BeiDou B1 and B3 double-frequency observations. The results, which are based on observational datas, show that LC fixed solution model is obviously better than B1+B3 model. At the same time, we compare the single ratio validation method with the joint ratio validation method. The results show that: because of the ill condition of BeiDou system, the single ratio method has a false phenomenon. On this basis, a new method which bases on the residual of observation is added. It can reduce the probability of error and has good application value in engineering practice.

Keywords Medium-long baseline · Static baseline solution · LC fixed solution model · Single ratio validation method · Joint ratio validation method

1 Introduction

In BeiDou static baseline solution with medium-long baseline (20–60 km), there are two problems: (1) selection of algorithm model: Due to outlier of observational datas, larger residual error of double-difference atmospheric and effect of

J. Ying (✉) · C. Sheng · J. Zhang
State Key Laboratory of Satellite Navigation System and Equipment Technology, No. 589 West Zhongshan Road, Shijiazhuang 050081, Hebei, China
e-mail: yingjjcetc@163.com

C. Sheng
e-mail: shengchuanzhen@163.com

J. Zhang
e-mail: cetc_zjk@163.com

J. Ying · C. Sheng · J. Zhang
The 54th Research Institute of China Electronics Technology Group Corporation, Shijiazhuang, China

© Springer Science+Business Media Singapore 2016

J. Sun et al. (eds.), *China Satellite Navigation Conference (CSNC) 2016 Proceedings: Volume III*, Lecture Notes in Electrical Engineering 390,
DOI 10.1007/978-981-10-0940-2_51

multi-paths uncorrected bias, severely restricting medium-long baseline static baseline solution accuracy, so it is essential to choose suitable algorithm model of BeiDou medium-long baseline solution; (2) selection of ambiguity validation value and validation methods: Using carrier phase to achieve high-precision positioning relies on resoluting ambiguity reliably, however, due to the multiple impacts of uncorrected bias, ambiguity properly fixed probability will be reduced. Error ambiguity will lead to decimeter level or even greater positioning error, and to determine ambiguity is fixed correctly whether or not, depending on effective ambiguity validation method. Traditional single ratio validation method based on ambiguity, in ultra-short baseline, short baseline and no ill-condition normal equation situation, the validation is reliable, but for the BeiDou system, due to the constellation design features, GEO satellites of BeiDou change slowly, carrier phase measurements have strong correlation, resulting in equation severely ill-condition [1–3], and substantial increase of ratio value less than 2.0, only relying on single ratio validation method, some of the desirable fixed solution situation mistakes float solution, dramatically reducing the accuracy of medium-long baseline static solution.

Single ratio validation method is a ambiguity validation method based on parameter field, the correlation between parameters will reduce the effectiveness of the method, if we can increase validation method based on the measurement fields for joint validation, it will be more stable and reliable. In this paper, on the basis of single ratio validation method, increasing new ratio validation method based on observation residual quadratic form, has good application value in engineering practice.

2 Medium-Long Baseline Algorithm Model

For 20–60 km medium-long baseline static baseline solution, some software such as Bernere5.0 in GPS dealing strategy uses L1 + L2 model. If we use L1 + L2 model in BeiDou medium-long baseline solution, meanwhile, compared to LC fixed solution model, what will be the conclusions. To discuss this issue, the following will be based on BeiDou system, focusing on these two algorithm models. This paper respectively based on BeiDou B1 and B3 double-frequency observations, for the convenience of narration, GPS L1 + L2 double-frequency model is to be known as BeiDou B1+B3 double-frequency model.

2.1 B1+B3 Double-Frequency Model

Observation equations of B1+B3 double-frequency model are:

$$\Phi_{\mathrm{rb},1}^{jk} = \rho_{\mathrm{rb}}^{jk} + \lambda_1(N_{\mathrm{rb},1}^{\mathrm{j}} - N_{\mathrm{rb},1}^{\mathrm{k}}) + \varepsilon_{\mathrm{rb},\Phi}^{\mathrm{jk}} = \rho_{\mathrm{rb}}^{jk} + \lambda_1 N_{\mathrm{rb},1}^{\mathrm{jk}} + \varepsilon_{\mathrm{rb},\Phi}^{\mathrm{jk}} \quad (1)$$

$$\Phi_{\mathrm{rb},3}^{jk} = \rho_{\mathrm{rb}}^{jk} + \lambda_3\left(N_{\mathrm{rb},3}^{\mathrm{j}} - N_{\mathrm{rb},3}^{k}\right) + \varepsilon_{\mathrm{rb},\Phi}^{jk} = \rho_{\mathrm{rb}}^{jk} + \lambda_3 N_{\mathrm{rb},3}^{jk} + \varepsilon_{\mathrm{rb},\Phi}^{jk} \quad (2)$$

$$P_{\mathrm{rb},1}^{jk} = \rho_{\mathrm{rb}}^{jk} + \varepsilon_{\mathrm{rb},p}^{jk} \quad (3)$$

$$P_{\mathrm{rb},3}^{jk} = \rho_{\mathrm{rb}}^{jk} + \varepsilon_{\mathrm{rb},p}^{jk} \quad (4)$$

Among these, $\Phi_{\mathrm{rb},i}^{jk}$ and $P_{\mathrm{rb},i}^{jk}$ are double difference carrier (unit: m) and code combination observation, ρ_{rb}^{jk} is double difference value of pseudorange, λ_i is the wavelength of corresponding frequency, $N_{\mathrm{rb},i}^{j}$ and $N_{\mathrm{rb},i}^{k}$ are satellite j's single difference ambiguity and k's single difference ambiguity, $N_{\mathrm{rb},i}^{k}$ is satellite j's double difference ambiguity and k's double difference ambiguity, $\Delta \mathrm{I}_{r,i}^{s}$ is double difference ionospheric delay, $\varepsilon_{\mathrm{rb},\Phi}^{jk}$ and $\varepsilon_{\mathrm{rb},p}^{jk}$ are carrier's residual error and code's residual error (observational noise and not corrected model error).

The processing mode of B1+B3 double-frequency is based on observational datas for a long time. Firstly, expansion in accordance with the observation equation, solving ambiguity $N_{\mathrm{rb},1}^{jk}$ and $N_{\mathrm{rb},3}^{jk}$ float solution and position coordinates parameters, and then through searching to fix ambiguity, finally, return the result of fixed ambiguity to the above equation to obtain precise position coordinates.

2.2 LC Fixed Solution Model

For the medium-long baseline (20–60 km), the ionospheric correlation over two receivers weakens, the ionospheric delay of double difference residual is still bigger, so we can't take ignored process. Taking into account that ionospheric delay impact and frequency are closely related, through double-frequency elimination ionosphere combination, but the combination does not have integral characteristics, so we can't directly use the LAMBDA and other searching algorithm to make ambiguity fixed, but by decomposition, we can solve this problem. Equation of ionosphere-free linear combination and decomposed observation equation are as follows:

$$
\begin{aligned}
\mathrm{DD_{L3}} &= \frac{f_1^2\mathrm{DD_{L1}} - f_2^2\mathrm{DD_{L2}}}{f_1^2 - f_2^2} = DD_\rho - \frac{f_1^2\lambda_1\mathrm{DD}_{N1} - f_2^2\lambda_2\mathrm{DD}_{N2}}{f_1^2 - f_2^2} + \mathrm{DD_{trop}} + \mathrm{DD}_\varepsilon \\
&= \mathrm{DD}_\rho - \frac{f_1^2\lambda_1 \times (\mathrm{DD}_{N1} - \mathrm{DD}_{N2}) + \mathrm{DD}_{N2} \times \left(f_1^2\lambda_1 - f_2^2\lambda_2\right)}{f_1^2 - f_2^2} + \mathrm{DD_{trop}} + \mathrm{DD}_\varepsilon \\
&= \mathrm{DD}_\rho - \left(\frac{\mathrm{vlight} \times f_1 \times \mathrm{DD}_{N5}}{f_1^2 - f_2^2} + \frac{\mathrm{DD}_{N2} \times \mathrm{vlight}}{f_1 + f_2}\right) + \mathrm{DD_{trop}} + \mathrm{DD}_\varepsilon \\
&\quad or \\
\mathrm{DD_{L3}} &= \frac{f_1^2\mathrm{DD_{L1}} - f_2^2\mathrm{DD_{L2}}}{f_1^2 - f_2^2} = \mathrm{DD}_\rho - \frac{f_1^2\lambda_1\mathrm{DD}_{N1} - f_2^2\lambda_2\mathrm{DD}_{N2}}{f_1^2 - f_2^2} + \mathrm{DD_{trop}} + \mathrm{DD}_\varepsilon \\
&= \mathrm{DD}_\rho - \frac{f_1^2\lambda_1\mathrm{DD}_{N1} - f_2^2\lambda_2\mathrm{DD}_{N2} + f_2^2\lambda_2\mathrm{DD}_{N1} - f_2^2\lambda_2\mathrm{DD}_{N1}}{f_1^2 - f_2^2} + \mathrm{DD_{trop}} + \mathrm{DD}_\varepsilon \\
&= \mathrm{DD}_\rho - \left(\frac{\mathrm{vlight} \times f_2 \times \mathrm{DD}_{N5}}{f_1^2 - f_2^2} + \frac{\mathrm{DD}_{N1} \times \mathrm{vlight}}{f_1 + f_2}\right) + \mathrm{DD_{trop}} + \mathrm{DD}_\varepsilon
\end{aligned}
\tag{5}
$$

In the equation, $\mathrm{DD_{LC}}$, $\mathrm{DD_{L1}}$, $\mathrm{DD_{L3}}$ are double difference of ionosphere-free linear combination, double difference of B1 frequency, double difference of B3 frequency, f_1 and f_3 are B1's frequency and B3's frequency, DD_{N1}, DD_{N3} are double difference ambiguity of B1 and B3, DD_{N5} is wide-lane ambiguity, $\mathrm{DD}\rho$ is double difference of pseudorange, $\mathrm{DD_{trop}}$ is tropospheric error, DDs is residual error, and vlight is velocity of light.

Static baseline solution with Medium-long baseline is based on the above formula, the specific approach is: based on observational data for a long time, the first is to use the wide lane (B1 − B3) carrier double difference datas to solve the wide lane ambiguity DD_{N5}, then the width lane ambiguity DD_{N5} is substituted into the ionosphere-free linear combination, estimating DD_{N1} or DD_{N3} float solution and the coordinates (implicit in $\mathrm{DD}\rho$), and then through searching method to make DD_{N1} or DD_{N3} float solution fix, the final is to return the DD_{N1} or DD_{N3} integer solution to the above equation to get the precise location coordinates.

3 Two Kinds of Ambiguity Validation Methods

Static baseline solution of Medium-long baseline uses elimination ionosphere combination as the basic observation, when in the ambiguity solution, firstly, based on the principle of least squares to obtain ambiguous estimates, to get float ambiguity and covariance matrix, but because of big noise of elimination ionosphere combination observation, the initial solution of float ambiguity has large deviation, to get various ambiguity alternate groups with integer properties based on the float ambiguity, must through effective ambiguous validation methods. In the following, we will focus on the single Ratio validation method and joint validation method.

3.1 Single Ratio Validation Method

After searching the ambiguity, R_i, which is residual quadratic form of ambiguity, can be expressed as:

$$R_i = \left(\breve{N} - \widehat{N}\right)^T Q_{\widehat{N}}^{-1} \left(\breve{N} - \widehat{N}\right) \tag{6}$$

$$\text{Ratio} = R_s / R_m \tag{7}$$

In the above formula, $\breve{N}$ is ambiguity fixed solution, $\widehat{N}$ is ambiguity float solution, R_s is the second smallest residual quadratic form of ambiguity, R_{m} is the minimum value of ambiguity residual quadratic form, Ratio is their ratio. The statistics can be easily obtained after the ambiguity search, and the operation is simple. Meanwhile, the result of this test is more consistent with the actual situation, which is also the current main ambiguity confirmation method [4]. In GPS actual production, the statistic threshold is usually set as 3.0 [4], in some BeiDou literature [5], Ratio threshold is set as 2.0, according to BeiDou static baseline solution engineering practice, Ratio threshold can be set as 1.6.

3.2 Joint Validation Method

Usually, in the no ill-condition normal equation, Ratio value is greater than 2.0, single ratio validation method can be considered as reliable integer ambiguity solution, but for BeiDou system, due to the normal equation is in seriously ill condition, often can't meet the condition that Ratio value is greater than 2.0 [6], and therefore, we can use the following method which is based on measurement fields to assist validation:

$$V^T P V = R_v \tag{8}$$

$$R_{v,i-1} / R_{v,i} = \text{Ratio}_v \tag{9}$$

In the equation, V is the observational residual, P is the weight of observation, $R_{v,i-1}$ represents the second smallest sum of squared residuals, $R_{v,i}$ represents the minimum sum of squared residuals. Engineering practice shows that for the BeiDou medium-long baseline, using Ratio value and Ratiov value to validate, the validation accuracy of ambiguity improves significantly. Joint validation method specific implementation process is: when the Ratio value is greater than or equal to 1.6, the ambiguity is properly fixed, get the fixed solution, but when Ratio is less than 1.6, continue to increase Ratiov value to determine, if the Ratiov value is greater than or equal to 2.0, ambiguity is fixed, if Ratiov value is less than 2.0, the ambiguity is not fixed properly, then we get the float solution.

4 Experimental Data Analysis

4.1 Comparative Analysis of LC Fixed Solution Model and B1+B3 Model

Selecting BeiDou's static observation datas, in North China, December 12th, 2013, the baseline length is 41 km, the sampling interval is one second, a total of 11 observation periods, four hours for each period. LC fixed solution processing mode of self-developed software and B1+B3 static mode of RTKLIB software are used for processing, cut-off angles of satellites are set as 15° in calculating.

Figures 1 and 2 are respectively plane accuracy and vertical accuracy comparison chart of LC fixed solution model and B1+B3 model, we can see from the figures: LC fixed solution model's plane accuracy and vertical accuracy are in the centimeter level, B1+B3 model's plane accuracy and vertical accuracy are in the decimeter level, LC fixed solution model is significantly better than B1+B3 model.

Practice has proved that because of BeiDou system constellation design and GEO satellite multi-path effect is more serious than GPS, BeiDou static baseline solution with medium-long baseline is not suitable to use B1+B3 mode, but suitable to use LC fixed solution model.

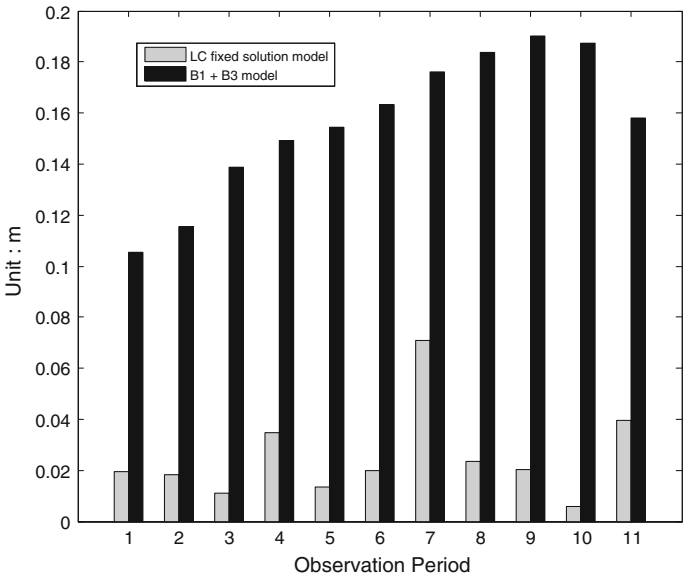

Fig. 1 Horizontal accuracy comparison chart of LC fixed solution model and B1+B3 model

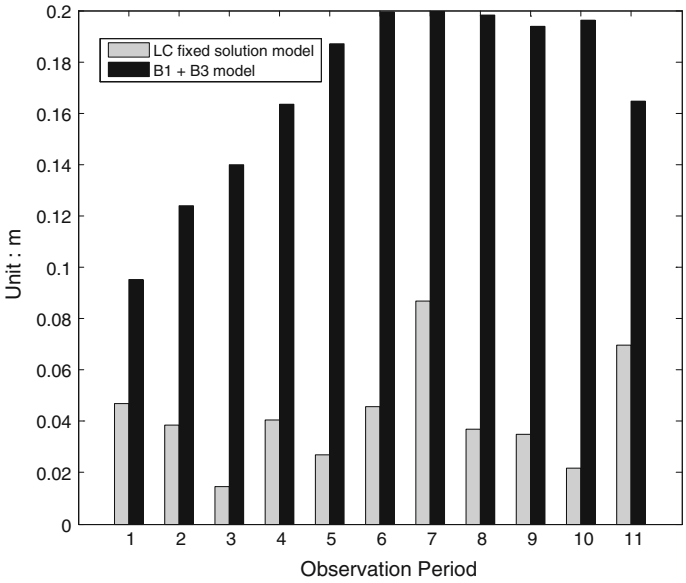

Fig. 2 Vertical accuracy comparison chart of LC fixed solution model and B1+B3 model

4.2 Comparative Analysis of Two Ambiguity Validation Methods

Selecting BeiDou static observation data, November 21st, 2013, in North China, baseline length is 43 km, a total of 15 observation periods, sampling interval is one second, four hours for each period, using LC fixed solution model of self-developed software for processing, the cut-off angles of satellite are set as 15° in calculating. Table 1 shows the plane accuracy and vertical accuracy comparison of two validation method, the single Ratio validation method is a method for using only traditional ambiguity residuals quadratic, Ratio + Ratiov validation method is a ambiguity validation method on the basis of Ratio increasing the observed value of residual quadratic, namely Ratio + Ratiov joint validation method.

Figure 3 is horizontal accuracy comparison of two kinds of methods for ambiguity validation. Figure 4 is vertical accuracy comparison of two kinds of methods for ambiguity validation.

From the chart and the table we can see: (1) When Ratio value is greater than 1.6, plane accuracy and vertical accuracy of single Ratio validation method and Ratio + Ratiov joint validation method are the same; (2) When Ratio value is less than 1.6, only using single Ratio validation method, taking ambiguity float solution, the plane accuracy and vertical accuracy are at or near decimeter magnitude, while using Ratio + Ratiov joint validation method, it will greatly reduce ambiguity validation error probability, at the same time, the plane and vertical accuracy reach

Table 1 Accuracy comparison of two kinds of methods for ambiguity validation

Period	Validation method	Validation value	Plane accuracy (m)	Vertical accuracy (m)
1	Single ratio validation method	1.40	0.0439	0.1256
	Ratio + Ratiov validation method	1.40 & 5.77	0.0273	−0.0139
2	Single Ratio validation method	1.79	0.0252	0.0263
	Ratio + Ratiov validation method	1.79 & 7.88		
3	Single Ratio validation method	1.63	0.0235	0.0258
	Ratio + Ratiov validation method	1.63 & 6.53		
4	Single Ratio validation method	1.42	0.0821	0.0803
	Ratio + Ratiov validation method	1.42 & 2.97	0.0215	−0.0154
5	Single Ratio validation method	1.28	0.1028	0.0700
	Ratio + Ratiov validation method	1.28 &1.29	0.1028	0.0700
		Mandatory fixation	0.0204	−0.0168
6	Single ratio validation method	1.31	0.0849	0.0904
	Ratio + Ratiov validation method	1.31 & 2.56	0.0190	−0.0182
7	Single Ratio validation method	1.41	0.0819	0.0927
	Ratio + Ratiov validation method	1.41 & 2.54	0.0181	−0.0186
8	Single Ratio validation method	1.53	0.0862	0.0957
	Ratio + Ratiov validation method	1.53 & 2.06	0.0181	−0.0191
9	Single Ratio validation method	1.93	0.0165	0.0173
	Ratio + Ratiov validation method	1.93 & 2.22		
10	Single Ratio Validation method	2.16	0.0167	0.0210
	Ratio + Ratiov validation method	2.16 & 3.15		
11	Single Ratio validation method	2.10	0.0163	0.0221
	Ratio + Ratiov validation method	2.10 & 3.28		

(continued)

Table 1 (continued)

Period	Validation method	Validation value	Plane accuracy (m)	Vertical accuracy (m)
12	Single Ratio validation method	2.10	0.0165	0.0223
	Ratio + Ratiov validation method	2.10 & 3.27		
13	Single Ratio validation method	2.11	0.0180	0.0256
	Ratio + Ratiov validation method	2.11 & 3.3		
14	Single Ratio validation method	2.11	0.0181	0.0258
	Ratio + Ratiov validation method	2.11 & 3.29		
15	Single Ratio validation method	2.11	0.0182	0.0259
	Ratio + Ratiov validation method	2.11 & 3.28	0.0182	0.0259

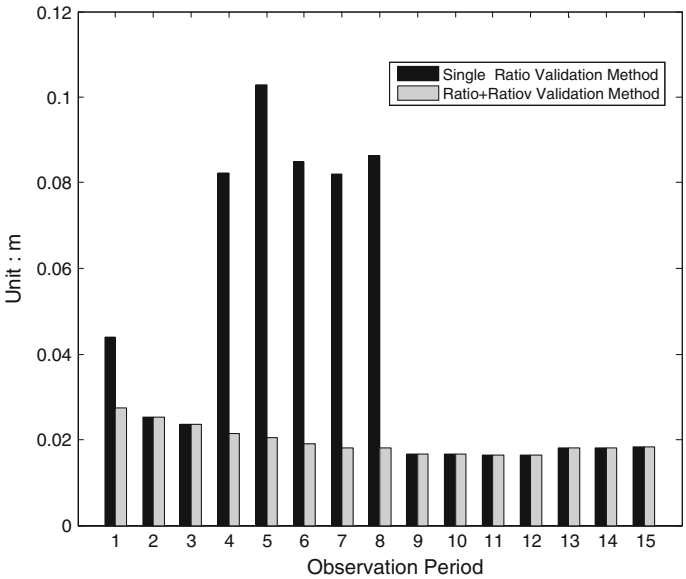

Fig. 3 Horizontal accuracy comparison of two kinds of methods for ambiguity validation

centimeter level; (3) Usually, Ratiov value is greater than Ratio value, and when both are similar and less than 1.6, there is a possibility of mistaking float solution, such as group 5 in the chart, if we enforce to take the fixed solution, the plane

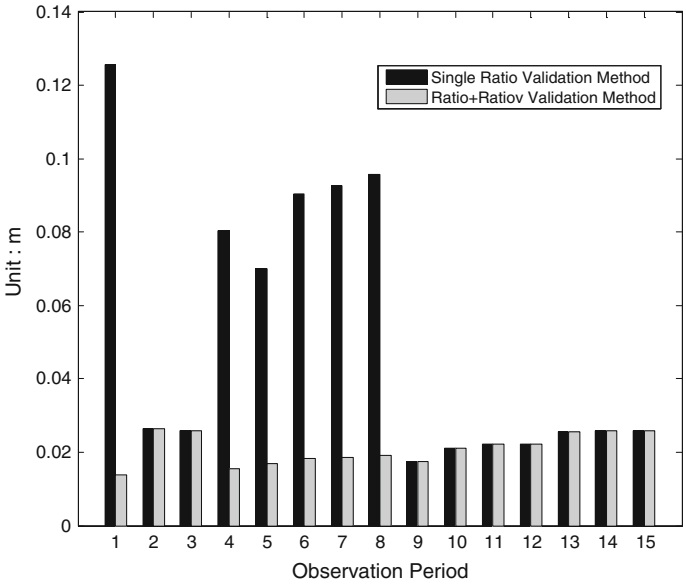

Fig. 4 Vertical accuracy comparison of two kinds of methods for ambiguity validation

accuracy and vertical accuracy are obviously better than taking the float solution accuracy. Despite the possibility of joint validation mistakes, but overall, Ratio + Ratiov joint validation method is superior to single Ratio validation method, it can substantially increase the probability of correctly validating ambiguity.

5 Conclusion

In this paper, we discuss two problems of static baseline solution with BeiDou medium-long baseline: selection of algorithm model and selection of ambiguity validation value and validation methods. The results show that: for BeiDou medium-long baseline solution, LC fixed solution model is significantly better than B1+B3 model. Because of BeiDou system's ill condition, ratio value is small, the traditional single ratio method has error phenomenon of validation, but on the basis of single ratio validation method, adding a valid method based on observation value residuals square, reduces the probability of ambiguity validation errors, has realistic significance in engineering practice.

Acknowledgement This research was supported by Research on Precision Positioning Technology with Terminal based on Satellite-Based Augmentation by State Key Laboratory of Satellite Navigation System and Equipment Technology (EX1501D0063).

References

1. Wang S, Wang Q, Nie W, Pan S (2013) Analysis and solution of Ill-conditioned Problems in BeiDou system high-precision high-orbit satellite positioning model. J Navig Positioning, 1(3):31–32
2. Qiu X, Liu G, Duan P, Wang B, Sha W (2015) Comparison analysis of Ill-condition for GPS and BeiDou carrier phase positioning, Sci Surv Mapp 40(7)
3. Wang S, Wang Q, Gao W, Pan S (2013) Analysis and valuation of Ill-condition in GNSS Multi-system baseline solution. J Southeast Univ (Nat Sci Ed) 43(4):753–757
4. Liu J, Deng C, Tang W (2014) Research progress on the theory and method of ambiguity validation of GNSS. Geomatics Inf Sci Wuhan Univ 39(9)
5. Yang Y, Li J, Wang A et al. (2014) Preliminary assessment of the BeiDou regional satellite navigation system basic navigation and positioning performance. Earth Sci 57(1):144–152
6. Luo X (2007) Theory and data processing of network RTK. Doctoral dissertation of Chinese Academy of Sciences

A Modified Algorithm of Phase-Smoothed Pseudorange Based on Doppler Frequency Shift

Zhiyong Lu, Ye Jin, Yuanhao Yu and Lijun Ma

Abstract Phase-smoothed pseudorange algorithm is the commonly used pseudorange smoothing algorithm in navigation receivers. This paper analyses characteristics of weight factors of traditional smoothing algorithms and correlations in epochs. Proposes a modified smoothing algorithm based on Doppler frequency shift. This paper compares precisions of M-order, Hatch and this modified smoothing algorithm using original data from BeiDou receivers. Results show the modified algorithm obviously improves precisions of traditional smoothing algorithms, which can offer great reference for designation of pseudorange algorithm of navigation receivers.

Keywords Pseudorange algorithm of navigation receiver · Phase-smoothed pseudorange · Hatch filter · Doppler frequency shift

1 Introduction

The error of carrier phase measurement in range is of centimeter level or below, while the error of code pseudorange measurement is two orders larger than carrier phase measurement, but ambiguity resolution is not existed in code pseudorange measurement. Carrier phase smoothing code pseudorange algorithm is the foundation of positioning in the navigation receiver and it is commonly used in single or

Z. Lu (✉) · Y. Yu · L. Ma
Unit 61876, no. 27, ShiBu Farm Road, Sanya, Hainan, China
e-mail: livingmore@163.com

Y. Yu
e-mail: yyhpla@126.com

L. Ma
e-mail: 25995327@qq.com

Y. Jin
School of Information Science and Technology, Peking University, Beijing, China
e-mail: jinye@pku.edu.cn

© Springer Science+Business Media Singapore 2016

J. Sun et al. (eds.), *China Satellite Navigation Conference (CSNC) 2016 Proceedings: Volume III*, Lecture Notes in Electrical Engineering 390,
DOI 10.1007/978-981-10-0940-2_52

dual-frequency positioning [1]. The smoothing algorithm is also used in precise orbit determination based on multi-frequency measurements [2].

Hatch filtering is the basic algorithm of carrier phase smoothing code pseudo-range [1, 3]. Modified algorithms are proposed based on Hatch filtering. Fan Shijie improved Hatch algorithm by considering the elevation angle [4]. Yang Chunyan proposed an algorithm based on complementary Kalman filtering [5]. Lee proposed an optimal recursion estimation algorithm considering pseudorange error covariance [6]. Sun Zhengming discussed the smoothing effects of different weight factors in dual-frequency positioning [7]. He Haibo compared Hatch filtering of different weight factors [8]. Taking the random relative motion between the receiver and satellites into consideration, weight factors of smoothing should be affected by random motion. The paper proposed a modified algorithm of carrier phase smoothing code pseudorange based on Doppler frequency shift. The algorithm can improve the effect of smoothing by modifying the weight factor of Hatch filtering.

2 Analyze of Correlations in Epochs of Different Smoothing Algorithm

Take single-frequency measurement for example, the equation of carrier phase smoothing code pseudorange is:

$$\hat{P}_i = w_i \cdot P_{i-1} + (1 - w_i) \cdot (\hat{P}_{i-1} + \Delta\Phi_i) \tag{1}$$

$$\hat{P}_1 = P_1$$

$\hat{P}_{i-1}$, $\hat{P}_i$ is the pseudo-range results in t_{i-1}, t_i, $\Delta\Phi_i = \Phi_i - \Phi_{i-1}$, Φ_{i-1}, Φ_i is the carrier phase in range in t_{i-1}, t_i, w_i is the weight factor in epoch t_i. $\Delta\Phi_i$ has no cycle slip if the receiver is in continuous tracking. $w_i = 1/M$ in M-order filtering and $w_i = 1/i$ in Hatch filtering. w_i can also be modified by elevation angle in epoch t_i.

Transform Eq. (1) into non-recursion equation:

$$\begin{aligned}
\hat{P}_i &= w_i \cdot P_{i-1} + (1 - w_i) \cdot \Delta\Phi_i + (1 - w_i) \cdot \hat{P}_{i-1} \\
&= w_i \cdot P_{i-1} + (1 - w_i) \cdot \Delta\Phi_i + (1 - w_i) \\
&\quad \cdot \left(w_{i-1} \cdot P_{i-2} + (1 - w_{i-1}) \cdot \Delta\Phi_{i-1} + (1 - w_{i-1}) \cdot \hat{P}_{i-2}\right) \\
&= w_i \cdot P_{i-1} + (1 - w_i) \cdot \Delta\Phi_i + \sum_{k=1}^{i-2} (1 - w_{k+2}) \\
&\quad \cdot w_{k+1} \cdot P_k + \sum_{k=2}^{i-1} (1 - w_{k+1}) \cdot (1 - w_k) \cdot \Delta\Phi_k
\end{aligned} \tag{2}$$

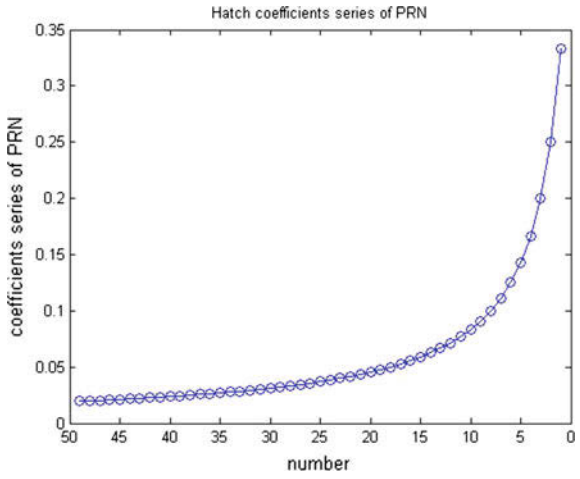

Fig. 1 Coefficients of PRN in Hatch smoothing at each epoch

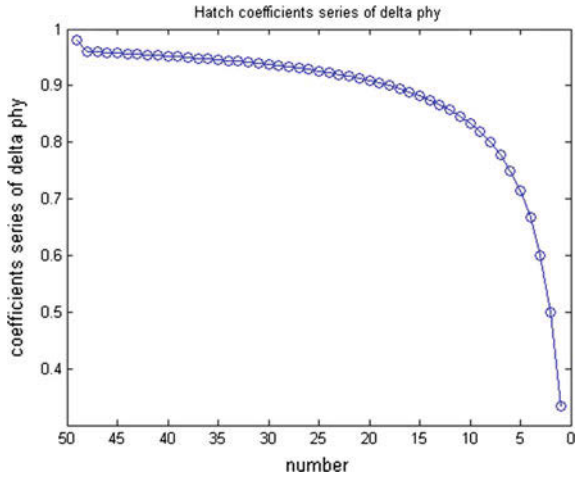

Fig. 2 Coefficients of phase difference in Hatch smoothing at each epoch

50 epoch are selected for analyze. The coefficients of P_k and $\Delta\Phi_k$ are drawn in Figs. 1, 2, 3 and 4.

The figure obviously shows that the coefficients of P_k and $\Delta\Phi_k$ are almost equal, which means the estimated value of pseudo-range of epoch t_i is equal-weighted depends on the M epochs before. In Hatch smoothing algorithm, the coefficients of P_k decreases gradually where the coefficients of $\Delta\Phi_k$ increases gradually as the epoch increases, which means the estimated value of pseudorange of epoch t_i basically depends on the increments of $\Delta\Phi_k$. The coefficients in previous epochs can be understood as the correlations of current epoch and previous epochs. So the correlations from $\Delta\Phi_k$ is higher as the epochs are closer in Hatch filtering and the correlations from $\Delta\Phi_k$ is basically equal in previous M epochs in M-order filtering.

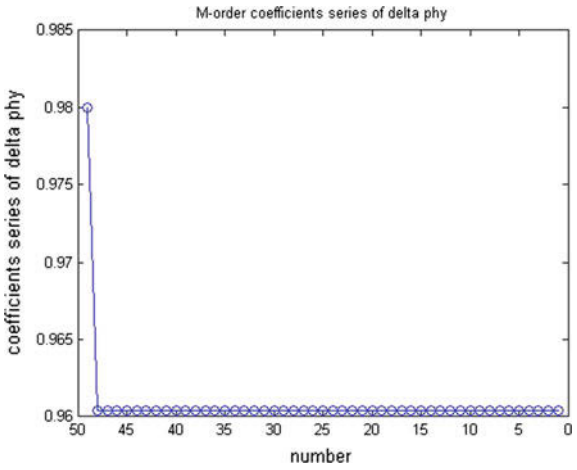

Fig. 3 Coefficients of PRN in M-order smoothing at each epoch

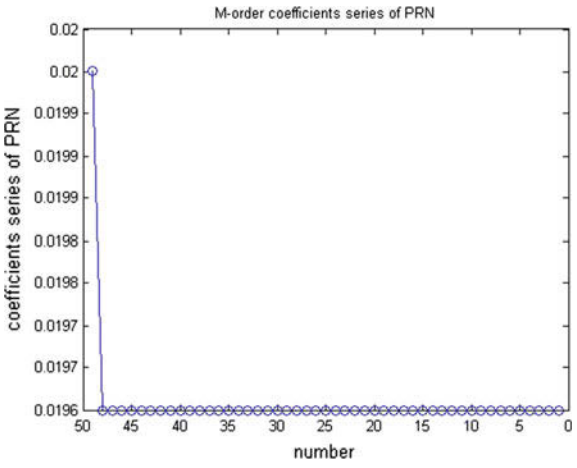

Fig. 4 Coefficients of phase difference in M-order smoothing at each epoch

The receiver and satellite are in random motion in most application scenario, the correlation of current epoch and previous epoch decreases as epoch furthers. Obviously, weight factors of Hatch filtering are more suitable for smoothing algorithm from perspective of correlations in epochs.

3 Weight Factors Based on Doppler Frequency Shift

Pseudorange varies as range of receiver and satellite varies. It is more precise to measure range change in phase difference between adjacent epochs because of the high precisions of carrier measurements. So the weight factor of $\Delta\Phi_k$ should be

greater when the relative motion velocity is larger. From perspective of correlations in epochs, the larger of the relative random motion velocity, the smaller correlations generated in previous epochs. The coefficients of P_k should be smaller and the coefficients of $\Delta\Phi_k$ should be larger.

From equation $f_d = \frac{\vec{v}\cdot\vec{e}_r}{\lambda} = \frac{\delta(d_r)}{\lambda}$, we can know the radial range change (or radial velocity) is in proportion to the Doppler frequency shift measured by receiver. Therefore the weight factors $\Delta\Phi_i$ of should be greater when the Doppler frequency shift is higher. Proposed a modified algorithm expressed in Eq. (3):

$$\hat{P}_i = w_i^d \cdot P_{i-1} + (1 - w_i^d) \cdot (\hat{P}_{i-1} + \Delta\Phi_i) \tag{3}$$

$w_i^d = \beta_i(f_{d,i}) \cdot w_i$, where $f_{d,i}$ is the Doppler frequency shift in epoch t_i and $\beta_i(f_{d,i})$ is the modification factor related to $f_{d,i}$. Based on discussions before, w_i should be smaller to better indicate the random motion when the $f_{d,i}$ is greater. A method of determine $\beta_i(f_{d,i})$ is given in Eq. (4):

$$\beta_i(f_{d,i}) = \left(1 + \frac{f_{d,i}}{(f_d)_{\max}}\right)^{-1} \tag{4}$$

4 Calculation Examples

To verify validity of modified algorithm, calculate data of 300 epochs in Nov, 2015 from BeiDou receiver in Hainan. The data include B1IW pseudo-range, carrier phase and Doppler frequency shift measurements of an IGSO satellite and a MEO satellite. Compares the modified algorithm based on Doppler frequency shift with traditional M-order and Hatch smoothing algorithm. Residuals are drawn in Figs. 5, 6, 7 and 8.

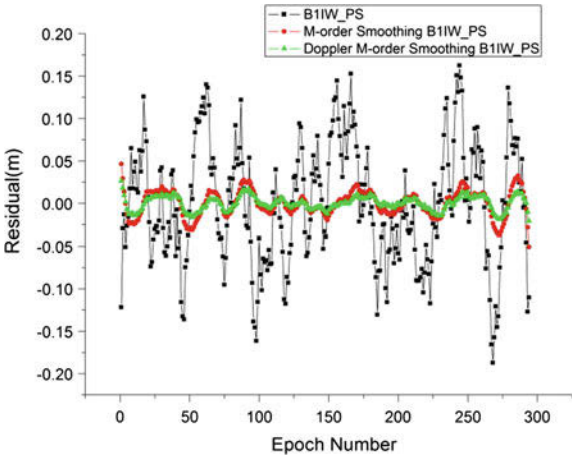

Fig. 5 Modified M-order smoothing algorithm of IGSO B1IW_PS

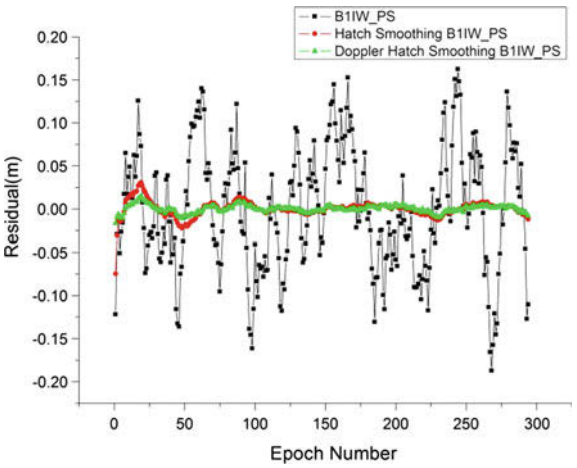

Fig. 6 Modified Hatch smoothing algorithm of IGSO B1IW_PS

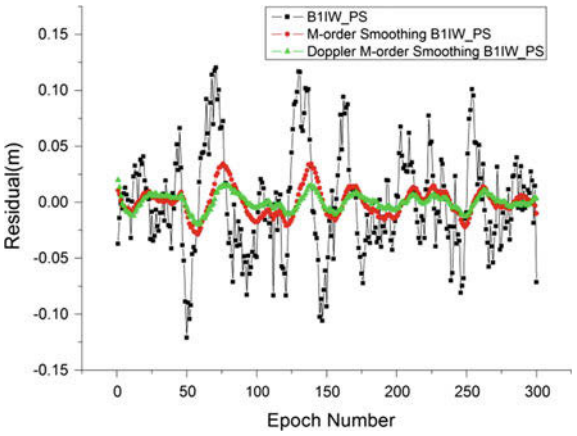

Fig. 7 Modified M-order smoothing algorithm of MEO B1IW_PS

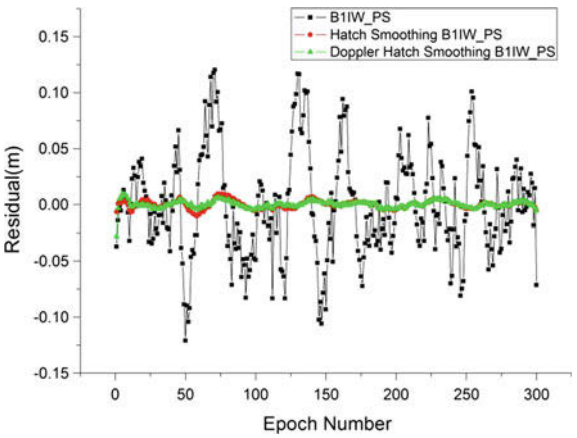

Fig. 8 Modified Hatch smoothing algorithm of MEO B1IW_PS

Table 1 Comparisons of residual variance of different algorithms (m in unit)

Satellite type	B1IW code pseudo-range residual variance	B1IW code carrier phase residual variance	M-order smoothing	Modified M-order smoothing	B1IW Hatch smoothing	Modified B1IW Hatch smoothing
MEO	0.0472	0.0015	0.0128	0.0072	0.0036	0.0028
GSO	0.0720	0.0033	0.0151	0.0082	0.0092	0.0045

Residual variances of different algorithms are shown in Table 1.

Results show that: (1) Smoothing algorithm can notably improve the precisions of pseudorange measurements and Hatch smoothing is better than M-order smoothing, which can verify the methods and conclusion of analyze of correlations in epochs; (2) Smoothing algorithm-based Doppler frequency shift can improve the precisions of traditional algorithm such as Hatch and M-order; (3) Calculations of original data from BeiDou receiver shows algorithm based on Eq. (4) can improve the residual variance by 22–50 %.

5 Conclusion

The modified algorithm of phase-smoothed pseudorange based on Doppler frequency shift gives adequate consideration in affection of random motion between navigation receiver and satellite. Precision of traditional smoothing algorithm such as M-order and Hatch can be improved through adding modification factor based on Doppler frequency shift. Results of calculation of original data from BeiDou receiver show that precisions can be improved by 22–50 %, which means the modified algorithm is effective in carrier phase smoothing code pseudorange. The algorithm has practical value and can be used in combination of phase and code observations in navigation receivers.

References

1. Misra P, Enga P (2006) Global positioning, system signal, measurements, and performance, 2nd edition. Ganga-Jamuna Press, Massachusetts, pp 137–141
2. Sun B, Ou J (2010) Precise orbit determination of GEO navigation satellites based on multi-frequency carrier phase measurements, vol 1, pp 688–700
3. Hatch R (1982) The synergism of GPS code and carrier measurements. In: Proceedings of the third international symposium on satellite doppler positioning, vol 2, pp 1213–1231
4. Fan S, Guo J (2005) Accuracy research on GPS dual frequency phase-smoothed pseudo-range and tis point positoing. In: Engineering of surveying and mapping, vol 14, No 4, pp 1006–7949 (04-0039-04:39-42)
5. Yang C, Wu D (2008) A phase-smoothed pseudo-range algorithm based on complementary Kalman filtering. J Air Force Eng Univ (Nat Sci Ed) 9(25):1009–3516 (05-0052-05:52-56)

6. Lee HK, Rizos C, Jee IG (2003) Design and analysis of DGPS filters with consistent error covariance information. In: Proceedings of 6th international symposium on satellite navigation technology including mobile positioning and location services, vol a, p 47
7. Sun Z, Gao J (2007) Discussion on weighting factors of GPS dual frequency phase smoothed pseudo-range. Hydrogr Survey Charting 24(4):1671–3044 (04-0013-04:39-42)
8. He H, Guo H (2005) Re-evaluation of two carrier smoothed code algorithms for WADGPS reference stations. J Institude Survey Mapp 22(3):1009-427X (03-0157-03:157-159)

VTEC Modeling and Analysis for Single Station Based on Moving Time Window

Yadong Bao, Changjian Liu, Hongzhou Chai and Xu Feng

Abstract The principle of VTEC modeling for single station based on moving time window was introduced. First, extract STEC between station and satellites using the combination observations of dual-phase (or pseudo-range), and convert STEC to VTEC using projection function. Then, fit the regional VTEC by moving the time window to achieve continuous modeling of single station regional VTEC. Two IGS stations (REDU and LHAZ) at DOY 300 in year 2015 were carried out modeling practices according to this method. The answers were compared and analyzed with GIMs. The results show that: the modeling answer based on moving time window shared similar characteristics in space change with GIMs, but most of VTEC values in this method were lower than GIMs. The result of REDU was closer to GIMs than LHAZ's, which was mainly caused by the uneven distribution of IGS stations. The modeling method based on moving time window had a higher temporal and spatial resolution, and not affected by the density of the stations distribution. The results could be used instead GIMs instead of GIMs.

Keywords Moving time window · VTEC modeling · GIMs · Combination observations · Polynomial fitting

1 Introduction

With the rapid development and continuous improvement of multi-band and multi-mode GNSS technology, the methods to establish ionospheric VTEC model using GNSS data are gradually mature [4, 10]. The ionospheric models that can be applied to engineering practice are always divided into two [6]: empirical models and mathematical models. The empirical models are statistical models which are established by a large number of long-term observations to describe the ionospheric activities in the silent states. They are always used by single-frequency GNSS users

Y. Bao (✉) · C. Liu · H. Chai · X. Feng
Institute of Geospatial Information, Information Engineering University, Zhengzhou, China
e-mail: geoboydong@163.com

© Springer Science+Business Media Singapore 2016

J. Sun et al. (eds.), *China Satellite Navigation Conference (CSNC) 2016 Proceedings: Volume III*, Lecture Notes in Electrical Engineering 390,
DOI 10.1007/978-981-10-0940-2_53

because of the poor accuracy and correction effects. The mathematical models are fitting models according to actually measured values within a certain period or a region. The mathematical models always include polynomial model, triangular series model, spherical harmonics model, etc. [8]. Global Ionosphere Maps (GIMs), a gridded result from the spherical harmonic model, is widely recognized with the reliable data quality and wider scope of application, but the needed values of VTEC in applications should always be gotten by interpolation because of the limited spatial resolution of 2.5° × 5° and time resolution of 2 h [3, 7]. Meanwhile, the precision of GIMs grid between different regions may be in a large difference because of the uneven distribution of observation stations. Therefore, it becomes particularly necessary to conduct multi-station or single station modeling in the station-less areas. The polynomial model, as one of the main methods to simulation regional VTEC, is widely used [2]. Liu et al. [6] applied the polynomial model to China's wide area differential positioning system for ionospheric TEC modeling, and reached a good result. It is also used in some GNSS data processing software, such as BERNESE developed by the University of Bern [1]. Some other scholars also studied the polynomial model, and the results show that it has a good effect on regional ionospheric VTEC modeling. But the continuity is usually not enough when using polynomial to model the regional VTEC, because the time windows are segmented. The ideal results are still hard to reach, even though restrictions were imposed at junctions [5]. For this reason, applying moving time window into polynomial model is proposed to improve convergence at junctions. This paper will analyze the moving time window method by practicing single station modeling, so as to provide a reference for the study of regional VTEC modeling methods.

2 Principle of Polynomial Model Based on Moving Time Window

2.1 Extraction of VTEC

GNSS observations mainly include carrier phase and pseudorange for VTEC extracting. The observation equations only first-order ionospheric delay considered can be expressed by

$$L_i^s(t) = \rho^s(t) + \lambda_i N_i^s(t) - \frac{40.308}{f_i^2} \cdot \mathrm{STEC}(t) + v_{i,L}^s(t) \tag{1}$$

$$P_i^s(t) = \rho^s(t) + \frac{40.308}{f_i^2} \cdot \mathrm{STEC}(t) + v_{i,P}^s(t) \tag{2}$$

where i is the number of frequency, s represents satellite, L represents carrier phase, P represents pseudo-range, f_i is frequency, t is the observation time, $L_i^s(t)$ and $P_i^s(t)$

is observed value, $\rho^s(t)$ is the geometric distance between the satellite and the receiver, λ_i is the length of signals, $N_i^s(t)$ is the ambiguity of $L_i^s(t)$, $I_i^s(t)$ is the ionospheric delay, $v_{i,L}^s(t)$ and $v_{i,L}^s(t)$ represent the other factors of error, where mainly includes the Differential Code Bias (DCB). STEC(t) is the total electrons along the ray-path. According to single-layer ionospheric theory, the relation between STEC(t) and VTEC(t) can be expressed as

$$\mathrm{VTEC}(t) = \cos z' \cdot \mathrm{STEC}(t) \tag{3}$$

where is the zenith of the Ionospheric Pierce Point (IPP) along the ray-path. From Eqs. (1) and (2), when the effects of $v_{i,L}^s(t)$ and $v_{i,P}^s(t)$ were neglected, the geometry-free linear combinations of carrier phase and pseudo-range can be derived as

$$\begin{aligned} L_4^s(t) = L_2^s(t) - L_1^s(t) = -\left(\frac{40.308}{f_2^2} - \frac{40.308}{f_1^2}\right) \cdot \mathrm{STEC}(t) \\ + \lambda_2 N_2^s(t) - \lambda_1 N_1^s(t) \end{aligned} \tag{4}$$

$$P_4^s(t) = P_2^s(t) - P_1^s(t) = \left(\frac{40.308}{f_2^2} - \frac{40.308}{f_1^2}\right) \cdot \mathrm{STEC}(t) \tag{5}$$

where $L_4^s(t)$ and $P_4^s(t)$ are geometry-free linear combinations of carrier phase and pseudo-range. From Eqs. (3), (4) and (5), VTEC can be shown as:

$$\mathrm{VTEC}(t) = -\frac{L_4^s(t) - \lambda_2 N_2^s(t) + \lambda_1 N_1^s(t)}{40.308/f_2^2 - 40.308/f_1^2} \cos z' \tag{6}$$

$$\mathrm{VTEC}(t) = \frac{P_4^s(t) - v_{2,P}^s(t) + v_{1,P}^s(t)}{40.308/f_2^2 - 40.308/f_1^2} \cos z' \tag{7}$$

According to Eqs. (6) and (7), when $\lambda_2 N_2^s(t) - \lambda_1 N_1^s(t)$, DCB, etc., were clear, the VTEC series can be easily extracted from the dual observations.

2.2 *Establishment of Polynomial Model Based on Moving Time Window*

The polynomial models of ionospheric VTEC can be shown as a function of hour angle difference and latitude difference (Eq. (8)).

$$\mathrm{VTEC} = \sum_{i=0}^{n} \sum_{k=0}^{m} C_{i,k} (B - B_0)^i (L + t - L_0 - t_0)^k \tag{8}$$

where n and m are the maximum order, (B_0, L_0) is geodetic coordinate of the development point, t_0 is the mid-time of single time window, (B, L) is the geodetic coordinate of IPPs, t is the real time of VTEC, $C_{i,k}$ is the parameter to be estimated. When the area to be modeled is not wider than a state's, the polynomial models can reach a good result by setting period length as 4 h, m as 2–4, and n as 1–2 [9]. But it is obvious that the difference between the model results from Eq. (8) and the actual VTEC will get enhanced with the increases of $|t - t_0|$. However, the idea of establishing polynomial models based on moving time windows will reduce this problem in some cases. The basic process of moving time windows can be described as follows: First, model the VTEC at the time window from T_1 to T_2 using polynomial according to Eq. (8), and only retain the results around $(T_1 + T_2)/2$; Then, move the time window for Δt, and model for the time widow from $(T_1 + \Delta t)$ to $(T_2 + \Delta t)$. Repeat the above methods until the time windows through the entire observation period.

3 Simulation and Analysis

Here, the VTEC values observed by REDU (in Europe) and LHAZ (in China) on the day 300/2015 (dd/yy) are extracted according to Eqs. (6) and (7). Finally, regional VTEC grid map with a spatial resolution of 1° × 1° and at the height of 450 km is established according the method of moving time widow. In order to reduce the impact from multi-path effects, atmospheric, etc., the cut-off elevation angle of IPPs is set as 20°. Figure 1 shows the distribution of grid in the polar coordinates based on azimuth and geocentric angle from station's. There are total

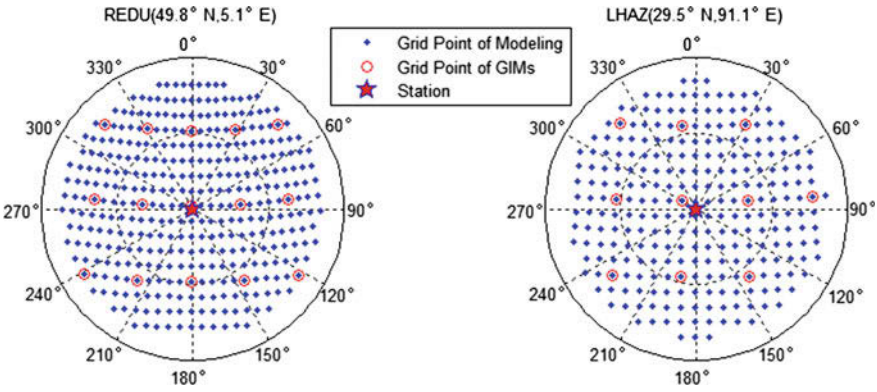

Fig. 1 Distribution of grid point in station polar coordinates

366 grid points at station REDU (267 grid points at LHAZ), and 15 points shared with GIMs (10 at LHAZ). Figure 2 shows the distribution of IPPs according to the data from IGS.

In this paper, the parameters are set as follows: $n = 1$, $m = 2$, $T_2 - T_1 = 4$ h, and $\Delta t = 30$ s. Considering that the ionospheric influence on carrier phase is always opposite to the influence on pseudorange, this paper will take the average value of the results from $L4$ and $P4$ as the final results (VTEC series with a time resolution of 30 s at the grid points with the spatial resolution of $1° \times 1°$) to reduce the influence of some systematic errors. To simplify the content, the paper just gives the results at UTC = 4 h and 16 h (Fig. 3).

Figure 3 shows a strong consistency of trend in space. Therefore, the model at the parameters in this paper is able to reflect the variation of VTEC in spatial. However, the difference between GIMs and LHAZ's results is much larger than the difference between GIMs and REDU's. The maximum at REDU is less than 3TECu, but it can reach 12TECu at LHAZ. This phenomenon is mainly caused by the distribution of IGS stations. Where there are more IGS station, there are more data to determine the GIMs results. For the reason that the density of IGS stations in Europe is much higher than the density in China, GIMs can fit the real VTEC in Europe better than in China, and the difference at REDU will show smaller than LHAZ. It also shows that the values of difference between REDU's and GIMs will get reduced with the azimuth increasing from Fig. 3. This phenomenon is mainly related to the distribution of IPPs (Fig. 2). It can be considered as that the modeling results of south are better than the results of north because of the influence of the distribution of IPPs. Moreover, this paper compared the VTEC series between single station and GIMs at the shared grid points (Fig. 4), and compiles the statistics of difference in Table 1.

As shown in Fig. 4, most of the VTEC modeling results in this paper are smaller than GIMs'. However, there are some regular patterns contained by the difference series: the higher density of deviations mainly happen during UTC = 6 and 8 h, and the deviations are negative; the positive deviations are mainly at around

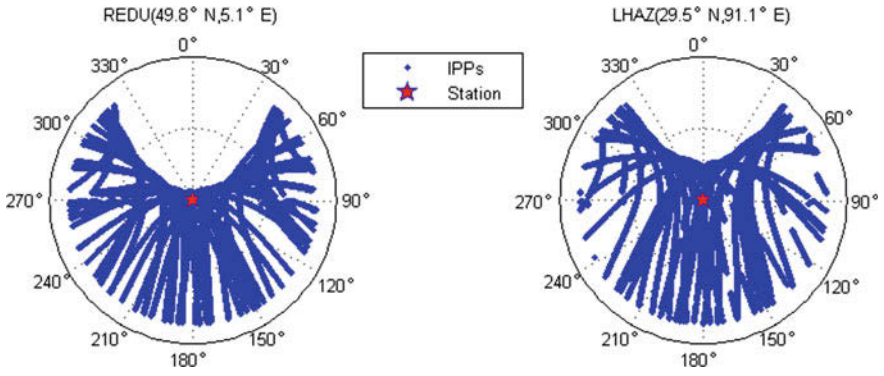

Fig. 2 Distribution of IPPs in station polar coordinates

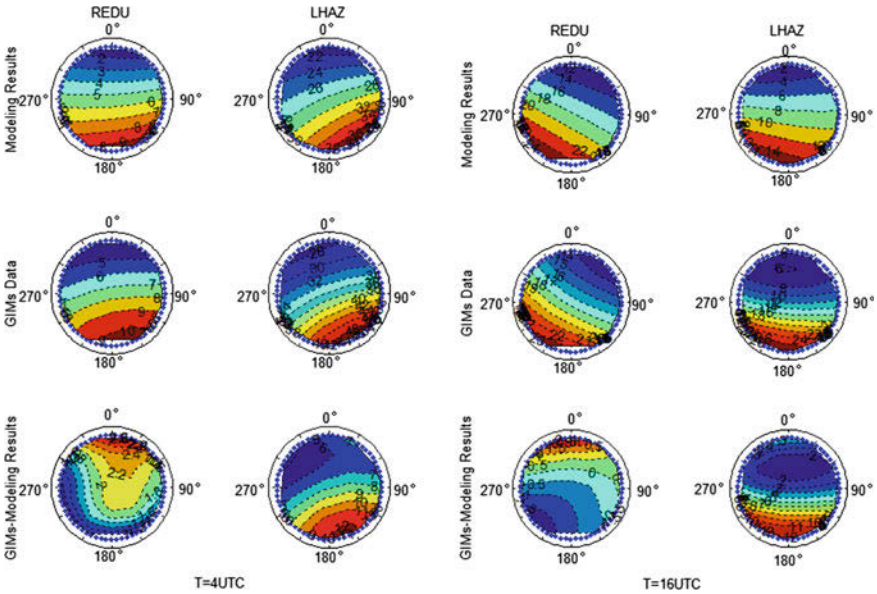

Fig. 3 Comparison of the results under moving time window with GIMs

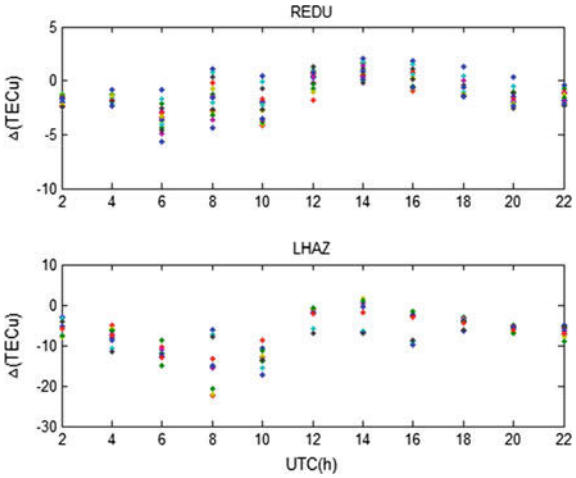

Fig. 4 Series of VTEC difference at the shared grid points

UTC = 14 h, and the absolute values are smaller; and there is a clear trend of upward (or downward) between the positive and negative deviations. Comparing the differences between the two stations', it will be found that the modeling results at REDU have a higher consistency with GIMs than the results at station LHAZ. The main reason for this feature in this paper is considered as the uneven

Table 1 Statistics of differences (%)

Bias (TECu)	REDU	LHAZ
$\|\Delta\| \leq 0.5$	15.76	1.82
$0.5 < \|\Delta\| \leq 1.0$	15.76	2.73
$1.0 < \|\Delta\| \leq 2.5$	52.73	10.91
$2.5 < \|\Delta\| \leq 5.0$	15.14	13.64
$5.0 < \|\Delta\| \leq 10$	0.61	46.36
$\|\Delta\| > 10$	0	24.54

distributions of IGS. From Table 1, the differences at REDU (LHAZ) are mainly for 1–2.5TECu (5–10TECu), maximum for 7TECu (23TECu), which is consistent to the results in Fig. 3. Therefore, the method based on moving time windows is reliable, and it can make up for the defect GIMs in the area with less IGS stations. By the way, the method based on moving time windows for single station can reduce the influence of interpolating for the higher spatial and temporal resolutions than GIMs.

4 Conclusion

The principle of modeling method based on moving time window for single station VTEC is introduced in this paper. By experimenting and comparing the results with GIMs, some conclusions can express as follows:

1. The modeling results based on moving time windows have a consistence of space characteristics with GIMs, but most of the values are lower than GIMs';
2. The differences between sing station modeling with GIMs are smaller than in China, which is mainly caused by the uneven density of IGS station. Therefore, the grid VTEC maps in the area with less IGS stations can be modeled by the method based on moving time window instead of GIMs.
3. The single station VTEC models based on moving time windows have higher time and spatial resolutions than GIMs, which can release the influence when interpolating.

Acknowledgments The authors are grateful to IGS for providing GIMs and GNSS observations to download.

References

1. Dach R, Hugentobler U, Fridez P, Meindl M (2011) Bernese GPS software version 5.0. Astronomical Institute, University of Bern
2. Fan G, Wang W, Xi X (2010) Modeling of ionosphere VTEC using generalized regression neutral network. Acta Geod Cartogr Sin 39(1):16–21

3. Hernández-Pajares M, Juan JM, Sanz J et al (2009) The IGS VTEC maps: a reliable source of ionospheric. J Geodesy 83(3):263–275
4. Hernández-Pajares M et al (2011) The ionosphere: effects, GPS modeling and the benefits for space geodetic techniques. J Geodesy 85:887–907
5. Liu C (2011) Study on modeling method and model quality control of ionosphere based on GNSS. Information Engineering University, China, Zhengzhou
6. Liu J, Chen J et al (1999) Method and principles of wide area differential GPS. Surveying and Mapping Press, Peking
7. Schaer S (1999) Mapping and predicting the Earth's ionosphere using the global positioning system. der Universität Bern, Bern
8. Zhang H (2006) Study on China's regional ionospheric monitoring and delay correction based on GPS. Shanghai Astronomical Observatory, Shanghai
9. Zhang X, Li Z, Cai H (2001) Study on regional ionospheric modeling using dual-frequency gps measurements. Geomatics Inf Sci Wuhan Univ 26(2):140–143
10. Zhang S, Tu R, Zhang Q, Huang G (2011) The establishment of ionospheric second-order model and the analysis of ionospheric variation. Acta Geod Cartogr Sinica 40(S):105–110

Relative Positioning with Undifferenced Observations: Concept and Application/Experiments with BDS

Wei Zhou, Rengui Ruan, Hao Zhang and Feijuan Yao

Abstract This paper reviews the history and evolution of the relative positioning based on the undifferenced (UD) observation. The internal mechanism of this method is explained by error division, that is, adopting the model of estimating quasi-clock parameter, which absorbs the unmodeled error of the receiver and the satellite to achieve the same effect of eliminating the common error explicitly by double differenced (DD) observation. With UD observation of Beidou Navigation Satellite System (BDS), various experiments are carried out to demonstrate the flexibility of the relative positioning mode presented, including network solution, static/kinematic baseline solution, and kinematic reference (kinematic for kinematic) solution. In the case of the experiment for network solution with baselines up to thousands of kilometers (2000–5000 km), precise post-processed orbit are used to cancel the influence of orbit errors, the repeatability within 1.1 cm in horizontal direction can be reached, the repeatability in vertical direction is less than 3 cm. The relative positioning precision of BDS on the condition of long baseline also needs to be improved because the phase center offset and variation of satellite antenna and receiver antenna have not been accurately calibrated, and there is still a gap of orbit precision between the current of BDS satellite and GPS. In the static baseline experiments, the broadcast ephemeris is adopted. For baseline of 800 m, the repeatability in horizontal and vertical are 3 and 8 mm, respectively, while for

W. Zhou (✉) · F. Yao
LuoYang Electronic Equipment Testing Center, LuoYang, China
e-mail: zhouweiz-0611@163.com

R. Ruan
Institute of Surveying and Mapping, Information Engineering University, Zhengzhou, China

R. Ruan
Xi'an Research Institute of Surveying and Mapping, Xi'an, China

H. Zhang
College of Navigation and Aerospace Engineering, Information Engineering University, Zhengzhou, China

© Springer Science+Business Media Singapore 2016

J. Sun et al. (eds.), *China Satellite Navigation Conference (CSNC) 2016 Proceedings: Volume III*, Lecture Notes in Electrical Engineering 390,
DOI 10.1007/978-981-10-0940-2_54

30 km static baseline, they are 10 and 13 mm. In the experiments of kinematic baseline and kinematic reference solutions both horizontal and vertical precisions are in several centimeters; the latter is slightly worse because the coordinates of reference station are not accurate.

Keywords BDS · Relative positioning · Undifferenced observation · Double differenced observation · Quasi-clock · Kinematic for kinematic relative positioning

1 Introduction

In the GNSS precise positioning, the undifferenced (UD) observation and the double differenced (DD) observation are widely used. These two kinds of measurements have advantages and disadvantages (Sect. 2) [1–4]. Instead of the algorithm of using DD between two receivers and two simultaneously observed satellites to eliminate the common errors of the satellites and receivers, errors will be estimated as unknown parameters in the processing of UD observation, which will achieve the same effect. This has been proved to be equivalent in theory and practice [5–7]. In recent years, with the construction of multiple new navigation satellite systems such as Galileo, QZSS, IRNSS, and BDS, as well as the advancement of GLONASS, there will be more and more observational data to be used in the application of precise positioning. Because of the mutual independence between the UD measurement, the observation data from different GNSS with different frequency and modulation code is more convenient when data processing. Even for some applications such as relative positioning which has been dominated by DD observation data for a long time, researchers start to reconsider the advantageous of the UD observation, i.e., the mode for relative positioning based on the UD observation. Salazar [8] used this mode for network solution and baseline solution, called precise orbits positioning (POP) model, Zhou [9] and Pan [10] carried out the experiments of Beidou Navigation Satellite System (BDS) relative positioning, Wang [11] used it to resolve the long baseline, and named it as double station observation processing (DSOP). In fact, this is not a new concept, but in the multi GNSS era, the processing procedure with UD observation may indeed be more convenient than double differential observation, because the latter requires a complex structure of DD measurement process. In this paper, the concept is used to solve the BDS relative positioning in a variety of applications, including network solution, single baseline static/kinematic solution, and kinematic for kinematic relative positioning.

In this paper, the history and evolution of this technology is reviewed, the basic principle of this model is introduced, and the internal mechanism of the high precise positioning by using UD measurement is explained. Finally, the experiments and results of different modes of the BDS UD observation are demonstrated.

2 History and Evolution

For more than two decades, the GPS system has been used for precise (geodetic) positioning applications. The observations used can be the undifferenced/differenced original/combined observations (carrier phase, sometimes code may also be used) [7]. The advantage to use differenced observation is that some unknown parameters, such as satellite/receiver clock offsets, are eliminated so that the problem to be solved becomes smaller. Among various differenced observations (single-differenced or SD, DD, and triple-differenced), the DD between two receivers and two simultaneously observed satellites is most favorable because the common part of model errors belongs to receivers or satellites that are explicitly eliminated together with receiver and satellite clock offsets, which is helpful for quality control, moreover, the DD ambiguities possess the property of integer and can be fixed to integers with some ambiguity resolution algorithms such as the LAMBDA method [12], which will greatly improve the quality of solution and has been wildly used for various applications such as precise orbit determination, static/kinematic relative positioning, attitude determination, and so on. Just as a coin has two sides, the disadvantage is that the differenced observations become correlative with each other . The covariance matrix of differenced observation is not a diagonal matrix, which makes the computation complicated. For the DD observations, the clock offset has been eliminated and therefore cannot be used for clock solution. On the contrary, the UD observations reserves all information (unknown parameters), therefore can be used for more applications including for satellite or station clock determination and those the DD observation works. Meanwhile the data processing for UD observation is mathematically more simple (actually the data processing procedure is as complicated and trivial as that for DD observations) since the observations are independent from each other (a basic hypothesis and is usually correct). For a not short time, researchers argued against the problem that which observation is better between the differenced mode represented by DD and UD, and either DD or UD observation has been adopted by different groups [2, 3, 13]. It is demonstrated that the results for baseline of different lengths with UD, DD (and SD) are practically identical as long as the correlation is considered [5], and the equivalent effect with UD and DD (or differenced) observations is theoretically a proof [6, 7]. For quit a long time the UD observation are mainly used for network (or long baseline) solution, orbit determination, and clock solution adopted by GIPSY/EPOS software. With the intuitive merit and convenient for ambiguity resolution, the DD observation is dominant for various application fields where the clock offsets of satellite or receiver are not interested until the precise point positioning (PPP) mode is proposed. In 1997 the PPP mode with UD code and phase data together with precise orbit and clock for large-scale network was implemented to amend errors caused by orbit and clock for broadcast ephemeris is proposed by Zumberge [14]. The PPP mode shows great advantage of economic and efficiency compared with relative positioning mode and shares comparative precision for many applications, and becomes one of the most interesting research fields [15–23].

The PPP technology calls more and more people to pay attention to high precision satellite clock solution. The UD observation which is adopted by all the new software packages (e.g., PANDA, GINS, NAPEOS, and SPODS) [24–27] for data processing to provide orbit and clock products developed by the Analysis Centers of the International GNSS Service or the international GNSS Monitoring and Assessing Service. Along with the great improvement of the achievable precision of clock and orbit, ambiguity resolution for a single receiver or even UD carrier phase has become possible with estimation of the fractional cycle biases (FCBs) or "integer" clock or other equivalent method [26, 28, 29]. The PPP with integer ambiguity resolution can theatrically lead to identical result as DD mode, which used to enjoy more precise and less time to converge exclusively benefited from the ambiguity resolution technique. As several upcoming GNSS, such as Galileo, Beidou, QZSS, IRNSS, are underdeveloped and the modernization of GLONASS is ongoing, it can be foreseen that more and more satellites with different frequency and coding signal can be involved in various applications. Because of the advantage of simplicity, data processing with UD observations are causing more and more interest even for those applications with DD observation traditionally, e.g., relative positioning. As mentioned above, in the early days of positioning with GPS, both UD and differenced (especially) observation have been tested and used by different research teams for various applications including relative positioning. Several famous software packages using UD observations are developed and play an important role in the geodetic field, such as the pioneers, as GIPSY and EPOS, and follow as PANDA, GINS, and NAPEOS, which are also used for network or baseline solution by fixing the satellite orbit to known values without euphemize on the concept of "relative positioning", although it is. The concept of relative positioning with UD observation is revitalized by Salazar [8] to position a network of stations (baseline is a special case of network with only two stations) with respect to a selected master station and is named as called "Precise Orbits Positioning (POP)". This mode is also adopted for BDS relative position for baseline by Zhou [9], Pan [10] and Wang [11] and is renamed as DSOP by M. Wang. We here conclude that the idea of "relative positing with UD observation" is not a new concept but on the contrary it as old as the history of GPS or concept of the relative positioning itself.

3 Mathematical Principle

The observation equation of pseudorange P_i^k and phase L_i^k for satellite k observed by receiver/station i are usually written as [7]

$$P_i^k = \rho_i^k + c \cdot (dt_i - \delta t^k) + T_i^k + I_i^k + e_i^k \tag{1}$$

$$L_i^k = \rho_i^k + c \cdot (dt_i - \delta t^k) + T_i^k + I_i^k + \lambda \cdot N_i^k + \varepsilon_i^k \tag{2}$$

where $\rho = \left| r_i - r^k \right|$ is the geometric distance between the satellite at the emission time and the station at the reception time, while $r_i = [x_i, y_i, z_i]^T$ and $r^k = \left[x^k, y', z^k\right]^T$ are respectively the coordinates of the satellite and station expressed in a common reference frame. dt_i and δt^k are clock offset of station and satellite. c is velocity of light. T_i^k and I_i^k are the troposphere path delay and group delay caused by ionosphere. N_i^k is the ambiguity with wavelength of N. e_i^k and ε_i^k are the measurement noise for pseudorange and phase accumulated with multipath delay.

Linearization for the above equation must be conducted so that the problem can be solved with linear optimal estimator e.g., the least square method. For the sake of simplicity, only linearization for the phase observation is presented as below

$$\tilde{L}_i^k = L_i^k - \bar{L}_i^k = \boldsymbol{u}_i^k \delta \boldsymbol{r}_i + c \cdot (dt_i - \delta t^k) + \lambda \cdot N_i^k + m \cdot z + \tilde{\varepsilon}_i^k \tag{3}$$

where $\tilde{L}_i^k$ are the observed minus computation (OMC) observation while $\tilde{L}_i^k = \left| \bar{r}_i - \bar{r}^k \right| + \bar{T} - \bar{I}$ are the computed ones. $\bar{r}_i^k = \left[\bar{x}_i^k, \bar{y}_i^k, \bar{z}_i^k\right]^T$ is the position of satellite k from broadcast ephemeris or precise orbit products and $\bar{r}_i = \left[\bar{x}_i, \bar{y}_i, \bar{z}_i\right]^T$ is the apriori value of station coordinate. $\bar{T}$ and $\bar{I}$ are troposphere delay and ionosphere correction if any apriori model is used otherwise they are equal to zero. In the right side of Eq. (3), $u_i^k = \left.\frac{\partial \rho_i^k}{r_i}\right|_{\bar{r}_i, \bar{r}^k}$ is the partial derivative of ρ_i^k, δr_i is correction of station coordinates, $m \cdot z$ is the delay compensation for the troposphere, z is zenith delay of wet weight, m is mapping function, such as GMF [30], for the short baseline, this one is usually ignored, $\tilde{\varepsilon}_i^k$ is sum of unmodeled errors and noise, including measurement noise, multipath delay, tropospheric and ionospheric errors, and orbit error, and it can be expressed as

$$\tilde{\varepsilon}_i^k = \varepsilon_i^k + \delta T + \delta I - \boldsymbol{u}_i^k \delta \boldsymbol{r}^k \tag{4}$$

$\delta \mathbf{r}^k$: indicates deviation between the calculated value and the actual position of the satellite orbit. In order to understand how the unmodeled errors are eliminated through UD observation, $\tilde{\varepsilon}_i^k$ is decomposed into three parts.

$$\tilde{\varepsilon}_i^k = \bar{\varepsilon}_i + \bar{\varepsilon}^k + v_i^k \tag{5}$$

$\bar{\varepsilon}_i$: the sum of errors belongs to the station, which mainly includes the hardware delay of receiver, the same part of error for all satellites, including the troposphere and ionosphere delay. It will be superimposed on the receiver clock offset.

$\bar{\varepsilon}^k$: the sum of the errors belong to the satellite, which mainly includes the hardware delay of the satellite and the same part of error for all stations, including the satellite position error, the attitude error, and the error of the antenna model. It will be superimposed on the satellite clock error.

v_i^k: the remaining part of errors with the above two parts taken out, mainly including the multipath effect, the measurement noise, and those different for

stations and satellites. The value and probability distribution of this part will determine the precision of positioning result. This part mainly reflects the measurement noise and multipath effect in the case of a short baseline or long baseline with a precise model used.

After the division of the unmodeled errors, Eq. (3) can be rewritten as

$$\tilde{L}_i^k = L_i^k - \bar{L}_i^k = \boldsymbol{u}_i^k \delta \boldsymbol{r}_i + \delta_i - \delta^k + \lambda \cdot N_i^k + m \cdot z + v_i^k \tag{6}$$

where $\delta_i = c \cdot dt_i + \bar{\varepsilon}_i$ and $\delta^k = c \cdot \delta t^k - \bar{\varepsilon}_i$, and they are named as the quasi-clock offsets of the receiver and the satellite in this paper, which absorbs the respective unmodeled errors. They are explicitly eliminated with DD measurement and they will be estimated together with other unknown parameters with UD measurement.

When more than two stations are used and the total number of observation is greater than the number of unknown parameters, the unknown parameters including station coordinate correction δr_i, quasi-clock offsets of receiver δ_i, and satellite δ^k, ambiguity N_i^k, tropospheric parameters z (zenith delay + horizontal gradient, if it exists) can be solved through the linear estimation methods such as least square method. In order to obtain the spatial datum, at least one station should be selected as the reference station, with its coordinates fixed or constrained to a given value. Note that, when more than one station is used as reference stations, the precision of these stations coordinates will affect the precision of the results. Since the final solution of the station coordinates are determined with respect to the selected reference station, so this mode is called relative positioning. Similarly, in order to obtain a time datum, one and only one (the value of the clock offset usually cannot be known accurately in advance) quasi-clock parameter fixed or bound to the apriori value (usually zero or navigation solution). In addition, because the ambiguity parameter and the quasi-clock error parameters are linearly related, after introducing spatial and time datum, the system is still rank deficient, which can be eliminated by using pseudorange measurement. The clock offset may vary greatly with time, and should be estimated epoch by epoch, while the tropospheric delay changes considerably slowly, it can expressed with piecewise constant or linear function, or estimated epoch by epoch constrained to a random walk model. The solution of station coordinate correction is depend on its movement, for static station, only one set of coordinate correction is estimated, while for kinematic station, the coordinate correction is estimated epoch by epoch.

Depending on the number of stations involved and the movement state of the receivers, different modes of relative positioning can be summarized in the following:

1. Baseline solution: two stations, one of which is selected as reference station, and the other, the rover station, can be static or kinematic.
2. Network solution: more than two stations, at least one is selected as reference station; the rover stations can be static or kinematic.
3. Kinematic reference solution: at least two stations, all stations are kinematic, including at least one station that is selected as the base station (need to pay

special attention to the consistency of datum on the condition of multi base solution), the coordinate correction of the base station is constrained to the navigation solution.

Because the UD measurement is independent of each other, it is convenient to realize the above varied positioning mode by taking different apriori information for the reference and rover stations and by taking different process noise for the static and kinematic stations.

Although, in this paper, only formula for the single frequency observation is presented, to implement the relative positioning mode with UD observations, users can select observation from different frequency or linear combinations according to different application requirements. For example, when the distance of reference station and the rover station is short, the single frequency measurement has advantages because of its lower noise. When the distance is long, the ionospheric free combination of two frequencies is more favorable, because it can greatly eliminate the ionospheric delay [7]. The method of using the DD combination of UD ambiguity to fix the ambiguity has been used in many softwares [24, 27, 31, 32]. After the selection of independent DD ambiguity combination, various ambiguity resolution strategies, such as LAMDA [12], can be used to improve the positioning result.

4 Analysis of Experiment

The BDS constellation is announced to operate on December 20, 2012, presently consisting of 14 satellites, including 4 MEO, 5 IGSO, and 5 GEO. These satellites are transmitting signals on three frequencies, B1 (1561.098 MHz), B2 (1207.14 MHz), and B3 (1268.52 MHz). GEO and IGSO satellites cover the longitudinal band from 50E to 170_E and are thus best observed from East Asian and Australian stations (Fig. 1).

In order to demonstrate the accuracy of the BDS relative positioning and the flexibility of the application of the UD observation, in this paper, the experiments are carried out using BDS data and broadcast ephemeris (or precision ephemeris) for the following four modes: network solution, static/kinematic baseline solution, kinematic reference solution. This paper is based on the SPODS [27] software, which is developed by Xi'an Institute of Surveying and Mapping. The procedure of data processing is quite similar to that presented in paper [27] except that the orbit is fixed to the broadcast ephemeris or other orbit products. The prior accuracy of the ionosphere-free linear combination of pseudorange and carrier phase is 2 and 0.02 m, respectively. We do not eliminate the coordinates corrections of the reference stations and the reference clock offsets. Instead, they are constrained to the apriori values, for the reference station coordinates, apriori constrain of $\sigma = 10^{-4}$ m is applied, and $\sigma = 10^{-6}$ m is adopted for the reference clock offsets.

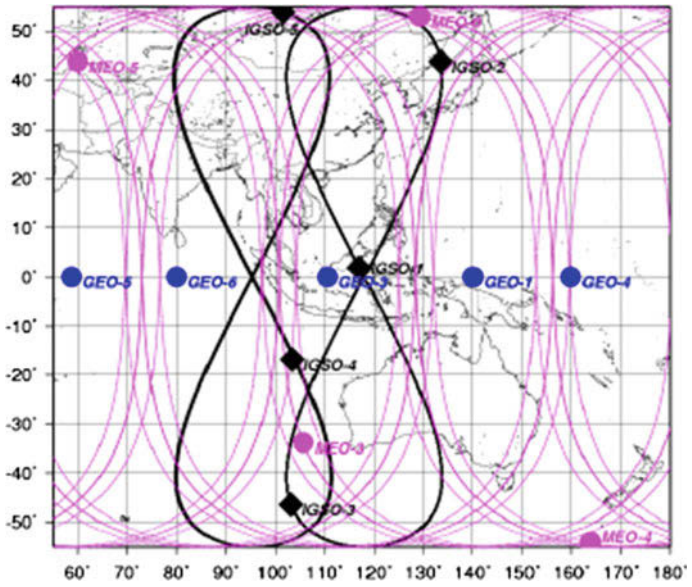

Fig. 1 Point track under the satellite of BDS

4.1 Network Solution

Observations during DOY 230–243, 2015 from 10 stations operating by the International GNSS Service are collected. These stations are located in South Pacific and their distribution is shown in Fig. 2. All of these stations are equipped with NETR9 TRIMBLE except UNX3 with SEPT ASTERX3. The UNX3 is chosen as the reference station, with its coordinates constrained to that obtained by PPP solution using GPS data and it clock offsets fixed to zero. The apriori value of the tropospheric zenith delay is calculated by the Saastamoinen model and then GMF is used for the mapping function. The wet zenith delays are estimated for every 2 h with piecewise constant model [27], every 24 h one set of horizontal gradient is estimated. Since there is no data variable to correct the antenna PCV and PCO for BDS observation, the GPS values provided by IGS in the ANTEX file igs08.atx are used. The distance of rover stations to the base station is from 1900 to 5000 km (Table 1), in order to reduce the satellite orbit errors, the BDS orbit products provided by the Xian Institute of Surveying and Mapping are used which is one of the Analysis Centers of the International GNSS Monitoring and Assessment Service (iGMAS). The correction of satellite antenna is provided by IGS-MGEX [33], and the attitude of different satellites [34] and phase windup effect [35] are also to be considered. The deformation of the tidal station is consistent with the IERS convention 2003 [36].

We use the repeatability of the coordinates to measure the quality of the solution. It is obvious that the repeatability in *N* direction is less than 0.1 cm, and smaller

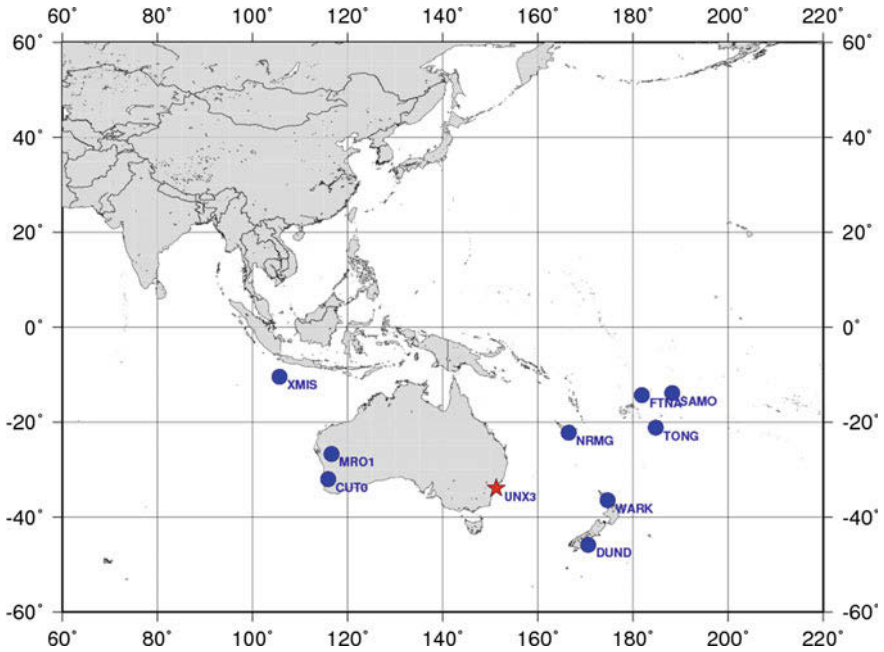

Fig. 2 Distribution map of the stations

Table 1 9 repeatabilities of the station coordinates in network solution (m)

Station	*N*	*E*	*U*	Distance
NRMG	0.005	0.006	0.016	1969.1
DUND	0.003	0.010	0.014	2103.7
WARK	0.004	0.007	0.021	2137.1
CUT0	0.003	0.007	0.017	3258.0
MRO1	0.002	0.006	0.014	3365.1
TONG	0.007	0.009	0.018	3539.1
FTNA	0.006	0.010	0.026	3717.8
SAMO	0.007	0.009	0.026	4257.7
XMIS	0.006	0.011	0.027	5155.5

than the other two directions, because it is benefited from the wide range motion of IGSO satellite in the North and South direction, which makes the observation geometry structure strong in North direction. The repeatability in *U* direction is the maximum, ranging from 0.014 to 0.027 m, while that in *E* direction is from 0.006 to 0.011 m. From the table, it can be seen that with the increase in distance the precision of the coordinates is reduced, and it is particularly evident in the *U* direction, because the correlation of the orbit error for stations decreases as the distance increases. Overall, based on the BDS precise post-processed orbit, in the mode of the relative positioning, the accuracy of mm level in the horizontal

direction and cm level in vertical direction for static positioning can be obtained for the baseline of thousands of kilometers' long, which is consistent with the experimental results presented by Wang [11].

4.2 Static Baseline Solution

Two baselines (XIAN-BGLG and XIAN-NTSC) are selected to carry out the static baseline solution experiment, the three stations are equipped with UNICORE receivers. The length of baseline XIAN to BGLD is about 786 m, and the length of baseline XIAN to NTSC is about 30 km. The observation time is during DOY 168–170, 2012, when the C13–C14 satellite is not enabled. In the mode of baseline solution, data processing is carried out baseline by baseline, which is quite different for the network solution in which observation from all the stations involved are processed together in an integration mode. In this experiment, satellite position is calculated from broadcast ephemeris, since the two baselines belong to short–middle length baseline, respectively, the tropospheric parameters will not be estimated, and the coordinates of reference station (XIAN) will be constrained to the GPS PPP solution (Fig. 3).

In order to evaluate the positioning results with BDS, the result with GPS data is taken as reference values, the positioning errors are expressed in three directions (*N*/*E*/*U*). Table 2 shows the errors of the baseline results in *N*, *E,* and *U* directions: the mean deviation and STD. The STDs in *E*/*N* of the baseline XIAN-BGLG are 0.003 m, and in *U* is 0.008 m; the STD in *E*/*N* of the baseline XIAN-NTSC are respectively 0.010 and 0.007 m, and the STD in *U* is 0.013 m. With the increase of the baseline length, the STD is obviously increasing, which is mainly due to the decrease of the spatial correlation of the tropospheric delay. It should be noted that

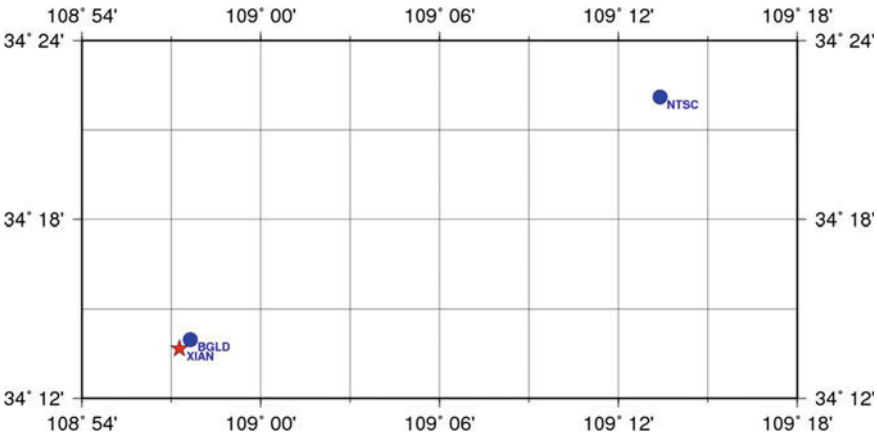

Fig. 3 The distribution of baselines

Table 2 Relative positioning errors of baseline solution (unit: m)

Station	Component	168	169	170	Mean	STD
BGLD	*N*	0.004	0.011	0.011	0.009	0.003
	E	−0.001	0.004	0.008	0.003	0.003
	U	0.007	−0.005	−0.016	−0.005	0.008
NTSC	*N*	0.005	−0.007	−0.013	−0.005	0.007
	E	0.005	−0.018	−0.017	−0.010	0.010
	U	−0.010	0.019	0.023	0.011	0.013

the mean value of error cannot be ignored, which may reflect the systematic differences between the BDS and GPS positioning results.

4.3 Kinematic Baseline Solution

Since we do not have any real BDS observation data from kinematic receiver, the data from baseline XIAN-NTSC (Sect. 4.2) are used in the following experiments to simulate the kinematic baseline solution. The configuration for this experiment is quite the similar with the static baseline solution, except that the coordinate correction of the rover station NTSC is estimated epoch by epoch. Comparing with the result of static baseline solution with GPS, the position errors are calculated and expressed in *N*/*E*/*U* directions, as shown in Fig. 4, the statistics of the mean deviation and the STD are in Table 3, it demonstrates that the STDs in *E*/*N*/*U* direction are 0.012, 0.012, and 0.036 m, respectively.

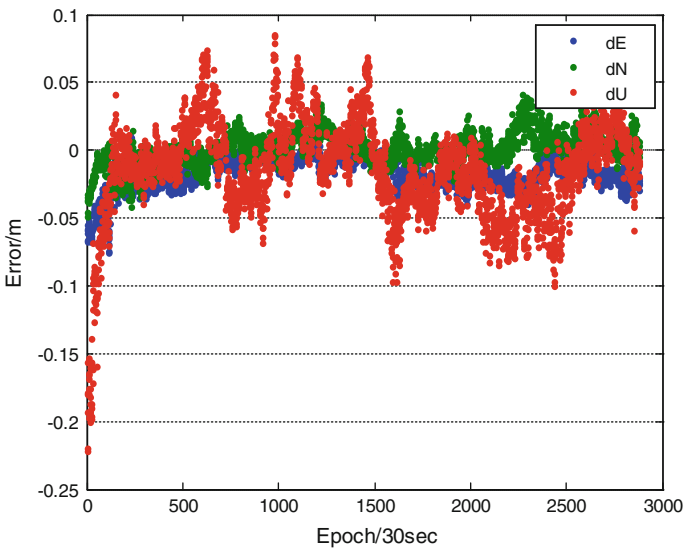

Fig. 4 The positioning error of the station NTSC

Table 3 Means and STDs of the kinematic positioning result (unit: m)

Direction	Mean	STD
N	−0.017	0.012
E	0.001	0.012
U	−0.015	0.036

4.4 Kinematic Reference Solution

The above three experiments have one thing in common: the reference station is static, in this section we will demonstrate the effectiveness of BDS positioning when the reference station is kinematic. Sometimes users are interesting in the relative position of the two receivers, and the precision of absolute position of the carrier is interested, such as the relative position measurement of aircraft and ship formation, the relative position measurement of satellite formation, this mode is refer to kinematic reference in this paper, which is wildly used in aircraft and ship formation.

We also use data from XIAN and NTSC to simulate the kinematic reference positioning experiment and the former is selected as the base station. In this mode, we assume that the base station is moving, so the coordinates of the base station are constrained to those obtained by single point positioning with pseudorange and broadcast ephemeris epoch by epoch, besides, the data processing procedure is quite similar to the mode of kinematic baseline solution presented in the Sect. 4.3. Figures 5 and 6 show the series of absolute coordinates errors of the NTSC and

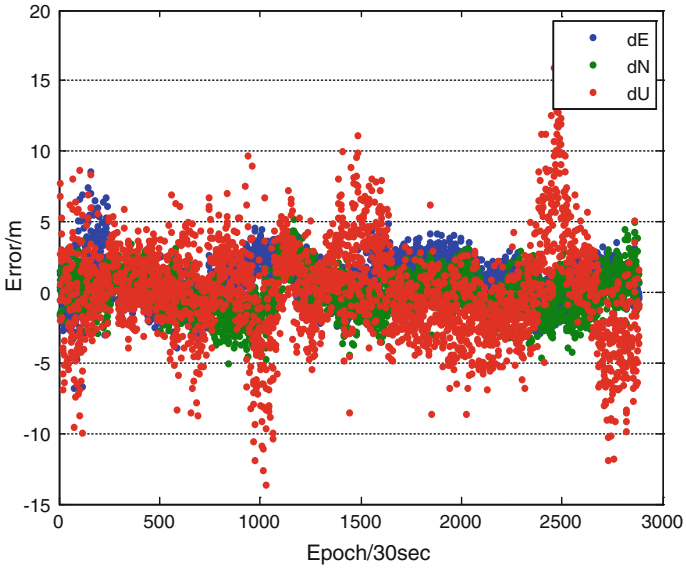

Fig. 5 Absolute position error of the NTSC station

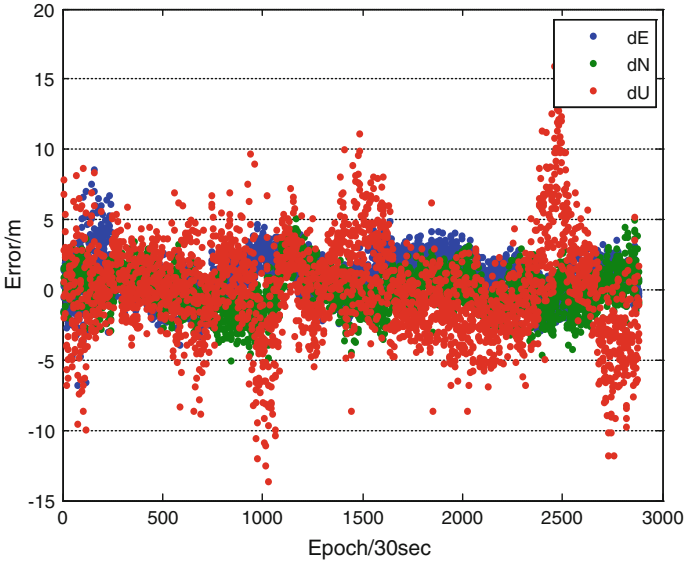

Fig. 6 The absolute position error of the XIAN station

Table 4 Statistics of positioning error (unit: m)

Station	Mean			STD		
	E	*N*	*U*	*E*	*N*	*U*
XIAN	0.973	−0.039	0.052	1.499	1.459	3.397
NTSC	0.963	−0.041	0.045	1.498	1.461	3.397
Baseline (XIAN-NTSC)	−0.010	−0.001	−0.007	0.016	0.016	0.039

XIAN; the two has a similar trend. It can be seen that the absolute coordinate errors of the NTSC and XIAN stations are mainly within 10 m, which are consistent with the single frequency positioning accuracy based on the pseudorange. Figure 7 shows the relative positioning error of NTSC relative to XIAN, which is all smaller than 0.1 m. Table 4 shows the statistic of the mean deviation and STD of the absolute coordinates error of XIAN and NTSC, the baseline solution errors from XIAN to NTSC. The absolute position errors of the two stations is are at the level of a few meters, while the relative position error in the *E*/*N*/*U* direction is 0.016, 0.016, and 0.039 m, respectively. On Comparing with Sect. 4.3, the positioning accuracy is slightly degraded, which reflects the influence of the positioning error by the accuracy of reference station coordinates.

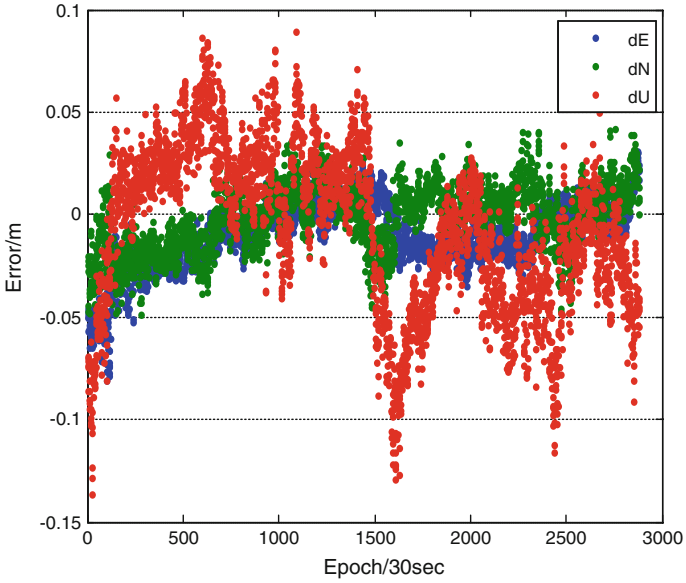

Fig. 7 Baseline error

5 Conclusion

In this paper, the history of relative positioning based on undifferenced observation is reviewed, and it is pointed out that the internal mechanism of the UD relative positioning is estimating the quasi-clock offsets, which absorb the common errors of receivers and satellites. The relative positioning experiments using BDS UD observation in different modes are conducted including the network solution (with baseline up to 5000 km), static baseline solution, kinematic baseline solution, and kinematic reference solution. These experiments demonstrate the flexibility of the UD observation in terms of data processing. In term of positioning precision, in the case of the network solution using post precision orbit, for thousands of kilometers (2000–5000 km) of the baseline, the repeatability of 11 mm in horizontal direction can be reached, while the repeatability in vertical direction is less than 3 cm. The relative positioning precision on the condition of long baseline also needs to be improved, because the satellite antenna phase center and receiver antenna phase center have not been accurately calibrated, and there is still a gap of orbit precision between the current BDS satellite and GPS. When the broadcast ephemeris is adopted for the static baseline of 800 m, the repeatability in horizontal direction is 3 mm and in vertical direction it is 8 mm; for 30 km static baseline, the repeatability in horizontal direction is less than 10 mm and about 13 mm respectively. In the case of kinematic baseline and kinematic for kinematic solutions, both horizontal and

vertical precision are in several centimeters, for the latter, because the initial coordinates of base station are not accurate, the precision is slightly worse.

Acknowledgements The work of this paper is supported by Sate Key Laboratory of Geodesy and Earth's Dynamics (project number: SKLGED2014-3-4-E). Thanks to the IGS and BDS Test and Evaluation Network for providing experimental data, and the precise orbit products in experiment is also calculated with MGEX data.

References

1. Bock Y, Abbot RI, Counselman CC III et al (1985) Establishment of three-dimensional geodetic control by interferometry with the global positioning system. J Geophys Res Solid Earth 90(B9):7689–7703
2. Remondi RW (1985) Global positioning system carrier phase: description and use. Bull Geod 59:361–377
3. Lichten SM, Border JS (1987) Strategies for high-precision global positioning system orbit determination. J Geophys Res 92(B12):12751–12762
4. Dong DN, Bock Y (1989) Global positioning system network analysis with phase ambiguity resolution applied to crustal deformation studies in California. J Geophys Res 94 (B4):3949–3966
5. Ashkenazi V, Yau J (1986) Significance of discrepancies in the processing of GPS data with different algorithms. Bull Geodesique, 229–239
6. Jonge de PJ (1998) A processing strategy for the application of the GPS in networks. Delft University of Technology, Delft, p 238
7. Xu G (2007) GPS theory, algorithms and applications, 2nd edn. Springer, Berlin, p 353
8. Salazar D, Hernandez-Pajares M, Juan JM et al (2010) GNSS data management and processing with the GPSTk. GPS Solutions 14:293–299
9. Zhou W (2013) Research and realization on theories and methods of precise positioning base on BeiDou navigation satellite system. PLA Information Engineering University, Zhenghzou, China, p 172
10. Pan Z, Chai H, Wang M et al (2014) A new relative positioning method based on un-differenced BDS observation. In: 2014 Proceedings of China satellite navigation conference (CSNC). Springer, Nanjing, pp 165–174
11. Wang M, Cai H, Pan Z (2015) BDS/GPS relative positioning for long baseline with undifferenced observations. Adv Space Res 55(1):113–124
12. Jonge de P, Tiberius C (1996) The LAMBDA method for integer ambiguity estimation: implementation aspects
13. Bock Y, Abbot RI, Counselman CC III et al (1986) A demonstration of 1–2 parts in 107 ACCURACY using GPS. Bull Geod 60:241–245
14. Zumberge J, Heflin M, Jefferson D et al (1997) Precise point positioning for the efficient and robust analysis of GPS data from large networks. J Geophys Res 102(B3):5005–5017
15. Gao Y, Shen X (2001) Improving ambiguity convergence in carrier phase-based precise point positioning. In: Proceeding of ION GPS 2001, Salt Lake City, US
16. Kouba J, Heroux P (2001) Precise point positioning using IGS orbit and clock products. GPS Solutions 5(2):12–28
17. Shen X, Gao Y (2002) Kinematic processing analysis of carrier phase based precise point positioning. FIG XXII International Congress, Washington, DC, USA
18. Beran T, Kim D, and Langley RB (2003) High-precision single-frequency GPS point positioning. ION GPS/GNSS 2003, Portland, pp 1192–1200

19. Kouba J (2003) A guide to using international GPS service (IGS) products, p 31. Date accessed: 15 Sept 2008. ftp://igscb.jpl.nasa.gov/igscb/resource/pubs/GuidetoUsingIGSProducts.pdf
20. Muellerschoen RJ, Iijima B, Meyer R et al (2003) Real-time point positioning performance evaluation of single-frequency receivers using NASA's global differential GPS system
21. Beran T, Bisnath SB, Langley RB (2004) Evaluation of high-precision, single-frequency GPS point positioning models. ION GNSS 2004, Long Beach CA, pp 1893–1901
22. Gao Y, Wojciechowski A (2004) High precision kinematic positioning using single dual-frequency GPS receiver. Remote Sens Spat Inf Sci, 34
23. Zhang X (2005) Precise point positioning evaluation and airborne lidar calibration. Danish National Space Center
24. Jing-nan L, Mao-rong G (2003) PANDA software and its preliminary result of positioning and orbit determination. Wuhan Univ J Nat Sci 8(28):603–609
25. Springer T, Dilssner F, Escobar D et al (2011) NAPEOS: The ESA/ESOC tool for space geodesy. The European Geosciences Union 2011 General Assembly, Vienna, Austria
26. Loyer S, Perosanz F, Mercier F et al (2012) Zero-difference GPS ambiguity resolution at CNES-CLS IGS analysis center. J Geodesy
27. Wei Z, Ruan R, Jia X et al (2014) Satellite positioning and orbit determination system SPODS: theory and test. Acta Geodaetica et Cartographica Sinica 43(1):1–4
28. Collins P, Lahaye F, Heroux P et al (2008) Precise point positioning with ambiguity resolution using the decoupled clock model. ION GNSS 2008, Savannah, Georgia
29. Ge M, Gendt G, Rothacher M et al (2008) Resolution of GPS carrier-phase ambiguities in precise point positioning (PPP) with daily observations. J Geodesy 82:389–399
30. Beohm J, Neill A, Tregoning P et al (2006) Global mapping function (GMF): a new empirical mapping function based on numerical weather model data. Geophys Res Lett, 33
31. Blewitt G (1989) Carrier phase ambiguity resolution for the global positioning system applied to geodetic baselines up to 2000 km. J Geophys Res 94(B8):187–203
32. Ge M, Gendt G, Dick G et al (2005) Improving carrier-phase ambiguity resolution in global GPS network solutions. J Geodesy 2005:103–110
33. Montenbruck O, Schmid R, Mercier F et al (2015) GNSS satellite geometry and attitude models. Adv Space Res 56:1015–1029
34. Dai X, Ge M, Lou Y et al (2015) Estimating the yaw-attitude of BDS IGSO and MEO satellites. J Geodesy 89:1005–1018
35. Wu JT, Wu SC, Hajj GA et al (1993) Effects of antenna orientation on GPS carrier phase [J]. Manuscripta Geodaetica 18:91–98
36. McCarthy DD, Petit G (2003) IERS conventions (2003): Verlag des Bundesamtes für Kartographie und Geodäsie, Frankfurt am Main 2004, p 127

Part III
Atomic Clock and Time-Frequency Technology

Experimental Study on Improvement of Discharge Bulb Aging of Hydrogen Maser

Wenming Wang, Hefei Zheng, Guohui Shen and Jing Li

Abstract The preparation of atomic hydrogen has a significant effect on the operation of the hydrogen maser. The paper presents radio frequency (RF) discharge source and discharge bulb as the necessary conditions for the preparation of atomic hydrogen. Based on the current technical status of the RF discharge source and the main reaction of the plasma inside the discharge bulb, a new improved technique for the discharge bulb aging consisting in a series of experiments of different proportions of HF solution, acid etching time, and inner wall purification. The new method described here fulfils the time, that the discharge bulb from the first light reached a normal rose red and the photoelectric diode light detection voltage reached equilibrium value, cut from more than one week to less than two days, the spectral intensity reached 16,500 after two days while the traditional technology reaches 14,000 after one week, and the aging success rate of this batch reached 100 %.

Keywords Hydrogen maser · Discharge bulb · Plasma · Aging

1 Introduction

Hydrogen maser has become one of the most widely used frequency standard in the world at present with excellent frequency stability and low drift characteristics. It has been applied to many fields of society, such as punctuality, timing,

W. Wang (✉) · H. Zheng · G. Shen · J. Li
Beijing Institute of Radio Metrology and Measurement, Beijing, China
e-mail: wwm_kingdom@163.com

H. Zheng
e-mail: zhenghefei1@sina.com

G. Shen
e-mail: shenguohui@163.com

J. Li
e-mail: lijing@yahoo.com

© Springer Science+Business Media Singapore 2016

J. Sun et al. (eds.), *China Satellite Navigation Conference (CSNC) 2016 Proceedings: Volume III*, Lecture Notes in Electrical Engineering 390,
DOI 10.1007/978-981-10-0940-2_55

navigation, deep space exploration, time synchronization, basic scientific research, space applications, and communication synchronization.

The atomic hydrogen is an essential material for the hydrogen maser, affecting the performance of the maser. The electromagnetic wave, produced by the transition of atomic hydrogen ground-state hyperfine levels and processed by a series of frequency control, provides a high accuracy and stability integer frequency signal for users. The process of preparing the atomic hydrogen is one of the components of the plasma, which is formed by the molecular hydrogen (H_2) entered into the discharge bulb of quartz material, under the action of the external radio frequency (RF) field. The atomic hydrogen through the collimator and injection into the magnetic state selector will deflect. Finally, the high-energy state atomic hydrogen enters the storage bulb to create stimulated emission [1].

The proportion of atomic hydrogen in the discharge bulb is not only restricted by the dissociation efficiency of molecular hydrogen, but also by the recombination of H_2^+ ions. Therefore, the RF discharge source and discharge bulb are particularly important in the preparation of atomic hydrogen. Among them, the application of the RF discharge source has been relatively mature with fixed technology, which is equal to the foreign level [2]. At present, it is not the main factor that affects the efficiency of the preparation of atomic hydrogen. However, the effect of the discharge bulb with the same kind of material but different aging processes is different. For many years, the aging process of hydrogen maser is one of the bottlenecks that restricted the improvement of the technology of hydrogen maser.

2 Effects and Evaluation Method of Discharge Bulb

The complex reactions of plasmas can be classified into two types in the discharge bulb [3]. The first type is the reaction of plasmas, and the second is the reaction of plasma and the inner wall of the discharge bulb. These two reactions have a decisive effect on the preparation of atomic hydrogen, and ultimately affect the proportion of target hydrogen atom in the discharge bulb.

The reaction of plasmas, which plays a major role in the preparation of atomic hydrogen, is expressed as follows.

$$H_2{}^+ + e \rightarrow H + H \tag{1}$$

This reaction with a large cross section, especially in the time when the electron energy level is low, can produce the target atomic hydrogen. However, the concentration of H_2^+ ions must be high enough, depending on the intensity of the ionization process and the rate of ion depletion. In fact, most of the H_2^+ ions react with the inner wall of discharge bulb instead of the above reaction, so, it is necessary to avoid the second type of reaction in the process of the preparation of atomic hydrogen. The materials used in the discharge bulb require resistance from the bombardment of plasmas, having smooth surface, small composite coefficient,

Fig. 1 The discharge bulb of hydrogen maser

and little impurity. The most common materials are glass of Pyrex 7740 and fused silica.

At present, the domestic and international size of the structure of discharge bulb is basically similar (Fig. 1), while the only difference is the aging process of its inner wall.

The experimental results show that the reasonable aging of the inner wall of discharge bulb can effectively reduce the consumption of H_2^+ ion reacted with the inner wall, and increase the proportion of target atomic hydrogen in the bulb. Eliminating the common factors such as RF discharge source and the size of discharge bulb, the effect of different aging processes is significant.

The minimum energy required for hydrogen dissociation is 8.5 eV, while the energy of atomic hydrogen recombined is 4.7 eV, which indicates that the energy of the decomposition of atomic hydrogen is at least 2 eV [4]. The energy can be reflected in the speed of the atomic hydrogen, where the velocity distribution of the atomic hydrogen from the discharge bulb becomes the Gauss distribution, rather than the usual Maxwell distribution.

The energy also excites the hydrogen atoms to a high-energy level and then emit photons. The light in this process is the red or purple light of Ballmer system, which is rose-red light seen by eyes. The working level of the discharge bulb is evaluated according to the detection of the luminous state, which mainly includes visual inspection (rose red), photoelectric diode (voltage value), and laboratory of spectrometer (light intensity).

3 Existing Aging Technological Procedure of Discharge Bulb

The following is the existing aging technological procedure of discharge bulb.

(a) Take the qualified discharge bulbs from the same batches on the aging experimental platform. Check the inner wall of discharge bulbs whether there are particulate impurities one by one.

(b) Put the discharge bulbs with particulate impurities into a flume filled with water. Inject a half of the bulb with 25 % HF solution from the air inlet into the discharge bulbs by means of a syringe. Take out the syringe and then shake the bulbs vigorously until the impurities fall off.
(c) Expel the 25 % HF solution from the discharge bulbs with a syringe.
(d) Fill the discharge bulbs with absolute ethyl alcohol and then put them into the flume. Expel the absolute ethyl alcohol from the bulb with a syringe after 4 h.
(e) Inject branch water into the discharge bulbs to clean them again by a new syringe.
(f) Use the absolute ethyl alcohol to dehydrate the discharge bulbs and then connect them to the collimator.

The existing aging technological procedure of discharge bulb has been used for many years. It will take one or two weeks from injecting the hydrogen into the discharge bulb to normal. Worse yet, some of the discharge bulbs cannot work after a long time and need to be changed. The duplicate work leads that the development cycle is not controllable, the product consistency is poor and the manpower and capital are wasted.

4 Experimental Study of Discharge Bulb Aging Improvement

The main limiting factor of the traditional technology, which leads one or two weeks from the first light to a normal rose red and a low aging success rate, is that the aging of the inner wall of the discharge bulb is not enough or scientific. Based on the research and analysis of the theories and a large number of exploratory tests, the new aging technological procedure of discharge bulb is described as follows.

(a) Take the qualified discharge bulbs from the same batches on the aging experimental platform. Inject branch water into the discharge bulbs to clean them at least three times by a syringe and then put the bulbs without water on the silk used for vacuum.
(b) Pour the quantitative HF solution to a beaker and then dilute it to a certain dilution ration with a pair of acid proof gloves. Fill the discharge bulbs with the solution and then put them into the flume.
(c) After a certain time, expel the solution from the discharge bulbs, inject branch water to clean them at least three times and put them on the silk.
(d) Wear another pair of clean gloves and inject deionized water into the discharge bulbs to clean them at least three times.
(e) Use the absolute ethyl alcohol to dehydrate the discharge bulbs.
(f) Place the discharge bulbs in a vacuum cabinet and set aside.

5 Comparison of the Two Kinds of Aging Process

Discharge bulbs with the improved aging process are assembled in the verification subject of hydrogen maser test pieces, electrical parts, and small titanium pump, using the same ionization method as previous, in order to test the effect of the improved aging process.

After monitoring of the working state of a few discharge bulbs (Figs. 2 and 3), the results show that the time from injecting the atomic hydrogen into the discharge bulb to normal state, which is less than two days, is significantly shorter than using the traditional process, and there is no failure.

The working states of the discharge bulbs with the two kinds of aging process are given by Table 1.

In addition, the discharge bulb cannot work alone and it must be matched with the magnetic state selector, in order to transfer the hydrogen atoms in the high-energy state to the storage bulb. This requires that the velocity of the hydrogen atoms from discharge bulb to be as low as possible, so that the resolving power of

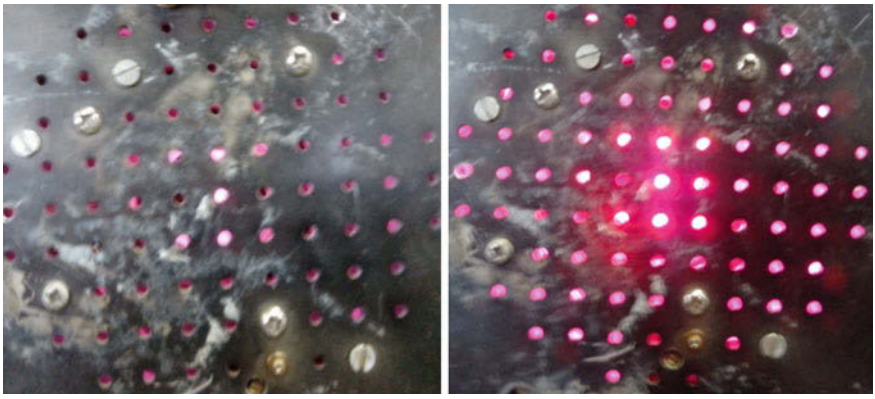

Fig. 2 The change of color after two days

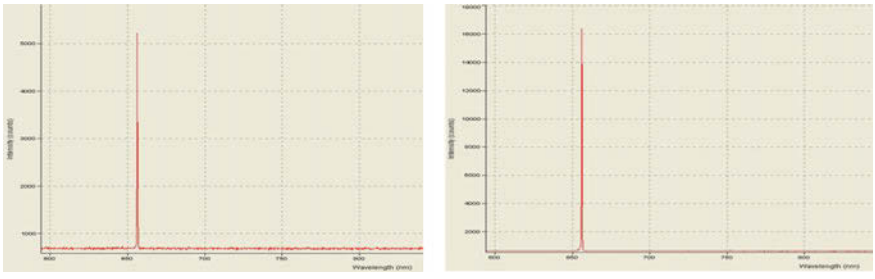

Fig. 3 The change of light intensity after two days

Table 1 The working states of the discharge bulbs with the two kinds of aging process

Quantity of contrast	Existing aging technological procedure of discharge bulb	Improved aging technological procedure of discharge bulb
Color contrast (by naked eye)	The color changes to red rose after a week	The color changes to red rose after two days
Voltage of light detection contrast (photoelectric diode)	The voltage is still rising slowly after a week	The voltage reaches balance after two days
Spectral intensity contrast (ocean optics spectrasuite)	14,000 after a week	16,500 after two days
Success rate	<100 %	100 %

the magnetic state selector can be strong. In addition, it is required that the velocity distribution of the atomic hydrogen from discharge bulb to be narrow, in order to improve the resolving power of the magnetic state selector. Macroscopically, this requires that the electron temperature to be as low as possible, because the lower the electron temperature is, the lower the transmit energy from the dissociation of molecular hydrogen to the atomic hydrogen is. The high-energy hydrogen molecules penetrating the silicon dioxide react with the various ingredients in the wall, causing the change in the nature of the cell wall (e.g. the crystallization) or the introduction of impurities in the plasmas which lead to the deterioration of the performance of discharge bulb. The above process has a significant relationship with the material, the impurity, and the surface state of the wall, especially the temperature. Therefore, the working temperature of the aging discharge bulb should be reduced as far as possible and air cooling or alloy heat conduction cooling can be usually used in engineering.

6 Conclusion

The aging discharge bulb is effectively improved through the reform and innovation of the unreasonable process, and operation method which are based on the theory investigation and analysis of the early stage, multiple exploratory tests, and according to the process control of HF solution with different ratio, acid etching time, and purification of the inner wall. The time reaching to normal state, which shorten to less than two days from a week, has a remarkable effect on shortening the production cycle, especially in the development of the national space strategy with the urgent need of hydrogen maser. At the same time, the qualified rate of the test batches of discharge bulb is 100 %, saving the raw materials, reducing the cost, improving the product consistency and making an outstanding contribution to improve the product quality and labor productivity. In particular, the new aging process has successfully overcome the difficulties in the aging process through hydrogen maser and solved one of the bottlenecks that restricted the improvement of the technology of hydrogen maser.

References

1. Wang Y, Wang Q, Fu J (1986) The theory of quantum frequency standard. Science Press, Beijing, p 450
2. Peng J (1996) A new RF dissociator for hydrogen maser of Shanghai observatory. Ann Shanghai Astron Observatory 17:310–313
3. Maleki L (1980) A study of the processes in the RF hydrogen gas dissociator. TDA Progress Report, pp 42–59
4. Hernqvist KG (1978) The hydrogen dissociator. IEEE Trans Plasma Sci 6(3):238–243

Analysis on Factors Influencing Frequency Drift of Rubidium Clocks for Satellite Navigation

Chang Liu, Feng Xu, Yongsheng Qu, Yu Zhang, Erwang Du, Min Cheng, Tao Yang and Wei Zhang

Abstract The output frequency of the atomic clock drifts slowly, called frequency drift, which is a major feature of the satellite rubidium (Rb) clock and determines the autonomic running duration of the satellite navigation system. Evaluation on frequency drift of satellite rubidium clocks and analysis on factors contributing to frequency drift are carried out. Primary factors leading to frequency drift of rubidium clocks are pointed out and proposals aiming at reducing frequency drift are put forward.

Keywords Satellite rubidium clock · Frequency drift · Light shift

1 Introduction

The satellite rubidium clock has good frequency stability, with characteristics of a relatively small volume, low power consumption, and good space environmental adaptability, which is widely used in global navigation and positioning systems [1, 2]. Compared with the passive hydrogen maser and the cesium beam clock, satellite rubidium clocks generally show a greater frequency drift which has a significant impact on the retention time of the satellite navigation system. In order to improve satellite navigation system with more auto-running time, it requires a small frequency drift rate for the rubidium clock.

Satellite rubidium clocks have a greater drift rate during the equilibrium stage. In order to meet requirements of the satellite navigation system, satellite rubidium clocks should have a frequency drift rate less than 10^{-14} per day, which requires effective measures to be taken to minimize the frequency equilibration time, and to speed satellite rubidium clock into the linear frequency aging stage. Therefore, it is

C. Liu · F. Xu (✉) · Y. Qu · Y. Zhang · E. Du · M. Cheng · T. Yang · W. Zhang
CAST-Xi'an Institute of Space Radio Technology, China Academy of Space Technology, Xi'an 710010, China
e-mail: xufeng1355@163.com

© Springer Science+Business Media Singapore 2016

J. Sun et al. (eds.), *China Satellite Navigation Conference (CSNC) 2016 Proceedings: Volume III*, Lecture Notes in Electrical Engineering 390,
DOI 10.1007/978-981-10-0940-2_56

necessary to study on factors influencing the frequency drift in the frequency equilibration stage for the satellite rubidium clock.

J. Camparo and M. Bloch [3–5] have done some studies on frequency drift and proposed some possible mechanism hypotheses of frequency drift, comprising: the intensity-dependent light shift, helium permeation, position shift, but there are some shortcomings for all these hypotheses. So far, the mechanism influencing frequency drift of the rubidium atomic clock is not clear yet and further experimental study is needed. Here we will do some discussion and analysis, trying to figure out the major mechanism accounting for frequency drift of the satellite rubidium clock.

2 Frequency Characteristics of the Satellite Rubidium Clock

The satellite rubidium clock warmed up to its steady state a few days later after it was powered on. The long-term output frequency characteristics of the clock are generally shown in Fig. 1 [6], the output frequency of the clock often exhibits unidirectional drift over time. The long-term frequency drift characteristic of the satellite rubidium clock can be divided into two stages called the frequency equilibration stage and the linear frequency aging stage. In the frequency equilibration stage, the output frequency decays exponentially with time, the time constant usually ranges from dozens of days to a few hundred days. At this stage frequency drift rate is high, usually in the 10^{-12} per day to 10^{-13} per day. After the frequency equilibration stage, the rubidium clock enters its linear frequency aging stage, showing a slow linear frequency drift of the 10^{-14} per day of magnitude.

The frequency characteristic of the satellite rubidium clock can be described as below

$$\Delta y(t) = \Delta y_0 \exp\left(-\frac{t}{\tau_{\mathrm{EQ}}}\right) + Kt \tag{1}$$

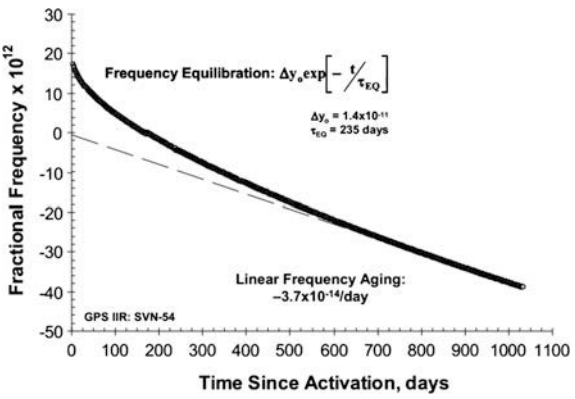

Fig. 1 Fractional frequency history for the rubidium clock on the GPS satellite SVN-54

Where Δy_0 is the total amount of frequency drift during the equilibration stage, τ_{EQ} is the time constant of the equilibration stage, which characterizes the length of time required for the rubidium clock to enter into the linear frequency drift stage, K is the frequency drift rate of the linear frequency aging stage, usually in a small coefficient of 10^{-14} per day.

3 Mechanisms of the Frequency Drift

3.1 Light Shift

Light shift of the rubidium atomic clock originates from interaction between the pumping light and ^{87}Rb atoms in absorption cell. It is the secondary AC Stark effect. Assuming that the ground state of the rubidium atom is $|i>$, and excited state is $|\alpha>$, if the pumping light of the frequency ω and the electric field amplitude ε interacts with the ^{87}Rb atom, according to quantum mechanical calculations, we can obtain the amount of light shift of the ground level as follows: [7]

$$\delta v = \frac{\left|\langle i|\vec{P}\cdot\vec{\varepsilon}|a\rangle\right|^2}{2\pi\hbar^2} \times \frac{\omega-\omega_{ai}}{(\omega-\omega_{ai})^2+\frac{\Gamma^2}{4}} \tag{2}$$

$$\omega_{ai} = (E_a - E_i)/\hbar \tag{3}$$

Where $\vec{P}$ is the electric dipole moment operator, $\vec{\varepsilon}$ is the complex amplitude of light, $1/\Gamma$ is the lifetime of the excited state, E_α and E_i are energy symbols of the two energy levels of the transition.

The formula (2) shows that the amount of light shift is proportional to the light intensity, and also relates with the frequency detuning between the pumping light and resonance absorption of the ^{87}Rb atom. Since the pumping light is not monochromatic, but has a certain spectral profile, therefore, the total amount of light shift not only has a linear relationship with the light intensity, but also relates to the overlap degree of absorption spectrum of ^{87}Rb atoms inside the absorption cell and pumping light spectrum profile.

For the rubidium clock, the light shift can be abbreviated as follows:

$$(\nu_{LS}/\nu_{hfs}) = \alpha(I/I_0) \tag{4}$$

where ν_{LS} is the light frequency shift, ν_{hfs} is the frequency of the clock transition, I_0 is the normalized light intensity, α is the intensity-dependent light-shift coefficient related to the light spectrum. Frequency drift rate due to light-shift effect can be written as

$$A = \frac{1}{\nu_{\mathrm{hfs}}} \frac{\delta \nu_{\mathrm{LS}}}{\delta t} \cong \dot{\alpha} + \alpha \left(\frac{\dot{I}(t)}{I_0} \right) \tag{5}$$

Formula (5) shows that the slow change of light intensity and slow variation of light spectrum over time will bring to frequency drift. Phenomenon has been observed in experiments that the intensity of the pumping light decays over time with a rate of generally 10^{-3} per day to 10^{-4} per day, which is due to physical and chemical interactions between rubidium atoms and the glass of the lamp bulb.

The slow decay of light intensity affects the output frequency of the rubidium atomic clock through the light-shift effect, so researchers often speculate that the frequency shift due to light intensity is an important mechanism of frequency drift. Experimentally, we can see that the light intensity curve shows a strong correlation characteristic with the output frequency curve of the rubidium clock. Figure 2 shows the light intensity and output frequency curves of the Rubidium clock on GPS IIR satellite SVN-54 [8], it can be seen that jumps in the lamp light intensity coincided with jumps in the output frequency.

For GPS IIR satellite rubidium clock SVN-54 [8], the aging-removed frequency and light intensity curves are shown in Fig. 3. As it can be seen, during the overall

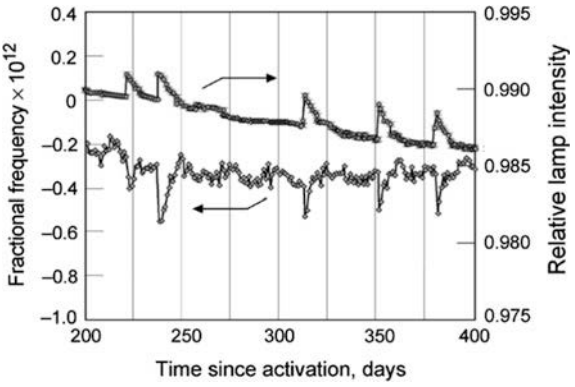

Fig. 2 Jumps in the lamp light intensity that coincide with jumps in the clock frequency for the Rb atomic clock on the GPS satellite SVN-54

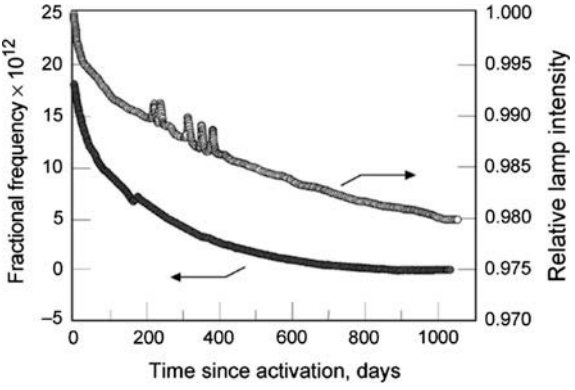

Fig. 3 Aging-removed fractional frequency and relative light intensity history for the Rb atomic clock on the GPS satellite SVN-54

frequency equilibration stage, the light intensity decayed about 2 %. The average intensity-dependent light-shift coefficient is about -1.4×10^{-12}/%, thus the decay in light intensity during the frequency equilibration stage contributes to a frequency change of -2.8×10^{-12}. However, the practical output frequency of rubidium clock shifted -1.4×10^{-11}, so the frequency change caused by intensity-dependent light-shift effect is far less than the total amount of variation in output frequency of the satellite Rb clock, which indicates that relevance between the intensity-dependent light-shift effect and the frequency drift of the Rb clock is very small. The results are consistent with the studies of Volk-Frueholz [9]. Meanwhile, for the GPS IIR Rb clocks it was also found that the intensity-dependent light shift and the frequency drift of the Rb clock have a opposite direction. Therefore, it can be inferred that intensity-dependent light shift is not the main mechanism affecting the frequency drift for the satellite Rb clock.

The light shift is not only relevant with light intensity but also with the spectrum overlap between pumping light spectrum passing through the filtering cell and the absorption spectrum of rubidium atoms inside the absorption cell. It can be seen from Eq. (4), in addition to changes in light intensity, slow variation in spectral profile of pumping light can also cause frequency shift. The temperature of spectrum lamp, the power of RF excitation circuit, temperature of the filtering cell and other factors will alter the spectrum profile of the pumping light within the absorption cell, leading to a slow change in output frequency of the Rb clock. Camparo [10] found that the spectral-dependent light shift was not zero, but in the same order of magnitude with frequency drift rate A of the Rb clock. Therefore, the light shift relating to the variation in the spectral profile of pumping light may be an important mechanism influencing frequency drift of the Rb clock.

3.2 Helium Permeation

Bloch et al. [6] showed that the slow frequency drift of the vapor cell Rb atomic clock may be caused by helium permeation of absorption cell through helium pressure shift effect. Rubidium absorption cells are generally filled with a certain pressure of buffer gasses, such as N_2, Ar, etc. These buffer gas molecules serve to eliminate the Doppler broadening and quench fluorescence through frequent collisions with rubidium atoms. The absorption cells are often made of a certain material of anti-alkali glass which is impermeable for buffer gasses, such as N_2, Ar, etc. However, the phenomenon that helium molecules can penetrate the glass material because of its small atomic radius has been confirmed by many experiments [11]. Permeation of helium will cause the pressure variation inside the absorption cell, thus causing output frequency shift of the rubidium atomic clock.

Atmospheric pressure of helium is 0.53 Pa. Pressure frequency shift coefficient of helium is 7.88×10^{-10} Pa. Therefore, the maximum frequency shift caused by

helium permeation is 4.2×10^{-10}. In the atmospheric environment, the helium in air will slowly penetrate into the absorption cell and the increase of helium pressure will cause a positive frequency shift. However, in vacuum helium will come out of the absorption cell, contributing to a positive frequency shift.

When working under vacuum, helium pressure inside the absorption cell changes with time as follows:[8]

$$P_{\text{cell}} = P_0 \cdot e^{-t/\tau} \tag{6}$$

Where P_0 is the initial helium pressure in cell, $\tau = 1/k\eta\Gamma$ is the time constant for the helium permeability coefficient in glass, η is the coefficient associated with temperature T, Γ is the coefficient associated with cell dimensions.

Frequency drift caused by helium permeation relates to the initial helium pressure P_0 and the time constant τ related. Helium leak is a slow process that the helium pressure inside the cell is difficult to measure.

Bloch [5] found that in the atmosphere rubidium clocks exhibited a positive frequency drift, while in vacuum it exhibited a negative frequency drift. Helium permeation mechanism can explain frequency shift in experiments and the total amount of the frequency shift during in frequency equilibration stage is also within the range of the frequency shift caused by helium permeation, which are the strong support of helium permeation mechanism. However, the time constant of the frequency equilibration stage of each GPS IIR rubidium clock distributed widely, according to statistics time constant ranged in 100–600 days [8], which helium permeation mechanism is difficult to explain. Because these satellite rubidium clocks are developed by the same manufacturer, utilizing the same material, design, and craftsmanship. Meanwhile, according to estimates, the effect due to helium permeation in the lamp bulb and the filtering cell should be negligible.

Therefore, helium permeation mechanism is difficult to satisfactorily explain frequency drift during the frequency equilibrium stage.

3.3 *Other Mechanisms Affecting Frequency Drift*

During the frequency equilibration stage, a variety of physical and chemical interactions occur, accompanying with redistribution of metal rubidium in the lamp bulb, the filtering and absorption cells. Migration of liquid metal rubidium in the lamp bulb can cause slow variation in quality factor Q value of radio frequency oscillation circuit, thus changing the lamp operating status thereby affecting the output frequency. At the same time, studies have shown that the metal rubidium redistribution on wall surface of absorption cell will cause a slow variation in Q value of the microwave cavity [12] with time constant of 10^2 days, which affects the output frequency of the rubidium atomic clock through cavity pulling effects.

4 Discussion and Conclusion

This paper studies on mechanisms influencing frequency drift for the satellite rubidium atomic clock, including the light shift, helium permeation, cavity pulling frequency shift. Studies have shown that frequency drift of the satellite Rb atomic clock should be caused by the combined effect of a variety of mechanisms, and the light shift related to slow variation of light spectrum profile may be the main factor affecting frequency drift during the frequency equilibration stage. By means of adequate advance aging of the rubidium spectrum lamp, the filter cell, and the absorption cell, it will help to reduce frequency drift due to the spectrum-related light shift, thus shortening the duration required for frequency equilibration. At the same time, reducing the storage time of absorption cells in the atmosphere and the choice of a special material glass with a small helium permeation coefficient will help reduce frequency drift due to the helium permeation. Migration of liquid metal rubidium in lamp bulbs, filtering and absorption cells, which slowly changes Q value of light excitation oscillator circuit and the microwave cavity, thus causes frequency shift. Thus, the appropriate cold end for storage of metal rubidium should be set for the lamp bulb, the filtering and absorption cells in order to avoid rubidium redistribution, which may reduce frequency drift for the satellite rubidium clock, requiring further experimental verification.

References

1. Busca G, Frelechoz C (2003) Space clocks for navigation satellite. In: Proceedings of the 2003 IEEE international frequency control symposium and PDA exhibition jointly with the 17th European frequency and time forum, pp 172–178
2. Vannicola F, Beard R, White J (2011) GPS block IIF atomic frequency standard analysis. 42nd annual Precise Time and Time Interval (PTTI) meeting, pp 181–195
3. Coffer JG, Camparo JC (2000) Long-term stability of a rubidium atomic clock in geosynchronous orbit. 31st annual Precise Time and Time Interval (PTTI) systems and applications meeting, pp 65–73
4. Bloch M (1996) Performance data on the milstar rubidium and quartz frequency standard: comparison of ground test in a simulated space environment to results obtained on orbit. In: IEEE international frequency control symposium, pp 1057–1065
5. Bloch M, Mancini O, McClelland T (2002) Performance of rubidium and quartz clocks in space. In: Proceedings of the 2002 IEEE international frequency control symposium & PDA exhibition, pp 505–509
6. Camparo J, Klimcak C (2008) Influence of the atmosphere on a rubidium clock's frequency aging. 39th annual Precise Time and Time Interval (PTTI) meeting, pp 317–322
7. Wang YQ (1986) The quantum physics of atomic frequency standards. Beijing Science Publishing House, pp 386
8. Camparo J, Klimcak C, Herbulock S (2005) Frequency equilibration in the vapor-cell atomic clock. IEEE Trans Instrum Meas 51:1873–1880

9. Volk CH, Frueholz RP (1985) The role of long-term lamp fluctuations in the random walk of frequency behavior of the rubidium frequency standard: a case study. J Appl Phys 57(3):980–983
10. Camparo J (2005) Does the light shift drive frequency aging in the rubidium atomic clock? IEEE Trans Ultrason Ferroelectr Freq Control 52:1075–1078
11. Altemose VO (1954) Helium diffusion through glass. J Appl Phys 32(7):868–875
12. Coffer J, Sickmiller B, Camparo J (2004) Cavity-Q aging observed via an atomic-candle signal. IEEE Trans Ultrason Ferroelectr Freq Control, 51:139–145

Development of a New Type of Spaceborne Miniaturized Rubidium Clock

Rongyan Zhang, Yu Zhang, Jiayu Hu, Feng Xu, Chang Liu, Tao Yang and Min Cheng

Abstract Spaceborne rubidium clock has been widely used in the fields of navigation satellites, remote sensing satellites, and so on. With the continuous expansion of application fields, spaceborne rubidium clock miniaturization put forward higher requirements. This paper introduces a new type of miniaturized spaceborne rubidium clock. By optimizing the design, performance reached the level of similar foreign rubidium clock (3E-12/1s). The whole mass of the clock is less than 1.5 kg, half of the similar foreign clock, the Volume is less than 2L.

Keywords Spaceborne rubidium clock · Miniaturized

1 Introduction

Rubidium atomic frequency standard has been widely used for its small size and low power consumption. It occupies the largest market share of atomic frequency standards. Currently rubidium frequency standards developed in two directions: First, continue to improve performance and meet the needs of satellite navigation and other high end applications; second is to continuously reduce the size, power consumption, to meet the needs of the information industry.

With the rapid development of technology, the rubidium clock performance has surpassed the early prediction, GPS Block IIR and IIF spaceborne rubidium clocks exhibit excellent ground and in-orbit performance [1, 2] proved rubidium clock has great potential in spaceborne applications. The long-term stability, accuracy, and aging rate of atomic frequency standards is higher than quartz oscillator by two to three orders of magnitude, combined the good phase noise of crystal oscillator and

R. Zhang · Y. Zhang (✉) · J. Hu · F. Xu · C. Liu · T. Yang · M. Cheng
China Academy of Space Technology (Xi'an), 710100 Xi'an, China
e-mail: 635753365@qq.com

© Springer Science+Business Media Singapore 2016

J. Sun et al. (eds.), *China Satellite Navigation Conference (CSNC) 2016 Proceedings: Volume III*, Lecture Notes in Electrical Engineering 390,
DOI 10.1007/978-981-10-0940-2_57

low aging rate, high accuracy rate of the atomic frequency standard, use miniaturization technology to reduce the atomic frequency standard size, weight, power consumption, at the same time broaden the application temperature range, to meet the demand for high precision time and frequency source of more satellite system. Such atomic oscillator as one of the atomic frequency standards, in addition to small size, light weight, except that for phase noise and high short-term stability requirements while without requiring long-term stability.

China domestic has accumulated a wealth of experience in small commercial rubidium frequency standard research and have relevant batch of products, but in spaceborne miniaturized rubidium clock had not yet been publicly corresponding product. This paper introduces a new type of small onboard rubidium, by adopting new materials, new processes, new technology applications, and optimization of the design, the lightweight and miniaturization of the whole machine is realized. At the same time, ensure that the short-term stability, phase noise, and other electrical performance of the miniaturization clock comparable to the clocks used in the current Beidou navigation satellites, able to meet the demands of formation flying satellite, military communications satellite system. Miniaturized spaceborne rubidium clock can be directly used in high orbit early warning satellites, formation flying satellites. It can also replace the high stability crystal oscillator used in communication satellite, provides high performance, high reliability, and lightweight frequency standard to the satellite system.

2 Machine Design and Technical Features

2.1 Machine Design

Rubidium clock generally consists of a voltage-controlled crystal oscillator (VCXO), frequency integrated circuit, the physical part and the servo circuit. VCXO output signal generating 6.83468 GHz FM signal by frequency multiplication and frequency synthesizer, comprehensive measures, 6.83468 GHz signal is send into the physical part, excitation rubidium atoms hyperfine levels of the ground state transition, produce a resonance signal, this signal changes the light intensity when the rubidium light in the physical part through the absorption bulb, and we get photodetector signal of the physical part (the physical part is to change the difference between the 6.83468 GHz excitation signal frequency and rubidium atomic transition line center frequency into an error voltage output, play the role of a frequency discriminator). The servo circuit makes the phase comparison between the photodetector signal and the discriminator signal, gets the correction voltage obtained by integrating, then the voltage feedback to a voltage-controlled crystal oscillator, realize the automatic control of the physical part to the voltage-controlled oscillator frequency. With this loop, voltage-controlled oscillator output frequency is locked at the resonance frequency of the physical part of rubidium clock [3].

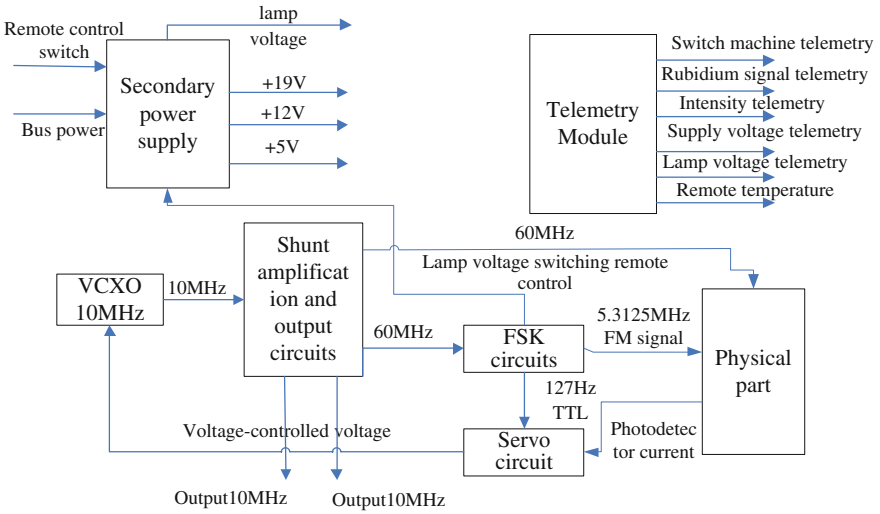

Fig. 1 Block diagram of miniaturized rubidium clock

In order to achieve lightweight, compact design goals, we design on the basis of past experience, uses a modular design, the miniaturized rubidium clock according to the function is divided into four modules, two circuit boards. Among them, the four modules are: the physical part, the secondary power, integration module, and high stable oscillator. Two circuit boards, respectively: telemetry, adapter and FSK circuit, a servo circuit. As shown in Fig. 1.

Specific functions of each part are as follows:

The physical part: the physical part is the core components of miniaturized rubidium clock, play the role of the frequency reference and frequency discriminator, realize automatic frequency control loop with circuit parts together.

Secondary power supply: the primary bus voltage is converted into an internal voltage that other modules needed, four output voltages are +19, +12, +5 V, and the lamp voltage (adjustable).

Integration Module: integration module is the important component of the second generation of miniaturized rubidium atomic clock, mainly consists of two functional modules: shunt amplification and output circuitry temperature control circuitry. 10 MHz signal put into shunt amplifier circuit, and out put two way 10 MHz signal and two way 60 MHz signal. Temperature control circuit is used to implement the temperature control of the second mounting surface of the physical part.

The servo circuit: Change the photodetector current signal into a frequency discriminator error voltage-controlled oscillator to achieve locking.

Telemetry adapter and frequency synthesizer (FSK) circuit: telemetry transfer circuit implementation of rubidium clock status monitoring, and line transfer, commissioning, testing point settings, and other functions. At the same time input

60 MHz signal, output 82 Hz TTL, and 5.3125 MHz FSK signal and outputs a lamp voltage switching command.

2.2 Technical Features

Miniaturized rubidium clock adopts a number of measures to ensure that in the case of the performance satisfy the requirements, minimize weight and volume. Mainly in the following aspects:

2.2.1 Structural Design

Miniaturized onboard rubidium clock is designed with a modular design, integrate the traditional rubidium clock as far as possible, After determining the functions and interfaces of each module, using the optimized structure design, so that each modules and single board closely surrounds the physical part, so that both reduces the volume and weight, but also to avoid wiring complex problems caused by excessive circuit board.

In the rubidium clock the structure accounted for most of the weight of the machine, by using a new type of alloy materials, the whole weight can be greatly reduced, while ensuring stable and reliable structure.

The structural design fully consider the thermal characteristics and mechanical characteristics of the machine, each module stress distribution conducted a simulation analysis, improved the weakness part of the analysis results, takes the methods of strengthen the tendons and so on to ensures its mechanical properties meet the requirements.

2.2.2 Circuit Design

Power supply module uses a single-ended flyback topology circuit program, for the flyback circuit does not need an output inductor, and will not increase the reset circuit, small devices, the circuit is simple, when multi-output this kind of circuit will reflect on the advantages of volume, it is the low power common circuit topology scheme.

In the circuit design inside the clock, synthesizer circuit, telemetry circuit, switching circuit of the three merged into a single board, the PCB layout process digital and analog isolation, and use a flexible printed circuit board technology. This program is not only greatly reduce the board size and wires between various boards, but also simplified the manufacture and test process, it is beneficial to reduce manufacturing costs and batch production.

The servo circuit uses a single power supply design helps reduce the volume of the power module.

Many of miniaturized rubidium clock circuit is low frequency circuit, in order to further reduce the volume of rubidium clock, ascertain board technical state, reduce testing and assembly work, these separate components of the circuit can use hybrid integrated circuits. Hybrid IC has a long application history in the satellite. Nowadays the hybrid IC can make a relatively large capacitance values and relatively high voltage solid tantalum capacitors together. It is suitable for rubidium clock circuit requirements, most of the active component are operational amplifiers, others are the resistance and capacitance (including tantalum capacitance), and they are all low power consumption components, beneficial to hybrid integration. By using a hybrid integrated circuits, servo circuit noise can be further reduced, improving short-term frequency stability of the clock, and also facilitate the realization of the whole circuit miniaturization design.

In addition, in order to improve overall performance, the clock also used the scanning capture circuit and FSK phase adjust circuit, the scan capture circuit will adjust the oscillator frequency over a wide range when the clock is power on, ensure the oscillator frequency quickly get into the capture range of the clock, this will improve the successful lock rate of the clock, meanwhile reduce the lock time. FSK phase adjust function can fine tune the 5.3125 MHz signal phase, make the phase aligning with 82 Hz modulation signal. In the test, after using a phase adjust function, Vss signal waveform has significantly improved, 1 s stability can be increased from 6×10^{-12} to about 2×10^{-12}.

2.2.3 Design of Physical Part

The physical part of the miniaturized rubidium clock use three bulb separation filter system program, the filter and the resonance transition completed in a separate filter bulb and absorption bulb, respectively, a separate filter bulb is conducive to optimizing the filter effect, the density of inverse population is high, so the SNR is high too. The lamp cavity, the filter bulb and absorption bulb execute temperature control, respectively, in favor of adjusting the optical frequency shift and temperature coefficient. Using intracavity frequency doubling scheme and photocell as photodetector, help to improve the efficiency of light detection and rubidium clock miniaturized. Compared to the past, the physical part of rubidium clock has the following characteristics:

1. TE_{011} magnetron microwave cavity and the intracavity frequency doubling technology
   Small rubidium atomic clock technology based on preliminary research and studies, the microwave cavity design uses a TE_{011} mode magnetron microwave cavity and the intracavity frequency doubling technology program. The magnetic field component of the electromagnetic field in the TE_{011} cavity is near the axis of the cavity (just the microwave-atomic interaction area), parallel with the chamber axial (Z direction) line and densely distributed, so this field mode is

ideal for excitation ^{87}Rb atom 0-0 transition, and the Q value is high, you can achieve a high signal to noise ratio.

Meanwhile, the intracavity frequency doubling efficiency is high, and SRD is in a temperature controlled microwave cavity, help to reduce the overall temperature coefficient.

2. Use silicon photovoltaic cells for signal detection
   Silicon photocell works photovoltaic effect, it is a large area photodiode, it can convert the light energy incident on its surface to electric energy. The design chosen a single large area silicon photocell 2CR43 instead of photodiodes, reduce the volume of photodetector unit and simplify the circuit.
3. Temperature control circuit design
   This design uses two temperature control scheme, one way to control the temperature of the rubidium bulb separately, use film heater heating method, provide temperature stable working environment for the rubidium lamp, for stable light intensity and lower rubidium spectrum lamp power consumption purposes. Another temperature control way using optical absorption bulb and filter bulb temperature compensation scheme, namely the absorption bulb and filter bulb using the same temperature control device, set a temperature point, use thin-film heater heating, further reducing the size and weight of the temperature section, simplify temperature control device. The lamp chamber and resonator are each buried two thermistor MF-51-33 k-3900 as temperature control thermistor and temperature measurement thermistor, in which the temperature measurement thermistor was threaded as the telemetry signal of the physical part.

   Through the above measures, the final design of the whole mass is less than 1.5 kg, smaller than 2 L, compared with similar imported clock is reduced by 1/2. The whole clock is in accordance with the requirements of aerospace product design, with high reliability, to meet the demand for the use of satellites.

3 Performance Test Results

After the machine design is completed, we conducted a number of test, the final test results obtained are shown in Table 2 and Fig. 1, where the short-term stability and phase noise was measured by TSC5115, the reference source is the hydrogen clock in laboratory (Fig. 2; Table 1).

As can be seen from the test results, short-term stability within a hundred seconds is good, but after 1000 s stability performance got worse, a preliminary analysis the reason for the machine temperature control, and is currently being resolved.

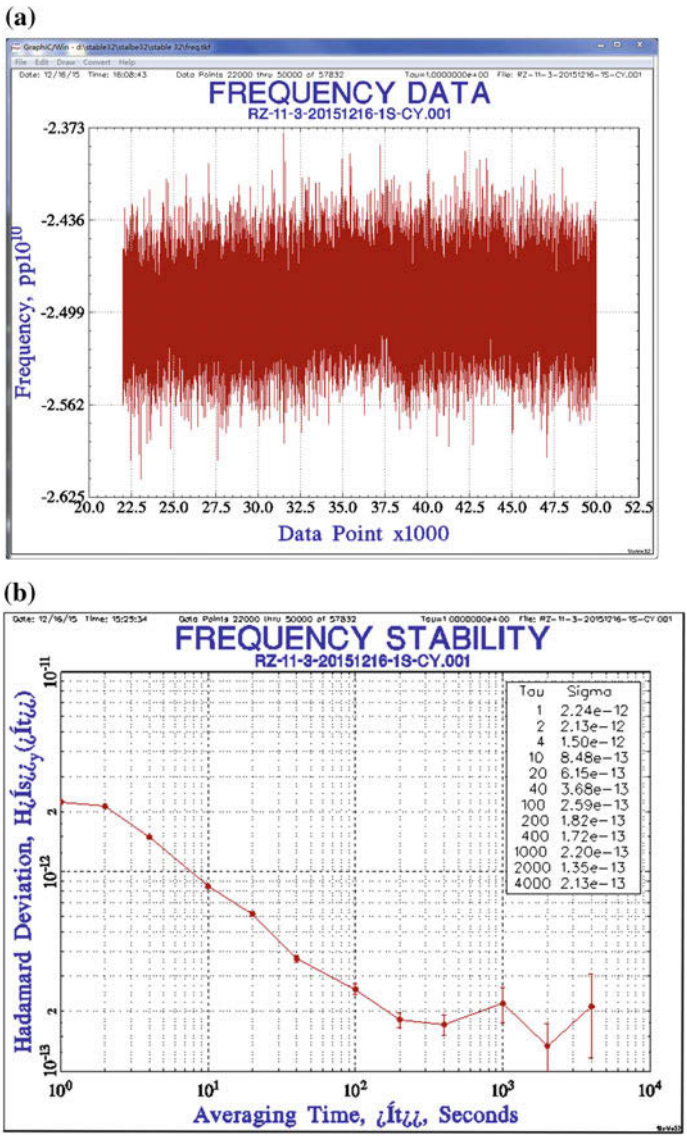

Fig. 2 Frequency stability test results of miniaturized rubidium clock. **a** Frequency data. **b** Frequency stability

Table 1 Phase noise of miniaturized rubidium clock

Phase noise (dBc/Hz)	
1 Hz	−106.4
10 Hz	−125.1

4 Conclusion

This paper introduces a new type of miniaturized onboard rubidium clock, through the optimization of structure, circuit, and physical part, the performance is similar to the imported rubidium clock, while significantly reducing the mass and volume of the clock. The next step will be integrated servo circuit in film thick, while continuing to optimize the circuit parameters, further reducing the overall size and weight and improve overall performance. The latter will follow on the aerospace standard to conduct temperature and mechanical tests, in order to meet the needs of aerospace applications.

References

1. Dass T, Freed G, Petzinger J et al (2002) GPS clocks in space: current performance and plans for the future. In: 34th annual precise time and time interval (PTTI) meeting. Virginia, USA
2. Vannicola F, Beard R, White J et al (2010) GPS block IIF atomic frequency standard analysis. In: 42nd annual precise time and time interval (PTTI) meeting. Virginia, USA
3. Yiqiu W, Qingji W, Jishi F et al (1986) Principle of quantum frequency standard. The Science Publishing Company, Beijing

Analyzing Prediction Methods and Precision of GNSS System Time Offset Using End-Point and Kalman Filter

Lin Zhu, Huijun Zhang, Xiaohui Li, Ye Ren and Longxia Xu

Abstract GNSS compatibility and interoperability is one of the most significant problems in multi-system navigation and position. The precise prediction of system time offset is one of the most important problems for application of GNSS compatibility and interoperability. To increase the prediction precision of system time offset and meet the requirement of multi-system users, this essay studies the prediction algorithm of system time offset. First, based on research on the prediction principle of end-point (EP) and Kalman filter, the feature of GNSS system time offset is analyzed. The initial values of Kalman filter parameters are determined to reduce the uncertainty and error caused by it. In addition, the real-time measurement data is provided by a platform that monitors GNSS system time offset at National Time Service Center (NTSC). It verifies the applicability of two methods to predict the system time offset and compares the precision of EP and Kalman filter. The result shows that for any type data of system time offset, when real-time precision prediction is required, Kalman filter provides higher precision and will be influenced less significantly by other factors: For GPS data, precision is about 1 ns and for GLONASS data, it is 2 ns. It is 0.5 times higher than that of EP. In other cases, EP is more precise.

Keywords GNSS · System time offset · End-Point · Kalman · Prediction

L. Zhu (✉) · H. Zhang · X. Li · Y. Ren · L. Xu
National Time Service Center, The Chinese Academy of Sciences,
Lintong, Shaanxi, China
e-mail: zhulin@ntsc.ac.cn

L. Zhu · H. Zhang · X. Li · Y. Ren · L. Xu
Key Laboratory of Precision Navigation Positioning and Timing,
Chinese Academy of Sciences, Lintong, Shaanxi, China

Y. Ren
Graduate School of Chinese Academy of Sciences, Beijing, China

© Springer Science+Business Media Singapore 2016

J. Sun et al. (eds.), *China Satellite Navigation Conference (CSNC) 2016 Proceedings: Volume III*, Lecture Notes in Electrical Engineering 390,
DOI 10.1007/978-981-10-0940-2_58

1 Introduction

GNSS compatibility and interoperability is one of the most significant problems in multi-system navigation and position. Since every system has independent system time, one of the most important issues to make GNSS compatibility and interoperability applicable is to measure and predict GNSS system offset precisely. GNSS system time offset is the difference of between any two navigation system times. It is also called system time offset [1].

Normally, the methods being used for prediction are Kalman filter, gray model, end-point (EP), etc. [2]. Kalman filter is built-up based on dynamic system. It can reduce influence from random interference and can gradually get the unknown parameters, according to the characteristics of the filter [3]. Gray model method fits for data which has incomplete volume of data. According to essay of D.W. Allen, if the target is time and frequency data set, EP method is more appropriate and it is easier to ensure the parameter. Considering the feature of system time offset data, EP, and Kalman filter method are mainly compared to choose the most appropriate prediction method for system time offset.

2 Analysis of Prediction Principle

Basically, the relationship between reference time scale T and time of navigation system time scale GNSST can always be describe be a quadratic polynomial [3–6]:

$$T - \mathrm{GNSST} = a_0 + a_1 * (\mathrm{t} - \mathrm{t}_0) + a_2 * (\mathrm{t} - \mathrm{t}_0)^2 \tag{1}$$

where a_0, a_1, a_2 are time offset, frequency offset, and linear frequency drift offset of GNSST about T at epoch, t_0 is the reference time.

Defining z to be observed value, that is $z(t) = T - \mathrm{GNSST}$, if observation epoch is t_i, the observed residual at that t_i is v_i, let $\hat{a}_0, \hat{a}_1, \hat{a}_2$ to be the estimate value of a_0, a_1, a_2, then have [4, 6]

$$z(t_i) + v_i = \hat{a}_0 + \hat{a}_1 * (t_i - t_0) + \hat{a}_2 * (t_i - t_0)^2 \tag{2}$$

First, mathematical model is built by least squares criterion to get the fitting parameters of system time offset. As defining the optimal probability value to be calculated is z^*, then the residual of observe value is $v_i = z_i - z^*$. As least square criterion is to choose the z^* that makes the residual to be the minimum, z^* must be satisfied to Eq. 4 [6].

$$\sum_{i=1}^{N} v_i^2 = \sum_{i=1}^{N} [z_i - z^*]^2 = \min \tag{3}$$

After getting the fitting parameters of system time offset, it use EP and Kalman filter, respectively, to evaluate the fitting parameters. Then, the prediction model parameters of system time offset is achieved. Finally, the prediction is completed. The principle to apply EP and kalman filter on the known fitting model parameters is introduced in the rest of the essay.

2.1 Principle for End-Point Prediction

The principle for end-point prediction is to use the previous data as the evaluate value of time offset in the forecast model parameters. Characteristics of other parameters are gotten through different methods. For example, for white noise PM, the best estimation for time offset is average, for frequency offset is linear least square fitting, and for linear frequency drift offset is quadratic least square fitting. For white noise FM, the best estimation for time is the previous data and both frequency and linear frequency drift offset is got from linear least square fitting [7].

For system time offset, it can be viewed as time offset that two sets of atomic clocks which keeps their time scale. It has the same characteristic with atomic clock. Meanwhile, it also has attribute of time, which is accumulation. Therefore, like quadratic polynomial prediction principle, fitting result of previous time can be used as the estimation of time offset in best prediction model parameters. Also, the best frequency offset and linear frequency drift offset can be acquired from quadratic least square fitting.

2.2 Principle of Kalman Filter Prediction

Since Kalman filter prediction contains unknown parameters, the principle of prediction has two parts: process of principle and determination of parameters.

2.2.1 Principle and Process of Kalman Filter Prediction

Kalman filter is a kind of linear minimum mean square error estimation. Defining $\hat{X}$ to be the estimation of X, then $\hat{X}(Z) = AZ + b$, that is, $\hat{X}$ have to satisfies Eq. 5 at least.

$$E[(X - \hat{X})^T (X - \hat{X})]|_{\hat{X}=\hat{X}(Z)} = \min \tag{4}$$

In addition, Kalman filter has time updating process and measurement updating process during every period of the filter. These two processes rely on each other, to estimate state parameters.

Based on the fitting model parameter of system time offset that is already known, according to the rule of Kalman prediction, following processes is executed to complete the estimation [5, 7, 8].

State equation is:

$$X_k = \Phi_{k,k-1} X_{k-1} + W_{k-1} \tag{5}$$

Measurement matrix is described as:

$$Z_k = H_k X_k + V_k \tag{6}$$

The estimation state values after k times of measurement:

$$\hat{X}_{k/k-1} = \Phi_{k,k-1} \hat{X}_{k-1} \tag{7}$$

Determine current estimation state values based on before estimation state values and current measurements:

$$\hat{X}_k = \hat{X}_{k/k-1} + K_k\left(Z_k - H \cdot \hat{X}_{k/k-1}\right) \tag{8}$$

Mean square error matrix after $k - 1$ times of measurement is:

$$P_{k/k-1} = \Phi_{k,k-1} P_{k/k-1} \Phi_{k,k-1}^T + N_k \tag{9}$$

Defined the filter gain which produce the minimum mean square error matrix is:

$$K_k = P_{k/k-1} H_k^T (H_k P_{k/k-1} H_k^T + R)^{-1} \tag{10}$$

Finally mean square error matrix after updating:

$$P_k = (I - K_k H) P_{k/k-1} \tag{11}$$

X_k is state matrix,$\Phi_{k,k-1}$ is the one step transfer matrix from t_{k-1} to t_k; W_{k-1} is excitement noise sequence of the system, Z_k is measurement at k epoch, H_k is unity vector, V_k is measure noise matrix, $\hat{X}_k$ is the estimation of X_k, N_k is extra noise matrix, R is measure noise matrix.

Above is the process for state estimation using Kalman filter. The best estimation $\hat{X}_k$ is achieved by Multiiterating. Because every kind of data has different features, when using Kalman filter to make prediction appropriate parameters has to be chosen according their trait.

2.2.2 Determination of Kalman Prediction Parameters

According to analysis prediction principle, when using Kalman filter to predict system time offset, following parameters have to be determined [7, 9].

1. State matrix
   According to the characteristic of system time offset, the least square fitting model being used is quadratic. Therefore, three parameters of fitting model parameters to be estimated is the elements of state matrix, that is $X(t)$ is 3 dimensional vectors.

$$X(t) = \begin{bmatrix} a_0 \\ a_1 \\ a_2 \end{bmatrix} = \begin{bmatrix} x_1(t) \\ x_2(t) \\ x_3(t) \end{bmatrix}$$

   $x_1(t)$ is time offset, $x_2(t)$ is frequency offset, $x_3(t)$ is linear frequency time drift offset.
2. Mean square error matrix

$$P(t) = \begin{bmatrix} p_{11}(t) & p_{12}(t) & 0 \\ p_{21}(t) & p_{22}(t) & 0 \\ 0 & 0 & 0 \end{bmatrix}$$

   The unit of $p_{11}(t)$ is s^2, of $p_{12}(t)$ and $p_{21}(t)$ is s^2/s and of $p_{22}(t)$ is s^2/s^2
3. State noise matrix
   For state noise matrix, it contains not only white noise but many kinds of noise. There are many ways of expression. For example:

$$Q = \begin{bmatrix} q_1\tau + q_2(\tau^3/3) & q_2(\tau^2/2) & 0 \\ q_2(\tau^2/2) & q_2\tau & 0 \\ 0 & 0 & 0 \end{bmatrix}$$

4. Measure noise matrix
   Measure noise mainly considers the noise during the measurement of system time offset. Measure noise matrix is R.
5. State propagation matrix
   According to the order of state matrix, state propagation matrix is a 3×3 matrix and it is based on the quadratic model of data at before epoch [7]:

$$\Phi(\tau) = I + F_k T + \frac{T^2}{2!} F_k^2 + \ldots$$

$$\Phi(\tau) = \begin{bmatrix} 1 & 0 & 0 \\ 0 & 1 & 0 \\ 0 & 0 & 1 \end{bmatrix} + \begin{bmatrix} 0 & \tau & 0 \\ 0 & 0 & \tau \\ 0 & 0 & 0 \end{bmatrix} + \begin{bmatrix} 0 & 0 & \frac{\tau^2}{2!} \\ 0 & 0 & 0 \\ 0 & 0 & 0 \end{bmatrix} = \begin{bmatrix} 1 & \tau & \frac{\tau^2}{2!} \\ 0 & 1 & \tau \\ 0 & 0 & 1 \end{bmatrix}$$

6. Unity vector
   This matrix is used to describe the relationship between measurement value and state vector at one epoch.

$$H = [1 \quad 0 \quad 0]$$

3 Analysis of Prediction Performance

Based on the analysis of prediction principle in part 2, using specific data to analyze the performance of two kinds of prediction method.

3.1 Method to Analyze

The essay chooses the data provided GNSS system time offset monitoring platform of Chinese academy of Science, National time server center. First, it bases on two prediction principles to construct the predicting functions, and the related parameters are estimated, the results are calculated. Then calculate the precision (root mean square, RMS) and compare them taking measurement data at the same time as the reference.

3.2 Determine the Initial Values of Prediction Parameters

During EP prediction, it only need to consider whether or not the data at previous epoch is reliable, and does not have to consider the dynamic information which is related to the estimated parameters and the statistic information about measure noise, so the prediction parameters need not to determine. During Kalman prediction, although some prediction parameters can be acquired from the iterating calculation during the prediction, the prediction speed and precision will effect on this procedure. Therefore, following parameters are determined before Kalman filter prediction.

3.2.1 State Noise Variance Matrix

System time offset contains multiple kinds of noise. Therefore, it is necessary to determine the state noise variance matrix according to noise attributes. The determine methods have following:

1. Based on the type of state noise
   The unknown parameters in state noise matrix are determined based on the stability of system time offset and following equation [10]:

$$\sigma^2 = (q_1)/\tau + (q_2) * \tau/3$$

   σ^2 is variance of measure results stability, q_1 and q_2 are parameters of state noise variance matrix, τ is the data interval.
   Refer to third party data, the performance of system time offset is evaluated with RMS. q_1 and q_2 are hard to determine, but q_1 are corresponding to q_2 each other. Thus, this essay views both $q1$ and q_2 as unknown. It determines q_1 in a range and then determines the according q_2.
   Because stability is different between UTC(NTSC)-GPST/GLONASST, separate calculation is needed. The parameter and result of the calculation is shown in Table 1.
2. Dynamic estimation of state noise variance matrix
   Use dynamic estimation to estimate the state noise matrix. According to Eq. (5) [3]

$$W(k-1) = X(k) - \Phi(k-1)X(k-1)$$

   Estimate state noise matrix through iteration estimation:

$$Q(k) = \frac{Q(k-1) + [W(k-1)W(k-1)^T]}{2}$$

3. Unit matrix
   Because that system time offset contains multiple noises, and it is difficult to separate them, to simplify the calculation, its initial value is assigned to be a 3×3 unit matrix.
   Taking three methods above in the Kalman filter method, and the monitoring data of system time offset as reference, RMS is determined, as been shown by Table 2.
   According to table above, the result gotten by different methods are not different significantly. Therefore, each one of the methods is ok. This essay chooses second method to determine the state noise variance matrix.

Table 1 Parameter and result during calculation of state noise variance matrix

Data type	RMS (s)	Optimal parameters	
		q_1 (s^2/s)	q_2 (s^2/s^3)
UTC(NTSC)-GPST	1.14×10^{-9}	1.10×10^{-9}	-9.17×10^{-13}
UTC(NTSC)-GLONASST	2.61×10^{-9}	2.60×10^{-9}	-2.17×10^{-12}

Table 2 The results comparison table with different methods

Evaluation result		Methods		
		Method 1	Method 2	Method 3
RMS(ns)	UTC(NTSC)-GPST	0.95	0.94	0.95
	UTC(NTSC)-GLONASST	1.89	1.89	1.89

3.2.2 Measure Noise Matrix

For the measurement of system time offset, the error caused by measurement during the process of transiting and receiving is eliminated. The measuring noise is negligible. Therefore, measure noise matrix considers mainly the noise in navigation system which is user range accuracy (URA). It can be determined by URA parameter which is broadcasted in navigation message. The method is as shown following equation [9, 11, 12].

$$(URA)^2(ns^2) \cong R(s^2)$$

Because URA will update in random time, it is necessary to update that data during the calculation.

3.2.3 Mean Square Noise Matrix

Because the mean square noise matrix of system time offset varies according to the variation of time offset, this essay assigns the initial value of that matrix to be

$$P(t) = \begin{bmatrix} 1 & 0 & 0 \\ 0 & 1 & 0 \\ 0 & 0 & 0 \end{bmatrix}$$

Through multiple iterate to update that matrix, the result from calculation is closer to real value.

3.3 Result Analysis of Prediction Experience

According to the methods of verification above, taking monitoring results of system time offset from 0:00 September 1, 2015 to 23:59 September 21, 2015 to be the original value. Predicts with EP and Kalman filter methods, and assigns different parameters (fitting length, prediction length, reference point of prediction, prediction frequency), and then the following results are achieved through calculation. As shown in Table 3.

From the result analysis it can be known

Table 3 Comparison table of prediction precision

Prediction parameters (fitting length, prediction length, reference point of prediction, and prediction frequency)	The prediction precision of UTC(NTSC)-GPST(ns)		The prediction precision of UTC(NTSC)-GLONASST (ns)	
	Kalman	EP	Kalman	EP
60/1/1/1	**0.95**	**1.37**	**1.89**	**2.68**
60/10/1/10	8.65	1.41	17.25	2.79
60/10/5/10	4.72	1.38	9.45	2.73
60/30/1/30	25.43	1.67	52.98	3.35
60/30/5/30	20.58	1.60	42.90	3.18
60/30/10/30	15.50	1.54	32.34	3.04
120/1/1/1	**0.95**	**1.35**	**1.89**	**2.65**
120/10/1/10	9.55	1.39	18.31	2.73
120/10/5/10	5.22	1.38	10.05	2.71
120/30/1/30	28.56	1.57	56.32	2.97
120/30/5/30	23.10	1.54	45.60	2.93
120/30/10/30	17.41	1.51	34.40	2.89
120/60/1/60	59.27	1.93	111.92	3.48
120/60/5/60	53.46	1.88	100.96	3.40
120/60/10/60	46.58	1.82	88.00	3.31
120/60/30/60	29.60	1.67	55.87	3.10
180/1/1/1	**0.95**	**1.39**	**1.89**	**2.65**
180/10/1/10	10.13	1.43	19.52	2.73
180/10/5/10	5.55	1.42	10.71	2.71
180/30/1/30	30.68	1.57	60.66	2.93
180/30/5/30	24.81	1.55	49.09	2.9
180/30/10/30	18.70	1.53	37.03	2.87
180/60/1/60	63.56	1.80	121.76	3.32
180/60/5/60	57.32	1.78	109.83	3.28
180/60/10/60	49.95	1.74	95.71	3.23
180/60/30/60	31.83	1.66	60.95	3.10

1. For two types (UTC (NTSC)-GPST/GLONASST), if the same prediction method is used, the trend for the variation of precision of date are the same with whatever parameters. That is, under the same situation, one method can be used to predict both types of data.
2. For each prediction method and any type of system time offset, when real-time precision prediction is required, the prediction precision is the best. Kalman filter can provide higher precision: for GPS data, the precision is about 1 ns, for GLONASS data, it is 2 ns. It is 0.5 times more precise EP. But in other cases, EP is more precise.

3. When others prediction parameters are same, the fitting length is 60, the prediction precision of Kalman filter is higher, and when the fitting length is 120, the prediction precision of EP filter is higher.
4. Kalman filter prediction precision will be more significantly influenced by other factors than EP.

4 Conclusion

This essay first introduces the prediction principle of nd-point and Kalman filter and, based on the principle, use the data of system time offset to compare the precision of both methods and get following conclusions: (1) when predicting UTC (NTSC)-GPST/GLONASST, when parameters are same, it can use only one process of prediction; (2) Real-time prediction is the most accurately for whichever methods; (3) When applying real time prediction, Kalman filter is more precise and receives less influence from other factors. Otherwise EP prediction is more precise. This essay compares the precision of two prediction methods mainly through analysis of real data. However, theoretically, Kalman filter method of prediction and parameters determination can be further improved.

Acknowledgments Funded by the National Natural Science Foundation of China (Grant No. 11503030) and the State Key Laboratory of Geo-information Engineering, No. SKLGIE2014-M-2-5.

References

1. Li X, Xu L, Zhang H et al (2011) Study on the interoperability of system time. China Satellite Navigation Conference, Shanghai, pp 319–325
2. Allan DW (1987) Time and frequency (time-domain) characterization, estimation, and prediction of precision clocks and oscillators. IEEE Trans Ultrason Ferroelectr Freq Control 34:647–654
3. Li X, Wu H, Gao H et al (2007) Clock disciplined method by using kalm an filter. Control Theor Appl 20(4):P551–P554
4. Liu X-G, Li J, Li Y et al (2008) The study of time prediction based on the methods of least square and kalman filter. Hydrogr Surv Chart Ing 28(3):24–26
5. Zhu S, Zhang S, Zhang Y Estimate and predict satellite clock error using Kalman filter. http://www.paper.edu.cn, pp 1–5
6. Ding Y (1998) Astronomical data processing method, Nanjing University Press, p 95
7. Davis JA, Stacey PW, Harris PM et al (2002) Combining time transfer measurements using a kalman filter. 34th Annual Precise Time and Time Interval (PTTI) meeting, pp 53–68
8. Qin Y, Zhang H, Wang S (2012) Kalman filter and integrated navigation principle. Northwest Industrial University press, p 35
9. Hutsell ST, Kalman filtering USNO's GPS observations for improved time transfer predictions

10. Brown KR (1991) The theory of the GPS composite clock. In: Proceedings of ION GPS-91, 11–13 Sept 91
11. ARINC Research Corporation (2004), Navstar GPS Space Segment/Navigation User Interfaces, ICD-GPS-200D. El Segundo, CA (12 Dec 2004)
12. GLONASS Interface Control Document (2008) Moscow

Analysis of the Effect of ODTS System Noise on the Performance Estimation of On-Board Clock

Dawei Sun, Xaolin Jia and Na Cheng

Abstract Depending on the orbit determination and time synchronization (ODTS) process, we consider at least two receivers driven by active hydrogen maser on the ground and then we analyze the effect of ODTS system noise on the performance estimation of on-board clock based on the difference between the clock offset of these two receivers. The IGS and GBM clock products are calculated in the method of ODTS, therefore the products contain the ODTS system noise. We could determine the system noise of ODTS quantitatively based on the method above, and the results show that system noise of IGS and GBM clock products is acceptable in the midterm and long term, and the IGS and GBM clock products could be used to estimate the mid-term and long-term performance of on-board clock.

Keywords System noise · Clock products · Orbit determination and time synchronization

1 Introduction

As the core component of satellites, atomic clock is essential to the navigation and positioning [1]. Therefore, monitoring and estimation to on-board clock are necessary [2, 3].

GPS satellites embark Rubidium clocks and Cesium clocks, BDS satellites embark Rubidium clocks, Galileo satellites are equipped with Rubidium clocks and Passive Hydrogen clocks, in addition, Cesium clocks are used in GLONASS [4].

D. Sun (✉)
Chang'an University, Xi'an, Shanxi, China
e-mail: 382481321@qq.com

X. Jia (✉)
Xi'an Research Institute of Surveying and Mapping, Xi'an, Shanxi, China
e-mail: 13891907401@139.com

N. Cheng
Xi'an Aerors Data Technology Co. Ltd, Xi'an, Shanxi, China

© Springer Science+Business Media Singapore 2016

J. Sun et al. (eds.), *China Satellite Navigation Conference (CSNC) 2016 Proceedings: Volume III*, Lecture Notes in Electrical Engineering 390,
DOI 10.1007/978-981-10-0940-2_59

Due to the complexity of the environment in space, it is more difficult to estimate the on-board clock than that on the ground. The clock performance is connected to the orbit determination and time synchronization (ODTS) method and error sources including receiver noise, orbital residuals [5], etc. The combined effects in the ODTS method [6] (called system noise), shall be determined quantitatively, which is critical to the on-board clock assessment.

ODTS method calculates the data collected from the stations to acquire the satellites orbit parameters, and based on the orbit and coordinates of stations, ODTS provides the offset between on-board clock and reference timescale on the ground.

The clock products provided by IGS or GBM [7, 8] could be used to estimate the performance of the GNSS on-board clock, but these products contain the ODTS system noise, which needed to be evaluated, its effect on the performance estimation of on-board clock.

2 Analysis on ODTS System Noise

Taking into account the time difference between the clocks are measured on the ground, we consider at least two stations on the ground which the receiver is connected to an atomic clock, which is more stable than the GNSS clock to be estimated, and acquire the clock offset. The clock offset between the two stations could be considered as the ODTS system noise effect.

Based on this thought, we choose several stations driven by a high precision atomic clock (we choose hydrogen clock), then we estimate the ODTS system noise using the clock offset between the two stations.

IGS and GBM provide precise clock products by the global network, and the nominal accuracy clock error is 0.1–0.2 ns. Several stations in the network are connected to the high precision frequency standard, and some are driven by the UTC main clock. Therefore, using these products, the performance of the satellite clocks can be investigated. Precise clock products are calculated in the method of ODTS, therefore the products contain the ODTS system noise. We could determine the system noise of ODTS quantitatively based on the method above.

3 Results of ODTS System Noise

We consider the system noise of IGS and GBM clock products separately. By the stations around the world, IGS and GBM process the ODTS method, and some stations [9] are listed in the Table 1.

We select the IGS precise clock products in January 2015, and the sampling rate is 300 s. Taking the station clock offset of amc2, ptbb, wab2, and usno, we calculate that the difference between two clocks can get ODTS system noise, and we

Table 1 Information of IGS stations (partly)

IGS stations	Clock standard style	Input frequency (MHz)	Commissioning date
algo	Active hydrogen masers	5	2015-03-23
amc2	Active hydrogen masers	5	1998-03-24
ieng	Active hydrogen masers	20	2014-02-05
irkj	Active hydrogen masers	5	2001-07-24
ptbb	Active hydrogen masers	20	2010-01-28
wab2	UTC (CH) main clock	20	2011-08-08
usno	Active hydrogen masers	5	1997-04-24

calculate the frequency offset and the Allan deviation [10–12] of clock offset difference. The results are shown in Figs. 1, 2, 3.

As shown in Figs. 1, 2, 3, the Allan deviations of clock offset difference of two AHM are generally the same: The Allan deviation of 10,000 s is about 5×10^{-15}, and the Allan deviation of 86,400 s is at the 2–3 $\times$ 10^{-15} level, which is better than

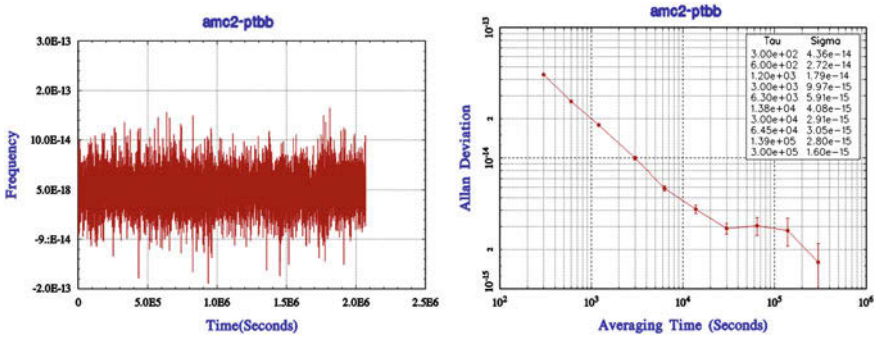

Fig. 1 Frequency offset, Allan deviation of clock offset difference of amc2-ptbb

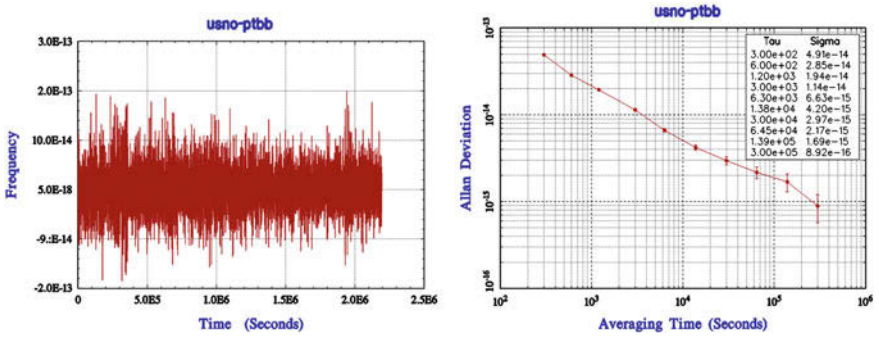

Fig. 2 Frequency offset, Allan deviation of clock offset difference of usno-ptbb

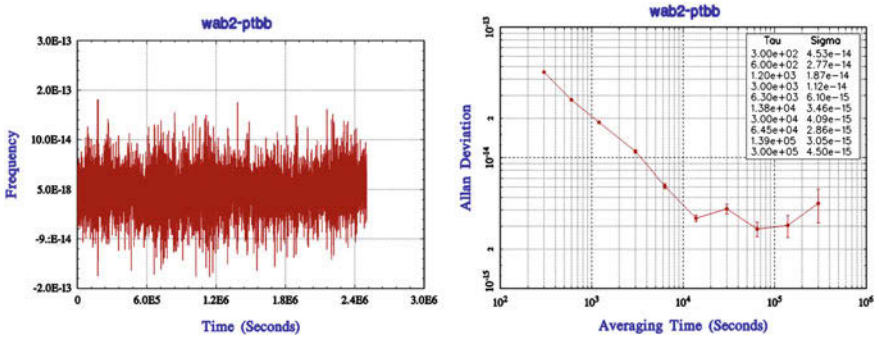

Fig. 3 Frequency offset, Allan deviation of clock offset difference of wab2-ptbb

the Allan deviation of Rubidium Atomic Frequency Standards and Cesium Atomic Frequency Standards on-board. But the short-term stability of ODTS system noise is at the same level as the frequency standards on-board. The result shows that IGS clock products could be used to estimate the long-term (10,000 s or longer) performance of GPS on-board clock, but not the short-term (300 s) performance.

To estimate BDS on-board clocks, we should use Multi-GNSS clock products, such as the products produced by GBM and iGMAS. The system noise of these products shall be analyzed, too. In this paper, we take the GBM precise clock products in June 2015, and the sampling rate is 300 s. The stations driven by active hydrogen masers are chosen to analyze the ODTS system noise, and we choose five stations: kour, mgue, usn4, usn5, and usn4. Like the system noise of IGS clock products, we do the same process on GBM clock products, and the results are shown in Figs. 4, 5, 6.

As shown in Figs. 4, 5, 6, the Allan deviations of clock offset difference of two AHM are generally the same: The Allan deviation of 10,000 s is about $1–2 \times 10^{-14}$, and the Allan deviation of 86,400 s is at the $2–4 \times 10^{-15}$ level, which is better than the Allan deviation of Rubidium Atomic Frequency Standards and on

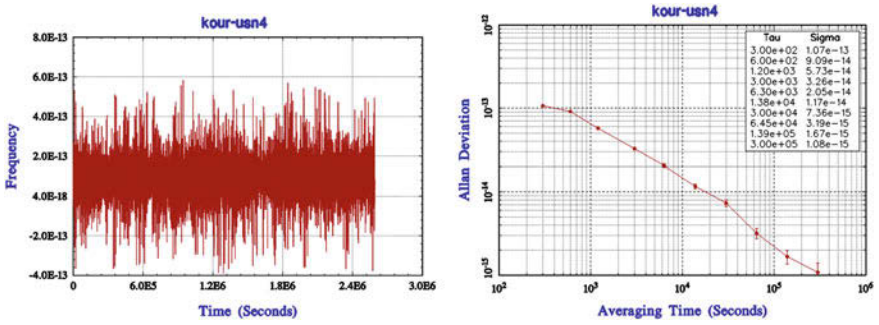

Fig. 4 Frequency offset, Allan deviation of clock offset difference of kour-usn4

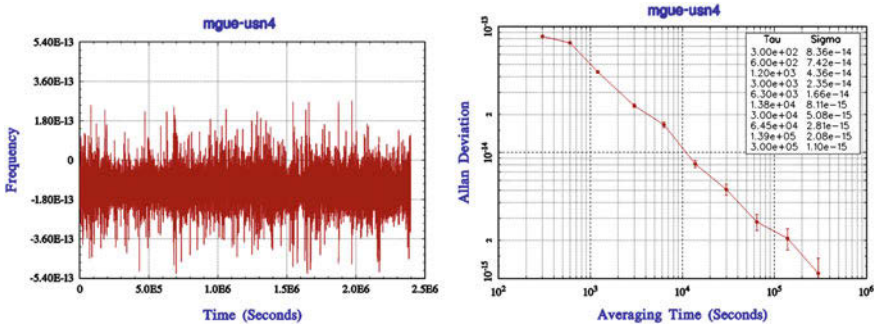

Fig. 5 Frequency offset, Allan deviation of clock offset difference of mgue-usn4

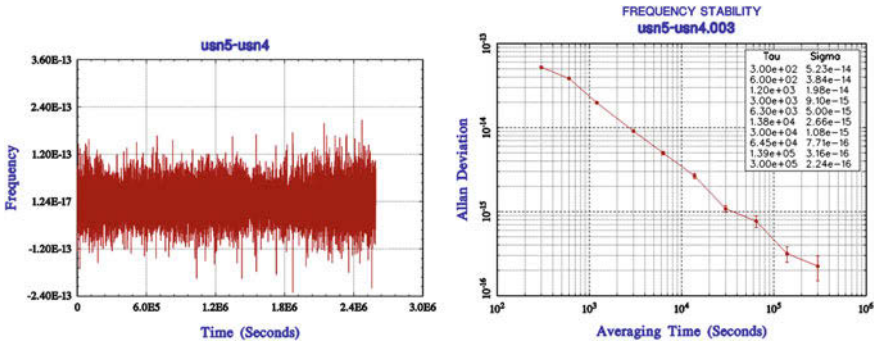

Fig. 6 Frequency offset, Allan deviation of clock offset difference of usn5-usn4

the ground. For the passive hydrogen masers on the ground, the results are only better when time goes to 86,400 s but to 10,000 s (the Allan deviation of passive hydrogen masers on ground is 1×10^{-14}). Additionally, the short-term stability of ODTS system noise of GBM clock products is at the same level as the ground frequency standards. From the analysis above, we could conclusion that the GBM products could be used to estimate the mid-term and long-term (10,000 s or longer) performance of on-board Rubidium clock, but not the short-term (300 s) performance, and we could only estimate the passive hydrogen masers on-board when time interval goes to more than 10,000 s. With the clock products by GBM, we could estimate the long-term performance of BDS on-board clock.

4 Conclusion

The clock offset between the two stations that are driven by ground high precision clocks could be considered as the ODTS system noise effect, and the analysis on the clock offset could show the effect on the on-board clock performance of ODTS

system noise quantitatively. From the tests above, we could see that the effect of system noise of clock products is optimistic, and we could use the clock products of IGS or GBM to estimate performance of on-board clock in the midterm and long term. Additionally, the Multi-GNSS products could be used to estimate BDS on-board clock.

References

1. Huang G, Zhang Q, Li H et al (2013) Quality variation of GPS satellite clocks on-orbit using IGS clock products. Adv Space Res 51(6):978–987
2. Jia XL, Feng LP, Mao Y et al (2010) Performance evaluation of GPS on-board clock. J Time Freq
3. Guo H (2004) Study on the analysis theories and algorithms of the time and frequency characterization for atomic clocks of navigation satellites. The PLA Information Engineering University, Zhengzhou
4. Cernigliaro A, Valloreia S, Fantino G et al (2013) Analysis on GNSS space clocks performances. In: European frequency and time forum and international frequency control symposium (EFTF/IFC), 2013 Joint. IEEE, pp 835–837
5. Waller P, Gonzalez F, Binda S et al (2010) The in-orbit performances of GIOVE clocks. IEEE Trans Ultrason Ferroelectr Freq Control 57(57):738–745
6. Cerretto G, Guyennon N, Sesia I, Tavella P, Gonzalez F, Hahn J, Fernandez V, Mozo A (2008) Evaluation of the ODTS system noise in the Galileo GIOVE mission. In: Proceedings of European frequency and time forum '08, Toulouse, France
7. ftp://cddis.gsfc.nasa.gov/
8. http://igs.org/mgex/
9. IGS Tracking Network Web Site, IRKT log. http://igs.org/network/site/irkt.html
10. Galleani L, Tavella P (2009) The dynamic Allan variance. IEEE Trans Ultrason Ferroelectr Freq Control 56(3):450–464
11. Galleani L, Tavella P (2007) Interpretation of the dynamic Allan variance of nonstationary clock data. In: Proceedings of joint IEEE international frequency control symposium and European frequency and time forum, Geneve, Switzerland
12. Sesia I, Tavella P (2008) The Allan variance for measurements with long periods of missing data and outliers. Metrologia 45(6):134–142

Research on the MAI Model of TWSTFT System and MAI Suppression Algorithm

Yachuan Bao and Baoguo Yu

Abstract Because of the advantage of high precision and long operating range, TWSTFT is becoming more and more important in the areas including time reference system establishment and maintenance, construction of GNSS and aerospace measurement and control. Focus on the multiple access interference (MAI) produced with the multiple signals in the same frequency in TWSTFT system, deep analysis is given in the article. Quantitative research of the influence of MAI to the measurement precision of spread spectrum signal and time comparison is made based on the theory simulation and experiment. The error model of MAI of TWSTFT is established, which is the basis of the signal link design and system performance evaluation. A MAI suppression algorithm of TWSTFT system is given in the article, and its effectiveness of the improvement of measurement precision is proved by experiments.

Keywords TWSTFT · MAI · Error model · MAI suppression algorithm

1 Introduction

Two-way satellite time and frequency transfer (TWSTFT) is a high precision long-range time synchronisation technology which is widely used at present. Because of its advantage of long range and high precision, it is used in time reference system establishment and maintenance, time synchronization between stations in GNSS area.

Scientists of nations have done wide research on TWSTFT. The error source of TWSTFT includes ionosphere error, troposphere error, Sagnac effect, equipment delay error, measure error, and so on. Following the wider usage of TWSTFT, multiple access interference (MAI) becomes one error source which needs to be

Y. Bao (✉) · B. Yu
State Key Laboratory of Satellite Navigation System and Equipment Technology, Shijiazhuang, China
e-mail: baoyachuan@126.com

© Springer Science+Business Media Singapore 2016

J. Sun et al. (eds.), *China Satellite Navigation Conference (CSNC) 2016 Proceedings: Volume III*, Lecture Notes in Electrical Engineering 390,
DOI 10.1007/978-981-10-0940-2_60

considered in some systems with big number of links. James Caffery has done some research on MAI influence on NC-DLL [1, 2]. The inland research about MAI influence on TWSTFT signal track and measure is less. Analysing the reason, one is because the MAI problem can be managed with a reasonable signal design in full wireless resource scene, and the other is the influence of MAI on measure precision in traditional system is small and can be ignored. But with the development of TWSTFT, precision requirement is higher and higher, and the influence of MAI cannot be ignored any more. The technology of anti-MAI becomes an important way to improve the precision of TWSTFT system.

Focus on the TWSTFT in multiple access scene, the article derivate the error model of TWSTFT with MAI. The MAI suppression method is given in the article. With the method the measure precision can be improved.

2 System Model of TWSTFT

2.1 Theoretical Principle of TWSTFT

Station A and B transmit measure signal at the moment t_{TA} and t_{TB}, and the time space counter is triggered. The signal transmitted by A is received by B at the moment t_{RB} and the counter in B stops to count. The signal propagation time is τ_{AB}, and the time measured by B is T_B. As well, the signal transmitted by B is received by A at the moment t_{RA} and the counter in A stops to count. The signal propagation time is τ_{BA}, and the time measured by B is T_A. The measurement results of station A and B are transmitted to the comprehensive process centre, and the clock difference between station A and B will be got after computation (Fig. 1).

If the signal propagation path and device process delay are absolutely symmetrical, TWSTT will eliminate all system errors. It is just the reason why TWSTT achieves the highest precision.

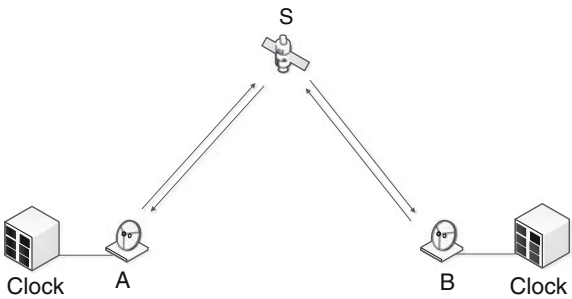

Fig. 1 Curve: TWSTFT system figure

2.2 Signal Model with MAI

When numbers of stations perform TWSTFT with central station, the multiple signals received by central station can produce MAI problem, which will make the measure precision worse.

On the assumption that there are N signals received by central station, signals are modulated by BPSK. In the scene of Gauss noise, the received signal can be written as

$$r(t) = a_0 p_0(t-\tau_0)\cos(\omega t+\theta_0) + \sum_{n=1}^{N-1} a_n p_n(t-\tau_n)\cos(\omega t+\theta_n) + N_0 \quad (1)$$

The first part of the formula is $a_0 p_0(t-\tau_0)\cos(\omega t+\theta_0)$, the expected signal, a_0 is the amplitude of expected signal, $p_0(t)$ is the pseudo-code wave form of expected signal, ω is the carrier frequency, τ_0 and θ_0 is the time delay and carrier phase of expected signal. N is the access number. a_n is the amplitude of signal n, $p_n(t)$ is the pseudo-code wave form of signal n, τ_n 和 θ_n is the time delay and carrier phase of signal n. N_0 is the power of noise.

Assume that the local carrier can track the signal frequency exactly, and the local signal is $\cos(\omega t+\tilde{\theta})p(t-\tilde{\tau}_0)$ and $\sin(\omega t+\tilde{\theta})p(t-\tilde{\tau}_0)$, in which $\tilde{\theta}$ is the estimated carrier phase and $\tilde{\tau}_0$ is the estimated code phase delay. Make the received signal and local signal correlation and sum computation, the correlation output of I and Q branch are

$$I_P = a_0 R(r)\cos\left(\tilde{\theta}-\theta_0\right) + \sum_{n=1}^{N-1} a_n R_n(r-\tau_n)\cos\left(\tilde{\theta}-\theta_n\right) \quad (2)$$

$$Q_P = a_0 R(r)\sin\left(\tilde{\theta}-\theta_0\right) + \sum_{n=1}^{N-1} a_n R_n(r-\tau_n)\sin\left(\tilde{\theta}-\theta_n\right) \quad (3)$$

In the formula, r is the time delay estimate error, $r = \tilde{\tau}_0 - \tau_0$. $R(r)$ is the self-correlation of expected signal, $R_n(r)$ is the cross-correlation of expected signal with other signals.

Pseudo-code-track loop uses the results of I and Q branch, estimate the code phase error with phase discriminator and loop filter. The delay of local pseudocode is adjusted constantly and the measure of expected signal is achieved.

The second part of formula (2) and (3) is the MAI to the expected signal. Assume the estimated carrier phases of signals are the same with the real one. The output of I branch is the sum of self-correlation of expected signal and cross-correlation of expected signal with other signals. In the MAI experiment using the pseudocode with 2000 period, the correlation peak distortion with 20 signals is shown in Fig. 2. Figure 2a is the self-correlation shape, and the peak is symmetrical and side lobe is small. Figure 2b is the scene with 20 accesses. The

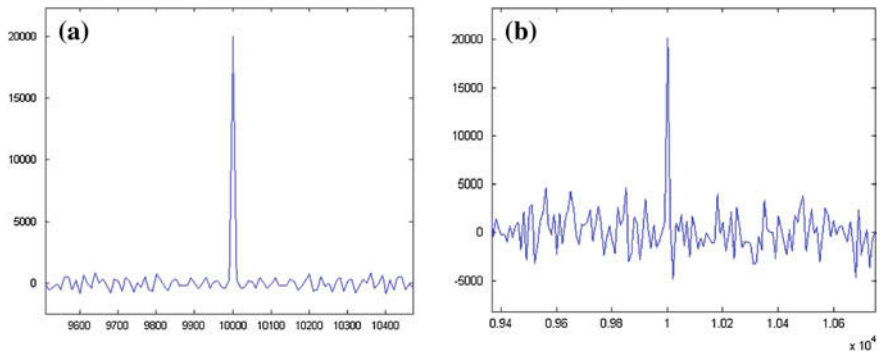

Fig. 2 Curve: system result of standard experiment. **a** Curve: correlation peak of one signal. **b** Curve: correlation peak of expected signal with MAI

peak is asymmetrical, which is caused by the sum of cross-correlation. It is the primary cause of the worse measure precision.

For the asynchronous spread spectrum signal measure system, the influence of MAI is time varying. The sum of correlation peak, the asymmetrical shape of main peak is time varying. The track adjust range of DLL is bigger, results in worse variance of measurement. For the synchronous spread spectrum signal measure system, the asymmetrical shape of main peak caused by MAI is relative constant. During the signal tracking process of DLL, constant error will occur on the code delay estimation. It will cause relative constant error during the period.

3 MAI Error Estimate Method

The measure precision of spread spectrum signal can be evaluated by uncertainty and stability. The influence of MAI is on the stability, which can be measured by the code track loop variance. The track error concerns with the design parameter of loop, including phase discriminator, noise bandwidth, correlation space, and so on. The references [3, 4] give the compute formula of code track error. Formulas (4)–(6) are the measure error compute formula with different phase discriminators including Non-coherent-amplitude method, Non-coherent-power method and coherent dot product method.

$$\sigma_{t\mathrm{DLL}} = \begin{cases} \sqrt{\frac{B_L}{2\cdot C/N_0} D\left(1+\frac{2}{(2-D)T_{\mathrm{coh}}\cdot C/N_0}\right)} \\ \sqrt{\frac{B_L}{2\cdot C/N_0}\left(\frac{1}{B_{\mathrm{fe}}T_C}+\frac{B_{\mathrm{fe}}T_C}{\pi-1}\left(D-\frac{1}{B_{\mathrm{fe}}T}\right)\right) D\left(1+\frac{2}{(2-D)T_{\mathrm{coh}}\cdot C/N_0}\right)} \\ \sqrt{\frac{B_L}{2\cdot C/N_0}\frac{1}{B_{\mathrm{fe}}T_C}\left(1+\frac{2}{(2-D)T_{\mathrm{coh}}\cdot C/N_0}\right)} \end{cases} \quad (4)$$

$$\sigma_{t\mathrm{DLL}} = \sqrt{\frac{B_L D}{2 \cdot C/N_0}\left(1 + \frac{1}{T_{\mathrm{coh}} \cdot C/N_0}\right)} \tag{5}$$

$$\sigma_{t\mathrm{DLL}} = \sqrt{\frac{B_L D}{2 \cdot C/N_0}} \tag{6}$$

In the formulas, B_L is the loop noise bandwidth, T_{coh} is the coherent time, D is the space between early and late correlation. B_{fe} is the RF front-end bandwidth, T_C is the code width of pseudocode.

There are numbers of methods to compute the SNR influence of MAI including Gaussian Approximation, Improved Gaussian Approximation, and Simple Gaussian Approximation and so on. The following formula is widely used in engineering SNR computation.

$$\left(\frac{C}{N_0}\right)_{\mathrm{eff}} = \frac{1}{\left(\frac{C}{N_0}\right)^{-1} + \frac{4\lambda}{3W}(k-1)} \tag{7}$$

λ is the bandwidth correction factor. W is the signal bandwidth.

Using the above formulas, the measure error of pseudo-code-track loop with MAI can be estimated in theory.

Figure 3 is the measure error of pseudo-code-track loop using Non-coherent-amplitude method. Figure 4 is the measure error of pseudo-code-track loop with MAI. The signal CNR is 70 dBHz and bandwidth is 4 MHz. Bandwidth correction factor is 1.15. The measure error is 4.3144×10^{-4} code with 20 access.

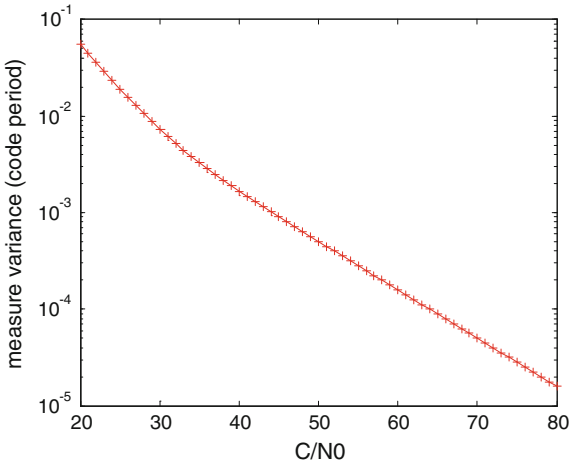

Fig. 3 Curve: measurement error of NC-DLL

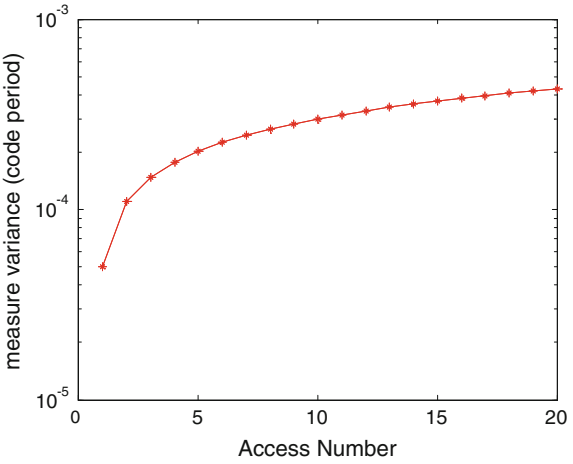

Fig. 4 Curve: measurement error of NC-DLL with MAI

4 MAI Suppression Method Focus on Pseudo code Measure

Focus on the MAI influence of time measure signal measure precision, MAI suppression method can be used to decrease the error.

At present, there are many kinds of MAI Suppression methods, but most of them focus on the improvement of BER. There are two groups of methods including multi-user joint detection and MAI cancellation. Joint detection method includes ML, ZF and MMSE methods, and MAI cancellation includes SIC and PIC methods [5–8].

But unfortunately, using the methods above directly cannot improve the measurement precision. The problem is that the traditional methods are used behind the signal track apartment. Without information feedback to code track loop, the signal track precision cannot be improved.

Anti-MAI spread spectrum method transfers MAI information to special signal tracking module to suppress the MAI influence to the signal measure. The process can use PIC method, to reduce the processing delay. The architecture of the method is shown in Fig. 5.

Main procedure of the method:

(a) All signals are acquired, tracked, power estimated and demodulated, respectively. Buffer the IF signal, the buffer size is decided by bit rate.
(b) Compute the relative time delay and correlation of the signals. Transfer the bit information and power estimation to the anti-MAI signal tracking module, using the buffer signal to achieve the signal measure with MAI suppression.

In the anti-MAI module, the phase discriminator must be reformed. Take coherent dot product method as example, the traditional code phase error compute method is

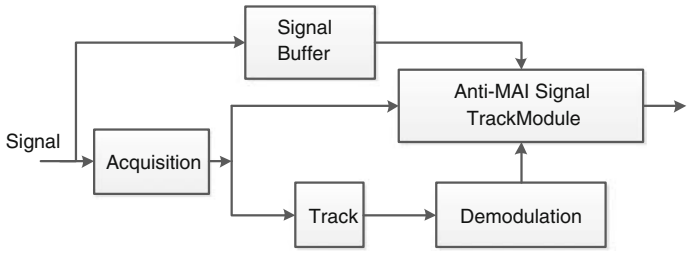

Fig. 5 Curve: MAI suppression algorithm aimed to improve measurement precision

$$\delta_{\text{cp}} = \frac{1}{4}\frac{I_E - I_L}{I_P} \tag{8}$$

The coherent integration is

$$I = \int_{t=0}^{T_{\text{coh}}} r(t) \times p_0(t) \times \cos\left(\omega t + \tilde{\theta}\right) \mathrm{d}t \tag{9}$$

To cancel the MAI influence in coherent integration it must be computed as following:

$$I' = \int_{t=0}^{T_{\text{coh}}} r(t) \times p_0(t) \times \cos\left(\omega t + \tilde{\theta}\right) \mathrm{d}t - \sum_{n=1}^{N-1} a_n R_n(r - \tilde{\tau}_n) \cos(\tilde{\theta} - \tilde{\theta}_n) \tag{10}$$

In the formula, $\tilde{a}_n$, $\tilde{\theta}_n$ is the estimation of amplitude, carrier phase of other signals. $\tilde{\tau}_n$ is the relative time delay between other signals and expected signal.

Using the method above, the MAI element can be cancelled in the coherent integration or Non-coherent integration. As a result, the MAI influence can be suppressed in signal track and measure module.

5 Simulation Analysis

Simulation research is performed on the spread spectrum signal measurement.

Assume that there are 20 users, and the code track loop use different phase discriminators including non-coherent power method and non-coherent amplitude method. The CNR of signal is 60 dBHz. Compute hundred variance of error between code phase measure value and code phase real value.

Figure 6a is the result of NC-power-DLL result. The single signal error is 1.3175×10^{-4} code, and the error in MAI scene is 4.8009×10^{-4} code. Figure 6b

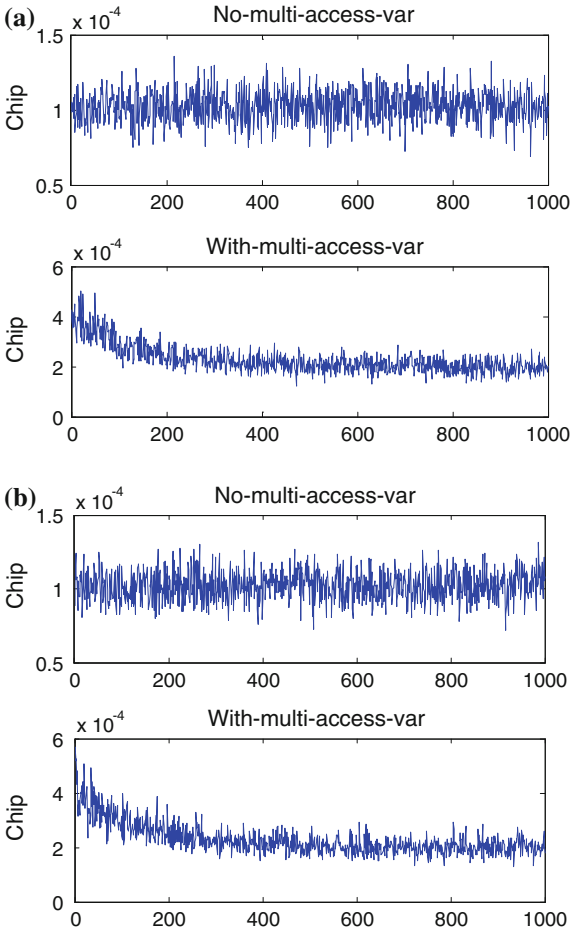

Fig. 6 Curve: measurement variance with MAI. **a** NC-Power-DLL, **b** NC-Amplitude-DLL

is the result of NC-amplitude-DLL result. The single signal error is 1.3286×10^{-4} code, and the error in MAI scene is 5.6793×10^{-4} code. The result shows that MAI can make big influence on signal measurement, and NC-power-DLL performs better than NC-amplitude-DLL.

Figure 7 is the result with the anti-MAI method. The error with anti-MAI method is 3.0109×10^{-4} code, and the error without anti-MAI method is 5.0112×10^{-4} code. The mean value of error is 1.4×10^{-4} code compared with 2.2×10^{-4} code. The measure precision improves 36 %.

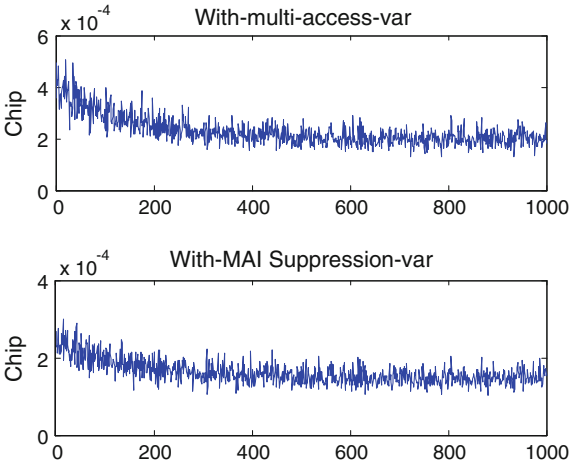

Fig. 7 Curve: measurement variance with MAI suppression algorithm

6 Summary

The article makes a research on the MAI influence on the spread spectrum signal measurement in the TWSTFT. The signal model is given in the article, and the reason how the MAI influence the signal measure is analysed. The MAI error estimate method is given in the article. Focus the MAI problem for measurement, a anti-MAI measure method is given. Based on the simulation, the error estimate method and the anti-MAI signal measure method is verified.

References

1. Caffery J (2000) Effects of multiple-access interference on the noncoherent delay lock loop. IEEE Trans Commun 48(12):2109–2112
2. Betz JW, Kolodziejski K (2009) Generalized theory of code tracking with an early-late discriminator part II: noncoherent processing and numerical results. IEEE Trans Aerosp Electron Syst 45(4):1551–1564
3. Betz JW, Kolodziejski K (2000) Extended theory of early-late code tracking for a band limited gps receiver. Navig J Inst Navig 47(3):211–226
4. Kaplan E (2006) Understanding GPS: principles and applications, 2nd edn. Artech House
5. Zheng W, Li J, Luo Y, Chen J Wu J (2013) Multi-user interference pre-cancellation for downlink signals of multi-beam satellite system. Intell Agent Multi-Agent Syst (IAMA) 415–418
6. Klein A, Baier PW (1993) Linear unbiased data estimation in mobile radio systems applying CDMA. IEEE J Select Areas Commun 1058–1066
7. Alam MZ, Alom MZ, Molla MKI, Hirose K, Sobhan MA (2008) OFDM based multi-path channel modeling using sub-carrier frequency shuffling to reduce ISI and ICI Effect. In: Proceedings of APPC, pp 1–4
8. Ei Barbary K, Alneyadi HM (2005) Comparison of the behavior of MMSE detection scheme for DS-CDMA and MC-CDMA. Second IFTP international conference, pp 490–495

Study on the Time Delay Calibration Method of TWSTFT Link

Ya Liu, Chen Shi, Xiao-tang Chen and Xiao-hui Li

Abstract Two-way satellite time and frequency transfer (TWSTFT) using geo-stationary telecommunication satellites has proven to be one of the most appropriate means of comparing time scales and atomic frequency standards with an uncertainty less than 1 ns. This paper analyzes what are the main errors sources of TWSTFT. And then, concludes that the main limiting factors for the improvement of the accuracy of TWSTFT are the calibration level of the equipment delay. A new method is used to calibrate link delay of TWSTFT based on double portable stations that has been proposed. A set of double portable stations (DPS) has been developed. To evaluate the performance of DPS, a compare and test platform has been designed including DPS, fixed ground stations of TWSTFT, fiber-based links. When the distance of two compared clocks are around 60 km, the DPS and fiber links are tested synchronously. The measurement results show that the systematic deviation of DPS is less than 0.1 ns, and the standard deviation is less than 0.2 ns. When the distance between two sites is around 3000 km, DPS compared with fixed ground stations, the standard deviation of the difference between the two systems measurement results are less than 0.3 ns. So we can get conclusion, the DPS calibrates links delay that the uncertainty of calibrating achieves less than 0.5 ns. It is helpful to improve the performance of TWSTFT.

Keyword Fiber links · TWSTFT · Portable station · Double portable stations (DPS)

Y. Liu (✉) · X. Li
National Time Service Centre, Chinese Academy of Sciences, Xi'an 710600, China
e-mail: liuya@ntsc.ac.cn

Y. Liu · X. Li
Key Lab. of Time and Frequency Primary Standards, CAS, Xi'an 710600, China

C. Shi · X. Chen
University of CAS, Beijing 100049, China

© Springer Science+Business Media Singapore 2016

J. Sun et al. (eds.), *China Satellite Navigation Conference (CSNC) 2016 Proceedings: Volume III*, Lecture Notes in Electrical Engineering 390,
DOI 10.1007/978-981-10-0940-2_61

1 Introduction

Two-way satellite time and frequency transfer (TWSTFT) using geostationary telecommunication satellite is the most appropriate means of comparing time scales and atomic frequency standards [1]. It is not only used to compare the time and frequency among various atomic frequency standards, but also used in satellite navigation system which contains multiple precision time units and distributes in different locations. Since the clocks of different sites need high-precision synchronization, the uncertainty of TWSTFT links time delay calibration is around 1 ns [2] and it represents the current level in time of TWSTFT too. According to the different transmission medium, link delay can be divided into two categories, including instrument delay and space propagation delay. The main sources of instrument delay are ground stations delay and satellite transponder delay. Equipment delay changes due to environment condition, equipment aging or other factors will change the delay and therefore increase the uncertainty. It is hard to be calibrated accurately, compared with the equipment delay, the sources of the signal in space propagation delay are much more complicated and changing variable including the ionosphere, troposphere, satellite motion, Sagnac effect, etc.

After years of research, there are a serious of means to reduce the uncertainty of signal in space propagation. Its influence is far less than the equipment delay currently. Therefore, uncertainty is a measure of the time transfer accuracy, which is dominated by the uncertainty of equipment delay calibration. This paper proposed a new method to calibrate link delay of TWSTFT system. It can also be used to calibrate the delay of other remote time comparison systems.

2 TWSTFT Basics

TWSTFT is used to compare remote clocks of frequency standards. At both clock sites, the time signals are transmitted at the same instance and on both sides the signal from the other clock is received and measured. Each measurement represents the determination of the time of arrival of a radio signal that is transmitted from the remote station and that is phase-coherent with the remote reference clock. The measurement result obtained at site 1, $\mathrm{TW}(1,2)$, is the time difference reading from a time interval counter (TIC) at site 1 receiving the signal from site 2. It includes the difference between the two clocks, $\mathrm{CL}(1) - \mathrm{CL}(2)$, and also the complete delay along the signal path. After the exchange of the measured data, the difference of the two clocks is calculated. The delays cancel due to the complete reciprocity.

But ideal reciprocity is non-existent. We need to apply some means to correct these effects to improve accuracy. The accuracy of the result then depends on the residual effects due to the incomplete reciprocity. The non-reciprocity factors are further addressed in the following sections.

Non-reciprocity due to satellite equipment delays, which can be reduced to less than 80 ps when using same transponder. The Sagnac effect correction can be operated using typical formula. Ionospheric delay is closely related to the carrier frequency and the total electron content along the signal path. It can be corrected using dual-frequency receiver [3, 4]. Ground station equipment delay refers to the difference of transmit and receive section including the up and down converters, modulator and demodulator, feeds, wiring, etc., has to be determined at each station. A portable station is colocated with the ground stations involved in the link, which mainly means that it has been demonstrated before that this method can very likely provide the required calibration uncertainty of 1 ns. The uncertainty of equipment delay is much higher than other non-reciprocity factors. So corrections equipment delay can be used to improve accuracy.

Research shows that the difficulties of accuracy calibration equipment delay were as follows:

1. Equipment delay changes with its environment condition, such as temperature, humidity, etc. Different environment should be calibrated to make sure accuracy;
2. NIST research shows that the relative change between GPS and TWSTFT transfer links can be as large as 6–7 ns over 7 years [5]. The change contributed by equipment delay could not be canceled or added in the opposite direction, because of its change direction being random. The study results point out the need for frequency calibration campaigns if accuracies at the nanosecond level are required;
3. In many cases, calibration campaigns have been very infrequent due to the expense and lack of suitable equipment.

In conclusion, in order to acquire higher accuracy, we need to improve the equipment delay calibration or propose better means instead of portable station method. In the next section, we will analyze current equipment delay means.

3 Calibration of Ground Stations

ITU recommends three methods to obtain this equipment delay including colocation of both stations, subsequent colocation of a third (transportable) ground station at both stations, and use of a satellite-simulator and calibrated cable. Despite the high accuracy, moving the fixed ground station is hard, resulting in colocation of both stations' unavailability [6]. Satellite-simulator is very expensive and each station needs one or portable, so it is difficult to operate. Another scholars put forward triangle closure condition, based on the known link calibrates unknown link time delay. It has the lowest cost, and the accuracy can only reach 2 ns level. Transportable ground station method is applied widely to calibrate equipment delay among Europe or America. Therefore, this paper will focus on transportable ground

station method. In addition, we propose a double portable stations (DPS) method to improve accuracy of TWSTFT.

3.1 The Portable TWSTFT Station

The method of portable station is a ground station instrument delay calibration method and recommended by ITU, the portable station (PS) is operated at two different sites A and B, respectively. At each site both the PS and the under calibrated station are connected to the same clock. The result between the colocated stations is the difference of the internal delays, which is named as the common clock difference CCD [2]. The CCD includes reference delay and relative delay between fixed ground station and PS. The reference delay refers to the transmission delay from the output port of under test clock to input port of equipment of fixed ground station or PS. It is measured easily. So we can acquire the relative equipment delay according to the CCD(A, PS) results. Then, the PS is transported to station B and connected with the reference clock there. The second CCD(B, PS) is acquired. So the relative delay between ground station A and B can be determined.

Based on previous experience, the calibration campaign was finished with a closure measurement at first site in order to demonstrate that the PS did not change significantly compared to expected uncertainties during the campaign. So the last step, PS should be moved back to the station A, and connected to the same clock with station A [2].

The Technical University of Graz in Austria (TUG), US Naval Observatory (USNO), and other agencies had developed themselves portable station. 21 links of European institutes participated in a TWSTFT calibration campaign to determine the equipment delay of fixed ground stations relative to the PS of TUG. The PS of USNO is used to calibrate the relative delay between USNO and five remote stations. Reference shows that the calibration uncertainty of slightly above 1 ns.

PS is the main means to determine relative equipment delay of TWSTFT. Nevertheless, PS calibrates the ground station delay is not perfect, there are several questions

1. The uncertainty is: 0.8–3 ns, it is difficult to improve and limits accuracy of TWSTFT;
2. The signal needs to be transmitted and received between PS and fixed ground station each other when do calibration campaign. So the PS has to use same frequency with fixed ground station, such as both are Ku or C bands;
3. PS is not sensitive for the under test station environment condition, because they are installed and measured at same location, respectively. So they suffer same effects from environment. But different sites may have different environment. The effect of measurement environment is hard to be reflected;
4. During the equipment delay calibration, the fixed ground station needs to communicate with portable station. So the fixed ground has to interrupt the

normal remote time comparison work, and it is not acceptable for the occasion which needs to be continually time comparison. In addition, even the comparison links can be interrupted temporarily, it can't be occupied either. It goes against to find some daily periodic phenomenon.

3.2 *The Double Portable TWSTFT Stations (DPS)*

In order to further improve the accuracy of TWSTFT, solve the problems of PS. This paper proposes a new double portable TWSTFT stations means to calibrate complete link delay. Its basic components include two sets of identical and movable TWSTFT ground stations [4]. It is called DPS. The calibration practice process is depicted by Fig. 1. The first step, two DPS are installed on site A and connected to the same clock, respectively. This step is used to calibrate DPS relative equipment delay; the second step, DPS 1 and DPS 2 are installed on site A and B and connected clock A and B as reference signal, respectively. This step is operated to acquire the time difference of two clocks; the third step, two DPS are installed on site B and connected to the same clock, respectively. This step is used to calibrate DPS relative equipment delay again.

The process of DPS 1 and 2 are used to measure link delay $\mathrm{CAL}(\mathrm{B},\mathrm{A})$ of TWSTFT A and B as follows:

First, DPS are installed on site A using same clock as reference signal, measure the relative equipment delay of DPS $\mathrm{CAL}(P_2,P_1)_{\mathrm{A}}$, expressed in Eq. (1):

$$\mathrm{CAL}(P_2,P_1)_A = 1/2[\mathrm{TW}(P_2,P_1) - \mathrm{TW}(P_1,P_2)] + [RDY(P_2) - RDY(P_1)] \quad (1)$$

where RDY is reference delay, TW is CCD measurement results, CAL is relative equipment delay.

Then, DPS are installed on site A and B, respectively. Time difference between site A and B can be measured synchronously by both fixed ground TWSTFT

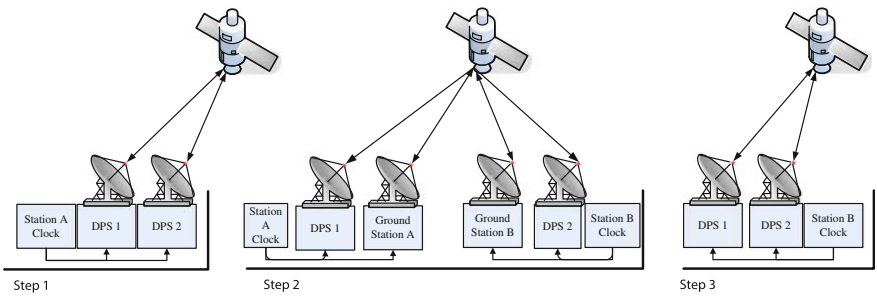

Fig. 1 Schematic of the double portable stations calibrated equipment delay

stations and DPS. The measurement results are expressed by Eq. (2) and (3), respectively.

$$\mathrm{CL(B)} - \mathrm{CL(A)} = 1/2[\mathrm{TW(B,A)} - \mathrm{TW(A,B)}] + [\mathrm{RDY(B)} - \mathrm{RDY(A)}] + \mathrm{CAL(B,A)} \quad (2)$$

$$\mathrm{CL(B)} - \mathrm{CL(A)} = 1/2[\mathrm{TW}(P_2, P_1) - \mathrm{TW}(P_1, P_2)] + [\mathrm{RDY}(P_2) - \mathrm{RDY}(P_1)] + \mathrm{CAL}(P_2, P_1) \quad (3)$$

where CL represents reference signal.

Finally, DPS is installed on site B using same clock as reference signal, measure the relative delay of DPS $\mathrm{CAL}(P_2, P_1)_{\mathrm{B}}$ again. In order to acquire the DPS delay change during the campaign. It can be expressed in Eq. (4):

$$\mathrm{CAL}(P_2, P_1)_{\mathrm{B}} = 1/2[\mathrm{TW}(P_2, P_1) - \mathrm{TW}(P_1, P_2)] + [\mathrm{RDY}(P_2) - \mathrm{RDY}(P_1)] \quad (4)$$

Equations (1) and (4) represent relative equipment delay of DPS, respectively, under the environment of station A and B. Then, we can calculate the relative equipment delay of DPS according to the Eq. (5) $\mathrm{CAL}(P_2, P_1)$.

$$\mathrm{CAL}(P_2, P_1) = 1/2\left[\mathrm{CAL}(P_2, P_1)_{\mathrm{A}} + \mathrm{CAL}(P_2, P_1)_{\mathrm{B}}\right] \quad (5)$$

Put Eq. (5) into (3), and using known reference delay RDY, so we can acquire the real time difference according to the Eq. (3). Then, the real time difference is substituted Eq. (2) to calculate the link delay $\mathrm{CAL(B,A)}$ of fixed ground TWSTFT station between site A and B. $\mathrm{CAL(B,A)}$ absorbs all influence of the link delay, including the ground stations delay, space propagation delay, etc.

The DPS combine the advantages of the colocation of both stations and PS means. It has the accuracy of colocation means and more flexible than PS means. It can improve significantly the accuracy of link delay of TWSTFT. Experiment shows that it can calibrate the link delay of TWSTFT to below 0.5 ns. It is better than all other means of calibration equipment delay. In addition, the DPS can work independently, unlimited by frequencies, equipment type, which decide that it not only be used to calibrate TWSTFT, but also be used for calibrating any other high-precision remote time comparison system. During calibration, DPS can work parallel with under test ground stations and uninterrupted normal operate. It is apparent difference with PS means that has to interrupt comparing time.

4 Experimental Results

The performance of DPS will be validated using following experiments including comparing with fiber-based time transfer system and fixed ground TWSTFT stations. Because the performance of fiber-based time transfer system is better than TWSTFT, we can use its measurement results as the true time difference of two clocks. Then comparing the measurement results with the true value, we can

evaluate the performance of DPS. The another experiment is that comparing with the fixed ground station distance from 3000 km, in order to test the capacity of DPS calibrating link delay of TWSTFT. The test case is described in detail below.

4.1 Comparison Test with Fiber

In order to test the performance of time comparison and equipment delay of DPS, making use of the approximately 60 km length of fiber link between Xi'an and Lintong, carried out comparing experiment. DPS and fiber link measured simultaneously two clocks that are located in Xi'an and Lintong, respectively. Test structure is shown in Fig. 2.

The output of the atomic clocks in Lintong and Xi'an, respectively, is used as reference signal, and use the equal length of cable access reference signal to DPS, eliminate the influence of the reference delay, and then used the DPS to test the time difference between two reference signals. At the same time, using fiber-based link measure time difference between two reference signals.

Taking into account the uncertainty of fiber-based link is less than 0.1 ns, therefore, the test result of fiber-based link can be considered as the true value of time difference of two clocks. According to the measurement principle shown in Fig. 2, for the same measurement object, ideally two systems should get exactly same measurements results.

Test time occurred July 10, 2015 05:42:00 to July 17, 2015 11:07:00, lasted about a week time and the difference in results are shown in Fig. 3.

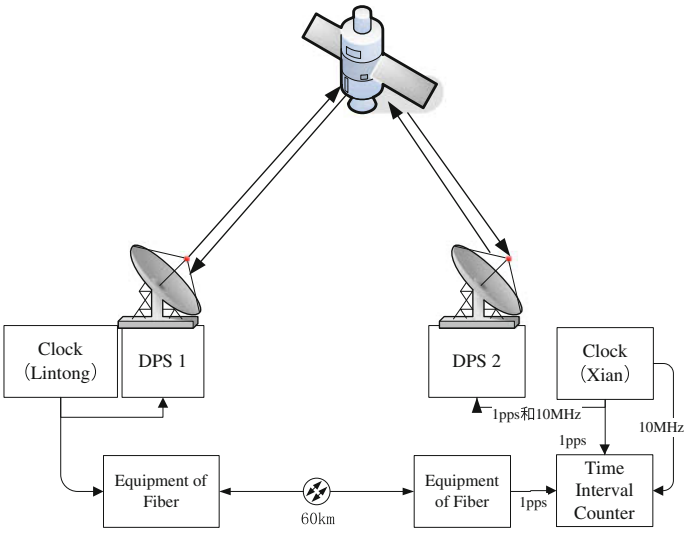

Fig. 2 Compare DPS with and fiber-based link

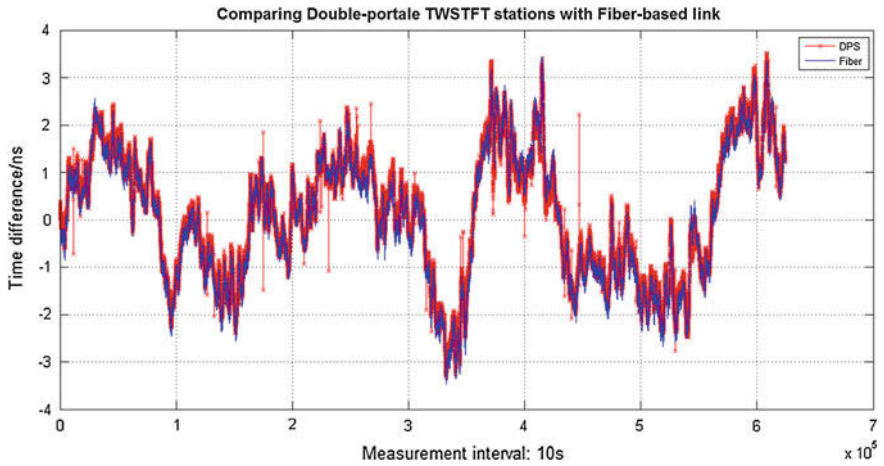

Fig. 3 Test results of DPS and fiber-based link

The red star line in the diagram indicates that the test results of DPS, blue solid lines represent fiber-based link test results. It can be found that the two curves of the change trend of the time difference between the two references signals completely coincide, which indicates that the two sets of system can truly reflect the changes of the two reference signals. The figure used in the same line width, but can be found directly that the solid blue line is narrower than the red asterisks line. It indicates that the results of fiber-based link have smaller discrete degree than the DPS. It is truthfulness too.

Figure 4 shows the difference of two sets systems, and it represents the degree of inconsistency.

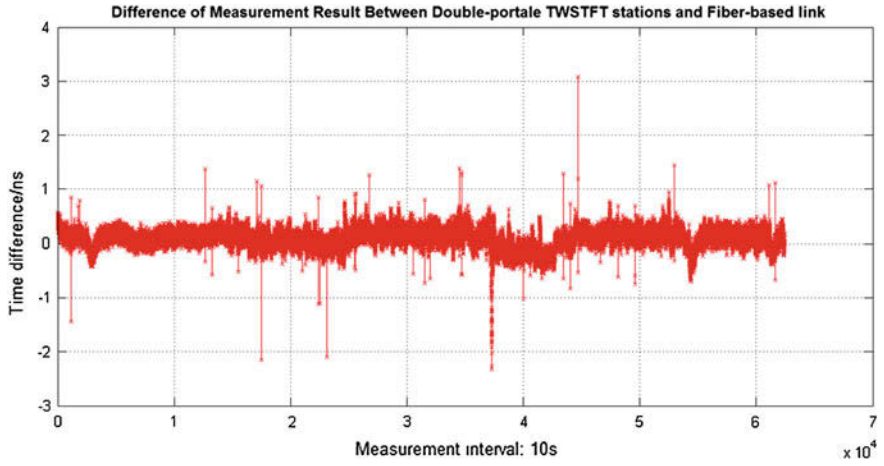

Fig. 4 The difference of results between DPS and fiber-based link

According to data from Fig. 4, we can acquire that the mean value is 0.095 ns, standard deviation is 0.17 ns. The fiber-based link test results were used as the true time difference values of the two clocks. So the mean value of difference of two sets systems represents the system deviation of DPS, and the standard deviation reflects the uncertainty of DPS. It indicates that the DPS can be used to compare time difference or calibrate the link delay up to the sub-nanosecond level.

4.2 Calibrating Link Delay of Ground TWSTFT Stations

Evaluating measurement system performance, the most objective method is to compare with a higher performance system, such as fiber-based link. But when distance is 1000 km even longer, it is harder to find out a suitable experimental condition. So it is unreality using fiber link to verify remote comparison performance of DPS. But the application of long distance comparison is the main engineering value of DPS. In order to test its performance and to test its ability to calibrate the link delay, this paper designs the comparison platform both DPS and fixed ground stations distance more than 3000 km. Two systems are operated parallel and connected same clock as reference signal. Figure 5 gives the schematic.

The experiment was conducted between Xi'an and Kashi, using the hydrogen atomic clock as reference signal source respectively. The sites have been built in fixed ground stations before experiment. It consists of transmitter, receiver and 3.7 m antenna, and the carrier frequency is C band. When the ground stations regularly work, they use four different satellites taking turns to relay signal. Every satellite kept working half an hour, and two hours finished a period. Before calibration test, the DPS has to be calibrated themselves relative delay.

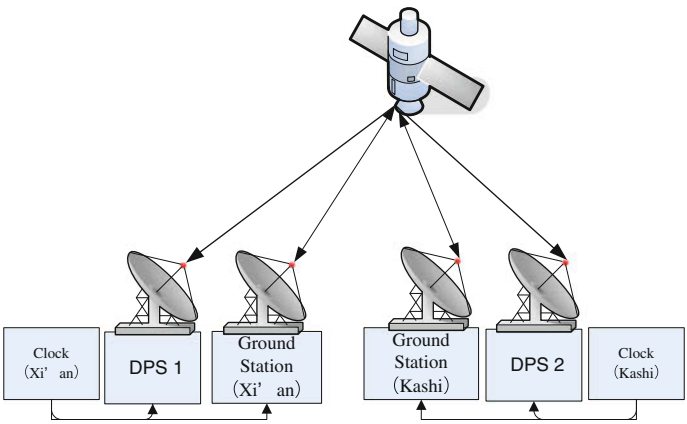

Fig. 5 Schematic of calibrating link delay of ground TWSTFT stations

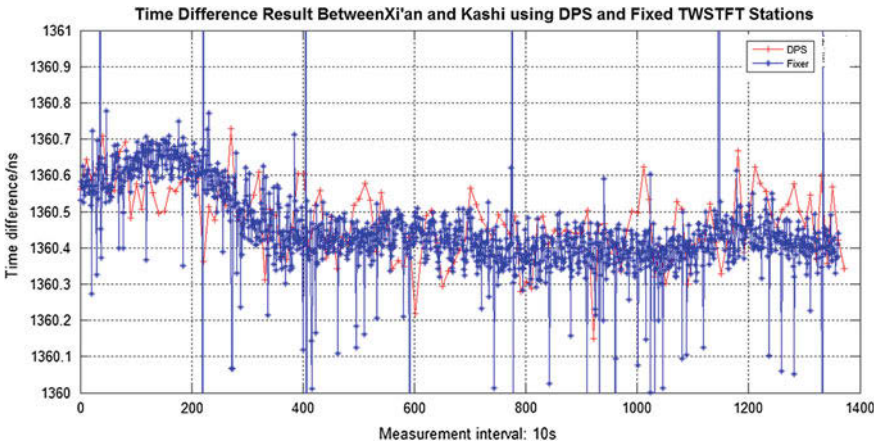

Fig. 6 Time difference between Xi'an and Kashi using DPS and Fixed TWSTFT stations

Fixed ground stations maintain normal observing schemes to measure the time difference between two clocks using different satellites. In addition, during entire experiment, DPS are used to measure continuously the time difference between two sites. Ideally, same results should be acquired by two systems. The reality results are show in Fig. 6.

In view of Xi'an and Kashi fixed ground stations using four different satellites compare time difference at different time, in order to eliminate the impact of the reference signal to the measurement results, choice the same period data with fixed ground station to compare, Fig. 6 is one of a period of observation data. Experimental results show that the change trend of the time difference between the two reference signals is completely consistent with the DPS and the fixed ground stations. The mean value of difference of two set systems is 14.5 ns, standard deviation is 0.27 ns. The mean value reflected the link delay of the fixed ground station, which is the sum of the equipment delay and the delay of space propagation. Standard deviation reflects the whole uncertainty of two measurement results.

Experimental results show that the two systems reflect the same change trend, and have a good consistency and Can be concluded as follows:

1. When they are measured at the same environment and the same parameter configuration, link delay of ground stations can be reproduced. So delay can be measured accurately;
2. The uncertainty of measurement results comes from combined action of two sets of systems. The biggest uncertainty is less than 0.3 ns of two systems;
3. The link delay absorb kinds of residual delay terms, including to ground station delay, signal space propagation, satellite motion, and Sagnac effect, etc. Therefore, the test results are closely related to the environment condition and parameters. Any of changes will lead to link delay change.

5 Conclusions

In this paper, we analyse the main errors sources of TWSTFT link, and give the correction methods of the delay in the signal propagation path. And then introduce kinds of the method of calibrating equipment delay. Based on this, we propose a method of link delay calibration based on double portable stations, in order to improve comparison accuracy of long distance TWSTFT. In this way, we can decrease the uncertainty from 1 ns to less than 0.5 ns.

In conclusions, DPS can be used to calibrate the link delay of TWSTFT. It has realized to calibrate the system deviation of TWSTFT link to sub-nanosecond level. Other advantages of DPS include the parallel test with the under test stations, do not need to interrupt the regular comparison, DPS can work independently very well; unrelated with the under test stations of equipment type and carrier frequencies, so DPS can be adopted by any remote comparison links, etc.

Acknowledgments This study is funded by the National Science Foundation of China (61127901). This work is also supported by the Youth Innovation Promotion Association CAS.

References

1. Piester D, Bauch A, Breakiron L, Matsakis D, Blanzano B et al (2008) Time transfer with nanosecond accuracy for the realization of international atomic time. Metrologia 45:185–198
2. Bauch A, Piester D (2009) Results of the 2008 TWSTFT calibration of seven European stations. IEEE 1209–1215
3. Wu W, Li Z, Yang X et al (2012) Sagnac effect in satellite two way time frequency transmission. J Astronaut 33(7):936–941
4. Wang G (2015) Study on the error calibration method based on two—mobile station for satellite transmission system. Chinese Academy of Sciences University doctoral dissertation, pp 13–34
5. Zhang V, Parker T, Yao J (2015) Long-term uncertainty in time transfer using GPS and TWSTFT Techniques. 727–727
6. ITU Recommendation TF.1153–2 (2003) The operational use of two-way satellite time and frequency transfer employing PN codes. ITU-R TF. 1153–2

A Quick Method of Measuring the Transmission Time of Optical Fiber

Bo Zhu, Yong Zhu, Lin Lu, Baofu Zhang, Chuanxin Wu, Yimei Wei and Longqiang Yu

Abstract It is difficult to determine the peak of optical signal transmission time in the time transfer system based on single photon detector. In order to solve the problem, a novel scanning measurement method is proposed to quickly measure the optical signal transmission time, taking the advantages of the remainder theorem and the peak scanning means. The experimental results demonstrate that the new method can not only achieve high accuracy of less than 10 ns between the computed result and the real peak, but also save time in the peak determination.

Keywords Single photon detector · Peak scanning · Quick measurement · Remainder theorem · Time transfer

1 Introduction

Time transfer in optic fiber has become a promising mean for time transfer [1, 2]. Compared with the free space channel, fiber-based time transfer has advantages in stability, resistance to electromagnetic interference ability, and precision. The accuracy of time transfer in fiber relies on the precise measurement of one-way optical signal transmission time. State of the art, the measurement of transmission time is estimated by measuring the round-trip time using the same clock. So, the symmetry of the transmission time in two directions decides the estimation precision of one-way transmission time [3]. Generally speaking, among fiber-based time transfer systems, the schemes that passively reflect the optical signal at the remote end have the best symmetry in the bidirectional transmission time, but also twofold power loss. It is inadvisable to use optical amplifier because of the backscattering in fiber, which restricts the measuring accuracy and transfer distance.

B. Zhu (✉) · Y. Zhu · L. Lu · B. Zhang · C. Wu · Y. Wei · L. Yu
Institute of Communication Engineering, PLA University of Science and Technology, Jiangsu, China
e-mail: ny_zhu_bo@163.com

© Springer Science+Business Media Singapore 2016

J. Sun et al. (eds.), *China Satellite Navigation Conference (CSNC) 2016 Proceedings: Volume III*, Lecture Notes in Electrical Engineering 390,
DOI 10.1007/978-981-10-0940-2_62

Traditionally, the detection of optical signals is based on optical power detection. Therefore, it is not suitable to fiber links with great attenuation. The single photon detector [4], by contrast, can detect very weak optical signal because of its high sensitivity, and consequently it plays an important role in the ultraweak biochemiluminescence detection [5], 3D imaging [6], laser ranging [7], the space timing [8], and other fields. The main principle is to amplify the weak photoelectric current, and distinguish desired signals from the background noise using the screening technique. In order to keep the fiber link symmetrical and expand the time transfer distance, we combine the method of passively reflecting the optical signal with the single photon detection technique, so that the mutual constraint between the timing distance and accuracy in a fiber-based time transfer system can be eliminated.

2 The Peak Scanning Measurement

When the single photon detector receives optical signals, it will generate photoelectric current. The variation of the response time induces time jitter. The time jitter will affect the measure precision of the transmission time, and finally degrade the stability and accuracy of the time transfer system. There are two reasons causing the time jitter. First, as few photons arriving at the single photon detector, it is the Gaussian-type envelope of the pulses in time domain that decides the arrival time, which is in fact uncertain [9]. On the other side, the initial power of the carrier produced by photon detector is also uncertain. Therefore, the time for carrier reaching power threshold and generating avalanche current is random [10].

To reduce the time jitter of time transfer system, we design a method of peak scanning measurement based on single photon detection [11]. By adjusting the open time of the gating signal and monitoring the photon counting rates of the single photon detector in unit time, we take the open time corresponding to the peak count rate as the arrival time of the optical pulse. In this way, we can get the photon flight time. The open time of gating signal, rather than the photoelectric current, serves as the stop signal of the time interval counter (TIC), which effectively avoids the error caused by time jitter and improves the accuracy of the system. The specific scheme is shown in Fig. 1.

In the experiments, G.652 optical fiber of 125 km is employed in total. The attenuation coefficient is 0.2 dB/km. We use the gain-switched semiconductor laser as light source, and the time-domain envelope of the optical pulses are Gaussian-type with wavelength of 1530 nm and full width at half maximum (FWHM) of about 40 ps. In the scheme, we use the TIC and take the launching time of the laser as the start of the TIC. The optical signals reflect from the fiber end and come into the single photon detector. A variable optical attenuator (VOA) is used to control the power of the arrival optical signal to a single photon state. The arrival time of the optical pulses is roughly estimated by optical fiber length at first. Then we use the time-delay control module to adjust the open time of the gating signal by

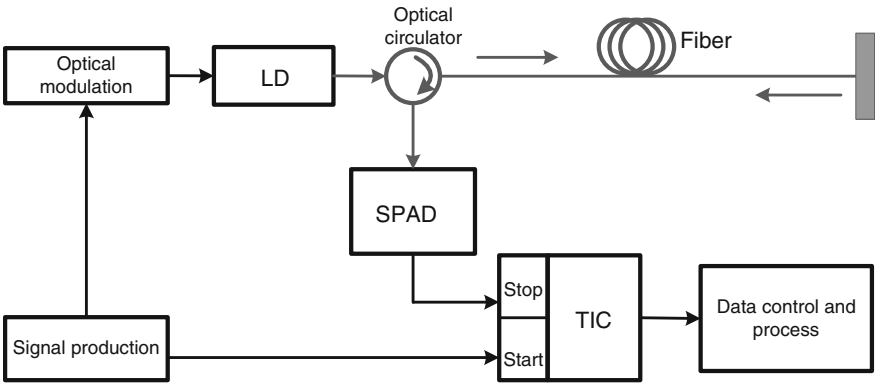

Fig. 1 Principle diagram of peak scanning scheme

preset step to finely scan the count rate of the single photon detector. The curve of the count rate in a certain period could be drawn versus different delays of the gating signal. The gating time corresponding to the peak of the curve is taken as the arrival time of the photons. And then the time interval can be measured by TIC.

In this method, we estimate the two-way transmission delay of the optical pulse first, according to the rough length of the fiber. Then we choose a range of time to scan the peak based on the estimated delay. Usually, in order to make sure that the real peak is located in the chosen scope, the selected range should be as large as possible. However, the peak scanning time will also increase. Moreover, if there is a large deviation in estimating the optical fiber length, no peak will be obtained even if the whole time period is scanned since the real peak is beyond the selected range. In the time transfer systems based on peak scanning method, getting the peak is just the primary step. So how to determine the peak position quickly is a key criterion of the performance of a time transfer system.

3 Remainder Theorem

If an integer is divided by several coprime integers, we could get different quotients and remainders. The remainder problem is to deduce the dividends from the already known divisors and remainders when the corresponding quotients are unknown. More than two thousand years ago, the Chinese Remainder Theorem was put forward to solve the problem. Further, strictly proved by modern mathematical deduction, the problem has been solved in theory [12], as follows:

Assuming that $m_1, m_2, \ldots, m_k$ are coprime positive integers, and X is the unknown dividend, $M_i = m/m_i,\ i = 1, 2, \ldots, k,$ where the total modulo $m = m_1 m_2 \ldots m_k$, the congruencies are:

$$\begin{cases} X \equiv b_1 (\text{mod } m_1) \\ X \equiv b_2 (\text{mod } m_2) \\ \cdots \\ X \equiv b_3 (\text{mod } m_3) \end{cases} \tag{1}$$

And the solution is:

$$X \equiv M_1' M_1 b_1 + M_2' M_2 b_2 + \cdots + M_k' M_k b_k (\text{mod } m) \tag{2}$$

where b_k are integers, $M_1' M_1 b_1, M_2' M_2 b_2, \ldots M_k' M_k b_k$ are basic number of the divisors, $M_i' M_i \equiv 1 (\text{mod } m_i)$, and M_i' are the inverse elements of $M_i (i = 1, 2, \ldots, k)$.

So the dividend is

$$X = X' + k * m \tag{3}$$

X' is the minimum dividend, $k = 1, 2, 3, \ldots$.

4 The Quick Scanning Measurement Method

In general, the length of optical fiber is a constant in a short time. So the transmission time of an optical pulse is a constant too. We can neglect the deviation caused by the changed temperature. If the transmission time is divided into different intervals, we can get different corresponding quotients and remainders. If the optical pulses are sent with equal interval, there will be integral numbers of pulses in the fiber link at the same time. Therefore, the transmission time of the fiber link can be divided into corresponding integral multiple of the pulse interval plus an extra short time within a single pulse interval. Theoretically, the peak count rate is expected to appear within the scan scope of a pulse interval. The corresponding time delay of the gating signal is the extra fractional pulse interval and therefore can be viewed as the remainder of the total transmission time divided by pulse interval. Based on the remainder theorem, we can take T which is the transmission time of the optical pulse as the dividend, N as the selected pulse interval, q as the quotient and b as the remainder. The relation is: $T = N \times q + b$. Choosing different pulse intervals, we can get a congruence group and then deduce the transmission time of the fiber link by the Euclidean Algorithm.

During the experiments, we choose 23, 29, and 37 as the coprime integers. The optical pulse width is 40 ns, and the pulse intervals are set as 230, 290, and 370 ns for the convenience of peak scanning. The final m is 246,790. But in the calculation, the mathematical relations are converted to those of the prime numbers 23, 29, and 37. Four fiber spools are used in the experiments, with length of 13, 25, 25, and 50 km, respectively. The results are shown in Tables 1 and 2.

We can calculate the value based on the data got by the quick scanning method, and the peak will be found soon if we take the calculated value as the basic time

delay of the gating signal in the sequent measurement of the actual transmission time of the fiber link. In the experiments of testing the 13 and 25 km fiber spools, the error between the measured value and the calculated value is within 10 ns (shown in Tables 1 and 2).

As is shown in Table 3, the two-way flight time of the optical pulse in 25 km fiber spool is about 244,852 ns. By the quick scanning method, we get the calculated value of 990 ns using the three intervals. It is far less than the estimated value. To get the right value, multiples of the total modulo *m* (246,790 ns in this case) are needed to add to the calculated value.

In the experiment of testing the 50 km fibers spool, we get the solution of 500,310 ns by adding the twofold modulo m using the three intervals. In the case that the fiber length is undetermined, it is quite possible to get the wrong solution if the multiple of modulo m is uncertain. A viable way to solve the problem is to introduce another pulse interval. In Table 4, there are two solutions based on the data got using three and four intervals respectively, and it shows that the more measurement intervals we use, the more likely we get the direct solution.

In the previous peak scanning methods, it is the rough estimating accuracy of the fiber length that decides how long it will take to get the first sample of the scanning peak. In most case, the estimation is not accurate enough, and therefore large scanning range, i.e., long scanning time is needed. By contrast, the quick scanning method proposed in this manuscript can greatly minish the scanning range, which is only 890 ns at most in the demonstrated case with the three pulse intervals 230, 290, and 370 ns.

Table 1 The calculated value of quick scanning method and the real measured value (13 km)

Pulse interval (ns)	230	290	370
Peak position (ns)	120	190	50
Calculated value (ns)	132,140		
Measured value (ns)	132,146		

Table 2 The calculated value of quick scanning method and the real measured value (25 km)

Pulse interval (ns)	230	290	370
Peak position (ns)	220	30	200
Calculated value (ns)	242,180		
Measured value (ns)	242,188		

Table 3 The calculated value of quick scanning method and the real measured value (25 km)

Pulse interval (ns)	230	290	370
Peak position (ns)	70	120	250
Calculated value (ns)	990 + 246,790		
Measured value (ns)	247,783		

Table 4 The calculated value of quick scanning method and the real measured value (50 km)

Pulse interval (ns)	230	290	370	310
Peak position (ns)	60	60	70	280
Calculated value (ns)	(6730 + 246,790 * 2) 500,310			
Measured value (ns)	500,315			

5 Conclusion

The peak scanning method based on single photon detection is a new method for the measurement of transmission time of the optical pulse. In order to locate the uncertain peak position for the first measurement, we propose a quick scanning method to realize the quick measurement of the optical signal transmission time based on the Chinese remainder theorem. Experiments show that the new method can not only keep the high precision within 10 ns between the measured value of the peak position and the calculated value, but also save scanning time. We can use a small step to scan the small time scale which is based on the calculated value giving by the quick measurement, and get the precise time of the optical signal transmission time in the end.

References

1. Jaldehag K, Ebenhag SC, Hedekvist PO et al (2009) Time and frequency transfer using asynchronous fiber-optical networks: progress report. In: Proceedings of the 41st annual precise time and time interval (PTTI) systems and applications meeting, vol 11, pp 383–296
2. Wang B, Cao C, Wang LJ et al (2012) Precise and continuous time and frequency synchronisation at the 5×10^{-19} accuracy level. Nat/Sci Rep 2:556
3. Krehlik P, Sliwczynski L, Buczek L et al (2012) Fiber-optic joint time and frequency transfer with active stabilization of the propagation delay. IEEE Trans Instrum Meas 61(10): 2844–2851
4. Huang J, Wu G, Zeng H (2014) Study of 1.5 GHz harmonics ultrashort pulse gated InGaAs/InP avalanche photodiode single-photon detection. Acta Optica Sinica 34(2):0204001
5. Isoshima T, Isojima Y, Hakomori K, Kikuchi K, Nagai K, Nakagawa H (1995) Ultrahigh sensitivity single—photon detector using a Si avalanche photodiode for the measurement of ultraweak biochemiluminescence. Rev Sci Instrum 66:2922–2926
6. Wallace AM, Buller GS, Walker AC (2001) 3D imaging and ranging by time-correlated single photon counting. Comput Control Eng J 12(4):157–168
7. Ren M, Gu X, Liang Y et al (2011) Laser ranging at 1550 nm with 1 GHz sine-wave gated InGaAs/InP APD single-photon detector. Opt Express 19(14):13497
8. Laas-Bourez M, Samain E, Courde C et al (2013) Time and frequency distribution improvement in Calern/Geoazur laboratory for T2L2 campaigns. In: European frequency and time forum and international frequency control symposium, joint, pp 869–872
9. Li X, Ding J, Tang R et al (2014) Research on quantum statistic properties of photon number in pulse mode nonlinear frequency up-conversion. Acta Optica Sinica 34(5):0527002
10. Rosfjord KM, Yang JKW, Dauler EA, Kerman AJ, Anant V, Voronov BM, Gol'Tsman GN, Berggren KK (2006) Nanowire single-photon detector with an integrated optical cavity and anti-reflection coating. Opt Express 14(2):527–534
11. Zeng Z, Zhu Y, Lu L et al (2015) Research of peak count rate scanning method for single photon detector used in high precision optical transfer time measurement. Chin Laser 42(5):0508003
12. Yang Y (2009) The Chinese remainder theorem and the system of congruence. J Anshun Univ 2:87–89

Design of a High-Performance Compact Rubidium Frequency Standard

Chunjing Li, Dongliang Cong, Nina Ma, WenChong Zhang and Qing He

Abstract In this paper, a high-performance compact rubidium frequency standard (CRFS) has been successfully developed, of which the frequency stability (Allan variance) reached $3E{-}12/\tau^{0.5}$ (τ = 1–1000 s) and frequency drift was reduced to below 1E−12/1d. The frequency stability is less than ±2E−10 at the temperature range of −45 to +60 °C. Powered by modern electronic technology, the bulk is controlled to about 0.5 L and the mass is about 0.4 kg.

Keyword Compact rubidium frequency standard (CRFS)

1 Introduction

The compact rubidium frequency standard (CRFS) has a nice short and medium term frequency stability, and its long-term frequency stability and drift can be greatly be improved when it is locked to a 1PPS from a COMPASS or GPS time receiver. Thus, CRFS becomes one of the most popular frequency standard in the industries of electricity, telecommunication, time frequency, measurement and calibration, radar, etc.

The domestic development of CRFS began mainly in late twentieth century and early this century, which reaches a certain level, especially to deserve to be mentioned, the frequency stability can reach 5E−12/1 s [1, 2]. Moreover, the research on vibration resistance was further carried out and gained some achievements, for example, the product's frequency stability was in a magnitude order of 10^{-11} [3].

The Beijing Institute of Radio Metrology and Measurement (BIRMM) began to engage in the rubidium frequency standard research and the products are commonly

C. Li (✉) · D. Cong · N. Ma · W. Zhang
Beijing Institute of Radio Metrology and Measurement, Beijing 100854, China
e-mail: 18600019689@163.com

D. Cong · N. Ma · W. Zhang · Q. He
Southwest China Research Institute of Electronics Equipment, Chengdu 610036, China

© Springer Science+Business Media Singapore 2016

J. Sun et al. (eds.), *China Satellite Navigation Conference (CSNC) 2016 Proceedings: Volume III*, Lecture Notes in Electrical Engineering 390,
DOI 10.1007/978-981-10-0940-2_63

used as spaceborne time base of COMPASS, whose long-term frequency stability reaches the order of 10^{-15}. In this paper, by using but not to be confined to the development experience of high-performance spaceborne rubidium clock, the CRFS makes innovative improvements on microwave synthesis design, physics package, low frequency servo circuit, power supply, etc. Many new industrial devices were used in the design for achieving high performance and satisfactory productbility.

2 Design Approach

The rubidium frequency standard is a passive standard in which a specified hyperfine transition of electrons in ^{87}Rb atoms is used to control the output frequency. In engineering implementation, since the factors such as the S/N ratio of frequency discrimination signal, microwave performance, and system complexity need to be considered, the separated filter technique (i.e., SFT, in which the physics package is designed with three gas cells, i.e., a pure ^{87}Rb lamp, a pure ^{85}Rb filter cell, and a pure ^{87}Rb absorption cell) or the integrated filter technique (i.e., IFT, in which there are only two gas cells, i.e., a mixed isotopes lamp and a mixed isotopes cell) can be selected.

In the SFT, the product achieves optimal performance by properly adjusting the buffer gas pressure and temperature to enable the physics package to work at the ZLS point, and the physics package has low sensitivity to the microwave power. On the contrary, in the system of IFT, the physics package reaches the ZLS point by the design of isotopic ratio and work temperature. In this scheme, the product has the merits of simple structure and low cost, but its performance is comparatively poor. Therefore, the SFT scheme is adopted in this paper for the purpose of improving the product performance and batch consistency while slightly compromising the cost, and thus increases the yield and user satisfaction.

The schematic diagram of the CRFS is shown in Fig. 1. The physics package adopts the SFT with three cells integrated in two ovens. Analog electronics components are mainly used for amplifier, synchronous detector, integrator and phase-locked loop, and an 8-bit RISC microprocessor for the detector signal generation and control circuit design, which guarantees agility and simplicity.

In the design of the circuit system, a 10 MHz crystal oscillator is employed for frequency synthesis to obtain a 6.83 GHz microwave signal for the physics package. A direct digital synthesizer (DDS) is introduced for matching the mantissa frequency of the microwave signal, which nearly omits fine adjustment of the frequency of absorption cell by special measures and thus greatly improves the production efficiency and also helps the physics package focus on the improvement of key performances. This circuit design is different from that of high-performance space rubidium frequency standard developed by BIRMM, in which the 6.8346875 GHz signal is obtained by ×540 frequency doubling of 12.6568387 MHz from an OCVCXO. Thus, clutter spectrum will not appear within the range of 12 MHz of

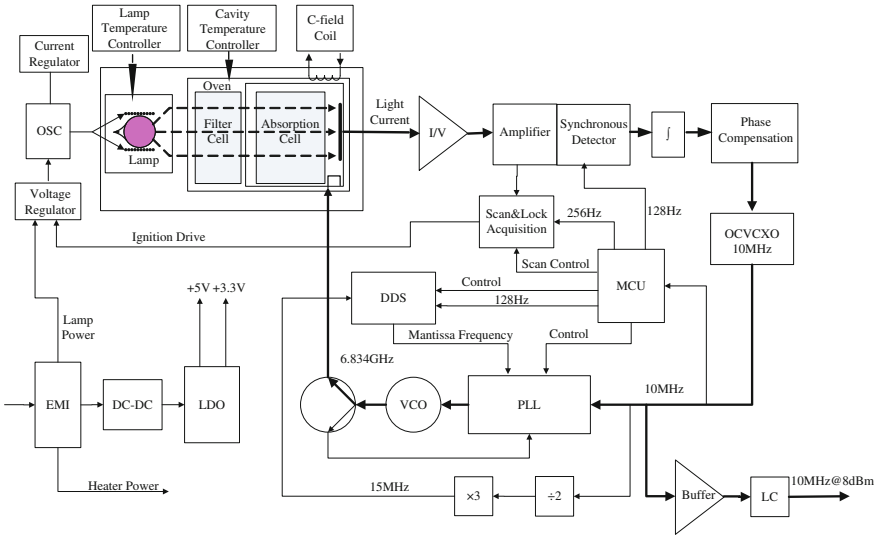

Fig. 1 Diagram of the CRFS

the microwave signal, and the design does not need highly integrated devices. As a result, it is suitable for high-reliability space products. However, it is necessary to introduce analog phase modulation at front end of doubling, and further two crystal oscillators are required to achieve high-quality 10 MHz signal, which is not suitable for the design of compact product.

There are many significant advantages of using DDS, including restriction removing of absorption cell frequency, accurate control of the microwave frequency, phase modulation, and digital automatic control which are vital to control the consistency of batch production and improve the applicability.

Another feature of the circuit design is that, a 6.8 GHz VCO is employed to generate the microwave signal directly, whose frequency is locked to the 10 MHz OCVCXO by using a low noise PLL with a DDS integrated. Without using the traditional transistor and step recovery diode (SRD) for frequency multiplication, the adjustment for matching can be omitted; moreover, the temperature coefficient of microwave power can be controlled effectively, which makes contribution to the frequency of the product in all range of temperature at an order as small as 10–11. For the rubidium frequency standard, BIRMM usually prefers external frequency multiplication mode (i.e., the 6.83 GHz signal is generated outside the quantum transition resonator and then is fed to the resonator). This mode can accurately measure and control the quality of microwave signal for servo quantum transition, including the signal frequency spectrum, power stability, temperature coefficient, etc., which greatly contributes to quality control.

To guarantee the technical indexes and vibration sensitivity, a 3rd SC-cut crystal is used in the design of 10 MHz VCXO and shared the oven with the absorption cell, which guarantees the performance of oscillator without extra power and obtains a

trade-off between performance and cost. In fact, the temperature needs to be adjusted according to the characteristics of physics package, and the optimal temperature points of the crystal have certain discreteness, so the crystal does not always work at the inflection point temperature. But none of this matters much on performance.

3 Physics Package

The Rb physics package is the SFT and two-oven design with the use of a Xe buffer gas lamp and a thin-film optical interference filter. This thin-film filter passes both Rb D-lines while blocking essentially all of the buffer gas emissions. This design provides significant performance improvement in frequency stability by both raising the rubidium error signal and lowering the shot noise. This system can be adjusted to ZLS point by operating the lamp at about +120 °C while the absorption cell and filter cell is at about +75 °C. Evaluation indicates that the frequency stability base level of the physics package is better than $2E{-}12/\tau^{0.5}$. Moreover, no deviant frequency hopping appears in long time test.

A mixture of buffer gasses is used in the absorption cell, and ratio and pressure are optimized according to the S/N radio and temperature coefficient. The test shows that the frequency change of CRFS is below 2E−10 in the ambient temperature range of −45 to +60 °C. In addition, the frequency still keeps small deviation even if the temperature of absorption cell is slightly out of control.

The quantum transition resonator still adopts a TE_{111} microwave cavity, which has the merits of easy processing, low cost, high reliability, and appropriate size. It is really an eclectic choice after considering the performance, size, and cost for industrial and military CRFS.

The detector uses a 10 mm × 20 mm photodiode, which is welded in the bottom of the microwave cavity. The experimental results prove that it is reliable and excellent in performance.

The lamp is a key part of the physics package, and its noise and stability affects much on the product's performance. It is a big challenge in design when CRFS works at the ambient temperature of −45 to +60 °C, especially there is no extra circuit temperature control. In this paper, with the purpose of improving the stability of lamp and lowering spectral background noise, a Colpitts oscillator with collector grounded is used for lamp excitation, and a linear power supply with the temperature coefficient of less than 100 ppm/°C is employed as the power supply. Moreover, the temperature coefficient of the oscillator current is also controlled below 100 ppm/°C which guarantees the temperature adaptability.

Generally, the oscillator circuit works at +15 to +20 V. But in this design, the start voltage is +12.8 V, and the proper level for continuous operation is only +10 V. Low voltage is beneficial to lamp stability, and besides, the RF heating effect on the lamp cell is remarkably reduced. The experimental result indicates that the change of lamp status is very small even put into vacuum, and the frequency change of the CRFS can be ignored.

In the design, the lamp and filament are isolated from each other, i.e., the lamp is not in contact with the filament, which avoids direct heating of the lamp by the filament and disturbance of rubidium microscopic motion. The experimental results prove that this measure effectively improves the working stability of the rubidium lamp.

The temperature control of the rubidium lamp is realized by a bridge circuit, which has the merits of simple and reliable structure and good performance. But in improvement, the circuit is of PID control mode with long time constant for the purpose of accomplishing large-loop gain and good stability. Darlington transistors are used as heating elements, and a small resistor is also used for cooperating current sampling; as a result, the temperature-controlled heating efficiency is up to 98 % or above, which reduces power consumption, lowers the temperature of the whole set, and improves the reliability.

4 Structure

In order to adapt the CRFS to work at the temperature of −45 to +60 °C, it is necessary to ensure good heat dissipation while achieving good temperature coefficient for the circuit. Additionally, the structure should be as simple as possible to reduce connectors and installation complexity for the purpose of controlling failure rate of products in batch production. Therefore, a single PCB design is adopted for the CRFS, i.e., all circuits are integrated in one circuit board, and what's more, it is convenient to be connected to the physics package, as shown in Fig. 2.

Fig. 2 Internal structure diagram of CRFS

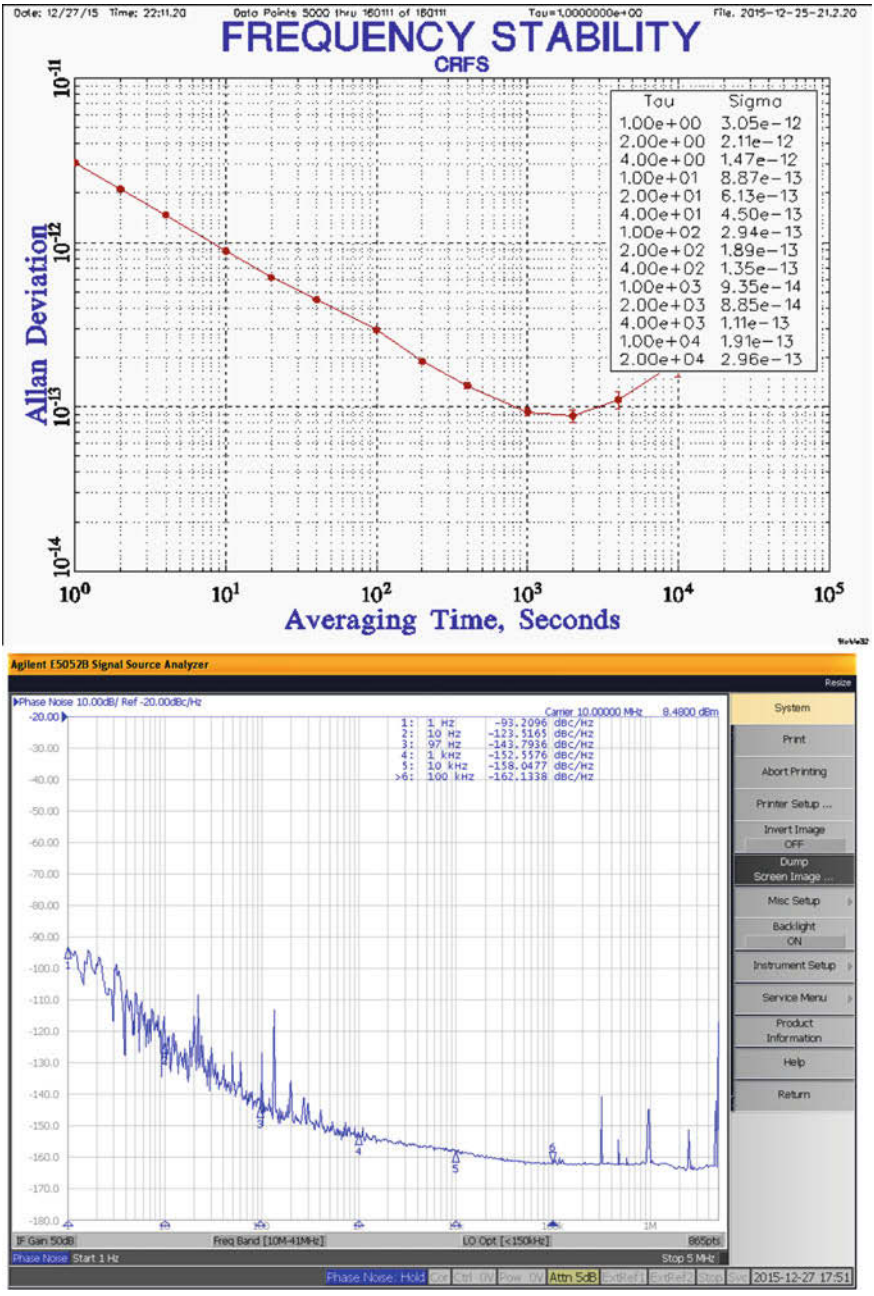

Fig. 3 Frequency stability and phase noise of CRFS

In order to decrease magnetic sensitivity, a magnetic shielding structure is designed for the physics package, and is installed together with the circuit board.

Aluminum is used for the bottom plate and case of the whole set due to its light weight, good thermal conductivity, and easy processing, and the PCB is directly mounted on the bottom plate. With this structure, good heat dissipation performance can be guaranteed, deformation of the circuit board caused by machining error of common sheet metal parts can be avoided, and thus the reliability is improved.

5 Performance and Subsequent Work

Currently, three rubidium clocks are manufactured. The products have good performance and consistency. The frequency stability (Allan variance) is shown in Fig. 3, in which the frequency stability reaches $3E{-}12/\tau^{0.5}$ (τ = 1–1000 s). In addition, the drift is better than 1E−12/d and generally falls into 1 ∼ 3E−13/d after operation for dozens of days. The typical indexes are given in Table 1.

From the test results, the performance of the products can meet most commercial and military demands, and the frequency stability nearly reaches the nominal indexes of high-precision space rubidium frequency standard. Moreover, the products have good environmental adaptability.

Table 1 Electrical test result of CRFS

1	Frequency	10 MHz
2	Settability	<5E−11
3	Retrace	<2E−11
4	Frequency stability	3.0E−12/1 s
		8.9E−13/10 s
		2.9E−13/100 s
		9.4E−14/1000 s
5	Long-term stability	3E−13/d
6	SSB phase noise offset from signal	−93 dBc/Hz@1 Hz
		−124 dBc/Hz@10 Hz
		−144 dBc/Hz@100 Hz
		−152 dBc/Hz@1 kHz
		−158 dBc/Hz@10 kHz
		−162 dBc/Hz@100 kHz
7	Harmonic distortion	−30 dBc
8	Non-harmonically	−70 dBc
9	RF power	8 dBm

(continued)

Table 1 (continued)

10	Warm-up time	1E−9@25 °C 5 min
		1E−10@25 °C 10 min
11	Power consumption	During warm-up 1.45 A × 24 V
		After warm-up <0.6 A × 24 V@25 °C
12	Operating	−45 to +60 °C
13	Frequency TC	1E−10@(0–50 °C)
14	Size	125 × 92 × 42 mm^3
15	Weight	0.41 kg
16	RF connector	SMA
17	DC connector	DB-9
18	Voltage	+13 to +24 VDC

In the subsequent work, the research team will carry out environmental test according to the military standard, make improvement on the product accordingly, and on the basis of this, develop high-performance military rubidium frequency standard.

6 Summary

In this paper, the CRFS developed by BIRMM is introduced. The research team makes good use of advanced component technique, makes the most of their previous research experience of high-performance space rubidium frequency standard, and now achieves some new breakthroughs in technical indexes, especially to deserve to be mentioned, the frequency stability of the product is very close to that of the space rubidium frequency standard, which provides a more flexible choice for the users.

References

1. Li C, Gao W et al (2009) Development progress of miniature rubidium frequency standard. CTFS2009
2. Xiang J, Cao Y, Liu Y et al (2009) Development of a miniature high-performance rubidium clock. CTFS2009
3. Li C, Yang T (2013) Development of new-generation space-borne rubidium clock. In: China Satellite Navigation Conference (CSNC)

Part IV
Standardization, Intellectual Properties, Policies, and Regulations

Analysis on the Standard Structure for the Ground Control Segment of Beidou Navigation Satellite System

Zhixue Zhang, Zhiheng Zhang, Jie Xin, Jinxian Zhao, Chunxia Liu, Wei Zhao, Na Zhao and Xiaofei Li

Abstract Identical with the other satellite navigation systems, such as GPS and Glonass, Beidou navigation satellite system is composed of space segment, ground segment, and user segment. This paper focuses on the demand of standards for the ground segment of Beidou navigation satellite system. Based on the existing standards both home and abroad, this paper discusses the principles of building the standard structure and proposes an architecture of the standard structure for the ground segment. Some standards which are urgently needed by the construction, operation, and maintenance of the Beidou regional and global system are proposed as well. This paper could provide references for drawing up and amendment of Beidou ground control segment standards.

Keywords Satellite navigation · Ground control segment · Operation and maintenance · Standard structure

1 Introduction

Beidou navigation satellite system has officially provided services to the Asia Pacific region in 2012. At present, the Beidou global system construction has been under construction and intends to provide service in 2020. Satellite navigation system which gradually occupies an important position in the national economy is an important national information infrastructure. The Beidou system urgently needs standardization methods to ensure the system construction and operation [1].

Satellite navigation is a strategic emerging industry in China. Beidou is a new type of space infrastructure and national strategic resources, but few standard is drawn up and published, nor to say form a complete standard system. The existing standards mainly concentrated on the basic standards and application standards [2]. Some domestic scholars researched on the standard structure for Beidou navigation

Z. Zhang (✉) · Z. Zhang · J. Xin · J. Zhao · C. Liu · W. Zhao · N. Zhao · X. Li
Bejing Satellite Navigation Center, Beijing, China
e-mail: zzx6057@sina.com

© Springer Science+Business Media Singapore 2016

J. Sun et al. (eds.), *China Satellite Navigation Conference (CSNC) 2016 Proceedings: Volume III*, Lecture Notes in Electrical Engineering 390,
DOI 10.1007/978-981-10-0940-2_64

satellite system [3–7] and mainly in the application standard structure [8, 9]. However, few standard of ground operation control technology is published, and only Ref. [10] researched on the standard structure of satellite navigation system operation and maintenance. On April 28, 2014, the national Beidou satellite navigation Standardization Technical Committee (referred as Beidou Standard Technical Committee) was established, which is the first military and civilian satellite navigation standards organization. The committee is mainly responsible for standardization of system management, construction, operation, application, and service [11].

In November 2015 Beidou Standard Technical Committee officially published the national satellite navigation system (version 1.0), which is conductive to the development of satellite navigation standards to provide guidance for the development of satellite navigation standards.

Like GPS, GLONASS and other navigation system, Beidou system is composed by the space segment (satellite constellation), ground control segment, and application equipment segment. The constellation configuration of Beidou regional system is 5GEO+5IGSO+4MEO. The constellation configuration of the Beidou global system will be 3GEO+3IGSO+24MEO. The main functions of satellite constellation include receiving navigation messages uploaded by the ground control segment and propagating the messages to the user equipment. Ground operation control segment is mainly composed of master station, monitoring stations, and time synchronization stations. The user segment mainly receives satellite navigation signal and provides positioning, speed testing and timing services for different users. The standards of Beidou ground control segment is demanded by the system construction and constant improvement. It is necessary for us to develop the standard of the ground control segment, which is the core of the operation, management, and control of satellite navigation system.

In this paper, the development status and the existing standard system of the ground operation control technology of the satellite navigation system are analyzed, and the principle of the standard system is put forward, and the standard system is designed.

2 Current Status of Navigation Signal Construction Design

Foreign satellite navigation systems mainly include GPS, GLONASS, and Galileo. All of the three satellite navigation systems consist of the space segment, the ground control segment, and the user device segment. The ground control system is primarily responsible for satellite constellation monitoring and controlling, satellite navigation signal monitoring, and navigation messages upload [12]. Foreign satellite navigation related standards mainly focus on user interface control document (ICD), service performance and evaluation. However, no standard related to

system construction especially to the ground control segment is published. The standard architectures abroad related to satellite navigation systems mainly are the NASA standard system and EU's ECSS standard system, which are both the aerospace universal standard system, and cannot fully reflect the characteristics of the satellite navigation system standard.

At present, the relevant domestic satellite navigation standard consists of 100 items. The application of satellite navigation system in China started with GPS. GPS currently has very extensive applications in China, so the GPS satellite navigation standards mainly focus on the application standards. Only in recent years several Beidou satellite navigation standards have been issued, including spatial signal ICD, Beidou communication protocol, and so on.

Before the Beidou Standard Technical Committee was established, the domestic related standard systems of satellite navigation include military standard system, aerospace equipment standard system, and astronavigation standard system. These standard systems are on behalf of the national level, industry level, and aerospace construction level, respectively. These standard systems mainly work for their own industry and cannot fulfill the requirements of Beidou navigation system. Therefore, in November 2015 the Beidou Standard Technical Committee released the national satellite navigation system of version 1.0 which is the first national satellite navigation standard structure. However, that standard structure still does not cover the ground operation control segment.

3 Demand Analysis for Operation Control Standards of Beidou System

The standard system research of Beidou navigation satellite system is the inherent requirement of system construction and improvement. From the first generation system to current regional system, the testing and engineering construction cost only 10 years. According to the engineering planning of Beidou global system, it will provide service in 2020. To realize rapid construction, we need advanced and mature technology standard and management technology to guarantee the timetable and construction quality. Therefore, the research on operation control standard is the inevitable demand of standard structure for Beidou system. The ground operation control technology is the core technology for the system operation, management and control, and the research and establishment of its standard system is a significant part of standard structure for Beidou navigation satellite system.

All navigation satellite systems go through two stages, construction and operation maintenance. At present, Beidou regional system has stepped into maintenance stage, and Beidou global system is engaged in developing construction stage which will provide official service in about 2020 and then go into operation maintenance stage. Though the working content and targets are very different in two stages, their basic goals are approximately the same, i.e., service performances must

be guaranteed in both of the two stages. Hence, we need to analyze the standard demands in three aspects including service performance, construction, and operation maintenance.

3.1 Demand Analysis of Operation Service Standard

In order to define the service and performance in the system construction and operation maintenance, the service standard should be first established, regulating the navigation signal, service and performance requirements which should be maintained by the system. The user conducts positioning and timing by receiving RNSS satellite signals and the corresponding navigation message. The navigation message contains various information formed by the ground control stations, such as satellite ephemeris, satellite clock error, ionospheric delay correction parameters, almanac data, wide-area difference correction data and integrity information. Each kind of data plays an important role to the user performance. Users must closely follow the data format and accurately employ the navigation parameters to get high precision navigation and positioning performance. Therefore, it is necessary to establish the ground operation control service agreement to regulate the messages use and create conditions for users to understand and employment.

3.2 Demand Analysis of Construction Standards

As the formal operation of Beidou regional system, it is urgent to put the mature technical requirements and regulations into standard for the ground control segment, especially for monitoring stations, key components and test devices with large quantity, wide application and vast subsequent demand. These need more guidance and constraint by the technical specification standard to complete the following production and provide reference for the development of the global system construction. But the global ground control and regional ground segment contain different systems and devices. Therefore, the existing specifications for the regional system ground control segment cannot be directly applied to the construction of the global system. As a result, the ground control segment technical specification standards should not only reflect the technical achievements of the regional system construction, but also reflect the generalization for the construction of the global system. The ground operation control segment is mainly composed of master control station, time synchronization upload station, monitoring stations, key components, and test devices. Therefore, we need to set standard in master control station, time synchronization upload station, monitoring stations, key components, and test devices respectively.

The ground operation control segment is an enormous system with large sets of devices and the interface between devices is rather complicated which forms a large

number of interface documents in the process of system construction. Global system is the upgrade of regional system, requiring the existing regional system interfaces be summed up to form standard for global system design. The ground operation control system interface can be summarized as satellite-ground interface, station-station interface, inter-station interface (inter-system interface and internal interface) and key components interface. In conclusion, the interface standard should be designed with the above expects.

In the construction process of Beidou regional system, testing assessment has been done throughout the whole construction. Comprehensive test of the ground system, subsystem, and key components need corresponding testing outlines and regulations. The subsystems and key devices of the ground operation control system have the characteristic of long development cycle and large quantity. As the system is put into formal operation, some devices have come into the end of life, which need authoritative testing standard to conduct spare devices production, purchasing, testing, and application. These testing specification files provide guidance for spare device testing and acceptance inspection.

3.3 Demand Analysis of Operation Maintenance Standard

The operation maintenance standards should be drawn with the guarantee of system service. During the process of operation maintenance, the work related to system services mainly include six aspects including performance evaluation, safety protection, constellation maintenance, operation maintenance, fault disposal and equipment replacement. Therefore, the standard should be formulated with these aspects into account.

In order to guarantee the service performance of the system, it is necessary to establish the system performance evaluation standard in the long-term operation stage to provide the evaluation basis for navigation satellite system operation and thus provide the basis for long-term service performance optimization. In the long term, the performance evaluation criteria also provide technology support for service performance evaluation system and engineering construction of Beidou global system. Therefore, we need to establish performance evaluation standard of Beidou navigation satellite system, providing systematic and normative basic to estimate the operation condition of the navigation system.

In order to guarantee the service performance of the system, maintenance the performance of the Beidou navigation constellation is the foundation. To maintain the constellation performance, backup satellites and complementary satellites should be launched. Before the satellite goes into the constellation, on-orbit estimation should be conducted. When the satellite iscoming to its life expectancy, de-orbit steps should be implemented. Then, satellite networking and retirement standard should be formulated to clarify strategies, principles, and operation procedures.

In order to guarantee the service performance and maintain the continuity of the system, the system devices should be maintained at regular intervals. At the same time, different devices should be operated according to different control instructions. Therefore, it is necessary to formulate operation and maintenance standard for satellite and ground system devices to ensure the accuracy of each operation.

In order to guarantee the service performance of the system, fault location and disposal should be carried out in time when the system failure occurs. For Beidou satellite failure, including satellite platforms and payload fault, there must be a set of fault diagnosis and disposal procedures to ensure satellite recovery and reduce the impact on the navigation users. In the process of testing of the control segment, hundreds of system failures have been found and solved and a lot of system management experience has been accumulated. It is necessary to formulate the existing failures and fault disposal scheme and classify the common failures in the process of operation to ensure the continuous and stable operation of the system.

In order to guarantee the service performance of the system, devices should be replaced when cannot be repaired. The ground control system consists of master station, monitoring station, and upload station with different devices and compositions, which require different equipment replacement specifications. Therefore, it is necessary to establish requirements for the equipment replacement, which guarantees the stable operation of the equipment.

4 Standard Structure Design of Ground Control Segment

4.1 Design Principle

1. The unity principle: standard system should focus on unity of engineering construction and technical requirements and the development of the industrialization for Beidou navigation satellite system, establishing a unified standard for navigation satellite system, which should not only consider the need of the regional system operation maintenance, but also take the needs of Beidou global system construction into account.
2. The openness principle: standard system should make full use of domestic and foreign existing standards resources and research achievements, and comprehensively connect with international navigation satellite standard to carry out international exchanges, cooperation, and competition conveniently.
3. The autonomy principle: standard system should be based on Beidou navigation satellite system with Chinese characteristics and the core independent intellectual property rights.
4. The compatibility principle: standard system should be compatible with other exiting global navigation satellite system (GPS, GLONASS, Galileo) to build an open and compatible standard system, meeting the needs of compatible interoperability and realize global application.

5. The progressive principle: standard system should be based on our national reality of the technical and economic development, follow the step-by-step model, combine with the development of the specific schedule and key technology research, compile required standards hierarchically, and gradually improve to eventually form a comprehensive and complete standard system.

4.2 Standard Structure Design

According to the requirement analysis above, the standard system for the ground operation control segment of Beidou navigation satellite system can be designed. As shown in Fig. 1, the operation control standard can be divided into three parts including operation service, system construction, and operation maintenance. The operation service standard includes service protocol and service requirement standard. The system construction standard includes the system standard, interface standards, and test standard. The operation maintenance standard includes performance evaluation, security protection, on-orbit management, operation and maintenance, fault disposal and the replacement of the equipment.

1. The operation service standard
   The operation service standard mainly defines the interface between the navigation satellite and the ground operation control segment and the specific performance requirements of various services. It can be divided into two branches including service agreement and service requirements.

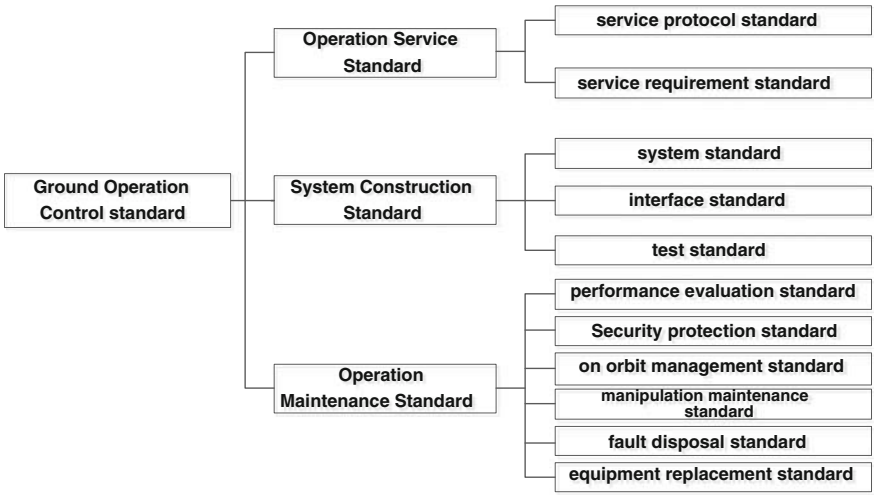

Fig. 1 The standard structure of the ground operation control segment for Beidou navigation satellite system

The service protocol standard is mainly for the interface between satellite and the ground control segment, and establishes common specification for navigation message process.

The service requirements mainly provide specific performance requirements for the ground operation control segment, such as the wide-area differential service, precise ephemeris service, ionospheric model service, timing services, service system.

2. The system construction standard

   The system construction standard mainly includes system technical requirements and standard correlated with system design, internal interface of the ground operation control segment, and unity test and key components examination standard, which can be divided into system standard, interface standard and test standard.

   The system standard mainly defines the system technical requirements and construction requirement of the master station, monitoring stations and time synchronization/upload station, key components and testing devices.

   The interface standard defines the design of satellite-ground, station-station and key components interfaces.

   The test standards mainly guide the test and estimation the monitoring station and key components.

3. The operation maintenance standards

   The operation maintenance standard is used for the maintenance procedures of the master station, monitoring station, upload station, key component and testing devices, which can be divided into performance evaluation, security protection, on-orbit management, operation and maintenance, fault disposal and the replacement of the equipment.

   The performance evaluation standard includes performance assessment criteria and evaluation methods mainly based on the service performance of Beidou navigation satellite system.

   The security protection standard defines the safety requirements by the on-orbit satellite and information security requirements by the system.

   The on-orbit management standard mainly formulates the operation management to the networking and on-orbit satellite.

   The operation and maintenance standard mainly formulates constellation maintenance and single on-bit satellites management, and operation procedures and maintenance process of the master station, upload station, monitoring station and key components.

   The fault disposal standard mainly formulates fault diagnostic criteria and disposal procedures for control segment.

   The equipment replacement standard is mainly used to define replacement rules and operation procedures of the master station, upload station, monitor station, and key components.

4.3 Urgent Standard Demand of the Ground Control Segment for Beidou Navigation Satellite System

According to the actual demand of the regional and global system, the service requirements standard in service protocol standard and performance estimation standard in operation maintenance should be preferentially considered. The service requirements standard mainly refers to performance specification in RNSS and RDSS service and service interface specification standard of Beidou system; the performance evaluation criteria mainly include Beidou performance evaluation standard in RNSS and RDSS service, and evaluation standard of the master station, upload station and monitoring station. These standards can regulate service performance and evaluation methods of the regional system, providing significant basis for the stable operation of the regional system. At the same time, it can also set up targets and guidance for Beidou global system construction.

5 Conclusion

In this paper, the current status of GNSS Standards both at home and abroad are analyzed. Considering the construction and maintenance of Beidou navigation satellite system, the standard demand of the Beidou ground operation control segment is analyzed. The operation control standard structure is designed and the suggestions on urgent standards are given. The results of this paper can provide references for the design of Beidou ground control standard structure.

References

1. Xu R, Zhu X, Zhao J (2010) Some considerations for establishing the standard structure of navigation systems. Bull Surveying Mapp 11:195–197
2. Zhu X, Xu R, Zhao J et al (2010) Analysis on specifications of satellite navigation system. Radio Eng 40(12):31–41
3. Wu H, Li Z, Liu H (2014) Analysis and countermeasure on working status of international standard for the satellite navigation system. Geomatics World 06
4. Wang H (2014) Reflections on the construction of Beidou satellite navigation standard architecture. Satell Appl 07
5. Liu C, Zhao J (2014) Analyzing the construction of Beidou navigation satellite standard system. In: The 5th China satellite navigation conference, Nanjing, 2014, 05
6. Lu J, Zhou Y, Zhang H (2010) Research on the Beidou satellite navigation standard system. In: The first China satellite navigation conference, Beijing, 2010, 05
7. Li D (2012) On the basic framework and multiple perspectives of the satellite navigation's standard system. Digit Commun World 2
8. Chen Q (2009) Standard system for satellite navigation positioning application. Inform Technol Stand 3

9. Liu C, He H, Zheng C, Dai X (2014) The framework of standard system for BeiDou civil application. In: The 5th China satellite navigation conference, Nanjing, 2014, 05
10. Zhang Z, Zhao J, Liu C, Zhao N, Ren H (2014) Research on the operation and maintenance standard structure for satellite navigation system. In: The 5th China Satellite Navigation Conference, Nanjing, 2014, 05
11. Zhao Z (2014) Setup of National Beidou Satellite Navigation standardization Committee. China Stand, 2014
12. Kaplan ED (2002) Understanding GPS principles and applications. Publishing House of Electronics Industry

The Management Pattern of Intellectual Property for Enterprises of Beidou Satellite Navigation

Ping Wang

Abstract The idea of the paper: In the aspect of technical level, enterprises need to manage patent technology according to different categories. In the aspect of enterprise institutional framework, build specific organization that supports enterprise's intellectual property strategy. In the aspect of business operation, pursuit of profit maximization is the company's basic business objective, which is also the goal of intellectual property strategy. In the aspect of resource utilization, deeply grasp the national planning and policy, fully collect and use all resources.

Keywords Beidou · Intellectual property · Management pattern

1 Introduction

Beidou industry belongs to the sunrise industry in China. In April 2007, China launched its first satellite Beidou second generation, which is expected to reach global coverage in 2020. So far, China has successfully launched 20 satellites, successfully completing to provide positioning, navigation, timing, and the goal of short message communication service in the Asia-Pacific region. It is also accelerating the process of global coverage [1]. Beidou satellite navigation, a typical technology-intensive industry, the core technology research and development, the protection and utilization is fundamental to the survival and development. How to complete scientific management and effective utilization is the key influencing factor to get advantages over big dipper companies in the fierce international competition. This article analyzes the management pattern of intellectual property for enterprises of Beidou satellite navigation from the following four aspects.

P. Wang (✉)
School of Management, Huazhong University of Science and Technology,
1037 Luoyu Road, Wuhan, China
e-mail: wp0127@126.com

© Springer Science+Business Media Singapore 2016

J. Sun et al. (eds.), *China Satellite Navigation Conference (CSNC) 2016 Proceedings: Volume III*, Lecture Notes in Electrical Engineering 390,
DOI 10.1007/978-981-10-0940-2_65

2 Aspect of Technical Level

The outward sign of Beidou technology advantage is its holdings of the patent. Based on the background of public intellectual property, the article gives a simple summary and analysis on the present condition of the related patents in China. In the state intellectual property office patent database retrieval and analysis [2] (Patent Search and Analysis of SIPO), using "Beidou" as the keyword to search related patents, the pieces information can be as much as 5629. Similarly, in the U.S. Patent office is (USPTO Patent Full—Text and Image Database) [3], searching "GPS" and won the 99240 article of information related to patent. Only from the perspective of the patent number of publicly, Beidou industry in China has a large gap to catch up with the world advanced level.

2.1 The Annual Quantity of Application for Patents Related to Beidou Satellite Navigation

First of all, the study began from the analyzing its development over time according to the Beidou-related-patents situation from database for patent retrieval.

Figure 1 showed that the relevant patent application of Beidou has been low before 2007. From 2008 to 2012, it began to grow. Since 2013, it showed a trend of rapid growth, especially in 2013, the number has more than doubled compared to 2012.

2.2 The Areas of Technology that Beidou Related Patents are Concentrated in

In order to get more detailed understanding of Beidou main technical direction and application field of industry, this article selects the top ten related patents technology classification that Beidou is greatest concentrated of. They can be shown in Table 1.

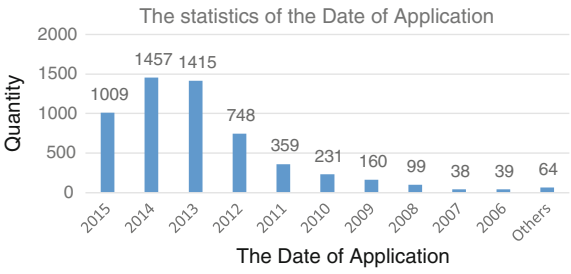

Fig. 1 The statistics of the date of application

Table 1 The top ten related patents technology

Rank	Technology areas	Main direction	Quantity of application	Proportion (%)
1	G01	Measurement; test	1976	29.44
2	H04	The electric communication technology	1357	20.21
3	G08	Signal unit	670	9.98
4	G06	Calculation; count	413	6.15
5	G05	Control; adjust	374	5.57
6	H01	Basic electrical components	246	3.66
7	B60	General vehicles	236	3.52
8	G07	Accounting device	220	3.28
9	G04	Time measuring	200	2.98
10	H02	Power generation; substation and power distribution	152	2.26

2.3 The Proportion of Participation in Research and Development by Enterprises in Beidou Related Patents

The core of this paper is to explore management mode of intellectual property rights for enterprises related to Beidou. So it is necessary to clear the enterprise research and development of patent in the proportion of all patent.

Figure 2 indicates that the enterprises in the development of patents related to Beidou played a dominant role, accounting for 69 %, this shows that with the development of industrialization of Beidou, enterprises, as the main body of the market, will be more and more important. The national policy guidance of Beidou industry will gradually change to mature industry dominated by market demand model.

Fig. 2 The type of applicants

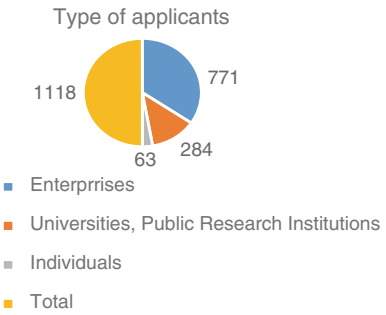

3 Aspect of Institutional Framework

3.1 The Main Function of Intellectual Property Management Department of Enterprise

With the standardization of management, large-scale operations of the enterprise, setting up special department which is responsible for technical innovation is the inevitable choice of technology-intensive enterprises. In the enterprise, intellectual property management departments mainly charge of the following tasks.

3.1.1 The Strategy Management of Intellectual Property

As the important part of enterprise overall strategy, intellectual property strategy of enterprise has a decisive role in the development of Beidou related businesses, which is both export-oriented and technology oriented. This strategy should be a macro, long-term, at the same time is also the result of the enterprise internal department coordination. It will eventually be in the form of company system as the direction of the effort to each employee, finally forming the enterprise development goals.

3.1.2 The Development and Application of Intellectual Property Rights

The development of intellectual property rights is mainly to inforce R&D cooperation with enterprises internally and strengthen links with universities and research institutes. In accordance with the planning of intellectual property strategy, integrate internal and external resources, focusing on breakthrough in technology and technological innovation, forming the enterprise core technology, thus creating a high technology core product with market competitiveness. The application of intellectual property rights is mainly cooperated with enterprise production, sales department, focusing on intellectual property into production capacity, and market acceptance of the product.

3.1.3 Intellectual Property Management

The management of intellectual property rights mainly has the following several aspects: daily management, dispute handling, and information gathering process. Daily management is mainly transactional work. Dispute handling can be divide two kinds: intellectual property disputes involving internal and external contradiction disputes between departments. The management department of intellectual property should monitor the bank industry in the forefront of research, and

collecting information on research and development related to intellectual property rights is the important content of work.

3.1.4 Communication and Cooperation

In terms of international, enterprises should strive to join international organizations of relevant industries, accessing to industry at the forefront of the dynamic, knowing technology development trend in the future, participating in the development of international rules, etc. In domestic, the enterprises should strengthen the cooperation with other enterprises on the chain, integrating various enterprise resource advantages, with major technological breakthrough. At the same time, it should also strengthen the cooperation with universities, scientific research institutes in order to realize the coordinated development of the study. Then strengthen the cooperation between the government department, the financial sector and the intellectual property agency, enterprises from different angles to create conditions to achieve breakthroughs in key technology areas.

3.2 The Status quo of Management Department of Intellectual Property of Key Enterprises in Beidou Industry

To analyze the actual situation of enterprise intellectual property management, this paper is based on factors such as sales, net income, industry enterprise reputation in the relevant enterprises to select the Beijing Beidouxingtong navigation technology Co., Ltd., Beijing Hualichuangtong technology Co., Ltd.

- Beijing Beidouxingtong navigation technology Co., Ltd.
  Beijing Beidouxingtong navigation technology Co., Ltd. is China's one of the earliest engaged professional company in navigation and positioning. Beidouxingtong technology center is the core of the enterprise technology innovation system, which is mainly rely on technological progress and technological innovation. Its main functions include: study the formulation and organize the implementation of enterprise technology innovation strategy planning; Organize technology development, transfer, management and services; Industry-university-institute cooperation and foreign exchange; Cultivate the enterprise technology innovation team, etc. Within the company, systems have been built up and down to achieve management and technology research and development of science and technology. In the future, through the central research institute and a line of research and development institutions to coordinate, linkage, the flux in the technology strategy research, basic research, and applied research can be deepening and accumulation, and the strong support may have new business development.

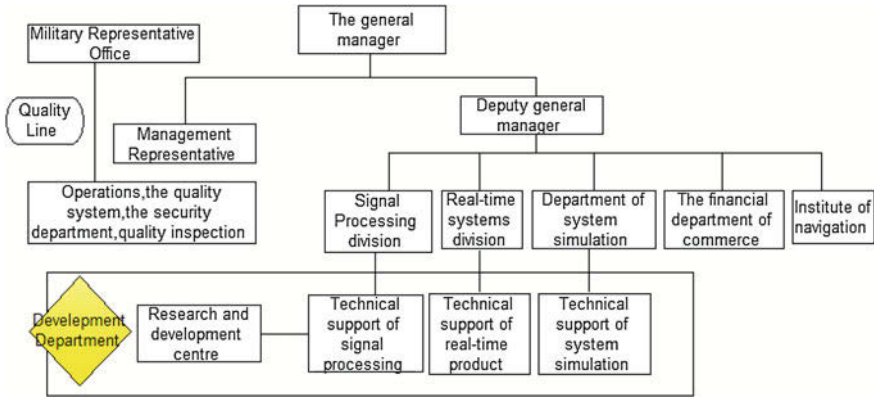

Fig. 3 Company's organization chart

- Beijing Hualichuangtong technology Co., Ltd., China
  The company has set up a navigation technology research institute and a research and development centers, research and development personnel accounted for more than 60 % of the total employees. The company's organization chart is as shown in Fig. 3.

As you can see, the R&D department is the core of the corporate sector, the financial support and human resources are fully equipped. The company has made nearly 70 items of intellectual property rights, forming solid core technology and research and development ability.

3.3 Summary and Analysis

According to the analysis of the two companies in the second part, as well as to the survey of other related industry enterprise, it showed that Beidou enterprise did not establish a separate intellectual property management department at the present stage, and the general situation is relied on a research and development center or institute for all intellectual property rights innovation, management and application. Doing so is actually the fruits of research and development department and R&D management department, the comprehensive utilization of human resources. In the starting stage, because of money and human resources are limited, this is a lot of enterprises in general.

4 Aspect of Business Operation

Any kind of management is to improve management effectiveness, which is ultimately in order to increase corporate profits, bigger, and stronger. The management of the enterprise intellectual property rights is to serve the ultimate goal. This paper

selected Guoteng electronics, the representative company to analyze its profitability and R&D, the excavation of the optimized management method to improve the efficiency of the enterprise.

Table 2 shows, the volatile of Beidou business achievements. At the beginning of the industrial development, the research on the high cost has outstanding performance in the enterprise intangible assets and increases the cost of management. Although the larger investment can make the enterprise fund chain tight, the industry as a whole is located in the high-speed development stage. This technology is essential for the survival and development. Beidou industry, as the representative of advanced technology in China, has to get advantage in the international competition, keeping the leading core technology. In this regard, the development of Beidou enterprises can draw lessons from the development of China's high-speed rail industry. High-speed rail can be used as China's technology business card to the world. The most basic point lies in the high technology and low cost. Beidou enterprises should develop, using its leading core technology as the basic elements. Beidou industry, of course, has a special relationship to national security industry. Considering the interests of the enterprise at the same time, attention should be given to positive externalities, namely, social effect.

Table 2 The basic financial data of Guoteng electronic

The basic financial data of Guoteng electronic						
Subject\year	2014	2013	2012	2011	2010	2009
Basic earnings per share	0.19	−0.06	0.09	0.34	0.95	0.76
Net profit	5151.93	−1533.2	2434.52	4778.09	5640.15	3961.57
Year-on-year growth rate	436.04	−162.98	−49.05	−15.28	42.37	34.54
Buckle the net profit	4422.35	−1673.6	2340.33	4487.15	5348.41	3749.13
Income	40719.7	26080.1	20229.3	19753.1	20056.3	17568.8
Revenue year-on-year growth rate	56.13	28.92	2.41	−1.51	14.16	28.07
Net assets per share	2.73	2.56	2.68	5.32	10.26	2.91
Equity	7.03	−2.11	3.29	6.61	14.37	29.19
Equity-diluted	6.79	−2.16	3.27	6.46	7.91	26.14
Liability ratio	31.9	24.62	14.62	6.57	7.56	28.31
Capital reserve fund	1.17	1.19	1.2	3.4	7.8	0.77
Profit per share	0.49	0.31	0.41	0.82	1.33	1.05
Operating cash flow per share	0.68	0.07	0.07	0.01	0.71	0.69
Sales gross profit margin	54.19	45.51	57.02	52.55	64.5	63.66
Turnover	0.99	1.17	1.13	1.94	1.71	1.18

5 Aspect of Resource Utilization

5.1 National Industry Policy

According to the state council general office on October 9 2013 issued by "the national satellite navigation industry long-term development planning", can see clearly the current support of the state encourages the key development direction is: improving the navigation infrastructure, the core technology breakthrough. In the core technology, core device and the universal product breakthrough, to strengthen the construction of innovative ability, promoting application of time frequency safeguard, promoting the industry innovative applications, expand the scale of the masses and promoting the overseas market development. Main task is to overseas demonstration project construction, global marketing and service network construction, and internationalization development service system construction. These six points can be as Beidou macro industrial development direction the future 5 years, which has a guiding effect on related businesses. Enterprise intellectual property strategy should revolve around the six major development direction to develop, complying with the national industrial development trend, getting the support of the government in the policy, funding, which will enhance the status of enterprise in the industry.

5.2 Cooperation with Universities and Scientific Research Institutes

High-tech enterprise and scientific research institution have close relationships. It is clear in the example of the Silicon Valley in the United States and Japan Tsukuba science city. In the study of the concrete enterprise, the enterprise cluster effect obviously, mostly located in high-tech industrial park and concentration areas in colleges and universities. The most prominent is the Beijing Zhongguancun science park, where gathered the Beidou system civil research and development and industrialization of leading enterprises. At the same time, it has the no. 1 Beidou satellite navigation and positioning system and sorting service qualification units. Associated with a cluster of Beidou enterprises coexist is composed of a large number of research institutes of colleges and universities to provide rich intellectual resources, including China's satellite navigation application center, satellite navigation and positioning terminal management institution, China academy of space technology, Chinese academy of sciences, the second generation navigation special China academy of surveying and mapping science, Beidou navigation application major project office in Beihang University, Zhongguancun aerospace science and technology innovation park research resources, etc.

5.3 The Integration of Internal Resources in Enterprises

Nonaka's SECI model argues that knowledge innovation can be divided into four stages: socialization, externalization, combination, and internalization. In the transformation of the four steps, a lack of incentive constraint mechanism is the common fault of the domestic enterprise technology innovation. Beidou enterprises also exists such problems.

To solve these problems, management department of intellectual property needs to strengthen the enterprise internal mechanism of incentive and constraint, to integrate resources, promote technological innovation. Specifically, there are following points: First, project management. The work of the project scheme design utmost to adapt to the characteristics of the research and development work is complicated, giving full play to the group, which is advantageous to the secondary development of technology to product. Second, incentive and constraint mechanism. Incentive mechanism in salary incentive and equity incentive, for ordinary technicians take differential compensation system, for developers to use with outstanding contribution of equity incentive to make them closely connected with the enterprise development. Constraint mechanism mainly lies in establishing a professional assessment team. Third, the establishment of technology standards. In order to avoid duplication and inefficient work, enterprises should optimize the existing intellectual property management pattern, forming the modular management, the existing intellectual property classification. Each corresponding intellectual property in enterprise's products or services can increase the rate of utilization of patent and transition.

6 Conclusions

From the above, the optimization of Beidou enterprise intellectual property management mode needs to improve from four aspects, namely at the technical level, to strengthen the enterprises in the main role in technology innovation, to strengthen the market orientation of technology innovation; At the organization level, according to the enterprise development situation, set the competent intellectual property, shall be formulated by the enterprise top directly responsible for intellectual property strategy, enterprise development of guidance documents written to enterprise strategic planning; In the enterprise management level, strengthen technology to the secondary development of products, to the project team working mode to promote the efficiency of each of the intellectual property rights and profitability; In resource utilization level, study relevant government policy documents, and make full use of the government all preferential measures for industry development, to strengthen the coordination development and personnel training of scientific research institutes, promoting the combination of production, and between the various departments within the enterprise, through the project management,

incentive constraint mechanism, and establishing method of fusion technology standard internal resources, stimulate innovation consciousness, create a good research, and development team.

References

1. Beidou Website. http://www.beidou.gov.cn/
2. Website of Patent Search and Analysis of SIPO. http://www.pss-system.gov.cn visiting time 10 Dec 2015
3. Website of USPTO Patent Full—Text and Image Database. http://www.uspto.gov/ visiting time 10 Dec 2015
4. Xu Q, Liu Y, Chen M (2014) Analysis of the situation of patent for Beidou satellite navigation. Chin J Intellect Property Rights 92
5. The IPC classification of most of the invention or utility model is divided into 8, respectively is: part A—human life essential (agriculture, light, medicine); Part B—operations, transportation; Part C—chemical, metallurgy; Part D—textile, paper making; E department—fixed building (building, mining); F department—mechanical engineering; G department—physical; H department—electrical
6. http://www.pss-system.gov.cn/ the state intellectual property office patent database retrieval and analysis. Patent analysis. Rapid analysis. The analysis of access time: 12 Dec 2015

Erratum to: China Satellite Navigation Conference (CSNC) 2016 Proceedings: Volume III

Jiadong Sun, Jingnan Liu, Shiwei Fan and Feixue Wang

Erratum to:
J. Sun et al. (eds.), *China Satellite Navigation Conference (CSNC) 2016 Proceedings: Volume III*, Lecture Notes in Electrical Engineering 390,
DOI 10.1007/978-981-10-0940-2

The book was inadvertently published without including many changes in Chapters 21, 25, and 45. The changes included language enhancements, capitalization changes, and addition in affiliation the same has been incorporated and the chapter and the erratum book has been updated.

The updated original online version for this book can be found at
DOI 10.1007/978-981-10-0940-2

J. Sun (✉)
Chinese Academy of Sciences, China Aerospace Science and Technology Corporation, Beijing, China
e-mail: csnc@aoe.ac.cn

J. Liu
Wuhan University, Wuhan, China
e-mail: jnliu@whu.edu.cn

S. Fan
China Satellite Navigation Office, Beijing, China
e-mail: fansw@beidou.gov

F. Wang
National University of Defense Technology, Changsha, China
e-mail: Wangfeixue365@sina.com

© Springer Science+Business Media Singapore 2016

J. Sun et al. (eds.), *China Satellite Navigation Conference (CSNC) 2016 Proceedings: Volume III*, Lecture Notes in Electrical Engineering 390,
DOI 10.1007/978-981-10-0940-2_66